12-4-91

CM

AJR

Cuk-H08511-81-P024460 (31)

American
Journal of
Roentgenology

November 1990

SonoVu US™—A visible improvement in ultrasound-guided aspiration.

The clearly visible bright echoes on the real-time sonogram below mark a breakthrough in accuracy and safety for fine-needle aspiration under ultrasound guidance.

SonoVu US, from E-Z-EM, is the first in a family of procedural needles designed specifically for enhanced ultrasound visualization.

Precisely formed 0.44 mm distal side holes on the cannula closely match the wavelength of ultrasound generated by a 3.5 MHz transducer. Uniform diffraction of the wave at each hole creates a highly visible echo on the US display.

The side holes also provide a significant increase in needle flow rate, and ensure free flow should the tip become occluded—often the case with spinal or chiba needles.

Developed for use in amniocentesis, the SonoVu design can offer similar benefits in such procedures as US-monitored biopsy and cyst aspiration. For more information on 20- and 22-gauge SonoVu US needles from E-Z-EM, call 1-800-544-4624.

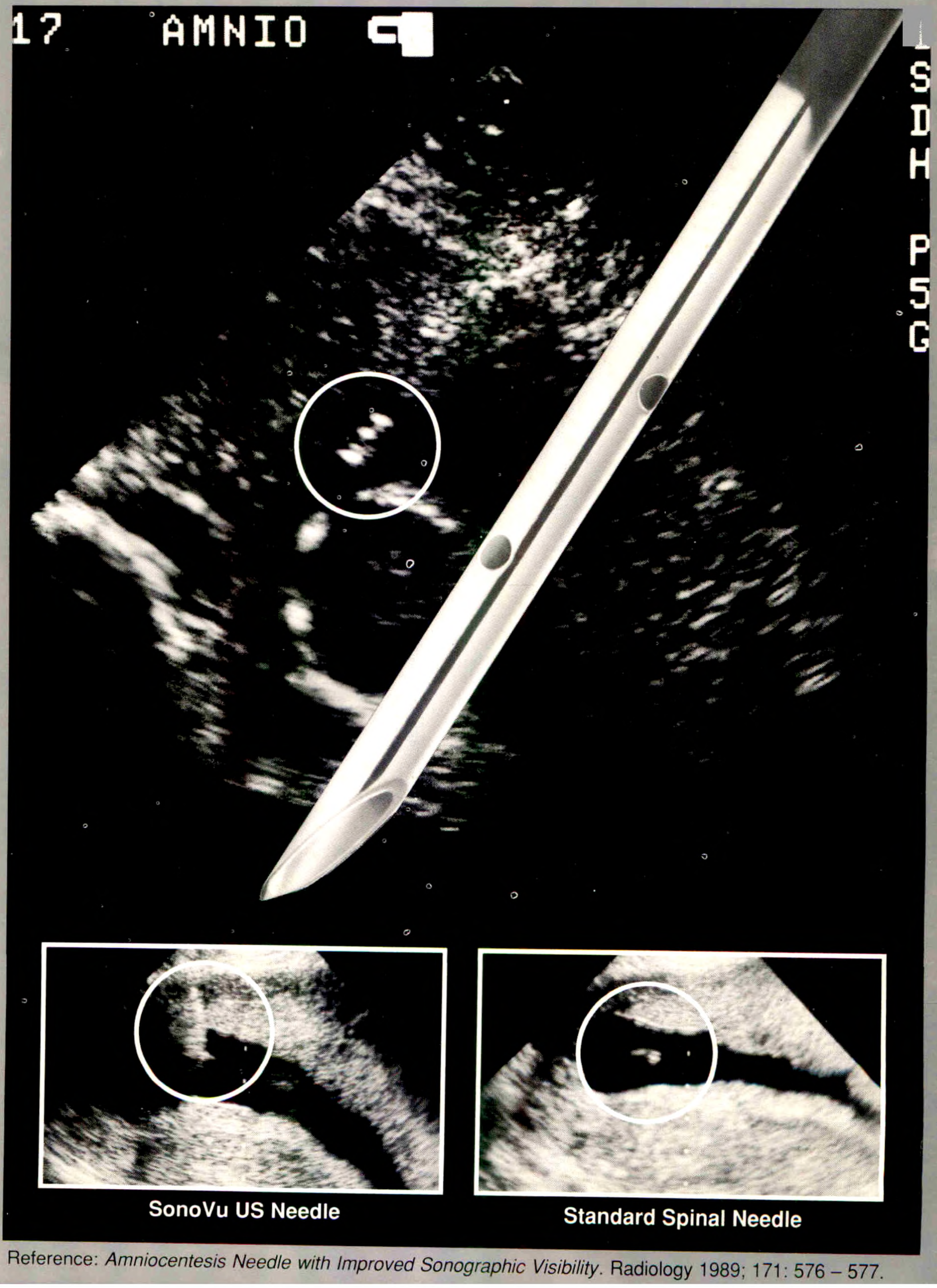

SonoVu US Needle

Standard Spinal Needle

Reference: *Amniocentesis Needle with Improved Sonographic Visibility*. Radiology 1989; 171: 576 – 577.

For both the patient and the practitioner, E-Z-EM products set the standards for convenience, safety, and quality in:

- **GI Radiology**
- **Interventional Radiology**
- **CT Scanning**
- **Ultrasound**
- **Magnetic Resonance Imaging**
- **Angiography**
- **CEA Immunostaining**
- **Radiation Oncology**
- **Patient Prepping**
- **Protective Products**
- **Computerized Information Management Systems**

E-Z-EM®

E-Z-EM, Inc.
Westbury, NY 11590

© 1990, E-Z-EM, Inc.

12.4.91

Official Journal of the American Roentgen Ray Society

AJR

American Journal of Roentgenology
Diagnostic Imaging and Related Sciences

P 24.460

Editor-In-Chief	Robert N. Berk, *La Jolla, California* *University of California, San Diego* *School of Medicine and Medical Center*
Editor Emeritus	Melvin M. Figley, *Seattle, Washington*
Associate Editor	Saskia von Waldenburg Hilton, *San Diego, California*
Consulting Editor	Michael S. Huckman, *Chicago, Illinois*
Statistician	Charles C. Berry, *San Diego, California*

Editorial Board

John R. Amberg
Itamar Aviad
Mark E. Baker
Lawrence W. Bassett
Michael A. Bettmann
Felix S. Chew
N. Reed Dunnick
David K. Edwards
Ronald G. Evens
David S. Feigin
Sandra K. Fernbach
Richard H. Gold
William R. Hendee
John R. Hesselink
Charles B. Higgins
Melvyn T. Korobkin
Faye C. Laing
Thomas L. Lawson
Robert G. Levitt
Bruce L. McClennan
Richard P. Moser
Albert A. Moss
Jeffrey H. Newhouse
Donald L. Resnick
Stewart R. Reuter
Charles A. Rohrmann, Jr.
Peter M. Ronai
Sjef H. J. Ruijs
Stuart S. Sagel
David J. Sartoris
Stefan C. Schatzki
William P. Shuman
Edward A. Sickles
Barry A. Siegel
David D. Stark
Edward T. Stewart
Murali Sundaram
Eric vanSonnenberg
Robert K. Zeman

Editorial Staff: Margaret Levene, *managing editor*; Katie L. Spiller, Barbara Rose, Barbara L. Halliburton, and Janine Anderson, *manuscript editors*; Nancy Rydbeck, *office manager*; Sheri Smith, *administrative assistant*; Matthew M. McCormick, *administrative secretary*.

AJR, AMERICAN JOURNAL OF ROENTGENOLOGY (ISSN 0361 803X) is the official journal of the American Roentgen Ray Society and is published monthly by Williams & Wilkins, 428 E. Preston St., Baltimore, MD 21202. Annual dues include $50 for journal subscription. Second-class postage paid at Baltimore, MD, and at additional mailing offices. Postmaster, send address changes (Form 3579) to AJR, 428 E. Preston St., Baltimore, MD 21202. Subscription rates $110 ($155 foreign, $244 Japan); institutions $120 ($165 foreign, $254 Japan); in training $25 ($70 foreign, $159 Japan); single copy $16 ($19 foreign). Japanese rates include airfreight. Japanese yen price is available from our sole agent USACO Corporation, 13-12, Shimbashi 1-Chome, Minato-Ku, Tokyo 105, Japan, telephone 03-502-6471. Airmail rates furnished on request. Indexed by *Current Contents* and *Index Medicus*. Copyright © 1990 by American Roentgen Ray Society.

0361–803X/90$2.00

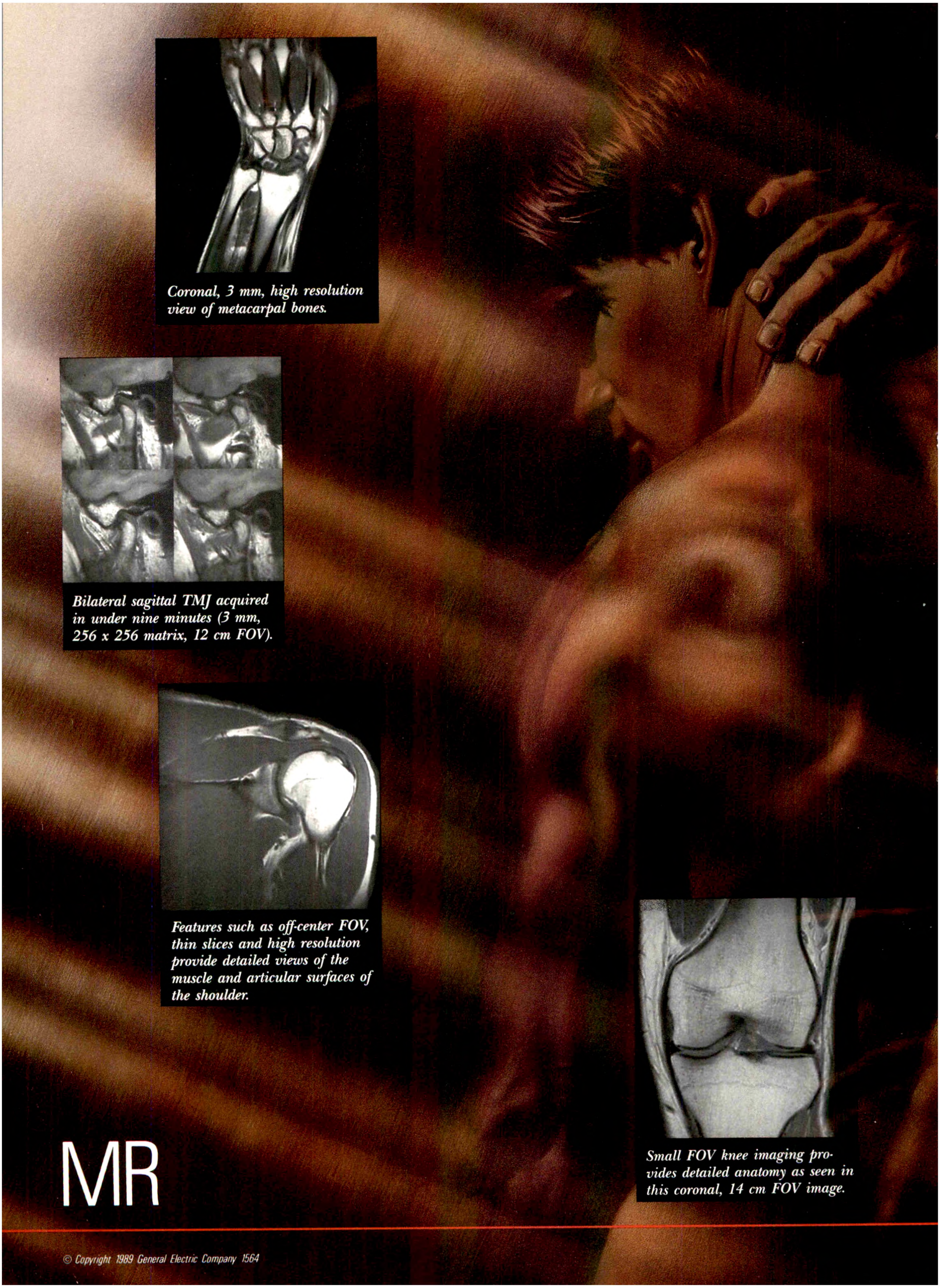

Coronal, 3 mm, high resolution view of metacarpal bones.

Bilateral sagittal TMJ acquired in under nine minutes (3 mm, 256 x 256 matrix, 12 cm FOV).

Features such as off-center FOV, thin slices and high resolution provide detailed views of the muscle and articular surfaces of the shoulder.

Small FOV knee imaging provides detailed anatomy as seen in this coronal, 14 cm FOV image.

MR

© Copyright 1989 General Electric Company 1564

SIEMENS

Beyond Imaging

Beyond each imaging modality and support service we offer there is a commitment to be in touch with the state of your art...and with you, the professionals who practice it.
Once a year the RSNA gives us that opportunity.

A time for professional enrichment. The exchange of ideas. A welcome chance to learn more about your requirements for tomorrow. And the opportunity to show you the technological advancements and services we have today.

Computed tomography • PACS • Lithotripsy • Linear accelerators • Magnetic resonance • Therapy planning • Mobile image intensifier • Diagnostic ultrasound • X-ray mammography • R/F systems • Data management • Education programs • Digital imaging • Therapy simulator • Uro-radiology • Mobile MR • Nuclear medicine • Site planning • Service plans • Mobile CT • Cardiovascular imaging • Financial services • Mobile X-ray • Preventive maintenance • Special procedures • Health physics • Diagnostic imaging centers • In-service education • Positron emission tomography • Mobile cath. lab

© Siemens Medical Systems, Inc. 1990 MG/5000-274 3575

AJR Business and Subscriber Information

The American Roentgen Ray Society

AJR, American Journal of Roentgenology, is published monthly to disseminate research on current developments in the radiologic sciences and commentary on topics related to radiology. It is published by the American Roentgen Ray Society, 1891 Preston White Dr., Reston, VA 22091; (703) 648-8992. Inquiries regarding society business, the annual ARRS meeting, and membership should be addressed to the Society at the above address.

Correspondence Concerning the *AJR*

Correspondence regarding display (not classified) advertising, subscriptions, address changes, reprints, and permission requests should be addressed to Williams & Wilkins, 428 E. Preston St., Baltimore, MD 21202; (301) 528–4000.

Correspondence regarding editorial matters and classified advertising should be addressed to Editorial Office, AJR, 2223 Avenida de la Playa, Ste. 103, La Jolla, CA 92037-3218; telephone (619) 459-2229; FAX (619) 459-8814. For information on manuscript submission, see Guidelines for Authors, pages A19–A21.

Subscriber Information

Subscription requests and inquiries should be sent to Williams & Wilkins, 428 E. Preston St., Baltimore, MD 21202. ARRS annual dues include $50 for journal subscription. Subscription rates are as follows: nonmembers, $110/year ($155 foreign, $244.00 Japan); institutions, $120 ($165 foreign, $254.00 Japan); nonmember in-training, $25 ($70 foreign, $159.00 Japan). Single copies of the Journal may be purchased for $16 ($19 foreign). Airmail rates will be furnished on request.

Japanese rates include airfreight. Japanese yen price is available from our sole agent, USACO Corporation, 13-12, Shimbashi 1-Chome, Minato-Ku, Tokyo 105, Japan; telephone 03-502-6471.

Call toll-free, 1-800-638-6423 (in Maryland call 1-800-638-4007), with subscription questions or problems. Please have the mailing label from your latest issue available when you call.

If a subscriber receives a damaged copy of the *AJR* or fails to receive an issue, the subscriber should notify Williams & Wilkins (428 E. Preston St., Baltimore, MD 21202) within 60 days of publication (90 days for foreign subscribers) and that issue will be replaced.

Change of address information should be sent to Williams & Wilkins, 428 E. Preston St., Baltimore, MD 21202. Allow 90 days for address changes.

Copyrights, Permissions, and Reprints

The American Roentgen Ray Society holds the copyright for all material published in the *AJR*. No part of this publication may be reproduced without permission from the ARRS. Requests for such permission should be addressed to Williams & Wilkins, 428 E. Preston St., Baltimore, MD 21202.

For reprints of a particular article, please contact the author designated in the footnotes for that article.

Indexes

The *AJR* provides volume and yearly indexes (subject and author) in the June and December issues each year. *AJR* articles are also indexed in *Current Contents*, *Index Medicus*, and the cumulative index published by *Radiology*.

AJR Guidelines for Authors

Address new and revised manuscripts, correspondence, and classified ads to the Editor:

AJR Editorial Office
2223 Avenida de la Playa, Suite 103
La Jolla, CA 92037-3218
Telephone: (619) 459-2229; FAX: (619) 459-8814

Inquiries regarding subscriptions, display advertising, reprints, or permission to republish *AJR* material should be addressed to the publisher:

The Williams & Wilkins Co.
428 E. Preston St.
Baltimore, MD 21202 Telephone: 1-800-638-6423

The *AJR* publishes original contributions to the advancement of medical diagnosis and treatment. Submitted manuscripts should not contain previously published material and should not be under consideration for publication elsewhere. Papers dealing with neuroradiology should be addressed to: American Journal of Neuroradiology, Dept. of Radiology, Massachusetts General Hospital, Boston, MA 02114. At the discretion of the *AJR* Editor, *AJNR* articles that are of interest to the general reader may be republished in the *AJR*. Neuroradiologic papers sent to the *AJR* will be forwarded to the Editorial Office of the *AJNR*.

Manuscript decisions are based on peer review. Reviewers receive manuscripts without title pages to ensure an unbiased review. Statements made in the article, including changes made by the Editor or manuscript editor, are the responsibility of the author and not of the *AJR* or its publisher. Authors will be sent the edited manuscript, galley proof, and proofs of illustrations. If the corresponding author will be unavailable to review galleys, arrangements should be made for a coauthor or colleague to read and return the proof.

The following guidelines are based on instructions set forth in the **Uniform Requirements for Manuscripts Submitted to Biomedical Journals** (*Ann Intern Med* **1988;**108:258–265). Articles will be edited, however, to conform to the individual style of AJR.

General Guidelines for Major Papers

Abstract. Clearly state (in 200 words or less) the purpose, methods, results, and conclusions of the study. Include actual data.

Introduction. Briefly describe the purpose of the investigation and explain why it is important.

Methods. Describe the research plan, the materials (or subjects), and the methods used, in that order. Explain in detail how disease was confirmed and how subjectivity in observations was controlled.

Results. Present results in a clear, logical sequence. If tables are used, do not duplicate tabular data in text, but do describe important trends and points.

Discussion. Describe the limitations of the research plan, materials (or subjects), and methods, considering both the purpose and the outcome of the study. When results differ from those of previous investigators, explain the discrepancy.

AUTHOR'S CHECKLIST

For priority handling, complete the following checklist, sign the copyright form on the reverse side of this page, and include both with the manuscript.

________ Two copies of the manuscript (the original and a photocopy) and two complete sets of figures are submitted. One copy has been retained by the author.

________ If appropriate, *AJR* Guidelines for case reports, technical notes, pictorial essays, or letters to the Editor have been followed. (See page A5.)

________ The manuscript, including references, figure legends, and tables, is typed double-spaced on 8½ × 11 in. (21.6 × 27.9 cm) *nonerasable* paper. Right-hand margins are not justified.

________ All manuscript pages are numbered consecutively beginning with the abstract. Authors' names do not appear on the manuscript pages.

________ The manuscript is organized as follows: title page, blind title page (title only), abstract, introduction, methods, results, discussion, acknowledgments, references, tables, figure legends, and figures.

________ Informed consent has been obtained from patients who participated in clinical investigations. If experiments were performed on animals, authors complied with NIH guidelines for use of laboratory animals.

________ Use of unfamiliar acronyms and abbrevations is kept to a minimum. When abbreviations are used they are defined at first mention, followed by the abbreviation in parentheses.

________ Metric measurements are used throughout, or the metric equivalent is given in parentheses.

________ Names and locations (city and state only) of manufacturers are given for equipment and nongeneric drugs.

Title Page

________ The following information is given: title of article; names and complete addresses (including zip code) of all authors; current addresses of authors who have moved since study; acknowledgment of grant or other assistance. The corresponding author is clearly identified, and a current address, phone number, and FAX number are given.

________ Two copies of a blind title page are included giving only the title (without the authors' names) for use in the review process.

Abstract

________ An abstract of approximately 200 words concisely states the purpose, methods, and results of the study in one paragraph. Actual data are included. Conclusions are stated in a second, summary paragraph.

________ No abbreviations or reference citations are used.

References

______ References (not to exceed 35) are typed double-spaced starting on a separate page and are **numbered consecutively in the order in which they appear in the text**.

______ All references are cited in the text and are enclosed in brackets and typed on line with the text (not superscript).

______ Unpublished data are not cited in the reference list, but are cited parenthetically in the text, for example, (Smith DJ, personal communication), (Smith DJ, unpublished data). This includes papers submitted, but not yet accepted, for publication.

______ Inclusive page numbers (e.g., 333–335) are given for all references.

______ Journal names are abbreviated according to *Index Medicus*.

______ Style and punctuation of references follow the format illustrated in the following examples (all authors are listed when six or fewer; when seven or more authors, the first three are listed, followed by "et al."):

Journal article

1. Long RS, Roe EW, Wu EU, et al. Membrane oxygenation: radiographic appearance. *AJR* **1986**;146:1257–1260

Book

2. Smith LW, Cohen AR. *Pathology of tumors*, 6th ed. Baltimore: Williams & Wilkins, **1977**:100–109

Chapter in a book

3. Breon AJ. Serum monitors of bone metastasis. In: Clark SA, ed. *Bone metastases*. Baltimore: Williams & Wilkins, **1983**:165–180

Paper presented at a meeting

4. Lau FS, Kirk AN. MR imaging of the spine. Presented at the annual meeting of the American Roentgen Ray Society, Washington, DC, April **1986**

Tables

______ Each table is typed double-spaced on a separate page without vertical or horizontal rules; each has a short, descriptive title. Tables do not exceed two pages in length and contain at least four lines of data.

______ Tables are numbered in the order in which they are cited in the text.

______ Abbreviations are defined in an explanatory note below each table.

______ Tables are self-explanatory and do not duplicate data given in the text or figures.

______ All arithmetic (percentages, totals, differences) has been double checked for accuracy, and tabular data agree with data given in the text.

Figures and Legends

______ Two complete sets of original figures are submitted unmounted in labeled envelopes.

______ Figures are clean, unscratched, 5 × 7 in. (13 × 18 cm) glossy prints with **white borders.** A separate print is submitted for each figure *part*.

______ All figure parts relating to one patient have the same figure number.

______ Each figure is labeled on the back with the figure number and an arrow indicating "top." For black-and-white figures, labeling is done on a gummed label, which is then affixed to the back of the print. **Never** use labels on **color** *figures, but write figure number on the back lightly in pencil. Never* use ink on front or back of any figures.

______ Author's names are *not* written on the backs of figures.

______ Only removable (rub-on) arrows and letters are used on the figures. Symbols are uniform in size and style and are not broken or cracked.

______ Images are uniform in size and magnification.

______ Line drawings are done in black ink on a white background. They are professional in quality, and all use the same size type. (Only glossy prints are acceptable.)

______ Written permission has been obtained for use of all previously published illustrations (and copies of permission letters are included), and an appropriate credit line is given in the legends.

______ Legends are typed double-spaced, and figure numbers correspond with the order in which the figures are cited in the text.

Transfer of Copyright Agreement, Conflict of Interest Acknowledgment, Certification of Coauthors, and Exclusive Publication Statement

Complete copyright to the article entitled: ______________________________

____

is hereby transferred to the American Roentgen Ray Society (for United States government employees to the extent transferable), effective if and when the article is accepted for publication in the *American Journal of Roentgenology*. In the case of the authors who are officers or employees of the United States government, the American Roentgen Ray Society recognizes that works prepared by officers or employees of the United States government as part of their official government duties are in the public domain.

Authors reserve all proprietary rights other than copyright, such as patent rights and the right to use all or part of this article in future works of their own. The authors retain the right of replication, subject only to crediting the original source of publication and receiving written permission from the publisher.

Authors guarantee that this manuscript contains no matter that is libelous or otherwise unlawful, invades individual privacy, or infringes any proprietary rights.

Authors understand that they will receive no royalty or other compensation from the American Roentgen Ray Society or the publisher.

Authors guarantee that the editor has been or will be informed of any proprietary or commercial interest or conflicts of interest the authors may have that relate directly or indirectly to the subject of this article.

All authors certify that they have made substantive and specific intellectual contributions to the article and assume public responsibility for its content.

Finally, the authors certify that none of the material in this manuscript has been published previously or is currently under consideration for publication elsewhere.

______________________ First author/date	______________________ Second author	______________________ Third author
______________________ Fourth author	______________________ Fifth author	______________________ Sixth author

This agreement must be signed by all authors in order for the manuscript to be published.

Case Reports

A case report is a brief description of a special case that provides a message that transcends the individual patient.

Format. There is no abstract. The introduction should be a short paragraph giving the general background and the specific interest of the case. No more than one case should be described in detail (similar ones can be mentioned briefly in the discussion). Emphasis should be on the radiologic aspects; clinical information must be limited to that necessary to provide a background for the radiology. The discussion should be succinct and should focus on the specific message and relevance of radiologic methods. A review of the literature is not appropriate.

Length. Maximum of five double-spaced, typewritten pages, including the references but not the title page or figure legends.

References. Maximum of eight.

Figures. Maximum of three or four, unless the text is shortened accordingly. Legends must not repeat the text.

Tables and Acknowledgments. Not appropriate in case reports.

Technical Notes

A technical note is a brief description of a specific technique or procedure, modification of a technique, or equipment of interest to radiologists.

Format. No abstract, headings, or subheadings are required. If headings are used, they should be a combination of "Case Report," "Materials and Methods," "Results," and "Discussion." A brief one-paragraph introduction should be included to give the general background. Discussion should be limited to the specific message, including the uses of the technique or equipment. Literature reviews and lengthy case reports are not appropriate.

Length. Maximum of five double-spaced, typewritten pages, including the references but not the title page or figure legends.

References. Maximum of eight.

Figures. Maximum of two, unless the text is shortened accordingly.

Tables and Acknowledgments. Not appropriate in technical notes.

Pictorial Essays

A pictorial essay is an article that conveys its message through illustrations and their legends. Unlike other *AJR* articles, which are based on original research, pictorial essays serve primarily as teaching tools, like exhibits at a scientific meeting. They are not encyclopedic book chapters. The abstract should be a short, introductory paragraph.

Length. Maximum of four double-spaced, typewritten pages, including the references but not the title page or figure legends.

References. Maximum of four.

Figures. Maximum of 30 figure *parts*. Number should be as few as necessary to convey the message of the paper.

Tables and Acknowledgments. Not appropriate in pictorial essays.

Letters to the Editor and Replies

Letters to the Editor and Replies should offer objective and constructive criticism of published articles. Letters may also discuss matters of general interest to radiologists. Do not end a letter with a hand-written signature.

Format. All letters should be typed double-spaced on nonletterhead paper, with no greeting or salutation. Name and affiliation should appear at the end of the letter. Titles for letters should be short and pertinent. The title for a reply is simply "Reply."

Length. Maximum of two double-spaced, typewritten pages, including references.

References. Maximum of four.

Figures. Maximum of two.

Tables and Acknowledgments. Not appropriate in Letters to the Editor and Replies.

Opinions, Commentaries, and Perspectives

Opinions, commentaries, and perspectives are special articles dealing with controversial topics or issues of special concern to radiologists.

Format. Include a title page but no abstract. Headings may be used to break up the text.

Length. Maximum of five double-spaced, typewritten pages.

References. Maximum of five.

Tables and Figures. Maximum of four.

Computer Page Articles

Articles published on the computer page deal with practical computer applications to radiology.

Format. Include a title page but no abstract.

Length. Maximum of eight double-spaced, typewritten pages.

References. Maximum of five.

Figures and Tables. Maximum of five. Computer printouts are not acceptable. Figures must be submitted as 5 × 7 in. glossy prints.

All submissions to the *AJR* must be accompanied by a completed copy of the Author's Checklist and the signed Copyright Agreement.

AJR: AMERICAN JOURNAL OF ROENTGENOLOGY

Bound Volume Offer

A trouble-free way to keep your reference library up to date

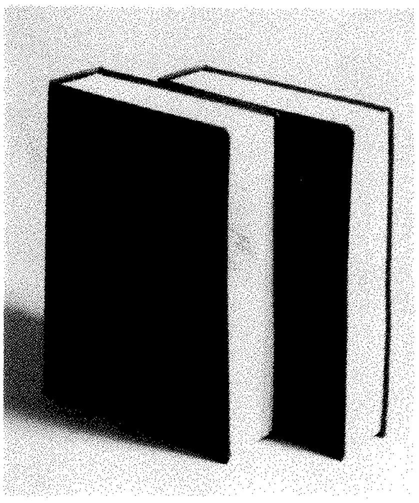

As an **AJR: American Journal of Roentgenology** subscriber, you know how much useful information is packed into each issue. But you also probably know how frustrating and time-consuming it can be to try and locate one particular article from a back issue.

Find that back issue quickly and easily

Now you can get a year's worth of articles in bound volume form — a special offer available only to subscribers. So the information you need will be at your fingertips, handsomely preserved and ready for years of future reference.

You get the timely coverage only a journal can provide — penetrating discussions of the topics that interest you most, by the brightest names in your field — with all the durability and convenience of a hardcover edition. With bound volumes, you'll never again spend frustrating hours sifting through dog-eared back issues, only to discover that the article you need has been torn out. You'll have a year's worth of vital information all arranged and indexed in one sturdy source. And each carefully crafted volume will make a handsome addition to your permanent library.

Send in your paid order by October 31, 1990 and SAVE

Act now and receive the **1990 Bound Volumes** for only $88.00 for all prepaid orders, $2.00 off the regular price of $90.00. (Please add $15.00 to all orders outside the US.) Bound volumes are available for the current year only, and are in addition to the regular subscription price.

We'll help you keep your reference library up to date

Once a year, we'll send you a reminder so you can order the latest bound volumes. When you send in your paid order, a set will be reserved for you, to be sent as soon as available on 30-day approval. If you do not want the bound volumes for any reason, simply return them to us within 30 days for a courteous refund. It's that easy.

Williams & Wilkins

P.O. Box 23291 Baltimore, Maryland 21203-9990
Broadway House 2-6 Fulham Broadway London SW6 1AA

EASY ORDERING

Please send me the **AJR: American Journal of Roentgenology 1990 Bound Volumes** at $90.00 ($105.00 outside the US). I understand that I can save $2.00 by sending in my prepaid order (check or charge) by October 31, 1990. I also understand that this offer is in addition to my regular subscription, that it is available only to subscribers, and that I will have the option of ordering bound volumes for subsequent years as long as I remain a subscriber. I will receive my 1990 bound volumes in early 1991.

☐ Check enclosed ☐ Bill me
☐ VISA ☐ MasterCard ☐ American Express

Card # Exp. date

Signature/P.O. #

Please pay in US dollars. MD residents, please add 5% sales tax. Orders outside the US and Canada must be prepaid. Rates subject to change without notice. **All orders must be received by December 31, 1990.**

Name

Address

City/State/Zip

Date of order

ORDER FREE BY PHONE.
Call **1-800-638-6423** from anywhere in the US.
In Canada, call collect **301-528-4223.**

Williams & Wilkins

P.O. Box 23291 Baltimore, Maryland 21203-9990
Broadway House 2-6 Fulham Broadway London SW6 1AA

Printed in US

AJRBV 52426

Merrill C. Sosman Lecture

Drugs, Behavior, and Brain Chemistry

Henry N. Wagner, Jr.[1]

Elson-Alexandre

In a 1955 article in the *Saturday Evening Post* magazine, Merrill Sosman was described as a "doctor who sees through you," the most famous radiologist in the United States. In Sosman's day, chest radiographs comprised 25% of radiology; another 15% involved bones. Radiologists could be recognized by their lead aprons and red goggles. Sosman was famous for his caring, humanitarian approach to patients, displayed even in the darkness of the fluoroscopy room. His diagnostic accuracy was equally renowned. For example, he diagnosed Harvey Cushing's gastric ulcer as benign, a diagnosis that proved to be correct when the ulcer healed completely without surgery. In interpreting well over one million radiographs, Sosman taught his devoted students and house staff that "we only see what we know."

Today is also a celebration of James Adelstein, on the 20th anniversary of the Joint Program in Nuclear Medicine, a program that originally included the Peter Bent Brigham and Children's Hospital, and now also includes the West Roxbury Veteran's Administration Hospital, the Dana Farber Cancer Institute, and the Beth Israel Hospital. Stimulated by Herbert Abrams, Jim created the joint program that during the past two decades has produced scores of leaders in nuclear medicine and over 1200 scientific publications. Nothing could be a greater honor than to be invited to deliver the Sosman lecture on such an occasion.

The Mind/Brain Interface

Physicians, psychologists, and neuroscientists try to relate human behavior to biological processes within the human brain in a variety of ways: (1) by studying the functional deficits of patients with focal diseases of the brain, (2) by measuring electrical activity at the surface of the brain (electroencephalography), or (3) by implanting electrodes in the brain of patients with epilepsy. Focal electrical stimulation of the brain in such patients at times results in visual hallucinations, often of remote events, but it has not been possible to relate electrical activity to specific mental functions. One problem is that the spatial resolution of the electrical measurements is poor, while surface measurements integrate the electrical activity associated with neuronal activity within relatively large regions of the brain. Tomography makes possible more precise anatomical localization and is the basis of positron emission tomography (PET), single-photon emission CT (SPECT), MR imaging, and CT. Magnetoencephalography (MEG), a technique currently under development, applies the principle of tomography to magnetic field measurements and may help solve the problem of achieving adequate spatial localization of electromagnetic events in the living brain. Nevertheless,

---

Received May 21, 1990; accepted June 18, 1990.
Presented as the 28th Merrill C. Sosman Lecture, Brigham and Women's Hospital, Boston, MA, March 1990.
This work was supported by U.S. Public Health Service grant number NS 15090.

[1] Divisions of Nuclear Medicine and Radiation Health Sciences, The Johns Hopkins Medical Institutions, 615 N. Wolfe St., Baltimore, MD 21205-2179. Address reprint requests to H. N. Wagner, Jr.

AJR 155:925-931, November 1990 0361-803X/90/1555-0925 © American Roentgen Ray Society

the degree of localization of mental functions in different parts of the human brain remains a topic of current research.

Most neurophysiologists believe that mental phenomena will someday be able to be assigned to collections of neurons in specific regions, called modules. In primary sensory perception, "receptive fields" of specific neurons that correspond to sensory input are located in columns in the somatic and visual cortex [1]. In these regions, point-to-point relationships between sensory stimulation and neuronal modules exist; as incoming information is transferred beyond primary sensory regions, such as the retina, progressively larger areas of the brain become involved. Axonal arborization spreads the information into association areas of the brain, where sensory input is converted eventually into perception, cognition, emotion, and movement.

Certain regions, such as the frontal lobes, do not correlate with *specific* primary sensation, but are involved in higher perceptual and executive functions. Persons with frontal lobes damaged in automobile accidents, brain tumors, or stroke often are apathetic and distractible, with periods of restlessness, boastfulness, euphoria, and outbursts of aggressive behavior. They have lapses in judgment and decision making, and fail to synthesize information properly.

The localization of the pathways in the brain involved in memory is a major focus of neurobiology. In some patients, deficits in memory involve primarily short-term recall while longer term memory involving recognition and recall remains intact. They have difficulty in remembering new facts, but can recall former events and can carry out complex behavior learned in the past. Images involve different memory mechanisms from those involved with verbal recognition memory and/or semantic memory. Language is a uniquely human characteristic. After surgical removal of both medial temporal lobes in the treatment of epilepsy, memory involving storage of new information is impaired, but the function of subcortical regions, such as the caudate nuclei, which are involved in retrieval of stored information, remains intact.

Emotions

Emotions are important determinants of memory, possibly related to attention. A frequently cited example is the observation that virtually everyone alive at the time of President Kennedy's assassination remembers what he or she was doing when they heard the news. Apparently, the emotional content etched the event permanently in long-term memory.

Nearly 100 years ago, William James commented on the question of localization of emotions in brain centers:

> Concerning the emotions . . . either separate and special centers, affected to them alone, are their brainseat, or else they correspond to processes occurring in the motor and sensory centers already assigned, or in others like them, not yet known.

The PET/SPECT Era

PET and SPECT make it possible to determine the relative involvement of cortical and subcortical regions in both conscious and unconscious mental processes. Questions being addressed include: How much brain activity is involved in exteroceptive mental activity, as distinct from memory, enteroceptive, or proprioceptive mental functions? What fraction of the total brain neuronal activity is involved in consciousness, in verbal language, and in other brain functioning occurring in the human brain at a particular time? Why are the brains of porpoises, elephants, and blue whales larger than the brains of human beings, even though language is lacking in these species? Results of fluorine-18 deoxyglucose studies have so far indicated that regional increases in glucose utilization associated with sensory stimulation or simple movements account for a relatively small fraction of total basal glucose utilization, the principal source of the energy required to repolarize neurons. Regional increases in glucose utilization or blood flow brought about by sensory or simple motor stimulation amount of approximately 10% of basal activity in the involved areas of the brain. Perhaps over 90% of neuronal activity does not seem to be related to exteroceptive functions of the brain, but rather to memory or to the control of the respiratory, gastrointestinal, cardiovascular, genitourinary, and musculoskeletal systems.

PET and, more recently, SPECT provide images of regional chemical reactions within the brain, which are related to mental functions [2-17]. The images portray global and regional brain blood flow, glucose utilization by using fluorine-18 2D-deoxyglucose (FDG) as a tracer, other metabolic processes involved in energy supply, neurotransmitter synthesis, or neuroreceptor density and availability (Figs. 1-5).

Regional neuronal activity stimulated in human beings or experimental animals by sensory activation or movement results in increased regional blood flow or increased glucose utilization. In this way, certain mental processes can be assigned to "seats" or anatomic regions of the brain, and spatial and temporal patterns of neuronal activation can be traced. Involvement of subcortical and cortical regions in the performance of various mental tasks is being addressed. In addition to experiments involving normal persons during different states and conditions, studies are also being done in patients with various mental diseases, including schizophrenia, depression, mania, obsessive-compulsive disorders, abnormal aggressiveness, and Tourette syndrome. The effects of legal and illegal drugs on brain chemistry also are being examined.

Drugs and Receptors

At the turn of the century, Paul Ehrlich proposed that the pharmacologic response to drugs might be due to the drug's binding to a specific chemical group on a cell that served as a recognition site, the function of which is to pass on information to the site at which the drug acts [18]. The opiates involve such "receptors," but it was not until 1973 that their existence in the mammalian brain was proved [19]. Radioactive naloxone, a so-called "antagonist" drug that blocks the pharmacological action of opiates, was found to bind to sites along pain and respiratory pathways in the brain. Naloxone that is bound to the receptors could be readily measured despite the exceedingly small chemical quantity of receptors present in the brain. The finding that the receptors were

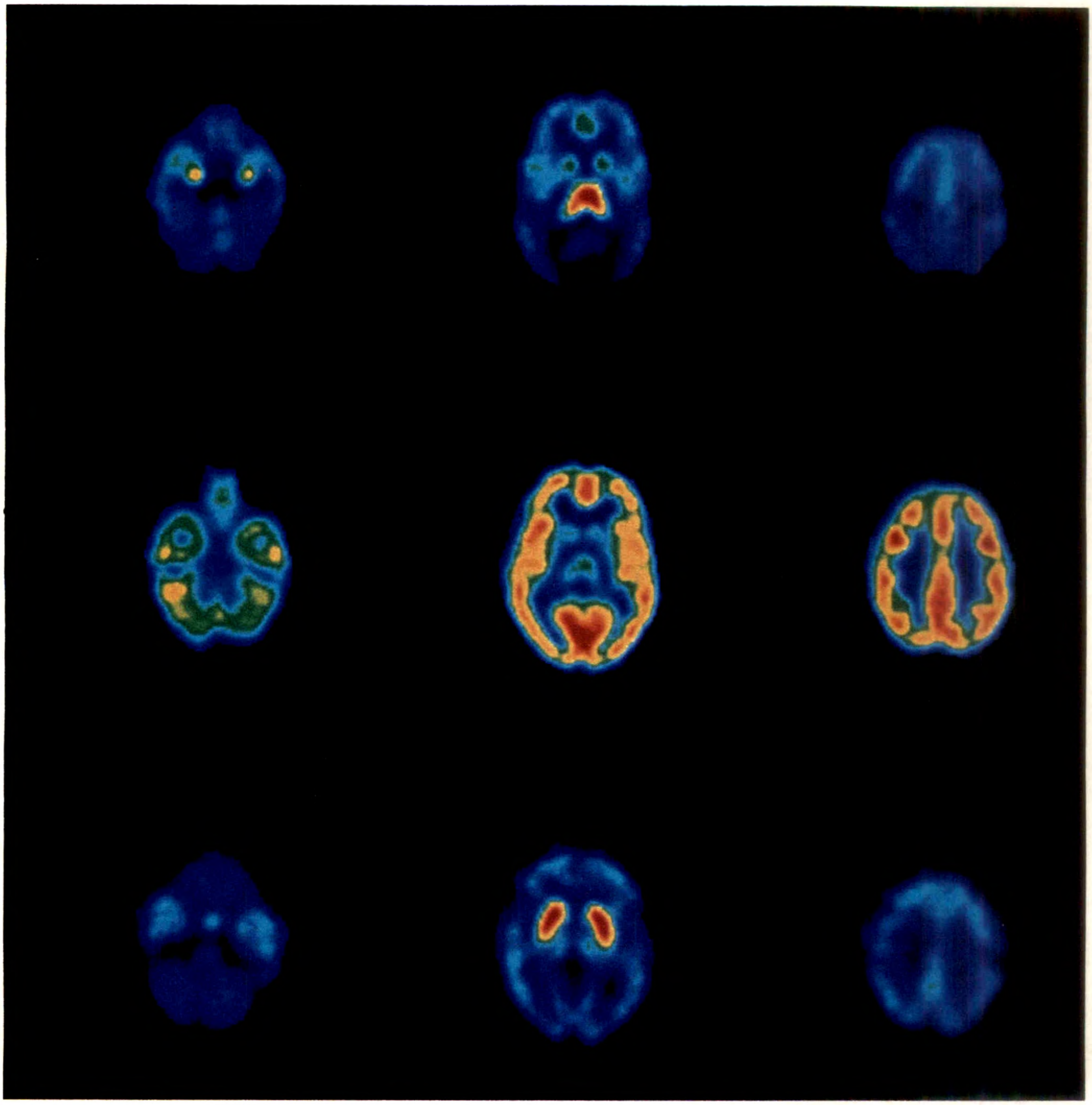

Fig. 1.—Three types of neuroreceptors imaged in transaxial cross sections of a normal person with positron emission tomography (PET). Upper row shows high concentration of opiate (^{11}C-carfentanil) receptors in amygdala and thalamus, with low concentrations in somatosensory and visual cortex. Middle row shows wide distribution of benzodiazepine (^{11}C-Ro15-1788) receptors. Lower row shows high concentration of dopamine and serotonin (^{11}C-methyl spiperone) receptors in caudate nucleus and putamen.

distributed along pain and respiratory neuronal pathways indicated their role in the process of neurotransmission.

Neuroreceptors vary in number in different parts of the brain and from one person to another; they can alter their molecular structure rapidly, serving an excitatory function under certain conditions and an inhibitory function under other conditions. Many drugs act by stimulating or blocking receptors. For example, drugs that block dopamine receptors diminish delusions and hallucinations in psychotic patients and improve their cognitive function. Other drugs that block receptors are cimetidine, which blocks histamine receptors; propranolol, which blocks beta adrenergic receptors; and haloperidol, which blocks D2 dopamine receptors.

Some drugs modulate the response to external stimuli, determining whether and to what degree an external event is perceived, and how long the event will be recalled or recognized. Neuroreceptors are involved in this process of "receptivity." For example, in the retina, the neurotransmitter dopamine increases the sensitivity of retinal neurons to dim light [20]. Dopamine does this by inhibiting the inhibitory neurons that encircle excitatory neurons. This arrangement of an excitatory neuron surrounded by inhibitory neurons is a mechanism for increasing spatial resolution in bright light. In dim light, sensitivity is increased because the inhibitory neurons are inhibited by dopamine, but visual acuity (spatial resolution) is less.

Another example is the inhibition in responsiveness to external events that occurs with persistent or repeated stimuli. Again, inhibitory neurotransmitters may be involved. The lack of inhibition may allow new and unexpected events to be more readily perceived and remembered.

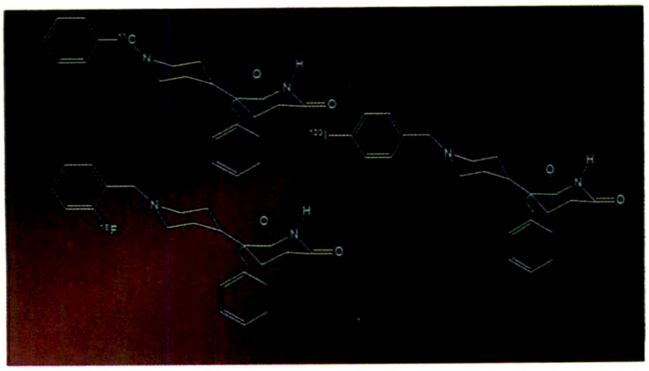

Fig. 2.—Dexetimide-levetimide analogs are used to image acetyl choline (muscarinic) receptors and can be labeled with carbon-11, fluorine-18, or iodine-123. Iodine-123 makes possible single-photon emission CT (SPECT), and ^{11}C and ^{18}F are used in positron emission tomography (PET).

The Dopaminergic System

Studies of neuroreceptors in experimental animals extended to living human beings with the development of carbon-11 N-methyl spiperone (NMSP), a drug that binds to dopamine receptors of the D2 subtype [21]. This radiotracer made possible the first successful imaging of neuroreceptors in the brain of a living human being. Most of the dopamine receptors are in the caudate nucleus and putamen, parts of the brain concerned with movement and emotion. D2 dopamine receptor density decreases dramatically between the ages of 19 and 73 years, most of the decrease occurring before the age of 40 [22].

Many patients with schizophrenia were found to have increased concentrations of D2 dopamine receptors in the caudate nucleus and putamen [23], which could be the result of deficiencies of presynaptic neurons and a consequent

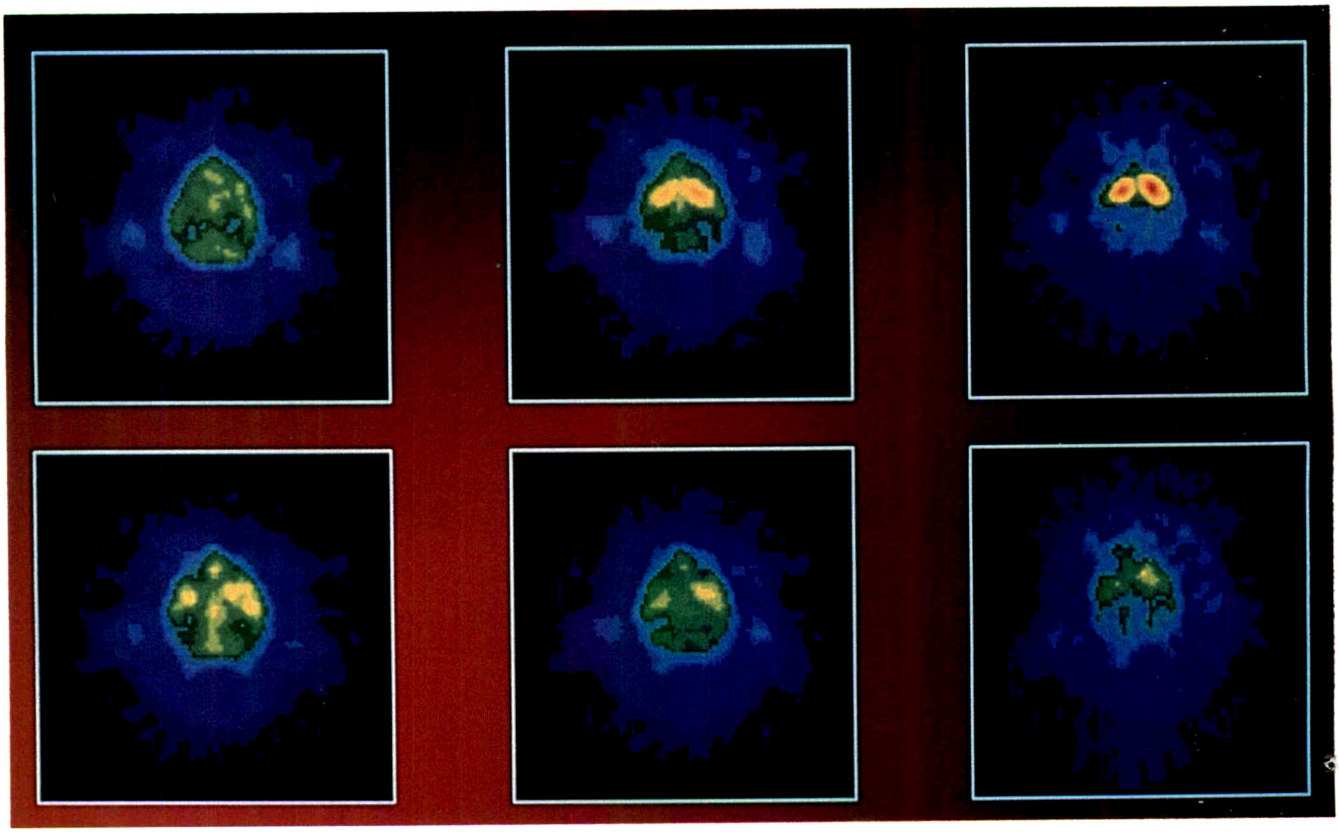

Fig. 3.—^{11}C WIN 35, 428 positron emission tomography study in baboon shows that both presynaptic and postsynaptic receptors can be imaged. Upper row (control) shows distribution of presynaptic dopamine uptake sites. Cocaine acts by blocking these sites, as shown in lower row where accumulation of WIN tracer is reduced by 80 min after injection. Left, 9 min after injection; center, 27 min; right, 80 min.

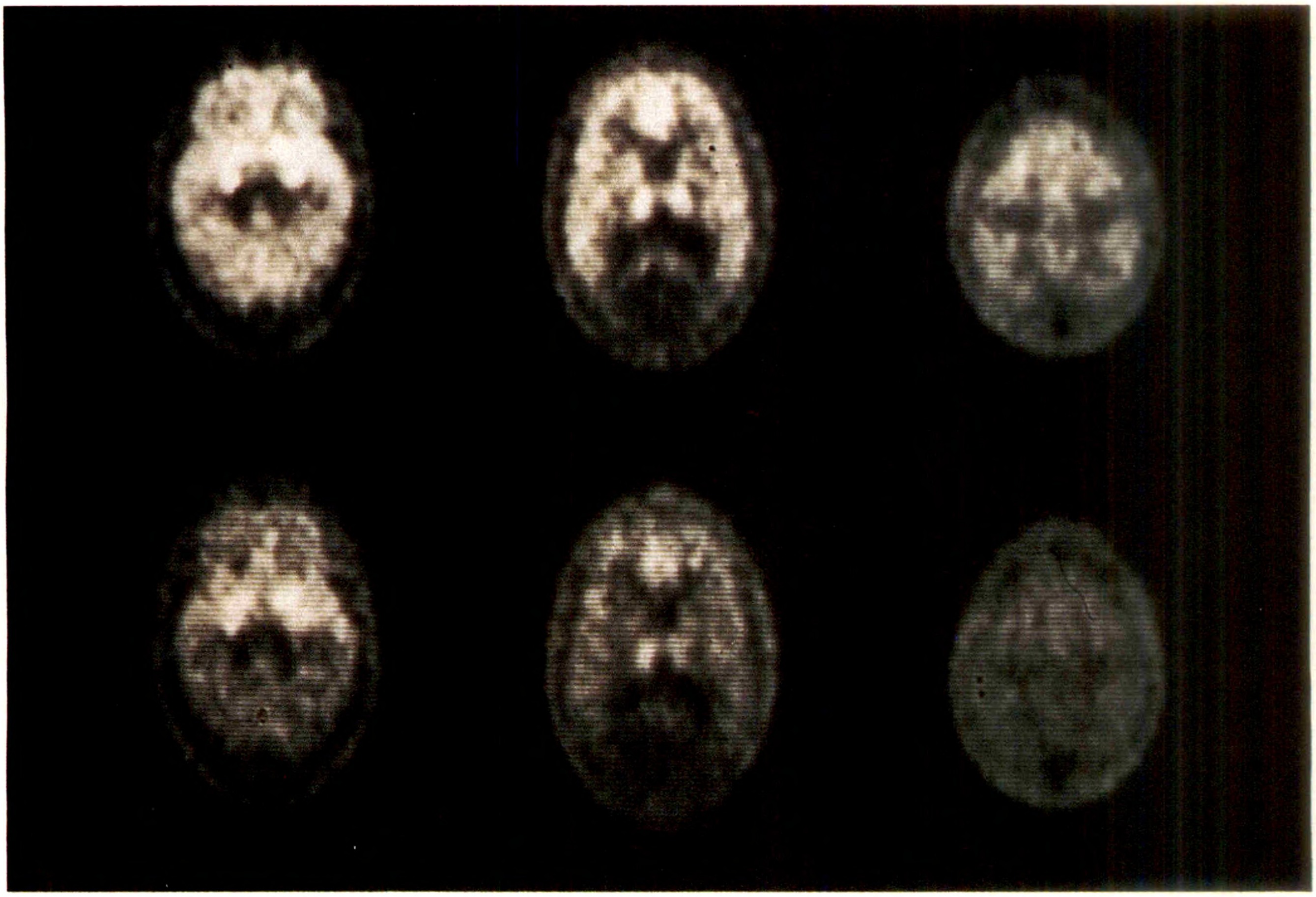

Fig. 4.—Upper row shows distribution of opiate (^{11}C-carfentanil) receptors imaged in a normal person by positron emission tomography. In lower row, receptors have been partially blocked by prior administration of naloxone (0.001 mg/kg), used to treat narcotic addiction.

decreased release of neurotransmitters into synapses in these regions, a process related to "supersensitivity." D2 dopamine receptors also were elevated in other types of mental illness [24]. For example, some patients with psychotic depression who have delusions, hallucinations, and thought disorder, even though classifiable as suffering from depression rather than schizophrenia on the basis of standardized clinical criteria, were found to have elevated D2 dopamine receptor densities in the caudate nucleus and putamen. In patients with bipolar manic/depressive illness who were not on medication, receptor levels in nonpsychotic patients did not differ from those in age-matched normal persons, but psychotic patients, whether in a manic or depressed phase of illness at the time of PET imaging, had dopamine receptor density values that were two or three times higher than those in age-matched control subjects.

Patients suffering stroke also may suffer from persistent mood disorders [25]. Between 30% and 50% of patients who have had a stroke suffer from persistent depression not related to the degree of physical impairment caused by stroke. Sixty percent of the time, depression is related to involvement of the left frontal lobe, particularly the anterior part.

Serotonin Receptors

Mayberg and colleagues [26] also observed, in patients with strokes damaging the right cerebral hemisphere, evidence of increased availability of serotonin receptors of the S2 type, resulting from an increased number of receptors, increased affinity of the receptors, or decreased occupancy by endogenous serotonin. Serotonin receptors also seemed to be involved in depressed patients with Parkinson disease. These preliminary findings support the concept that there are "seats" of emotion in the brain, just as there are certain areas concerned chiefly with somatosensory or visual perception.

Opiates and the Limbic System

An area of special interest in the control of emotions is the limbic system. In 1984, opiate receptors of the mu-type were imaged for the first time in living human beings with carbon-11 carfentanil, a drug that stimulates opiate receptors [27]. The highest concentrations were found in the limbic system, especially the amygdala.

Molecular Psychiatry

Traditionally, neurology and psychiatry have involved the search for the specific cause of disease by identifying focal pathologic changes, either in whole organs or in chemically stained cells. The cell remains the basic unit of biology, but PET and SPECT move the focus to the subcellular, molecular level of brain function. Carbon-14 and tritium revolutionized biochemistry after World War II ended. Today, PET/SPECT

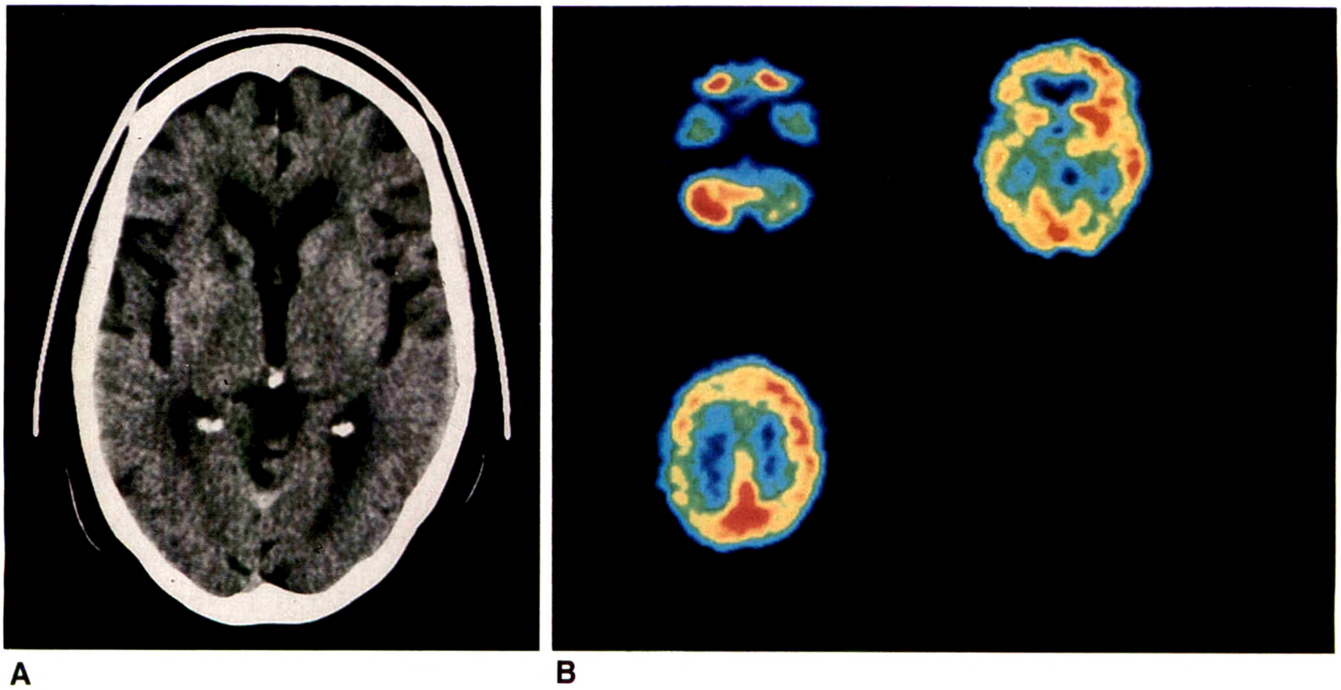

Fig. 5.—*A*, CT scan of patient with lacunar infarct of left caudate nucleus (seen from above).

***B*, Fluorine-18 deoxyglucose (FDG) positron emission tomography (PET) scan shows large area of reduced glucose utilization in left cerebral hemisphere (seen from above), with a decrease in contralateral glucose utilization in right cerebellar hemisphere. Patient was suffering from persistent depression after a stroke 6 months before.**

extend biochemistry to the living human being, creating a *molecular medicine*, the domain beyond even the resolution of the electron microscope. The study of molecules is chemistry, which emphasizes process and change rather than structure.

A neuroanatomist, James Papez [28], and a psychiatrist, Paul MacLean [29], focused on certain regions of the brain in the control of emotions. MacLean called these regions the limbic system, comprising the temporal lobes, midbrain, areas around the third ventricle and cerebral aqueduct, the amygdala, hippocampus, hypothalamus, fornix, cingulate gyri, and septum pellucidum. The neocortex, which evolved later, was postulated to be responsible for conscious, rational, chiefly verbal thought and for the initiation of voluntary motion.

In human beings, the limbic system is the site of action of many mood-altering neurotropic drugs, including narcotics and cocaine. For example, receptors for opiate drugs have been shown by PET to be present in high concentrations in the limbic system of human beings [27]. Cocaine binds to receptors in the caudate nucleus and putamen [30]. Other drugs such as phenobarbital and tranquilizers are more effective on cortical regions. One of the main approaches to human neurobiology by use of PET/SPECT is to examine the effects of drugs. In searching for the mechanism of action of drugs, we first look for regions of the brain where the drugs concentrate and then try to relate the chemical effects within these regions to the behavioral effects of the drugs.

Mood-altering drugs, such as narcotics and cocaine, bind to structures of the limbic system, supporting the hypothesis that human beings turn to drugs because of emotional problems, such as excessive aggressive inclinations. PET studies are being directed toward the phenomenon of craving, including studies of possible differences between human beings in their response to drugs. PET can facilitate the design, development, evaluation, and application of drugs in the treatment of various types of mental dysfunction, including schizophrenia, depression, and dementia, by direct measurement of the effects of drugs on the target organs.

When diseases such as stroke or Parkinson disease involve parts of the limbic system, they are often associated with emotional disturbances. The diagnosis of "organic personality disorder, explosive type" is observed in some patients with diseases involving the prefrontal and frontal lobes, parts of the limbic system.

Because of the episodic nature of many aggressive acts, one theory is that they are related to focal epilepsy and originate at sites of excessive focal neuronal activity. In some patients with partial complex epilepsy, psychotic symptoms, such as hallucinations, delusions, and abnormal thought patterns, seem to be associated with abnormal neuronal firing. PET made it possible to identify more precisely the sites of origin of the seizures and identify abnormalities of neurotransmitters or neuromodulators in such regions [31].

Obsessive-compulsive disorder (OCD) and Tourette syndrome are impulsive disorders that also may involve neurotransmission. The symptoms of patients with OCD are greatly diminished by the administration of clomipramine, a drug that blocks catecholamines from being taken up again by presynaptic neurons, thus increasing the concentration of synaptic dopamine. The drug dampens urges to carry out certain compulsive acts, such as excessive hand washing. The frontal lobes may be involved.

One third of patients with schizophrenia have structural abnormalities of the brain revealed by CT, including stenosis of the aqueduct of Sylvius, ventricular dilatation, and subependymal hemorrhages. Abnormalities in frontal lobe phosphoesters have been shown by MR spectroscopy. Such abnormalities may reflect regional neuronal injury involving the mesolimbic dopaminergic system with a resultant secondary increase in postsynaptic dopamine receptor concentrations in later stages of the disease.

Beyond Genotype to Molecular Phenotype

In theory, whenever a chemical process can be measured anywhere in the body, including the brain, there are at least two possible diseases, one in which the process is abnormally slow and another in which the process is abnormally fast. Hyper- and hypothyroidism were among the earliest examples. In epilepsy, regional changes in glucose metabolism and neuroreceptor concentrations can be measured at the site from which the seizures originate [32]. The cause of these changes remains to be determined. Endogenous neurotoxins are a possible factor.

Although it is frequently helpful to search for chemical abnormalities in specific regions of the brain, overall or global brain chemistry also is of interest. As stated previously, increases in regional glucose utilization that occur in the involved regions of the brain are small relative to the total utilization of glucose by the entire brain. For example, in patients with Parkinson disease, global glucose utilization is reduced by about 20%, although the most severely affected regions include the inferior frontal cortex [33].

In the future, patients with mental symptoms may be characterized according to their chemical phenotype, such as "excessive dopaminergic reactions" or other biochemical abnormalities, rather than by anatomic or clinical phenotype.

ACKNOWLEDGMENT

I acknowledge the contributions of many investigators who took part in this work, including J. J. Frost, D. F. Wong, R. F. Dannals, J. M. Links, H. S. Mayberg, U. S. Scheffel, E. D. London, A. A. Wilson, and J. R. Lever.

REFERENCES

1. Edelman GM, Mountcastle VB. *The mindful brain.* Cambridge, MA: MIT Press, **1978**
2. Reivich M, Kuhl D, Wolf A, et al. The [18F]fluorodeoxyglucose method for the measurement of local, cerebral glucose utilization in man. *Circ Res* **1979**;44:127–137
3. Reivich, M, Alavi A, eds. *Positron emission tomography.* New York: Alan R. Liss, **1982**
4. Phelps ME, Huang SC, Hoffman EJ, Selin C, Sokoloff L, Kuhl, DE. Tomographic measurement of local cerebral glucose metabolic rate in humans with (F-18) 2-fluoro-2-deoxy-D-glucose: validation of method. *Ann Neurol* **1979**;6:371–388
5. Phelps ME, Mazziotta JC. PET: Human brain function and biochemistry. *Science* **1985**;228:799–809
6. Phelps ME, Mazziotta JC, Schelbert HR. *Positron emission tomography and autoradiography: application in the brain and heart*. New York: Raven Press, **1986**
7. Sokoloff L, Reivich M, Kennedy C, et al. The [14C]deoxyglucose method for the measurement of local cerebral glucose utilization: theory, procedure, and normal values in the conscious and anesthetized albino rat. *J Neurochem* **1977**;28:897–916
8. Sokoloff L. The radioactive deoxyglucose method, theory, procedure and applications for the measurement of local glucose utilization in the central nervous system. In Agranoff BW, Aprison MH, eds. *Advances in neurochemistry*, vol 4. New York: Plenum **1982**:1–82
9. Ter-Pogossian MM, Phelps ME, Hoffman EJ, Mullani NA. A positron emission transaxial tomograph for nuclear imaging (PETT). *Radiology* **1975**;114:89–98
10. Ter-Pogossian MM, Mullani NA, Hood J, Higgins CS, Currie CM. A multislice positron emission computed tomograph (PETT IV) yielding transverse and longitudinal images. *Radiology* **1978**;18:477–484
11. Ido T, Wan CN, Casella V, Fowler JS, Wolf AP. Labeled 2-deoxy-D-glucose analogs: ^{18}F-labeled 2-deoxy-2-fluoro-D-glucose, 2-deoxy-2-fluoro-D-mannose and ^{14}C-2-deoxy-2-fluoro-D-glucose. *J Label Compds Radiopharm* **1978**;14:175–183
12. Tewson TJ, Welch MJ, Raichle ME. [18F] labeled 3-deoxy-3-fluoro-D-glucose: synthesis and preliminary biodistribution data. *J Nucl Med* **1978**;19:1339–1345
13. Raichle ME. Measurement of local brain blood flow and oxygen utilization using oxygen-15 radiopharmaceuticals: a rapid dynamic imaging approach. In Reivich M, Alavi A, eds. *Positron emission tomography*. New York: Alan R. Liss, **1985**:241–247
14. Raichle ME, Martin WRW, Herscovitch P, Mintun MA, Markham J. Brain blood flow measured with intravenous $H_2{}^{15}O$. II. Implementation and validation. *J Nucl Med* **1983**;24:790–798
15. Mintun MA, Raichle ME, Martin WR, Herscovitch P. Brain oxygen utilization measured with O-15 radiotracers and positron emission tomography. *J Nucl Med* **1984**;25:177–187
16. Ter-Pogossian MM, Herscovitch P. Radioactive oxygen-15 in the study of cerebral blood flow, blood volume, and oxygen metabolism. *Semin Nucl Med* **1985**;15:377–394
17. Frackowiak RSJ, Lammertsma AA. Clinical measurement of cerebral blood flow and oxygen consumption. In Reivich M, Alavi A, eds. *Positron emission tomography*. New York: Alan R. Liss, **1985**:153–181
18. Ehrlich P. Address in pathology on chemotherapeutics: scientific principles, methods and results. *Lancet* **1913**;2:445–451
19. Pert CB, Snyder SH. Opiate receptors: demonstration in nervous tissue. *Science* **1973**;179:1011–1014
20. Knapp AG, Dowling JE. Dopamine enhances excitatory amino acid-gated conductances in cultured retinal horizontal cells. *Nature* **1987**;325: 437–439
21. Wagner HN Jr, Burns HD, Dannals RF, et al. Imaging dopamine receptors in the human brain by positron tomography. *Science* **1983**;221:1264–1266
22. Wong DF, Wagner HN Jr, Dannals RF, et al. Effects of age on dopamine and serotonin receptors measured by positron tomography in the living human brain. *Science* **1984**;226:1393–1396
23. Wong DF, Wagner HN, Tune LE, et al. Positron emission tomography reveals elevated D2 dopamine receptors in drug-naive schizophrenics. *Science* **1986**;234:1558–1563
24. Wong DF, Pearlson G, Tune L, et al. In vivo measurement of D2 dopamine receptor abnormalities in drug-naive and treated manic depressive patients. *J Nucl Med* **1987**;28:611
25. Robinson RGH, Kubos KL, Starr LB, Rao K, Price TR. Mood disorders in stroke patients: importance of lesion location. *Brain* **1984**;107:81–93
26. Mayberg HS, Robinson RG, Wong DF, et al. PET imaging of cortical S2 serotonin receptors following stroke: lateralized changes and relationship to depression. *Am J Psychiatr* **1988**;145:937–943
27. Frost JJ, Wagner HN, Dannals RF, et al. Imaging opiate receptors in the human brain by positron tomography. *J Comput Assist Tomogr* **1985**; 9:231–236
28. Papez JW. A proposed mechanism of emotion. *Arch Neurol Psychiatr* **1937**;38:725–743
29. MacLean PD. *A triune concept of the brain and behavior*. Toronto: University of Toronto Press, **1973**
30. Fowler JS, Volkow ND, Wolf AP, et al. Mapping cocaine binding sites in human and baboon *in vivo*. *Synapse* **1989**;4:371–377
31. Frost JJ, Mayberg HS, Fisher RS, et al. Mu-opiate receptors measured by positron emission tomography are increased in temporal lobe epilepsy. *Ann Neurol* **1988**;23:231–237
32. Engel J, Kuhl DE, Phelps ME, Mazziotta JC. Interictal cerebral glucose metabolism in partial epilepsy and its relation to EEG changes. *Ann Neurol* **1982**;12:510–517
33. Mayberg HS, Starkstein SE, Sadzot B, et al. Selective hypometabolism in the inferior frontal lobes in depressed patients with Parkinson disease. *Ann Neurol* **1990**;28:57–64

Book Review

Practical Color Atlas of Sectional Anatomy. Chest, Abdomen, and Pelvis. By E. A. Lyons. New York: Raven, 320 pp., 1990. $56, softcover

This text is a revision of the original atlas published in 1978. The book is now smaller and therefore easier to carry and use. It is a purportedly a handy reference not only for the medical imaging specialist but also for all practitioners and medical students who must be aware of sectional anatomy in order to review imaging procedures on their patients intelligently.

The text is divided into three parts: transverse, parasagittal, and coronal sections. Each contains subdivisions depicting the chest, abdomen, and male and female pelvis, respectively. Each image pair, on facing pages, consists of a line drawing on the left-hand page and the appropriate 1-cm-thick frozen cadaveric section on the right-hand page. Use of color makes it possible to identify certain structures rapidly and to follow them from section to section. Structures are marked clearly on the line drawing, but the cadaveric sections are unmarked. A specific attempt was made to not mark every structure on every page, an intelligent choice considering the necessity for a relatively uncluttered page in a smaller sized text. An unmarked structure usually can be found easily on one of the immediately adjacent sections.

Preceding each major part is a series of lines drawn through a figure to depict the sections to be illustrated, and, most helpful, a similar depiction with only the appropriate line accompanies each page with a line drawing. The cadaveric sections all have red and blue coloring to accentuate the major branches of the arterial and venous vasculature, respectively, and this is helpful.

The book concludes with a seven-page index. The small size and softcover format might be considered advantageous for quick reference use and portability but possibly could result in a shorter useful life. Also, at times the natural coloring of the cadaveric sections makes structures difficult to distinguish. All these are in contradistinction to a classic larger, hardcover cross-sectional anatomy text with clearly delineated artistic drawings rather than cadaveric sections, such as the one by Eycleshymer and Schoemaker.

Except for the fact that in my copy the coronal and parasagittal sections are upside-down, I have found this book, with its softcover format, a handy ready reference, particularly while reading cross-sectional imaging examination. I therefore recommend it to all who might be in need of such a reference.

Hano A. Siegel
Mercy Hospital
San Diego, CA 92103

Review

Update on Esophageal Radiology

Marc S. Levine,[1] Stephen E. Rubesin,[1] and David J. Ott[2]

This article reviews the current status of double-contrast radiography in diagnosing pharyngeal tumors and opportunistic esophagitis and the radiologic evaluation of esophageal motility disorders in patients with chest pain. Double-contrast pharyngography is a valuable technique for detecting pharyngeal tumors. These lesions may be manifested by an intraluminal mass, mucosal irregularity, or asymmetric distensibility. Furthermore, barium studies may demonstrate lesions involving the valleculae, tongue base, lower hypopharynx, and pharyngoesophageal segment that are difficult to visualize at endoscopy. Double-contrast radiography is also a valuable technique for detecting opportunistic esophagitis and for differentiating the underlying causes. Mucosal plaques should suggest *Candida* esophagitis, whereas discrete ulcers should suggest herpes esophagitis, and one or more large, relatively flat ulcers should suggest cytomegalovirus esophagitis. Finally, in evaluating patients with chest pain, in only a small percentage are esophageal motility disorders found to be a possible cause of their pain. Instead, the majority are found to have cardiac disease, structural esophageal lesions, or gastroesophageal reflux, so that barium studies are more useful in documenting normal motility or structural abnormalities in these patients.

Double-Contrast Radiography of Pharyngeal Tumors

The radiologist often is the first physician to suggest the diagnosis of pharyngeal carcinoma (Fig. 1) [1]. Some patients are asymptomatic, and the tumors are detected on barium studies performed for other reasons. Other patients who are symptomatic may undergo pharyngography as the initial diagnostic examination. Thus, the radiologist must be familiar with the morphology and behavior patterns of pharyngeal carcinoma.

Anatomy and Technique

During double-contrast pharyngography, high-density barium (E-Z-HD, E-Z-EM Co., Westbury, NY) coats the squamous mucosa overlying the muscular tube of the pharynx [2, 3]. Longitudinal striations are often observed on the posterior or lateral pharyngeal wall because of the close apposition of the mucosa to the inner longitudinal muscle layer (palatopharyngeus, stylopharyngeus) and its pharyngeal aponeurosis (Fig. 2) [3]. In contrast, horizontal striations may be seen overlying the muscular processes of the arytenoid cartilages owing to redundant mucosa in this region (Fig. 2) [3]. The mucosa overlying the palatine and lingual tonsils may also have a finely nodular appearance due to lymphoid hyperplasia [4].

The radiologic study should include double-contrast spot films to assess morphology and a dynamic examination (cine- or videofluoroscopy) to assess function [5]. For the double-contrast examination, vertically split two-on-one spot films are obtained in a lateral projection during suspended respiration and during phonation with the sound "Eee. . ." [6]. Frontal spot films are also obtained during suspended respiration and during maximal distension by a modified Valsalva

---

Received April 30, 1990; accepted after revision June 10, 1990.
Presented at the annual meeting of The Society of Gastrointestinal Radiologists, Hawaii, HI, January 1990.

[1] Department of Radiology, Hospital of the University of Pennsylvania, 3400 Spruce St., Philadelphia, PA 19104. Address reprint requests to M. S. Levine.
[2] Department of Radiology, Bowman Gray School of Medicine, Winston-Salem, NC 27103.

AJR 155:933-941, November 1990 0361-803X/90/1555-0933 © American Roentgen Ray Society

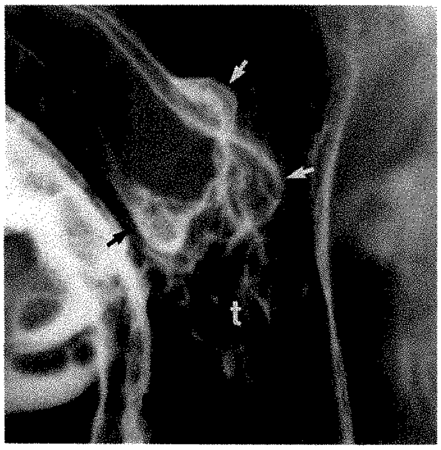

Fig. 1.—Unsuspected squamous cell carcinoma of soft palate in 80-year-old man with dementia and epigastric pain. Lateral view from double-contrast pharyngogram shows large, lobulated mass (*arrows*) arising from soft palate. Note how distal soft palate and uvula have been obliterated. Nodular mucosa in region of tonsilar fossa (t) also indicates tumor spread into palatine tonsil. (Reprinted with permission from Rubesin and Glick [1].)

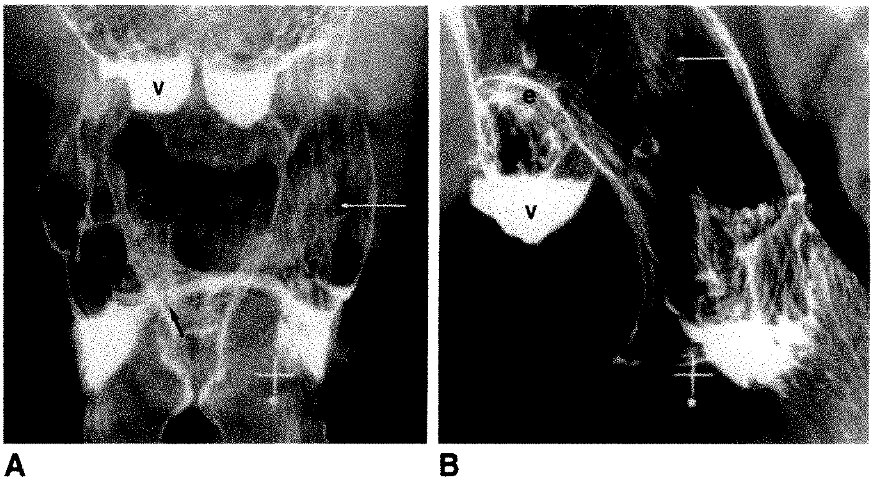

Fig. 2.—Normal lines of pharynx.

A and *B*, Frontal (*A*) and lateral (*B*) views from double-contrast pharyngogram show longitudinal striations in hypopharynx (*white arrows*) due to close apposition of squamous mucosa to inner longitudinal muscle layer and pharyngeal aponeurosis. Transverse lines overlying muscular processes of arytenoid cartilages reflect redundant mucosa (*black arrow*). v = vallecula, e = epiglottis. (Reprinted with permission from Rubesin and Glick [1].)

maneuver (blowing against closed lips) [7]. Oblique films may provide additional information.

Radiologic Evaluation

The radiologic findings of pharyngeal carcinoma include (1) an intraluminal mass, (2) mucosal irregularity, and (3) asymmetric distensibility [7–10]. An intraluminal mass may be manifested by an abnormal luminal contour, extra barium-coated lines in an abnormal location (Fig. 3), a focal area of increased radiodensity, or a filling defect in the barium pool. Mucosal irregularity may be recognized by abnormal barium collections due to ulceration or by a nodular surface pattern due to mucosal elevations (Fig. 4). Lymphoid hyperplasia of the lingual tonsil may result in small, uniform nodules that are distributed symmetrically at the base of the tongue [4]. However, nonuniform nodules that have an asymmetric distribution should be considered suspicious for tumor in this region. Finally, asymmetric distensibility may be caused by an infiltrating tumor or extrinsic nodal mass impinging on the pharynx.

Squamous cell carcinoma of the palatine tonsil is the most common malignant lesion arising in the pharynx [11]. Bulky, exophytic tumors are easily detected radiologically. However, infiltrative tumors may be obscured by the nodular mucosa overlying the lymphoid tissue of the tonsillar fossa. Palatine tonsil tumors frequently spread to the soft palate, lateral base of the tongue, and posterior pharyngeal wall.

Most squamous cell carinomas of the base of the tongue are clinically silent until they are advanced lesions with nodal metastases, so that affected patients have a 5-year survival rate of only 15% [12]. These tumors may be manifested by polypoid or ulcerated lesions at the base of the tongue [13]. The tumors subsequently may spread to the palatine tonsils, valleculae, and pharyngoepiglottic folds.

Supraglottic squamous cell carcinomas are defined as "laryngeal" tumors even though they arise in the pharyngobuccal anlage [11]. They may involve various portions of the epiglottis, aryepiglottic folds, arytenoid cartilages, false vocal cords, laryngeal ventricle, and preepiglottic space (Fig. 3). Affected individuals may present with respiratory symptoms such as coughing, choking, or hoarseness. About 30% of patients have nodal metastases at the time of diagnosis, and the 5-year survival rate is 40% [8].

Patients with squamous cell carcinoma of the piriform sinus often present with a neck mass or hoarseness. At the time of diagnosis, 70% of patients already have metastases to jugular lymph nodes [11]. Early lesions may be recognized by relatively subtle areas of mucosal nodularity in the piriform sinus (Fig. 4). However, more advanced lesions typically appear as bulky, exophytic masses in this region. Tumors arising on the medial wall of the piriform sinus may invade the paraglottic space and cause hoarseness. Tumors arising on the lateral wall of the piriform sinus may invade the thyroid gland and carotid sheath.

Squamous cell carcinomas of the posterior pharyngeal wall are usually bulky, fungating tumors (Fig. 5). They often spread vertically into the naso- and oropharynx or cervical esophagus. Affected patients usually present with a neck mass. About 50% of patients have metastases to jugular and/or retropharyngeal lymph nodes at the time of diagnosis, so that 5-year survival rates are poor. This is the type of pharyngeal carcinoma that is most frequently associated with a synchronous malignancy in the pharynx or esophagus.

Postcricoid squamous cell carcinomas are rare lesions, except in northern Europe, where they are encountered more

Fig. 3.—Squamous cell carcinoma of left aryepiglottic fold.

A, Frontal view from double-contrast pharyngogram shows abnormal line (*arrows*) coursing from level of obliterated left vallecula to lower right aryepiglottic fold. Note preservation of lateral walls of hypopharynx and tip of epiglottis (e).

B, Lateral view shows mass of aryepiglottic fold depicted by elevated contour of left aryepiglottic fold (*arrows*) with nodular mucosa and abnormal lines in this region. Note how tip of epiglottis is spared.

(Reprinted with permission from Rubesin et al. [3].)

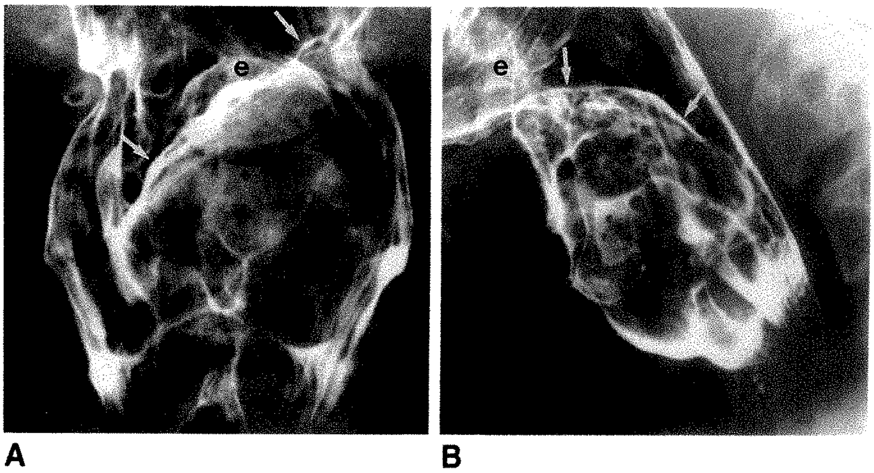

Fig. 4.—Nodular mucosa in pharyngeal carcinoma in 43-year-old woman with known squamous cell carcinoma of tip of tongue.

A and *B*, Frontal (*A*) and lateral (*B*) views from double-contrast pharyngogram show focal area of mucosal nodularity (*arrows*) in anterolateral region of right piriform sinus. Endoscopic biopsies revealed a synchronous primary squamous cell carcinoma of piriform sinus invading the submucosa.

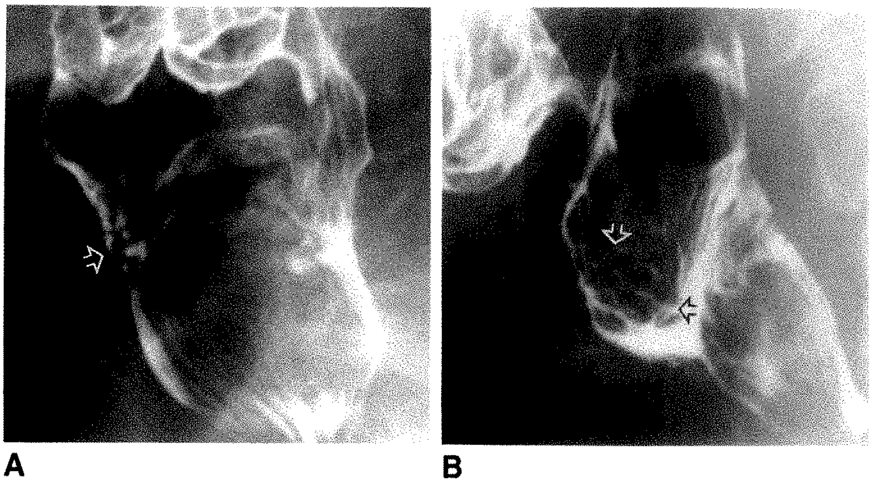

Fig. 5.—Squamous cell carcinoma of posterior pharyngeal wall in 62-year-old patient with dysphagia and smoking and alcohol addiction. Lateral view from double-contrast pharyngogram shows large, lobulated mass (*arrows*) on posterior pharyngeal wall, extending from level of uvula to mucosa overlying muscular processes of arytenoid cartilages (a). Initial barium study alerted endoscopist to size of tumor. At panendoscopy, endoscope could not safely pass this lesion. (Reprinted with permission from Rubesin and Glick [1].)

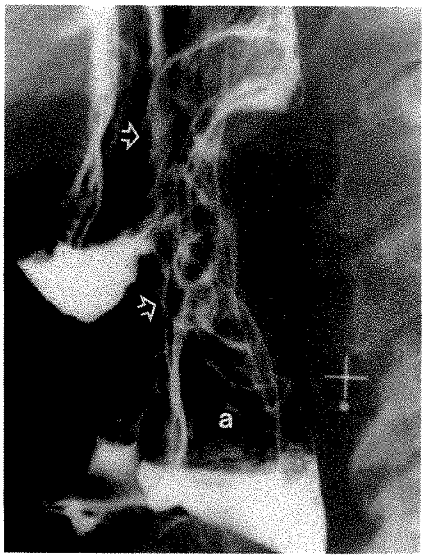

5

Fig. 6.—Postcricoid carcinoma. Lateral view from double-contrast pharyngogram shows irregular contour and fine lobulations of mucosa in distal hypopharynx and pharyngoesophageal segment (*arrows*).

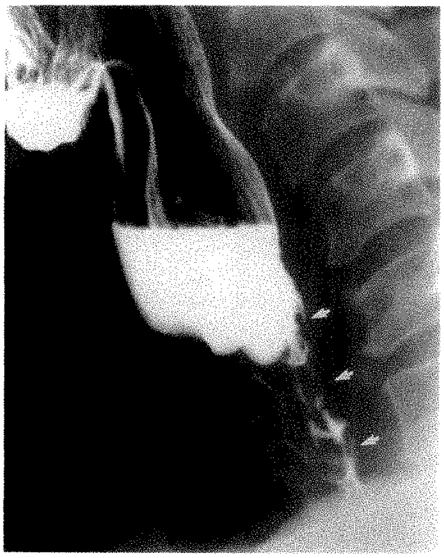

6

often. The association between postcricoid carcinomas, iron-deficiency anemia, and webs is controversial and probably does not occur in the United States. These tumors usually appear radiologically as anular, infiltrating lesions (Fig. 6). They often spread vertically into the hypopharynx or cervical esophagus and mediastinum. Occasionally, skip lesions may occur.

Lymphomas constitute 15% of oropharyngeal tumors [8]. They usually involve the lingual and palatine tonsils. Lymphomas arising in the hypopharynx are rare. Most lymphomas appear radiologically as large, lobulated tumors.

Clinical Perspective

Symptoms of pharyngeal carcinoma are nonspecific and may include a sore throat, odynophagia due to mucosal ulceration, and dysphagia due to blockage of the passage of a bolus. The patient may experience coughing or choking due to laryngeal penetration during swallowing or aspiration of a bolus trapped in an ulcerated tumor. Hoarseness may be caused by laryngeal or supraglottic carcinomas. Voice changes may also occur when tumors arising on the medial wall of the piriform sinus infiltrate the cricoarytenoid joint or arytenoid cartilage. Some patients may have referred pain from the pharynx, producing an earache. Some asymptomatic patients may have a palpable neck mass.

Double-contrast pharyngography is a valuable technique for diagnosing pharyngeal tumors. It is particularly helpful for evaluating the hypopharynx. In one study, about 97% of lesions below the pharyngoepiglottic fold were detected radiologically [14]. Pharyngography is also helpful for determining the size, extent, and inferior limit of the tumor and the degree of functional impairment. However, the barium study is of much less value in detecting lesions in the oral cavity. Flat, infiltrating lesions arising in the palatine tonsils also may be missed radiologically. Thus, it is important to be aware of the limitations of pharyngography in these patients.

At the same time, endoscopy is not an infallible technique for examining the pharynx. Barium studies may detect lesions in the valleculae, vertical surface of the tongue base, lower hypopharynx, and pharyngoesophageal segment, which are difficult to visualize at endoscopy. Barium studies may also demonstrate bulky tumors, pharyngoesophageal narrowing, or Zenker diverticula that are difficult to circumvent safely at endoscopy (Figs. 5 and 6). Therefore, the complementary roles of these techniques should be recognized.

In patients with known pharyngeal carcinoma, barium studies are also helpful for detecting separate, coexisting carcinomas of the pharynx or esophagus. About 10% of patients with squamous cell carcinomas of the head and neck develop a second primary lesion [15], and 1% develop synchronous or metachronous carcinomas of the esophagus [16, 17]. Thus, a double-contrast esophagogram should be obtained when a lesion is detected in the pharynx on double-contrast pharyngography.

Opportunistic Esophagitis

Clinical Perspective

Because of the increased use of steroids, cytotoxic drugs, and other immunosuppressive agents, opportunistic esophagitis has become an increasingly common problem in modern medical practice. *Candida albicans* is the usual offending organism, but the herpes simplex virus and cytomegalovirus (CMV) also have been recognized with increasing frequency as opportunistic invaders of the esophagus. The recent AIDS epidemic has led to the development of more fulminant forms of fungal and viral esophagitis, accentuating the need for early diagnosis and treatment.

Opportunistic esophagitis may be manifested clinically by odynophagia, dysphagia, chest pain, or, less frequently, upper gastrointestinal bleeding. Although many patients with *Candida* esophagitis have associated lesions in the oropharynx (i.e., thrush), esophageal symptoms in some patients with oropharyngeal candidiasis result from herpes or CMV esophagitis. Thus, it is often difficult or impossible to differentiate fungal and viral esophagitis on clinical grounds.

Radiologic Evaluation

Although conventional single-contrast esophagography has been considered an unreliable technique for diagnosing opportunistic esophagitis, double-contrast esophagography has dramatically improved the ability of the radiologist to detect this condition and to differentiate the various underlying causes. The accurate diagnosis of fungal or viral esophagitis on barium studies is particularly important for patients with AIDS, as gastroenterologists are reluctant to perform endoscopy in these individuals because of fear of contaminating their endoscopic instruments or exposing themselves to the AIDS virus. Thus, double-contrast radiography has an important role in examining these patients.

Candida *esophagitis*.—The radiologic diagnosis of *Candida* esophagitis has been limited by the fact that it tends to be a superficial disease with mucosal abnormalities that are difficult to recognize on conventional single-contrast barium studies. As a result, endoscopy has been advocated as a more reliable test for this disease. However, recent studies have shown that double-contrast esophagography has a sensitivity of approximately 90% in diagnosing *Candida* esophagitis [18, 19]. The major advantage of this technique is its ability to demonstrate mucosal plaques that cannot be seen easily on single-contrast studies. As a result, only mild cases of *Candida* esophagitis are likely to be missed on the double-contrast examination.

Candida esophagitis is usually manifested on double-contrast radiographs by discrete plaquelike lesions corresponding to the characteristic white plaques seen at endoscopy. The plaques tend to be longitudinally oriented, appearing as linear or irregular filling defects with normal intervening mucosa (Fig. 7) [18, 20]. Because these lesions have discrete borders, they may be etched in white by a thin layer of barium trapped between the edge of the plaque and the adjacent mucosa (Fig. 7B). Some patients may have giant plaques or pseudomembranes in the esophagus, whereas others may have tiny, nodular lesions producing a granular appearance of the mucosa (Fig. 8) [20]. Thus, the classic radiologic features of *Candida* esophagitis are not present in all patients.

Patients with AIDS may have a more fulminant form of *Candida* esophagitis, manifested by a grossly irregular or

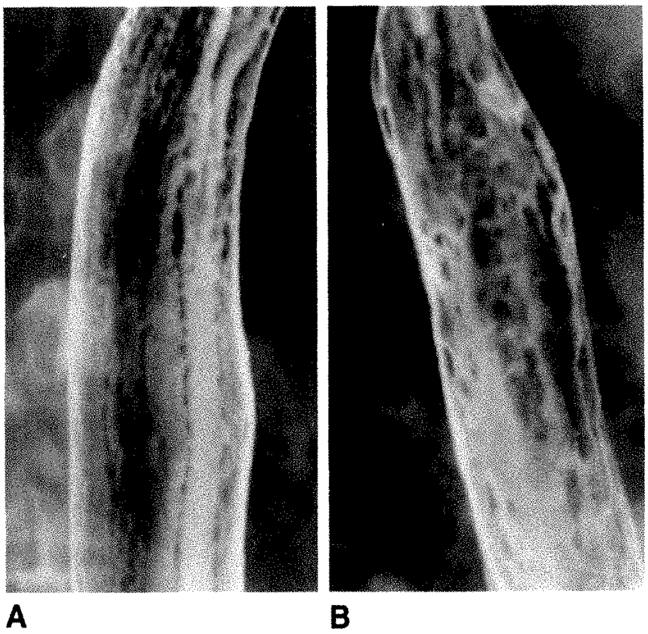

Fig. 7.—*Candida* esophagitis with plaques.

A, Double-contrast esophagogram shows classic appearance of candidiasis with multiple linear plaques. Note how lesions have well-defined borders and longitudinal orientation in relation to long axis of esophagus.

B, More irregular plaquelike lesions in different patient. Note how some lesions are etched in white owing to barium trapped between edge of plaque and adjacent mucosa.

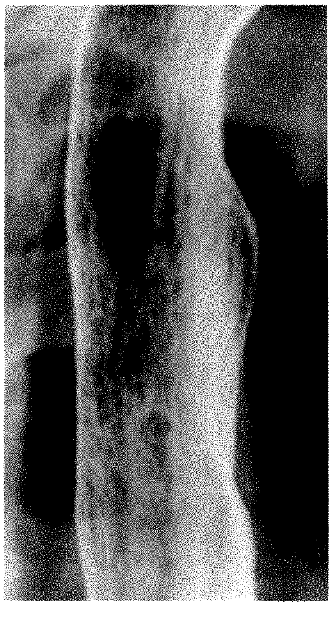

Fig. 8.—Double-contrast esophagogram in patient with *Candida* esophagitis shows tiny, nodular elevations, producing granular appearance of mucosa.

"shaggy" esophagus owing to coalescent plaque and pseudomembrane formation with barium trapped between these plaques and pseudomembranes (Fig. 9) [20]. Occasionally, the shaggy esophagus of candidiasis may be the initial manifestation of AIDS [20]. Because this degree of esophagitis rarely occurs in other immunocompromised patients, the possibility of AIDS should be suspected when a shaggy esophagus is detected on barium studies [21].

Although the presence of mucosal plaques should be highly suggestive of *Candida* esophagitis, glycogenic acanthosis also may be manifested radiologically by plaques or nodules in the esophagus (Fig. 10) [22, 23]. Glycogenic acanthosis is a benign, degenerative condition characterized by accumulation of cytoplasmic glycogen in squamous epithelial cells lining the esophagus [22, 23]. However, it rarely causes esophageal symptoms, so that the clinical history is extremely helpful in distinguishing this condition from *Candida* esophagitis. Occasionally, an undissolved effervescent agent, air bubbles, or debris in the esophagus can also be mistaken for the plaques of candidiasis. If an artifact is suspected, however, additional double-contrast radiographs should be obtained to demonstrate the transient nature of these findings.

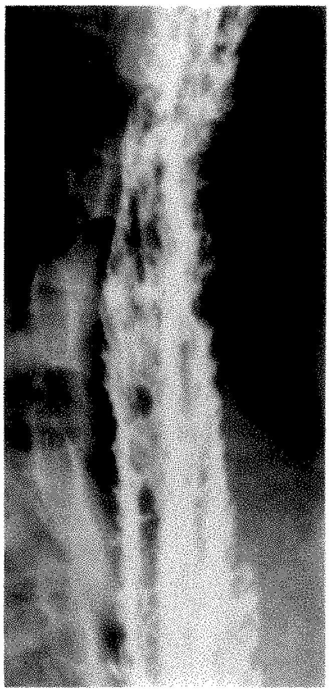

Fig. 9.—Double-contrast esophagogram in patient with AIDS shows severe *Candida* esophagitis with shaggy esophagus owing to multiple coalescent pseudomembranes and plaques.

Herpes esophagitis.—Herpes esophagitis is initially manifested by esophageal blisters or vesicles that subsequently rupture to form discrete, punched-out ulcers on the mucosa. Although esophageal vesicles rarely have been demonstrated on radiologic examinations, discrete, superficial ulcers may be visualized on double-contrast esophagograms in more than 50% of patients with endoscopically proved herpes esophagitis [24]. These ulcers may have a punctate, linear, ringlike, or stellate configuration and often are surrounded by a radiolucent halo of edematous mucosa (Fig. 11) [20, 24–26]. The ulcers can be clustered together in the mid esophagus or widely separated by normal mucosa. In the appropriate clinical setting, the presence of discrete ulcers on an otherwise normal mucosa should be highly suggestive of herpes esophagitis, as ulceration almost always occurs on a background of diffuse plaque formation in patients with candidiasis [18, 20].

Although discrete ulcers are characteristic of herpes esophagitis, other conditions such as drug-induced esophagitis, reflux esophagitis, and, less frequently, Crohn disease may produce similar findings. Oral medications, particularly tetracycline and doxycycline, may produce a focal contact esoph-

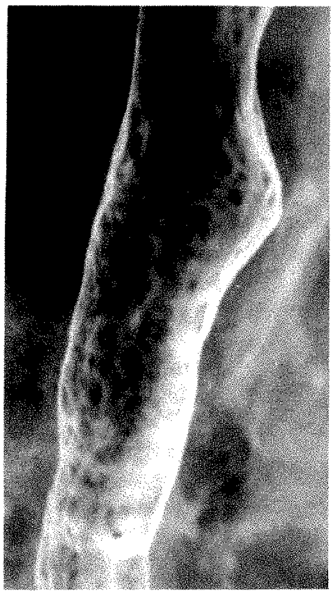

Fig. 10.—Glycogenic acanthosis with multiple plaquelike lesions in mid esophagus, mimicking appearance of *Candida* esophagitis. However, this patient had no esophageal symptoms. (Reprinted with permission from Levine [21].)

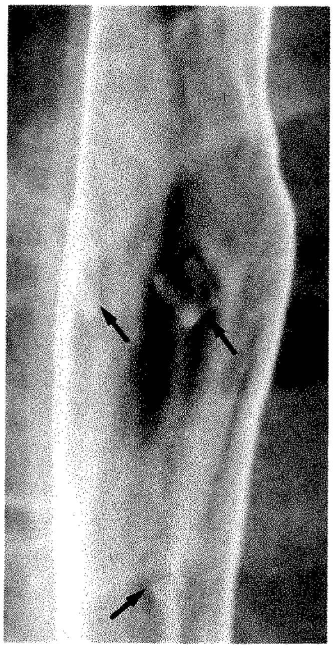

Fig. 12.—Double-contrast esophagogram in patient with drug-induced esophagitis shows several shallow ulcers (*arrows*) in mid esophagus. Although herpes esophagitis could produce similar findings, the correct diagnosis was suggested by the patient's recent history of ingesting doxycycline.

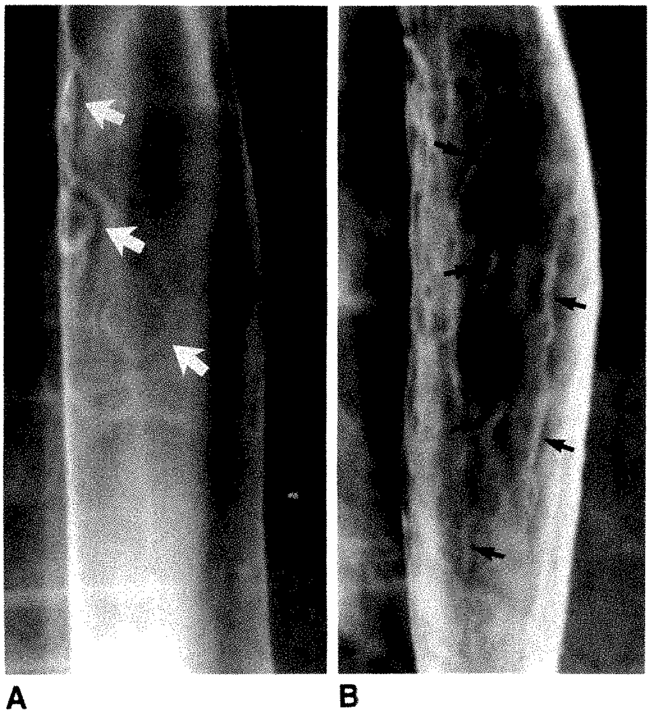

Fig. 11.—Herpes esophagitis with ulcers.

A, Double-contrast esophagogram shows discrete, widely separated ulcers (*arrows*) in mid and distal esophagus on otherwise normal background mucosa. Ringlike appearance of some ulcers is due to barium coating rim of crater.

B, Different patient with multiple linear and serpiginous ulcers (*arrows*). (Reprinted with permission from Levine [21].)

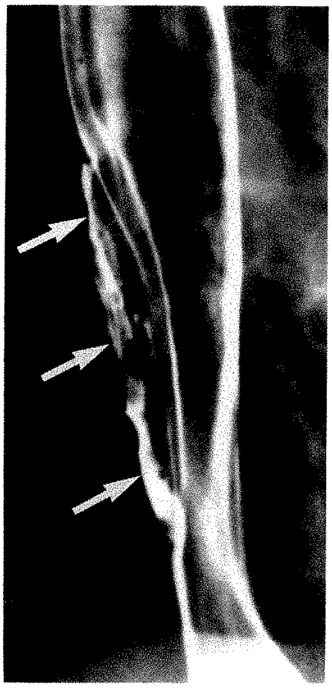

Fig. 13.—Patient with AIDS and cytomegalovirus esophagitis. Double-contrast esophagogram shows giant, relatively flat ulcer (*arrows*) in distal esophagus. Because herpetic ulcers rarely become so large, this finding should be highly suggestive of cytomegalovirus infection in patients with AIDS. (Courtesy of P. C. Freeny, Seattle, WA.)

agitis with superficial ulceration, most frequently in the mid esophagus at the level of the aortic arch or left main bronchus (Fig. 12) [27, 28]. Although the radiologic findings may be indistinguishable from those of herpes esophagitis, a history of recent drug ingestion should suggest the correct diagnosis. The ulcers of reflux esophagitis almost always can be distinguished from the ulcers of herpes esophagitis by their characteristic location in the distal esophagus at or near the gastroesophageal junction. Rarely, esophageal involvement by Crohn disease can be manifested by discrete aphthous ulcers in the esophagus [29, 30]. However, these patients almost always have associated Crohn disease involving the lower gastrointestinal tract, so that this diagnosis should be considered only if there is known Crohn disease in the small bowel or colon.

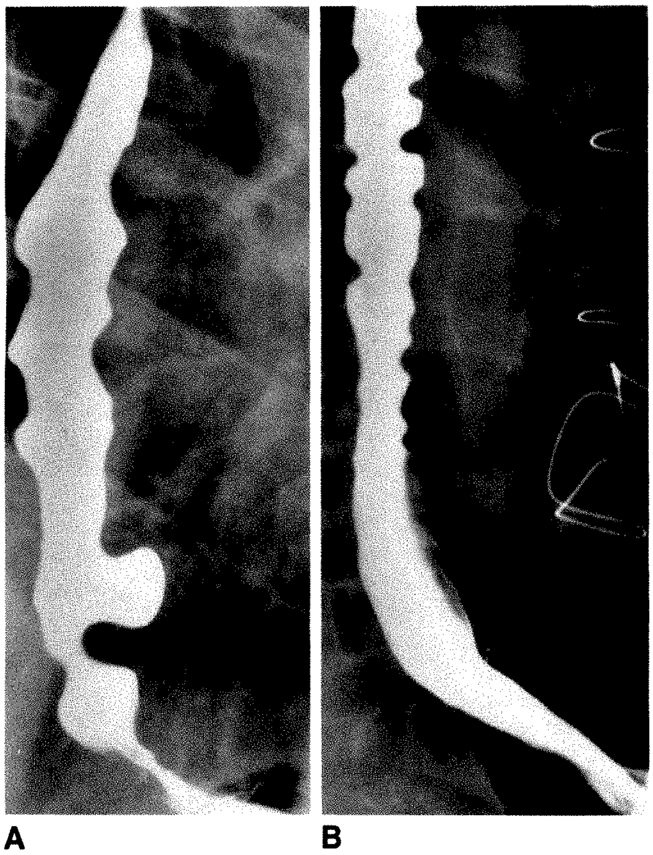

Fig. 14.—Nonspecific esophageal motility disorder (NEMD).
***A*, Spot film of esophagus in patient without esophageal symptoms shows simultaneous tertiary contractions. This patient had intermittent disruption of primary peristalsis at fluoroscopy. NEMD was diagnosed manometrically.**
***B*, Spot film of disrupted primary peristalsis with tertiary contractions in another patient with NEMD. Clinical and manometric correlation is needed to distinguish this disorder from diffuse esophageal spasm.**

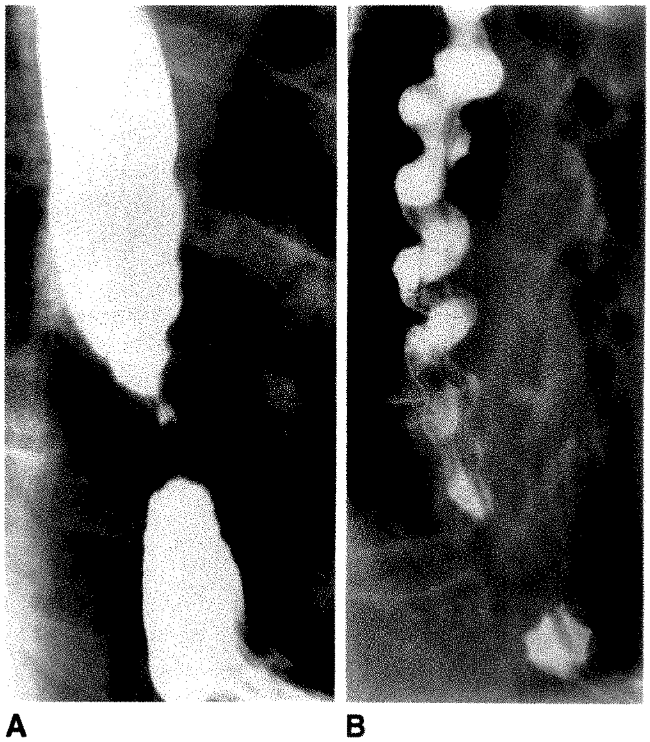

Fig. 15.—Diffuse esophageal spasm (DES).
***A*, Spot film of esophagus in patient with DES shows disrupted peristalsis with obliterative focal contraction in lower esophagus.**
***B*, Spot film of another patient with DES shows typical "corkscrew" or "curling" appearance.**

Cytomegalovirus (CMV) esophagitis.—CMV is another member of the herpes virus group that has recently been recognized as a cause of opportunistic esophagitis in patients with AIDS. CMV esophagitis may also be manifested radiologically by discrete, superficial ulcers in the mid or distal esophagus [31–33]. In other patients, however, CMV may lead to the development of one or more large, relatively flat ulcers, surrounded by a radiolucent rim of edematous mucosa (Fig. 13) [20, 31, 33]. Because ulcers in herpes esophagitis rarely become this large, the presence of one or more giant esophageal ulcers should be highly suggestive of CMV esophagitis in patients with AIDS. However, endoscopic brushings, biopsies, or cultures are required for a definitive diagnosis.

Conclusions

The double-contrast esophagogram is a valuable technique for diagnosing opportunistic esophagitis. The presence of mucosal plaques should suggest *Candida* esophagitis, whereas discrete ulcers should suggest herpes esophagitis, and one or more large, relatively flat ulcers should suggest CMV esophagitis, particularly in patients with AIDS. Thus, fungal and viral esophagitis often can be differentiated by their characteristic features on double-contrast radiographs, eliminating the need for endoscopic intervention [21]. Nevertheless, endoscopy may be required for a definitive diagnosis if the radiologic findings are equivocal or if appropriate treatment with antifungal or antiviral agents fails to produce an adequate clinical response in these patients.

Esophageal Motility Disorders as a Cause of Chest Pain

Recurrent chest pain is a serious complaint because of the possibility of cardiac disease. Patients often remain anxious even after reasonable exclusion of coronary artery disease, making evaluation of a noncardiac cause of the pain paramount. The enormity of this problem is evident by the finding of normal coronary arteries at cardiac catheterization in up to 30% of patients with anginal symptoms [34]. Structural and functional esophageal abnormalities are potential causes of noncardiac chest pain. This discussion concerns esophageal motility disorders as a possible explanation of anginalike symptoms and the contribution of radiologic evaluation.

Clinical Perspective

To place this clinical problem into perspective, an algorithm can be suggested for evaluating all patients with recurrent

P24,460

chest pain. Cardiac disease must be excluded first, because about 70–80% of those with anginalike chest pain will have coronary artery disease [35]. Only 10–15% will have an esophageal cause, which may include structural disease, gastroesophageal reflux, or a motility disorder. Structural disease of the esophagus, such as neoplasm or esophagitis, is diagnosed by endoscopic or radiologic examination, which is done next if the chest pain is believed to be of noncardiac origin.

If cardiac disease and a structural esophageal disorder have been excluded, the presence of gastroesophageal reflux as a cause of chest pain is then evaluated. About 40% of patients with symptomatic reflux will have normal esophageal mucosa at endoscopy, and even about 40% of those with endoscopic esophagitis do not show radiologic abnormalities [36]. These patients with reflux disease and normal esophageal mucosa need to be identified by histologic examination, acid perfusion testing, or prolonged pH monitoring of the lower esophagus. Indeed, ambulatory pH monitoring for 24 hr is the simplest and most sensitive means of diagnosing abnormal gastroesophageal reflux [37].

After these exclusions, a small minority of patients remain for whom an esophageal functional disorder might explain their chest pain. In a recent study of 910 patients with noncardiac chest pain, only 255 (28%) had abnormal esophageal motility on manometric examination [38]. Nutcracker esophagus (122/255), nonspecific esophageal motility disorder (NEMD) (92/255), and diffuse esophageal spasm (DES) (26/255) accounted for 94% of the abnormal manometric diagnoses. Achalasia, which more often presents with dysphagia and is the motility disorder best detected radiologically [39], was rare (5/255) in patients with chest pain. A hypertensive lower esophageal sphincter was uncommon (10/255), but it is a controversial entity without radiologic findings [40].

Radiologic Evaluation

The role of radiologic evaluation of abnormal esophageal motility as a cause of chest pain will apply to a small proportion of these patients, especially if cardiac disease has not been excluded. Most patients with noncardiac chest pain have normal esophageal motility on manometric examination [38]. Proper fluoroscopic observation accurately assesses normal esophageal peristalsis with reported specificities of 91–95% [41–43]. Multiple single swallows of barium must be observed with the patient prone to determine the actual prevalence of primary peristalsis. The use of five separate swallows is recommended and has shown a 92% agreement with synchronous manometric evaluation [43].

Radiologic detection of esophageal motility disorders depends on the disorder being evaluated and on the quality of the examination done. In the previously quoted manometric study of 910 patients with noncardiac chest pain, nutcracker esophagus was present in 48% of those with abnormal motility [38]. Nutcracker esophagus is a manometric diagnosis showing normal peristalsis but high-amplitude lower esophageal contractions. Radiologic examination is normal, although nonspecific tertiary contractions are seen occasionally [44]. NEMD accounted for 36% of abnormal manometric diagnoses, and is a catchall term to describe those motility disturbances that defy specific classification. Radiologic findings in NEMD are also nonspecific and include primary peristaltic disturbance and tertiary contractions (Fig. 14). In our retrospective experience, about half of NEMD cases are detected radiologically [42]. DES was responsible for only 10% of abnormal manometric findings, and is seen as intermittent absence of peristalsis with spontaneous, repetitive nonperistaltic contractions on fluoroscopic examination (Fig. 15). The reported radiologic sensitivity in DES is about 75% [45], although with careful fluoroscopic observation of five single swallows, detection of NEMD and DES probably would improve [43].

With these detection rates and the spectrum of motility disorders seen in the 255 patients with noncardiac chest pain, the overall radiologic sensitivity in this selected population translates to nearly 30% (71/255). What are the general implications of this sensitivity rate for the role of radiologic evaluation of esophageal motility in patients with chest pain? If 1000 patients presented with anginalike chest pain, cardiac disease would be found in approximately 750, esophageal disorders in 150, and miscellaneous causes in 100. Structural esophageal disease and gastroesophageal reflux would account for most causes of esophageal origin, leaving perhaps 50 patients with motility disorders on manometric examination. Of these 50 patients, about 15 cases would be detected radiologically for an overall return of 1.5% (i.e., 15/1000). Indeed, the radiologic examination has greater impact in diagnosing normal motility and the presence of structural abnormalities of the esophagus.

Caveats and Conclusions

Several caveats in this scenario must be mentioned. First, the concept of "microvascular angina" warrants discussion, since some patients with small-vessel disease and normal coronary arteries on angiography would be categorized as having noncardiac chest pain [34]. These patients would dilute the pool of those with a potential esophageal cause of chest pain. The relative importance of microvascular angina in this analysis is not known. Second, as patients age, the chance of coexisting cardiac and esophageal disease increases and may confuse the attribution of symptoms. Finally, recognition of abnormal esophageal motility does not prove an esophageal origin for the chest pain [35]. Most patients with chest pain and abnormal motility do not have symptoms at the time of manometric or radiologic examination, and only a minority respond to provocative testing with acid perfusion or drugs, such as edrophonium. Furthermore, prolonged ambulatory monitoring of esophageal function has shown changing motility patterns, questioning the validity of the short temporal sampling of esophageal function done with most standard manometric examinations.

In conclusion, the efficacy of the radiologic examination of the esophagus is related, in part, to the presenting complaint of the patient. Dysphagia is more effectively evaluated radiologically because structural disease is often found and achalasia is an important component of the spectrum of abnormal motility [39]. However, only a minority of those with recurrent chest pain will have symptoms originating in the esophagus. Structural disease and gastroesophageal reflux account for most esophageal causes of chest pain. This leaves only a small fraction of patients in whom abnormal esophageal motility is a potential source of their pain, and the radiologic examination is normal in many of these patients.

REFERENCES

1. Rubesin SE, Glick SN. The tailored double-contrast pharyngogram. *Crit Rev Diagn Imaging* **1988**;28:133–179
2. Ekberg O, Nylander G. Double contrast examination of the pharynx. *Gastrointest Radiol* **1985**;10:263–271
3. Rubesin SE, Jessurun J, Robertson D, Jones B, Bosma JF, Donner MW. Lines of the pharynx. *RadioGraphics* **1987**;7:217–237
4. Gromet M, Homer MJ, Carter BL. Lymphoid hyperplasia at the base of the tongue. *Radiology* **1982**;144:825–828
5. Levine MS, Rubesin SE. Radiologic investigation of dysphagia. *AJR* **1990;**154:1157–1163
6. Rubesin SE, Jones B, Donner MW. Contrast pharyngography: the importance of phonation. *AJR* **1987**;148:269–272
7. Jing BS. The pharynx and larynx: roentgenographic technique. *Semin Roentgenol* **1974**;9:259–265
8. Balfe DM, Heiken JP. Contrast evaluation of structural lesions of the pharynx. *Curr Probl Diagn Radiol* **1986**;15:73–160
9. Seaman WB. Contrast radiography in neoplastic disease of the larynx and pharynx. *Semin Roentgenol* **1974**;9:301–309
10. Jing BS. Roentgen examination of the larynx and hypopharynx. *Radiol Clin North Am* **1970**;8:361–386
11. Silver CE. Surgical management of neoplasms of the larynx, hypopharynx and cervical esophagus. *Curr Probl Surg* **1977**;14:2–69
12. Dockerty MD, Parkhill EM, Dahlin DC, Woolner LB, Soule EH, Harrison EG. *Tumors of the oral cavity and pharynx*. Washington, DC: Armed Forces Institute of Pathology, **1968**
13. Apter AJ, Levine MS, Glick SN. Carcinoma of the base of the tongue: diagnosis using double-contrast radiography of the pharynx. *Radiology* **1984**;151:123–126
14. Semenkovich JW, Balfe DM, Weyman PJ, Heiken JP, Lee JKT. Barium pharyngography: comparison of single and double contrast. *AJR* **1985**; 144:715–720
15. Wagonfeld DJH, Harwood AR, Bryce DP, et al. Secondary primary respiratory tract malignant neoplasms in supraglottic carcinoma. *Arch Otolaryngol Head Neck Surg* **1981**;107:135–137
16. Goldstein HM, Zornoza J. Association of squamous cell carcinoma of the head and neck with cancer of the esophagus. *AJR* **1978**;131:791–794
17. Thompson WM, Oddson TA, Kelvin F, Daffner R, Postlethwait RW. Synchronous and metachronous squamous cell carcinoma of the head, neck, and esophagus. *Gastrointest Radiol* **1978**;3:123–127
18. Levine MS, Macones AJ, Laufer I. *Candida* esophagitis: accuracy of radiographic diagnosis. *Radiology* **1985**;154:581–587
19. Vahey TN, Maglinte DDT, Chernish SM. State-of-the-art barium examination in opportunistic esophagitis. *Dig Dis Sci* **1986**;31:1192–1195
20. Levine MS, Woldenberg R, Herlinger H, Laufer I. Opportunistic esophagitis in AIDS: radiographic diagnosis. *Radiology* **1987**;165:815–820
21. Levine MS. Infectious esophagitis. In: Levine MS, ed. *Radiology of the esophagus*. Philadelphia: Saunders, **1989**:49–71
22. Berliner L, Redmond P, Horowitz L, Ruoff M. Glycogen plaques (glycogen acanthosis) of the esophagus. *Radiology* **1981**;141:607–610
23. Glick SN, Teplick SK, Goldstein J, Stead JA, Zitomer N. Glycogen acanthosis of the esophagus. *AJR* **1982**;139:683–688
24. Levine MS, Loevner LA, Saul SH, Rubesin SE, Herlinger H, Laufer I. Herpes esophagitis: sensitivity of double-contrast esophagography. *AJR* **1988**:151:57–62
25. Levine MS, Laufer I, Kressel HY, Friedman HM. Herpes esophagitis. *AJR* **1981**:136:863–866
26. Agha FP, Lee HH, Nostrant TT. Herpetic esophagitis: a diagnostic challenge in immunocompromised patients. *Am J Gastroenterol* **1986**;81: 246–253
27. Creteur V, Laufer I, Kressel HY, et al. Drug-induced esophagitis detected by double-contrast radiography. *Radiology* **1983**;147:365–368
28. Bova JG, Dutton NE, Goldstein HM, Hoberman LJ. Medication-induced esophagitis: diagnosis by double contrast esophagography. *AJR* **1987**; 148:731–732
29. Gohel V, Long BW, Richter G. Aphthous ulcers in the esophagus with Crohn colitis. *AJR* **1981**;137:872–873
30. Degryse HRM, DeSchepper AM. Aphthoid esophageal ulcers in Crohn's disease of ileum and colon. *Gastrointest Radiol* **1984**;9:197–201
31. Balthazar EJ, Megibow AJ, Hulnick DH. Cytomegalovirus esophagitis and gastritis in AIDS. *AJR* **1985**;144:1201–1204
32. Teixidor HS, Honig CL, Norsoph E, Albert S, Mouradian JA, Whalen JP. Cytomegalovirus infection of the alimentary canal: radiologic findings with pathologic correlation. *Radiology* **1987**;163:317–323
33. Balthazar EJ, Megibow AJ, Hulnick D, Cho KC, Berenbaum E. Cytomegalovirus esophagitis in AIDS: radiographic features in 16 patients. *AJR* **1987**;149:919–923
34. Richter JE, Bradley LA, Castell DO. Esophageal chest pain: current controversies in pathogenesis, diagnosis, and therapy. *Ann Intern Med* **1989**; 110:66–78
35. Richter JE. Noncardiac chest pain: use of esophageal manometry and provocative tests. In: Castell DO, Richter JE, Dalton CB, eds. *Esophageal motility testing*. New York: Elsevier, **1987**:143–155
36. Ott DJ. Barium esophagram. In: Castell DO, Wu WC, Ott DJ, eds. *Gastroesophageal reflux disease: pathogenesis, diagnosis, therapy*. Mount Kisco, NY: Futura, **1985**:109–128
37. Wiener GJ, Morgan TM, Cooper JB, et al. Ambulatory 24-hour esophageal pH monitoring: reproducibility and variability of pH parameters. *Dig Dis Sci* **1988**;33:1127–1133
38. Katz PO, Dalton CB, Richter JE, Wu WC, Castell DO. Esophageal testing in patients with noncardiac chest pain or dysphagia. *Ann Intern Med* **1987**;106:593–597
39. Ott DJ. Radiologic evaluation of esophageal dysphagia. *Curr Probl Diagn Radiol* **1988**;17:1–33
40. Waterman DC, Dalton CB, Ott DJ, et al. Hypertensive lower esophageal sphincter: what does it mean? *J Clin Gastroenterol* **1989**;11:139–146
41. Dodds WJ. Current concepts of esophageal motor function: clinical implications for radiology. *AJR* **1977**;128:549–561
42. Ott DJ, Richter JE, Chen YM, Wu WC, Gelfand DW, Castell DO. Esophageal radiography and manometry: correlation in 172 patients with dysphagia. *AJR* **1987**;149:307–311
43. Ott DJ, Chen YM, Hewson EG, et al. Esophageal motility: assessment with synchronous video tape fluoroscopy and manometry. *Radiology* **1989**;173:419–422
44. Ott DJ, Richter JE, Wu WC, Chen YM, Gelfand DW, Castell DO. Radiologic and manometric correlation in "nutcracker esophagus." *AJR* **1986**;147: 692–695
45. Chen YM, Ott DJ, Hewson EG, et al. Diffuse esophageal spasm: radiographic and manometric correlation. *Radiology* **1989**;170:807–810

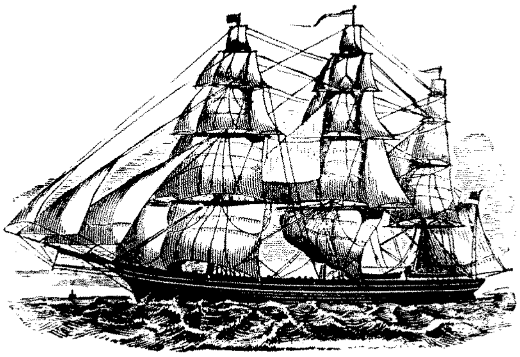

Come to the
American Roentgen Ray Society

91st

ANNUAL MEETING

Boston, MA

Sheraton Boston Hotel
May 5-10, 1991

Scientific Program (200 papers)
Instructional Courses (60 hours)
Categorical Course on Body MR Imaging
The Caldwell Lecture
Award Papers
Scientific Exhibits
Social, Golf, and Tennis Programs
Guest Programs

Review Article

Iron Oxide–Enhanced MR Imaging of the Liver and Spleen: Review of the First 5 Years

Joseph T. Ferrucci[1] and David D. Stark

Superparamagnetic iron oxide (SPIO) particles are a potent new class of MR contrast agents affording improved detection of hepatic and splenic neoplasms. In this report we review the development of this agent through preclinical studies and early clinical results at Massachusetts General Hospital during a 5-year investigation. SPIO particles are sequestered by normal phagocytic Kupffer cells of the reticuloendothelial system (RES) but are not retained in tumor tissue. Consequently, there is a fivefold increase in T2 relaxation between normal RES tissue and tumor, with a comparable advantage in quantitative signal-to-noise ratio, contrast-to-noise ratio, and lesion detectability in the liver and spleen on MR imaging. Increased lesion conspicuity can be exploited to decrease threshold size for lesion detection to less than 3 mm. Clinically beneficial effects occur with a variety of mildly T2-weighted spin-echo pulse sequences; gradient-echo techniques show even greater benefit after administration of SPIO. Metabolically, pharmaceutical-grade preparations are biodegradable and bioavailable, being rapidly turned over into body iron stores and incorporated into erythrocyte hemoglobin. Early dose-escalation clinical trials have identified a probable clinical dose range of 10–20 μmol Fe/kg body weight. In the United States, SPIO compounds evaluated to date are still approved for use in investigational studies only. Newer commercial formulations currently being evaluated may extend clinical safety margins.

Iron oxide, in the form of superparamagnetic particles, is a powerful tissue-specific MR contrast agent used for enhanced detection of tumors in the liver and spleen. Extensive preclinical studies at the Massachusetts General Hospital from 1985 through 1988 elucidated the biological and pharmaceutical principles for MR imaging [1–7] and led to the first clinical trial in 1988, in which greatly enhanced detection of liver lesions was confirmed [8]. Additional clinical trials are now in progress in the United States as well as in France, Belgium, and Japan, and early results from one European center recently have been reported [9]. The potential benefits of superparamagnetic iron oxide (SPIO) particles have been widely recognized by the MR contrast media research community, but, in the United States, these agents are still approved for use only in investigational studies.

This article reviews the development of iron oxide–enhanced MR imaging of the liver and spleen during the past 5 years. The emphasis is on work carried out by the Division of Gastro-Intestinal Radiology at the Massachusetts General Hospital.

Superparamagnetic Iron Oxide: Physical Properties

SPIO particles are crystalline structures with the general formula $Fe^{3+}{}_2O_3M^{2+}O$, where M^{2+} is a divalent metal ion like iron, manganese, nickel, cobalt, or magnesium. SPIO is similar to magnetite, a naturally occurring ferrite, in which the metal ion (M^{2+}) is ferrous iron (Fe^{2+}) with the formula Fe_3O_4 (Fig. 1).

Received May 11, 1990; accepted after revision June 14, 1990.

Presented at the International Symposium on Liver Imaging, Harvard Medical School, Boston, June 1990.

[1] Both authors: Department of Radiology, Massachusetts General Hospital and Harvard Medical School, 55 Fruit St., Boston, MA 02115. Address reprint requests to J.T. Ferrucci.

AJR **155:943–950, November 1990** 0361–803X/90/1555–0950 © American Roentgen Ray Society

Because of its ubiquitous presence in living tissue, iron is a natural candidate for manipulation of MR signal. Indeed, the ferrite magnetite is particularly suitable because this iron oxide has been isolated from certain birds, fish, and bacteria in which its interaction with the magnetic field of the earth has been found to play a critical role in navigation [10].

Pharmaceutical-grade preparations suitable for clinical use have evolved rapidly since the earliest characterization studies of magnetic particles for possible medical applications were performed [1-3]. Superparamagnetic iron oxide crystals by themselves are 5-50 nm in size. However, these crystals are usually formed by precipitation of iron salts with coating material to form larger composite particles. The median diameter of composite particle size has been varied from the 1000-nm range used in early studies to less than 10 nm (Fig. 2). The smaller size of newer particles accelerates degradation of SPIO into paramagnetic forms of iron. Biocompatible coatings such as starch (dextran), protein, glycoprotein, or lipid allow safe IV administration and ready biodegradability. The compound used in our initial clinical trials was a stable colloidal aqueous suspension of iron oxide-dextran, reddish brown to black, formulated at 0.2 mmol/l Fe and designated AMI-25 or Feridex (Advanced Magnetics, Inc., Cambridge, MA).

The magnetic properties of these materials were first referred to as superparamagnetic in 1955 [11]. The term refers to the extremely large magnetic moments they acquire when placed in external magnetic fields. This sensitivity to magnetic fields is the result of the crystalline matrix, which facilitates the alignment of adjoining spins to an applied field. This is so efficient that even at low field strengths all available spins can be recruited, and no further gain in magnetization is achieved by increasing the applied field strength. Superparamagnetic materials differ from ferromagnetic substances because, like diamagnetic and paramagnetic materials, they do not retain any magnetization once the external field is removed. In contrast, once magnetized, ferromagnetic materials show remanence (i.e., remain partially magnetized even in the absence of an applied field), and therefore are used as recording materials and to make permanent magnets.

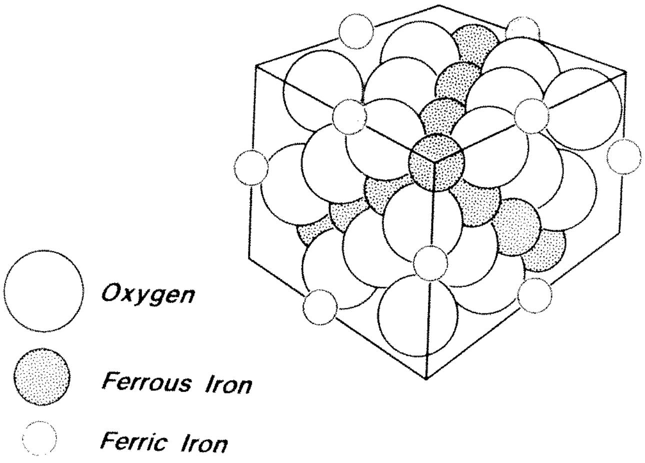

Fig. 1.—Drawing shows spinel crystal structure characteristic of superparamagnetic iron oxides.

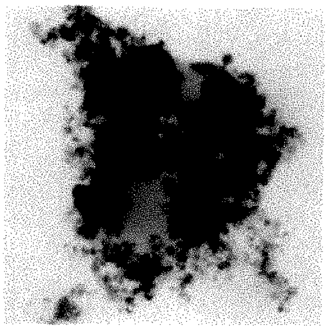

Fig. 2.—Electron micrograph of superparamagnetic iron oxide particle (M4125, Advanced Magnetics, Inc., Cambridge, MA) magnified ×82,000 shows an irregularly shaped structure approximately 1 μm in size. Particle shape and size are stabilized by coating a cluster of iron oxide crystals with a hydrophilic polymer. Individual superparamagnetic ferrite crystals can be seen. (Reprinted with permission from Saini et al. [1].)

In tissue, the large magnetic moments associated with superparamagnetic iron particles result in local magnetic field inhomogeneities. Diffusion of water through these local field disturbances produces rapid proton dephasing, which results in preferential shortening of transverse relaxation time, T2, with little effect on longitudinal relaxation time, T1. The T2 relaxivity (R2) of 1×10^5 sec^{-1} $(\text{mol/l})^{-1}$ and T1 relaxivity (R1) of 3×10^4 sec^{-1} $(\text{mol/l})^{-1}$ of iron oxide are substantially larger than the relaxation of paramagnetic molecules such as gadopentetate dimeglumine: $R2 = 6 \times 10^3$ and $R1 = 4 \times 10^3$ sec^{-1} (mol/l^{-1}) [1-7].

Superparamagnetic Iron Oxide: Physiologic Considerations

Pharmacokinetic behavior of SPIO is generally comparable in animals and humans [1-7]. The injected particles are smaller than erythrocytes (which are approximately 7 μm in diameter), so they successfully traverse capillary beds in the lung, brain, heart, and kidney. Particles are promptly sequestered by the reticuloendothelial system (RES). The RES cells have a scavenging function and, by phagocytosis, readily remove particulate materials from the circulation. AMI-25 shows a blood clearance half-life of about 10 min with uptake by hepatic RES Kupffer cells accounting for 80% of the injected dose [1-7]. Thus, T2 relaxation times of blood, liver, and spleen decrease promptly after IV injection, but only blood quickly returns to normal. The extremely powerful effect that SPIO particles have on proton relaxation is attested to by the observation that even in minute doses (8 μmol/kg), which are located in a very small (approximately 2%) portion of the hepatic cellular volume (i.e., Kupffer cells), there is essentially complete signal loss from the entire liver.

Because neoplastic tumor nodules are devoid of the phagocytic Kupffer cells, they do not sequester SPIO (Fig. 3). As a consequence, the signal difference between normal RES tissue and tumor is greatly enhanced. After administration of SPIO, no change occurs in relaxation times of tumor, whereas normal liver shows an almost threefold decrease in T2. The resulting difference in T2 relaxation between tumor and liver, expressed as a percentage of T2 of normal liver, increased from 49% to 280% in ex vivo studies of a rat liver-tumor model [2].

To date, newer formulations of SPIO have been evaluated in animals only. Ferrosomes are a class of SPIO encapsulated

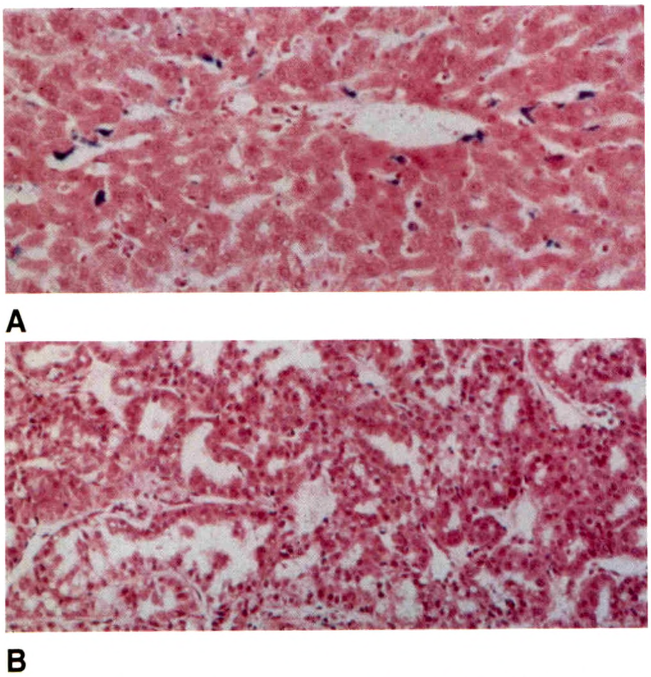

Fig. 3.—Reticuloendothelial sequestration of IV administered superparamagnetic iron oxide particles in normal liver but not in tumor tissue.

***A* and *B*, Light microscopic sections of normal rat liver (*A*, ×320) and tumor tissue (*B*, ×200) stained for iron (Prussian blue). Superparamagnetic iron oxide particles are stained blue and can be identified readily in hepatic reticuloendothelial cells. No such particles are present in hepatocytes or in tumor tissue. (Reprinted with permission from Saini et al. [2].)**

in lipid vesicles (liposomes) developed by Vestar, Inc. (San Dimas, CA) that have prolonged blood circulation (clearance half-life, 4 hr). Prolonged circulation allows increased delivery of SPIO to tissues other than the liver and spleen. For example, ferrosomes show distribution to macrophages located at the periphery of tumors [12].

Metabolically, AMI-25 iron is biodegradable and bioavailable, being rapidly turned over into the body iron stores and incorporated into erythrocytes as hemoglobin [6]. In studies that used light microscopy, stainable iron disappears from rat liver within 2 weeks, whereas radiolabeled ^{59}Fe iron oxide shows a liver-spleen half-life of 3–4 days [7]. With in vivo MR imaging in animals as well as humans, liver signal blackening shows a reversal toward normal baseline tissue characteristics over 3–7 days [1, 8].

Bioavailability is demonstrated by the incorporation of molecular iron into hemoglobin after administration of ^{59}Fe AMI-25. Twenty percent of radiolabeled iron is found in hemoglobin 14 days after IV administration. Similar rates of erythrocyte incorporation (21%) occur with administration of radiolabeled ferritin. Bioavailability is shown also by the ability of SPIO to reverse iron-deficiency anemia in rats to an extent similar to that of hematinic iron-dextran [6].

Extensive toxicity studies in animals have disclosed no acute toxic effects (LD_{50} in rats) or chronic injury at doses greater than 100 times the clinically effective dose of 20 μm Fe/kg body weight [3, 6]. Even at the subcellular level, when a massive dose of 250 mg Fe/kg was given to rats, Bacon et al. [3] were unable to detect hepatic mitochondrial dysfunction or microsomal lipid peroxidation, both sensitive biochemical indicators of iron-induced hepatotoxicity. Despite the large increase in hepatic iron concentrations at 10 weeks after SPIO administration, biochemical and morphologic studies give no evidence of chronic injury.

Toxicity in Humans

Despite these wide margins of safety in animals, dose escalation in human clinical trials with AMI-25 has shown dose-dependent acute hypotensive reactions when more than 40 μmol/kg is administered at rates greater than 1000 μmol/min [8]. So far, in the United States, 40 patients have received 20 μmol Fe/kg administered at the recommended rate of 200 μmol/min, and in only one patient was there a drop in systolic blood pressure of 20 mm Hg; no treatment was required. The mechanism of these adverse reactions is unknown. They have been reversed by infusions of saline. Further clinical trials are being conducted to explore safety and efficacy. Newer formulations with enhanced safety profiles can be anticipated also, but currently all SPIO compounds have investigational status in the United States.

Effects on MR Imaging

Numerous beneficial effects of SPIO MR contrast agents have been documented with in vivo imaging. Liver and spleen signal intensity decreases, whereas tumor nodules are displayed as areas of bright signal intensity with a variety of pulse sequences (Fig. 4) [2]. Quantitative measurements of signal-to-noise ratio (SNR) and contrast-to-noise ratio (CNR) show marked enhancement after SPIO (Table 1). Maximal decrease in signal from liver occurs on more heavily T2-weighted spin-echo (SE) pulse sequences (TR > 1000, TE > 50 msec), although relaxation effects can be shown by using a wide variety of sequences. Pulse sequences in which tumor and liver appear essentially isointense before SPIO, such as

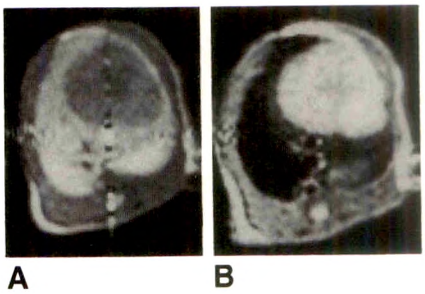

Fig. 4.—Effects of superparamagnetic iron oxide (30 μmol Fe/kg) on liver/tumor visibility in mammary carcinoma implanted in a rat.

***A*, T1-weighted MR image, SE 500/15, shows bright signal from liver outlining tumor nodule, which has slightly longer T1 relaxation time.**

***B*, MR image, SE 500/30, obtained after administration of superparamagnetic iron oxide shows complete loss of signal intensity from normal hepatic parenchyma. Tumor nodule has slightly brighter signal compared with unenhanced image because of longer TE and greater T2 weighting. Overall liver/tumor contrast is markedly increased after administration of superparamagnetic iron oxide.**

TABLE 1: Quantitative MR Image Analysis: Contrast- and Signal-to-Noise Ratios

Pulse Sequence	Cancer SNR	Liver SNR	Spleen SNR	Cancer-Liver CNR
Unenhanced (before drug administration)				
SE 260/14	28.7 ± 17.5	39.5 ± 12.5	27.4 ± 11.4	−10.8 ± 9.6
SE 500/28	28.1 ± 10.7	31.4 ± 9.4	26.2 ± 9.4	−3.3 ± 4.4
SE 1500/40	24.6 ± 10.9	23.9 ± 9.3	25.6 ± 13.3	+0.6 ± 4.9
SE 1500/80	19.4 ± 6.3	14.9 ± 3.9	21.3 ± 6.4	+3.4 ± 3.8
Ferrite-enhanced (1–2 hr after administration)				
SE 500/28	37.3 ± 14	21.8 ± 10.6[a]	28.5 ± 11.3	+15.9 ± 7.6[a]
SE 1500/40	24.4 ± 11.6	8.1 ± 3.7[a]	11.6 ± 4.9[a]	+16.3 ± 9.6[a]
SE 1500/80	18.9 ± 10.8	4.3 ± 3.1[a]	4.8 ± 2.3[a]	+14.5 ± 9.8[a]

Note.—Adapted from Stark et al. [8]. CNR = contrast-to-noise ratio, SNR = signal-to-noise ratio.

[a] $p < .01$; ferrite-enhanced values are significantly different from unenhanced values.

SE 500/30 (TR/TE), show great increase in tumor conspicuity after SPIO.

A further beneficial effect of increased lesion conspicuity is reduction in threshold size for lesion detection. Tsang et al. [5] conducted a detailed MR imaging/pathologic correlation of mammary tumors smaller than 1 cm implanted in rat livers. They imaged 39 separate tumor nodules 1–10 mm in diameter before and after SPIO and correlated MR appearances with thin-slice necropsy measurements. With contrast enhancement, the mean threshold size for lesion detectability decreased from 1 cm to < 3 mm in diameter. This increase in sensitivity was obtained with a 0.6-T clinical MR system by using a widely available SE 500/32 pulse sequence. These investigators further noted that even these tiny millimeter-sized nodules were not obscured on imaging or underestimated in size. Comparison of actual pathologic measurements with MR images confirmed that extremely high accuracy can be expected for clinical MR assessment of lesions. Furthermore, this study showed that enhanced CNR correlates with improved detection of lesions.

Kawamura et al. [13] confirmed these results in similar studies using a slightly larger 100-nm particle obtained from a Japanese supplier. The detection rate for 89 implanted rat tumors, including some less than 2 mm in diamter, increased from 10% (9/89) before to 65% (58/89) after ferrite injection.

The breadth of clinically advantageous SPIO effects with a variety of pulse sequence parameters was stressed in a study by Fretz et al. [14]. A range of conventional mildly T2-weighted SE sequences (500–1500/30–80) showed excellent enhancement of liver/tumor CNR at 0.6 T. Gradient-echo techniques, irrespective of TE and flip angle, showed the greatest benefit after administration of iron oxide. Gradient-echo techniques are well known to be exceptionally sensitive to the presence of local field inhomogeneities such as those produced by the presence of iron particles. Local magnetic field disturbances caused by the particles result in both irreversible (T2) and reversible dephasing of transverse coherence. Together, this transverse relaxation enhancement (T2* effect) causes extra signal loss detectable by gradient-echo techniques. The added sensitivity of gradient-echo methods may be superior to the exploitation of T2 effects with SE imaging. In our initial clinical study [8] we confirmed this effect in humans.

Clinical Results

Our group has imaged more than 40 patients with liver tumors at two sites by using mid-field systems (0.3 and 0.6 T); detailed analysis of the results in 15 of those patients has been reported [8]. Initially, doses of SPIO ranging from 10 to 50 μmol/kg were administered IV at a rate of 1 ml (11.2 mg Fe)/min in a dose-escalation study. On the basis of toxicity data, the recommended clinical dose for AMI-25 has been set at 10–20 μmol Fe/kg body weight. The ultimate dose of SPIO that will be allowed by the Food and Drug Administration (if approved) has yet to be established. Imaging usually has been performed within 1 hr after injection, although satisfactory clinical imaging results easily could be achieved as late as 48 hr.

Profound reduction in both liver and spleen signal intensity was seen in all patients, even as early as 5 min after SPIO administration (Fig. 5). As expected, cancer tissue was unaffected, and striking improvements in the sensitivity of lesion detection occurred when compared with unenhanced images (Fig. 6). The beneficial effect on lesion detection occurred with a range of conventional pulse sequences. Overall, the number of lesions detected after contrast administration increased from 89 to 349 on SE 500/28 images, from 21 to 325 on SE 1500/40 images, and from 20 to 271 on SE 1500/80 images (of a total of 370 lesions identified). Quantitative analyses of lesion/liver CNR values confirm the subjective visual appearances, as shown in Table 1.

In patients with known hepatic metastases, lesions smaller than 1 cm in diameter were not visible on unenhanced SE images with TRs of 500 and 1500 msec, whereas threshold size for lesion detection on unenhanced SE 260/14 images was 0.5 cm when a 0.6-T MR imaging system was used. After administration of contrast material, many lesions 0.3–1.0 cm could be detected (Fig. 7). The size threshold for lesion detectability decreased from 1.5 to 0.3 cm on SE 500/28 images, from 2.1 to 0.3 cm on SE 1500/40 images, and from 1.9 to 0.4 cm on SE 1500/80 images. These results were statistically significant at $p < .005$.

In order to provide more objective documentation of the benefits of SPIO for detection of liver cancer, quantitative comparisons of diagnostic accuracy were made by using receiver-operating-characteristic (ROC) analysis. Fretz et al.

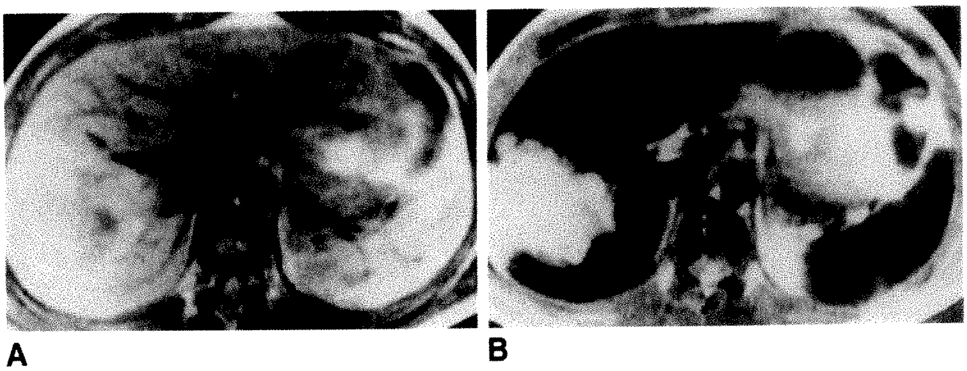

Fig. 5.—Metastatic colonic cancer.

A, Unenhanced SE 1500/40 MR image shows a mass displacing vessels in posterior segment of right hepatic lobe. Contrast between tumor and liver is low and exact margins of tumor are difficult to delineate.

B, 1 hr after IV administration of superparamagnetic iron oxide (AMI-25, 40 μmol Fe/kg). Tumor is now easily detected, sharply delineated, and distinguished from adjacent blackened liver tissue. Note corresponding signal decrement in the spleen.

(Reprinted from Weissleder et al. [15].)

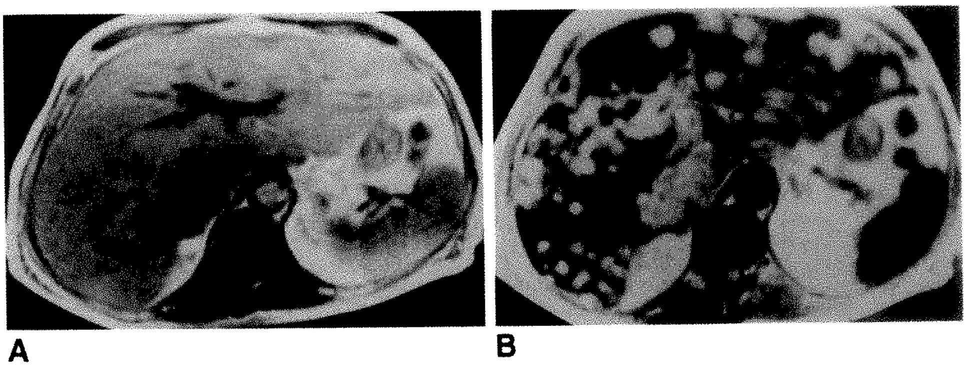

Fig. 6.—Improvement in sensitivity for lesion detection in patient with metastatic renal cell carcinoma.

A, T1-weighted SE 500/28 MR image before ferrite administration shows normal upper abdominal anatomy. Poorly defined region of low intensity is seen near caudate lobe of liver.

B, Same sequence at same anatomic level 15 min after administration of AMI-25 (20 μmol/kg). Diffuse hepatic metastases, many smaller than 0.5 cm in diameter, can be identified. Large lesion in region of caudate lobe corresponds to area of abnormal signal on unenhanced image. Note reduction in signal of spleen.

(Reprinted with permission from Stark et al. [8].)

[17] performed a controlled observer-performance test of contrast-enhanced CT, unenhanced MR, and MR after AMI-25 on 731 individual images from our clinical trial material. Contrast-enhanced MR yielded significantly better observer-performance scores than did bolus contrast-enhanced CT images, whereas enhanced SE 1500/40 and 1500/80 sequences yielded significantly greater areas under the ROC curve than did standard MR sequences. The superiority of SPIO-enhanced MR over iodine-enhanced CT and unenhanced MR imaging was statistically significant ($p < .01$) in both cases.

In a study of 15 patients in whom liver metastases were imaged at high field (1.5 T), Marchal et al. [9] found comparable quantitative gains in CNR on all sequences except heavily T2-weighted SE (2200/70) [9]. With this sequence there was only marginal benefit after SPIO administration. The optimal relation between imager field strength, pulse sequence, and SPIO needs to be clarified in future clinical studies.

Enhanced Spleen Imaging

None of the currently available techniques, including CT scanning, are very sensitive to either metastatic disease or lymphomatous involvement of the spleen. Detection of splenic deposits by MR also has been unreliable because of the similarity of spleen relaxation times (T1 and T2) and proton density to the MR characteristics of tumor tissue. As a result, there is little net difference in the tumor-spleen signal intensity on most pulse sequences. However, as in the case of hepatic metastases, SPIO selectively alters the tissue characteristics (T2) of spleen without affecting tumor, producing a marked increase in image contrast and detectability of splenic tumor deposits.

Early studies by Weissleder et al. [4] from our group showed that 4- to 6-mm splenic tumors implanted in animal models become readily visible after SPIO administration (Fig. 8). Tumors appear hyperintense against the black background of spleen tissue because, again, the SPIO is not sequestered by tumor tissue. Quantitative measurements of lesion conspicuity measured by tumor-spleen CNR ratios also showed 40- to 50-fold increases. In a subsequent series of 18 patients, SPIO-enhanced MR revealed 45 individual splenic nodules (four patients were positive) as opposed to four lesions on unenhanced images (two patients were positive) (Fig. 9) [16]. Because the effect of SPIO is less in splenic pulp than in liver, the dose of iron necessary to achieve comparable degrees of spleen blackening may be slightly larger (i.e., 20–30 μmol Fe/kg body weight).

Of perhaps even greater clinical significance is the ability of SPIO to reveal diffuse lymphomatous involvement of the spleen. In lymphoma patients, splenomegaly per se is an unreliable indicator of active neoplastic infiltrate. Our group developed techniques for SPIO-enhanced MR to detect both micronodular lymphoma and diffuse lymphoma in animal models [7]. Moreover, benign splenomegaly was differentiated by its preservation of complete blackening after SPIO, whereas spleens with diffuse malignant lymphoma showed no iron uptake. Lymphomatous spleens retained their diffuse bright signal after SPIO, presumably because RES phagocytic

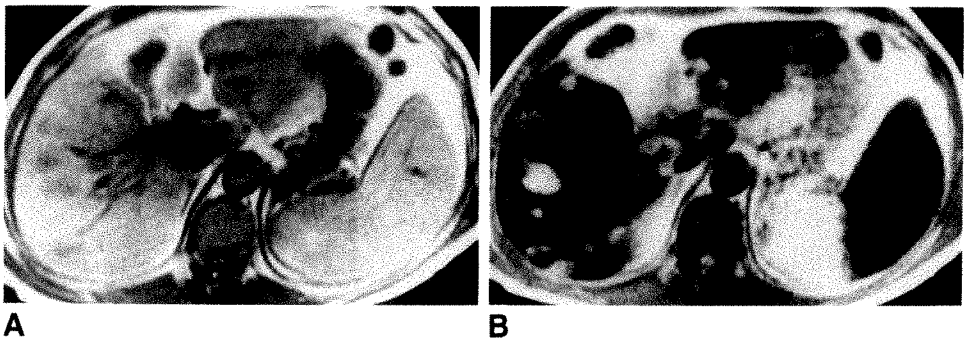

Fig. 7.—Demonstration of hepatic and splenic metastases after AMI-25 administration.

A, Unenhanced T1-weighted SE 500/28 MR image. Several 1- to 3-cm metastases are visible in right hepatic lobe. Questionable area of reduced signal intensity in medial portion of spleen was thought to be an artifact.

B, Mildly T2-weighted SE 1500/42 sequence 1 hr after injection of contrast material. Multiple additional small hepatic lesions measuring 5–10 mm are evident in both right and left hepatic lobes. In addition, entire medial portion of spleen is replaced by large solitary metastatic deposit. Splenic tumor was confirmed at splenectomy.

(Reprinted with permission from Weissleder et al. [16].)

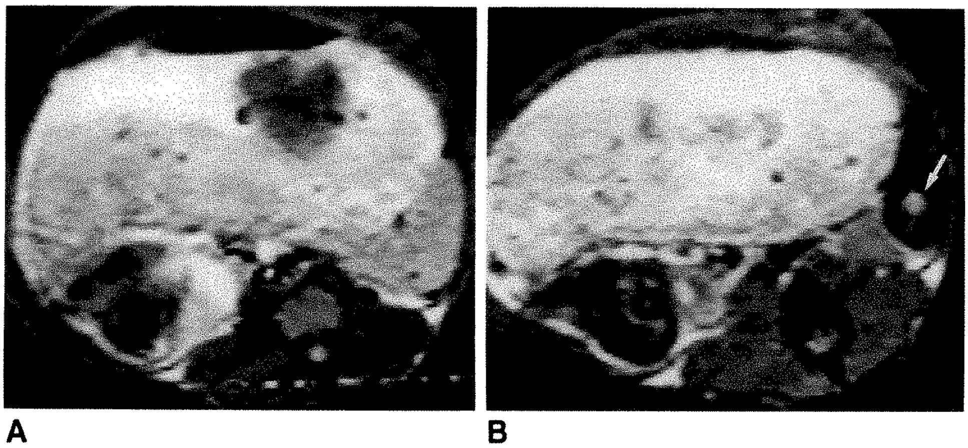

Fig. 8.—Demonstration of splenic tumor in animal model after administration of superparamagnetic iron oxide (SPIO).

A, SE 500/32 MR image before SPIO shows no abnormality within spleen.

B, After administration of SPIO, blackening of spleen parenchyma shows tumor nodule because of markedly enhanced tumor/spleen contrast (*arrow*).

activity was blocked by malignant infiltrate. In patients with normal spleens and in those with benign splenomegaly, spleen signal intensity showed the typical marked blackening after ferrite. These findings were confirmed in four subjects in a preliminary clinical investigation [15].

The results suggest that both metastatic and lymphomatous neoplasms of the spleen, whether focal or diffuse, may be diagnosed with improved accuracy with SPIO-enhanced MR images.

Cirrhosis and Hepatitis

Striking morphologic and functional effects were seen after SPIO administration in a small pilot series of seven patients with cirrhosis and active alcoholic hepatitis [18]. Cirrhotic liver tissue showed an inhomogeneous decrease in liver signal intensity with a superimposed reticular nodular pattern of thin septa of high signal intensity believed to represent collagenous bands. Splenomegaly with marked signal loss confirmed the well-known redistribution of particulate matter occurring in cirrhotic portal hypertension. Patients with active hepatitis showed a markedly reduced hepatic response to iron oxide, with effective preservation of normal signal intensity. This effect was thought to reflect diminished Kupffer cell activity. The results were considered highly promising as a means to further characterize diffuse liver disease.

Image Interpretation

As with any fundamentally new imaging technique, SPIO-enhanced MR imaging raises complex interpretative issues for the radiologist.

Because the liver turns dark on all pulse sequences, tumor nodules are always higher in signal intensity than surrounding liver. However, signal in blood vessels viewed in cross section may resemble millimeter-sized tumors. To overcome this pitfall, Hahn et al. [19] performed imaging during the first 12 min after ferrite injection while the contrast agent remains in circulation (distribution phase). They showed reduction of signal from small intrahepatic blood vessels, as the entire liver became uniformly blackened, allowing greater confidence in distinguishing tumor from vessels in cross section. Distribution-phase images showed little or no signal loss from cancer tissue. Vascular signal was restored on images at 1–2 hr (retention phase).

A further major problem in clinical cancer imaging is differentiation of malignant nodules from incidental coexisting benign tumors, especially the common cavernous hemangioma. In the same study, Hahn et al. [19] found that hemangiomas showed greater signal loss on retention-phase images (1–2 hr after injection) than did metastatic lesions (Fig. 10). Intralesional signal intensity loss of 60% or more of the unenhanced intensity was characteristic of cavernous hemangioma. These findings confirm the slower and prolonged perfusion of cav-

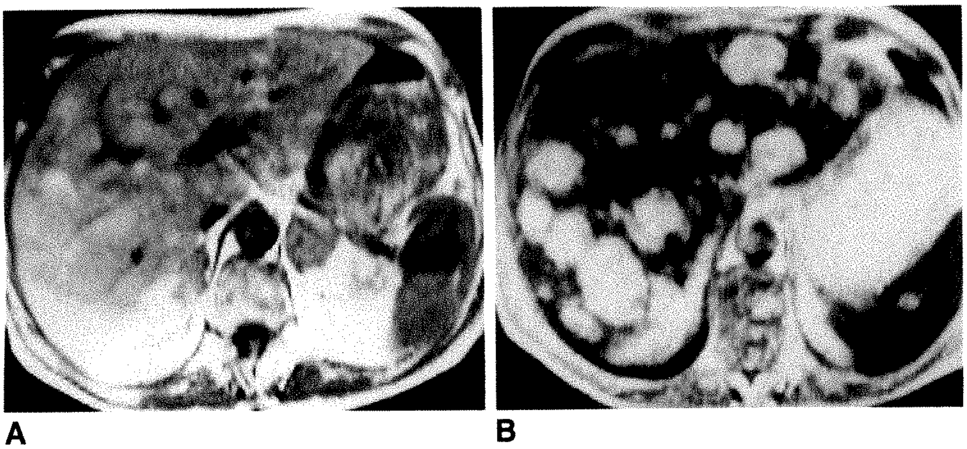

Fig. 9.—Enhanced detection of splenic tumor nodules in a patient with widespread hepatic metastases.

A, SE 1500/40 MR image faintly shows several bright-signal liver metastases. No definite abnormality is evident in spleen.

B, After AMI-25 administration, a single discrete tumor nodule is visible in spleen. Liver metastases are more visible, with numerous small subcentimeter nodules now evident.

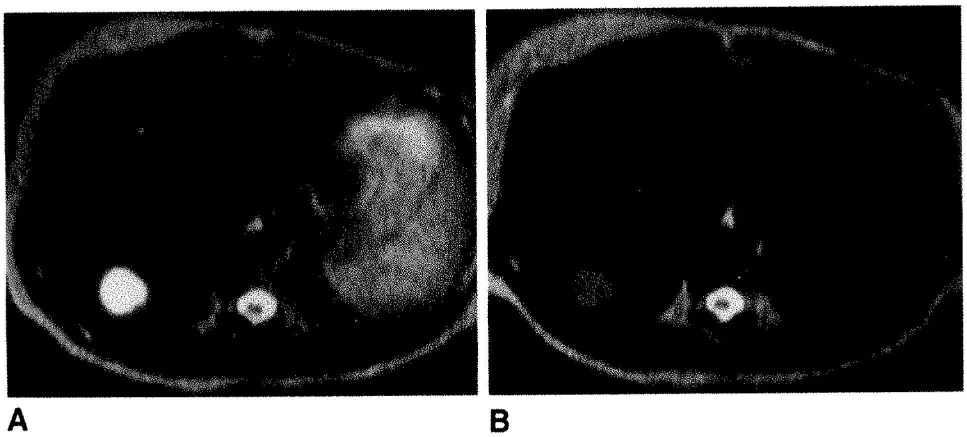

Fig. 10.—Cavernous hemangioma showing negative contrast enhancement after AMI-25 administration. The lesion was considered atypical because of poor contrast enhancement on CT.

A and *B*, Heavily T2-weighted SE 2350/180 MR images before (*A*) and 2 hr after (*B*) injection of AMI-25 (20 μmol Fe/kg). Hemangioma loses signal because of retention of agent in vascular pool of lesion. (Reprinted with permission from Hahn et al. [19].)

ernous hemangiomas observed with other imaging studies. Although SPIO perfusion effects hold great promise for providing tissue characterization, more studies are required for confirmation. Similar strategies are used to diagnose hemangiomas by blood-pool imaging of iodine (CT), ^{99m}Tc-labeled erythrocytes (nuclear medicine), or gadopentetate dimeglumine–enhanced MR.

In the context of tissue characterization by MR, there are two further caveats. First, the use of signal-intensity measurements or calculated T2 relaxation times may give spurious results when lesion/liver ratios are applied to patients in whom liver T2 is shortened by iron [20]. Specifically, the presence of exogenously administered iron oxide variably alters both hemangioma and liver signal intensities, eliminating the very long T2 of hemangiomas while changing (unpredictably) their signal-intensity ratio relative to liver.

Second, certain primary liver tumors or tumorlike conditions, such as hepatic adenoma and focal nodular hyperplasia, may contain Kupffer cells. SPIO may cause such lesions to lose signal, even in the retention phase. This would tend to obscure the lesion but might have value in suggesting a tissue-specific diagnosis.

Conclusions

The value of SPIO-enhanced MR imaging of the liver and spleen has been accepted rapidly by the medical research community. Further clinical experience must be accumulated to validate its clinical role. A first priority will be to establish a clear safety profile for the various formulations under development. New commercial formulations may extend the safety margins. Biodistribution, clearance, and protocols for clinical administration may or may not be altered for various SPIOs.

Future research directions will involve the use of SPIO for splenic neoplasia, especially lymphomas; diffuse liver diseases; bone marrow and lymph node imaging; and perfusion studies. Cardiac studies in which SPIO is combined with high-speed gradient-echo or echo planar imaging techniques offer an especially interesting possibility. The ability of these methods to permit further reduction of the SPIO dose certainly will be studied extensively in clinical trials. Finally, in the liver, where the first clinical applications are likely, more detailed definition of cellular function and temporal profiles of SPIO retention within benign and malignant liver tumors will be necessary to refine diagnostic criteria for clinical use. The agent appears to have a promising future in clinical MR imaging.

REFERENCES

1. Saini S, Stark DD, Hahn PF, Wittenberg J, Brady TJ, Ferrucci JT Jr. Ferrite particles: a superparamagnetic MR contrast agent for the reticuloendothelial system. *Radiology* **1987**;162:211–216

2. Saini S, Stark DD, Hahn PF, et al. Ferrite particles: a superparamagnetic MR contrast agent for enhanced detection of liver carcinoma. *Radiology* **1987**;162:217–222
3. Bacon BR, Stark DD, Park CH, et al. Ferrite particles: a new magnetic resonance imaging contrast agent: lack of acute or chronic hepatotoxicity after intravenous administration. *J Lab Clin Med* **1987**;110(2):164–171
4. Weissleder R, Hahn PF, Stark DD, et al. MR imaging of splenic metastases: ferrite-enhanced detection in rats. *AJR* **1987**;149:723–726
5. Tsang YM, Stark DD, Chen MCM, Weissleder R, Wittenberg J, Ferrucci JT. Hepatic micrometastases in the rat: ferrite-enhanced MR imaging. *Radiology* **1988**;167:21–24
6. Weissleder R, Stark DD, Engelstad BL, et al. Superparamagnetic iron oxide: pharmacokinetics and toxicity. *AJR* **1989**;152:167–173
7. Weissleder R, Stark DD, Rummeny EJ, Compton CC, Ferrucci JT. Splenic lymphoma: ferrite-enhanced MR imaging in rats. *Radiology* **1988**;166: 423–430
8. Stark DD, Weissleder R, Elizondo G, et al. Superparamagnetic iron oxide: clinical application as a contrast agent for MR imaging of the liver. *Radiology* **1988**;168:297–301
9. Marchal G, Van Hecke P, Demaerel P, et al. Detection of liver metastases with superparamagnetic iron oxide in 15 patients: results of MR imaging at 1.5 T. *AJR* **1989**;152:771–775
10. Blakemore RP, Frankel R. Magnetic navigation in bacteria. *Sci Am* **1981**;246:58–65
11. Bean CP. Hysteresis loops of mixtures of ferromagnetic micropowders. *J Appl Phys* **1955**;26:1381–1383
12. Patrizio G, Elizondo G, Fretz C, Eley CGS, Stark DD, Ferrucci JT. Cancer targeted liposomes containing superparamagnetic iron oxide: ferrosomes (abstr.). In: *Book of abstracts. Society of Magnetic Resonance in Medicine. Eighth annual meeting,* vol. 1. Berkeley, CA: Society of Magnetic Resonance in Medicine, **1989**:327
13. Kawamura Y, Endo Y, Watanabe Y, et al. Use of magnetite particles as a contrast agent for MR imaging of the liver. *Radiology* **1990**;174:357–360
14. Fretz CJ, Elizondo G, Weissleder R, Hahn PF, Stark DD, Ferrucci JT Jr. Superparamagnetic iron oxide-enhanced MR imaging: pulse sequence optimization for detection of liver cancer. *Radiology* **1989**;172:393–397
15. Weissleder R, Elizondo G, Stark DD, et al. The diagnosis of splenic lymphoma by MR imaging: value of superparamagnetic iron oxide. *AJR* **1989**;152:175–180
16. Weissleder R, Hahn PF, Stark DD, et al. Superparamagnetic iron oxide: enhanced detection of focal splenic tumors with MR imaging. *Radiology* **1988**;169:399–403
17. Fretz CJ, Stark DD, Metz CE, et al. Detection of hepatic metastases: comparison of contrast-enhanced CT, unenhanced MR imaging, and iron oxide-enhanced MR imaging. *AJR* **1990**;155:763–770
18. Elizondo G, Weissleder R, Stark DD, et al. Hepatic cirrhosis and hepatitis: MR imaging enhanced with superparamagnetic iron oxide. *Radiology* **1990**;174:797–801
19. Hahn PF, Stark DD, Weissleder R, Elizondo G, Saini S, Ferrucci JT. Clinical application of superparamagnetic iron oxide to MR imaging of tissue perfusion vascular liver tumors. *Radiology* **1990**;174:361–366
20. Mirowitz S, Heiken JP, Lee JKT. Potential MR pitfall in relying on lesion/liver ratio in presence of hepatic hemochromatosis. *J Comput Assist Tomogr* **1988**;12:323–324

Review

Fast MR Imaging: Techniques and Clinical Applications

E. M. Haacke[1] and J. A. Tkach[2]

Fast MR imaging has matured in the past few years and is now of established value for several aspects of clinical MR imaging. The initial impetus for rapid imaging was to reduce scan times. Today its usefulness includes reducing motion artifacts, improved contrast per unit time, three-dimensional (3-D) imaging, real-time imaging, cine-mode imaging, and flow imaging. The focus of this review is on short-TR steady-state gradient-echo imaging. We discuss the basic sequence design of the mainstream fast techniques. Many important applications exist, including gadopentetate dimeglumine-enhanced MR imaging of the brain and spine, subsecond imaging of real-time applications, myelographic imaging of the spine, cardiac cine-mode imaging; 3-D musculoskeletal (knee) imaging, 3-D pituitary imaging; two-dimensional and 3-D body imaging; 3-D carotid and intravascular imaging, and reformatting 3-D images into arbitrary planes.

Fast imaging has its impetus in improving throughput of patients and reducing motion artifacts. With respect to acquisition time, MR imaging can be classified into four regimens: (1) conventional scans taking minutes, as in normal SE imaging; (2) intermediate savings in time (by factors of 2 or 4) such as with hybrid imaging [1, 2], multiecho techniques [3], partial-Fourier imaging [4–8], or improved reconstruction with limited data [9–11]; (3) rapid GFE scanning with partial flip angles [12–23] requiring on the order of 1–10 sec; and (4) snapshot imaging, actually a subset of rapid GFE scanning [24, 25] (collected in less than 1 sec) and EPI [26–29] (collecting the data in a single readout in 20–100 msec). The focus of this article is on rapid partial-flip-angle GFE techniques. The MR abbreviations and symbols used throughout this article are defined in the Appendix.

The last few years have seen a resurgence of earlier attempts at fast, short TR techniques (known as SSFP imaging), thanks to improvements in field homogeneity, higher signal-to-noise (S/N) at higher fields, and higher gradient strengths. Much of the theoretical foundation for these techniques was laid several decades ago [15, 30–33]; its reincarnation in the last few years has appeared in the guise of techniques like FLASH [13, 14, 18, 20] and FISP [12, 21, 22]. Many important contributions regarding contrast-to-noise (C/N) [12, 34–45] and other issues such as spoiling [46, 47], slice profile [36, 44], missing pulse acquisition [48], and clinical usefulness [49–51] are now being carefully examined. There are also a great many ways to approach steady state and to acquire the data [16, 17, 22, 23, 48, 52–54].

In this article, the basic concept of steady state is reviewed, followed by a summary of the different Fourier-transform MR sequence types available on modern whole-body MR systems. Their physical differences are addressed, with special emphasis on the consequences for imaging parameters such as measuring time, spatial resolution, S/N, and C/N. The effects of slice profile, resonance offset variations, and local field inhomogeneities on image contrast are also mentioned. Clinical examples of 2-D and 3-D implementations [55, 56] are then presented for CNS, musculoskeletal, cardiac, and vascular imaging.

Received January 17, 1990; accepted after revision May 21, 1990.

[1] Department of Radiology, University Hospitals of Cleveland, and the Department of Physics, Case Western Reserve University, Cleveland, OH 44106. Address reprint requests to E. M. Haacke, Department of Radiology, University Hospitals of Cleveland, 2074 Abington Rd., Cleveland, OH 44106.

[2] Department of Radiology, The Cleveland Clinic Foundation, Cleveland, OH 44195-5129.

AJR 155:951–964, November 1990 0361–803X/90/1555–0951 © American Roentgen Ray Society

Techniques

Because of recent improvements in field homogeneity, S/N, and gradient strengths, GFE imaging has become a viable means of signal acquisition. In conventional SE imaging, the minimum TR and TE are limited by the fact that two RF pulses, 90° and 180° (Fig. 1A), are applied per cycle. Both TR and TE can be reduced when the signal is formed by gradient reversal alone. For these short-TR GFE sequences, only one RF pulse is applied per cycle (Fig. 1B), reducing RF power deposition. With present gradient strengths of 10 mT/m, by using a short RF pulse, small sampling intervals, and reduced resolution, it is possible to reduce TEs to 2–5 msec and TRs to 4–8 msec [24, 25, 57]. A scan with 128 phase-encoding steps can then be acquired in roughly 0.5–1.0 sec. Reducing the number of phase-encoding steps would allow faster image acquisition at the expense of resolution. RF times can be selective at 1–3 msec and nonselective (covering the whole volume) at 500 μsec or less. Both 2-D and 3-D acquisitions are possible. Flip angles of less than 90° are then selected to optimize contrast. This inherent contrast can be altered by the application of various preparation schemes (e.g., π saturation pulse) prior to image acquisition [24, 25].

Owing to the absence of the 180° refocusing pulse in GFE sequences, only the dephasing induced by the imaging gradients (with the exception of phase-encoding) is refocused at the TE. Dephasing due to local field inhomogeneities remains, acting to accelerate the rate of decay of the transverse

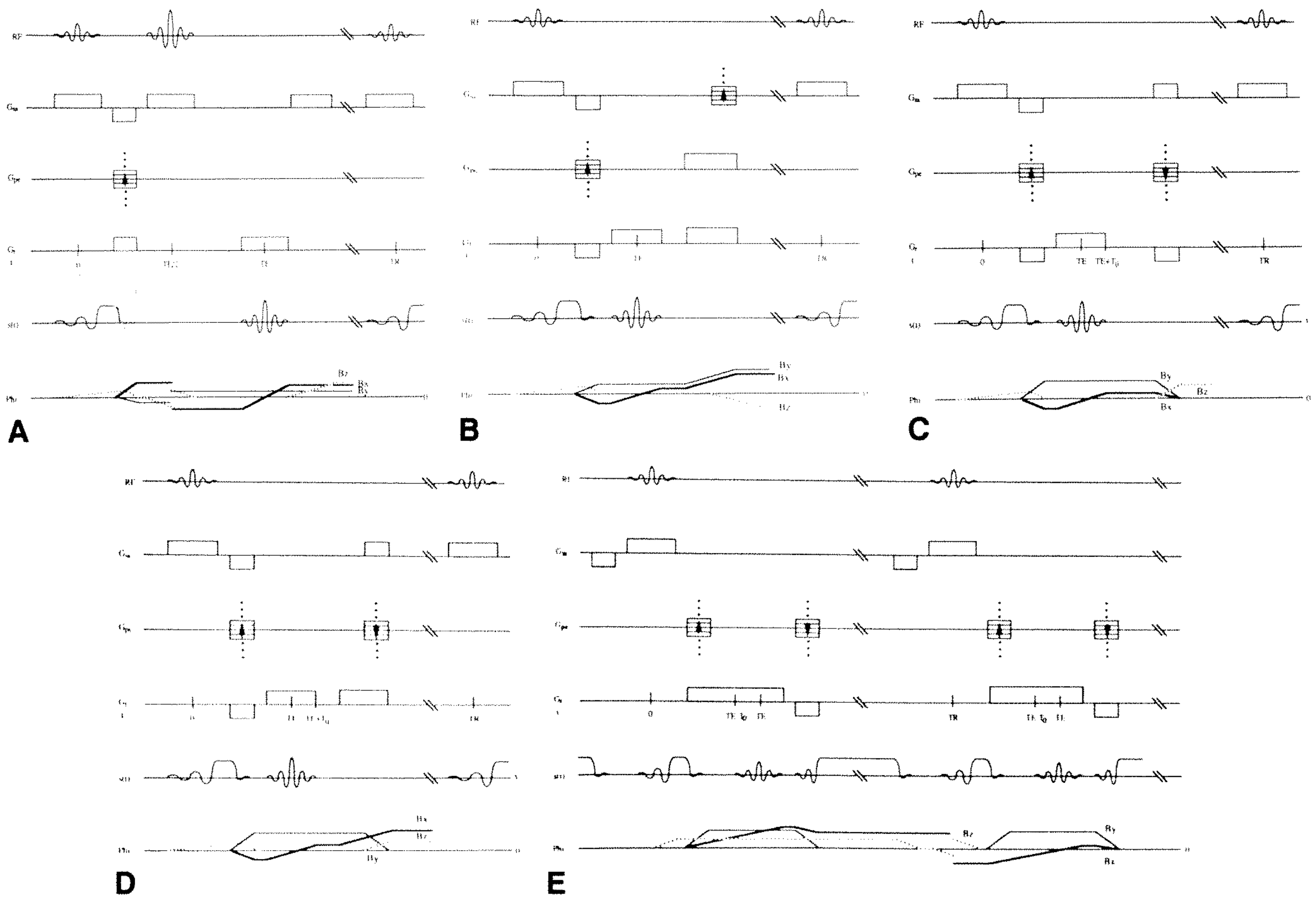

Fig. 1.—*A*, Usual SE sequence ($\pi/2$ first RF, π second RF pulse) refocuses all spins at TE, even in presence of static local field inhomogeneities. Alternatively, dephasing gradient before the π pulse can be inverted and moved to after the π pulse (the broken line along G_r). Similarly, the polarity of the rephasing gradient pulse (as well as phase-encoding gradient) in the slice direction can be inverted and placed after the π pulse. S (+) represents the signal during the pulse sequence. Phi represents the phase evolution for an isochromat in all directions. The dotted line (labeled Bz) corresponds to slice-select gradient (G_{ss}), thin solid line (labeled By) to phase-encoding gradient (G_{pe}), and dark solid line (labeled Bx) to read gradient (G_r). Phi is shown in each sequence diagram.

B, FLASH gradient-echo sequence. Unbalanced gradients and changing gradient table in slice-select direction are used as spoilers. Elongation of read gradient beyond sampling window ensures that if spoiling is incomplete, no RF echoes begin to form during data collection, as well as providing for integration over resonant offset. Both are essential to avoiding image artifacts.

C, SSFP, true FISP sequence, measures total signal FID and RF echo portions superimposed. Associated sequence structure is characterized by balanced imaging gradients in all three directions (using the broken line in G_{ss}). Rare ROAST is balanced in all but the slice-select direction (using the solid line in G_{ss}). It could have been unbalanced in the read direction instead.

D, ROAST sequence. Only gradients in phase-encoding direction are balanced. This is common version of FISP, which collects just the FID. Rare ROAST integrates the SSFP signal from a voxel across a 0–2π range of resonant offset as a consequence of unbalanced gradient structure along G_{ss} (or G_r). For ROAST, this integration occurs along both G_{ss} and G_r.

E, Contrast-enhanced ROAST sequence collects only RF portion of data. Two repeat intervals are shown to highlight phase behavior. As in ROAST, integration across resonant offset occurs along G_{ss} and G_r for the sequence structure shown.

magnetization (referred to as T2*). This vulnerability has proved to be a limitation of these techniques. Alternative rapid techniques have been implemented to avoid T2*-related signal and resolution loss [52, 54, 56, 57], the details of which are discussed later under imaging difficulties.

SSFP

SSFP implies that both longitudinal and transverse magnetization reach a dynamic equilibrium that is the same from cycle to cycle [31] (from one RF excitation pulse to the next). Considering only the behavior of the transverse magnetization over one cycle, the steady-state signal is characterized by an exponentially decreasing function, reaching a minimum near the center of the interval, followed by an exponentially increasing function of opposite polarity reaching its maximum just prior to the next RF pulse. The initial decaying portion of this complete SSFP signal is typically referred to as the FID and the regrowth as the RF echo. The RF echo is similar to the 90–180° echo, in that dephasing due to local field inhomogeneities is refocused at the RF pulse.

As long as the interval between RF pulses remains constant and no imaging gradients are applied (or the gradient structure is constant from cycle to cycle), all echoes will occur at a time nTR, where n is an integer. The components that refocus to form the echoes continue to undergo T1 growth and T2 decay during the intervals in which they are stored along the longitudinal axis or lie in the transverse plane, respectively. However, they are continually augmented by those echo trains initiated by subsequent RF pulses so that a steady-state signal is obtained. Echo amplitude is dependent on T1, T2, TR, flip angle (α), and precession angle or resonant offset (β). As shown by Kaiser et al. [32], the expression for the SSFP signal can be determined by summing the appropriate refocusing echo trains, treating them as a geometric series. The result is identical to that obtained by solving the phenomenologic Bloch equations of motion for equilibrium conditions [33].

When balanced imaging gradients are applied (i.e., the gradient-induced phase accumulation before the gradient-echo time, TE, of the FID is equal and opposite to that which accumulates over the TR-TE interval), all echoes occur simultaneously with the gradient echo of the FID at TE (this sequence is shown in Fig. 1C, broken-line box in G_{ss}). Alternatively, the gradients can be purposely unbalanced and the associated sequence designed so that only the gradient echo of the FID (Figs. 1C and 1D) or RF echo (Fig. 1E) forms and is acquired at TE.

Whenever a TR less than or on the order of T1 is used, it will take several RF pulses or sequence repetitions for the spin system to reach an equilibrium (where the dynamic behavior of the magnetization during any interpulse interval is identical to that during any other) to some chosen degree of accuracy. The exact number of cycles required will differ depending on T1, T2, TR, α, β, and the sequence structure. The approach to equilibrium can be quite long when TR or α or both are small.

In the rotating frame of reference, the resonant offset rotation angle, β, is the angle through which the spin precesses in the transverse plane from one RF pulse to the next (i.e., over one TR interval). In practice, β is determined by the RF phase, imaging gradients, and local field inhomogeneities [57], all of which shift the frequency off resonance.

Nomenclature.—The widespread simultaneous development of many of the sequences designed to acquire the FID and RF echo portions of the SSFP signal has led to a proliferation of names. For example, the incompletely refocused (with respect to the zero moment of the imaging gradients in the slice and/or read directions) SSFP sequence designed to acquire the FID portion of the SSFP signal is called FAST, GRASS, and modified FISP (true FISP actually includes balanced gradients along all axes) [30]. Because the signal acquired with this intermediate sequence reflects an average over the resonant offset angle induced by the remnant imaging gradients and other static field inhomogeneities across a voxel, we propose to lump the three names into resonant offset averaged steady state, or ROAST, to reflect the actual spin system behavior. "Rare ROAST" is used to denote those sequences in which the gradients along only one of the imaging directions is left unbalanced. As is true for ROAST sequences (Fig. 1D), the net effect of the imaging gradients in contrast-enhanced FAST or contrast-enhanced ROAST, also called PSIF, the sequence designed to acquire the SE portion of the SSFP signal, is nonzero in the slice or read directions or both. An SSFP sequence can also be structured to collect a gradient echo of both the FID and the RF echo simultaneously [21].

In the original article by Hahn [30], the concept of SSFP was used for conditions in which "coherence" of the transverse and longitudinal magnetization was maintained. We recommend classifying sequences such as FISP, ROAST, or CE-ROAST, in which the net effect of the imaging gradients is constant from cycle to cycle, as in SSC sequences. Sequences such as FLASH or spoiled GRASS, in which the transverse magnetization is spoiled (when TR is much less than T2 or when β is randomized), would then be referred to as steady-state incoherent (SSI) sequences.

SSC behavior.—When TR $\ll$ T2, $\beta = 0$ and alternating RF pulses are applied (equivalent to $\beta = \pi$ and nonalternating RF), the resulting FID signal is

$$M_y^+ = \frac{M_o \sin\alpha}{1 + T1/T2 - \cos\alpha(T1/T2 - 1)}. \qquad (1)$$

This approach is referred to as true FISP [21]. It should be noted that equation 1 serves only as an approximation because the usual SSC sequences require integration over resonant offset. The signal is acquired as demonstrated in Figure 1D. The sequence structure can be time reversed, as is done in CE-ROAST (Fig. 1E), so that the RF echo can be acquired. Signal and contrast behavior are similar to that of FISP with the exception of some additional T2 weighting. The effective TE (with respect to T2* decay) for this sequence is defined as the time between the center of the acquisition interval and the succeeding RF pulse.

We have not dealt with another fast imaging approach, driven equilibrium [58–60], which requires precisely refocused transverse coherence. This concept assumes a uniform field so that after a $\pi/2$ pulse and read gradient, the magnetization is returned to the positive z axis by a $\pi/2$ pulse of opposite polarity. This only works well if the resonant offset is constant across the image; otherwise, signal from a homogeneous object will vary from one point to the next.

SSI behavior.—Historically, SSFP had its origins in spectroscopy. Consequently, it has been the FID portion of the MR signal that has been of primary interest. In order to prevent signal associated with the RF echo from entering the data window, additional gradient pulses were applied after data acquisiton. The amplitude and/or duration of these gradients (spoilers) was changed from cycle to cycle (Fig. 1B) [46, 47]. Since the gradient structure was no longer constant from cycle to cycle, the build-up of transverse coherence was minimized if not eliminated even for TR ≪ T2. Similarly, a degree of transverse incoherence can be introduced into the system by incorporating a variable-phase RF pulse into the sequence structure [15]. With either "spoiling" strategy, only the longitudinal magnetization reaches a nonzero steady state. Signal and contrast are determined primarily by T1. When applied to GFE sequences, these techniques are referred to as FLASH or spoiled GRASS. The general SSFP equations for the transverse magnetization associated with the FID acquired with these techniques reduces to

$$M_y^+ = \frac{M_o \sin\alpha(1 - E1)}{(1 - \cos\alpha E1)}, \tag{2}$$

where $E1 = \exp(-TR/T1)$.

Signal-to-Noise

SE imaging.—Several important limits of S/N behavior for the various sequences need to be considered [54]. For short TR, SE varies as TR/T1. Hence, in the region in which TR ≪ T1, doubling TR nearly doubles the signal (this is especially true for CSF) and potentially doubles the contrast between short and long T1 tissues. Partial-Fourier imaging collects roughly half of the usual number of phase-encoding steps and hence loses roughly $\sqrt{2}$ in S/N. In theory, no resolution is lost with this method. It can be used to collect data with 2TR in the same time as the usual scan time with TR and actually improves the C/N for CSF/gray or white matter (owing to the long T1 of CSF [5]).

SSC imaging.—At the optimal flip angle, the signal for FISP varies as $\sqrt{T2/T1}$ for TR ≪ T2. Therefore, FISP and its variants should always be run at the shortest possible TR for a given TE since the signal does not depend on TR. In the body, this TR-independent behavior is observed approximately for TR ≤ 25 msec. By reducing TE, TR can be reduced further. However, the expected increase in S/N, for a fixed spatial resolution, will not be realized owing to the concomitant decrease in sampling time. Signal bandwidth (and the amplitude of the read gradient) varies inversely with sampling time, and the noise varies as the square root of the bandwidth (although T2* dephasing is reduced with the shorter TE). As an example, using a TR of 6 msec and averaging over eight scans can give up to a $2\sqrt{2}$ improvement in S/N for CSF over a single scan with a TR of 48 msec. When longer TEs are acceptable (i.e., when field inhomogeneities are not a problem) the bandwidth can be reduced by a factor of 4–8, recovering most S/N per unit time (but the increase in T2* dephasing may prevent this full increase in S/N from being realized).

SSI imaging.—For FLASH imaging at the optimal (Ernst) angle and TR ≪ T1, signal varies as $\sqrt{TR/T1}$. When TR is doubled, the increase in S/N is $\sqrt{2}$. If motion is present and approximately periodic, as is true for respiratory motion in the abdomen, it is preferable to use the shorter TR and take multiple acquisitions, N_{acq}, as opposed to a single acquisition at a longer TR. Not only will S/N be increased by $\sqrt{N_{acq}}$, but motion artifacts will be reduced by pseudogating, particularly if $N_{acq}TR$ is equal to some integer multiple of the period of motion [61].

Contrast

The major factors affecting contrast are the tissue properties ρ (spin density), T1, and T2; the imaging parameters α, β, TR, and TE; the slice profile; motion; Gibbs ringing; and S/N via the matrix size, gradient strength (bandwidth), number of acquisitions, and reconstruction technique. Both the slice profile and resonant offset effects must be integrated over to properly take into account their effects on the image contrast. Motion can cause either a large signal from the inflow of fast spins (as in blood flow) or a loss of signal owing to the inability of the transverse magnetization for these spins to reach a steady state, as in pulsatile CSF flow [57, 62]. The consideration of all these variables is beyond the scope of this review and the reader is referred to the various articles covering these topics [12, 34–45, 54, 63, 64] and some further information in the Discussion section.

Applications and Results

In imaging, it is the signal from a voxel that must be considered. Practically, for 2-D imaging, the slice profile is not uniform. In 2-D FLASH imaging, this leads to a shift in the optimal flip angle for a given tissue to a higher flip angle and a flattening of the curve thereafter (Fig. 2A). In 3-D imaging, although the flip angle distribution is now approximately constant across each partition, the flip angle varies across the slab, leading to a variation in signal intensity and contrast from 3-D partition to 3-D partition.

In SSC imaging, the resonant offset angle (β) also must be considered. Integration across β over a multiple of 2π leads to the contrast shown in Figure 2B. Tissues with low values of T1/T2 (e.g., CSF) appear bright at the large flip angles, as expected. In reality, owing to the imperfect slice profiles, integration over slice profile and resonant offset also should be incorporated into the conventional SE signal calculations.

With low flip angles, spin density/T1 contrast is possible and useful in CSF/myelographic spine imaging. Figure 3A shows the expected low-S/N FLASH image with a 10° flip angle and TR of 320 msec. Figure 3B shows a T1/T2-weighted FISP image at 70° (obtained by combining two

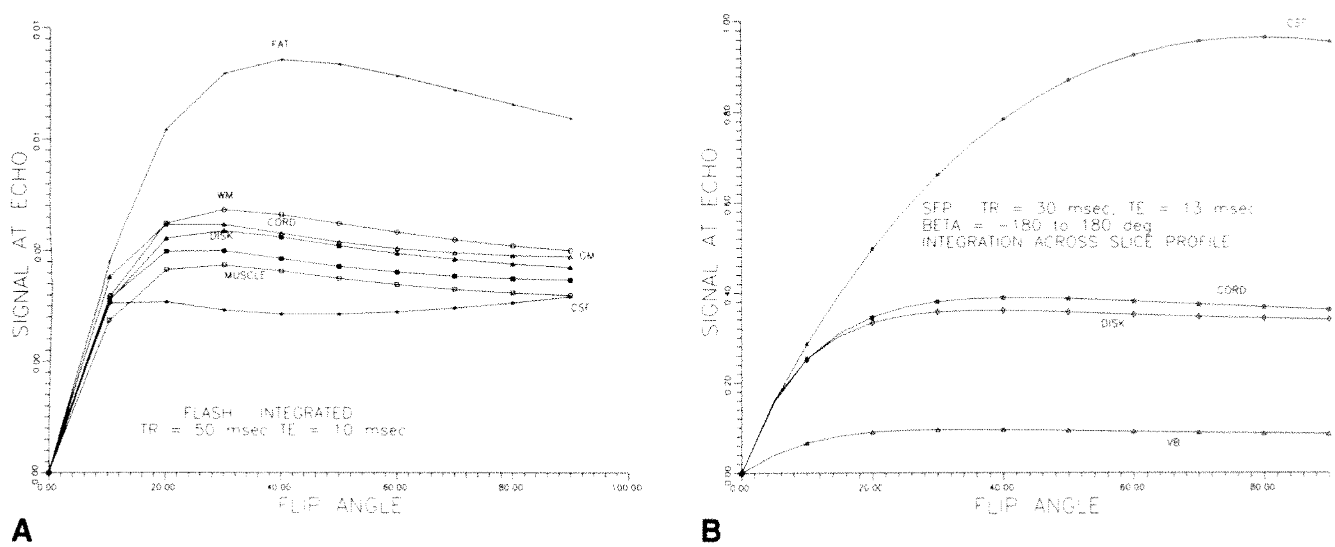

Fig. 2.—Ideally, flip angle distribution should be uniform across slice. In practice, the RF pulse is often an apodized (Hanning window) low-bandwidth sinc pulse and resulting flip angle distribution is not uniform.

***A*, T1-weighted FLASH image contrast from integrated RF profile over a 5-mm-thick slice. There is a shift in optimal flip angle to the right and little change in contrast past 40°. If the profile were perfectly square, the signal at higher flip angles would be more T1 weighted (lower in amplitude).**

***B*, FISP signal integrated over β and slice profile. The tissue parameters used to generate all plots are given in Table 4.**

WM = white matter, GM = gray matter, VB = vertebral body.

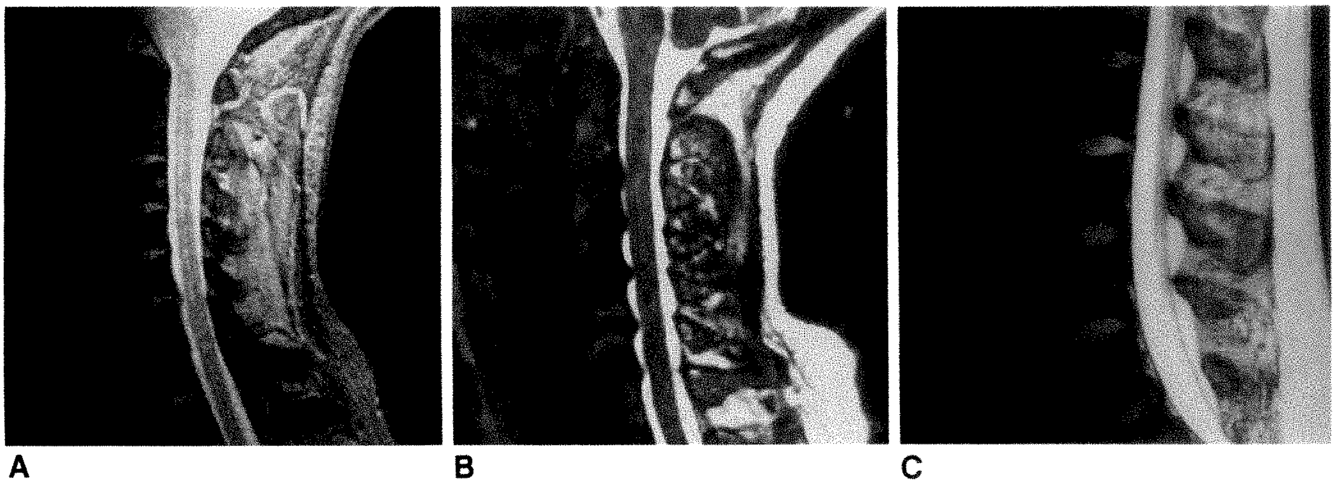

Fig. 3.—Multiple contrast mechanisms can be exploited to obtain CSF/myelographic spine MR images.

***A*, Spin-density-weighted 2-D FLASH image (10°, TR = 320 msec, TE = 18 msec, four acquisitions) shows enhanced CSF but suffers from poor S/N and C/N owing to small flip angle. Enhanced disk/vertebral body reflects T2* dephasing in fatty parts of vertebral body.**

***B*, Contrast is improved on the 3-D FISP 70° image obtained from a combination of two FISP 3-D partitions. One source image was acquired with 180° phase-alternated RF ($\beta_o = \pi$), the other with non-phase-alternated RF ($\beta_o = 0$). Otherwise, imaging parameters were identical for the two scans (TR = 20 msec, TE = 7 msec, one acquisition, $N_z = 32$, $R_x = R_y = 0.9$ mm, $R_z = 2$ mm).**

***C*, Comparable contrast can be obtained in the lumbar spine with a single 25° rare ROAST 3-D study (TR = 15 msec, TE = 6 msec, four acquisitions, $N_z = 32$, $R_x = R_y = 0.9$ mm, $R_z = 2$ mm [two adjacent images added]).**

images with alternating RF pulses [57, 62]). The CSF is reasonably bright and there are no apparent artifacts. Similar results can be obtained in the lumbar spine in one scan by using rare ROAST (Fig. 3C). Myelographic T2-weighted images (TEs of several hundred milliseconds) are also possible by using RARE [64]. (Recall that rare ROAST implies balanced gradients in two directions [Fig. 3C], whereas RARE refers to the technique of phase encoding between echoes [3]).

T2*-related signal and resolution loss are common to all gradient-echo imaging techniques. These effects are minimized by the use of a short TE or are eliminated with SE equivalents of FLASH, such as FATE [54]. Recent work has also shown that 3-D GFE imaging [56] and 2-D variants of the same [65] can reduce the T2* effect significantly because dephasing across a voxel is reduced as a consequence of phase encoding in the slice-select direction (Fig. 4). There is excellent gray-matter/white-matter contrast. Missing pulse schemes also can eliminate these problems [48].

One area of the musculoskeletal system in which routine use of fast imaging is important is in thin-slice 3-D imaging of the knee. Three scans are obtained to reveal spin density (Fig. 5A), T1 weighting (Fig. 5B), and T1/T2 weighting (Fig. 5C). The spin-density image with a larger TR and low flip angle (10°) clearly shows the cartilage-bone/marrow contrast (since at 1.5 T, the T2* of marrow is low, roughly 8–10 msec). The synovial fluid is particularly bright on the FISP image.

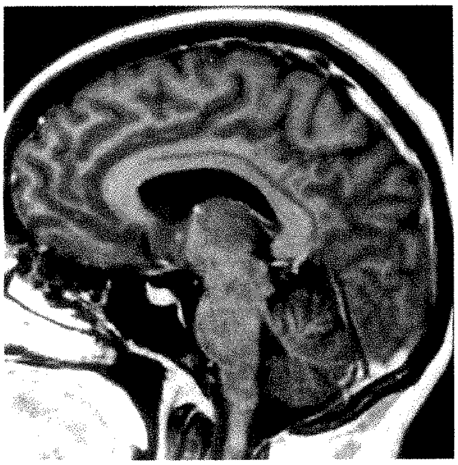

Fig. 4.—S/N and resolution in GFE MR images are typically poor in regions of large changes in local magnetic susceptibility unless short-TE 3-D images are acquired. Note that even at 1.5 T, short TEs and 3-D imaging with a large number of partitions leads to high-quality pituitary imaging and excellent gray/white matter contrast. FLASH imaging parameters: single acquisition 3-D, TR = 50 msec, TE = 5 msec, N_z = 64, R_x = R_y = 1.0 mm, R_z = 3 mm, α = 40°.

FISP contrast requires that both the longitudinal and transverse magnetization reach a steady state. Any motion during the scan can prevent a transverse steady state from being established, leading to artifacts and a loss of signal. This motion-induced loss in transverse coherence is minimized by the use of a short TR. Comparisons of 2-D data sets for SE (Fig. 6A), ROAST 40° (Fig. 6B), FISP 40° (Fig. 6C), and FISP 70° (Fig. 6D) images show the advantage of the velocity-compensated (at the RF) FISP over the uncompensated ROAST. Clearly, regions of motion for CSF are well represented in the former and compare nicely with the usual T2-weighted results. The true FISP images are obtained from combining two corresponding FISP images acquired with alternating and nonalternating RF. Nevertheless, each eight-acquisition 2-D image took only 40 sec to acquire.

Fast imaging plays a key role for dynamic display of events. The most important use is in cine cardiac imaging [66–68]. Since the time required for spatial encoding and data collection is short, 20 msec or so, many images, each associated with a different cardiac phase, can be acquired over each R-R interval. Contrast between blood and myocardium is good because inflow of unsaturated spins leads to flow-related enhancement of the blood signal while muscle becomes saturated (even though it also moves). Standard FISP or FLASH sequences with velocity-rephasing gradients are typically used. The contrast behavior of the muscle and rapidly moving blood is the same for each technique. Since both are moving, there is little or no buildup of transverse coherence for these sequence structures. Example gradient-echo images show bright signal from the blood and less intense myocardium (Fig. 7). Recently, TRs ranging from 4 to 6 msec have been used [24, 25] to obtain a snapshot image with reduced resolution in the head, abdomen, spine, and heart.

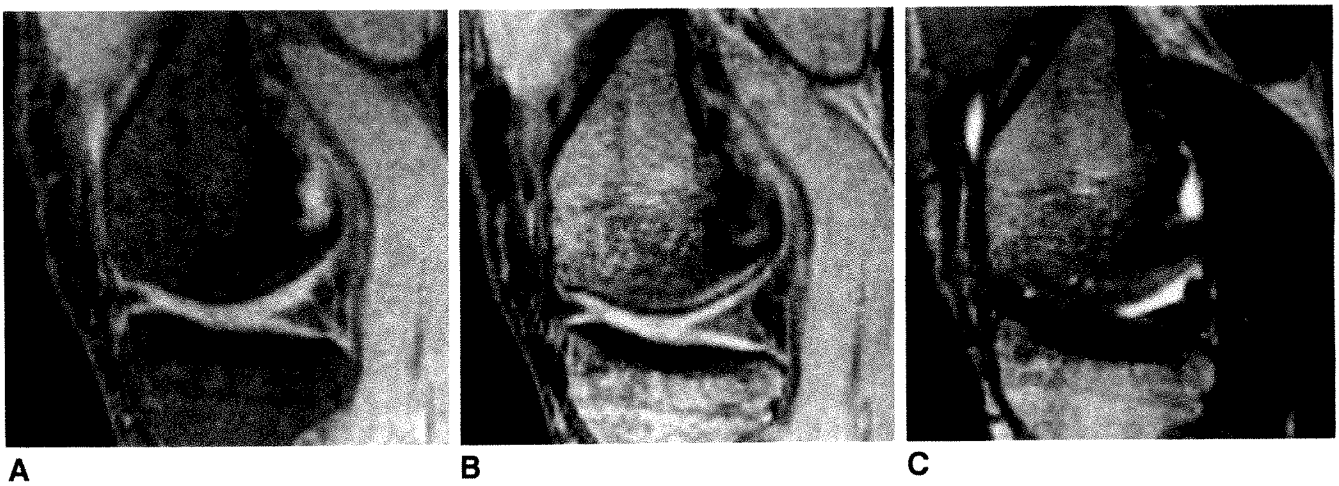

Fig. 5.—The knee often requires very-high-resolution 3-D MR images to appreciate tears and small abnormalities. Various types of contrast have proved useful.

A, Spin-density-weighted 10° FLASH image.

B, T1-weighted 40° FLASH image.

C, T1/T2-weighted 40° FISP image.

High signal from synovial fluid is reminiscent of T2-weighted SE images. Imaging parameters: 2-mm slice thickness; 3-D; 32 partitions; 1.0 × 1.0 mm^2 in-plane resolution; TE = 10 msec, TR = 100 msec for FLASH images and TR = 20 msec for FISP. Marrow appears hypointense in *A* because of its short T2*.

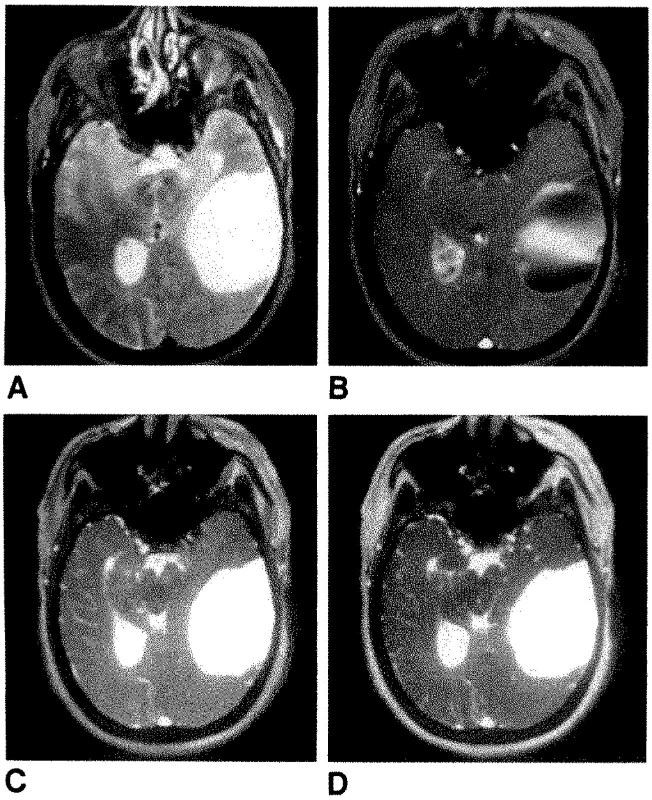

Fig. 6.—Motion acts as a natural spoiler, often preventing a true SSC equilibrium and hence expected ROAST contrast from being obtained for the corresponding tissues (e.g., CSF). The balanced symmetric gradient structure of FISP renders it less sensitive to the detrimental effects of motion. Consequently, the expected SSC signal and contrast can be obtained even for nonturbulent moving tissues. This is well shown in the following set of 2-D MR images.

A, Conventional T2-weighted SE image.
B, 40° ROAST image.
C, 40° combined FISP image.
D, 70° combined FISP image.

Imaging parameters: TR = 2500 msec, TE = 90 msec, single acquisition, $R_x = R_y = 0.9$ mm, $R_z = 5$ mm for 2-D SE (*A*); TR = 16 msec, TE = 10 msec, eight acquisitions, $R_x = R_y = 0.9$ mm, $R_z = 5$ mm for 2-D 40° ROAST (*B*); and TR = 16 msec, TE = 6 msec, eight acquisitions, $R_x = R_y = 0.98$ mm, $R_z = 5$ mm for 2-D 40° and 70° FISP (*C* and *D*).

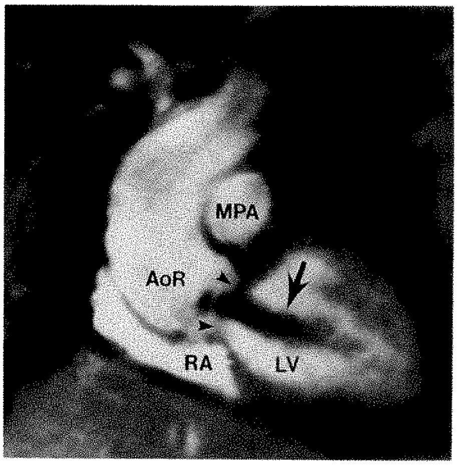

Fig. 7.—Cine cardiac imaging has been exploited to examine morphologic as well as dynamic abnormalities. Use of gradient rephasing schemes in both read (at the echo) and slice-select directions reveals much reduced ghosting and allows visualization of heart at different points in cardiac cycle. This MR image shows aortic regurgitation caused by an incompetent aortic valve acquired with a prospective ECG-triggered 40° modified FISP (i.e., ROAST) sequence with velocity compensation and TR of 20 msec, TE of 10 msec, and four acquisitions. Turbulent diastolic blood flow retrograde through incompetent aortic valve (*arrowheads*) constitutes aortic regurgitation (*arrow*). This dark jet of signal void passes almost to left ventricular apex. A dilated aortic root (AoR) is also visualized. MPA = main pulmonary artery, RA = right atrium, RV = right ventricle. (Courtesy of R. White, Cleveland, OH.)

Fast flow can be taken advantage of in transverse (Fig. 8A) or sagittal (Fig. 8B) imaging. (Although not shown, similar results can be obtained with coronal acquisitions.) To enhance blood/stationary signal contrast, optimal angles, TR, and slice thickness are chosen differently in each case. Data can be collected in the 2-D and 3-D modes, but the 3-D nature of the coverage is crucial to the separation of arteries and veins through their slices [69–75]. In the former example, reformatting the 3-D slices with enhanced vessels yields an excellent MR angiogram (Figs. 8C and 8D), which can be displayed at various angles. The very short TEs used here require the collection of an asymmetric echo.

The sequential application of single-slice fast imaging should prove useful in abdominal imaging, where motion is a problem. Any scan acquired within a respiratory cycle will have no ghosting artifacts and is effectively a form of ordered phase encoding. Repeating the scans one after another and adding the raw data sets before reconstruction will improve S/N but blur the images somewhat if motion has occurred (residual ghosting due to flow will still remain). An example cut through the liver and kidneys shows contrast changes for a conventional SE (Fig. 9A) vs a 40° FLASH acquisition with a TR of 100 msec (Fig. 9B). This scenario suggests running the scan as fast as possible without incurring T2 coherence artifacts and repeating it several times to improve S/N and then shifting to a new slice location (known as serial single-slice acquisition). This approach is also useful in 2-D flow imaging [69, 71].

Even though equilibrium may not be reached, very rapid scans maintain sufficient contrast while avoiding transverse coherence loss problems due to motion, as demonstrated in the short TR/TE (6/2.5 msec) 2-D image of the head and spine in Figure 10A. This snapshot imaging can be extended to 3-D acquisitions within a breath-hold (Fig. 10B). An example in the heart with reduced resolution with only 64 phase-encoding steps is shown in Figure 10C.

Discussion

This section comprises a review of a variety of technical and practical details relating to the implementation and interpretation of short-TR fast imaging sequences with a brief mention of RARE imaging and EPI.

Slice Profile

FLASH (SSI).—For FLASH imaging, the observations in Figure 2 imply that at low flip angles, contrast between most

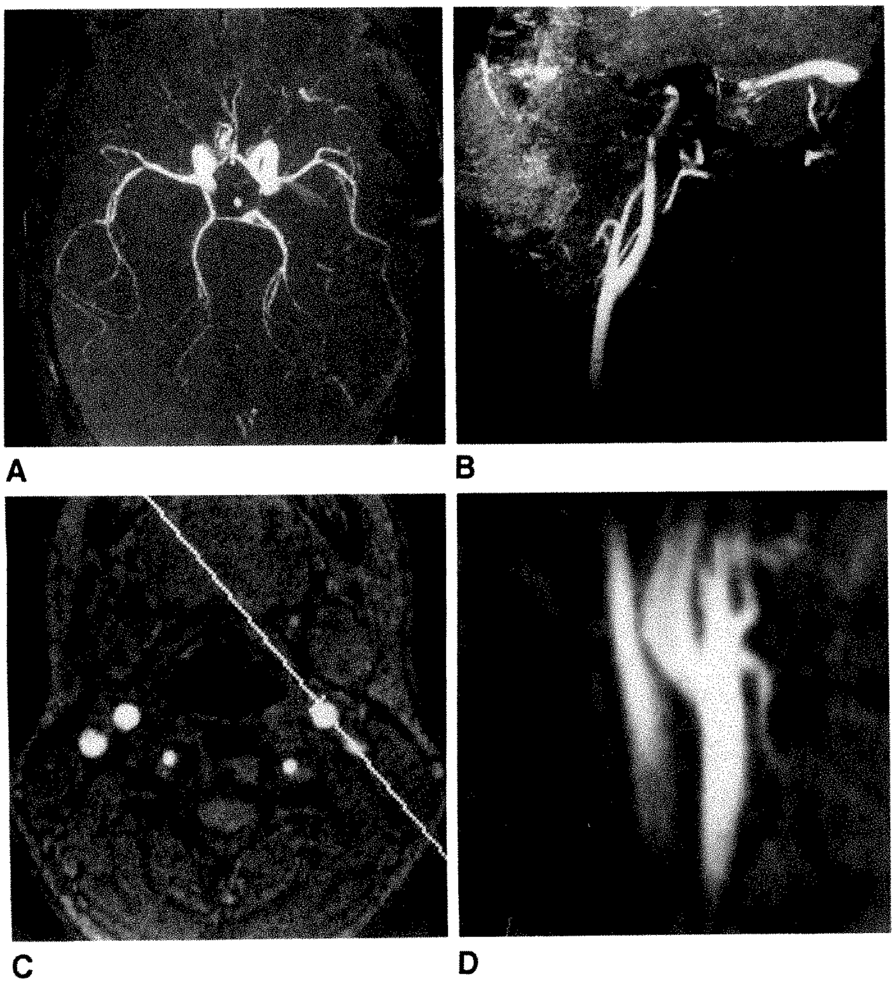

Fig. 8.—Fast 3-D imaging can be used with motion-compensation sequences to reveal vascular information. For thin slices, spin dephasing is reduced and blood is so much brighter than stationary tissue that no background suppression or subtraction is required.

A, Maximum-intensity projection from a set of 1.25-mm-thick transverse slices through the intracranial vessels extracted from 3-D sequence where $N_z = 16$ partitions. Even the communicating vessels can be visualized here. Imaging parameters: TR = 30 msec, TE = 7 msec, $R_x = R_y = 0.765$ mm, $R_z = 1.25$ mm, $\alpha = 15°$, and one acquisition.

B, Projected set of 2-mm sagittal slices through the carotid arteries. Imaging parameters: TR = 100 msec, TE = 12 msec, $N_z = 16$, $R_z = 2$ mm, $R_x = R_y = 1$ mm, $\alpha = 40°$, and one acquisition.

C, Example of usefulness of 3-D isotropic acquisitions and MPR from one of a set of 3-D transverse images.

D, Parasagittal image extracted from 3-D transverse images along line in *C*. Imaging parameters: TR = 40 msec, TE = 7 msec, $R_x = R_y = R_z = 1$ mm, $\alpha = 15°$.

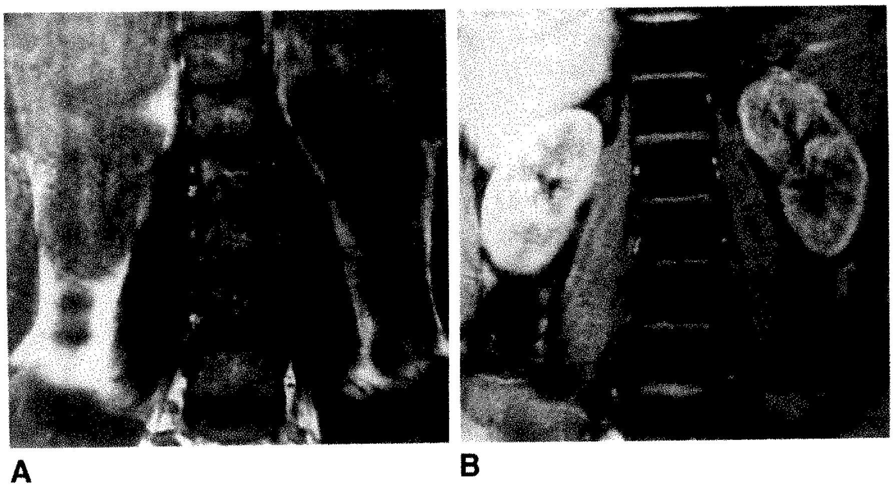

Fig. 9.—T1-weighted single-acquisition 2-D MR images of the abdomen at 1.5 T.

A, Conventional SE MR image. (TR = 550 msec, TE = 15 msec, $R_x = R_y = 1.3$ mm, $R_z = 8$ mm, 256 × 256 matrix).

B, 40° FLASH image (TR = 100 msec, TE = 12 msec $R_x = R_y = 1.3$ mm, $R_z = 8$ mm, 256 × 256 matrix).

tissue becomes spin-density weighted at about 5–10° for a TR of 50–200 msec. The signal from CSF is maximized at these low angles so that for CSF, some T1 weighting is still present. This low flip angle provides an alternative means of obtaining the CSF myelographic effect that was shown in Figure 3A. A broad slice profile reduces this effect somewhat. Nevertheless, because of the relatively short overall imaging time, it has been used as a replacement for T2-weighted SE imaging in some cases. The reduction in contrast that results from integration over the slice profile increases with increasing

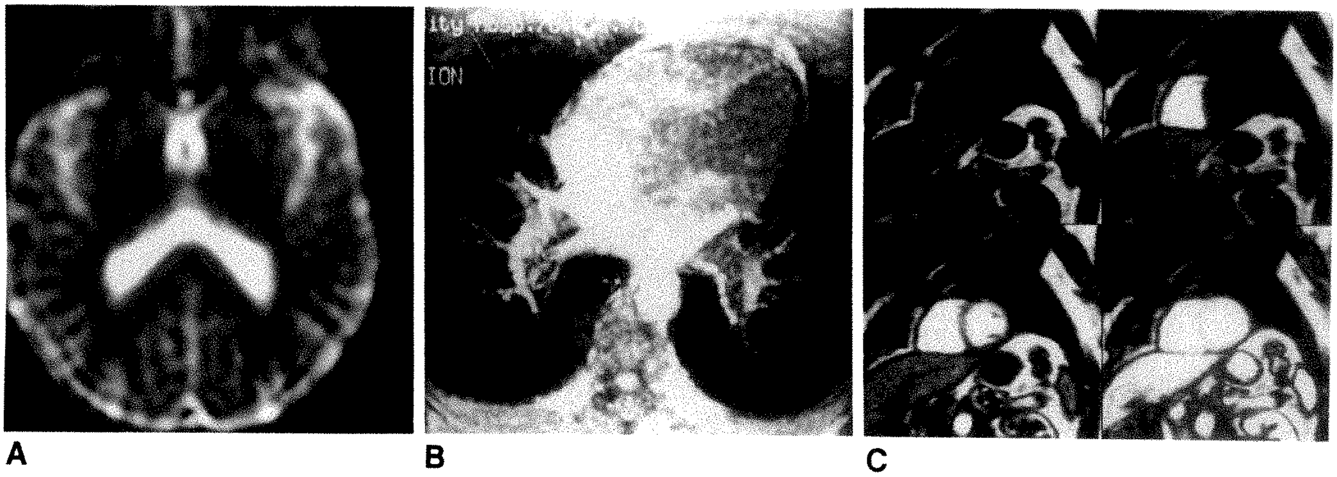

Fig. 10.—Very short TRs of 5 msec with FISP allow low-resolution images of 32 to 128 phase-encoding steps to be acquired in less than 1 sec.

A, Sample head scan (TR = 6 msec, TE = 2.5 msec, $R_x = R_y = 2.4$ mm, $R_z = 5$ mm, $\alpha = 40°$, $N_x = N_y = 128$).

B, 30-sec, breath-hold, 3-D pulmonary artery snapshot FLASH study. Maximum intensity projection of data. An inversion pulse can be added before the data are acquired.

C, Before (top left) and after (one scan every three cardiac cycles with 2.5 sec between scans) administration of gadopentetate dimeglumine. Snapshot FLASH with a preparatory inversion pulse (TI = 650 msec, TE = 3 msec, TR = 7 msec, $N_x = 128$, $N_y = 64$). (Courtesy of D. Finelli, Cleveland, OH.)

flip angle. For flip angles of roughly 40° and greater, the contrast is ρ and T1 weighted and does not change much between the tissues examined here. For flip angles in which $\theta^2 \ll 2TR/T1$, the signal remains independent of slice profile and is spin-density weighted.

ROAST (SSC).—In ROAST-like sequences, resonant offset, β, also must be considered. The effect of resonant offset on signal and contrast is not as straightforward as is that of the slice profile. Practically, the resonant offset angle depends on the static local field inhomogeneities, the net effect of the imaging gradients over each cycle, and the phase of the RF. When the distribution of β across a pixel is approximately 2π, the signal from the voxel is independent of the central value of β in a pixel and the signal from a homogeneous phantom will be uniform. By dephasing more than 2π across a pixel, some remnant inconsistencies remain but are continually reduced (by roughly $1/n$ as the phase wraps the *nth* time). It should be noted that the steady-state solution for the signal is a function of T2, not T2* (see also equation 2). Local field inhomogeneities affect the intrinsic SSC signal through their influence on β. At low flip angles, $\theta^2/2 \ll TR/T1$ (i.e., θ much less than the Ernst angle) and the contrast is spin-density weighted, but with one half the signal of FLASH. In practice, flip angles are larger and integration over resonant offset occurs, leaving a larger signal—ironically, one that behaves much like that for FLASH.

Motion Effects

Motion can prevent the buildup of transverse coherence in ROAST/FISP imaging [57]. The signal in the enhanced ROAST-type sequences is even more motion sensitive. The subsequent loss of SSC signal in any of these techniques may be used for diffusion or slow-flow measurements. When the dephasing is large, the system is naturally spoiled and a FLASH equilibrium is attained. This can cause moving tissues such as the CSF in the spine to exhibit a FLASH-like contrast even though a ROAST sequence is used. When properly compensated [76, 77], the signal from FISP reaches the expected steady state (Fig. 6).

Body Imaging

Once a given TR and flip angle have been chosen, if TR is short enough, single-slice abdominal imaging can be done in a breath-hold [78]. Recently, an SE sequence was implemented with very short TEs (8–10 msec), a short TR (250–300 msec), and 11 to 19 slices (usually about 1 cm thick) [78]. Acquisition times can be 18–22 sec with half-Fourier reconstruction and equivalent 128 × 256 sampling points. Of course, the short TR reduces contrast but is nevertheless proving sufficient for liver imaging, especially when gadopentetate dimeglumine is used. It also has the distinct advantage of reducing motion artifacts, because the scan can be taken in a breath-hold. Snapshot 3-D imaging [79, 80] can be used but will suffer more from motion artifacts, although the acquisition of very thin contiguous 3-D slices is possible within a breath-hold. Sequential 2-D flow imaging also is likely to prove useful in the body.

Contrast

Spin-density and T1 weighting are the types of contrast available with FLASH imaging. For tissues in the range of $T1 < 1000$ msec and TR = 50 msec, spin-density weighting occurs at very small angles (roughly 5°) and T1 weighting occurs at angles above roughly 40° (theoretically Fig. 2A and clinically Figs. 3A and 4). The exact choice of angle depends on TR as well as the slice profile. As TR increases, the flip angle can be increased for improved S/N (representing a linear increase with angle). Similarly, FISP or ROAST images show spin-density weighting at low angles and T1/T2 weighting at high angles (Fig. 2B). Once again, a T2-like contrast is obtained for CSF (Figs. 3B and 3C). CE-ROAST provides additional T2 weighting to the T1/T2 images by a factor of roughly exp(−2TR/T2) [32, 38, 41], although the images are much noisier.

Contrast-to-Noise per Unit Time

With respect to C/N per unit time, a short-TE (≈6 msec) 5° FLASH sequence with a TR of 100 msec repeated 25 times gives a signal of roughly 0.390 for CSF and 0.360 for gray matter. Greater contrast is present in an image obtained from the combination of two FISP 70° images, one in which successive RF pulses were phase alternated and the other in which successive RF pulses were not phase alternated. Assuming both images are acquired with a TR of 20 msec, TE of 6 msec, and 62.5 acquisitions, the resulting FISP 70° signal is roughly 3.33 for CSF and 0.87 for gray matter. Compare this with the usual T2-weighted SE sequence with a TR of 2500 msec and TE of 90 msec; the CSF signal is roughly 0.530 whereas that for gray matter is 0.320. Clearly, in this application, FISP is superior with respect to C/N per unit time.

T2*, Field Inhomogeneities, and Chemical Shift

GFEs are sensitive to field inhomogeneities through T2*. This sensitivity is proving useful in studies involving finite microspheres in the liver and in studies of perfusion and hemorrhage [81]. They also exhibit an in-/opposed-phase behavior as a function of TE owing to chemical shift. This can lead to black boundaries at water/fat interfaces. Lipid components will also be amplitude modulated. For a field strength of 1.5 T and a chemical shift of 3.5 ppm, the in-phase images appear at TEs of 4.5 and 9.0 msec, and so on. The T2* in marrow when measured for these first two TE values is roughly only 8–10 msec. This short T2* is the cause of the dark marrow and fat (Fig. 9B) relative to disk and muscle on images with TE values even as short as 9 msec [82]. The existence of the phase error also causes problems with half-Fourier imaging [6]. It has been suggested that reducing TE and/or using 3-D or 4-D acquisitions can alleviate this problem [56]. Other approaches have included SE substitutes [54] and SSFP missing pulse measurements [48].

3-D Imaging

Three-dimensional imaging is not completely successful in obtaining contiguous thin-slice images because RF profiles are not perfect and Gibbs ringing along the third dimension also exists [55]. This can be especially problematic when the tissue properties vary dramatically along the slice-select direction or thick 3-D slices (partitions) are acquired. In either case, false information appears on the images. In addition, since information is phase encoded along the third dimension, motion artifacts appear along both the slice-select and in-plane phase-encoding directions. If the motion is approximately periodic, the associated artifacts can be minimized if not eliminated by setting the TRs multiplied by the number of partitions to be equal to the period of motion or some integer multiple thereof [61]. With high-quality 3-D data sets, preferably with isotropic resolution, MPR allows for viewing the data in any arbitrary orientation (Figs. 8C and 8D). MPR capability, in combination with high-quality spin-density T1- and T1/T2-weighted acquisition techniques, may make it possible to acquire clinically comprehensive MR examinations in some areas with only three 3-D GFE scans.

RARE Imaging

The RARE [3] technique allows heavy T2 weighting but at the expense of resolution (owing to T2 decay across phase-encoding views) and RF power deposition. Signal and contrast obtained with RARE sequence variations that use small flip angles, FLARE [83], are based on the same theory presented in the previous SSFP discussions.

EPI

EPI allows real-time imaging with optimal contrast for long T1 and T2 tissues since TEs can be varied from 26 msec to very large values while keeping TR essentially infinite. Its rapid acquisition allows for snapshot pictures and for movies to be made of motion throughout the cardiac or respiratory cycles. Resolution generally is limited to a voxel size of 1.5 × 1.5 × 4 mm^3, owing to gradient strength limitations and S/N arguments [28]. Nevertheless, applications may include cardiac, abdominal, CSF, cine, perfusion, 3-D, and flow imaging with the use of contrast agents in some cases. Some concern exists that high-resolution EPI applications possibly cause nerve stimuli.

Reconstruction Schemes

Partial-Fourier imaging can be used to reduce imaging time by reducing the number of phase-encoding steps needed. The reduction can be almost a factor of two when applied in the phase-encoding direction, but the concept has difficulties for 3-D GFE imaging when rapid local phase changes exist. Recently, sophisticated algorithms have been developed and these difficulties have been largely overcome [6]. Partial-Fourier imaging can be used in conjunction with any of the previously mentioned imaging techniques to reduce acquisition time. This technique also can be applied in the frequency-encoding direction to reduce TEs [5]. Although overall imaging time is not decreased, the increased ringing associated with the asymmetric echo acquisition in the read direction will be is reduced. The latter restriction continues to diminish as computer technology advances. The method may be particularly useful for improving resolution in EPI and snapshot

TABLE 1: Properties and Applications of Fast Scan MR Sequences

Sequence Type	Time	Clinical Applications[a]	Advantages/Disadvantages
EPI or instant scan	26–100 msec	1–6	Can give excellent spin-density or T2 contrast but needs special hardware
SSI			
FLASH or spoiled GRASS	1–5 sec	1, 2, 4, 7	Optimal S/N for T1 contrast with reduced flip angles but difficult to spoil transverse coherence for TR shorter than T2; significant T2* effects can degrade images (particularly with 2-D)
FATE or LASE	30 sec	3, 5, 6	No T2* decay; double echoes can be acquired but high RF power and sensitive to RF profile
SSC			
Rare ROAST and FISP	1–5 sec	2, 4–7	Short TR but sensitive to field inhomogeneities (via T2* and resonant offset for FISP)
ROAST, FAST, GRASS, FADE	1–5 sec	1, 2, 4, 6, 7	T2* signal loss as above and signal loss from moving tissue
CE-ROAST or CE-FAST	10–30 sec	2, 6, 7	T2* signal loss and poor S/N and signal loss from moving tissue
STAT (missing pulse)	1–10 sec	1, 2, 6, 7	No T2* loss but some loss of signal
RARE	5 sec	3, 6	Heavily T2 weighted but T2 filtered data and high RF power

Note.—All sequences can be acquired with $R_x = R_y = 0.5$ mm and $R_z = 2$ mm, except in 3-D, where $R_z = 0.5$ mm, and EPI, where $R_x = R_y = 4$ mm and $R_z = 5$ mm. Here, R_i refers to resolution in the *ith* direction. The times listed give the lower range of scan times, although longer TRs can always be used (except for the SSC techniques).

[a] 1 = cardiac; 2 = real time; 3 = conventional C/N; 4 = reduced motion artifacts; 5 = reduced flow artifacts; 6 = extra T2 weighting; 7 = low RF (not for large-angle 3-D).

TABLE 2: S/N at Optimal Flip Angles

Sequence	S/N Equation
FLASH	$S/N_1 = 2^{-1/2}(TR/T1)^{1/2}e^{-TE/T2^*}$
ROAST/FISP	$S/N_2 = \frac{1}{2}(T2/T1)^{1/2}e^{-TE/T2^*}$
CE-ROAST	$S/N_3 = S/N_2e^{-2TR/T2}$
FATE	$S/N_4 = S/N_1(1 - 2TI/TR)e^{-TE(1/T2 - 1/T2^*)}$
HYBRID/EPI	$S/N_5 = [1 - e^{-Q \cdot TR/T1)}e^{-TE/T2}]/Q^{1/2}$
SE	$S/N_6 = (TR/T1 - TE/T1)e^{-TE/T2}$

Note.—The factor of exp(−2TR/T2) in the CE-ROAST signal is valid when the signal is integrated over a 0–2π range of β. Note, for TR = T2 $\sqrt{2}$, FISP and FLASH signals are equal. Note the TR independence of FISP (for TR $\ll$ T2) for a fixed value of sampling time, TS, and gradient strength, G. Clearly, if TR is to be reduced below the given sampling time, then G (and signal bandwidth) increases (TS decreases), and hence the sequence acquires a $\sqrt{TR}$ dependence through G. Similarly, HYBRID has a $\sqrt{TR}$ dependence through Q (since as Q increases the effective TR decreases, i.e., Q·TR is fixed). Lastly, the SE is seen to suffer a linear loss with TR. The RF is assumed to be ideal and is applied along the $\hat{x}$ axis for all examples.

TABLE 3: Practical S/N Normalized to a Circularly Polarized Head Coil at 1.0 T for 2-D Applications

Sequence	CSF	Gray Matter	White Matter
FLASH	18.3	29.1	31.0
FISP	85.6	28.4	28.6
Enhanced ROAST	81.7	9.9	8.8
FATE	11.0	17.5	18.6
HYBRID/EPI	16.4	21.7	18.7
SE	3.3	9.4	12.8
Signal maximum	200	180	150

Note.—The values can be scaled according to field strength, tissue properties, TR, and TE so as to be generalized to any set of tissues and set of imaging parameters. For tissues such as blood, which are refreshed as they move, the most efficient sequences for obtaining peak signal may be the EPI-like sequences. The ratio of 200:1 is used for TE = 0 and TR = ∞ for voxel dimensions of 1 × 1 × 5 mm^3. The values were calculated by using the S/N equations shown in Table 2 with TR = 50 msec, TE = 0 msec, TI = 10 msec, and Q = 64. The values of ρ, T1, and T2 can be found in Table 4. Changing slice thickness, resolution, etc., will accordingly change the scale. For the gradient-echo sequences, T2* rather than T2 appears in the exponential weighting term at the echo. T2* will vary with voxel size, 2-D vs 3-D acquisition, and field strength.

TABLE 4: Tissue Parameters at 1.0 T

Tissue	T1	T2	T1/T2	Spin Density
White matter	585	85	6.9	0.75
Gray matter	955	95	10.5	0.90
CSF	3000	2200	1.4	1.00
Vertebral body	554	50	11.1	0.80
Intervertebral disk	934	90	10.4	0.80
Spinal cord	700	90	7.8	0.75
Fat	284	50	5.7	0.90
Muscle	758	45	16.8	0.75

Note.—Spin densities are relative, normalized to that of CSF. Since $T2^*$ varies as a function of spatial parameters, acquisition mode (i.e., 2-D or 3-D), and location in the body, $T2^*$ was set equal to T2 for all simulations. (The T1 of CSF may be higher than the value of 3 sec used here.)

imaging without compromising overall imaging time. Further reductions in time and/or ringing may be possible with the use of constrained reconstruction techniques [10]. These latter methods currently suffer from long reconstruction times.

Summary

Some of the different techniques and their signal and contrast properties are shown in Table 1. The S/N obtained with each technique under ideal imaging conditions is shown in Table 2. In Table 3, some practical values of signal intensity are presented for the various techniques and a variety of tissues. The tissue parameters used for all signal and contrast calculations are shown in Table 4.

Conclusions

Fast imaging has matured to the point where it has become clinically viable for many real-time and morphologic studies. We have discussed the numerous factors affecting the contrast in MR fast imaging and have shown how each type may have its own unique role in some part of the clinical domain. Some important characteristics of fast imaging that can be exploited include (1) use of the shortest TR possible with ROAST and FISP; (2) pseudogating to reduce motion artifacts; (3) 2-D and 3-D angiographic imaging for flow visualization; (4) 3-D imaging with short TE for high resolution and reduction of $T2^*$ effects (as in MR arthrography or pituitary studies); (5) preferably isotropic 3-D data for MPR in any orientation; (6) the use of FLASH or ROAST for cardiac cine imaging; (7) the use of snapshot 2-D and 3-D abdominal and cardiac imaging; and (8) the combined use of FISP and FLASH for rapid acquisition of spin density-, T1-, and T1/T2-weighted imaging for CSF myelographic or pathologic studies in the CNS or musculoskeletal system.

ACKNOWLEDGMENT

One of us (J. A. T.) would like to thank Siemens Medical Systems, Inc., Iselin, NJ, for support during the preparation of this review.

Appendix: Definitions of MR Abbreviations and Symbols Used in this Article

2-D	two dimensions, two-dimensional
3-D	three dimensions, three-dimensional
CE	contrast enhanced
C/N	contrast to noise
EPI	echo planar imaging
FADE	SSFP sequence
FAST	fast steady state
FATE	SE equivalent of FLASH ($\alpha \leq 90$)
FID	free induction decay
FISP	fast imaging with steady-state precession
FLARE	RARE sequence with small flip angles
FLASH	fast low-angle shot
G	gradient strength
G_{pe}	phase-encoding gradient
G_r	read gradient
G_{ss}	slice-select gradient
GFE	gradient field echo
GRASS	gradient-recalled acquisition in the steady state
HYBRID	combination of EPI and normal SE
LASE	large-angle spin echo ($\alpha > 90$)
M_o	equilibrium value of magnetization
M_y	transverse magnetization when $\beta = 0$
MIP	maximum intensity projection
MPR	multiplanar reconstruction
N_{acq}	number of times a sequence has repeated
N_i	number of sample points in *ith* direction
Phi	phase evolution for an isochromat in all directions
PSIF	sequence designed to acquire SE portion of SSFP signal
Q	time reduction in HYBRID
R_i	resolution in the *ith* direction
RARE	technique of phase encoding between echoes (rapid acquisition with repeated echoes)
Rare ROAST	ROAST sequence in which gradients along only one of the directions is left unbalanced
ROAST	resonant offset average steady state
SE	spin echo
SFP	SSFP
Spoiled GRASS	GRASS sequence in which the TR is much greater than the T2 or β is randomized (FLASH)
SSC	steady-state coherent
SSFP	steady-state free precession
SSI	steady-state incoherent
S/N	signal to noise
STAT	missing pulse SFP technique
TE	echo time
TH	slice thickness
TI	inversion time
TR	repetition time
α	flip angle
β	resonant offset angle
ρ	spin density

REFERENCES

1. Haacke EM, Bearden FH, Clayton JR, Linga NR. Reduction of MR imaging time by hybrid fast-scan technique. *Radiology* **1986**;158:521–529
2. Van Uijen CMJ, Den Boef JH, Verschuren FJJ. Fast Fourier imaging, *Magn Reson Med* **1985**;2:203–217

3. Hennig J, Nauerth A, Friedburg H. RARE imaging: a fast imaging method for clinical MR. *Magn Reson Med* **1986**;3:823–833
4. Feinberg DA, Hale JD, Watts JC, Kaufman L, Mark A. Halving MR imaging time by conjugation: demonstration at 3.5 kG. *Radiology* **1986**;161:527–531
5. Haacke EM, Mitchell J, Lee D. Improved contrast using half-Fourier imaging: application to spin echo and angiographic imaging. *Magn Reson Imaging* **1989**;8:79–90
6. Lindskog E, Haacke EM, Mitchell JD, Liang Z. Half Fourier imaging: a partially phase constrained iterative reconstruction scheme and an evaluation of several fast reconstruction schemes (abstr). In: *Book of abstracts. Society of Magnetic Resonance in Medicine. Eighth Annual Meeting.* Berkeley, CA: Society of Magnetic Resonance in Medicine, **1989**:363
7. MacFall JR, Pelc NS, Vavrek RM. Correction for spatially dependent phase shifts for partial Fourier imaging. *Magn Reson Imaging* **1988**;6:143–155
8. Margosian P, Schmitt F, Purdy D. Faster MR imaging: imaging with half the data. *Health Care Instrum* **1986**;1:195–197
9. Haacke EM, Liang ZP, Izen SH. Constrained reconstruction: a superresolution optimal signal-to-noise alternative to the Fourier transform in magnetic resonance imaging. *Med Phys* **1989**;16:388–397
10. Liang ZP, Haacke EM, Thomas CW. High resolution inversion of finite Fourier transform data through localized polynomial approximation. *Inverse Prob* **1989**;5:831–838
11. Smith MR, Nichols ST, Henkelman RM, Wood ML. Applications of ARMA parametric modeling in MRI reconstruction. *IEEE Trans Med Imaging* **1986**;MI-5:132–139
12. Bruder H, Fischer H, Graumann R, Diemling M. A new steady-state sequence for simultaneous acquisition of two MR images with clearly different contrasts. *Magn Reson Med* **1988**;7:35–42
13. Frahm J, Hasse A, Matthaei D. Rapid three dimensional MR imaging using the FLASH technique. *J Comput Assist Tomogr* **1986**;10:363–368
14. Frahm J, Haase A, Mathaei D. Rapid NMR imaging of dynamic processes using the FLASH technique. *Magn Reson Med* **1986**;4:48–60
15. Freeman R, Hill HDW. Phase and intensity anomalies in Fourier transform NMR. *J Magn Reson* **1971**;4:366–383
16. Gyngell ML. The application of steady state free precession in rapid 2D-FT imaging: FAST and CE-FAST Sequences. *Magn Reson Imaging* **1988**;6:415–419
17. Haase A, Frahm J, Matthaei D, Hanicke W, Merboldt K-D. FLASH imaging. Rapid NMR imaging using low flip-angle pulses. *J Magn Reson* **1986**;67:256–266
18. Haase A, Matthaei D, Hanicke W, Frahm J. Dynamic digital subtraction MR imaging using the FLASH method. *Radiology* **1986**;160:537–541
19. Johnson G, Hutchinson JMS. The limitations of NMR recalled-echo imaging techniques. *J Magn Reson* **1985**;63:14–30
20. Matthaei D, Frahm J, Haase A, Hanicke W, Merboldt KD. 3D FLASH MR imaging of the thorax and abdomen without triggering or gating. *Magn Reson Imaging* **1986**;4:381–386
21. Oppelt A, Graumann R, Barfuss H, Fischer H, Hertl W, Schajor W. A new fast MRI sequence. *Electromed* **1986**;3:15–18
22. Sekihara K. Steady-state magnetizations in rapid NMR imaging using small flip angles and short repetition intervals. *IEEE Trans Med Imaging* **1987**;MI-6:157–164
23. Van der Muelen P, Groen JP, Cuppen JJM. Very fast MR imaging by field echoes and small angle excitation. *Magn Reson Imaging* **1985**;3:297–299
24. Frahm J, Merboldt KD, Bruhn H, Gyngell ML, Hanicke W, Chien D. 0.3 second FLASH MRI of the human heart. *Magn Reson Med* **1990**;13:150–157
25. Haase A. Snapshot FLASH MRI applications to T1, T2 and chemical shift imaging. *Magn Reson Med* **1990**;13:77–89
26. Mansfield P, Pykett IL. Biological and medical imaging by NMR. *J Magn Reson* **1978**;29:355–373
27. Ordidge RJ, Howsemann A, Coxon R, et al. Snapshot imaging at 0.5 T using echo planar techniques. *Magn Reson Med* **1988**;8:110–115
28. Rzedzian RR, Pykett IL. Instant images of the human heart using a new, whole-body MR imaging system. *AJR* **1987**;149:245–250
29. Ordidge RJ, Howseman A, Coxon R, et al. Snapshot imaging at 0.5T using echo-planar techniques. *Magn Reson Med* **1980**;10:227–240
30. Hahn EL. Spin echoes. *Phys Rev* **1950**;80:580–594
31. Carr HY. Steady-state precession in nuclear magnetic resonance. *Phys Rev* **1958**;112:1693–1701
32. Kaiser R, Bartholdi E, Ernst RR. Diffusion and field-gradient effects in NMR Fourier spectroscopy. *J Chem Phys* **1974**;60:2966–2979
33. Hinshaw WS. Image formation by nuclear magnetic resonance: the sensitive-point method. *J Appl Phys* **1976**;47:3709–3721
34. Buxton RB, Edelman RR, Rosen BR, Wismer GL, Brady TJ. Contrast in rapid MR imaging: T1- and T2-weighted imaging. *J Comput Assist Tomogr* **1987**;11:7–16
35. Gyngell ML. The steady state signal in short repetition time sequences. *J Magn Reson* **1989**;81:474–483
36. Hanicke W, Merboldt KD, Frahm J. Slice selection and T_1 contrast in FLASH NMR imaging. *J Magn Reson* **1987**;77:64–74
37. Hawkes RC, Patz S. Rapid Fourier imaging using steady-state free precession. *Magn Reson Med* **1987**;4:9–23
38. Hawkes RC, Patz S. Some factors that influence the steady state in steady-state free precession. *Magn Reson Imaging* **1988**;6:405–413
39. Hendrick RE, Kneeland JB, Stark DD. Maximizing signal-to-noise and contrast-to-noise ratios in FLASH imaging. *Magn Reson Imaging* **1989**;5:117–127
40. Lee SY, Cho ZH. Fast SSFP GE sequences for simultaneous acquisition of FID and echo signals. *Magn Reson Med* **1988**;8:142–150
41. Matsui S, Kuroda M, Kohno H. A new method of measuring T2 using steady-state free precession. *J Magn Reson* **1985**;62:12–18
42. Van der Meulen P, Groen JP, Tinus AMC, Bruntink G. Fast field echo imaging: an overview and contrast calculations. *Magn Reson Imaging* **1988**;6:355–368
43. Young IR, Payne JA, Collins AG, Bydder GM. MRI: the development of T2 contrast with rapid field echo sequences. *Magn Reson Med* **1987**;4:333–340
44. Young IR, Bryant DJ, Payne JA. Variations in slice shape and absorption as artifacts in the determination of tissue parameters in NMR imaging. *Magn Reson Med* **1985**;2:355–389
45. Zur Y, Stokar S, Bendel P. An analysis of fast imaging sequences with steady state transverse magnetization refocusing. *Magn Reson Med* **1988**;6:175–193
46. Crawley AP, Wood ML, Henkelman RM. Elimination of transverse coherences in FLASH MRI. *Magn Reson Med* **1988**;8:248–260
47. Frahm J, Merboldt K-D, Hanicke W. Transverse coherence in rapid FLASH NMR imaging. *J Magn Reson* **1987**;27:307–314
48. Patz S, Wong STS, Roos MS. Missing pulse steady-state free precession. *Magn Reson Med* **1989**;10:194–209
49. Bydder GM, Payne JA, Collins AG, et al. Clinical use of rapid T2 weighted partial saturation sequences in MR imaging. *J Comput Assist Tomogr* **1987**;11:17–23
50. Jolesz FA, Patz S. Clinical experience with rapid 2DFT SSFP imaging at low field strengths. *Magn Reson Imaging* **1988**;6:397–403
51. Mills TC, Ortendahl DA, Hylton NM, Crooks LE, Carlson JW, Kaufman L. Partial flip angle MR imaging. *Radiology* **1987**;162:531–539
52. Hackney DB, Lenkinski RE, Grossman RI, et al. Initial experience with fast low-angle multiecho (FLAME) imaging of the central nervous system. *J Comput Assist Tomogr* **1988**;12:171–174
53. Redpath TW, Jones RA. FADE—a new fast imaging sequence. *Magn Reson Med* **1988**;6:234–244
54. Tkach JA, Haacke EM. A comparison of fast spin echo and gradient field echo sequences. *Magn Reson Imaging* **1988**;6:373–389
55. Carlson J, Crooks L, Ortendahl D, Kramer D, Kaufman L. Signal-to-noise ratio and section thickness in two-dimensional versus three-dimensional Fourier transform MR imaging. *Radiology* **1988**;166:266–270
56. Haacke EM, Tkach JA, Parrish TB. Reducing $T2*$ dephasing in gradient field-echo imaging. *Radiology* **1989**;170:457–462
57. Haacke EM, Wielopolski P, Tkach JA, Modic MT. Steady state free precession imaging in the presence of motion: an application to cerebrospinal fluid. *Radiology* **1990**;175:545–552
58. Iwaoka H, Sugiyama T, Matsura H, Fujino K. A new pulse sequence for "fast recovery" fast-scan NMR imaging. *IEEE Trans Med Imaging* **1984**;MI-3:41–46
59. Maki JH, Johnson GA, Goefer GP, MacFall JR. SNR improvement in NMR microscopy using DEFT. *J Magn Reson* **1988**;80:482–492

60. Van Uijen CMJ, Den Boef JH. Driven-equilibrium radiofrequency pulses in NMR imaging. *Magn Reson Med* **1984**;1:502-507
61. Haacke EM, Lenz GW, Nelson AD. Pseudo-gating: elimination of periodic motion artifacts in MRI without gating. *Magn Reson Med* **1987**;4:162-174
62. Patz S, Hawkes RC. The application of steady-state free precession to the study of very slow fluid flow. *Magn Reson Med* **1986**;3:140-145
63. Haacke EM. Image behavior: resolution, signal-to-noise, contrast and artifacts. In: Modic MT, ed. *Magnetic resonance imaging of the spine*. Chicago: Year Book Medical, **1988**:1-34
64. Hennig J, Friedburg H. Clinical applications and methodological developments of the RARE technique. *Magn Reson Imaging* **1988**;6:391-395
65. Frahm J, Merboldt KD, Hanicke W. Direct FLASH MR imaging of magnetic field inhomogeneities by gradient compensation. *Magn Reson Med* **1988**;6:474-480
66. Lenz GW, Haacke EM, White R. Retrospective cardiac gating: a review of technical aspects and future directions. *Magn Reson Imaging* **1989**;7:445-455
67. Lipton MJ, Higgins CB. Ultrafast CT and dynamic MR. *Dynamic Cardiovasc Imag* **1987**;1:40-48
68. Spritzer CE, Herfkens RJ. Magnetic resonance of the heart. In: Kressel HY, ed. *Magnetic resonance annual 1988*, vol. 6. New York: Raven, **1988**:121-139
69. Edelman RR, Wentz KU, Mattle H, et al. Projection arteriography and venography: initial clinical results. *Radiology* **1989**;172:351-357
70. Frahm J, Merboldt K-D, Hanicke W, Haase A. Flow suppression in rapid T2 contrast with rapid FLASH NMR imaging. *Magn Reson Med* **1987**;4:327-377
71. Keller PJ, Drayer BP, Fram EK, Williams KD, Dumoulin CL, Souza SP. MR angiography with two-dimensional acquisition and three-dimensional display. Work in progress. *Radiology* **1989**;173:527-532
72. Masaryk TJ, Ross JS, Modic MT, Lenz GW, Haacke EM. Carotid bifurcation: MRI. *Radiology* **1988**;111:461-466
73. Masaryk TJ, Modic MT, Ruggieri PM, et al. Three-dimensional (volume) gradient-echo imaging of the carotid bifurcation: preliminary clinical experience. *Radiology* **1989**;171:801-806
74. Lenz GW, Haacke EM, Masaryk TJ, Laub G. In-plane vascular imaging: pulse sequence design and strategy. *Radiology* **1988**;166:875-882
75. Gullberg GT, Wehrli F, Shimakawa A, Simons MA. MR vascular imaging with a gradient refocussing pulse sequence and reformatted images from transaxial sections. *Radiology* **1987**;165:241-246
76. Haacke EM, Lenz GW. Improving image quality in the presence of motion by using rephasing gradients. *AJR* **1987**;148:1251-1258
77. Nishimura DG, Macovski A, Pauly JM. Magnetic resonance angiography. *IEEE Trans Med Imaging* **1986**;MI-5:140-151
78. Mirowitz SA, Lee JKT, Brown JJ, Eilenberg SS, Heiken JP, Perman WH. Rapid acquisition spin-echo (RASE) MR imaging: a new technique for reduction of artifacts and acquisition time. *Radiology* **1990**;175:131-135
79. Brookeman JR, Mugler JP III. High-speed MR imaging at high field. *Appl Radiol* January **1990**:12-16
80. Henrich D, Haase A, Matthaei D. 3D-snapshot FLASH NMR imaging of the human heart. *Magn Reson Imaging* **1990**;8:377-379
81. Edelman RR, Johnson K, Buxton R, et al. MR of hemorrhage: a new approach. *AJNR* **1986**;7:751-756
82. Haacke EM, Patrick JL, Lenz GW, Parrish TB. The separation of water and lipid components in the presence of field inhomogeneities. In: *Reviews of Magnetic Resonance in Medicine*, **1986**;1:123-154
83. Hennig J. Multiecho imaging sequences with low refocusing flip angles. *J Magn Reson* **1988**;78:397-407

Pictorial Essay

Malignant Pleural Mesothelioma: CT Manifestations in 50 Cases

Akira Kawashima[1] and Herman I. Libshitz

Malignant pleural mesothelioma, a rare and usually fatal neoplasm that is associated with asbestos exposure, is being encountered with increasing frequency. Pretreatment CT findings from 50 patients with malignant pleural mesothelioma are illustrated. Pleural thickening was found in 46 (92%) of the 50 patients, thickening of the pleural surfaces of the interlobar fissures in 43 (86%), pleural calcifications in 10 (20%), and pleural effusions in 37 (74%). The volume of the involved hemithorax varied appreciably. Contractions of the involved hemithorax was noted in 21 (42%) of 50 patients and contralateral mediastinal shift in seven (14%). Disease beyond the parietal pleura was found in the chest wall (nine patients), mediastinum, lymph nodes, and diaphragm.

Malignant pleural mesothelioma (MPM) is a rare and usually fatal neoplasm that is increasing in frequency [1, 2]. It is associated with exposure to asbestos [1, 2]. The clinical signs and symptoms are nonspecific. The histologic diagnosis of MPM by light microscopy may be difficult and require the aid of electron microscopy and immunohistochemistry. In this essay, we present our experience with pretreatment CT findings in 50 patients, 25 of whom had follow-up studies.

Materials and Methods

Pretreatment CT findings in 50 patients (45 men and five women) seen at our institution from June 1980 through January 1990 were reviewed retrospectively. The mean age was 59 years (range, 37–85 years). A definite history of asbestos exposure was present in 24 (48%). One patient had had radiation therapy to the thorax 30 years before for breast cancer.

The diagnoses were verified by more than one pathologist at our institution. Twenty patients underwent radical surgery and/or autopsies. Histologic subtyping was possible in 44 patients. The MPMs were classified as epithelial (tubulopapillary) in 30, sarcomatoid (fibrous, fibrosarcomatous) in 11, and mixed (biphasic) in three [1, 2].

Twenty-five patients had from two to seven (average, 3.6) follow-up CT scans. The mean observation period per patient spanned 8.2 months (range, 3–44 months).

Pleural Disease

Pleural Thickening

The most common finding was pleural thickening that varied in extent, thickness, and nodularity. This was seen in 46 (92%) of 50 patients. Associated pleural effusions were present in 33 (72%) of the 46 patients. The pleural thickening ranged from nonspecific plaquelike lesions seen in three patients (Fig. 1) to a complete or nearly complete rindlike encasement of the entire lung (Fig. 2). The great variability in pleural thickening can be appreciated on other CT images as well.

Focal pleural masses were seen in four patients (8%), all of whom had pleural effusions. The masses ranged from 7 to 18 cm in maximum diameter. Two of these four patients had chest wall invasion.

Received March 26, 1990; accepted after revision May 30, 1990.
Presented in part at the annual meeting of the Society of Thoracic Imaging, Naples, FL, January 1990.

[1] Both authors: Department of Diagnostic Radiology, The University of Texas M. D. Anderson Cancer Center, 1515 Holcombe Blvd., Houston, TX 77030. Address reprint requests to H. I. Libshitz.

AJR **155:965–969, November 1990** 0361–803X/90/1555–0965 © American Roentgen Ray Society

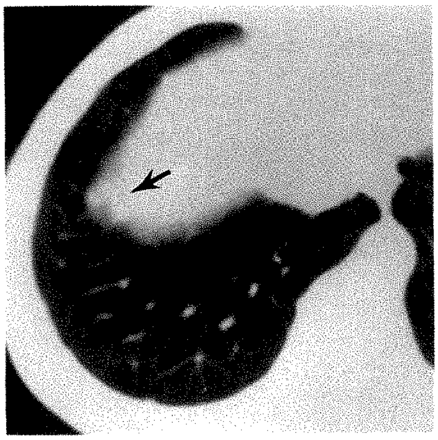
1

Fig. 1.—51-year-old man with an epithelial malignant pleural mesothelioma diagnosed at pleuroscopic biopsy. CT scan shows nonspecific plaques (*arrow*) abutting right hemidiaphragm.

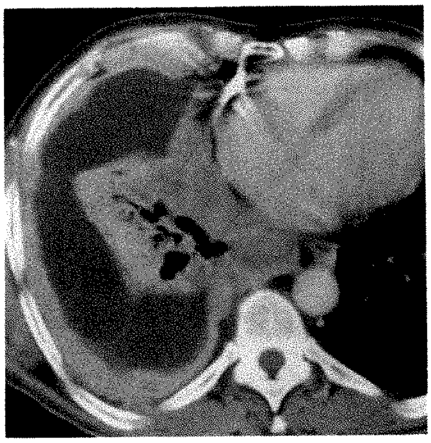
2

Fig. 2.—65-year-old man with epithelial malignant pleural mesothelioma and a history of asbestos exposure. CT scan shows diffuse, irregular pleural thickening involving both parietal and visceral pleurae. Pleural effusion is present and lung is markedly contracted.

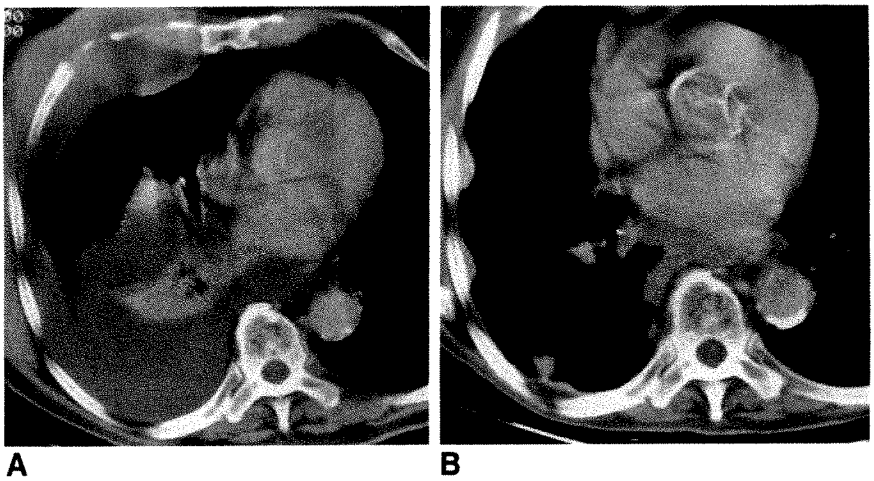

Fig. 3.—85-year-old man with an unclassified malignant pleural mesothelioma.

A, CT scan shows infiltrating chest wall mass destroying ribs and associated moderate pleural effusion.

B, 15 months after tangential external beam radiation therapy, chest wall mass and pleural effusion have markedly diminished. However, nodular pleural thickening has developed.

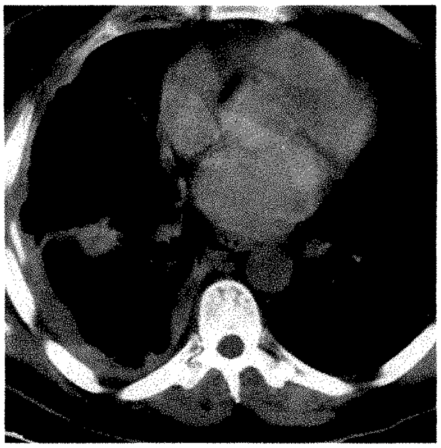

Fig. 4.—56-year-old man with mixed malignant pleural mesothelioma. CT scan shows nodular pleural thickening in major interlobar fissure on right that is contiguous with pleural thickening in periphery of lung.

In 22 medically treated patients with serial CT scans, interval progression occurred in 16, no appreciable change in three, improvement in two, and mixed response in one. Progression of the pleural disease can be seen in Figure 3 in a patient who also had a focal infiltrating chest wall mass that diminished with radiotherapy.

Fissural Involvement

Thickening of the pleural surfaces of the interlobar fissures was seen in 43 (86%) of 50 patients. Like the pleural involvement elsewhere, this may be seen as thickening and/or nodularity (Fig. 4). However, pleural effusion is difficult to distinguish from true pleural thickening, particularly in the absence of nodularity when the involvement is not extensive. Because of its horizontal orientation, involvement of the minor fissure may be difficult to identify on CT scans.

Pleural Calcifications

Pleural calcifications were seen in 10 patients (20%). The calcifications were seen in the mesothelioma in six cases. In five, they appear to have originated in a pleural plaque (Fig. 5). A history of asbestos exposure was present in three of the five. The calcification was stippled in the sixth mass. Calcified plaques in keeping with asbestos-related disease were seen bilaterally in four patients (Fig. 6). None of our patients had radiologic evidence of pulmonary fibrosis, although thin-section CT scans were not obtained.

Pleural Effusion

Pleural effusions were present in 37 (74%) of 50 patients. The volume of the pleural effusion was estimated as composing less than one third of the hemithorax in 18 patients, one

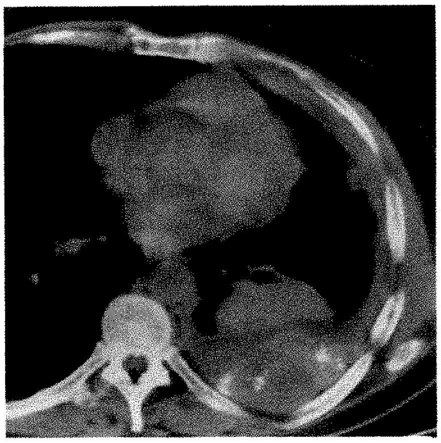

5

Fig. 5.—46-year-old man with sarcomatoid malignant pleural mesothelioma and history of asbestos exposure. CT scan shows calcification in tumor in left chest. Consolidated lung anterior to calcified mass was invaded by tumor.

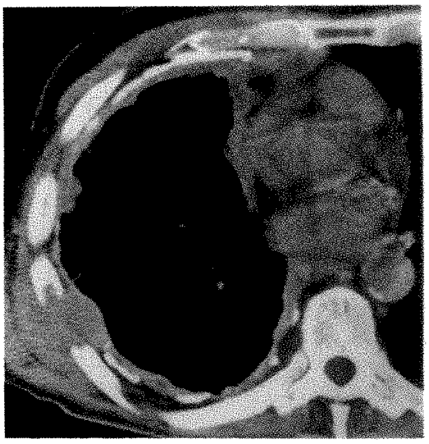

6

Fig. 6.—72-year-old man with mixed malignant pleural mesothelioma (MPM) and history of asbestos exposure. CT scan shows bilateral calcified pleural plaques in keeping with asbestos-related disease. MPM is nodular mass invading chest wall and destroying ribs on right.

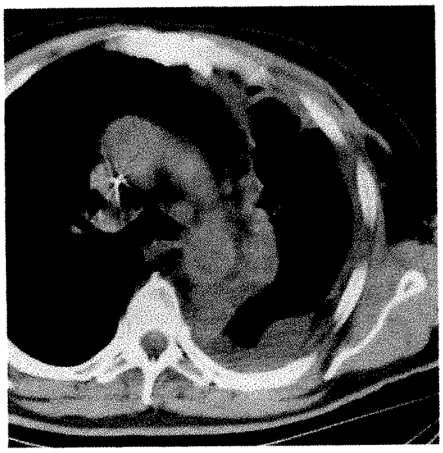

7

Fig. 7.—65-year-old man with epithelial malignant pleural mesothelioma. CT scan shows volume loss in left hemithorax, but there is no mediastinal shift.

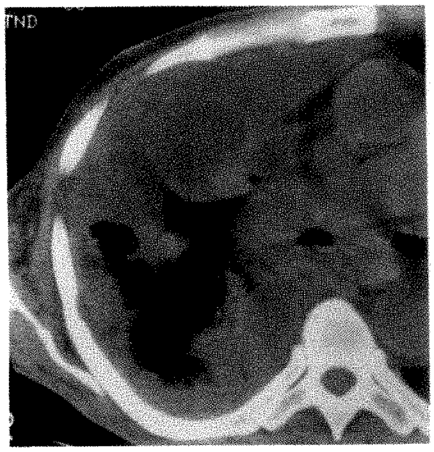

8

Fig. 8.—74-year-old man with unclassified malignant pleural mesothelioma (MPM). CT scan shows bulky pleural disease and pleural effusion associated with this right-sided MPM, which has caused contralateral mediastinal shift. Of note is pleural thickening across mediastinum into contralateral hemithorax along aorta.

to two thirds of the hemithorax in 15 patients, and more than two thirds in four patients.

Volume of the Involved Hemithorax

The volume of the involved hemithorax varied appreciably. There was contraction of the involved hemithorax with or without ipsilateral mediastinal shift, no difference between hemithoraces, and increased volume with contralateral mediastinal shift.

Contraction of the involved hemithorax was noted in 21 patients (42%). It was associated with ipsilateral mediastinal shift in 11 and was without obvious shift in 10 (Fig. 7). Other signs of volume loss on CT included narrowed intercostal spaces and elevation of the ipsilateral hemidiaphragm.

Contralateral mediastinal shift was seen in seven patients (14%). It was due to a large effusion in five patients and both effusion and tumoral mass in two patients (Fig. 8). No difference in the volume of the hemithoraces or position of the mediastinum was seen in 22 patients (44%).

A "frozen" mediastinum and loss of volume of the involved hemithorax have been suggested as diagnostic features of malignant pleural mesothelioma [1, 3]. However, a sufficiently large pleural effusion and/or bulky mass may cause mediastinal shift to the contralateral side so that volume loss or fixation of a hemithorax need not be present.

Serial CT scans in eight patients with contraction of the hemithorax on the initial study showed progressive volume loss in three and no change in five. Two of 10 patients with neither mediastinal shift nor volume loss at presentation developed contralateral shift owing to increase in the effusion in one and increase of both the effusion and tumor in the other. Ipsilateral volume loss developed in three of the 10. Five remained midline. In no patient with ipsilateral mediastinal shift did the mediastinum return to midline even with progression of disease.

Disease Beyond the Parietal Pleura

MPM spreads primarily by local extension throughout the pleural cavity, with subsequent invasion of the chest wall, mediastinum, and diaphragm, and into the abdomen and retroperitoneum [1, 2, 4]. Hematogenous metastatic disease is less common [2]. CT is valuable in determining the extent of disease beyond the parietal pleura at the initial evaluation and in the follow-up of patients during treatment [4].

Chest Wall Invasion

Chest wall invasion was noted in nine patients (18%), with obvious rib involvement in five (10%) (Figs. 3 and 6). Of interest, chest wall invasion was present in five (45%) of 11 sarcomatoid MPMs, four of which had rib destruction. Serial CT scans revealed development of chest wall invasion in four additional patients and invasion of the dorsal spine in one. Rusch et al. [4], in a surgical series, noted that CT underestimates chest wall invasion and may suggest it when it is not present.

Mediastinal Invasion

Mediastinal pleural involvement often was associated with pericardial thickening to various degrees. In many cases it was virtually impossible to distinguish pleural disease alone from associated pericardial disease. Pericardial disease is certainly more common than in the eight patients in whom it was proved at either surgery or autopsy (Fig. 9). Three patients developed pericardial effusion. It caused pericardial tamponade in two and was asymptomatic in the third. When involvement of the mediastinal pleura was bulky or extensive, involvement of other mediastinal structures was thought to be likely. Extension of the tumor into the contralateral hemithorax was seen in two patients (Fig. 8).

Lymph Node Involvement

All nodal groups were examined with the American Thoracic Society classification, and the sizes of the nodes were noted. Nodes 1 cm or larger in maximum diameter were found in 61 nodal groups in 29 patients. These included 13 patients with nodes 1 cm or larger in 15 nodal groups of the anterior diaphragmatic (Fig. 10) and internal mammary nodal areas. This indicates not only central lymphatic spread along the course of the tracheobronchial tree but also subpleural and/or chest wall lymphatic spread of this tumor.

Extensive pleural disease frequently enveloped and obscured the nodal anatomy in the hilar and middle mediastinal nodal groups. This was noted in 15 patients and involved 50 nodal groups.

In the 20 cases with either radical surgery or autopsy, the lymph nodes were proved to be involved with metastases in eight. Nodes 1 cm or larger in diameter were proved to be involved in four cases in six nodal groups (Fig. 11), and nodes less than 1 cm in diameter in four cases in seven nodal groups.

Of 22 patients with serial CT scans who were treated medically, new nodes 1 cm or larger in diameter developed in 13 patients in 20 nodal groups.

Diaphragmatic and Infradiaphragmatic Invasion

Thickening of the hemidiaphragm, presumably due to pleural disease, is common. Diphragmatic involvement does not preclude radical surgery; however, spread below the diaphragm does. Direct hepatic involvement was seen in two patients and proved at autopsy in one (Fig. 12). Direct retroperitoneal extension was present in four patients (Fig. 13); in two of these it was proved at surgery. This included retrocrural lymphadenopathy, which was seen in three patients (Fig. 14).

Serial CT scans revealed new hepatic invasion in one patient who also developed liver and lung metastases (Fig. 15).

Rusch et al. [4] found that involvement of the undersurface of the diaphragm was underestimated on CT in operated patients.

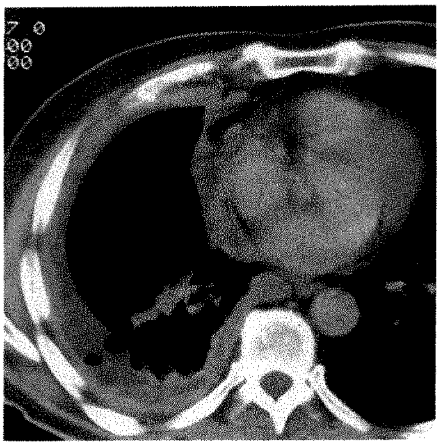

Fig. 9.—77-year-old man with epithelial malignant pleural mesothelioma. CT scan shows pericardial and pleural thickening in right hemithorax. Pericardial invasion was proved at surgery.

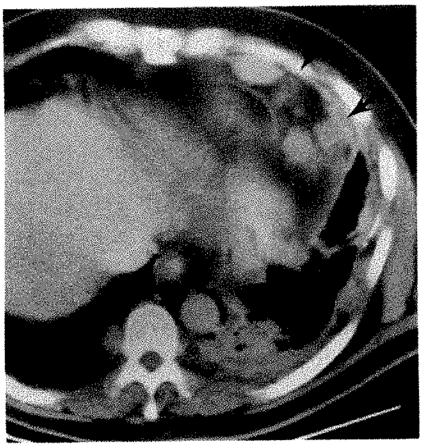

Fig. 10.—60-year-old man with epithelial malignant pleural mesothelioma and history of asbestos exposure. CT scan shows extensive anterior diaphragmatic adenopathy on left side (*arrows*). Ovoid density to right of spine is believed to represent paraspinous lymph node.

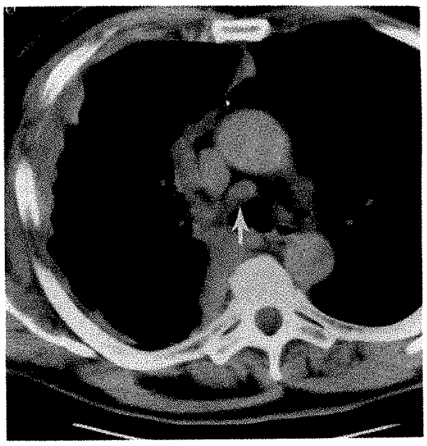

Fig. 11.—65-year-old man with epithelial malignant pleural mesothelioma. CT scan shows 2.0-cm node in right paratracheal region (*arrow*). Metastases to node were proved at surgery. Nodular, diffuse pleural thickening is seen as well.

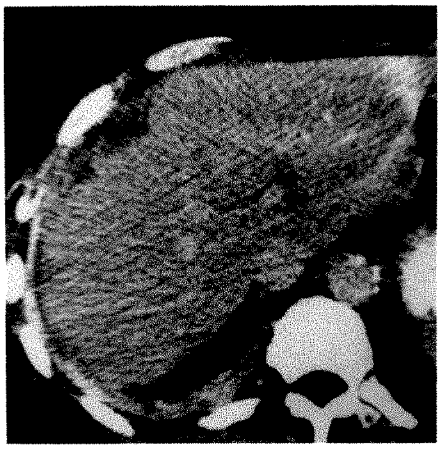

12

Fig. 12.—72-year-old man with epithelial malignant pleural mesothelioma and history of asbestos exposure. Contrast-enhanced CT scan shows direct extension of malignant pleural mesothelioma into liver as an area of decreased attenuation along lateral aspect of liver. Involvement was proved at autopsy.

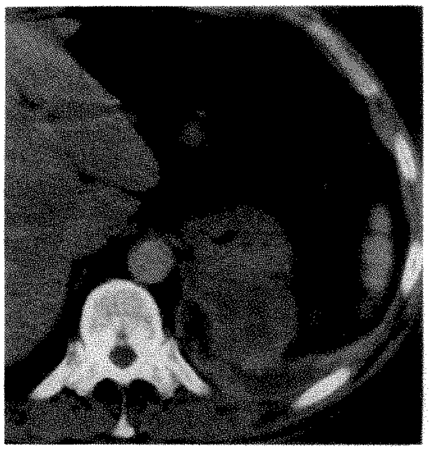

13

Fig. 13.—63-year-old man with sarcomatoid malignant pleural mesothelioma. CT scan shows direct extension into abdomen on left side. Mass of tumor abuts stomach.

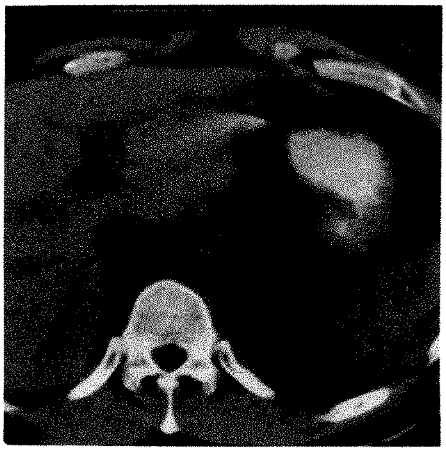

14

Fig. 14.—46-year-old man with epithelial mesothelioma and history of asbestos exposure. CT scan shows bilateral retrocrural nodal extension of left-sided tumor.

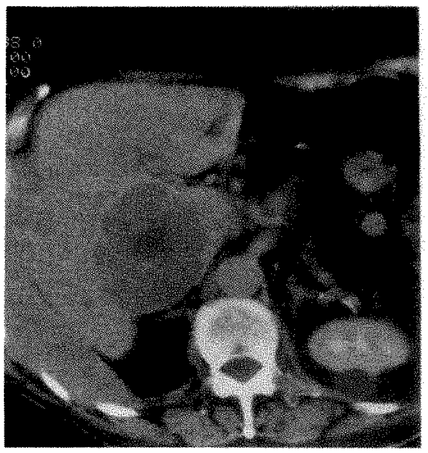

15

Fig. 15.—15-month follow-up CT scan of patient in Fig. 3 shows large mass with central necrosis in liver. This was presumed to represent metastatic disease as it was not present on the initial study. Direct hepatic invasion and chest wall invasion are also seen laterally on right side. Left renal lesion is a cyst.

REFERENCES

1. Antman KH. Clinical presentation and natural history of benign and malignant mesothelioma. *Semin Oncol* **1981**;8:313–320
2. Brenner J, Sordillo PP, Magill GB, Golbey RB. Malignant mesothelioma of the pleura: review of 123 patients. *Cancer* **1982**;49:2431–2435
3. Rabinowitz JG, Efremidis SC, Cohen B, Dan S, et al. A comparative study of mesothelioma and asbestos using computed tomography and conventional chest radiography. *Radiology* **1982**;144:453–460
4. Rusch VW, Godwin JD, Shuman WP. The role of computed tomography scanning in the initial assessment and follow-up of malignant pleural mesothelioma. *J Thorac Cardiovasc Surg* **1988**;96:171–177

Book Review

CT and MRI of the Thorax. Edited by Elias A. Zerhouni. (Vol. 11 in Contemporary Issues in Computed Tomography.) New York: Churchill Livingstone, 222 pp., 1990. $62

The principal aim of this book as stated by the editor is to evaluate the current status and future applications of CT and MR imaging of the chest. The book focuses primarily on CT, however. This can be explained easily by the greater wealth of clinical experience with CT than with MR. It would be impossible for a book of this size to be all inclusive, but the important areas of interest in thoracic imaging are included.

I thought it curious that the overview of CT and MR imaging is placed as the third chapter and not the first. It is probably fortunate, however, as this is perhaps the weakest chapter in the book. Virtually everything in this chapter is covered in more detail in the other chapters. My primary complaint is that this chapter makes bold statements about indications for MR imaging but then fails to illustrate these findings convincingly.

The first two chapters focus on clinical problems and not anatomic regions. CT of the immunocompromised (chapter 1) and MR imaging of lymphoma (chapter 2) are concise, informative, and well-illustrated discussions. Chapter 4 on the mediastinum overlaps with chapter 3 considerably. The focus of chapter 4 is clearly applications of MR imaging.

The next two chapters do more than simply recite what is in the literature. They are instructive. Someone attempting to acquire an understanding of high-resolution CT in diffuse lung disease (chapter 5) or of the use of CT and MR in focal lung disease (chapter 6) will enjoy these extremely well-focused discussions.

Chapter 7 on CT of the pleura is perhaps the most inclusive of all the chapters. In fact, it makes the subsequent chapter on the diaphragm redundant. I particularly liked the way this chapter blends radiologic and clinical information. The final chapter, on CT and MR of the airways, focuses on the CT anatomy of the lower lobe bronchi. It is well illustrated and one of the most instructive chapters in the book.

Five case presentations are found at the end of this book. I was a little surprised to find only CT cases, particularly in light of the preceding discussions of the increasing indications for MR of the chest.

Who should buy this book? For the actual amount of new material, I would say that it is a little overpriced for those actively involved in thoracic imaging on a day-to-day basis. Pulmonologists or general radiologists probably would benefit the most from this book.

David W. Nelson
Oregon Health Sciences University
Portland, OR 97201

Tuberculous Bronchial Stenosis:
CT Findings in 28 Cases

Kyu Ok Choe[1]
Hyeon Joo Jeong[2]
Hee Young Sohn[3]

Bronchial stenosis is a complication of tuberculous parenchymal or lymph node disease and may adversely affect its treatment. Findings on plain radiographs may be nonspecific or simulate malignancy. The purpose of this study was to evaluate the role of CT in diagnosing this abnormality. We reviewed the findings in 28 patients who underwent CT to evaluate bronchial stenosis proved by bronchoscopy. Eighteen had evidence of tuberculosis on bronchial biopsy. In the other 10 the biopsy findings were nonspecific, but tuberculous lesions were elsewhere in the thorax. Twelve patients (43%) had CT findings of concentric bronchial stenosis, uniform thickening of the bronchial wall, and involvement of a long segment of the bronchi. In 14 patients (50%), CT showed obliteration of bronchial outlines by adjacent lymphadenopathy, parenchymal consolidation, and absence of intraluminal air. In two patients, the abnormality was not visible on CT.

Our experience shows that CT is useful for identifying bronchial stenosis caused by tuberculosis. However, the findings vary, and in more than half of the patients concentric narrowing and uniform thickening of the bronchi are not seen.

***AJR* 155:971-976, November 1990**

The assessment of tuberculous bronchial stenosis is important in the management of patients with pulmonary tuberculosis. The stenosis may adversely affect treatment in some patients [1, 2]; in others, it may pose a serious diagnostic challenge because its appearance is similar to that of other pulmonary lesions, including cancer [3, 4]. The reported prevalence of tuberculous bronchial stenosis in patients with pulmonary tuberculosis varies from 40% in an autopsied series in the preantibiotic era [5] to 10% in patients who have undergone routine bronchofibroscopy in more recent years [6].

The use of chest radiographs is limited to evaluating the presence and degree of bronchial stenosis in these patients, often showing only secondary changes in the lung parenchyma [1-4, 7]. CT, however, is able to outline the encroached bronchus and identify changes in adjacent lymph nodes and in the lung parenchyma distal to the stenosis.

The purpose of this study was to review the CT findings in 28 patients with tuberculous bronchial stenosis in an attempt to define the role of CT in the diagnosis and management of these patients.

Materials and Methods

The 28 patients included in this study were seen between 1983 and 1988 and had tuberculous bronchial stenosis proved by bronchofibroscopy. The mean age was 49 years (range, 5-83 years); all except one were adults. There were eight men and 20 women.

In all patients, bronchofibroscopy showed bronchial stenosis with mucosal changes compatible with the hyperplastic or fibrostenotic stage of tuberculous bronchial stenosis. In 18 patients, tuberculous changes were found in the biopsy specimen from the affected bronchial

Received April 6, 1990; accepted after revision June 4, 1990.

[1] Department of Diagnostic Radiology, Yonsei University College of Medicine, C.P.O. Box 8044, Seoul, Korea. Address reprint requests to K. O. Choe.

[2] Department of Pathology, Yonsei University College of Medicine, Seoul, Korea.

[3] Department of Medicine, Section of Pulmonology, Yonsei University College of Medicine, Seoul, Korea.

0361-803X/90/1555-0971
© American Roentgen Ray Society

wall (Fig. 1). Acid-fast bacilli were detected in the sputum or the bronchial washing in 10 of the 18 and in the pleural fluid in one. The 10 patients without tuberculous changes also had bronchial stricture, but histologic examination of the bronchial wall revealed only nonspecific inflammatory changes in three, fibrosis in four, and both in three. These 10 patients were included in the study because the bronchial lesion was thought to represent later stages of tuberculous bronchial stenosis and there was also evidence of tuberculous lesions elsewhere in the thorax. Among the 10 patients, acid-fast bacilli were found in the sputum or bronchial washings in seven patients and tuberculous granulomata in the pleural biopsy specimen of one. Two patients who underwent a lobectomy and a pneumonectomy to manage stenotic lesions of the major bronchi had tuberculous lesions in the distal lung parenchyma and mediastinal lymph nodes (Figs. 2 and 3).

CT scans were obtained after contrast enhancement and during breath holding with the use of a GE 9800 (General Electric Medical Systems, Milwaukee, WI) or Philips Tomoscan 540 (Best, Holland) unit with a slice thickness of 1.0 cm. In six patients, additional 1.5-mm-thick high-resolution CT scans were obtained at the level of the diseased bronchi. CT images were analyzed retrospectively for changes in the size and shape of the bronchial lumen, structures around the bronchus, lung parenchyma, and adjacent lymph nodes. Bronchial luminal changes seen on CT were described as (1) diffuse, if the walls of the stenotic segment were parallel to each other (Fig. 2); (2) funnel-shaped, if the luminal narrowing was gradual, tapering off distally (Fig. 4); (3) complete obstruction, if there was no intraluminal gas (Fig. 5); and (4) extrinsic narrowing, if the bronchial lumen changed to a polygonal shape from diffuse compression of the wall (Fig. 6). The thickness of the bronchial wall could be measured only if there was air within the bronchus and mediastinal fat or aerated lung parenchyma around the bronchus (Figs. 2–4). Abnormalities in the lung parenchyma distal to the diseased lobar branches as well as elsewhere in the lung and changes in hilar and mediastinal lymph nodes were noted also.

The most proximal extent of bronchial stenosis, as seen at the time of bronchofibroscopy, was the trachea in two patients, the right or left main bronchus in 10, the right intermediate bronchus in five, the lobar bronchus in eight, and the segmental bronchus in three. The stenotic lesion, however, had a general tendency to involve a fairly long segment of the bronchus. In only two patients was disease confined to the right main and right intermediate bronchi (Fig. 6). In the remaining 15 patients who had proximal lesions in the trachea, the right and left main and the intermediate bronchi had extension of the disease into the lobar bronchi (Figs. 2–4). Consequently, the lobar distribution of the bronchial disease as seen by bronchofibroscopy and CT in these 26 patients was to the right upper lobe in eight patients, both right upper and middle lobes in two, right middle lobe in two, right middle and lower lobes in two, right lower lobe in one, left upper lobe in nine, and left lower lobe in two. The upper lobar bronchus was found to be the most frequently affected site ($n = 19$).

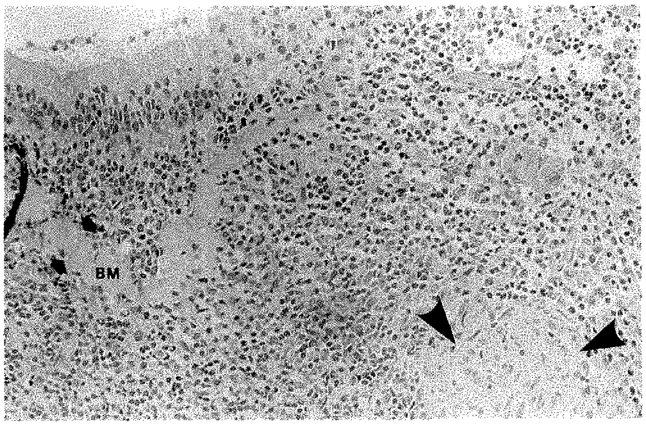

Fig. 1.—Bronchial biopsy specimen by bronchofibroscopy. Submucosa is diffusely infiltrated by lymphoplasmocytic cells with a small epitheloid granuloma in lower right corner (*arrowheads*). This granuloma does not show caseation necrosis, but there were other areas with granulomas associated with caseation necrosis. Overlying mucosa is intact. BM = basement membrane (between *arrows*). (H and E, ×100)

Results

CT confirmed the presence of bronchial stenosis in 26 (93%) of the 28 patients. In two patients, slight luminal narrowing of the right main and the right upper lobar bronchi seen on bronchoscopy was not present on the CT scan. In one of these patients, enlarged mediastinal lymph nodes adjacent to the bronchial lesion and, in the other, air-space nodules in the right upper lobe parenchyma were the only changes shown by CT. Even high-resolution CT with 1.5-mm slice thicknesses failed to show the bronchial abnormality in these patients.

The patterns of bronchial stenosis seen on CT images in the 26 patients were divided into two groups. Twelve patients had concentric bronchial stenosis with mild and uniform thickening of the bronchial wall (Figs. 2–4). The stenosis was funnel-shaped in seven patients and diffuse in five; all stenoses were located in the lobar bronchi with or without more proximal extension. In 14 patients, it was difficult to evaluate the status of the stenotic bronchus because the inner or outer wall of the bronchus was obliterated by enlarged lymph nodes or peribronchial abnormalities or both (Figs. 6 and 7). In nine patients, the enlarged lymph nodes were adjacent to the bronchial stenosis, causing loss of the silhouette of the outer wall of the bronchus. CT in three patients showed a polygonal stenosis of the right intermediate bronchus caused by extrinsic compression (Fig. 6). In the remaining patients it was not possible to define the nature of the luminal stenosis as being intrinsic or extrinsic (Fig. 7). CT showed mediastinal lymphadenopathy remote from the bronchial lesion in another two patients, unenlarged calcified mediastinal nodes in four (Fig. 2), and no evidence of lymphadenopathy in 12.

Three patients had bronchial lesions at the level of the segmental bronchus, all producing abrupt and complete obstruction of the lumen (Fig. 5). In these patients, it was impossible to assess the thickness of the bronchial wall, and, therefore, it was difficult to tell whether the endobronchial obstruction was caused by tumors, stagnant inflammatory exudates, or inflammatory changes of the bronchial wall. In two patients in whom CT showed either funnel-shaped or diffuse narrowing of the bronchial lumen, the stenotic bronchus was surrounded by homogeneous consolidation, making it difficult to exclude stenosis caused by enlarged peribronchial lymph nodes or transbronchial tumor growth.

In two patients, no abnormality was seen in the lung parenchyma on CT. In these patients the bronchial lesion was confined to the right main and right intermediate bronchi (Fig. 6), in close contact with the mediastinal adenopathy. The

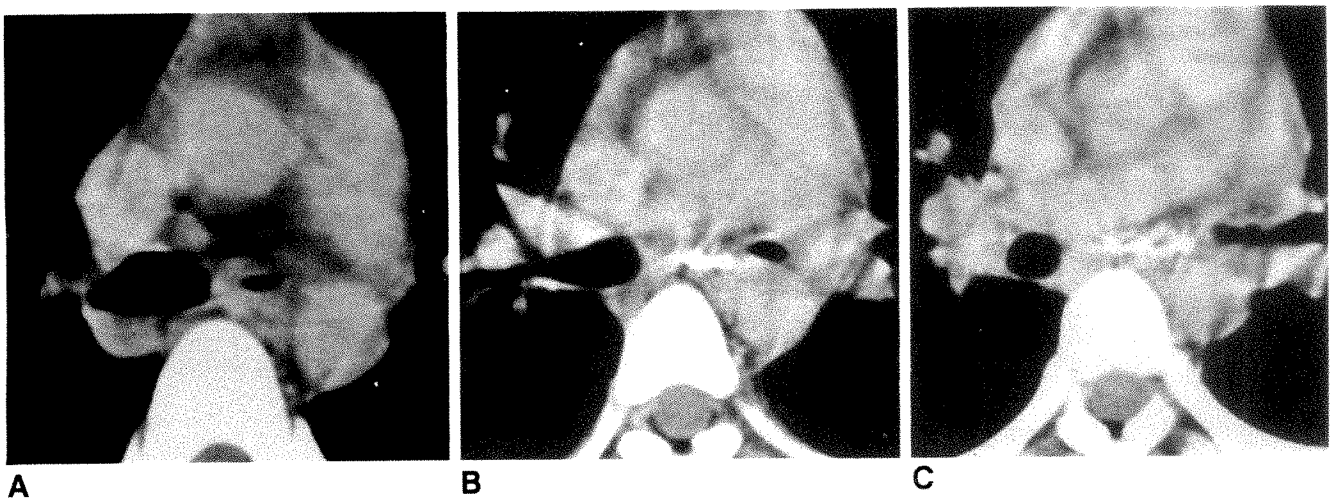

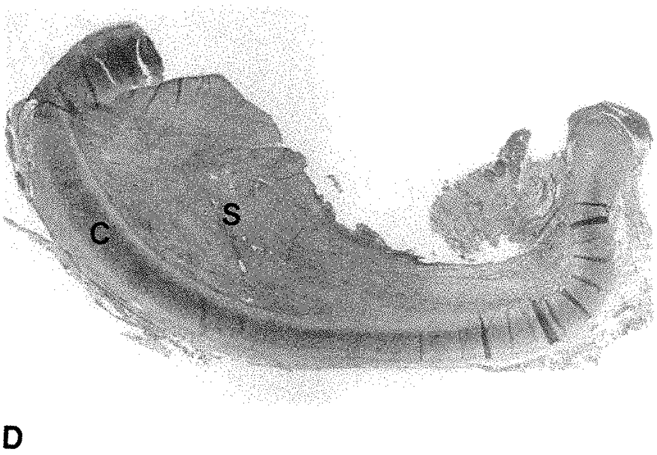

Fig. 2.—22-year-old woman with nonspecific bronchial biopsy results.

A–C, CT shows diffuse luminal obstruction of left main (*A* and *B*) and left upper lobar (*C*) bronchi with diffuse thickening of bronchial wall. Multiple nonenlarged calcified nodes are seen in subcarinal area.

D, Cross-section photomicrograph of left main bronchus shows marked submucosal fibrosis, especially on left, and minimal vascular proliferation and ectasia, but without obvious inflammatory reaction or granuloma. C = cartilage, S = submucosa. (H and E, ×4)

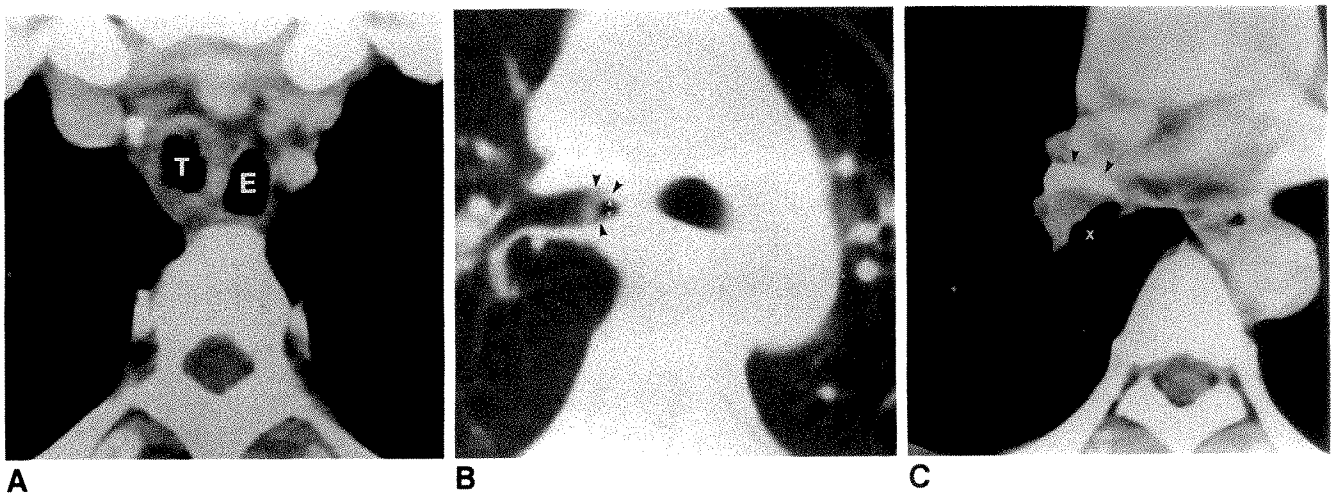

Fig. 3.—51-year-old man with nonspecific bronchial biopsy results.

A and *B*, CT shows diffuse thickening of tracheal wall (*A*) with disease extending over right main (*black arrowheads*, *B*) and right intermediate (*white arrowheads*, *B*) bronchi. E = esophagus; T = trachea.

C, Right middle lobar bronchial wall was extensively calcified with complete obstruction of its lumen (*arrowheads*), proved histologically. Right middle lobe was totally collapsed. X = right lower lobar bronchial lumen.

other 26 patients showed consolidation and/or collapse of the distal lung parenchyma supplied by the diseased bronchi. In addition to these changes, necrotic cavities (Fig. 4), dilated bronchial lumina filled with air and/or fluid (Fig. 4), and diffuse thickening of bronchovascular bundles (Fig. 7) were found (Table 1). Chest radiographs failed to show tubular densities in the patients in whom thickening of the bronchovascular bundles was seen on the CT scan. Other portions of the lung

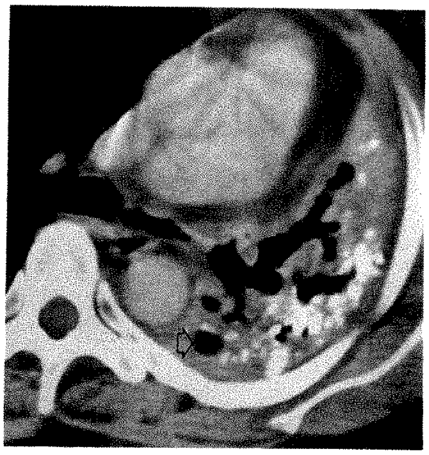

Fig. 4.—54-year-old woman with positive bronchial biopsy results. CT shows a funnel-shaped obstruction of left main and left upper lobar bronchi. Left main bronchus lies horizontally because of collapse of left lung. Its distal airways are bronchiectatic. Necrotic cavity (*arrow*) is noted in superior segment.

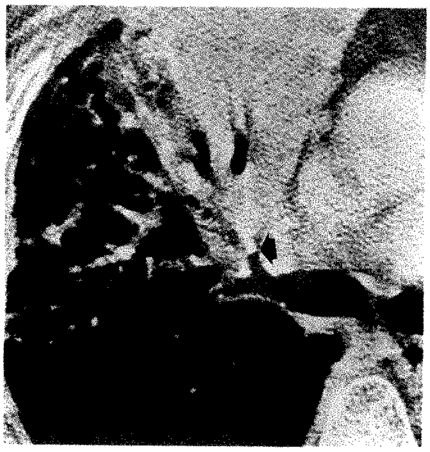

Fig. 5.—63-year-old woman with positive bronchial biopsy results. High-resolution CT scan, 1.5-mm slice thickness, shows abrupt total obstruction of anterior segmental bronchus of right upper lobe (*arrow*) associated with homogeneous consolidation of distal segment and scattered acinus nodules in other segments.

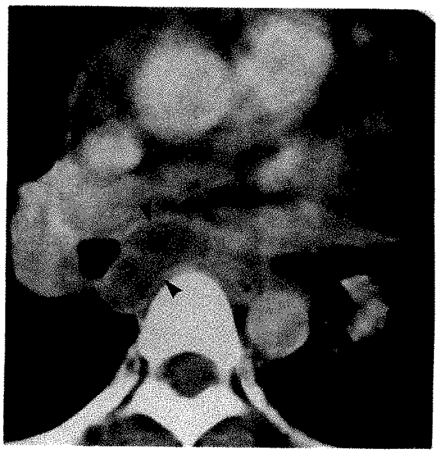

Fig. 6.—27-year-old woman with positive bronchial biopsy results. CT shows enlarged subcarinal (*arrowheads*) and right hilar lymph nodes with central low densities, capsular enhancement, and pericapsular coalescence. Massive pericardial effusion is seen also. Right intermediate bronchus is compressed. Bronchofibroscopy showed diffuse extrinsic compression of right major airway and hyperplastic lesion of right intermediate bronchus.

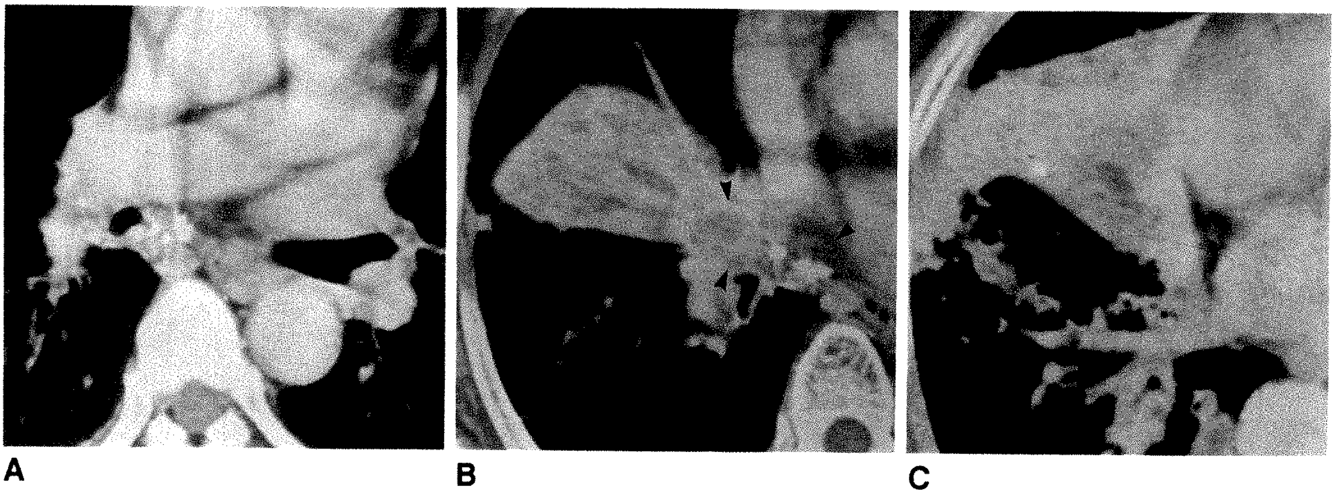

Fig. 7.—41-year-old man with nonspecific bronchial biopsy results.

A and *B*, CT shows partial narrowing of right intermediate (*A*) and right lower lobar (*B*) bronchi and complete obstruction of right middle lobar bronchus (*B*). Subcarinal and right hilar nodes are coalesced and of low density (*arrowheads*) compared with collapsed right middle lobe, closely mimicking enhancement seen in central bronchogenic cancer.

C, Consolidation and diffuse thickening of bronchovascular bundle are noted in right lower lobe. Multiple necrotic cavities are seen also.

parenchyma were normal on the CT scan of 13 patients. Some lesion was seen in the remaining portions (Table 1). The parenchymal consolidation was thought to be active pulmonary tuberculosis because of its response to antituberculous medication. A solitary pulmonary nodule was confirmed to be a tuberculoma by fine-needle aspiration. Two patients had pleural effusion, which was confirmed to be of tuberculous origin.

Comparing the CT findings in 18 patients with tuberculous lesions and in the other 10 patients with nonspecific histologic findings from the stenotic bronchi, the age of the patients and the distribution of the diseased bronchi were similar. However, lymphadenopathy, necrotic cavity in the parenchyma, and peripheral bronchial dilatation were seen more often in the group with positive biopsy results. Conversely, the number of patients with features of concentric bronchial stricture was greater in the group with negative biopsy results (Table 2). Four patients with calcified mediastinal lymph nodes were in the latter group.

Discussion

Bronchial stenosis resulting from tuberculosis may be caused by granulomatous changes in the bronchial wall [3–5, 8] or by extrinsic pressure from enlarged peribronchial lymph nodes, a common finding in children [9]. When tuberculosis involves the bronchial wall directly, the disease goes

TABLE 1: Pulmonary Parenchymal Changes Noted on CT in 28 Patients with a Tuberculous Bronchial Stricture

CT Finding	No. of Patients (n = 28)	
	Lobes Supplied by Diseased Bronchus	Other Lobes
Normal	2	13
Collapse, consolidation	26	13
Cavity	11	1
Bronchial dilatation	12	0
Thickening of bronchovascular bundle	4	0
Mucoid impaction	1	0
Solitary pulmonary nodule	0	2

TABLE 2: CT Findings in Groups with Positive and Negative Biopsy Results

CT Findings	No. of Patients	
	Positive (n = 18)	Negative (n = 10)
Intrinsic stenosis[a]	5	7
Lymphadenopathy	10	2
Parenchymal cavity	11	1
Distal bronchial dilatation	10	2

Note.—*Positive* and *negative* mean that biopsy results of the mucosa of bronchostenosis reveal tuberculous granuloma and nonspecific histology, respectively.

[a] Combination of radiologic findings of concentric bronchostenosis and even thickening of bronchial wall on CT.

through several evolutionary stages including early formation of tubercles in the submucosal layer (hyperplastic stage) (Fig. 1), ulceration and necrosis of the bronchial wall, and finally residual stenosis (fibrostenotic stage) [2, 3, 8]. However, various stages of the disease may coexist [5, 8]. Tuberculomas are absent in the diseased bronchial wall in the fibrostenotic stage (Fig. 2D) [1–3, 8].

In our cases, a positive diagnosis of tuberculosis was obtained from the site of the bronchial stenosis in 18 patients. In the remaining 10 patients, the bronchial biopsy was nonspecific and the diagnosis of tuberculous bronchial stenosis could only be inferred from the presence of tuberculous lesions elsewhere in the lungs. The group with negative biopsy findings may include patients in whom the biopsy material was obtained from a superficial region in the hyperplastic stage of the disease [10] or patients who were in the late fibrotic stage of this disease. This is supported by the findings that signs of active tuberculosis such as lymphadenopathy and cavity formation were seen less often in this group than in the group with positive biopsy findings (Table 2). On the CT scan, typical bronchial changes compatible with inflammatory stricture were encountered more often in this group of patients, probably because of the relative paucity of associated lymphadenopathy or adjacent consolidation.

There are two main theories concerning the development of tuberculous bronchial stenosis. One holds that the bronchial changes originate from the contact of the mucosa with the infected sputum from the lesions in the distal lung parenchyma, particularly those with cavities [5, 8]. This theory cannot explain the mechanism in patients who have few acid-fast bacilli in the sputum or have noncavitary parenchymal lesions. The other more recent theory suggests a submucosal spread of tubercle bacilli through lymphatics from the lung parenchyma, which is followed by the formation of submucosal tubercles and subsequent mucosal ulceration [2, 3]. In support of this theory, in many patients in our series in whom the bronchial biopsy was positive for tuberculosis, the main tuberculous lesions were confined to the submucosa and the mucosa was either intact (Fig. 1) or revealed only shallow ulcerations. Another possibility is the direct extension of the tuberculous process from an adjacent parenchymal lesion or tuberculous lymphadenitis [3, 4], as was shown in two patients in whom tuberculous lesions were seen in the major airway, contiguous with lymphadenopathy on CT (Fig. 6). Both cases were thought to be primary pulmonary tuberculosis because of the coexisting absent parenchymal lesion [11].

It is difficult to distinguish primary from postprimary tuberculosis unless there is a clinical history of recent purified protein derivative conversion. Most of our cases are believed to be cases of postprimary pulmonary tuberculosis because (1) the upper lobe bronchus was involved most frequently (19/28), (2) many (12/28) showed necrotic cavities in the distal lung parenchyma, and (3) almost 90% of Korean adults have positive purified protein derivative skin tests [12]. This may explain the different manifestations of this disease in reports from Western countries, where conventional chest radiographs frequently show noncavitary infiltrates in unusual locations or no recognizable parenchymal abnormality [3, 4, 13].

Lymphadenopathy compatible with active tuberculous adenitis (Figs. 6 and 7) [14] was noted on CT in a fairly large number of cases (43%) in this study. Woodring et al. [15], studying conventional radiographs, reported a 35% prevalence of lymphadenitis in primary infections and a 5% prevalence in the postprimary types. In contrast, Salkin et al. [5] reported a 70% prevalence of caseating lymphadenitis in their autopsied cases of tuberculous bronchitis during the preantibiotic era, compared with 43% in our study. It is difficult to speculate about the exact relationship between tuberculous bronchitis and lymphadenopathy, but the high prevalence of lymphadenopathy supports the concept that the lymphatic system plays an important role in the pathogenesis of tuberculous bronchial lesions, even in cases of postprimary tuberculosis.

Anatomic studies reveal that the disease usually begins in the small distal airways near the parenchymal lesion and spreads to the larger proximal airways [5, 8]. Both CT and bronchofibroscopy can observe changes down to the proximal segmental bronchi only; anything beyond that is out of reach. This may explain the difference in prevalence between the autopsy and bronchofibroscopy series [5, 6], and also the fact that, in our series, all lesions were in bronchi that were proximal to the proximal segmental level. In patients with lung cancer, the CT scan can localize the diseased subsegmental bronchi before bronchofibroscopy and provide a useful guide for the bronchoscopist. In tuberculous bronchial stenosis affecting the subsegmental level, however, CT was not very helpful to the bronchofibroscopist; bronchial disease was not suspected on CT because of coexisting parenchymal lesions in most cases, and granulation tissue obtained from the peripheral airway could not differentiate bronchial from parenchymal tuberculosis, unless the normal bronchial mucosa adjacent to the granuloma was included in the specimen.

CT was reported to be accurate in detecting focal bronchostenotic lesions, but inaccurate in predicting endobronchial, submucosal, and extrinsic diseases [16]. This disease is mainly of the submucosal thickening, and, in the hyperplastic stage, inflammation and ulceration of the mucosal layer are combined. However, CT could not resolve the existence of changes in the mucosal layer in this study. The recognition of intrinsic stenosis, including both submucosal and mucosal lesions, could be possible only when the outer wall of the diseased bronchus was contrasted with aerated lung parenchyma or the mediastinal fat on the CT scan. In only 12 patients in this series was bronchial stenosis seen on CT characterized by a concentric narrowing of the lumen, uniform thickening of the wall, and involvement of a long bronchial segment, features expected to reflect pathologic changes [17]. The findings varied in 16 patients. The diagnostic difficulty encountered most frequently in these patients was the presence of enlarged lymph nodes lying close to the stenotic bronchus, which made it impossible to differentiate the intrinsic from the extrinsic cause of stenosis. The lymph nodes almost always showed areas of low density in the central portion, probably from caseating necrosis [14], and often coalesced to form a large, low-density mass. These findings, when combined with peripheral parenchymal collapse or consolidation, were similar to the differential enhancement between a central tumor mass and a collapsed distal lung found in lung cancer [18]. Also, it was not possible to accurately assess the thickness of the bronchial wall in many cases, either because of loss of the silhouette of the outer wall of the involved bronchus by the adjacent consolidation, or of the inner wall by the absence of intraluminal air. In such cases, the possibility of a tumor with transbronchial growth and adjacent lymph-node metastasis or the presence of an endobronchial tumor could not be ruled out.

Further difficulty in the differential diagnosis may arise from the fact that minimal and uniform thickening of the bronchial wall may be found in other diseases including early bronchogenic cancer [19, 20] and that patients with bronchogenic cancer are known to have a high rate of reinfection with pulmonary tuberculosis [21]. Because of these overlapping CT manifestations between tuberculous bronchial stenosis and lung cancer, the scan should always be supplemented by bronchofibroscopy to confirm the diagnosis. The advantages of CT over bronchofibroscopy are that it can visualize airways beyond a severe stenosis that are not accessible to bronchofibroscopy, and that it is beneficial in following the response to treatment, especially when the bronchial biopsy shows only nonspecific changes.

REFERENCES

1. Albert RK, Petty TL. Endobronchial tuberculosis progressing to bronchial stenosis. *Chest* **1976**;76:1133–1148
2. Case records of the Massachusetts General Hospital (case 32-1976). *N Engl J Med* **1976**;295:328–334
3. Smith LC, Schillaci RF, Sarlin RF. Endobronchial tuberculosis. Serial fiberoptic bronchoscopy and natural history. *Chest* **1987**;91:644–647
4. Matthews JI, Matarese SL, Carpenter JL. Endobronchial tuberculosis simulating lung cancer. *Chest* **1984**;19:236–242
5. Salkin D, Cadden AV, Edson RC. The natural history of tuberculous tracheobronchitis. *Am Rev Respir Dis* **1943**;47:351–369
6. Jokinen K, Palva T, Nuutinen J. Bronchial findings in pulmonary tuberculosis. *Clin Otolaryngol* **1977**;2:139–148
7. Birkelo CC, Poznak LA. The radiologic findings in tracheobronchial tuberculosis. *Chest* **1945**;11:26–35
8. Medlar EH. The behavior of pulmonary tuberculous lesions. *Am Rev Respir Dis* **1955**;71:1–245
9. Weber AL, Bird TK, Janower ML. Primary tuberculosis in childhood with particular emphasis on changes affecting the tracheobronchial tree. *AJR* **1968**;103:123–132
10. Kim SK, Kim JM, Oh SH, et al. Fiberoptic bronchoscopy in the diagnosis of pulmonary and endobronchial tuberculosis. *Tuberc Respir Dis* **1982**;29:152–156
11. Khan MA, Kovnat DM, Bachus R, Whitcomb ME, Brody JS, Snider GL. Clinical and roentgenographic spectrum of pulmonary tuberculosis in the adult. *Am J Med* **1977**;62:31–38
12. Ministry of Health and Social Affairs and Korean National Tuberculosis Association. *Report on the 5th tuberculosis prevalence survey in Korea*. Seoul, Korea: Yoo Poong, **1985**:23–24
13. Volchaert V, Roels P, Van der Niepen P, Schandevyl W. Endobronchial tuberculosis; report of three cases. *Eur J Respir Dis* **1987**;70:99–101
14. Im JG, Song KS, Kang HS, et al. Mediastinal tuberculous lymphadenitis: CT manifestations. *Radiology* **1987**;164:115–117
15. Woodring JH, Vandiviere HM, Lee C. Intrathoracic lymphadenopathy in postprimary tuberculosis. *South Med J* **1988**;81:992–997
16. Naidich DP, Lee JJ, Garay SM, McCauley DI, Aranda CP, Boyd AD. Comparison of CT and fiberscopic bronchoscopy in the evaluation of bronchial disease. *AJR* **1987**;148:1–7
17. Gamsu G. Computed tomography of the trachea and central bronchi. In: Moss AA, Gamsu G, Genant HK, eds. *Computed tomography of the body*. Philadelphia: Saunders, **1983**:145–194
18. Naidich DP, McCauley DI, Khouri NF, Leitmen BS, Hulnick DH, Seigelman SS. Computed tomography of lobar collapse: 1. Endobronchial obstruction. *J Comput Assist Tomogr* **1983**;7:745–757
19. Schnur MJ, Winkler B, Austin JHM. Thickening of the posterior wall of the bronchus intermedius. *Radiology* **1981**;139:551–559
20. Foster WL, Roberts L, McLendon RE, Hill RC. Localized peribronchial thickening: a CT sign of occult bronchogenic carcinoma. *AJR* **1985**; 144:906–908
21. Ting YM, Church WR, Ravikrishnan KP. Lung carcinoma superimposed on pulmonary tuberculosis. *Radiology* **1976**;119:307–312

Mammography-Guided Stereotactic Fine-Needle Aspiration Cytology of Nonpalpable Breast Lesions:

Prospective Comparison with Surgical Biopsy Results

Laurie L. Fajardo[1]
John R. Davis[2]
Julie L. Wiens[2]
Douglas C. Trego[2]

We assessed the usefulness of fine-needle aspiration cytology (FNAC) in evaluating nonpalpable breast abnormalities by prospectively performing stereotactic mammography-guided FNAC on 100 women undergoing surgical excisional biopsy. Mammographic and cytologic diagnoses, on a scale of 1 (benign) to 4 (malignant), were assigned for each case and compared with the surgical pathologic diagnosis. Sensitivity and specificity were examined at different diagnostic cutoff points for regarding a mammographic or cytologic diagnosis as positive or negative. Of the 100 breast biopsy specimens, 70 were benign and 30 were malignant. For both mammography and FNAC, the optimal diagnostic cutoff point was between diagnosis 2 (mammography, probably benign; cytology, atypical) and 3 (mammography and cytology both suspicious for malignancy). At this cutoff point, FNAC had a sensitivity of 0.77 and specificity of 1.00, vs 0.73 sensitivity and 0.79 specificity for mammography. Pearson coefficient analysis revealed significant correlations between both mammographic and FNAC diagnoses and surgical pathology ($p < .001$ for both).

Our results suggest that use of mammography-guided FNAC may reduce the number of breast biopsies performed for benign lesions.

***AJR* 155:977–981, November 1990**

Most suspicious breast lesions currently are evaluated by surgical excisional biopsy and histologic examination. Approximately 287,000 breast biopsies are performed in the United States annually (B. Gilbert, personal communication). Of these, about 250,000 are open surgical procedures, and the remaining 37,000 are percutaneous needle biopsies of palpable breast lesions. The positive rate for breast biopsies performed for mammographically identified nonpalpable abnormalities is 11–36% [1–16]. Two large screening studies, the Breast Cancer Detection Demonstration Project (BCDDP) [16] and the Nijmegen Project [17], reported positive biopsies of 16% and 35%, respectively, for patients with mammographic findings, but these series did not distinguish between palpable and nonpalpable lesions.

Improvements in the accuracy of mammography-guided localization of breast abnormalities, particularly with the use of stereotactic devices, might allow radiologists to perform fine-needle aspiration cytology (FNAC) of suspicious, nonpalpable breast lesions. These procedures might reduce the number of surgical breast biopsies currently performed for benign breast lesions and could reduce patients' costs and morbidity. However, mammography-guided FNAC must detect breast cancer with accuracy similar to that of surgical biopsy. Significant numbers of false-negative and false-positive diagnoses are unacceptable, and these metrics must be closely examined to determine the clinical usefulness and limitations of these procedures.

In an ongoing study, we are performing FNAC on patients undergoing mammography-guided stereotactic localization of breast lesions before open surgical biopsy. Data on the first 100 patients are presented here.

Received March 28, 1990; accepted after revision June 15, 1990.

[1] Department of Radiology, University of Arizona and University Medical Center, 1501 N. Campbell Ave., Tucson, AZ 85724. Address reprint requests to L. L. Fajardo.

[2] Department of Pathology, University of Arizona and University Medical Center, Tucson, AZ 85724.

0361-803X/90/1555-0977
© American Roentgen Ray Society

Materials and Methods

Patient Population and Mammographic Evaluation

One hundred sixteen consecutive women undergoing mammography-guided needle-wire localization of nonpalpable breast lesions were enrolled in this study between July 1988 and January 1990. Informed consent was obtained from all patients, and no one refused to participate. Sixteen patients were excluded from the study because their breast lesions were found to be cysts at the time of localization. The cysts were aspirated, and the patients' biopsies were cancelled. Data from the 100 patients who had surgical biopsies are presented in this report.

Patients ranged in age from 28 to 81 years (mean age, 59 years). All abnormalities were nonpalpable on physical examination and included 59 manifested as microcalcifications, 35 as masses, and six as both masses and microcalcifications on mammograms. Abnormalities varied from 0.5 to 3.0 cm in largest diameter (Table 1). Before the localization procedure, the characteristics of each breast lesion visible on radiographs were evaluated by a single radiologist who assigned a mammographic diagnosis as follows: 1 = benign lesion; 2 = probably benign; 3 = suspicious for malignancy; 4 = malignant. Criteria for these diagnoses are detailed in Table 2.

TABLE 1: Distribution of Breast Lesions by Size

Lesions	Longest Diameter (mm)			
	<5	6–10	11–20	>20
Masses	8	22	21	2
Microcalcifications	6	18	9	2
Mass and microcalcifications	2	3	5	2
Total	16	43	35	6

Stereotactic Localization and Pilot Studies

A prototype of a stereotactic device (LoRad Medical Systems, Inc., Danbury, CT) was used to localize the breast masses under mammographic guidance. This device uses +15° and −15° angled views to calculate the three-dimensional location of a lesion within the breast. It attaches easily to a standard mammography unit and functions similarly to other recently described stereotactic devices [18, 19].

Before starting the clinical study, we evaluated the stereotactic device for accuracy in a pilot study that used simulated lesions in a phantom. We performed 26 localizations with a variety of needle-wire devices. The distance of the wire from the center of the simulated lesion was measured on orthogonal radiographs by using a comparator reticle (12× magnification, Edmund Scientific, Barrington, NJ). The larger of these two distances was used as the measured value. Wires were placed a mean distance of 0.5 ± 0.9 mm standard deviation (SD) from the center of the simulated lesions in the phantom. Results in 20 consecutive patients undergoing needle-wire localization were similar. Distances were measured by the same method on craniocaudad and 90° mediolateral views obtained before biopsy; wires were placed a mean distance of 1.2 ± 1.1 mm SD from the center of the breast lesions.

To optimize the radiologist's sampling technique and familiarize the pathologist and technologists with the cytologic appearance of a variety of breast lesions, we sampled all breast biopsy and mastectomy specimens submitted to our pathology department during a 4-month period before starting the clinical study.

Performance of Fine-Needle Aspiration Cytology and Pathologic Evaluation

All FNACs were performed by the same radiologist. After the location of a breast abnormality was calculated in three dimensions, four needle passes for FNAC were made on each patient. Twenty-

TABLE 2: Mammographic and Fine-Needle Aspiration Cytology Diagnoses

Diagnosis	Mammographic Findings	Fine-Needle Aspiration Cytology
0	Not applicable	Inadequate, acellular specimen
1	Benign Circumscribed, low-density mass, or Round, uniformly dense microcalcifications, few in number (<5)	Benign Normal epithelial pattern of aggregates and cytologic features
2	Probably benign Low-density mass with partial border loss, or Round, uniformly dense microcalcifications (<15)	Atypical Atypical with regard to cell groupings and nuclei
3	Suspicious for malignancy Low-density mass with architectural distortion, or Circumscribed, high-density mass, or Small stellate mass without architectural distortion, or Microcalcifications of irregular shapes and density	Suspicious for malignancy Malignancy-suspect cells, not interpretable as carcinoma with certainty
4	Malignant Circumscribed, high-density or stellate, spiculated mass with architectural distortion, or Microcalcifications of irregular shape and density with architectural distortion	Malignant Cells indicative of malignancy

two gauge, 3½-in. (8.9 cm) spinal needles (Sherwood Medical, St. Louis, MO) were used, and the slides were prepared by the radiologist. After the samples were obtained, the breast abnormality was localized with a Homer needle-wire localizer (Namic, Glens Falls, NY) and the patient underwent surgical biopsy. An average time of 28 ± 6 min SD was required to localize the abnormality and obtain and prepare the specimens. Radiographs of all surgical specimens confirmed the excision of the mammographic abnormality.

Later, the fixed smears from the FNAC aspirates were stained by the Papanicolaou method. All specimens were evaluated independently by both a senior cytotechnologist and a cytopathologist who had no knowledge of the mammographic findings or the results of surgical pathology. Cytologic samples were evaluated for cellularity, cellular arrangements, nuclear-to-cytoplasmic ratio, and the characteristics of cell nuclei and nucleoli. Samples were classified on a scale of 0 to 4 as follows: 0 = inadequate; 1 = benign; 2 = atypical; 3 = suspicious for malignancy; 4 = malignant (Table 2) [20].

Analysis

Sensitivity and specificity rates were calculated for mammographic and FNAC diagnoses on the basis of various cutoff points for designating a diagnosis as positive or negative. Pearson coefficient correlation, a nonparametric analog of regression analysis, was used to evaluate for possible correlations between mammographic diagnosis and pathologic findings at surgery and between FNAC diagnosis and pathologic findings at surgery.

Results

Of the 100 breast biopsy specimens, 70 were benign and 30 were malignant on histologic examination. The histologic type and size of carcinomas is given in Table 3. Nineteen cancers (63%) were less than or equal to 1 cm in size and 10 (33%) were noninvasive.

TABLE 3: Histologic Type and Size of the 30 Nonpalpable Malignant Breast Lesions

Histologic Type	Tumor Size (mm)		
	<5	6–10	11–20
Ductal carcinoma in situ	2	3	3
Lobular carcinoma in situ	1	0	1
Infiltrating ductal carcinoma	3	10	3
Infiltrating lobular carcinoma	0	0	2

Note.—There was one combined infiltrating ductal carcinoma and lobular carcinoma in situ that was larger than 20 mm and one combined infiltrating ductal carcinoma and infiltrating lobular carcinoma that was 11–20 mm.

Benign specimens included nine fibroadenomas and one lymph node. The remainder of the benign biopsies showed one or more of the following: fibrocystic disease (five), fibrosis (three), intraductal papilloma (one), papillomatosis (two), sclerosing adenosis (three), dysplasia (39), intraductal hyperplasia (three), lobular hyperplasia (five), apocrine metaplasia (six), atypical lobular hyperplasia (three), atypical ductal hyperplasia (20), and severe atypical ductal hyperplasia (two).

All 100 cases had at least two FNAC slides containing sufficient cellular material for diagnosis, thus there were no FNAC diagnoses of 0 in the study. Table 4 compares the FNAC and mammographic diagnoses with the surgical pathologic diagnosis. No surgically benign lesions were interpreted as suspicious (3) or malignant (4) on the basis of FNAC (i.e., no false-positive FNAC diagnoses). Pearson coefficient analysis showed a significant correlation between FNAC diagnosis and the surgical diagnosis ($p < .001$, $r = .81$, 98 degrees of freedom [d.f.]). Similar correlation was also found between mammographic diagnosis and surgical pathologic findings ($p < .001$, $r = .55$, 98 d.f.).

In three cases in which carcinoma was present on surgical biopsy, the FNAC was interpreted as benign (FNAC diagnosis 1). One case had an incidental focus of lobular carcinoma in situ, which was not related to the suspicious microcalcifications that were localized. A second case of microcalcifications contained a microscopic focus of intraductal carcinoma, less than 1 mm in size, that was not sampled by the 22-gauge fine needle. The third case, a 10-mm mass with multifocal intraductal carcinoma, appears to have been missed by FNAC because of an error in localization, as the cytology slides showed normal cells only. Table 5 compares the false-negative diagnoses for FNAC and mammography with the pathologic findings at surgery.

Discussion

Fine-needle aspiration biopsy has been accepted as a means of diagnosing palpable breast lesions for years. The reliability of this technique has been widely tested, with sensitivities ranging from 0.53 to 0.99 and specificities from 0.96 to 1.00 [21–29]. By comparison, experience with nonpalpable lesions is more limited. Recent studies report sensitivity rates of 0.71–1.00 and specificity rates of 0.91–1.00 for FNAC of nonpalpable breast abnormalities [19, 30–33]. Our results are

TABLE 4: Comparison of Fine-Needle Aspiration Cytology (FNAC) and Mammographic Diagnoses with Pathologic Findings at Surgery

Surgical Histologic Diagnosis	FNAC/Mammographic Diagnosis			
	Benign/ Benign	Atypical/ Probably Benign	Suspicious/ Suspicious	Malignant/ Malignant
Benign (n = 70)	54/37	16/18	0/13	0/2
Ductal carcinoma in situ (n = 8)	2/1	1/2	1/2	3/2
Infiltrating ductal carcinoma (n = 16)	0/1	1/1	4/4	12/11
Infiltrating ductal carcinoma and lobular carcinoma in situ (n = 1)	0/0	0/0	0/0	1/1
Infiltrating ductal carcinoma and infiltrating lobular carcinoma (n = 1)	0/0	0/0	1/0	0/1
Lobular carcinoma in situ (n = 2)	1/1	1/1	0/0	0/0
Infiltrating lobular carcinoma (n = 2)	0/0	1/0	0/1	1/1

TABLE 5: Comparison of False-Negative Diagnosis for Mammography and Fine-Needle Aspiration Cytology (FNAC)

Surgical Histologic Diagnosis	FNAC Diagnosis[a]	Mammographic Diagnosis[b]
Ductal carcinoma in situ	1	1
Ductal carcinoma in situ	1	4
Ductal carcinoma in situ	2	2
Ductal carcinoma in situ	4	2
Invasive ductal carcinoma	3	1
Invasive ductal carcinoma	2	2
Lobular carcinoma in situ	1	1
Lobular carcinoma in situ	2	2
Invasive lobular carcinoma	2	3

[a] FNAC diagnoses: 1 = benign, 2 = atypical, 3 = suspicious, 4 = malignant.
[b] Mammographic diagnoses: 1 = benign, 2 = probably benign, 3 = suspicious, 4 = malignant.

in agreement with these data; however, it is difficult to compare the results of these studies directly with our own results. Specifically, there are differences in the categorization of data from study to study; some use only three categories of FNAC diagnoses. In addition, a significant number of fine-needle biopsies were inadequate or acellular in these studies, and typically, the inadequate cytologic samples were omitted from statistical analysis.

Because investigators in previous studies did not define their cutoff points for interpreting an FNAC reading as positive or negative, it is difficult to apply the reported sensitivities and specificities to clinical situations. It is important to recognize how the choice of cutoff points will affect medical decision making should FNAC become more widely incorporated into the evaluation of nonpalpable breast abnormalities. For example, sensitivity and specificity for FNAC diagnosis, based on different cutoff points for regarding an FNAC diagnosis as positive or negative for malignancy, are shown for our data in Table 6. The same results for mammographic diagnosis are shown in Table 7. These tables show how different physicians' attitudes toward FNAC or mammography diagnosis will change sensitivity and specificity. As the diagnostic cutoff is shifted to the right, specificity improves, but more false-negative diagnoses result. For instance, if only diagnosis 1 is regarded as negative (i.e., benign, requiring no further patient workup) and diagnoses 2, 3, and 4 are regarded as positive (i.e., malignant, requiring further patient workup or intervention), sensitivity is high—0.90 for both mammography and FNAC—but specificity is poor. By this scenario, mammography would result in 34 false-positive diagnoses and FNAC would result in 17. If diagnoses 1, 2, and 3 are treated as negative and diagnosis 4 as positive, specificity is high (0.97 for mammography and 1.00 for FNAC), but sensitivity falls and false-negative rates rise.

For both mammography and FNAC, regarding diagnoses 1 and 2 as negative and diagnoses 3 and 4 as positive results in the best compromise between false-positive and false-negative rates. At this cutoff point, FNAC results in sensitivity of 0.77 and specificity of 1.00, vs 0.73 sensitivity and 0.79 specificity for mammography.

The major disadvantage of FNAC for nonpalpable breast lesions is the potential for sampling error that could result in a false-negative cytologic diagnosis. Good sampling techniques avoid the problem of inadequate specimen retrieval; however, accurate placement of the biopsy needle is crucial. Stereotactic techniques have improved the accuracy of needle placement [19, 31, 32], but, as evidenced in our results, potential pitfalls still exist that can result in improper needle placement. A cooperative patient is important because the patient's motion is an obstacle to accurate placement. Patients must sit motionless for 20–30 min. Care must be exercised when making measurements of the lesion. Although not performed in this study, we think that additional 15° angled views should be performed after the needle is placed to ensure that the radiologist is actually sampling the lesion. This, of course, would lengthen the procedure and add radiation exposure, but might be necessary only for the initial needle placement. If a coaxial system is used, the location of the stationary, 20-gauge outer sheath can be confirmed on radiographs and multiple samples can be obtained with the inner 23-gauge needle. The disadvantage of a coaxial system is that it may restrict the area of the lesion that is sampled.

TABLE 6: Sensitivity and Specificity of Fine-Needle Aspiration Cytology (FNAC) According to Different Cutoff Points for Positivity

	FNAC Diagnoses Considered Positive for Malignancy		
	2, 3, 4	3, 4	4
Sensitivity	0.90	0.77	0.57
Specificity	0.76	1.00	1.00
	(3 FN)	(7 FN)	(13 FN)
	(17 FP)	(0 FP)	(0 FP)

Note.—FNAC diagnosis considered positive for malignancy: 1 = benign, 2 = atypical, 3 = suspicious, 4 = malignant. FN = false-negative, FP = false-positive.

TABLE 7: Sensitivity and Specificity of Mammography According to Different Cutoff Points for Positivity

	Mammographic Diagnoses Considered Positive for Malignancy		
	2, 3, 4	3, 4	4
Sensitivity	0.90	0.73	0.40
Specificity	0.51	0.79	0.97
	(3 FN)	(8 FN)	(18 FN)
	(34 FP)	(15 FP)	(2 FP)

Note.—Mammographic diagnoses considered positive for malignancy: 1 = benign, 2 = probably benign, 3 = suspicious, 4 = malignant. FN = false-negative, FP = false-positive.

Fine-needle aspiration cytology cannot be successfully incorporated into the workup of nonpalpable breast lesions unless the radiologist works closely with an experienced cytologist. Under ideal circumstances, a cytotechnologist or cytopathologist would be present during the procedure to stain and examine the specimens immediately. As this requires about 5–7 min per slide, the total procedure would take longer. The cytologist must use strict interpretation criteria to avoid false-positive diagnoses. In previous work with FNAC of palpable breast masses, very low false-positive rates, ranging from 1% to 4%, have been reported [22–30].

Our results indicate that with proper localization, sampling, and evaluation techniques, FNAC of nonpalpable lesions might be refined to increase sampling accuracy and optimize sensitivity and specificity for the diagnosis of breast cancer. If this is the case, then the cost of diagnosing breast cancer could be reduced significantly.

Fine-needle aspiration cytology of nonpalpable lesions might reduce this cost by separating out those patients with benign abnormalities who do not need surgical biopsy, hence, improving the positive-to-negative ratio for surgical biopsy.

However, the cost of a false-negative FNAC also must be considered, and follow-up schemes for these patients must be examined. For example, at what interval should follow-up mammography be performed for patients with negative FNAC results? Should some patients with negative FNAC undergo subsequent excisional biopsy on the basis of clinical history and mammographic findings? It is likely that decisions for follow-up care will need to be tailored for each patient. Such decisions should be based on clinical factors (such as patient/family history) and FNAC and mammographic findings. For example, some of our FNAC samples contained small cores of tissue that allowed our cytopathologist to diagnose fibroadenoma. For these patients, no additional workup is needed, and they can return to routine breast screening. However, a patient with a suspicious, spiculated mass on mammography, but negative FNAC results might be treated with excisional biopsy, on the basis of the suspicious mammographic findings. Management decisions must involve a team approach with input from the radiologist, pathologist, and breast surgeon.

Whether all nonpalpable lesions can be accurately evaluated by FNAC has not been closely evaluated. In our experience, well-defined lesions are easier to localize and tend to yield more cellular FNAC samples than poorly defined, spiculated lesions. With only 30 cancers in our series, we are unable to detect significant differences among lesions that differ in mammographic character. More extensive, well-controlled clinical trials comparing FNAC with surgical biopsy are needed to determine the accuracy and yield of FNAC for a spectrum of breast lesions. Only after these are accomplished can we develop appropriate follow-up regimens for patients with negative FNAC results and address the potential medicolegal issues related to false-negative FNAC diagnoses.

By which scheme mammography-guided FNAC is integrated into breast cancer diagnosis will determine the extent of financial savings that might accrue. However, there are other, nonfinancial, benefits attributable to FNAC. First, it is cosmetically more acceptable to patients than surgical biopsy. In addition, FNAC will not interfere with the interpretation of subsequent mammograms because it does not produce the architectural distortion that occurs after open surgical biopsy. Finally, the procedure can be performed on an outpatient basis, with minimal discomfort and complications for the patient.

REFERENCES

1. Hermann G, Janus C, Schwartz IS, Krivisky B, Bier S, Rabinowitz JG. Nonpalpable breast lesions: accuracy of prebiopsy mammographic localization. *Radiology* **1987**;165:323-326
2. Meyer JE, Kopans DB, Stomper PC, Lindfors KK. Occult breast abnormalities: percutaneous preoperative needle localization. *Radiology* **1984**;150:335-337
3. Grisvold JJ, Martin JK. Prebiopsy localization of nonpalpable breast lesions. *AJR* **1984**;143:477-481
4. Ciatto S, Cataliotti L, Distante V. Nonpalpable lesions detected with mammography: review of 512 consecutive cases. *Radiology* **1987**;165:99-102
5. Rosenberg AL, Schwartz GF, Feig SA, Patchefsky AS. Clinically occult breast lesions: localization and significance. *Radiology* **1987**;162:167-170
6. Proudfoot RW, Mattingly SS, Stelling CB, Fine JG. Nonpalpable breast lesions: wire localization and excisional biopsy. *Am Surg* **1986**;52:117-122
7. Schwartz GF, Patchefsky AS, Feig SA, Schwartz AB. Clinically occult breast cancer: multicentricity and implications for treatment. *Ann Surg* **1980**;191:8-12
8. Marrujo G, Jolly PC, Hall MH. Nonpalpable breast cancer: needle-localized biopsy for diagnosis and considerations for treatment. *Am J Surg* **1986**;151:599-602
9. Solmer R, Goodstein J, Abliozzo C. Nonpalpable breast lesions discovered by mammography. *Arch Surg* **1980**;115:1067-1069
10. Wilhelm MC, de Paredes ES, Pope T, Wanebo HJ. The changing mammogram: a primary indication for needle localization biopsy. *Arch Surg* **1986**;121:1311-1314
11. Bigelow R, Smith R, Goodman PA, Wilson GS. Needle localization of nonpalpable breast masses. *Arch Surg* **1985**;120:565-569
12. Hoehn JL, Hardacre JM, Swanson MK, Williams GH. Localization of occult breast lesions. *Cancer* **1982**;49:1142-1144
13. Homer MJ, Smith TJ, Marchant DJ. Outpatient needle localization and biopsy for nonpalpable breast lesions. *JAMA* **1984**;252:2452-2454
14. Poole GV, Choplin RH, Sterchi JM, Leinbach LB, Myers RT. Occult lesions of the breast. *Surg Gynecol Obstet* **1986**;163:107-110
15. Landercasper J, Gunderson SB, Gunderson AL, Cogbill TH, Travelli R, Strutt P. Needle localization and biopsy of nonpalpable lesions of the breast. *Surg Gynecol Obstet* **1987**;164:452-456
16. Baker LH. Breast Cancer Detection Demonstration Project: five-year summary report. *CA* **1982**;32:194-225
17. Verbeek ALM, Hendriks JHCL, Holland R, Mravunac M, Sturmans F, Day NE. Reduction of breast cancer mortality through mass screening with modern mammography: first results of the Nijmegen Project, 1975-1981. *Lancet* **1984**;1:1222-1224
18. Lofgren M, Andersson I, Lindholm K. Stereotactic fine-needle aspiration for cytologic diagnosis of nonpalpable breast lesions. *AJR* **1990**;154:1191-1195
19. Evans WP, Cade SH. Needle localization and fine-needle aspiration biopsy of nonpalpable breast lesions with use of standard and stereotactic equipment. *Radiology* **1989**;173:53-56
20. McDivitt R, Stewart F, Berg J. Tumors of the breast. In: *Atlas of tumor pathology*. Washington DC: Armed Forces Institute of Pathology, **1969**:22-86
21. Silverman JF, Lannin DR, O'Brian K, Norris HT. The triage role of fine needle aspiration biopsy of palpable breast masses: diagnostic accuracy and cost-effectiveness. *Acta Cytol* **1987**;31:731-750
22. Grant CS, Goellner JR, Welch JS, Martin JK. Fine-needle aspiration of the breast. *Mayo Clin Proc* **1986**;61:377-381
23. Adye B, Jolly PC, Bauermeister DE. The role of fine-needle aspiration in the management of solid breast masses. *Arch Surg* **1988**;123:37-39
24. Hammond S, Keyhani-Rofagha S, O'Toole RV. Statistical analysis of fine needle aspiration cytology of the breast: a review of 678 cases plus 4,265 cases from the literature. *Acta Cytol* **1987**;31:276-284
25. Carlson GW, Ferguson CM. Needle aspiration cytology of breast masses. *Am Surg* **1987**;53:235-237
26. Bell D, Hajdu S, Urban J, Gaston J. Role of aspiration cytology in the diagnosis and management of mammary lesions in office practice. *Cancer* **1983**;51:1182-1189
27. Kline T, Joshi L, Neal H. Fine-needle aspiration of the breast—diagnoses and pitfalls: a review of 3545 cases. *Cancer* **1979**;44:1458-1464
28. Abele J, Miller T, Goodson W, Hunt T, Hohn D. Fine-needle aspiration of palpable breast masses. *Arch Surg* **1983**;118:859-863
29. Azzarelli A, Guzzon A, Pilotti S, Quagliuolo V, Bono A, DiPietro S. Accuracy of breast cancer diagnoses by physical, radiologic, and cytologic combined examinations. *Tumori* **1983**;69:137-141
30. Dowlatshahi K, Gent HJ, Schmidt R, Jokich PM, Bibbo M, Sprenger E. Nonpalpable breast tumors: diagnosis with stereotaxic localization and fine-needle aspiration. *Radiology* **1989**;170:427-433
31. Svane G. Stereotaxic needle biopsy of nonpalpable breast lesions: a clinical and radiologic follow-up. *Acta Radiol [Diagn]* (Stockh) **1983**;24:385-390
32. Svane G, Silfverward C. Stereotaxic needle biopsy of nonpalpable breast lesions: cytologic and histologic findings. *Acta Radiol [Diagn]* (Stockh) **1983**;24:283-288
33. Azavedo E, Svane G, Auer G. Stereotactic fine-needle biopsy in 2594 mammographically detected nonpalpable lesions. *Lancet* **1989**;1:1033-1036

Book Review

Progress in Cardiology. Update on Cardiac Imaging. Edited by Douglas P. Zipes and Derek J. Rowlands. Philadelphia: Lea & Febiger, 1990;3(2):1–239, softcover; by subscription, 2 issues (1 year) for $49.50; 4 issues (2 years) for $85

This softcover volume is part of a series, with two issues each year, that concentrates on current cardiology topics. Its up-to-the-minute articles make it, as the publishers say, "current as a journal—complete as a book!" This issue deals with advances in cardiac imaging and includes eight sections divided into 15 chapters. It was written by 31 international contributors, all of whom are "major players" in the field of cardiac imaging. Of these 31, only five represent radiology departments. Most of the authors are cardiologists, and the text is definitely biased to that discipline. This issue is an update on cardiac imaging. For diversity, it has two chapters on cardiac infections and one thorough summary on coronary thrombolysis. The latter topic will be considered further in the next issue.

In section 1, a comparison of modern imaging techniques is offered. The tables in the introductory chapter are concise and informative, comparing the usefulness of conventional and evolving imaging techniques and giving the radiation exposure to the patient from various cardiac imaging techniques. A brief but significant discussion of cost-benefit considerations is quite pertinent.

Section 2 includes three chapters dealing with MR imaging. In the first, Julsrud explains the principles and normal cardiac anatomy in a simplistic but thorough fashion. The illustrations show normal cardiac anatomy in all three planes, with excellent anatomic correlation. The next chapter deals with MR evaluation of ventricular function. The final chapter deals with cine-MR in acquired and congenital heart disease, describing the technical considerations and the importance of ECG gating. All three of these chapters are well laid out with little overlap and redundancy. The cited references are complete.

The third section, on echocardiography and Doppler imaging, consists of three chapters. The first deals with color Doppler imaging in valvular regurgitation, discussing the principles, benefits, and limitations. The second chapter deals with myocardial tissue characterization, quantified by using sonography and measurements of integrated back scatter, but the conclusions are not definitive. The final chapter deals with stress echocardiography. It defines the various types of stress to be used and demonstrates the analysis of wall motion. A concise table of advantages and disadvantages is helpful in deciding whether to use this technique. Comparison with radionuclide imaging techniques and validation with coronary angiography is necessary.

The next section deals with positron emission tomography (PET) and comprises two chapters. The first deals with the technique's initial evolution. PET is a another major advance that has changed our approach to cardiovascular disease by providing new information about patients that was unavailable by other means. The traditional well-established approach to medical management, the "symptoms and salvage approach," has changed. The new approach is based on a "screen and clean" philosophy and use of noninvasive PET. Five separate case studies are presented to show the value and merit of the PET studies. The technique with the isotopes now in use is compared to the thallium technique. The chapter on practical aspects states that PET probably will become the gold standard by which all other methods will be judged. Differentiation of planar imaging vs emission CT is explained. A thorough description of a PET facility so far as personnel, financial considerations, physical layout, and so forth is well offered.

The section on digital subtraction angiography starts out with a historical description of the technical advances and the evolution from IV to intraarterial studies. The table of the sources of error in quantitative video densitometry is enlightening. The next chapter on the evaluation of coronary flow by using digital subtraction angiography and video densitometry is well described and the limitations are included.

The next section describes cardiac sympathetic imaging with metaiodobenzylguanidine (MIBG). The chemistry and radioiodination of MIBG and its comparison with norepinephrine are detailed. The use of this technique first in animal models of myocardial disease and then finally in humans is compared with thallium-201 imaging, and illustrations are provided. The section on cardiac infections describes the return of rheumatic fever in the United States and the relationship of viruses and atherosclerosis.

The final chapter is the longest of all (40 pages) and is a thorough review of coronary thrombolysis. Description and discussion of the various types of thrombolytic agents and their advantages and disadvantages are thoroughly detailed. Extensive sections of smaller print show that the contributors wanted to pack these 40 pages with information.

Overall, this "journallike" book thoroughly describes the evolving newer cardiac imaging techniques, with good comparisons back to coronary arteriography and with honest descriptions of advantages and disadvantages. Cost relationships not only to the patient (both monetary and biologic risk) but also to the institutions pursuing such studies are included. One major area of weakness, however, is the lack of editorial attention to the illustrations. The color plates, beginning after page 63, are beautiful. However Color Plates 2 and 3 show translocated images that do not correspond to the legends beneath them. Similar types of mismatched images, labels, and legends are found throughout the text and will be confusing for novices in these new techniques if this text is to be their introduction. For radiologists involved in cardiac imaging, a subscription to this series would be worthwhile and most appropriate.

Patricia A. Randall
SUNY Health Science Center
Syracuse, NY

Radiologic Evaluation of Esophageal Motility: Results in 170 Patients with Chest Pain

David J. Ott[1]
William B. Abernethy[1]
Michael Y. M. Chen[1]
Wallace C. Wu[2]
David W. Gelfand[1]

The role of radiologic evaluation of esophageal motility in patients with chest pain has been studied rarely. Consequently, we compared the results of radiologic and manometric examinations of the esophagus in 170 patients (106 women, 64 men; mean age, 53 years) with chest pain. Manometry, used as the standard, was normal in 114 (67%) patients, and showed the following abnormal diagnoses in the remaining 56 (33%): nonspecific esophageal motility disorder in 27 (48%), nutcracker esophagus in 16 (29%), diffuse esophageal spasm in 11 (20%), and achalasia in two (4%). Radiologic specificity was 93% (106/114) and overall sensitivity only 36% (20/56). Sensitivity increased to 50% by excluding those with nutcracker esophagus, a purely manometric diagnosis. Of the 20 patients in whom nonspecific esophageal motility disorder and diffuse esophageal spasm were undetected on radiologic examination, minimal manometric criteria for diagnosis were available in 18.

Our results show that radiologic recognition of normal esophageal peristalsis is excellent. However, the vast majority of patients with chest pain do not appear to have abnormal esophageal motility on radiologic evaluation.

***AJR* 155:983-985, November 1990**

Chest pain is a potentially serious complaint because of the risk of cardiac disease. Patients often remain anxious even after coronary artery disease has been reasonably excluded, making evaluation of a noncardiac cause of pain important [1]. Correlative radiologic and manometric studies in patients with dysphagia have been reported, but similar comparisons in those presenting with chest pain are uncommon [2]. Chest pain may result from abnormal esophageal motility, but the efficacy of radiology in this evaluation has not been clarified. As a result, we reviewed the radiologic and manometric records of 170 patients with chest pain to clarify the role of the radiologic examination for assessing normal and abnormal esophageal motility.

Materials and Methods

The radiologic and esophageal manometric records for a 3-year period were reviewed. Patients in whom chest pain was the major symptom were selected consecutively on the basis of having had both examinations done within 2 weeks of each other. A total of 170 patients entered the study, which comprised 106 women and 64 men with a mean age of 53 years (range, 23–87 years). Esophageal manometry, used as the standard, was normal in 114 patients (67%). Manometry was abnormal in 56 patients (33%), with the following disorders diagnosed: nonspecific esophageal motility disorder (NEMD) in 27 (48%), nutcracker esophagus in 16 (29%), diffuse esophageal spasm (DES) in 11 (20%), achalasia in two (4%).

Esophageal manometry was performed with a round, eight-lumen polyvinyl catheter. The lumens were infused continuously by using a low-compliance infusion system (Arndorfer Specialties, Inc., Greensdale, WI). The pressure of the lower esophageal sphincter was measured and relaxation was assessed at mid-expiration by the station pull-through technique. The catheter was then positioned in the esophageal body with catheter openings 3, 8,

Received May 11, 1990; accepted after revision June 22, 1990.

Presented at the annual meeting of the American Roentgen Ray Society, Washington, DC, May 1990.

[1] Department of Radiology, Bowman Gray School of Medicine, Wake Forest University, Winston-Salem, NC 27103. Address reprint requests to D. J. Ott.

[2] Department of Medicine, Bowman Gray School of Medicine, Wake Forest University, Winston-Salem, NC 27103.

0361-803X/90/1555-0983
© American Roentgen Ray Society

13, and 18 cm above the lower esophageal sphincter. The esophageal contractions were recorded in response to 10 wet swallows (5 ml H_2O) at 30-sec intervals. The normal mean distal amplitude in our laboratory is 100 ± 80 mm Hg (mean ± 2 SD) [3].

Standardly accepted criteria for abnormal manometric diagnoses were used [1, 2, 4]. NEMD, a catchall term, included manometric abnormalities that defied specific classification, such as intermittent absence of peristalsis, low-amplitude peristalsis, prolonged duration or repetitive contractions, or incomplete relaxation of the lower esophageal sphincter. Nutcracker esophagus was defined as normal esophageal peristalsis but with distal peristaltic contractions with mean amplitudes above 180 mm Hg [5]. DES showed intermittently abnormal peristalsis and simultaneous contractions on more than 10% of wet swallows [6]. The manometric criteria for achalasia were esophageal aperistalsis and lower esophageal sphincter dysfunction.

A multiphasic radiologic examination of the esophagus was done with remote-control machinery [2, 7]. Esophageal motility was assessed fluoroscopically with the patient in the prone oblique position by observing single swallows of barium traversing the length of the esophagus. All examinations were done by gastrointestinal radiologists or residents, the latter being supervised during film interpretation but not always during fluoroscopy. The status of primary esophageal peristalsis and other functional abnormalities was noted. Radiologic criteria for achalasia included aperistalsis and smooth tapering of the lower end of the esophagus due to failure of relaxation of the lower esophageal sphincter. Radiologic findings suggesting DES included intermittently uncoordinated peristalsis and segmental nonperistaltic contractions. Other less specific abnormalities of esophageal motility were diagnosed as NEMD. No specific radiologic criteria have been determined for nutcracker esophagus [5].

Results

Of 114 patients in whom manometry was normal, normal motility was seen fluoroscopically in 106, for a specificity of 93%. In this group, eight false-positive diagnoses of NEMD were made radiologically. The overall radiologic sensitivity was only 36% (20/56), and there was a wide range of detection rates (Table 1). Nutcracker esophagus was not diagnosed radiologically, although NEMD was suggested in four patients. The radiologic sensitivity increased to 50% (20/40) when diagnoses of nutcracker esophagus are excluded.

Of 20 patients in whom NEMD (15) and DES (five) went undetected radiologically, minimal manometric criteria for diagnosis were available in 18. In all five patients with DES, the prevalence of disrupted peristalsis and spontaneous contractions on manometric examination was only 20%. Of the 15 patients with NEMD who were not diagnosed, the frequency of interrupted peristalsis in 11 patients was 20% (eight patients) or 30% (three patients), while triple-peaked contractions were seen in two.

TABLE 1: Radiologic Sensitivity in 56 Patients with Chest Pain and Abnormal Esophageal Manometry

Manometric Diagnosis	No. (%)	
	Total	Radiologic Detection
Nonspecific esophageal motility disorder	27	12 (44)
Nutcracker esophagus	16	0[a]
Diffuse esophageal spasm	11	6[b] (55)
Achalasia	2	2 (100)
Total	56	20 (36)

[a] Nonspecific esophageal motility disorder diagnosed radiologically in four patients.

[b] Diffuse esophageal spasm diagnosed in two patients and nonspecific esophageal motility disorder in four.

Discussion

In a patient with recurrent chest pain, cardiac disease must be excluded first, since about 70–80% of those with angina-like pain will have coronary artery disease [1, 4]. Only 10–15% of patients with chest pain will have an esophageal cause, most commonly structural disease or gastroesophageal reflux. This leaves a small minority of patients with chest pain that may result from abnormal esophageal motility. We studied 170 patients with chest pain to assess the role of radiology in evaluating this symptom for abnormal esophageal motility.

In those patients with chest pain, esophageal manometry was normal in 67%; the radiologic specificity was 93%. This true-negative rate agrees with other reports showing radiologic specificities of 91–95% in assessing normal esophageal peristalsis [2, 8, 9]. Multiple single swallows of barium must be observed to evaluate esophageal motility accurately [9]. Similarly, a previous manometric study at our institution of 910 patients with noncardiac chest pain showed normal esophageal motility in 72% [10]. Thus, the results of these studies indicate that manometric and radiologic evaluation of esophageal motility usually is normal in patients with chest pain.

In this series, esophageal manometry was abnormal in 56 patients; NEMD, nutcracker esophagus, and DES accounted for 96% of the positive diagnoses. The overall radiologic sensitivity was only 36%, indicating that manometric verification of an esophageal motility disorder diagnosed radiologically was available in 20 (12%) of 170 patients. This was a selected group of patients with chest pain, consisting mainly of those in whom cardiac disease and structural disorders of the esophagus had been largely excluded. In a more general group of individuals with chest pain in which abnormal esophageal function on manometry would possibly explain the pain, radiologic detection of abnormal motility would be only about 1–2% [1, 4, 10].

Thus, this small radiologic yield reflects both the low prevalence of esophageal motility disorders as a cause of recurrent chest pain and the poor sensitivity of the fluoroscopic examination in evaluating the spectrum of functional disorders exhibiting this symptom. Even by eliminating nutcracker esophagus, the radiologic sensitivity increased to only 50%. This low return is in part due to the rarity of achalasia as a cause of chest pain. Achalasia is the motility disorder best diagnosed radiologically and the one found in about 36% of patients with functional dysphagia [7, 10]. The poor radiologic sensitivities also are related to the presence of minimal manometric criteria for the diagnoses of NEMD and DES in 18 of the 20 patients in whom these disorders were not detected fluoroscopically. More careful fluoroscopic observation using five single swallows of barium would improve detection in these cases [9], but at most would probably only double the already low radiologic yield found in patients with chest pain.

Several caveats in attributing chest pain to abnormal esophageal function must be mentioned. The concept of "microvascular angina" warrants discussion since some patients with small-vessel disease and normal coronary arteries at angiography would be labeled as having noncardiac chest pain [1]. These patients would expand the pool of those being evaluated for a possible esophageal cause of pain and would lower the percentage having abnormal esophageal function. Also, as patients age, the chance of coexisting cardiac and structural disease of the esophagus increases, making attribution of symptoms more difficult. Obviously, these combinations reduce the specificity of abnormal esophageal function.

Finally, the presence of abnormal esophageal motility does not prove an esophageal origin for the chest pain [1, 4]. Nearly half of our abnormal manometric diagnoses were NEMD, a common motility disorder of uncertain significance that often is not associated with chest pain [1]. Most patients with chest pain and abnormal motility will not have symptoms during the standard manometric or radiologic examinations. Furthermore, only a minority of those with chest pain respond to provocative testing by esophageal acid perfusion or the injection of drugs, such as edrophonium [10]. Prolonged ambulatory monitoring of esophageal function has further shown changing motility patterns in the same individual, questioning the brief temporal sampling of esophageal pressures done on routine manometric examination [11-13]. In one study of 60 patients with noncardiac chest pain, an esophageal origin was shown to be likely in 27% by using standard testing but increased to 48% by adding 24-hr recording of esophageal pressures [11]. The occasional observation of transitional motility disorders also emphasizes the difficulty of correlating symptoms and abnormal esophageal function [14-16].

In conclusion, the majority of patients with chest pain who undergo radiologic evaluation will have normal esophageal motility. In only a minority will the symptom originate in the esophagus, and structural disease or gastroesophageal reflux accounts for most esophageal causes of chest pain. This leaves a small fraction of patients in whom abnormal esophageal motility is a potential source of the pain, and the radiologic examination is usually normal in these patients. The contribution of radiology and standard manometry in evaluating this symptom is further compromised because the attribution of chest pain to many of these esophageal motility disorders remains problematic.

REFERENCES

1. Richter JE, Bradley LA, Castell DO. Esophageal chest pain: current controversies in pathogenesis, diagnosis, and therapy. *Ann Intern Med* **1989;**110:66-78
2. Ott DJ, Richter JE, Chen YM, Wu WC, Gelfand DW, Castell DO. Esophageal radiography and manometry: correlation in 172 patients with dysphagia. *AJR* **1987;**149:307-311
3. Richter JE, Wu WC, Johns DN, et al. Esophageal manometry in 95 healthy adult volunteers. *Dig Dis Sci* **1987;**32:583-592
4. Richter JE, Castell DO. Esophageal disease as a cause of noncardiac chest pain. *Adv Intern Med* **1988;**33:311-336
5. Ott DJ, Richter JE, Wu WC, Chen YM, Gelfand DW, Castell DO. Radiologic and manometric correlation in "nutcracker esophagus." *AJR* **1986;**147: 692-695
6. Chen YM, Ott DJ, Hewson EG, et al. Diffuse esophageal spasm: radiographic and manometric correlation. *Radiology* **1989;**170:807-810
7. Ott DJ. Radiologic evaluation of esophageal dysphagia. *Curr Probl Diagn Radiol* **1988;**17:1-33
8. Dodds WJ. Current concepts of esophageal motor function: clinical implications for radiology. *AJR* **1977;**128:549-561
9. Ott DJ, Chen YM, Hewson EG, et al. Esophageal motility: assessment with synchronous video tape fluoroscopy and manometry. *Radiology* **1989;**173:419-422
10. Katz PO, Dalton CB, Richter JE, Wu WC, Castell DO. Esophageal testing in patients with noncardiac chest pain or dysphagia. *Ann Intern Med* **1987;**106:593-597
11. Janssens J, Vantrappen G, Ghillebert G. 24-hour recording of esophageal pressure and pH in patients with noncardiac chest pain. *Gastroenterology* **1986;**90:1978-1984
12. Peters L, Maas L, Petty D, et al. Spontaneous noncardiac chest pain—evaluated by 24-hour ambulatory esophageal motility and pH monitoring. *Gastroenterology* **1988;**94:878-886
13. Soffer EE, Schalabrini P, Wingate DL. Spontaneous noncardiac chest pain: value of ambulatory esophageal pH and motility monitoring. *Dig Dis Sci* **1989;**34:1651-1655
14. Vantrappen G, Janssens J, Hellemans J, Coremans G. Achalasia, diffuse esophageal spasm, and related motility disorders. *Gastroenterology* **1979;** 76:450-457
15. Shiflett DW, Wu WC, Ott DJ. Transition from nonspecific motility disorder to achalasia. *Am J Gastroenterol* **1980;**73:325-328
16. Longstreth GF, Forouzan P. Evolution of symptomatic diffuse esophageal spasm to achalasia. *South Med J* **1982;**75:217-220

Technical Note

Use of C-Arm Fluoroscope to Examine Patients with Swallowing Disorders

Michael Davis,[1] Phyllis Palmer,[2] and Charles Kelsey[1]

Barium swallow examinations are routinely performed with conventional radiographic fluoroscopic equipment. Patients sit or stand on a radiographic table footboard and are given barium to swallow on command. Certain patients cannot be examined in this manner because of illness or physical disability that mandates the use of other types of radiographic equipment. Remote-control fluoroscopic units with an overhead image tube, radiographic tables that have been mounted with a cross-table X-ray tube for horizontal-beam imaging of a patient in the supine position [1], and portable C-arm fluoroscopic units are available. Special chairs also are available that are narrow enough to be placed between the radiographic table and the image intensifier [2, 3]. To the best of our knowledge, there have been no reports describing the use of the C-arm fluoroscopic units for swallowing studies.

Materials and Methods

We examined 74 patients confined to wheelchairs (Fig. 1) or stretchers (Fig. 2) with a mobile C-arm fluoroscope. None of the patients could be examined in the routine manner with standard fluoroscopic equipment. Forty-four patients were examined while in a wheelchair, and 30 patients were examined while on a stretcher. All patients were adequately studied in anteroposterior and lateral projections. The examinations were performed with a mobile C-arm unit (Series 9000 Mobile C-Arm, OEC-Diasonics Inc., Salt Lake City, UT) consisting of a microprocessor-controlled X-ray mainframe and dual-screen monitor with integrated real-time digital image processing. The system has a 0.3-mm focal spot with 40–120 kVp and 0.5- to 5.0-mA boost capability, a high-resolution television camera with 360° motorized rotation, choice of 6- or 9-in. (15- or 23-cm) input screen with central resolution of 4.4 pixels/mm and peripheral resolution of 3.6 pixels/mm, a 512 × 512 image matrix, and an image storage system with videocassette recorder and videodisk recorder. The unit can be powered by any 115-V, 20-A electrical outlet.

Different consistencies of barium-laden substances were used for the swallowing examinations. Medium-density barium (55% w/v), high-density barium (200% w/v), barium paste (100% w/v), and food substances including cereal, cookies, and marshmallows were mixed with high-density barium. The swallowing examinations were recorded on ¾-in. (2-cm) videocassette tape with a video recorder (5600 Series, Sony, Park Ridge, NJ). Selected video images were later either digitized on videodisk, and when necessary hard copies were generated from the videodisk, or recorded freeze frame from a video recorder by using a conventional multiformat imager. The hard-copy images from videodisk or from freeze-frame videotape do not have the sharpness of conventional spot films or 105 photospots, but they are clear enough to identify abnormalities.

Radiation Exposure and Dosimetry of the Fluoroscopic C-Arm

The entrance skin exposure rate varies with field size, patient age, and neck thickness but is usually around 1500 mR (387×10^{-6} C/kg)/min at 65 kVp. The unit operates in the automatic brightness mode so it will automatically adjust the kilovoltage and amperage to optimize the image brightness. These values are approximately the same as would be encountered with conventional fluoroscopy.

During recording of images the output rises to approximately 9.5 R (2.5 mC/kg)/min. This is considerably lower than the 30–60 R (7.7–15.5 mC/kg)/min measured during cinefluoroscopy.

Received March 8, 1990; accepted after revision May 20, 1990.

[1] Department of Radiology, University Hospital, University of New Mexico Medical Center, Albuquerque, NM 87131. Address reprint requests to M. Davis.

[2] Department of Speech Pathology, University Hospital, University of New Mexico Medical Center, Albuquerque, NM 87131.

***AJR* 155:986–988, November 1990** 0361–803X/90/1555–0986 © American Roentgen Ray Society

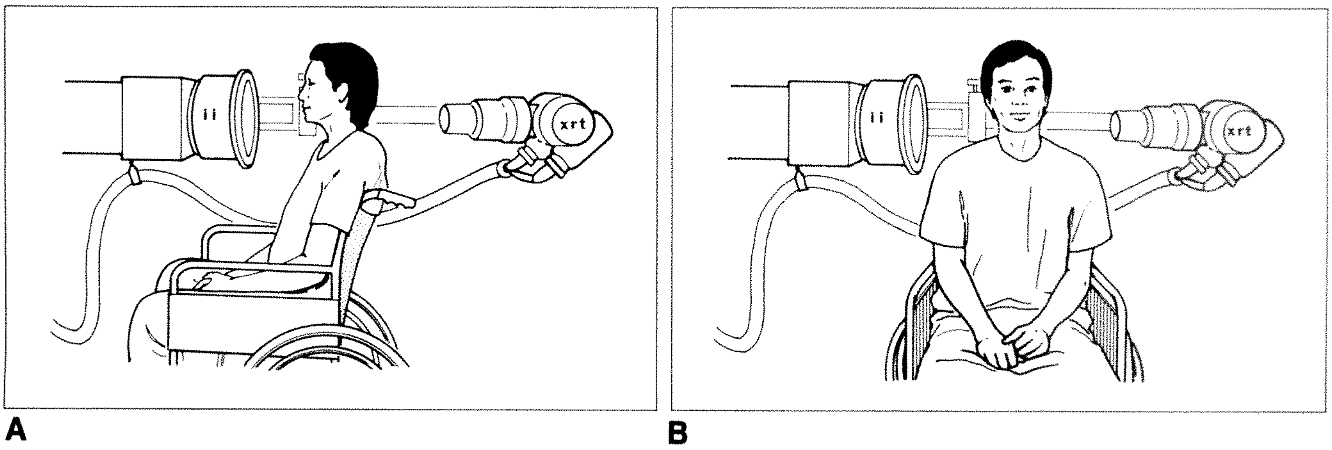

Fig. 1.—*A* and *B*, Illustrations show orientation of C-arm fluoroscope for imaging in anteroposterior (*A*) and lateral (*B*) positions with patient sitting in wheelchair. ii = image intensifier, xrt = X-ray tube.

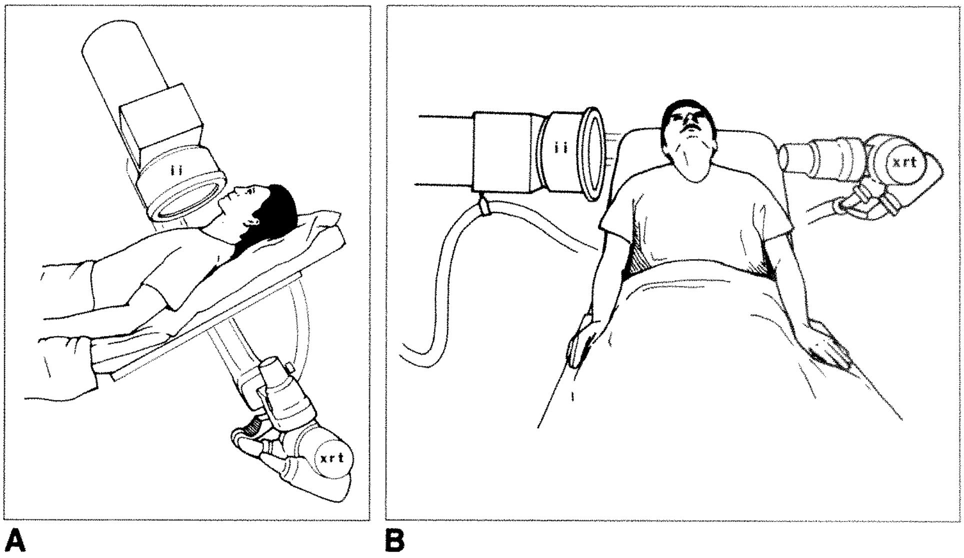

Fig. 2.—*A* and *B*, Illustrations show orientation of C-arm fluoroscope for imaging in anteroposterior (*A*) and lateral (*B*) positions with patient on a stretcher. ii = image intensifier, xrt = X-ray tube.

The radiation dose to the patient's thyroid is three to five times lower when the X-ray beam enters from the posterior side as compared with an anterior entrance. This is because attenuation in the tissues will reduce the beam intensity before it reaches the thyroid if the beam enters from the rear.

The scattered radiation levels measured at the control panel 2 m from the X-ray beam were 25 mR (6.5×10^{-6} C/kg)/hr. For a lateral beam the scattered radiation levels to a staff member standing next to the patient will be 50 to 100 times greater if he or she stands on the entrance side rather than the exit side of the patient. This is because the radiation is scattered uniformly in all directions. The scattered radiation is attenuated in passing through the patient and less reaches the opposite side.

Results

All examinations were judged by an experienced observer to be of high quality. At fluoroscopy the examination quality was considered equal to that obtained with conventional fluoroscopic equipment. Patients were diagnosed with labial and buccal abnormalities, abnormal tongue movement, nasopharyngeal reflux (Fig. 3), premature oropharyngeal leakage from mouth, pharyngeal paresis, aspiration (Fig. 4), cricopharyngeal muscular dysfunction, vallecular and piriform sinus pooling, pharyngeal diverticula, pharyngeal perforation, esophageal motility disorders, and esophageal perforation.

Discussion

The mobility of the C-arm fluoroscope allows an easier examination of patients confined to a wheelchair than do special chairs that are narrow enough to be placed between the X-ray table and image intensifier. Sometimes it is difficult to manage patients with the latter method because of decreased transfer skills related to deficits in mobility and stability. Examination time varied according to patient's ability to comply, but average fluoroscopic time was approximately 3 min and average time in the room was 15 min.

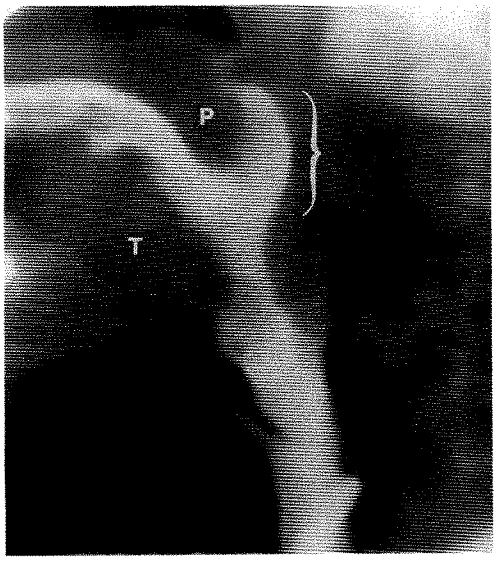

3

Fig. 3.—Lateral pharyngogram shows extensive nasopharyngeal reflux of barium. Reflux (*bracket*). P = soft palate, T = tongue.

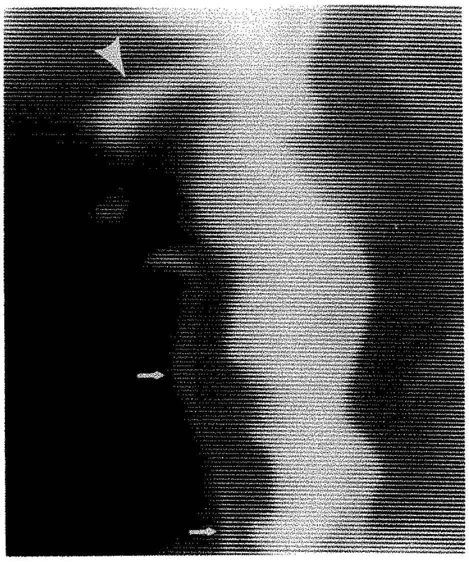

4

Fig. 4.—Lateral pharyngogram shows penetration of barium into laryngeal airway (*arrowhead*) and spillage of barium on posterior wall of trachea (*arrows*).

At our institution, the fluoroscopic C-arm unit is also used to diagnose vascular abnormalities in seriously injured patients who are on treatment tables in the emergency department. The C-arm also has been used under these conditions to diagnose pharyngeal and esophageal trauma usually from penetrating knife or gunshot wounds. The reduced time required to diagnose these acute injuries is significant compared with time required to transport injured patients to the radiology department for examination with conventional equipment. In some instances there was no time for a conventional examination and patients were rushed to emergent surgery and the swallowing examination was done later. A C-arm examination in the emergency department could obviate a second operation.

In patients with suspected swallowing disorders studied by C-arm fluoroscopy, the emphasis was to image the dynamic process of swallowing rather than the static condition seen with double-contrast pharyngography. Therefore, video recording was emphasized.

In patients unable to sit or stand comfortably on a conventional fluoroscopic table, the fluoroscopic C-arm is an effective tool for evaluating patients with dysphagia, aspiration symptoms, suspected esophageal motility disorders, and other suspected swallowing disorders. Limitations in using the C-arm for swallowing disorders include inability to check for gastroesophageal reflux in the usual manner, although the fluoroscopic C arm is capable of imaging esophageal motility throughout the entire esophagus. The procedure has been accepted at our institution by patients, technologists, radiologists, referring physicians, speech pathologists, and others involved in the diagnosis and treatment of swallowing disorders.

REFERENCES

1. Jones B. Examination of the patient with dysphagia. *Radiology* **1988**;167:319–326
2. Logemann JA. *Evaluation and treatment of swallowing disorders.* San Diego: College-Hill, **1983**
3. Logemann JA. *Manual for the videofluorographic study of swallowing.* San Diego: College-Hill, **1986**

Case Report

Primary Aortoesophageal Fistula After Chronic Aortic Dissection

Barry S. Rose,[1] Douglas M. Gordon, and James D. Geihsler

Aortoenteric fistula is an unusual condition accounting for a small proportion of gastrointestinal hemorrhages. The preoperative diagnosis may be difficult, even when it is considered in the differential diagnosis of gastrointestinal hemorrhage. We describe a case in which a primary aortoesophageal fistula in association with chronic aortic dissection was detected with CT before clinical suspicion of the condition.

Case Report

A 68-year-old hypertensive man originally presented in 1985 with a DeBakey type III aortic dissection extending from the distal aortic arch to the abdominal aortic bifurcation. This was associated with no neurologic deficit or visceral branch occlusion. The patient was treated medically and evaluated periodically. Four years later, CT showed enlargement of the thoracic component. The patient declined surgical treatment. Regular follow-up including antihypertensive therapy continued.

The patient remained in his usual state of health for another 11 months until he presented to the emergency department with a 4-day history of nausea, vomiting, and diarrhea. He described a 3-hour episode of sharp retrosternal chest pain occurring the preceding day. He was febrile (102°F) with shaking chills. The patient denied the presence of blood in the vomitus or stool. Guaiac tests were negative on admission. Blood pressure was 196/100. The patient was admitted for regulation of his blood pressure and evaluation of gastrointestinal symptoms and fever. Plain films of the chest showed linear gas collections along the margins of a thoracic aortic aneurysm (Figs. 1A and 1B).

The next day, CT examination of the chest and abdomen showed the large, chronic aortic dissection and, in addition, gas within the false lumen of the thoracic aorta (Fig. 1C). No contrast enhancement was present within the false lumen. No additional evidence of aortic rupture was detected. The CT findings were thought to represent a communication between the false lumen and an air-containing structure, most likely the esophagus, possibly with concurrent infection of the thrombus.

Antibiotic therapy was instituted, and the patient's course was initially relatively uneventful. Five days later, the patient had an episode of massive hematemesis and hypotension. An aortogram showed a type III dissection without communication of the true and false channels and without extravasation of contrast material. The renal, celiac, and mesenteric branches were adequately perfused from the true lumen. Endoscopy revealed a clot and surrounding bluish discoloration on the posterior midesophageal wall consistent with an aortoesophageal fistula.

The patient's condition rapidly deteriorated. Approximately 24 hr after the initial gastrointestinal hemorrhage, the patient had another episode of hematemesis and hypotension. He responded briefly to resuscitative efforts, but died that evening.

At autopsy, an aortoesophageal fistula was found with the defect in the posterior esophageal wall just below the level of the carina (Fig. 1D). The stomach was grossly distended with 5000 g of clotted blood. A large amount of blood also was present throughout the intestinal tract.

Discussion

Aortoenteric fistulas are classified as primary (uncommon) or secondary (more common). Secondary aortoenteric fistulas are usually related to aortic prosthetic grafts and most commonly involve the duodenum. Recent reports of secondary aortoesophageal fistula after aortic grafts and aortic wall reinforcement with Dacron wraps have appeared. Primary aortoenteric fistulas are most commonly caused by atherosclerotic aneurysms and most commonly rupture into the duodenum (80%) [1]. The esophagus (10%), stomach, and jejunum are less common sites. Primary aortoenteric fistulas rarely involve the colon or other portions of the small bowel.

Aortoesophageal fistula is a rare complication of aortic dissection, occurring much less frequently than aortoesophageal fistulas caused by atherosclerotic thoracic aneurysms uncomplicated by dissection. Hirst et al. [2], in their exhaus-

---

Received March 19, 1990; accepted after revision April 24, 1990.

[1] All authors: Department of Radiology, Aultman Hospital, 2600 Sixth St., S.W., Canton, OH 44710. Address reprint requests to B. S. Rose.

AJR 155:989-990, November 1990 0361-803X/90/1555-0989 © American Roentgen Ray Society

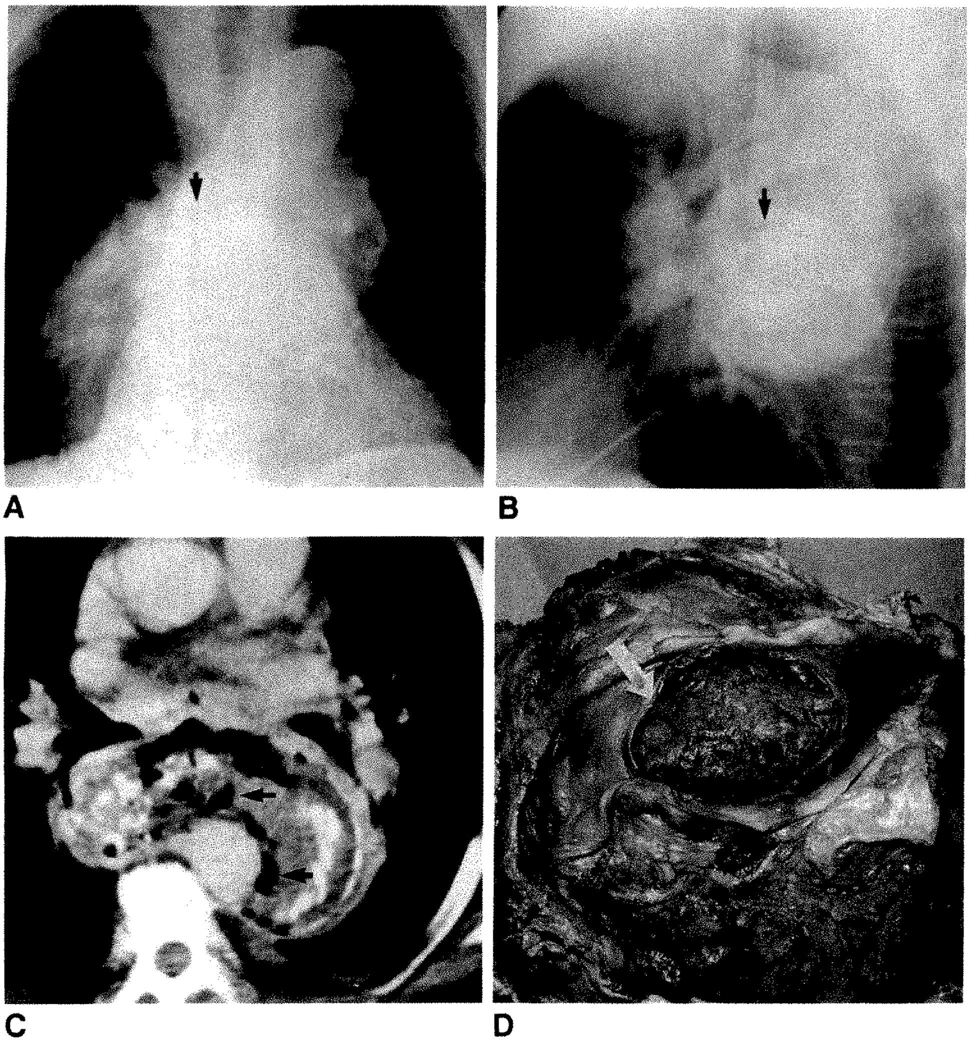

Fig. 1.—*A* and *B*, Posteroanterior (*A*) and lateral (*B*) chest radiographs show linear gas collections along margins of thoracic aneurysm (*arrows*).

C, CT scan shows gas collections in false lumen of aneurysm (*arrows*). White material is calcification of thrombus in false lumen.

D, Gross specimen with anterior esophageal wall slit longitudinally showing clot (*arrow*) extending through a large defect in posterior esophageal wall.

tive review of the literature spanning a 21-year period, noted four reports of this condition. Aortoesophageal fistula has occurred with subacute [3] and chronic [4] dissections. The exact mechanism of rupture of the aorta into the gastrointestinal tract is not clearly established. Pressure necrosis and infection are probably major factors.

Aortoesophageal fistula may cause sudden massive exsanguinating hemorrhage, but, in most patients, sentinel or herald hemorrhage occurs. Brief episodes of bleeding followed by a latent period of minutes to several weeks are sufficiently common to be considered a hallmark of the condition. The Chiari triad of midthoracic pain, sentinel hemorrhage, and final exsanguination after an asymptomatic interval describe the clinical syndrome [5]. The most important factor in diagnosis is awareness of the condition. A chest radiograph may show mediastinal widening, most often indicating an aneurysm. Upper gastrointestinal contrast series have occasionally been useful. Angiography and endoscopy have been used in diagnosis with partial success.

Although no single imaging study has proved completely reliable, CT has been used to diagnose aortoenteric fistula [6–8]. Localized disruption of the conspicuity of the aortic wall on a contrast-enhanced examination in combination with effacement of the fat plane between the aneurysm and the juxtaposed enteric structure is an important finding [8]. The presence of intraluminal air is a specific sign for aortoenteric fistula [7].

In summary, aortoesophageal fistula is a rare consequence of aortic dissection. Pressure necrosis due to an enlarging aneurysm most likely accounts for the presence of the fistula in our patient. The chest radiograph suggested this condition by showing gas in the aneurysm. The diagnosis was confirmed with CT and endoscopy. To the best of our knowledge, CT diagnosis of a primary aortoesophageal fistula after aortic dissection has not been reported before. The presence of gas in the false lumen is a unique feature in this case.

REFERENCES

1. Hooper WL. Hematemesis and melana due to rupture of a saccular aneurysm of the aorta into the esophagus. *Postgrad Med J* **1962**;38: 297–301
2. Hirst AE, Johns VJ Jr, Kime SW Jr. Dissecting aneurysm of the aorta: a review of 505 cases. *Medicine* **1958**;37:217–279
3. Gittleman SE, Leichtling M. Dissecting aneurysm of aorta with perforation into esophagus. *NY State J Med* **1952**;52:2517–2519
4. Baer S, Loewenberg SA. Aortic aneurysms simulating organic disease of the gastrointestinal tract. *Gastroenterology* **1948**;10:617–625
5. Chiari H. Uber Premdkorperverletzung des oesophagus mit aortenperforation. *Klin Wochenschr* **1914**;51:7
6. Kukora JS, Rushton FW, Cranston PE. New computed tomographic signs of aortoenteric fistula. *Arch Surg* **1984**;119:1073–1075
7. Mark AS, Moss AA, McCowin M. CT of aortoenteric fistulas. *Invest Radiol* **1985**;20:272–275
8. Raptopoulos V, Cummings T, Smith EH. Computed tomography of life-threatening complications of abdominal aortic aneurysm: the disrupted aortic wall. *Invest Radiol* **1987**;22:372–376

Obliteration of the Fat Surrounding the Celiac Axis and Superior Mesenteric Artery Is Not a Specific CT Finding of Carcinoma of the Pancreas

Mark E. Baker[1]
Richard H. Cohan
Scott N. Nadel
Richard A. Leder
N. Reed Dunnick

Partial or complete obliteration of the fat surrounding the celiac axis and superior mesenteric artery on CT is considered so characteristic of pancreatic carcinoma that many consider it diagnostic. However, this finding may be present on CT scans of some treatable tumors. During a 2-year period, we retrospectively collected 10 cases of nonpancreatic tumors that obliterated the fat surrounding the celiac axis and/or superior mesenteric artery. Four patients had metastatic disease, three had lymphoma, two had primary small-bowel adenocarcinoma, and one had a diffuse retroperitoneal endocrine tumor. The scans were analyzed for presence, location, and morphology of the mass and biliary and/or pancreatic ductal dilatation. Of the patients with metastatic disease, three had focal, retropancreatic, periceliac masses without ductal dilatation. One had an infiltrative retroperitoneal process enveloping the pancreas and causing biliary dilatation. Of the patients with lymphoma, two had focal masses in the mesenteric root without ductal dilatation, and one had an infiltrative retroperitoneal process. Of the two patients with primary carcinoma of the small bowel, one had a mesenteric mass without ductal dilatation and the other had an infiltrative retroperitoneal process enveloping the pancreatic head and obstructing the ducts. The patient with the neuroendocrine tumor had an infiltrative retroperitoneal process enveloping the pancreas without ductal dilatation.

Obliteration of the fat surrounding the celiac axis and superior mesenteric artery is not a specific CT finding of carcinoma of the pancreas. One cannot rely solely on its presence for the diagnosis of pancreatic carcinoma but should use other important findings such as a focal pancreatic mass and ductal dilatation.

***AJR* 155:991–994, November 1990**

Pancreatic carcinoma often infiltrates posteriorly to involve the peripancreatic vessels, principally, the celiac axis and/or the superior mesenteric artery. Megibow et al. [1] described the CT manifestations of this process as "thickening" of the arteries. As the tumor progresses, the artery becomes encased and the surrounding fat is obliterated. The importance and frequency of this finding have been confirmed and emphasized in subsequent work [2–4]. Currently, arterial thickening and/or obliteration of the fat surrounding the celiac axis and superior mesenteric artery is so characteristic that many consider it almost diagnostic of pancreatic carcinoma [5]. Although this finding has been described for nonpancreatic tumors [6], it has not been widely accepted. Recently, a case of chronic pancreatitis with obliteration of periarterial fat was described [5]. In the past 2 years, we have seen 10 cases of nonpancreatic tumors obliterating a portion or all of the fat surrounding the celiac axis and superior mesenteric artery. These cases form the basis of this report.

Materials and Methods

During a 2-year period, 10 cases of nonpancreatic tumors obliterating the fat surrounding the celiac axis and superior mesenteric artery were detected on CT and retrospectively

Received April 23, 1990; accepted after revision June 7, 1990.

[1] All authors: Department of Radiology, Box 3808, Duke University Medical Center, Durham, NC 27710. Address reprint requests to M. E. Baker.

0361-803X/90/1555-0991
© American Roentgen Ray Society

collected. The patients' age range was 47–67 years. There were six men and four women. Four patients had metastatic disease (three with squamous cell carcinoma of the esophagus and one with prostatic adenocarcinoma). Three patients had lymphoma (one nodular small-cell type, one histiocytic cell type, and one diffuse large-cell type). Two had primary small-bowel adenocarcinomas, one arising from the third portion of the duodenum and the other arising from the duodenal-jejunal junction. The last patient had a diffuse, retroperitoneal neuroendocrine tumor, either representing a carcinoid or a nonfunctioning islet cell tumor. In all but the four patients with metastatic disease, the mass was the initial manifestation of disease. The three patients with esophageal carcinoma were scanned 9, 31, and 37 months after esophagectomy. The patient with metastatic prostatic carcinoma was scanned 30 months after the initial diagnosis. All four patients with metastatic disease had received chemotherapy and/or radiation therapy. In the patient with carcinoma at the duodenal-jejunal junction, the scan was obtained 16 months after resection. Nonetheless, at the original surgery, the mass abutted the mesenteric vessels and was not resected completely.

Histologic confirmation was obtained at surgery in five patients, and cytologic confirmation was obtained by percutaneous biopsy in four patients. In the last patient, metastases of prostatic carcinoma to the liver, lungs, and retroperitoneal lymph nodes provided compelling clinical evidence that the pancreatic mass was a metastasis.

All patients were examined on the 9800 QUICK (General Electric Medical Systems, Milwaukee, WI) by using 2-sec scans acquired with dynamic, incremental scanning techniques. During scanning, 150 ml of Iopamidol-300 (Squibb Diagnostics, New Brunswick, NJ) was injected at a rate of 2.5 ml/sec for 20 sec and then at 1.2 ml/sec in a medially placed antecubital vein by using a MedRad Mark IV automated injector (MedRad, Pittsburgh, PA). Scanning was delayed until 20 sec after infusion of contrast material was started. Ten-millimeter contiguous slices were obtained in nine patients, and 5-mm contiguous slices were obtained in one patient.

The patients' charts were reviewed for history of neoplastic disease and elevation of bilirubin and alkaline phosphatase levels. The scans were analyzed for mass morphology, location, and density, biliary and/or pancreatic ductal dilatation, liver metastases, retroperitoneal lymphadenopathy, and other ancillary findings.

Results

Of the patients with metastatic disease, three had a low-density, periceliac, retropancreatic mass and one had an extensive infiltrative, confluent, retroperitoneal process. In those patients with the periceliac mass, all had metastatic esophageal carcinoma and presented with normal levels of alkaline phosphatase and bilirubin. These masses were unifocal and encased the celiac axis and superior mesenteric vessels (Fig. 1), with two partially encasing the renal vessels and only one involving the aorta and inferior vena cava. Mild biliary dilatation was present in only one patient, and pancreatic ductal dilatation was absent in all three patients. In one patient, the mass was contiguous with the left kidney and posterior wall of the stomach, causing ulceration of the gastric mucosa. Hepatic metastases and adenopathy were present in one patient each.

The patient with metastatic prostatic carcinoma showed an infiltrative, retroperitoneal process on CT. This patient had markedly elevated levels of alkaline phosphatase and bilirubin. On CT, the entire upper retroperitoneum, including the pancreas, was completely enveloped by an extensive soft-tissue process. As a result, all of the major upper retroperitoneal vessels, including the aorta and inferior vena cava, were completely encased. Marked biliary ductal dilatation, liver metastases, and retroperitoneal lymphadenopathy were present.

Of the patients with lymphoma, two had a low-density mass in the mesenteric root, and one had an infiltrative, retroperitoneal process. Those patients with a mesenteric root mass had normal alkaline phosphatase and bilirubin levels. On CT, these patients had a soft-tissue mass adjacent to the superior mesenteric vessels, infralateral to the pancreas (Fig. 2). The superior mesenteric artery was completely or partially encased in both, and the superior mesenteric vein was thrombosed in one. Only one of these patients had retroperitoneal lymphadenopathy.

The patient with lymphoma who had an infiltrative, retroperitoneal process had elevated levels of alkaline phosphatase and bilirubin. The extensive soft-tissue process was primarily retropancreatic, completely encasing the retroperitoneal vessels (occluding the inferior vena cava) with only partial encasement of the head and uncinate process of the pancreas (Fig. 3). Biliary air was present as a result of a choledochojejunostomy. No lymphadenopathy was seen.

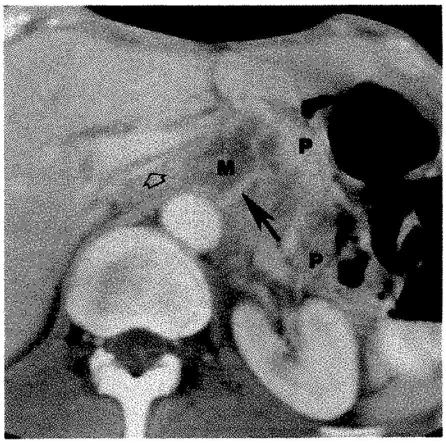

1

Fig. 1.—CT scan of patient with metastatic esophageal carcinoma shows a periceliac, retropancreatic mass (M) that obliterates fat surrounding celiac axis (*solid arrow*) and narrows inferior vena cava (*open arrow*). Mass is clearly retropancreatic (P), and no pancreatic ductal dilatation is present. Mild biliary dilatation is due to mass effect.

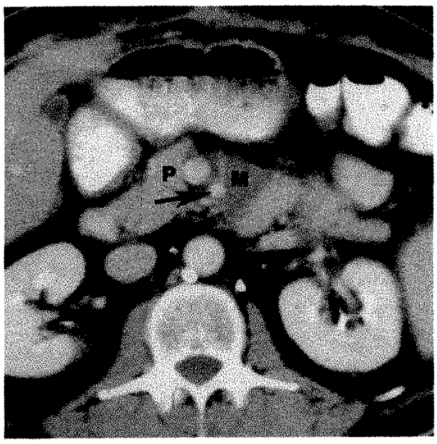

2

Fig. 2.—CT scan of patient with lymphoma shows a mesenteric root mass. Mass (M) obliterates fat surrounding superior mesenteric artery (*arrow*) and also abuts superior mesenteric vein. Mass is clearly not pancreatic (P).

Of the two patients with primary, small-bowel adenocarcinoma, one had a low-density mass in the mesenteric root, and the other had an infiltrative retroperitoneal process. The patient with a mesenteric root mass had normal levels of alkaline phosphatase and bilirubin. This low-density mass partially encased only the superior mesenteric artery. Left paraaortic lymphadenopathy was present.

The patient with primary adenocarcinoma of the small bowel and an infiltrative retroperitoneal process had markedly elevated levels of bilirubin and alkaline phosphatase. Although the process was primarily retropancreatic, the pancreatic head and major upper retroperitoneal vessels were encased, with complete occlusion of the superior mesenteric and portal veins and inferior vena cava (Fig. 4). Massive biliary and pancreatic ductal dilatation, ascites, and retroperitoneal lymphadenopathy were present.

The one patient with a diffuse, retroperitoneal neuroendocrine tumor had an infiltrative retroperitoneal process and normal levels of alkaline phosphatase and bilirubin. This process was partially calcified, primarily retropancreatic, and encased the pancreatic head, the third portion of the duodenum, and the upper retroperitoneal vessels. Liver metastases, ascites, and lymphadenopathy also were present.

None of the patients had the combination of a focal, pancreatic mass associated with periarterial fat obliteration and biliary or pancreatic ductal dilatation, findings considered classic for pancreatic carcinoma.

Discussion

Pancreatic carcinoma is a common tumor with characteristic radiologic findings. A classic feature of this tumor is infiltration around the celiac axis and superior mesenteric artery, giving a thickened appearance to these vessels [1, 2]. As the tumor progresses, the fat surrounding these vessels may be obliterated. In the original CT description, Megibow et al. [1] found thickening of the celiac axis and superior mesenteric artery in 20 of 53 patients with pancreatic carcinoma. In the larger series of Freeny et al. [2] of 175 patients with pancreatic carcinoma, 92% had a pancreatic mass with one or more findings of tumor extension. Vascular involvement (usually encasement) was the most common ancillary finding (84%). As result, obliteration of this periarterial fat has been considered almost diagnostic of pancreatic carcinoma [5].

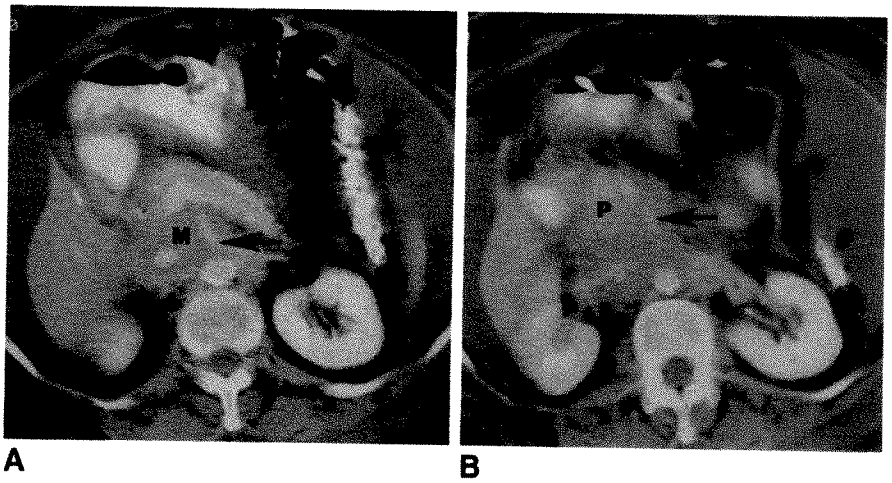

Fig. 3.—CT scans of patient with lymphoma show an extensive, infiltrative, retroperitoneal process.

***A*, Homogeneous soft-tissue mass (M) obliterates fat surrounding superior mesenteric artery (SMA, *arrow*) and encases inferior vena cava (IVC).**

***B*, Mass encases SMA (*arrow*), narrows IVC, and surrounds renal vessels and pancreatic head (P).**

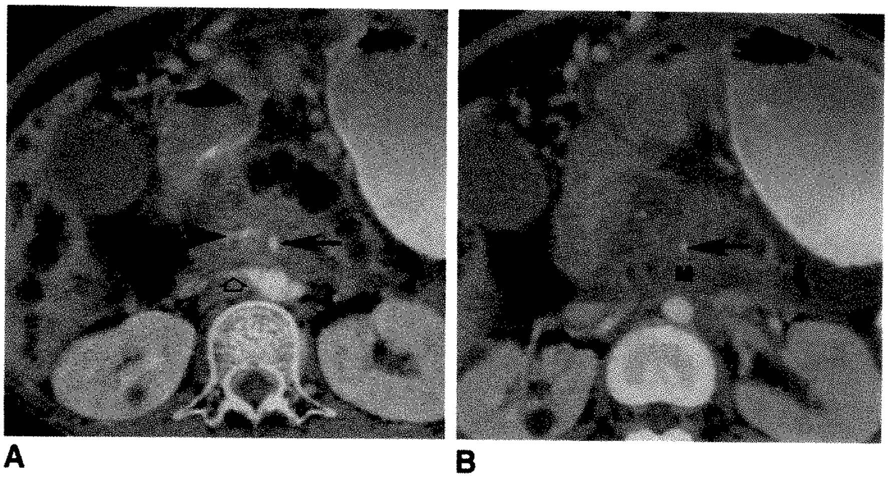

Fig. 4.—CT scans of patient with small-bowel carcinoma show an extensive, infiltrative, retroperitoneal process.

***A*, Homogeneous, soft-tissue mass obliterates fat surrounding superior mesenteric artery (SMA, *solid arrow*) and portal vein (*arrowhead*), surrounds renal vessels (*open arrow*), and obstructs biliary and pancreatic ducts.**

***B*, Mass (M) encases SMA (*arrow*). Superior mesenteric vein is absent, and collaterals (*arrowheads*) are present.**

Obliteration of perivascular fat associated with a pancreatic mass has been described in metastatic disease and lymphoma [6]. A case of chronic, fibrous pancreatitis manifesting as a pancreatic mass with celiac axis and superior mesenteric artery encasement also has been described [5].

Our series confirms that not all tumors that obliterate the periarterial fat are pancreatic carcinomas. In those patients with the infiltrative, retroperitoneal process, the tumor mass and involvement of contiguous organs was much more extensive than would be expected for a pancreatic carcinoma. All patients with a celiac axis mass had clearly extrapancreatic masses. Furthermore, only one patient had biliary dilatation, and none had pancreatic ductal dilatation. Finally, all patients with the mesenteric root mass had extrapancreatic lesions.

The mechanism of periarterial fat invasion in these tumors is not known. Presumably, in pancreatic carcinoma and other tumors, the perivascular lymphatics are infiltrated by neoplastic cells or the tumor directly invades the fat to involve the vessels. In our cases, we had no surgical visualization of this area to determine the cause of fat obliteration.

Obliteration of the periarterial fat by lymphoma [6] has not been emphasized and its occurrence may not be universally recognized. Indeed, experienced observers have been impressed with how seldom the arteries are thickened and the fat obliterated in lymphoma as opposed to pancreatic carcinoma (Megibow AJ, presented at the 12th annual meeting of the Society of Computed Body Tomography, April 1989). Although it is conceivable that lymphoma could invade the lymphatics surrounding these vessels, our experience with lymphoma suggests that this finding is rare.

Other regional tumors, such as gastric or duodenal carcinoma, can invade the lymphatics or the fat surrounding the vessels in the upper adbomen. Fortunately, proximal small-bowel adenocarcinomas (especially duodenal carcinomas) are uncommon.

Metastases to gastrohepatic ligament lymph nodes are common, especially with esophageal squamous cell carcinoma [7]. As these metastases are often clinically silent, they may attain a large size before detection. When large enough, these nodal masses could engulf or invade the periarterial fat.

Half of our cases presented without a known diagnosis. Some of these patients (especially those with lymphoma) had tumors with a much better prognosis than pancreatic carcinoma. Thus an accurate histologic diagnosis must be obtained in these patients.

These cases illustrate that the presence of periarterial fat obliteration is not enough for a specific diagnosis of pancreatic carcinoma in a patient who has a pancreatic mass. Other findings, such as pancreatic and biliary dilatation, also should be used in arriving at the most likely diagnosis. Although we think that the sign of vascular invasion remains reliable in the diagnosis of pancreatic carcinoma in patients who have pancreatic masses detected by CT, its presence also should be weighed with other radiologic features such as mass pattern, extent, and the presence of biliary and pancreatic ductal dilatation [3]. Further, the mass must be scrutinized carefully to determine that it is not subtly peripancreatic. Finally, when atypical characteristics are present (such as very extensive infiltration without ductal dilatation), a diagnosis of nonpancreatic tumor must be considered.

REFERENCES

1. Megibow AJ, Bosniak MA, Ambos MA, Beranbaum ER. Thickening of the celiac axis and/or superior mesenteric artery: a sign of pancreatic carcinoma on computed tomography. *Radiology* **1981**;141:449–453
2. Freeny PC, Marks WM, Ryan JA, Traverso LW. Pancreatic ductal adenocarcinoma: diagnosis and staging with dynamic CT. *Radiology* **1988**; 166:125–133
3. Ward EM, Stephens DH, Sheedy PF. Computed tomographic characteristics of pancreatic carcinoma. *RadioGraphics* **1983**;3:547–565
4. Wittich GR, van Sonnenberg E, Willson SA, Tobin RS, Cubberley DA, Marx MQ. Computed tomography of peripancreatic fat planes. *Europ J Radiol* **1987**;7:253–256
5. Luetmer PH, Stephens DH, Fischer AP. Obliteration of periarterial retropancreatic fat on CT in pancreatitis: an exception to the rule. *AJR* **1989**;153:63–64
6. Mitchell DG, Hill MC, Cooper R, et al. The superior mesenteric artery fat plane: is obliteration pathognomonic of pancreatic carcinoma? *CT* **1987**; 11:247–253
7. Balfe DM, Mauro MA, Koehler RE, et al. Gastrohepatic ligament: normal and pathologic CT anatomy. *Radiology* **1984**;150:485–490

Case Report

Low-Density Insulinoma on Dynamic CT

Theodore R. Smith[1] and Mordecai Koenigsberg

Tumors of functioning beta cells of the islets of Langerhans (insulinomas) are usually characterized radiologically by their tendency to enhance significantly with contrast material on angiography and CT. Most commonly, a localized area of "blush" extends from the arterial into the capillary phase. In some cases, isodense lesions may occur. Recently, we encountered a small noncystic insulinoma that had low density on contrast-enhanced lesions on CT.

Case Report

This 37-year-old woman was well until 8 months before admission, when paroxysmal dizziness, irritability, and syncope developed. After worsening of symptoms, symptomatic hypoglycemia with hyperinsulinemia was diagnosed on outpatient workup. Endocrinologic study revealed symptoms of neuroglycopenia 10 hr after fasting and blood glucose of 31 mg/dl (1.7 mmol/l) with simultaneous insulin level of 31 μU/ml (220 pmol/l). She was admitted for localization of an insulinoma and surgery. CT scans (GE 9800) were obtained, including dynamic scans (50 ml Reno-M-Dip [Squibb Diagnostics, New Brunswick, NJ] at 5-mm sections) through the pancreas. An area of approximately 1 cm in diameter in the posterior caudal head of the pancreas had low density compared with the surrounding pancreatic tissue (Figs. 1A and 1B). It appeared to flatten the adjacent anterior aspect of the inferior vena cava. An associated extrinsic pressure defect on the adjacent second portion of the duodenum was seen on multiple scans through the area. Real-time sonography and Doppler imaging confirmed the presence of a nonvascular lesion in the head of the pancreas (Fig. 1C). The biliary tree was not dilated. Results of angiography, including subselective injections of the gastroduodenal, splenic, and superior mesenteric arteries, were negative. At surgery, intraoperative sonography showed a 1 × 2 × 2 cm mass in the head of the pancreas, correlating perfectly with the preoperative CT and sonographic findings. It was just anterior to the inferior vena cava, to the right of the superior mesenteric vein, and inferior to the common duct. The mass was enucleated. Pathology revealed a well-circumscribed solid 2.0 × 1.7 × 1.2 cm mass consistent with insulinoma, with no evidence of pleomorphism, nuclear atypia, or adenopathy. Immunocytochemical staining showed 80% insulin-secreting cells. The patient became asymptomatic and had normal glucose levels postoperatively.

Discussion

Insulinoma can be diagnosed medically on the basis of the presence of periodic hypoglycemic episodes, which are relieved by IV glucose administration, and in conjunction with fasting blood sugar levels below 50 mg/100 ml (termed "Whipples triad") [1]. Approximately 90% are benign, less than 2 cm in diameter, and solitary, but preoperative localization is important for surgical planning and for exclusion of metastases. In the past, angiography, including selective injections, had been considered the gold standard in demonstration of insulinoma, with an intense hypervascular blush reported in 50–80% of cases in various series [2]. Preoperative sonographic sensitivity has been reported in the 25–60% range [2–4]. More recently, intraoperative sonography coupled with surgical palpation has been cited as being 90–100% effective [3, 4]. Stark et al. [2] reported the effectiveness of thin-section (5 mm) rapid IV bolus contrast CT scanning of the pancreas in detecting islet cell tumors, including localization of approximately 50% of insulinomas (average size, 1.5 cm). Results of pancreatic venous sampling were positive in 75% of those insulinomas not detected by CT. Rossi et al. [5]

Received April 6, 1990; accepted after revision May 1, 1990.

[1] Both authors: Department of Radiology, The Jack D. Weiler Hospital of the Albert Einstein College of Medicine, 1825 Eastchester Rd., Bronx, NY 10461. Address reprint requests to T.R. Smith.

AJR 155:995–996, November 1990 0361-803X/90/1555-0995 © American Roentgen Ray Society

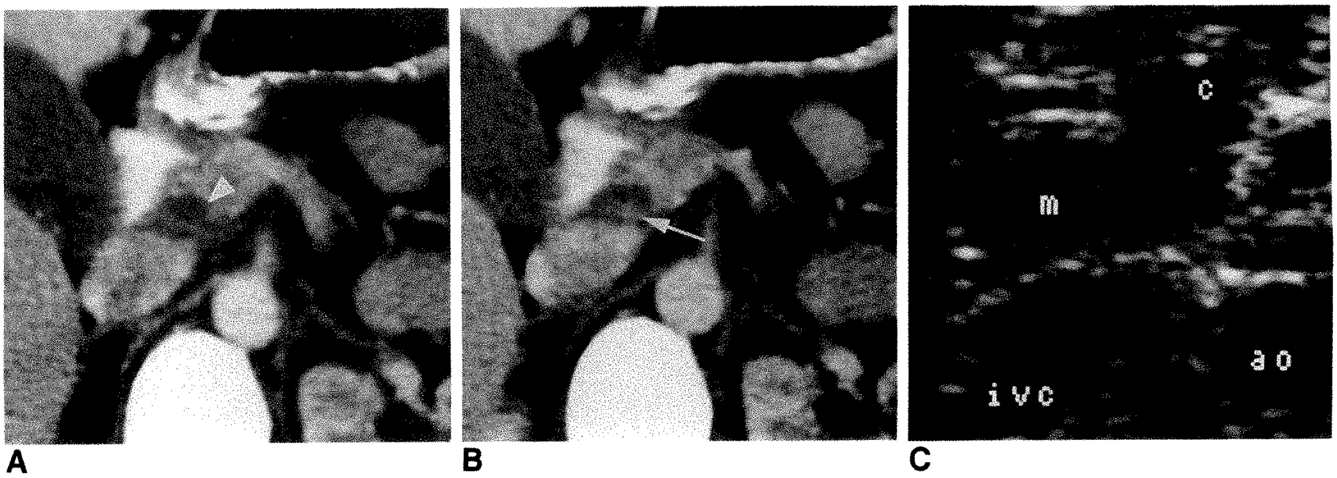

Fig. 1.—*A*, Dynamic IV CT shows well-demarcated low-density insulinoma (*arrowhead*) in pancreatic head. Note extrinsic pressure effect on inferior vena cava and duodenum.

B, 5 sec later, slight central increasing vascularity (*arrow*) is visible in relatively lucent tumor.

C, Transverse sonogram; c = confluence of superior mesenteric vein and splenic vein; m = mass; ao = aorta; ivc = inferior vena cava.

reported only one false-negative of 21 insulinomas studied with CT combined with angiography, and 66% sensitivity with dynamic CT alone. Most insulinomas are hyperdense on CT, and a minority of those detected are isodense (19% in Rossi's series). The latter may be diagnosed on the basis of their abnormal contours.

We found one reported case [6] of a hypovascular solid insulinoma on CT. Dynamic CT was performed after bolus intraarterial contrast administration through a catheter in the dorsal pancreatic artery; the lesion was identified by the surrounding normally enhanced tissue. However, findings on an IV dynamic CT scan obtained several days later were negative. A cystic hypodense insulinoma has been reported on IV contrast-enhanced CT by Pogany et al. [7].

The marked vascular blush of most insulinomas, as seen on CT or angiograms, is assumed to be due to hypervascularity. However, Fulton et al. [8], on pathologic review of 15 insulinomas that were visualized angiographically, found eight of them to be hypovascular. It would therefore appear that rich vascularity does not necessarily correlate with angiographic demonstration.

In the case reported here, the tumor was detectable as a low-density lesion on IV bolus dynamic CT, presumably because it was less vascularized than was the surrounding normal pancreatic parenchyma.

REFERENCES

1. Katz LB, Aufses AH Jr, Rayfield E, Mitty H. Preoperative localization and intraoperative glucose monitoring in the management of patients with pancreatic insulinoma. *Surg Gynecol Obstet* **1986**;163:509–512
2. Stark DD, Moss AA, Goldberg HI, Deveney CW. CT of pancreatic islet cell tumors. *Radiology* **1984**;150:491–494
3. Gunther RW, Klose KJ, Ruckert K, Beyer J, et al. Localization of small islet cell tumors: preoperative and intraoperative ultrasound, computed tomography, arteriography, digital subtraction angiography, and pancreatic venous sampling. *Gastrointest Radiol* **1985**;10:145–152
4. Galiber AK, Reading CC, Charboneau JW, Sheedy PF, et al. Localization of pancreatic insulinoma: comparison of pre- and intraoperative US with CT and angiography. *Radiology* **1988**;166:405–408
5. Rossi P, Baert A, Passariello R, Simonetti G, Pavone P, Tempesta P. CT of functioning tumors of the pancreas. *AJR* **1985**;144:57–60
6. Fink IJ, Krudy AG, Shawker TH, Norton JA, Gordon P, Doppman JL. Demonstration of an angiographically hypovascular insulinoma with intraarterial dynamic CT. *AJR* **1985**;144:555–556
7. Pogany AC, Kerlan RK Jr, Karam JH, LeQuesne LP, Ring EJ. Cystic insulinoma. *AJR* **1984**;142:951–952
8. Fulton RE, Sheedy PF, McIlrath DC, Ferris DO. Preoperative angiographic localization of insulin producing tumors of the pancreas. *AJR* **1975**; 123:367–377

Detection of Pancreatic Fluid and Urine Leakage After Pancreas Transplantation: Value of CT and Cystography

Deborah G. Longley[1]
David L. Dunn[2]
Rainer Gruessner[2,3]
Robert A. Halvorsen, Jr.[1]
David E. R. Sutherland[2]
Janis Gissel Letourneau[1]

Leakage from the urinary bladder or duodenal stump after pancreas transplantation with urinary bladder drainage of the graft is difficult to diagnose clinically. We retrospectively reviewed our experience with fluoroscopic cystography and CT to determine their relative merit in the diagnosis of pancreatic fluid and urine leakage as documented by surgical exploration in pancreas transplant recipients. Thirteen leaks were diagnosed by fluoroscopic cystography or by CT in 11 patients after pancreas transplantation with urinary bladder drainage of pancreatic fluid. Conventional retrograde fluoroscopic cystography showed 11 leaks; CT with retrograde bladder opacification showed three leaks. Of the five CT studies that did not show a leak and that also were done within 7 days of a cystogram with abnormal findings, failure to use retrograde bladder opacification accounted for the majority (three cases) of missed diagnoses. Focal or free peritoneal abdominal fluid was seen in all CT examinations, with extravasation of contrast material seen into both walled-off collections and free ascites.

Our experience suggests that retrograde bladder and duodenal stump opacification should be a routine part of the CT evaluation performed to detect leakage from the urinary bladder or duodenal stump after pancreas transplantation.

***AJR* 155:997–1000, November 1990**

Pancreas transplantation is an increasingly common procedure performed for treatment of selected patients with type I diabetes mellitus [1]. The goal is to abort or delay systemic complications of severe diabetes. Successful management of pancreatic secretions is the most critical technical aspect of pancreas transplantation and usually is accomplished by using enteric or urinary bladder drainage [2]. Currently, at our institution urinary bladder drainage is the preferred method [3]. Among the advantages of this method is accessibility of urine for enzymatic assay; this facilitates monitoring of pancreatic function and diagnosis of early rejection without the need for allograft biopsy [3].

With bladder drainage of pancreatic fluid, leakage of pancreatic secretions and urine into the peritoneal cavity can occur. Surgical repair of the leak is usually the definitive treatment and must be performed immediately. Because of the nonspecific clinical signs and symptoms of leaks, imaging plays an important role in the detection of bladder leakage.

In this paper, we retrospectively review our experience with leaks after pancreatic transplantation with bladder drainage. Specifically, we identify pitfalls in the imaging diagnosis and attempt to define the relative roles of fluoroscopic cystography and CT in the diagnosis.

Subjects and Methods

The subjects for this study were culled from the 130 whole cadaveric pancreas transplantations that used urinary bladder drainage of pancreatic fluid. The grafts were placed intraperitoneally with vascular anastomoses made to the iliac vessels (Fig. 1) [4]. Two techniques were used for duodenocystostomy for drainage of pancreatic secretions: (1) the

---

Received March 12, 1990; accepted after revision May 30, 1990.

[1] Department of Diagnostic Radiology, Box 292, University of Minnesota, Harvard St. and E. River Rd., Minneapolis, MN 55455. Address reprint requests to J. G. Letourneau.

[2] Department of Surgery, University of Minnesota, Minneapolis, MN 55455.

[3] Present address: Department of Surgery, Philipps University, Marburg, E. Germany.

0361-803X/90/1555-0997
©American Roentgen Ray Society

patch or button technique, in which a 3- to 6-cm button of duodenum surrounding the papilla of Vater and the duct of Santorini was used for anastomosis with the bladder, and (2) the whole duodenal technique, in which a 7- to 14-cm length of duodenum was used [4]. When the whole duodenal technique was used, three surgical anastomoses resulted: one at each blind end of the duodenal stump and one at the duodenocystostomy site (Fig. 1).

Only patients in whom a leak of the duodenocystostomy site or of the blind end of duodenal stump was shown by fluoroscopic cystography or CT and in whom the leak was confirmed by surgical exploration were included for review. Thirteen leaks were diagnosed in 11 patients, eight women and three men (age range, 24–42 years). The medical records and all radiologic studies of the 11 patients were reviewed retrospectively. A total of 50 CT scans and 36 cystograms were obtained postoperatively on the 11 patients during several years of follow-up. Leaks were recognized on 11 fluoroscopic cystograms and on three CT scans. When leakage was shown by fluoroscopic cystography or CT cystography, results of the corresponding studies performed within 7 days of the diagnosed leak were analyzed also. Using this method, we compared 13 cystograms and 8 CT scans to obtain our final results. Two radiologists reinterpreted the examinations; original reports were not used.

Retrograde cystography was performed under fluoroscopic control through a urethral catheter with 75–350 ml of diatrizoate meglumine (14% iodine). Contrast medium was instilled by gravity only. Overhead spot films and photospots were obtained in anteroposterior and oblique projections.

CT studies were done by using 8-mm sections taken at 10- or 15-mm intervals through the abdomen and pelvis before and after retrograde instillation of contrast material into the bladder. Oral contrast material was administered for all CT examinations. (IV contrast material is rarely used in pancreas recipients at our institution because of the risk of nephrotoxic reactions.) Contrast material (125–400 ml of diatrozoate meglumine [14% iodine]) was instilled through a bladder catheter in 14 (28%) of the 50 CT scans; the end point for gravity filling was patient discomfort. CT scans were obtained for comparison after the instillation of contrast material into the bladder. CT scans were analyzed for the presence of focal or free intraabdominal fluid and the presence of extravasated bladder contrast material.

All patients presented with abdominal pain and/or distension. Three patients with ascites shown by CT underwent paracentesis; chemical analysis of the fluid obtained showed high levels of amylase (3,200–11,000 IU). These laboratory findings increased the clinical suspicion of leakage.

Leakage of pancreatic fluid occurred as early as 16 days and as late as 3.5 years after transplantation. The leak was from the duodenal stump in seven instances and at the duodenocystostomy in six instances. In all 13 instances, patients were taken to the operating room immediately after diagnosis. Ten leaks were repaired by oversewing. Three were treated by graft pancreatectomy. Reasons for graft removal were concurrent peritonitis (two cases) and vesicocutaneous fistula (one case).

Results

Overall, 12 leaks were eventually diagnosed by use of fluoroscopic cystography (Fig. 2). However, three leaks were not diagnosed initially with fluoroscopic cystography. In two cases, cystography under fluoroscopic control failed to detect a leak diagnosed by CT with retrograde bladder opacification. In one of these cases, a small leak from the proximal end of the duodenum was shown on follow-up fluoroscopic cystography that same day (Fig. 3). In the last case, fluoroscopic cystography was not performed.

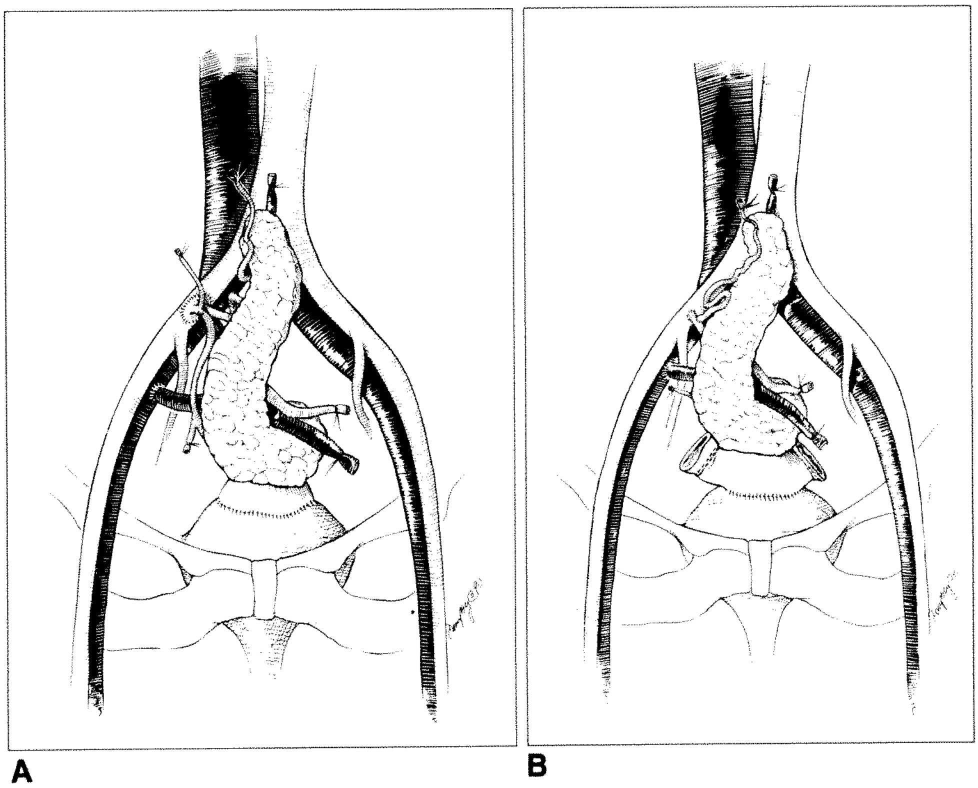

Fig. 1.—Schematic drawings of surgical anastomoses for pancreas transplantation with duodenocystostomy.
***A*, Patch technique.**
***B*, Whole duodenum technique.**

Leaks were diagnosed by use of CT in three of the eight examinations reviewed. Leakage was not recognized on CT in five instances in which the leak was diagnosed with fluoroscopic cystography. Three of these five examinations were done without retrograde bladder opacification (Fig. 3). However, one CT study with IV contrast administration failed to document leakage from the duodenal stump that was seen by fluoroscopic cystography; in this case distension of the urinary bladder and duodenal stump was incomplete. In one instance, CT failed to document leakage seen with cystography despite adequate bladder opacification; the CT scanning was performed 5 days before fluoroscopic cystography showed duodenal stump leakage.

In two instances, the sole means of detecting leakage was CT with retrograde bladder opacification (Fig. 4). One of these patients did not undergo fluoroscopic cystography. In the other, fluoroscopic cystography 1 day before the diagnostic CT examination did not show the leak from the proximal duodenal stump.

The CT studies done showed generalized ascites in eight patients and focal fluid collections in three.

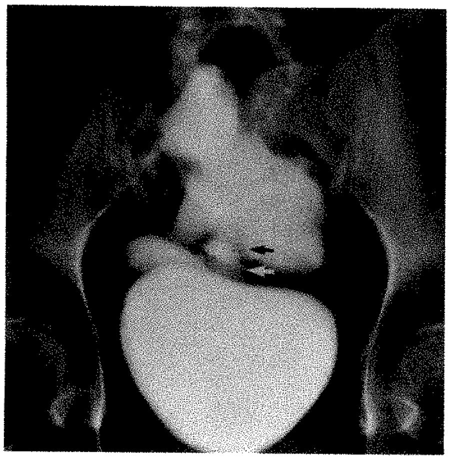

Fig. 2.—Leakage from duodenal stump in a 24-year-old woman 29 days after pancreatic transplantation with duodenocystostomy. Fluoroscopic cystogram shows extravasation of contrast material (*black arrow*) from proximal end of duodenum (*white arrow*).

Discussion

After pancreas transplantation, technical complications are common. Vascular thrombosis and intraabdominal infection are the two most common complications resulting in graft failure [5]. Other complications include graft rejection, hemorrhage, ischemic injury, pancreatitis, ascites, and leakage [4]. CT commonly is used to help diagnose posttransplantation complications [5] and frequently is done in the nonspecific clinical setting of abdominal pain and/or distension. Fluoroscopic cystography, on the other hand, is done specifically to evaluate the possibility of pancreatic enzyme and urine leakage [6].

Leakage from the duodenal stump, the duodenocystostomy, or the bladder is a complication of pancreas transplantation with bladder drainage of the pancreatic fluid. Why such leaks develop is not well understood and may be related in part to infection, rejection, immunosuppression, and technical factors, such as enteric stapling. In our review, leakage of pancreatic fluid and urine occurred in 10% of whole pancreas transplants with duodenal-bladder anastomoses. Treatment of such leakage is generally surgical repair, but in 23% of instances of leaks diagnosed in this series, simple repair of the leak could not be done; the presence of secondary or concomitant infection or vesicocutaneous fistula necessitated graft removal when the leak was diagnosed. Two additional small leaks were identified, but not included in this series, because surgical exploration was not done to confirm the diagnosis. These were recognized by fluoroscopic cystography, but not conventional CT, and were located in the bladder

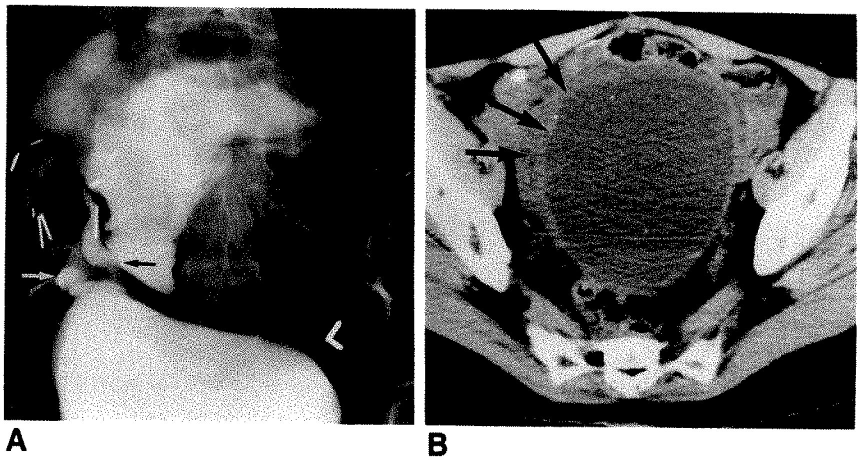

Fig. 3.—33-year-old man with abdominal pain and distension 2 years after pancreas transplantation.

A, Fluoroscopic cystogram shows extravasation of contrast material (*black arrow*) from proximal duodenum (*white arrow*).

B, CT scan without bladder opacification obtained 5 days before cystogram (*A*) shows large loculated fluid collection (*arrows*).

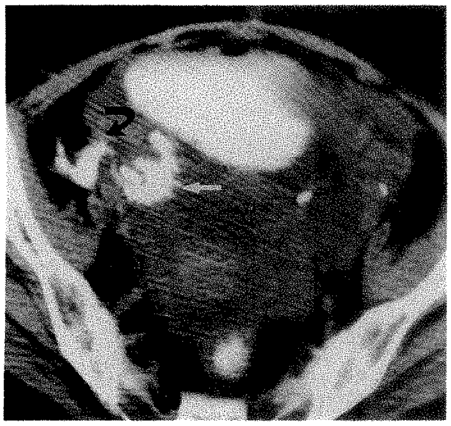

Fig. 4.—CT cystogram in a 46-year-old woman shows a small leak (*black arrow*) from duodenal pouch (*white arrow*) 52 days after pancreas transplantation.

and in the duodenum distant from the bladder anastomosis or stump closure. Both of these leaks were treated conservatively with bladder decompression and resolved as evidenced by follow-up fluoroscopic cystography.

Both fluoroscopic cystography and CT with retrograde bladder opacification can be used to diagnose leakage of pancreatic fluid after duodenocystostomy anastomoses in pancreatic transplantation patients. In our series, leakage was diagnosed more frequently with fluoroscopic cystography than with CT; however, in most of the CT studies, the urinary bladder and duodenal stump were not opacified. However, transplant recipients frequently undergo CT examination first, because of the nonspecific clinical presentation and because CT is useful to detect a variety of posttransplantation surgical complications. CT with retrograde bladder opacification should be performed in all pancreatic transplant recipients undergoing CT examination, particularly if intraabdominal fluid is seen. As leaks can occur any time after pancreas transplantation, CT cystography should be performed even if there is no or only a small suspicion of a leak. If CT with retrograde bladder opacification shows no leak, but a leak is suspected clinically, fluoroscopic cystography is indicated.

Leakage can be missed by fluoroscopic cystography or CT with retrograde bladder opacification if the bladder is not filled completely or if the duodenal stump is not distended completely. With fluoroscopic cystography, multiple projections must be used to optimize visualization of small or posterior leaks. Some small leaks may be intermittent; therefore, if symptoms are persistent, repeated fluoroscopic cystography or CT with retrograde bladder opacification is warranted. In one of our patients, findings on the initial fluoroscopic cystogram were negative, but CT cystography and fluoroscopic cystography the next day showed a leak. Because of the superior contrast resolution of CT compared with fluoroscopic cystography, CT may detect smaller leaks even in the presence of ascites; our experience is too limited to establish if this is the case.

Peritoneal fluid commonly is seen on CT and sonography after transplantation and is a nonspecific finding [5, 7]. When the patient has generalized ascites or a focal fluid collection, an elevated amylase level in fluid obtained by paracentesis increases clinical suspicion of a leak; markedly elevated levels of amylase also are seen with perigraft pseudocysts [8]. Localized fluid collections also may occur, presumably with walled-off leaks.

Routine use of retrograde bladder opacification for CT studies of pancreas recipients with duodenocystostomies and abdominal fluid could hasten diagnosis of such leaks.

REFERENCES

1. Sutherland DER, Chow SY, Moudry-Munns KC. International Pancreas Transplant Registry Report—1988. *Clin Transplant* **1989**;3:129–149
2. Najarian JS, Goetz FC, Sutherland DER. Pancreas transplantation: the Minnesota experience. *Transplant Proc* **1988**;20[suppl 1]:859–861
3. Prieto M, Sutherland DER, Goetz FC, Rosenberg ME, Najarian JS. Pancreas transplant results according to the technique of duct management: bladder versus enteric drainage. *Surgery* **1987**;102:680–691
4. Hanto DW, Sutherland DER. Pancreas transplantation: clinical considerations. *Radiol Clin North Am* **1987**;25:333–343
5. Letourneau JG, Maile CW, Sutherland DER, Feinberg SB. Ultrasound and computed tomography in the evaluation of pancreatic transplantation. *Radiol Clin North Am* **1987**;25:345–355
6. Woolsey EJ, Tauscher JR, Dafoe DC. Pancreas transplantation with pancreatico-duodeno-cystostomy for exocrine drainage: cystographic findings. *AJR* **1987**;149:507–509
7. Moulton JS, Munda R, Weiss MA, Lubbers DJ. Pancreatic transplants: CT with clinical and pathologic correlation. *Radiology* **1989**;172:21–26
8. Letourneau JG, Hunter DW, Crass JR, Thompson WM, Sutherland DER. Percutaneous aspiration and drainage of abdominal fluid collections after pancreatic transplantation. *AJR* **1988**;150:805–809

Review Article

Radiologic Findings of Clonorchiasis

Jae Hoon Lim[1]

Clonorchiasis is a trematodiasis caused by chronic infestation of liver flukes, *Clonorchis sinensis*. The adult flukes reside in the medium-sized and small intrahepatic bile ducts and, occasionally, in the extrahepatic bile ducts, gallbladder, and pancreatic duct. The result is mechanical obstruction, inflammatory reaction, adenomatous hyperplasia, and periductal fibrosis. Signs and symptoms are usually mild and nonspecific, but heavy infestation results in obstructive jaundice. The disease has a close relationship with recurrent pyogenic cholangitis and cholangiocarcinoma. In this article, the radiologic findings, including cholangiography, sonography, and CT of clonorchiasis are reviewed in light of the pathophysiology of the disease. The relationship to recurrent pyogenic cholangitis and to cholangiocarcinoma is discussed.

Epidemiology

The geographic distribution of clonorchiasis is largely confined to the Orient, from Japan to Vietnam. The endemic areas include Japan, Southern Korea, the mainland of China (except the northwest), Taiwan, and Northern Vietnam [1]. There are some 38 million carriers throughout the world [2]. The disease has been encountered in nonendemic areas as well [3–6] and may be recognized with increasing frequency in the Western world, because the flukes live for decades and the infested person may emigrate or travel anywhere in the world.

Human infestation depends on eating habits [1]. Persons with a marked preference for raw fish in their diet are infested more often. In Korea, 30- to 50-year-old men are infested most often. This is explained by social customs. Korean men have a tradition of eating raw freshwater fish, soaked simply in vinegar or red-pepper mash, as an appetizer when drinking at social gatherings. Children and women infrequently join in such gatherings, so they have much less exposure to the infestation.

Parasitology

The adult fluke of *Clonorchis sinensis* is a flat, elongated, leaflike, flabby worm tapered anteriorly and somewhat rounded posteriorly [1] (Fig. 1). The size ranges from 8.0 to 15.0 mm long by 1.5 to 4.0 mm wide and about 1.0 mm thick. The fluke has two suckers, oral and ventral; it sucks the blood of the host through the mucous membrane of the bile ducts. The fluke may persist for 15–20 years or more.

Humans are the most suitable definitive hosts. Animal reservoir hosts are dogs, hogs, wildcats, martens, badgers, minks, weasels, and rats [1]. One adult fluke lays approximately 2000–4000 eggs each day. The eggs, laid within the biliary tree of the definitive host, are carried down the common bile duct and passed in the stools. On reaching fresh water, the eggs are eaten by some genus of snail, mostly *Parafossarulus*, *Bithynia*, and *Alocinma*, the first intermediate host.

Within the snail, the eggs undergo metamorphosis, after which the cercariae escape. The cercariae penetrate the scales of suitable freshwater fish, mostly the Cyprinidae, the second intermediate host. Within the muscles of the fish, the cercariae encyst and become metacercariae to be ingested

---

Received April 20, 1990; accepted after revision May 30, 1990.

[1] Department of Diagnostic Radiology, Kyung Hee University Hospital, 1, Hoeki-dong, Dongdaemun-ku, Seoul 130-702, Korea. Address reprint requests to J. H. Lim.

AJR 155:1001–1008, November 1990 0361–803X/90/1555–1001 © American Roentgen Ray Society

by the final host. When a person ingests the flesh of raw fish containing metacercariae, the cyst is freed from the flesh by the action of gastric juice in the stomach, and the cyst wall is dissolved by trypsin in the duodenum. The larva excyst and migrate from the duodenum via the ampulla of Vater into the bile ducts, where they become mature worms in about 25 days. They usually reside in the intrahepatic bile ducts (Fig. 2) but also occasionally in the extrahepatic ducts and the gallbladder, as well as the pancreatic duct.

Pathophysiology

The main factor in pathogenesis is a mechanical obstruction of the biliary tract by the flukes, congestion of bile, and the effects of soluble substances (metabolites) released from the flukes into the ducts and surrounding tissues [1]. The severity of the dysfunction depends on the number of flukes present and the repetition and period of infestation. Most human infestation is chronic, perhaps from several years to several decades because of repeated ingestion of raw fish. Adult flukes living within the medium-sized and small intrahepatic ducts (i.e., tertiary, quaternary, and more peripheral tributaries) (Fig. 2) produce mechanical obstruction and inflammatory reaction [7].

In the early stage, edema and desquamation of epithelium, proliferation of bile ducts, and an inflammatory reaction occur. In the later stage, metaplastic squamous cells appear in conjunction with glandular proliferation, resulting in adenomatous hyperplasia [8, 9]. Bile ducts become dilated, thick, and infiltrated with lymphocytes, plasma cells, histiocytes, and fibroblasts. In heavy infestations, the main bile ducts and gallbladder are involved. Later, marked periductal fibrosis occurs with pronounced thickening of the walls of biliary passages [9].

In heavy infestation, flukes may reside in the pancreatic duct, within the main pancreatic duct of the tail portion, and within its tributary ducts [1, 10]. These ducts are dilated and packed with flukes. Flukes in the ducts produce squamous metaplasia, mucous gland hyperplasia, and fibrous thickening of the ductal wall [10].

Clinical Manifestations

Clinical manifestations depend on the number of flukes, the period of infestation, and complications [1]. Lightly infected persons usually have no signs or symptoms. In moderate or progressive cases, the clinical signs and symptoms are loss of appetite, indigestion, fullness of the abdomen, epigastric distress unrelated to meals, discomfort in the right upper quadrant, diarrhea, edema, and some hepatomegaly. In heavy infestations, the signs and symptoms are weakness and lassitude, epigastric discomfort, paresthesia, loss of weight, palpitation, tachycardia, diarrhea, vertigo, tetanic cramps and tremors, and toxemia from liver impairment. Jaundice is caused by obstruction of the intrahepatic biliary trees by worms or inflammatory changes. In patients with complications, such as pericholangitic abscess or recurrent pyogenic cholangitis, the signs and symptoms are those of acute infection, including fever, chills, and abdominal pain. In patients with cholangiocarcinoma, jaundice and pruritus predominate over other minor symptoms because of the obstruction of the passage of bile. Laboratory abnormalities include eosinophilia and an increased level of serum alkaline phosphatase. In cases with significant obstruction of the bile passage, levels of serum bilirubin, cholesterol, aspartate aminotransferase (GOT), and alanine aminotransferase (GPT) are increased [1].

Cholangiographic Findings

Cholangiography once played a major role in the assessment of the biliary tract in clonorchiasis. With the advent of sonography and CT, the role of cholangiography has decreased because the diagnosis usually is made on the basis of sonographic or CT findings and subsequent examination of the stool for ova. Cholangiography is indicated in heavy infestation as a workup for obstructive jaundice, or in patients with clonorchiasis complicated with recurrent pyogenic cholangitis or cholangiocarcinoma.

Cholangiographic findings reflect the basic disease: flukes within the lumen of the bile ducts, gallbladder, and pancreatic duct and resultant obstruction; ductal dilatation; and periduc-

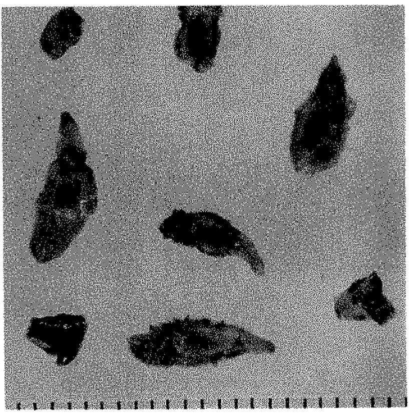
1

Fig. 1.—Photograph shows gross appearance of adult flukes of *Clonorchis sinensis* collected from feces of a patient. (Reprinted with permission from Lim et al. [19].)

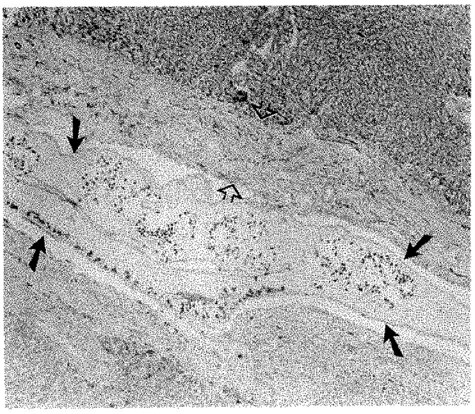
2

Fig. 2.—Photomicrograph of liver biopsy specimen shows adult fluke of *Clonorchis sinensis* (*solid arrows*) within dilated small intrahepatic bile duct. Wall of bile duct shows adenomatous hyperplasia of periductal glands, inflammatory cell infiltration, and fibrosis. Note severe thickening of wall of bile duct (between *open arrows*). (H and E, ×40)

tal tissue reaction, including adenomatous hyperplasia and periductal fibrosis. Okuda and colleagues [11] described (1) many round filling defects of several millimeters in diameter, a size compatible with the width of the fluke; (2) dilatation of intrahepatic ducts, which was more pronounced in the peripheral portion; and (3) hazy appearance of the intrahepatic duct. The filling defects within the bile ducts represent adult flukes (Figs. 3 and 4). The defects have been described as linear [3], round [11], filamentous [12], ricelike [13], and oval or elliptic [12, 14]. The shape of defects depends on whether the flukes are seen en face or in profile, as the flukes are flat and leaflike [14]. The size of filling defects varies from 2 to 10 mm. These defects occur mostly within the smaller intrahepatic bile ducts and tertiary, quaternary, and more peripheral tributaries [11-15].

In mild infestation, the defects are scattered within the dilated bile ducts. In severe infestation, the tributaries of the biliary tree are obstructed, and peripheral filling by contrast medium is interrupted. The tips of these ducts are blunt [5, 12]. This is because flukes or aggregates of flukes pack and block the small peripheral intrahepatic bile ducts. The defects often are encountered within the extrahepatic ducts. In heavy infestation, the defects (Fig. 5) are seen in the gallbladder as well [4, 11, 13]. These defects are distinguished from stone by their elliptic or oval appearance, the frequent change of position in the course of examination, and their uniformity in size [12]. Sometimes the outline of bile ducts is irregular, singly or in a series, showing a small indentation or hemispherical defects [6, 12, 13, 15] (Fig. 4). These irregularities reflect filling defects of flukes abutting the margin of the ducts and adenomatous hyperplasia [12].

The small or medium-sized intrahepatic bile ducts are dilated diffusely [11-15]. However, the extrahepatic bile ducts are not dilated or are slightly dilated (Figs. 3 and 4). Dilatation of smaller bile ducts most likely is caused by the fluke itself. The 8- to 15-mm fluke or aggregates of flukes easily could occlude small peripheral ducts, but larger ducts such as right and left hepatic ducts and extrahepatic ducts are wide enough to be patent, even if flukes are lodged within them. However, the mechanism of obstruction cannot be explained on the basis of fluke size alone, as the flukes are flat, 1.5-5 mm thick. Adenomatous hyperplasia, mucus in the bile ducts caused by cholangitis [11], and periductal fibrosis [7] and stricture may play additional roles in the occlusion of ducts and the resultant dilatation of proximal intrahepatic ducts. Uncommonly short segmental stenosis is seen also [12, 13, 15] (Fig. 3).

Often the peripheral intrahepatic bile ducts are poorly defined (Fig. 4) [11, 15]. Okuda et al. [11] attributed this to increased mucous material within the bile ducts. An amount of contrast medium insufficient to visualize the dilated peripheral ducts and poor mixing due to increased secretion within the ducts may play an additional role.

Differential diagnosis of clonorchiasis includes cancer along the bile ducts, choledocholithiasis with recurrent pyogenic cholangitis, sclerosing cholangitis, Caroli disease, and *Fasciola hepatica* infestation. In cancer of the bile ducts, including Klastkin tumor, and cancer of the pancreas or ampulla of Vater, the obstructing lesion usually can be visualized, and the entire biliary tree proximal to the obstructing level is dilated diffusely, not just the peripheral small bile ducts as in clonorchiasis. In patients who have stones in the bile duct and recurrent pyogenic cholangitis, small crescentic filling defects within the bile ducts easily are distinguished from those caused by the stone on the basis of the defects' size and shape [12]. Furthermore the pattern of dilatation is quite

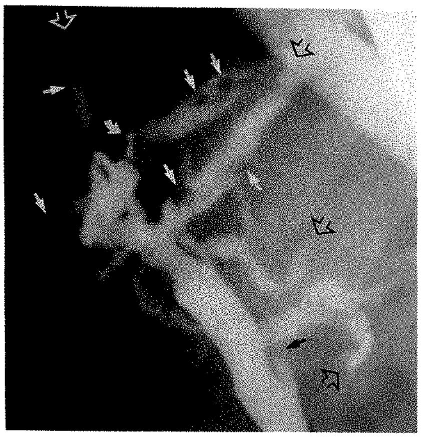

Fig. 3.—Endoscopic retrograde cholangiogram shows severe dilatation of intrahepatic ducts with narrowing (*curved arrow*). Intraductal ovoid or elliptic filling defects (*straight white arrows*) in medium-sized bile ducts are caused by adult flukes. Peripheral small ducts and cystic duct (*solid black arrow*) are obstructed, resulting in blunt end (*open arrows*). Note minimally dilated common hepatic duct. (Reprinted with permission from Lim et al. [19].)

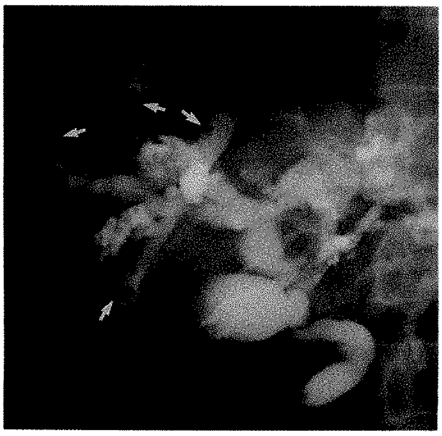

Fig. 4.—Endoscopic retrograde cholangiogram shows severe dilatation of intrahepatic bile ducts and innumerable oval or elliptic filling defects (*arrows*) of adult flukes in medium-sized and small bile ducts. Peripheral duct filling is interrupted by those filling defects. Contour of bile ducts is irregular and ragged because of defects abutting margin of ducts. Bile ducts in left hepatic lobe are hazy because of poor mixing of contrast medium with mucous material. Note relatively slightly dilated extrahepatic ducts (13 mm).

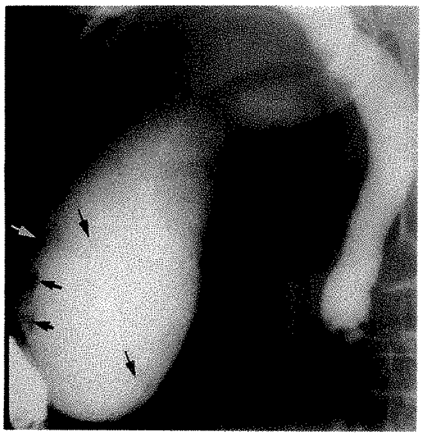

Fig. 5.—Endoscopic retrograde cholangiogram shows opacification of gallbladder. Multiple elliptic filling defects (*arrows*) represent adult flukes. Gallbladder is distended moderately.

different. In recurrent pyogenic cholangitis, the intrahepatic bile ducts are not dilated or are dilated minimally, but the extrahepatic bile ducts are much more dilated [14, 16]. Sclerosing cholangitis usually shows dilatation of the intrahepatic bile duct, but the ducts are much more irregular and serpiginous and appear to be discontinuous, rather than diffusely dilated, and, unlike in clonorchiasis, the extrahepatic ducts also are involved [14]. In Caroli disease, the bile ducts appear to be saccular rather than diffusely dilated [14]. In biliary tract diseases other than parasitic disease, characteristic oval or elliptic filling defects of flukes are not encountered. *Fasciola hepatica* infestation may result in dilatation of bile ducts and similar filling defects on cholangiograms, and thus differentiation can be difficult [17, 18].

Sonographic and CT Findings

Sonography is usually the first technique used to examine patients with clonorchiasis, as symptoms of clonorchiasis are vague and nonspecific. In severe cases with jaundice or increased levels of alkaline phosphatase, sonography is still the procedure of choice. For this reason, it is important for radiologists to recognize the varied sonographic appearances in order to suggest that clonorchiasis may be present and to recommend additional studies for correct diagnosis. CT is more or less the same, although CT usually is not the initial technique. Sonographic and CT findings are based on the same pathologic processes as cholangiography (i.e., flukes within the dilated bile ducts and periductal changes) [19, 20]. Flukes within the bile ducts usually are difficult to show with sonography and CT [19, 20]. With the advent of newer high-resolution sonographic equipment, the flukes or aggregates of flukes can be shown as a nonshadowing echogenic focus or cast (Fig. 6A) within the bile ducts [19, 21]. The bile ducts may be obstructed [5, 16] (Fig. 7). Morikawa et al. [22] described linear echoes moving quickly in the peripheral bile ducts; the movements were clearly apparent on M-mode sonograms.

Flukes within the gallbladder are much easier to see [19]. The gallbladder may have floating or dependent, discrete, nonshadowing echogenic foci in the lumen (Fig. 8). Usually flukes sink in the dependent portion, but float with a change in position or a light blow on the gallbladder with the transducer; the change in position or the light blow causes swirling movement of bile within the gallbladder, and the flukes float. Flukes occasionally float spontaneously, and these motions are considered to be caused by the movement of living flukes [19]. These discrete, echogenic foci are not considered stones because they are fusiform, weakly echogenic, and nonshadowing.

CT is of little value in the delineation of flukes [20]. To the best of my knowledge, no description concerning CT visualization of flukes in the bile ducts or gallbladder has been published. In my experience, CT of some patients showed high-density foci scattered within the dilated intrahepatic bile ducts, assumed to be aggregates of flukes (Figs. 9 and 10A).

As with cholangiograms, sonograms [19, 21, 22] and CT scans [20, 23, 24] show diffuse, uniform dilatation of the small intrahepatic bile ducts with no or minimal dilatation of the large bile ducts and no focal obstructing lesion (Figs. 6A, 9, and 10A). This characteristic finding of clonorchiasis is not encountered in other bile duct diseases, such as tumors along the bile duct or choledocholithiasis, as discussed with cholangiography. My colleagues and I, in prospective studies

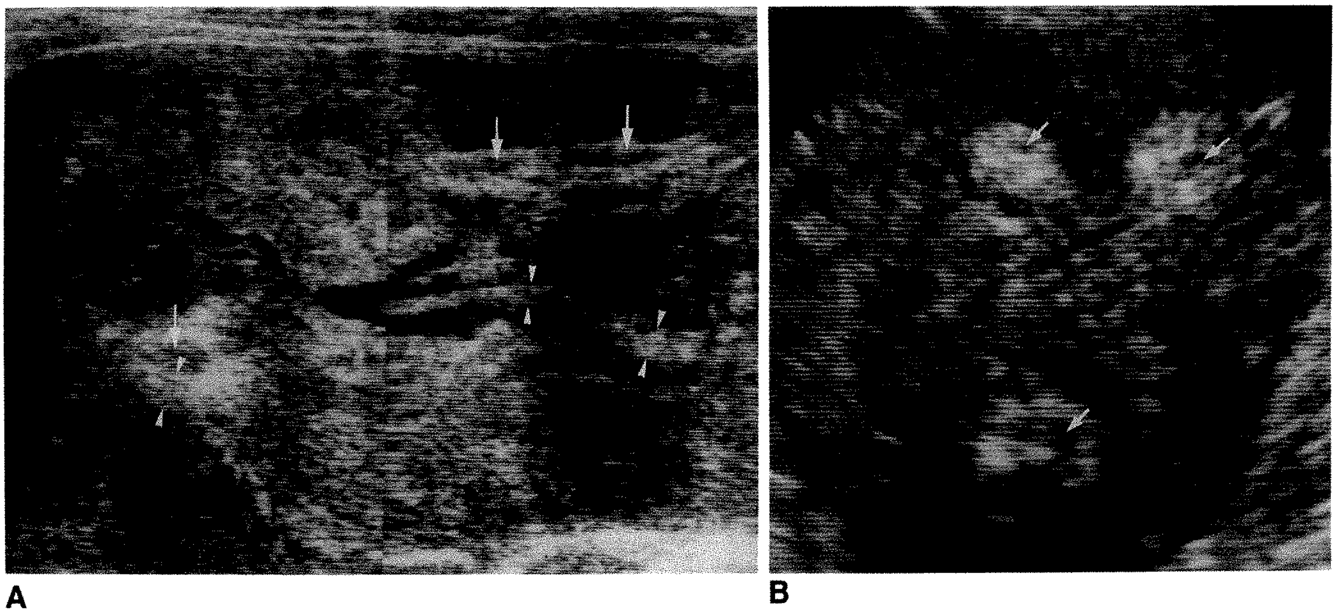

Fig. 6.—Sonograms of patient with severe infestation show dilatation and fibrous thickening of bile ducts.

A, Transverse scan of left hepatic lobe shows severe dilatation of bile ducts within which echogenic casts fill lumen (*arrows*), suggesting adult flukes. Note parallel echogenic bands (between *arrowheads*) along dilated bile ducts, indicating severe fibrous thickening of wall.

B, Longitudinal scan of left lobe shows markedly thickened bile ducts, mimicking echogenic nodules. Hepatic parenchymal echotexture is coarse. Note dilated small bile ducts (*arrows*) in center of thick echogenic wall.

(Reprinted with permission from Lim et al. [19].)

[25], stressed that clonorchiasis could be suspected with a high degree of confidence on the basis of dilatation of the peripheral intrahepatic bile duct without dilatation of the extrahepatic bile duct.

Thickening of the bile ducts can be shown with sonography and CT. Adenomatous hyperplasia, inflammatory cell infiltration, and periductal fibrosis produce diffuse thickening of the bile ducts. Sonograms show diffuse echogenic thickening of bile ducts [19, 26]. When the transducer is parallel to the bile ducts, the thick wall of the bile ducts can be seen as echogenic bands (Fig. 6A). When the transducer is tangential to the direction of the bile ducts, the thick bile ducts simulate echogenic nodules (Fig. 6B) [19, 26]. However, in clonorchiasis each nodule has a small echolucent center representing a dilated duct. The overall hepatic echogenicity becomes coarse [19].

Choi et al. [20] reported that CT failed to show the thickening of the bile ductal wall. On the contrary, Kim et al. [26] showed periductal contrast enhancement in half of their cases, suggesting periductal fibrosis. We have experienced several cases in which periductal contrast enhancement was shown, suggesting periductal fibrosis (Figs. 10B and 10C). Not infrequently the gallbladder is distended, the wall becomes thick, and gallstones may be present [19, 20].

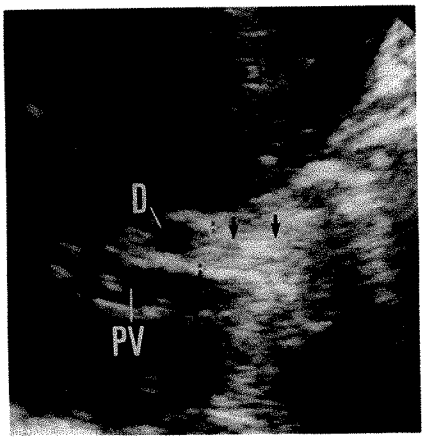

Fig. 7.—Oblique sonogram of right upper abdomen shows mild dilatation of common hepatic duct (D) (8 mm in diameter) filled by echogenic cast (*arrows*). This may represent an aggregate of adult flukes. PV = portal vein. (Reprinted with permission from Lim et al. [19].)

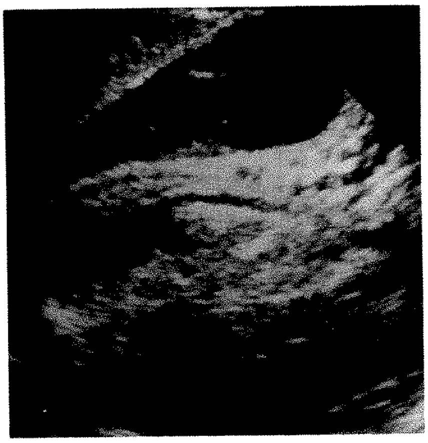

Fig. 8.—Sonogram of gallbladder shows several discrete, fusiform, floating and dependent echogenic foci measuring 5–10 mm, representing flukes.

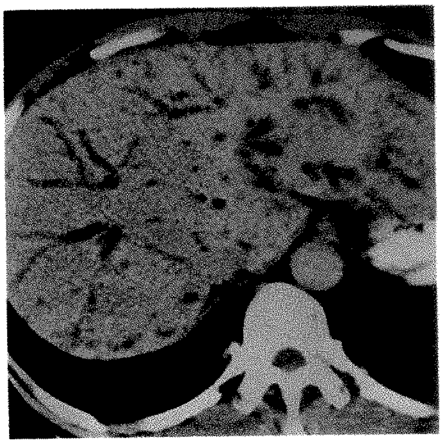

Fig. 9.—CT scan shows diffuse, uniform dilatation of intrahepatic ducts in periphery of liver and innumerable tiny hyperdense foci within dilated ducts, apparently due to aggregates of flukes. Extrahepatic duct was dilated minimally.

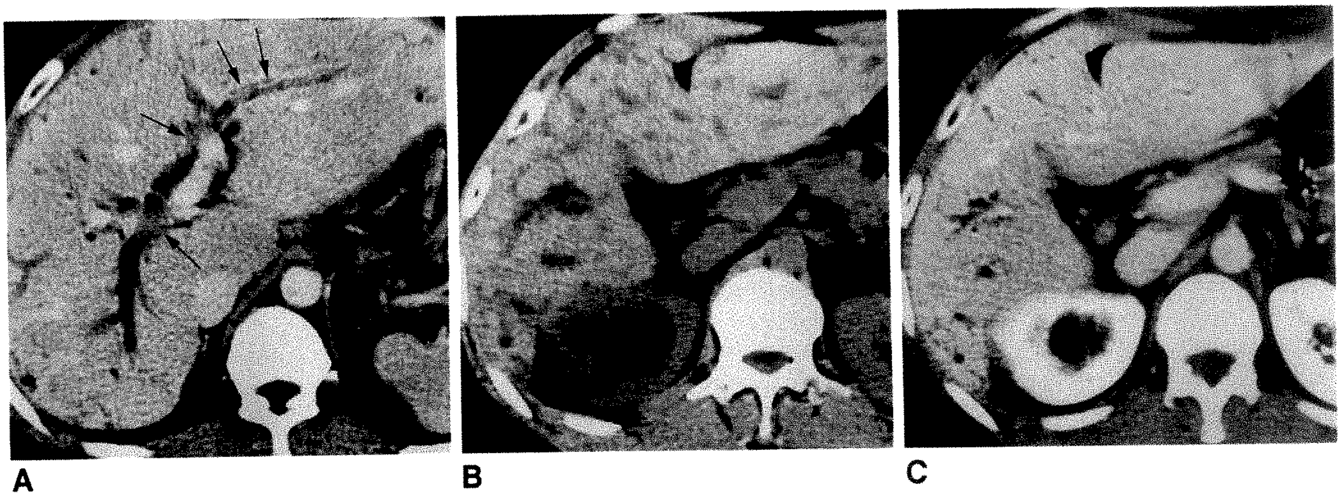

Fig. 10.—CT scans show liver flukes within dilated bile ducts and severe periductal fibrosis.

A, Postcontrast CT scan through middle of liver shows dilatation of intrahepatic ducts up to periphery of liver. Note high-density casts (*arrows*), assumed to be aggregates of flukes within dilated bile ducts. These intraductal flukes were depicted by cholangiography (Fig. 3) and sonography (Fig. 6A) as well. After administration of praziquantel, a lump of flukes was expelled, intermingled with feces. Flukes were collected and photographed (Fig. 1).

B and *C*, CT scans before (*B*) and after (*C*) administration of contrast medium show extensive periductal fibrous thickening. Branching low densities in *B* decrease in diameter in *C*, and only lumen of dilated ducts is visualized. Periductal fibrous tissue is enhanced and blends imperceptibly with adjacent liver parenchyma.

Sclerosing cholangitis may cause dilatation of intrahepatic bile ducts and concentric thickening of the intra- and extrahepatic biliary tree [27], but the thickening of the bile duct is more severe than that seen in clonorchiasis, and bile duct dilatation is focal and discontinuous [28]. Thickening of the bile duct may be encountered in cholangitis in AIDS [29]. Infestation of *Fasciola hepatica* results in biliary dilatation and thickening of the bile ducts, thus sonographic and CT findings are similar [30]. Furthermore, mobile vermiform structures [30] within the gallbladder are virtually the same as the echogenic foci in clonorchiasis [19].

Clonorchiasis of the Pancreas

In heavy infestations, flukes may reside in the pancreas [7, 10, 31]. Choi and Yang [32] studied 699 cases with surgical intervention of the hepatobiliary tract and confirmed pancreatitis in five cases (8%). Hou and Pang [31] reported that 19 of 300 patients with clonorchiasis had pancreatic involvement, and Chan and Teoh [10] found involvement in 24 of 64 cases. Patients with clonorchiasis are usually asymptomatic, but 83% of the patients who had acute pancreatitis of unknown cause were found to have a coexistent *Clonorchis* infestation [33]. The flukes were found in the main and tributary ducts of the pancreatic tail, and these ducts were dilated and packed with worms [10].

Only one paper has been published on pancreatography in pancreatic clonorchiasis [34]. On endoscopic retrograde pancreatograms, the pancreatic duct in the tail and its tributaries are dilated diffusely (Figs. 11A–11C). However, the main pancreatic duct and its tributaries in the head and body are not dilated. Sometimes small filling defects that might be caused by adult flukes are found in the main pancreatic duct. This characteristic pattern of dilatation of the pancreatic duct in clonorchiasis of the pancreas is quite different from dilatation due to other causes. In chronic pancreatitis, the main pancreatic duct is dilated irregularly, resulting in a beaded appearance, whereas in carcinoma of the pancreas, the main pancreatic duct frequently is dilated uniformly.

Relationship to Recurrent Pyogenic Cholangitis

Recurrent pyogenic cholangitis, which is also known as Oriental cholangitis, Oriental cholangiohepatitis, or intrahepatic pigment stone disease, is characterized by intrahepatic formation of pigmented stones with recurrent exacerbation and remissions of abdominal pain frequently associated with jaundice, chills, and fever [35–38]. The geographic distribution of the disease is similar to clonorchiasis. Unlike both suppurative and nonsuppurative cholangitis in the West, recurrent pyogenic cholangitis does not develop as a consequence of obstruction by primary calculi, strictures, or neoplasm. The stones in recurrent pyogenic cholangitis are usually muddy and claylike and are often multiple, packing the intra- and extrahepatic bile ducts with casts [35–37]. These stones are bilirubin stones, clearly different from cholesterol stones passed from the gallbladder and resulting in ascending cholangitis of Western people [36, 37].

The relationship between recurrent pyogenic cholangitis and clonorchiasis has been disputed. In fact, large proportions of persons in endemic areas are infested with liver flukes without ever having the development of recurrent pyogenic cholangitis [5, 39, 40]. Most persons who have clonorchiasis are male [19, 20], but there is no sex predilection in recurrent pyogenic cholangitis [36, 38]. Ong [36] suggested that the primary cause is portal septicemia resulting from poor eating habits, and that *C. sinensis* need not be present in all cases of recurrent pyogenic cholangitis. Carmona et al. [38] suggested low-protein diet and portal bacteremia as causes of recurrent pyogenic cholangitis. This theory was supported by animal experiments [40, 41].

However, evidence is ample that clonorchiasis is closely related to recurrent pyogenic cholangitis, and that a cause-and-effect relationship exists. Hou [7] reported that 20 of 31 patients with intrahepatic stone had clonorchiasis. In a clinical study in an endemic area in Korea, Choi and Yang [32] reported that 26% of patients with chronic cholecystitis, 19% of patients with gallstones, and 17% of patients with bile duct stones had clonorchiasis. Recent articles [19, 20] have reported that some 15% of persons with clonorchiasis have concomitant gallstones (Fig. 12).

Rim [1] and Hou [7] have asserted that *C. sinensis* infestation causes recurrent pyogenic cholangitis. As adult flukes, eggs, and desquamated epithelial cells block the intrahepatic ducts, partially or completely, bile stasis is sure to follow [7]. Stagnation not only favors bacterial infection but also leads to reflux of bile into the smaller branches of the bile ducts and consequent cellular infiltration of the portal spaces and liver parenchyma. When pyogenic infection occurs in the bile ducts, *C. sinensis* are killed [1, 7]. Bile stasis and the presence of flukes and ova or their debris may be important. The flukes and ova or their debris can form a nucleus for the formation of gallstones or bile duct stones [42], and this could instigate all the consequent abnormalities, resulting in a vicious cycle of repeated bouts of cholangitis and stone formation [37]. Chemically, such stones are composed almost entirely of bilirubin [1]. The formation of bilirubin stones may be attributed to bacterial deconjugation of bilirubin diglucuronide with the formation of insoluble bilirubin during bouts of cholangitis [43].

The Relationship to Cholangiocarcinoma

The close correlation between *C. sinensis* infestation and bile duct carcinoma has long been emphasized [8, 24, 43–48]. Hou [44] reported that in at least 15% of patients with primary carcinoma of the liver, the cancer was caused by infestation with *C. sinensis*. Belamaric [45] found that most patients with cholangiocarcinoma had adenomatous hyperplasia and ductal fibrosis characteristic of clonorchiasis. Kim [46] and Chung and Lee [47] also found that the prevalence of clonorchiasis was significantly higher in cholangiocarcinoma than in hepatocellular carcinoma. In a cholangiographic

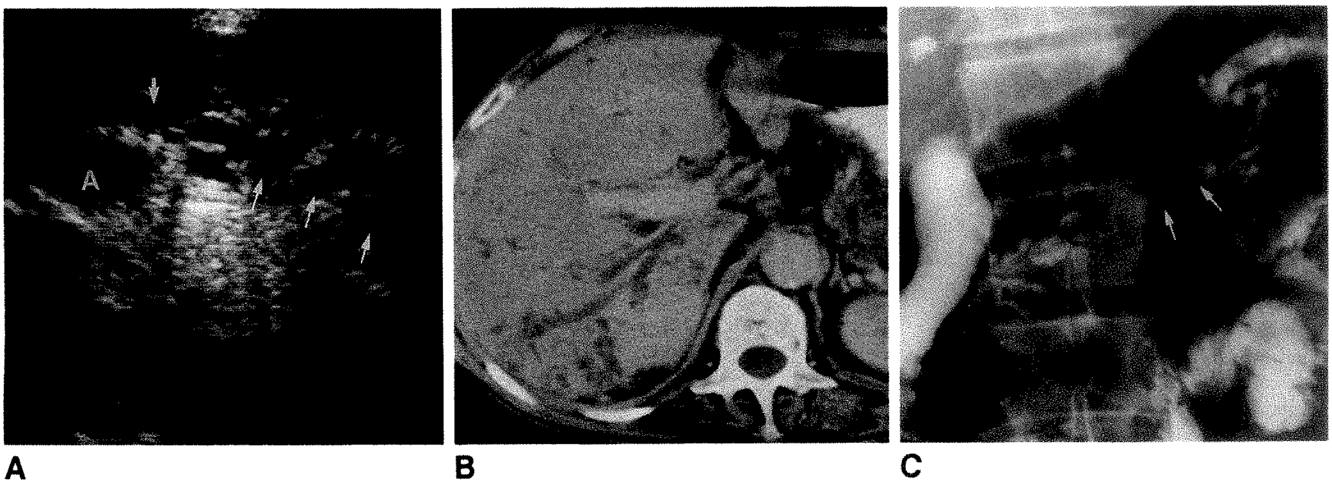

Fig. 11.—Clonorchiasis of pancreas.

A, Sonogram of pancreas shows severe dilatation of main pancreatic duct (*thick arrow*) and tributaries (*thin arrows*) in tail of pancreas. A = aorta.

B, CT scan shows tortuous dilatation of tributary ducts of tail of pancreas. Pancreatic parenchyma is virtually absent. Note diffuse dilatation of intrahepatic bile ducts in periphery of liver.

C, Endoscopic retrograde pancreatogram shows marked dilatation of main pancreatic duct and tributaries in tail of pancreas. Oval filling defects (*arrows*) are presumed to be flukes. Note relatively normal pancreatic duct in head of pancreas.

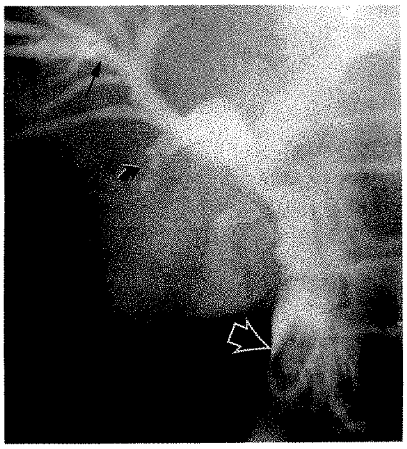

Fig. 12.—Recurrent pyogenic cholangitis associated with clonorchiasis. Endoscopic retrograde cholangiogram shows a stone in common bile duct (*open arrow*). Note obstruction (*curved arrow*) and elliptic filling defect caused by flukes (*straight solid arrow*).

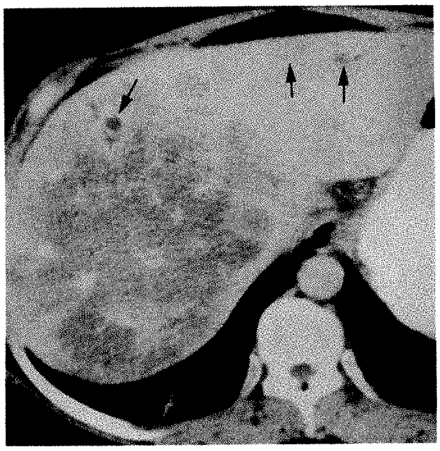

Fig. 13.—Cholangiocarcinoma, peripheral type associated with clonorchiasis. CT scan shows poorly defined, large, irregular hypodense mass with small enhancing foci in middle of tumor. Peripheral intrahepatic bile ducts are dilated (*arrows*).

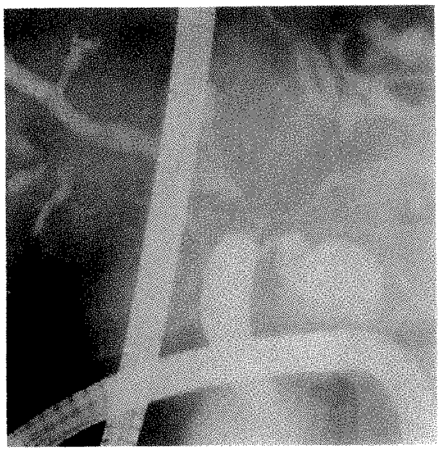

Fig. 14.—Cholangiocarcinoma, hilar type associated with clonorchiasis. Endoscopic retrograde cholangiogram shows severe segmental narrowing of right hepatic duct, left hepatic duct, and proximal common hepatic duct due to infiltrating carcinoma at porta hepatis. Note dilatation of intrahepatic ducts with small elliptic filling defects in peripheral small bile ducts.

study of patients with clonorchiasis (Lim et al., unpublished data), seven of 46 patients had cholangiocarcinoma (Figs. 13 and 14). In studies in cats and dogs with clonorchiasis, Hou [8, 48] advocated that adenomatous tissue formation of bile ducts regressed and was replaced by fibrous thickening or progressed to malignant change.

The considerably higher prevalence of clonorchiasis in patients with cholangiocarcinoma, the close physical relationship of the main tumor mass to infested ducts, the frequent coexistence in the same duct of focally atypical epithelial hyperplasia and invasive cancer, and the results of animal experiments all support a cause-and-effect relationship between clonorchiasis and cholangiocarcinoma.

ACKNOWLEDGMENTS

I thank Jong Kwon Won and Byung Do Kim for sonographic assistance, Mun Young Roh for preparation of photographs, and Nan Ok Yeo for secretarial assistance in manuscript preparation.

REFERENCES

1. Rim HJ. The current pathobiology and chemotherapy of clonorchiasis. *Korean J Parasitol* **1986**;24[suppl]:7–20

2. Peters W. Medical aspects: comments and discussion. II. In: Taylor AER, Muller R, eds. *The relevance of parasitology to human welfare today.* Oxford: Blackwell Scientific, **1978**:25-40
3. Cremin BJ. Biliary parasites. *Br J Radiol* **1969**;42:506-508
4. Hartley JPR, Doughlas AP. A case of clonorchiasis in England. *Br Med J* **1975**;6:575
5. Ameres JP, Levine MP, DeBlash HP. Acalculous clonorchiasis obstructing the common bile duct: a case report and review of the literature. *Am Surg* **1976**;42:170-172
6. Baker MS, Baker BH, Woo R. Biliary clonorchiasis. *Arch Surg* **1979**; 114:748
7. Hou PC. The pathology of *Clonorchis sinensis* infestation of the liver. *J Pathol* **1955**;70:53-64
8. Hou PC. Pathological changes in the intrahepatic bile ducts of cats (*Felis catus)* infested with *Clonorchis sinensis. J Pathol Bacteriol* **1965**;89: 357-364
9. Lee SH, Shim TS, Lee SM, Chi JG. Studies on pathological changes of the liver in albino rats infected with *Clonorchis sinensis. Korean J Parasitol* **1978**;16:148-155
10. Chan PH, Teoh TB. The pathology of *Clonorchis sinensis* infestation of the pancreas. *J Pathol Bacteriol* **1967**;93:185-189
11. Okuda K, Emura T, Morokuma K, Kojima S, Yokagawa M. Clonorchiasis studied by percutaneous cholangiography and a therapeutic trial of toluene-2, 4-diiso-thiocyanate. *Gastroenterology* **1973**;65:457-461
12. Choi TK, Wong KP, Wong J. Cholangiographic appearance in clonorchiasis. *Br J Radiol* **1984**;57:681-684
13. Lee JI, Yoo JH, Lim GS, Lee CH, Min YI, Lim JH. ERCP findings in clonorchiasis. *J Korean Soc Gastrointest Endosc* **1981**;1:29-32
14. Clemett AR. The interpretation of the direct cholangiogram. In: Berk RN, Clemett AR, eds. *Radiology of the gallbladder and bile ducts.* Philadelphia: Saunders, **1977**:285-330
15. Kang IW, Seo HS, Lim DR, Yeon KM. Radiological findings of clonorchiasis. *J Korean Radiol Soc* **1980**;16:159-162
16. Chau EMT, Leong LLY, Chan FL. Recurrent pyogenic cholangitis: ultrasound evaluation compared with endoscopic retrograde cholangiopancreatography. *Clin Radiol* **1987**;38:79-85
17. Clemett AR. Radiology of the liver and biliary tract. In: Margulis AR, Burhenne HJ eds. *Alimentary tract radiology.* St. Louis: Mosby, **1989**: 1260-1261
18. Ham SY, Park CM, Chung KB, et al. A case of fascioliasis in common bile duct. *J Korean Radiol Soc* **1989**;25:783-785
19. Lim JH, Ko YT, Lee DH, Kim SY. Clonorchiasis: sonographic findings in 59 proved cases. *AJR* **1989**;152:761-764
20. Choi BI, Kim HJ, Han MC, Do YS, Han MH, Lee SH. CT findings of clonorchiasis. *AJR* **1989**;152:281-284
21. Kim JW, Kim JG, Sol CH, Kim BS. An observation of ultrasonographic findings in clonorchiasis. *J Korean Radiol Soc* **1983**;19:538-545
22. Morikawa P, Ishida H, Niizawa M, Komatsu M, Arakawa H, Masamune O. Sonographic features of biliary clonorchiasis. *JCU* **1988**;16:655-658
23. Kim SY, Ko YT, Suh SJ. Computed tomography in evaluation of jaundiced patients due to *Clonorchis sinensis. J Korean Radiol Soc* **1978**;14: 460-464
24. Choi BI, Park JH, Kim YI, et al. Peripheral cholangiocarcinoma and clonorchiasis: CT findings. *Radiology* **1988**;169:149-153
25. Lim JH, Ko YT, Lee DH, Min YI. Ultrasound findings of clonorchiasis. *J Korean Soc Med Ultrasound* **1987**;6:193-194
26. Kim MJ, Yoo HS, Lee JT, Jung SH. Radiologic imaging of the bile duct changes by clonorchiasis. *J Korean Radiol Soc* **1988**;24:878-882
27. Carrol BA, Oppenheimer DA. Sclerosing cholangitis: sonographic demonstration of bile duct wall thickening. *AJR* **1982**;139:1016-1018
28. Ferrucci JT, Adson MA, Mueller PR, Stanley RJ, Stewart ET. Advances in the radiology of jaundice: a symposium and review. *AJR* **1983**;141:1-20
29. Dolmatch BL, Laing FC, Federle MP, Jeffrey RB, Cello J. AIDS-related cholangitis: radiographic findings in nine patients. *Radiology* **1987**;163: 313-316
30. Van Beers B, Pringot J, Geubel A, Trigaux J-P, Bigaignon G, Dooms G. Hepatobiliary fascioliasis: noninvasive imaging findings. *Radiology* **1990**;174:809-810
31. Hou PC, Pang SC. *Clonorchis sinensis* infestation in man in Hong Kong. *J Pathol Bacteriol* **1964**;87:245-250
32. Choi JM, Yang DH. Clinical study on clonorchiasis of hepatobiliary tract. *J Korean Surg Soc* **1974**;16:245-253
33. McFadzen PJS, Young RTT. Acute pancreatitis due to *Clonorchis sinensis. Trans R Soc Trop Med Hyg* **1966**;60:466-470
34. Lim JH, Ko YT. Clonorchiasis of the pancreas. *Clin Radiol* **1990**;41: 195-198
35. Cook J. Hou PC, Ho HC, McFadzean AJS. Recurrent pyogenic cholangitis. *Br J Surg* **1954**;42:188-203
36. Ong GB. A study of recurrent pyogenic cholangitis. *Arch Surg* **1962**; 84:199-225
37. Seel DJ, Park YK. Oriental infestational cholangitis. *Am J Surg* **1983**; 146:188-203
38. Carmona RH, Crass RA, Lim RC, Trunkey DD. Oriental cholangitis. *Am J Surg* **1984**;148:117-124
39. Sullivan WG, Koep LJ. Common bile duct obstruction and cholangiohepatitis in clonorchiasis. *JAMA* **1980**;243:2060-2061
40. Chou ST, Chan CW. Recurrent pyogenic cholangitis: a necropsy study. *Pathology* **1980**;12:415-428
41. Matsushiro T, Susuki N, Sato T, et al. Effects of diet on glucaric acid concentration in bile and the formation of calcium bilirubinate gallstones. *Gastroenterology* **1977**;72:630-633
42. Teoh TB. A study of gallstones and included worms in recurrent pyogenic cholangitis. *J Pathol Bacteriol* **1963**;86:123-129
43. Flavell DJ. Liver-fluke infection as an aetiological factor in bile-duct carcinoma of man. *Trans R Soc Trop Hyg* **1981**;75:814-824
44. Hou PC. The relationship between primary carcinoma of the liver and infestation with *Clonorchis sinensis. J Pathol Bacteriol* **1956**;72:239-246
45. Belamaric J. Intrahepatic bile duct carcinoma and clonorchiasis infection in Hong Kong. *Cancer* **1973**;31:468-473
46. Kim YI. Liver carcinoma and liver fluke infection. *Arzneimittelforschung* **1984**;34:1121-1126
47. Chung CS, Lee SK. An epidemiological study of primary liver carcinoma in Busan area with special reference to clonorchiasis. *Korean J Pathol* **1976**;10:33-46
48. Hou PC. Hepatic clonorchiasis and carcinoma of the bile duct in a dog. *J Pathol Bacteriol* **1965**;89;365-367

Case Report

MR Imaging of Hepatic Adenoma

Toshifumi Gabata,[1] Osamu Matsui,[1] Masumi Kadoya,[1] Tsutomu Takashima,[1] Yoshimichi Ueda,[2]
Yoshikazu Komatsu,[3] and Makoto Sasaki[4]

Hepatic adenoma is a rare benign tumor composed of benign hepatocytes in sheets and cords without an acinar architecture [1]. It is difficult to distinguish from well-differentiated hepatocellular carcinoma (HCC), both pathologically and radiologically [2]. MR imaging has become an important diagnostic technique for detecting and differentiating hepatic tumors [3, 4]. The MR appearance of hepatic adenoma is variable, and MR has been unable to provide the specific diagnosis in reported cases [3–5]. We report a case of hepatic adenoma with a characteristic appearance on MR images.

Case Report

A 38-year-old woman had a 2-week history of epigastric pain and nausea. She had taken oral contraceptives for 3 months 10 years ago. Results of physical examination were normal. A sonogram revealed a single, well-circumscribed mass protruding from the medial segment of the liver, which was slightly hyperechoic with inhomogeneity. CT showed a hypodense mass, 10 cm in diameter, with an isodense central area relative to the surrounding liver parenchyma both before and after IV administration of contrast medium. Hepatic angiography showed a moderately hypervascular mass with tumor vessels entering from the periphery during the arterial phase and a faint tumor stain during the capillary phase. MR imaging was performed with a 1.5-T Signa imaging system (General Electric Medical Systems, Milwaukee, WI). On T1-weighted (SE) images, spin-echo 500/20 (TR/TE), the hepatic mass was hyperintense relative to the liver except for the central zone of hypointensity with a hypointense rim (Fig. 1A). On T2-weighted images (SE 2500/80), the mass was slightly hypointense compared with normal liver and its central zone showed hyperintensity. The peripheral rim of the mass was double layered with inner hypointensity and outer hyperintensity (Fig. 1B). On gradient-recalled acquisition into steady state (GRASS, 22/13/10° flip angle), the central zone of the mass was markedly hypointense, which we considered to be indicative of central hemorrhage. Resection of the tumor revealed a giant (maximal diameter, 11.5 cm) tumor, encapsulated by a thin fibrous capsule, in the medial segment of the liver. It was partially lobulated and had central hemorrhage (Fig. 1C). Histologically, the tumor was composed of normal-sized or slightly larger cells resembling normal hepatocytes arranged in sheets and cords. There were no Kupffer cells or bile ducts within the tumor. The tumor scarcely had fatty metamorphosis within it. The fibrous capsule was a pseudocapsule composed of compressed normal hepatic parenchyma. The pathologic diagnosis was hepatic adenoma (Fig. 1D).

Discussion

To our knowledge, few reports have been published about MR imaging of hepatic adenomas [3–5]. Moss et al. [3] reported two cases of hepatic adenomas that were hyperintense on long TR/TE pulse sequences on a 0.35-T MR imaging system. Rummeny et al. [4] reported four cases that were isointense or slightly hyperintense on T1-weighted images and hyperintense on T2-weighted images on a 0.6-T MR imaging system. They considered adenoma in many cases to be indistinguishable from HCC on MR images. However, they used midfield superconducting systems (0.35 and 0.6 T), and the images of the cases reported by Moss et al. were not clear and could not be obtained with strictly T2-weighted pulse sequences. Conversely, Nokes et al. [5] reported a case of a hepatic adenoma that was nearly isointense relative to normal liver on T1- and T2-weighted images,

---

Received March 7, 1990; accepted after revision April 24, 1990.

[1] Department of Radiology, School of Medicine, Kanazawa University, 13-1 Takara-machi, Kanazawa 920, Japan. Address reprint requests to T. Gabata.
[2] Department of First Pathology, School of Medicine, Kanazawa University, Kanazawa 920, Japan.
[3] Department of Internal Medicine, Kanazawa Red Cross Hospital, 2-251 Minma, Kanazawa 920, Japan.
[4] Department of Surgery, Kanazawa Red Cross Hospital, Kanazawa 920, Japan.

AJR 155:1009–1011, November 1990 0361–803X/90/1555–1009 © American Roentgen Ray Society

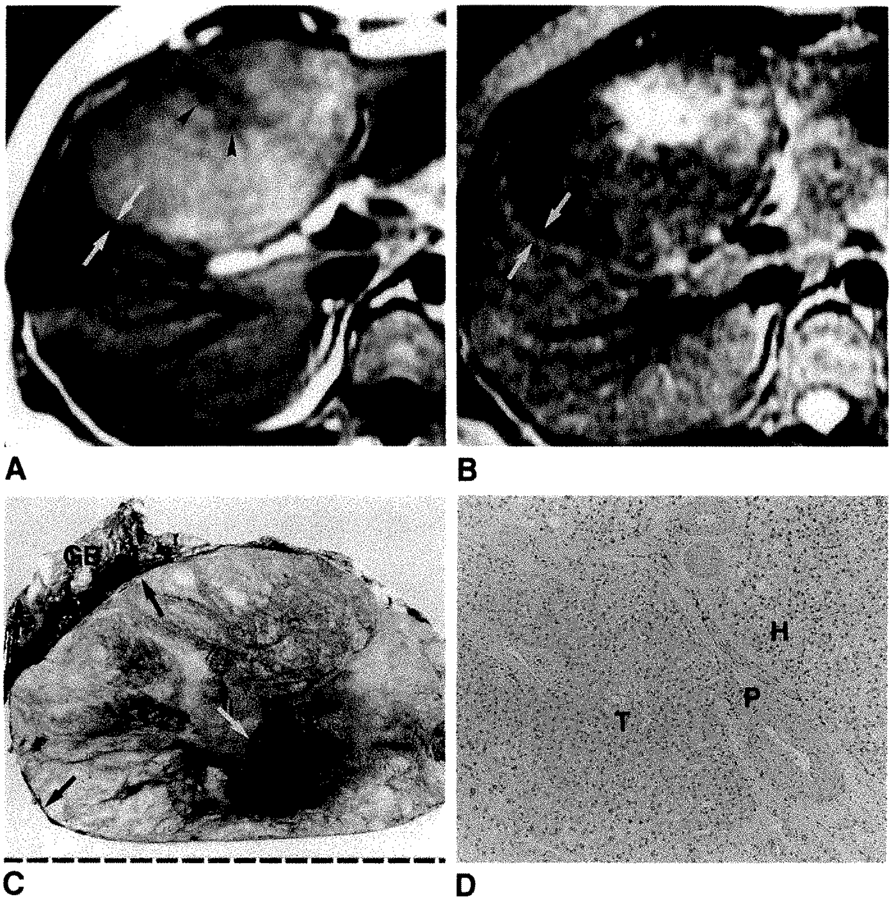

Fig. 1.—*A*, T1-weighted MR image (SE 500/20). Large tumor is hyperintense relative to liver with central hypointense zone (*arrowheads*). Rim is hypointense (*arrows*).

B, T2-weighted MR image (SE 2500/80). Tumor is hypointense relative to liver. Central zone is markedly hyperintense (*arrowheads*). Peripheral rim of tumor has double layers with inner hypointensity and outer hyperintensity (*arrows*).

C, Resected tumor, sectioned in sagittal plane. Tumor is partially lobulated and encapsulated with thin fibrous capsule (*black arrows*). Note central hemorrhage (*white arrow*). GB = gallbladder.

D, Microscopic section shows pseudocapsule (P) composed of compressed hepatic portal tract; outside of it, compressed normal hepatic parenchyma is seen. T = tumor, H = hepatic parenchyma.

mimicking focal nodular hyperplasia, which has been reported to show similar intensity relative to normal liver on both pulse sequences [4, 6].

Almost all hepatic tumors, such as hemangioma, metastasis, and cholangiocarcinoma, are seen as hypointense on T1-weighted images and hyperintense on T2-weighted images [3, 4]. It has been reported that 31% of HCCs are hyperintense on T1-weighted images, while 97% are hyperintense on T2-weighted images [7]. Hyperintensity of HCC on T1-weighted images was thought to be one of the important characteristics allowing differentiation of HCC from other tumors [7].

Hyperintensity of HCC on T1-weighted images is generally thought to be related to steatosis of cancer tissue, but we saw many cases of HCC that had increased signal intensity on T1-weighted images, and scarcely had steatosis histologically (unpublished data). Therefore, any other cause of the increased signal intensity is unknown. Our case of hepatic adenoma, which also scarcely had fatty metamorphosis histologically, was hyperintense on T1-weighted images, similar to some cases of HCC. However, it was hypointense on T2-weighted images, in distinct contrast to HCCs, which are usually hyperintense. So we were able to differentiate our case of adenoma from HCC. Hypointensity on T2-weighted images is very unusual and has not been reported in any hepatic tumors.

Recently we reported that hepatic adenomatous hyperplastic nodules in the cirrhotic liver, which are possibly precancerous lesions of HCC, also show hyperintensity on T1-weighted images and hypointensity on T2-weighted images [8]. Itoh et al. [7] suggested that well-differentiated HCCs tend to show higher intensity on T1-weighted images. Adenomatous hyperplastic nodules and our case of adenoma, which are all difficult to distinguish from well-differentiated HCC, also show hyperintensity on T1-weighted images. Therefore, we speculate that benign hepatic tumor composed of cells resembling normal hepatocytes such as focal nodular hyperplasia, adenoma, and adenomatous hyperplastic nodules may be isointense or hypointense on T2-weighted images; these can be differentiated from malignant hepatic tumors, which almost always are hyperintense on T2-weighted images.

In our case, the adenoma had a hypointense rim on T1-weighted images and a double-layered (inner low intensity and outer high intensity) rim on T2-weighted images. Comparison of the MR images and pathologic findings showed that the inner hypointense rim corresponds to the pseudocapsule and the outer hyperintense rim to the compressed normal hepatic parenchyma. Similar MR findings were reported in HCCs [7]. The central hypointense area of the tumor on GRASS images was related to hemosiderin deposition as a result of hemorrhage. We think that GRASS images are useful in the detection of intratumoral hemorrhage.

Our case illustrates that MR can differentiate benign hepatic tumors originating from hepatocytes from malignant tumors on the basis of the intensity pattern, especially on T2-weighted images. However, further examinations will be necessary to confirm the usefulness of MR imaging for differentiating hepatic tumors.

REFERENCES

1. Goodman ZD. Benign tumor of the liver. In: Okuda K, Ishak KG, eds. *Neoplasm of the liver*. Tokyo: Springer, **1987**:105–125
2. Kerlin P, Davis GL, McGill DB, Weiland LH, Adson MA, Sheedy PF. Hepatic adenoma and focal nodular hyperplasia: clinical, pathologic, and radiologic features. *Gastroenterology* **1983**;84:994–1002
3. Moss AA, Goldberg HI, Stark DD, et al. Hepatic tumors: magnetic resonance and CT appearance. *Radiology* **1984**;150:141–147
4. Rummeny E, Weissleder R, Stark DD, et al. Primary liver tumor: diagnosis by MR imaging. *AJR* **1989**;152:63–72
5. Nokes SR, Baker ME, Spritzer CE, Meyers W, Herfkens RJ. Hepatic adenoma: MR appearance mimicking focal nodular hyperplasia. *J Comput Assist Tomogr* **1988**;12:885–887
6. Mattison GR, Glazer GM, Quint LE, Francis IR, Bree RL, Ensminger WD. MR imaging of hepatic focal nodular hyperplasia: characterization and distinction from primary malignant hepatic tumors. *AJR* **1987**;148:711–715
7. Itoh K, Nishimura K, Togashi K, et al. Hepatocellular carcinoma: MR imaging. *Radiology* **1987**;164:21–25
8. Matsui O, Kadoya M, Kameyama T, et al. Adenomatous hyperplastic nodules in the cirrhotic liver: differentiation from hepatocellular carcinoma with MR imaging. *Radiology* **1989**;173:123–126

FORTHCOMING ARTICLES

1990 ARRS PRESIDENT'S AWARD PAPER

MR receptor imaging: ultrasmall iron oxide particles targeted to asialoglycoprotein receptors. *Weissleder R, Reimer P, Lee AS, Wittenberg J, Brady TJ*

REVIEW ARTICLE

Fracture of the pelvis: current concepts of classification. *Young JWR, Resnik CS*

CHEST RADIOLOGY

Assessing the patency of mediastinal and thoracic inlet veins: value of MR imaging. *Hansen ME, Spritzer CE, Sostman HD*

Case report. Misdiagnosis or missed diagnosis? Thoracic actinomycosis and carcinoma on sequential CT-guided lung biopsies. *Macaulay SE, vanSonnenberg E, Casola G, Harrell JH II*

Case report. Peripheral carcinoid tumor of the lung: CT diagnosis. *Davis SD, Zirn JR, Govoni AF, Yankelevitz DF*

BREAST RADIOLOGY

Comparison of 3-min and 90-sec mammography processing in 44 patients. *Skubic SE, Yagan R, Oravec D, Shah Z*

Perspective. Nonpalpable, probably benign breast lesions: follow-up strategies after initial detection on mammography. *Adler DD, Helvie MA, Ikeda DM*

Case report. Mammographic appearance of the retained Dacron cuff of a Hickman catheter. *Beyer GA, Thorsen MK, Shaffer KA, Walker AP*

GASTROINTESTINAL RADIOLOGY

Pictorial essay. Gastrointestinal lipomas: a radiologic and pathologic review. *Taylor AJ, Stewart ET, Dodds WJ*

Piezoelectric biliary lithotripsy: an in vitro study of factors affecting gallstone fragmentation. *Schulte SJ, Baron RL*

Nonaspiration fine-needle cytology of the liver: a new technique for obtaining diagnostic samples. *Fagelman D, Chess Q*

Treatment of hepatocellular carcinoma with percutaneous ethanol injection: analysis of 77 patients. *Shiina S, Tagawa K, Unuma T, et al.*

Regenerating nodules in hepatic cirrhosis: MR findings with pathologic correlation. *Murakami T, Kuroda C, Marukawa T, et al.*

Case report. Familial splenic epidermoid cyst. *Ragozzino MW, Singletary H, Patrick R*

Case report. Hemangiomatosis of the liver and spleen: successful treatment with embolization and splenectomy. *Tarazov PG, Polysalov VN, Ryzhkov VK*

Bright pleural effusion and ascites in gradient-echo MR images: a potential source of confusion in vascular MR studies. *Wallner B, Edelman RR, Finn JP, Mattle HP*

Sonography of abnormal lymph nodes in vitro: correlation of sonographic and histologic findings. *Rubaltelli L, Proto E, Salmaso R, Bortoletto P, Candiani F, Cagol P*

Case report. Well-differentiated papillary mesothelioma of the peritoneum. *Lovell FA, Cranston PE*

GENITOURINARY RADIOLOGY

Extraadrenal retroperitoneal paraganglioma: clinical, pathologic, and CT findings. *Hayes WS, Davidson AJ, Grimley PM, Hartman DS*

MUSCULOSKELETAL RADIOLOGY

Differentiation of benign and malignant soft-tissue masses with MR imaging: a blind study. *Berquist TH, Ehman RL, King BF, Hodgman CG, Ilstrup DM*

MR imaging findings in patients with bone-chip allographs. *Jelinek JS, Kransdorf MJ, Moser RP, Temple HT, Lenhart MK, Berrey BH*

PEDIATRIC RADIOLOGY

MR imaging of fractures of the growth plate: work in progress. *Jaramillo D, Hoffer FA, Shapiro F, Rand F*

Cloacal exstrophy: radiologic findings in 13 patients. *Meglin AJ, Balotin RJ, Jelinek JS, Fishman EK, Jeffs RD, Ghaed V*

Choledochal cyst and biliary atresia in the neonate: imaging findings in five cases. *Torrisi JM, Haller JO, Velcek FT*

Localization and guided removal of soft-tissue foreign bodies with sonography. *Shiels WE II, Babcock DS, Wilson JL, Burch RA*

Case report. Gastric hematoma and pneumatosis in child abuse. *Fulcher AS, Narla LD, Brewer WH*

NEURORADIOLOGY

MR imaging of the normal and abnormal clivus. *Kimura F, Kim KS, Friedman H, Russell EJ, Breit R*

Sarcoidosis of the CNS: comparison of unenhanced and enhanced MR images. *Sherman JL, Stern BJ*

Spinal cord ischemia after resection of thoracoabdominal aortic aneurysms: MR findings in 24 patients. *Mawad ME, Rivera V, Crawford S, Ramirez A, Breitbach W*

Wernicke encephalopathy: MR findings in five patients. *Gallucci M, Bozzao A, Splendiani A, Masciocchi C, Passariello R*

Commentary. Significance of MR in the diagnosis of Wernicke-Korsakoff syndrome. *Victor M*

COMPUTER PAGE

Computer-based learning in radiology: a hypermedia application in CT. *Hennessey JG, Fishman EK, Kuhlman JE, Ney DR, Magid D*

COMMENTARY

Europe 1992: consequences for European health care and radiology. *Schütte HE*

PERSPECTIVES

Physician referrals to radiologists. *Lopiano M, Stolz J, Sunshine J, Fisk T, Leepson E*

Antitrust principles for radiologists. *Reuter SR*

Case Report

Percutaneous Cholecystostomy Drainage for the Treatment of Acute Emphysematous Cholecystitis

Harlan L. Vingan,[1] Stephen D. Wohlgemuth,[2] and J. Sumner Bell III[3]

Recent reports document the usefulness of percutaneous cholecystostomy drainage in the therapy of acute inflammatory diseases such as cholecystitis or empyema of the gallbladder [1, 2]. It also has been shown that the gallbladder can be used as a site for draining the biliary system obstructed distal to the cystic duct [1, 3]. This approach is usually reserved for patients in whom a transhepatic approach is either unsuccessful or contraindicated.

We recently used the gallbladder as an approach for definitive therapy of a patient with complete distal common bile duct obstruction who secondarily developed emphysematous cholecystitis. The percutaneous cholecystostomy tube used to treat the acute infection was directly converted, via the cystic duct, into a permanent internal/external drain.

Case Report

The patient is an 81-year-old woman with a history of insulin-dependent diabetes mellitus and transitional cell carcinoma of the urinary bladder. She presented for evaluation of rapidly progressive jaundice.

On admission the patient was afebrile with a total bilirubin level of 12.1 mg/dl (207 μmol/l); SGOT, 74 IU/1; and alkaline phosphatase, 617 IU/l. Sonography and CT showed intrahepatic and extrahepatic bile duct dilatation due to a mass in the head of the pancreas. ERCP showed a malignant-appearing stricture of the distal common bile duct with proximal dilatation (Fig. 1A). Endoscopic drainage of the biliary tree was attempted, but despite being able to cross the obstruction with a guidewire, an indwelling endoprosthesis could not be advanced across the stricture. No further drainage was attempted, and the patient was started on antibiotics. Within the next 48 hr, fever, chills, and pain in the right upper quadrant developed. The WBC count rose to 29.4×10^9/l, bilirubin level was 22.9 mg/dl (392 μmol/l), and alkaline phosphatase level was 1001 IU/l. The patient was transferred to the intensive care unit with a diagnosis of Gram-negative sepsis. At this time, an abdominal radiograph and a CT scan showed air in the gallbladder wall and in the intrahepatic bile ducts (Fig. 1B).

Decompression of the entire biliary system via percutaneous cholecystostomy was attempted. This decision was made, in part, because the plain film of the abdomen showed contrast material in the gallbladder after the ERCP, suggesting cystic duct patency. A 12-French vanSonnenberg sump catheter (Medi-tech, Inc., Watertown, MA) was placed in the gallbladder by trocar technique. This was done by using a lateral transhepatic approach under CT guidance. The patient tolerated the catheter placement well, without evidence of vasovagal reaction. Three hundred milliliters of thick, foul-smelling bile was withdrawn, which subsequently grew *Klebsiella pneumoniae* and *Pseudomonas aeruginosa*. Bile cytology results were negative. External biliary drainage was continued, and the patient's condition improved rapidly. Within 24 hr, she was afebrile and alert. During the following week, the WBC count returned to normal, the bilirubin level was 11.4 mg/dl (195 μmol/l), and the alkaline phosphatase level was 268 IU/l.

The patient underwent cholangiography via the external drainage catheter after 1 week. This showed a patent cystic duct and the distal common bile duct stricture. One week later, this catheter was exchanged for an internal/external drain via the cystic duct. Side holes

---

Received April 5, 1990; accepted after revision May 29, 1990.

[1] Department of Radiology, Sentara Norfolk General Hospital and Eastern Virginia Medical School, Norfolk, VA 23507. Address reprint requests to H. L. Vingan, Medical Center Radiologists, Inc., 6161 Kempsville Circle, Norfolk, VA 23502.

[2] Department of Surgery, Sentara Norfolk General Hospital and Eastern Virginia Medical School, Norfolk, VA 23507.

[3] Department of Gastroenterology, Sentara Norfolk General Hospital and Eastern Virginia Medical School, Norfolk, VA 23507.

AJR 155:1013–1014, November 1990 0361–803X/90/1555–1013 © American Roentgen Ray Society

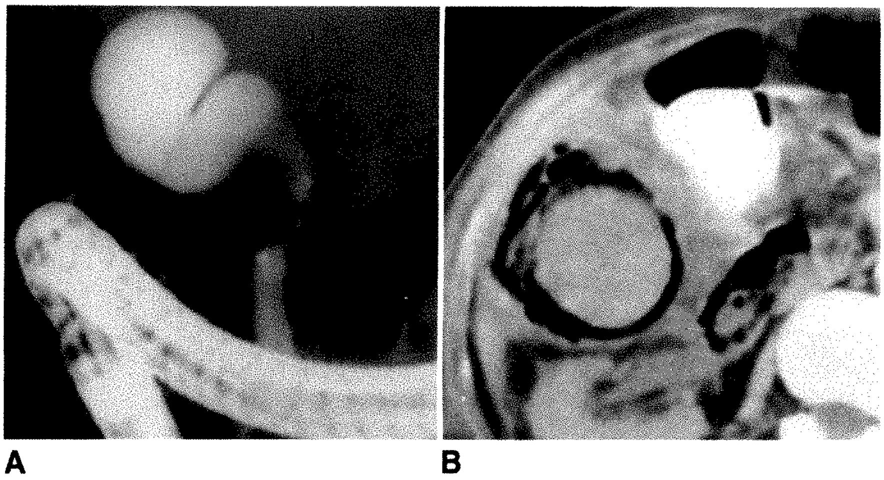

Fig. 1.—*A*, ERCP shows irregular, abrupt, malignant-appearing stricture of distal common bile duct with proximal dilatation.

***B*, CT scan shows air in gallbladder wall characteristic of emphysematous cholecystitis.**

were left in the gallbladder, bile duct, and bowel, establishing internal drainage. The patient was discharged with normal bilirubin and alkaline phosphatase levels.

When she returned for a tube change 3 months later, she was free of pain, anicteric, and had gained 25 pounds.

Discussion

Emphysematous cholecystitis is a particularly virulent infection most often seen in diabetic patients. Emphysematous cholecystitis related to ERCP has been described [4]. A characteristic feature is the presence of air in the gallbladder wall or lumen. The morbidity and mortality rates are higher than those associated with other forms of acute cholecystitis, and prompt surgery (cholecystectomy or cholecystostomy) is warranted [5–7].

Our patient was unusual in that her acute cholecystitis was superimposed on a malignant-appearing stricture of the distal common bile duct, presumably due to carcinoma of the pancreas. The exact cause of the obstruction was never actually determined, as multiple bile cytology specimens were negative. The patient was thought to be too ill for open or imaging-guided biopsy. After she recovered from the acute infection, a conservative, palliative management approach was decided on by the referring physicians, and no biopsy was performed.

The placement of the cholecystostomy catheter via a transhepatic approach healed the acute cholecystitis and provided an access to the biliary system for permanent internal/external biliary drainage. Sideholes in this catheter were placed in the gallbladder, bile duct, and bowel to ensure adequate drainage of the entire biliary system.

This case illustrates the successful percutaneous treatment of emphysematous cholecystitis. Percutaneous cholecystostomy should be considered as a temporizing procedure in critically ill patients with emphysematous cholecystitis in whom surgical intervention is contraindicated.

REFERENCES

1. Pearse DM, Hawkins IF, Shaver R, Vogel S. Percutaneous cholecystostomy in acute cholecystitis and common duct obstruction. *Radiology* **1984**;152:365–367
2. Lindemann SR, Tung G, Silverman S, Mueller P. Percutaneous cholecystostomy: a review. *Semin Intervent Radiol* **1988**;5:179–185
3. Vogelzang R, Nemcek A. Percutaneous cholecystostomy: diagnostic and therapeutic efficacy. *Radiology* **1988**;5:179–185
4. Baker JP, Haber GB, Gray RR, Handy S. Emphysematous cholecystitis complicating endoscopic retrograde cholangiography. *Gastrointest Endosc* **1982**;28:184–186
5. Glenn F. Cholecystostomy in the high risk patient with biliary tract disease. *Ann Surg* **1977**;185:185–191
6. Gingrich R, Awe W, Boyden A, Peterson C. Cholecystostomy in acute cholecystitis: factors influencing morbidity and mortality. *Am J Surg* **1968**;116:310–314
7. Sharp K. Acute cholecystitis. *Surg Clin North Am* **1988**;68:269–279

Carcinoma of the Prostate: Value of Transrectal Sonography in Detecting Extension into the Neurovascular Bundle

Ulrike M. Hamper[1]
Sheila Sheth[1]
Patrick C. Walsh[2]
Patrice M. Holtz[1]
Jonathan I. Epstein[3]

Detection of involvement of the neurovascular bundles (NVB) by tumor is important in deciding whether sexual function can be preserved in patients undergoing radical prostatectomy for prostatic cancer. The nerve branches innervating the corpora cavernosa have a rather constant association with the capsular arteries and veins of the prostate, forming the periprostatic neurovascular bundle, which can be identified intraoperatively and spared during radical surgery, thus preserving potency. We examined 160 patients with biopsy-proved clinical stage A or B adenocarcinoma with transrectal sonography before radical prostatectomy to determine how useful the procedure is for predicting tumor extension into the NVB. Correlation with pathologic serial sections was obtained in each patient. The sonograms depicted the NVB on both sides in 77 patients (50%), on the right side only in 13 (8%), and on the left side only in 36 patients (23%). In 29 patients (19%) neither neurovascular bundle could be identified on the sonograms. Ninety-one tumors in this series showed evidence of extraglandular spread pathologically, which was posterolateral or into the NVB in 70 tumors involving 82 hemispheres. Using transrectal sonography, we correctly identified invasion of the NVB in 54 cases and missed it in 28 cases. NVB invasion was predicted incorrectly with transrectal sonography in 51 cases; absence of involvement of the NVB was correctly predicted in 177 hemispheres. The sensitivity of sonography for predicting invasion of the NVB was 66%, with a specificity of 78% and an accuracy of 75%. Positive predictive values and negative predictive values were 51% and 86%, respectively.

We conclude that transrectal sonography currently suffers from lack of sufficient spatial resolution to detect accurately invasion of the NVB.

***AJR* 155:1015–1019, November 1990**

In past years, radical prostatectomy for the treatment of prostatic cancer has not been generally accepted, despite its proved effectiveness as a cure for localized disease [1, 2]. This was largely because the majority of patients undergoing prostatectomy were left impotent owing to surgical injury to the pelvic nerve plexus, which innervates the corpora cavernosa. Walsh et al. [3–8] revolutionized radical prostatic surgery by sparing these nerve bundles during surgery, after recognizing their rather constant association with the capsular vessels of the prostate (neurovascular bundle). As a result, sexual function in a large majority of patients is preserved without compromising treatment of the cancer [3–10].

Detection of neurovascular bundle involvement by tumor is key to deciding if sexual function can be preserved after radical surgery. We therefore undertook a sonographic-pathologic correlation study on a large series of patients with prostatic cancer in order to determine the usefulness of transrectal sonography for preoperative staging and especially for prediction of tumor extension into the neurovascular bundles (NVB).

Subjects and Methods

Between July 1987 and February 1989, we performed transrectal sonography on 160 men before radical prostatectomy was performed according to the method described by Walsh et

Received April 18, 1990; accepted after revision June 15, 1990.

Supported in part by NCI grant U01-CA-45202, RDOGI.

[1] Russell H. Morgan Department of Radiology and Radiological Science, The Johns Hopkins Medical Institutions, 600 N. Wolfe St., Baltimore, MD 21205. Address reprint requests to U. M. Hamper.

[2] James Buchanan Brady Urological Institute, The Johns Hopkins Medical Institutions, 600 N. Wolfe St., Baltimore, MD 21205.

[3] Department of Surgical Pathology, The Johns Hopkins Medical Institutions, 600 N. Wolfe St., Baltimore, MD 21205.

0361–803X/90/1555–1015
© American Roentgen Ray Society

al. [3]. All patients had biopsy-proved prostatic carcinoma and clinically localized disease, that is, stage A or B, which describes tumors confined to the gland. Thirty-two patients had clinical stage A disease, and 128 patients had clinical stage B disease. All patients were studied 6 weeks or longer after transperineal or transrectal biopsy. The age range of our patients was 43–74 years, with a mean age of 60 years. All patients were part of the Johns Hopkins study protocol for the Radiology Diagnostic Oncology Group (RDOGI).

All patients were examined with high-resolution biplane endorectal sonographic probes, defined as 5- to 7.5-MHz transducers with sharply focused near fields (Aloka SSD-256, Aloka, Japan; Brüel & Kjær 1850, 8538, and 8537, Marlborough, MA; General Electric RT 3600, Milwaukee, WI).

All sonograms were obtained within 24–48 hr of surgery. The examiner and the interpreter of the sonograms did not know the results of the other clinical examinations, other imaging studies, and previous pathology reports.

Sonographically, 320 prostatic hemispheres (right and left lobes) were evaluated separately in the 160 patients. Five patients were excluded from the study because of inadequate protocol (e.g., inadequate sonographic technique, pathologic processing problems).

The tumor was identified on the sonograms and the NVB were visualized sonographically (Fig. 1). Invasion of the NVB was diagnosed if the tumor was close to the posterolateral aspect of the gland, causing a bulge or irregularity of the posterolateral tumor outline and echogenic periprostatic fat line (Figs. 2–6). All sonograms were correlated with pathologic sections and surgical findings.

The pathologic evaluation included fixation of the gland, hemisectioning along the plane of the urethra, and subsequent contiguous axial sectioning at 2- to 3-mm intervals. The sections were labeled in a fashion that allowed exact localization of each tumor within the gland for correlation with the sonograms, and all sections were submitted for histologic examination. Tumor foci (>5 mm) were measured, and a mean average tumor diameter was obtained [1/3(a + b + c)]. In addition, the Gleason grade [11] of each tumor was determined, presence of tumor transgression into the NVB was noted and its maximal depth measured in millimeters, and the resection margins were evaluated for presence of tumor.

One hundred ninety-one separate tumors were found on pathologic examination of the posterior or posterolateral portion of the prostate in the 155 patients. Ninety-one of these tumors showed evidence of capsular penetration, which was posterior in 21 tumors or 23 hemispheres and posterolateral or into the NVB in 70 tumors involving 82 prostatic hemispheres. The mean size of tumors with capsular penetration was significantly larger, at 19.2 mm, than the size of tumors confined to the gland, which showed a mean average diameter of 9.4 mm.

Tumors demonstrating posterolateral penetration were moderately differentiated in 80% of cases and poorly differentiated in 20%, giving combined Gleason scores of 5–7 and 8–10, respectively. Fifty-two tumors (74%) penetrated 0–3 mm into the NVB, 12 tumors (17%) between 3 and 5 mm, and six tumors (9%) showed a penetration depth of more than 5 mm pathologically (Figs. 2–6).

At surgery the NVB were either preserved or partially or widely excised, depending on the intraoperative findings. Indications for wide excision of the NVB included: preoperative impotence, preoperative induration of the lateral sulcus, intraoperative induration of the lateral pelvic fascia, and fixation of the NVB to the prostate [6, 7]. Partial excision was performed either intentionally to obtain a wider surgical margin or inadvertently because of technical difficulties in freeing the NVB from the prostate.

At surgery, the NVB were excised widely in 39, partially in 10, and were preserved in 33 hemispheres in which tumor extension was present pathologically. In the 228 hemispheres without extraglandular tumor extension, the bundles were preserved in 179, resected partially in 22, and resected widely in 27 hemispheres. In cases where the bundles were thought to be uninvolved at surgery, the penetration was either very shallow or circumferential invasion was present and the contralateral bundle had already been excised. Only in two patients were the margins of resection positive in the posterolateral aspect of resection (Fig. 6).

Results

In the 155 patients included in the final evaluation, the sonograms depicted the NVB in the posterolateral aspect of the gland on both sides in 77 patients (50%), on the right side only in 13 patients (8%), and on the left side only in 36 patients (23%) (Fig. 1). In 29 patients (19%) neither bundle could be identified on the sonograms.

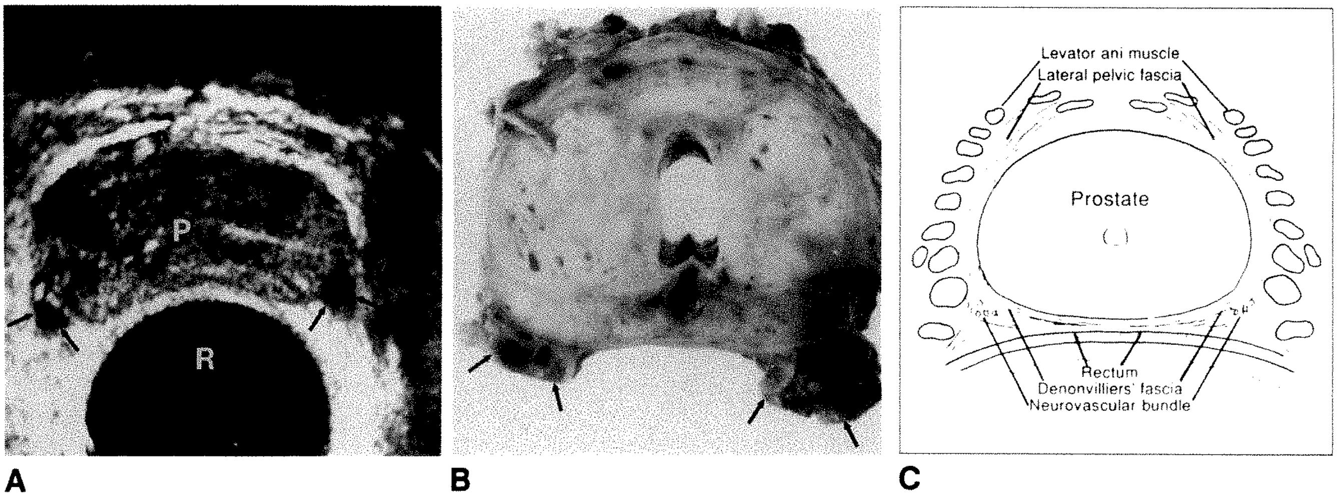

Fig. 1.—*A*, Radial transrectal sonogram of prostate shows hypoechoic area posterior to posterolateral aspects of gland representing neurovascular bundle (NVB, *arrows*). P = prostate, R = rectum.

B, Corresponding pathologic specimen shows NVB (*arrows*) posterolateral to prostate proper.

C, Schematic diagram depicts location of NVB. (Adapted from Walsh [3].)

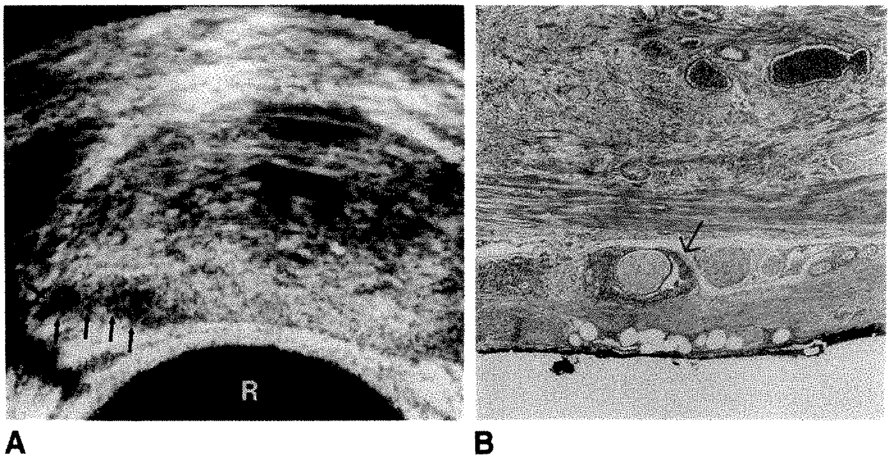

Fig. 2.—*A*, Radial transrectal sonogram shows right-sided hypoechoic tumor with subtle tumor bulge and irregularity posterolaterally at neurovascular bundles (NVB, *arrows*). During surgery, part of right NVB was resected. R = rectum.

B, Corresponding pathologic specimen shows adenocarcinoma with 0.3-mm penetration into region of NVB. Note gland showing perineural invasion immediately exterior to prostatic capsule (*arrow*). (H and E, ×55)

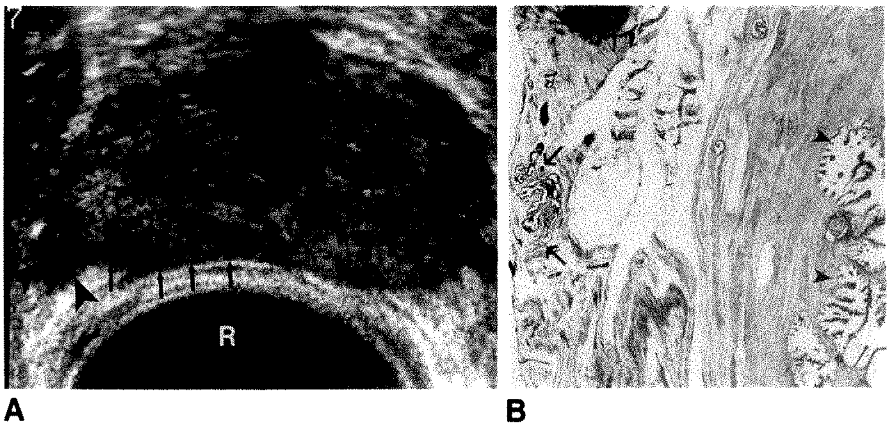

Fig. 3.—*A*, Radial transrectal sonogram shows hypoechoic right-sided tumor (*arrows*) with extension into neurovascular bundles (NVB, *arrowheads*). Note bulge and marked irregularity posterolaterally compared with left side. During surgery, NVB was thought to be uninvolved and was therefore partially preserved. R = rectum.

B, Pathologic specimen shows adenocarcinoma of prostate (*arrowheads*) with 2-mm penetration into NVB region (*arrows*). (H and E, ×38)

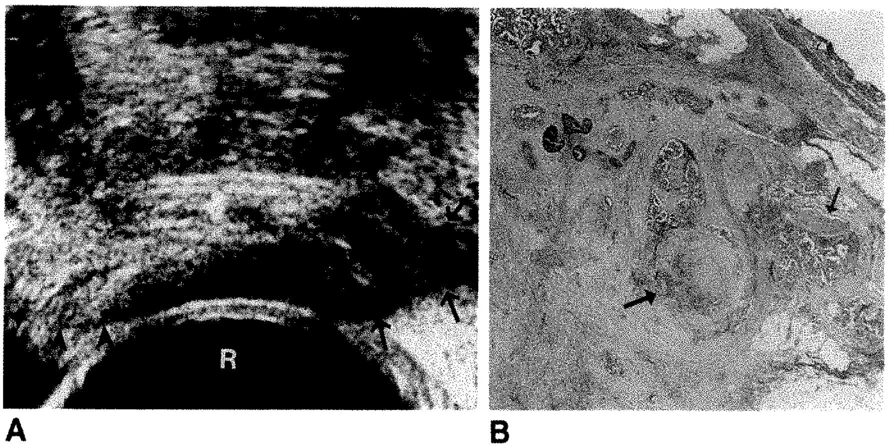

Fig. 4.—*A*, Radial transrectal sonogram shows large left-sided tumor with posterolateral bulge suggesting invasion of neurovascular bundles (NVB, *arrows*). Note smooth posterolateral border on right side (*arrowheads*). During surgery, left NVB was widely excised. R = rectum.

B, Pathologic specimen shows extensive penetration into NVB over distance of 7 mm (*arrows*). (H and E, ×55)

In the 310 hemispheres examined pathologically in the 155 patients, tumor extension into the NVB was present in 82; using transrectal sonography, we correctly identified 54 and missed 28. Using transrectal sonography, we incorrectly predicted NVB invasion in 51 hemispheres (Fig. 7) and correctly predicted tumor confinement to the gland in 177 hemispheres. The sonographic detection rate for tumors penetrating the NVB became increasingly more accurate with increasing depths of penetration, identifying 60% of tumors with penetration depths of 0–3 mm, 80% with depths of 3–5 mm, and 86% of tumors with a penetration depth of more than 5 mm into the NVB. This was despite the fact that the NVB themselves could only be visualized in about two thirds of the 82 hemispheres with NVB involvement by use of the criteria outlined previously. The sensitivity for transrectal sonography in detecting posterolateral or NVB invasion in our study was thus calculated to be 66% (54/82), with a specificity of 78% (177/228), and an accuracy of 75% (231/310). Positive and negative predictive values were 51% (54/105) and 86% (177/205), respectively.

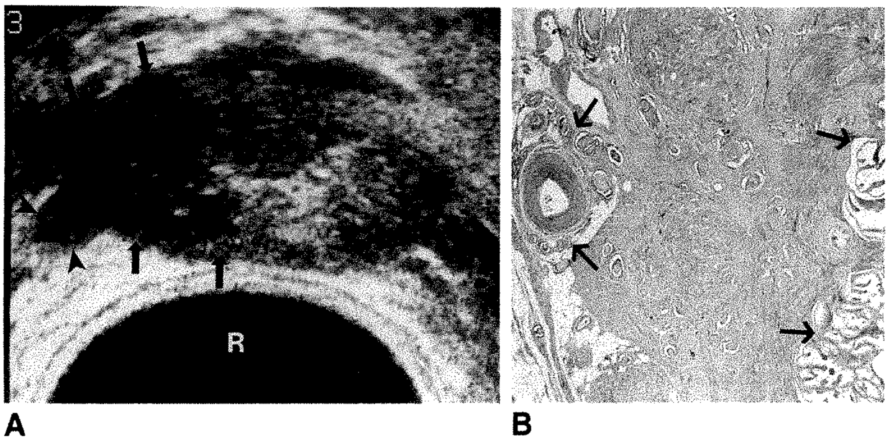

Fig. 5.—*A*, Radial transrectal sonogram shows large right-sided hypoechoic tumor (*arrows*) with obvious extension into right neurovascular bundle (NVB, *arrowheads*). R = rectum.

B, Pathologic specimen shows prostatic adenocarcinoma (*arrows*) penetrating 8 mm into region of NVB. (H and E, ×55)

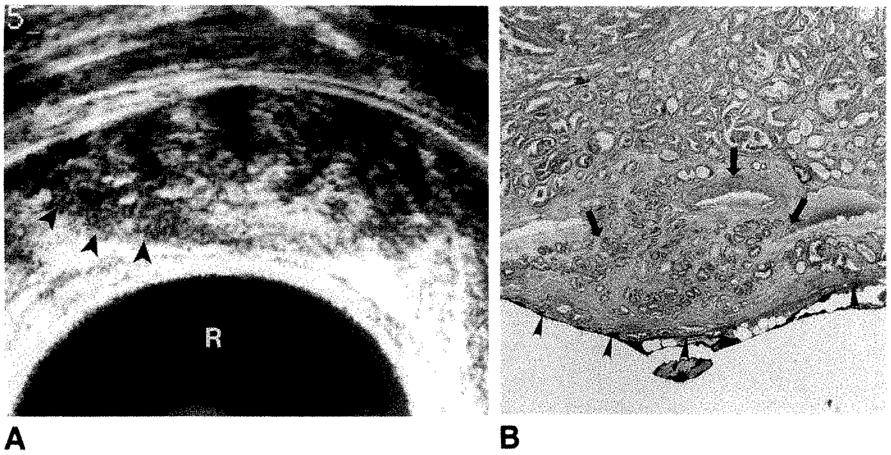

Fig. 6.—*A*, Radial transrectal sonogram shows vague right-sided tumor with only minimal posterolateral irregularity (*arrowheads*). Neurovascular bundles (NVB) were thought to be uninvolved at surgery and were therefore partially preserved. R = rectum.

B, Pathologic specimen shows 5-mm tumor penetration into NVB region (*arrows*). Tumor extended to inked margin of resection (*arrowheads*).

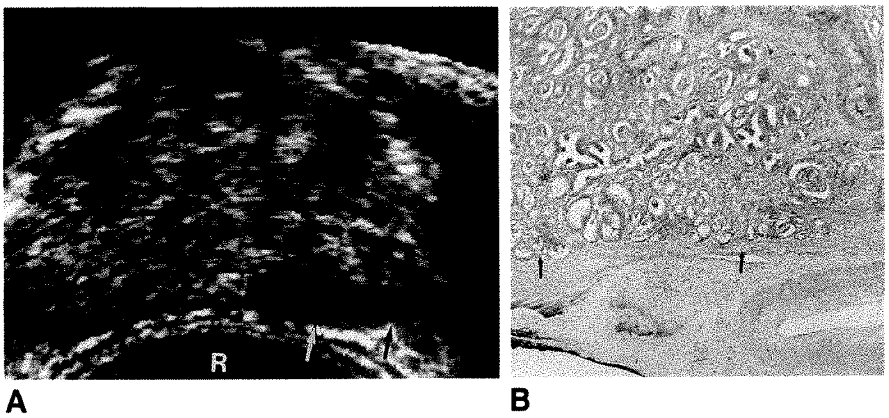

Fig. 7.—*A*, Radial transrectal sonogram shows left-sided hypoechoic mass (*arrows*) close to neurovascular bundle (NVB), suggestive of invasion. During surgery, left NVB was preserved.

B, Pathologic specimen shows adenocarcinoma of prostate, confined to gland (*arrows*) and showing no penetration into periprostatic adipose tissue. (H and E, ×55)

Discussion

Selection of appropriate therapy for prostatic carcinoma depends on accurate preoperative staging of the disease. Patients with tumors confined to the gland are usually considered candidates for radical surgery, whereas those with more advanced disease are usually treated by radiation therapy or chemotherapy [12, 13]. Extension of the tumor into the periprostatic tissues and seminal vesicles has been shown to affect prognosis and survival adversely [14]. Despite the availability of CT, transrectal sonography, and MR imaging, understaging of the disease occurs in a considerable number of patients [15–25].

Radical prostatectomy for patients with prostatic carcinoma was never widely adopted because most men were left impotent after the procedure as a result of injury to the pelvic nerve plexus, which provides anatomic innervation to the corpora cavernosa [1, 2]. Detection of involvement of the NVB by tumor is therefore extremely important in predicting whether sexual function can be preserved after radical surgery.

Walsh et al. [4, 8] modified the technique of radical prostatectomies in a way that enabled intraoperative visualization of these bundles, resulting in an operation that allowed preservation of one or both NVB and thus potency in a large majority of these patients. However, during surgery, it may be difficult for the surgeon to know whether or not to excise the NVB. For this reason, it is highly desirable to develop techniques that accurately predict whether it is safe to preserve the NVB in individual patients.

Previous sonographic-pathologic correlation studies have not focused on the evaluation of tumor extension in the NVB. Although not always easily seen, the NVB can be shown on transrectal sonograms as a slightly hypoechoic area in the posterolateral triangle of the prostate when meticulous imaging techniques and high-resolution systems are used (Fig. 1). These NVB are easily seen on transverse view of the prostate obtained with radial transducers, which allow a 360-degree image of the gland. The hypoechoic appearance of the NVB presumably reflects the pericapsular arteries and veins, because we observed changes in size and prominence with Valsalva maneuvers or positional changes; the nerve branches themselves are microscopic and are not expected to be visualized with current transrectal sonographic equipment. Knowing the anatomic location of the NVB, we could predict tumor extension into the NVB despite the lack of exact delineation of the NVB as separate structures in about one third of the hemispheres with bundle penetration, by using the criteria of a hypoechoic mass involving the posterolateral aspect of the gland showing a focal tumor bulge or irregularity of the tumor outlined posterolaterally (Figs. 2–6). Transrectal sonography in our series was more accurate in the prediction of invasion of the NVB when penetration depth was greater. Also the tumors showing posterior or posterolateral extraglandular spread were significantly larger than those confined to the gland. In addition, tumors with extension into the NVB were mostly moderately or poorly differentiated according to the Gleason grading system [11]. This confirms findings of other investigators [25].

In summary, our study has shown that 55% of patients in this series had extraglandular spread of tumor, with posterolateral or bundle invasion in 42% of the patients. Seventy of the 191 tumors involving 82 of the 310 hemispheres of the prostate pathologically extended into the region of the NVB. Transrectal sonography in the series was only moderately sensitive, specific, and accurate in detecting this posterolateral invasion, giving a positive predictive value of only 50% to detect invasion of the NVB. The detection rate for invasion of the NVB was increasingly more accurate with increasing depths of penetration.

Although our study has shown that transrectal sonography is of value in staging carcinoma of the prostate, it currently suffers from lack of sufficient spatial resolution to detect accurately invasion of the NVB. Future studies that use duplex or color flow Doppler endorectal probes might help to overcome these limitations and possibly provide a more accurate preoperative staging procedure for the urologist performing nerve-sparing radical prostatectomies.

ACKNOWLEDGMENTS

The authors thank Celia Jarvis for preparation of the manuscript and Henri Hessels for photography.

REFERENCES

1. Jewett HJ, Bridge RW, Gray GF Jr, Shelley WM. The palpable nodule of prostatic cancer: results 15 years after radical excision. *JAMA* **1968**;203: 403–406
2. Kopecky AA, Laskowski TZ, Scott R Jr. Radical retropubic prostatectomy in the treatment of prostatic carcinoma. *J Urol* **1970**;103:641–644
3. Walsh PC. Radical retropubic prostatectomy. In: Walsh PC, Gittes RF, Perlmutter AD, Stamey TA, eds. *Campbell's urology*, 5th ed. Philadelphia: Saunders, **1986**:2754–2775
4. Lepor H, Gregerman M, Crosby R, Mostofi FK, Walsh PC. Precise localization of the autonomic nerves from the pelvic plexus to the corpora cavernosa: a detailed anatomical study of the adult male pelvis. *J Urol* **1985**;133:207–212
5. Walsh PC, Lepor H, Eggleston JC. Radical prostatectomy with preservation of sexual function: anatomical and pathological considerations. *Prostate* **1983**;4:473–485
6. Walsh PC, Epstein JC, Lowe FC. Potency following radical prostatectomy with wide unilateral excision of the neurovascular bundle. *J Urol* **1987**;138:823–827
7. Walsh PC. Radical prostatectomy, preservation of sexual function, cancer control: the controversy. *Urol Clin North Am* **1987**;14:663–673
8. Walsh PC, Donker PJ. Impotence following radical prostatectomy: insight into etiology and prevention. *J Urol* **1982**;128:492–497
9. Pontes JE, Huben R, Wolf R. Sexual function after radical prostatectomy. *Prostate* **1986**;8:123–126
10. Catalona WJ, Dresner SM. Nerve-sparing radical prostatectomy: extraprostatic tumor extension and preservation of erectile function. *J Urol* **1985**;134:1149–1151
11. Gleason DF. Histologic grading and clinical staging of prostatic carcinoma. In: Sandberg AA, Murphy GP, Isaacs JT, eds. *Urologic pathology: the prostate*. Philadelphia: Lea & Febiger, **1977**:171–198
12. Vick CW, Walsh JW. CT staging of pelvic neoplasms. *Appl Radiol* **1984**;13:74–84
13. Catalona WJ, Scott WW. Carcinoma of the prostate. In: Walsh PC, Gittes RF, Perlmutter AD, Stamey TA, eds. *Campbell's urology*, 5th ed. Philadelphia: Saunders, **1986**:1453–1534
14. Jewett HJ, Eggleston JC, Yawn DH. Radical prostatectomy in the management of carcinoma of the prostate: probable causes of some therapeutic failures. *J Urol* **1972**;107:1034–1040
15. Emory TH, Reinke DB, Hill AL, Lange PH. Use of CT to reduce understaging in prostatic cancer: comparison with conventional staging techniques. *AJR* **1983**;141:351–354
16. Platt JF, Bree RL, Schwab RE. The accuracy of CT in the staging of carcinoma of the prostate. *AJR* **1987**;149:315–318
17. Hricak H, Dooms GC, Jeffrey BR, et al. Prostatic carcinoma: staging by clinical assessment, CT and MR imaging. *Radiology* **1987**;162:331–336
18. Brondetti PR, Lee JKT, Ling D, Catalona WJ. Clinical stage B prostate carcinoma: staging with MR imaging. *Radiology* **1987**;162:325–329
19. Friedman AC, Seidmon EJ, Radecki PD, Lev-Toaff A, Caroline DF. Relative merits of MRI, transrectal endosonography and CT in diagnosis and staging of carcinoma of prostate. *Urology* **1988**;6:530–537
20. Peeling WB, Griffiths GJ, Evans KT, Roberts EE. Diagnosis and staging of prostate cancer by transrectal ultrasonography. *Br J Urol* **1979**;51: 565–569
21. Scardino PT, Wheeler TM, Shinohara K, Harrison C, Fujino A, Carlton CE Jr. Confined or not confined: the value of transrectal ultrasonography in staging prostatic cancer (abstract). *J Urol* **1986**;135:149A
22. Mukamel E, Hanna J, Barbaric Z, DeKernion JB. The value of computerized tomography scan and magnetic resonance imaging in staging of prostatic carcinoma. *J Urol* **1986**;136:1231–1233
23. Salo JO, Kivisaari L, Ranniko S, Lehtonen T. Computerized tomography and transrectal ultrasound in the assessment of local extension of prostatic cancer before radical retropubic prostatectomy. *J Urol* **1987**;137:435–438
24. Pontes JE, Eisenkraft S, Watanabe H, Ohe H, Saitoh M, Murphy GP. Preoperative evaluation of localized prostatic carcinoma by transrectal ultrasonography. *J Urol* **1985**;134:289–291
25. McNeal JE, Kindrachuk RA, Freiha FS, Bostwick DG, Redwine EA, Stamey TA. Patterns of progression in prostate cancer. *Lancet* **1986**;2:60–63

Book Review

Genitourinary Radiology. A Multimodality Approach. By Rosalyn Kutcher and Everett M. Lautin. New York: Gower Medical, 280 pp., 1990. $95

When I obtained a copy of this book, I first read the preface by the authors and the two forewords by internationally known experts in the field, Milton Elkin, a uroradiologist, and Arthur D. Smith, a urologist. My purpose was to understand what the authors had in mind for this text and who its audience would be. From this initial reading, I gathered from the authors that the book was to be for the general radiologist and that therefore it would deal with common conditions only. From Dr. Elkin I found out that the reader would learn about the various entities primarily from the illustrations and from the legends. Indeed, subsequent reading revealed that the book was designed to be a kind of atlas. The pages are large, and each page has several images. The text itself is brief, even skimpy. The value of the book truly lies in the illustrations and in the legends. Perhaps the book's purpose could have been made clearer in its title.

In keeping with its nature, the book has no discussion of contrast material or systemic reactions to contrast medium. This is understandable in an atlas but unconventional in a book for the general radiologist or for the resident in training. Similarly, the references are limited, usually only a few key ones for each topic. In most cases, the illustrations are relevant, and the vast majority make excellent teaching points. The book's 19 chapters cover imaging of the urinary tract, developmental anomalies and normal variants of the kidney, urinary tract calcifications, renal infections, renal obstructions, renal trauma, medical diseases of the kidney, vascular diseases of the kidney, renal cystic disease, renal masses, the ureters, the urinary bladder, the prostate and seminal vesicles, the urethra and penis, the scrotum and its contents, the adrenal gland, imaging in renal transplantation and dialysis, interventional radiology, and postoperative radiologic evaluation.

The quality of the illustrations is mixed. The sonograms, CT scans, MR images, and diagrams are outstanding. The quality of the reproductions of the IV urograms, voiding cystourethrograms, and retrograde urethrograms is often poor; a number of these reproductions are so dark that I could not make out sufficient detail to see the point being illustrated. Future editions of the text will have to attend to this.

One major weakness is that the authors do not stress often enough when a given imaging examination is unnecessary. Figure 14.20A, for example, is an underpenetrated radiograph of a patient with Peyronie disease that is used to demonstrate the bending of the erect penile midshaft. Most urologists, however, would have had the patient bring in a photograph he had taken himself, to avoid unnecessary embarrassment and an unnecessary radiograph.

How useful will the general radiologist find this book? It could be used in two ways: as a kind of portable teaching file, which is compact and could be taken home, or as a relatively inexpensive atlas to be used with a problem case. In the latter situation, the radiologist could look up an entity and check the text, illustrations, and legends to see if the case findings fit the information given in the book. For these purposes, this volume would work quite well. It differs from currently available books in that it is illustrated much more profusely than the sections on uroradiology in general radiology textbooks or, indeed, than the smaller texts on uroradiology itself. It has, by design, less text than either. The book does fill a gap and addresses a need. It is a compact, relatively inexpensive, and usually reliable guide to the common genitourinary entities.

Gerald W. Friedland
Palo Alto Veterans Affairs Medical Center
Palo Alto, CA 94304

Cysts of the Prostate and Seminal Vesicles: MR Imaging Findings in 11 Cases

P. A. Gevenois[1]
M. L. Van Sinoy[1]
S. A. Sintzoff, Jr.[1]
B. Stallenberg[1]
I. Salmon[2]
G. Van Regemorter[3]
J. Struyven[1]

Cysts of the prostate and seminal vesicles are confusing abnormalities because they are uncommon and their origin is uncertain. Several approaches to diagnosis have been used, most recently CT and transrectal sonography. In this study, we investigated the value of MR imaging in the diagnosis of six cases of prostatic cyst and five cases of cysts of the seminal vesicles. All patients were symptomatic. T1- and T2-weighted spin-echo images were obtained in all cases; pathologic confirmation was available in four patients. MR images were analyzed prospectively without knowledge of clinical data or the results of other imaging procedures. In all cases, low- and high-signal masses were observed on T1- and T2-weighted images, respectively. The cysts were unilocular with a sharply defined margin, ranging from 0.5 to 3.0 cm in diameter. The thin wall was of low signal intensity on T2-weighted images.

Our experience suggests that MR imaging is useful in demonstrating the liquid content of prostatic and seminal-vesicle cysts and in establishing their size and location.

AJR **155:1021–1024, November 1990**

Cysts of the seminal vesicles are an uncommon congenital or acquired abnormality. In some cases, they are accompanied by ipsilateral renal agenesis [1]. The MR features of this disorder have been described [2, 3]. Prostatic cysts include utricular cysts, müllerian duct cysts, prostatic retention cysts, and cysts of the ejaculatory duct. The CT and sonographic findings of midline prostatic cysts have been reported. More recently, MR imaging has proved to be reliable in identifying müllerian duct cysts [1–9]. We report our experience in using MR imaging to diagnose cysts of the prostate and seminal vesicles in 11 patients.

Subjects and Methods

MR imaging was performed in six patients with prostatic cysts and in five patients with cysts of the seminal vesicles. The patients were 24–84 years old (mean, 60 years). All patients were symptomatic and were suspected clinically of having disorders of the prostate and seminal vesicles. The examinations were performed without knowledge of clinical or sonographic findings. Prostatism was present in six cases, acute prostatitis in two cases, and hemospermia in one case. Chronic prostatic abscess and urothelial cancer were present in one case each. Digital examination revealed a smooth cystic swelling of the prostate or of a seminal vesicle in two cases.

Pathologic confirmation was obtained in four patients by either transurethral resection (one prostatic cyst) or surgery (two seminal vesicle cysts associated with benign hyperplasia and chronic abscess and one prostatic cyst associated with benign hyperplasia). One patient has been treated by transrectal needle aspiration without histologic examination of any material. No chemical analyses of the cystic fluid were done. Other patients were treated conservatively. In these cases, the diagnoses were not confirmed by histologic examination.

MR images were obtained with a 1.5-T Gyroscan S15 MR imaging unit (Philips, Eindhoven, the Netherlands) that was operated at 0.5 T for one patient and at 1.5 T for the others. In all cases, a body coil was used, and the patients were examined while supine. A 256- by 256-

---

Received March 23, 1990; accepted after revision June 15, 1990.

[1] Department of Radiology, Cliniques Universitaires de Bruxelles, Hôpital Erasme, Route de Lennik 808, 1070 Brussels, Belgium. Address reprint requests to P. A. Gevenois.

[2] Department of Pathology, Cliniques Universitaires de Bruxelles, Hôpital Erasme, 1070 Brussels, Belgium.

[3] Department of Urology, Cliniques Universitaires de Bruxelles, Hôpital Erasme, 1070 Brussels, Belgium.

0361-803X/90/1555-1021
© American Roentgen Ray Society

pixel matrix was used. In all 11 patients, sagittal T1-weighted, 350/20 (TR/TE), and transaxial T2-weighted, 2020/20–100, images were obtained with 5-mm-thick sections and 0.5-mm gaps. Sagittal T2-weighted images were obtained in two patients. In one case, gadolinium 1,4,7,10-tetraazacyclododecane tetraacetic acid (Gd-DOTA) was used, and enhanced T1-weighted transverse images were obtained. MR images were analyzed prospectively by an experienced radiologist without knowledge of the clinical findings or the results of other imaging tests. The appearance of the cysts was analyzed for size, margins, location, and signal intensity.

One patient had transabdominal sonography and CT. The other patients had transrectal sonography. This method suggested the cystic nature of the abnormality in all but one case. In this patient, the cystic nature was revealed by transurethral resection.

Results

All cases had a similar appearance on MR images: low- and high-signal masses were observed on T1- and T2-weighted images, respectively. This feature suggests that the lesion was filled with fluid. The cysts were all unilocular with sharply defined margins. The thin wall was of low signal intensity on T2-weighted images. The cysts were similar in size, from 0.5 to 3.0 cm in diameter. They were hypointense with respect to the prostate on unenhanced T1-weighted images. After injection of Gd-DOTA (one case), no significant enhancement was noted. In the seminal vesicles (Figs. 1 and 2), cysts were localized on the left in three cases and on the right in two cases. In the prostate, they were in the midline in four cases (Figs. 3 and 4) and lateral in two cases (Figs. 5 and 6). When in the midline, they arose at the level of the verumontanum and, in one case, extended upward from the prostate between the seminal vesicle (Fig. 4).

Discussion

Midline Prostatic Cysts

Although the origin of midline prostatic cysts could not be determined noninvasively, it is likely that they were prostatic utricular or müllerian duct cysts. A true prostatic cyst cannot be excluded. Congenital enlargement of the utricle may occur and may be associated with hypospadias, cryptorchidism, or renal agenesis. Such association did not occur in any of our cases. Enlargement also can result from obstruction caused by inflammation. Müllerian duct cysts also are midline, but extend superiorly from the level of the verumontanum [9], even outside the prostate. The last feature was observed in one case (Fig. 4). On the basis of this feature, the mass was supposed to be müllerian in origin. Anatomically, midline prostatic cysts derive from the caudal fused ends of müllerian ducts at the level of the verumontanum. Recently, several reports have emphasized the differences in the embryologic origin of the urogenital sinus and the müllerian ducts from the entoderm and mesoderm, respectively [10]. Histopathologically, the distinction is confusing. Transitional epithelium, stratified squamous epithelium, cuboidal epithelium, and even no epithelial lining have been reported [11]. The contents of müllerian duct cysts vary (mucoid, purulent, serous, or hemorrhagic). When blood is present (not observed in our series), both T1- and T2-weighted images show a high signal within the cyst [9].

In a previous study [12] of 22 normal volunteers with no known urinary tract disorders who were less than 30 years old, we observed a high-intensity signal on T2-weighted images in the midline, between the peripheral and the central parts of the prostate. They were less than 3 mm in diameter in our three cases. The significance of such a finding is unclear.

The demonstration of a midline cystic structure relating to the prostate and the verumontanum is helpful in differentiating a müllerian duct cyst from other anomalies, including a cyst of the seminal vesicles or of the prostate, as well as from a posterior bladder diverticulum [8] or a mucinous cystadenoma of the appendix [9].

Lateral Prostatic Cysts

The cause of lateral prostatic cysts is unclear, and the embryologic origin is not established. Acquired cysts include

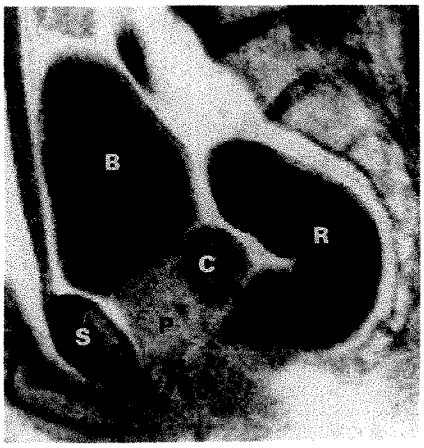

Fig. 1.—Seminal vesicle cyst (surgical confirmation). Sagittal MR image, 350/20, shows cyst (C) with low-intensity signal between prostate (P), rectum (R), and bladder (B). S = symphysis pubis.

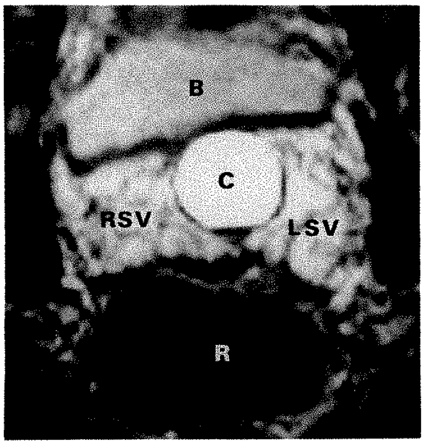

Fig. 2.—Seminal vesicle cyst (surgical confirmation). Transverse MR image, 2000/50, shows high-intensity signal in seminal cyst (C) arising in left seminal vesicle (LSV). RSV = right seminal vesicle, B = bladder, R = rectum.

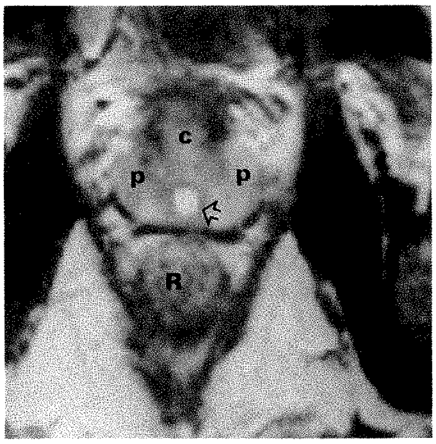

Fig. 3.—Midline prostatic cyst (confirmed by transurethral resection). Transverse MR image, 2000/50, shows a high-intensity signal between two parts of peripheral prostate (p), in midline (*arrow*). c = central prostate, R = rectum.

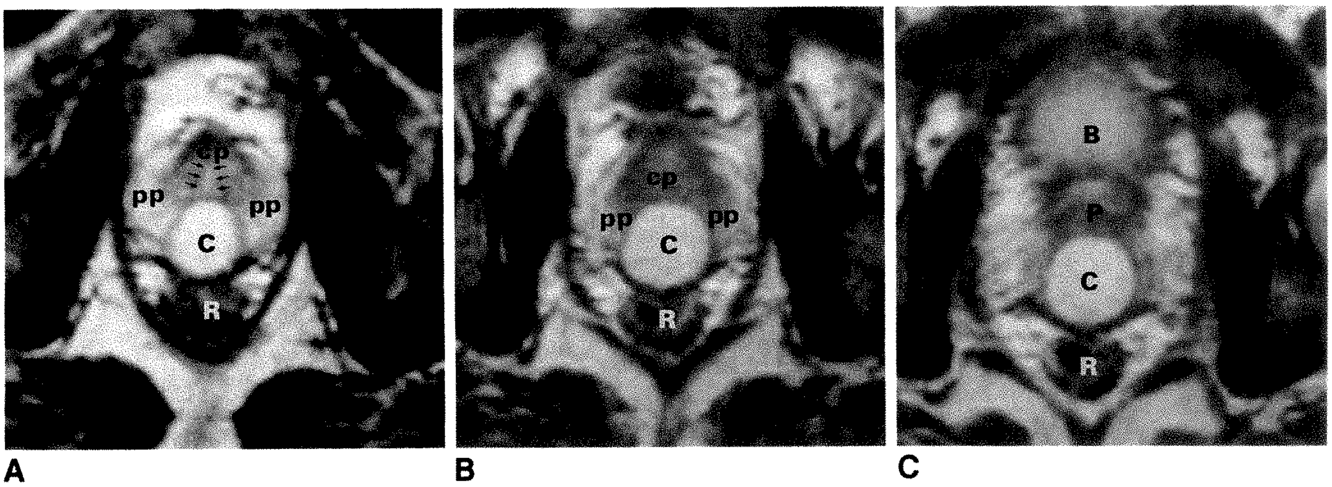

Fig. 4.—Midline prostatic cyst. Müllerian duct cyst (confirmed by transrectal needle puncture). Transverse MR images, 2000/50, show high-intensity signal between two parts of peripheral prostate (pp).

***A*, Cyst (C) arises at level of verumontanum (*arrows*), in posterior part of prostate, between two crescents of peripheral prostate (pp). cp = central prostate, R = rectum.**

***B*, Cyst extends superiorly between two parts of peripheral prostate, outside gland.**

***C*, Cyst extends outside gland, in prostatoseminal angle. P = prostate, B = bladder.**

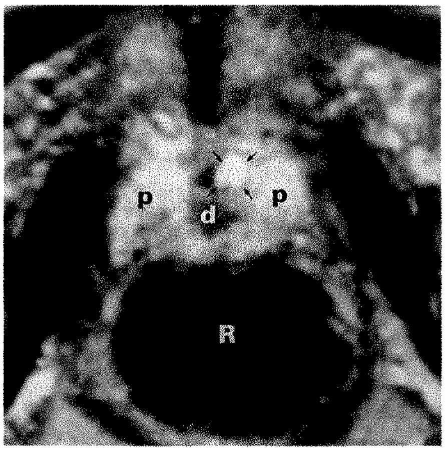

5

Fig. 5.—Lateral prostatic cyst. Transverse MR image, 2000/50. Cyst (*arrows*) in anterior part of left peripheral prostate (p) is associated with urothelial carcinoma in defect (d) after a surgical removal of adenoma. Because of no surgical confirmation, pseudodiverticulum resulting from irregular tumor growth cannot be excluded definitively. R = rectum.

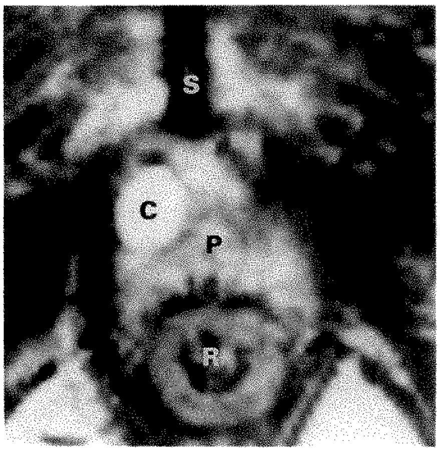

6

Fig. 6.—Lateral prostatic cyst (surgical confirmation). Transverse MR image, 2000/50, shows cyst (C) in anterior part of right peripheral prostate (P). Upper transverse images showed benign prostatic hyperplasia. S = symphysis pubis, R = rectum.

parasitic cysts, cysts associated with carcinoma, and retention cysts. One of our cases was associated with benign prostatic hyperplasia, and one was associated with urothelial carcinoma in the defect after surgical removal of an adenoma. In this case, a pseudodiverticulum resulting from irregular tumor growth could not be firmly excluded. Differentiation of a prostatic cyst from a dilated prostatic acinus is established arbitrarily by size: cysts are more than 7.5 mm in diameter [10]. In our series, there were two cases of lateral prostatic cyst, one less than and one more than 7.5 mm in diameter. Prostatic abscesses also cause fluid-filled masses in the prostate. These occur in symptomatic patients in association with complicated acute prostatitis.

Seminal Vesicle Cysts

Cysts of the seminal vesicles are uncommon, with fewer than 100 cases reported. This number does not reflect the real frequency. Diagnosis of these lesions has been uncommon in the past because of the difficulty in imaging these structures. Of cysts of the seminal vesicle, 32% are not associated with ipsilateral renal agenesis. In our series, no association with renal agenesis was found. Postinfection fibrosis has been suggested as the cause [13]. Infection of the prostate has been found in two cases, benign prostatic hyperplasia in three others. Acquired cysts are usually associated with obstruction of the ejaculatory ducts due to urinary tract infection, usually ascending from the lumen of the prostatic urethra into the seminal vesicles. Compression of the ejaculatory ducts by prostatic adenomatous nodules explains the association with benign prostatic hyperplasia. To our knowledge, no previous reports have mentioned this association.

Seminal-vesicle cysts must be differentiated from cysts arising from the prostate, utricle, or müllerian duct and from abscesses or tumors [2]. Investigation of the seminal tract has involved injection of the cyst with contrast material or vasovesiculography. Both CT and transrectal sonography can delineate a prostatic or a seminal-vesicle tumor. These techniques also allow a distinction between solid and cystic structures. In one report, it was mentioned that the cyst appeared as a solid mass [1]. Hemorrhagic seminal vesicle cysts have been reported [2]. In this study [2], no Hounsfield numbers were mentioned, but these cysts could appear with a high attenuation rate.

Transabdominal and transrectal sonography and CT should be used as the initial diagnostic studies; MR should be reserved for more complex situations. The nature of many, if not most, pelvic cysts can be determined invasively by injecting them with contrast material or by vasovesiculography. Noninvasive methods such as sonography, CT, or MR imaging should be performed before invasive techniques. Because of the capability of direct acquisition of multiplanar images, MR imaging is superior to CT and sonography in delineating the anatomic relationships. King et al. [14] reported a case in which the cystic architecture of a hemorrhagic seminal vesicle cyst was clearly depicted only on the MR image. In the same article, they stated that cysts of the male genital tract frequently are of high signal intensity on both T1- and T2-weighted images. On the basis of these features, the cysts are likely hemorrhagic and probably associated with hemospermia. It is important to show that vesicle cysts are unilocular, because malignant cystosarcoma phyllodes are described. In these malignant conditions, the tumor is multiloculated [15].

The clinical usefulness of MR imaging in evaluating seminal-vesicle and prostatic cysts is in the demonstration of a cystic tumor and the location of the mass by observation of contiguous thin slices. As the definitive diagnosis requires a histologic specimen obtained by an invasive procedure, diagnosis by noninvasive methods would be appropriate if conservative management is planned. Before surgical intervention, MR imaging provides full anatomic definition.

REFERENCES

1. Ejeckman GC, Govatsos S, Lewis AS. Cyst of seminal vesicle associated with ipsilateral renal agenesis. *Urology* **1984**;24:372–374
2. Kenney PJ, Leeson MO. Congenital anomalies of the seminal vesicles: spectrum of computed tomographic findings. *Radiology* **1983**;149:248–251
3. Kneeland JB, Auh YH, McCarron JP, Zirinsky K, Rubinstein WA, Kazam E. Computed tomography, sonography, vesiculography, and MR imaging of a seminal vesicle cyst. *J Comput Assist Tomogr* **1985**;9:964–966
4. Gevenois PA, Van Regemorter G, Van Gansbeke D, Kuhn G, Struyven J. Kyste de la vésicule séminale. Aspect en échotomographie, tomodensitométrie et résonance magnétique. A propos d'un cas. *J Radiol* **1987**;68:489–491
5. Van Poppel H, Vereecken R, De Geeter P, Verduyn H. Hemospermia owing to utricular cyst: embryological summary and surgical review. *J Urol* **1983**;129:608–609
6. Elder JS, Mostwin JL. Cyst of the ejaculatory duct/urogenital sinus. *J Urol* **1984**;132:768–771
7. Schwarts JM, Bosniak MA, Hulnick DH, Megibow AJ, Raghavendra BN. Computed tomography of midline prostatic cysts of the prostate. *J Comput Assist Tomogr* **1988**;12:215–218
8. Neustein P, Hein PS, Goergen TG. Chronic hemospermia due to müllerian duct cyst: diagnosis by magnetic resonance imaging. *J Urol* **1989**;142:828
9. Thurnher S, Hricak H, Tanagho EA. Müllerian duct cyst: diagnosis with MR imaging. *Radiology* **1988**;168:25–28
10. Emmett JL, Braasch WF. Cysts of the prostate gland. *J Urol* **1936**;36:236–249
11. Shuhrke TD, Kaplan GW. Prostatic utricle cyst (müllerian duct cysts). *J Urol* **1978**;119:765–767
12. Gevenois PA, Salmon I, Stallenberg B, Van Sinoy ML, Van Regemorter G, Struyven J. MR imaging of the normal prostate at 1.5 telsa. *Br J Radiol* **1990**;63:101–107
13. Haeney JA, Pfister RC, Maeres EM Jr. Giant cysts of the seminal vesicles with renal agenesis. *AJR* **1987**;149:139–140
14. King BF, Williamson B Jr, Hattery RR, Hartman GW, Lieber MM, Berquist TH. Seminal vesicle imaigng. *RadioGraphics* **1989**;9:653–674
15. Mazur MT, Myers JL, Maddox WA. Cystic epithelial-stromal tumor of the seminal vesicle. *Am J Surg Pathol* **1987**;11:210–217

Soft-Tissue Tumors of the Foot:
Value of MR Imaging for Specific Diagnosis

Louis H. Wetzel[1]
Errol Levine

We reviewed MR imaging findings in 14 patients with primary soft-tissue tumors of the foot and compared them with surgical and pathologic findings to determine the value of MR imaging in anatomic localization, delineation, and characterization of such lesions. Nine tumors (64%) were benign, and five (36%) were malignant. The anatomic location (compartment, space, relation to specific tendon) and extent of all tumors were accurately shown by MR imaging. Twelve tumors (86%) were correctly characterized as benign or malignant. Eight (89%) of nine benign lesions showed distinctive MR imaging features that correctly suggested a specific diagnosis. These included hemangioma (high T2-weighted intensity and internal septa), ganglion cyst (homogeneous, high T2-weighted intensity and peritendinous location), plantar fibromatosis (nodularity of plantar aponeurosis with low intensity on all sequences), and pigmented villonodular synovitis (low T2-weighted intensity and lower intensity rim). Aggressive fibromatosis (one case) could not be characterized. Four (80%) of five malignant neoplasms had MR imaging findings suggesting soft-tissue sarcoma. Two synovial sarcomas were inhomogeneous and showed extensive peritendinous growth. Two clear cell sarcomas arose at the origin of the plantar aponeurosis and infiltrated adjacent muscle. A small clear cell sarcoma could not be characterized as benign or malignant.

MR imaging of the foot is accurate in showing the extent of soft-tissue tumors, which is helpful for surgical planning. Determination of their specific anatomic location may help characterize some tumors. Although our series is small, it appears that MR imaging often suggests a specific diagnosis in certain benign soft-tissue tumors of the foot and may often correctly distinguish benign from malignant tumors.

***AJR* 155:1025–1030, November 1990**

Although superficial lesions in the foot are usually readily diagnosed by physical examination, deep soft-tissue tumors are often difficult to evaluate clinically and radiologically [1]. Accurate preoperative assessment and diagnosis of such lesions is important in determining the proper surgical approach and management [1]. The high soft-tissue contrast and multiplanar capability of MR imaging are particularly advantageous in evaluating the foot, owing to its compact soft tissues and paucity of deep fat planes [2]. To date, few reports of MR imaging of soft-tissue tumors in the foot have been published [3–6]. We describe our results in 14 patients with primary tumors in the foot evaluated with MR imaging.

Subjects and Methods

From December 1985 through October 1989, 29 patients were referred for MR imaging for evaluation of suspected soft-tissue tumors in the foot. Clinical data, imaging studies, and pathologic findings in these patients were reviewed. Five patients had infectious or inflammatory disorders and were excluded from the study. Six patients had normal MR examinations and normal findings on clinical and radiologic follow-up 3–12 months later. Four patients had clinical and imaging findings typical of benign tumors (two hemangiomas, one ganglion cyst, and one plantar fibromatosis) but did not have symptoms sufficient to warrant surgery and

Received April 4, 1990; accepted after revision June 1, 1990.

Presented at the annual meeting of the American Roentgen Ray Society, Washington, DC, May 1990.

[1] Both authors: Department of Diagnostic Radiology, University of Kansas Medical Center, 39th St. and Rainbow Blvd., Kansas City, KS 66103. Address reprint requests to L. H. Wetzel.

0361-803X/90/1555-1025
© American Roentgen Ray Society

were excluded from our study. Fourteen patients with surgical confirmation of foot tumors comprised our final study group. There were 11 males and three females, 7–59 years old (mean, 28 years). All patients presented with a palpable mass, and eight complained of pain.

Nine (64%) of 14 patients had benign tumors including cavernous hemangioma (four), ganglion cyst (one), plantar fibromatosis (one), pigmented villonodular synovitis (two), and aggressive fibromatosis (one). The tumors ranged in size from 2.2 to 10.0 cm in greatest dimension (mean, 5.4 cm). Five (36%) of 14 tumors were malignant: two synovial sarcomas and three clear cell sarcomas. They ranged from 3 to 17 cm in greatest dimension (mean, 7.1 cm). Diagnoses were confirmed histologically after complete or partial excision (nine) or amputation (five).

MR imaging was performed on a superconducting system (Magnetom, Siemens Medical Systems, Iselin, NJ) operated at 1.0 T. Conventional multisection two-dimensional Fourier transform spin-echo (SE) imaging was used with section thicknesses of 4–8 mm, intersection spacing of 1–4 mm, and one or two signal acquisitions. The acquisition matrix was 256 × 512 and the display matrix was 256 × 256. Two pulse sequences were always used: 500–600/17–30 (TR/TE) and 2000–2100/28–35, 80–90. At least two imaging planes were used in all patients, usually coronal and sagittal, and occasionally axial or oblique imaging also was done. A standard head coil with a 30-cm field of view was used in all cases with both feet positioned symmetrically as close as possible to zero degrees plantar flexion to simplify identification of anatomic structures. Plain films were available in all patients.

Because the authors were familiar with many of the cases at the time of review, a truly blinded retrospective evaluation was not possible. Instead, all MR imaging studies were reviewed and compared with surgical and pathologic findings to assess the usefulness of MR imaging for determining the anatomic location of tumors (compartment, space, relation to specific tendon or aponeurosis) and delineating their extent. We also analyzed the size, character of margins, internal morphology (septa, homogeneity), growth pattern, and signal intensity of tumors on MR scans to determine if there were MR imaging features that would help distinguish benign from malignant lesions or suggest a specific diagnosis.

Results

Benign Tumors

Cavernous hemangiomas were the most common tumors (44%) and had consistent MR imaging features. All were slightly higher in intensity than skeletal muscle on T1-weighted images and had markedly high intensity on T2-weighted images, with internal septa and slightly lobulated or irregular borders (Fig. 1). They were located in the intermediate (two) and lateral (one) plantar compartments and the pre-Achilles space (one). Two plantar lesions had flame-shaped dorsal extensions between the metatarsal shafts. The pathologic specimens showed vascular channels separated by various amounts of fat or fibrofatty septa.

A single ganglion cyst adjacent to the peroneus longus tendon was homogeneous, smooth-bordered, of lower intensity than muscle on T1-weighted images, and markedly high in intensity on T2-weighted images (Fig. 2). Plantar fibromatosis appeared as nodular thickening of the plantar aponeurosis, which was of low intensity on all pulse sequences, and dense fibrocollagenous tissue was verified histologically (Fig. 3). Both cases of pigmented villonodular synovitis involved the sinus tarsi and resulted in a palpable mass just anteroinferior to the lateral malleolus. They showed mildly inhomogeneous low-intensity signal on T2-weighted images and a smooth hypointense peripheral rim (Fig. 4). Hemosiderin deposition was prominent in both pathologic specimens. Aggressive fibromatosis consisted of a slightly lobulated, 10-cm mass with discrete high- and low-intensity areas (Fig. 5). Microscopy showed infiltrative sheets of fibrous tissue surrounding muscle bundles.

The anatomic location of all tumors was correctly identified by MR imaging. All benign tumors were well delineated from surrounding normal tissues on MR images because of high soft-tissue contrast. The size and soft-tissue extent of tumors were accurately shown by MR imaging when compared with surgical findings in all patients, and no areas of unsuspected tumor growth were encountered. Cortical bone erosion in one patient was shown by plain films and MR images.

Analysis of tumor margins and homogeneity was not reliable in identifying benign lesions: six had lobulated or irregular margins, and seven were inhomogeneous. However, benign tumors could be characterized by recognizing a distinctive combination of MR imaging findings that suggested a specific diagnosis (Figs. 1–4). The correct diagnosis was suggested by MR imaging in eight (89%) of nine benign tumors. Aggres-

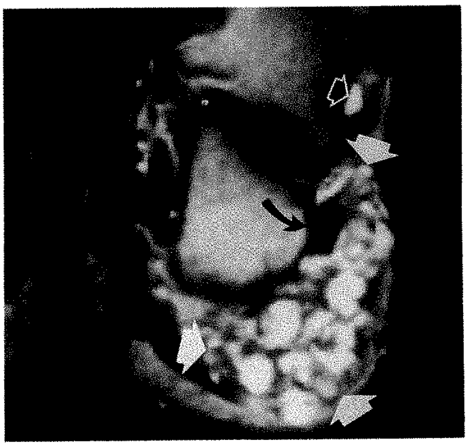

1

Fig. 1.—Cavernous hemangioma of lateral plantar compartment. Coronal T2-weighted MR image (SE 2100/90) shows inhomogeneous tumor (*solid white arrows*) with high intensity, comparable to that of joint fluid (*open arrow*). Lower intensity internal septa were more pronounced in this case than in other hemangiomas. At surgery, lesion was dissected free of peroneus tendons (*curved arrow*) without functional impairment.

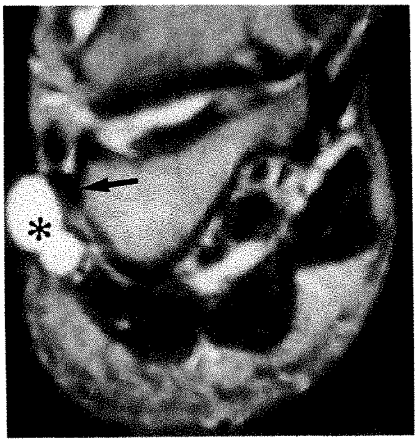

2

Fig. 2.—Ganglion cyst. Biloculated lesion (*asterisk*) has homogeneous high intensity on SE 2100/90 MR image. Cyst arose from sheath of peroneus tendons (*arrow* shows peroneus longus tendon) just distal to inferior peroneal retinaculum.

sive fibromatosis could not be distinguished from sarcoma, particularly malignant fibrous histiocytoma (Fig. 5).

Malignant Neoplasms

Both synovial sarcomas showed an extensive peritendinous growth pattern and internal inhomogeneity (Fig. 6). One had well-defined lobulated borders and one had irregular infiltrative margins. They were mildly to moderately higher in intensity than fat on T2-weighted images. Two of three clear cell sarcomas arose near the origin of the plantar aponeurosis. Both were oval with slightly lobulated borders and showed infiltration of adjacent muscle (Fig. 7). One small tumor (3 cm) adjacent to the extensor hallucis longus tendon was heterogeneous and had irregular margins. Clear cell sarcomas were mildly higher (two) or moderately lower (one) in intensity than fat was on T2-weighted images.

Four of five tumors were readily delineated from surrounding tissues on T2-weighted images. One clear cell sarcoma was nearly isointense with muscle on all pulse sequences, and tumor infiltration was evident as loss of intramuscular fat striations (Fig. 7). The anatomic location, growth pattern, and extent of all malignant tumors were accurately depicted by MR images when directly compared with gross sections of amputation specimens. Cortical bone erosion in two patients was shown by plain films and MR images, and early marrow invasion in one case seen by use of MR imaging was confirmed by pathologic analysis.

A soft-tissue sarcoma was correctly suggested by MR imaging in four (80%) of five malignant neoplasms by a combined analysis of the growth pattern, morphology, and

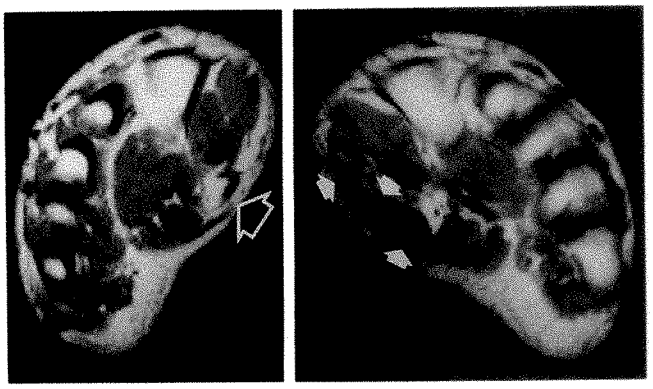

Fig. 3.—Plantar fibromatosis. Coronal SE 2100/30 MR image shows low-intensity nodular thickening (*solid arrows*) of medial aspect of plantar aponeurosis. Lesion remained very low in intensity on SE 2100/90 image owing to dense fibrous tissue. Note appearance of normal contralateral aponeurosis (*open arrow*).

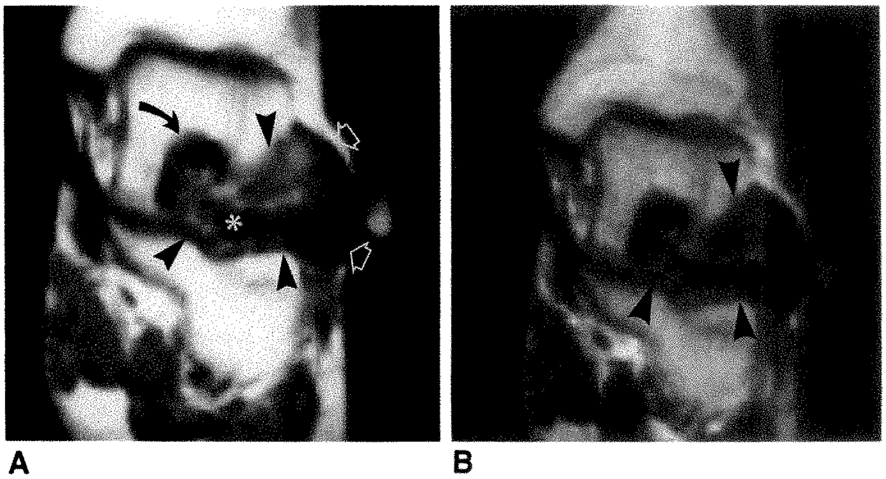

Fig. 4.—Pigmented villonodular synovitis arising in sinus tarsi.
A, Coronal SE 2100/28 MR image shows mass (*arrowheads*) surrounding interosseous talocalcaneal ligament (*asterisk*) and causing erosion (*curved arrow*) of talus. Note prominent lateral extension of tumor with hypointense peripheral rim (*open arrows*).
B, Lesion (*arrowheads*) has mildly inhomogeneous, low-intensity signal on SE 2100/90 MR image, reflecting hemosiderin deposition.

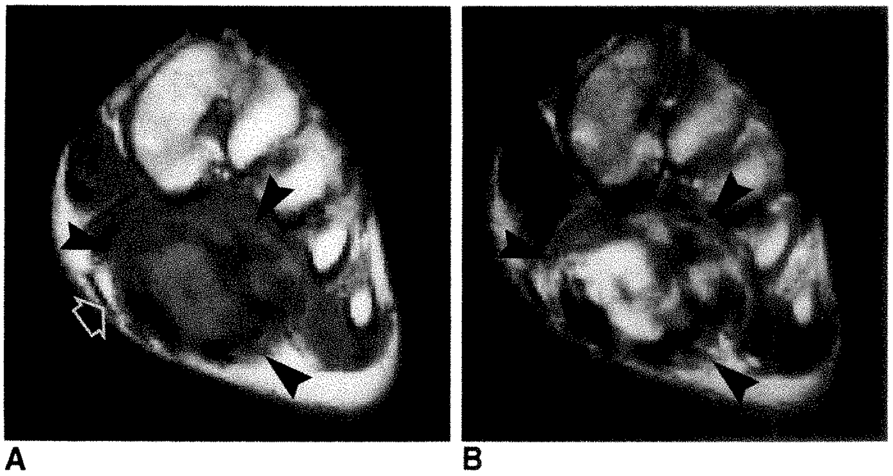

Fig. 5.—Aggressive fibromatosis.
A, Coronal SE 500/17 MR image shows oval mass (*arrowheads*) in intermediate plantar compartment. Note normal thickness of plantar aponeurosis (*open arrow*) as compared with plantar fibromatosis (Fig. 3).
B, High- and low-intensity areas are evident within tumor (*arrowheads*) on coronal SE 2100/90 MR image. Because of its size and marked inhomogeneity, lesion could not be distinguished from malignant neoplasm.

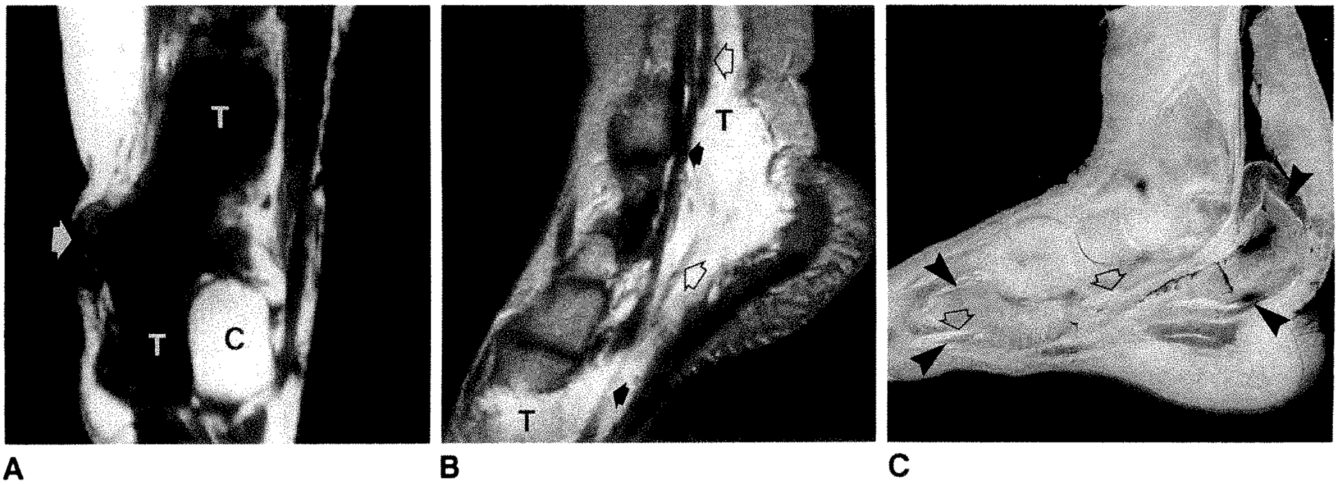

Fig. 6.—Synovial sarcoma.

A, Coronal SE 500/17 MR image shows large tumor (T) medial to calcaneus (C) extending into posterior compartment of leg, which was not detected clinically in obese patient. Small medial component (*arrow*) was palpable, and initial clinical diagnosis was ganglion cyst.

B, Sagittal SE 2100/90 MR image reveals longitudinal extent of tumor (T) with infiltrative margins and high intensity compared with fat. Note tumor growth along flexor digitorum longus (*solid arrows*) and flexor hallucis longus (*open arrows*) tendons.

C, Gross section of specimen confirms extent of neoplasm (*arrowheads*), which was firmly adherent to long flexor tendons in foot (*open arrows*).

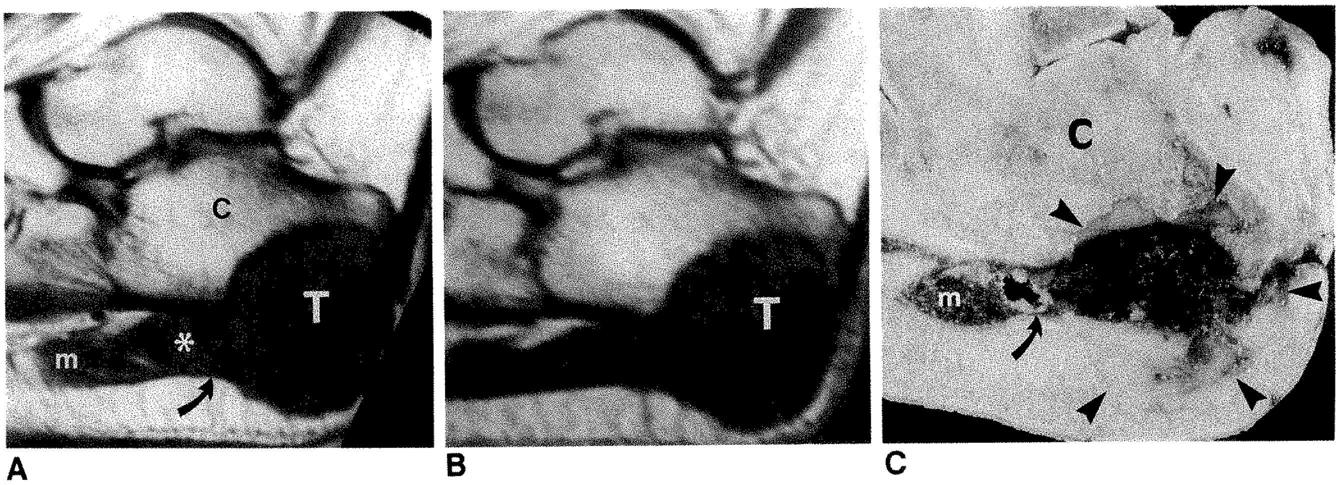

Fig. 7.—Clear cell sarcoma.

A, Sagittal SE 600/25 MR image reveals oval tumor (T) with intensity similar to that of muscle (m), arising near origin of plantar aponeurosis (*curved arrow* shows aponeurosis distal to origin). Note tumor infiltration (*asterisk*) of flexor digitorum brevis muscle (m) and erosion of calcaneus (C). Presumptive clinical diagnosis was lipoma of heel.

B, Neoplasm (T) has low intensity compared with intensity of fat on SE 2000/90 MR image, probably related to its melanin content.

C, Gross section just medial to plane of images confirms infiltration (*curved arrow*) of muscle (m) by tumor (*arrowheads*). C = calcaneus.

MR signal intensity. Apart from the low-intensity clear cell sarcoma, malignant tumors were intermediate in signal intensity on T2-weighted images, whereas nearly all benign tumors were either markedly high (five) or markedly low (three) in intensity. Because of its size and indeterminate imaging features, a small 3-cm clear cell sarcoma could not be characterized as benign or malignant.

Discussion

Deep soft-tissue tumors of the foot are uncommon and are difficult to evaluate clinically [1]. As metastases to the foot are extremely rare, most foot tumors are primary lesions [1]. MR imaging is now generally accepted as the most accurate method for detection and delineation of soft-tissue tumors [2, 7–11]. All tumors in our series were detected preoperatively with MR imaging. The ability to obtain images in multiple planes often clarified anatomic relationships and facilitated anatomic localization of tumors. This was useful in characterization of lesions because some foot tumors often occur in a specific anatomic location, for example, plantar fibromatosis (Fig. 3), or in relation to certain anatomic structures such as tendons, for example, ganglion cyst (Fig. 2) and synovial sarcoma (Fig. 6).

Our results show that MR imaging accurately delineates the extent of soft-tissue tumors in the foot, which is helpful in surgical planning for benign and malignant tumors. Preoperative demonstration of benign tumor relationships to major tendons and neurovascular bundles helps avoid injury to these structures during excision (Fig. 1). The full extent of benign tumors should be ascertained before surgery because many lesions, such as plantar fibromatosis, hemangioma, and pigmented villonodular synovitis, have a high recurrence rate if incompletely excised. Demonstration of the most proximal extent of malignant neoplasms determines the type of amputation necessary to achieve radical resection margins [1]. If wide excision and limb-sparing treatment is performed instead of amputation, then knowledge of exact tumor extent is essential for successful therapy [1, 12].

In our series and in previous studies [8, 9, 13, 14], analysis of general morphologic MR imaging features (tumor margin, homogeneity) and subjective assessment of signal intensity on T2-weighted images were not reliable in distinguishing benign from malignant tumors. However, nearly all benign tumors in our study were correctly identified by distinctive MR findings that suggested a specific diagnosis. Although not pathognomonic, the typical MR features of soft-tissue hemangioma [13, 15–18], pigmented villonodular synovitis [13, 19–21], and ganglion cyst [22, 23] have been well described and were evident in our cases (Figs. 1, 2, and 4).

Plantar fibromatosis typically presents as a nodular subcutaneous growth involving the medial aspect of the middle portion of the plantar aponeurosis and is bilateral in 10–25% of cases [24]. It is genetically linked to the other superficial fibromatoses, palmar fibromatosis (Dupuytren contracture) and penile fibromatosis (Peyronie disease), and these disorders may affect the same patient separated by a 5- to 10-year interval [24]. MR imaging confirmed the diagnosis in our patient by showing involvement of the plantar aponeurosis and low signal intensity at all pulse sequences due to dense fibrous tissue (Fig. 3) [25]. Aggressive fibromatosis (extraabdominal desmoid) is classified as a deep fibromatosis and occasionally involves the foot [24]. In aggressive fibromatosis, infiltrative fibrous tissue surrounds and entraps skeletal muscle, which may account for the disparate signal intensities seen in our case (Fig. 5) [24].

As malignant neoplasms of the foot are less common than benign tumors are, they are frequently misdiagnosed clinically and may be inappropriately managed surgically [1]. Four patients with sarcomas were referred to our hospital with presumptive diagnoses of gout, hemangioma, ganglion cyst (Fig. 6), and lipoma (Fig. 7). If a malignant tumor is initially approached by marginal excision—the standard treatment for benign lesions, instead of careful preliminary incisional biopsy–then tumor dissemination is much more likely [1]. In our study, MR imaging correctly suggested sarcomas in 80% of malignant tumors on the basis of their peritendinous or periaponeurotic growth, infiltrative margins, and intermediate signal intensity on T2-weighted images.

Although we did not attempt specific histologic diagnoses of sarcomas, extensive peritendinous tumor growth in two cases strongly suggested synovial sarcoma [26]. Synovial sarcoma is the fourth most common soft-tissue sarcoma after malignant fibrous histiocytoma, liposarcoma, and rhabdomyosarcoma [26]. However, nearly one fourth of all synovial sarcomas occur in the foot and ankle region, whereas the more common sarcomas rarely or seldom occur there [26–28]. Accordingly, synovial sarcoma is probably the most common malignant soft-tissue tumor arising in the foot. The reported tendency for some synovial sarcomas to have benign-appearing well-defined margins at imaging [13, 22], as did one of our cases, most likely results from the slow growth of such lesions [26].

Clear cell sarcoma is a rare deep-seated neoplasm of uncertain histogenesis that usually affects young adults [29]. As nearly half of these tumors produce melanin, clear cell sarcoma also has been called malignant melanoma of soft parts [29]. However, unlike cutaneous melanoma, it nearly always arises in intimate association with tendons or aponeuroses. Melanin, present in two of our cases, causes paramagnetic relaxation enhancement of surrounding tissues with shortening of T1 and T2 values, resulting in higher intensity on T1-weighted images and lower intensity on T2-weighted images [30]. This effect was particularly apparent on MR images in our case with the larger amount of melanin by pathologic analysis (Fig. 7). The foot and ankle region is the most common site of clear cell sarcoma (43%), and one fourth of tumors in this region involve the heel [29]. Regional lymph node and pulmonary metastases are common, and bone and myocardial metastases occur also. Unlike in synovial sarcoma, calcification and secondary bone involvement are uncommon [29].

Clear cell sarcoma, plantar fibromatosis, aggressive fibromatosis, and pigmented villonodular synovitis comprise a subset of tumors with diffuse low signal intensity or prominent foci of low intensity on T2-weighted images. Although the causes of a shortened T2 relaxation time in these tumors are different, they should be considered when prominent low-intensity areas are found in a soft-tissue tumor in the foot. Furthermore, on the basis of a limited number of cases, our findings suggest that these tumors may often be differentiated by MR imaging.

Our study was confined to a specific and unique anatomic region, and our results cannot be generalized to soft-tissue tumors in all parts of the body. We encountered a limited variety of histologic tumor types, most of which had distinctive MR imaging features. These factors contributed to our success in characterizing tumors, in contradistinction to other studies that have shown the inability of MR imaging to characterize soft-tissue tumors [8, 9, 13, 14]. Our study suggests that, in the foot, there may be a large percentage of lesions with recognizable anatomic and MR imaging features that allow a specific diagnosis. However, the relative frequency of different foot tumors is not well known, and in a small series this could be a fortuitous finding. Results similar to ours have recently been reported in evaluating tumors of the hand and wrist by MR imaging [22]. Although our initial results are encouraging, we anticipate that additional tumors with atypical or indeterminate MR imaging features will be encountered as experience with imaging of the foot increases.

In summary, MR imaging appears to be accurate for determining the precise anatomic location and delineating the extent of soft-tissue tumors in the foot. Knowledge of tumor extent is important in surgical planning, and attention to the specific anatomic location of tumors may help characterize some of them. Despite the small size of our series and other limitations, it appears that MR imaging often suggests a specific diagnosis in certain benign soft-tissue tumors of the foot and may often correctly distinguish benign from malignant tumors.

REFERENCES

1. Enneking WF. Musculoskeletal tumor surgery. New York: Churchill Livingstone, **1983**:719-740
2. Wetzel LH, Levine E, Murphey MD. A comparison of MR imaging and CT in the evaluation of musculoskeletal masses. *RadioGraphics* **1987**;7: 851-874
3. Keigley BA, Haggar AM, Gaba A, Ellis BI, Froelich JW, Wu KK. Primary tumors of the foot: MR imaging. *Radiology* **1989**;171:755-759
4. Sartoris DJ, Resnick D. Magnetic resonance imaging of podiatric disorders: a pictorial essay. *J Foot Surg* **1987**;26:336-350
5. Wu KK. Synovial sarcoma of the foot. *J Foot Surg* **1987**;26:359-364
6. Sherry CS, Harms SE. MR evaluation of giant cell tumors of the tendon sheath. *Magn Reson Imaging* **1989**;7:195-201
7. Hudson TM, Hamlin DJ, Enneking WF, Pettersson H. Magnetic resonance imaging of bone and soft tissue tumors: early experience in 31 patients compared with computed tomography. *Skeletal Radiol* **1985**;13:134-146
8. Petasnick JP, Turner DA, Charters RJ, Citelis S, Zacharias CE. Soft tissue masses of the locomotor system: comparison of MR imaging with CT. *Radiology* **1986**;160:125-133
9. Sundaram M, McGuire MH, Herbold DR. Magnetic resonance imaging of soft tissue masses: an evaluation of fifty-three histologically proven tumors. *Magn Reson Imaging* **1988**;6:237-248
10. Demas BE, Heelan RT, Lane J, Marcove R, Hajdu S, Brennan MF. Soft-tissue sarcomas of the extremities: comparison of MR and CT in determining the extent of disease. *AJR* **1988**;150:615-620
11. Pettersson H, Gillespy T, Hamlin DJ, et al. Primary muscoloskeletal tumors: examination with MR imaging compared with conventional modalities. *Radiology* **1987**;164:237-241
12. Kinsella TJ, Loeffler JS, Fraass BA, Tepper J. Extremity preservation by combined modality therapy in sarcomas of the hand and foot: an analysis of local control, disease free survival and functional result. *Int J Radiat Oncol Biol Phys* **1983**;9:1115-1119
13. Kransdorf MJ, Jelinek JS, Moser RP, et al. Soft-tissue masses: diagnosis using MR imaging. *AJR* **1989**;153:541-547
14. Totty WG, Murphy WA, Lee JKT. Soft-tissue tumors: MR imaging. *Radiology* **1986**;160:135-141
15. Levine E, Wetzel LH, Neff JR. MR imaging and CT of extrahepatic cavernous hemangiomas. *AJR* **1986**;147:1299-1304
16. Kaplan PA, Williams SM. Mucocutaneous and peripheral soft-tissue hemangiomas: MR imaging. *Radiology* **1987**;163:163-166
17. Cohen EK, Kressel HY, Perosio T, et al. MR imaging of soft-tissue hemangiomas: correlation with pathologic findings. *AJR* **1988**;150: 1079-1081
18. Yuh WTC, Kathol MH, Sein MA, Ehara S, Chiu L. Hemangiomas of skeletal muscle: MR findings in five patients. *AJR* **1987**;149:765-768
19. Jelinek JS, Kransdorf MJ, Utz JA, et al. Imaging of pigmented villonodular synovitis with emphasis on MR imaging. *AJR* **1989**;152:337-342
20. Spritzer CE, Dalinka MK, Kressel HY. Magnetic resonance imaging of pigmented villonodular synovitis: a report of two cases. *Skeletal Radiol* **1987**;16:316-319
21. Kottal RA, Vogler JB, Matamoros A, Alexander AH, Cookson JL. Pigmented villonodular synovitis: a report of MR imaging in two cases. *Radiology* **1987**;163:551-553
22. Binkovitz LA, Berquist TH, McLeod RA. Masses of the hand and wrist: detection and characterization with MR imaging. *AJR* **1990**;154:323-326
23. Weiss KL, Beltran J, Lubbers LM. High-field MR surface-coil imaging of the hand and wrist. Part II. Pathologic correlations and clinical relevance. *Radiology* **1986**;160:147-152
24. Enzinger FM, Weiss SW. Fibromatoses. In: *Soft tissue tumors*, 2nd ed. St. Louis: Mosby, **1988**:136-163
25. Sundaram M, McGuire MH, Schajowicz F. Soft-tissue masses: histologic basis for decreased signal (short T2) on T2-weighted MR images. *AJR* **1987**;148:1247-1250
26. Enzinger FM, Weiss SW. Synovial sarcoma. In: *Soft tissue tumors*, 2nd ed. St. Louis: Mosby, **1988**:659-688
27. Kearney MM, Soule EH, Ivins JC. Malignant fibrous histiocytoma. *Cancer* **1980**;45:167-178
28. Owens JC, Shiu MH, Smith R, Hajdu SI. Soft tissue sarcomas of the hand and foot. *Cancer* **1985**;55:2010-2018
29. Enzinger FM, Weiss SW. Malignant tumors of uncertain histogenesis. In: *Soft tissue tumors*, 2nd ed. St. Louis: Mosby, **1988**:945-951
30. Gomori JM, Grossman RI, Shields JA, Augsburger JJ, Joseph PM, DeSimeone D. Choroidal melanomas: correlation of NMR spectroscopy and MR imaging. *Radiology* **1986**;158:443-445

Injury of the Achilles Tendon:
Diagnosis with Sonography

Franz M. Kainberger[1]
Alfred Engel[2]
Peter Barton[1]
Peter Huebsch[1]
Andreas Neuhold[3]
Erich Salomonowitz[4]

We determined the diagnostic accuracy of sonography for the assessment of injury to the Achilles tendon. After anatomic investigations in three human cadavers, we performed a clinical study in 24 healthy volunteers and 73 symptomatic patients referred for achillodynia or signs of heel thickening or both in whom a clinical diagnosis of acute total rupture was excluded. High-resolution real-time sonography was performed and the results were compared with final clinical diagnoses (55 patients) and surgical findings (18 patients). Fifty-two of the patients had been involved in various sporting activities (long-distance runners, jumpers, and basketball players), three patients had familial hypercholesterolemia, five patients had systemic inflammatory disease, and 13 patients had no known underlying cause. Anatomic investigation demonstrated accurate assessment of tendon structure and thickness. Sonograms were abnormal in 53 patients (sensitivity, 0.72; specificity, 0.83), and the extent of structural disorders of the tendon could be assessed properly. Abnormalities occurred in the form of tendon swelling (45%), abnormal tendon structure (42%), rupture (15%), and peritendinous lesions (47%). No changes were detected in low-grade disease of short duration, which suggests symptoms caused by functional disorders.

Sonography is valuable in the diagnosis of various lesions of the Achilles tendon and its surrounding tissue. Furthermore, it can be used to estimate the degree of tendon abnormality and to differentiate between functional and morphologic conditions.

***AJR* 155:1031–1036, November 1990**

Acute total ruptures of the Achilles tendon are easily diagnosed clinically [1]. However, complex chronic trauma or partial ruptures hamper the clinical examination and the sensitivity of clinical diagnosis is only about 0.7–0.8 [2]. Tendinitis and peritendinitis may result in a painful thickening of the heel that cannot be accurately differentiated by using clinical examination alone [1, 2]. Considerable delays in surgical treatment have been shown to significantly worsen the eventual outcome in these patients [1]. Therefore, a sensitive imaging tool is needed to predict the risk for tendon rupture and to institute specific therapy and training programs in sports medicine [3].

Low-kilovoltage radiography and xeroradiography only outline the silhouette of the tendon and substantial fluid accumulation in the surrounding tissue [4]. MR imaging, with its excellent soft-tissue contrast resolution and multiplanar capabilities, shows structural abnormalities and fluid accumulations that may be differentiated into hematomatous and nonsanguineous types. Since 1979, sonography has been suggested to demonstrate tendon rupture, alterations of tendon structure, and abnormalities of the peritendinous soft tissues [4–13].

In several of these studies preliminary results were reported, some of them based on small sample populations. Our objective was to determine the value of sonography in detecting abnormalities of the tendo Achillis, using the results of surgery and clinical follow-up to establish the final diagnosis.

Received March 19, 1990; accepted after revision June 7, 1990.

[1] Department of Diagnostic Radiology, Second Medical Clinic, University of Vienna, Garnisongasse 13, A-1090 Vienna, Austria. Address reprint requests to F. M. Kainberger.

[2] Orthopedic Clinic, University of Vienna, A-1090 Vienna, Austria.

[3] Department of Diagnostic Imaging, KA Rudolfinerhaus, Billrothstrasse 78, A-1090 Vienna, Austria.

[4] Central Institute of Diagnostic Radiology, University of Vienna, A-1090 Vienna, Austria.

0361-803X/90/1555-1031
© American Roentgen Ray Society

Subjects and Methods

We compared sonographic and macroscopic sagittal and transverse sections in three anatomic specimens. After obtaining the sonograms, anatomic sections were obtained with a cryomicrotome. Blocks of tissue were frozen and, as each millimeter of tissue was removed, a photograph was taken of the surface. Normal structure, contour, and diameters of the Achilles tendon and the peritendinous tissue and bursae were evaluated.

We investigated 73 symptomatic patients (54 men and 19 women 13-60 years old; mean age, 38 years) referred for achillodynia and/or thickening of the heel due to tendon enlargement or involvement of the peritendinous soft tissue. Achillodynia is defined as pain at the posterior part of the heel on flexion movements of the foot. Patients with a definite clinical diagnosis of acute total rupture were excluded from the study since clinical assessment is usually sufficient for starting proper therapy. The group consisted of 52 athletes (long-distance runners, jumpers, and basketball players) or patients involved in sporting activities when younger. Another three patients had extensive familial hypercholesterolemia, five patients had systemic inflammatory disease (rheumatoid arthritis in two, systemic lupus erythematosus in three), and 13 patients had no known underlying cause.

After informed consent, 24 healthy volunteers—most of them young athletes (17 men, seven women)—were examined as a control group.

We used McNemar's test to establish the value of sonography in comparison with clinical and surgical data and analysis of variance to test the relationship of tendon thickness between normal and abnormal individuals.

Clinical symptoms and signs were evaluated by experienced orthopedic surgeons or rheumatologists. Depending on the duration of achillodynia, patients were grouped into those with a history of complaints lasting (1) 2 months or less, (2) 2-12 months, and (3) longer than 1 year. Sensations of pain were evaluated, as were signs of swelling, which were documented as diffuse or circumscribed (swelling at the level of insertion of tendon or palpable nodules). Diagnosis of rupture was made by means of the Thompson test (in which pressure on the calf does not result in plantar flexion of the foot), assessed by an inability to stand on tiptoe or palpation of a localized groove.

At the time of diagnostic imaging, the final diagnoses and the results of other imaging techniques (low-kilovoltage radiography in 34 patients) were not known to any of the four investigators. We used linear phased-array and real-time sector scanners with frequencies of 5-10 MHz (Acuson, Mountain View, CA, and Advanced Technology Laboratories, Bothell, WA). The optimal focal zone of the transducer was placed at the level of the tendon. Patients were placed prone with their feet overhanging the end of the scanning table. If necessary, an acoustic standoff was placed on the skin (Kitecko, 3M, St. Louis, MO) to decrease artifacts in the near field. Documentation included sagittal imaging of the entire tendon and transverse sections. Comparison with the contralateral Achilles tendon and dynamic investigation during plantar and dorsiflexion also were done.

Variables evaluated included tendon swelling, abnormal tendon structure, and peritendinous lesions. Tendon thickness was measured on the anteroposterior scan with a neutral position of the talocrural joint. We used the shorter diameter at the point where the tendon was most thickened. Tendon structure was interpreted as abnormal when there was any disturbance of homogeneous structure in the form of hypoechoic signals with vanishing internal echoes, hyperechoic signals with or without inhomogeneity, or echogenic spots with acoustic shadowing indicating calcification. Analysis of the peritendinous tissue included defects of tendon contours, fluid accumulations, and estimated thickness of the subcutaneous tissue. Contour defects were described as abrupt narrowing of tendon diameter with irregular acoustic shadowing, undulating defects, and/or vanishing borders. Depending on the anatomic location, hypoechoic fluid was interpreted as hematoma, bursitis, or fat pad necrosis. The superficial bursa of Achilles was not evaluated, as clinical findings are specific and diagnostic imaging is not needed.

We compared sonographic results with clinical outcomes in all 73 patients (one to four follow-up investigations within 1-17 months) and with operative diagnoses in 18 patients. A final clinical diagnosis of Achilles tendon injury due to mechanical stress was established if there was a typical clinical history with exaggeration of symptoms during walking or flexion maneuvers. Systemic inflammatory and metabolic diseases were confirmed by means of specific laboratory tests.

Repeated sonographic examinations were performed in 34 patients. Nine of the patients undergoing surgery had at least two postoperative sonographic examinations.

Results

Normal Anatomy

The Achilles tendon originates at the point where the posterior fascia of the triceps surae unites with the fibers of the soleus muscle. Its insertion at the midportion of the posterior aspect of the os calcis can be depicted as a strong echogenic border against the bone. The tendon flattens and covers the calcaneus like a cuff. In children, a broad layer of hyaline cartilage covers the posterior aspect of the calcaneus. With high-resolution equipment, the structure of the hyaline cartilage is hypoechoic with speckled hyperechoic foci that correspond to the calcified posterior epiphysis calcanei.

In the group of normal control subjects, all tendons showed a homogeneous fibrillar structure on sagittal scans (Fig. 1), with six to eight characteristic undulated lines of internal echoes that reflect the acoustic borders between twisted collagen fibrils and loose connective tissue permeating between fasicles. On transverse scans, they appeared in a honeycomb pattern. Tendon echogenicity depends on the angle between the sound beam and collagen fibers. Because of the normal convex course of the tendon, focal artifactual changes in echo texture are almost always visible and should not be mistaken for localized abnormality. The tendon is demarcated against the surrounding fatty tissue by its epitendineum, which is visible as an echogenic line. Its form is oval and may be ventrally concave and its orientation is generally oblique, with the transverse axis oriented from posterolateral to anteromedial. In some individuals, the tendon is subdivided by an echogenic septum, which may be visible sonographically and should not be misinterpreted as a sign of rupture.

Normal tendon thickness ranged from 4.0 to 6.7 mm (mean, 5.2 mm) in our group of 24 healthy adults. Those asymptomatic subjects with tendon thickness of more than 6 mm were involved in intensive sports activities suggesting physiologic adaptation to mechanical stress or beginning painless tendinitis.

The pretendinous fat pad, radiologically referred to as Kager's triangle, shows a mottled echo texture with a broad

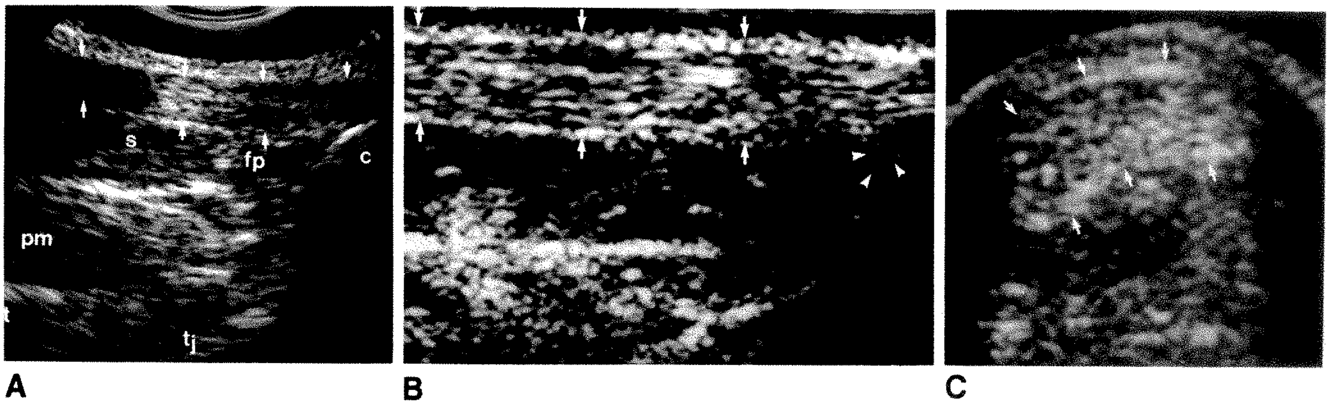

Fig. 1.—31-year-old healthy man.

A, Normal sonogram. Achilles tendon (*arrows*) originates from distal soleus muscle fibers (s), uniting with posterior fascia of triceps surae. With a sector scanner, which provides a larger field of view, typical amplification of tendon signals is visible in center of image. Tendon inserts at os calcis (c). Pre-Achilles fat pad structure (fp) varies among individuals. Anterior fascia of triceps surae muscle covers deep crural and peroneal muscles (pm), which run behind posterior aspect of tibia (t) and tibiotalar joint (tj).

B, Zoomed sagittal linear sonogram. Homogeneous linear structures within tendon correspond to collagen fibers. Tendon borders (*arrows*); normal sub-Achilles bursa (*arrowheads*).

C, Transverse sonogram. Oval tendon fibers (*arrows*) and loose connective tissue between fascicles appear in a honeycomb pattern.

spectrum of variation among people. Consequently, differentiation between normal structure and inflammatory swelling may not be possible. Together with the Achilles tendon it fills the distal part of the triceps surae compartment of the calf. Sometimes the tendon of the plantaris muscle is visible as a linear structure running through the distal part of the pre-Achilles fat pad, with its shape and course varying considerably. Ventrally, it ends at the deep layer of the crural fascia, which covers the flexor hallucis longus and the peroneus brevis muscles.

A crescent-shaped deep sub-Achilles bursa forms between the tendon and the upper posterior edge of the calcaneus. It was visible as a thin hypoechoic structure in all of the subjects examined. Its form depends on the amount of flexion and varies from person to person.

As the posterior epitendineum is the continuation of the superficial crural fascia, the Achilles tendon lies under the subcutaneous tissue. At the skin, an echogenic band delineates the acoustic border between coupling gel and skin. Echogenic structures below represent the epidermis and the corium with an indistinct border to the more hypoechoic subcutaneous tissue.

Pathologic Findings

Abnormalities (Table 1) were found in 53 patients. Sonographic detection had a sensitivity of 0.72 and a specificity of 0.83 (chi-square = 9375, $p = .002$). In 20 patients with Achilles tendon injury due to mechanical stress, no sonographic abnormalities were found. Retrospective analysis revealed that 14 of the 20 patients had achillodynia lasting not longer than 2 months. In none of these 14 cases were clinical signs of swelling detected or function tests abnormal, and in 11 patients the symptoms subsided within 4–8 weeks after the first onset of achillodynia. This suggests the complaints were due to functional disorders without structural derangements of the tendon and its surrounding tissue. Calculating the numbers excluding the group of patients with low-grade symptoms increased the sensitivity to 0.9. In nine cases, sonographic examination of the contralateral asymptomatic heel revealed abnormalities in tendon structure that were not detected clinically. Thorough reexamination disclosed the source of former pain in the contralateral heel in seven patients.

Tendinitis and tendon necrosis.—Changes were found in 32 patients who had one or more than one of the following abnormalities.

Focal or diffuse thickening of the tendon occurred in 24 (45%) of 53 patients. There was a significant difference ($p = .0001$ with alpha = 0.05) between tendon thickness in normal control subjects (4.0–6.7 mm; mean, 5.15), patients with Achilles tendon injury without operation (4.0–14 mm; mean, 7.58), and postoperative patients (7.0–15.0 mm; mean, 10.43 mm).

Tendon structure was altered in 22 patients (42%), and the degree of tendon abnormalities could be estimated. Focal hypoechoic lesions generally occurred 2–5 cm above the calcaneus in the medioventral part of the tendon. In four patients, surgery disclosed focal necrosis. Extensive inhomogeneity of tendon structure indicating chronic tendinitis was observed in 13 cases. It occurred in seven of the surgically treated patients and four of those with a ruptured tendon.

Calcifications at the site of insertion were found in three patients and could also be seen on lateral radiographs. In four patients, tiny intratendinous echogenicities with acoustic shadowing suggesting focal abnormalities with the beginning of little calcifications were invisible on corresponding radiographs.

Tendon lesions of patients with systemic metabolic or inflammatory disease could not be differentiated from tendinitis resulting from mechanical stress. In the two patients with rheumatoid arthritis, no calcaneal erosions were seen, nor

TABLE 1: Correlation of Sonography with Duration of Symptoms and Surgical Findings

Sonographic Result	No. of Patients		
	All Patients	With Symptoms of 2 mo or Longer	Surgical Correlation
True positive	53	53	17
False positive	4	4	0
True negative	20	20	0
False negative	20	6	1
Total	97[a]	83[b]	18

[a] Sensitivity = 0.72; specificity = 0.83.
[b] Sensitivity = 0.90; specificity = 0.83.

were erosions visible on other radiographs. A hypoechoic oval lesion was seen in one, connected to the tibiotalar articulation, corresponding to joint effusion. In two of the three patients with familial hypercholesterolemia, type II, thickened echogenic tendons were found bilaterally.

Peritendinous lesions.—Changes in the peritendinous tissue were found in 25 (47%) of 53 patients. Defects in tendon contour indicating acute peritendinitis showed poorly defined borders with the surrounding tissue, with or without semicircular fluid accumulations. Peritendinous swelling could be estimated by the thickening of the subcutaneous tissue. However, in four patients, the clinical sign of edematous swelling of the heel was invisible on sonography, probably because of compression effects from the transducer during investigation. In one patient, a hypoechoic tumor shown compressing the tendon was surgically proved to be a cutaneous fibroma.

Anterior Achilles bursitis (Albert disease) was found in four patients. In two of them a round or oval hypoechoic lesion (Fig. 2) could be documented, suggesting an intrabursal fluid collection. In the other two patients only indirect signs of hypoechoic transformation of adjoining tendon fibers were seen and there was no enlargement of the bursa. In two patients, sonographically guided intrabursal injection of a soluble corticosteroid was effective in relieving the symptoms; sonographic follow-up studies after 1 month showed a normal tendon.

Tendon rupture and postoperative changes.—Incomplete tendon ruptures were diagnosed in eight (15%) of 53 patients. Six of them had recent rupture and showed one or more of the following sonographic signs: localized reduction of tendon diameter (five cases), contour defect (five cases), irregular acoustic shadowing (owing to rolled fibers in three patients), intra/peritendinous fluid (hematoma) of more than 1 cm in diameter (three cases), and thickening of the severed ends of the tendon (five patients).

All but two clinically diagnosed tendon ruptures were identified correctly with sonography. One partial rupture at the site of insertion of the soleus muscle was overlooked. In one patient, a false-positive diagnosis of rerupture was made on the basis of a bizarre hyperechoic strand of soft tissue that had been used by the orthopedic surgeon to bridge the defect. Conversely, two clinically occult ruptures were detected with sonography. They were overlooked by the clinician because a dense fibrous scar and granulomatous tissue masked the defect (Fig. 3).

Old ruptures were diagnosed in two of the eight patients who had a positive Thompson test and had experienced trauma 8 and 17 weeks earlier, respectively. With sonography, a characteristic cuff of hypoechoic and inhomogeneous echoes (Fig. 4) surrounded the torn tendon, indicating repair with granulomatous tissue.

One to four postoperative sonographic follow-up studies were performed in nine patients. A thickened inhomogeneous tendon was found in seven patients and did not change during 4–16 months. The two patients without tendon thickening had undergone surgery for peritendinous abnormalities (one focal necrosis due to instillation of a corticosteroid, as reported previously [5]), and complete restitution could be demonstrated. Intratendinous sutures were visible in two cases in the form of echogenic lines and spots. In five patients, a flattened upper posterior edge of the calcaneus indicated operative removal of a prominent bursal projection.

Discussion

The most common cause of achillodynia is degeneration of tendon fibers due to mechanical stess. Metabolic diseases (hypercholesterolemia and disorders in steroid metabolism, particularly Cushing syndrome) and weakening due to systemic inflammatory diseases such as rheumatoid arthritis, psoriasis, Reiter syndrome, ankylosing spondylitis, juvenile chronic arthritis, and gout are uncommon causes [1]. Experimental and clinical studies [1] show that a normal tendon ruptures only from an extreme pulling force (4.3–9.12 kN) or after pretraumatic degeneration. Therefore, most ruptures occur because of predisposing destruction of tendon texture, as suggested by pathologists. Localized hypovascularization [14] and asynchronous rubbing of inadequately weaved collagen bundles [15] have been proposed to cause circumscribed degeneration and increase the risk of rupture. The clinical term achillodynia summarizes at least five different

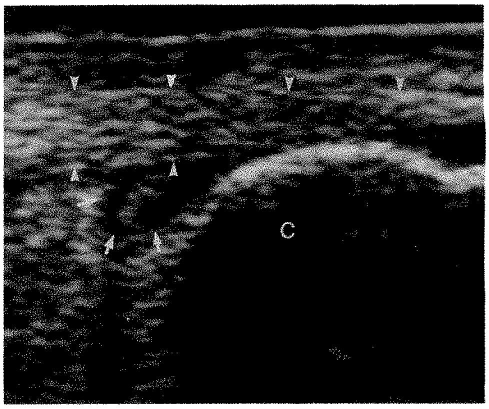

Fig. 2.—53-year-old man. Sagittal sonogram shows enlarged sub-Achilles bursa containing some fluid (*arrows*) in angle between os calcis (c) and Achilles tendon (*arrowheads*).

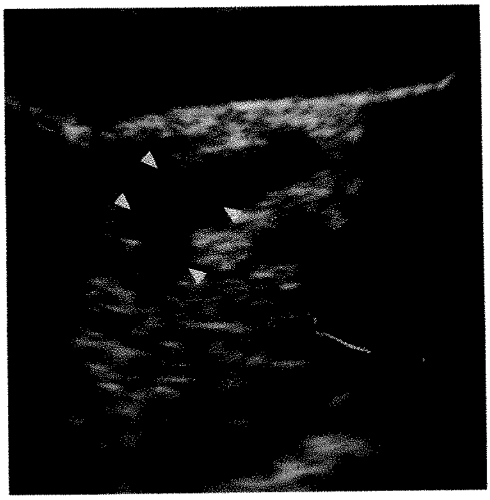

Fig. 3.—42-year-old male jogger. Transverse sonogram shows anechoic tendon defect (*arrowheads*). Surgery disclosed partial rupture (overlooked clinically because of extensive peritendinous fibrosis).

3

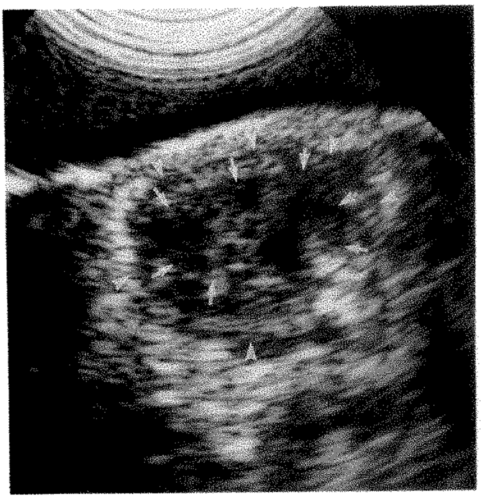

Fig. 4.—35-year-old male athlete. Transverse sonogram shows typical cuff of scar tissue in old rupture not treated surgically. Inhomogeneous tendon thickening (*arrows*) is surrounded by echogenic granulomatous tissue (*arrowheads*).

4

morphologic entities (tendinitis, peritendinitis, inflammation of the deep or superficial bursa of Achilles, and enthesopathy at the tendon insertion). Differentiation among them is necessary for adequate treatment but is not always possible with clinical investigation alone [1, 4].

Tendon structure is seen sonographically in the form of linear echoes representing acoustic borders between collagen fibers and loose connective tissue permeating between fascicles. On the basis of the phenomenon of acousic fiber anisotropy as described by Dussik et al. [16], tendon echogenicity is angle-dependent. Crass et al. [17] found that tendons appear hypoechoic when scanned at an angle greater than 2–7°. They would become hyperechoic at smaller angles. With a sector transducer or when studying the somewhat curved Achilles tendon, circumscribed, angle-dependent, artifactual inhomogeneities of tendon structure almost always occur. They should not be mistaken for focal tendinitis. At the site of interdigitation of soleus muscle fibers with the tendon, small hypoechoic spots may appear [10] that reflect a special form of angle-dependent tendon echogenicity. All non-artifactual disturbances of homogeneous tendon structure indicate abnormality. We interpret small hypoechoic nodules, corresponding to "nodular tendinitis" [4], to be the correlate of areas of focal degeneration with unmasking of collagen fibers [1, 18]. Their typical echogenic appearance may be influenced by the amount of water stored by the proteoglycans [18]. The hypoechoic nodules are the earliest form of tendinitis without tendon thickening and are the possible site of initiation of tendon rupture. Tiny calcifications may be detected earlier with sonography than with plain film radiology.

Eleven of the 20 symptomatic patients without evidence of abnormal sonographic findings had had achillodynia for less than 2 months. This suggests the diagnosis of tenalgia, which is defined as functional disorders of the dorsal muscle apparatus of the leg without evidence of morphologic alterations [19], predicting a good result with conservative therapy. Our results correspond to those reported by Mathieson et al. [10], who describe all patients with normal sonographic findings as recovered completely with conservative treatment in less than 4 months.

In xanthomatosis, large amounts of cholesterol may be deposited in the tendon. In two of our patients, tendon thickening and inhomogeneity of tendon structure could be documented. Although these findings seem to be nonspecific for hyperlipoproteinemia, type II, sonography can be used to monitor patients with this disease [13].

Tendon thickness can be determined exactly. Consequently, palpable nodules may be assigned as intratendinous or originating from the epitendineum. In accordance with Fornage [4], we measured tendon size by using the shorter diameter on transverse scans in order not to overestimate the true transverse diameter of the obliquely oriented Achilles tendon. As focal swelling may occur [1, 4], we measured tendon thickness at the level of its widest diameter. Measuring at the standard level 1 cm above the superior calcaneal surface may lead to false-negative findings. We assume divergent interpretations in the literature concerning the value of tendon diameter are due to different ways of taking the measurements [4, 10, 13].

Peritendinitis manifests itself as tendon contour alteration and soft-tissue thickening, which may be estimated by the amount of subcutaneous tissue swelling. However, compression effects from the transducer may hide peritendinitis. Several of the false-negative sonographic findings in our series may be from peritendinous edema or tiny fibrous strands at the tendon border. Fluid accumulation around the tendon may occur with peritendinitis, as a result of tendon rupture or as an indication of necrosis of the pre-Achilles fat pad. Cutaneous lesions may be demonstrated and their extension, such as compression of the tendon surface or invasiveness, determined. With modern high-resolution equipment, the normal retrocalaneal bursa is always visible. Variations between subjects may account for difficulties in demonstrating inflammation in the generally flattened or wrinkled bursa [20]. There-

TABLE 2: Summary of Sonographic Findings in the Literature

Study	Year	*n*	Rupture (%)	Tendinous Lesions (%)		Peritendinous Lesions (%)[a]
				Tendon Swelling	Abnormal Structure	
Mayer et al. [6]	1984	16	63	NE	NE	NE
Fornage [4]	1986	67	13	42	49	NE
Maffulli et al. [7]	1987	47	NE	51[b]	–	40
Laine et al. [8]	1987	38	37	NE	13	71
Milbradt et al. [9]	1988	86	30	+	+	+
Mathieson et al. [10]	1988	20	15	15	15	35
Merk [11]	1989	91	13	22[b]	–	35
Present study	1990	97	15	45	42	47

Note.—The discrepancies in demonstrated ruptures are attributed to different study design. NE = not evaluated; + = positive findings.

[a] Includes defects of tendon contour.

[b] Includes both tendon swelling and abnormal structure.

fore, bursitis will be detectable only with considerable fluid accumulation or on the basis of accompanying focal tendinitis in the vicinity of the bursa. Sonographically guided injection of a corticosteroid into the bursa with exact positioning of the needle may avoid intratendinous installation, which has a high risk of tendon necrosis [1].

Our results and those of others show that tendinitis, peritendinous lesions, and rupture may be determined properly with the help of sonography (Table 2). Signs of focal tendinitis were found accidentally in nine cases in the contralateral heels. This supports the high value of sonography in detecting abnormalities of tendon structure. Peritendinous changes can be diagnosed only on the basis of semicircular fluid accumulation or considerable fibrous scars. Edema of the peritendinous tissue is assessed to better advantage with clinical examination; tiny fibrous strands may be missed by either method. Equivocal symptoms and signs of incomplete or old rupture can be specified with the help of sonography.

With plain films and xeroradiographs, internal anatomy of the tendon is poorly delineated [4]. The sensitivity of these methods in depicting ruptures is very low, and diagnosis of tendons at higher risk of rupture is based merely on indirect signs [3,20]. Opacification of Kager's triangle is visible only with considerable fluid accumulation. However, films should be exposed to prove or rule out bony fracure with accompanying ruptures. Furthermore, radiographic techniques may be useful in evaluating Haglund syndrome, which is the result of a prominent bursal projection of the calcaneus, and in detecting calcaneal spurs or calcifications [3, 20].

Therefore, high-resolution sonography should play a central role in imaging the Achilles tendon. It helps in classifying different nosologic entities included under the term achillodynia. Sonography specifies the clinical diagnosis and may reduce delay in treatment. A normal sonogram in a symptomatic patient with a short duration of achillodynia will reliably predict a successful response to conservative treatment and aid in establishing proper training programs. Clinically occult ruptures may be detected [4, 10]. Because of the possibility of a false-negative result in diagnosing peritendinous edema, a combined clinical and sonographic evaluation is mandatory.

REFERENCES

1. Schoenbauer HR. Diseases of the Achilles tendon. *Wien Klin Wochenschr Suppl* **1986**; 98[168]:1–47
2. Ingliss AE, Scott WN, Sculco TP, Patterson AH. Ruptures of the tendo Achilles. *J Bone Joint Surg [Am]* **1976**; 58-A:990–993
3. Pavlov H, Torg JS. *The running athlete: roentgenograms and remedies*. New York: Year Book Medical, **1987**:95–111
4. Fornage BD. Achilles tendon: US examination. *Radiology* **1986**; 159: 759–764
5. Kainberger F, Fruehwald F, Engel A, Windhager R, Schwaighofer B, Seidl G. Sonography of the tendo Achilles and its bursa. *ROFO* **1988**; 148: 394–397
6. Mayer R, Wilhelm K, Pfeifer KJ. Ultrasound examination of subcutaneous Achilles tendon rupture. *Digitale Bilddiagn* **1984**; 4:185–189
7. Maffulli N, Regine R, Angelillo M, Capasso G, Filice S. Ultrasound diagnosis of Achilles tendon pathology in runners. *Br J Sports Med* **1987**; 21: 158–162
8. Laine HR, Harjula ALJ, Peltokallio P. Ultrasonography as a differential diagnostic aid in achillodynia. *J Ultrasound Med* **1987**; 6:351–362
9. Milbradt H, Reimer P, Thermann H. Sonomorphology of the normal Achilles tendon and the pattern of pathological changes. *Radiologe* **1988**; 28:330–333
10. Mathieson JR, Connell DG, Cooperberg PL, Lloyd-Smith DR. Sonography of the Achilles tendon and adjacent bursae. *AJR* **1988**; 151:127–131
11. Merk H. High-resolution real-time sonography in the diagnosis of lesions of Achilles tendon. *Ultraschall Med* **1989**; 10:192–197
12. Harcke HT, Grisson EL, Finkelstein MS. Evaluation of the musculoskeletal system with sonography. *AJR* **1988**; 150:1253–1261
13. Steinmetz A, Schmitt W, Schuler P, Kleinsorge F, Schneider J, Kaffarnik H. Ultrasonography of Achilles tendons in primary hypercholesterolemia. Comparison with computed tomography. *Atherosclerosis* **1988**; 74: 321–239
14. Lagergren C, Lindholm A. Vascular distribution in the Achilles tendon—an angiographic and microangiographic study. *Acta Chir Scand* **1959**; 116:491–495
15. Christensen IB. Rupture of the Achilles tendon, analysis of 57 cases. *Acta Chir Scand* **1953**; 106:50–56
16. Dussik KT, Fritch DJ, Kyriazidou M, Sear RS. Measurements of articular tissues with ultrasound. *Am J Phys Med Rehabil* **1958**; 37:160–165
17. Crass JR, van de Vegte GL, Harkavy LA. Tendon echogenicity: ex vivo study. *Radiology* **1988**; 167:499–501
18. Ruggeri A, Benazzo F. Collagen, proteoglycans and elastin interactions. In: Ruggeri A, Motta PM, eds. *Ultrastructure of connective tissue matrix*. The Hague, the Netherlands: Martinus Nijhoff, **1984**:113–120
19. Puddu G, Ippolito E, Postacchini F. A classification of Achilles tendon disease. *Am J Sports Med* **1976**; 4:145–149
20. Resnick D, Feingold ML, Curd J, Niwayama G, Goergen TG. Calcaneal abnormalities in articular disorders. *Radiology* **1977**; 125:355–366

Congenital Absence of a Cervical Spine Pedicle: Clinical and Radiologic Findings

M. David Wiener[1]
Salutario Martinez
David A. Forsberg

Congenital absence of a cervical pedicle is an unusual disorder with potentially confusing clinical and radiologic manifestations. A review of the previously reported 42 cases as well as 13 new cases is presented. Congenital absence of a cervical pedicle was an incidental finding in 10 of the 55 total patients (age range, 3–65 years; mean 31 years). The remainder presented with an array of symptoms; the most common was cervical pain (31 patients), often after trauma (19/31). Neurologic examination was normal in the majority (65%) of patients. The most common neurologic finding, in an additional 19% of patients, was isolated diminished sensation in an upper extremity. Imaging included conventional radiographs, tomograms, myelograms, and CT. The typical radiologic triad of findings included (1) the false appearance of an enlarged neural foramen owing to the absent pedicle; (2) a dysplastic, dorsally displaced ipsilateral articular pillar and lamina; and (3) a dysplastic ipsilateral transverse process. The spectrum of this disorder also included absence of the ipsilateral pillar in four of 55 patients and absence of the entire ipsilateral neural arch in five of 55 patients. Other osseous anomalies were present in 28 (51%) of 55 cases. In 10 of 55 cases, initial misdiagnosis resulted in inappropriate therapy, with a poor clinical outcome after therapy in three cases. Conservative therapy was the only successful management in all cases in which follow-up information was available, with the exception of one patient who had partial improvement after surgery.

Careful analysis of radiologic images and knowledge of the specific findings of absent cervical pedicle should decrease the potential for misdiagnosis and inappropriate, potentially harmful therapy.

AJR **155:1037–1041, November 1990**

Since the original description in 1946 by Hadley [1] of three patients with congenital absence of a cervical pedicle, 39 additional cases have been reported in the world literature [2–31]. Hadley described the associated findings on radiographs of absent cervical pedicle and concluded that the disorder alone was probably asymptomatic, though secondary degenerative changes may have contributed to symptoms of cervical pain in one of his patients. Eight subsequent reports detailed misdiagnoses based on the radiologic findings and consequent misguided therapy, including radiation and surgical exploration for presumed tumor [3, 11, 14, 24] and application of a cervical halo and traction under general anesthesia for presumed facet fracture-dislocation [7, 14, 27, 29]. We report an additional 13 cases and review the clinical and radiologic spectrum of findings, including those on radiographs, tomograms, myelograms, and CT.

Materials and Methods

The available medical records and radiologic images of 13 patients in whom absent cervical pedicle was diagnosed at our institution during a 13-year period were reviewed retrospectively. In addition, the 42 previously reported cases in the world literature were reviewed. The medical records and reported case histories were examined for patient age, sex, presenting

Received April 2, 1990; accepted after revision June 7, 1990.

[1] All authors: Department of Radiology, Box 3808, Duke University Medical Center, Durham, NC 27710. Address reprint requests to S. Martinez.

0361-803X/90/1555-1037
© American Roentgen Ray Society

symptoms, neurologic examination, clinical diagnosis, specific therapy, and therapeutic outcome. Imaging of the 13 patients seen at our institution included anteroposterior, lateral, and oblique radiographs of the cervical spine in all patients, coronal and sagittal tomography in five, myelography in three, and CT in three. The diagnostic images of our patients and those described in the literature were evaluated for location of the absent pedicle, spectrum of the anomaly (i.e., absent ipsilateral pillar or lamina), associated dysplastic and degenerative changes in the cervical spine, and the contribution of the different imaging techniques.

Results

Clinical Presentation

Fifty-five patients with absent cervical pedicle were reviewed. Medical records were not available for one patient seen at our institution. The remaining 54 included 32 males and 22 females 3–64 years old (mean age, 31). Ten patients had no complaints referable to the cervical spine or upper extremities at the time of incidental radiologic diagnosis of absent cervical pedicle. Thirty-one patients had cervical pain, often after trauma (19/31) and often with radiation of pain, numbness, or tingling to one or both upper extremities (17/31) or associated headache (6/31). Ten patients had isolated upper extremity symptoms, and an isolated headache [22], torticollis [13], and a "popping sensation" with neck motion were each reported by one patient.

Of the 43 patients for whom the results of a neurologic examination were available, 28 (65%) had no abnormalities other than cervical tenderness or slight limitation of motion, nine (21%) had subjective diminished sensation over a distal upper extremity, one (2%) had hyperalgesia confined to a cervical dermatome [22], one had an isolated brisk unilateral knee jerk [7], and one had triceps weakness that progressed to atrophy [9]. One patient with multiple other congenital anomalies of the cervical spine had decreased upper extremity muscle strength [19], another patient with an Arnold-Chiari malformation and syringomyelia had upper extremity muscle atrophy [14], and one patient with a herniated cervical disk had motor and sensory radicular findings [10].

Diagnostic Imaging

In our study group of 13 patients, absent cervical pedicle occurred most commonly at C6 (five of 13 cases; four left, one right). Other involved levels included C2 (one right), C3 (one right, one left), C5 (one right), and C7 (three right, one left). All of our cases were unilateral.

Combining imaging results from our 13 cases and the 42 previously reported cases, absent cervical pedicle occurred most often at the C6 level (23 of 55 cases; 13 left, 10 right) and next most often at the C5 level (14 of 55 cases; 10 left, four right), though it was found at all levels from C2 through C7 (including one patient with bilateral absent pedicles at C2 through C7 [19]). The ipsilateral articular pillar was absent in four of 55 cases and the entire ipsilateral neural arch was absent in five of 55 cases. Other associated osseous anomalies of the cervical spine were present in 28 (51%) of 55 patients. These anomalies included spina bifida occulta at the absent pedicle level in nine patients, other hypoplastic pedicles in nine, vertebral body fusion in five, vertebral arch fusion in two, anomalies of the atlas in two, spondylolysis at another cervical level in one, and sagittal vertebral body cleft in one.

Radiologic Findings

The typical triad of radiologic findings (seen in eight of our 13 cases) included (1) the false appearance of an enlarged neural foramen owing to the absent pedicle; (2) a dysplastic, dorsally displaced ipsilateral articular pillar and lamina; and (3) a dysplastic ipsilateral transverse process.

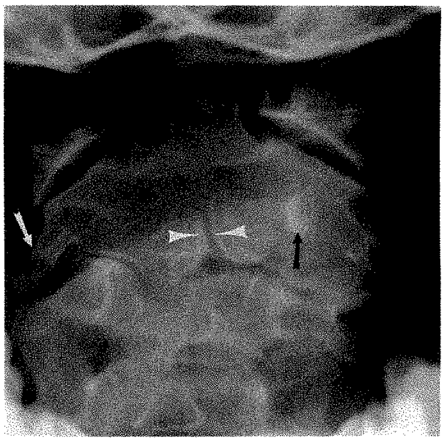

Fig. 1.—53-year-old man who had had cervical pain and numbness in his right hand for 2 years and no history of trauma. Anteroposterior radiograph shows congenital absence of right C2 pedicle as compared with normal left pedicle (*black arrow*), dysplastic right C2 transverse process (*white arrow*), and spina bifida (*arrowheads*).

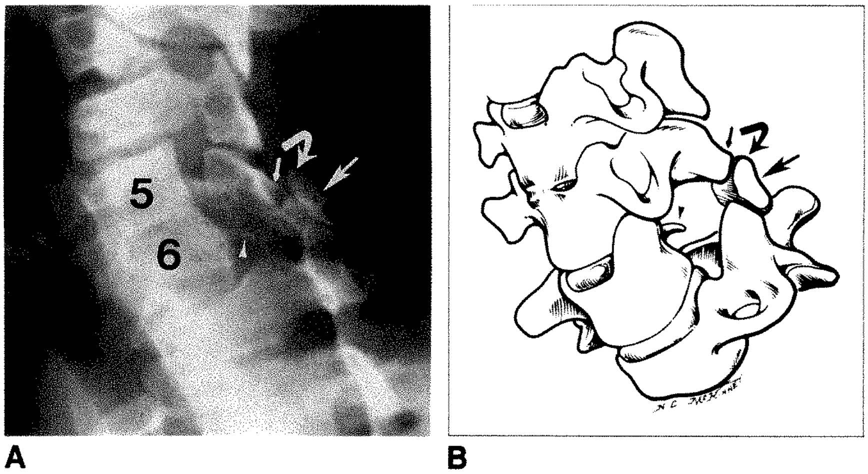

Fig. 2.—25-year-old man without cervical symptoms who was seen in the emergency department immediately after a motor vehicle accident.

***A* and *B*,** Right posterior oblique radiograph (*A*) and corresponding illustration (*B*) show absence of left C6 pedicle, with characteristic appearance of dorsally displaced ipsilateral articular pillar (*large straight arrows*) with its superior articular facet (*curved arrows*) situated dorsal to left C5 inferior articular facet (*small straight arrows*). Dysplastic left C6 transverse process is seen projecting through apparently enlarged neural foramen (*arrowheads*). There is partial fusion of C5 and C6 vertebral bodies.

Conventional Radiographs

Absence of the pedicle could be appreciated at the involved level on the anteroposterior view (Fig. 1), particularly when compared with the symmetric appearance of the pedicles projecting en face at other levels. The dysplastic, asymmetric transverse process could be identified, particularly at the lower cervical levels. Associated spina bifida was seen only on the anteroposterior view.

The lateral view was the least helpful view, as the appearance was often confusing and did not allow a specific diagnosis. Dorsal displacement of the ipsilateral pillar at the involved level (when present) usually could be appreciated, though the appearance suggested a unilateral facet dislocation. However, an important distinction was the absence of vertebral body anterolisthesis. Vertebral body fusion, when present, was recognized easily.

The contralateral posterior 45° oblique view (Fig. 2) was the most helpful and characteristic. Absence of the pedicle was recognized when compared with other levels, which resulted in the false appearance of an enlarged neural foramen actually representing the two adjacent neural foramina above and below the absent pedicular level. The dysplastic transverse process often could be identified projecting obliquely through the enlarged neural foramen. In the most common type of isolated absent cervical pedicle, the dorsally displaced, dysplastic articular pillar had a characteristic appearance. The superior articular facet was deficient, resulting in the pillar being situated dorsal to the inferior articular facet of the vertebra above. Secondary degenerative changes of the dysplastic facets were best defined by this view. Occasionally, associated laminar fusion also was identified, as was hypoplasia of pedicles or pillars at other levels.

With more severe dysplasia, absence of the ipsilateral pillar or the entire neural arch could be identified. In these cases, the inferior articular facet of the vertebra above and the superior articular facet of the vertebra below were hyperplastic and articulated with one another (Fig. 3).

Tomography

Tomograms in the coronal and sagittal planes more clearly outlined the described features of absent pedicle than did conventional radiographs alone and allowed confirmation of the specific diagnosis. No diagnostic features of absent cervical pedicle were unique to tomography, however.

CT

Axial CT most clearly revealed absence of the pedicle and the relatively horizontal and posterior orientation of the ipsilateral lamina (Fig. 4A). Also spina bifida was seen easily. The dorsally displaced articular pillar, with the dysplastic superior articular facet situated posterior to the inferior articular facet of the vertebra above, could mimic the "naked" facet sign [32] of facet dislocation on CT if the absent pedicle was not appreciated. Because of the axial plane of CT, the full morphology of the dysplastic pillar and any associated osseous fusion were not depicted as well as on oblique radiographs and sagittal tomography.

Myelography

In nine of 19 patients, myelography revealed a common dural sheath for the nerve roots at and below the level of the absent pedicle, which exited the common enlarged neural foramen together (Fig. 4B). No other myelographic abnormalities were unique to absent cervical pedicle.

Clinical Outcome

In three patients, other correct diagnoses were made that accounted for their neurologic symptoms, including a thoracic outlet syndrome [20], a herniated cervical disk [10], and an Arnold-Chiari malformation with syringomyelia [12]. The disorders in 11 of 55 patients were misdiagnosed initially as either facet fracture-dislocation (six patients) [7, 22, 27, 29], neoplasm (four patients) [3, 11, 19, 24], or herniated nucleus pulposus (one patient). Misdiagnosis resulted in inappropriate therapy in 10 of 11 patients, consisting of halo application with traction (five patients), exploratory surgery (four patients), and radiation (one patient). In three patients explored surgically, the postoperative course was poor [3, 24]; this occurred in one patient in our series who had perioperative cord ischemia with a resultant central cord syndrome. Decom-

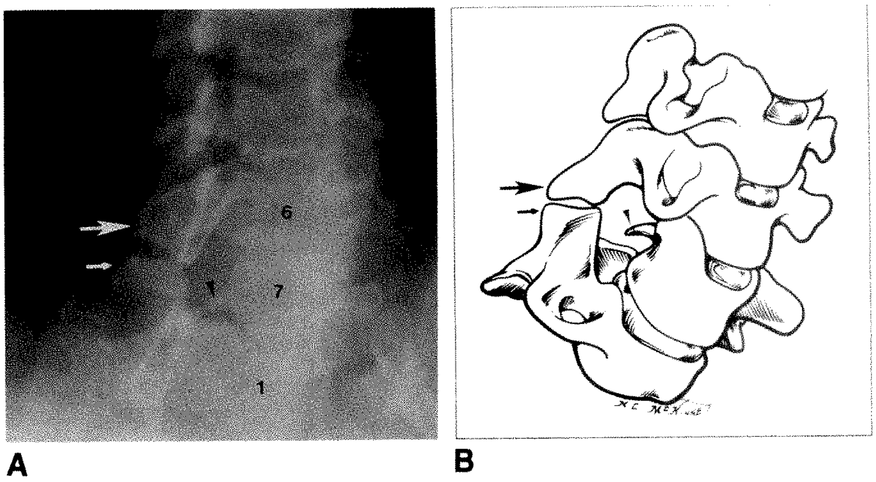

Fig. 3.—24-year-old man who had had cervical and left shoulder pain for 9 months and no history of trauma.

A and *B*, Left posterior oblique radiograph (*A*) and corresponding illustration (*B*) show absence of right C7 pedicle and articular pillar. Hyperplastic right superior articular facet of T1 (*small arrows*) articulates directly with hyperplastic inferior articular facet of C6 (*large arrows*). Dysplastic right C7 transverse process projects through apparently enlarged neural foramen (*arrowheads*).

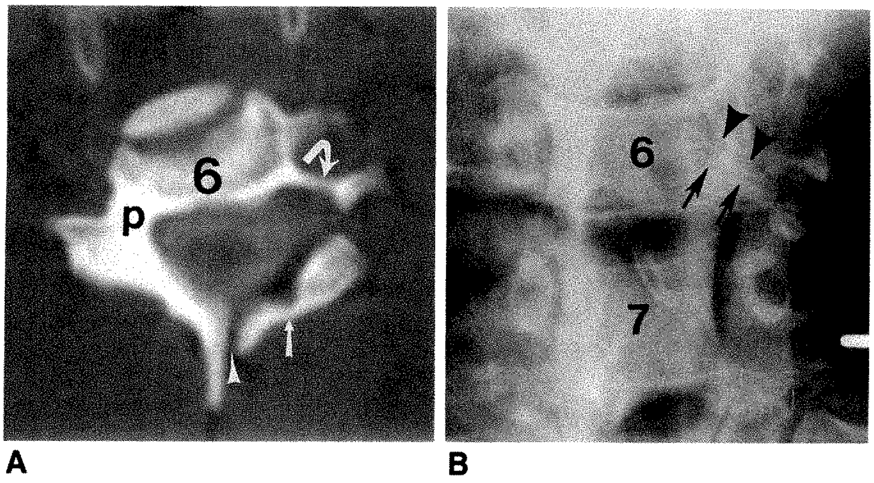

Fig. 4.—31-year-old man who had had cervical pain for 2 years after a traumatic hyperextension injury.

A, Axial CT image at level of C6 pedicle shows absence of left pedicle as compared with normal right pedicle (p). Left C6 lamina (*straight arrow*) is more posterior and horizontal in position than normal right C6 lamina. Also, spina bifida (*arrowhead*) and dysplastic left C6 transverse process (*curved arrow*) are present.

B, Anteroposterior view from cervical myelogram shows left C6 (*arrowheads*) and C7 (*arrows*) nerve roots exiting together via common dural sheath.

pressive laminectomies were performed in two patients with correct preoperative diagnoses, one without relief of symptoms [26] and the other with some improvement in symptoms [9].

In only one patient were symptoms thought to be directly attributable to a congenitally absent pedicle [9]. A 28-year-old woman had cervical pain associated with numbness and weakness of the right upper extremity and numbness of both lower extremities that had progressed for 2 months. Radiographs showed an absent C4 pedicle on the right with a spina bifida occulta at C4 resulting in an "unstable lamina." At surgery, the common dural investments of the right C4 and C5 nerve roots appeared stretched around the inferior surface of the dorsally displaced articular pillar of C4. The intraspinal portion of the pillar was removed, and 2 months later the patient reported only slight numbness of the feet and right hand.

No therapy or conservative therapy, consisting of rest, analgesics, muscle relaxants, and/or physical therapy, was successful in alleviating symptoms in all of the remaining 25 cases for which follow-up information was available.

Discussion

Unfamiliarity with the findings on radiographs in absent cervical pedicle probably contributed to the misdiagnoses in 11 of the 55 reported patients. The dominant radiologic features of absent cervical pedicle are a triad of findings: (1) the false appearance of an enlarged ipsilateral neural foramen owing to the absent pedicle; (2) a dysplastic, dorsally displaced ipsilateral articular pillar and lamina; and (3) a dysplastic ipsilateral transverse process (Figs. 1 and 2). On closer inspection, the superior articular facet of the dysplastic pillar is situated dorsal to the inferior articular facet of the vertebra above (Fig. 2). The pillars of the adjacent vertebrae may be hyperplastic in an effort to articulate with the deficient involved pillar. The extreme of this spectrum occurs when there is associated absence of the ipsilateral pillar or the entire ipsilateral posterior neural arch and the hyperplastic pillars of the adjacent two vertebrae articulate directly with one another (Fig. 3). Other osseous anomalies were present in 51% of cases and include spina bifida, vertebral body fusion, other hypoplastic pedicles, and vertebral arch fusion. Interestingly, hyperplasia of the contralateral pedicle at the involved level was not encountered, as is seen in absent or hypoplastic lumbar pedicle [32]. This difference probably is related to the lack of significant weight bearing on the cervical vertebrae.

The embryology of the vertebral spine is controversial. Not surprisingly, the pathogenesis of absent cervical pedicle is unknown. We think that this condition results from a total defect in formation of the pedicle, pedicle and pillar, or entire ipsilateral neural arch. This embryologic defect would be expected to occur during the early stages of development, either the blastema or chondrification phase, but before ossification takes place.

The differential diagnosis of an enlarged neural foramen includes a dumbbell neurofibroma, dural ectasia, neoplastic osseous destruction, surgical foraminotomy, and osseous erosion by a tortuous or aneurysmal vertebral artery [31]. None of these entities has the triad of radiologic findings seen in absent cervical pedicle. The most common misdiagnosis is of facet fracture-dislocation (6/55 cases). The appearance of the dysplastic, dorsally displaced pillar on initial inspection can mimic a facet fracture-dislocation, particularly on the lateral radiographs and CT images through the pillar. On axial CT, the appearance is similar to the naked facet sign of facet dislocation [33]. However, careful inspection of the anteroposterior and oblique radiographs, biplanar tomograms, and CT images at the pedicle level will reveal absence of the pedicle. Moreover, anterolisthesis, a common observation in patients with facet fracture-dislocation, is not seen with absent pedicle. A more rare differential diagnostic possibility is cervical spondylolysis, which often is confused with traumatic injury because this condition also includes a posteriorly positioned articular pillar and a hypoplastic pedicle. However, a well-marginated spondylolytic cleft in the articular pillar separating two triangular pillar fragments is a finding unique to spondylolysis [34].

Tomography and CT are useful only in confirming the diagnosis of absent cervical pedicle, which should at least be suspected on the basis of conventional radiographs alone. CT optimally shows the anomaly in a single axial plane (Fig. 4A), thereby excluding all other differential diagnostic possibilities. However, CT may be of limited value in assessing the full morphology of the dysplastic pillar. Although myelography can shown a common dural nerve root sheath at the involved level (Fig. 4B), its usefulness lies only in excluding the rare possibility of coexisting disk herniation [10]. MR now can usually supplant myelography. However, MR probably has little value in the initial diagnosis of absent cervical pedicle, as cortical bone detail is not well delineated by this technique.

In 10 cases, the radiologic finding of absent cervical pedicle was incidental. Of the remaining patients for whom clinical information was available, the most commonly encountered presenting symptom was cervical pain, often after trauma and sometimes associated with pain, numbness, and/or paresthesias of an upper extremity. Of greater importance in the evaluation of this group of patients were the overall benign results of the neurologic examination. Of the 43 patients for whom results were available, the examination was normal in 28 (65%). The most common abnormal finding in nine of the remaining 15 patients was a subjective decrease in sensation over a distal upper extremity. Only one author believed that neurologic symptoms in one patient were directly attributable to an absent cervical pedicle [9]. As previously outlined, this patient had associated spina bifida occulta at the level of the absent pedicle, resulting in an unstable pillar and lamina with intraoperative documentation of nerve root compression by the dysplastic pillar. On the other hand, three reports [3, 24, 26] concluded after surgical exploration that an absent cervical pedicle without evidence of nerve root compression accounted for the presenting symptoms. At surgery in each case, only loose areolar connective tissue was found within the enlarged neural foramen. Histologic analysis of this tissue in one patient was reported as "hyperplastic connective tissue" and was ascribed pathologic significance by Tiyaworabun et al. [24], though neither their patient nor the other two patients who underwent surgery experienced relief of symptoms after surgery. Although Hadley [1], in his original description of absent cervical pedicle, speculated that superimposed degenerative changes may have contributed to the neck pain in one patient, advanced degenerative changes were a distinctly unusual finding in only two previously reported cases [1, 4] and in one of our case. This absence of associated degenerative disease is at least in part related to the relatively young mean age at diagnosis, 31 years, but also further supports the benign nature of the anomaly. Though Brugman et al. [18] stated that the anomaly can cause some instability and can predispose to greater vulnerability in cases of trauma, there is no documentation among the 19 patients who related their symptoms to a specific traumatic event that significant neurologic injury resulted.

In conclusion, careful inspection of cervical spine radiographs with knowledge of the radiologic triad of findings in absent cervical pedicle should allow proper diagnosis in all cases. When plain films are inconclusive, tomography and CT will confirm the diagnosis. A prudent clinical course is suggested when the radiologic diagnosis of absent cervical pedicle is made. Cervical pain and/or radicular symptoms should not be attributed to the absent cervical pedicle per se until other causes are excluded. Even then, conservative nonoperative therapy is recommended, as it was successful in 96% of reported cases.

REFERENCES

1. Hadley LA. Congenital absence of pedicle from the cervical vertebrae. *AJR* **1946**;55:193–197
2. Perlman CR, Hawes LE. Cervical spondylolisthesis. *J Bone Joint Surg [Am]* **1951**;33-A:1012–1013
3. Steinback HL, Boldrey EB, Sooy FA. Congenital absence of the pedicle and superior facet from a cervical vertebrae. *Radiology* **1952**;59:838–840
4. Buetti C. Zur Rontgendiagnostik seltener Fehlbildungen der Halswirbelsaule. *Radiol Clin* (Basel) **1953**;22:141–161
5. Grasser BH, Klien E. Differentialdiagnose seltener Wirbelsaulenveranderungen. *Z Orthop* **1957**;88:550–553
6. Abel MS. Moderately severe whiplash injuries of the cervical spine and their rank and neurologic diagnosis. *Clin Orthop* **1958**;12:189–208
7. Zatz LM, Burgess PW, Hanbery JW. Agenesis of a pedicle in the cervical spine. *J Neurosurg* **1963**;20:564–569
8. Gaizler G. Fehlen einer Bogenwarzel an der Halswirbelsaule. *ROFO* **1963**;99:421–423
9. Wilson CB, Norrell HA. Congenital absence of a pedicle in the cervical spine. *AJR* **1966**;97:639–647
10. Louyot P, Gaucher A, Laxenaire M, Combebias JF. Agenesie du pedicule droit de la sixieme vertebre cervicale et syndrome radiculaire C7 par hernie discale. *Rev Rhum Mal Osteoartic* **1967**;34:276–279
11. Brocher J, Etter H. Eine komplexe Fehlbildung der Halswirbelsaule. *ROFO* **1967**;107:559–561
12. Oestreich AE, Young LW. The absent cervical pedicle syndrome: a case in childhood. *AJR* **1969**;106:505–510
13. Holland C, Stolle W. Fehlbildungen der Wirbelbogenreihe. *ROFO* **1970**; 112:120–122
14. McLoughlin DP, Wortzman G. Congenital absence of a cervical vertebral pedicle. *Can Assoc Radiol J* **1972**;23:195–200
15. Kanshepolsky J, Agnew D, Echols C, Hodak J. The missing cervical spine pedicle. *Bull Los Angeles Neurol Soc* **1973**;38:85–90
16. Danziger J, Jackson H, Bloch S. Congenital absence of a pedicle in a cervical vertebrae. *Clin Radiol* **1975**;26:53–56
17. Chapman N. Case report 6. *Skeletal Radiol* **1976**;1:65–66
18. Brugman E, Palmers Y, Staelens B. Congenital absence of a pedicle in the cervical spine: a new approach with CT scan. *Neuroradiology* **1979**;17: 121–125
19. Archer E, Batnitzky S, Franken EA, Muller J, Hale B. Congenital dysplasia of C2–6. *Pediatr Radiol* **1977**;6:121–122
20. Liliequist B. Absent cervical pedicle. *Acta Neurochir* (Wien) **1977**;38: 125–128
21. Gehweiler JA, Martinez S, Clark WM, Miller MD, Stewart GC. Spondylolisthesis of the axis vertebrae. *AJR* **1977**;128:682–684
22. Vencken LN. Absent pedicle in the cervical spine. *Radiol Clin* (Basel) **1978**;47:190–194
23. Lauten GJ, Wehunt WD. Computed tomography in absent cervical pedicle. *AJNR* **1980**;1:201–203
24. Tiyaworabun S, Beeko D, Bock WJ. Congenital absence of a pedicle in the cervical spine. *Acta Neurochir* (Wien) **1982**;61:303–317
25. Schwartz AM, Wechsler RJ, Landy MD, Wetzner SM, Goldstein SA. Posterior arch defects of the cervical spine. *Skeletal Radiol* **1982**;8: 135–139
26. Sakou T, Morizono Y. Congenital absence of a vertebral pedicle in the cervical spine. *Clin Orthop* **1983**;175:51–55
27. Cox HE, Bennett WF. Computed tomography of absent cervical pedicle. *J Comput Assist Tomogr* **1984**;8:537–539
28. Jamjocn ZB. Die Bogenwarzelagenesie in Cervikalbereich. *ROFO* **1987**;146:551–554
29. Van Dijk Azn R, Thigssen Hom, Merx JL, Lemmens Jam, Wackenhein A. The absent cervical pedicle syndrome. *Neuroradiology* **1987**;29:69–72
30. Douillet P, Lascaux JP, Faure C. Absence congenitale d'un pedicule vertebral. *J Radiol* **1977**;58:459–463
31. Schimmel DH, Newton PH, Mani J. Widening of the cervical intervertebral foramen. *Neuroradiology* **1976**;12:3–10
32. Wortzman G, Steinhardt MI. Congenitally absent lumbar pedicle: a reappraisal. *Radiology* **1984**;152:713–718
33. O'Callaghan JP, Ullrich CG, Yunn HA, Kieffer SA. CT of facet distraction in flexion injuries of the thoracolumbar spine: the "naked" facet. *AJNR* **1980**;1:97–102
34. Forsberg DA, Martinez S, Wiener MD, Vogler JB. Cervical spondylolysis: imaging findings in 12 patients. *AJR* **1990**;154:751–755

Book Review

New Techniques in Metabolic Bone Disease. By John C. Stevenson. Butterworths, Stoneham, MA: 287 pp., 1990. $175

This text has 17 chapters and 28 contributing authors, of whom 24 are from the United Kingdom. A broad range of topics includes physiology of bone cells, measurement of hormones, hormone replacement therapy, histomorphometry, neutron activation analysis, bone and collagen disorders, osteoporosis, osteomalacia, Paget disease, and physiology and function of parathyroid hormone. Chapters are likely to be of unequal interest, as they cover many different disciplines. The chapters most likely to be of interest to radiologists include "Photon Absorptiometric Techniques," "Computerized Axial Tomography in Bone Disease Measurements," "Magnetic Resonance Imaging of Bone Marrow," "The Pathogenesis, Prevention and Treatment of Osteoporosis," and "Current Problems with Rickets and Osteomalacia and Paget's Disease of Bone."

Twenty-five pages devoted to MR imaging of bone marrow seems an anomaly in a text discussing new techniques in metabolic bone disease. This chapter is well written in its own right but appears out of place in the context of the text. It is a chapter devoted to those diseases in which MR imaging has had strong clinical impact, such as primary bone tumors, metastatic disease, infection, infarction, and trauma. No surprises are found here and certainly no indication of any application, as yet, for MR imaging in metabolic or endocrine diseases of the skeleton. The chapters on photon absorptiometric techniques and CT in measurements of bone disease are succinct but not comprehensive reviews of the subject. The organization and chapters in this book derive their origin from a postgraduate course conducted by the main author and it is not meant to be a comprehensive text. Although it has several quite readable, well-written chapters, at $175, its value to radiologists, even for those with a special interest in metabolic bone disease, is limited.

Murali Sundaram
St. Louis University Medical Center
St. Louis, MO 63110-0250

Detection of Malignant Bone Tumors: MR Imaging vs Scintigraphy

Joseph A. Frank[1,2]
Alexander Ling[1,2]
Nicholas J. Patronas[1,2]
Jorge A. Carrasquillo[3]
Klara Horvath[1,2]
Ann M. Hickey[1]
Andrew J. Dwyer[1]

One hundred six patients with a known or suspected diagnosis of bone cancer (11 patients with biopsy-proved primary tumors, 95 patients with metastatic disease) were evaluated with scintigraphy and MR imaging to determine the relative sensitivity of each technique in the detection of bone disease. MR imaging was performed at 0.5 T as part of the entry evaluation into Intramural Research Board protocols (30%), for evaluation of cord compression, or because of an equivocal scintigram. MR was performed with T1-weighted (e.g., 300–500/10–20 [TR/TE]), T2-weighted (e.g., 2000/80) spin-echo (SE), and a short-TI inversion recovery (STIR) pulse sequence. Scintigrams were performed with ^{99m}Tc-methylene diphosphonate. A retrospective analysis showed that in 30 (28%) of 106 patients, MR imaging performed over a limited region of interest revealed a focal abnormality consistent with tumor that was not observed on scintigraphy. Only one patient had an abnormality on scintigraphy, caused by a metastasis, that was not found on MR images. In 73 (69%) of the 106 patients, the results of MR imaging and scintigraphy were equivalent; in 41 cases results of both techniques were normal. A McNemar analysis of the discordant cases showed MR imaging to be more sensitive than scintigraphy was ($p < .001$).

Our results suggest that although MR imaging has a greater sensitivity in detecting focal disease, scintigraphy is still the most useful screening test for evaluating the *entire* skeleton. MR imaging should be reserved for clarification of scintigraphic findings when suspicion is high for tumor.

***AJR* 155:1043–1048, November 1990**

Accurate evaluation of the presence and extent of malignant bone tumors, both primary and metastatic, is crucial to proper staging and treatment of these diseases. Various imaging techniques are available for the evaluation of bone metastases, including plain film radiographs, CT, scintigraphy, and MR imaging [1, 2]. Scintigraphy is the most commonly used imaging technique for the staging and evaluation of bone metastases [3, 4]. MR imaging has recently been shown to be a sensitive technique for the detection of tumor involvement within the bone; however, only a few studies have compared the findings on scintigraphy with those on MR imaging [5–9].

The purpose of this study was to determine the relative sensitivities of MR imaging and scintigraphy for detecting primary malignant bone tumors and bone metastases.

Materials and Methods

We retrospectively reviewed MR images and scintigrams obtained from 1986 to 1988 in 106 patients who were being considered for study or as part of entry criteria onto National Cancer Institute Intramural Research Board–approved protocols (32 patients) or who had clinically indicated follow-up examinations for spinal cord compression, focal pain, or equivocal findings on scintigraphy of the primary or metastatic disease (74 patients). Patients were included in this study only if MR imaging and scintigraphy were performed within 36 days of

Received March 5, 1990; accepted after revision June 4, 1990.

[1] Department of Diagnostic Radiology, Bldg. 10, Rm. 1C660, National Institutes of Health, Bethesda, MD 20892. Address reprint requests to J. A. Frank.

[2] Department of Radiology, Georgetown University Medical Center, Washington, DC 20007.

[3] Department of Nuclear Medicine, National Institutes of Health, Bethesda, MD 20892.

0361-803X/90/1555-1043
© American Roentgen Ray Society

each other. In more than 80% of the cases, MR imaging and scintigraphy were performed within 20 days of each other. In 64 (60%) of 106 patients, MR imaging was performed after scintigraphy, and in 13% of the patients, MR imaging and scintigraphy were performed on the same day. Patients and lesions were considered evaluable for this study only to the extent that comparable regions of anatomy were examined with scintigraphy and MR imaging (i.e., if the lumbar spine was examined for cord compression by MR imaging, the finding was compared only with the corresponding lumbar region on the scintigram). In 91 (86%) of the 106 patients, the comparison of the two techniques involved regions of the spine and pelvis, with the rest (14%) of the patients' examinations limited to examination of only the long bones in the upper and lower extremities.

The demographic data and distribution of the number of patients per tumor type are listed below. Forty-one males and 65 females ranged in age from 4 to 71 years (mean 41 ± 14 years). Most (90%) patients studied had proved or suspected metastatic tumor to the bone; the rest had a primary malignant tumor of bone or bone marrow. Twenty-three patients had breast cancer; 16 patients had lymphoma (both Hodgkin and non-Hodgkin); 15 patients had hypernephroma; 15 patients had various sarcomas; 13 patients had Ewing sarcoma; six patients had adenocarcinoma of the colon; four patients had melanoma; three patients had prostatic cancer; two patients had esophageal cancer; and one patient each had rectal cancer, adenocarcinoma with an unknown primary tumor, small-cell lung cancer, germ cell tumor, adrenal cell carcinoma, hepatoma, testicular cancer, non-small-cell lung cancer, and acute leukemia.

MR images were obtained on a 0.5-T Picker International Vista HP MR unit (Highland Heights, OH) by using a T1-weighted spin-echo (SE), 300-500/10-26 (TR/TE) sequence (SE 300/10), a T2-weighted sequence (SE 2000/80), and an inversion recovery (STIR) sequence (IR 1500/100) [10]. MR images were obtained in up to three planes, as dictated by the evaluation protocol. MR imaging was performed with 5- to 10-mm contiguous slices with fields of view from 20 to 50 cm and 128 phase-encoded steps, resulting in a 1-4 mm^2 pixel. MR images were displayed on a 256 × 256 image matrix.

Bone scans were obtained by using a gamma camera 2-3 hr after injection of ^{99m}Tc-methylene diphosphonate. Patients younger than 18 years old received 0.3 mCi/kg (11.1 MBq/kg), and all adults received 25 mCi (925 MBq).

MR images and scintigrams were reviewed separately by two to three radiologists who were blinded to findings of related imaging tests, then jointly reviewed and classified according to relative performance of corresponding images. Focal or diffuse areas with high signal intensity on T2-weighted or STIR images and low signal intensity on T1-weighted images relative to signal intensity of normal bone or bone marrow were considered abnormal when shown in two different scanning planes or two distinct pulse sequences. On scintigrams, areas of excess radiotracer uptake and photopenic areas were considered abnormal. Because many studies identified multiple lesions, these studies were considered positive only if they showed all abnormal foci identified by either MR imaging or scintigraphy. Scintigraphically detected lesions outside the field of view of the corresponding MR images were excluded. Lesions shown on the scans were confirmed with bone marrow biopsies, imaging studies, or documented clinical progression of response to therapy on follow-up bone scans or MR images. Most of the follow-up examinations were performed within 6 months of the MR imaging or scintigraphy compared in this study. Confirmation of lesions depicted by MR imaging and/or scintigraphy was sought only for patients whose scans were discordant, 33 (31%) of 106 patients. Follow-up studies, histologic confirmation, or both were available for 24 (73%) of 33 patients. The presumption made was that all focal lesions on scintigrams or MR images were considered tumor unless proved otherwise.

Patients whose MR imaging studies comprised only images of either the brain or liver were excluded from this study. MR imaging was not performed in the appropriate scanning plane or with breath-holding techniques to evaluate the ribs for tumor involvement. MR images of the head also were not included in the study.

Statistical analysis was performed by using a McNemar test [11]. The McNemar test is a useful method for comparing paired data or studies (i.e., the relative sensitivity of MR imaging and scintigraphy) in the detection of diffuse or focal involvement of the bone with tumor [11]. By using the McNemar test, we can assume that the patients serve as their own control subjects.

Results

The appearance of malignant lesions on MR images depends on the pulse sequence used. On T1-weighted images, tumors appear hypointense (i.e., dark) compared with the normal marrow (Figs. 1 and 2). On T2-weighted images, metastatic disease can appear isointense (i.e., similar in signal intensity) to normal marrow [12]. Focal lesions on the STIR images, because of the suppression of the fat signal, appeared bright and were easily differentiated from the red and yellow marrow [12-14] (Fig. 2 and 3).

In 41 (39%) of the 106 patients, no tumor involvement of the bone was detected in the regions of interest covered by both techniques. In 32 (30%) patients, both techniques had positive findings and showed similar anatomic distribution of the tumor involvement in the bone. MR imaging showed areas of presumed metastatic tumor involvement in the bone not observed on scintigraphy in 30 (28%) of the 106 patients. The distribution of the number of patients per tumor type is as follows: eight patients with breast cancer, six patients with various sarcomas, six patients with lymphoma, four patients with renal cell carcinoma, four patients with Ewing sarcoma, and one each with a germ cell tumor and leukemia. In 16 (53%) of these 30 cases in which MR imaging findings were positive and scintigraphic findings were negative, MR imaging was performed 1-35 days after scintigraphy either to resolve a focal clinical problem (i.e., pain, equivocal findings) or for the evaluation of cord compression. Twenty-one (70%) of the 30 patients in whom MR imaging findings were positive and scintigraphic findings were negative had follow-up imaging studies as a means of confirmation 0-6 months after the comparative studies (Fig. 1). Four of the 21 patients had biopsy-proved malignant tumors. In nine of these 30 patients, findings on scintigraphy were normal, whereas MR images showed focal areas of abnormal signal intensity that were presumed to be tumors; pathologic confirmation was not available. In almost all 30 cases, MR imaging was performed in the coronal or sagittal plane, which efficiently encompassed the greatest extent of bone at risk on a single image.

Scintigraphic findings were positive in two cases (Ewing sarcoma, colonic carcinoma) and indeterminate in one case (lymphoma) in which MR imaging findings were negative. Only one of these three cases (colonic carcinoma) was subsequently proved to be a metastatic lesion (Fig. 4) on the basis of follow-up imaging studies. The other two cases were considered clinically and radiologically compatible with stress or compression fractures.

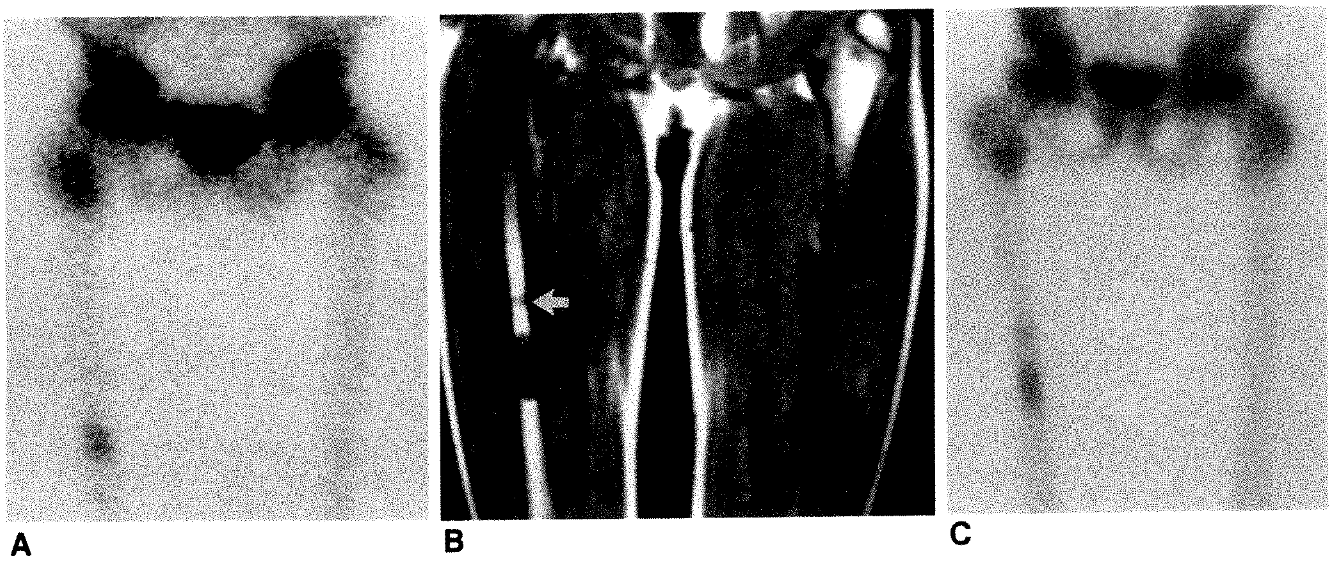

Fig. 1.—11-year-old boy initially presenting with a primary Ewing sarcoma of fibula. MR imaging showed another focus of tumor that was observed on scintigram obtained 3 months after initial examination.

A, Scintigram shows a solitary metastasis to right femoral diaphysis.

B, T1-weighted SE MR image, 300/26, obtained 11 days after scintigraphy clearly shows a smaller satellite lesion (*arrow*) and tumor in contralateral femur.

C, Scintigram obtained 3 months after initial scintigraphy shows second focus of tumor. Patient later died of diffuse metastatic Ewing sarcoma.

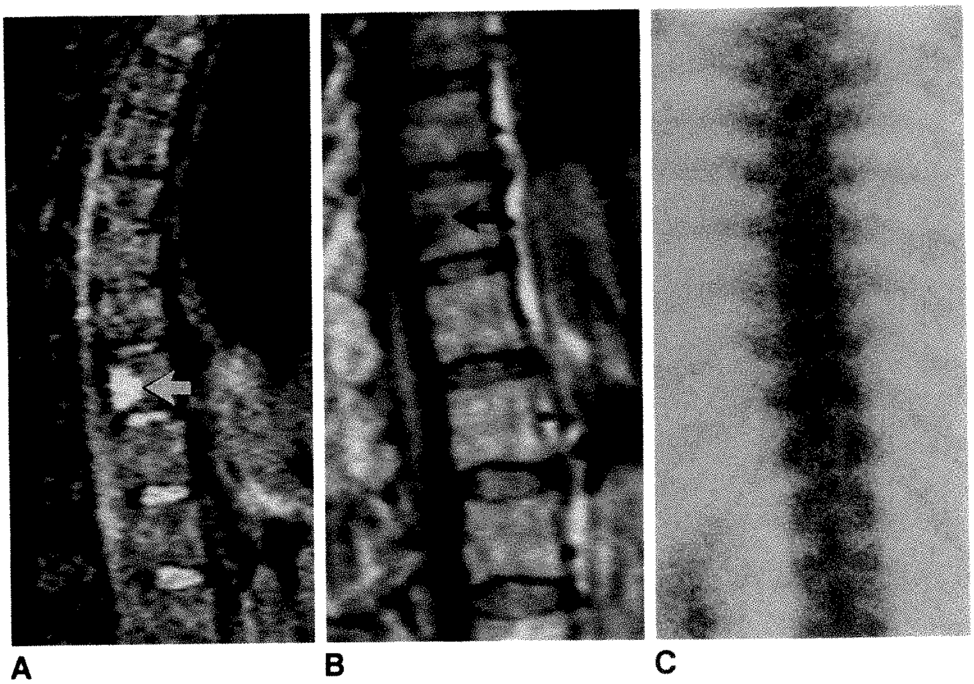

Fig. 2.—46-year-old man with renal cell carcinoma. MR imaging has greater sensitivity for metastases than scintigraphy does.

A and *B*, MR imaging performed as part of staging evaluation reveals vertebral lesion (*arrow*) on STIR (IR 1500/100) (*A*) and T1-weighted SE 433/26 (*B*) MR images.

C, Posterior scintigram obtained 1 day after MR imaging is normal.

The two-sided McNemar test demonstrated that the overall positive rates for a case-by-case analysis of MR imaging differed from scintigraphy at $p < .001$. The advantage of the McNemar test in the analysis of matched comparisons is its sole dependence on discordant cases (i.e., MR imaging findings positive, scintigraphic findings negative or MR imaging findings negative, scintigraphic findings positive). If we disregard the nine (30%) of 30 unconfirmed (either by biopsy or follow-up examination) cases in which MR imaging findings were positive and scintigraphic findings were negative, the relative sensitivity of MR imaging differed from that of scintigraphy at $p < .003$. As a worst case, MR imaging was shown to have a higher sensitivity than scintigraphy did for all bony lesions in patients at risk of metastatic disease.

Discussion

MR imaging has been shown to be sensitive for the detection of bone marrow metastases [5–10, 12, 13–16]. Normal red and yellow marrow can be distinguished on an MR image because of differences in signal intensity or morphology [16, 17]. A significant variety of diseased tissues (e.g., tumor, inflammation, and infection) have relaxation times that differ from normal marrow to a similar degree, resulting in similar appearances on MR images [14, 18–20] and a lack of histologic specificity. Scintigraphy is a sensitive but not specific imaging technique for the detection of malignant tumors because benign conditions such as degenerative joint disease, trauma, and infection can result in positive test results. The lack of histologic specificity stems from the mechanisms of isotope uptake ("hot spot") or lack of tracer uptake (photopenic) areas on the bone scan. Hot spots predominately reflect the pattern of bone response to a local insult, and focal decreases in skeletal tracer uptake result from bone destruction without repair [21].

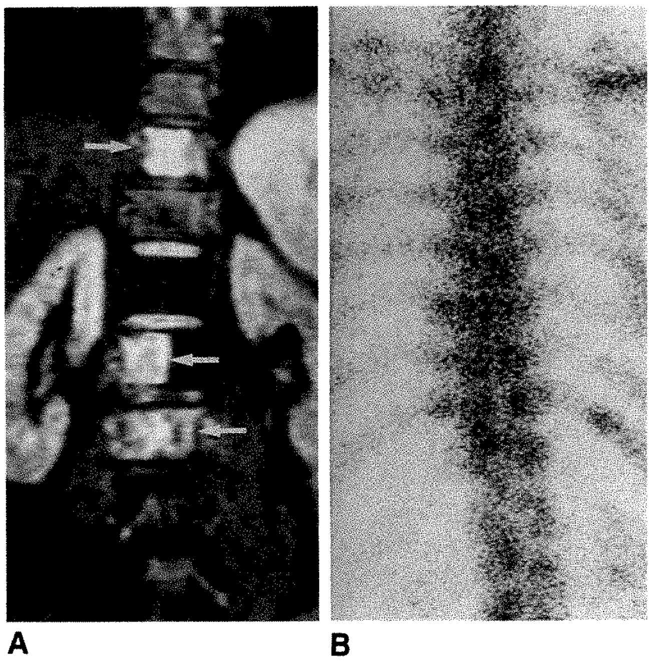

Fig. 3.—58-year-old man with nodular poorly differentiated lymphoma. MR imaging was performed as a basis for monitoring the patient's response to therapy.

A, Coronal STIR MR image obtained for evaluation of retroperitoneal adenopathy clearly shows multiple focal thoracolumbar vertebral lesions (*arrows*).

B, Posterior scintigram of spine obtained 2 days later is unremarkable. Rib lesion, not seen on MR, is evident.

We found MR imaging to be more sensitive than scintigraphy was for the detection and delineation of bone tumor. A possible explanation for MR imaging's superiority is that hematogenously seeded intramedullary metastasis produces detectable lesions by replacement of marrow. This occurs before either intrinsic or reactive metabolic changes in cancellous and cortical bone can be detected scintigraphically or radiologically. Usually, destruction of bony trabeculae and mobilization of osteoclastic reparative mechanisms are prerequisites for positive findings on a scintigram [21].

In a preliminary study examining the extent of bone marrow involvement in patients with small-cell lung carcinoma, 10 (42%) of 24 patients who were considered to have limited disease by standard staging criteria (including scintigraphy) had their stage of disease changed to extensive disease after MR imaging [9]. In these cases, focal or diffuse abnormalities in signal intensity were noted on T1-weighted images of the pelvis and proximal femur not observed on bone scans. In a study of 50 patients with malignant tumors and suspected skeletal involvement, MR imaging was shown to have a lower false-positive rate than scintigraphy and 100% sensitivity and specificity in patients with multiple myeloma with marrow

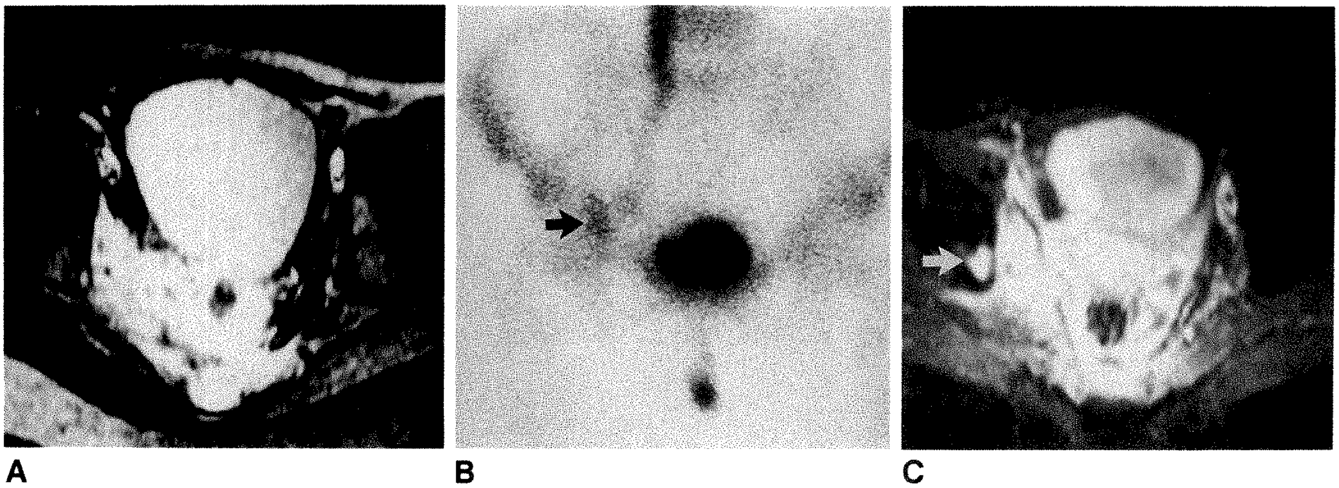

Fig. 4.—44-year-old man with metastatic adenocarcinoma of colon. This is only case in this series in which scintigraphy showed a malignant lesion before MR imaging.

A, STIR MR image fails to reveal posterior acetabulum lesion.

B, Scintigram made 1 month before MR image shows lesion (*arrow*).

C, MR image obtained 4 months after scintigraphy shows lesion (*arrow*).

involvement [6]. There are also reports of patients with lymphoma in whom MR imaging showed marrow involvement despite a normal iliac crest bone marrow biopsy [7, 8]. These studies support our results.

It could be argued that during the 36-day (maximum) interval between scintigraphy and MR imaging, a new malignant lesion could develop, which would result in positive findings for one scanning technique while the other showed negative findings. In addition, delay between the two studies might introduce a selection bias. In only nine of the 31 malignant cases in which the MR imaging findings differed from scintigraphy was there a delay of more than 20 days between the two examinations. Deleting these patients from the statistical analysis would not change the overall results of this study ($p < .003$). If an MR imaging examination was ordered or not obtained on the basis of results of a scintigram, then it is possible that the number of cases of positive scintigraphic/negative MR imaging findings reported may underestimate the true incidence of false-negative MR imaging examinations. In 16 (53%) of the 30 cases with negative scintigraphic findings and positive MR imaging findings, MR imaging was performed after scintigraphy. If these studies were excluded from the analysis, the sensitivity of MR imaging would differ from that of bone scanning at $p < .01$.

Under ideal circumstances, a comparison study would relate results of two imaging techniques to the true condition of a patient *at every lesion described by either test*. Unfortunately, although histology is a universally accepted estimate of "truth," percutaneous biopsy of even a single site, much less at every one of multiple sites, has not been possible in our population of patients. Noninvasive assessment through follow-up imaging studies, although frequently available in our series, is burdened by ambiguity—if a marrow lesion disappears during therapy, did it represent a metastasis or a focal site of "reconverted" red marrow responding to cytotoxic drugs or radiation? Observing progression toward a subsequently unambiguous state without treatment is universally feasible only in an animal study.

It is important to note that red marrow can have an appearance on MR images similar to focal or diffuse tumor involvement depending on lesion location and age of the patient. In patients with aplastic anemia, focal islands of hematopoietic marrow can have signal-intensity pattern and distribution mimicking metastatic disease [22]. We encountered insufficient numbers of patients with predominantly red marrow to establish whether our overall results would apply to this group [17]. Distinction between hyperplastic red marrow, particularly when focally deposited, and neoplasm may be difficult with MR imaging. Although only additional study of such patients can resolve this issue, behavior similar to that exhibited by metastases in response to therapy, that is, either replacement with fatty marrow [23] or overpopulation with hematopoietic elements (i.e., stress) after chemotherapy [24], also may complicate both experimental design and clinical diagnosis.

The high sensitivity of MR imaging in relation to that of scintigraphy by itself does not alter scintigraphy's role as the most useful screening examination for primary and metastatic disease. Scintigraphy examines 100% of the skeleton, is widely available, and at present is less expensive than MR imaging. The use of MR imaging to evaluate skeletal metastases is limited by its expense, lesser availability, and regional purview. Lesions of the ribs and skull were excluded from this study principally because so few images included them. However, rib metastases might prove difficult to show on MR images because of respiratory motion, paucity of at-risk tissue (red marrow), or lack of a convenient imaging plane (Fig. 3). Metastasis to the skull would normally be included on a separate MR imaging examination of the brain; these were not reviewed as part of this study.

Although MR imaging as currently practiced is not an efficient technique for screening the entire skeleton, we find it extremely valuable in clarifying equivocal or (suspected) falsely positive or negative bone scans. Because of MR imaging's inherent anatomic detail, we also may find it useful as a localization technique for directed biopsies of suspected lesions [5–8]. Future improvement in MR imaging techniques (e.g., development of faster scanning techniques or surface coils) may make MR imaging an efficient screening technique for detecting and staging bone marrow metastasis.

ACKNOWLEDGMENTS

The authors thank Anna Scheib for her preparation of the manuscript. In addition, the authors acknowledge the work of the MR technologists who performed the studies.

REFERENCES

1. Volger JB, Murphy WA. Bone marrow imaging. *Radiology* **1988**;168:679–693
2. Kagan AR, Bassett LW, Gold RH. Radiologic contributions to cancer management. *AJR* **1986**;147:305–312
3. McNeil BJ. Value of bone scanning in neoplastic disease. *Semin Nucl Med* **1984**;14:277–286
4. Krishnamurthy GT, Tubis M, Hiss J, Bland WH. Distribution pattern of metastatic bone disease: a need for total body skeletal image. *JAMA* **1977**;237:2504–2506
5. Khurana JS, Rosenthal DI, Rosenberg AE, Mankia HJ. Skeletal metastases in liposarcoma detectable only by magnetic resonance imaging. *Clin Orthop* **1989**;243:204–207
6. Daffner R, Lupetin A, Dash N, Beeb Z, Sefczek R, Shapiro R. MRI in the detection of malignant infiltration of bone marrow. *AJR* **1986**;146:353–358
7. Dohner H, Guckel F, Knauf W, et al. Magnetic resonance imaging of bone marrow in lymphoproliferative disorders: correlation with bone marrow biopsy. *Br J Haematol* **1989**;73:12–17
8. Linden A, Zankovich R, Theissen P, Diehl V, Schicha H. Malignant lymphoma: bone marrow imaging versus biopsy. *Radiology* **1989**;173:335–339
9. Carney DN, Redmond O, Harford P, Stark J, Ennis J. Bone marrow involvement (BMI) by small cell lung cancer (SCLC) using magnetic resonance imaging. *Proc Am Soc Clin Oncol* **1989**;8:228
10. Dwyer AJ, Frank JA, Sank VJ, et al. Short TI inversion recovery pulse sequence: analysis and initial experience in cancer imaging. *Radiology* **1988**;168:827–836
11. Conover WJ. *Practical nonparametric statistics*, 2nd ed. New York: Wiley, **1980**:130
12. Porter BA, Shields AF, Olson DO. Magnetic resonance imaging of bone marrow disorders. *Radiol Clin North Am* **1986**;24:269–289
13. Shields AF, Porter BA, Churchley S, et al. The detection of bone marrow involvement by lymphoma using magnetic resonance imaging. *J Clin Oncol* **1987**;5:225–230
14. Frank JA, Dwyer AJ, Doppman JL. Magnetic resonance imaging in oncology. In: DeVita VT, Hellman S, Rosenberg SA, eds. *Important advances in*

oncology 1987. Philadelphia: Lippincott, **1987**:133–174

15. Fruehwald FJ, Tscholakoff D, Schwaighofer B, et al. Magnetic resonance imaging of the lower vertebral column in patients with multiple myeloma. *Invest Radiol* **1988**;23:193–199
16. Smoker WRK, Godersky JC, Knutzon RK, Keyes WD, Norman D, Bergman W. The role of MR imaging in evaluating metastatic spinal disease. *AJR* **1987**;149:1241–1248
17. Kricun ME. Red-yellow marrow conversion: its effect on the location of solitary bone lesions. *Skeletal Radiol* **1985**;14:10–19
18. Unger E, Moldofsky P, Gatenby R, Hartz W, Broden G. Diagnosis of osteomyelitis by MR imaging. *Radiology* **1987**;164:449–454
19. Mitchell DG, Rao VM, Dalinku MK, et al. Femoral head avascular necrosis: correlation of MR imaging, radiographic staging, radionuclide imaging and clinical finding. *Radiology* **1987**;162:709–715
20. Modic MT, Masaryk TJ, Paushter D. Magnetic resonance imaging of the spine. *Radiol Clin North Am* **1986**;24:229–245
21. Charkes ND. Mechanisms of skeletal tracer uptake. *J Nucl Med* **1979**;20:794–795
22. Kaplan PA, Asleson RJ, Klassen LW, Duggan MJ. Bone marrow patterns in aplastic anemia: observations with 1.5T MR imaging. *Radiology* **1987**;164:441–444
23. Ramsey RG, Zacharias CE. MR imaging of the spine after radiation therapy: easily recognizable effects. *AJR* **1985**;144:1131–1135
24. McKinstry CS, Steiner RE, Young AT, Jones L, Swirsky D, Aber V. Bone marrow in leukemia and aplastic anemia: MR imaging before, during, and after treatment. *Radiology* **1987**;162:701–707

Osteochondral Impaction of the Femoral Head Associated with Hip Dislocation: CT Study in 35 Patients

Jamshid Tehranzadeh[1]
William Vanarthos[2]
M. Joyce Pais[1]

Chondral and osteochondral impactions are insults to articular cartilage and subchondral bone of the femoral head during hip dislocation. To evaluate the frequency and sites of femoral head impaction, we reviewed CT scans of 35 patients with hip dislocation (32 posterior and three anterior). Osteochondral impaction fractures were present in 20 (63%) of the 32 patients with posterior hip dislocation and in all three patients with anterior dislocation. In patients with posterior dislocation, the impaction occurred anteriorly in an arc between the 11-o'clock and 1-o'clock positions in all seven cases (100%) of right-sided dislocation and in eight (61%) of 13 cases of left-sided dislocation. Twelve (60%) of the 20 patients with femoral head impaction fracture underwent surgery; osteochondral impaction was substantiated in all 12. In those with anterior dislocation, osteochondral impaction occurred at the posterolateral aspect of the femoral head in an arc between the 4-o'clock and 5-o'clock positions.

A high rate of osteochondral impaction after hip dislocation was detected in this series. Observing the site of femoral head impaction allows determination of the type of original dislocation. Alternatively, when the type of original dislocation is known, the site of femoral head impaction can be predicted.

***AJR* 155:1049–1052, November 1990**

Chondral and osteochondral damage are important predisposing factors in the development of posttraumatic osteoarthritis [1, 2]. Although femoral head impaction in association with hip dislocation has been recognized for many decades, it has been estimated to occur in only 7–16% of cases [3–6]. Many of these impaction injuries may not be recognizable on plain radiographs [7, 8] and are subtle even on CT. They often appear as a minimal localized flattening of the femoral head on CT and easily could be overlooked. Chondral impaction injuries are probably more common than recognized even on CT, as only those in which the subchondral bones are affected are appreciated.

With the use of CT, we have shown a higher prevalence of femoral head impaction after hip dislocation than previously reported. Additionally, anterior and posterior hip dislocations were associated with impaction fractures of the femoral head at specific sites.

Materials and Methods

CT scans of 100 patients with acetabular fracture were reviewed by two radiologists independently without knowledge of operative findings. Among these, 32 patients had posterior dislocation. Three cases of anterior hip dislocation were also included to compare the site of femoral head impaction in this less common type of dislocation.

All patients had supine CT scans of the pelvis and acetabulum with the GE 8800 and GE 9800 scanners (General Electric, Milwaukee, WI). Sections were 5 mm thick at 3-mm intervals throughout the acetabulum. Adult (large) calibration was used. Images were filmed with both bone and soft-tissue windows. Sixteen of 32 patients with posterior dislocation and 12 of 20 patients with femoral head impaction underwent surgery.

Received April 19, 1990; accepted after revision June 6, 1990.

[1] Department of Radiological Sciences, University of California, Irvine Medical Center, 101 City Dr., Orange, CA 92668. Address reprint requests to J. Tehranzadeh.

[2] Department of Radiology, University of Miami Medical Center, P.O. Box 016960, Miami, FL 33101.

0361-803X/90/1555-1049
© American Roentgen Ray Society

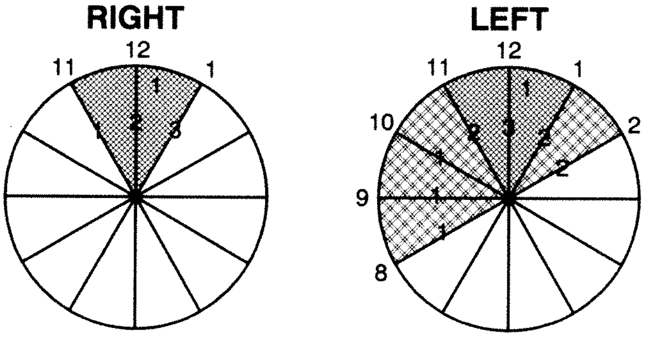

Fig. 1.—Diagram shows spectrum of 20 sites (clock positions) of osteochondral impaction of femoral head in 32 cases of dislocation of the right or left posterior hip.

Results

One hundred patients had 112 acetabular fractures. Twenty (63%) of 32 cases of posterior hip dislocation showed osteochondral impaction fractures of the femoral head. Thirteen osteochondral impactions occurred on the left side and seven on the right. Impaction of the femoral head occurred anteriorly in an arc between the 11-o'clock and 1-o'clock positions in all seven right-sided cases (100%) and in eight (61%) of 13 left-sided cases. The other five cases of impaction of the left femoral head included two at the 2-o'clock position and three at the 8-, 9-, and 10-o'clock positions, respectively (Fig. 1). All patients with osteochondral impaction of the femoral head had a history of dislocation. The three cases of anterior hip

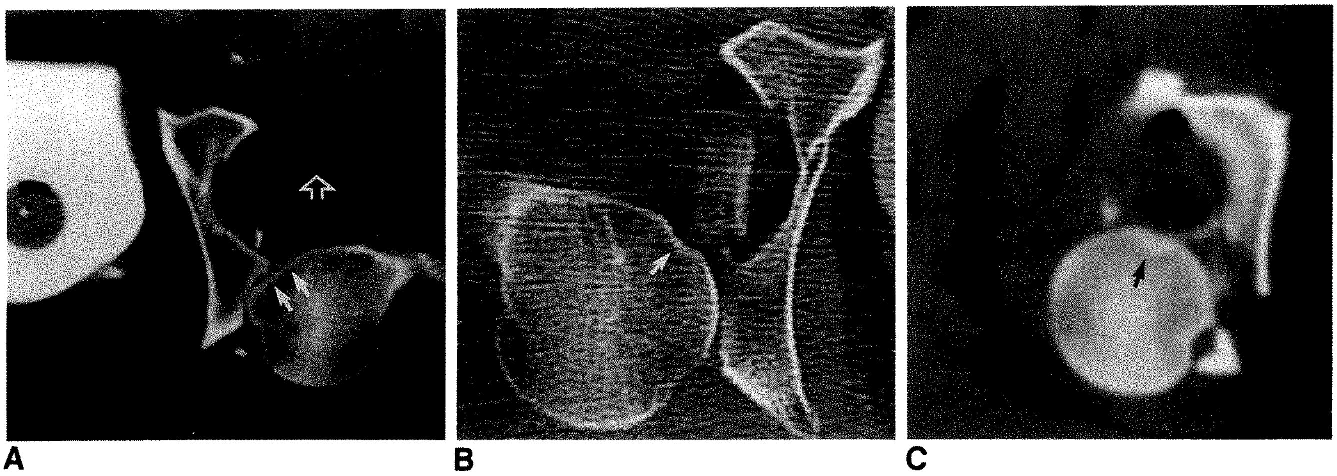

Fig. 2.—Three different patients, all involved in motor vehicle accidents, had posterior hip dislocation. CT scans before reduction show osteochondral impaction of femoral head at 11- or 12-o'clock position and posterior acetabular fracture.

A, CT scan of 43-year-old man shows flattening of left femoral head, free osseous fragment, fat-fluid level (*open arrow*) in joint, and flattening of superior aspect of femoral head (*solid arrows*).

B, CT scan of 43-year-old man shows depression of femoral head (*arrow*) and large osseous fragment in joint.

C, CT scan of 33-year-old man shows subtle impaction of femoral cortex (*arrow*) with comminuted posterior acetabular fracture.

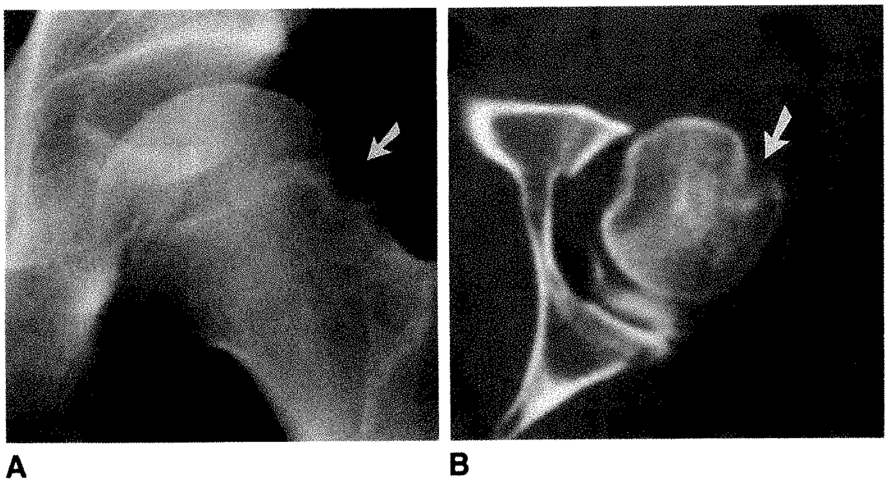

Fig. 3.—24-year-old man involved in motor vehicle accident had posterior hip dislocation and posterior acetabular fracture.

A, Plain radiograph after reduction shows osteochondral impaction of lateral aspect of femoral head (*arrow*) and widening of joint due to intraarticular osseous fragment.

B, CT scan shows impaction of left femoral head at 2-o'clock position (*arrow*) with osseous fragment in joint.

dislocation showed osteochondral impaction posterolaterally in an arc between the 4- and 5-o'clock positions.

Sixteen of 32 patients with posterior dislocation (12 of 20 with femoral head impaction) underwent surgery. Osteochondral impaction was documented in the 12 cases; the remaining four cases proved to be true-negative for impaction fracture of the femoral head at surgery.

In 22 cases (20%) of acetabular fractures, intraarticular fracture fragments were recognized on CT. Of these, 11 cases (50%) were related to posterior hip dislocation. Seven of the 11 patients underwent surgery.

Discussion

Dislocation of the hip is not common. It accounts for only 5% of all dislocations and is seen most often after vehicular injury (Figs. 2 and 3) [5, 9, 10]. Hip dislocations are classified simply as posterior, anterior, and central. Posterior dislocation, the most common, occurs with the hip in flexion as severe forces are applied on the knee [9]. The femur acts as a long lever to force the femoral head through the joint capsule. When the knee is abducted at the time of impact, the posterior acetabular rim is often fractured [7, 9]. Birkett [11], who in 1869 originally described femoral head impaction in association with posterior hip dislocation, postulated that either the head was split by being driven forcefully against the strong edge of the acetabulum or that the strength of the ligamentum teres was sufficient to overpower the cohesion of the bony tissues, while the femur was driven violently upward and backward. Associated fracture of the femoral head is reported as a relatively uncommon injury [9]. However, we report a high prevalence (63%) of osteochondral impaction fractures of the femoral head after posterior hip dislocation and speculate that even this rate may be an underestimation, as an isolated chondral injury without subchondral bone impaction often remains undetected. These fractures, which usually result from impaction of the anterior femoral head onto the posterior acetabular rim, may appear as a subtle flattening of the femoral head on CT. Rarely, these osteochondral fractures are more prominent with deeper "slice" fractures [7] and separated osteochondral fragments in the joint [4, 10]. In our series, impaction of the femoral head occurred at specific sites with both posterior and anterior hip dislocation. It is imperative to search for these impaction fractures of the femoral head at the acetabular level on CT examination. Minimal flattening of the femoral head and neck junction at the inferior sections at the level of the lesser trochanter, which is a normal finding, should not be mistaken for the impaction fracture (Fig. 4).

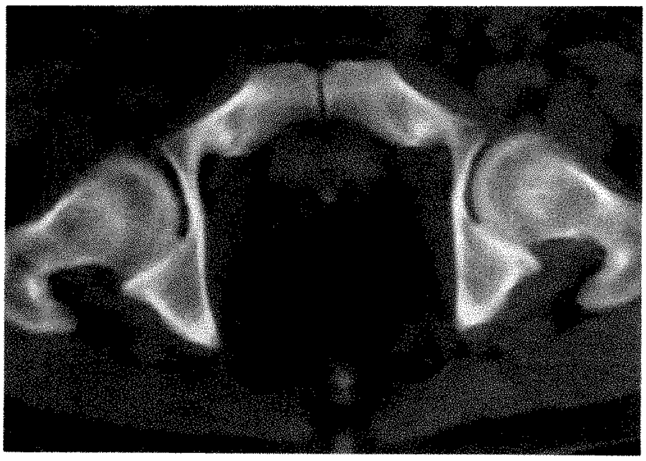

Fig. 4.—CT scan at level of lesser trochanter in a normal hip of a 45-year-old man shows femoral heads are normally flat on lateral aspect at junction of head and neck.

We may assume that the degree of the impaction and the site and size of fracture of the femoral head and posterior

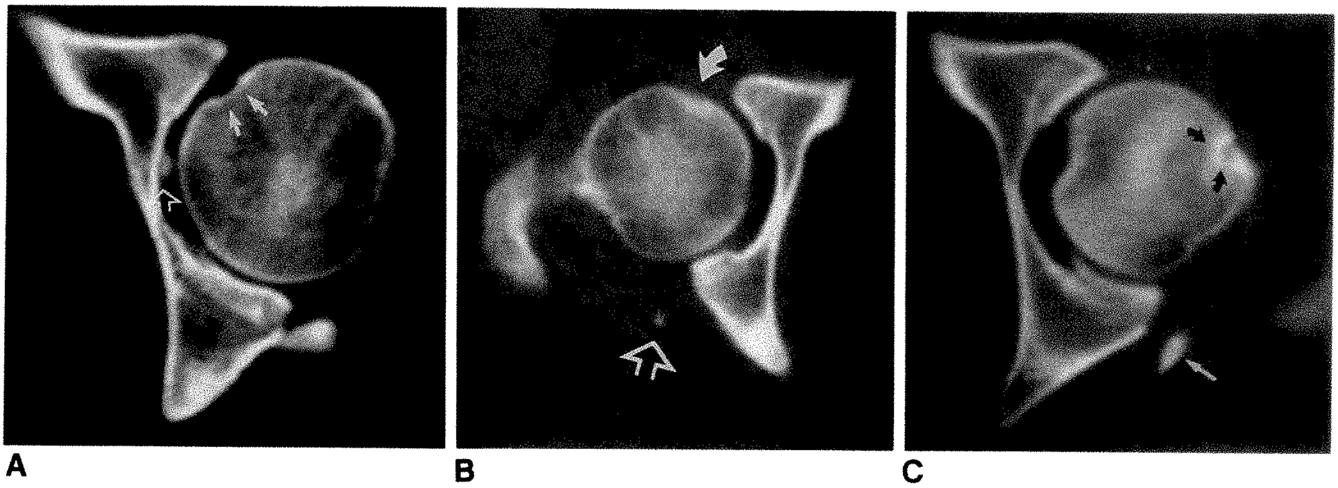

Fig. 5.—CT scans of three different patients, all involved in motor vehicle accidents, with dashboard-type posterior hip dislocations. The femur was in partial adduction at time of impact, causing small fracture of posterior acetabular lip associated with subtle osteochondral flattening or depression of femoral head.

A, CT scan of 45-year-old man shows cortical depression at 11-o'clock position (*solid arrows*), small osseous fragment in joint (*open arrow*), and small fracture of posterior lip of acetabulum.

B, CT scan of 25-year-old woman shows subtle flattening of right femoral head at 12-o'clock position (*curved arrow*) and small fracture of posterior lip (*open arrow*).

C, CT scan of 15-year-old boy shows osteochondral depression at 2-o'clock position (*black arrows*), small fracture of posterior lip of acetabulum (*white arrow*), and tiny osseous debris in joint.

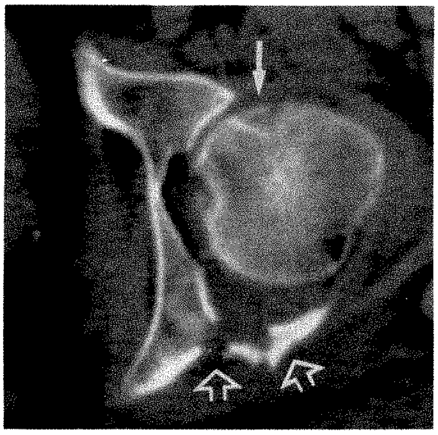

Fig. 6.—CT scan after reduction of posterior hip dislocation in a 67-year-old man shows large fracture of posterior acetabular wall (*open arrows*) and "buttonhole" type of osteochondral defect of femoral head (*solid arrow*).

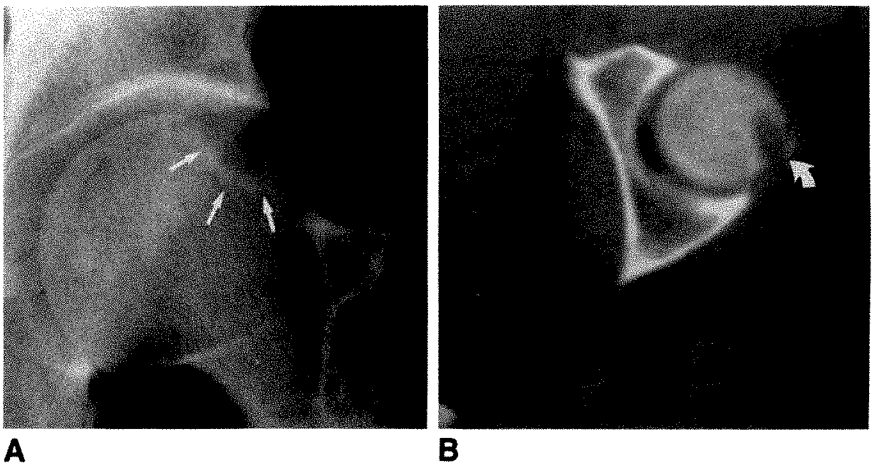

Fig. 7.—31-year-old man involved in car accident with anterior hip dislocation.

A, Plain radiograph after reduction shows osteochondral impaction on lateral aspect of femoral head (*arrows*).

B, CT scan after reduction shows osteochondral defect at an arc between 4- and 5-o'clock positions at posterolateral aspect of femoral head (*arrow*). (Reprinted with permission from Tehranzadeh [12].)

wall of the acetabulum may be directly related to the degree of abduction of the femur and flexion of the hip, as this impaction becomes less likely after hip dislocation when the hip is significantly adducted and flexed (Figs. 5 and 6) [9].

In the more common obturator type of anterior dislocation, when the hip is flexed and externally rotated at the time of injury, the femoral head dislocates anteriorly after sudden forceful abduction and external rotation. This extreme abduction abutment of the femoral neck against the posterior margin of the acetabulum forces the femoral head out of and in front of the acetabular cavity. The posterosuperior and lateral portions of the femoral head impinge against the anteroinferior margin of the acetabular rim, producing an impaction fracture of the femoral head (Fig. 7) and occasionally an osteochondral fracture of the anterioinferior margin of the acetabulum [13]. Impaction fracture of the femoral head was noted in eight of 11 patients after anterior hip dislocation in the series of Dussault et al. [13]. In the same series, osteochondral fracture of the acetabular rim was noted in three cases.

Impaction fracture of the anteriosuperior surface of the femoral head in association with posterior hip dislocation is analogous to a "trough line" fracture of the humeral head in posterior shoulder dislocation. Anterior hip dislocation, in contrast, creates an osteochondral impaction on the posterolateral margin of the femoral head analogous to Hill-Sachs fracture of the humeral head in anterior shoulder dislocation.

Assessment of the extent of direct damage to the articular surface of the femoral head is important in the management of hip injury. Difficulty arises in viewing the plain radiograph, since the posterior, posteroinferior, and inferomedial aspects are in a blind spot [7]. Shirkhoda et al. [14] showed the value of CT of acetabular fractures in influencing management planning. The presence of intraarticular fragments, large defects of the femoral head, or femoral head–acetabular incongruity indicates the need for surgery. Determination of the position of fragments also may help in planning the surgical approach. If CT after reduction reveals an anatomic placement of the fragment, surgical intervention may be avoided [3]. Knowledge of the significance of the site of impaction of the femoral head alerts the radiologist to the presence and type of earlier hip dislocation. Momentary hip dislocation followed by instantaneous relocation may not be appreciated after a traumatic event and may not leave any trace of dislocation except for femoral head impaction or acetabular lip fracture.

REFERENCES

1. Stewart MJ, Milford LW. Fracture-dislocation of the hip: an end result study. *J Bone Joint Surg [Am]* **1954**;36-A:315–342
2. Hougaard K, Lindquist S, Nielsen LB. Computerised tomography after posterior dislocation of the hip. *J Bone Joint Surg [Br]* **1987**;69-B:556–557
3. Ordway CB, Xeller CF. Transverse computerized axial tomography of patients with posterior dislocation of the hip. *J Trauma* **1984**;24(1):76–79
4. Epstein H. Posterior fracture-dislocation of the hip: Long-term follow-up. *J Bone Joint Surg [Am]* **1974**;56-A:1103–1127
5. Larson CB. Fracture dislocations of the hip. *Clin Orthop* **1973**;92:147–154
6. Pipkin G. Treatment of grade IV fracture-dislocations of the hip. *J Bone Joint Surg [Am]* **1957**;39-A:1027–1042
7. Stein H. Computerized tomography for ascertaining osteocartilagenous intra-articular (slice) fracture of the femoral head. *Isr J Med Sci* **1983**;19:180–184
8. Urist MR. Fracture dislocation of the hip joint. *J Bone Joint Surg [Am]* **1984**;30-A:699–727
9. Rogers LF. The hip and femoral shaft. In: Rogers LF, *Radiology of skeletal trauma*, vol. 2, 1st ed. New York: Churchill-Livingstone, **1982**:653–712
10. Epstein HC. Traumatic dislocations of the hip. *Clin Orthop* **1973**;92: 116–142
11. Birkett J. Description of a dislocation of the head of the femur complicated with its fracture. *Med Chir Trans London* **1869**;52:133–138
12. Tehranzadeh J. Avulsion and avulsion-like injuries of the musculoskeletal system. In: Tehranzadeh J, Serafini AN, Pais MJ. eds. *Avulsion and stress injuries of the musculoskeletal system*, 1st ed: Basel: Karger, **1989**:1–64
13. Dussault RG, Beauregard G, Fauteaux P, Laurin C, Boisjoly A. Femoral head defect following anterior hip dislocation. *Radiology* **1980**;135: 627–629
14. Shirkhoda A, Brashear HR, Staab EV. Computed tomography of acetabular fractures. *Radiology* **1980**;134:683–688

K-Edge Digital Subtraction Arthrography of the Painful Hip Prosthesis: A Feasibility Study

Frederick Kelcz[1]
Walter W. Peppler[2]
Charles A. Mistretta[2]
Arthur DeSmet[1]
Andrew A. McBeath[3]

K-edge energy subtraction radiography is a method for detecting the presence of iodinated contrast material by subtracting two digital radiographs produced by X-ray beams with energies above and below the iodine K edge. We performed a feasibility study on the application of K-edge energy digital subtraction arthrography (KEDSA) to painful hip prostheses. During arthrography, loosening of the prosthesis is implied if contrast material is seen dissecting around the prosthesis, an often difficult detection task because of adjacent prosthesis metal or cement. In conventional arthrography a preliminary mask image is thus used from which films obtained after injection of iodinated contrast material are subtracted. Movement by the patient during this process may preclude subsequent subtraction. With KEDSA, since multiple image pairs may be obtained after the injection of contrast material, the problem of patient motion is virtually eliminated. A conventional X-ray tube operating between 55 and 65 kVp was alternately filtered by iodine and cerium filters to produce the KEDSA images. The apparatus was capable of producing a subtracted image within 3 sec. The technique was applied to phantoms and to six patients immediately after hip arthrography that had been positive for prosthesis loosening. Although of lower spatial resolution, the KEDSA images were, in all cases, positive for loosening in a pattern consistent with the conventional arthrographic images.

KEDSA was shown to be successful in detecting extraarticular contrast material. During a single study, subtraction in various imaging planes as well as postexercise subtraction imaging can be accomplished—techniques not heretofore possible in routine subtraction arthrography.

***AJR* 155:1053–1058, November 1990**

One of the common long-term complications of placement of a hip prosthesis is pain associated with loosening at the interface with either bone or cement. During hip arthrography, dissection of contrast material around the extraarticular portions of the prosthesis is positive evidence of loosening. Since both the metal prosthesis and surrounding barium-impregnated cement are radiopaque, a small sliver of contrast material adjacent to them may be difficult to detect on conventional radiographs. Traditionally, this problem has been overcome by obtaining radiographs before (mask image) and after the injection of iodinated contrast material into the joint. If no motion occurs between the views, subtraction of the mask image from the postinjection view leads to enhanced detection of the small collections of iodinated contrast material that can be seen with loosening. Subtraction arthrography has been shown to be more sensitive than conventional arthrography or scintigraphy in the detection of hip prosthesis loosening [1, 2]. Recently, digital subtraction imaging has been applied to arthrography, resulting in the immediate availability of subtracted images [3, 4]. By using a digital subtraction apparatus to rapidly subtract a precontrast mask from subsequent images, it is possible to view, in real time, the iodinated contrast material as it enters the hip joint, separately from overlying bone, soft tissue, and barium-impregnated cement [4].

Received April 30, 1990; accepted after revision June 25, 1990.

[1] Department of Radiology, University of Wisconsin Hospitals and Clinics, 600 Highland Ave., Madison, WI 53792. Address reprint requests to F. Kelcz.

[2] Department of Medical Physics, University of Wisconsin Hospitals and Clinics, Madison, WI 53792.

[3] Department of Surgery, Orthopedics Division, University of Wisconsin Hospitals and Clinics, Madison, WI 53792.

0361-803X/90/1555-1053
© American Roentgen Ray Society

All subtraction techniques have several fundamental shortcomings. Patient motion after the subtraction mask image has been obtained interferes with the subsequent subtraction. For this reason, postexercise subtraction is not possible, because once the limb is exercised, repositioning it into exactly the same position is practically impossible. Finally, dissecting contrast material is best detected when viewed tangentially, a serendipitous factor in traditional film subtraction, as only a single projection is obtained.

We evaluated the feasibility of K-edge energy digital subtraction arthrography (KEDSA) as a supplementary technique in imaging painful hip prostheses. After contrast material is injected into the joint, pairs of images are obtained, with each image of the pair made at a different effective X-ray energy. Subtraction of these images permits selective imaging of the iodinated contrast material. Since only 1–3 sec separate the two images of the subtraction pair, the chance of patient motion is decreased. Furthermore, even if the patient were to move during this short interval, repeat images are easily obtained.

The energy-dependent method of subtraction arthrography also permits, as part of the same examination, multiple subtraction views to be made in any imaging plane, limited only by the range of motion of the image intensifier. Furthermore, subtraction imaging performed after exercise, not heretofore possible, can be performed.

Theoretical Principles

The principles of KEDSA were developed in this laboratory over 10 years ago [5, 6] and have been applied by others, primarily for applications in cardiovascular radiology [7–9] and the evaluation of calcification in pulmonary nodules [10].

The dual-energy difference image, DE, is formed by combining the log-transformed low- and high-energy images in the following way:

$$DE = \ln(L) - R \times \ln(H),$$

where L and H represent the low- and high-energy images, ln is the natural log operation, and R is a constant that can be varied to cancel a particular material in the subtraction image. In general, the best choice for R is given by the ratio of the attenuation coefficients, at the low and high beam energies, of the material to be canceled. For example, to cancel tissue, R is chosen to equal the ratio of the low to high X-ray attenuation coefficients for tissue. In practice, one material may be canceled relative to another only if its R value is significantly different from that of the other material. In K-edge imaging it is the small R value for iodine, due to the sharp discontinuity in the attenuation coefficient at the K edge, that permits its differentiation from other tissues whose R values are close to unity.

One potential problem with this technique is that with a polychromatic spectrum the effective energy of the beam changes with tissue thickness. Therefore the R value used to cancel tissue at one thickness would not be correct at another thickness. Another problem is that hip replacement prostheses are often secured in place with barium-impregnated cement. The K edge of barium is close to that of iodine (37 vs 33 keV), which may cause difficulty in distinguishing the two elements. To understand the spectral behavior of the X-ray beams over a physiologic range of bone and tissue thickness, a computer simulation was performed.

We used a computer program called DXSPEC [11] to simulate the behavior of a Bremstrahlung spectrum as it is attenuated through various materials (e.g., tissue, bone, iodine) of various thicknesses. The DXSPEC program uses a polynomial interpolation to generate mass attenuation coefficients as published by McMaster et al. [12]. In our simulation, the thickness of tissue was varied from 15 to 25 cm and that of bone from 0 to 1 g/cm^2. The barium and iodine signals were calculated assuming thicknesses of 100 mg/cm^2 for each (about 3-mm thickness for 60% iodinated contrast material). The spectral shaping filters were chosen to be iodine (200 mg/cm^2) and cerium (230–380 mg/cm^2) for the low- and high-energy beams, respectively. The thickness of the cerium filter was adjusted for each kVp studied to give equal detected signal at a tissue thickness of 15 cm. This yielded roughly equal required mAs for the two beams. The X-ray tube voltage was varied from 55 to 65 kVp, but calculations were performed using the same kVp for both beams.

We imposed the requirement that the R value be such as to produce equal signals of opposite polarity for barium and iodine. This eliminates the possible confusion between the two signals, which are often equal on a conventional radiograph. The R value at which this balance occurred changed by less than 5% for tissue thicknesses from 15 to 25 cm. By using this balance condition, the iodine difference signal was approximately 20% of the difference signal that would have been obtained had temporal subtraction been used instead of energy subtraction. Herein lies a key distinction between energy subtraction and temporal subtraction methods. With the former, some iodine signal is present in each image of the subtraction pair. Thus, the maximum iodine difference signal achieved is always less than that obtained with temporal subtraction, where no iodine signal is present in the mask image. Furthermore, the subtraction process itself increases noise in all portions of the subtracted image. The final result is that the signal-to-noise ratio of iodinated contrast material imaged with KEDSA is significantly less than it would be were it imaged with standard temporal subtraction techniques. The ratio of iodine-to-bone subtraction signals changes significantly as a function of tissue thickness. The ratio peaks sharply between 20 and 22.5 cm for the 60-kVp beam and between 17.5 and 20.0 cm for the 62-kVp beam. Since, to enhance iodine visibility, we want this ratio to be large, our calculations show that the kVp should be adjusted to compensate for patient body habitus. Once kVp is set, the thickness of the tissue over the hip is nearly constant so that tissue cancellation should be relatively well maintained.

Subjects and Methods

Because digital subtraction radiography equipment has become almost routine in many diagnostic imaging centers, our interest was in developing an energy-dependent technique that could most easily retrofit existing equipment. Thus, we constrained ourselves to a single-kVp, two-filter subtraction technique that would require only the mounting of rapidly switched filters above the X-ray tube. For the two X-ray beam filters, we used CeO_2 and NaI powders embedded in epoxy. In order to compensate for attenuation by the filters, tube loading was increased by a factor of 10 when using the iodine filter and by 18 when using the cerium filter. A Philips Optimus M200 generator, 6- to 9-in. (15- to 23-cm) image intensifier and XTV6 Plumbicon video camera (Philips Medical Systems, Shelton, CT) were used to acquire all the digital subtraction images used in this study. The images were processed by using a dedicated image processor, DVIP II described by Peppler et al. [13]. For each filter, a test exposure was produced by using a wide-imaging-aperture, low-dose technique. The imaging aperture was then reduced and both final images were acquired in rapid succession. Exposure times ranged from 0.8 to 3.2 sec with an interval of approximately 2 sec between images. Tube current ranged from 200 to 830 mA (necessitated by the required filtration). Patient exposure (skin entrance exposure measured in air) ranged from 3.1×10^{-5} to 6.4×10^{-5} C/kg (120–250 mR) per image pair.

To demonstrate the physical principles of the technique, images of a phantom were generated illustrating how the changes in contrast produced by spectral filtering are transformed into images in which iodine is preferentially imaged (Fig. 1).

Before using the system on cadavers and human volunteers, we constructed a second phantom that more closely modeled the loosened hip prosthesis. Images of this phantom are shown in Figure 2.

Our clinical study population included six patients (two men and four women 54–83 years old) who had undergone standard film subtraction arthrography immediately before KEDSA. Four patients had total hip prostheses; three of these four were of the cementless design. One patient had a cemented femoral prosthesis. One patient had a cemented acetabular prosthesis and a resurfacing prosthesis of the femoral head. Patients had signed an informed consent prior to arthrography so that after this procedure they could be brought immediately to the medical physics laboratory for KEDSA. Nevertheless, this meant a delay of approximately 20 min between the end of standard arthrography and the first KEDSA images, probably enough time for some absorption and redistribution of contrast material. For this feasibility study no attempt was made to blindly evaluate the KEDSA method. Rather, direct comparison with film images were performed by an observer already familiar with the results of the arthrography.

Results

The machined, loosened prosthesis model was first imaged at 55 kVp over 15 cm of Lucite. The resulting KEDSA image

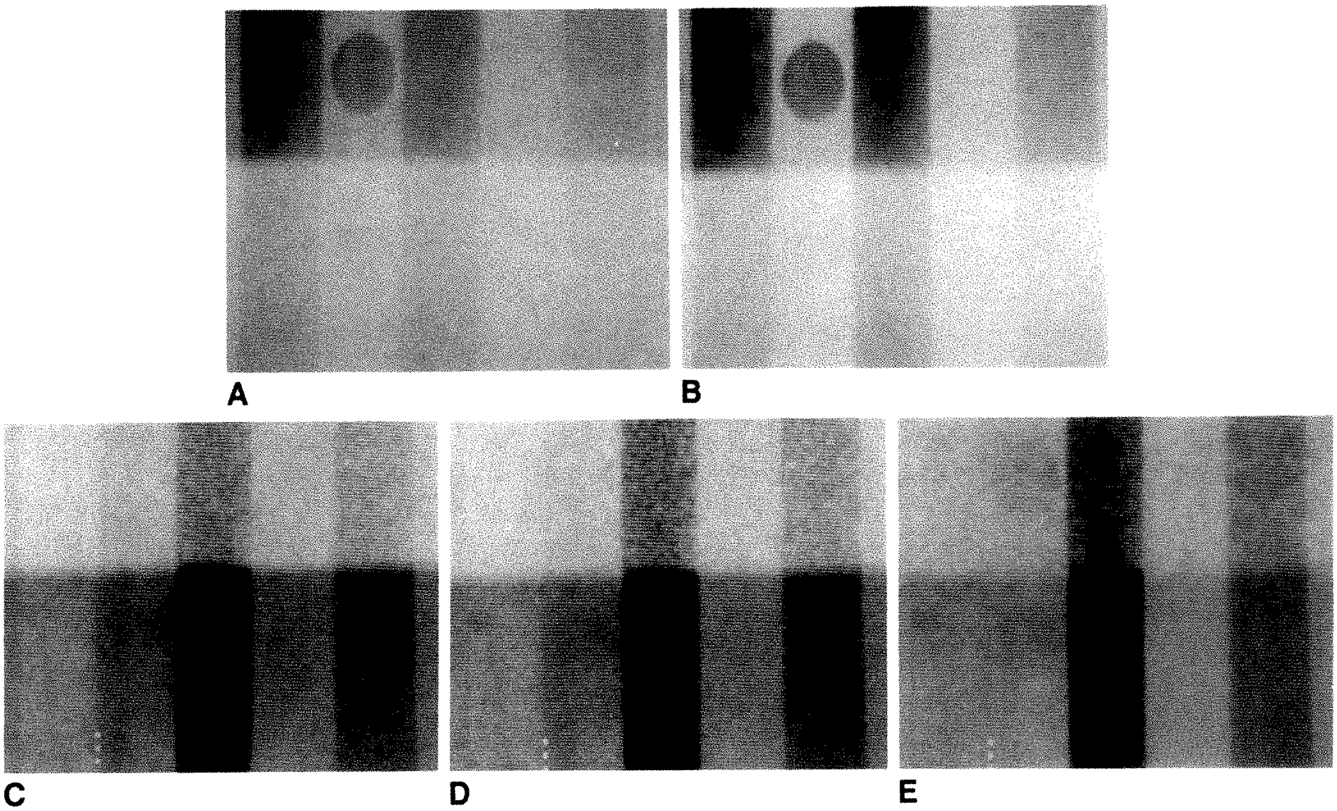

Fig. 1.—Phantom consisting of three fluid-filled channels overlying tissue-equivalent step wedge (15 and 20 cm of Lucite). From left to right, channels contain dilute barium, 53 mg/cm² Renovist 60%, and 18 mg/cm² Renovist 60%. A round bone-equivalent cylinder (1 g/cm², RMI, Middleton, WI) overlies thicker (top) portion of tissue wedge.

***A* and *B*, Iodine- (*A*) and cerium- (*B*) filtered beams were used to produce images. Note that greatest contrast change, when switching between spectra, occurs for iodine-containing channels, permitting selective enhancement of iodine signals. The two images were electronically subtracted by using a weighting factor, z, as a multiplier for the iodine image.**

***C–E*, Difference images using z values of 1.2, 1.3, and 1.35, respectively, with iodine displayed as a black signal. The choice of z value will determine how barium is displayed relative to iodine. Bone is well suppressed in all cases shown. By using only two spectra, it is not possible to simultaneously cancel the tissue step signal.**

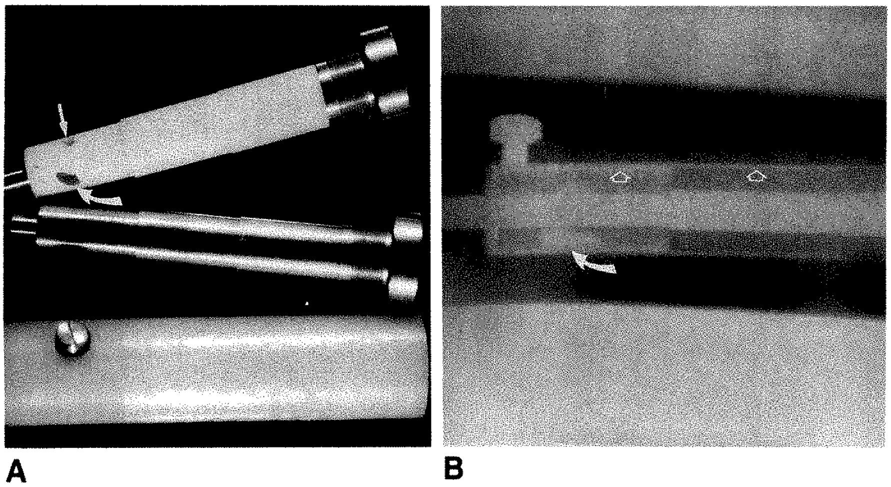

Fig. 2.—Phantom to simulate loosened hip prosthesis with 0.5, 1, and 2 mm of loosening.

A, Two metallic inserts were machined to fit into a bone-equivalent tube (*bottom*, RMI, Middleton, WI). One insert (*top*) was coated with barium-impregnated methyl methacrylate and contains machining defects (*arrows*). After insert is screwed into tube, iodine contrast material is placed into phantom via screw plug.

B, Dual-energy digital subtraction image of phantom with cement-coated insert. Iodine, imaged as white, is clearly seen in 2- and 1-mm spaces (*open arrows*), as well as within machining defects (*solid arrow*), demonstrating that iodine can be isolated from adjacent barium and bone.

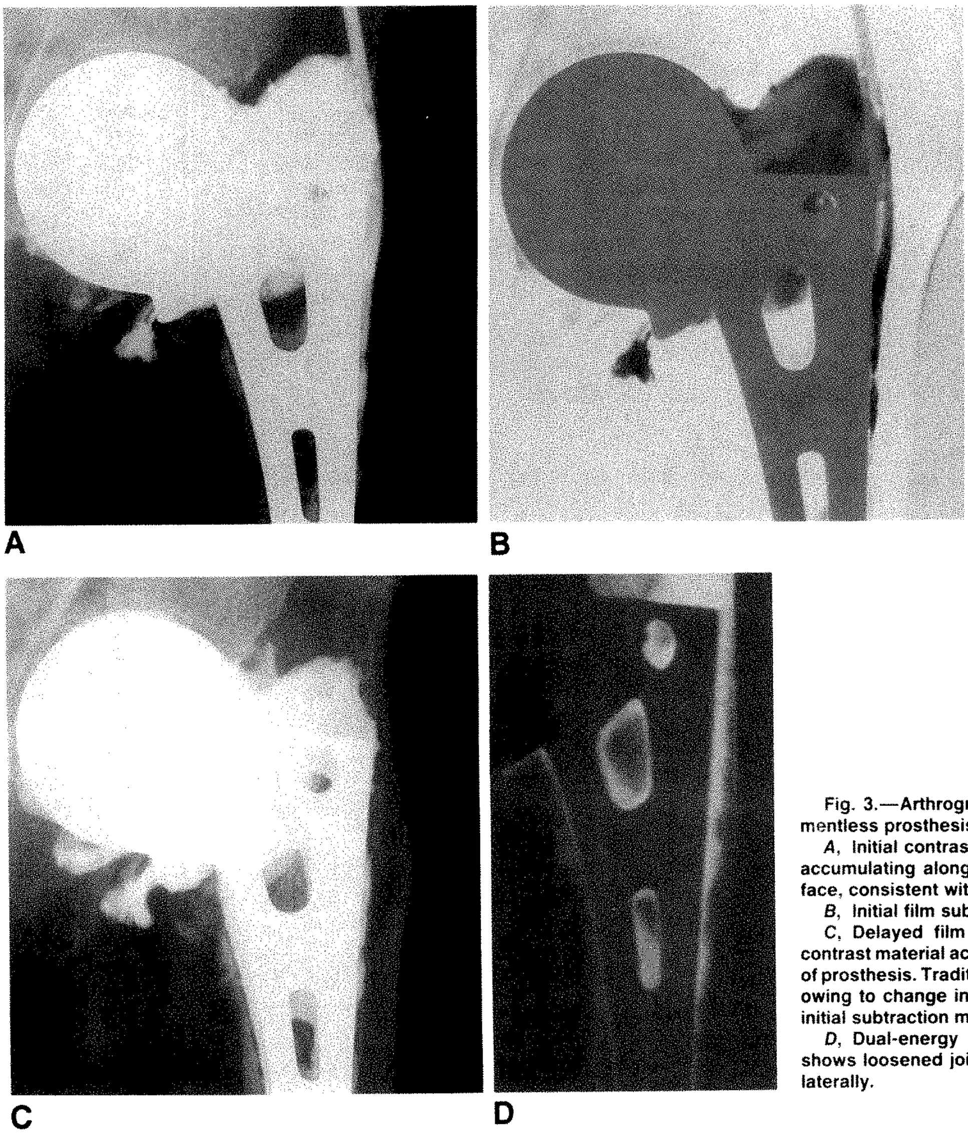

Fig. 3.—Arthrogram of a 60-year-old woman with left cementless prosthesis.

A, Initial contrast-enhanced view shows contrast material accumulating along lateral portion of bone-prosthesis interface, consistent with loosening.

B, Initial film subtraction confirms impression from *A*.

C, Delayed film after exercising joint shows additional contrast material accumulating medially and within interstices of prosthesis. Traditional film subtraction is no longer possible owing to change in limb position from that used to produce initial subtraction mask.

D, Dual-energy subtraction image (iodine is white) also shows loosened joint with iodine accumulating medially and laterally.

(Fig. 2B) again verifies that iodinated contrast material can be successfully isolated from the barium-impregnated cement.

All four patients with total hip prostheses had conventional arthrographic evidence of acetabular and femoral component loosening. KEDSA was positive as well in each of these patients. All of these patients had surgical confirmation of the suspected loosening and there were no false-negative or false-positive conventional or KEDSA arthrographic findings.

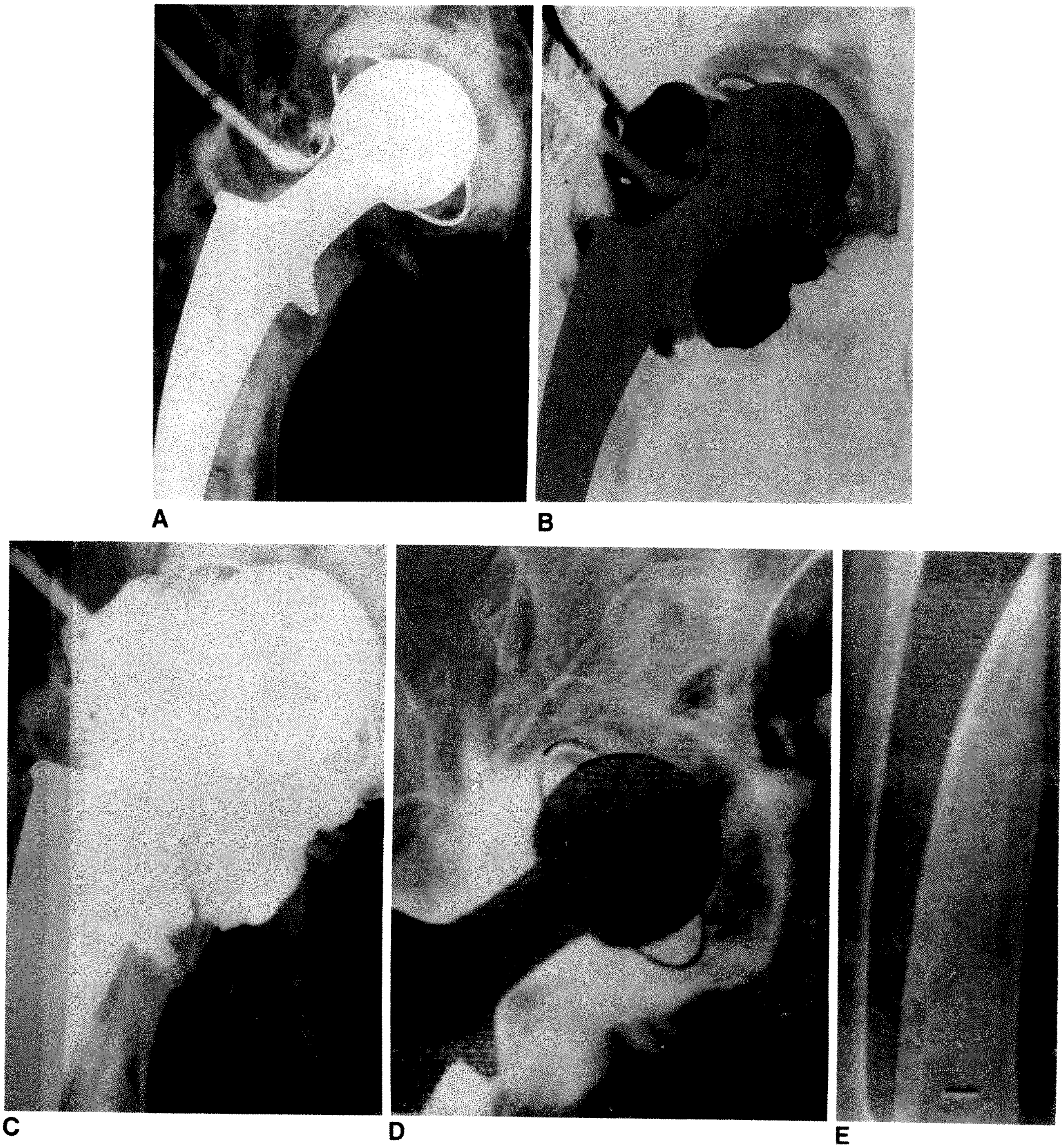

Fig. 4.—Arthrogram of a 75-year-old woman with right cemented prosthesis.

A, Preinjection view shows distribution of barium-impregnated cement.

B, Initial film subtraction shows no significant accumulation along shaft, despite initial impression on plain film of loosening due to lucency near inferior prosthesis tip (*not shown*) and actual observation of movement during fluoroscopy.

C, After exercise, contrast material is now seen along medial aspect of prosthesis. Shading along left portion of film is due to fogging.

D and *E*, Dual-energy subtraction confirms loosening by imaging contrast material accumulating along medial acetabular component cement-bone interface and along medial shaft. Comparison with *A* and *B* shows that barium-impregnated cement has been well canceled.

The single patient with the femoral head resurfacing prosthesis also had a positive arthrogram and KEDSA for acetabular loosening. At surgery, no gross loosening was reported, but as nonunion at the femoral neck necessitated replacement of the femoral component (which then would not have matched the existing acetabular component), it was simply elected to replace the acetabular component as well without closer examination. The patient with a femoral prosthesis had an arthrogram and KEDSA that were positive for loosening, but surgical confirmation could not be obtained because of multiple, unrelated medical complications. The results in two of the six patients are illustrated (Figs. 3 and 4).

Discussion

Although we have presented some initial images supporting the feasibility of KEDSA, many questions remain. Equipment modification would be required to enable a solenoid-operated dual-element filter to be placed in the X-ray beam. Of course, both filters would have to be moved out of the beam for routine imaging. The digital subtraction apparatus software may also have to be modified to permit low-dose test exposures. Possibly, further experience could result in technique tables based on patient measurements, permitting a simpler conversion of existing equipment.

Fundamental questions persist about how stable the balance conditions are that permit isolation of the iodine signal in the clinical situation. We have observed that by varying the relative weighting of the iodine- and cerium-filtered images, the final image can be greatly altered and the determination of the presence of iodine can be confusing. In such cases, comparison with the prior film subtraction results has proved invaluable. Only more experience will determine whether KEDSA can become a reliable technique.

Finally, physical considerations prevented us from performing KEDSA in the same room as the routine arthrography so that comparison of imaged iodine collections would be more reliable. Prospective, randomized studies are required in which blinded observers would compare these images with traditional arthrographic findings, using operative reports as the standard.

In conclusion, we have conducted a feasibility study of a new method for imaging the painful hip prosthesis that does not require a traditional mask image, yet permits multiple subtraction images to be obtained after the injection of iodinated contrast material. KEDSA, with its increased complexity and reduced spatial resolution and sensitivity to iodine, will probably not replace conventional subtraction arthrography. However, it may become a helpful adjunct in the patient with prior negative or ambiguous studies, but in whom clinical suspicion for loosening is high. In such cases, KEDSA permits subtraction images in multiple projections as well as after exercise, techniques heretofore unavailable to the radiologist and orthopedist. We believe this method is now worthy of a well-controlled clinical evaluation.

ACKNOWLEDGMENTS

We thank David R. Fisher and Mark Burnstein, Department of Radiology, Henry Ford Hospital, Detroit, MI, for support in referring patients for our study; Richard W. Glad and Raymond Vanderby, Department of Surgery, Division of Orthopedics, for help with cadaver material in the early part of this study; and Carrie Poole for careful attention in the preparation of this manuscript.

REFERENCES

1. Lyons CW, Berquist TH, Lyons JC, Rand JA, Brown ML. Evaluation of radiographic findings in painful hip arthroplasties. *Clin Orthop* **1985**;195: 239-251
2. Baretsz JO, Lemmens JM, Slooff TJJH. The use of subtraction arthrography in total hip arthroplasties. *ROFO* **1986**;144:440-446
3. Newberg AH, Wetzner SM. Digital subtraction arthrography. *Radiology* **1985**;154:238-239
4. Resnick D, Kerr R, Andre MG Jr, et al. Digital arthrography in the evaluation of painful joint prostheses. *Invest Radiol* **1984**;19:432-437
5. Kelcz F, Mistretta CA. Absorption edge fluoroscopy using a three spectrum technique. *Med Phys* **1976**;3:159-168
6. Kelcz F, Mistretta CA, Riederer SJ. Spectral considerations for absorption-edge fluoroscopy. *Med Phys* **1977**;4:26-35
7. Brody WR. Hybrid subtraction for improved arteriography. *Radiology* **1981**;141:828-831
8. Van Lysel MS, Dobbins JT, Peppler WW, et al. Hybrid temporal-energy subtraction in digital fluoroscopy. *Radiology* **1983**;147:869-874
9. Molloi SY, Mistretta CA. Quantification techniques for dual-energy cardiac imaging. *Med Phys* **1989**;16:209-217
10. Fraser RG, Hickey NM, Niklason LT, et al. Calcification in pulmonary nodules: detection with dual-energy digital radiography. *Radiology* **1986**; 160:595-601
11. Ergun DL. *A slow-scan video technique for digital IV subtraction angiography* [PhD thesis]. Madison, WI: University of Wisconsin, 1983
12. McMaster WH, DelGrande NK, Mallet JH, Hubbell JH. *National Bureau of Standards. Compilation of x-ray attenuation coefficients*, UCRL-50174, sec II, rev 1. Berkeley, CA: University of California, **1969**
13. Peppler WW, VanLysel MS, Dobbins JT, et al. Progress report on the University of Wisconsin digital video image processor DVIP II. In: Heintzen PH, Brennecke R, eds. *Digital imaging in cardiovascular radiology*. Stuttgart: Georg Thieme Verlag, **1983**:55-66

Diffusion-Weighted MR Imaging of the Brain: Value of Differentiating Between Extraaxial Cysts and Epidermoid Tumors

Jay S. Tsuruda[1]
Wil M. Chew
Michael E. Moseley
David Norman

This study demonstrates the use of diffusion-weighted MR imaging in improving the specificity of the diagnosis of extraaxial brain tumors. Three surgically proved lesions (one arachnoid cyst and two epidermoid tumors) and two nonsurgically proved lesions (arachnoid and ependymal cysts) were evaluated with T1- and T2-weighted spin-echo studies followed by intravoxel incoherent motion (IVIM) MR imaging. The IVIM images of the lesions were displayed as an apparent diffusion coefficient (ADC) image obtained at 0.65 G/cm (maximum gradient b value = 100 sec/mm^2) and compared with external oil and water phantoms. The ADC of arachnoid cysts was similar to stationary water whereas the ADC of epidermoid tumors was similar to brain parenchyma, indicating the solid nature and the slower diffusion rate of the epidermoid tumors. Cisternal CSF demonstrated uniformly high ADC, primarily because of bulk flow, which enhanced image contrast. Improved delineation of postsurgical changes was also possible.

Our preliminary results show that diffusion-weighted MR imaging can be useful in distinguishing between arachnoid cysts and epidermoid tumors.

***AJNR* 11:925–931, September/October 1990; *AJR* 155:1059–1065, November 1990**

The application of strong magnetic field gradients during proton MR imaging allows one to observe differences in molecular self-diffusion [1]. The basis for this diffusion is molecular translational (Brownian) motion, which leads to attenuation of signal intensity in each image voxel. Proton diffusion rates differ according to the tissue type; and specific techniques, such as intravoxel incoherent motion (IVIM) imaging, resulting in an apparent diffusion coefficient (ADC) image, have been developed to exploit these differences [1]. Early findings with diffusion-weighted imaging of normal patients [1–8] have yielded variable results in quantifying diffusion differences between CSF, gray matter, and white matter. Preliminary examples of intraparenchymal tumors and associated edema [1, 3, 5, 6], infarcts [1, 7], normal pressure hydrocephalus [7], and benign intracranial hypertension [1, 7, 8] have shown regions of either increased or restricted diffusion when compared with normal parenchyma.

Clinical application of this technique is significantly hindered by physiological pulsatile and uncontrolled patient motion. Artifacts generated by motion limit quantitative measurements and differentiation of critical anatomic structures; for example, gray/white matter interfaces [6]. This motion-generated artifact may be used to advantage in the case of in vivo macroscopic CSF motion, where the apparent diffusion value of CSF is increased when compared with stationary fluid [2]. This phenomenon may assist in accentuating image contrast between normal CSF and extraaxial tumors on a diffusion-weighted image. Additionally, further characterization of a mass lesion based on intrinsic diffusion values should be possible.

The purpose of this study was to demonstrate the utility of ADC imaging in improving conspicuity and specificity of extraaxial lesions in three surgically proved cases. We applied the knowledge gained from these three cases to assist in the

Received September 23, 1989; revision requested December 14, 1989; revision received February 5, 1990; accepted February 22, 1990.

Presented at the annual meeting of the Society of Magnetic Resonance in Medicine, Amsterdam, August 1989.

[1] All authors: Department of Radiology, Box 0628, 505 Parnassus Ave., University of California School of Medicine, San Francisco, CA 94143. Address reprint requests to J. S. Tsuruda.

0361-803X/90/1555-1059
© American Roentgen Ray Society

therapeutic management of two nonsurgically proved cases. The limitations of this technique and some pitfalls in image interpretation are also described.

Material and Methods

All studies were performed on a 1.5-T GE Signa system using a self-shielded RF gradient coil (1 G/cm maximum) and standard quadrature head coil. Prior to scanning, the patients were immobilized within the head coil with a vacuum-assisted device (size 20, Olympic Medical, Seattle, WA). In the majority of patients, an external phantom consisting of plastic tubing filled with mineral oil and water was simultaneously imaged. Care was taken to position the phantom such that it would be seen on any orthogonal slice through the brain. Acetone was also included as an external reference in one patient. All patients were initially studied with a multislice T1-weighted sagittal sequence, 600/20/2 (TR/TE/excitations), 5-mm-thick slices, 1-mm interslice gap, 22-cm field of view, and 192 × 256 matrix. This was followed by a multislice, multiecho T2-weighted sequence (2800/30,80/1), 5-mm thick, 2.5-mm interslice gap, 20-cm field of view, and 192 × 256 matrix. Gradient-moment nulling (Flow Compensation, General Electric) without cardiac gating was used on the long TR images. Additional T1-weighted sagittal and coronal images were obtained if additional anatomic detail was desired.

Multislice ADC images [1] were obtained in the axial plane using a cardiac-gated spin-echo sequence 900–1000 (effective TR)/100/2–4. The diffusion-gradient pulse duration was 30 msec with a gradient separation of 43 msec and a maximum gradient strength of 0.65 G/cm corresponding to a maximum gradient b value of approximately 100 sec/mm^2 [3]. The final ADC image reflects the ratio of signal intensities between two images obtained with either high b and low b gradient values. This method has been previously described in detail [1]. The diffusion gradient was applied along the frequency-encoding axis, which was oriented along the anterior-posterior direction on axial sections and along the superior-inferior direction on both the sagittal and coronal sections. Slice thickness was 5 mm with a field of view of 24 cm and a 128 × 256 matrix. Imaging time was approximately 8–13 min.

In three patients, surgical confirmation of the MR findings was obtained. In addition, the second patient also underwent axial and coronal CT cisternography immediately after a lumbar intrathecal injection of 5 ml of iohexol (Omnipaque 240, Winthrop). The fourth and fifth patients were also studied by contrast-enhanced MR immediately following IV injection of 0.1 mmol/kg gadopentetate dimeglumine (Magnevist, Berlex).

Results

Patient 1

A 40-year-old woman presented with a 1-year history of vertigo, nausea, right ear pain without hearing loss, and transient right upper extremity numbness with poor coordination. Short and long TR spin-echo images demonstrated a mass in the right cerebellopontine angle and lateral medullary cisterns with extrinsic compression of the brainstem and isointensity with CSF in all sequences (Figs. 1A–1C). On the

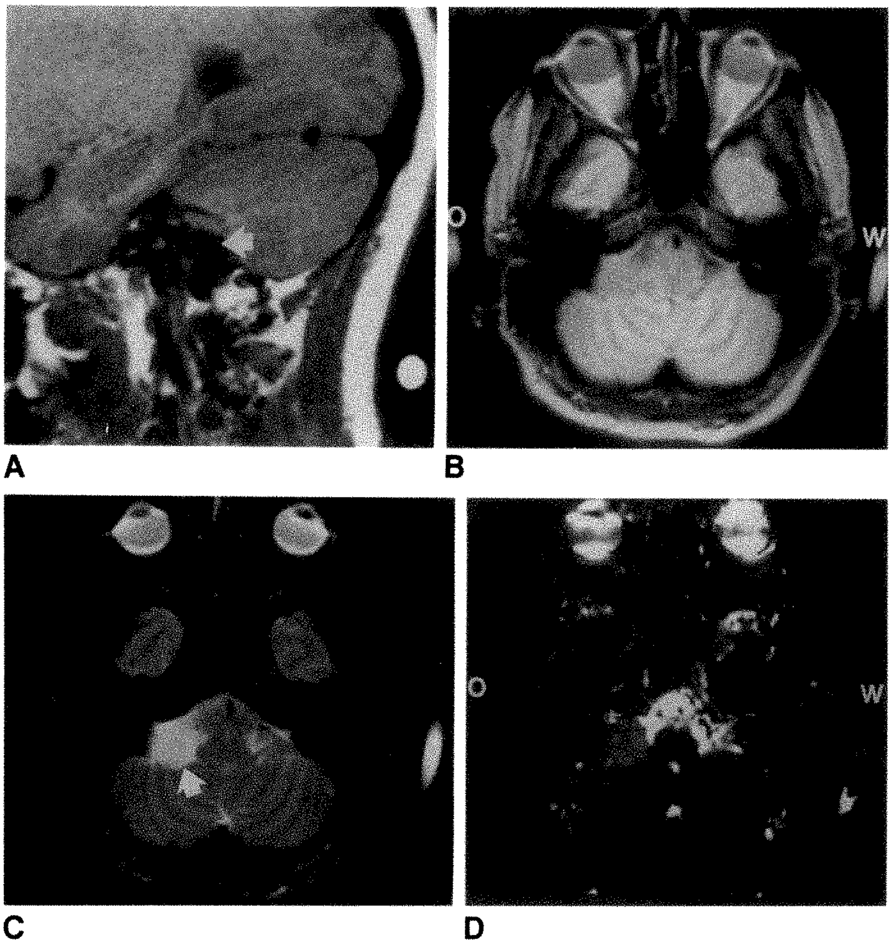

Fig. 1.—Patient 1: Arachnoid cyst of the posterior fossa.

***A*, Parasagittal T1-weighted image (600/20) shows widening of right cerebellopontine angle cistern (*arrow*). Note that a portion of the external oil phantom is seen posterior to upper neck.**

***B* and *C*, T2-weighted images (2800/30/80) confirm the presence of an extraaxial mass (*arrow* in *C*) of CSF signal intensity. Portions of the oil (O) and water (W) phantoms are shown.**

***D*, Apparent diffusion coefficient (ADC) image (gated/100) shows a distinct boundary between cisternal CSF and the mass, which is higher in signal intensity than adjacent cerebellum but similar in intensity to stationary water phantom (W). The oil phantom shows nearly complete loss of signal, compatible with its relatively slow diffusion constant. The increased signal within the eyes is due to orbital motion during image acquisition, causing an increase in the ADC. Slight heterogeneity of signal intensity is noted in lateral aspect of both cerebellar hemispheres due to phase artifact generated from orbital motion projecting posteriorly.**

ADC images, the mass was isointense with the stationary water phantom, and had slightly greater intensity compared with normal brain parenchyma. Cisternal CSF exhibited greater intensity than the stationary water phantom (Fig. 1D). The interface and contrast between the mass and the cistern was well defined. Because of the similarity in ADC signal intensity between the mass and stationary water, a diagnosis of a locculated fluid collection, compatible with an arachnoid cyst, was suggested and subsequently confirmed surgically.

Patient 2

A 55-year-old man who had had surgical resection of an intracranial epidermoid tumor at age 35 presented with complaints of progressive visual loss. A recurrence of the tumor was suspected clinically. Short and long TR spin-echo MR images (Figs. 2A–2F) showed an intraaxial anteromedial left frontal lesion and the suggestion of an extraaxial suprasellar lesion extending into the middle cranial fossa; both were isointense with CSF on all sequences.

CT cisternography (Figs. 2G–2J) demonstrated a CSF density mass in the suprasellar cistern, enlarged CSF spaces in the medial aspect of the left temporal lobe, and low density in the frontal lobe, the latter compatible with either encephalomalacia due to prior surgery or, less likely, epidermoid tumor. With CT cisternography, discrimination between enhancing cisternal CSF and tumor was possible; however, the low-density encephalomalacia could not be distinguished from the cisternal mass.

The ADC images (Figs. 2K–2M) showed uniformly increased signal intensity of the cisternal CSF, markedly decreased signal within the tumor (similar to normal brain parenchyma), and intermediate signal within the encephalomalacia. Orbital motion, resulting in phase artifact, degraded the phantom images, so quantitative comparison with tumor was not possible. However, qualitatively the ADC study indicated that the cisternal mass was solid in nature, indicating recurrence of epidermoid tumor and that separation between tumor and encephalomalacia was possible. These findings were confirmed surgically.

Patient 3

A 58-year-old woman was evaluated by MR for the diagnosis of left-sided tic douloureux. The short TR and long TR spin-echo MR images (Figs. 3A and 3B) demonstrated an asymmetric widening of the left cerebellopontine angle cistern with a mass of CSF-like intensity. Morphologically, this lesion most likely represented an epidermoid tumor; however, an arachnoid cyst could not be entirely excluded. The axial ADC image (Fig. 3C) revealed that the lesion was heterogeneous with signal intensity predominantly similar to brain parenchyma as opposed to either stationary water or cisternal CSF. The ADC image identified the solid nature of the mass and confirmed the presence of an epidermoid tumor, which was proved surgically.

Patient 4

A 5-year-old boy presented with a history of petit mal seizures, which were well controlled by medication. ECG indicated bihemispheric epileptogenic foci. Short and long TR images demonstrated a well circumscribed mass with intensity similar to CSF filling the right temporal horn and extending into the adjacent choroidal fissure. A preliminary diagnosis of an atypical arachnoid cyst was made. The ADC study (Fig. 4) confirmed the presence of stationary fluid intensity. The patient will be electively followed without surgical intervention.

Patient 5

A 26-year-old man presented with a several-month history of progressive dizziness associated with nausea and vomiting. The screening MR scan demonstrated moderate third and lateral ventriculomegaly requiring decompression by shunt tube placement and a mass in the posterior third ventricle, which was isointense with CSF. There was no enhancement on the postcontrast examination. The ADC image confirmed that this lesion behaved similarly to the stationary water phantom. The presumptive diagnosis was that of a third ventricular ependymal cyst rather than a solid neoplasm. Since ependymal cysts are a benign process, the patient will be electively followed without any further surgical intervention at this time.

Discussion

IVIM MR imaging, first described by Le Bihan and coworkers [3], is a method of obtaining images sensitive to microscopic translational motions that occur in each MR imaging voxel. The effect of IVIM is to cause an apparent reduction of the spin-echo signal and therefore a reduction of signal intensity. In biological tissue, this reduction is thought to be due primarily to molecular self-diffusion and perfusion (capillary flow). IVIM may be quantified by the use of different gradient b values [9] for different sequences (keeping all other parameters identical). In this fashion, magnitude images with differing b values are obtained. From two resulting magnitude images, an ADC image is constructed. In this study, we found that the ADC image was preferred over the magnitude image, since image contrast is independent of spin density, T1, and T2 differences. On the ADC image, relative signal intensity is due to differences in tissue diffusion and perfusion (if present). By using this method, one can calculate reproducible diffusion coefficients, in units of 10^{-5} cm^2/sec, of stationary fluids such as acetone, oil, water, and cyclohexane and compare them favorably with published values [10].

The application of ADC imaging in vivo has been met with limited success because of artifacts [6]. This image degradation is caused by the presence of coherent or incoherent macroscopic motion from either gross patient motion and/or physiological brain motion due to cardiac or respiratory pulsations. This increased sensitivity to patient motion is accentuated by the long imaging times required to obtain a diffusion-weighted spin-echo image [4]. An attempt was made to reduce unwanted motion by immobilizing the patient with a vacuum device originally suggested by Thomsen and coworkers [7]. An occasional image artifact was still present in some of our clinical cases, resulting in degradation of parenchymal detail with associated nonuniformity of signal intensity (Figs.

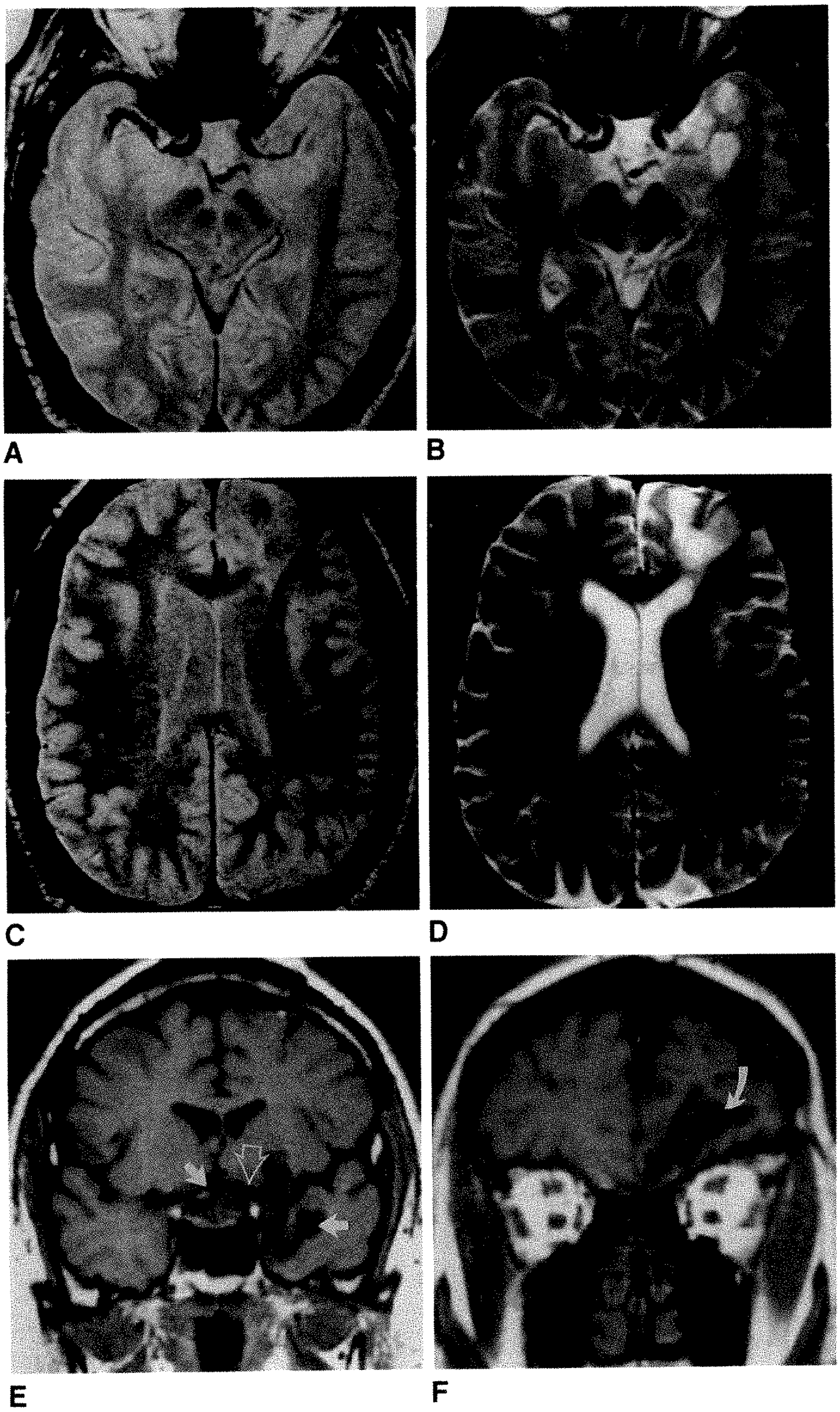

Fig. 2.—Patient 2: Epidermoid tumor and postoperative encephalomalacia.

A–D, Axial T2-weighted MR images (2800/30/80) show region of epidermoid tumor and encephalomalacia that is nearly isointense with CSF.

E and *F*, Coronal T1-weighted MR images (600/20) show that the region of suspected tumor (*solid arrows* in *E*) cannot be easily separated from cisternal CSF (*open arrow* in *E*) or from frontal lobe encephalomalacia (*curved arrow* in *F*).

(Fig. 2 is continued on the opposite page.)

2K–2M). Despite these limitations, diagnostic images were successfully obtained in all cases.

Physiological brain pulsations (up to 5 mm/sec) as a function of the cardiac cycle [11] have been observed in humans. These pulsations are several orders of magnitude greater than diffusion of water in the brain. Sensitivity to the pulsatile motion of the brain is unavoidable owing to the relatively long diffusion-gradient duration resulting in an echo delay time of 100 msec. These factors are required on our system in order to achieve high b values for our imaging sequences. These macroscopic motions are significant enough that measurements of diffusion coefficients of brain parenchyma may not be totally accurate [6]. An attempt was made to reduce physiological motion by the application of cardiac gating. The

Fig. 2—(continued).

G and *H*, Axial (*G*) and coronal (*H*) CT cisternogram images show presence of a low-density mass (*solid arrows*) in suprasellar cistern extending into left middle cranial fossa. Note the normally enhancing basal cisterns (*open arrows*).

I and *J*, More anteriorly, axial (*I*) and coronal (*J*) CT cisternogram images depict an additional region of low density (*curved arrows*) within frontal lobe consistent with either postoperative encephalomalacia or epidermoid tumor.

K–M, Axial (*K*) and coronal (*L* and *M*) apparent diffusion coefficient (ADC) (gated/100) images show epidermoid tumor (*solid straight arrows*) with signal intensity that is isointense with brain parenchyma, indicating solid nature of mass. The high signal intensity of cisternal CSF (*open arrow* in *L*) correlates quite well with the normally enhancing CSF seen previously on CT cisternogram. The region of left frontal encephalomalacia (*curved arrow* in *M*) has intermediate intensity and is uniquely different from cisternal CSF, epidermoid tumor, and brain parenchyma. Note the shading artifact throughout the brain parenchyma, best appreciated on the coronal images, caused by patient motion. Marked heterogeneity and signal loss within lateral ventricles is noted on coronal ADC images, and presumably is due to complex CSF motion. Orbital motion degrades external phantom detail as a result of phase artifact.

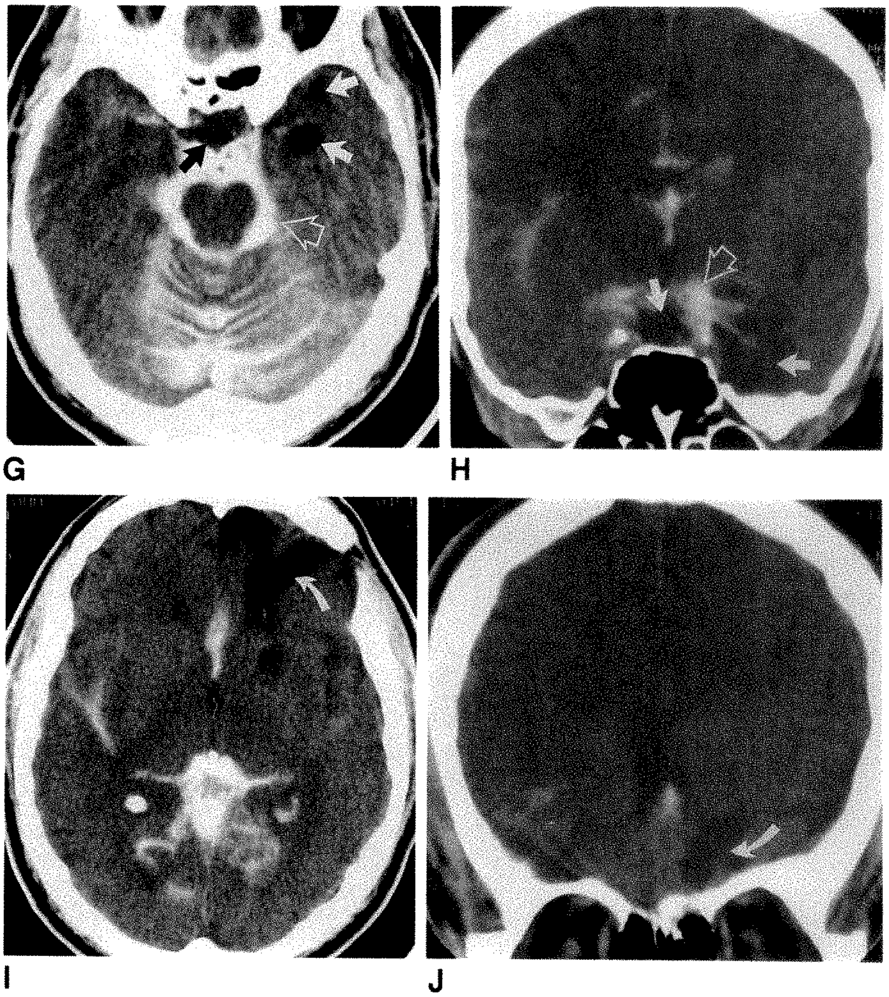

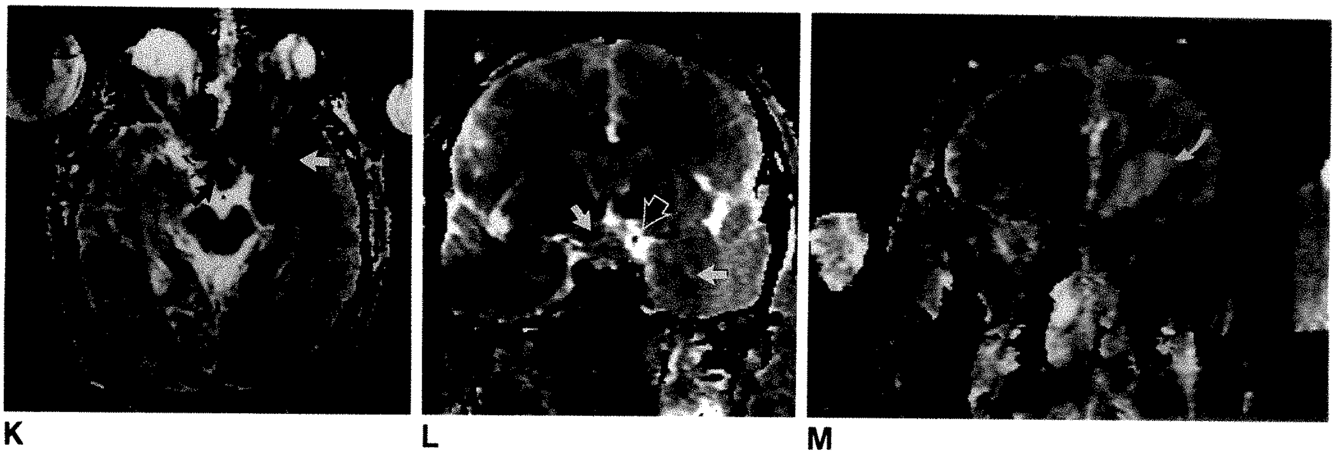

contribution of tissue perfusion to the ADC may not be observed, since the capillary bed only represents a small fraction (<5%) [1] of the total brain volume and is overshadowed by macroscopic brain motion, which has similar velocity as capillary flow. In addition, macroscopic fluid motion—such as bulk, nonuniform CSF flow—is also a contributing factor to image degradation [7].

Since macroscopic motion significantly contributes to ADC image artifact, alternative methods for reducing the overall scan time have been proposed. These include CE-FAST [6], steady-state free precession [4], and echo planar imaging [12, 13]. For spin-echo imaging, adequate motion suppression has been obtained on a small-bore system in anesthetized animals [10]. In the present study, oral sedation (chloralhydrate) was used for patient 4 (Fig. 4) with favorable results. The additional use of signal averaging up to 8–16 times can also decrease apparent motion artifact [6]. However, signal averaging will increase total acquisition to an unacceptably

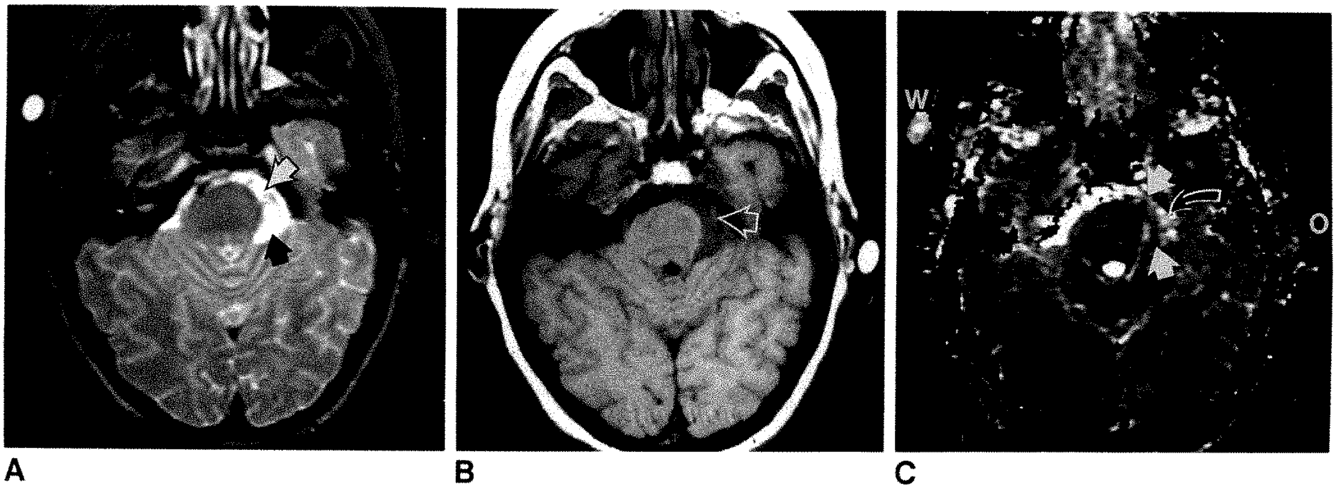

Fig. 3.—Patient 3: Epidermoid tumor.

A, Axial T2-weighted image (2800/80) depicts asymmetric widening of left cerebellopontine angle cistern by a lesion (*arrows*) with predominantly CSF intensity.

B, Axial T1-weighted image (600/20) confirms these findings. A portion of the left fifth cranial nerve can be identified (*open arrow*) within the lesion.

C, Apparent diffusion coefficient (ADC) (gated/100) study shows that this lesion (*straight arrows*) has similar signal intensity to the adjacent pons but quite distinct from either cisternal CSF or the stationary water phantom (W). The oil phantom (O) is also shown. The interface between tumor and cisternal CSF is well seen. Note that there appears to be minimal hyperintense CSF (*curved arrow*) lateral to mass.

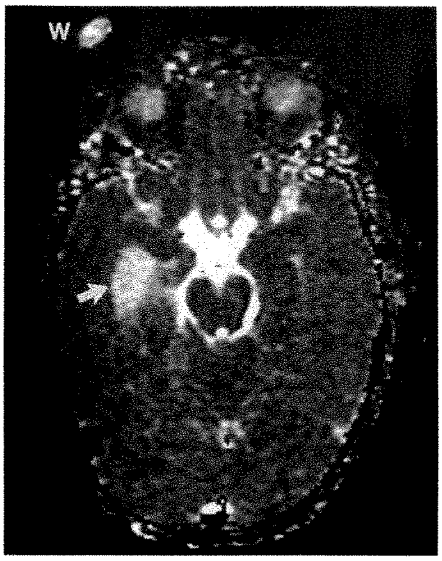

Fig. 4.—Suspected arachnoid cyst of right middle cranial fossa. Axial apparent diffusion coefficient (ADC) (gated/100) image confirmed that this lesion (*arrow*) has signal intensity similar to the water phantom (W). The lack of motion artifact was due to cardiac gating and patient immobilization. Slight heterogeneity was noted in the water phantom presumably due to truncation artifact.

long time for clinical application. To our knowledge, sequence optimization of spin-echo diffusion-weighted parameters, such as varying TR and gradient b values, in order to reduce motion artifact and improve signal-to-noise ratio has not been performed. This is an area that is currently under investigation in our laboratory.

Despite these limitations, we have noted that the ADC images have yielded consistently good results in delineating cisternal CSF. This is due to (1) the fast diffusion of CSF associated with water (2.5×10^{-5} cm^2/sec) [14]; (2) slowed diffusion associated with biological soft tissue, which is approximately 50% that of pure water [5]; and (3) macroscopic CSF flow, such as cisternal CSF, which further elevates its ADC over stationary water by up to 400% [2, 14]. From a quantitative standpoint, the differences in the ADC between brain parenchyma and CSF may be significantly different by several orders of magnitude. This potential for high dynamic range can be qualitatively seen on the ADC images as very high image contrast. In addition, any lesion that inhibits bulk CSF flow will be easily detected.

Variable success in obtaining homogeneously high signal intensity on the ADC images within the lateral ventricle was noted, presumably as a result of a greater degree of pulsatile motion leading to phase ghosting [6], especially if the flow is perpendicular to the imaging plane [7]. An example of this complex CSF flow artifact was noted in patient 2 (Fig. 2L). Phase artifact was also generated by orbital motion (Figs. 1D and 2K). This ghosting may be reduced with the application of gradient-moment nulling. Unfortunately, this technique was not available for our current diffusion-weighted sequences.

Determining tissue specificity on the basis of spin-echo images as well as calculated T1, T2, and proton-density values has been unreliable [15, 16]. In some cases complicated cysts may mimic solid neoplasms if there is alteration in protein content [17]. Additional factors such as the presence of paramagnetic substances may alter the signal intensity of cystic lesions [18]. Arachnoid cysts are typically isointense with CSF on all pulsing sequences [19–21] and are usually not a diagnostic challenge. Epidermoid tumors, on the other hand, may have variable signal intensity. According to some investigators [22–25], they are typically isointense or slightly hyperintense relative to CSF on both T1- and T2-weighted MR images. More definite diagnosis is valuable in planning the optimal surgical approach [23]. In our experience, there are cases in which the MR signal intensity of epidermoid tumors may closely approach that of CSF, thus leading to diagnostic uncertainty and poor definition of the surgical anatomy. These difficulties were encountered in patients 2 and 3. CT cisternography may still be indicated in problematic cases.

ADC imaging yielded additional specificity in distinguishing between the cystic and solid nature of these tumors. External oil and water phantoms provided a more objective reference intensity value for identifying slowed diffusion within the epidermoid tumors. Improved delineation of the interface between the lesion and adjacent CSF was possible owing to the replacement of normally pulsatile cisternal CSF. In one sense, ADC imaging represents a physiological MR "cisternogram." In the second patient, ADC imaging, as compared with routine spin-echo MR and CT cisternography, was the only method that could distinguish between epidermoid tumor and postoperative encephalomalacia. While no definitive conclusions can be drawn from this single example, with improvements such as higher b values and/or faster imaging schemes, more valid conclusions on analyzing brain parenchyma may be obtainable while reliable quantitative diffusion numbers may provide additional tissue specificity. Furthermore, analysis of brain-water content may also be feasible. For example, initial studies have shown that early brain ischemia can be detected by changes in diffusion-restricted water and may function as an indicator of early cytotoxic edema [10].

Conclusions

Our preliminary results show that diffusion-weighted MR imaging is helpful in characterizing and distinguishing between arachnoid cysts and epidermoid tumors that may be difficult to distinguish from CSF on spin-echo MR images. Improved differentiation of postsurgical changes was also possible. Several factors contribute to the increase in intensity of cisternal CSF on the ADC images, most importantly bulk flow. This effect will enhance image contrast between normally pulsatile CSF and nonpulsatile extraaxial tumors. Proper patient immobilization is important. Despite limitations imposed by macroscopic motion, we have adopted this technique as a routine tool in further characterizing challenging extraaxial lesions.

ACKNOWLEDGMENTS

We thank James R. MacFall and Ann Shimakawa for their support and helpful comments.

REFERENCES

1. Le Bihan D, Breton E, Lallemand D, Aubin M-L, Vignaud J, Laval-Jeantet M. Separation of diffusion and perfusion in intravoxel incoherent motion MR imaging. *Radiology* **1988**;168:497–505
2. Chien D, Buxton R, Rosen B, Johnson K. MR imaging of restricted diffusion in biological systems. *Proceedings of annual meeting Soc Magn Reson Med*, New York City, **1987**:887
3. Le Bihan D, Breton E, Lallemand D, Grenier P, Cabanis E, Laval-Jeantet M. MR imaging of intravoxel incoherent motions: application to diffusion and perfusion in neurologic disorders. *Radiology* **1986**;161:401–407
4. Le Bihan D. Intravoxel incoherent motion imaging using steady-state free precession. *Magn Reson Med* **1988**;7:346–351
5. Le Bihan D, Breton E, Lallemand D, Brugieres P, Gueron M. Tissue characterization by molecular diffusion using intravoxel incoherent motion (IVIM) MR imaging. *Proceedings of annual meeting Soc Magn Reson Med*, San Francisco, **1988**:306
6. Merboldt K-D, Bruhn H, Frahm J, Gyngell M, Hanicke W, Deimling M. MRI of "diffusion" in the human brain: new results using a modified CE-FAST sequence. *Magn Reson Med* **1989**;9:423–429
7. Thomsen C, Henriksen O, Ring P. In vivo measurement of water self diffusion in the human brain by magnetic resonance imaging. *Acta Radiol* **1987**;28:353–361
8. Thomsen C, Gjerris F, Sørensen S, Ring P, Henriksen O. Increased water self diffusion in the brain white matter in patients with abnormal CSF hydrodynamics. *Proceedings of annual meeting Soc Magn Reson Med*, San Francisco, **1988**:118
9. Carr H, Purcell E. Effects of diffusion on free precession in nuclear magnetic resonance experiments. *Physiol Rev* **1954**;94:630–635
10. Cohen Y, Mintorovitch J, Chileuitt L, et al. Early detection of ischemic injury: comparison of diffusion and T2-weighted MRI and spectroscopy during regional cerebral ischemia in cats. *Proceedings of annual meeting Soc Magn Reson Med*, Amsterdam, **1989**:42
11. Feinberg D, Mark A. Human brain motion and cerebrospinal fluid circulation demonstrated with MR velocity imaging. *Radiology* **1987**;163:793–799
12. Le Bihan D, Turner R, MacFall J. Artifacts in intravoxel incoherent motion (IVIM) MR imaging. *Proceedings of annual meeting Soc Magn Reson Imaging*, Los Angeles, **1989**:172
13. Turner R, Le Bihan D, Delannoy J, Pekar J. Echo-planar diffusion and perfusion imaging at 2.0 Tesla. *Proceedings of annual meeting Soc Magn Reson Med*, Amsterdam, **1989**:139
14. Le Bihan D, Breton E, Barth M, Aubin M, Lallemand D, Vignaud J. CSF flow and diffusion mapping using intra-voxel incoherent motion (IVIM) imaging. *Proceedings of annual meeting Soc Magn Reson Med*, New York City, **1987**:313
15. Komiyama M, Yagura H, Yasui T, Hakuba A, Nishimura S, Inoue Y. MR imaging: possibility of tissue characterization of brain tumors using T1 and T2 values. *AJNR* **1987**;8:65–70
16. Just M, Thelen M. Tissue characterization with T1, T2, and proton density values: results in 160 patients with brain tumors. *Radiology* **1988**;169:779–785
17. Haimes A, Zimmerman R, Morgello S, et al. MR imaging of brain abscesses. *AJNR* **1989**;10:279–291
18. Hackney D, Grossman R, Joseph P, Goldberg H, Bilaniuk L, Spagnoli M. Low sensitivity of clinical MR imaging to small changes in the concentration of nonparamagnetic protein. *AJNR* **1987**;8:1003–1008
19. Harsh G, Edwards M, Wilson C. Intracranial arachnoid cysts in children. *J Neurosurg* **1986**;64:835–842
20. Wiener S, Pearlstein A, Eiber A. MR imaging of intracranial arachnoid cysts. *J Comput Assist Tomogr* **1987**;11:236–241
21. Garcia-Bach M, Ismat F, Vila F. Intracranial arachnoid cysts in adults. *Acta Neurochir Suppl* (Wein) **1988**;42:205–209
22. Vion-Dury J, Vincentelli F, Jiddane M, et al. MR imaging of epidermoid cysts. *Neuroradiology* **1987**;29:333–338
23. Olson J, Beck D, Crawford S, Menezes A. Comparative evaluation of intracranial epidermoid tumors with computed tomography and magnetic resonance imaging. *Neurosurgery* **1987**;21:357–360
24. Steffey D, De Filipp G, Spera T, Gabrielsen T. MR imaging of primary epidermoid tumors. *J Comput Assist Tomogr* **1988**;12:438–440
25. Tamperi D, Melanson D, Ethier R. MR imaging of epidermoid cysts. *AJNR* **1989**;10:351–356

The reader's attention is directed to the commentary on this article, which appears on the following pages.

Commentary

Diffusion-Weighted MR Imaging: A Useful Adjunct to Clinical Diagnosis or a Scientific Curiosity?

R. Mark Henkelman[1]

It has been appreciated from the earliest development of MR imaging that MR images are exquisitely sensitive to motion. This sensitivity remains the major limitation in the application of MR to the body. However, it also has been appreciated that motion is not simply a problematic source of artifact. Motion sensitivity can be used to advantage in sequences designed to highlight the flow sensitivity in blood, making possible MR angiography. Provided flow and pulsatile motion can be controlled satisfactorily, motions as small as those arising from perfusion and diffusion can be used to enhance contrast in specially sensitized MR imaging sequences.

The pioneering work of Le Bihan et al. [1] in 1986 showed that MR pulse sequences can be sensitized to perfusion and diffusion. This sensitization showed specificity for certain neurologic disorders. The diffusion sensitivity of such images was based on straightforward physical principles, which had been elucidated two and three decades earlier [2, 3]. The MR acquisition records two interleaved images: (1) a standard spin-echo image and (2) an identical image with additional balanced diffusion-gradient pulses that have no effect on static spins but result in a loss of phase coherence for randomly diffusing spins. Subtraction of the second diffusion-sensitive image from the first reference image results in a much noisier image in which the contrast is proportional to the diffusion coefficient at least for pure static liquids. In a patient, a large number of additional factors contribute to this different image. The contrast is therefore referred to as an apparent diffusion coefficient (ADC). If the diffusion-encoding gradients are comparatively weak, the contrast in the ADC image will depend on susceptibility, perfusion, and restricted diffusion [4], but as the strength of the diffusion-encoding gradients becomes greater, the contrast becomes dependent primarily on diffusion [5].

By 1988, ADC imaging had attracted the attention of a number of groups. More than a dozen papers at the Society of Magnetic Resonance in Medicine meeting in San Francisco in 1988 reported preliminary results of the appearance of a variety of pathologic conditions on ADC images.

Despite the interest and enthusiasm, it was clear that ADC imaging still had a number of technologic problems: (1) Persistent eddy currents arising from large pulse gradients can contribute to signal intensity in nondiffusing tissue. This problem has been resolved to a large degree with the advent of self-shielded gradients with markedly diminished eddy current properties (Le Bihan et al., paper presented at the annual meeting of the Society of Magnetic Resonance Imaging, Los Angeles, 1989). (2) Motion seriously degrades ADC images. The sensitivity of ADC imaging to the small motion associated with diffusion makes the technique highly sensitive to any displacement motion of the tissue. Restriction of motion has required restraint of the head by means of sophisticated packing techniques and even sedation. Multiple averages and gradient-moment-nulling techniques also reduce the effect of patient motion and flow. Nonetheless, use of ADC imaging is restricted to the head, and even there residual motion of the

---

This article is a commentary on the article by Tsuruda et al.

[1] Department of Medical Biophysics, University of Toronto, 500 Sherbourne St., Toronto, Ontario, Canada M4X 1K9. Address reprint requests to R. M. Henkelman.

AJNR 11:932-934, September/October 1990; AJR 155:1066-1068, November 1990 0361-803X/90/1555-1066 © American Roentgen Ray Society

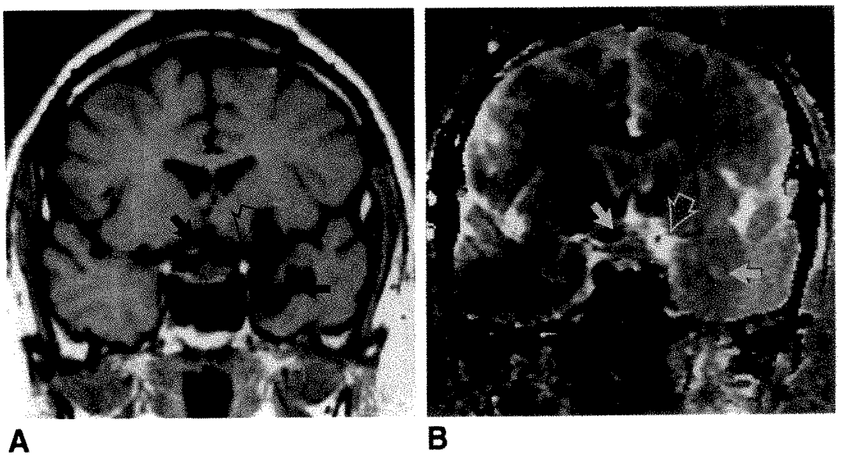

Fig. 1.—*A* and *B*, On T1-weighted MR image (*A*), regions of suspected tumor (*solid arrows*) cannot be distinguished from cisternal CSF (*open arrow*). On apparent diffusion coefficient (ADC) image (*B*), ADC of tumor is equivalent to that of parenchyma brain (*solid arrows*), indicating solid nature of mass. (Reprinted with permission from Tsuruda et al. [6].)

orbits can seriously degrade ADC images. More recently, apparent diffusion sensitization has been combined with echo-planar imaging to diminish some of the impact of tissue motion. (3) Even when gross tissue motion is controlled, small-amplitude pulsatile motion makes significant contributions to the ADC. Cardiac gating is required to diminish this effect in ADC imaging, although it is unlikely to eliminate pulsation completely as a source of some of the contrast.

Thus, reliable ADC imaging requires careful control of other confounding sources of motion that could contribute apparent contrast. The appropriate management of all motion other than diffusion is essential for reliable ADC contrast. Although many helpful techniques have been worked out, reliable ADC contrast cannot be achieved in every study.

What kind of medically useful information can be obtained from ADC images? Does it provide a useful adjunct for differential diagnosis? Or is ADC imaging simply another example of MR technical wizardry? Will it remain simply a scientific curiosity?

This issue of *AJNR* presents an example [6] of clinical problems for which ADC imaging provides additional useful information. Tsuruda et al. have shown that ADC imaging can help differentiate between extradural cysts and epidermoid tumors, which can appear identical on T2-weighted sequences. The epidermoid tumors, which are generally more solid than arachnoid cysts, lead to less ADC contrast than is seen in CSF (Fig. 1). Bulk flow of nonencapsulated CSF yields an even greater ADC and allows ready distinction of arachnoid cysts from the surrounding CSF. This appears to be a better method for differentiating arachnoid cysts than the one that uses the flow sensitivity of gradient-echo sequences [7].

The article by Moseley et al. [8] in the May/June 1990 issue of *AJNR* reports that regions of brain ischemia show a twofold decrease in ADC 1 hr after the loss of vascular supply, whereas T2 contrast changes require 5 hr to develop. The cause of the decrease in ADC is not yet fully understood. It is unlikely to be due to changes in intracellular edema at this early time and simply may arise from reduced pulsatility in the ischemic region. Alternatively, it could arise from a decrease in temperature in the infarcted region with an associated decrease in the diffusion coefficient. Whatever the mechanism of action may be, it appears to be a reproducible and reliable correlate of ischemia.

ADC imaging also can be used to distinguish necrotic regions within tumors from viable tumor cells. The necrotic region with degraded cell walls shows a higher ADC than the viable tumor tissue does. Enhanced apparent diffusion contrast correlates with extracellular gadolinium contrast en-

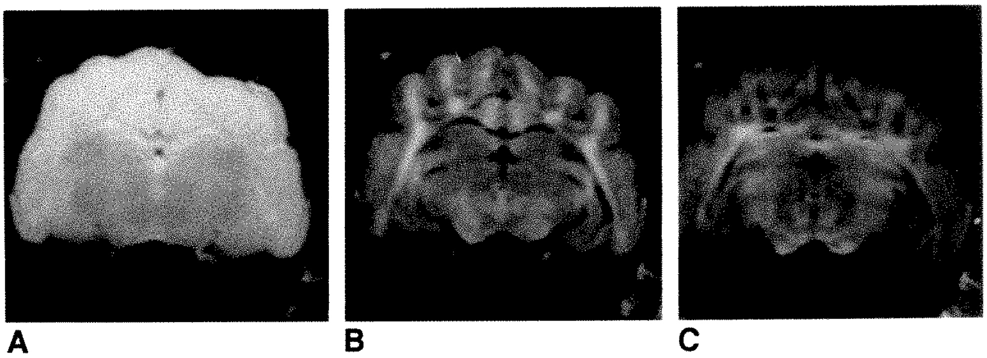

Fig. 2.—*A–C*, T2-weighted (*A*) and diffusion-weighted (*B* and *C*) coronal MR images of cat brain. Direction of diffusion-sensitizing gradient is left to right in *B* and top to bottom in *C*. When white-matter tracts are oriented parallel to direction of diffusion gradient, fast directional diffusion of water is indicated by regions of hypointensity. (Reprinted with permission from Moseley et al. [7].)

hancement in the necrotic regions (Moseley ME, personal communication).

Thus, several areas of clinical diagnosis already are benefiting from ADC imaging. As the technique becomes more widely established, undoubtedly additional problems in differential diagnosis will benefit from the unique information provided by this new form of MR contrast.

Beyond immediate diagnostic applications, ADC imaging is providing fundamental insights into the nature of relaxation processes in MR imaging. Recent work by Moseley et al. (personal communication) shows that the ADC has a marked directional dependence in white matter, which is probably a reflection of the restricted diffusion of water within the layers of the myelin sheath (Fig. 2). Similar restricted diffusion has been detected in MR spectroscopy of phosphorus metabolites in muscle [9]. These kinds of measurement, which are unlikely to be of immediate diagnostic use, provide deeper insight into the mechanistic processes that give rise to relaxation contrast in MR imaging. As these processes are understood more completely, it is likely that much more specific imaging acquisition sequences with unique contrast characteristics can be developed to exploit such contrast mechanisms.

Diffusion-weighted MR imaging is here to stay. It already has demonstrated its ability to provide differential diagnostic information. It also is beginning to give us new information that enhances our understanding of the mechanisms of tissue relaxation themselves, satisfying our scientific curiosity *and* promising further contributions to reliable clinical diagnoses.

REFERENCES

1. Le Bihan D, Breton E, Lallemand D, Grenier P, Cabanis E, Laval-Jeantet M. MR imaging of intravoxel incoherent motions: applications to diffusion and perfusion in neurologic disorders. *Radiology* **1986**;161:401–407
2. Stjskal EO, Tanner JE. Spin diffusion measurements: spin echoes in the presence of a time-dependent field gradient. *J Chem Phys* **1965**;42:288–292
3. Carr HY, Purcell EM. Effects of diffusion on free precession in nuclear magnetic resonance experiments. *Phys Rev* **1954**;94:630–638
4. Zhong J, Gore JC. Studies of restricted diffusion in heterogeneous media containing variations in susceptibility. In: *Future directions in MRI of diffusion and microcirculation: workshop syllabus*. Berkeley: Society of Magnetic Resonance in Medicine, **1990**:166–179
5. Le Bihan D, Breton E, Lallemand D, Aubin ML, Vignaud J, Laval-Jeantet M. Separation of diffusion and perfusion in intravoxel incoherent motion MR imaging. *Radiology* **1988**;168:497–505
6. Tsuruda JS, Chew WM, Moseley ME, Norman D. Diffusion-weighted MR imaging of the brain: value of differentiating between extraaxial cysts and epidermoid tumors. *AJNR* **1990**;11:925–931
7. Henkelman RM, McVeigh ER, Crawley AC, Kucharczyk W. Very slow flow in-plane flow with gradient echo imaging. *Mag Res Imag* **1989**;7:383–393
8. Moseley ME, Kucharczyk J, Mintorovitch J, et al. Diffusion-weighted MR imaging of acute stroke: correlation with T2-weighted and magnetic susceptibility-enhanced MR imaging in cats. *AJNR* **1990**;11:423–429
9. Moonen CTW, Van Zijl PCM, Le Bihan D, DesPres D. In vivo NMR diffusion spectroscopy: ^{31}P application to phosphorus metabolites in muscle. *Mag Res Med* **1990**;13:467–477

MR Imaging of CSF-like Choroidal Fissure and Parenchymal Cysts of the Brain

John L. Sherman[1,2]
Ernest Camponovo[3]
Charles M. Citrin[1,2]

The purposes of this study were to delineate the MR characteristics of CSF-like parenchymal or fissural cysts of the brain and to correlate them with the clinical findings. Clinical data and MR images of 34 patients with these abnormalities were reviewed. Pathologic correlation was not available. Two types of cystic lesions were identified and separated by location: medial temporal lobe cysts arising in or near the choroidal fissure (26 patients) and parenchymal or pseudoparenchymal cysts not related to the choroidal fissure (eight patients). The choroidal fissure cysts simulated intraparenchymal cysts on axial images but their extraaxial location was well portrayed on the coronal images. Choroidal fissure cysts had a characteristic spindle shape on sagittal images. The other cysts were found in the temporal lobe (seven patients) or thalamus (one patient) and appeared parenchymal but situated close to the subarachnoid space. These lesions were round or ovoid. There was no abnormal enhancement in 10 patients studied with gadopentetate dimeglumine. Coronal images were most useful, revealing the cysts as focal CSF-intensity lesions expanding the choroidal fissure of the temporal lobe. All the cysts appeared to represent incidental findings that did not correlate with the clinical signs and/or symptoms that prompted the imaging evaluations.

The MR characteristics of CSF-like cysts are important to recognize so that they are not confused with other, more serious entities, such as intraaxial cystic tumors, infarctions, or parasitic lesions.

***AJNR* 11:939-945, September/October 1990; *AJR* 155:1069-1075, November 1990**

Cysts of the CNS are categorized in a variety of ways. However, the most important consideration is whether the lesion is neoplastic or nonneoplastic. If it is nonneoplastic, it is then important to determine the potential clinical significance of the cyst. We have encountered a variety of cystic lesions involving the temporal lobe, including a group with strikingly similar imaging characteristics. We examined the MR characteristics and determined the clinical significance of these cysts with emphasis on lesions that invaginate the temporal lobe.

Patients and Methods

Thirty-four patients with CSF-like paramedian temporal lobe or basal ganglia cysts were prospectively identified over a 3-year period by one of the authors. All examinations included at least three sequences: T1-weighted spin-echo, 500–600/20–25/2 (TR range/TE range/excitations), intermediate spin-echo (2400–2700/30–40/1, 2), and T2-weighted spin-echo (2200–2700/60–90/1, 2). Section thickness was 5 or 7 mm. Without surgical exploration, we determined that the lesions were benign cysts on the basis that they had characteristics typical of cysts in the brain and other anatomic areas; that is, no detectable wall or associated soft-tissue mass, homogeneous consistency, signal intensity identical to CSF, absence of surrounding edema or gliosis, and lack of contrast enhancement (selected cases) [1, 2]. Gadopentetate-dimeglumine–enhanced MR imaging was performed in 10 patients. CT scans were obtained by us or were available for review in 20 patients. We obtained clinical correlation by conferring with the referring physician and by reviewing the patient charts. Follow-up MR examinations, made 2–24 months after the initial study, were acquired in 10 patients.

Received October 30, 1989; revision requested January 2, 1990; revision received February 23, 1990; accepted February 23, 1990.

Presented in part at the annual meeting of the American Society of Neuroradiology, Chicago, May 1988.

[1] Wheaton Magnetic Imaging, Washington Imaging Center, 2801 University Blvd., Kensington, MD 20895. Address reprint requests to J. L. Sherman.

[2] Department of Radiology, Uniformed Services University of the Health Sciences, Bethesda, MD 20814.

[3] Department of Radiology, National Naval Medical Center, Bethesda, MD 20814.

0361-803X/90/1555-1069
© American Roentgen Ray Society

Results

Two types of cystic lesions were identified: medial cysts that were shown to arise in or near the choroidal fissure on coronal images and parenchymal or pseudoparenchymal cysts not related to the choroidal fissure. All cysts were sharply demarcated from the adjacent brain. There was no discernible wall or evidence of surrounding gliosis. There was no evidence of mass effect or edema. The cysts were isointense with CSF on all sequences. None of the patients had surgery on the cysts or died during the period of the study; thus, there is no histopathologic correlation.

Group 1

Group 1 consisted of 26 patients in whom the cysts were identified in or near the choroidal fissure of the medial temporal lobe. These patients ranged in age from 5 to 74 years (mean, 38 years). There were 16 females and 10 males. The cysts were bilateral in two patients, and typically were ovoid in shape with the long axis in the anteroposterior plane parallel to the choroidal fissure (Figs. 1–5). The cysts typically appeared intraaxial on axial images but their relationship with the choroidal fissure was apparent on coronal images. On sagittal images the cysts were spindle-shaped (Figs. 1 and 2). Cyst size varied from 5 × 4 × 4 mm to 30 × 20 × 18 mm. The average size was 11.0 × 8.7 × 8.7 mm. Gadopentetate-dimeglumine–enhanced MR imaging was performed in five of these patients and revealed no evidence of enhancement on T1-weighted images (Fig. 4). CT scans with and without contrast enhancement were available in 10 patients, while only noncontrast scans were available in five patients. The cysts were not seen owing to artifact in three patients. In the other eight patients the cysts appeared isodense (cursor density measurements were not available) with CSF (Figs. 2 and 5).

Clinical Correlation: Group 1

The MR studies were performed to evaluate for suspected tumor, brain trauma, infarct, or demyelinating disease. Primary symptomatology included complex migraine headache syndrome (five patients) (Figs. 3 and 4), seizure disorder (five patients), gait disturbance/tremor (four patients), vertigo/hearing loss (three patients), head trauma (two patients) (Fig. 1), paresthesia (two patients), hemiparesis (three patients), visual scotomata (one patient) (Fig. 5), and positive HIV test (one patient) (Fig. 2). The combined imaging and clinical assessment was that the cysts could not explain the patients' signs or symptoms. Clinical follow-up without development of signs or symptoms referable to the cysts varied from 3–34 months (average, 17.8 months). In the five patients with seizures the clinical assessment was that the cysts were probably unrelated to the seizures since there were no focal electroencephalographic signs or physical manifestations of the seizure disorders that corresponded to the cysts.

Group 2

Group 2 was composed of eight patients in whom the cysts were unrelated to the choroidal fissure and appeared intraparenchymal in that a definite communication with the subarachnoid space could not be identified on images in all three planes. There were seven women and one man, ranging in age from 18 to 61 years (average, 46 years). Five patients were studied with gadopentetate dimeglumine without evidence of enhancement. The cysts were isodense with CSF on CT scans with and without contrast in five patients.

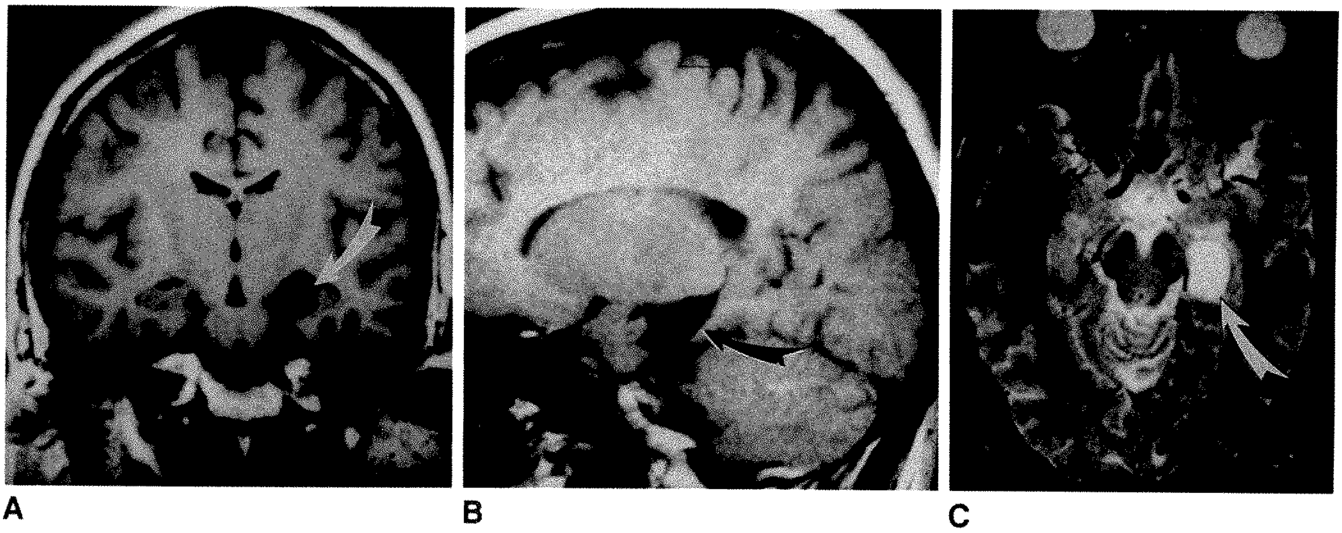

Fig. 1.—Left choroidal fissure cyst (*arrows*) in 36-year-old man who had CT scan (not shown) for head trauma. MR was obtained to evaluate hypodensity in left temporal lobe.

A, Coronal T1-weighted spin-echo image (600/20).

B, Sagittal T1-weighted spin-echo image (500/20) reveals typical spindle-shaped cyst.

C, Axial T2-weighted spin-echo image (2600/80).

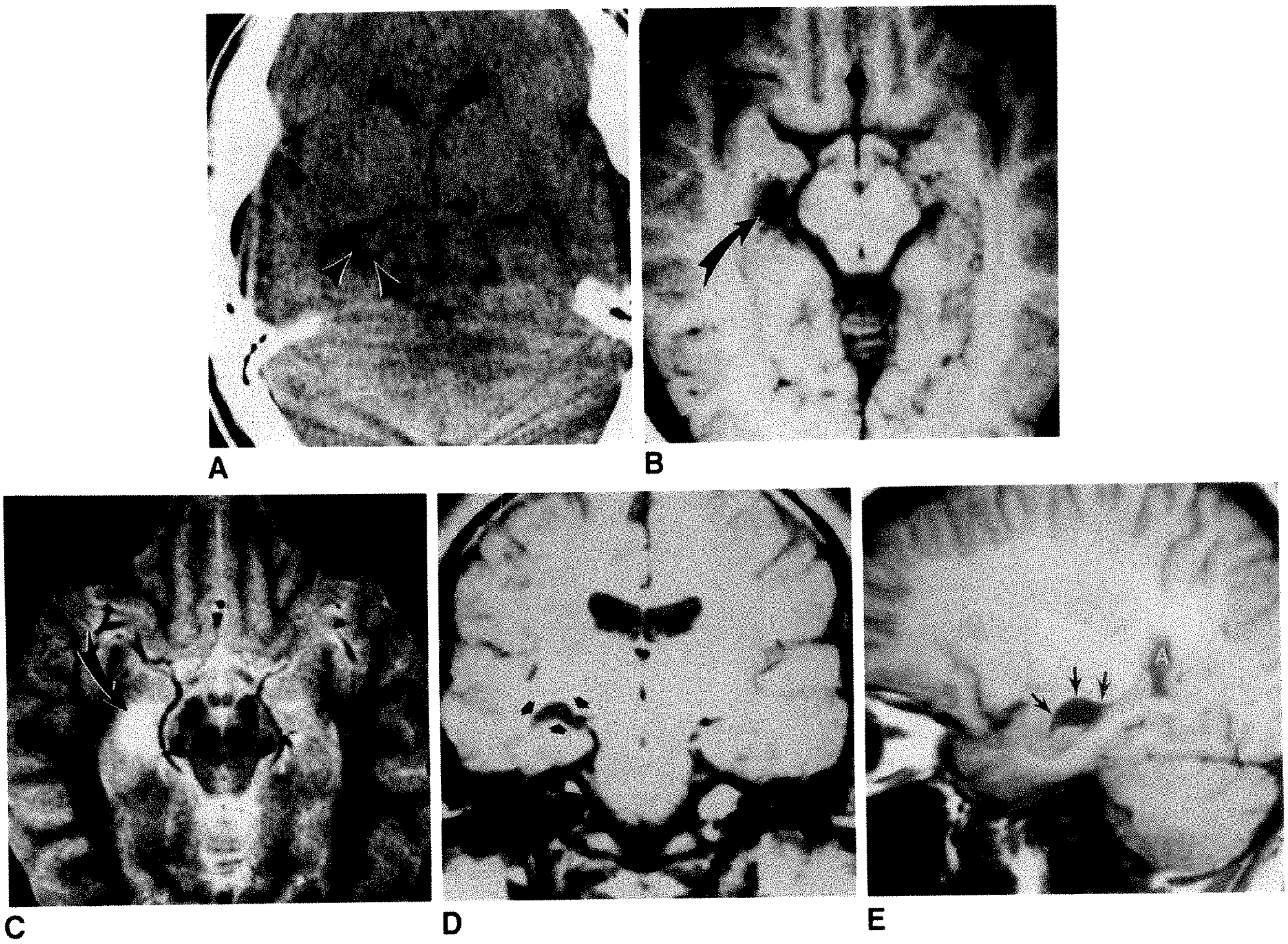

Fig. 2.—Right choroidal fissure cyst (*arrows*) in 31-year-old HIV-positive man who had MR after CT demonstrated lesion in right temporal lobe.

A, Noncontrast CT scan. Poorly demarcated right temporal lobe lesion (*arrowheads*) is difficult to differentiate from ventricle.

B–E, MR images clearly reveal characteristics of cyst in all three planes. The cyst appears intraparenchymal on axial images. Axial T1-weighted spin-echo image (600/20) (*B*). Axial T2-weighted spin-echo image (2600/80) (*C*). Coronal T1-weighted spin-echo image (600/20) (*D*) most clearly shows cyst origin in choroidal fissure. Sagittal T1-weighted spin-echo image (600/20) (*E*) reveals typical spindle-shaped cyst. (A = atrium of lateral ventricle.)

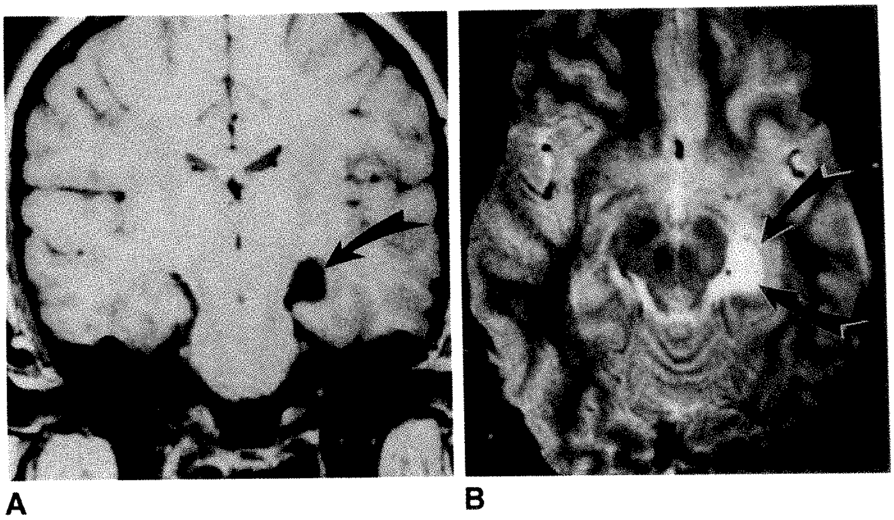

Fig. 3.—Left choroidal fissure cyst (*arrows*) in 13-year-old girl who had MR for evaluation of complex migraine headache and paresthesia.

A and *B*, Typical appearance of cyst between mesial temporal lobe and brainstem is seen on coronal T1-weighted spin-echo image (600/20) (*A*) and axial T2-weighted spin-echo image (2500/80) (*B*).

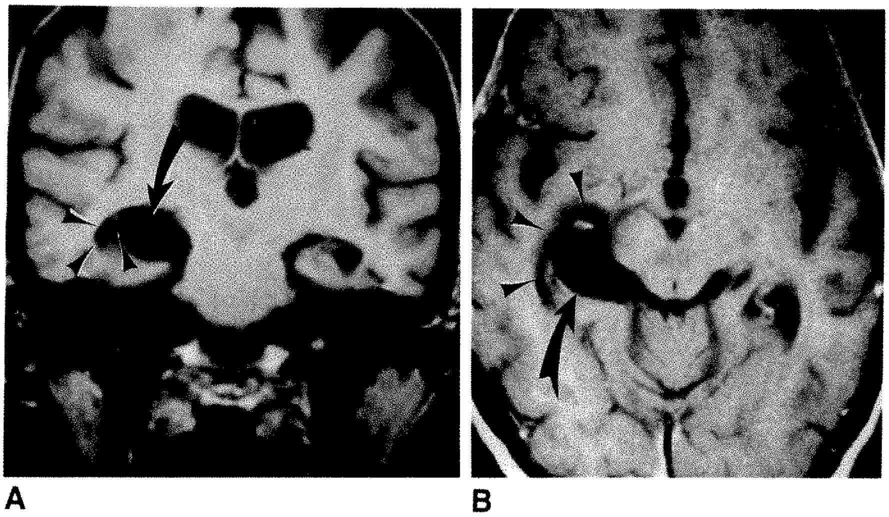

Fig. 4.—Right choroidal fissure cyst in 74-year-old woman with cerebral atrophy who was evaluated for migraine headaches and depression.

A and *B*, Large cyst (*arrows*) medial to temporal tip of lateral ventricle (*arrowheads*) is seen on coronal T1-weighted spin-echo image (600/25) (*A*) and gadopentetate-dimeglumine-enhanced axial T1-weighted spin-echo image (500/20) (*B*). There is no enhancement of lesion.

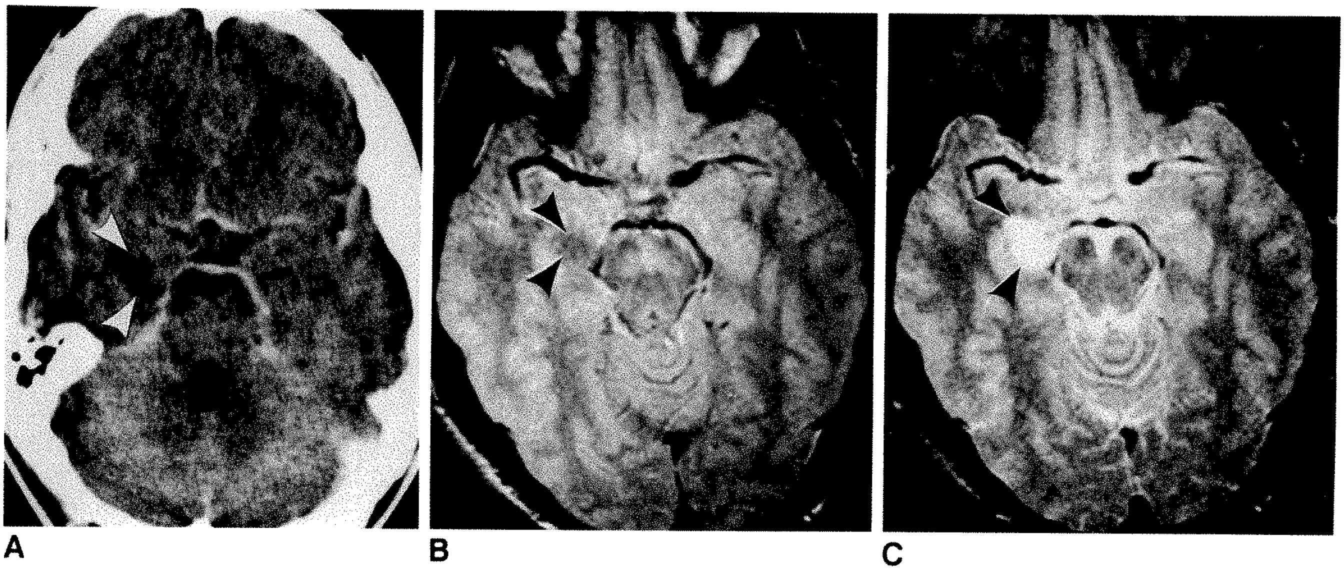

Fig. 5.—Right choroidal fissure cyst (*arrowheads*) in 27-year-old man with visual scotomata.

A–C, CSF-density cyst was discovered on contrast CT scan (*A*). Cyst is isointense with CSF on axial proton-density-weighted spin-echo MR image (2600/30) (*B*) and axial T2-weighted spin-echo MR image (2600/80) (*C*).

The cysts in this group were more rounded and irregular in shape than those in Group 1. They varied in size from 6 × 5 × 5 mm to 20 × 12 × 22 mm. Five patients had cysts near the sylvian fissure (Figs. 6 and 7). These patients (ages 42, 48, 49, 54, and 61) had lesions that were just inferior to the sylvian fissure and in three cases were indented or invaginated by a branch of the middle cerebral artery. On T1-weighted images this appearance simulated a giant aneurysm. Two patients (ages 58 and 31) each had a cyst just superior to the temporal tip of the lateral ventricles. These did not appear to communicate with the ventricles or with the adjacent subarachnoid space. One patient (66 years old) had a septated cyst extending into the thalamus (Fig. 8) measuring 25 × 15 × 15 mm, which did not appear directly related to the choroidal fissure or the adjacent ventricle.

Clinical Correlation: Group 2

None of these patients had seizure disorders. Of the five patients with cysts near the sylvian fissure one was evaluated for diplopia, one for hearing loss, one for paranasal sinus disease, one for mild head trauma, and one for vertigo. This subgroup of patients has been followed clinically for an average of 17 months (4–24 months) without development of symptomatology related to the temporal lobe. A 31-year-old woman had MR imaging for evaluation of hemifacial pain. The cyst was unrelated to her symptoms. She has been followed for 6 months. A 55-year-old woman had a cystic lesion in the thalamus. It appeared septated and did not change over a 3-year period. The patient was originally evaluated for migraine headache and had no signs or symptoms that were related

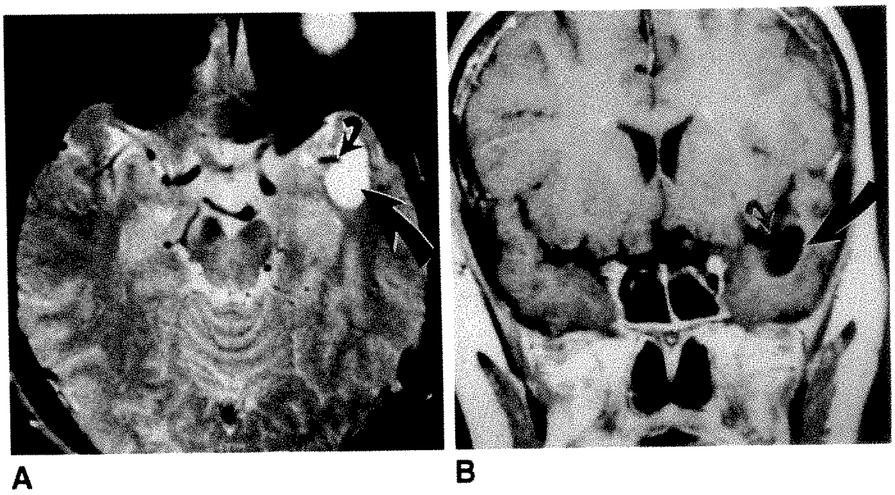

Fig. 6.—Left juxtasylvian cyst in 49-year-old woman who had CT for evaluation of sinus disease. This lesion was incidentally detected and further evaluated with pre- and postcontrast MR.

A, Axial T2-weighted noncontrast spin-echo image (2600/80) shows loop of middle cerebral artery (*small curved arrow*) indenting cyst (*large arrow*).

B, Gadopentetate-dimeglumine-enhanced coronal T1-weighted spin-echo image (600/20) shows no abnormal enhancement in or around cyst (*large arrow*).

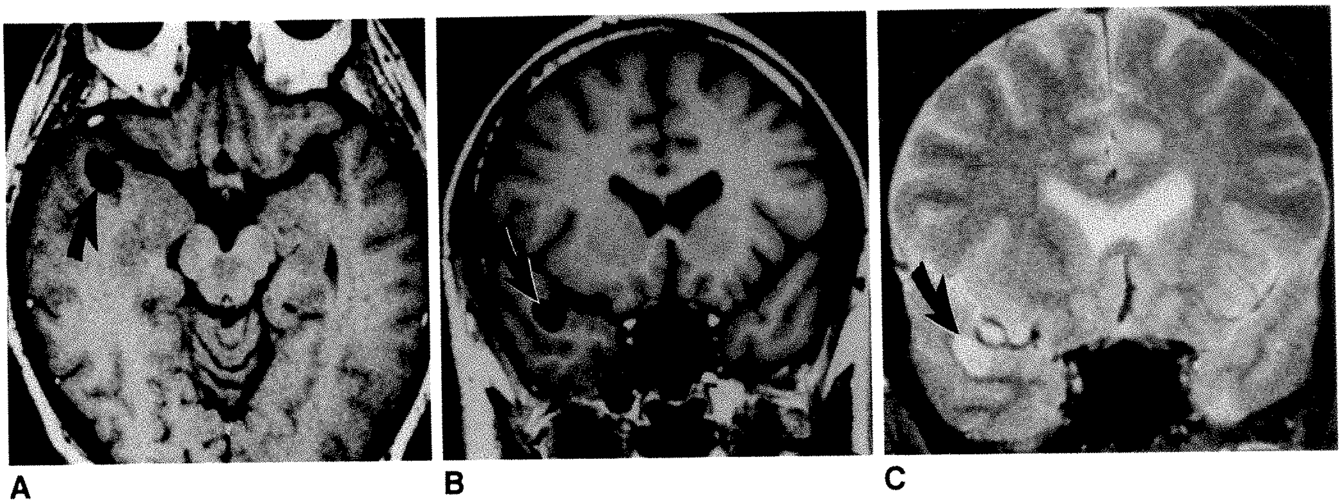

Fig. 7.—Right juxtasylvian cyst (*arrows*) in 54-year-old man. Note similarity in shape and location to Figure 5. Branch of middle cerebral artery indents cyst. Also note similarity to aneurysm.

A–C, Axial T1-weighted spin-echo image (600/20) (*A*). Coronal T1-weighted spin-echo image (600/20) (*B*). Coronal T2-weighted spin-echo image (2500/80) (*C*).

to the thalamus. There was no histopathologic proof of this lesion or of the other cysts.

Discussion

The improved soft-tissue contrast and lack of artifact that is inherent in the MR imaging process has allowed the visualization of minute anatomic and pathologic features of the brain that were not previously detectable. As previously unrecognized benign lesions are detected they must be differentiated from the pathologic lesions with which we are more familiar. We used a combination of three methods to determine that the lesions we encountered represented benign cysts. First, we required that they have characteristics that are typical of cysts in the brain and other anatomic areas; that is, no detectable wall or associated soft-tissue mass, homogeneous consistency, signal intensity identical to CSF, absence of surrounding edema or gliosis, and lack of contrast enhancement [1, 2]. Second, we correlated the cysts with clinical signs and symptoms. And, finally, when possible, we determined that no change in cyst size occurred by obtaining follow-up MR or by comparing MR with previous CT scans.

The cysts that we discovered appeared to fit into two groups. Group 1 consisted of spindle-shaped or ovoid cysts whose shape and location indicated probable origin in the choroidal fissure (Figs. 1–5). The location of these cysts may be a clue to their development. The anatomy of this area has been described in exquisite detail by Naidich et al. [3]. The choroid fissure is the CSF space between the fimbria of the hippocampus and diencephalon. It is normally a shallow fissure that curves posterosuperiorly from the anterior temporal lobe to the atrium of the lateral ventricle. The tela choroidea is a double layer of the pia mater that invaginates through the choroid fissure to reach the lateral ventricles. Developmental errors may occur at the time of formation of primitive choroid plexus anywhere along the choroid fissure, thus forming a cyst. The cysts may be of the neuroepithelial or arachnoid

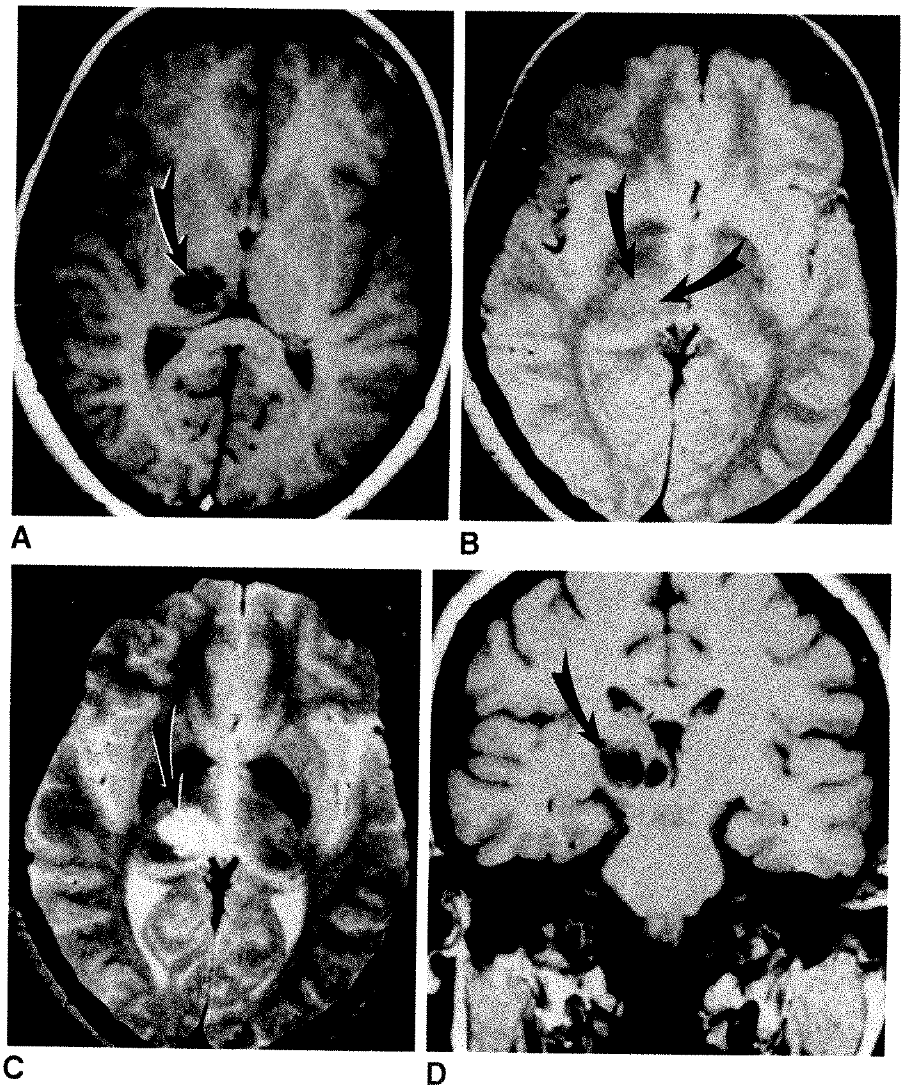

Fig. 8.—Right thalamic multiseptated cyst (*arrows*) in 66-year-old woman with migraine headaches. There was no change in this lesion over a 3-year period. Note isointensity of cyst with CSF.

A–D, Axial T1-weighted spin-echo image (500/20) (*A*). Proton-density-weighted spin-echo image (2500/30) (*B*). T2-weighted spin-echo image (2500/80) (*C*). Coronal T1-weighted spin-echo image (600/20) (*D*).

type. Focal temporal lobe hypoplasia adjacent to the choroidal fissure could lead to ex vacuo enlargement of the fissure with resultant accumulation of CSF, which could simulate a cyst in some patients. Cysts could be acquired if adhesions developed as a result of hemorrhagic or inflammatory arachnoiditis.

Neuroepithelial cysts have features of primitive ependyma and/or choroid plexus [4]. They are lined by epithelium and may or may not have a basement membrane [5]. Choroid plexus cysts measuring less than 10 mm in diameter are common [6]. Cysts arising in the choroid fissure may be similar to choroid plexus cysts. Sequestration of neuroectoderm and vascular pia mater could lead to cyst formation [5]. Another explanation is that of an ependymal diverticulum that "pinches off," giving rise to an isolated ependymallined cavity [7].

Arachnoid cysts are formed between the layers of the arachnoid or between the dura and the arachnoid and usually are not lined by epithelium [8]. The cysts in our patients may develop in the arachnoid space surrounding the penetrating pial vessels or between the arachnoid and the dura.

Group 2 was composed of seven patients with benign noninflammatory, nonneoplastic cysts that were either true parenchymal cysts or communicated with the subarachnoid space through a small opening [9] or through a diverticulum of the subarachnoid space (Figs. 6–8). The cysts were indented by a branch of the middle cerebral artery in two cases (Figs. 6 and 7), possibly indicating a point of communication of the cyst with the investing arachnoid sheath around the vessel. True parenchymal cysts are considered rare and must be differentiated from cystic neoplasm, cystic encephalomalacia, porencephalic cysts, dermoid cysts, epidermoid cysts, abscess, and parasitic cysts [4]. Intracerebral benign cysts have been reported mostly in the cerebral hemisphere, thalamus, midbrain, and cerebellar vermis [4, 5, 10, 11]. Thalamic cysts with pathologic correlation and imaging characteristics similar to those in one of our patients have been reported in the literature. In two cases the cysts had no epithelial lining (however, histologic material was very limited) [10] and in one case a single layer of epithelium was identified [4]. None of these cysts could be attributable to previous infarction or hemorrhage.

The development of these intraparenchymal cysts is difficult to explain. They appear less common than the cysts occurring near the choroidal fissure and they are more likely to raise concern of a cystic neoplasm, parasitic cyst, or old infarction. The diagnosis of a benign neuroepithelial cyst is one of exclusion in these patients. They most likely develop as a result of sequestration or infolding of neuroectodermal tissue [9, 12] or possibly as a manifestation of a local neuronal migration disorder [13, 14]. The latter is more likely to be associated with localized neurologic and intellectual deficits.

An extensive search of the pathologic, medical, and radiologic literature failed to uncover a report of cyst formation in the choroidal fissure. Rengachary and Watanabe [15] reported the location of 208 arachnoid cysts. They stated that the sylvian fissure is the most common location and that all the cysts in their study were associated with arachnoid cisterns; however, they did not report on any cysts in the choroidal fissure. Friede and Yasargil [13] in a study of 17 intracerebral cysts that did not communicate with the ventricular system mentioned cysts in the ambient cistern without further elaboration. The lack of previous reports may reflect their small size, benign clinical nature, and possible collapse or compression at the time of autopsy.

Clinically, both groups of patients in our study presented with a variety of symptoms unrelated to the temporal lobe. However, there were five patients in whom a seizure disorder was the reason for the scan (15%). It was clinically determined that the cysts were probably not related to the seizure disorders. In these patients and in the others, we concluded that the cysts were incidental findings unrelated to the patients' symptomatology; however, since we have no pathologic correlation, we believe that limited follow-up examinations are probably indicated for most of these lesions. The follow-up interval will be determined by the individual clinical setting. We would generally recommend more frequent examinations with the parenchymal cysts than with the choroidal fissure cysts. We have no evidence of enlargement of the cysts or subsequent development of neurologic signs or symptoms in our patients. However, we recognize that such enlargement is possible as a result of chronic CSF pulsation, ball-valve effect, or heterotopic choroid plexus and cyst loculation. Symptoms may occur from the compressive effects of a cyst. Nakasu et al. [10] reported neurologic deficits in two patients with benign thalamic cysts. Both patients improved after surgical drainage procedures.

We believe that the use of T1-weighted, T2-weighted and proton-density-weighted sequences in every patient is necessary. The use of gadopentetate dimeglumine depends on the individual case, but is useful to exclude a defect in the blood-brain barrier along the margins of the lesions. Contrast enhancement would be considered suspicious for a neoplastic or inflammatory cyst.

In summary, we have described a series of CSF-like cysts that, in our opinion, are benign and important to recognize so that they are not confused with intraaxial cystic tumors, infarctions, parasitic lesions, and other entities that have significant clinical implications.

ACKNOWLEDGMENTS

Our thanks to Darlene Markett and Kathy Kimball for their administrative and organizational support.

REFERENCES

1. Czervionke LF, Daniels DL, Meyer GA, Pojunas KW, Williams AL, Haughton VM. Neuroepithelial cysts of the lateral ventricles: MR appearance. *AJNR* **1987**;8:609–613
2. Kjos BO, Brant-Zawadzki M, Kucharczyk W, Kelly WM, Norman D, Newton TH. Cystic intracranial lesions: magnetic resonance imaging. *Radiology* **1985**;155:363–369
3. Naidich TP, Daniels DL, Haughton VM, et al. Hippocampal formation and related structures of the limbic lobe: anatomic-MR correlation. Part I. surface features and coronal sections. *Radiology* **1987**;162:747–754
4. Numaguchi YH, Connolly ES, Kumra AK, Varga EF, Gum GK, Mizushima A. Computed tomography and MR imaging of thalamic neuroepithelial cysts. *J Comput Assist Tomogr* **1987**;11:583–585
5. Andrews BT, Halks-Miller M, Berger MS, Rosenblum ML, Wilson CB. Neuroepithelial cysts of the posterior fossa: pathogenesis and report of two cases. *Neurosurgery* **1984**;15:91–95
6. Fakhry J, Schecter A, Tenner MS, Reale M. Cysts of the choroid plexus in neonates: documentation and review of the literature. *J Ultrasound Med* **1985**;4:561–563
7. Hamby WB, Garder WJ. An ependymal cyst in the quadrigeminal region: report of a case. *Arch Neurol Psychiatry* **1935**;33:391–398
8. Ludwin SK, Norman MG. Congenital malformations of the nervous system. In: Davis RL, Robertson DM, eds. *Textbook of neuropathology*. Baltimore: Williams & Wilkins, **1985**:176–242
9. Starkman SP, Brown TC, Linell EA. Cerebral arachnoid cysts. *J Neuropathol Exp Neurol* **1958**;17:484–500
10. Nakasu Y, Handa J, Watanabe K. Progressive neurological deficits with benign intracerebral cysts. *J Neurosurg* **1986**;65:707–709
11. MacGregor BJL, Bawler J, South JR. Intracranial epithelial cysts. Report of two cases. *J Neurosurg* **1976**;44:109–115
12. Bouch DC, Mitchell I, Maloney AFJ. Ependymal lined paraventricular cerebral cysts: a report of three cases. *J Neurol Neurosurg Psychiatry* **1973**;36:611–617
13. Friede RL, Yasargil MG. Supratentorial intracerebral epithelial (ependymal) cysts: review, case reports, and fine structure. *J Neurol Neurosurg Psychiatry* **1977**;40:127–137
14. Gilles FH. Perinatal neuropathology. In: Davis RL, Robertson DM, eds. *Textbook of neuropathology*. Baltimore: Williams & Wilkins, **1985**:243–283
15. Rengachary SS, Watanabe I. Ultrastructure and pathogenesis of intracranial arachnoid cysts. *J Neuropathol Exp Neurol* **1981**;40:61–83

Book Review

Magnetic Resonance Imaging of the Spine. By Michael T. Modic, Thomas J. Masaryk, and Jeffrey S. Ross. Chicago: Year Book Medical, 280 pp., 1989. $110

In the rapidly evolving field of imaging, MR has established itself as the best initial imaging technique for most clinical situations that require spinal imaging. This book discusses the diagnostic applications of MR imaging in the detection and evaluation of spinal disease. The three major authors have an international reputation in the subject reviewed. The stated objective is to impart the present status of MR, in terms of both technique and clinical applications, in a logical fashion. The authors are successful in meeting this objective.

The book has 10 chapters and 280 pages. The text is well organized and is written in an easy manner that flows from one subject to another. Each chapter is illustrated extensively, and the book features nearly 800 MR images. These are of an extremely high quality and represent state-of-the-art MR images. Each chapter is supported by an abundant, but not exhaustive, up-to-date reference list.

The first chapter deals with the physical principles behind imaging strategies. Although clinical correlates are discussed, the mathematics of image behavior is overemphasized. The next chapter deals with normal anatomy and consolidates the technical principles with the anatomic substrate of the MR signal. This chapter is the highlight of the book and has 26 full-color illustrations, most of which are photographs of anatomic cross sections. These anatomic images are derived from the cryomicrotome methodology developed by Dr. Wolfgang Rauschning, and each such image was generated in his laboratory. The remainder of the book concerns itself with pathologic processes of the spine and its contents, both congenital and acquired, again integrating technical considerations with clinical conditions and suggesting reasonable imaging strategies.

The authors present a strong case for MR imaging as the primary diagnostic technique in their evaluation of the spine. However, the one major criticism of this book is that is suffers from a lack of comparative analysis between MR imaging and the other various imaging techniques currently being used in the evaluation of the spine.

Magnetic Resonance Imaging of the Spine is aimed at all clinical scientists whose interest is the spine. I can recommend this book highly as an excellent reference text for radiologists, neuroradiologists, neurosurgeons, neurologists, and orthopedic surgeons as well as residents in these specialties. The book is reasonably priced at $110. Although changes undoubtedly will occur in MR imaging over the next few years, this book will continue to provide the basic information necessary to build on.

Solomon Batnitzky
University of Kansas Medical Center
Kansas City, KS 66103

Spinal Cord Pial Metastases: MR Imaging with Gadopentetate Dimeglumine

Vivian Lim[1,2]
David F. Sobel[1]
Jack Zyroff[1]

The purpose of this investigation was to describe gadopentetate-dimeglumine–enhanced MR findings in metastatic disease to the pial lining of the spinal cord. Correlation was made with clinical data, other radiologic studies, and pathologic findings. Eighty-six patients with a known malignancy and unexplained neurologic signs or symptoms were studied with pre- and postcontrast T1-weighted images. In seven of these patients, abnormal enhancement of the pial lining of the cord was seen on the sagittal postcontrast T1-weighted images. This appeared as a thin rim of enhancement along the surface of the cord in six patients and as a focal, thick rim of enhancement in addition to the thin rim of enhancement in the seventh patient. Axial images confirmed the location along the pial lining in each case. Precontrast T1-weighted images in all seven cases and precontrast T2-weighted images in five cases failed to detect any focal abnormalities of the pial lining of the cord. Pathologic confirmation was available in five of the seven patients. Pirmary malignancies in these patients included breast carcinoma (two), lymphoma (one), leukemia (one), adenocarcinoma of the lung (one), prostate carcinoma (one), and malignant melanoma (one). Three of seven patients had metastatic disease evident only within the CNS, while four patients had widespread disease outside the CNS.

We conclude that contrast-enhanced MR imaging is useful in the diagnosis of pial spread of metastatic disease in patients with a known primary malignancy and unexplained neurologic signs or symptoms.

***AJNR* 11:975–982, September/October 1990; *AJR* 155:1077–1084, November 1990**

MR imaging is rapidly replacing myelography in the evaluation of patients with suspected metastatic disease to the spine. The MR appearances of extradural, intradural, and intramedullary metastases have been described previously [1–8]. However, the MR appearance of pial metastases has heretofore received little or no attention in the radiology literature. In this report we describe seven patients with malignant disease who demonstrated abnormal enhancement of the pial lining of the spinal cord, and we correlate this finding with clinical and pathologic findings. The purpose of this report is to describe the appearance of spinal cord pial metastases on gadopentetate-dimeglumine–enhanced MR imaging.

Subjects and Methods

One hundred and thirty-five patients underwent MR of the spine during a 12-month period from August 1988 to August 1989 to evaluate for possible spinal metastases. Forty-nine of these patients presented with back pain or a positive radionuclide bone scan but had no neurologic signs or symptoms. These patients had noncontrast studies only. Eighty-six patients had unexplained neurologic signs or symptoms in association with a history of a primary malignancy; these patients underwent MR both with and without gadopentetate dimeglumine. In each patient the examination was targeted to the sites of clinical suspicion. Twenty-four of these 86 patients had surveys of the entire spine, 43 had thoracic/lumbar

Received October 31, 1989; revision requested December 15, 1989; revision received February 21, 1990; accepted March 5, 1990.

[1] Department of Radiology, Division of Neuroradiology, Scripps Clinic and Research Foundation, 10666 N. Torrey Pines Rd., La Jolla, CA 92037. Address reprint requests to D. F. Sobel.

[2] Department of Radiology, University of California, San Diego, CA 92103.

0361-803X/90/1555-1077
© American Roentgen Ray Society

surveys, 13 had cervical/thoracic examinations, and six patients had thoracic studies. In seven of the 86 patients, gadopentetate dimeglumine MR studies demonstrated abnormal contrast enhancement of the pial lining of the spinal cord. These seven patients form the basis of this report.

MR studies were performed on a GE Signa 1.5-T system. Precontrast sequences consisted of sagittal T1-weighted, 400–600/20 (TR range/TE), images of the cervical, thoracic, and lumbar spine. Gadopentetate dimeglumine was then administered IV at a dose of 0.1 mmol/kg. Postcontrast images were initiated at the same levels using the same TR and TE immediately after contrast injection. A slice thickness of 5 mm with a 1-mm skip was used throughout with two excitations and a matrix of 128 × 256 or 256 × 256 precontrast, and 256 × 256 postcontrast. Axial images were obtained either before or after contrast injection whenever it was deemed necessary to complement the findings on sagittal scans. Abnormal pial enhancement was always confirmed with axial images. Precontrast sagittal T2-weighted images (2000–2500/30,90) were obtained in five of the seven patients with pial enhancement.

We also reviewed gadopentetate dimeglumine–enhanced T1-weighted MR scans of the cervical, thoracic, or lumbar spine in 50 control patients who underwent MR to exclude a myelopathy and who had no history of a malignant, infectious, or inflammatory disease. In each patient we looked specifically for the presence or absence of pial enhancement.

Results

Clinical data and imaging results from our seven patients are presented in Table 1. Abnormal enhancement appeared

TABLE 1: Pial Metastases: Clinical, Pathologic, and MR Findings

Case No.	Age (years)	Sex	Diagnosis and Documentation	Neurologic Signs and Symptoms	CSF*	Location of Pial Enhancement	Other MR Abnormalities
						Precontrast T1/ Postcontrast T1/T2	
1	30	M	Malignant melanoma, Clark IV; lumbar arachnoid biopsy positive for melanoma	Headache, nausea and vomiting, photophobia, left face/arm weakness	Protein 600 mg/dl, glucose 14 mg/dl, 400 wbc/cu mm, 15 rbc/cu mm (90% lymphocytes, 10% monocytes), cytology negative for melanoma	−/+/− Diffuse	Cranial nerves 7/8, clumped lumbar nerve root with abnormal root and arachnoid enhancement
2	72	M	Chronic lymphocytic leukemia, positive biopsy of leptomeninges and CSF	Low back pain, right greater than left; lower extremity weakness	Cytology positive, no chemistry or cell count	−/+/− Thoracic lumbar-conus	Lumbar nerve roots enhanced with clumped roots, herniated nucleus pulposus
3	72	M	Prostate carcinoma, widespread metastases	Headache, cranial nerve palsies	Not performed	−/+/not performed Diffuse	Clivus plus right cavernous sinus involvement dural and arachnoid
4	62	F	Breast carcinoma with diffuse bone metastases	Bilateral lower extremity decreasing sensation, cauda equina syndrome	Not performed	−/+/not performed Low thoracic	Postradiation changes in thoracic/lumbar spine-compression of T11 and bone metastases in L3–L5
5	72	F	Breast carcinoma with malignant pleural effusion and rib metastases; postmortem examination was positive	Polyneuropathy both upper and lower extremities, decreased bladder control	Protein 700, glucose 45 cytology showed atypical cells	−/+/− Dorsal cervical spine only	Not applicable, sequence not performed
6	39	M	Lung adenocarcinoma with metastasis to brachium pontis	Seizures, neck pain, confusion, decreased bowel/bladder control	Protein 73, glucose 23, 21 wbc/cu mm/rbc/cu mm (51% lymphocytes, 47% monocytes), cytology positive	−/+/− Diffuse	Not applicable, sequence not performed
7	48	M	Hi-grade large-cell lymphoma, Postmortem examination positive)	Low back pain, bilateral sciatica with lower extremity numbness	Not performed	−/+/− Diffuse	Retroperitoneal mass

* Normal total protein = 15–45 mg/dl, normal glucose = 40–80 mg/dl

as a thin rim on the cord periphery in six patient (Figs. 1–3). One of these had focal linear enhancement along the dorsal aspect of the cervical cord (Fig. 4). In the seventh patient, linear enhancement was observed in conjunction with a focal area of thick enhancement along the surface of the cord (Fig. 5). In three patients the enhancement was observed at one segment of the cord only, whereas in the other four patients it involved the entire cord. Two of the seven patients also had clumping of the cauda equina with nerve root and arachnoid enhancement (Figs. 1 and 2). In the patient with linear enhancement on the dorsum of the cervical cord, pathologic examination revealed circumferential pial infiltration with focal areas of invasion into the cord substance (Figs. 4E and 4F). Long TR, long TE sequences performed on this patient and four other of the seven patients failed to demonstrate any focal cord or pial abnormalities (Fig. 4D).

The onset of clinical symptoms ranged from 6 months to 17 years from the time of initial diagnoses. Three of the seven

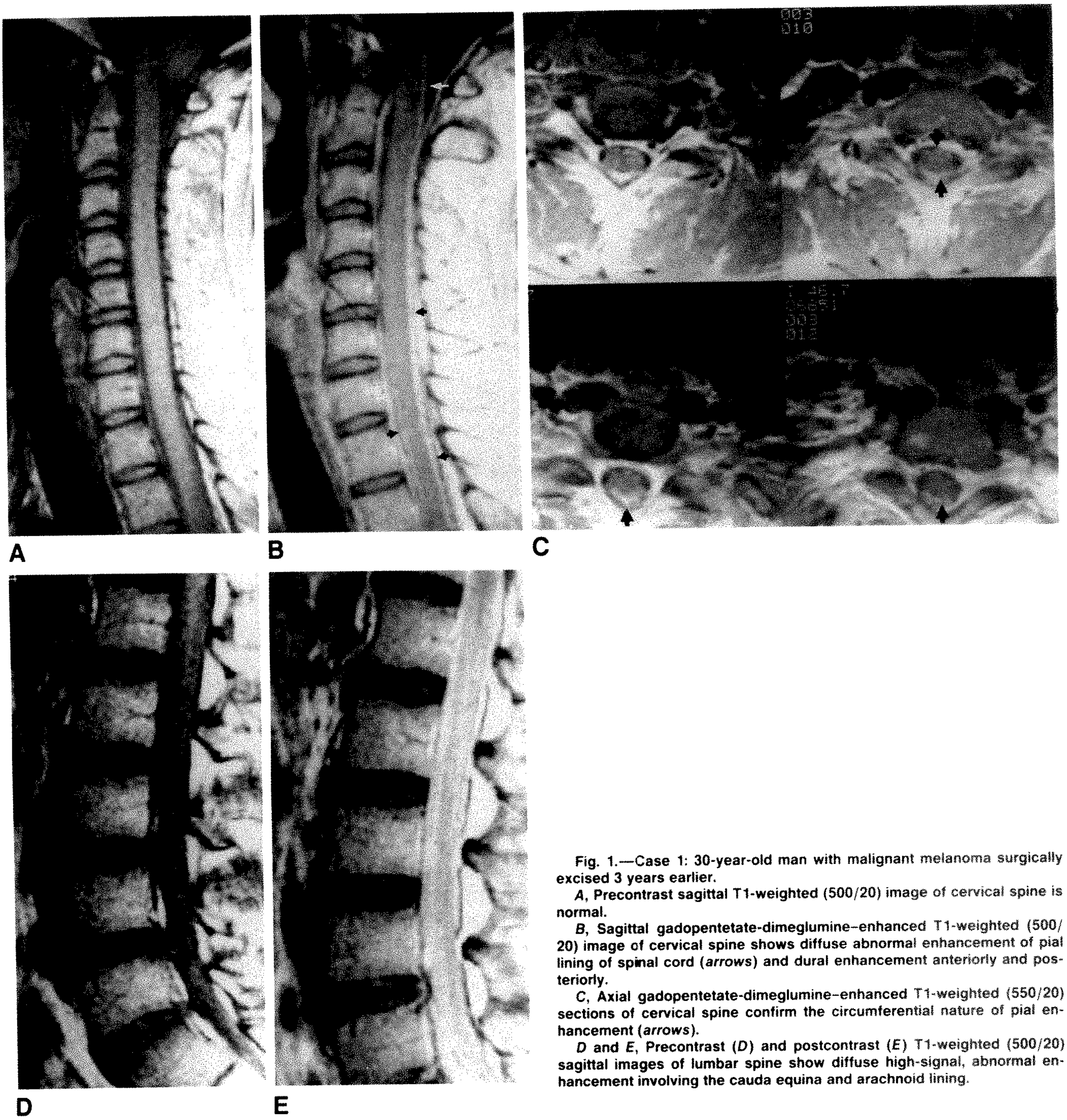

Fig. 1.—Case 1: 30-year-old man with malignant melanoma surgically excised 3 years earlier.

A, Precontrast sagittal T1-weighted (500/20) image of cervical spine is normal.

B, Sagittal gadopentetate-dimeglumine-enhanced T1-weighted (500/20) image of cervical spine shows diffuse abnormal enhancement of pial lining of spinal cord (*arrows*) and dural enhancement anteriorly and posteriorly.

C, Axial gadopentetate-dimeglumine-enhanced T1-weighted (550/20) sections of cervical spine confirm the circumferential nature of pial enhancement (*arrows*).

D and *E*, Precontrast (*D*) and postcontrast (*E*) T1-weighted (500/20) sagittal images of lumbar spine show diffuse high-signal, abnormal enhancement involving the cauda equina and arachnoid lining.

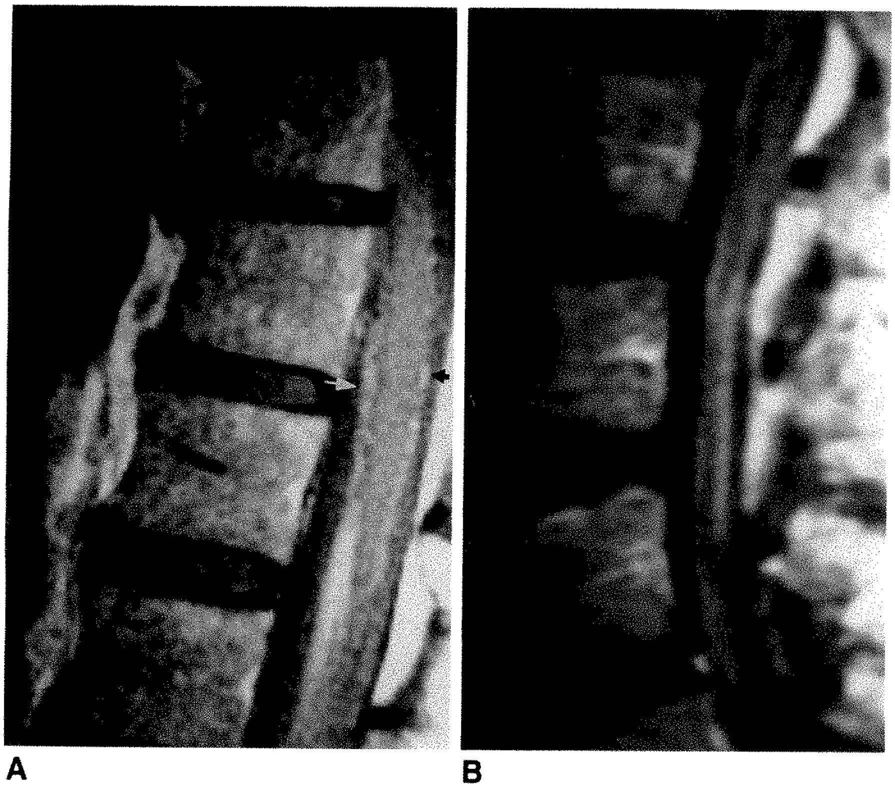

Fig. 2.—Case 2: 72-year-old man with chronic lymphocytic leukemia.

A, Sagittal gadopentetate-dimeglumine–enhanced T1-weighted (500/30) image of lumbar spine shows abnormal rim of enhancement outlining the conus (*arrows*) with involvement of the proximal cauda equina.

B, Sagittal gadopentetate-dimeglumine–enhanced T1-weighted (500/20) image of lumbar spine shows clumping and abnormal enhancement of lumbar roots.

patients died within 4 months of their MR examination. Two of these patients had received treatment with intrathecal methotrexate after the MR studies were performed. One of these two patients died 2 months after therapy from an unknown cause. The other patient withdrew from all therapy after one dose of intrathecal methotrexate and died a week later with postmortem examination revealing terminal pneumonia, urinary tract infection, pleural metastases, and metastatic breast cancer involving the pia/arachnoid and nerve roots of the entire spinal cord (case 5). At the time of this report, three patients were undergoing radiation therapy to the spine, two with a combination of osseous and pial involvement by malignancy and one with pial/arachnoid involvement by melanoma. One patient was undergoing experimental systemic chemotherapy.

Pial enhancement was not observed in the control patients except for minimal enhancement anterior to the conus in 30% of patients. We believe this was probably related to the anterior spinal artery (Fig. 6). Gibbs artifact was considered less likely, since this finding was not seen on the precontrast images.

Discussion

Leptomeningeal metastases may be seen with CNS neoplasms or with primary malignancies outside the CNS. The diagnosis can be difficult to establish, as both CSF cytologic analysis and myelography have significant false-negative rates [9–11]. Patients may present with nonspecific symptoms—including headache, neck or back pain—or with focal neurologic deficits, including cranial nerve palsies, motor or sensory dysfunction, and loss of sphincter control. Early recognition and treatment of this disease, usually with intrathecal chemotherapy or radiation, can offer these patients palliation and in some cases improved survival rates [9, 11].

Gadopentetate-dimeglumine–enhanced MR imaging has been shown to be superior to noncontrast images in the evaluation of intramedullary and intradural extramedullary processes [1–5, 8]. However, little distinction is made in the literature between clinical findings and significance of metastases involving the arachnoid lining of the dural sac, the pial lining of the nerve roots, and the pial lining of the brain and spinal cord.

In this report, we focus on metastases to the pial lining of the spinal cord although coexisting involvement of the arachnoid, dura mater, or nerve roots was present in at least three patients. Autopsy proof of spinal cord pial metastases was available in two of the seven patients. Two patients had positive arachnoid biopsies, two patients had positive CSF cytology including one of the two patients who underwent arachnoid biopsy, and two patients had widespread metastatic disease with no evidence of an infectious or inflammatory process. Pial enhancement with gadopentetate dimeglumine was not observed in the control population except for minimal enhancement seen occasionally along the anterior aspect of the conus. Therefore, the enhancement that we observed along the surface of the spinal cord can be consid-

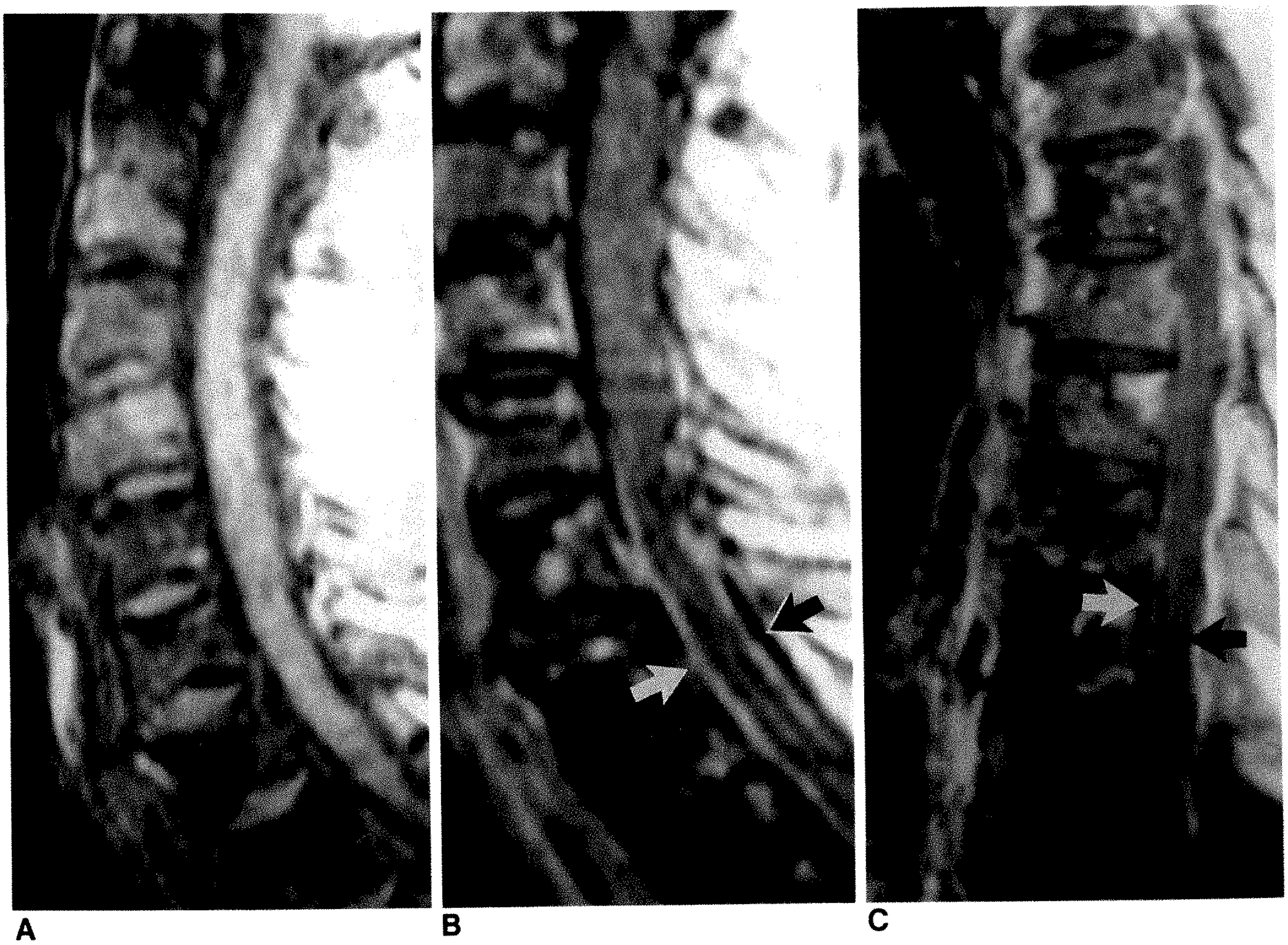

Fig. 3.—Case 3: 72-year-old man with metastatic prostate carcinoma.

A, Precontrast sagittal T1-weighted (600/20) image of cervical spine shows metastatic disease to cervical vertebrae and a normal appearance to cervical cord.

B, Sagittal gadopentetate-dimeglumine-enhanced T1-weighted (600/20) image of cervical spine shows abnormal rim enhancement of cervical cord (*arrows*).

C, Sagittal gadopentetate-dimeglumine-enhanced T1-weighted (500/20) image of thoracic spine shows continuation of abnormal rim enhancement of thoracic cord (*arrows*) and vertebral metastases. Pial location confirmed on axial images (not shown).

ered abnormal and due to pial metastatic disease. When the enhancement is clearly applied to the surface of the cord on both sagittal and axial images, and is surrounded by low signal CSF on postcontrast T1-weighted images, it is thought to be pial in nature. This is to be distinguished from dural enhancement where there is enhancement of the outlying dural sac, and arachnoid enhancement where there is enhancement within the CSF space between the pial and dural lining of the sac or along nerve roots. In some patients, all three may coexist.

Our observations are further supported by a recent report of an animal tumor model that demonstrated similar-appearing pial enhancement on postcontrast T1-weighted images. Serial MR examinations of rabbits inoculated with tumor suspension into the cisterna magna demonstrated pial and arachnoidal enhancements synchronous with the development of neurologic dysfunction [12]. T2-weighted images were nondiagnostic in the rabbits as in our series, since meningeal involvement by tumor cannot be distinguished from CSF on the basis of signal intensity.

While it can be argued that radiation therapy may have contributed to the abnormal enhancement in the patient with a thick rim of enhancement and radiation changes in the bone (case 4), no evidence of radiation-induced arachnoiditis was seen. Furthermore, pial enhancement was not observed in other patients who had received similar spinal radiation for bony metastases.

All seven of our patients had focal neurologic findings or symptoms; however, this number is biased since we did not administer contrast material to patients with nonfocal com-

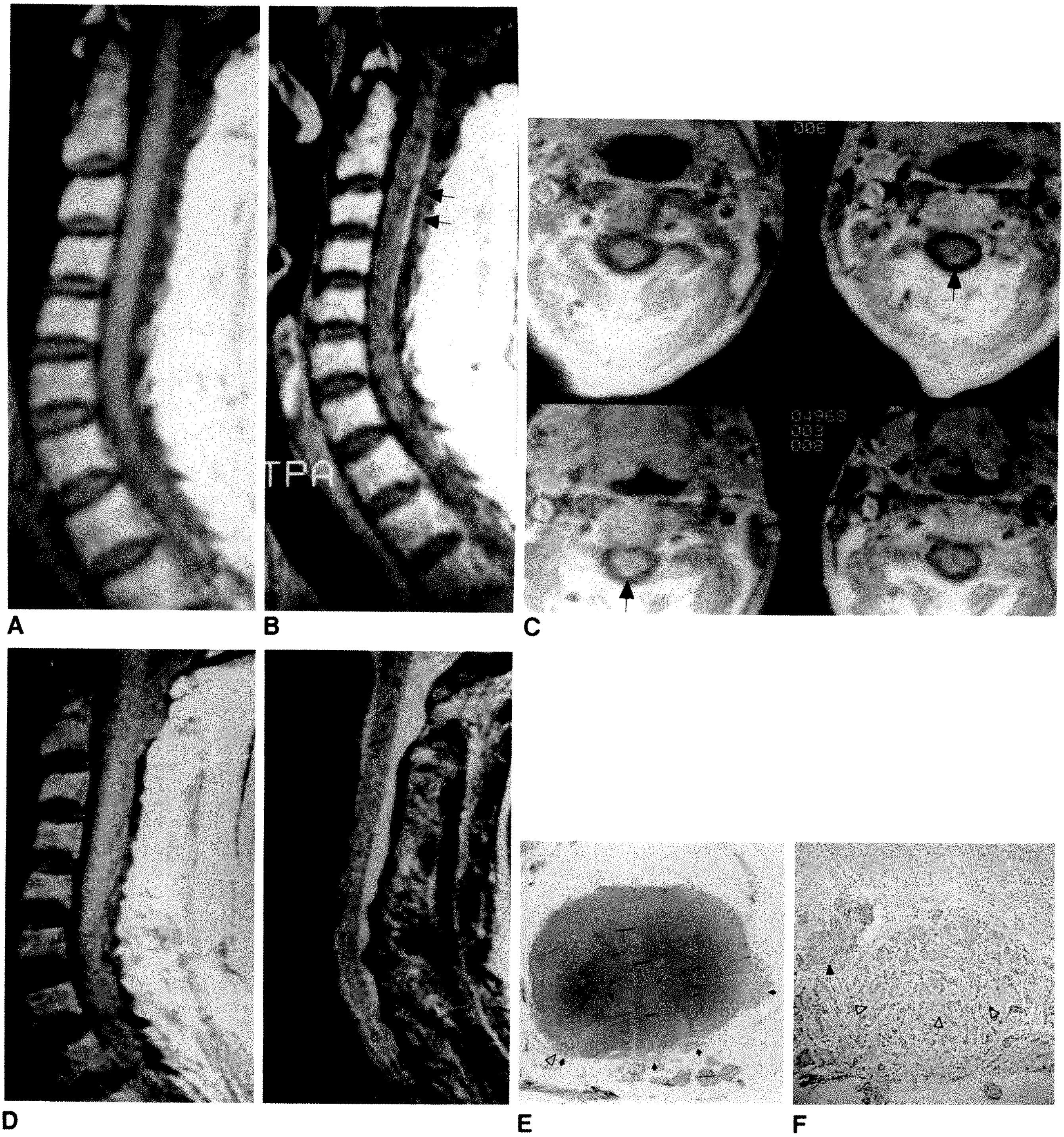

Fig. 4.—Case 5: 72-year-old woman with breast cancer treated 17 years prior to admission.

A, Precontrast sagittal T1-weighted (400/20) image of cervical spine is normal.

B, Sagittal gadopentetate-dimeglumine–enhanced T1-weighted (400/20) image of cervical spine shows a thin linear streak of enhancement along dorsal surface of cord (*arrows*).

C, Axial gadopentetate-dimeglumine–enhanced T1-weighted (800/20) images confirm the abnormal enhancement along dorsal surface of cervical cord (*arrows*).

D, Precontrast sagittal intermediate and T2-weighted (2000/30,80) images show no evidence of cord or pial abnormality.

E, Cross section of cervical spine with low-power magnification shows increased thickness of pial lining (*solid arrows*) due to metastatic infiltration. An area of cord invasion by tumor cells is magnified in part *F* (*open arrow*).

F, High-power magnification shows pial infiltration by metastatic adenocarcinoma of the breast (*open arrows*) as well as focal invasion of cervical cord (*solid arrow*).

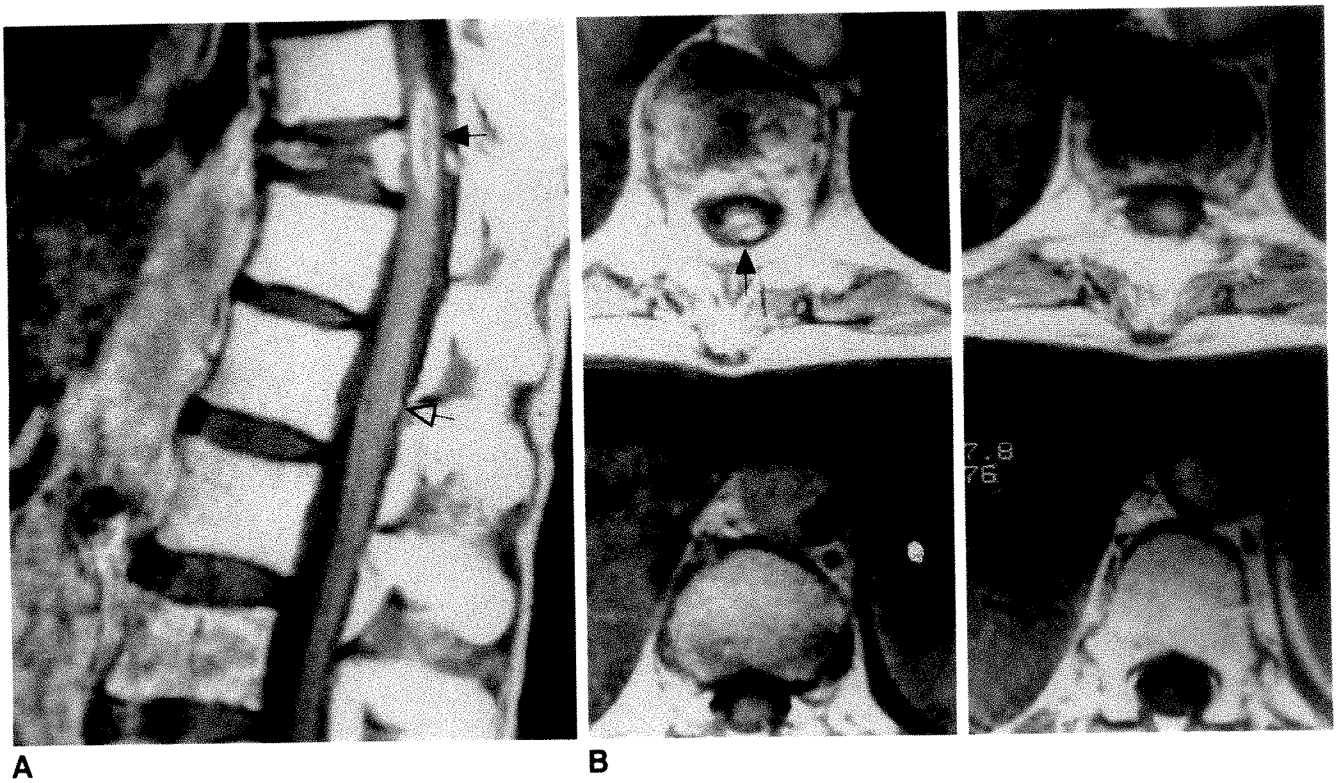

Fig. 5.—Case 4: 62-year-old woman with metastatic breast cancer.

A, Sagittal gadopentetate-dimeglumine-enhanced T1-weighted (500/20) image of lumbar spine shows both a thick (*closed arrow*) and thin (*open arrow*) rim of abnormal enhancement. Note the radiation change with increased fatty marrow and collapsed T11 vertebral body and vertebral metastases involving L3–L5.

B, Axial gadopentetate-dimeglumine-enhanced T1-weighted images confirm the circumferential thick rim of enhancement (*arrow*).

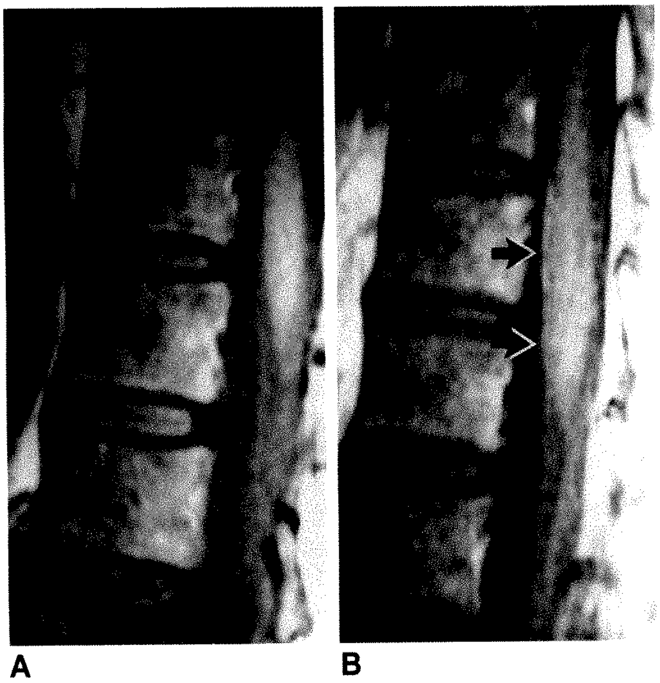

Fig. 6.—Normal patient.

A, Sagittal precontrast T1-weighted image of conus.

B, Sagittal postcontrast T1-weighted image shows minimal enhancement along anterior surface of conus (*arrows*).

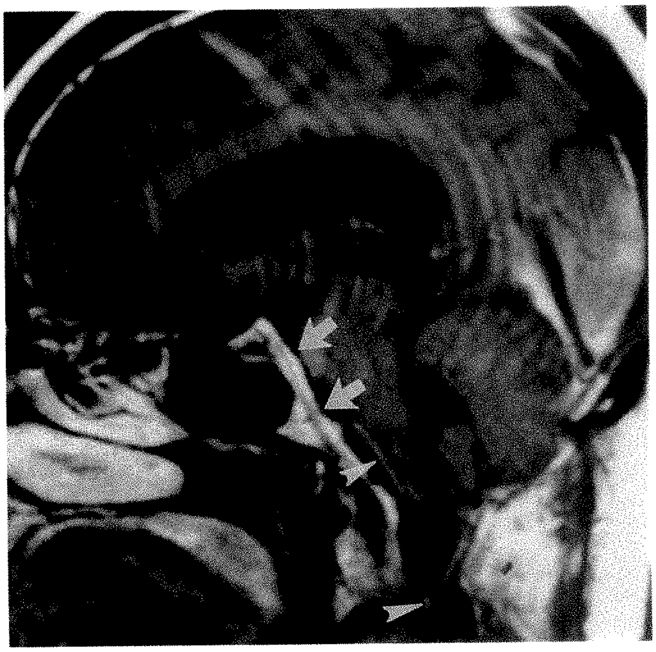

Fig. 7.—Chronic meningeal fibrosis caused by shunting for Arnold Chiari I complicated by syrinx. Sagittal postcontrast T1-weighted (750/20) image of brain and upper cervical cord shows both dural enhancement along clivus (*arrows*) and pial enhancement along surface of midbrain and upper cervical cord (*arrowheads*).

plaints. Since this is not an autopsy study, we cannot comment on the sensitivity or false-negative rate of contrast-enhanced MR in the detection of spinal cord pial metastases. However, one of the two patients who had a postmortem examination (case 5) demonstrated diffuse involvement of the pial lining of the cord, while contrast-enhanced MR performed 2 months earlier showed only abnormal cervical pial enhancement.

Metastatic disease to the leptomeninges is being found increasingly as a complication of systemic cancer. There is speculation that these findings are a result of improved systemic therapy for certain malignancies [11, 13]. The most common primary malignancies reported include breast carcinoma, small-cell and non-small-cell lung carcinoma, malignant melanoma, gastrointestinal carcinomas, and lymphoma [10, 12, 14]. Up to 50% of patients with acute lymphoblastic leukemia may develop this complication, and a similar phenomenon has been observed in the myelogenous leukemias [11]. Malignancies in our series included breast carcinoma, chronic lymphocytic leukemia, large-cell lymphoma, lung adenocarcinoma, melanoma, and prostate carcinoma.

Abnormal pial enhancement on MR is not unique to metastatic disease. We have observed similar findings with both infectious and inflammatory conditions, such as meningeal fibrosis caused by chronic shunting (Fig. 7). Pial involvement by spinal sarcoidosis has also been described recently [15]. Clinical correlation and CSF analysis including cytology are necessary to make a specific diagnosis. In our series, five of seven patients were treated for leptomeningeal spread of malignancy with either intrathecal methotrexate or radiation. One patient underwent experimental chemotherapy. A longer period of follow-up and a larger series of patients with this complication of malignancy are necessary to determine the impact of our observation of pial enhancement and of the subsequent therapy.

In conclusion, metastatic disease to the pial lining of the spinal cord may present as a focal or diffuse rim of increased signal along the surface of the cord on contrast-enhanced T1-weighted MR images. Metastatic screening studies performed without the use of gadopentetate dimeglumine may miss the diagnosis of pial metastases.

REFERENCES

1. Parizel PM, Baleriaux D, Rodesch G, et al. Gd-DTPA-enhanced MR imaging of spinal tumors. *AJNR* **1989**;10:249-258, *AJR* **1989**;152:1087-1096
2. Sze G, Abramson A, Krol G, et al. Gadolinium-DTPA in the evaluation of intradural extramedullary spinal disease. *AJNR* **1988**;9:153-163, *AJR* **1988**;150:911-921
3. Valk J. Gd-DTPA in MR of spinal lesions. *AJNR* **1988**;9:345-350, *AJR* **1988**;150:1163-1168
4. Dillon WP, Norman D, Newton TH, Bolla K, Mark A. Intradural spinal cord lesions: Gadolinium DTPA-enhanced MR imaging. *Radiology* **1989**; 170:229-237
5. Breger RK, Williams AL, Daniels DL, et al. Contrast enhancement in spinal MR imaging. *AJNR* **1989**;10:633-637, *AJR* **1989**;153:387-391
6. Krol Y, Sze G, Malkin M, Walker R. MR of cranial and spinal meningeal carcinomatosis: comparison with CT and myelography. *AJNR* **1988**;9:709-714, *AJR* **1988**;151:583-588
7. Post MJD, Quencer RN, Green BA, et al. Intramedullary spinal cord metastases, mainly of nonneurogenic origin. *AJNR* **1987**;8:339-346, *AJR* **1987**;148:1015-1022
8. Sze G, Krol G, Zimmerman RD, Deck MDF. Intramedullary disease of the spine: diagnosis using gadolinium-DTPA-enhanced MR imaging. *AJNR* **1988**;9:847-858, *AJR* **1988**;151:1193-1204
9. Olson ME, Chernik NL, Posner JB. Infiltration of the leptomeninges by systemic cancer: a clinical and pathologic study. *Arch Neurol* **1974**;30: 122-137
10. Little JR, Dale AJD, Okazaki H. Meningeal carcinomatosis: clinical manifestations. *Arch Neurol* **1974**;30:138-143
11. Wasserstrom WR, Glass JP, Posner JB. Diagnosis and treatment of leptomeningeal metastases from solid tumors: experience with 90 patients. *Cancer* **1982**;4:759-772
12. Frank JA, Girton M, Dwyer AJ, Wright DC, Cohen PJ, Doppman JL. Meningeal carcinomatosis in the VX2 rabbit tumor model: detection with Gadolinium DTPA-enhanced MR imaging. *Radiology* **1988**;167:825-829
13. Bigner SH, Johnston WW. The cytopathology of cerebrospinal fluid. II. Metastatic cancer, meningeal carcinomatosis and primary central nervous system neoplasms. *Acta Cytol* **1981**;25:461-477
14. Sorenson SC, Eagan RT, Scott M. Meningeal carcinomatosis in patients with primary breast or lung cancer. *Mayo Clin Proc* **1984**;59:91-94
15. Nesbit GM, Miller GM, Baker HL, Ebersold MJ. Scheithauer BW. Spinal cord sarcoidosis: a new finding at MR imaging with Gd-DTPA enhancement. *Radiology* **1989**;173:839-843

Determination of the Extent of Lower-Extremity Peripheral Arterial Disease with Color-Assisted Duplex Sonography:

Comparison with Angiography

Joseph F. Polak[1]
Mitchell I. Karmel[1]
John A. Mannick[2]
Daniel H. O'Leary[1]
Magruder C. Donaldson[2]
Anthony D. Whittemore[2]

Color-assisted duplex sonography combines color Doppler flow imaging with duplex sonography to rapidly survey the vasculature. Color Doppler sonography displays the motion of flowing blood on a sonogram and is used to visualize directly arterial lumen narrowing of greater than 50%. Absence of Doppler signals signifies arterial occlusion. Preangiographic triage of patients for surgical or interventional therapy requires that a rapid and accurate survey be performed of the extent of arterial disease. Color-assisted duplex sonography was applied prospectively in 17 consecutive patients with the clinical diagnosis of peripheral arterial disease who had not previously undergone angiography. Results of angiography of the femoropopliteal arteries were graded and localized in one of seven approximately equal arterial segments. These were compared with similar segmental maps made with sonography. For the detection of stenosis or occlusion in any of the 238 segments, the sensitivity was 0.88 (49/56), specificity 0.95 (173/182), and accuracy 0.93 (222/238). The average time taken to survey both limbs was 29 min.

We conclude that color-assisted duplex sonography is an accurate and rapid tool for the noninvasive mapping of the extent of femoropopliteal arterial disease.

***AJR* 155:1085–1089, November 1990**

Patients with peripheral arterial disease of the lower extremities who undergo angiography may have long stenoses and occlusions suitable for surgical bypass or shorter segmental lesions amenable to percutaneous intervention [1–3]. It has previously not been possible to noninvasively predict the extent and severity of segmental arterial lesions [4, 5].

Increasing clinical experience with color Doppler flow sonography suggests this technique can facilitate the preangiographic determination of the nature and extent of segmental arterial disease in the legs. We propose that the subjective grading of narrowing of the arterial lumen by color flow imaging be combined with Doppler spectral analysis, a technique that by itself is accurate yet time-consuming [6, 7]. This combined approach can then map out the extent of segmental disease in symptomatic patients with suspected peripheral arterial disease.

Subjects and Methods

Seventeen consecutive symptomatic patients who had not previously undergone arteriography or surgical revascularization of the lower extremities were examined with sonography prospectively before arteriography. The patient population consisted of 13 men and four women 21–82 years old (mean age, 62). The indications for arteriography consisted of claudication in 10 patients, cellulitis in one patient, nonhealing foot ulcer in one patient, foot ulcer and claudication in one patient, foot ulcer and rest pain in one patient, acute rest pain (possible embolic disease) in two patients, and vasculitis in one patient.

Each lower extremity was scanned 1–4 hr before arteriography with the sonographer blinded to the type and location of symptoms as well as to the results of previous noninvasive pressure measurements. Imaging was performed from the groin crease to just below the knee (i.e., along the course of the femoral and popliteal arteries). Each extremity was divided

Received April 2, 1990; accepted after revision June 1, 1990.

[1] Department of Radiology, Harvard Medical School and Brigham and Women's Hospital, 75 Francis St., Boston, MA 02115. Address reprint requests to J. F. Polak.

[2] Department of Surgery, Harvard Medical School and Brigham and Women's Hospital, Boston, MA 02115.

0361-803X/90/1555-1085
© American Roentgen Ray Society

into seven arterial segments consisting of the common femoral artery; the profunda femoris artery; the proximal, mid, and distal superficial femoral arteries; and the proximal and distal popliteal arteries.

Color Doppler imaging was performed prospectively with a 5-MHz sonographic system (Acuson Computed Sonography, Mountain View, CA) in conjunction with both pulsed Doppler (3.5 MHz) and standard high-resolution sonography by means of a linear-array transducer.

Each segment was imaged transversely, to size the colored flow in the lumen with respect to the arterial walls and express it as percent narrowing of the lumen diameter, and longitudinally, for measurement of peak systolic velocity from the Doppler spectrum.

Arterial segments were scanned contiguously in the transverse plane for assessment of lumen diameter. The transducer, although transverse to the vessel, was angled 30° to the vertical plane in order to encode arterial color signals. Relative narrowing of the lumen, when present, was graded as percentage of lumen narrowing with respect to the visualized arterial walls by using the smallest lumen diameter either in the left-to-right or anteroposterior direction. The transducer was held static for one to two cardiac cycles, then displaced by 1-cm increments down the leg.

Once the vessels were mapped in the transverse plane, color imaging parallel to the vessel was used to place the Doppler sampling gate in the lumen and to angle-correct it parallel to the flow in the lumen. A Doppler spectrum was then obtained and the peak systolic velocity calculated from it. Doubling of the peak systolic velocity expressed as a peak systolic velocity ratio was used as the criterion for a significant stenosis. This ratio was determined with respect to a point with a normal color flow pattern in the lumen situated at least 4 cm proximally.

After both extremities were scanned and before arteriography, an arterial map was drawn summarizing the location of normal segments (0–49%), significant stenoses (50–99%), and occlusions (100%). The duration of the color-assisted duplex sonographic evaluation was recorded in minutes.

Arteriography was performed by using a four-station cut-film technique and injections of 77–84 ml of Hypaque-76 (Winthrop Pharmaceuticals). When completed, the arteriograms were evaluated blindly by consensus opinion of two angiographers. Each segment was graded as being without significant narrowing (0–49%), significantly narrowed (50–99%), or occluded (100%). The segments were graded on the basis of the most severe component. Of the 34 extremities studied, 11 had significant femoropopliteal stenoses, eight had occlusions, six had a combination of occlusions and stenoses, and nine had no significant femoropopliteal disease.

Sensitivity and specificity were calculated according to previous recommendations [8, 9]. The accuracy of the technique was determined both for the combined 238 arterial segments as well as for the 34 lower extremities. Confidence limits are given at the 95% level [9].

Results

All 25 limbs that had at least one diseased segment were detected with sonography, whereas three examinations were false-positive in nine limbs without femoropopliteal disease, two for stenoses and one for an occluded segment, giving a sensitivity of 1.0 (0.87, 1.0 [95% confidence intervals]), a specificity of 0.66 (0.35, 0.87), and an accuracy of 0.9 (0.77, 0.97). The two examinations false positive for stenoses were distal to iliac artery occlusions and the one false positive for occlusion was in a limb with severely diseased tibioperoneal branch arteries.

Three limbs had long isolated femoral artery stenosis (12, 11, and 30 cm). The average of the velocities measured in the corresponding six arterial segments was 0.54 m/sec (± 0.38 m/sec SD; range, 0.3–1.3 m/sec). The average velocity in nine extremities without diseased femoral segments was 0.97 m/sec (±0.31 m/sec SD). Seven limbs had isolated short segmental stenosis of the superficial femoral arteries. The average velocity at the stenoses was 2.53 ± 0.93 m/sec (range, 1.47–3.84 m/sec), whereas it was 0.77 ± 0.51 m/sec in the segment above. The average peak systolic velocity ratio was 5.3 ± 5.5 (range, 2.0–17.0).

A total of 238 arterial segments were evaluated for peak systolic velocity and color flow characteristics. Twenty-two significant stenoses were predicted and confirmed on arteriography. Three (14%) were predicted by a doubling of the peak systolic velocity. Nine (41%) were predicted by a marked narrowing of the transverse lumen seen with color Doppler

TABLE 1: Summary of the Results of Color-Assisted Duplex Sonography Compared with Arteriography for the Detection of Arterial Segment Stenosis and Occlusions

Artery	True Positive		False Positive		True Negative
	Stenosis	Occlusion	Stenosis	Occlusion	
Common femoral	1	0	0	0	32
Profunda femoris	1	0	0	0	30
Superficial femoral					
Proximal	4	5	1	0	24
Mid	7	5	1	0	20
Distal	4	7	0	4	17
Popliteal					
Proximal	3	4	2	0	25
Distal	2	6	1	0	25
Total	22	27	5	4	173

Note.—Results of seven examinations were false negative for stenosis. Three of these resulted from dense calcifications, one each in the common femoral and mid and distal superficial femoral arteries. Four lesions were distal to a more proximal high-grade stenosis or occlusion, with three in the profunda femoris artery and one in the distal superficial femoral artery. No examination results were false negative for occlusion.

imaging; and 10 lesions (45%) had both increased peak systolic velocity and narrowing of the lumen on color-assisted duplex imaging. Five significant stenoses were predicted but not confirmed by arteriography. These predictions were all based on the subjective view that the lumen was narrowed on color flow images. A doubling of the peak systolic velocity was not found at any of these sites.

Seven significant stenoses were found at arteriography but not predicted prospectively (Table 1). Of these seven lesions, two were immediately distal to occluded segments, two were immediately distal to tight stenoses, and three were in heavily calcified segments.

No arterial occlusions were missed (Table 1). Twenty-seven occlusions were correctly predicted on the basis of absence of both color flow and duplex Doppler signals. Four occluded segments were predicted but not confirmed by arteriography. All four of these were at the adductor canal in the distal superficial femoral artery and two were also distal to more proximal occlusions of the superficial femoral artery.

Incidental findings included two popliteal aneurysms, one thrombosed and the other with significant intramural thrombus. The arteriogram was not diagnostic in either case.

One hundred seventy-three segments were correctly predicted to be patent and without stenosis on the basis of colored flow in the lumen of greater than 50% and absence of a doubling of peak systolic velocities in these segments.

The sensitivity of the technique for detecting a segmental stenosis, exclusive of an occlusion, was 0.76 (22/29), for a specificity of 0.97 (173/178) and an accuracy of 0.94 (195/207). When both occluded and stenotic segments were ana-

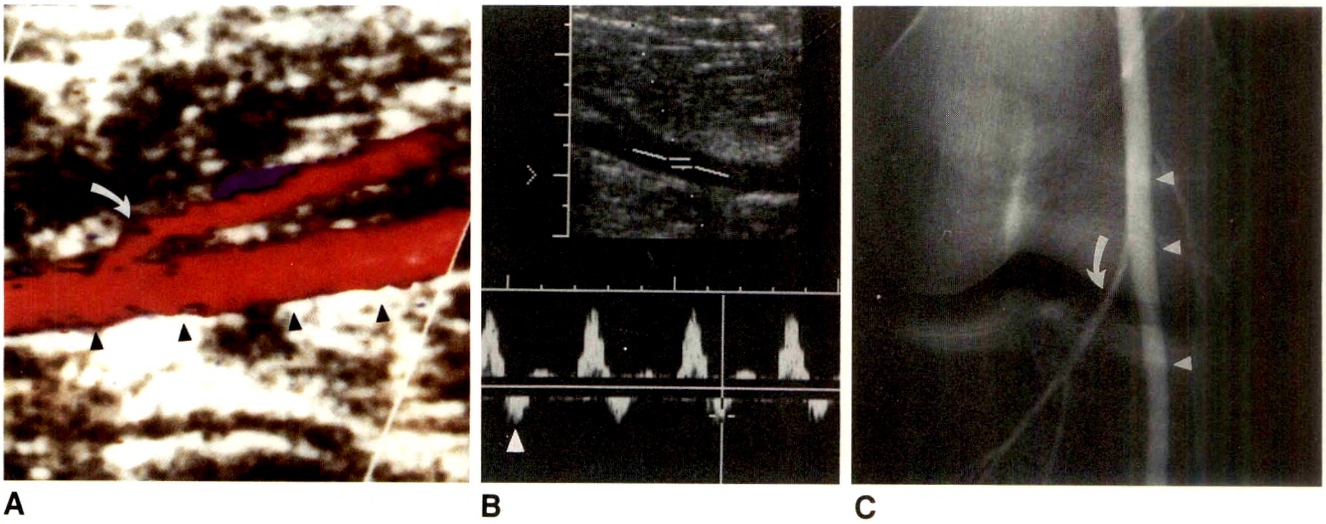

Fig. 1.—Images showing ease with which color Doppler sonography helps in identifying normal arterial branches. This 21-year-old woman with vasculitis affecting the tibioperoneal arteries has, nevertheless, a normal femoropopliteal system.

A, Longitudinal color flow image clearly shows popliteal artery (*arrowheads*) and smaller geniculate branch (*arrow*).

B, Doppler spectrum is sampled from corresponding popliteal artery. This shows normal triphasic velocity profile with late systolic reversal (*arrowhead*). (Figure is printed with cephalad to reader's right and caudad to reader's left.)

C, Corresponding arteriogram shows normal popliteal artery (*arrowheads*) and geniculate branch (*arrow*), which courses superficial to popliteal artery.

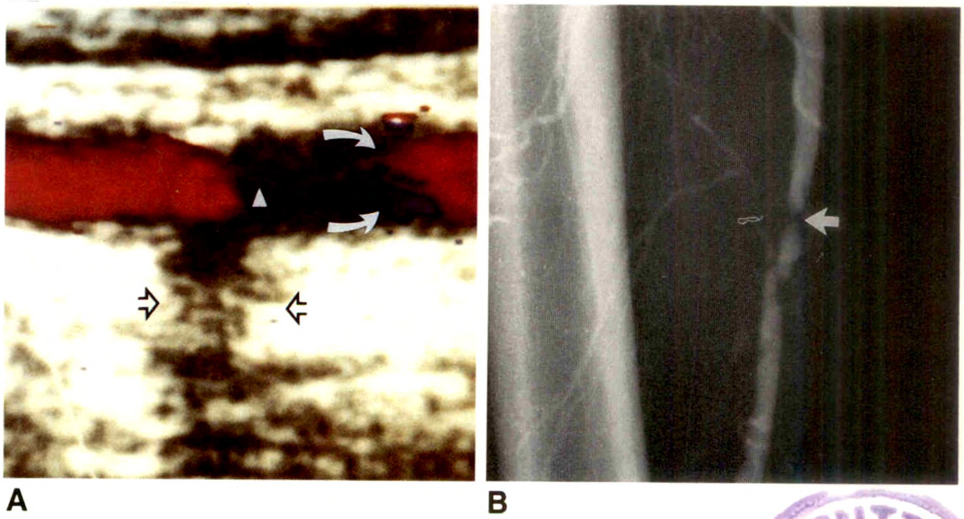

Fig. 2.—Images showing typical example of focal lesion amenable to angioplasty detected prospectively by color-assisted duplex sonography. This 76-year-old man had claudication.

A, Longitudinal color flow scan of mid superficial femoral artery (right side is proximal, left is distal) shows marked narrowing of flow channel (*arrowhead*). Note also shadowing from calcific plaque (*open arrows*). Distal to lesion, note turbulence with flow reversal encoded as blue and red adjacent to each other (*curved arrows*).

B, Corresponding arteriogram confirms high-grade stenosis (*arrow*) seen on color Doppler sonogram. Lesion was subsequently dilated with balloon angioplasty.

CALCUTTA CENTRAL

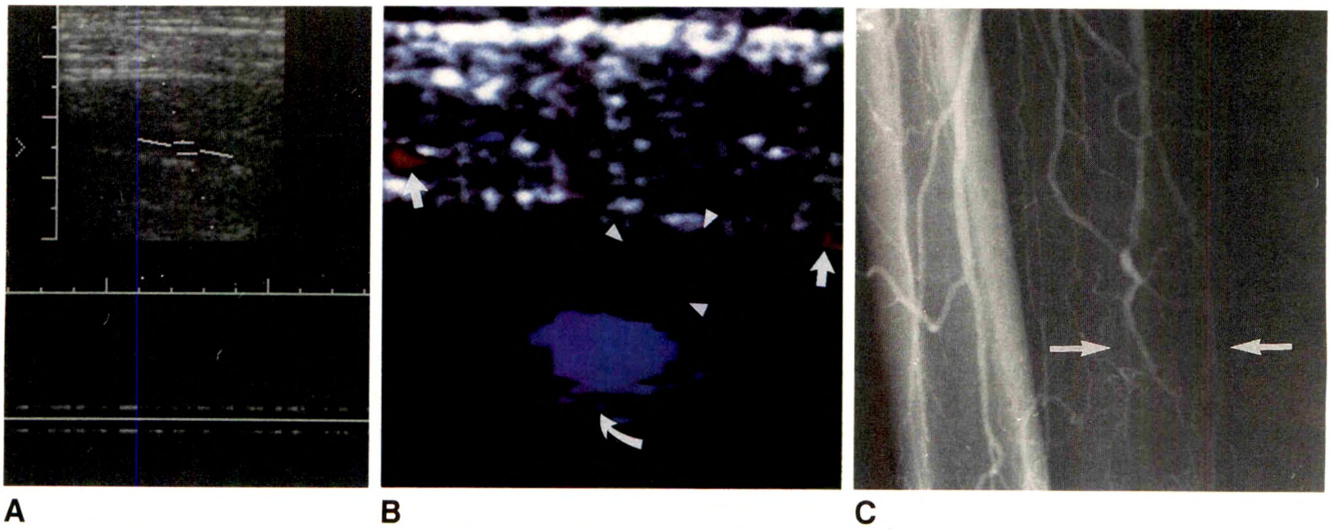

Fig. 3.—Images showing typical example of occluded superficial femoral artery, making patient an unlikely candidate for angioplasty. Duplex sonography is used to confirm diagnosis of occlusion suggested by absence of color flow signals. This 59-year-old man had severe claudication.

A, Longitudinal sonogram of distal superficial femoral artery with Doppler gate over artery reveals no detectable flow. Deflections above and below baseline represent noise due to high gain setting.

B, Corresponding transverse color flow sonogram at same level shows flow in superficial femoral vein (*curved arrow*). No flow is seen in superficial femoral artery, which is immediately superficial to vein (*arrowheads*). Small flow channels encoded as red (*straight arrows*) are due to flow in multiple small collateral arteries.

C, Arteriogram confirms occlusion of distal superficial femoral artery with multiple collaterals. *A* and *B* were obtained at level of *arrows*.

lyzed, sensitivity was 0.88 (49/56), specificity 0.95 (173/182), and accuracy 0.93 (222/238).

The average length of the duplex sonographic evaluation of both lower extremities in a given patient was 29.5 min (± 4.9 min SD; range, 20–38 min).

Discussion

We have used color-assisted duplex sonography, a technique that combines the subjective assessment of the lumen of flowing arterial blood with the selective sampling of Doppler spectra and the derived peak systolic velocity ratio, to rapidly evaluate lower-extremity arterial segments for stenoses, occlusions, or patency (Fig. 1).

In our series of 17 patients, 238 arterial segments were evaluated, 29 of which had stenoses and 27 of which were occluded. Twenty-two of the 29 stenotic segments and all occluded segments were correctly predicted before arteriography (Figs. 2 and 3).

In the stenotic segments, an isolated doubling of peak systolic velocity was present in three instances, diminished color flow in nine instances, and both criteria in 10 instances. In vessels that were heavily calcified, the only marker of a significant stenosis was the isolated increase of peak systolic velocity. In less calcified vessels with focal stenoses 0.5–4 cm long, an increase in peak systolic velocity and narrowing of the lumen were readily definable. In irregular stenotic segments longer than 5 cm, instead of an increase in velocity, there was in fact a velocity decrease. These lesions were identified only by a narrowed lumen seen on transverse color sonography. The false-positive diagnosis of stenosis was always made by a narrowed transverse colored lumen (five cases). This occurred contiguous to long segmental narrowings, where velocities are low. The size of the colored flow in the lumen was most likely underestimated because blood flow velocities dropped below the flow sensitivity of the device near the wall of the arteries. We were careful to visualize each segment transversely, because nonsignificant (<50%), focal, eccentric stenoses can be accentuated and made to look significant when viewed longitudinally if the transducer is also positioned eccentrically over the lesion. Such an effect, although present when the probe is held transverse and angled to the artery, seems to be less noticeable than on longitudinal imaging.

Assessment of blood flow velocities is best made in the longitudinal plane by using doubling of peak systolic velocity as a criterion for significant stenosis. All segments that had a doubling of peak systolic velocity were significantly stenosed.

All of the group of seven significant stenoses that were missed by prospective duplex and color Doppler sonography were in regions where visualization or assessment was altered by adjacent or intrinsic abnormalities. Four were immediately distal to occluded or highly stenotic segments with three of the four being at the origin of the profunda femoris arteries. The amount of blood flow in these segments was markedly diminished, and abnormal flow was not resolved by sonography. Three stenoses were in heavily calcified segments, where beam attenuation probably played a major role in decreased visualization.

No occlusions were missed. In the group of occlusions predicted with sonography and not confirmed with arteriography, all four were in the distal superficial femoral artery at the level of the adductor canal. This region is the most difficult to visualize and in some patients may be a blind spot. The increased depth of the vessel in the thigh causes decreased penetration of the ultrasound beam. These four false-positive segments were distal to high-grade stenoses or to occlusions. Large collateral branches were present and decreased the amount of blood carried by these segments. The velocity of blood traveling within was therefore decreased and more difficult to detect with Doppler imaging.

Could we have improved the sensitivity of the technique?

Forty-one percent of significant stenoses were detected only on the color examination. Duplex sonography performed poorly in these segments, where velocities and blood flow are uniformly low owing to parallel flow through developing collaterals. Conversely, 14% of stenoses were detected solely by the duplex component of the examination. This may be due to the lowered temporal resolution of color Doppler imaging. In peripheral arterial disease, the diastolic component can disappear while the systolic component of the Doppler spectrum can be quite short [6] and seen on only one to three frames of the color images obtained during each cardiac cycle. This may have altered the perception of relative lumen narrowing or had an effect on the digital processing used to create the color flow image [10]. Could the specificity of the examination have been improved? If assessment of the colored flow in the lumen is removed from the arterial maps, specificity is improved but sensitivity decreases dramatically because identification of long-segment stenoses was based only on a subjective assessment of the size of the colored lumen. Increasing the sensitivity of color Doppler imaging to lower velocities could have helped in excluding false-positive findings of occlusion. Unfortunately, this lowered sensitivity is more common at higher ultrasound frequencies (i.e., 7.5 MHz), where beam penetration causes more of a problem at the level of the adductor canal.

In this study, duplex sonography coupled with color flow sonography had a sensitivity of 0.88 for detecting significant stenoses or occluded segments. Specificity was 0.95 and accuracy was 0.93. This is equivalent, if not slightly more accurate, than rates reported for duplex sonography [6, 7]. The major advantage of color-assisted duplex imaging is the time taken to survey the femoropopliteal arterial system of both lower extremities. Typically, our average examination time was 29 min. This compares quite favorably with the range of 1-2 hr reported for duplex sonography alone [7].

We believe the technique is an improvement over the noninvasive use of segmental Doppler pressure measurements. Segmental disease is inferred when a pressure drop (>30 mm Hg) is measured between two cuffs at different locations in the extremity (i.e., upper thigh and lower thigh) [4, 5]. Accuracy of segmental Doppler pressures for femoropopliteal disease (>50% narrowing of lumen diameter) is moderate, with a sensitivity varying from 0.67 to 0.89 depending on the presence or absence of concomitant aortoiliac disease [11-12]. The technique cannot determine the nature of lower-extremity arterial lesions (i.e., occlusion vs focal stenosis) or their respective lengths.

Preangiographic color-assisted Doppler sonography influenced the diagnostic approach in six patients. Of the four patients in whom severely diminished inflow at the level of the common femoral artery was caused by severely diseased or occluded iliac arteries, two cases had not been predicted clinically. The two cases of common femoral artery disease were not obvious clinically. Focal stenoses of the superficial femoral artery in two patients were correctly predicted to be amenable to angioplasty. The angioplasties were performed after the diagnostic studies. An additional patient was found to have bilateral popliteal aneurysms, one of which was thrombosed. The popliteal aneurysm that was patent was not apparent on angiography because of the amount of mural thrombus lining it. Negative arteriographic findings such as these are thought to occur in up to 36% of diagnosed popliteal aneurysms [13]. This patient has now had arterial bypass surgery after ligation of the popliteal aneurysm.

Our experience suggests color-assisted Doppler sonography should be performed with longitudinal color flow imaging to locate sites where the Doppler spectrum is to be sampled [14]. This approach may also decrease study variability caused by the sonographer [15]. Transverse color Doppler imaging would then be used only as an adjunct for long segmental stenoses. The choice of sonographic imaging device also is important. We believe that steering the color Doppler angle separately from the gray-scale image and a high frame rate make it feasible to perform the examination in a reasonable amount of time.

In summary, color-assisted Doppler sonography is a noninvasive tool helpful in assessing the extent of peripheral arterial disease. Subjective evaluation of the colored flow in the lumen and determination of peak systolic velocity can be used to rapidly predict segmental stenoses and occlusions in the lower limb arteries.

ACKNOWLEDGMENTS

We thank Vennetta Hanley for secretarial assistance; Jo-Anne Polak for editorial aid; and the technological staff of both the noninvasive laboratory and angiography suites, without whom this study would not have been possible.

REFERENCES

1. Murray RR Jr, Hewes RC, White RI Jr, et al. Long-segment femoropopliteal stenoses: is angioplasty a boon or a bust? *Radiology* **1987**;162:473-476
2. Krepel VM, van Andel GJ, van Erp WF, Breslau PJ. Percutaneous transluminal angioplasty of the femoropopliteal artery: initial and long-term results. *Radiology* **1985**;156:325-328
3. McLean L, Jeans WD, Horrocks M, Baird RN. The place of percutaneous transluminal angioplasty in the treatment of patients having angiography for ischaemic disease of the lower limb. *Clin Radiol* **1987**;38:157-160
4. Lynch TG, Hobson RW II, Wright CB, et al. Interpretation of Doppler segmental pressures in peripheral vascular occlusive disease. *Arch Surg* **1984**;119:465-467
5. Cutajar CL, Marston A, Newcombe JF. Value of cuff occlusion pressures in assessment of peripheral vascular disease. *Br Med J* 1973; 2:392-395
6. Kohler TR, Nance DR, Cramer MM, Vandenburghe N, Strandness DE Jr. Duplex scanning for diagnosis of aortoiliac and femoropopliteal disease: a prospective study. *Circulation* **1987**;76:1074-1080
7. Jager KA, Phillips DJ, Martin RL, et al. Noninvasive mapping of lower limb arterial lesions. *Ultrasound Med Biol* **1985**;11:515-521
8. McNeil BJ, Keller E, Adelstein SJ. Primer on certain elements of medical decision making. *N Engl J Med* **1975**;293:211-215
9. Berry CC. A tutorial on confidence intervals for proportions in diagnostic radiology. *AJR* **1990**;154:477-480
10. Kasai C, Namekawa K, Koyano A, Omoto R. Real-time two dimensional blood flow imaging using an autocorrelation technique. *IEEE Trans Sonics Ultrason* **1985**;SU-32:458-463
11. Bell G, Nielsen PE, Wolfson B, Ulrich J, Engell HC, Lassen NA. Measurements of systolic pressure in the limbs of patients with arterial occlusive disease. *Surg Gynecol Obstet* **1973**;136:177-181
12. Heintz SE, Bone GE, Slaymaker EE, Hayes AC, Barnes RW. Value of arterial pressure measurements in the proximal and distal part of the thigh in arterial occlusive disease. *Surg Gynecol Obstet* **1978**;146:337-343
13. MacGowan SW, Saif MF, O'Neill G, Fitzsimons P, Bouchier-Hayes D. Ultrasound examination in the diagnosis of popliteal artery aneurysms. *Br J Surg* **1985**;72:528-529
14. Polak JF, Donaldson MC, Dobkin GR, Mannick JA, O'Leary DH. Early detection of saphenous vein arterial bypass graft stenoses by color-assisted duplex sonography: a prospective study. *AJR* **1990**;154:857-861
15. Polak JF, Dobkin GR, O'Leary DH, Wang A-M, Cutler SS. Internal carotid artery stenosis: accuracy and reproducibility of color-Doppler-assisted duplex imaging. *Radiology* **1989**;173:793-798

Book Review

Duplex Doppler Ultrasound. (Vol. 26 in Clinics in Diagnostic Ultrasound.) Edited by Kenneth J. W. Taylor and D. Eugene Strandness, Jr. New York: Churchill Livingstone, 182 pp., 1990. $55

This book attempts to present the leading edge of applications of Doppler ultrasound. The editors did not intend to produce a comprehensive textbook on this technique but rather to provide an up-to-date authorative overview of new developments in this area. Color Doppler sonography is not dealt with because a separate issue of *Clinics in Diagnostic Ultrasound* will be devoted to this topic.

The first chapter gives a broad overview of clinical applications of Doppler ultrasound in the assessment of arterial disease and provides several insightful comments on the pathophysiology of atherosclerosis. However, much of the content reflects current routine practice in vascular imaging. Furthermore, 22 of the 30 references at the end of this chapter were published before 1985. The same can be said of the chapter on hemodynamic considerations in the evaluation of arterial disease. It is well written but does not provide any insights not already available in numerous textbooks, including one for which Dr. Taylor is a coauthor.

The chapter by D. J. Phillips on recent advances in evaluation of the carotid artery has an excellent section on hemodynamics of the human carotid bifurcation. In fact, some of the earliest understanding of these hemodynamics was presented by Dr. Phillips working in conjunction with Dr. Strandness. The summary and conclusions are prophetic, and this chapter is a tribute to its author.

The section on deep venous thrombosis offers a brief but well-written description of standard techniques for evaluation of deep venous thrombosis of the lower extremities. However, for a chapter that purports to be about the leading edge of the technology, it would be helpful if the authors discussed the problem of differentiating acute from chronic deep venous thrombosis and the ability of low-flow detection Doppler systems to detect calf vein thrombosis. Furthermore, some mention of the potential role of MR imaging of the deep venous system would be useful.

The discussion of Doppler ultrasound evaluation of portal hypertension is excellent and well referenced. The illustrations are outstanding, and the diagram of potential surgical shunts is most enlightening. The only shortcoming of this chapter is failure to mention the potential of color Doppler sonography for evaluation of the hepatic venous system.

The chapter on Doppler evaluation of mesenteric and renal vascular disease presents controversial material. It is obvious that these authors advocate use of Doppler sonography as a screening test for patients with suspected renal vascular hypertension. This point of view is one that many challenge, and the excellent results achieved in the authors' laboratory are not duplicated readily by numerous others across the United States. The section on renal transplants includes a potentially misleading statement suggesting that high-resistance waveforms are characteristic of rejection but less so of other processes. Numerous recently published articles have shown that a variety of processes, including infection, acute tubular necrosis, and obstruction, can result in abnormal resistance patterns identical to those seen in acute vascular rejection. This section of the chapter is a bit brief when compared with the extensive discussion of portal hypertension. Similarly, the section on mesenteric arteries is brief and somewhat anecdotal.

Application of Doppler sonography in the female pelvis and in the first trimester of pregnancy, including technique, instrumentation, and safety, is discussed nicely. This chapter, however, would be more state of the art if more of it were devoted to discussion of endovaginal sonography, which is widely available in institutions that are performing evaluations of high-risk pregnancies, and which also entails the ability to provide color and pulsed Doppler evaluation of adnexal masses and intrauterine contents. The section on the vascularity of gynecologic tumors would be stronger if it included the work by Hatta et al. (*J Ultrasound Med*, 1989) describing relative nonspecificity of decreased resistivity indexes and increased blood flow.

One of the coauthors of the chapter on the use of Doppler ultrasound in high-risk pregnancies is a leading authority in the field. However, a major omission in this chapter is reference to the work of Benson and Dubilet (*J Ultrasound Med*, 1988), which shows quite clearly that Doppler studies are not a particularly sensitive or specific means of screening for intrauterine growth retardation and that Doppler sonography of umbilical arteries provides no more accurate detection of intrauterine growth retardation than standard biometric measurements of the fetal abdomen, femur, and head do.

The section on Doppler evaluation of lower limb vessels provides a succinctly written review, and the section on assessment of tumor vascularity offers an up-to-date look at the topic of Doppler analysis of tumor blood flow. The chapter by Wells on future development in Doppler ultrasound is delightfully written and touches on many areas in which advances in the field of ultrasound should be expected.

Most of these chapters provide concise summaries of applications of Doppler ultrasound; however, few actually accomplish the stated purpose of providing a leading-edge assessment of technology not already available in a number of excellent textbooks dealing with clinical applications of Doppler ultrasound, one of which was written by Taylor, Burns, and Wells. Although this issue of *Clinics in Diagnostic Ultrasound* is well written, it suffers from a shortcoming typical of most books: it cannot encompass recent advances in a rapidly evolving field of investigation.

Barbara A. Carroll
Duke University
Durham, NC 27710

Duplex Doppler Sonography of the Carotid Artery: False-Positive Results in an Artery Contralateral to an Artery with Marked Stenosis

William W. Beckett, Jr.[1]
Patricia C. Davis
James C. Hoffman, Jr.

Anecdotal reports have described a false-positive "jet effect" or velocity increase in the carotid artery contralateral to an artery with significant stenosis or occlusion when using duplex Doppler sonography. In this study, the frequency, significance, and possible reasons for this finding were evaluated by a retrospective comparison of duplex sonography and angiography. Twenty-three patients with unilateral 81–100% carotid artery stenosis who underwent both duplex sonography (16 Acuson, seven Quantum) and angiography were evaluated. In 14 patients, there was an accurate or slight underestimate (<20%) of stenosis present in the internal carotid artery contralateral to an artery with tight stenosis/occlusion. In nine, a velocity increase in the internal carotid artery resulted in overestimation (10–80%) of the actual degree of stenosis. In one of these nine patients, real-time images were sufficient to explain the velocity increase on the basis of vessel tortuosity. In one, falsely elevated velocity resulted from inaccurate assignment of the Doppler angle of incidence in a patient in whom real-time visualization of a distal internal carotid lesion was poor. In four of the nine patients, cross filling via the circle of Willis toward the side of greater stenosis occurred. However, seven of 14 patients in whom there was duplex sonography/angiography agreement or slight duplex sonography underestimation also had cross filling. Vertebral artery patency did not correlate well with the presence of a "jet effect."

These findings suggest that an increase in blood flow velocity with duplex Doppler sonography in the internal carotid artery on the side opposite an artery with a tight stenosis is a common source of error and is not readily explained by angiographic evidence of collateral flow.

***AJNR* 11: 1049–1053, September/October 1990; *AJR* 155:1091–1095, November 1990**

Duplex sonography (real-time imaging combined with Doppler) evaluation of the internal carotid artery contralateral to an artery with a significant (81–100%) stenosis/occlusion occasionally reveals a "jet effect" or an increase in velocity that is disproportionately high for the degree of stenosis actually present. Although this finding has been anecdotally reported as a pitfall of duplex sonography (Zweibel WJ, Dreisbach JN. Paper presented at annual meeting of RSNA, December 1986) and [1, 2], the frequency and cause of this false-positive velocity increase have not been studied in detail. For this reason, we undertook a retrospective study of duplex sonography findings in the common carotid/internal carotid arteries in a series of patients with a contralateral, angiographically proved, high-grade internal carotid artery stenosis/occlusion.

Materials and Methods

Between January 1987 and May 1988, 23 consecutive patients who had duplex sonography followed by carotid angiography and who had a proved unilateral 81–100% carotid stenosis by angiography were evaluated retrospectively. These patients ranged in age from 58 to 82 years (17 men, six women). Indications for duplex sonography included clinical suspicion of carotid artery disease (21) or preoperative screening for significant coronary or peripheral atherosclerosis (two).

Received June 27, 1989; revision requested October 2, 1989; revision received March 12, 1990; accepted March 12, 1990.

Presented at the annual meeting of the American Society of Neuroradiology, Orlando, March 1989.

[1] All authors: Department of Radiology, Section of Neuroradiology, Emory University School of Medicine, 1364 Clifton Rd., N.E., Atlanta, GA 30322. Address reprint requests to P. C. Davis.

0361-803X/90/1555-1091
© American Roentgen Ray Society

Duplex sonography was performed on an Accuson scanner with a 5.0-mHz real-time-pulsed Doppler transducer in 16 patients and a Quantum 7.5- and/or 5.0-mHz color real-time-pulsed Doppler transducer in seven patients. The sonographic study was always performed before the angiographic study, with a mean time interval between the two of 10 days (range, 0–42 days).

Standard duplex techniques included real-time imaging in the sagittal and transverse planes and multiple Doppler velocity measurements throughout each vessel. The Doppler angle of incidence was assigned parallel to the direction of blood flow in the portion of the vessel under evaluation, and was always less than 70°. Peak systolic and diastolic velocity data were recorded in the common carotid artery (CCA), internal carotid artery (ICA), and external carotid artery (ECA), and pre-, at, and poststenosis. Peak systolic velocity ratio was defined by Bluth et al. [3] as the peak velocity in systole at the ICA point of maximum stenosis divided by the peak velocity in the CCA 1 cm or more below the bifurcation. Percent stenosis by diameter was determined from real-time images by measuring plaque width relative to vessel diameter. Vessel tortuosity and shadowing plaque were noted.

Criteria for duplex sonography quantification of degree of stenosis are charted in Table 1 (Zweibel and Dreisbach, paper presented at RSNA, 1986) [3, 4].

Angiographic evaluation was performed by using selective intraarterial digital subtraction arteriography in 20 patients and biplane magnification cut-film angiography in three patients. Angiographic interpretation included location of plaque, percent stenosis by diameter based on the ratio of the greatest diameter of the plaque to the normal diameter distal to the lesion, the presence and direction of vertebral artery flow, and the presence and direction of cross filling intracranially via the circle of Willis. Percent stenosis by diameter was estimated to the closest tenth percentile.

Images obtained by duplex sonography and angiography were interpreted separately and independently by an experienced observer. Studies were considered to agree if the diagnostic range demonstrated by duplex sonography included the percent stenosis by diameter determined by angiography.

Results

In 11 (48%) of 23 patients, the duplex sonographic and angiographic interpretation agreed. The degree of stenosis determined by duplex sonography was overestimated in nine (39%) and underestimated in three (13%) compared with angiographic findings. Data were calculated both by using the peak systolic velocity ratio with the peak end diastolic velocity (Table 1) and by the ratio between the peak systolic velocity at the lesion and the peak systolic velocity just proximal to the lesion within the ICA with the peak end diastolic velocity. The results obtained from both velocity ratio measurements were identical, as noted above.

The presence or absence, and direction of cross filling angiographically via the circle of Willis are charted in Table 2.

The majority of patients in each category demonstrated bilateral vertebral artery patency, as reported in Table 2. Unilateral vertebral patency was noted in three of 11 patients in the duplex sonography/angiography agreement category, in one of three patients with duplex sonography underestimation, and in one of nine patients with duplex sonography overestimation. Subclavian steal was present in one patient in the duplex sonography overestimation category.

Recognizable causes for falsely elevated velocity ratios were found in two of nine patients. These included marked vessel tortuosity confirmed at angiography (one patient) and poorly visualized distal ICA stenosis, which resulted in inaccurate Doppler angle assignment (one patient). Of the remaining seven patients, no apparent explanation was found for the elevated velocity ratio measurements (Figs. 1 and 2). A case-by-case display of this data is found in Table 3.

The three patients in whom the degree of stenosis was underestimated by duplex sonography include: one patient with a 30% proximal ICA stenosis by sonography, and a 50% stenosis at angiography; one patient with the peak systolic velocity ratio of 2.91 and peak end diastolic velocity of 60 cm/sec, placing the patient in the 61–80% stenosis category (however, angiography demonstrated a 90% ICA lesion); and one patient with a 61–80% lesion by duplex sonography but a 90% lesion on angiography.

TABLE 1: Quantification of Degree of Stenosis by Duplex Sonography*

SVR[a] < 1.5	<50% stenosis by diameter (rely on real-time measurements in orthogonal planes)
SVR ≥1.5 and SVR <1.8	50–60% stenosis by diameter
SVR ≥1.8 and PEDV[b] <100 cm/sec	61–80% stenosis by diameter
SVR ≥1.8 and PEDV ≥100 cm/sec	81–99% stenosis by diameter
No Doppler shift	"String" (99%) stenosis or occlusion

* Criteria adopted from Zweibel and Dreisbach (paper presented at RSNA, December 1986) and Bluth et al. [3].

[a] SVR (systolic velocity ratio) is defined as the peak systolic velocity within the ICA at the point of maximum stenosis divided by the peak systolic velocity within the CCA, 1 cm or more below the bifurcation.

[b] PEDV (peak end diastolic velocity) is defined as the maximum velocity at end diastole.

Discussion

Velocity ratio measurements are an essential component of duplex sonography in the assessment of the degree of stenosis of the carotid arteries. These depend on accurate Doppler angle selection and sample volume placement, as well as adequate signal-to-noise ratio. The angle between the axis of the ultrasound beam and the long axis of the vessel studied must be less than 70° to assure an accurate velocity measurement. Accurate angular correction is achieved by manually assigning the angle of incidence of the Doppler beam relative to the direction of blood flow in the vessel. Finally, the sample volume gate should be centered within the blood vessel in order to encompass the entire laminar distribution of velocities for flow data [5].

Known causes of falsely low velocity measurements resulting in quantitative errors in stenoses include: (1) an angle greater than 70° between the ultrasound beam axis and the vessel; (2) suboptimal visualization of the vessel in question (or marked attenuation of the Doppler signal) resulting from

TABLE 2: Correlation Between Findings on Duplex Sonography and Angiography

	Cross-Filling Toward the Side of Greater Stenosis	No Cross-Filling	Cross-Filling Away from the Side of Greater Stenosis	Bilateral Antegrade Vertebral Flow
Duplex sonography overestimate (9)	4	5	0	7
Duplex sonography/angiography agreement (11)*	6	3	1	8
Duplex sonography underestimate (3)	1	1	1	2

* One patient in this category did not undergo evaluation of the intracranial vessels.

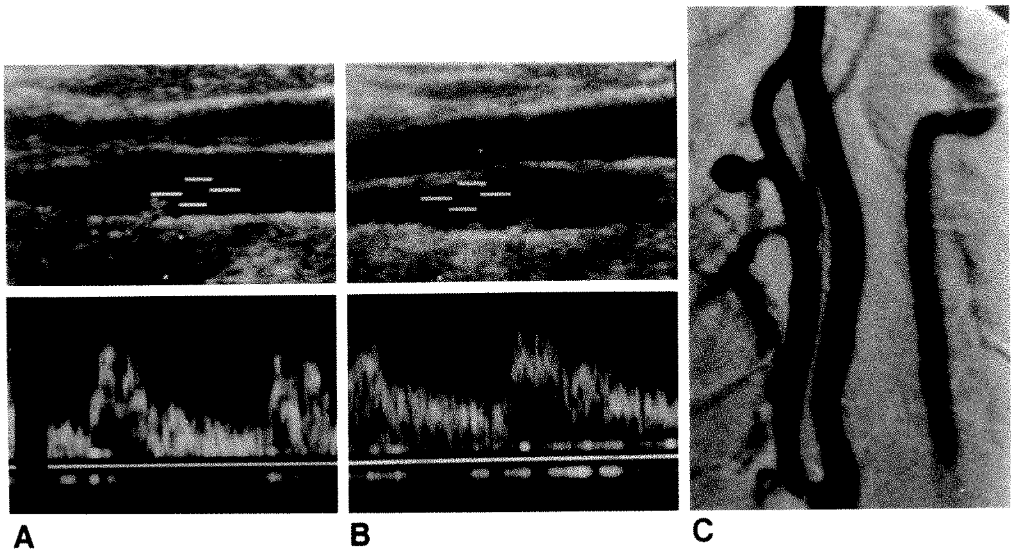

Fig. 1.—*A* and *B*, Distal CCA and proximal ICA duplex sonography images in a patient with an SVR of 2.2 (maximum systolic velocity in the ICA [*B*] divided by maximum systolic velocity in the CCA [*A*]), and a PEDV of less than 100 cm/sec, place the patient in the 61–80% stenosis category.

C, Carotid digital angiogram demonstrates 20% stenosis, indicating gross overestimation by duplex sonography. This patient did have collateral cross filling toward the side of greater stenosis, but no other explanation for the false "jet effect" with sonographic or angiographic evaluation could be found.

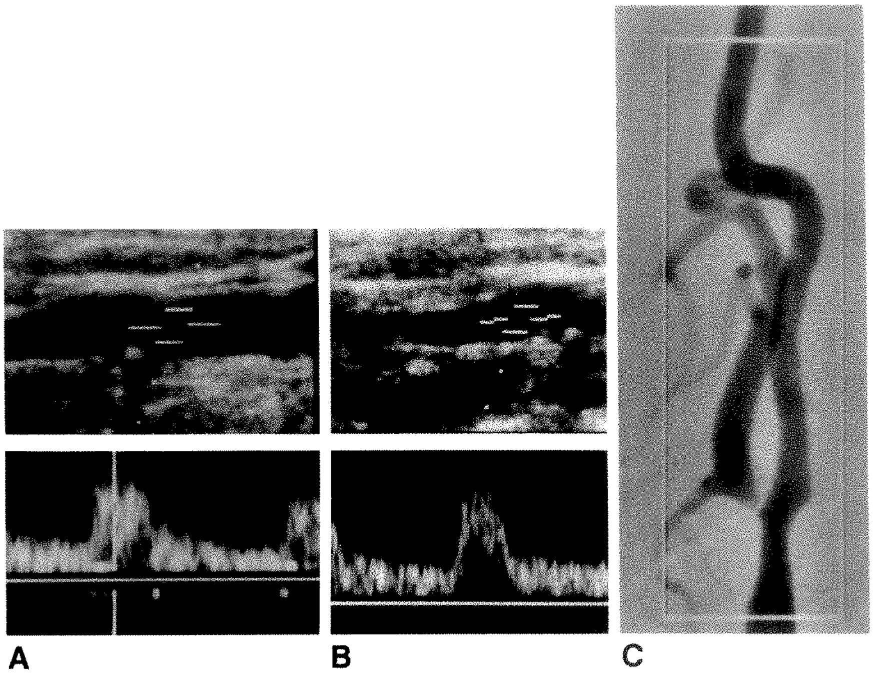

Fig. 2.—*A* and *B*, Representative duplex sonography images with an SVR of 2.0 and a PEDV equal to 36 cm/sec indicate a 61–80% lesion.

C, Angiogram shows a 50% CCA/ICA lesion and high-grade ECA stenosis. This is an example of mild duplex sonography overestimation.

TABLE 3: Duplex Sonography Findings Correlated with Angiography Findings in the Duplex Sonography Overestimation Group

Case No.	Side	SVR	PEDV (cm/sec)	% Stenosis by Duplex Sonography	% Stenosis by Angiography	Vertebral Patency by Angiography	Cross-Filling via Circle of Willis	Comments
1	Right	3.10	42	61–80	50	Antegrade	None	
2	Right	2.31	30	61–80	20	Antegrade	Right to left, MCA, ACA	Tortuous vessels on both real-time and angiography images
6	Right	2.17	50	61–80	10	Antegrade	Right to left, ACA	
7	Left	2.08	30	61–80	30	Subclavian steal	Left to right, ACA, MCA	
13	Right	1.94	33	61–80	10	Antegrade	None	Real-time images high in ICA, difficult to image
16	Left	2.73	43	61–80	50	Antegrade	None	
18	Left	1.80	36	61–80	50	Antegrade	None	
22	Right	1.64	35	50–60	30	Antegrade	Right to left, ACA	
23	Left	1.50	33	50–60	20	Antegrade	None	

Note.—SVR = systolic velocity ratio, PEDV = peak end diastolic velocity, MCA = middle cerebral artery, ACA = anterior cerebral artery, ICA = internal carotid artery.

such factors as depth or inaccessibility; and (3) multiple or serial stenoses (Zweibel WJ, Stavros AT. Paper presented at annual meeting of RSNA, December 1988).

Causes of falsely high velocities include erroneous assignment of an angle of incidence that is wider than the actual angle of incidence. This is evident upon review of the equation used to calculate such velocities:

$$V = FC/(2F_0 \cos \theta)$$

where V represents the velocity of the flowing blood, F is the Doppler frequency shift, C is the speed of sound in tissue, F_o is the frequency of the transducer, and θ is the angle of incidence of the Doppler beam relative to the direction of blood flow [5]. If θ is assigned in error as too great an angle, the velocity is overestimated. Practically, this occurs in studies of tortuous vessels in which it is difficult to set the angular correction to reflect the true direction of blood flow throughout a sharp curvature in the vessel. Simultaneous real-time imaging is helpful in identifying tortuosity and, thus, in preventing spurious velocity values. Additional sources of error in evaluation of lesions in the distal ICA include interference from the mandible, shadowing plaques, and vessel depth.

Intracranial collateral flow via the circle of Willis toward the cerebral hemisphere supplied by a significantly stenosed/occluded ICA has been implicated as a cause of the false "jet effect" in the more widely patent ICA (Zweibel WJ, Stavros AT. Paper presented at annual meeting of RSNA, December 1988). Flow equals velocity multiplied by the cross-sectional area of the vessel. If flow increases with a constant cross-sectional area (i.e., due to contralateral occlusion), then velocity must increase, resulting in a falsely elevated systolic velocity ratio. Other authors have anecdotally described examples of accelerated velocity in the absence of angiographically identifiable stenosis contralateral to a tight lesion [1, 2]. In this study, angiographic evidence of intracranial cross filling via the circle of Willis was equally common in patients with and without accurate duplex sonography studies. Superficially, this suggests that this explanation for error is overly simplistic. It is reasonable to suspect, however, that angiographic demonstration of cross filling via the circle of Willis is a relatively insensitive index of collateral flow. Xenon CT or radionuclide studies (single proton emission CT [SPECT] or positron emission tomography [PET]) more accurately reflect cerebral perfusion; thus, these studies might provide additional insight as to the cause of falsely elevated velocity ratios in our patients. Unfortunately, these studies are not routinely performed in patients thought to have carotid stenosis. Vertebral artery patency and antegrade flow as potential sources of collateral intracranial flow similarly correlated poorly with our duplex sonography results, since most patients in all categories demonstrated bilateral antegrade flow.

In summary, quantitation by duplex sonography of the degree of stenosis in the carotid artery contralateral to a high-grade or occluded ICA is more prone to error than duplex sonography in general, with the error generally resulting in an overestimation of the degree of stenosis actually present. This potential source of error should be anticipated contralateral to a high-grade stenosis, and the performance of angiography considered to most accurately assess the extent of carotid vascular disease. A possible explanation for the error is increased flow caused by intracranial cross filling to the contralateral hemisphere; however, this could not be confirmed by angiographic data.

Conversely, observation of a velocity increase or "jet effect" out of proportion to real-time vessel characteristics should prompt a careful sonographic search for high-grade stenosis of the contralateral ICA.

ACKNOWLEDGMENTS

We gratefully acknowledge the expert assistance of Roz Vecchio (photography), Francine Hollowell (manuscript preparation), and our referring physicians.

REFERENCES

1. Satiani B, Porter R, Biggers K, Burns R. Evaluation of the color coded Doppler ultrasound in detecting carotid bifurcation disease. *J Cardiovasc Surg* **1988**;29:196-200
2. White DN, Curry GR. A comparison of 424 carotid bifurcations examined by angiography and the Doppler echoflow. In: White D, Lyons EA, eds. *Ultrasound in medicine*, vol 4. New York: Plenum Press, **1978**:363-376
3. Bluth EI, Stavros AT, Marich KW, Wetzner SM, Aufrichtig D, Baker JD. Carotid duplex sonography: a multicenter recommendation for standardized imaging and Doppler criteria. *RadioGraphics* **1988**;8:487-506
4. Dreisbach JN, Seibert CE, Smazal SF, Stavros AT, Daigle RJ. Duplex sonography in the evaluation of carotid disease. *AJNR* **1983**;4:678-680
5. Nelson TR, Pretorius DH. The Doppler signal: where does it come from and what does it mean? *AJR* **1988**;151:439-447

American Roentgen Ray Society Residents' Award Papers, 1991

The ARRS announces competition for the 1991 President's Award and two Executive Council Awards for the best papers concerning the clinical application of the radiologic sciences.

Awards

The winner of the President's Award will receive a certificate and a $2000 prize. The winners of the two Executive Council Awards will each be given a certificate and a prize of $1000. The winners will be announced on March 15, 1991. Winning papers will be presented at the ARRS annual meeting at the Sheraton Boston Hotel, Boston, MA, May 5-10, 1991. Winning papers will be submitted for early publication in the *American Journal of Roentgenology*. All other papers will be returned to the authors.

Regulations

Eligibility is limited to residents or fellows in radiology who have not yet completed 4 years of approved training in a radiologic discipline. A letter from the resident's department chairman attesting to this status must accompany the manuscript. The resident must be the sole or senior author and be responsible for all or most of the project.

Submitted manuscripts must not exceed 5000 words and have no more than 10 illustrations. Four copies of the manuscript and illustrations are required. Submitted manuscripts should not contain previously presented or published material and should not be under consideration for publication elsewhere.

Deadline for submissions is February 15, 1991. Send papers to

Nancy O. Whitley, M.D.
Chairman, Committee on Education & Research
American Roentgen Ray Society
Department of Radiology
University of Maryland Medical Systems Hospital
22 South Greene St.
Baltimore, MD 21201

Memorial

John T. Keller, 1922–1990

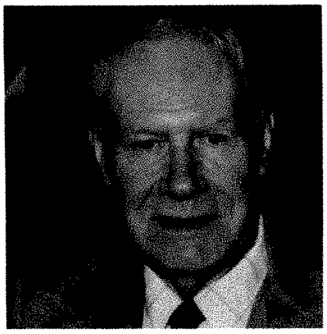

John T. Keller died on March 17, 1990. His family and friends mourn his demise. To us, St. Patrick's Day—the day he was buried—will always bring back sad memories.

Jack graduated from high school when he was 15 years old and then attended Loras College in Dubuque, IA. World War II called him to active duty; he flew 488 combat missions in a C-47 transport over China, Burma, and India. He received two Distinguished Flying Crosses and 24 Air Medals.

After the war, Jack returned to Loras College. Then he attended Creighton Medical School. After training in radiology, he joined the medical faculty of the University of Iowa College of Medicine, where he spent 14 years. He was a highly respected radiologist and was loved by residents and fellow faculty members. He left the university for private practice in 1971. In 1975, he joined the Veterans Affairs Medical Center in Providence, RI, where he worked till the end.

His hobbies were flying, singing, and watching action or comedy movies. Jack was a caring, loving, and giving person. We will miss him a lot.

Subhash G. Lathi
Providence, RI

Percutaneous Placement of Hickman Catheters: Comparison of Sonographically Guided and Blind Techniques

Johan S. Laméris[1]
Pieter J. M. Post[1]
Harmine M. Zonderland[1]
Pieter G. Gerritsen[2]
Mies C. Kappers-Klunne[3]
Henri E. Schütte[1]

We studied the value of sonographically guided puncture of the subclavian vein for placement of indwelling right atrial and permanent subcutaneously tunneled catheters (Hickman) for long-term venous access. The commonly used blind puncture is associated with complications such as pneumothorax, arterial puncture, and hemothorax. The results and complications of 40 sonographically guided punctures and fluoroscopically controlled catheterizations of the subclavian vein (group 1, 31 patients) performed in the radiology department were compared with those of 40 blind percutaneous punctures and fluoroscopically controlled catheterizations (group 2, 29 patients) performed in the operating room. The patients were selected consecutively. The groups were comparable in age, sex, and indication for catheter placement; administration of chemotherapy for hematologic malignancies was the major indication (group 1, 84%; group 2, 83%). All punctures in group 1 were successful; group 2 had two failures (5%). Puncture-related complications occurred significantly more in group 2 (10%) than in group 1 (0%) ($p <$ .05). These complications were pneumothorax in three cases and hemothorax in one. Complications not related to the puncture technique were prolonged bleeding at the entrance site (groups 1 and 2, two cases each), local infection (group 1, one case), thrombosis (group 1, three cases; group 2, two), catheter sepsis (group 1, 10 cases; group 2, 14), catheter occlusion (group 2, three cases), and catheter migration (groups 1 and 2, two cases each).

We conclude that sonographically guided puncture increases the success rate and significantly decreases the puncture-related complications of percutaneous placement of Hickman catheters.

AJR **155:1097–1099, November 1990**

Catheterization of the subclavian vein is a procedure commonly used to obtain central venous access for hemodialysis and long-term administration of fluids, antibiotics, or chemotherapy. Indwelling right atrial and permanent subcutaneously tunneled catheters such as the Hickman catheter are widely accepted for these purposes [1]. Such catheters can be placed by using either the surgical cutdown method or percutaneous puncture of the vein. In general, the percutaneous method is preferred, because it decreases the time and cost of the procedure [2]. Complications of this technique—arterial puncture, hemothorax, nerve injury, and pneumothorax—occur in 1–7% [2–4].

Of the technical improvements that have been proposed, the use of sonographic and fluoroscopic guidance seems the most logical and the most valuable [5–8]. Demonstrating the target vein and its surrounding anatomic structures could prevent complications and enable easy recognition of malposition. These considerations encouraged us to place the Hickman catheters in the patients in the radiology department, where both sonography and fluoroscopy are available.

The results and the complications of 40 procedures in which puncture of the subclavian vein was done under sonographic guidance and catheter placement was controlled by fluoroscopy were compared with those in a control group in

Received March 26, 1990; accepted after revision June 1, 1990.

[1] Department of Radiology, University Hospital Dijkzigt, Erasmus University, Dr. Molewaterplein 40, 3015 GD, Rotterdam, the Netherlands. Address reprint requests to J. S. Laméris.

[2] Department of Surgery, University Hospital Dijkzigt, Erasmus University, 3015 GD Rotterdam, the Netherlands.

[3] Department of Hematology, University Hospital Dijkzigt, Erasmus University, 3015 GD Rotterdam, the Netherlands.

0361-803X/90/1555-1097
© American Roentgen Ray Society

which 40 Hickman catheters were inserted by the surgeon in the operating room by using blind percutaneous puncture and fluoroscopy to control the guidewire and catheter positions.

Subjects and Methods

Group 1 consisted of 31 patients in whom 40 Hickman catheters were placed by the radiologist in the radiology department. The subclavian vein was punctured under sonographic guidance. We used a freehand approach in which the needle was inserted through the skin directly into the plane of a 5- or 7.5-MHz linear-array transducer (Aloka Co., Japan) in which the infraclavicular subclavian vein was visualized. The positions of the guidewire and catheter were controlled by fluoroscopy. Group 2 consisted of 29 patients in whom 40 Hickman catheters were placed by the surgeon in the operating room. The infraclavicular subclavian vein was punctured blindly in a standard fashion from a position 2–3 cm below the middle third of the clavical [9–10]. The positions of the guidewire and catheter were controlled also by fluoroscopy.

The procedures were done between January 1987 and November 1989. Waiting periods for the operating room influenced patient selection during the first few months. Later on, patients were selected consecutively. After September 1988, only sonographically guided procedures were done.

Patients of both groups were comparable in sex, age, underlying disease, and indication for long-term venous catheter access. In group 1 there were 15 men and 16 women, in group 2 13 men and 16 women. The mean age in group 1 was 44 (range, 16–70); in group 2 it was 49 (range, 20–77). The indications for catheter placement were administration of chemotherapy for hematologic malignancies in 26 patients (84%) in group 1 and 24 patients (83%) in group 2, parenteral nutrition in two patients (7%) in group 1, administration of antibiotics in one patient (3%) in group 1 and three patients (10%) in group 2, and hemodialysis and other miscellaneous indications in two patients (7%) in each group. Platelet transfusion was necessary before catheter placement in 18 patients with thrombocytopenia in both groups.

In all procedures, a 14-French double-lumen silicone central venous access catheter was used (Gish Biomedical Inc., Santa Ana, CA). Local anesthesia and IV sedation were used for both techniques. In the operating room an anesthesiologist was standing by in case failure of the puncture necessitated a cutdown approach.

In both groups puncture of the left subclavian vein was preferred, because the longer distance to the superior vena cava facilitates positioning of the catheter [11] and prevents kinking of the introducer sheath. When thrombosis was detected sonographically (group 1) or the left vein was catheterized (either group) before placement, the right subclavian vein was punctured. In both groups the puncture site and subcutaneous tract for the catheter were anesthetized with 1% lidocaine, and two small incisions were made. The subclavian vein was punctured with an 18-gauge needle. In group 1 the tip of the needle was continuously monitored by sonography (Fig. 1). In both techniques a flexible J wire was introduced through the needle into the vein and the position of the wire was controlled by fluoroscopy. Then, a subcutaneous tunnel was made. The catheter was passed through the tunnel and shortened to its appropriate length. A 14-French dilator with peel-away sheath was subsequently introduced over the wire into the subclavian vein. The dilator and the wire were then removed and the catheter was led through the gradually split and withdrawn sheath, leaving the catheter in place.

The position of the catheter was again controlled by fluoroscopy. The catheter was immediately flushed with heparin saline. The two incisions were closed and covered with a sterile dressing.

In both groups patency of the subclavian vein after placement was checked only when clinical signs suggested thrombosis. Sonography was the method of choice in detecting thrombosis. Differences in success rate and puncture-related complications were analyzed by means of a statistical test for difference between sample proportions.

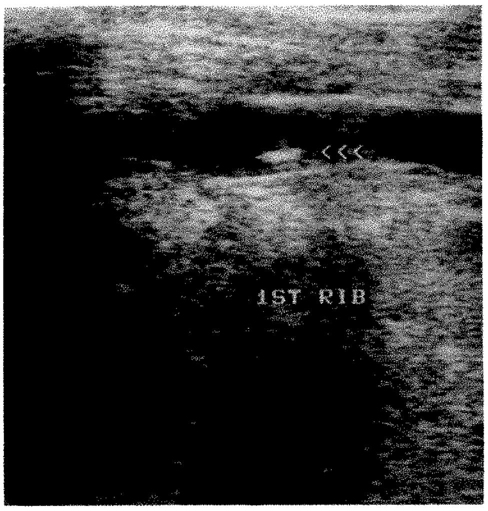

Fig. 1.—Sonogram showing infraclavicular part of left subclavian vein. Reflection of needle tip can be seen within vein (*arrowheads*).

Results

The results and complications are summarized in Table 1.

All sonographically guided punctures in group 1 were successful. In two patients, sonographic examination before the procedure showed clinically unsuspected thrombosis of the left subclavian vein; therefore, the right vein was punctured. One patient had stenosis of the subclavian vein due to the earlier presence of an infected catheter. This prevented correct positioning of the catheter in the superior vena cava and a malposition was accepted. Unfortunately, thrombosis of the punctured vein occurred within 2 days. The two other cases of thrombosis were diagnosed 7 and 59 days after placement. The patients with prolonged bleeding at the insertion site were treated with several platelet transfusions. In one patient local infection developed on the fourth day. Nine catheters were removed because of suspected infection and two after migration and malposition of the catheter tip.

Blind puncture of the subclavian vein in group 2 failed in two patients. In the first patient, the cutdown technique was subsequently used; in the second, the catheter was ultimately placed under sonographic guidance. One malpositioned catheter was removed the same day. Pneumothorax occurred in three patients; two needed a chest tube, one was treated conservatively. In one of these patients in whom puncture on the contralateral side was attempted, hemothorax occurred, which was treated conservatively. Thrombosis was seen in two patients after 30 and 103 days. Sepsis was the reason for removing 14 catheters (one was occluded also); two catheter migrated and were subsequently removed.

The differences in success rates between the two groups were not statistically significant. The occurrence of puncture-related complications, however, showed a statistically significant difference in favor of group 1 ($p < .05$).

Discussion

Sonographically guided percutaneous placement of Hickman catheters combines several advantages of existing methods for central venous access and at the same time avoids their drawbacks. As with the surgical cutdown method, the target vein is visualized during the procedure; and as with the

TABLE 1: Results and Complications in the Percutaneous Placement of Hickman Catheters With (Group 1) and Without (Group 2) Sonographic Guidance

Variable	No. (%)	
	Group 1 (*n* = 40)	Group 2 (*n* = 40)
Successful catheterization	40 (100)	38 (95)
Catheter site	27 L 13 R	24 L 14 R
Malposition	1	1
Duration (days)		
Mean	89	66
Range	2–415	1–214
Puncture-related complications		
Pneumothorax	0	3 (7.5)
Hemothorax	0	1 (2.5)
Early complications (<1 wk)		
Thrombosis	2 (5)	0
Prolonged bleeding at entrance site	2 (5)	2 (5)
Local infection	1 (2.5)	0
Late complications		
Thrombosis	1 (2.5)	2 (5)
Sepsis	10 (25)	14 (35)
Catheter occlusion	0	3 (7.5)
Catheter migration	2 (5)	2 (5)

blind percutaneous method, sonographically guided placement is a fast and successful procedure. The main drawbacks of the cutdown method are the low success rate (75%), the long operating time, and the compromising of the vein for future use [2]. The blind percutaneous method is associated with a 1–7% puncture-related complication rate [2, 3]. Inadvertent puncture of the subclavian artery or the pleural space, causing hemothorax or pneumothorax, is one of the most severe complications. However, the success rate of this technique is as high as 96%, and the same vein can be reused if necessary.

The most striking difference between the two groups of patients was the absence of severe puncture-related complications such as hemo- or pneumothorax in the 40 cases of sonographically guided placements. Sonographically guided puncture of the subclavian vein succeeded in all cases. The use of sonography also has the advantage that before the vein is punctured the patency of the vein can be checked. In two cases, a clinically unsuspected thrombosis of the left vein prompted us to choose the contralateral side. Constant monitoring of the needle point will prevent inadvertent puncture of adjacent anatomic structures. Unlike the blind technique, only the anterior wall of the vein is punctured, leaving the posterior wall undisturbed.

Early thrombosis of the vein after catheter placement is often ascribed to damage of the wall of the vessel owing to the puncture and subsequent manipulations with the guidewire, sheath, and catheter [7]. The duration of the procedure therefore should be as short as possible and manipulations within the vein should be limited. There is no reason to assume that sonographic guidance will reduce the chance of this complication because this technique only reduces the number of unsuccessful needle passes. Once the vein is punctured, both methods are identical. Early thrombosis occurred in two sonographically guided procedures and only after difficult placement: in one patient, after kinking of the sheath, and in another, after a failed attempt to catheterize the superior caval vein because of subclavian vein stenosis.

Placement of Hickman catheters is usually done in the operating room, where strict sterile conditions are assured. Moreover, when the percutaneous technique fails, the cutdown method can be applied, and when complications occur, surgery is directly available. The overall infection rate of the sonographically guided procedures does not support reservations about the sterility of the radiology department. Sonographic guidance seems to guarantee not only a highly successful but also a safe procedure. The low rate of failures or complications therefore will seldom make surgical interventions necessary. Another consideration that led us to perform the procedure in the radiology department was that scheduling is far more flexible than in the operating room.

Two other reports have advocated placement of large venous access catheters in the radiology department [8, 12]. In one, only fluoroscopy was used to control the position of the guidewire and the catheter; in other words, the technique was identical to the surgical percutaneous method. Here, puncture-related complications still occurred [12]. In the other report, fluoroscopy was used for angiographic visualization of the subclavian vein during the puncture by injecting contrast material in a peripheral vein. Here, puncture-related complications were prevented [8]. However, disadvantages of this indirect method, compared with direct sonographic visualization of the subclavian vein, are the length of the procedure, the radiation exposure to the hands of the radiologist, and the fact that this method is applicable only when peripheral venous access for contrast administration is possible.

In conclusion, we consider sonographically guided placement of Hickman catheters superior to other methods.

REFERENCES

1. Hickman RO, Buckner CD, Clift RA, et al. A modified right arterial catheter for access to the venous system in marrow transplant recipients. *Surg Gynecol Obstet* **1979**;148:871–875
2. David SJ, Thompson JS, Edney JA. Insertion of Hickman catheters; a comparison of cutdown and percutaneous technique. *Am Surg* **1984**; 50:673–676
3. Ryan JA Jr, Abel RM, Abbot WM, et al. Catheter complications in total parenteral nutrition: a prospective study of 200 consecutive patients. *N Engl J Med* **1984**;290:757–761
4. Padberg FT Jr, Ruggiero J, Blackburn GL, Bristrian BR. Central venous catheterization for parenteral nutrition. *Am Surg* **1982**;193:264–270
5. Sukigara M, Yamazaki T, Hatanaka M, Nagashima N, Omoto R. Ultrasonic real time guidance for subclavian venipuncture. *Surg Gynecol Obstet* **1988**;167:239–242
6. Nolsoe C, Nielsen L, Karstrup S, Lauritzen K. Ultrasonically guided subclavian vein catheterization. *Acta Radiol [Diagn]* (Stockh) **1989**;30:108–109
7. Machi J, Takeda J, Kakegawa T. Safe jugular and subclavian venipuncture under ultrasonographic guidance. *Am J Surg* **1987**;153:321–323
8. Selby JB, Tegtmeyer CJ, Amedo C, Bittner L, Atuk NO. Insertion of subclavian hemodialysis catheters in difficult cases: value of fluoroscopy and angiographic technique. *AJR* **1989**;152:641–643
9. Hawkins J, Nelson E. Percutaneous placement of Hickman catheter. *Am J Surg* **1982**;144:624–626
10. Kirkemo A, Johnstron MR. Percutaneous placement of the Hickman catheter. *Surgery* **1982**;91:349–351
11. Bonventre EV, Lally K, Chwalls WJ, Hardin WD, Atkinson JB. Percutaneous insertion of subclavian venous catheters in infants and children. *Surg Gynecol Obstet* **1989**;169:203–205
12. Robertson LJ, Mauro MA, Jaques PF. Radiologic placement of Hickman catheters. *Radiology* **1989**;170:1007–1009

Case Report

The Mechanism of Peripheral Recanalization by Laser-Assisted Thermal Angioplasty: Confirmation by Intravascular Sonography

Jonathan M. Tobis,[1] Cres P. Miranda,[1] Larry Deutsch,[2] Jim Griffith,[3] Jim Gessert,[3] Avi Bergman,[3] Michael Berns,[4] and Walter Henry[1]

The mechanism of recanalization during laser-assisted angioplasty in the treatment of obstructive atherosclerotic vascular disease has been controversial. Initial reports claimed that the laser-heated metal-tipped probe ablated atheroma as the hot tip "sought the lumen" and progressed down the artery as it created a new lumen in the central portion of the plaque [1-3]. In distinction to the initial animal and clinical studies, an in vitro study of the mechanism of recanalization with laser-assisted thermal angioplasty found it to be a predominantly mechanical process in which the laser probe was deflected by the hard, fibrocalcific plaque away from the true lumen and followed a dissection plane between the intimal plaque and the arterial media [4]. However, in human clinical trials, it is difficult to prove the exact pathway of the laser probe by using angiography or angioscopy.

Recent work has documented the feasibility of imaging arteries in cross-section with a miniaturized catheter-mounted sonographic transducer that generates arterial images from inside the artery lumen [5, 6]. This report documents that the information obtained from the intravascular sonographic device in vivo is consistent with the hypothesis derived from our in vitro study for the mechanism of recanalization by the laser probe.

Case Report

A 73-year-old man with claudication had bilateral superficial femoral artery (SFA) occlusions at the bifurcation with the common femoral artery. Both popliteal arteries were reconstituted, and distal runoff was good. The patient refused surgical intervention but was willing to undergo percutaneous angioplasty. The length of the occlusion of the right SFA was 20 cm, and the left SFA was occluded 23 cm.

The right femoral artery was recanalized in a retrograde fashion from a puncture in the popliteal fossa. A 1.5-mm-diameter laser probe (Model PLR-plus, Trimedyne Inc., Santa Ana, CA) was inserted and advanced under fluoroscopic control through an introducing sheath and an 8-French angioplasty guiding catheter. The laser probe was used as a cold mechanical device without turning on the argon laser. The laser probe was advanced by using intermittent forward pressure to puncture the occlusive atheroma. The course of the laser probe was followed under fluoroscopic control until it advanced to the proximal end of the SFA and reentered the lumen of the common femoral artery. The laser probe was then removed, and a guidewire was inserted through a 7-French diagnostic catheter, which was used in a rotary maneuver to enlarge the communication between the SFA and the common femoral artery. The 20-MHz sonographic catheter (InterTherapy, Inc., Costa Mesa, CA) was advanced in the new channel to the level of the common femoral artery.

Figure 1A shows the intravascular sonogram that was obtained at the level of the distal SFA before the sonographic catheter entered

---

Received February 12, 1990; accepted after revision April 27, 1990.

[1] Division of Cardiology, University of California, Irvine, Medical Center, P.O. Box 14091, Orange, CA 92668. Address reprint requests to J. M. Tobis.

[2] Division of Radiologic Sciences, University of California, Irvine, Medical Center, Orange, CA 92668.

[3] InterTherapy Inc., Santa Ana, CA 92705.

[4] The Beckman Laser Institute, Irvine, CA 92717.

AJR 155:1100-1102, November 1990 0361-803X/90/1555-1100 © American Roentgen Ray Society

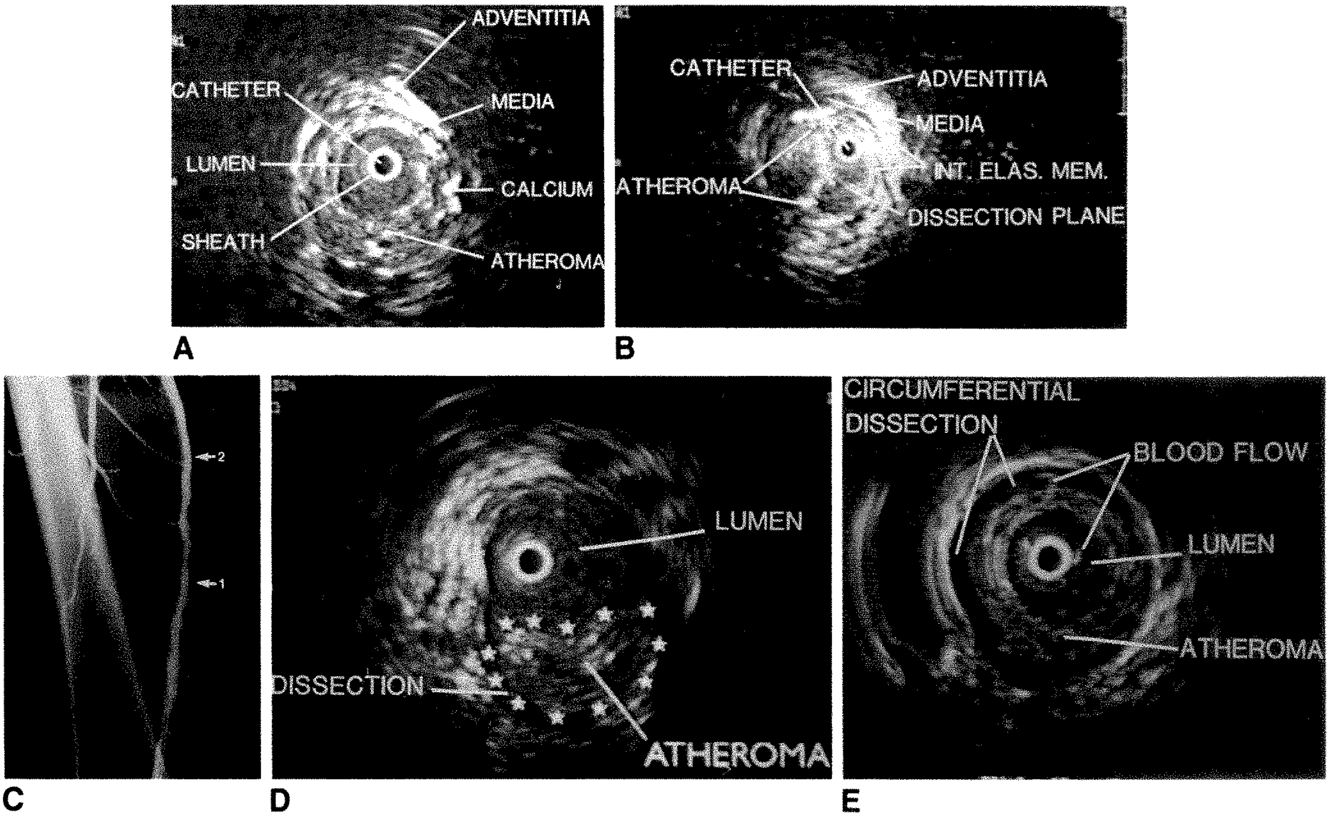

Fig. 1.—*A*, Intravascular sonogram in distal superficial femoral artery before entering area of recanalization. Central black area is from catheter; around this is a white echo reflection from plastic sheath. In a radial distribution is echolucent lumen, then a thick atheroma with variable echo reflections depending on amount of collagen within plaque or presence of calcium.

***B*, Sonogram shows path of laser probe in vivo. Instead of recanalizing artery through central atheroma, catheter is in a dissection plane between atheroma and internal elastic membrane.**

***C*, Angiogram of superficial femoral artery after laser-probe recanalization and balloon angioplasty shows a patent vessel with areas of dissection.**

***D*, Sonogram obtained at level 1 in *C* shows an eccentric atheroma that has been deformed by balloon. Note dissection around capsule of atheroma that separates atheroma from media.**

***E*, Sonogram obtained at level 2 in *C* shows concentric atheroma that has not been torn at this level, but has been separated from media almost circumferentially. Real-time sonography showed blood pulsating in dissection plane and in lumen.**

the area of recanalized SFA. The echolucent media, which defines the extent of the atheroma, can be seen in the superior and inferior portions of the image. The dimensions of the lumen are 4.4 × 3.6 mm or 14.0 mm^2 by planimeter measurement. Calcification is observed on the right side as intense echo-reflectance with dropout of echoes and shadowing peripherally to this area. The total atheroma area is 30 mm^2, which is 68% of the total available cross-section area within the boundary of the media. The artery at the level where this sonogram was obtained appeared to be normal angiographically.

At a more proximal level, in the area of the SFA that was recanalized, the sonogram showed the pathway that was taken by the laser probe (Fig. 1B). Moving from the peripheral portion of the artery on the right side of the image across to the left, the following structures are visualized: The adventitia is intensely echo-reflective followed by an echolucent circumferential line of media, followed by the echogenic thin line from the reflections from the internal elastic membrane. More central is a dissection plane in which the sonographic imaging catheter is situated. To the left and medial to the catheter are dense echo-reflections from calcium and atheroma that had previously occluded this portion of the SFA, but were mechanically pushed aside by the laser probe and guiding catheter as they created the dissection plane between the atheroma and the internal elastic membrane.

After this initial observation with the sonographic catheter, balloon angioplasty was performed from the level of the adductor canal to the common femoral artery. The angiogram (Fig. 1C) showed adequate patency of the SFA. The sonographic catheter was reinserted, and multiple images were obtained along the length of the SFA. Examples of the effect of balloon dilatation as visualized by the sonographic catheter in vivo are shown in Figures 1B and 1C. At the midportion of the SFA (Fig. 1B), the lumen is reconstituted and measures 6.1 × 5.2 mm in diameter or 23.8 mm^2 in cross-sectional area. In addition, a dissection is present around the eccentric atheroma plaque, which separates the atheroma from the media. The atheroma plaque is 16.4 mm^2 in area and has a deformation consistent with a compression effect of the balloon. In addition, there is a central echolucent arc in the atheroma that is interpreted as representing the original lumen after it was compressed by the balloon inflation in the new periatheroma dissection plane.

At a more proximal portion of the SFA (Fig. 1C), the balloon inflation created almost a complete circumferential dissection with separation of the atheroma from the wall of the artery for 300°. In real time on the video monitor, the atheroma appeared to move independently of the media and external wall of the artery. In addition, because of the relatively slow flow in the lumen, intermittent pulsations of echo-reflectance were seen in the central lumen around the sonographic catheter sheath and also in a portion of the dissection plane (at 12 o'clock), indicating that blood was flowing within this newly created dissection. This type of dissection plane suggests that the atheroma plaque was torn away from the media wall by a force of torsion, which might explain why the dissection was completely circumferential. This type of torsion dissection was observed in our in vitro study [4]; however, it was believed that this was an artifact of the in vitro preparation. The observation from the intravascular sonographic study shows that this type of dissection also exists in vivo and is not due to manual manipulation or histologic preparation.

Discussion

Although laser angioplasty has tremendous potential for expanding the treatment of obstructive atherosclerotic disease, serious complications such as vasospasm, thrombogenicity, and vessel perforation have diminished the initial enthusiasm. This case adds evidence that the predominant mechanism of recanalization in laser-assisted thermal angioplasty is a mechanical process in which the laser probe is deflected by the atheromatous plaque to follow a dissection plane along the arterial wall within the boundary of the internal elastic membrane [4]. In addition, this case demonstrates that the laser-probe catheter can successfully recanalize an occluded artery without the use of laser energy.

Given the technology and cost required to perform laser angioplasty, a definitive demonstration of its superiority over conventional techniques in the treatment of obstructive atherosclerotic vascular disease is necessary [7]. In fact, the application of thermal energy to this process may be detrimental; therefore, randomized clinical trials are necessary to compare the two techniques directly [8].

This report supports the hypothesis that the pathway of recanalization by the laser probe observed in the in vitro studies also occurs in vivo. Not only does intravascular sonography provide a means to study the effect of balloon or laser angioplasty, it also allows accurate quantification of the lumen and atheroma cross-sectional areas. Intravascular sonography could significantly increase our understanding of the pathophysiology of atherosclerotic peripheral disease.

REFERENCES

1. Lee G, Ikeda RM, Chan MC, et al. Dissolution of human atherosclerotic disease by fiberoptic laser-heated metal cautery cap. *Am Heart J* **1984**; 107:777–778
2. Cumberland DC, Sanborn TA, Tayler DI, et al. Percutaneous laser thermal angioplasty: Initial clinical results with a laser probe in total peripheral artery occlusions. *Lancet* **1986**;1:1457–1459
3. Sanborn TA, Cumberland DC, Greenfield AJ, et al. Peripheral laser-assisted balloon angioplasty. *Arch Surg* **1989**;124:1099–1103
4. Tobis J, Smolin M, Mallery J, et al. Laser-assisted thermal angioplasty in human peripheral artery occlusions: mechanisms of recanalization. *J Am Coll Cardiol* **1989**;13:1547–1554
5. Tobis JM, Mallery JA, Gessert J, et al. Intravascular ultrasound cross-sectional arterial imaging before and after balloon angioplasty in vitro. *Circulation* **1989**;80:873–882
6. Yock PG, Johnson EL, Linker DT. Intravascular ultrasound: development and clinical potential. *Am J Cardiac Imaging* **1988**;2:185–193
7. Society of Cardiovascular and Interventional Radiology. SCVIR position statement on thermal laser angioplasty. *Radiology* **1989**;172:944
8. Sanborn TA, Greenfield AJ. Response. Peripheral laser angioplasty: need for organized clinical trials. *Radiology* **1989**;172:943

Case Report

Splaying of Titanium Greenfield Inferior Vena Caval Filter

Parvati Ramchandani,[1] Harvey A. Koolpe,[2] and Robert M. Zeit[2]

The titanium Greenfield filter, which was developed to overcome some of the shortcomings of the stainless steel Greenfield filter, has had its own set of problems, as reported by Teitelbaum et al. [1] in their three patients. We report our experience in placing titanium Greenfield filters in seven patients, four of whom were followed up with radiographs.

Case Report

A 65-year-old woman with scleroderma had deep venous thrombosis (DVT) in the left lower extremity. Anticoagulation was contraindicated because of a recent stroke. Inferior vena cavography was performed via the right femoral vein and showed the proximal inferior vena cava (IVC) to be narrowed and irregular (Fig. 1A); a large lower lumbar collateral was seen. The abnormality was thought to be most likely a sequela of old caval thrombosis. A titanium Greenfield filter (Medi-tech, Watertown, MA) was placed in the normal part of the infrarenal portion of the IVC. The insertion was relatively easy, despite the distorted IVC. A postinsertion scout radiograph showed a filter span of 27 mm (all measurements take into account an estimated magnification factor of 20% and are corrected measurements) with no significant tilt (Fig. 1B). The cavogram obtained a few moments later showed an increase in the filter span to 35 mm (Fig. 1C), with two of the filter legs protruding beyond the caval lumen. The vertical alignment of the filter remained satisfactory. The apical cap of the filter was located at the level of the T12–L1 interspace.

The patient recovered uneventfully and was discharged. She returned 5 months later with bilateral edema in the lower extremities. A plain radiograph of the abdomen (Fig. 1D) showed marked splaying of the filter with a span of 64 mm and a tilt angle of 30 degrees to the left. The filter cap was displaced caudally by 68 mm. A cavogram (Fig. 1E) showed thrombosis of the infrarenal part of the IVC with at least three filter legs protruding from the IVC. The patient had no symptoms referable to the malpositioned filter.

Discussion

The titanium Greenfield filter was developed for percutaneous insertion through a 14-French sheath. Early animal experiments [2] and clinical experience [3] indicated that the filter was both effective and safe. However, as clinical experience accumulated, the titanium Greenfield filter was found to have an unacceptably high predisposition to splaying (increase in filter span beyond immediate postinsertion value), causing IVC perforation and injury to pericaval organs and blood vessels [1, 4]. Significant splaying, ranging from 8 to 37 mm occurred in two patients (Figs. 1A–1E). Caudal migration of the filter was associated with the splaying in both patients and also occurred in a third patient in whom the filter span remained unchanged. A fourth patient had stable filter position but a decrease in filter span, indicating caval thrombosis. In vitro experiments have demonstrated that the titanium Greenfield filter may remain splayed even in the face of clot retraction after IVC thrombosis [1], unlike the stainless steel Greenfield filter.

The titanium Greenfield filter is made of a flexible Beta III titanium alloy and has longer hooks, a larger span, and a larger hook angle than the standard stainless steel filter does. These factors appear to allow the struts greater caval penetration with potential for damage to pericaval organs and blood vessels. The flexibility of the filter also appears to predispose it to caudal migration.

Received February 8, 1990; accepted after revision April 27, 1990.

[1] Department of Radiology, Hospital of the University of Pennsylvania, 3400 Spruce St., Philadelphia, PA 19104. Address reprint requests to P. Ramchandani.

[2] Department of Radiology, Albert Einstein Medical Center, York and Tabor Rds., Philadelphia, PA 19141.

AJR 155:1103–1104, November 1990 0361–803X/90/1555/1103 © American Roentgen Ray Society

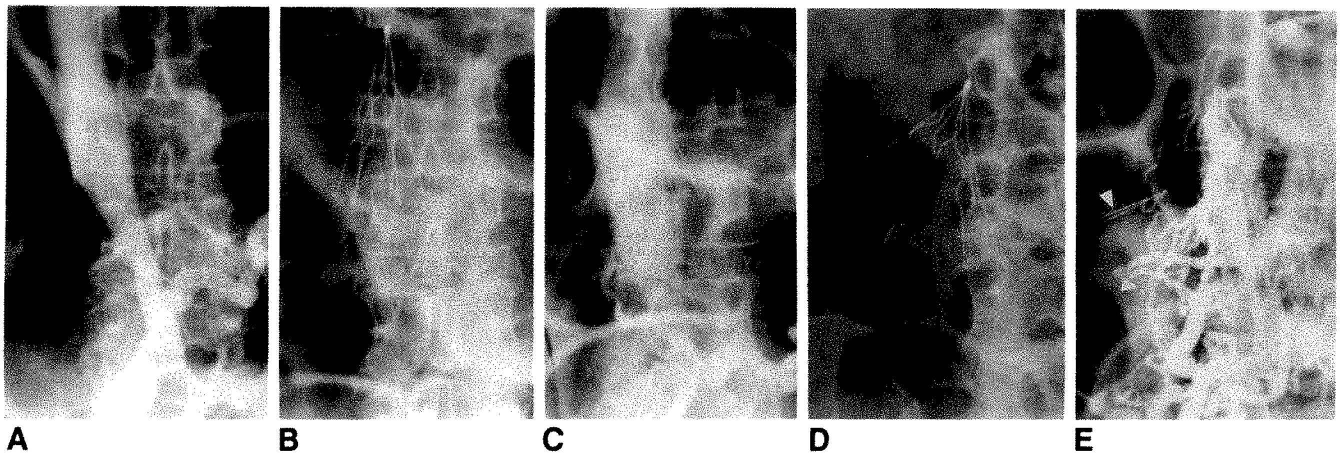

Fig. 1.—*A*, Cavogram obtained before filter placement shows narrowing and irregularity of proximal cava.

***B*, Postplacement plain radiograph. Filter span is 27 mm.**

***C*, Cavogram obtained moments after *B* shows filter span expansion to 35 mm with protrusion of two filter legs beyond caval lumen.**

***D*, Plain radiograph obtained 5 months later shows marked filter splaying with span of 64 mm, tilt angle of 30 degrees to left, and caudal migration of apical cap by 68 mm.**

***E*, Cavogram shows caval thrombosis with large collaterals opacifying normal suprarenal portion of inferior vena cava. Note filter legs outside caval lumen (*arrowheads*).**

Splaying has been described in three patients thus far [1]. Our experience brings the number to five. Approximately 200 titanium Greenfield filters have been implanted in humans (Teitelbaum GP et al., presented at the annual meeting of the Radiological Society of North America, November 1989). The filter has been withdrawn by its manufacturer for further design modifications. Despite the marked splaying, none of the five patients had complications directly attributable to the hook fixation in the pericaval tissues.

REFERENCES

1. Teitelbaum GP, Jones DL, Van Breda A, et al. Vena caval filter splaying: potential complication of use of the titanium Greenfield filter. *Radiology* **1989**;173:809–814
2. Burke PE, Michna BA, Harvey CF, Crute SL, Sobel M, Greenfield LJ. Experimental comparison of percutaneous vena caval devices: titanium Greenfield filter versus bird's nest filter. *J Vasc Surg* **1987**;6:66–70
3. Greenfield LJ, Cho KJ, Pais SO, Van Aman M. Preliminary clinical experience with the titanium Greenfield vena cava filter. *Arch Surg* **1989**;124:657–659.

Thermal Effects of MR Imaging:
Worst-Case Studies on Sheep

B. J. Barber[1]
Daniel J. Schaefer[2]
Christopher J. Gordon[3]
D. C. Zawieja[1,4]
Jamie Hecker[2]

The objective of this study was to provide a worst-case estimate of thermal effects of MR imaging by subjecting anesthetized unshorn sheep to power deposition at specific absorption rates (SARs) well above approved standards for periods of time in excess of normal clinical imaging protocols. A control period with no RF power was followed by 20–105 min of RF power application. Afterward, there was a 20-min or longer recovery period with no RF power. Eight sheep were given whole-body RF exposure (1.5- to 4-W/kg SAR) while rectal and skin temperatures were monitored. Four sheep were subjected to 4-W/kg head scans for an average of 75 min while temperatures of the cornea, vitreous humor, head skin, jugular vein, and rectum were measured. In head scanning experiments, skin and eye temperatures increased about 1.5°C. Jugular vein temperature rose a maximum of 0.4°C after an average exposure of 75 min. In whole-body exposures, elevation of rectal temperature was correlated with energy input. Deep-body temperature rises in excess of 2.0°C were attained for 4-W/kg whole-body exposure periods greater than 82 min. Animals exposed for 40 min to 4 W/kg in either body coil (three sheep) or head coil (two sheep) were recovered and observed to be in good health for 10 weeks; no cataracts were found.

MR power deposition at SAR levels well above typical clinical imaging protocols caused body temperature to increase. For exposure periods in excess of standard clinical imaging protocols the temperature increase was insufficient to cause adverse thermal effects. Studies in healthy humans are needed to determine whether enhanced heat-loss effector mechanisms are likely to cause deep-body temperatures to plateau at an acceptable level, and to elucidate mechanisms that determine subcutaneous temperature.

***AJR* 155:1105–1110, November 1990**

MR imaging is widely used for clinical imaging and diagnosis [1]. During a typical 20-min MR imaging examination, the body is exposed to an RF near field (64 MHz for a 1.5-T magnet) that is primarily magnetic. The induction heating from MR imaging typically leads to selective elevations in body temperature. The largest increase in tissue temperature occurs near the body surface [2].

MR imaging systems have now been approved [3, 4] for operation at whole-body specific absorption rates (SARs) of RF energy up to 0.4 W/kg. Further increases in SAR above 0.4 W/kg raise important safety questions because little is known about the thermal responses of animals comparable in size to humans during exposure to MR imaging or other sources of RF radiation [5].

The objective of this study was to provide a worst-case estimate of thermal effects of 4-W/kg head and 1.5- to 4-W/kg whole-body MR scans on a 70-kg anesthetized homeotherm such as a human.

Materials and Methods

Animals

Power deposition during MR imaging is related to the area of the eddy current loop [2]. For constant energy deposition and specific heat, the temperature rise in a passive object is

Received February 27, 1990; accepted after revision May 30, 1990.

[1] Department of Physiology, The Medical College of Wisconsin, Milwaukee, WI 53226.

[2] General Electric Company, Medical Systems Group, Milwaukee, WI 53201. Address reprint requests to D. J. Schaefer.

[3] U.S. Environmental Protection Agency, Research Triangle Park, NC 27711.

[4] Department of Physiology, College of Medicine, Texas A & M University, College Station, TX 77843.

0361-803X/90/1555-1105
© American Roentgen Ray Society

inversely proportional to mass. Many heat loss mechanisms are functions of surface area, which is proportional to the two-thirds power of mass [6]. For these reasons, it is important to study thermal effects from MR imaging in a homeotherm comparable in mass to humans.

Adult sheep were selected for study because (1) a sheep's body mass is close to that of a human; (2) metabolic rate per kilogram of body mass is nearly identical to that of humans [5]; (3) existing data [7-9] for sheep and human thermoregulatory effector mechanisms indicate that the heat stress thermoregulatory capability of an anesthetized, unshorn, nonpanting sheep is less than that of an unanesthetized, less insulated, sweating human; (4) invasive studies of temperature distribution are possible in sheep; and (5) anesthetized sheep can be subjected to heat stress of unknown severity.

Unshorn female sheep, numbered 1 through 12 throughout this article, were studied. Their body weights were 1: 73.2 kg; 2: 73.2 kg; 3: 62.2 kg; 4: 63.5 kg; 5: 75.5 kg; 6: 64.5 kg; 7: 54.6 kg; and 8: 81.8 kg. The four sheep exposed on the last day weighed 9: 80.0 kg; 10: 72.0 kg; 11: 83.5 kg; 12: 77.8 kg. All animals used in the study were housed and cared for in an on-site American Association for Laboratory Animal Sciences-approved facility; experiments were conducted in accordance with the National Institute of Health guidelines for use of laboratory animals. Two days before the experiment, animals were deprived of food to minimize bloating and regurgitation under anesthesia, but were allowed water ad libitum.

The sheep were anesthetized with a priming dose of sodium pentobarbital (10 mg/kg), and a surgical plane of anesthesia was maintained throughout the experiment (approximately 8 hr) by supplemental infusions (2 mg/kg) via an indwelling 18-gauge angiography catheter placed into the right jugular vein. All sheep were intubated with an endotracheal tube to minimize respiratory problems.

The animals were placed supine in the MR scanner with the hindlegs extended as far back as possible by tying them to the table with tape. Forelegs were folded, taped, and drawn together so the animal would fit in the body coil. Five animals (sheep 1 and 9-12) in which no thermocouples were surgically implanted were recovered after the experiments and held for a 10- to 12-week observation period. The remaining animals (sheep 2-8) were given a lethal injection of sodium pentobarbital after the experiment.

Experimental Protocols

A control period with no RF power was followed by 20-105 min of RF power application. Afterward, there was a 20-min or longer recovery period with no RF power. Three exposure protocols were used: 4-W/kg whole-body exposure (sheep 1-4, 9, 10); 4-W/kg head only exposure (sheep 5, 11, 12); and 4-W/kg head only exposure followed by a 45-min delay, followed by a low-power (1.5- or 2-W/kg) body exposure (sheep 6-8).

Rectal temperature was measured in animals 1-8 by inserting a thermocouple 25 cm into the colon via the rectum. Vena caval blood temperature was measured in whole-body nonrecovery protocols (sheep 2-4) by using a thermocouple placed in the superior vena cava by threading it through a 14-gauge angiography catheter inserted into the left external jugular vein.

Subcutaneous temperature-measuring thermocouples were placed on the abdomen (subdermally, 10 cm off midline and 8 cm below xiphoid process) and on the chest (subdermally, proximal to xiphoid process on midline) of sheep 6-8 (nonrecovery protocol) by inserting an 18-gauge needle subdermally, pushing the thermocouple through the needle, and withdrawing the needle leaving the thermocouple in place. Subcutaneous thermocouples were secured with a suture and contact cement [10].

In the 4-W/kg head exposure nonrecovery protocol (sheep 5-8), a minute thermocouple probe was inserted into the vitreous body of the eye. This was done by manually rolling the eye downward to expose the sclera just behind the equator and then making a hole through the sclera with an 18-gauge needle. The thermocouple was inserted through this hole to a depth of 1 cm, and sewn in place with 6-0 Vicryl suture material. A thermocouple was placed on the eye surface (cornea) and secured by taping the eyelid closed. A thermocouple was introduced into the external jugular and threaded cranially. Subcutaneous thermocouples were placed on the forehead (subdermally, on midline) over the frontal aspect of the skull about 5 cm above the eyes, and on the neck (subdermally, on midline above hyoid muscles).

Temperature Measurement Methods

Vinyl-insulated 24-AWG copper-constantan thermocouple wire was used for rectal temperature probes. A minute thermocouple probe was constructed to measure internal eye temperature by using 0.025-mm copper and constantan wires (type IRCO-001, Omega Engineering, Stamford, CT); the junction was dipped in polystyrene (Q-Dope, GC Electronics, Rockford, IL) and allowed to dry for 24 hr. Teflon-insulated 36-AWG copper-constantan thermocouple wire was used for all other thermocouple probes [10]. Cold junction compensation was performed by monitoring the temperature (Thermistor type 44202, Yellow Springs Instruments, Yellow Springs, OH) of the terminal block where the 10-m-long thermocouple leads were connected (a copper-constantan junction was formed at the block by the constantan wire). Thermocouple voltages were digitized (model DT2801-A, Data Translation, Marlboro, MA), processed, and stored on a computer. Calibration was performed by using a National Bureau of Standards traceable precision thermistor (model 49TA, Yellow Springs Instruments) with a resolution of 0.01°C and three precision-temperature baths (model FE, Haake, Saddle Brook, NJ) at 35, 40, and 45°C. Self-heating of the thermocouple by the RF field was tested by placing the thermocouple in open air (in the same location it would have been in the animal) and applying maximal RF power for 10 min; no change occurred in thermocouple voltage, indicating a lack of measurable self-heating. Furthermore, the thermocouples had no discernible effect on image quality, indicating a lack of RF field perturbation.

Ambient temperature was 19°C and relative humidity was 50%. Initial and final rectal temperatures were measured in sheep 9-12 by using a glass mercury thermometer.

RF Exposure

These experiments were conducted on a 1.5-T (64-MHz) MR imager by using quadrature circularly polarized magnetic field (vector) excitation (Signa, General Electric, Milwaukee, WI). In such a system the RF field was circularly polarized, had very little electric component (near field), and was oriented with the magnetic vector normal to the long axis of the animal.

Whole-body SAR was calculated as average RF power absorbed by the animal divided by the total body mass of the animal. Local average SAR levels in head experiments were calculated by dividing the net power absorbed by the sheep in the head coil by head mass (4.2 kg was measured for the head in one sheep and head dimensions were relatively invariant). To obtain desired SAR in the animal [1], peak forward power (P_f) was adjusted according to the animal mass (MASS), desired SAR, coil efficiency (ϵ), RF duty cycle (DC), forward power transmission line attenuation (α), load power transmission line attenuation (β), and reflection coefficient (Γ):

$$P_f = (\mathrm{SAR} \times \mathrm{MASS})/[\epsilon \times \mathrm{DC} \times (\alpha - |\Gamma|^2/\beta)]. \qquad (1)$$

A hybrid splitter was used to drive the RF body coil in quadrature. No splitter was used for the head scans. The P_f was measured remote from the RF body coil and corrected to values present at the input to the RF coil. For body scans the peak reflected power (P_r) (which was measured remote from the RF coil) is nearly zero (it never exceeded 0.2% of the forward power). The very small value of P_r in body scans results from the presence of the hybrid splitter. The hybrid splitter is a four-port device that divides the forward power into two signals of equal magnitude, 90° out of phase. When equivalent impedances appear at the two RF coil ports, then no reflected power will appear at the forward power port. Under these circumstances, all the reflected power will appear at the fourth port of the splitter, which is terminated in a matched load. During body scanning, then, P_r may be neglected. The ratio of the peak power delivered to the load port to the forward peak power in body scanning is a constant for a given load. It is analogous to the square of the magnitude of the reflection coefficient.

The accuracy of SAR calculations was verified experimentally by subjecting phantoms to 60-min, 4.0-W/kg scans. The SAR was determined from the specific heat of the material (C), the initial temperature (T_i), the final temperature (T_f), and the duration of exposure (τ). If the measured temperatures were the average temperatures of the phantom material and if the phantom were perfectly insulated, then:

$$SAR = C(T_f - T_i)/\tau. \quad (2)$$

The 11% maximal deviation between the theoretical and experimental values was due to imperfect thermal insulation, imperfect stirring of the phantom solution, and imperfections in temperature and power measuring devices. The calorimetry experiments validated the SAR calculations used for the animal exposures.

Statistical Methods

Data were recorded to 0.001°C resolution, and three decimal places were carried throughout all calculations. Reported values are rounded to one decimal place to reflect a conservative estimate of measurement precision. Data were self-paired by averaging only temperature changes, that is, each animal and each thermocouple channel was used as its own control. All averages are stated as mean ± standard error of the mean. Each regression analysis was accompanied by a one-way analysis of variance, which yielded an F statistic having a statistical significance level comparable to that of the t value for the regression analysis.

Results

Control Period with No RF Power Applied

Thermoneutrality of the sheep within the bore is indicated by the stability of body temperatures during the control period. Rectal and skin temperatures were monitored in seven animals for 30 min or more (skin temperatures were recorded for sheep 2–8). The average change in rectal temperature during the control period was −0.1 ± 0.1°C ($n = 7$), which was not significantly different from zero ($p = 1.0$). The grouped mean skin temperature change in the control period was 0.24 ± 0.11°C ($n = 7$), which was not significantly different from zero.

Whole-Body 4-W/kg Exposure

The effect on rectal temperature of whole-body exposure to 4 W/kg was measured in six sheep. Exposure times and temperature rises were 1: 20 min, 0.6°C (first of two exposures); 2: 82 min, 2.1°C; 3: 95 min, 2.0°C; 4: 104 min, 2.7°C; 9: 40 min, 0.9°C; and 10: 40 min, 0.9°C. The average rate of increase during RF exposure was 0.025 ± 0.003°C/min, which was significantly different from zero ($p < .01$). Body temperatures were not measured during the RF exposure period in sheep 1, 2, 9, and 10 to avoid any possibility of a reduction in temperature rise due to power interruptions.

To test for deviations from linearity during the temperature rise, rectal temperature was measured at approximately 20-min intervals in two sheep. For sheep 3 (Fig. 1A), linear

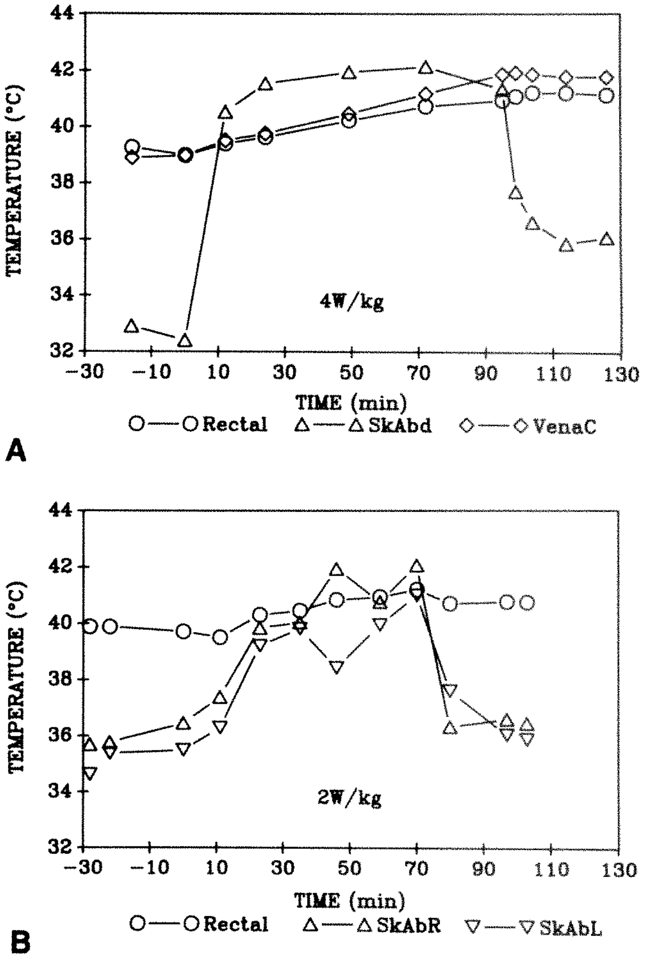

Fig. 1.—Time course of principal temperatures of skin and deep body in anesthetized, unshorn sheep subjected to whole-body MR imaging.

***A*, Response to 4 W/kg for 95 min. Subcutaneous temperature increases rapidly to a level just above deep-body temperature; this was largest change in subcutaneous temperature seen in this study. Near end of exposure period, all body temperatures were at about same level. SkAbd = abdominal skin, VenaC = vena cava.**

***B*, Response to 2 W/kg for 70 min. Rate of change in body temperatures and maximum increase is about one half of that seen in 4-W/kg experiment. Skin temperatures tend to change together. SkAbR = abdominal skin, right side; SkAbL = abdominal skin, left side.**

regression analysis yielded a slope of 0.020 ± 0.001°C/min ($p < 10^{-4}$). For sheep 4, regression analysis yielded a slope of 0.026 ± 0.003°C/min ($p < .001$). The closeness of fit to a straight line is indicated by the high level of statistical significance for the regression. This indicates that rectal temperature did not increase rapidly to a plateau nor did it lag for some time and then increase rapidly toward the end of the exposure period. However, no conclusions can be drawn about events that might have occurred during the 20-min periods when no measurements were taken. For the grouped data (all points from six sheep), the slope was 0.023 ± 0.002°C/min ($p < 10^{-4}$). Note that the brief (10- to 20-sec) power interruptions for temperature measurement had no discernible effect on the rate of rise in rectal temperature.

The effect on vena caval temperature of whole-body exposure to 4 W/kg was measured in three sheep. For sheep 2, the temperature rise was 2.3°C over 82 min. Regression analysis for sheep 3 yielded a slope of 0.028 ± 0.001°C/min ($p < 10^{-4}$). For sheep 4, the slope was 0.030 ± 0.001°C/min ($p < 10^{-4}$). No significant difference was seen in the rate of increase in vena caval temperature among the three sheep. Vena caval temperature increased at a higher rate ($p < .01$) than did rectal temperature.

The effect on subcutaneous temperatures of 4-W/kg whole-body exposure was studied in three sheep. In contrast to the high reproducibility of deep body temperature transients, responses varied widely. Subcutaneous temperature usually increased rapidly and reached a relatively stable level within 20 min. After this time, subcutaneous temperature either fell slightly or increased at a rate comparable to deep body temperature. Over the plateau interval, starting at 20 min after power went on and ending when power went off, the average change in subcutaneous temperature from time zero was 6.0 ± 1.2°C ($n = 8$ intervals; $p < .001$). The average rate of rise was 0.3°C/min during the first 20 min. This is roughly an order of magnitude higher than the rate of rise of deep body temperatures at 4 W/kg. The 95% confidence interval for the rise in skin temperature was 3.7–8.1°C.

Whole-Body 1.5- to 2.0-W/kg Exposure

Changes in body temperature (Fig. 1B) were smaller in the low-power experiments. At 1.5 W/kg (sheep 6), the slope of the rectal temperature regression line was 0.01 ± 0.001°C/min ($p < 10^{-4}$). Regression analysis for sheep 7 (2 W/kg) yielded a slope of 0.012 ± 0.001°C/min ($p < 10^{-4}$). For sheep 8 (2 W/kg), the slope was 0.018 ± 0.004°C/min ($p < .004$). Although the rate of rise of rectal temperature was lower at 1.5 W/kg, the difference was not statistically significant at the .05 level. If we combined the 1.5- and 2.0-W/kg data, then the regression slope for change in rectal temperature was 0.013 ± 0.0015°C/min ($p < 10^{-4}$) and the intercept was 0.105 ± 0.081°C ($p = .21$). Thus, the rate of increase in rectal temperature was about one half that seen in the 4-W/kg exposures.

The grouped mean change in skin temperature change while power was on was 3.9 ± 0.36°C ($n = 17$ intervals) in two sheep. The 95% confidence range for the difference between the change during the control period and the change during the power-on period was 2.5–4.9°C; the t value was 6.32 ($p < 10^{-4}$). Therefore, the change in subcutaneous temperature during 1.5- to 2.0-W/kg exposure was about half of that due to 4 W/kg.

The product of SAR and time gives the energy input to the animal. The rise in rectal temperature (Fig. 2) was correlated ($r = .92$) with energy input. A regression analysis of rectal temperature vs energy input gave a slope of 0.091 ± 0.005°C/(J/g), with a t value equal to 16.9 ($p < 10^{-4}$); the intercept was 0.100 ± 0.05°C ($p = .07$). Thus, whole-body scans in six sheep at SARs of 1.5–4 W/kg showed a highly significant relationship between energy input and rise in rectal temperature.

Head Exposure to 4 W/kg

During a 4-W/kg head scan (Fig. 3), internal eye temperature increased rapidly to a near steady-state value. During the control period the average of the temperature changes in four animals was −0.2 ± 0.1°C ($n = 22$ intervals). During the first 20 min of power application, the change in internal eye temperature from time zero was 0.8 ± 0.1°C ($n = 4$ intervals); at the end of approximately 75 min, the average change from time zero was 1.2 ± 0.1°C ($n = 4$). Regression analysis from the 20-min time to the end of the exposure yielded a slope of 0.005 ± 0.005°C/min ($p = .27$). During the same initial period the change in the temperature of the eye surface from time zero was 1.2 ± 0.1°C ($n = 4$); at the end of approximately 75 min, the change from time zero was 1.5 ± 0.1°C. Regression analysis from 20 min to the end of exposure yielded a slope of 0.008 ± 0.004°C/min ($p = .04$).

During the first 20 min of power application, the grouped mean change in jugular temperature was 0.3 ± 0.1°C ($n = 4$); at the end of approximately 75 min, the average change from time zero was 0.5 ± 0.20°C. Regression analysis from

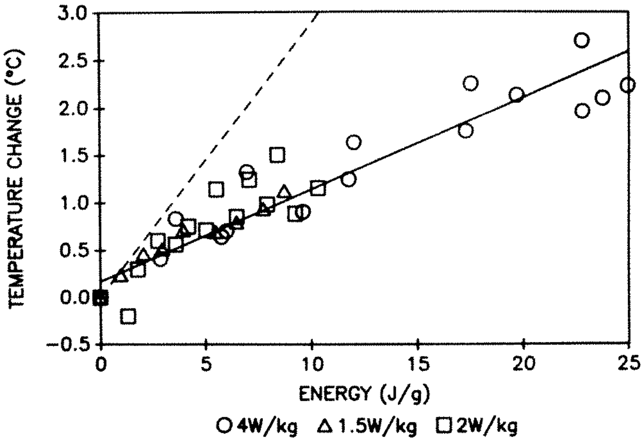

Fig. 2.—Relationship between energy input (the product of specific absorption rates and exposure time) and rise in rectal temperature in nine anesthetized, unshorn sheep subjected to whole-body MR imaging. *Broken line* represents predicted temperature rise under adiabatic conditions (no heat loss from the sheep). Exposure times range from 10 to 104 min; specific absorption rates range from 1.5 to 4.0 W/kg.

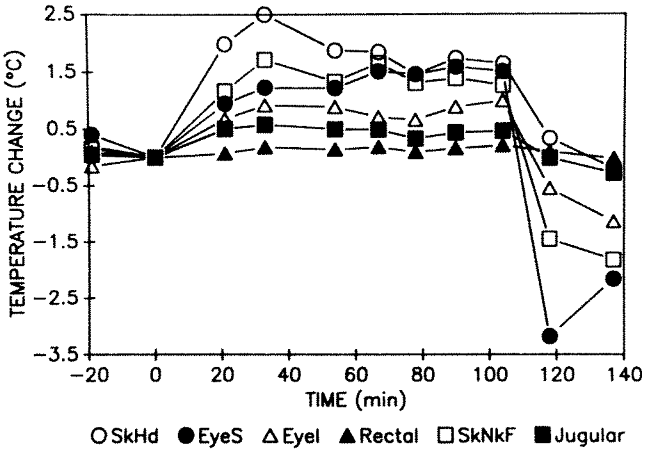

Fig. 3.—Time course of principal temperatures of head and core in an anesthetized, unshorn sheep subjected to MR imaging of head of 4 W/kg for a duration of 105 min. Body temperatures at time zero were rectal, 38.0°C; jugular, 37.9°C; eye internal (EyeI), 41.4°C; eye surface (EyeS), 44.3°C; skin from neck (SkNkF), 42.4°C; and head skin (SkHd), 35.2°C. Abrupt fall in temperatures at end of exposure period is due to moving sheep from bore of MR imaging machine to room.

the 20-min time to the end of the exposure yielded a slope of 0.003 ± 0.002°C/min ($p = .13$). During the first 20 min of power application the grouped mean change in rectal temperature was 0.06 ± 0.02°C; at the end of approximately 75 min the average change from time zero was 0.19 ± 0.04°C. Regression analysis from the 20-min time to the end of the exposure yielded a slope of 0.0018 ± 0.0009°C/min ($p = .05$). Therefore, the increase in rectal temperature was approximately linear. All other temperatures showed a rapid initial increase to a level from which little or no further increase occurred. The changes in rectal temperature were very small compared with those seen in the whole-body 1.5- to 2.0-W/kg exposures. Hence, little, if any, carryover effects were present in the low-power whole-body experiments conducted not less than 45 min later.

During the first 20 min of power application, the grouped mean change in skin head temperature was 0.9 ± 0.5°C ($n = 3$); at the end of approximately 75 min, the average change from time zero was 1.0 ± 0.2°C. Regression analysis from the 20-min time to the end of the exposure yielded a slope of 0.0083 ± 0.009°C/min ($p = .35$). During the first 20 min of power application, the grouped mean change in the temperature of the front skin neck was 1.3 ± 0.3°C ($n = 3$); at the end of approximately 75 min, the average change from time zero was 1.50 ± 0.5°C. Regression analysis from 20 min to the end of the exposure yielded a slope of 0.0046 ± 0.008°C/min ($p = .56$).

Examination After Exposure

No animal died during the course of the experimental protocols, nor did any animal exhibit either tetany or convulsions. Animals were euthanized after body temperature and respiratory rate had stabilized to within 10% of control values. Three animals exposed for 40 min to 4 W/kg in the body coil and two animals exposed for 40 min to 4 W/kg in the head coil were recovered and observed for 10 weeks. They were inspected weekly during this period by a licensed veterinarian and found to be in good health; no cataract formation was seen in any animals 10 weeks after the exposures.

Discussion

The worst possible case would have been the observation of metabolic control failure leading to fulminating hyperthermia and death. However, body temperatures consistently returned toward normal (Figs. 1 and 3) and appeared to be stabilizing. Moreover, a disturbance leading to a large increase in metabolic rate would have caused a temperature increase exceeding the prediction for adiabatic conditions. Clearly, this did not occur (Fig. 2). There are no reports of idiopathic hyperthermia in humans during exposure to RF fields; thus, there was little reason to expect this to occur in sheep.

The core temperatures (rectal and vena caval) were highly reproducible. In whole-body scans, these temperatures increased linearly with exposure time. The rate of increase was proportional to SAR. At 2 W/kg, about 1 hr would be needed to attain a 1° rise in core temperature, and about 30 min would be needed to achieve this increase at 4 W/kg.

In head scans, the temperature rise in jugular venous blood appears to be limited by blood flow to the head from the large unheated mass of the remainder of the body. Rectal temperature changed very little over the 60-min period because whole-body–averaged RF power input is reduced in proportion to the ratio of head to whole-body mass.

Subcutaneous temperatures were more variable and less clearly related to exposure time. The increase was approximately proportional to SAR and usually occurred rapidly. During the control period, subcutaneous temperature was well below deep-body temperatures, and the thermal gradient for heat loss was from deep-body to subcutaneous tissue. When RF power was applied, subcutaneous temperature increased rapidly to a level at which the temperature gradient was reversed. At this time, the rise in subcutaneous temperature leveled off; however, it is unclear whether this was due to circulatory vasodilator responses, an increase in heat transfer to both core and environment because of increased tissue temperature, or both.

Large rises in temperature at the skin are necessary to cause adverse effects. Human skin begins to redden after about 2 min at 45°C and blister at about 53–57°C [11, 12]. A 5-hr exposure to 44°C or 3-sec exposure to 60°C was needed to produce hyperemia without loss of epidermis; at 6 hr or 5 sec, respectively, complete necrosis occurred. Subcutaneous temperatures in the sheep did not attain these levels. On the basis of these data for humans, we would predict no adverse thermal effects on the integument of the sheep in future experiments at these exposure levels.

One potential mechanism for RF-induced cataractogenesis is thermal effects on the eye. Previous studies using 2450-MHz RF radiation showed cataractogenesis at relatively high SAR levels of at least 100 W/kg [13, 14]. Cataractogenesis has been produced experimentally at relatively high frequencies (≥2.4 GHz) and is always associated with extremely high tissue temperatures [15]. In the present study, a 4-W/kg head scan lasting at least 60 min led to a maximal increase in the temperature of the cornea and vitreous humor of 1.5 and 1.2°C, respectively. These temperature elevations appear to be insufficient to produce thermally induced tissue damage. No evidence of cataract formation was found in sheep 10 weeks after exposure to 4-W/kg whole-body or head MR imaging.

In these experiments, the ability of the sheep to withstand heat stress was compromised deliberately. All behavioral thermoregulatory capabilities were disabled by anesthesia. Furthermore, anesthetized animals have a reduced ability to lower body temperature when heat stressed [16]. The sheep is well insulated (about 7 clo), and clipping the fur greatly enhances passive heat loss from the skin of sheep [9]. Moreover, the sheep were intubated; therefore, panting was ineffective in producing increased evaporative water loss. This mechanism for heat dissipation is critical in the maintenance of homeothermy [7, 9] during heat stress in sheep.

The results of this study suggest the potential need for two different types of limits on RF power deposition. First, the rise in subcutaneous temperature was rapid and roughly proportional to SAR. Thus, it is likely that some value of SAR will result in adverse thermal effects to subcutaneous regions, and these effects could occur in a relatively short exposure time. The data on subcutaneous temperature suggest that the limiting average SAR for sheep, regardless of exposure time, is well above 4 W/kg but is likely to be less than 8 W/kg. Second, a limit on energy input (i.e., exposure time at a given SAR) is suggested by the steady increase in deep-body temperatures with time seen in this study. This steady increase would have eventually (in about 2 hr) produced potentially adverse thermal effects (a 2°C rise), even at an SAR of 2 W/kg.

Shellock and Crues [17] studied thermal effects in humans at lower SAR levels (0.4–1.2 W/kg) and shorter exposure times. Therefore, the increases in deep-body and surface temperatures were less than those seen in the present study. Similar conclusions were drawn regarding the importance of surface temperature. MR imaging systems have now been approved [3, 4] for operation at whole-body SARs of RF energy up to 0.4 W/kg, with the peak SAR in any gram of tissue less than 8 W/kg and SAR averaged over the head up to 3.2 W/kg. These SAR levels may be exceeded if it can be shown that the imaging system will produce a core temperature rise less than 1°C and localized heating to a temperature less than 38°C in the head, less than 39°C in the trunk, and less than 40°C in the extremities. A rise in sheep core temperature exceeding 1°C was seen at exposure levels well in excess of those currently typically used in clinical MR imaging. Studies in healthy humans are needed to determine whether enhanced heat-loss effector mechanisms are likely to cause deep-body temperatures to plateau at an acceptable level, and to elucidate the mechanisms that determine subcutaneous temperature.

ACKNOWLEDGMENTS

We thank J. Kusba for assistance in surgery and for evaluating the physical condition of the sheep and K. Strecker, D. Arndt, and V. Stanhope for technical assistance.

REFERENCES

1. Mansfield P, Morris PG. NMR imaging in biomedicine. In: Waugh JS, ed. *Advances in magnetic resonance*, suppl 2. New York: Academic Press, **1982**:181–191, 312–314
2. Bottomley PA, Andrew ER. RF magnetic field penetration, phase shift and power dissipation in biological tissue: implications for NMR imaging. *Phys Med Biol* **1978**;23:630–643
3. Department of Health and Human Services, Food and Drug Administration. *Magnetic resonance diagnostic device. Panel recommendation and report on petitions for MR reclassification*, docket nos. 87P-0214/CP through 87P-0214/CP0013. *Fed Reg* **1988**;53(46):7575–7579
4. Department of Health and Human Services, Food and Drug Administration. *Recommendation and report on petitions for magnetic resonance reclassification and codification of reclassification*, final rule, 21 CFR part 892. *Fed Reg* **1989**;54(20):5077–5088
5. Tell RA, Harlen F. A review of selected biological effects and dosimetric data useful for development of radiofrequency safety standards for human exposure. *J Microwave Power* **1979**;14:405–424
6. Schmidt-Nielsen K. Energy metabolism, body size, and problems of scaling. *Fed Proc* **1970**;29:1524–1532
7. Bligh J. The receptors concerned in the thermal stimulus to panting in sheep. *J Physiol* (Lond) **1959**;146:142–151
8. Carlson LD, Hsieh ACL. *Control of energy exchange*. New York: Macmillan, **1970**:63–65
9. Mount LE. *Adaptation to thermal environment, man and his productive animals*. Baltimore: University Park, **1979**
10. Barber BJ, Crawford EC Jr. Dual threshold control of peripheral temperature in the lizard *Dipsosaurus dorsalis. Physiol Zool* **1979**;52:250–263
11. Benjamin FB. Pain reaction to locally applied heat. *J Appl Physiol* **1952**;4:907–910
12. Guillemin V, Benjamin F, Cornbleet T, Grossman MI. A method of quantitative heat application to small skin areas at controlled temperature. *J Appl Physiol* **1952**;4:920–924
13. Carpenter RL, Biddle DK, Van Ummersen CA. Opacities in the lens of the eye experimentally induced by exposure to microwave radiation. *IEEE Trans Biomed Eng* **1960**;7:152–157
14. Guy AW, Lin JC, Kramer PO, Emery AF. Effect of 2450 MHz radiation on the rabbit eye. *IEEE Trans Microwave Theory Tech* **1975**;TT-23:492–498
15. Elder JE. Special senses. In: Elder JE, Cahill DF, ed. *Biological effects of radiofrequency radiation* (EPA-600/8-83-026F), section 5. Research Triangle Park, NC: U.S. Environmental Protection Agency, **1984**:64–78
16. Hunter WS, Holmes KR, Elizondo RS. Thermal balance in ketamine-anesthetized rhesus monkey *Macaca multatta. Am J Physiol* **1981**;241:R301–R306
17. Shellock FG, Crues JV. Temperature, heart rate, and blood pressure changes associated with clinical MR imaging at 1.5 T. *Radiology* **1987**;163:259–262

Fat-Saturation MR Imaging of the Upper Abdomen

Richard C. Semelka[1]
Wilbert Chew
Hedvig Hricak
Ernesto Tomei
Charles B. Higgins

The fat-saturation (fatsat) MR technique decreases the signal intensity of fat, thereby enhancing the definition of upper abdominal organs and reducing artifacts while maintaining the T1 and T2 information available on spin-echo sequences. To evaluate the potential of fatsat in examining the abdomen, we conducted a prospective study involving 30 subjects, including four normal volunteers, 18 patients investigated for liver disease, and eight patients studied for miscellaneous abdominal disease. Short TR, 300-600/15-20 (TR/TE), and long TR, 2000-2500/20-30, 70-80, spin-echo images with and without fatsat were compared. The images were evaluated both qualitatively and quantitatively. Qualitative assessment was made with receiver-operating-characteristic (ROC) curve analysis of the confidence level of observers to detect the presence of disease, comparing fatsat with standard spin-echo sequences. ROC analysis showed greater interpreter confidence and accuracy for fatsat sequences than for standard spin-echo sequences. The measured signal-difference-to-noise (SD/N) ratio comparing upper abdominal organs with surrounding tissue revealed the highest values for short TR/TE regular spin echo, followed by short TR/TE fatsat. The highest SD/N ratio for hepatic masses was with long TR/TE fatsat followed by short TR/TE fatsat.

The results of this study suggest that the fatsat technique may improve abdominal MR imaging.

AJR **155:1111-1116, November 1990**

Techniques have been devised to enhance contrast between diseased and normal tissue by attenuation of the signal from fat [1-13]. The fat-saturation (fatsat) technique suppresses the signal of fat by transmitting a low-amplitude, long-duration RF pulse centered on the frequency of lipid resonance followed by a gradient pulse to disperse this signal. A spin-echo sequence is then performed with signal reception centered on the frequency of water. T1 and T2 information is unaffected by this procedure, and therefore the specificity this information provides is not lost, unlike with short-T1 inversion recovery (STIR) [4, 5]. A disadvantage of the STIR sequence is substantial loss of signal intensity [4, 5]. This problem may not exist with the fatsat spin-echo technique. Reduction of fat signal intensity in the abdomen can be important because (1) the bright signal intensity of fat caused by cardiac and respiratory motion induces phase artifacts, degrading image quality [5], and (2) fat creates chemical-shift artifacts [14], which are particularly problematic for evaluation of the renal cortex. Fatsat MR imaging can be applied for short TR and long TR spin-echo sequences. Especially at high field strength, long TR/TE images have been effective and necessary for detection of hepatic lesions [15, 16].

To evaluate the potential of fatsat for MR imaging of the abdomen, we compared short and long TR sequences with fatsat and conventional spin echo in normal subjects and patients with abdominal disease, with qualitative assessment described by receiver-operating-characteristic (ROC) curve analysis and by measurement of signal-difference-to-noise (SD/N) ratios.

Received March 9, 1990; accepted after revision May 30, 1990.

[1] All authors: Department of Radiology, Box 0628, University of California Medical School, San Francisco, CA 94143. Address reprint requests to C. B. Higgins.

0361-803X/90/1555-1111
© American Roentgen Ray Society

Subjects and Methods

Patients

Thirty subjects were studied in a consecutive series, including four normal subjects, 18 patients investigated for liver disease (three with hepatocellular carcinoma, two with other primary malignant tumors, six with metastases, one with a hepatic hemangioma, three with cirrhosis, one with hepatic fibrosis, and two with masses of unknown cause), and eight patients with miscellaneous abdominal disease (two with malignant tumors, three with benign retroperitoneal fibrosis, one with benign renal calcifications, and two with no abnormalities). The study population included 18 men and 12 women 8–71 years old (mean, 54 years). Excluding the normal volunteers, correlation with other imaging studies was available for all patients, including CT within 1 month of the MR study ($n = 24$), sonography within 1 month of the MR study (patient with hepatic fibrosis), and serial CT and MR studies every 3–6 months for 3 years (one patient with metastases). MR findings were correlated with pathologic findings from surgery ($n = 11$) or biopsy ($n = 5$).

MR Imaging

Imaging was performed on a 1.5-T cryogenic magnet (Signa, General Electric, Milwaukee, WI). Short TR, 300–600/15–20 (TR/TE), and long TR, 2000–2500/20,70–80, spin-echo images were obtained, both with ($n = 30$, short TR; $n = 11$, long TR) and without ($n = 30$, short and long TR) fatsat. Long TR fatsat sequences were not acquired in the initial 19 subjects in this study. As implementation of the fatsat technique results in loss of approximately 15% of the slices obtained by regular spin echo when using the same TRs and TEs, slight variations (never exceeding 25%) in these parameters were necessary with fatsat in order to ensure the same coverage. Images of the abdomen were acquired in the axial plane. Respiratory compensation and superior and inferior saturation pulses were used in all studies. Matrix size was 256 × 192 with two excitations in all studies. Slice thickness and interslice gap were kept constant between all sequences in the same study (5- to 10-mm gap). Fatsat sequences were performed after regular spin-echo sequences.

Fatsat Technique

Fatsat was performed by transmitting a chemically selective RF pulse centered on the frequency of lipid resonance with subsequent dispersion of the signal with a slice-selective gradient pulse. The spin-echo sequence was then performed with signal reception centered on the frequency of water (Fig. 1).

Image Analysis

ROC analysis was performed by three independent radiologists. The various image sequences were randomly sorted and interpreted in a blinded fashion. Information provided by short TR and long TR sequences for regular spin echo was considered one information set and was compared with fatsat sequences, either short TR alone, or in combination with long TR in 11 cases. Short and long TR images were interpreted together in order to evaluate whether fatsat could substitute for spin echo in the clinical setting. Five categories of confidence were used: (1) definitely negative, (2) probably negative, (3) possibly positive, (4) probably positive, and (5) definitely positive. The presence of disease was evaluated. Determination of true presence was made on the basis of pathologic findings from surgery ($n = 11$) or biopsy ($n = 5$). When pathologic findings were not available, the maximum information from all imaging studies was treated as true presence of disease ($n = 10$). True-positive and false-positive fractions were calculated, comparing confidence of interpretation with true presence [17].

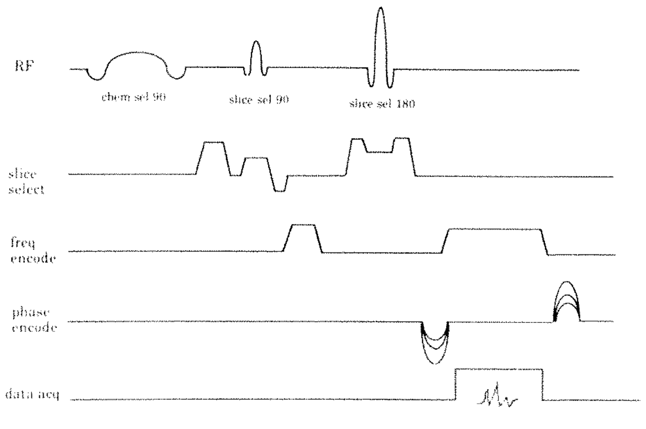

Fig. 1.—Pulse sequence for the fat-saturation spin-echo pulse sequence. chem = chemically, sel = select, freq = frequency, acq = acquisition.

An attempt was made to semiquantify the interpreters' overall impression of organ architecture in order to evaluate subjective information in a systematic way. To achieve this, definition of organ morphology was analyzed by three independent radiologists, concurrent with the ROC analysis. The ability to define internal structures and detect edges of normal organs and abnormalities was rated on the following scale: 0 = not visible, 1 = possibly visible, 2 = definitely visible, and 3 = easily visible and sharply defined. For individual organs, specific detail was assessed: for the liver, edge delineation; for the biliary tree and intrahepatic vasculature, sharpness; for the spleen, sharpness of the edge and hilar vasculature; for the pancreas, visualization of the uncinate process, head, body, tail, pancreatic duct in the body and tail, and common bile duct in the head of the pancreas; for the adrenal glands, visualization of both limbs and body (mean value for both glands); for the kidneys, corticomedullary differentiation and sharpness of renal outline.

Quantitative assessment of signal intensity was obtained by operator-defined regions of interest (ROIs). Data were expressed as the SD/N ratio of organs to surrounding tissue. The image display adds 1024 to pixel signal intensity and, therefore, this number was subtracted from all ROI determinations. Noise was measured by a large rectangular ROI anterior to the abdomen. The standard deviation of noise was used for calculations of SD/N. Liver, spleen, pancreas, and adrenal glands were compared with retroperitoneal fat; renal cortex was compared with medulla; liver lesions were compared with surrounding liver; and upper abdominal abnormalities were compared with retroperitoneal fat.

Statistical Analysis

All SD/N measurements and morphologic detail ratings were calculated as mean values ± standard deviation. Scheffe's test for multiple comparisons was applied to detect differences by multivariate analysis.

Results

ROC analysis by three independent radiologists comparing standard spin-echo and fatsat sequences showed a greater degree of confidence with fatsat in detecting the presence of disease. The higher confidence level is demonstrated by the position of the curve for the fatsat sequence compared with the curve for the regular spin-echo sequence (Fig. 2). A moderate statistical difference ($p < .05$) was present between the curves.

Table 1 contains SD/N data for short TR/TE, long TR/short TE, and long TR/TE sequences with and without fatsat. SD/N was greatest in short TR/TE regular spin-echo sequences for liver, spleen, pancreas, and adrenal glands, followed by long TR/short TE fatsat and short TR/TE fatsat. The values on regular short TR/TE images were negative because of the very bright signal intensity from fat. These values were all positive with the fatsat technique because the upper abdominal organs were higher in signal intensity than retroperitoneal fat was. Measured SD/N values for hepatic lesions were significantly higher for long TR/TE fatsat ($p < .01$) and moderately higher for short TR/TE fatsat ($p = .05$) than for all regular spin-echo sequences. No other statistically significant differences were observed between imaging sequences.

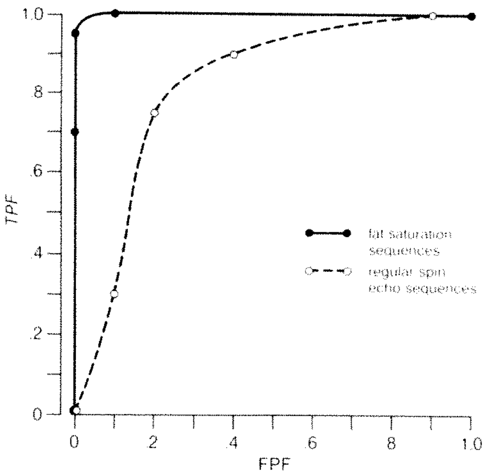

Fig. 2.—Receiver-operating-characteristic curve analysis for the presence of disease (*n* = 30). TPF = true-positive fraction, FPF = false-positive fraction.

Figure 3 illustrates the appearance of abdominal organs on images obtained by using the fatsat technique with short TR/TE and with long TR/TE sequences; the same levels were studied with regular spin-echo images for comparison. Compared with standard spin echo, images with fatsat showed improved delineation of the margins and internal morphology of liver, spleen, pancreas, adrenal glands, and kidneys. Improved definition of the abdominal organs is apparent owing to the relatively high signal intensity of these organs in the background of suppressed retroperitoneal fat.

In addition to the relative brightening of organs, the degree of noise was greatly diminished. Noise from respiratory and cardiac activity was greatly diminished, which permitted better visualization of the left lobe of the liver (Fig. 4). Fatsat sequences were more sensitive to lesion detection. In three of the five patients with hepatic metastases, long TR/TE fatsat permitted visualization of lesions not apparent on non-fat-suppressed sequences (51 vs 36 lesions) (Fig. 5).

The ability to define internal organ morphology was rated superior (27/30) and equivalent (3/30) when comparing fatsat and regular spin echo. Table 2 gives the data expressed as individual organs and hepatic disease. The subjective rating of the depiction of the pancreas and adrenal glands on short TR and long TR images and corticomedullary difference on short TR images was statistically superior ($p < .01$) for fatsat images compared with regular spin-echo images.

Fatsat was more specific in two of five cases of primary malignant tumor, by demonstrating sparing of the lateral segment of the left lobe, which was not evident on the standard spin-echo images.

On fatsat images, the signal intensity of fat was lowered to a level comparable to that of fibrous tissue, so that the contrast between the two was lessened. Fatsat showed diminished contrast between fibrous tissue and fat in patients with benign retroperitoneal fibrosis ($n = 3$), while standard spin-echo images showed clearly the presence of disease because of higher contrast.

Discussion

Various techniques are used to increase the signal difference between diseased tissue and surrounding structures

TABLE 1: Signal-Difference-to-Noise Ratios for Abdominal Organs and Liver Lesions

Region	Short TR/Short TE		Long TR/Short TE		Long TR/Long TE	
	Without Fatsat ($n = 30$)	With Fatsat ($n = 30$)	Without Fatsat ($n = 30$)	With Fatsat ($n = 11$)	Without Fatsat ($n = 30$)	With Fatsat ($n = 11$)
Liver	−19.4 ± 9.1	11.9 ± 4.8	−14.9 ± 5.0	11.3 ± 3.9	−8.6 ± 4.0	4.6 ± 5.1
Spleen	−23.2 ± 9.4	9.1 ± 4.4	−12.0 ± 4.9	12.2 ± 4.9	−4.2 ± 4.7	9.1 ± 6.4
Adrenal, fat	−19.3 ± 11.5	10.5 ± 4.0	−12.1 ± 4.5	11.8 ± 4.5	−4.9 ± 3.8	7.2 ± 4.0
Pancreas, fat	−19.5 ± 9.0	12.7 ± 5.7	−10.9 ± 4.8	15.4 ± 5.7	−4.9 ± 4.8	6.5 ± 1.7
Renal corticomedullary boundary	3.1 ± 2.0	7.7 ± 2.9	1.7 ± 1.4	5.0 ± 3.5	1.4 ± 0.9	3.2 ± 2.1
Lesion, liver	−3.8 ± 2.3	−7.3 ± 5.0[a]	1.3 ± 3.1	2.2 ± 3.8	4.2 ± 1.9	12.6 ± 3.1[b]

Note.—Values are means ± SD. Fatsat = fat saturation.

[a] Moderately significant ($p < .05$).

[b] Statistically significant ($p < .01$).

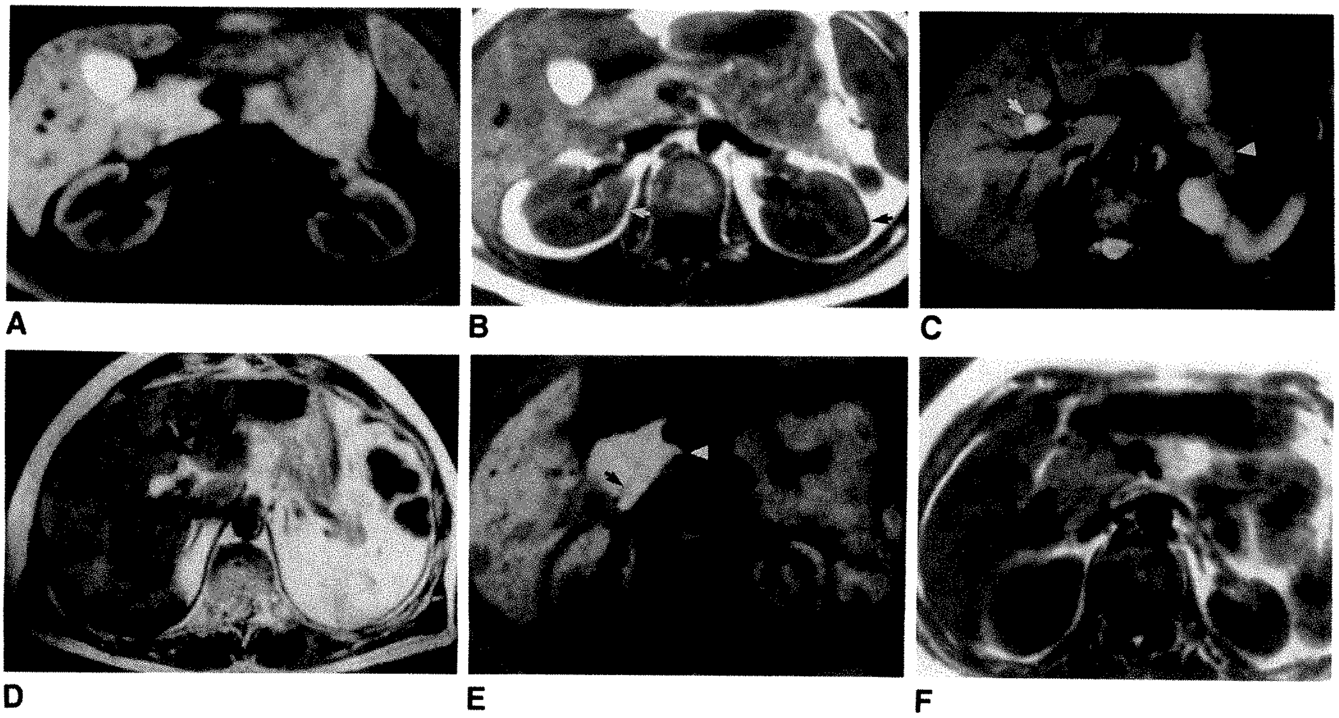

Fig. 3.—Images illustrating appearance of organs with and without fat saturation (fatsat).

A and *B*, Short TR/TE (600/20) fatsat (*A*) and regular spin-echo (*B*) images of normal kidneys. Improved corticomedullary differentiation and absence of chemical-shift artifact are apparent on fatsat image (*arrows* point to chemical-shift artifact on regular spin-echo image).

C and *D*, Long TR/TE (2000/70) fatsat (*C*) and regular spin-echo (*D*) images of normal adrenal glands in a patient with hepatic metastases from colonic cancer. Adrenal glands are better depicted and common hepatic duct (*arrow*) is sharply defined and separated from fat in the porta hepatis with fatsat technique. In addition, lobulations of pancreatic tail are apparent on fatsat image (*arrowhead*), but not on regular spin-echo image.

E and *F*, Short TR/TE (300/20) fatsat (*E*) and regular spin-echo (*F*) image of normal head of pancreas in a patient with gastrinoma metastatic to liver. Head of pancreas is relatively brighter than all surrounding tissue on fatsat compared with regular spin-echo image; common bile duct (*arrow*) is better delineated as it enters duodenum, and uncinate process is sharper in outline (*arrowhead*). Note also that hepatic metastases are better depicted with fatsat.

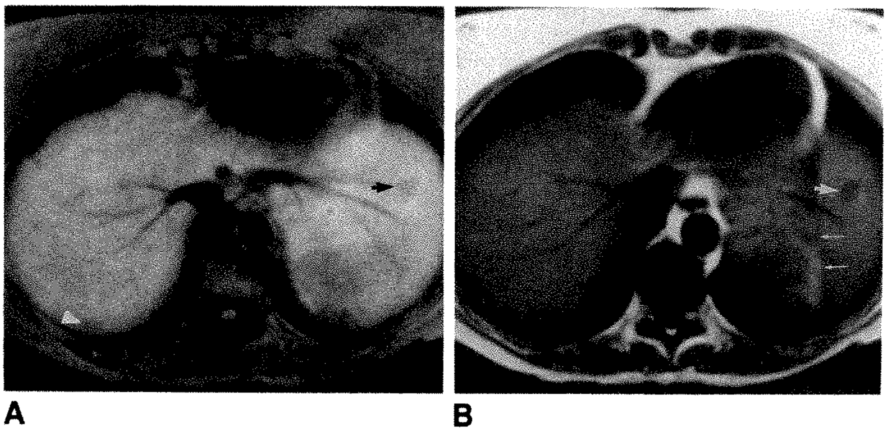

Fig. 4.—Patient with liver masses of unknown cause.

A and *B*, Short TR/TE (400/15) fat-saturation (fatsat, *A*) and short TR/TE (300/20) regular spin-echo (*B*) images. Fatsat image has less artifact from cardiac activity than does regular spin-echo image (*long arrows*), permitting improved visibility of left lobe of liver. Liver vasculature is more sharply defined. Low-intensity mass is apparent on both images (*short arrows*); a second lesion in posterior segment of right lobe on fatsat image (*arrowhead*) was not seen on short TR/TE regular spin-echo image, but was identified on TR/TE regular spin-echo image (*not shown*).

and hence the depiction of abnormalities by suppressing the high signal intensity of fat. Examples of fat-suppression techniques are the Dixon method [8–10], STIR [1–5], chopper fat suppression [6, 7], and chemical shift-selective (CHESS) imaging [11]. These techniques have been used in various anatomic sites where fat is a prevalent background tissue, and the suppression of fat permits better evaluation of disease. Fat suppression is useful in the upper abdomen because the motion of high-signal-intensity fat degrades image quality by inducing phase artifacts [5]. This can be diminished by fat-suppression techniques.

Fatsat is a modification of the spin-echo technique and therefore has the T1 and T2 information of regular spin-echo imaging. The specificity of lesion characterization provided by this information is maintained. With the STIR technique, there is signal addition of T1 and T2 information, which, among other things, renders the differentiation of tumor from edema difficult [5].

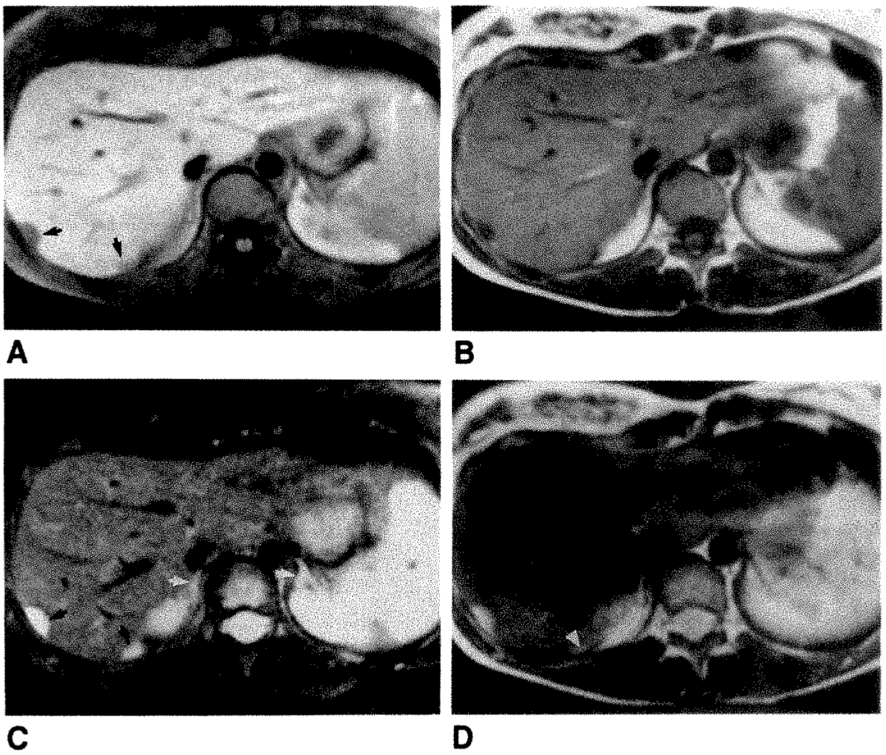

Fig. 5.—Patient with breast cancer metastatic to liver.

***A–D*, Short TR/TE (300/20) fat-saturation (fatsat, *A*) and regular spin-echo (*B*) and long TR/TE (2000/70) fatsat (*C*) and regular spin-echo (*D*) images. Two subcapsular metastatic deposits are well depicted on short and long TR fatsat images (*black arrows*), while on regular spin-echo images only one lesion was identified prospectively. Second lesion is apparent in retrospect on long TR/TE regular spin-echo image (*arrowhead*). Note high signal intensity of adrenal glands on long TR/TE fatsat image, providing excellent delineation from surrounding tissue (*white arrows*).**

TABLE 2: Definition of Morphology of Normal Organs and Liver Lesions

Region	Short TR/Short TE		Long TR/Short TE		Long TR/Long TE	
	Without Fatsat (*n* = 30)	With Fatsat (*n* = 30)	Without Fatsat (*n* = 30)	With Fatsat (*n* = 11)	Without Fatsat (*n* = 30)	With Fatsat (*n* = 11)
Liver	2.3 ± 0.08	2.9 ± 0.06	2.0 ± 0.06	2.7 ± 0.07	1.7 ± 1.0	2.2 ± 0.08
Spleen	2.3 ± 0.08	2.4 ± 0.07	2.3 ± 0.08	2.4 ± 0.07	1.7 ± 1.0	2.3 ± 0.07
Adrenals	2.0 ± 0.06	2.9 ± 0.03[a]	2.0 ± 0.06	2.9 ± 0.03[a]	1.3 ± 1.0	2.3 ± 0.08[a]
Pancreas	1.8 ± 0.07	2.8 ± 0.04[a]	1.8 ± 0.07	2.9 ± 0.04[a]	1.3 ± 1.0	2.2 ± 0.08[a]
Renal corticomedullary boundary	1.8 ± 0.07	2.4 ± 0.07[a]	0.4 ± 0.08	2.2 ± 0.08[a]	0.4 ± 0.08	1.6 ± 0.08
Liver disease	2.1 ± 0.08	2.7 ± 0.07[a]	0.6 ± 0.06	1.6 ± 1.0	2.2 ± 1.0	2.8 ± 1.2

Note.—Values are means ± SD. Internal morphology was rated on a scale of 0–3: 0 = not visible; 1 = possibly visible; 2 = definitely visible; 3 = easily visible, sharply defined. Fatsat = fat saturation.

[a] Statistically significant difference ($p < .01$).

The elimination of chemical-shift artifacts minimizes loss of anatomic detail around the edges of structures surrounded by fat [14]. The ability to visualize sharp margins of all abdominal organs with fatsat is to a large extent due to the removal of the chemical-shift artifact.

No postprocessing is required with fatsat, which is an advantage over other techniques [8–10]. However, approximately 15% of the slices are lost compared with regular spin echo with the same parameters, because of the time required to transmit the chemically selective pulse.

ROC analysis showed that greater confidence in evaluating disease was provided with fatsat than with standard spin echo, and fatsat was also better able to define organ morphology for the liver, pancreas, kidneys, and adrenal glands. This superior performance probably was due to three factors: (1) With fatsat phase artifacts are diminished and chemical-shift artifacts are absent, providing sharper depiction of organ architecture compared with regular spin echo. (2) With standard spin echo, other structures such as vessels, bowel, muscle, and fibrous tissue are also low in signal intensity, so that they can be difficult to distinguish from organs (particularly adrenal glands and pancreas), while with fatsat solid organs appear relatively bright and these other structures have lower signal intensity (see Fig. 3). Fatsat reduces the dynamic range of signal intensities in the abdomen, thereby expanding the signal intensity range between organs and nearby bowel and fibrous and vascular tissue, rendering the organs relatively bright in signal intensity. (3) Structures are more easily defined when they are of high intensity in a dark background rather than the reverse.

Fatsat sequences were useful in evaluating liver disease, increasing both sensitivity and specificity. In patients with hepatic metastases, greater confidence in detection was demonstrated with fatsat, in one of five, and fatsat identified more lesions in three of five cases. Improved specificity was shown in the ROC analysis, in which fatsat showed high confidence in sparing of the lateral segment in two cases of primary malignant tumor, while standard spin echo showed low confidence. In both cases, pathologic examination confirmed sparing of the lateral segment. The ability to define the extent of involvement (e.g., if segments are spared and the tumor is therefore resectable), is an important determination. The quantitative data for hepatic masses showed the highest values for long TR/TE fatsat, followed by short TR/TE fatsat (see Table 2). Comparable results at mid-field strength have been reported recently using the Dixon method of fat attenuation [10].

One drawback of fatsat is that contrast between fat, muscle, and fibrous tissue is lessened on all sequences. Therefore, if the disease is fibrous in nature, it may be less conspicuous with fatsat than with regular spin echo. This was the case for the patients with benign retroperitoneal fibrosis in our study. However, despite decreased contrast, the extent of disease may be better appreciated with fatsat.

The difficulties with fatsat are (1) the technical requirement of identification of the spectral peak of lipids on which to center the chemically selective pulse; (2) the slight inhomogeneity of the fat suppression at the periphery of the image and at the levels farthest from the central slice of an acquisition series, because the local resonant frequency of fat at these locations is slightly different from the chemically selective pulse [13]; and (3) that 15% fewer slices are obtained than with standard spin-echo sequences.

Although the results of this study are encouraging, this technique was not compared with other fat-attenuating sequences and pathologic proof was not available for all patients. Further evaluation in a larger prospective series is warranted before the role of fatsat in MR imaging is determined.

REFERENCES

1. Paling MR, Abbitt PL, Mugler JP, Brookeman JR. Liver metastases: optimization of MR imaging pulse sequences at 1.0 T. *Radiology* **1988**;167:695–699
2. Bydder GM, Steiner GM, Blumgart LH, Khenia S, Young IR. MR imaging of the liver using short T1 inversion recovery sequences. *J Comput Assist Tomogr* **1985**;9:1084–1089
3. Atlas SW, Grossman RI, Hackney DP, Goldberg HI, Bilaniuk LT, Zimmerman RA. STIR MR imaging of the orbit. *AJNR* **1988**;9:969–974
4. Bydder GM, Young IR. MR imaging: clinical use of the inversion recovery sequence. *J Comput Assist Tomogr* **1985**;9:659–675
5. Shuman WP, Baron RL, Peters MJ, Tanzioli PK. Comparison of STIR and spin-echo MR imaging at 1.5 T in 90 lesions of the chest, liver, and pelvis. *AJR* **1989**;152:853–859
6. Simon J, Szumowski J, Totterman S, et al. Fat suppression MR imaging of the orbit. *AJNR* **1988**;9:961–968
7. Szumowski J, Plewes DB. Separation of lipid and water MR imaging signals by chopper averaging in the time domain. *Radiology* **1987**;165:247–250
8. Lee JKT, Heiken JP, Dixon WT. Detection of hepatic metastases by proton spectroscopic imaging. *Radiology* **1985**;156:429–433
9. Scherty LD, Lee JKT, Heiken JP, Molina PL, Totty WG. Proton spectroscopic imaging (Dixon method) of the liver: clinical utility. *Radiology* **1989**;173:401–405
10. Rummeny E, Saini S, Stark DD, Weissleder R, Compton CC, Ferrucci JT. Detection of hepatic metastases with MR imaging: spin-echo vs phase-contrast pulse sequences at 0.6 T. *AJR* **1989**;153:1207–1211
11. Frahm J, Haase A, Hanicke W, Matthaei D, Bomsdorf H, Helzel T. Chemical shift selective MR imaging using a whole-body magnet. *Radiology* **1985**;156:441–444
12. Keller PJ, Hunter WW, Schmalbrock P. Multisection fat-water imaging with chemical shift selective presaturation. *Radiology* **1987**;164:539–541
13. Mitchell DG, Vinitski S, Rifkin MD, Burk DL Jr. Sampling bandwidth and fat suppression: effects on long TR/TE MR imaging of the abdomen and pelvis at 1.5 T. *AJR* **1989**;153:419–425
14. Daniels DL, Kneeland JB, Shimakawa AJ, et al. MR imaging of the optic nerve and sheath: correcting the chemical shift misregistration effect. *AJNR* **1986**;7:249–253
15. Foley WD, Kneeland JB, Cates JD, et al. Contrast optimization for the detection of focal hepatic lesions by MR imaging at 1.5 T. *AJR* **1987**;149:1155–1160
16. Marchal G, van Hecke P, Demaerel P, et al. Detection of liver metastases with superparamagnetic iron oxide in 15 patients: results of MR imaging at 1.5 T. *AJR* **1989**;152:771–775
17. Metz CE. Basic principles of ROC analysis. *Semin Nucl Med* **1978**;8:283–298

Spatial Misregistration of Vascular Flow During MR Imaging of the CNS: Cause and Clinical Significance

Theodore C. Larson III[1,2]
William M. Kelly[1,3]
Richard L. Ehman[4]
Felix W. Wehrli[5]

Spatial misregistration of signal recovered from flowing spins within vascular structures is a common phenomenon seen in MR imaging of the CNS. The condition is displayed as a bright line or dot offset from the true anatomic location of the lumen of the imaged vessel. Its origin is the time delay between application of the phase- and frequency-encoding gradients used to locate spins within the plane of section. The principal condition necessary for the production of spatial misregistration is flow oblique to the axis of the phase-encoding gradient. Flow-related enhancement (entry slice phenomenon), even-echo rephasing, and gradient-moment nulling contribute to the production of the bright signal of spatial misregistration.

Familiarity with the typical appearance of flow-dependent spatial misregistration permits confirmation of a vessel's patency; identification of the direction of flow; estimation of the velocity of flow; and differentiation of this flow artifact from atheromas, dissection, intraluminal clot, and artifacts such as chemical shift.

***AJNR* 11:1041–1048, September/October 1990; *AJR* 155:1117–1124, November 1990**

Vascular flow effects give rise to artifacts and variable intravascular signal intensity during MR imaging. As a noninvasive tool, MR imaging delineates the morphologic characteristics of the vascular system and provides insight into the physiological parameters of blood flow.

Several authors have reported spatial misregistration of flowing blood during routine spin-echo (SE) MR imaging [1–6]. The typical appearance of spatial misregistration as a bright line or oval adjacent to an imaged vessel is a common finding during MR imaging of the CNS. This article presents the theoretical basis for the misregistration artifact and how this knowledge can be used to determine vessel patency and direction of blood flow, to estimate its velocity, and to differentiate misregistration artifact from other artifacts and pathologic vascular processes.

Materials and Methods

MR scans of the head were reviewed to identify representative instances of spatial misregistration of intracranial vascular flow.

MR examinations were carried out on a 1.5-T MR unit (General Electric, Milwaukee, WI). Slice thickness was 3 or 5 mm and an intersection gap of 20% or 50% was used. The phase-encoding matrix was 128 or 256.

Most patients underwent short TR/short TE, 400–600/20–25/2 or 4 (TR/TE/excitations), and long TR/short and long TE, 2000/25–80/2, evaluations without flow-compensation gradients. Five patients were studied with T2-weighted examinations (2800/30,70/2) in which flow-compensation gradients were applied along the readout and slice-selection gradient axes [7–9]. One patient was examined with three axial T2-weighted scans consisting of a routine 2000/35,70/2 study, a four-echo 2000/25,50,75,100/2 sequence to generate even-echo rephasing, and a 2000/35,75/2 protocol in which the directions of the phase- and frequency-encoding gradients were exchanged relative to the routine study. One normal

Received October 30, 1989; revision received February 12, 1990; accepted February 23, 1990.

Presented at the annual meeting of the American Society of Neuroradiology, New York City, May 1987.

[1] Department of Radiology, University of California, San Francisco, San Francisco, CA 94143-0620.

[2] Present address: Department of Radiology, Nashville Memorial Hospital, 612 W. Due West Ave., Madison, TN 37115. Address reprint requests to T. C. Larson III.

[3] Department of Radiology, David Grant United States Air Force Medical Center (MAC), Travis Air Force Base, CA 94535-5300.

[4] Department of Radiology, Mayo Clinic, Rochester, MN 55905.

[5] Department of Radiology, Hospital of the University of Pennsylvania, 3440 Market St., Suite 420, Philadelphia, PA 19104.

0361-803X/90/1555-1117
© American Roentgen Ray Society

volunteer was examined first with 2000/40/2 and a second time with 2000/80/2, both studies using an SE sequence with flow-compensation gradients. Five patients were studied with a multiplanar gradient-recalled echo (MPGR) technique using 250–600/14–19/4 and flip angles of 35–60°. One patient was studied with sequential slice gradient-recalled echo acquisition in the steady state (GRASS) [7, 9, 10] using 100/12 and flip angle of 10°. Flow-compensation gradients were used with both the MPGR and GRASS sequences. Cardiac gating techniques were not used. The results of this study were considered to be representative of flow imaged randomly during the cardiac cycle.

The predicted appearance of spatial misregistration was tested by exchanging axes of the phase- and frequency-encoding gradients, by varying the TE after phase encoding, and by using a symmetric four-echo sequence. Because spatial misregistration was commonly demonstrated in venous angiomas, seven examples in six patients were included and analyzed. Several venous angiomas were examined further with angiography for confirmation of the vascular anomaly and its drainage pattern.

The velocity of vascular flow was estimated in seven venous angiomas by using SE series with even-echo techniques, in five convexity cortical veins in five different patients by using SE MR with flow-compensation gradients and the shortest TE value (30 msec) in a multiecho sequence for velocity calculations, and in five intracranial arteries (one vertebral, one proximal anterior cerebral, one proximal posterior cerebral, one proximal middle cerebral, and one distal middle cerebral) in five patients by using MPGR imaging. Because velocity (v) equals distance traveled (d) divided by time, knowledge of the time interval between application of the phase and readout gradients permits estimation of flow velocity:

$$v = d/(TE - t_{phase}); \qquad (1)$$

where t_{phase} is the time of the phase-encoding gradient application. Equation 1 was applied to examples of in-plane flow oblique to the axes of the phase- and frequency-encoding gradients. Calculations were based on measurement of the hypotenuse of a right triangle constructed with sides parallel to the phase- and frequency-encoding gradient directions and the hypotenuse lying along a straight segment of the imaged vessel (Fig. 1). This calculation provides the approximate velocity a flowing spin traveled between phase-encoding and readout steps.

Results

Spatial misregistration of vascular flow was routinely identified in all three standard MR imaging planes (sagittal, coronal, axial) used to examine the head. With the use of even-echo rephasing during a symmetric, multiecho SE sequence, bilateral cerebellar angiomas exhibited spatial misregistration on the second and fourth echoes of a four-echo series (Fig. 2). The misregistered line of the fourth echo was spatially mismapped a greater distance from the angioma than on the second echo.

The spatially misregistered bright line was found to be displaced on opposite sides of two different venous angiomas depending on the direction of their blood flow (Fig. 3). In each case, the spatially misregistered signal was displaced along that portion of its flow, which was directed along the frequency-encoding axis and mismapped upstream along the phase-encoding axis. Exchanging the orientations of the phase- and frequency-encoding gradients reversed the location of the bright line relative to the true lumen of a cerebellar venous angioma (Fig. 4).

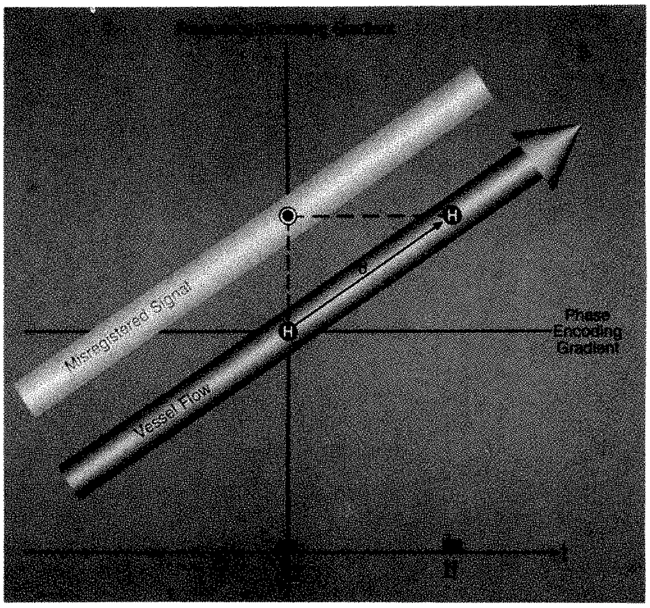

Fig. 1.—Diagram of in-plane vessel obliquely oriented to phase- and frequency-encoding gradients and geometric basis for derivation of equation 1 (see text). H = flowing spin, O = point of misregistered signal, d = measured distance traveled by flowing spin, t = time axis, t_p = time of phase-encoding gradient application, t_f = time of frequency-encoding gradient application.

The center of the spatially misregistered signal was always displaced the same distance from the imaged vascular structure when flow-compensation gradients were used regardless of TEs chosen. This was demonstrated on multiecho SE sequences and in the volunteer who underwent a head examination with two different TEs. Cortical veins imaged in the presence of flow-compensation gradients (Fig. 5) illustrated that the width of the spatially misregistered signal is of equal or slightly increased width with longer echo delays, the measured distances traveled by a flowing spin on both a single short TE/long TR and single long TE/long TR studies were approximately equal, and velocity calculations became dependent on the TEs selected.

Equation 1 was applied to estimate velocity of in-plane flow in venous angiomas and in normal intracranial veins and arteries. Flow rates were calculated to be 2.3–5.8 cm/sec (±0.21 cm/sec) in venous angiomas, 11.7–26.4 cm/sec (±0.35 cm/sec) in large cortical veins, and 26.8–42.6 cm/sec (±0.75 cm/sec) in intracranial arteries.

Discussion

The appearance of a bright line or oval adjacent to a CNS vascular structure is common during MR imaging. When an imaged vessel lies within the plane of section oblique to both the phase- and frequency-encoding gradients, spatial misregistration is represented as a bright white line of approximately uniform width offset slightly from the true anatomic

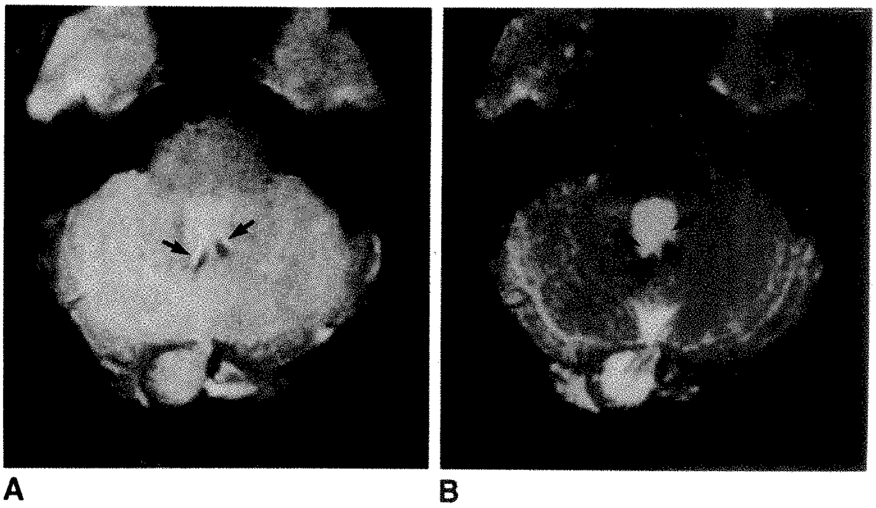

Fig. 2.—*A* and *B*, Axial second, SE 2000/50 (*A*), and fourth, SE 2000/100 (*B*), echoes of T2-weighted four-echo series (SE 2000/25,50,75,100) of the head. Centrally draining bilateral cerebellar venous angiomas show spatial misregistration (*arrows*) on second echo, which is further displaced from parent vessel on fourth echo, becoming indistinguishable from white CSF of fourth ventricle.

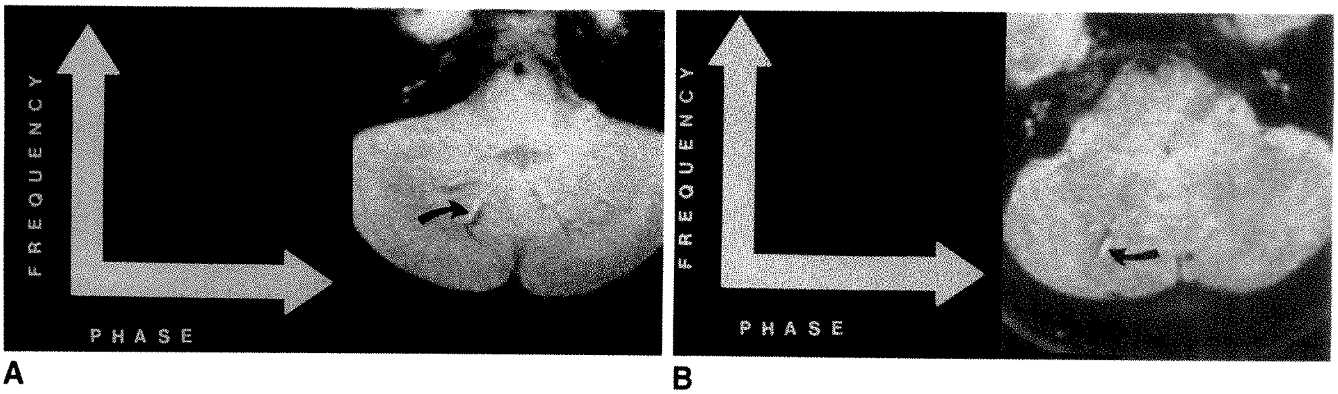

Fig. 3.—Axial T2-weighted second-echo images of cerebellum in two patients with venous angiomas.

A, Venous angioma and its accompanying bright misregistered signal (*arrow*) predict venous anomaly drains centrally.

B, Cerebellar venous angioma in this patient drains peripherally, and misregistered signal (*arrow*) is on opposite side of anomalous draining vein when compared with example in *A*.

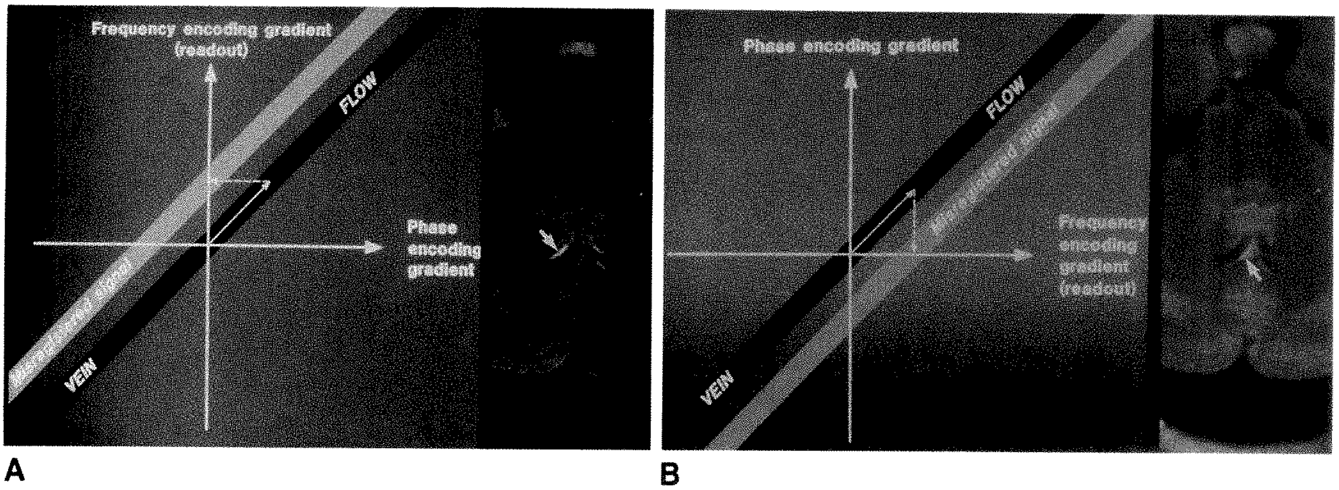

Fig. 4.—*A* and *B*, A patient with bilateral cerebellar venous angiomas was examined first with usual application of phase- and frequency-encoding gradients and then with axes of spatial-encoding gradients swapped. Second echo of each T2-weighted axial study shows spatially misregistered lines (*arrows*) to change their relationship to parent vessels depending on orientation of phase- and frequency-encoding gradients. Accompanying diagrams illustrate that misregistered signal of right cerebellar venous angioma is displaced along direction of its flow, which lies along frequency-encoding direction (upstream).

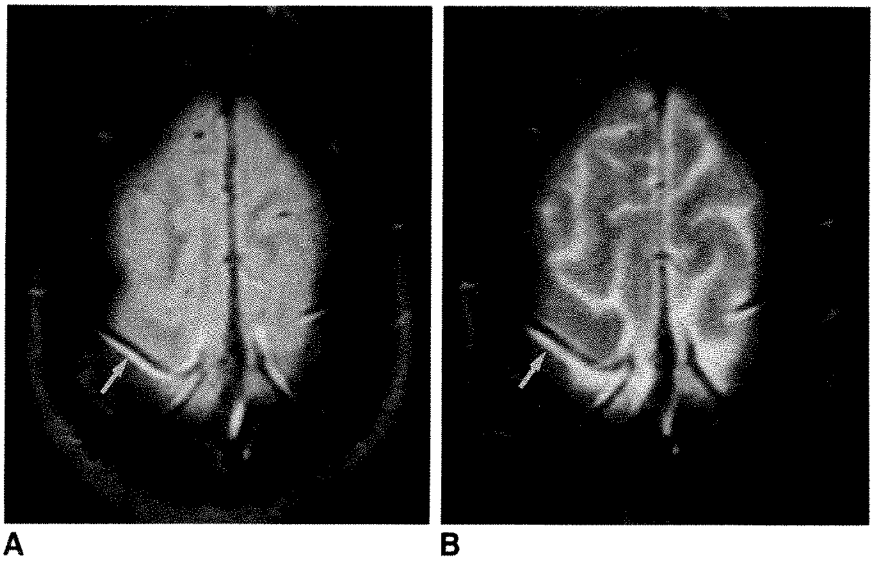

Fig. 5.—*A* and *B*, First- (*A*) and second- (*B*) echo T2-weighted axial images of head using flow-compensation gradients. Misregistered signal (*arrows*) occurs adjacent to normal superficial cortical draining veins on all echoes and is of equal width and misregistered equal distance from true vessel. Misregistered signal is more apparent on first-echo image.

location of the imaged vessel. This can be termed upstream spatial misregistration because the signal intensity of the moving spin is mapped at a more proximal position along the phase-encoding axis.

Downstream mismapped signal of flowing spins occurs when a vessel is parallel to the frequency-encoding gradient axis or the vessel traverses the plane of section. Spin position under these circumstances is determined solely at the time of frequency encoding as long as phase dispersal of the flowing spins has not occurred and there is no flow in the phase-encoding direction.

When the vessel is in plane and either aligned with the phase- or frequency-encoding gradients, the spatial misregistration artifact is difficult or impossible to identify because the mismapped signal is aligned with the vascular structure and has no lateral offset from the lumen of the parent vessel. Flow within a vessel coursing along the direction of the phase-encoding gradient causes signal from moving spins to be positioned upstream in line with the vessel's lumen. Flow within a vessel perpendicular to the phase-encoding gradient causes signal from moving spins to be located downstream, but again in alignment with the true vessel lumen. For spatial misregistration of vascular flow to be appreciated, the vessel examined must be oriented oblique to the axis of the phase-encoding gradient.

When the vessel traverses obliquely through the plane of section, the resultant misregistered signal is manifested as a dot or oval of high intensity adjacent to the imaged vessel and is always mismapped downstream. This resembles partial-volume averaging of the parent vessel and its misregistered signal when the three-dimensional section is transformed into a two-dimensional image (Fig. 6). A vessel perpendicular to the plane of section will produce no spatial misregistration. When signal intensity from the imaged intraluminal spins is present, it will be correctly placed within the vessel of origin when the vessel courses at a 90° angle through the plane of section (Fig. 7).

The bright white line or dot that appears adjacent to a vessel is explained as the signal of flowing blood spins assigned to pixel locations outside of the true vessel and superimposed on adjacent anatomy. The signal intensity from these spins is then summed with the signal of the stationary spins of the adjacent tissue. The vessel of interest demonstrates signal void because few spins are spatially mapped within its lumen.

The fundamental cause of the misregistered signal is the interval between the applications of the phase- and frequency-encoding gradients used during two-dimensional Fourier localization of spin signal intensity [1, 5, 6]. For the MR system used in this study, a phase-encoding gradient is applied 1.6 msec after delivery of the 90° nutation RF pulse to encode spins along one axis. This time interval is not altered by varying the TE. The frequency or readout gradient is applied later at time TE after the spins have traveled downstream (Fig. 8). The flowing spin first is given a phase coordinate identity and then downstream is read out with a frequency labeling process. The two coordinates for phase and frequency describe a point in a two-dimensional matrix and locate a position for the spin in the two-dimensional Fourier-transform reconstructed image.

Through-plane flow compounds this explanation of spatial misregistration by additionally contributing the time delay from the preceding RF pulse experienced by a slice-selected flowing spin to subsequent readout as another determinant of spin localization. This is the mechanism by which through-plane flow is always mismapped downstream.

The greater the time interval between the applications of the phase- and frequency-encoding gradients, the greater the distance the spatial misregistration is displaced from the parent vessel [5, 6]. This is evident in SE studies (without flow-compensation gradients) when comparing late-echo with early-echo spatial misregistration because the echoes are read out at progressively longer intervals from the application of the single phase-encoding gradient early in the timing sequence.

The longer the TE (time to readout), the more time is available for spins to dephase [5, 11]. Flowing spins with excessive dephasing or turbulent flow will not produce spatial

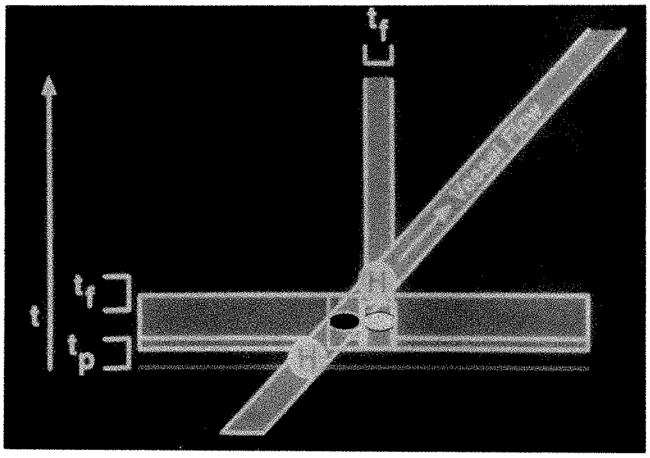

Fig. 6.—Schematic illustration of vessel that obliquely traverses plane of section and its downstream misregistered signal. Acquired slice is viewed in cross section with finite width. Flowing spin (H) experiences first phase-encoding gradient, t_p, then frequency-encoding gradient, t_f. Spatial-encoding gradients are oriented within plane of slice or perpendicular to its cross section. Frequency-encoding gradient application, t_f, is shown twice to illustrate both time elapsed between two localization gradients and their orthogonal relationship. t = time.

misregistration because signal intensity is reduced owing to the destructive interference of spins with many different phase angles [3, 5, 6]. Fundamental causes of flowing spin dephasing are the phase-encoding, slice-selection, and frequency-encoding gradients, which create phase shifts [1, 3, 6, 9, 11–21] dependent on the position of each spin within the intraluminal flow profile [1, 6, 12, 14]. This leads to intravoxel phase dispersion [1, 5, 6, 11, 12, 14, 17, 18] and phase modulation resulting in diminution of pixel signal amplitude [4, 12, 15, 19] for a wide distribution of phase angles [6, 13, 17], as well as to the commonly encountered phase-encoding artifact due to bulk motion, which generates a narrower range of phase shifts [6, 13, 17]. Even-echo rephasing [3, 5, 11] or flow-compensation gradients [6–9, 17] compensate for velocity-induced phase shifts.

Even-echo rephasing in slow flow (predominantly constant velocity) causes the majority of spins in the presence of balanced gradients to be in phase on even-numbered echoes [1, 3, 6, 11, 14–16, 19, 22]. Rephasing of spins is not always complete on even echoes when more complex flow is present involving acceleration or jerk [5, 11] and can occur on odd echoes, particularly with pulsatile flow [20].

Flow-compensation gradients (gradient moment nulling) attempt to correct for spin dephasing that is generated by gradients applied to differential velocity profiles [1, 6, 12, 14] normally found in intracranial vessels. Biphasic flow-compensation gradients are enabled during slice-selection and readout gradient applications. Rephased flowing spins become spatially misregistered with each TE because of the use of flow-compensation gradients with each readout. With flow-compensation gradients, each echo results in misregistered signal of equal width displaced an identical distance from the parent vessel. Flow-compensation gradients cannot compensate for phase shifts associated with flow of nonconstant velocity (due to acceleration and jerk) [7] nor for frequency shifts of flowing protons that are generated in the presence of gradients [21]. This latter effect may cause some of the blurred margins of the spatially misregistered signal and may be one of the mechanisms responsible for the roughly identical appearance of the misregistered signal on any echo when flow-compensation gradients are employed. Under the influence of flow-compensation gradients, spatial misregistration is more apparent on the first than on the second echo of an SE sequence (Fig. 5). By the time of the second echo, spin dephasing and washout effects diminish signal intensity, and the detection of the misregistered signal is more difficult against a background of bright CSF (Figs. 2 and 5B).

Slow flow, as is commonly present in intracranial veins and dural sinuses, produces spatial misregistration during SE imaging without flow-compensation gradients. If the vascular flow is very slow, no spatial misregistration will occur, or the mismapped signal will overlap the walls of the vessel imaged. Typical parabolic velocity flow profiles (e.g., venous) due to laminar flow [4, 5, 23] would cause the fastest flowing spins to be displaced greatest from the parent vessel lumen, slower flow the least, resulting in a band of mismapped parallel signal. Arterial flow, however, is nonlaminar, disturbed, pulsatile, and pluglike [1, 5]. Pulsatile flow has been shown to reverse the intraluminal velocity gradient with slower flow centrally and faster flow peripherally [23]. This should contribute greater width to the spatially misregistered signal band.

During spin-echo sequences, flowing spins must experience both the 90° and the 180° RF pulses to contribute signal intensity [3, 5, 11, 18, 22]. When the imaged vessel

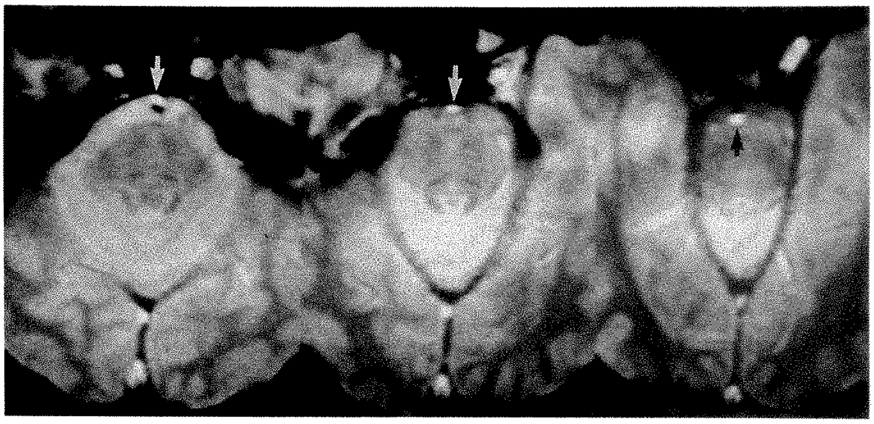

Fig. 7.—Three consecutive axial images of head using multiplanar gradient-recalled echo techniques. Basilar artery traverses axial plane and, depending on obliquity of its course through plane of section, oval or round dots of spatial misregistration (*arrows*) are mismapped anteriorly (left image) or posteriorly (right image), or not misregistered (central image).

courses orthogonal to the plane of section, the spin's flow velocity determines whether the flowing spins will experience the 90° and the 180° slice-selective pulses and the phase-encoding and readout gradients within the appropriate slice. Flow must be slow enough in a typical SE study for the bright dot or oval to be visibly registered next to the round signal void of the imaged vessel. At rapid flow rates, high-velocity washout effects [5, 11] and phase dispersal due to spin-velocity gradients [5, 9, 12] diminish or eliminate the signal source for spatial misregistration during routine SE imaging [3], particularly with longer TEs [5, 11]. However, fast flow, present in arteries and larger venous intracranial vessels, will produce spatial misregistration when gradient-recalled echo techniques are used (Fig. 9) [11].

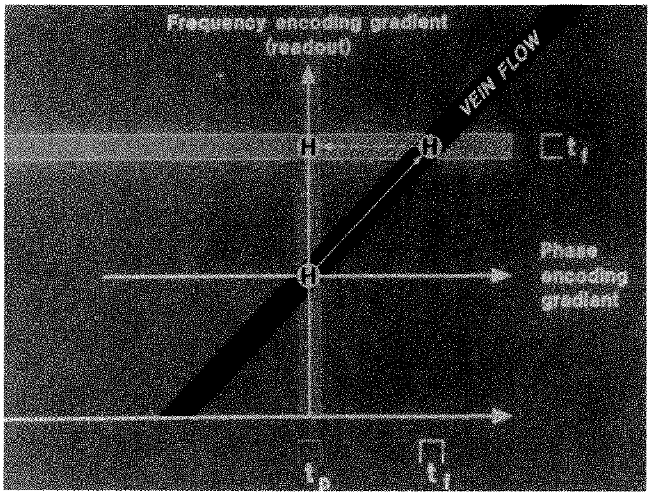

Fig. 8.—Simplified diagram of solitary spin traveling within vessel that is oblique to phase- and frequency-encoding gradients and in plane. Spin is first phase encoded and then frequency encoded, causing it to be localized outside parent vessel, upstream with respect to phase-encoding gradient axis. H = flowing spin, t_f = time of frequency-encoding gradient application, t_p = time of phase-encoding gradient application.

With gradient-recalled-echo imaging, the flowing spins must experience the initial nutation pulse, the phase-encoding step, and the refocusing readout gradient to produce MR signal. In this sequence a slice-selective 180° pulse is not used. Therefore, the signal of flowing spins can be spatially frequency encoded by using a gradient reversal technique (gradient applications are inherently nonselective), even though they have left the slice section at the time of readout [13]. This allows for signal generation from more rapid flow [5, 9, 13, 18, 24]. Flow-related enhancement is another significant source of MR signal from flowing spins during gradient-recalled-echo imaging [9, 13], particularly when slices are acquired sequentially.

Flow-related enhancement (entry slice) or even-echo rephasing are requisites for the production of spatial misregistration using routine SE MR techniques without flow-compensation gradients. Flow-related enhancement phenomena have been explained in detail by other authors [1, 5, 11, 14, 25]. They are also relevant when an interslice gap is interposed between slices, allowing more fully magnetized spins to enter the partially saturated plane of section and emit a strong echo. Flow-related enhancement in normal venous structures often results in spatial misregistration when short TE/short TR SE images are produced, especially in or near the end slices of a multislice sequence (Fig. 10).

By examining the relationship of the spatially misregistered signal to the linear signal void of the corresponding vessel and knowing the orientation of the phase- and frequency-

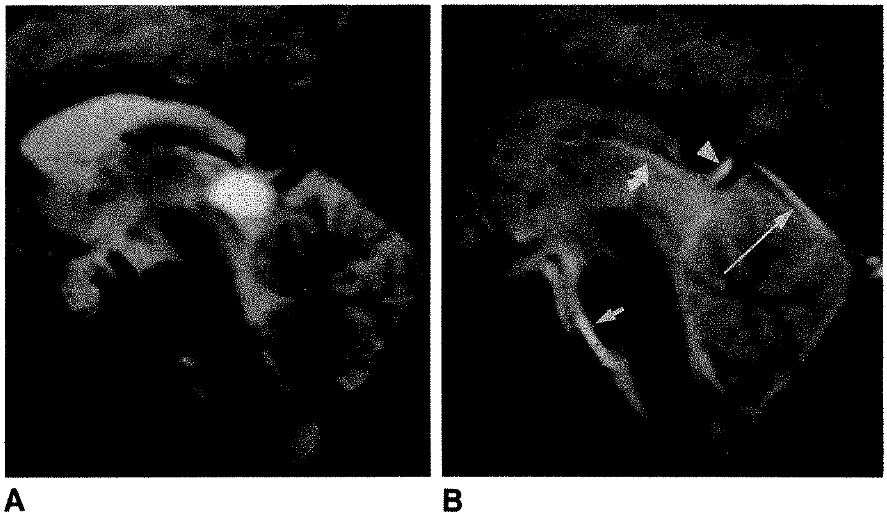

Fig. 9.—*A* and *B*, Second echo of T2-weighted sagittal study, SE 2000/70 (*A*), and sagittal GRASS examination, 100/12/10° (*B*), in patient with pineal cyst. Spatial misregistration adjacent to basilar artery (*short straight arrow*), internal cerebral vein (*curved arrow*), great vein of Galen (*arrowhead*), and straight sinus (*long straight arrow*) is apparent on GRASS scan. Note that misregistered signal is correctly placed depending on direction of flow within vessel and changes its orientation to parent vessel depending on vessel's obliquity to phase- and frequency-encoding gradients (compare great vein of Galen with straight sinus).

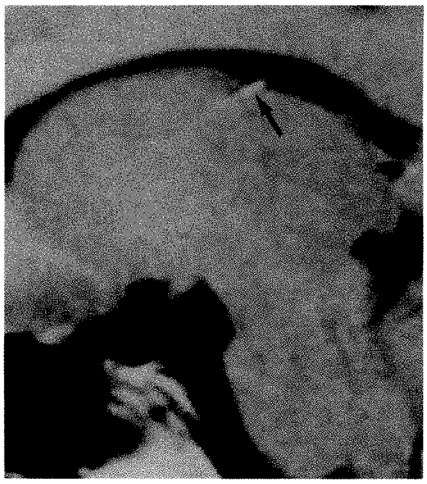

Fig. 10.—Parasagittal short TR/short TE SE image. Flow-related enhancement in left thalamostriate vein causes spatial misregistration, seen as bright white line (*arrow*) adjacent to black line of imaged vessel.

encoding gradients with respect to the plane of section, the direction of flowing blood can be determined (Fig. 11) [5]. In the most common situation, where the vessel is obliquely oriented to the phase- and frequency-encoding gradients, its directionality can be broken down into two vectors, one vector along the axis of the frequency-encoding gradient and the other along the axis of the phase-encoding gradient. This creates a right triangle with its hypotenuse along the imaged vessel. The corner of the right angle of this triangle marks the point of misregistered signal derived from a flowing spin (Fig. 1). The use of spatial misregistration to predict the direction of flowing blood is a practical aid to facilitate the correct distinction of normal patent arteries and veins or when evaluating supply and drainage of pathology with abnormal vascularity.

The relationship of the bright line or dot to the imaged vessel depends on the orientation of the phase- and frequency-encoding gradients for each particular plane of section and can be controlled through settings of operator preference. Different manufacturers orient the phase- and frequency-encoding gradients in various slice planes differently.

The velocity of in-plane flowing blood can be estimated through the use of simple geometry. The results of flow calculation in this study indicate that an approximation of venous or arterial flow can be achieved. The calculations for intracranial arteries are in general agreement with measurements of flow velocities in the middle cerebral, anterior cerebral, and posterior cerebral arteries by transcranial Doppler methods [26, 27]. Measurements of venous flow rates in cortical veins or venous angiomas are not available in the literature. Difficulties with the use of spatial misregistration to determine flow velocities lie in the tedious collection of the velocity data with calipers and in the potential error introduced when recording millimeter measurements. Additionally, the use of flow-compensation gradients causes equation 1 to become dependent on the TE values chosen for velocity calculation since the measured distance of a moving spin is approximately equal for each echo.

While any tubular flow in the CNS can produce spatial misregistration, such as that associated with flowing blood or CSF, recognition of this phenomenon is important in order to distinguish it from other artifacts or true disease. There should be no confusion with atheromas, dissections, or clotted blood, which have different appearances and cannot be altered by changing the directions of the phase- and frequency-encoding gradients. Atheromas should be concentric or eccentric and irregular. The signal intensity of arteriosclerotic plaques is complex, depending on composition [28]. Arterial dissections produce a peripheral crescent, spiral, tram track, ring, or line of nonuniform width of typically bright signal along the walls of the involved vessel owing to clotted blood within the false lumen [29]. Intraluminal clotted blood would lie within the vessel in question and would have complex signal intensity depending on the age of the clot, the field strength of the MR imaging system, and the pulse sequence parameters chosen [29–34]. Intravascular clotted blood is most easily recognized as increased signal intensity on short TR/short TE– and long TR/long TE–weighted images [33, 34]. None of these conditions would demonstrate even-echo rephasing or flow-related enhancement. The reproducible pattern of the spatial misregistration artifact distinguishes it from other MR artifacts, particularly the chemical-shift artifact, which occurs only in the direction of the frequency-encoding gradient at the interface between tissues of different resonant frequencies.

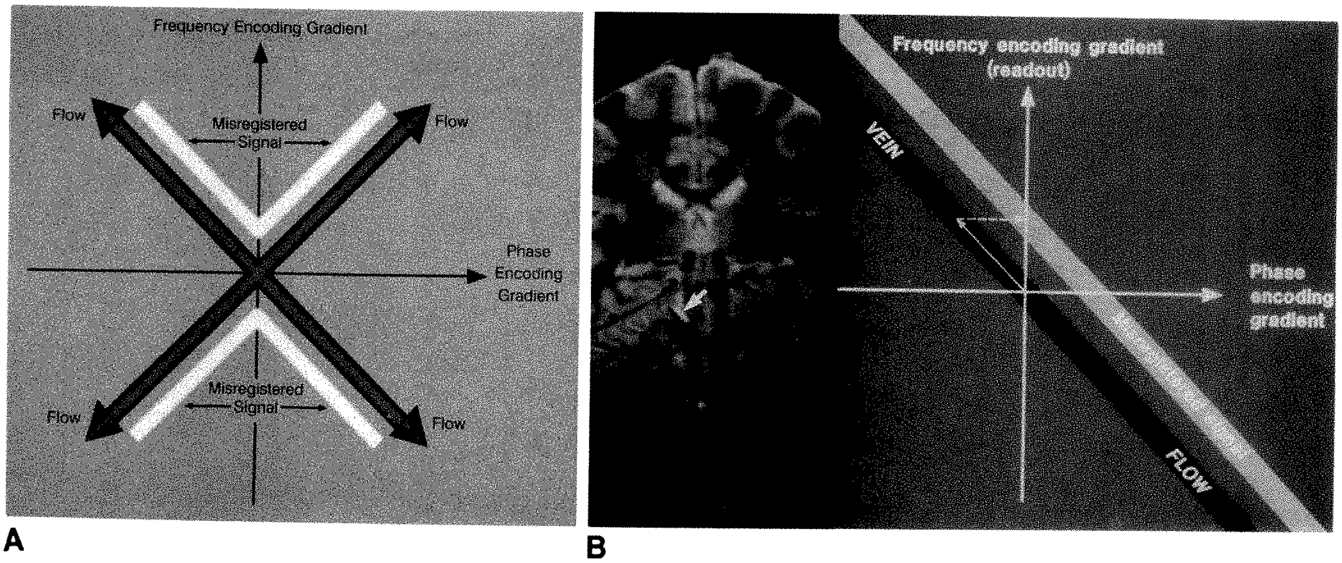

Fig. 11.—*A*, Schematic diagram used to predict direction of flow within vascular structure knowing orientation of phase- and frequency-encoding gradient axes and relationship of misregistered signal to parent vessel.

B, Second echo of T2-weighted coronal image (2000/35,70) and accompanying diagram of vessel and misregistered signal in relation to phase- and frequency-encoding gradients. Venous angioma drains peripherally toward tentorium, as would be predicted by displaced spatially misregistered signal (*arrow*).

ACKNOWLEDGMENTS

We thank Charles Higgins for reviewing the manuscript and constructive advice and Ann Shimakawa for helpful information.

REFERENCES

1. Von Schulthess GK, Higgins CB. Blood flow imaging with MR: spin-phase phenomena. *Radiology* **1985**;157:687–695
2. Bradley WG Jr, Waluch V, Lai K-S, Fernandez EJ, Spaller C. The appearance of rapidly flowing blood on magnetic resonance images. *AJR* **1984**;143:1167–1174
3. Bradley WG Jr, Waluch V. Blood flow: magnetic resonance imaging. *Radiology* **1985**;154:443–450
4. Axel L. Blood flow effects in magnetic resonance imaging. *AJR* **1984**;143:1159–1166
5. Von Schulthess GK. Blood flow. In: Higgins CB, Hricak H, eds. *Magnetic resonance imaging of the body.* New York: Raven, **1987**:119–143
6. Clark JA II, Kelly WM. Common artifacts encountered in magnetic resonance imaging. *Radiol Clin North Am* **1988**;26:893–920
7. Wehrli FW. *Advanced MR imaging techniques* (monograph). Milwaukee: General Electric Medical Systems, **1988**:6–7, 18–21
8. Pattany PM, Phillips JJ, Chiu LC, et al. Motion artifact suppression technique (MAST) for MR imaging. *J Comput Assist Tomogr* **1987**;11:369–377
9. Wehrli FW. Fast-scan imaging: principles and contrast phenomenology. In: Higgins CB, Hricak H, eds. *Magnetic resonance imaging of the body.* New York: Raven, **1987**:23–38
10. Wehrli FW. *Introduction to fast-scan magnetic resonance* (monograph). Milwaukee: General Electric Medical Systems, **1986**:3–13
11. Bradley WG Jr. Flow phenomena in MR imaging. *AJR* **1988**;150:983–994
12. Wehrli FW, Shimakawa A, MacFall JR, Axel L, Perman W. MR imaging of venous and arterial flow by a selective saturation-recovery spin echo (SSRSE) method. *J Comput Assist Tomogr* **1985**;9:537–545
13. Evans AJ, Hedlund LW, Herfleens RJ, Utz JA, Fram EK, Blinder RA. Evaluation of steady and pulsatile flow with dynamic MRI using limited flip angles and gradient refocused echoes. *Magn Reson Imaging* **1987**;5:475–482
14. Valk PE, Hale JD, Crooks LE, et al. MRI of blood flow: correlation of image appearance with spin-echo phase shift and signal intensity. *AJR* **1986**;146:931–939
15. Moran PA, Moran RA, Karstaedt N. Verification and evaluation of internal flow and motion. *Radiology* **1985**;154:433–441
16. Katz J, Peshock RM, Malloy CR, Schaefer S, Parkey RW. Even-echo rephasing and constant velocity flow. *Magn Reson Med* **1987**;4:422–430
17. Felmlee JP, Ehman RL. Spatial presaturation: a method for suppressing flow artifacts and improving depiction of vascular anatomy in MR imaging. *Radiology* **1987**;164:559–564
18. Wehrli FW, Shimakawa A, Gullberg GT, MacFall JR. Time-of-flight MR flow imaging: selective saturation recovery with gradient refocusing. *Radiology* **1986**;160:781–785
19. Wendt RE, Murphy PH, Ford JJ, Bryan RN, Burdine JA. Phase alterations of spin echoes by motion along magnetic field gradients. *Magn Reson Med* **1985**;2:527–533
20. Katz J, Peshock RM, McNamee P, Schaefer S, Malloy CR, Parkey RW. Analysis of spin-echo rephasing with pulsatile flow in 2DFT magnetic resonance imaging. *Magn Reson Med* **1987**;4:307–322
21. Wedeen VJ, Wendt RE III, Jerosch-Herold M. Motional phase artifacts in Fourier transform MRI. *Magn Reson Med* **1989**;11:114–120
22. Waluch V, Bradley WG Jr. NMR even echo rephasing in slow laminar flow. *J Comput Assist Tomogr* **1984**;8:594–598
23. George CR, Jacobs G, MacIntyre WJ, et al. Magnetic resonance signal intensity patterns obtained from continuous and pulsatile flow models. *Radiology* **1984**;151:421–428
24. Hearshen DO, Froelish JW, Wehrli FW, Haggar AM, Shimakawa A. Time of flight flow effects from gradient recalled echoes with short TR's (abstr.) In: *Book of abstracts. Society of Magnetic Resonance in Medicine. Fifth annual meeting.* Berkeley, CA: Society of Magnetic Resonance in Medicine, **1986**:94–95
25. Whittemore AR, Bradley WG, Jinkins JR. Comparison of cocurrent and countercurrent flow-related enhancement in MR imaging. *Radiology* **1989**;170:265–271
26. Aaslid R, Markwalder T-M, Nornes H. Noninvasive transcranial Doppler ultrasound recording of flow velocity in basal cerebral arteries. *J Neurosurg* **1982**;57:769–774
27. Grolimund P, Seiler RW. Age dependence of the flow velocity in the basal cerebral arteries—a transcranial Doppler ultrasound study. *Ultrasound Med Biol* **1988**;14:191–198
28. Merickel MB, Carman CS, Brookeman JR, Mugler JP III, Brown MF, Ayers CR. Identification and 3-D quantification of atherosclerosis using magnetic resonance imaging. *Comput Biol Med* **1988**;18:89–102
29. Goldberg HI, Grossman RI, Gomori JM, Asbury AK, Bilaniuk LT, Zimmerman RA. Cervical internal carotid artery dissecting hemorrhage: diagnosis using MR. *Radiology* **1986**;158:157–161
30. Gomori JM, Grossman RI, Goldberg HI, Zimmerman RA, Bilaniuk LT. Intracranial hematomas: imaging by high-field MR. *Radiology* **1985**;157:87–93
31. Rapoport S, Sostman HD, Pope C, Camputaro CM, Holcomb W, Gore JC. Venous clots: evaluation with MR imaging. *Radiology* **1987**;162:527–530
32. Alvarez O, Edwards JH, Hyman RA. MR recognition of internal carotid artery occlusion. *AJNR* **1986**;7:359–360
33. McMurdo SK, Brant-Zawadzki M, Bradley WG Jr, Chang GY, Berg BO. Dural sinus thrombosis: study using intermediate field strength MR imaging. *Radiology* **1986**;161:83–86
34. Sze G, Simmons B, Krol G, Walker R, Zimmerman RD, Deck MDF. Dural sinus thrombosis: verification with spin-echo techniques. *AJNR* **1988**;9:679–686

Meeting News

Liver Imaging—Current Trends in MRI, CT, and US: International Symposium and Course, June 1990

Elizabeth Whalen[1]

"Liver Imaging: Current Trends in MRI, CT, and US" (an international symposium and course sponsored by the Department of Radiology, Massachusetts General Hospital; The MGH Liver Biliary and Pancreas Center; and the Department of Continuing Education, Harvard Medical School) was held June 25-27, 1990, at the Copley Westin Hotel, Boston, MA. Some 60 invited lectures and 26 submitted scientific papers were presented by researchers from the United States and 10 foreign countries. The symposium was interdisciplinary as well as international: speakers included not only experts on liver imaging, but also gastroenterologists, biochemists, physicists, and representatives of the Food and Drug Administration (FDA) and the pharmaceutical and imaging industries.

Unfortunately, space limitations in the *AJR* preclude complete coverage of this intensive, 3-day symposium; however, we hope that this report will make our readers aware of the latest advances and future directions in liver imaging. The symposium director, Joseph T. Ferrucci, stated its purposes: to focus on "current and future trends in imaging diagnosis of the liver," "to identify the major trends that will affect radiologic diagnosis of abdominal diseases for the next decade," and "to set the research agenda for imaging diagnosis of liver disease." This report covers six major topics discussed during the symposium: imaging techniques to detect hepatic lesions, methods for characterization of hepatic tissue, imaging of hepatic metastases, the role of imaging in the planning and follow-up of hepatic surgery, new and developing techniques for liver imaging, and contrast agents for liver imaging.

Lesion Detection with MR Imaging, CT, and Sonography

After overview lectures by Dr. Ferrucci and by codirector David D. Stark (both Massachusetts General Hospital, Boston), the first topic was the detection of liver lesions by using imaging techniques. Lectures and scientific papers covered the use of different imaging methods and compared those methods.

CT

Patrick C. Freeny (Virginia Mason Clinic, Seattle, WA) discussed the techniques and results of four different CT methods: bolus dynamic CT, delayed iodine scanning, CT angiography, and CT arterial portography. Dr. Freeny suggested the following parameters as guidelines for these procedures: For bolus dynamic CT, effective scanning parameters include nine scans/sec, three-scan clusters, 2-sec scanning time, 3.5-sec interscan delay, 10-sec intergroup delay, and rapid uniphasic injection of 150-180 ml of 60% contrast material (ionic or nonionic); this technique works well in either abdominal surveys or liver surveys. For delayed iodine scanning, incremental CT is performed 4-6 hr after administration of a dose of 60 g or more of iodine; with these parameters, liver enhancement is 20 H greater than baseline enhancement, and accurate liver surveys can be obtained. The following parameters can be used for both CT angiography and CT arterial portography: A series of five to eight clusters of three 2-sec scans is obtained

---

[1] Contributing editor, *American Journal of Roentgenology*, Ste. 103, 2223 Avenida de la Playa, La Jolla, CA 92037.

Editor's note.—"Meeting News" articles report the highlights of important national radiology meetings. The intent is to provide Journal readers with succinct, substantive, and accurate reviews of topics of current interest, written in a readable fashion and published promptly after the meeting.

The articles will not undergo the peer review usually required of *AJR* publications, nor will they offer a critique of the information provided. The sole purpose of the series is to apprise *AJR* readers of topics of current concern in an interesting and timely fashion.

155:1125-1132, November 1990 0361-803X/90/1555-1125 © American Roentgen Ray Society

with a 3.5-sec interscan delay for table incrementation and a 10-sec intergroup delay for patients to breathe. CT angiography is performed with selective injection of the hepatic artery with a 15% contrast agent at 2 ml/sec during each three-scan cluster (total of 26 ml/cluster), and CT arterial portography is performed by selective injection of the superior mesenteric artery with 100–150 ml of a 60% contrast agent at a continuous rate of 2–3 ml/sec. CT angiography of CT arterial portography combined with delayed iodine scanning is the most useful protocol for hepatic lesion detection.

Dr. Freeny and colleagues have followed up 528 consecutive patients with various stages of cancer in whom CT was used to detect liver metastases; 40 of those patients have had liver metastases proved at surgery. For detecting liver metastases, CT had a sensitivity of 88% and a specificity of 99%. In another study of 25 resected livers with 35 lesions, Dr. Freeny found that, for hepatic lesion detection, CT angiography plus MR imaging had a sensitivity of 87%; CT angiography plus delayed iodine scanning had a sensitivity of 89%; and CT angiography plus delayed iodine scanning *and* MR imaging had the highest sensitivity, 97%.

MR Imaging

High-field MR imaging of hepatic lesions was discussed by W. Dennis Foley (Medical College of Wisconsin, Milwaukee). Image contrast is an important factor in lesion conspicuity, and contrast depends on both the MR field strength and the pulse sequence. Anecdotal evidence suggests that the difference between the T1 of liver and the T1 of lesion may be greater at low to intermediate field strength than at high field strength and that the T2 value of normal liver may be lower at 1.5 T than at 3.5 T. In a high-field MR study of 46 hepatic lesions, more lesions were detected by T2-weighted (44) than by either T1-weighted (30) or proton-density-weighted (35) imaging. Also, T2-weighted images had higher contrast-to-noise ratios. Presaturation reordered phase encoding and gradient moment nulling have become standard motion-compensation techniques for hepatic MR. Short inversion time recovery (STIR) pulse sequences null signal from subcutaneous fat while enhancing hepatic lesion contrast. However, image quality is degraded relative to standard spin-echo sequences. Recent evidence indicates that T1-weighted images with short echo times (TEs) may produce images with better contrast than that seen on standard T2-weighted images.

Dr. Stark compared midfield MR images with CT scans of liver lesions. A 0.6-T imager was used, with a 1.5-cm slice thickness, a 25% gap, 1.8 × 3.6 mm pixel size, two spin-echo sequences, and an inversion recovery sequence. The images produced with this midfield technique were retrospectively reviewed by three blinded, experienced radiologists, who compared them with CT scans obtained on a fourth-generation scanner (80% of the CT scanning was performed with rapid scanning after administration of >40 g of iodinated contrast material). Receiver-operating-characteristic (ROC) analysis of the results from 1000 patients showed that these MR images were slightly better than CT scans for lesions within the liver but inferior to CT scans for lesions outside the liver. Dr. Stark and his coworkers concluded that enhanced CT should still be used for routine abdominal imaging. Heavily T2-weighted MR imaging is effective for differential diagnosis of primary or secondary, benign or malignant liver lesions.

Preliminary data on the newer ultra-low-field MR units were presented by Ruedi F. Thoeni (University of California, San Francisco). Ultra-low-field MR imaging allows more comfort for the patient than other MR imaging methods because of the open design of the unit, which eliminates claustrophobia, and because of its silent operation. Low-field MR imaging is also more cost-effective; its purchase price, installation cost, and maintenance expenses are all lower than for mid- or high-field MR imaging. However, the current disadvantages of using low-field MR imaging include lower signal-to-noise ratio and spatial resolution than higher field techniques and the inadequate quality of short imaging sequences (particularly heavily T1-weighted sequences). Dr. Thoeni and colleagues compared low-field and midfield MR images in patients with primary or metastatic liver lesions. Low-field imaging was performed on a 0.064-T (640-gauss) permanent magnet with a vertically oriented field and a solenoidal body coil. For imaging liver lesions, low-field MR images were ranked equal to midfield MR images in 65% of the patients, worse than midfield in 4%, and better than midfield in 31%. Thus, in general, liver lesion margin and contrast was better on low-field images. However, low-field images were generally ranked lower for imaging of the rest of the abdomen (80% were considered worse than midfield images; 16% were considered equal; and 4% were considered better than midfield images). More research will be conducted to try to improve low-field imaging of the entire abdomen and to create adequate T1-weighted images with low-field MR imaging. At this point, low-field MR imaging is a cost-effective tool that provides excellent assessment of focal liver lesions.

Steven P. Braff (Clifton Springs Hospitals and Clinics, Clifton Springs, NY) discussed midfield MR imaging in a general clinical practice. Using a 0.4-T electromagnet, these radiologists obtained MR images on 15 patients for characterization of hepatic lesions. MR examinations included some short-TE, short-TR studies; some long-TE, long-TR studies; and studies both with and without cardiac gating. Midfield MR imaging helped in screening for liver metastases, characterizing a known mass, clarifying an abnormal or suboptimal CT study, obtaining images in patients who have had adverse reactions to contrast material, ruling out infiltrative disease, and ruling out liver lesions in patients with fatty infiltration of the liver. Dr. Braff said that MR imaging is now being used in 5–8% of their case load; he expects that percentage to increase as MR technology and their own expertise in MR imaging improve.

Comparative Studies

A comparison of MR, CT, and sonographic studies of focal liver lesions was presented by C. Dan Johnson (Mayo Clinic, Rochester, MN). All 30 patients in this prospective study had pathologically proved liver lesions; 25 (83%) had malignant lesions, and five (17%) had benign conditions. State-of-the-art MR imaging, CT, and sonography were compared in terms of sensitivity of liver lesion detection, diagnostic confidence level, and characterization of liver lesion. No significant differences were found in the sensitivities of the three techniques (MR imaging, 80%; CT, 77%; sonography, 73%). MR imaging was significantly better than sonography at characterizing lesions; no significant differences in lesion characterization were seen between MR imaging and CT or between CT and sonography. Analysis of the results indicated that sonography is best for studying cystic masses, CT is best for detecting lesions with calcification, and MR imaging is best for showing fat-containing lesions. Therefore, each patient's history and previous imaging studies can be used to predict the most likely type of lesion and thus to help select the best imaging method.

Imaging Methods for Characterizing Hepatic Tissue

In the presentations on liver tissue characterization, specific topics included color-flow sonography, MR imaging in hydatid cysts of the liver, and comparison of different imaging techniques in characterization of liver tumors.

Color Doppler Flow Sonography

F. Fobbe (Free University of Berlin, Berlin, West Germany) discussed the capability of color-coded duplex sonography to show the perfusion state of focal liver lesions. The specificity of real-time sonography is low for these determinations, and color sonography allows the display of flow from vessels too small to be seen on real-time images. Dr. Fobbe and colleagues performed a prospective study of color-coded duplex sonography in 96 patients; results were compared with CT, angiographic, and histologic results. Comparison of flow signals in the 41 patients with primary liver lesions showed that the vascularity of tumors was not significantly higher than that of normal liver tissue. In the 55 patients with secondary liver lesions, they once again found no significant difference in vascularity between tumor and normal tissue (59% of the colon metastases showed more blood flow than normal tissue, but increased blood flow was seen in only 29% of the breast, stomach, and pancreas metastases). Color-coded duplex sonography is a simple, accurate, and rapid technique for demonstrating the vascularization of liver lesions, but it cannot distinguish between primary and secondary tumors nor can it reveal the primary site of liver metastases.

In another study, Sachiko Tanaka and colleagues (The Center for Adult Diseases, Osaka, Japan) tried to establish which color flow patterns were most common to hepatocellular carcinomas by studying the color Doppler flow images of 31 patients with nodular hepatocellular carcinomas. Two characteristic pulsating-wave patterns were found: 22 (71%) displayed a basket pattern (a fine blood-flow network surrounding the tumor nodule), and 22 (71%) displayed vessels within the tumor (blood flow that runs into and branches within the tumor). Of the 11 tumors that were smaller than 2 cm, eight showed the basket pattern, and seven showed vessels within the tumor. Two constant-wave diagnostic patterns were seen: multiple hepatic metastases were often characterized by a detour pattern (a dilated portal vein meandering around the tumor nodules), and three of six hemangiomas had a spot pattern (color-stained dots in the tumor center). These results suggest the potential use of color flow patterns for distinguishing types of hepatic tumors; however, these patterns have not yet been proved to be definitive diagnostic signs.

MR Imaging of Hydatid Cysts of the Liver

Roberto Passariello (University of L'Aquila, L'Aquila, Italy) investigated the preoperative and postoperative use of 0.5-T MR imaging to evaluate hydatid liver cysts. The indications for MR imaging included doubtful sonographic findings, preoperative evaluation of extent of cyst and relationships of vessels, exact location of liver, characterization of lesion, identification of hepatic rupture, and postoperative evaluation of recurrent cyst. Preoperative MR evaluations were performed in 30 patients (cyst size, 3–10 cm), and postoperative MR images were obtained in three other patients. The cyst walls were best characterized on proton-density images; the wall was always hypointense (appearance of cyst content depended on lesion type), and a thickened wall indicated calcific areas. Three types of liver hydatid cysts can be defined on the basis of MR findings: type 1, serous ($n = 15$ in this series)—markedly and homogeneously hypointense on T1-weighted sequences; type 2, complex with daughter cysts ($n = 4$)—mildly hypointense on T1-weighted sequences and hyperintense on matrix T2-weighted sequences; and type 3, calcified ($n = 11$)—thickened hypointense wall with hyperintense contents, low signal intensity on T1-weighted images, and high signal intensity on T2-weighted sequences. MR imaging easily identified intrahepatic cyst rupture, and postoperative MR evaluation helped determine the serous or blood content of the residual and the recurrence and extent of vascular lesions. Thus, for hydatid liver cysts, MR imaging may be able to replace CT for clarification of cysts after indeterminate sonography, MR findings may help characterize the nature of a cystic lesion, and multiphasic MR imaging may assist in postoperative evaluation.

Comparative Studies

A prospective study comparing different imaging methods for characterization of liver tumors was presented by Meinhard Lüning (Charité Hospital, Humboldt University, Berlin, East Germany). The study group included 130 patients with histologically proved diagnoses of hemangioma (44), metastases (37), hepatocellular carcinoma (28), focal nodular hyperplasia (17), and adenoma (four). MR imaging was performed in all patients; dynamic CT in 122; sonography in 119; scintigraphy in 44; and CT arteriography in 15. In differentiating malignant from benign lesions, no significant difference was found between the imaging methods, although MR imaging appeared to have a moderate advantage (accuracies: MR imaging, 91%; CT, 89%, CT arteriography, 87%, sonography, 84%). MR imaging also had the highest accuracy in characterizing lesions (MR imaging, 80%; CT, 73%; CT arteriography, 73%; sonography, 69%; scintigraphy, 53%). The best disease-specific accuracy was found in the MR imaging diagnosis of hemangiomas; the worst disease-specific accuracy was the sonographic diagnosis of focal nodular hyperplasias.

Jeffrey C. Weinreb (New York University Medical Center, New York) presented the results of a retrospective study comparing MR imaging and ^{99m}TC-labeled-RBC single-photon emission CT (SPECT) in the definitive diagnosis of hepatic hemangiomas. In 38 patients, a total of 69 suspected cavernous hemangiomas had been detected by either CT or sonography. SPECT imaging was performed after the patient's blood was labeled with 30 mCi (1100 MBq) of technetium-99m; after acquisition of a dynamic flow phase followed by an interval of 90–120 min, delayed SPECT images were obtained, ultimately yielding 1.2-cm-thick axial, coronal, and sagittal slices. Low-field (0.5-T) MR imaging and T2-weighted spin-echo sequences were used. The images were reviewed by two pairs of experienced radiologists; the readers were told of the location and size of the reference lesion but were not given the previous CT or sonographic studies. The likelihood of hemangioma was graded on a five-point confidence scale. Overall, MR imaging was slightly superior in sensitivity (MR imaging, 91%; SPECT, 78%) and accuracy (MR imaging, 90%; SPECT, 80%). MR imaging was significantly more accurate in finding lesions less than 2 cm in diameter; there was no significant difference in accuracies for lesions larger than 2 cm. Also, MR imaging was more effective in identifying lesions less than 2.5 cm in diameter that were situated adjacent to major vessels or the heart. However, although MR imaging proved to be superior for lesions of certain size and location, its inability to differentiate hemangiomas from hypervascular metastases and its high cost make it an impractical first examination. Dr. Weinreb added that new triple-headed gamma cameras improve SPECT resolution dramatically and make detection of hemangiomas as small as 5 mm possible. After observing that "when working toward a solution to a problem, it always helps to know the answer," Dr. Weinreb noted that the radiologist will need to think of cavernous hemangiomas in order to see them on SPECT.

Imaging Diagnoses of Hepatic Metastases

To determine whether serial CT scans can help to predict the progression of liver metastases from colonic carcinoma, R. A. Halvorsen, Jr., and colleagues (University of Minnesota, Minneapolis) evaluated 127 CT scans in 27 patients. Factors evaluated included the number and size of metastases in each hepatic segment, percentage of liver involvement, and subjective estimate of change in metastases' volume; also, the metastases were characterized in terms of margination, contents (solid or cystic), calcification, mass effect, clefts, and rim enhancement. Changes in serial CT scans were correlated with each patient's clinical status, as defined by level of carcinoembryonic antigen, weight changes, and/or date of death. Direct correlations were found between these clinical indicators and a change in the size of the largest metastasis ($p = .004$: both sensitivity and specificity were 67% if a 1-cm increase in diameter was used as the criterion for progression); a change in metastasis volume ($p = .02$); and mass effect ($p = .024$). The change in percentage of involvement showed a borderline correlation with progression ($p = .085$). None of the other factors evaluated showed a significant correlation with clinical progression; Dr. Halvorsen noted that the lack of correlation was especially interesting for contents of the metastasis ($p = .71$) and clefts on the surface of the liver ($p = .95$). Perhaps the most surprising finding was that calcification showed no correlation with disease progression ($p = 1.00$). These researchers concluded that serial CT scans can be used to predict progression of hepatic metastases from colonic carcinoma: changes in the size of the largest metastasis and changes in its estimated volume on CT appear to correlate directly with clinical indicators of progression.

E. Rummeny (University of Münster, Münster, West Germany) discussed a study in which CT and high-field MR imaging were compared in regard to detecting hepatic metastases. Dr. Rummeny and colleagues studied the ROCs of MR images and both enhanced and unenhanced CT scans. In total, 900 images were studied; 450 of subjects without disease and 450 of patients with primary cancer proved at laparotomy. MR images were obtained at 1.5 T, by using T1-weighted spin-echo and gradient-echo, proton-density-weighted spin-echo, and T2-weighted presaturated spin-echo sequences. A third-generation CT scanner was used to obtain scans before, during, and 4–5 hr after a bolus injection of 200 ml of contrast material. ROC analysis indicated that, of all MR and CT techniques evaluated, the heavily T2-weighted MR sequence was the best technique for detecting liver metastases. Of the CT methods, contrast-enhanced CT scans were found to be more useful than either unenhanced or delayed scans; contrast-enhanced CT scans were approximately equivalent to gradient-echo T1-weighted MR images for detection of metastases.

Because CT scans show focal fatty infiltration of the liver and hepatic metastases as lesions of similar density, K. Neumann and colleagues (University Clinic Rudolf Virchow/Charlottenburg, Free University of Berlin, Berlin, West Germany) studied the use of MR imaging for the differential diagnosis of these two disease processes. Third-generation CT units were used to obtain enhanced and unenhanced scans; T1-weighted gradient-echo images and T2-weighted spin-echo images were generated on a 0.5-T MR imager. Of the 16 patients studied, 11 had liver metastases and five had focal fatty infiltration; CT scans of all 16 patients showed areas of decreased attenuation. On T1-weighted MR images, metastases were seen as areas of significantly decreased signal intensity (compared with normal liver); on T2-weighted MR images, they appeared as areas of significantly increased signal intensity. The signal intensity of areas of focal fatty infiltration on MR images was equal to or slightly different from the liver signal intensity. The mean values of differences between the signal intensity of metastases and that of liver were −36% on T1-weighted sequences and +132% on T2-weighted sequences; these values are significantly different from the mean values of differences in focal fatty infiltration (−1% and +4%, respectively; $p < .001$). These researchers conclude that MR imaging can differentiate between liver metastases and focal fatty infiltration when CT scans show a hypodense lesion in the liver of a patient with malignant disease.

Planning and Follow-up of Hepatic Surgery

Use of three-dimensional (3-D) CT imaging in preoperative planning for liver tumors was discussed by Pablo Ros (University of Florida College of Medicine, Gainesville). Two surgeons independently reviewed both two-dimensional and 3-D CT scans in 10 patients with liver tumors. For locating masses, one surgeon found the 3-D scans superior in all 10 cases, and the other surgeon found the 3-D scans superior in eight of 10 cases. For the first surgeon, the 3-D scans indicated a change in therapeutic approach in five cases; for the second, such a change was indicated by 3-D scans in four cases. Both surgeons preferred the 3-D coronal images to the other views; moreover, the 3-D image, especially in the coronal plane, was immediately accepted by the surgeons. With this technique, however, no more than two structures can be reconstructed at one time, real-time rotation capabilities are lacking, and much time is required of the radiologist (70–80 min/scan). However, 3-D CT seems to have great potential for liver imaging; not only do surgeons accept the technique and prefer the images to two-dimensional scans, but 3-D CT offers better visualization of central lesions and anatomic orientation.

A clinical hematologist, J. P. Kaltwasser (J. W. Goethe University, Frankfurt am Main, West Germany), discussed the possible role of MR imaging in the quantitative determination of liver iron in iron-overload syndromes. In iron storage disease, a progressive increase in total iron produces cellular damage and functional insufficiency of the involved organs. Hereditary hemochromatosis is primary iron-storage disease; acquired hemochromatosis (or secondary iron-storage disease) results from excessive dietary intake of iron. Usually, the liver is the first organ to be affected, and, to date, liver biopsy has been the most helpful clinical test to detect the distribution of iron, the extent of tissue injury, and the iron concentration in the liver. However, in order to find a noninvasive method to measure iron, Dr. Kaltwasser and colleagues studied MR images of 35 patients with various degrees of liver iron overload. To quantitate liver iron overload, they used 1.0- to 1.5-T MR images (T2-weighted sequences with very short TEs). Two findings suggested that MR imaging may be useful in measuring liver iron overload: (1) the T2 relaxation rate (1/T2) had a direct and significant correlation ($r = .79$) with the serum ferritin concentration, and (2) the T2 relaxation rate and liver iron concentration from biopsy specimens (the gold standard) showed a nearly linear correlation ($r = .90$).

Another study about the use of MR imaging to measure liver iron overload for surgical planning was presented by Yves Gandon (Pontchaillou Hospital, Rennes, France). Dr. Gandon and colleagues prospectively studied MR images of the liver in 40 patients with idiopathic hemochromatosis, 10 patients with chronic liver disease, and 10 normal subjects. On a 0.5-T MR unit, spin-echo, inversion-recovery, and breath-hold gradient-echo sequences were performed. Analyses of the images included regions of interest (ROIs) of signal intensity, calculation of signal-to-noise ratios and tissue ratios (e.g., liver to spleen or liver to muscle), and calculation of relaxation times. These values were then correlated with liver iron concentrations (LIC) from liver biopsy, which was performed in all patients. Biopsy results showed that LIC was normal in the 10 patients with chronic liver disease but ranged from 40 to 860 μmol/g in patients with hemochromatosis. In spin-echo MR sequences, liver signal-to-noise ratios were significantly lower in hemochromatosis patients than in either chronic liver disease patients or normal subjects; however, there was no significant difference in the signal-to-noise ratios of spleen, fat, or muscle among the three groups. Good correlations ($r = .8$) were found between LIC values and liver-to-spleen ratios and between LIC values and liver-to-muscle ratios, but slight iron overload could not be detected on spin-echo images. Gradient-echo T2-weighted sequences were more sensitive to slight iron overload, because such overload significantly decreased liver signal on these images. Also, these sequences provided excellent correlations ($r = .85$) between LIC values and liver-to-spleen ratios and between LIC values and liver-to-muscle ratios. With the more sensitive sequences, iron concentrations as low as 80 μmol/g can be detected by MR imaging. This information and MR-derived estimates of liver volume can aid the surgeon in determining how much iron must be withdrawn.

Special MR and CT Techniques for Liver Imaging

MR Imaging

STIR MR imaging of focal liver disease was discussed by Albert A. Moss (University of Washington Medical Center, Seattle). The advantages of a short inversion time (TI) include suppression of signal from fat and increased brightness of diseased tissue (and therefore increased contrast between diseased and normal tissue). However, limitations of STIR imaging include the equal brightness of tumor and edema, as well as the low signal-to-noise ratio, small number of slices per unit time, and low spatial resolution on STIR compared with spin-echo sequences. Dr. Moss and colleagues used a 1.5-T MR imager to study 41 proved liver lesions; they performed both STIR and double-echo spin-echo examinations. Three radiologists blindly evaluated both the STIR and spin-echo images for several factors, including presence of lesion, subjective lesion conspicuity, and lesion volume. All 41 lesions were seen clearly on STIR images; three lesions were missed on spin-echo images. STIR images were judged to provide better conspicuity in 66% of cases; lesion conspicuity was about equal in the other 34%. Lesion volume determinations by the two methods were within 20% of each other in 66% of the lesions; in 34%, the tumor volume measurement was larger on STIR than on spin-echo images. STIR can be a valuable adjunctive technique for liver imaging because the slightly higher lesion conspicuity on STIR can be helpful in showing lesions to a referring physician, the extent of abnormality and number of lesions can be judged more accurately with STIR, and because of STIR's higher sensitivity, a radiologist can have greater confidence in judging a study to be normal.

Joseph K. T. Lee (Mallinckrodt Institute of Radiology, Washington University School of Medicine, St. Louis, MO) discussed the phase-contrast technique of proton-spectroscopic MR imaging (PSI), which is also called chemical-shift imaging. A modification of the conventional spin-echo technique, phase-contrast PSI can produce—within less than 30 min—separate water and fat images with good spatial resolution. Dr. Lee reported that, in finding small fatty changes in the liver, out-of-phase (opposed) PSI is more sensitive than the conventional in-phase spin-echo imaging (with any echo time); PSI actually triples the difference between normal and fatty liver. Using a 0.5-T MR imager, these researchers compared images generated by T1- and T2-weighted PSI and spin-echo sequences for detecting liver metastases. In 24 patients, T1-weighted spin-echo images were better than T2-weighted PSI at showing the correct number of metastases in seven cases and at lesion conspicuity in 11 cases (the two methods were about equivalent in all other cases). In 27 patients, T2-weighted sequences for the two methods were compared; in counting of lesions and lesion conspicuity, T2-weighted PSI was better than T2-weighted spin-echo imaging in six and 12 cases, respectively (the two methods were about equivalent in almost all other cases). Therefore, the short-TR, short-TE spin echo sequence is the preferred method of lesion detection. For detecting fatty infiltration of the liver, T2-weighted PSI is preferred. Dr. Lee noted that PSI is most useful in determining the cause of focal low-attenuation lesions detected by CT.

The use of MR spectroscopy for differential diagnosis of liver tumors was the topic of a lecture given by Gary M. Glazer (Stanford University School of Medicine, Stanford, CA). The current limitations of ^{31}P MR spectroscopy include crude localization schemes, uncontrolled variability in histologic grades of tumors, and variability in the morphology of liver tumors. However, MR spectroscopy of tumorous tissue does differ from that of normal hepatic parenchyma: for tumors, phosphomonoester (PME) and phosphodiester (PDE) peaks are usually elevated relative to either the inorganic phosphate (PI) or a beta-adenosine triphosphate (β-ATP) peak. Dr. Glazer and colleagues used MR spectroscopy to evaluate 31 patients with liver metastases, eight patients with hepatomas, eight patients with hemangiomas, and five normal volunteers. Imaging parameters included use of a 8- to 14-cm surface coil over the lesion; proton shimming, and an average total acquisition time of 21 min 25 sec. Spectral quantitation parameters included operator-selected peak heights, peak areas via operator-selected border-to-border integration, and automatic curve-fitting with commercially available software. Dr. Glazer noted that spectral analysis is a crude estimation of the percentage of the spectral slice occupied by the tumor; at this point, there is always the question of how much the diseased tissue is "contaminated" by surrounding normal tissue. The peak-height PME/peak-height β-ATP ratios for the metastases and hepatoma groups comprising more than 50% of the spectral slice were significantly different from those ratios in the control subjects: normal subjects, 0.8262; patients with metastases, 2.1020 ($p < .001$); patients with hepatomas, 1.8034 ($p < .002$). A significant overlap was found between the spectral patterns of normal subjects and patients whose tumors occupied less than 50% of the spectral slice; this overlap is a limitation of the MR spectroscopic analysis and reflects the need for better localization methods. No significant difference was found among the spectral patterns of tumors of different malignant histologies. However, the most significant finding was a difference in spectra between hemangiomas and metastases in the calculation of the signal-to-noise ratio using β-ATP resonance (0.99 for hemangiomas compared with 5.99 for metastases; $p < .001$); this distinctive feature is important because the MR imaging features of hemangioma overlap those of metastases.

Yuji Yuasa (Keio University, Tokyo, Japan) discussed MR angiography of the hepatic vein and portal system. The indications for MR angiography of the upper abdomen include hepatobiliary and renal lesions; stenosis of portal, hepatic, and/or renal veins; and anatomic evaluation of portal or hepatic veins (especially for preoperative evaluation of neoplasms). Dr. Yuasa and colleagues used two-dimensional time-of-flight MR angiography to study 28 cases of liver disease (including 15 of hepatocellular carcinoma) and seven cases of biliary tract disease. MR angiography clearly showed venous obstruction in 12 of 15 cases of hepatocellular carcinoma. Not only did the results of MR angiography correlate well with the results of conventional angiography, but MR angiography also eliminated the problem of the superimposition of great vessels onto the portal and hepatic venous system and provided good visualization of organ contours (which was further improved with frequency-selective presaturation).

Three researchers presented studies on fast MR imaging techniques. Akihiro Tanimoto (Keio University Hospital, Tokyo, Japan) reported a study of a fast gradient-echo MR technique: spoiled gradient-recalled acquisition into steady state (spoiled GRASS or SPGR). SPGR was used to evaluate 50 patients (30 hepatomas, 10 hemangiomas, and 10 metastases). Dr. Tanimoto and colleagues compared images from conventional, spin-echo T1- and T2-weighted sequences; a fast T1-weighted sequence; and a T1-weighted SPGR sequence. Tumor-to-liver contrast-to-noise ratios were significantly higher on SPGR images than on fast and conventional T1-weighted images. Detectability rates were as follows for hepatocellular carcinomas smaller than or larger than 2 cm, respectively: conventional T1-weighted, 83% and 83%; conventional T2-weighted, 83% and 100%; fast T1-weighted, 91% and 83%; and SPGR, 100% and 100%.

Scott A. Mirowitz (Mallinckrodt Institute of Radiology, Washington University School of Medicine, St. Louis, MO) discussed a study of contrast-enhanced fast MR imaging. Rapid-acquisition spin-echo (RASE) MR images were obtained in 24 patients with liver lesions (total number of lesions, 62; size range of lesions, 1–15 cm). Four MR methods were used—conventional T2-weighted, conventional T1-weighted, and highly T1-weighted RASE—both before and after rapid

IV administration of gadopentetate dimeglumine. Both the contrast-to-noise and the contrast-to-artifact ratios were significantly higher on RASE images than on other images ($p < .05$), and both ratios are maximal immediately after injection of the contrast bolus. For example, contrast-to-artifact ratios were 2.7 on contrast-enhanced RASE sequences, 1.7 on unenhanced RASE sequences, 1.1 on conventional T2-weighted sequences, and 1.0 on conventional T1-weighted sequences. In this study, enhanced RASE imaging was used to screen the whole liver in less than 5 min with better lesion conspicuity than any other method.

Magnetization-prepared rapid gradient-echo (MP-RAGE) MR imaging of the liver was discussed by Eduard E. de Lange (University of Virginia Health Sciences Center, Charlottesville). Characterized by a rapid gradient-echo sequence preceded by magnetization-preparation pulses to provide T1- and T2-weighted tissue contrast, MP-RAGE MR imaging allows acquisition times of less than 1 sec and provides images that have virtually no motion artifacts. Four imaging studies were evaluated in 15 patients with liver lesions: T1-weighted MP-RAGE, T2-weighted MP-RAGE, T1-weighted spin-echo, and T2-weighted spin-echo sequences. The contrast-to-noise ratios, normalized for voxel volume and imaging time per slice, were significantly higher for T1-weighted MP-RAGE sequences than for any other sequence ($p < .01$); moreover, respiratory motion artifacts clearly evident on the spin-echo sequences were not noticeable on MP-RAGE images. These researchers are now developing and testing a 3-D technique for MP-RAGE MR imaging to evaluate the liver for focal disease.

CT Techniques

Ruth Langer (Free University of Berlin, Berlin, West Germany) reported the use of subsecond dynamic CT in 42 patients with malignant liver tumors (metastatic lesions, 20—two hypervascularized; hepatocellular carcinomas, 11; bile duct carcinomas, eight; gallbladder carcinomas, three). The examination protocol included a 0.7- to 1.0-sec scanning time, a 1- to 2-sec interscan delay, and computer-triggered injection of contrast material beginning 10 sec before the start of scanning. No studies were judged to be nondiagnostic; in 90%, image quality was excellent, and in the other 10%, image quality was good. In the arterial phase, 12 tumors (10 hepatocellular carcinomas and two metastases) appeared less dense than the normal liver, and 30 (18 metastases, 11 bile duct or gallbladder carcinomas, one hepatocellular carcinoma) appeared more dense than liver. A statistically significant difference ($p < .05$) was found when time-to-peak enhancement (T) and maximal contrast enhancement (D) of hepatocellular carcinomas were compared with those values for bile duct and gallbladder carcinomas (for hepatocellular carcinomas, $T = 0.33 \pm 0.2$ and $D = 1.2 \pm 0.4$; for bile duct and gallbladder carcinomas, $T = 3.1 \pm 1.8$ and $D = 0.7 \pm 0.2$). A great variability occurred in the T and D values for metastases ($T = 2.3 \pm 2.7$ and $D = 0.55 \pm 0.3$); this variability may be due to the heterogeneity of the primary malignant tumors. These researchers concluded that single-level, subsecond dynamic CT can help differentiate hepatocellular carcinomas from bile duct and gallbladder carcinomas; it cannot, however, distinguish hypervascularized metastases from either hepatocellular carcinomas or bile duct/gallbladder tumors.

In another study of fast, single-level dynamic CT, J. Gaa and colleagues (Municipal Hospital, Darmstadt, West Germany) studied 33 patients who had 38 liver hemangiomas (size range, 0.7–12.0 cm). Their CT technique included a 1-sec scanning speed and a bolus injection of 1 ml/kg of 30% nonionic contrast material. Thirty of the hemangiomas (all <1 cm) showed a characteristic and especially intense nodular enhancement in sharply delimited marginal areas; also noted on these scans was an increased spreading of nodular enhancement for more than 30 sec. These researchers tested these findings by comparing fast, single-level dynamic CT results in 43 liver metastases, five hepatocellular carcinomas, and two cases of focal nodular hyperplasia; they found that the intense nodular enhancement pattern described above was unique to the hemangiomas larger than 1 cm, and they suggest that fast, single-level dynamic CT can reliably differentiate these hemangiomas much faster than other techniques can.

New Contrast Agents for Liver Imaging

Effective, safe contrast agents for use in liver imaging have been an important subject for research in the last several years. After Dr. Stark provided a review of the physiologic principles for design of liver contrast media, John F. Palmer of the FDA gave the participants some very helpful advice about the design of clinical trials for pharmaceutical development. Dr. Palmer emphasized the importance of attention to detail in planning clinical trials of a new contrast material: the FDA does not want to reject a promising new agent because the clinical trials have been poorly executed (on the other hand, the FDA will not approve an ineffective or harmful drug just because the clinical trials have been beautifully executed and reported). Dr. Palmer listed some of the common design flaws in clinical trials of imaging agents: (1) poor chemistry (e.g., insufficient details on the chemistry of the drug); (2) inadequate pharmacology (e.g., lack of clearly specified pharmacology of the agent); (3) absence of care in collecting clear and accurate data on the population studied; (4) incorrect statistical analysis (e.g., invalid or unreliable specificity and sensitivity values); (5) poorly conceived medical objectives, including failure to decide clear objectives early in the process; (6) failure to maintain observer independence, including problems with blinding procedures; (7) unclear interpretation of contrast-enhanced and unenhanced images (e.g., use of words like "normal" or "non-normal" rather than "bright" or "dark"); (8) improper selection of a comparison imaging method or agent; and (9) insufficient numbers of subjects in one or more groups studied.

Dr. Ferrucci presented a lecture on the use of superparamagnetic ferrite particles for contrast enhancement in midfield MR imaging. He began with an interesting historical note: the first experiment in which his group performed ferrite-enhanced MR imaging in rats began exactly 5 years before that lecture (to the day—June 27, 1985). The contrast material consisting of superparamagnetic particles has undergone three name changes since its first appearance in experimental studies; first called *magnetite*, it was later known as *ferrite*, then as *iron oxide*, and now as *superparamagnetic iron oxide* (SPIO). Dr. Ferrucci's group has found that SPIO administration dramatically increased contrast-to-noise ratios (e.g., contrast-to-noise ratios: before SPIO administration, +0.6; after SPIO administration with same MR sequence, +16.3). Lesion conspicuity is also increased by use of SPIO: in a study of 370 lesions by midfield MR imaging, 5.7% of the lesions were seen before SPIO administration, but 88% were seen after contrast administration; among several different midfield imaging sequences, the best detection was 72% before and 94% after administration of contrast material. Furthermore, preliminary studies suggest that the use of SPIO can enable detection of much smaller lesions (0.3–0.4 cm) than is possible with nonenhanced MR imaging. Adverse effects appear to be dose-related (20 μmol Fe/kg body weight, with a 2% rate of adverse reactions, will probably be used in future studies), and studies of SPIO biodegradation rates have shown that 90% of the agent clears the system by 3–5 days after administration. Also important is the effectiveness of SPIO at midfield MR imaging (which is less expensive than high-field MR imaging).

Use of SPIO in high-field MR imaging was discussed by G. Marchal (University Hospitals, Leuven, Belgium). His group used a 1.5-T MR unit to study 15 patients with liver metastases. MR sequences used were intermediate-TR and long-TR spin-echo sequences before and 1 hr after IV injection of 20 μmol/kg of SPIO. Administration of SPIO particles did significantly increase the contrast-to-noise ratio by dramatically decreasing liver signal (e.g., in one sequence, the liver signal-to-noise ratio was 28 before and eight after contrast administration, whereas the tumor signal-to-noise ratio changed only from 28 to 29). However, SPIO administration was not found to significantly improve lesion detection (possibly because of the small number of patients studied). Future use of SPIO with breath-hold, gradient-echo sequences with vascular suppression may well allow improved lesion detection.

Attention *AJR* Contributors

As of October 1, 1990, the editorial office address has changed. The new address is

American Journal of Roentgenology
Editorial Office
2223 Avenida de la Playa, Suite 103
La Jolla, CA 92037
(619) 459-2229

Letters

Canadian National Breast Screening Study

We are grateful for the opportunity to respond to the comments of Dr. Kopans [1] on the Canadian National Breast Screening Study (NBSS). He raises a number of issues.

First, "the discouraging fact that almost 50% of the mammograms obtained during the first 2 years of screening were judged to be *unsatisfactory*," is perceived in a different light if the reader knows that only 5.1% of all NBSS mammograms were produced in the first 2 years of screening. Only five of the eventual 15 centers had opened during that period. Second, "two of the reviewers . . . felt it was the sharpness, contrast, and overall quality of the mammograms that was judged to be poor." This statement must be considered in relation to the actual scores recorded by the reviewers themselves, as displayed in Table 3 of the paper by Baines et al. [2]. Both contrast and image quality clearly improved over time. Third, "The Canadian sites were not required to have 'state-of-the-art equipment.'" In fact, the two largest centers in terms of recruitment, Toronto Mt. Sinai and Winnipeg, which entered the study in 1980 and 1981, respectively, began with new machines. Some later centers began with new equipment, and others acquired new equipment during the course of the study. All had dedicated equipment.

Fourth, "at least two of these advisors, recruited during the early years of the trial, resigned because one was not even permitted to view the images, and the other's recommendation . . . was not heeded earlier." Although Dr. Kopans was informed that only two resigned in disapproval, he chose to imply that more than two resigned. No advisor to the NBSS policy advisory group was ever refused permission to view images. To the contrary, they were invited to view images, and their remarks were shared with all NBSS radiologists. However, it was decided that NBSS mammograms should be reviewed in Toronto only and should not be shipped to the United States on a regular basis because of the risk of loss and also because our designated reference radiologist [3] was monitoring mammograms on a routine basis. It was essential to distinguish the role of the reference radiologist from the role of the advisor to the policy advisory group. As for disregarding recommendations, lengthy correspondence documents the extent to which we attempted to respond to Dr. S. Feig's suggestions. In general, advisors' recommendations reiterated those arising from quality control and audit mechanisms incorporated into the study design [4, 5].

Fifth, we agree with Dr. Kopans that breast cancer mortality in the NBSS will be judged in relation to some intermediated outcome measures expected from effective breast screening programs, such as sensitivity of the screening tests, detection of small invasive tumors, and reduction in advanced breast cancer. However, the Health Insurance Plan (HIP) trial was effective in reducing breast cancer mortality in women who were 50–64 years old on entry to the trial, despite a failure to achieve most of these indicators. Our success in relation to sensitivity of the screening has been reported [6–8]; we plan to publish other indicators later. In the meantime, we offer our cancer detection (Table 1) and interval cancer (Table 2) rates compared with those published for the Breast Cancer Detection Demonstration Project (BCDDP) [9], the only project other than the HIP study with a comparable screening procedure (annual mammography plus physical examination) described in the literature.

Sixth, "the decision to use the then 'current' level of mammographic quality . . . was ill conceived." In practice, we had no alternative. This was the level then accepted by many (including the American College of Radiology and the Canadian Association of Radiologists) as an appropriate basis for decisions on breast-screening policies. It is easy to judge by hindsight. It is ironic that single-view mammography, used in the Swedish two-county study, has now been replaced in Sweden by two-view mammography for the routine screening of women less than 55 years old. The NBSS used two-view mammography (mediolateral and craniocaudal) beginning in 1980, and in 1985 changed the mediolateral view to mediolateral oblique.

Seventh, the radiologists and technologists learned "as they [went] along." Although Dr. Kopans is critical of learning during the study, others might view this favorably. Such learning certainly occurred in the BCDDP, and has been acknowledged in all the European screening projects except the Swedish two-county study. We suspect, in the absence of information to the contrary, that it occurred in the

TABLE 1: Breast Cancers Detected per 1000 Women Screened

Year	Study	Age at Entry (years)			
		40–44	45–49	50–54	55–59
1	BCDDP	2.40	5.10	6.60	7.90
	NBSS	2.18	5.79	6.48	7.96
2	BCDDP	2.10	2.70	3.00	3.60
	NBSS	1.18	2.16	3.41	3.77
3	BCDDP	1.80	2.70	2.70	3.20
	NBSS	1.64	2.29	2.38	2.48
4	BCDDP	1.60	2.80	2.70	3.50
	NBSS	2.27	2.50	3.09	3.07
5	BCDDP	2.00	2.10	2.40	3.20
	NBSS	1.70	1.68	2.06	4.19

Note.—BCDDP = Breast Cancer Detection Demonstration Project; NBSS = National Breast Screening Study. Rates cited are for women allocated to mammography and physical examination of the breasts.

TABLE 2: Interval Cancers per 1000 Women Screened

Interval	Study	Age at entry (years)	
		40–49	50–59
1	BCDDP	0.68	0.93
	NBSS	0.86	0.88
2	BCDDP	0.80	0.94
	NBSS	0.78	0.71
3	BCDDP	0.82	0.84
	NBSS	0.40	0.52
4	BCDDP	0.86	0.85
	NBSS	0.58	0.61

Note.—BCDDP = Breast Cancer Detection Demonstration Project; NBSS = National Breast Screening Study. Rates cited are for women allocated to mammography and physical examination of the breasts.

Swedish two-county trial as well. As for the currently available accreditation and special training programs Dr. Kopans alludes to, they simply had not been started when the NBSS began. However, in response to a suggestion made by Dr. Feig, the NBSS invited Dr. L. Tabar in 1985 to meet with NBSS radiologists, who benefited from his inspired teaching.

The experience in the NBSS has been invaluable in pointing the way to the quality-control measures that must be built into screening programs. In the past, Canada accepted the challenge for evaluating screening recommended in the review of the BCDDP [10], a challenge rejected in the United States [11]. Canada continues to accept the challenge [12]. Before our findings are rejected, perhaps one should wait to see what NBSS breast cancer mortality results are.

A. B. Miller
C. J. Baines
E. A. Sickles
National Breast Screening Study
Toronto, Ontario, Canada M5S 1A8

REFERENCES

1. Kopans D. The Canadian screening program: a different perspective. *AJR* **1990**;155:748–750
2. Baines CJ, Miller AB, Kopans DB, et al. Canadian National Breast Screening Study: assessment of technical quality by external review. *AJR* **1990**;155:743–747
3. Baines CJ, McFarlane DV, Miller AB. The role of the reference radiologist in the Canadian National Breast Screening Study. *Invest Radiol* **1990**;25:971–976
4. Yaffe MJ, Mawdsley GE, Nishikawa RM. Quality assurance in a national breast screening study. *Soc Photo-optical Instrum Eng* **1983**;419:23–30
5. Baines CJ, McFarlane DV, Wall C. Audit procedures in the National Breast Screening Study: mammography interpretation. *Can Assoc Radiol J* **1986**;39:256–260
6. Baines CJ, Miller AB, Wall C, et al. Sensitivity and specificity of first screen mammography in the Canadian National Breast Screening Study: a preliminary report from five centres. *Radiology* **1986**;160:295–298
7. Baines CJ, McFarlane DV, Miller AB et al. Sensitivity and specificity of first screen mammography in 15 NBSS centres. *Can Assoc Radiol J* **1988**;39:273–276
8. Baines CJ, Miller AB, Bassett AA. Physical examination: its role as a single screening modality in the Canadian National Breast Screening Study. *Cancer* **1989**;63:1816–1822
9. Baker L. Breast Cancer Detection Demonstration Project: five-year summary report. *CA* **1982**;32:194–225
10. Beahrs O, Shapiro S, Smart C. Report of the Working Group to Review the National Cancer Institute American Cancer Society Breast Cancer Detection Demonstration projects. *J Natl Cancer Inst* **1979**;62:640–709
11. Thier SO. Breast cancer screening: a view from outside the controversy. *N Engl J Med* **1977**;297:1063–1065
12. The Workshop Group. Reducing deaths from breast cancer in Canada. *Can Med Assoc J* **1989**;141:199–201

The Radiologist, the Dictating Machine, and Transmission of Rhinovirus

The dictating machine is a necessity in the daily routine of radiologists, who must dictate reports in a timely manner. The handpiece of the machine must be grasped and placed near the mouth so that all words on the tape can be heard clearly by the transcriptionist. At times, the handpiece may be held in such a way that it comes in contact with the lips and mucosal surfaces of the mouth of the person dictating. Holding the handpiece this way is common and inadvertent, especially during pensive moments when the person dictating is studying radiographs. In addition, skin contact is made between the handpiece and the dictator's hand. These common maneuvers are excellent means for the spread of rhinoviruses, the agents most often associated with common colds.

The amount of virus shed by the donor, the length of time the recipient has contact with the virus, and the severity of the donor's signs and symptoms are important factors in the transmission of rhinoviruses [1]. Transmission from infected to susceptible persons under natural conditions may occur by transfer from the hands of an infected person to an intermediary surface or directly to the fingers of the susceptible recipient [2]. Infection results from self-inoculation of the eyes or nose with virus that is present on the fingers. The virus can be spread by aerosol, direct contact, or indirect contact with environmental objects [3]. It can be recovered from the fingers of persons with experimental and natural infections and from objects in the homes of persons who have colds. It can survive on various surfaces for hours, with subsequent hand-to-face contact during a person's daily routine. Hendley et al. [2] showed efficient fomite transmission via holding coffee cup handles or rubbing plastic tiles contaminated with fresh nasal secretions.

Measures to eliminate or reduce viral contamination of skin and environmental surfaces may be useful in interrupting viral spread between members of the health professions. We recommend several procedures that can be used in the workplace. We found that a plastic or paper condom, such as a plastic "baggy" or "surgical booty," placed over the handpiece of the dictating machine does not interfere with the transmission of sound or the use of hand controls. The covering is disposed of after the dictation is completed. This method is cost-effective and easily executed. Another method is to have each dictator carry a personal detachable mouthpiece that attaches to the base unit or simply carry a portable hand-held dictating machine. Several other methods have been described. Treatment of areas with a phenol/alcohol spray disinfectant was moderately effective in reducing viral contamination of fingers, but did not eliminate viral contamination completely [4]. Aqueous iodine (2%) applied to the hands was effective in blocking hand-contact transmission of experimental rhinovirus infection for up to 2 hr after application of the iodine solution to the hands [5].

We think that every effort must be made to maintain sanitary conditions in the workplace. Our goal is to shed light on a commonly used device that has significant impact on the health profession.

Perry Gerard
Ronald Frank
Anne Marie Mercanti
Edward Chapnick
Maimonides Medical Center
Brooklyn, NY 11219

REFERENCES

1. D'Alessio DJ, Meschievitz CK, Peterson JA, Dick CR, Dick EC. Short-duration exposure and the transmission of rhinoviral colds. *J Infect Dis* **1984**;150:189–194

2. Hendley JO, Wenzel RP, Gwaltney JM Jr. Transmission of rhinovirus colds by self-inoculation. *N Engl J Med* **1973**;288:1361–1364
3. Dick EC, Jennings LC, Mink KA, Wartgow CD, Inhorn SL. Aerosol transmission of rhinovirus colds. *J Infect Dis* **1987**;156:442–448
4. Gwaltney JM Jr, Hendley JO. Transmission of experimental rhinovirus infection by contaminated surfaces. *Am J Epidemiol* **1982**;116:828–833
5. Gwaltney JM Jr, Moskalski PB, Hendley JO. Interruption of experimental rhinovirus transmission. *J Infect Dis* **1980**;142:811–815

Atypical Distribution of Bacterial Pneumonia After Thoracic Radiation Therapy

Pulmonary infiltrates developing in patients with primary lung cancer can be the result of infection, neoplasm, or reaction to radiation or chemotherapy. The radiologic features of radiation pneumonitis are characteristic. Nonsegmental infiltrates with sharply marginated borders corresponding to the radiation portal usually occur several months after radiation therapy. We describe two patients with lung cancer in whom bacterial pneumonia confined to the nonirradiated parts of the lungs developed shortly after thoracic radiotherapy, as if the irradiated parts of the lung were protected by the irradiation.

The first patient was a 59-year-old woman with small-cell lung cancer of the bronchus of the right upper lobe (clinical stage, T4N2M1). She was treated with doxorubicin, cisplatin, and etoposide. One year later, the cancer recurred at the primary site. She had radiation therapy consisting of 50 Gy to the primary site and right hilum. Six days after completion of the treatment, alveolar infiltrates confined to the part of the lung not included in the radiotherapy appeared (Fig. 1A). Methicillin-resistant *Staphylococcus aureus* was detected in laryngopharyngeal aspirates. She was treated with antibiotics, and the infiltrates disappeared within 2 weeks.

The second patient was a 59-year-old man with squamous-cell lung cancer of the left lower lobe (clinical stage, T4N2M0). He was treated with 5-fluorouracil, cisplatin, and etoposide. Because the chemotherapy was not effective, he received radiation therapy consisting of 28 Gy to the primary site and left hilum. After irradiation, an esophageal bypass operation was performed to relieve severe dysphagia. Ten days after the operation, a chest radiograph showed alveolar infiltrates confined to the part of the left lung not included in the radiation portal (Fig. 1B). *Pseudomonas aeruginosa* was detected in the sputum. Despite antibiotic therapy, the patient died.

In both patients, within 2 weeks of completion of radiation therapy, bacterial pneumonia occurred in portions of the lung that had not been irradiated. A similar pattern has been described in patients given mediastinal radiation therapy in whom *Pneumocystis carinii* pneumonia develops [1–3]. Although the usual radiologic appearance of *Pneumocystis* pneumonia is perihilar infiltrates with peripheral clearing, in patients given radiation therapy, the infiltrates may not occur in the irradiated region, and only peripheral infiltrates are seen [3]. In addition, the term "reverse radiation pneumonitis" was used recently to describe pneumonia carcinomatosa, which occurs only outside the irradiated field [4]. The findings in our cases suggest that the distribution of bacterial pneumonia also can be altered by radiation therapy.

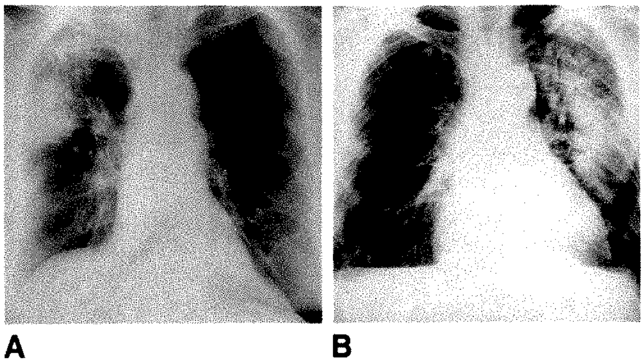

Fig. 1.—*A* and *B*, Chest radiographs of two patients show peripheral alveolar infiltrates that developed after radiation therapy for lung cancer. Infiltrates are confined to nonirradiated part of lungs: right upper lung in *A* and left lung in *B*.

Jiro Fujita
Masami Bungo
Hiroyuki Nakamura
Yasufumi Yamaji
Yuuki Hata
Taiichi Shiotani
Shozo Irino
Kagawa Medical School
Kagawa, 761-07, Japan

REFERENCES

1. Forrest JV. Radiographic findings in *Pneumocystis carinii* pneumonia. *Radiology* **1972**;103:539–544
2. Doppman JL, Geelhoed GW. Atypical radiographic features in *Pneumocystis carinii* pneumonia. *Natl Cancer Inst Monogr* **1976**;43:89–97
3. Panicek DM, Groskin SA, Chung CT, Heinzman ER, Sagerman RH. Atypical distribution of *Pneumocystis carinii* infiltrates during radiation therapy. *Radiology* **1987**;163:689–690
4. Adelstein DJ, Padhya T, Tomashefski JF, Park C. Pneumonia carcinomatosa from small cell undifferentiated carcinoma of the lung presenting as "reverse radiation pneumonitis." *Med Pediatr Oncol* **1988**;16:280–283

Interlobar Pneumothorax

We report a case of interlobar pneumothorax in a patient with bronchial asthma. A 54-year-old man with a history of asthma was admitted for treatment of right-sided pneumothorax of 1-day duration. Physical examination showed mild wheeze throughout both lungs, and a chest radiograph showed right-sided pneumothorax. Chest radiographs obtained 2 days later showed atelectasis of the right upper lobe, and 7 days later, atelectasis of the right middle and lower lobes was observed. Aspiration of mucous secretions via fiberoptic bronchoscopy relieved the atelectasis.

Eighteen days after the aspiration, the patient complained of additional chest discomfort. A frontal chest radiograph showed an

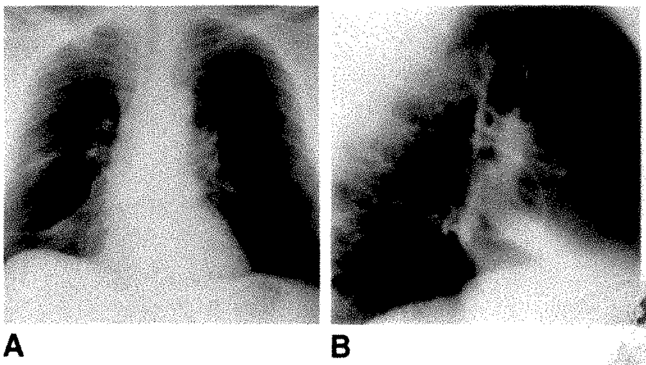

Fig. 1.—*A* and *B*, Frontal (*A*) and lateral (*B*) radiographs of lung show oval gas collection in right major fissure.

oval, radiolucent area in the region of the right major fissure (Fig. 1A). Lateral radiograph (Fig. 1B), tomogram, and CT scan showed that the radiolucency was located in the interlobar space. The air collection was considered to be an interlobar pneumothorax because of its shape and location and because no similar abnormality had been noted earlier when the pneumothorax was evident. Subsequently, an air-fluid level appeared in that space and gradually filled with fluid. A follow-up radiograph made 3 months later was normal.

Interlobar pneumothorax is extremely rare [1, 2]. Pleural adhesions are thought to cause the unusual loculation of air, but in our case, the presence of air in the pleural space on the initial radiographs appears to exclude this possibility. Adhesions may have developed in the interim.

Atsushi Watanabe
Kaoru Shimokata
Fumio Nomura
Hideo Saka
Nagoya University School of Medicine
Nagoya 466, Japan
Shuzo Sakai
Japanese Red Cross Nagoya First Hospital
Nagoya 453, Japan

REFERENCES

1. Vincent M, Tourville O, Beguier M, Brune J. Pneumothorax inter-lobaire. *Rev Pneumol Clin* **1984**;40:7–11
2. Bildstein F, Dalphin JC, Clement F, Coche G, Depierre A, Chanois AM. Pneumothorax interlobaire. *Rev Mal Respir* **1988**;5:407–408

Metastatic Anaplastic Thyroid Carcinoma to the Right Ventricle of the Heart

A 46-year-old woman had had increasing shortness of breath. Two years before this admission she had had a partial thyroidectomy for a stage III mixed anaplastic (mostly giant-cell) and follicular carcinoma. She was treated with postoperative irradiation to her neck.

Physical examination revealed the absence of a right thyroid gland. Cardiovascular examination was significant for a regular tachycardic rate and a grade III/VI holosystolic murmur at the left sternal border radiating throughout the precordium. Analysis of blood gases showed a pH of 7.48, P_{CO_2} of 28 mm Hg, and P_{O_2} of 56 mm Hg. Pulmonary function tests were normal. Chest radiograph was interpreted as showing left atrial and ventricular enlargement. An echocardiogram showed right-sided enlargement of the heart, an echogenic mass in the right ventricular apex, and tricuspid regurgitation. A CT scan showed right atrial and right ventricular enlargement and a mass in the right ventricular outflow tract extending into the pulmonary artery (Fig. 1). The patient had surgery for tumor debulking and closure of a patent foramen ovale. At surgery, a large mass in the right ventricle was seen extending into the pulmonary artery. The final pathologic examination showed anaplastic thyroid carcinoma. The patient declined further therapy.

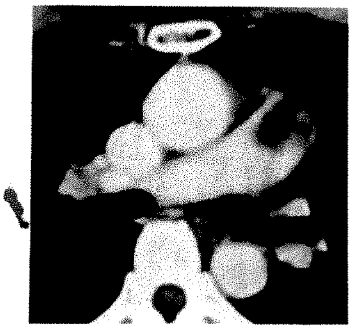

Fig. 1.—CT scan shows filling defect in right ventricle extending into pulmonary artery.

This is the only reported case that we are aware of that describes radiologic findings of metastatic thyroid carcinoma to the heart. Three cases of metastatic thyroid carcinoma to the right cardiac ventricle have been reported [1–3]. CT examination was helpful in our case in evaluating the mass detected by echocardiography. The differential diagnosis at the time of the CT included thrombus, metastatic tumor, and, less likely, a primary cardiac tumor. The chest radiograph was deceiving and appeared to show left atrial and ventricular enlargement. The CT showed that the apparent left-sided enlargement of the heart was the result of posterior displacement by the enlarged right ventricle with the intraventricular mass. Hara et al. [1] discuss a similar case in which echocardiography and CT were used to show the cardiac effects of metastatic carcinoma of the thyroid.

Michael F. Haggerty
Thomas M. Murphy
Tripler Army Medical Center
Honolulu, HI 96859-5000

REFERENCES

1. Hara K, Ohno M, Takenaga M, et al. Metastatic thyroid cancer to the right ventricle causing obstruction of the right ventricular outflow tract and associated with disseminated intravascular coagulopathy: a case report. *J Cardiogr* **1986**;16:765–773
2. Lind T, Jensen F, Petri C. Anaplastic carcinoma of the thyroid with metastases to the right cardiac ventricle. *Ugeskr Laeger* **1986**;148:1684–1685
3. Tolkacheva GA, Vasilyev SA, Kobozev VM, Balyaeva GP. A rare case of metastases of poorly differentiated thyroid carcinoma to the heart. *Ter Arkh* **1983**;55:107–109

Chest CT Scan Before Transplantation

In a recent issue of *AJR*, Carlsen and Bergin [1] reported a case of fatal reactivation of tuberculosis in a donor lung after it had been transplanted. Although organ transplantation is becoming more commonplace, and the overall results have improved markedly, infection remains an important cause of morbidity and mortality in transplant recipients.

A wide variety of approaches has been used to prevent infections associated with transplantation, including laboratory tests and radiologic examination of the recipient and use of antimicrobial prophylactic regimens after transplantation. The imaging examinations recommended in the protocol used at the University of Minnesota for recipients of renal transplants include chest radiographs, oral cholecystography, voiding cystourethrography, and upper gastrointestinal series. The need to examine the recipient for tuberculosis is questionable [2].

The reported prevalence of mycobacterial infection in renal transplant recipients is in the range of 0.65% to 1.7%, with relatively poor outcome because of uncontrolled infection. This rate is relatively low, but it is higher than would be expected in the general population in the United States [3].

We recommend that in areas where histoplasmosis and sarcoidosis are not endemic, every renal transplant recipient should have a routine chest CT scan before transplantation whenever the recipient's chest radiograph is normal and a tuberculin skin test is negative. As CT is better than plain radiographs for detecting pulmonary parenchymal changes and mediastinal and hilar calcified lymph nodes, the detection of such entities in these high-risk patients may indicate the need for prophylactic antituberculous therapy [4].

We think that because CT is noninvasive and easy to perform and does give additional contributing information, it is worthwhile to include it in the workup of transplant recipients before transplantation.

R. Zissin
M. Shapiro
Meir General Hospital
Kfar Saba, Israel

REFERENCES

1. Carlsen SE, Bergin CJ. Reactivation of tuberculosis in a donor lung after transplantation. *AJR* **1990**;154:495–497
2. Migliori RJ, Simmons RL. Infection prophylaxis after organ transplantation. *Transplant Proc* **1988**;20:395–399
3. Lloveras J, Peterson PK, Simmons RL, Najarian JS. Mycobacterial infections in renal transplant recipients. *Arch Intern Med* **1982**;142:888–892
4. Warren JB, Kreel L, Johnson NM, NcNicol MW. Use of computed tomography to demonstrate the extent of tuberculosis. *CT* **1981**;5:312–315

Reply

We appreciate the comments of Drs. Zissin and Shapiro on obtaining chest CT scans routinely in potential organ transplant recipients. We agree that CT noninvasively gives additional worthwhile information. The use of chest CT in screening for previous tuberculosis probably will have a different role in different types of organ transplantation.

The risk of transplanting an organ such as the lung, which may contain the tubercle bacillus, into a recipient who has no resistance to tuberculosis, and who will undergo immunosuppression, poses a unique problem compared with the risks of transplanting other organs. For organs other than the lung, skin testing with purified protein derivative as a screening procedure for tuberculosis is strongly recommended as a precaution in transplant recipients who will have to be immunosuppressed. The cost-effectiveness of using chest CT as a further screening procedure would depend on the prevalence of false-negative results when the skin test is used. In patients who are anergic, CT would be a useful addition to screen for calcified mediastinal or hilar lymph nodes or parenchymal abnormalities compatible with previous tuberculous disease. In patients with a negative skin test, who are not anergic, the usefulness of screening chest CT is questionable. In such patients, calcified lymph nodes may indicate granulomatous disease other than tuberculosis.

In lung transplantation, CT screening of the recipient's lungs before transplantation would not be indicated, but chest CT after transplantation would be useful to look for evidence of granulomatous disease transplanted into the patient, particularly if the recipient previously had a negative skin test. In transplant recipients who receive only one lung, perhaps preoperative screening may have a role.

Sandra E. Carlsen
Colleen J. Bergin
Stanford University School of Medicine
Stanford, CA 94305

Intraperitoneal Bile Leakage After Cholecystectomy

Accurate evaluation of the source of a bile leak after cholecystectomy is difficult. Sometimes, as in the following case, it is, in fact, impossible. Failure to find the source of bile leakage was encountered in 12 of the 20 cases of bile peritonitis reported by McKenzie [1]. We report another such case.

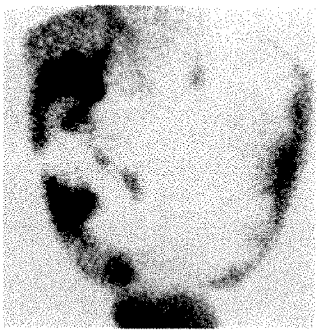

Fig. 1.—HIDA scan shows free biliary leakage into peritoneal cavity after cholecystectomy.

A 28-year-old woman had clinical signs and symptoms of acute cholecystitis. A sonogram showed the gallbladder had a thickened wall and contained multiple small stones. A small fluid collection around the gallbladder also was present. An HIDA scan confirmed obstruction of the cystic duct. Cholecystectomy was performed, and the wound was closed without drainage.

On the third postoperative day, the patient had severe upper abdominal pain accompanied by tenderness with guarding. Her temperature spiked at 102°F (38.9°C). An HIDA scan (Fig. 1) showed that the tracer material had collected in Morrison pouch and in the peritoneal cavity but did not show the site of the leak. An emergency ERCP was attempted, but the patient could not tolerate the procedure. Exploratory laparotomy was undertaken.

At surgery, 1.6 l of bile was found in the peritoneal cavity. A thorough attempt was made to find the source of the leak. The cystic duct ligature was intact as were the ligatures on the common bile duct and the hepatic duct. The fossa of the gallbladder was dry, and no biliary seepage was noted at that site. Furthermore, intraoperative cholangiography did not detect a site of biliary leakage. Choledochostomy was performed, and a T-tube was inserted. After surgery, about 25 to 30 ml of bile was collected for 2 days via a Jackson-Pratt drain in Morrison pouch; after the third day, no drainage occurred. On the sixth postoperative day, a T-tube cholangiogram showed a normal biliary tree without any leak. The T-tube was removed on the 10th day, and the patient was discharged.

This case emphasizes the difficulties of finding the precise source of a biliary leak. Although HIDA scanning is the best means of determining that a leak is present, it cannot localize its source. T-tube drainage of the common bile duct can be useful if the source of a leak cannot be identified.

Virendra Parikh
Sanjay Shah
Shihan Kim
Eugen Albu
Paul H. Gerst
Bronx-Lebanon Hospital Center
Bronx, NY 10457

REFERENCE

1. McKenzie G. Extravasation of bile after operation on biliary tract. *Aust NZ J Surg* **1954**;24:131–136

Pedunculated Hepatic Hemangioma: CT Findings

A 71-year-old man had his regular follow-up examination 6 months after surgery for an adenocarcinoma of the cecum. Increased levels of carcinoembryonic antigen prompted a CT study, which showed a

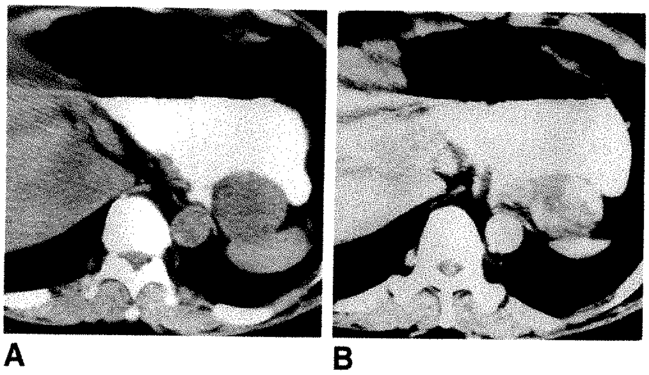

Fig. 1.—Pedunculated hepatic hemangioma.

A, Unenhanced CT scan shows soft-tissue mass in retrogastric region with an attenuation slightly less than that of liver.

B, CT scan obtained approximately 1 min after bolus injection of contrast material shows patchy nodular enhancement.

well-defined mass in the retrogastric region (Fig. 1A). The attenuation value of the mass was less than that of the hepatic parenchyma. CT after administration of contrast material showed nodular peripheral enhancement in the mass. A few clefts of unenhanced areas were evident (Fig. 1B). Surgery and histopathologic examination showed a pedunculated cavernous hepatic hemangioma in the retrogastric region. The tumor was adjacent to the posterior gastric wall, which was, however, uninvolved. The pedicle arose from the inferior surface of the left lobe of the liver.

Large hemangiomas may sag from the liver and form a pedicle [1]. The CT findings of a pedunculated hemangioma are similar to those of the usual hepatic hemangioma, with dense peripheral enhancement occurring in the early phase of bolus contrast study. Barnett et al. [2] postulated that the edge enhancement is produced by a combination of filling of vascular lakes and compressed hepatic parenchyma. The pedunculated hemangioma in our case showed edge enhancement, as did one in a case reported by Ellis et al. [3]. Both these cases show that compression of hepatic parenchyma does not contribute to edge enhancement as postulated by Barnett et al. [2].

Vipul P. Parikh
Ganesh N. Iyer
Tata Memorial Hospital
Parel, Bombay, 400 012, India

REFERENCES

1. Foster JH. Benign liver tumors. In: Blumgart LH, ed. *Surgery of liver and biliary tract.* Edinburgh, Churchill Livingstone, **1988**:1115–1127
2. Barnett PH, Zerhouni EA, White RI Jr, Siegelman SS. Computed tomography in the diagnosis of cavernous hemangioma of the liver. *AJR* **1980**;134:439–447
3. Ellis JV, Salazare JE, Gavant ML. Pedunculated hepatic hemangioma: an unusual case for anteriorly displaced retroperitoneal fat. *J Ultrasound Med* **1985**;4:623–624

Positional Hypoechoic Pseudolesions on Transrectal Sonography of the Prostate

Several sonographic-pathologic correlation studies have shown that early prostatic cancer is hypoechoic on sonograms in most patients [1, 2]. We report a hypoechoic artifact seen within the peripheral zone of the prostate that is related to positional changes and that creates the appearance of a lesion.

We used transrectal sonography to examine a large series of patients with biopsy-proved prostatic cancer before prostatectomy to evaluate the role of this procedure in preoperative staging. All examinations were performed with the patient in the left lateral decubitus, knee-chest position, and state-of-the-art, high-frequency endorectal probes were used. We noticed in several patients that hypoechoic lesions seen most often in the left peripheral zone did not correspond to tumor or any other abnormality on the pathologic step sections. We subsequently imaged all patients in whom we observed similar findings in a right-sided decubitus position to evaluate persistence or disappearance of these hypoechoic areas. We found that in a large number of patients, the left-sided hypoechoic areas disappeared when the patient was imaged in the opposite decubitus position.

Lesions with this characteristic often were easy to recognize because of their geographic nature. They involved a portion of the left posterior and anterior lobe, and the demarcation between the hypoechoic area and the remainder of the gland was sharp and linear (Figs. 1A and 1B). True hypoechoic left-sided prostatic cancers did not change their appearance when the opposite decubitus position was used for imaging and often showed an additional bulge without a linear geographic demarcation toward the remaining gland. Sometimes an overlap of the two echopatterns (tumor plus gravity-dependent artifact) was noted; however, the hypoechoic tumor nodule always persisted when the opposite decubitus position was used (Figs. 1C and 1D).

Artifacts should be recognized easily because of their linear demarcation toward the medial part and right side of the gland, their disappearance with positional changes (either opposite decubitus or

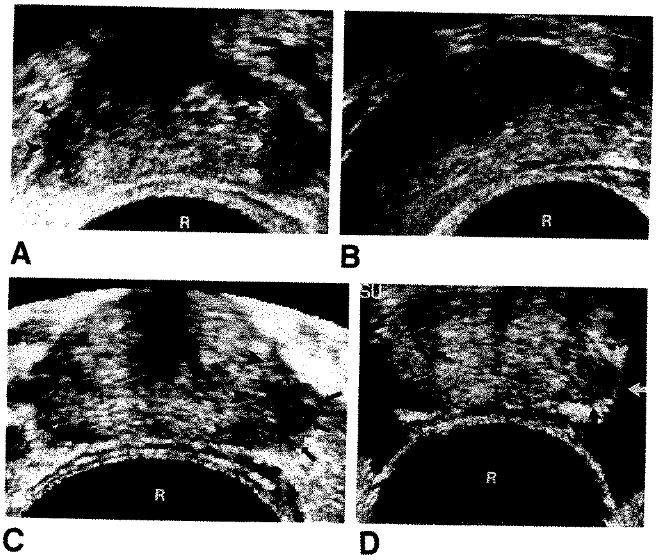

Fig. 1.—Artifact associated with body position of patient during transrectal sonography of prostate gland. R = rectum.

A and *B*, Pseudolesion. Sonogram (*A*) obtained with patient in left lateral decubitus position shows hypoechoic lesion in left peripheral zone (*arrows*) with anterolateral extension. Note geographic distribution; a carcinoma (*arrowheads*) is present on right side. Sonogram (*B*) obtained with patient in right lateral decubitus position shows complete disappearance of left pseudolesion.

C and *D*, Tumor. Sonogram (*C*) obtained with patient in left lateral decubitus position shows left-sided hypoechoic mass with lateral bulge (*arrows*) and sharp medial demarcation (*arrowheads*). Sonogram (*D*) obtained with patient in right lateral decubitus position shows decrease in size of lesion and loss of sharp medial border. Note persistence of tumor bulge laterally (*arrows*). Mass was adenocarcinoma.

lithotomy position), and their lack of focal volume increase or tumor bulge. Recognition of a left-sided lesion with these characteristics within the peripheral zone should prompt further evaluation of the gland after the patient changes position.

Ulrike M. Hamper
Sheila Sheth
Barbara L. Savader
The Johns Hopkins Medical Institutions, Baltimore, MD 21205

Supported in part by a grant from the NCI U01-CA-45202, RDOGI.

REFERENCES

1. Dahnert WF, Hamper UM, Eggleston JC, Walsh PC, Sanders RC. Prostatic evaluation by transrectal sonography with histopathologic correlation: the echopenic appearance of early carcinoma. *Radiology* **1986**;158:97-102
2. Lee F, Gray JM, McLeary RD, et al. Prostatic evaluation by transrectal sonography: criteria for diagnosis of early carcinoma. *Radiology* **1986**;158:91-95

Inverted Layering of Contrast Material and Urine in the Bladder on CT: Sonographic Correlation

CT nicely depicts fluid-fluid levels in the urinary bladder after IV injection of contrast material. The high specific gravity of the contrast material accounts for its layering in the dependent part of the bladder. Savit and Udis [1] reported "upside-down" layering of contrast material in the bladder of a patient who had non-insulin-dependent diabetes. This inverted layering was attributed to the high specific gravity of the urine caused by glycosuria.

In the past year, we have observed five cases of inverted layering of contrast material and urine in the bladder on contrast-enhanced CT (Fig. 1). In four cases, sonography was performed immediately after CT. In three patients who were not diabetic, sonograms showed intravesical sediment (Fig. 1C). The layered material was finely echoic and moved as the patient changed body position. Microscopic examination of the urine showed cellular debris mixed with fibrin. In the fourth patient, who was diabetic, sonograms did not show any abnormality in the bladder, and urinalysis showed glycosuria. In this case, the inverted layering of contrast material and urine seen on CT was attributed to the high specific gravity of the urine caused by glycosuria. No sonogram was obtained in the fifth case. The patient had diabetes, so the inverted layering on CT was assumed to be due to the high specific gravity of the urine. The CT features of the inverted layering were identical in both categories of patients (diabetes vs no diabetes). Thus, no CT sign established the origin of the abnormality.

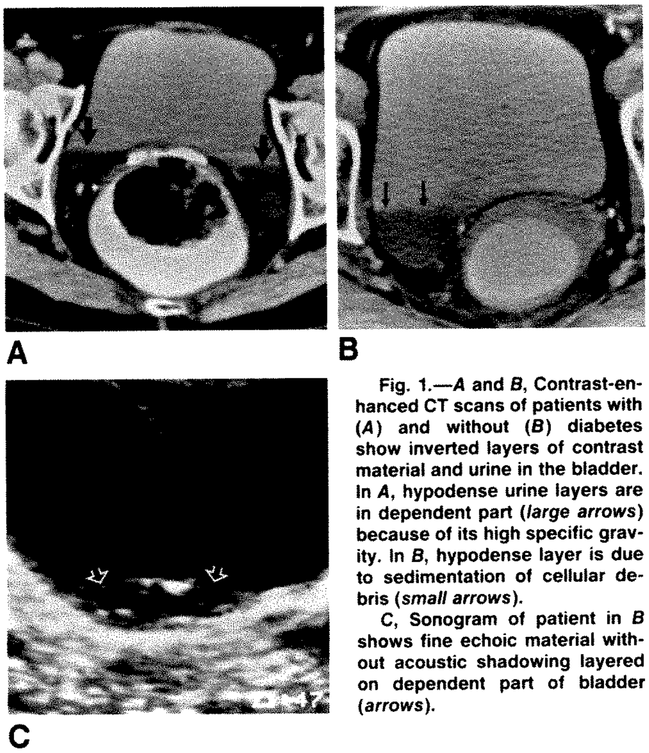

Fig. 1.—*A* and *B*, Contrast-enhanced CT scans of patients with (*A*) and without (*B*) diabetes show inverted layers of contrast material and urine in the bladder. In *A*, hypodense urine layers are in dependent part (*large arrows*) because of its high specific gravity. In *B*, hypodense layer is due to sedimentation of cellular debris (*small arrows*).

***C*, Sonogram of patient in *B* shows fine echoic material without acoustic shadowing layered on dependent part of bladder (*arrows*).**

Gadopentetate dimeglumine that collects in the bladder of a supine patient during MR imaging shows three defined layers, which are seen on both T1- and T2-weighted images [2]. This layering is actually artifactual; it is caused by high early concentration of excreted contrast material in the urine.

Although rare, inverted layering of contrast material and urine on contrast-enhanced CT should not be misdiagnosed or considered an artifact. Glycosuria in diabetic patients is a known cause of this phenomenon [1]. Sedimentation of cellular debris is another, more frequent, cause. Differentiation of both conditions is possible with sonography.

Bertrand Duvoisin
Dominique Fournier
University Hospital, CHUV
1011 Lausanne, Switzerland

REFERENCES

1. Savit RM, Udis DS. "Upside-down" contrast-urine level in glycosuria: CT features. *J Comput Assist Tomogr* **1987**;11:911-912
2. Elster AD, Sobol WT, Hinson WH. Pseudolayering of Gd-DTPA in the urinary bladder. *Radiology* **1990**;174:379-381

Retroperitoneal Extraskeletal Osteosarcoma

A 44-year-old man had had progressive pain in the left upper abdomen for 3 months. Serum alkaline phosphatase was 175 units/l and γ-glutamyl transferase was 39 units/l. Excretory urography showed a calcified mass that indented the upper pole of the left kidney. Plain abdominal CT showed a large and irregular calcified mass in the left retroperitoneum (Fig. 1A) that could not be delineated from the adrenal gland, kidney, stomach, or spleen. No involvement of adjacent bones was seen. Angiography showed an avascular mass (Fig. 1B). Technetium-99m bone scintigraphy showed increased uptake of radionuclide in the tumor and in multiple lesions in the lungs. Chest radiography showed multiple pulmonary metastases. The clinical diagnosis of a calcified adrenal tumor was considered. Results of percutaneous biopsies were repeatedly normal. At laparotomy, a large unresectable extraperitoneal mass was found that could not be separated from the left kidney, stomach, and spleen. Histopathologic examination showed well-differentiated bone-forming tissue, with mostly fine branching and foci of coarse trabecular formation of osteoid and bone. Around the edges were many polymorphous and partly multinucleated giant cells. No vascular pattern was prominent, and other components of the tumor could not be identified. On immunohistochemical staining, the tumor cells were positive for vementin and negative for keratin and other epithelial markers. A malignant bone-forming tumor or extraskeletal osteosarcoma was suggested. Follow-up CT showed rapid progression of the tumor and pulmonary metastases with an increase in the calcifications (Figs. 1C and 1D).

Primary extraskeletal osteogenic sarcoma of the soft tissues is a highly malignant neoplasm that accounts for approximately 1.2% of

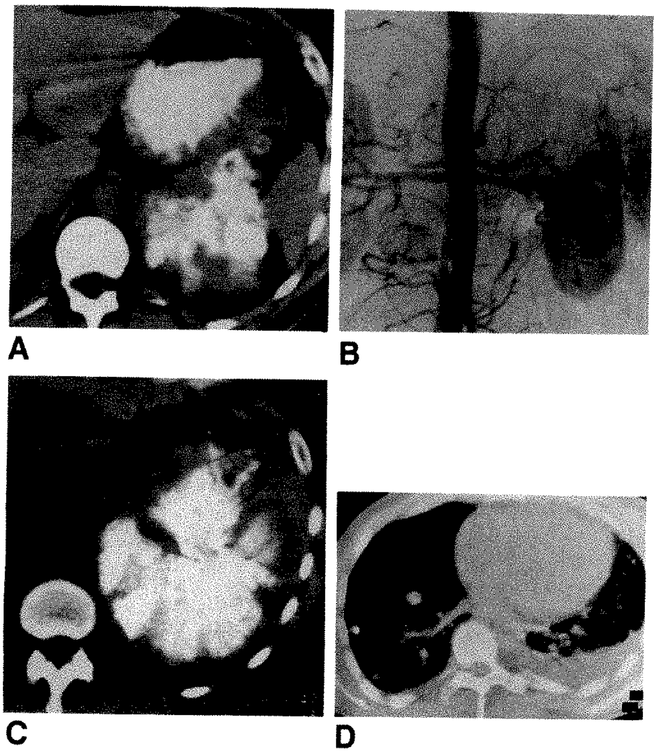

Fig. 1.—Retroperitoneal extraskeletal osteosarcoma.

***A*, Abdominal CT scan shows large calcified mass in retroperitoneum.**

***B*, Angiogram shows an avascular tumor and compression of upper pole of left kidney. Splenic artery is stretched and displaced cranially.**

***C* and *D*, Follow-up CT scans of abdomen (*C*) and lungs (*D*) show progression of tumor mass with calcifications of bone density (*C*) and multiple calcified metastases. Pleural effusion is result of surgery.**

all soft-tissue sarcomas and approximately 4% of all osteosarcomas [1, 2]. Although seen most frequently in patients in their fourth and fifth decades, it may occur at any age. This is unlike osteogenic sarcoma of bone, which usually is seen in children and adolescents. Common locations are the soft tissues of the lower extremities (47%) and the upper extremities (21%); less common are the breast, soft tissues of the face and trunk, and the retroperitoneum (17%) [2].

Radiologically, the tumors are usually large with spotty to massive calcifications. Especially in the retroperitoneum, they become large and bulky. None of the reported cases had evidence of bone involvement [2]. Angiographically they are usually highly vascular, in contrast to our case. CT in our case and in other cases showed a mass lesion with large calcifications scattered through the tumor [2]. An additional finding in our case was multiple calcified pulmonary metastases. This has not been reported before [1–3]. Osteosarcoma has a variable macroscopic appearance, depending on the main components of the tumor. Mostly it is firm to stony on palpation. The cut surface is granular white or partly yellow. Hemorrhage and necrosis are common. Microscopically the tumor shows neoplastic formation of osteoid and bone. In many cases, neoplastic cartilage and fibroblastic tissue are present also. These sarcomas usually are recognized as malignant bone-producing or cartilage-producing tumors. The relative amount of neoplastic tissue varies greatly [4].

The tumor should be distinguished from several benign and malignant processes that show bone formation. The most important benign conditions are exuberant fracture callus, posttraumatic calcified hematoma, and myositis ossificans. Malignant tumors that can have formation of bone are synovial sarcoma, epithelioid sarcoma, malignant fibrous histiocytoma, liposarcoma, and many other mesenchymal and epithelial tumors. When biopsy specimens are small, differential diagnosis between osteosarcoma and myositis ossificans can be difficult and sometimes impossible. Because of the invasive growth pattern and the formation of metastases, we think that in our case this diagnosis can be excluded. Distinction from parosteal osteosarcoma is usually clear on the radiographs, which show typical involvement of the adjacent bone.

Frank J. H. Wesseling
Richenel T. O. Tjon A Tham
Willem Breed
Paul J. J. M. Klinkhamer
Catharina Ziekenhuis and PAMM
5602 ZA Eindhoven, the Netherlands

REFERENCES

1. Sordillo PP, Hajdu SI, Magill GB, Golbey RB. Extraosseous osteogenic sarcoma. *Cancer* **1983**;51:727–734
2. Chung EB, Enzinger FM. Extraskeletal osteosarcoma. *Cancer* **1987**;60:1132–1142
3. Spjut HJ, Dorfman HD, Fechner RE, Ackerman LV, eds. *Tumors of bone and cartilage*. Washington, DC: Armed Forces Institute of Pathology, **1983**:166
4. Enzinger FM, Weiss SW. Soft tissue tumors. St. Louis: Mosby, **1988**: 892–905

Stress Fracture of the Acromion

Fatigue-type stress fractures are common among military recruits, athletes, joggers, and dancers. They occur mainly in the lower extremities but also in the lumbar spine and pelvis. Similar fractures involving the shoulder girdle and upper extremities are less common [1]. To our knowledge, this is the first report of a fatigue-type stress fracture of the acromion process of the scapula.

The patient was a 28-year-old offensive lineman for a professional football team. His training included daily weight-lifting sessions and repetitive blocking drills against other players and blocking sleds. While making a block, he experienced sudden pain in his left shoulder. Physical examination showed tenderness to palpation over the tip of the acromion, and the patient was unable to abduct his arm without significant pain. Conventional radiographs showed at least two inferior fissures in the medial aspect of the acromion (Fig. 1A). This site showed increased uptake of radionuclide on bone scan.

The patient stopped all training, and the pain progressively disappeared. Three months after the injury, the range of motion and the muscular strength of the left shoulder were normal. At that time,

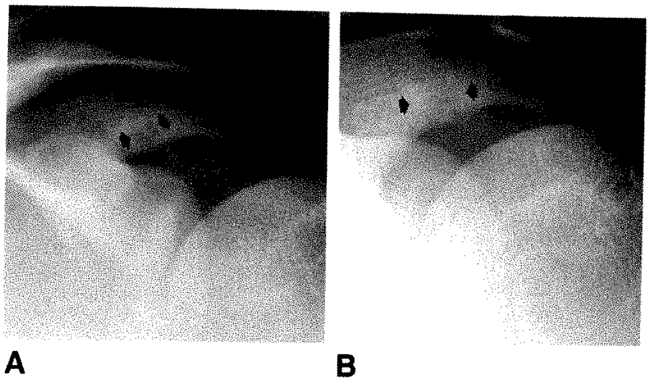

Fig. 1.—Stress fracture of acromion.

***A*, Anteroposterior radiograph of left shoulder shows two fissures (*arrows*) in inferior aspect of acromion near acromial angle.**

***B*, Anteroposterior radiograph obtained 3 months after *A* shows evidence of ongoing healing of fissures with callus formation (*arrows*).**

radiographs showed evidence of healing; the fissure was almost invisible (Fig. 1B).

Fatigue-type stress fractures are well-known complications of intense muscular activity, when abnormal muscular stress is applied to a bone with normal elastic resistance [1, 2]. In this case, the abnormal stresses were mainly weight lifting and blocking. The radiographs showed two incomplete fissures. This is different from a typical complete fracture resulting from a direct blow to the acromion from above. This appears to be the first reported case of a fatigue-type stress fracture involving the acromion. Stress fractures of the scapula involving the coracoid process, the spine, and the axillary border have been described [3]. As in the typical fatigue-type stress fracture, it is important to recognize the pathologic process; some of these fractures may become complete because of continued activity.

Jean P. Schils
Harris A. Freed
Bradford J. Richmond
David W. Piraino
John A. Bergfeld
George H. Belhobek
The Cleveland Clinic Foundation
Cleveland, OH 44195-5021

REFERENCES

1. Belkin SC. Stress fractures in athletes. *Orthop Clin North Am* **1980**;11:735–742
2. Pentecost RL, Murray RA, Brindley HH. Fatigue, insufficiency and pathologic fractures. *JAMA* **1964**;187:1001–1004
3. Vehnvohn P, Kohn HS, Guten GN, et al. Unusual stress fractures of the scapula in a jogger. *Clin Nucl Med* **1988**;13:531–532

Tuberculosis of the Skull

The diagnosis of tuberculosis often is not considered [1], and many radiologic presentations of the extrapulmonary forms of this disease are now rare. We report a case of tuberculosis in a woman with multiple skull lesions that was undiagnosed, despite a lengthy investigation, until *Mycobacterium tuberculosis* was isolated.

A 63-year-old woman had a 6-week history of mild headaches without neurologic signs or symptoms, a lump behind her right ear, night sweats, anorexia, and a weight loss of 20 lb (9.1 kg). Her history included a subtotal gastrectomy and polymyalgia rheumatica. She had been exposed, as a child, to tuberculosis (in her mother and sister) but had never taken antituberculous medications. Initial clinical findings were normal except for a nontender mass 2.5 cm in diameter over the right parietal bone, a microcytic anemia, mild leukocytosis, and a sedimentation rate of 55 mm/hr. Chest radiographs showed emphysema and collapse of the sixth thoracic vertebra. A skull radiograph showed multiple osteolytic lesions (Fig. 1), and a cranial CT scan showed epidural extensions of the lesions. A biopsy specimen of the mass showed necrotizing granulomas but no microorganisms, vasculitis, or malignancy. Biopsy specimens of two small hypoechoic lesions in the liver showed only leukocytes and necrosis. A radionuclide bone scan showed additional active foci in noncranial areas, but radiographs of these regions were normal. Skin testing showed anergy. *M. tuberculosis* was cultured from a repeat biopsy specimen. The patient received antituberculous therapy and continued to do well at follow-up 11 months later.

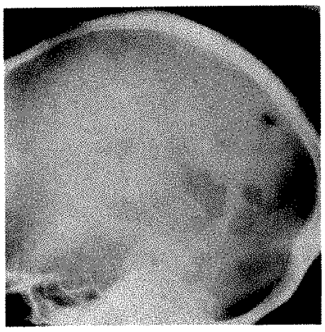

Fig. 1.—Skull radiograph shows multiple osteolytic lesions caused by tuberculosis.

Tuberculosis of the skull, once common in children, is now rare. Reviews of Straus [2] in 1933 and by Meng and Wu [3] in 1942 reported that 80% of patients with the skull form of the disease were 20 years old or less; only 0.54% were more than 60 years old. Based on a prevalence of skull disease in tuberculosis of 1% [4], the probability of a 63-year-old having this condition is only 0.000054. This may explain MacGregor's finding [1] that 44% of tuberculosis was misdiagnosed in a teaching hospital.

In a patient with multiple skull erosions on radiographs, tuberculosis should be considered, especially when the abnormality is painless and involves both tables of the calvarium.

Mark A. Miller
François Lebel
Montreal General Hospital
Montreal, Quebec, Canada H3G 1A4
Paul R. Fortin
Brigham and Women's Hospital
Boston, MA 02115

REFERENCES

1. MacGregor RR. A year's experience with tuberculosis in a private urban teaching hospital in the postsanitorium era. *Am J Med* **1975**;58:221–228
2. Straus DC. Tuberculosis of the flat bones of the vault of the skull. *Surg Gynecol Obstet* **1933**;57:384–398
3. Meng CM, Wu YK. Tuberculosis of the flat bones of the vault of the skull. *J Bone Joint Surg* **1942**;24:341–353
4. Nathanson L, Cohen W. A statistical and roentgen analysis of two hundred cases of bone and joint tuberculosis. *Radiology* **1941**;36:550–567

Endovascular Retention of a Ruptured Polyester Balloon in Femoral Angioplasty

Known complications of transluminal angioplasty include hematoma, acute arterial occlusion, subintimal dissection, distal embolization, rupture of the vessel [1] or balloon [2], false aneurysm [3], and detachment of the guidewire [4]. We recently encountered a complication of transluminal angioplasty that was related to use of a new balloon material, polyester, which produces a lower profile on a smaller shaft.

A 53-year-old man had claudication in the left lower extremity. A femoral angiogram showed multisegmental uncalcified stenotic disease of the distal superficial femoral artery. A left antegrade puncture was unsuccessful; therefore, a right femoral artery approach over the bifurcation was used for the angioplasty procedure. A polyester angioplasty balloon 5 mm in diameter and 4 cm long on a 5-French shaft (Ultra Thin, Medi-tech, Watertown, MA) was used for the dilatation. The balloon burst when it was inflated to a pressure of 7.5–8.0 atm (7.6×10^5 to 8.1×10^5 Pa). The recommended inflation pressure is 6 atm (6.1×10^5 Pa). The balloon was removed over a guidewire without difficulty through a 6-French femoral sheath. The balloon catheter was not inspected carefully. A second balloon catheter was used to complete the dilatation. Immediately after the

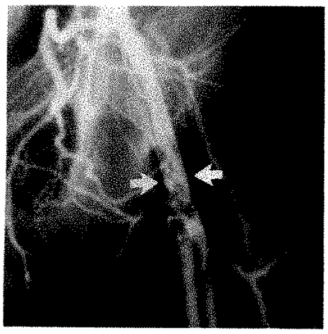

Fig. 1.—Angiogram of left common femoral artery shows a filling defect (*arrows*) caused by a retained angioplasty balloon. This represents thrombus surrounding detached balloon.

procedure, the pulse in the dorsal tibial artery was weakly palpable, which was an improvement.

Seven days after the procedure, the patient had pain in the left lower extremity and diminished peripheral pulses. Angiography showed a residual superficial stenosis of the femoral artery, which was dilated again via a contralateral approach. An arteriogram obtained after the angioplasty showed a filling defect of the common femoral artery, which was interpreted as thrombus (Fig. 1).

An end-hole catheter was left in place, and urokinase (60,000 units/hr) was infused intraarterially for 24 hr. A follow-up angiogram showed a persistent filling defect in the common femoral artery. A left common femoral arterotomy was performed, and the detached balloon was found embedded in thrombus. The detached balloon was approximately 4 cm long, and the circumferences of the balloon at both ends were intact. A vein patch was used to close the arterotomy, and the patient recovered without sequelae.

Transluminal angioplasty is an accepted and safe method for management of peripheral vascular disease. Significant complications are reported to be less than 5% [3]. The limits of angioplasty have been extended by new guidewire, catheter, and balloon technology. One important advance has been the development of a thinner balloon material made of polyester, which allows a lower balloon profile and a smaller diameter of the catheter shaft.

To date, no complications similar to the one we encountered have been reported. The manufacturer is aware of this complication and has notified the Food and Drug Administration. The detachment that occurred in our case is thought to be an isolated event involving a reliable and useful product.

Stephen F. Quinn
Good Samaritan Hospital
Portland, OR 97210
Oregon Health Sciences University
Portland, OR 97201
Roger Hallin
Good Samaritan Hospital
Portland, OR 97210

REFERENCES

1. Gardiner GA Jr, Meyerovitz MF, Stokes KR, Clouse ME, Harrington DP, Bettmann MA. Complications of transluminal angioplasty. *Radiology* **1986**;159:201–208
2. Berquist D, Jonsson K, Weibull H. Complications after percutaneous transluminal angioplasty of peripheral and renal arteries. *Acta Radiol* **1987**;28:3–12
3. Schwarten DE. Aortic, iliac and peripheral arterial angioplasty. In: Castaneda-Zuniga WR, Tadavarthy SM, eds. Baltimore: Williams & Wilkins, **1988**:268–294
4. Hartzer GO, Rutherford BD, McConaway DR. Retained percutaneous transluminal coronary angioplasty equipment components and their management. *Am J Cardiol* **1987**;60:1260–1264

Congenital Symmetrical Cerebral Intraventricular Membranes

CT study of a 6-month-old boy showed changes consistent with diffuse cerebral atrophy. No signs and symptoms of an inflammatory disease were evident. A striking finding was bilateral dilatation of the frontal horns of the lateral ventricles. A thin intraventricular membrane could be seen clearly on the right side, and a barely visible one was present on the left (Fig. 1).

It is known that intraventricular membranes may be extremely difficult to see on CT scans because of a volume-averaging effect: the membranes are so thin relative to the large volume of CSF [1]. These membranes usually develop as a result of inflammatory disease [1, 2], and in one reported instance, pathologic specimens showed "neurons" within the membrane, suggesting a congenital origin [2]. It is important to detect the membranes because multiple loculations within the ventricular system require shunts for decompression. When membranes are visualized, ventriculography with a positive contrast agent is of value in determining the degree of communication of the various compartments [1].

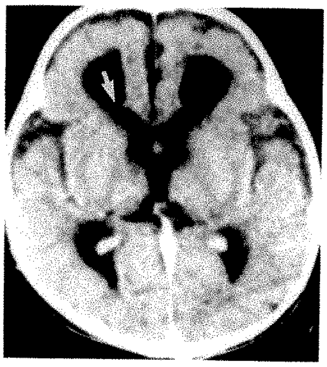

Fig. 1. — Contrast-enhanced CT scan shows diffuse cerebral atrophy and symmetrical dilatation of both anterior horns. Dilatation is much greater here than in other parts of ventricles. A thin membrane (*arrow*) can be seen on right side; membrane on left is less visible.

We think that this case is an example of congenital intraventricular membranes causing dilatation of the anterior horns of the lateral ventricles, although we had no opportunity to do a ventriculogram. Lack of evidence of inflammatory disease and symmetrically bilateral membranes suggest a congenital cause.

R. Nuri Sener
Abit Kaya
Muzaffer Eryilmaz
Macit Ariyurek
Hudaver Alper
Hospital of Ege University
Bornova, Izmir, Turkey

REFERENCES

1. Latchaw RE. *Computed tomography of the head, neck, and spine*. Chicago: Year Book Medical, **1985**:449
2. Savolaine ER, Gerber AM. Computerized tomography studies of congenital and acquired cerebral intraventricular membranes. *J Neurosurg* **1981**; 54:388–391

Spinal Cord Calcification in Congenital Cytomegalovirus Infection

Cytomegalic inclusion disease occurs in approximately one in 1000 newborns [1] and has profound effects on the nervous system. To

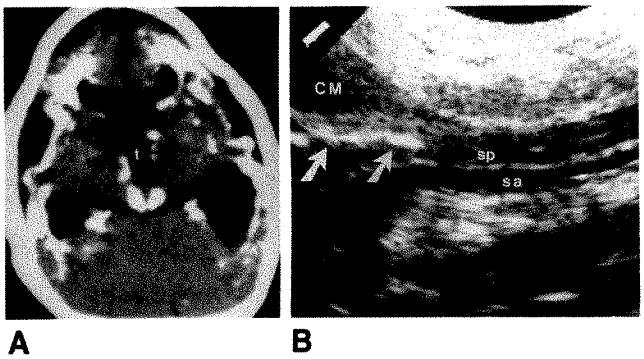

Fig. 1.—Cytomegalic inclusion disease.
***A*, Unenhanced cranial CT scan shows extensive calcification at level of third ventricle (t).**
***B*, Sagittal sonogram of craniocervical junction shows echogenicity indicative of calcification in central canal (*arrows*). CM = cisterna magna, sp = spinal cord, sa = subarachnoid space.**

our knowledge, spinal cord calcification associated with this condition has not been reported before.

A 29-year-old woman was delivered of a term female infant who had cytomegalic inclusion disease. The infant was severely microcephalic and had jaundice, a generalized petechial rash, and hepatosplenomegaly. Her birth weight, length, and head circumference were all well below the third percentile, consistent with severe intrauterine growth retardation.

A skull radiograph showed severe microcephaly with intracranial calcification. CT scan (Fig. 1A) showed the extensiveness of this calcification, which, in addition to being periventricular, was present in the basal ganglia and dentate nuclei. Ventricular dilatation was present also. A spinal sonogram showed calcification along the central canal in the upper cervical spinal cord (Fig. 1B). Abdominal sonography confirmed the presence of hepatosplenomegaly. In addition, the kidneys showed a generalized increase in echogenicity with loss of corticomedullary differentiation compatible with cytomegalovirus nephritis [2].

This case illustrates the diffuse manifestations of cytomegalic inclusion disease with extreme CNS involvement. The linear area of increased echogenicity seen on the sonogram within the central canal of the cervical spinal cord most likely represents an area of calcification. Although posterior acoustic shadowing was not seen, its absence in intracranial calcification has been shown before [3, 4]. The differential diagnosis includes hemorrhage, but our patient did not have neurologic signs referable to this level, making this possibility unlikely.

E. Walsh
B. Cramer
S. Shah
The Dr. Charles A. Janeway Child Health Centre
St. John's, Newfoundland, Canada A1A 1R8

REFERENCES

1. Bale JF, Blackman JA, Murph J, Andersen RD. Congenital cytomegalovirus infection. *Am J Dis Child* **1986**;140:128–131
2. Cramer BC, Jequier S, Chen MF. Sonographic appearances of cytomegalovirus nephritis in a neonate. *Pediatr Radiol* **1985**;15:56–57
3. Rumack CM, Johnson ML. *Perinatal & infant brain imaging*. Chicago: Year Book Medical, **1984**:197
4. Hayden CK, Swischuk LE. *Pediatric ultrasonography*. Baltimore: Williams & Wilkins, **1985**:66

Letters are published at the discretion of the Editor and are subject to editing.

Letters to the Editor must not be more than two *double-spaced*, typewritten pages. One or two figures may be included. Abbreviations should not be used. See Author Guidelines, page A5.

Material being submitted or published elsewhere should not be duplicated in letters, and authors of letters must disclose financial associations or other possible conflicts of interest.

Letters concerning a paper published in the *AJR* will be sent to the authors of the paper for a reply to be published in the same issue. Opinions expressed in the Letters to the Editor do not necessarily reflect the opinions of the Editor.

Review of Current Literature

Initials and addresses of corresponding authors are provided in parentheses for each article so that the reader can obtain reprints directly. Abstracts are printed verbatim from each journal.

Cancer

Sensitivity and specificity of computed tomography for the detection of adrenal metastatic lesions among 91 autopsied lung cancer patients. Allard P, Yankaskas BC, Fletcher RH, Parker LA, Halvorsen RA Jr (PA, Epidemiology Unit, Dept. of Social and Preventive Medicine, Laval University, Quebec, Canada G1K 7P4). *Cancer* 66:457-462, 1990

The ability of computed tomography (CT) to detect metastatic lesions in adrenal glands was evaluated on 91 autopsied lung cancer patients who died in 11 hospitals in the eastern United States and Canada from January 1983 to February 1988. Abdominal CT scans within 90 days of death were reviewed twice by two radiologists blinded to the autopsy diagnosis. The likelihood of metastatic spread in each adrenal gland was scored on a five-level scale. Histopathologic findings at autopsy were used to establish the presence or absence of metastases. The sensitivity of CT was low. Among 53 adrenal glands with proven metastatic lesions, the proportion with positive CT scans varied from 20.0% to 41.1%, according to the positivity threshold. In contrast, the specificity of CT was high, even at relaxed positivity thresholds, from 84.5% to 99.4%. The relatively low sensitivity of CT to detect adrenal metastatic lesions is explained to a large extent by the lack of substantial structural changes in many adrenal glands found to have metastases at autopsy. With a strongly positive CT scan, the probability of an adrenal metastatic lesion is high, and confirmatory adrenal biopsy may not be needed in patients with adrenocarcinoma and large cell carcinoma.

Reprinted by permission from the American Cancer Society.

Extraskeletal osteosarcoma: a clinicopathologic review of 26 cases. Bane BL, Evans HL, Ro JY, et al. (HE, Dept. of Pathology, Box 85, M. D. Anderson Cancer Center, 1515 Holcombe Blvd., Houston, TX 77030). *Cancer* 66:2762-2770, 1990

The clinical records and histopathologic features in 26 cases of extraskeletal osteosarcoma (ESOS) diagnosed at M.D. Anderson Cancer Center (Houston) between 1950 and 1987 were reviewed. Presentation was usually that of an enlarging soft tissue mass. The thigh (11 cases), upper extremity/shoulder girdle (three cases), and retroperitoneum (three cases) were the most common anatomic sites. Tumor size ranged from 2.5 to 30 cm. The predominant histologic pattern was osteoblastic in four cases, chondroblastic in two, fibroblastic or pleomorphic malignant fibrous histiocytoma (MFH)-like in four, giant cell type MFH-like in one, and small cell in one. Various mixtures of these patterns were seen in the remaining 14 tumors. The telangiectatic pattern was not seen as the predominant component in any primary tumor but was observed as a minor component. Thirteen tumors recurred locally and 16 metastasized; five patients had distant metastases at presentation. The lungs, bone, and soft tissue were the most frequent metastatic sites. Sixteen patients died of disease at 2 to 54 months, one patient died of unrelated causes at 61 months, seven patients were alive with no evidence of disease (NED) at 30 to 122 months, and two patients were alive with disease at 28 and 54 months, respectively. Tumor size (< 5 cm *versus* ≥ 5 cm) was the main prognostic factor; all patients alive with NED for whom accurate tumor measurements were available (six of seven) had neoplasms measuring < 5 cm that were amenable to complete surgical excision. Histologic pattern and other clinicopathologic features did not significantly affect outcome.

Reprinted by permission from the American Cancer Society.

Breast cancer diagnosis and prognosis in women augmented with silicone gel-filled implants. Silverstein MJ, Gierson ED, Gamagami P, Handel N, Waisman JR (MJS, The Breast Cancer, 14624 Sherman Way, Van Nuys, CA 91405). *Cancer* 66:97-101, 1990

From 1981 through 1988, 35 patients with prior augmentation mammoplasty were treated for breast carcinoma. Thirty-two patients had unilateral infiltrating carcinomas; three had noninvasive (*in situ*) lesions. Thirty-four of 35 (97%) lesions were palpable. One noninvasive cancer was occult, discovered mammographically in the absence of physical findings. Prebiopsy mammography was performed in 29 patients with palpable masses and failed to reveal an abnormality in 12 patients, a false-negative rate of 41%. Fifteen patients were treated with mastectomy; the remaining 20 with breast preservation. Thirty-two patients underwent axillary node dissection; 15 (47%) patients had lymph node metastases. There have been seven (20%) recurrences: one local and six metastatic. Four (11%) patients have died. The median follow-up time is 48 months. Women, previously augmented with silicone gel-filled implants, who develop breast cancer are similar in terms of nodal positivity and prognosis, to nonaugmented breast cancer patients who present with palpable masses. When compared with nonaugmented women whose cancers were found with screening mammography, augmented patients with breast cancer present with a higher percentage of invasive lesion and involved axillary lymph nodes, resulting in a poorer prognosis.

Reprinted by permission from the American Cancer Society.

Chest

Amyloidosis and pleural disease. Kavuru MS, Adamo JP, Ahmad M, Mehta AC, Gephardt GN (MA, Dept. of Pulmonary Disease, 9500 Euclid Ave., Cleveland, OH 44195). *Chest* 98(1):20-23, July 1990

Pleural involvement with systemic amyloidosis has been reported rarely in the literature. Diagnosis of this entity by percutaneous needle biopsy of the pleura has been described only in two prior case reports. We describe five patients in whom the diagnosis of pleural amyloidosis was established by Cope needle biopsy during evaluation of pleural effusions of indeterminate cause. Three patients presented with a history suggestive of multiorgan disease and a pleural biopsy performed despite a transudative effusion demonstrated amyloid infiltration of the pleura, obviating the need for other organ biopsies. We conclude that in patients with pleural effusions, if history suggests multiorgan involvement and there is suspicion for amyloidosis, then a closed pleural biopsy with special stains for amyloid should be performed even if the effusions are transudative. This may be the diagnostic procedure of choice in such patients.

The Journal of Bone and Joint Surgery

Fractures of allografts: frequency, treatment, and end-results. Berrey BH Jr, Lord CF, Gebhardt MC, Mankin HJ (BHB, Orthopaedic Oncology Unit, Orthopaedic Surgery, Walter Reed Army Medical Center, Washington, DC 20307-5001). *J Bone Joint Surg [Am]* 72-A(6):825–833, July 1990

One of the major complications of implantation of a massive frozen cadaveric allograft in the treatment of a tumor is fracture of the allograft. To determine the incidence, risk factors, appropriate management, and results of treatment of this complication, the records of the Orthopaedic Oncology Unit of the Massachusetts General Hospital were reviewed. Forty-three patients were identified in whom a tumor had been treated with an allograft that had subsequently fractured. The over-all incidence of fracture was almost 16 per cent. When the several risk factors (age and sex of the patient, stage and site of the lesion, and so on) for the forty-three patients who had a fracture were compared with those for the rest of the series, the only correlation was the incidence of non-union at the site of the host-donor junction, which was significantly higher in the patients who had a fracture.

The mean time to fracture was 28.6 months after the operation. Three types of fractures occurred: Type I (two patients), rapid dissolution of the graft; Type II (twenty-two patients), fracture of the shaft, which was observed more frequently in male patients and which occurred a mean of 27.6 months after the operation; and Type III (nineteen patients), fragmentation of the joint, which usually occurred later (a mean of 31.6 months postoperatively) and was found more frequently in female patients. All but four of the fractures (which healed after immobilization alone) were treated with an operation, which consisted initially of either open reduction, replacement of an internal fixation device, and addition of autogenous graft (mostly for Type-II fractures) or of conventional total joint replacement (mostly for Type-III fractures). After treatment, the results for the patients in whom the allograft had fractured approximated those for the entire series; the result was excellent or good in more than 75 per cent of each group. These data suggest that fracture of an allograft is a less severe complication than was originally thought.

Clinical Orthopaedics and Related Research

Periosteal chondroma: a report of ten cases and review of the literature. Lewis MM, Kenan S, Yabut SM, Norman A, Steiner G (MML, 5 E. 98th St., New York, NY 10029). *Clin Orthop* 256:185–192, July 1990

Periosteal chondroma is a slow-growing benign cartilaginous tumor of limited size arising within or under the periosteum, which, through constant pressure, induces cortical erosion and periosteal reaction. Ten new cases of periosteal chondroma are reported. All were treated by marginal or intralesional excision. No local recurrence was seen following this treatment. These patients demonstrated the clinical, roentgenographic, and pathologic features of this benign entity, which aid diagnosis, thereby avoiding overtreatment.

The Journal of Urology

Strategies for asymptomatic microscopic hematuria: a prospective study of 1,034 patients. Murakami S, Igarashi T, Hara S, Shimazaki J (SM, Dept. of Urology, Asahi General Hospital, Chiba, Japan). *J Urol* 144:99–101, July 1990

To establish strategies for treatment of asymptomatic microscopic hematuria we conducted a prospective study of 1,034 patients with this disease. The patients were examined by cystoscopy, urine cytology, abdominal ultrasound and excretory urography. On initial examination 30 highly significant lesions, including 24 cases of urological malignancies, 195 moderately significant lesions and 246 insignificant lesions were detected. In the remaining 563 patients no underlying lesion could be found. Of the 246 patients with insignificant lesions and 563 with unexplained asymptomatic microscopic hematuria followup was done in 421 at 6-month intervals for more than 1 year. A diagnosis became clear within 3 years in 22 patients, including 3 cases of bladder carcinoma and 1 of prostatic carcinoma.

Pediatrics

Prediction rules for selective radiographic assessment of extremity injuries in children and adolescents. McConnochie KM, Roghmann KJ, Pasternack J, Monroe DJ, Monaco LP (KMM, Dept. of Pediatrics, Rochester General Hospital, 1425 Portland Ave., Rochester, NY 14621). *Pediatrics* 86(1):45–57, July 1990

To assess the potential for selective use of roentgenography in evaluating extremity injuries, prediction rules were developed based on prospective observations for 617 injured children and adolescents examined in our Emergency Department (phase 1) and tested on 601 examined 1 year later (phase 2). Logit analysis produced best-fitting statistical models for phase 1 data with significant ($P < 0.05$) direct effects of gross signs, point tenderness, activity not routine, swelling moderate or severe, time from injury <6 hours, and pain with motion for upper extremity injuries; and, for lower extremity injuries, not knee injury, activity not routine, point tenderness, and foot injury. Prediction rules developed in phase 1 performed equally well when tested on phase 2 injuries. Data from both phases were combined, therefore, in analysis that produced risk estimates. For all injury types (ie, for injuries with all possible combinations of presence or absence of these findings), risk for fracture was derived. For upper extremity injuries, with a threshold risk for fracture of 20% used to select specific injury types for roentgenography, prediction rule outcomes were 18.1% of roentgenograms avoided and 5.3% of fractures missed. For lower extremity injuries, using a threshold risk of 10% to select injury types for roentgenography, outcomes were 25.8% of roentgenograms avoided and 5.3% of fractures missed. Alternative prediction rules allowed still greater roentgenogram avoidance, although missed fractures also increased. Risk of adverse functional outcome from missed fractures appeared small. Annual national cost savings from the elimination of 18.1% of upper and 25.8% of lower extremity roentgenographic evaluations was estimated at $103 million.

Reprinted by permission of PEDIATRICS © 1990.

Urinary N-acetyl-β-glucosaminidase and the selection of children for radiologic evaluation after urinary tract infection. Johnson CE, Vacca CV, Fattlar D, Fulton DJ, Hall PW (CEJ, Dept. of Pediatrics, MetroHealth Medical Center, 3395 Scranton Rd., Cleveland, OH 44109). *Pediatrics* 86(2):211–216, Aug. 1990

Urinary levels of N-acetyl-β-glucosaminidase (NAG) were measured in 147 consecutively enrolled children younger than 13 years of age with urinary tract infection to determine whether elevated levels were a predictor of urologic abnormalities. The children were classified as having cystitis if results of 0 or 1 of the following tests were positive and as having pyelonephritis if results of ≥2 tests were positive: (1) temperature >38°C, (2) serum C-reactive protein >1 mg/dL, (3) erythrocyte sedimentation rate >25 mm/h, and (4) 1-deamino-8-D-arginine vasopressin-renal concentrating protein <810 mOsm/kg. Urinary NAG to creatinine ratios did not distinguish cases of cystitis from those of pyelonephritis. Urinary NAG was useful in identifying children with cystitis who had vesicoureteral reflux of grades II through V. Of 6 children with cystitis and vesicoureteral reflux, 5 had levels of NAG more than 1 SD above the mean, whereas of 75 children without vesicoureteral reflux, only 15 had such an elevation ($P = .003$). Of those children with a normal NAG level, 60 (98.4%) had normal radiologic evaluation results, and only 1 child (1.6%) had vesicoureteral reflux. Levels of NAG did not identify children with pyelonephritis who had vesicoureteral reflux. It is concluded that (1) urinary NAG is of no value in localizing the site of urinary tract infection, and (2) an NAG level within 1 SD of the mean in a child with cystitis indicates a low risk of urologic abnormalities, and radiologic evaluation may be omitted unless infection recurs.

Reprinted by permission of PEDIATRICS © 1990.

The Journal of Pediatrics

Liquid ventilation of human preterm neonates. Greenspan JS, Wolfson MR, Rubenstein SD, Shaffer TH (JSG, St. Christopher's Hospital for Children, Section of Neonatology, Front St. and Erie Ave., Philadelphia, PA 19134). *J Pediatr* 117:106–111, July 1990

This report details the application of liquid perfluorochemical ventilation for investigational therapy in three human preterm neonates (gestational ages 28, 24, and 23 weeks) in whom conventional therapies for severe respiratory distress had failed. Liquid ventilation was performed without difficulty in each infant for two 3- to 5-minute cycles by means of gravity-assisted technique. Marked improvement in lung distensibility, without a change in cardiovascular status, occurred in all three infants after liquid ventilation; oxygenation improved in two. All infants died within 19 hours of liquid ventilation, and there was no evidence of retained perfluorochemical fluid in the lungs or pleural space. Death was probably related to the severity of lung disease before the initiation of liquid ventilation. This satisfactory initial outcome shows the feasibility and potential of this treatment of pulmonary dysfunction in the preterm neonate.

Vasoparalysis associated with brain damage in asphyxiated term infants. Pryds O, Greisen G, Lou H, Friis-Hansen B (OP, Dept. of Neonatology, Rigshospitalet, 2100 Copenhagen ø, Denmark). *J Pediatr* 117:119–125, July 1990

The relationship of cerebral blood flow to acute changes in arterial carbon dioxide and mean arterial blood pressure (MABP) was determined during the first day of life in 19 severely asphyxiated term infants supported by mechanical ventilation. For comparison, 12 infants without perinatal asphyxia were also investigated. Global cerebral blood flow (CBF_{∞}) was determined by xenon 133 clearance two or three times within approximately 2 hours. During the cerebral blood flow measurement, the amplitude-integrated electroencephalogram and visual-evoked potential were recorded. Changes in arterial carbon dioxide pressure followed adjustments of the ventilator settings, whereas MABP fluctuated spontaneously. Arterial oxygen pressure and blood glucose concentration were in the normal range. Five of the asphyxiated infants had isoelectric electroencephalograms and died subsequently with severe brain damage. They had a high CBF_{∞} (mean 30.6 ml/100 gm/min) and abolished carbon dioxide and MABP reactivity. Lower CBF_{∞} (mean 14.7 ml/100 gm/min) and abolished MABP reactivity were found in another five asphyxiated infants with burst-suppression electroencephalograms in whom computed tomographic or clinical signs of brain lesions developed. The carbon dioxide reactivity was preserved in these infants. In the remaining nine asphyxiated infants without signs of central nervous system abnormality, carbon dioxide and MABP reactivity were preserved, as was also the case in the control group. We conclude that abolished autoregulation is associated with cerebral damage in asphyxiated infants and that the combination of isoelectric electroencephalograms and cerebral hyperperfusion is an early indicator of very severe brain damage.

Angiotensin converting enzyme inhibitor therapy to decrease microalbuminuria in normotensive children with insulin-dependent diabetes mellitus. Cook J, Daneman D, Spino M, Sochett E, Perlman K, Balfe JW (DD, Hospital for Sick Children, 555 University Ave., Toronto, Ontario M5G 1X8, Canada). *J Pediatr* 117:39–45, July 1990

It has been proposed that lowering glomerular pressure in children with insulin-dependent diabetes mellitus will reduce microalbuminuria and that this reduction may preserve renal function. We therefore conducted a double-blind, placebo-controlled, crossover trial to compare 3 months of treatment with the angiotensin converting enzyme inhibitor captopril (0.9 mg/kg/day), and 3 months of placebo administration to 12 normotensive adolescents with insulin-dependent diabetes mellitus, 11 with microalbuminuria (albumin excretion rate of 15 to 200 μg/min) and one with early overt nephropathy. Mean age (±SD) was 14.4 ± 1.7 years, and disease duration was 5.1 ± 2.5 years. Albumin excretion rate decreased significantly during captopril therapy (baseline 78 ± 114 μg/min; mean of monthly measurements 38 ± 55 μg/min vs placebo 78 ± 140 μg/min; $p < 0.001$). During captopril therapy, albumin excretion was reduced by 41 ± 44% and decreased in 10 of 12 subjects, but was unchanged in two, one with a borderline albumin excretion rate (16.3 μg/min) and one with diabetes of short duration (2.9 years). Plasma renin activity rose significantly during captopril therapy, and mean arterial pressure decreased slightly (placebo 81 ± 7 mm Hg; captopril 76 ± 5 mm Hg; $p = 0.004$). After 3 months of captopril treatment, glomerular filtration rate and renal plasma flow did not change significantly. Hemoglobin A_{1c} values remained stable during the study. The only side effect of captopril was diarrhea in one patient. We conclude that, in the short term, captopril is effective in decreasing albumin excretion rate in normotensive children with insulin-dependent diabetes mellitus and microalbuminuria, without significant side effects. Longer trials are indicated in an attempt to delay or prevent overt nephropathy.

Journal of Thoracic Imaging

Imaging techniques for assessing pulmonary artery hypertension and right ventricular performance with special reference to COPD. Matthay RA, Shub C (RAM, Pulmonary and Critical Care Section (LCI 105), Yale Medical School, 333 Cedar St., New Haven, CT 06510). *J Thorac Imaging* 5(3):47–67, 1990

Several imaging techniques, both noninvasive and minimally invasive, have now been applied widely for determining cardiovascular performance in patients with chronic respiratory disease, particularly COPD. Moreover, some of these techniques are useful for evaluating response to therapeutic intervention in these patients. The plain chest radiograph is useful primarily for detecting the presence of pulmonary artery hypertension in patients with COPD. Radionuclide angiocardiography, using either first-pass techniques or the hypertension in patients with COPD. Radionuclide angiocardiography, using either first-pass techniques or the gated equilibrium technique, is particularly useful for determining right and left ventricular ejection fraction. Echocardiography has evolved as a technique for assessing right ventricular size and function and, in some cases, the degree of pulmonary artery hypertension.

Journal of Ultrasound in Medicine

Intrauterine fetal growth in discordant twin gestations. Rodis JF, Vintzileos AM, Campbell WA, Nochimson DJ (JFR, Dept. of Obstetrics and Gynecology, Division of Maternal-Fetal Medicine, University of Connecticut Health Center, Farmington, CT 06032). *J Ultrasound Med* 9:443–448, Aug. 1990

Twenty five discordant twin pairs were assessed ultrasonically in a longitudinal fashion and were compared with a group of 60 concordant twin pairs. The growth parameters of the larger fetus of the discordant pair did not differ significantly from the concordant twins, while the smaller of the discordant pair exhibited a slower rate of intrauterine growth as early as 23 to 24 weeks. We conclude that (1) twins who ultimately become discordant exhibit demonstrable differences as early as 23 to 24 weeks; (2) the smaller twin in a discordant pair has a much slower rate of growth between 33 to 37 weeks; and (3) using estimated fetal weight to predict concordancy and discordancy by Shepard's and Hadlock's tables are equally efficacious, although Hadlock's table can be used more often because biparietal diameter cannot be obtained as often as femur length.

Reprinted with permission by the American Institute of Ultrasound in Medicine.

Journal of Computer Assisted Tomography

Alveolar echinococcosis of the liver: MR findings. Claudon M, Bessieres M, Regent D, et al. (MC, Service de Radiologie, Centre Hospitalier Universitaire de Nancy, 54511 Vandoeuvre, France). *J Comput Assist Tomogr* 14(4):608–614, 1990

Nineteen cases of proven hepatic alveolar echinococcosis were examined by magnetic resonance (MR) and the results were compared with CT. Fibrous and parasitic tissue showed low signal both on T1- and, generally, on T2-weighted images. In a few cases a high signal on T2-weighted images may be observed, due either to central necrotic zones or to small peripheral cysts. Central necrosis was more easily identified by MR than by CT. However, MR seemed to be less effective than CT in allowing us to reach a positive diagnosis, due to its inability to show microcalcifications. In addition, MR may not reveal small lesions. In most cases T1-weighted images revealed more clearly than CT did the margins of the lesions and the hepatic extension, especially to hepatic veins, vena cava, and perihepatic spaces.

Lipomatous uterine tumors: diagnosis by ultrasound CT, and MR. Dodd GD III, Budzik RF Jr (GDD, University of Pittsburgh, Dept. of Radiology, Presbyterian-University Hospital, DeSoto at O'Hara Sts., Pittsburgh, PA 15213). *J Comput Assist Tomogr* 14(4):629–632, 1990

Lipomatous uterine tumors are rare benign neoplasms that can be difficult to differentiate from benign cystic ovarian teratomas. However, if a fat containing mass can be clearly identified to be of uterine origin, the diagnosis of a lipomatous uterine tumor can be made. We present two cases in which a lipomatous uterine tumor was suggested by ultrasound and confirmed by CT and magnetic resonance.

Systemic bone marrow disorders: characterization with photon chemical shift imaging. Gückel F, Brix G, Semmler W, et al. (FG, MR-Tomographie, Deutsches Krebsforschungszentrum Heidelberg, Institut für Radiologie und Pathophysiologie, Im Neuenheimer Feld 280, D-6900 Heidelberg, F.R.G.) *J Comput Assist Tomogr* 14(4):633–642, 1990

In a prospective clinical study, 26 patients (22 with malignant lymphoma and 4 with myelofibrosis) and 9 healthy volunteers were examined by conventional magnetic resonance and proton chemical shift imaging (CSI; modified Dixon method). On the basis of CSI data, a quantitative evaluation of the relative fat and water signal fractions in regions of interest of the femur, pelvis, and spine was performed. In 16 of 17 patients with biopsy-proven bone marrow disorders, CSI revealed a significant reduction in the fat fraction of the bone marrow relative to that of normal volunteers. The visual assessment could detect only 14 of the 17 pathological cases.

The September issue of *AJR: American Journal of Roentgenology* carried the incorrect Berlex Imaging Magnevist advertisement "Spinal Metastatic Disease." The correct advertisement should have been "Magnevist Brain Metastases."

News

Multidisciplinary Approach to CNS Tumors in Childhood

The International Symposium on Multidisciplinary Approach to CNS Tumors in Childhood will be held Nov. 7–10 at the Grand Hotel Miramare, Santa Margherita Ligure, Genoa, Italy. Topics will include basic research and pathology; primitive neuroectodermal tumors; sellar, opticochiasmatic, and third-ventricle tumors; CNS tumors in children less than 3 years old; tumors of the pineal region; brainstem tumors; the modern therapeutic approach to ependymomas; tumors of the skull base; the role of chemotherapy; and late effects of CNS tumors. The official languages will be Italian, English, and French. Simultaneous translations will be arranged. Course director: Luciano Andreussi. Course coordinator: Armando Cama. Fee: 350,000 Italian lire. Information: Dr. Armando Cama, Servizio di Neurochirurgia, G. Gaslini Children's Hospital, L.go G. Gaslini 5, 16147 Genoa, Italy; telephone: 39-10-5636515; fax: 39-10-5636461.

Society for Medical Decision Making Annual Meeting

The 12th annual meeting of the Society for Medical Decision Making will be held Nov. 11–14 at the Lafayette Hotel, Boston. The theme of the meeting will be outcomes research and its interfaces with medical decision making. William L. Roper, the director of the Centers for Disease Control, will be the keynote speaker. In addition to a course on outcomes research and an introductory course on practical applications of decision making, advanced courses will be offered on decision psychology, legal implications of decision making, cost-effectiveness analysis, and meta-analysis. Information: SMDM, 85 Mechanic St., Ste. 200, Lebanon, NH 03766; (603) 448-6808.

Digital Radiology and PACS

The 1st International Conference on Digital Radiology and PACS will be held Nov. 12–13 in Bologna, Italy. Topics to be covered are present and future digital radiology, clinical use of digital radiology, progress of PACS technologies, clinical and diagnostic impact of PACS, and problems and perspectives in PACS management. Italian and English will be the official languages. Simultaneous translation will be provided. Fee: 250,000 Italian lire. Information: Dr. Sandro Sartoni Galloni, Servizio di Radiologia I, Ospedale Maggiore, Largo B. Nigrisoli, 2, 40133 Bologna, Italy; telephone: 38-48-01.

ARNA Annual Meeting

The American Radiological Nurses' Association (ARNA) will hold its annual meeting Nov. 25–30 in Chicago in conjunction with the annual meeting of the Radiological Society of North America (RSNA). Registration fee for RSNA: $25. Registration fees for ARNA meeting: members, $175 and $200 (preregistered and at the door); nonmembers, $250 and $275; daily, $75 and $100. Information: Patsy Axley, R.N., Rural Route 2, Box 105, Eyota, MN 55934; (507) 876-2400.

CT/MRI Head to Toe

The 9th annual CT/MRI Head to Toe will be held at the Grand Hyatt New York, New York City, Dec. 17–22. The program will give a practical update of the entire field of CT and MR imaging. Correlative presentations of these two imaging techniques will be an important part of the course curriculum. The program will include plenary lectures and small group workshops on diseases of the head, neck, sinuses, thorax, abdomen, pelvis, spine, and musculoskeletal system and on interventional techniques. The program is divided into two sections, which can be taken independently or consecutively. Section I will include neurologic, spinal, and head and neck CT and MR. Section II will include chest and body CT and MR. Category 1 credit: entire course, 39.5 hr; part A, 19 hr; part B, 20.5 hr. Fee: entire course, $725; part A, $385; part B, $410. Information: NYU Medical Center, Post-Graduate Medical School, 550 First Ave., New York, NY 10016; (212) 340-5295.

Caribbean Cruise—Breast Imaging at Sea

Caribbean Cruise—Breast Imaging at Sea will be held Jan. 12–19, 1991. The course will be presented by Lawrence Bassett from the University of California, Los Angeles. Program director: Ronald J. Friedman. Lectures, seminars, and case discussions will be included. Category 1 credit is pending. Fee: through Nov. 15, 1990, $425; after Nov. 15, 1990, $460. Information: Caribbean Cruise, c/o Medical Seminars International, Inc., 18981 Ventura Blvd., Ste. 303, Tarzana, CA 91356; (818) 700-9821.

Seminars in MRI

The Medical College of Wisconsin is sponsoring Seminars in MRI, Jan. 19–26, 1991, at Marriott's Mark Resort, Vail, CO. The course will concentrate on the common and complex problems encountered in MR imaging of the body and neurologic system. Category 1 credit: 30 hr. Fee: $500. Information: Thomas L. Lawson, M.D., Dept. of Radiology, Milwaukee County Medical Complex, 8700 W. Wisconsin Ave., Milwaukee, WI 53226; telephone: (414) 257-6024; fax: (414) 257-7877.

Midwinter Radiological Conference

The Continuing Education Committee, Los Angeles Radiological Society (LARS), is sponsoring its 43rd annual Midwinter Radiological Conference, Feb. 1-3, 1991, at the Century Plaza Hotel, Los Angeles. The meeting will feature 16 30-min main lectures and 58 45-min seminars. In addition, a 1-day seminar on nuclear medicine, featuring 11 talks, will be offered. The lectures and seminars will cover six subject areas: MR imaging and neuroradiology, musculoskeletal imaging, general radiology, body imaging, mammography, and nuclear medicine. Category 1 credit: up to 17.25 hr. Fee: physicians, $395/$350/$175 (3 days/2 days/1 day); LARS members, $200/$150/$100; residents and technologists, $125/$100/$50; LARS resident members, $100/$70/$35. Information: Los Angeles Radiological Society—MWRC, P. O. Box 91215; Los Angeles, CA 90009-1215; (213) 827-9078 or (800) LARS-013.

Practical Aspects of Diagnostic Radiology/Medical Imaging IV

Vanderbilt University Medical Center is sponsoring Practical Aspects of Diagnostic Radiology/Medical Imaging IV, Feb. 2-8, 1991, at the Snowmass Conference Center, Snowmass Village, CO. Emphasis will be on the research interests of the faculty, not on everyday problems. Category 1 credit: 25 hr. Fee: physicians, $525 (through Dec. 2, 1990) and $550 (after Dec. 2, 1990); residents and fellows, $350 (letter required). Information: Marilyn D'Asaro, Vanderbilt Division of CME, CCC-5316 Medical Center North, Nashville, TN 37232; (615) 322-4030.

Big Sky Radiology Conference

The Dept. of Radiology, University of Wisconsin, is sponsoring the 15th annual Big Sky Radiology Conference, Feb. 3-7, 1991, at Huntley Lodge, Big Sky, MT. This general radiology conference will cover imaging techniques in musculoskeletal, gastrointestinal, pediatric, and obstetric radiology; neuroradiology; and mammography. Course director: Virgil B. Graves. Guest faculty: L. W. Bassett, R. I. Grossman, I. Laufer, D. H. Pretorius, and L. E. Swischuk. Category 1 credit: 20 hr. Fee: general, $400; residents, $200. Information: Sandy Yost or Virgil B. Graves, M.D., Clinical Science Center, University of Wisconsin, Dept. of Radiology E3/311, 600 Highland Ave., Madison, WI 53792; (608) 263-9179.

Mid-Pacific Radiological Conference

The Continuing Education Committee, Los Angeles Radiological Society (LARS), is sponsoring the 17th annual Mid-Pacific Radiological Conference, Feb. 5-9, 1991, at the Maui Marriott Hotel, Maui, HI. The conference will consist of 20 45-min lectures and two 30-min question-and-answer sessions. Topics will include mammography, neuroradiology, MR imaging, and interventional radiology. Faculty: C. Helms, M. Homer, A. Megibow, and M. Modic. Category 1 credit: up to 16 hr. Fee: physicians, $395; residents and technologists, $150. Information: Los Angeles Radiological Society—MPRC, P. O. Box 91215, Los Angeles, CA 90009-1215; (213) 827-9078 or (800) LARS-013.

Computed Body Tomography 1991—The Cutting Edge

The Johns Hopkins University School of Medicine is sponsoring Computed Body Tomography 1991—The Cutting Edge, Feb. 7-10, 1991, at the Peabody Orlando Hotel, Orlando, FL. The seminar will provide a comprehensive review of recent advances in CT of the chest and abdomen, including the spine, with some correlation with MR imaging. A series of 30-min lectures will concentrate on specific topics in depth. One-hour workshops will focus on problem-oriented topics, with emphasis on technique and differential diagnosis. Program directors: Elliot K. Fishman and Stanley S. Siegelman. Guest faculty: L. L. Berland, H. D. Curtin, G. M. Glazer, P. R. Mueller, and E. J. Russell. Category 1 credit: 22 hr. Fee: physicians, $500; residents and fellows, $375 (letter required); technologists, $375. Information: Program Coordinator, The Johns Hopkins Medical Institutions, Office of Continuing Education, Turner Bldg., 720 Rutland Ave., Baltimore, MD 21205; (301) 955-2959.

Annual Intermountain Imaging Conference

The Medical College of Wisconsin is sponsoring the 12th annual Intermountain Imaging Conference, Feb. 9-16, 1991, at the Sheraton at Steamboat, Steamboat Springs, CO. A series of lectures and seminars will cover imaging of the chest and abdomen, mammography, neurologic imaging, and obstetric and gynecologic imaging. The focus will be on integrated imaging and the advantages of various radiologic techniques and problem solving. Category 1 credit: 33 hr. Fee: $500. Information: Thomas L. Lawson, M.D., Dept. of Radiology, Milwaukee County Medical Complex, 8700 W. Wisconsin Ave., Milwaukee, WI 53226; telephone: (414) 257-6024; fax: (414) 257-7877.

Sun Valley Imaging Meeting

The 7th annual Sun Valley Imaging Meeting will be held Feb. 23–March 2, 1991, at the Sun Valley Lodge, Sun Valley, ID. The course will review important aspects and the latest developments in body imaging and intervention. Course coordinator: Peter L. Cooperberg. The speakers will be Dr. Cooperberg, Michael Federle, Thomas Lawson, Patrice Bret, Matthew Rifkin, and Bruce McClennan. Category 1 credit: 20 hr. Fee: $495. Information: Ethel Inglis, Dept. of Radiology, St. Paul's Hospital, 1081 Burrard St., Vancouver, B.C., Canada V6Z 1Y6; (604) 631-5026.

Principles and Practice of Clinical MRI

The Dept. of Radiology, Division of Magnetic Resonance Imaging, The Johns Hopkins Medical Institutions, is sponsoring Principles and Practice of Clinical MRI, Feb. 28–March 3, 1991, at Buena Vista Palace, Walt Disney World Village, Lake Buena Vista, FL. Category 1 credit: 20 hr. Fee: physicians, $495; residents, fellows, and technologists, $250. Information: Program Coordinator, The Johns Hopkins Medical Institutions, Office of Continuing Education, Turner Bldg., 720 Rutland Ave., Baltimore, MD 21205; (301) 955-2959.

Advanced Seminars in Diagnostic Imaging

The Dept. of Radiology, University of California, San Diego School of Medicine, will present Advanced Seminars in Diagnostic Imaging, March 1-3, 1991, at the Ritz-Carlton Resort Hotel, Laguna Niguel, CA. The course will consist exclusively of small group sessions rather than lectures. Instruction will be tailored individually to meet the needs, interests, and desires of registrants. The course is intended for experienced imagers and other physicians thoroughly sophisticated in the fundamentals of radiology. Program director: David S. Feigin. Category 1 credit: 18 hr. Fee: physicians, $400; residents, fellows, and technologists, $275. Information: Dawne Ryals, Ryals & Associates, P. O. Box 1925, Roswell, GA 30077-1925; telephone: (404) 641-9773; fax: (404) 552-9859.

Course on MR Imaging

The Dept. of Radiology, University of California, San Diego School of Medicine, is sponsoring Magnetic Resonance Imaging, March 4-8, 1991, at the Hotel del Coronado, Coronado (San Diego), CA. Program directors: John R. Hesselink, Robert F. Mattrey, and Donald S. Resnick. Information: Dawne Ryals, Ryals & Associates, P. O. Box 1925, Roswell, GA 30077-1925; telephone: (404) 641-9773; fax: (404) 552-9859.

Musculoskeletal Imaging

Boston University, School of Medicine, is offering Musculoskeletal Imaging for Orthopedic Surgeons and General Radiologists, March 4-8, 1991, at Heywoods Resort, Barbados. Course director: Peter D. Franklin. Category 1 credit: 21 hr. Fee: physicians, $435; residents, $300. Information: Maryjane Nolan, Dept. of Continuing Medical Education, 80 E. Concord St., Boston, MA 02118-2394; (617) 638-4605.

Orthopedic Radiology 1991

The Dept. of Radiology, Brigham and Women's Hospital, and Harvard Medical School are offering Orthopedic Radiology 1991, March 25-27, 1991, at The Ritz-Carlton Hotel, Boston. Program director: Barbara Weissman. Category 1 credit: approximately 22 hr. Fee: physicians, $450; residents, fellows, and technologists, $350. Information: Harvard Med-CME, P. O. Box 825, Boston, MA 02117; (617) 432-1525.

Ultrasound 1991

The Dept. of Radiology, Brigham and Women's Hospital, and Harvard Medical School will offer the 16th annual postgraduate course, Ultrasound 1991, April 2-5, 1991, at the Westin Hotel, Copley Place, Boston. A special feature will be Basics of Ultrasound, to be held April 2. Program directors: Peter M. Doubilet and Carol B. Benson. Category 1 credit: approximately 26 hr. Fee: physicians, $525; residents, fellows, and technologists, $350; Basic day, $130. Information: Dept. of Continuing Education, Harvard Med-CME, P. O. Box 825, Boston, MA 02117; (617) 432-1525.

National Council on Radiation Protection and Measurements

The 27th annual meeting of the National Council on Radiation Protection and Measurements will be held April 3-4, 1991, at the Mayflower Hotel, Washington, DC. The principal scientific session will be on biological research relating to radiation protection. Information: National Council on Radiation Protection and Measurements, 7910 Woodmont Ave., St. 800, Bethesda, MD 20814; telephone: (301) 657-2652; fax: (301) 907-8768.

Society for Magnetic Resonance Imaging Annual Meeting

The 9th annual meeting of the Society for Magnetic Resonance Imaging will be held April 13-17, 1991. Information: Kristen Coe, SMRI, 213 W. Institute Pl., Ste. 501, Chicago, IL 60610; (312) 751-2590.

Clinical Nuclear Medicine 1991

Harvard Medical School and the Joint Program in Nuclear Medicine at the Beth Israel Hospital, the Brigham and Women's Hospital, The Children's Hospital, Dana-Farber Cancer Institute, and the West Roxbury VA Medical Center are offering the 15th annual postgraduate course, Clinical Nuclear Medicine, April 22-25, 1991, at the Westin Hotel, Copley Place, Boston. Program director: William D. Kaplan. Category 1 credit: 25 hr. Fee: physicians, $500; residents, fellows, and technologists, $350. Information: Harvard Med-CME, P. O. Box 825, Boston, MA 02117; (617) 432-1525.

Cleveland Radiological Society Officers

The officers of the Cleveland Radiological Society for the year 1990-1991 are as follows: president, David M. Paushter; president-elect, Peter B. O'Donovan; secretary-treasurer, David M. Einstein; past-president, James A. Patterson; program chairman, Gary K. Lammert; and members-at-large, William K. Bishop, Joseph P. LiPuma, and Riaz A. Tarar.

The American Board of Radiology Examinations

Written examinations for the American Board of Radiology (ABR) are scheduled for Oct. 3-4, 1991. Oral examinations will be held at the Executive West Hotel in Louisville, KY, June 3-7, 1991. The ABR will accept applications for admission to the examinations after July 1, but not later than Sept. 30, in the year *preceding* the year in which the examination is to be taken. For application forms and further information: Office of the Secretary, The American Board of Radiology, 300 Park, Ste. 440, Birmingham, MI 48009.

Meeting and Course Review

For the reader's convenience, a summary of upcoming meetings and courses is provided. Detailed listings are given in the *AJR* issue given in parentheses.

Cyanoacrylate Embolization Course, times arranged, Baltimore (July)
Visiting Fellowships in Ultrasound, times arranged, Baltimore (Aug)
Visiting Fellowships in Interventional Radiology, times arranged, Baltimore (Oct)
Advances in Diagnostic Radiology, Oct. 28-Nov. 1, Tucson, AZ (July)
Courses in MR Imaging at Emory University: course for physi-

cians, Oct. 29–Nov. 2, Nov. 12–16, and Dec. 3–7; **course for technologists,** Nov. 4–10; Atlanta (June)
International Seminar on Medical Imaging, Oct. 29–Nov. 3, Hong Kong (Sept)
Melvin M. Figley Fellowships in Radiology Journalism, application deadline, Nov. 1 (Sept)
Course on CT and MR Imaging, Nov. 1–2, Chicago (Sept)
Advances in Color Doppler Sonography, Nov. 1–3, White Sulphur Springs, WV (May)
Principles and Practice of MRI, Nov. 1–4, Baltimore (Sept)
Musculoskeletal MRI for the Clinician, Nov. 3, Boston (Oct)
MR Imaging Review Course in Australia, Nov. 3–4, Brisbane, and Nov. 10–11, Sydney (Oct)
Color Doppler Ultrasound, Nov. 5, Philadelphia (Oct)
Obstetrics and Gynecology, Nov. 5–9, Philadelphia (July)
Diagnostic Radiology Seminars, Nov. 5–9, Maui, HI (Oct)
Intraluminal Ultrasound and Basic Introduction to Doppler Principles, Nov. 6, Coronado (San Diego), CA (Oct)
Symposium on Bone and Soft-Tissue Tumors, Nov. 9–10, Sacramento, CA (May)
Tomography for Technologists, Nov. 12–13, Atlanta (June)
Abdominal Ultrasound, Nov. 12–15, Philadelphia (July)
Prostate Ultrasound, Nov. 16, Philadelphia (July)
MRI for Radiologic Technologists, Dec. 7–8, Houston (July)
Advanced Seminars in Diagnostic Imaging, Dec. 7–9, Laguna Niguel, CA (Sept)
MRI Fellowships at Johns Hopkins, Dec. 10–14, 1990; Jan 7–11, 1991; April 8–12, 1991; and June 17–21, 1991; Baltimore (Oct)
MR Imaging Update, Dec. 13–15, New York City (Aug)
Future and Present MRI, Jan. 9–13, 1991, Naples, FL (Aug)
Advanced Seminars in Diagnostic Imaging, Jan. 19–21, 1991, Laguna Niguel, CA (Aug)
Park City 1991: MRI Update, Jan. 20–24, 1991, Park City, UT (Oct)
Diagnostic Imaging in Aruba, Jan 20–26, 1991, Aruba (Aug)
International Symposium on MR Imaging, Jan. 23–27, 1991, Garmisch-Partenkirchen, Bavaria (Aug)
Society for Pediatric Radiology Research and Education Grants, application deadline, Feb. 1, 1991 (Sept)
Angio-Interventional Radiology, Feb. 4–5, 1991, Coronado (San Diego), CA (Oct)
Duplex Imaging Tutorial Conference and Exhibit, Feb. 7–9, 1991, San Diego (Oct)
Contemporary Diagnostic Imaging, Feb. 11–15, 1991, Mauna Lani, HI (Oct)
Society of Gastrointestinal Radiologists Annual Meeting and Postgraduate Course, Feb. 17–21, 1991, Carlsbad, CA (Oct)
Imaging the Head, Spine, and Musculoskeletal System, Feb. 17–22, 1991, Kauai, HI (Oct)
MR Imaging Course at Disney World, Feb. 17–22, 1991, Orlando, FL (Oct)
Practicum in Diagnostic Ultrasound, March 4–8, 1991, and April 22–26, 1991, Baltimore (Oct)
International Pediatric Radiology '91, May 27–31, 1991, Stockholm (Aug)
International Congress of Radiation Research, July 7–12, 1991, Toronto. Deadline for abstracts, Jan. 15, 1991 (May)
World Congress in Ultrasound, Sept. 1–6, 1991, Copenhagen (Sept)
European Congress of Radiology 1991, Sept. 15–20, 1991, Vienna, Austria (Oct)

AJR carries announcements of courses, symposia, and meetings of interest to its readers if received a minimum of 5 months before the event. There is no charge; receipt of items by the *AJR* Editorial Office is not acknowledged. Submit items for publication typed double-spaced. Provide title, date, location, brief description, sponsor, course directors, fees, category I credit, and address and telephone number for additional information. Faculty from the host institution will not be listed. Guest faculty names will appear **only** if initials are provided. Mail news items to *AJR* Editorial Office, 2223 Avenida de la Playa, Ste. 103, La Jolla, CA 92037-3218.

American Roentgen Ray Society:

Officers, Committees, and Membership Information

Officers

President: M. Paul Capp
President-elect: John A. Kirkpatrick, Jr.
1st Vice-president: A. Everette James, Jr.
2nd Vice-president: Andrew K. Poznanski
Secretary: Joseph T. Ferrucci, Jr.
Treasurer: Beverly P. Wood

Executive Council: R. J. Alfidi, R. N. Berk, M. P. Capp, W. J. Casarella, N. R. Dunnick, R. G. Evens, J. T. Ferrucci, Jr., A. E. James, Jr., J. A. Kirkpatrick, Jr., A. M. Landry, Jr., J. E. Madewell, A. A. Moss, A. K. Poznanski, L. F. Rogers, R. J. Stanley, J. H. Thrall, K. H. Vydareny, N. O. Whitley, B. P. Wood, G. R. Leopold, chairman

Committees

Editorial Policy: R. N. Berk, E. Buonocore, Melvin M. Figley, S. v. W. Hilton, M. S. Huckman, C. A. Rohrmann, Jr., R. J. Stanley, R. I. White, W. J. Casarella, chairman

Education and Research: C. B. Higgins, B. J. Hillman, R. A. McLeod, R. J. Stanley, W. M. Thompson, N. O. Whitley, chairman

Finance and Budget: R. J. Alfidi, R. K. Gedgaudas-McClees, J. R. Thornbury, K. H. Vydareny, J. H. Thrall, chairman

Nominating: G. A. W. Gooding, L. F. Rogers, K. H. Vydareny, chairman

Publications: E. Buonocore, C. A. Rohrmann, Jr., R. J. Stanley, R. I. White, W. J. Casarella, chairman

Membership: J. E. Madewell, A. A. Moss, K. H. Vydareny, R. J. Alfidi, chairman

Representatives to Other Organizations

American Board of Radiology: J. A. Kirkpatrick, Jr., E. C. Klatte, L. F. Rogers

American College of Radiology: J. M. Dennis, R. A. Gagliardi, J. E. Madewell, B. L. McClennan, R. J. Stanley

American Medical Association: S. F. Ochsner, delegate; K. L. Krabbenhoft, alternate; K. L. Kidd, CPT Advisory Committee

American National Standards Institute: M. E. Haskin

National Council on Radiation Protection and Measurements: F. Miraldi, E. L. Saenger

Armed Forces Institute of Pathology: J. E. Madewell

Meeting Arrangements

Annual Meetings: May 5–10, 1991, Sheraton Boston, Boston; May 10–15, 1992, Marriott's World Center, Orlando, FL

Annual Meeting Committee: H. C. Carlson, J. K. Crowe, N. R. Dunnick, R. R. Lukin, R. J. Stanley, R. D. Steele, Jr., A. M. Landry, Jr., chairman

Instructional Courses: R. J. Stanley, chairman

Scientific Program: P. Arger, E. Buonocore, D. O. Davis, K. B. Hunter, D. Kushner, T. C. McLoud, W. A. Murphy, Jr., L. B. Talner, J. H. Thrall, J. A. Kirkpatrick, chairman

Scientific Exhibits: J. R. Haaga, R. G. Ramsey, N. R. Dunnick, chairman

ARRS Membership

An application form is printed in the September issue of the Journal. For consideration at the 1991 ARRS meeting, send completed forms before February 1, 1991, to American Roentgen Ray Society, 1891 Preston White Dr., Reston, VA 22091. Active members are graduates of an approved medical or osteopathic school or hold an advanced degree in an allied science. They must practice radiology or work in an associated science in the United States or Canada and be certified by the American Board of Radiology, American Osteopathic Board of Radiology, or Royal College of Physicians of Canada or otherwise adequately document training and credentials. Corresponding members are foreign radiologists or scientists who are active in radiology or an allied science. Members-in-training are residents or fellows in radiology or postgraduate students in an allied science. Additional application forms can be obtained from the ARRS offices in Reston, VA.

Business Office

Paul Fullagar, Executive Director, American Roentgen Ray Society, 1891 Preston White Dr., Reston, VA 22091; (703) 648-8900.

Classified Advertisements

Positions Available

BROAD SPECTRUM RADIOLOGIST/UPSTATE NEW YORK—Radiologist wanted for hospital-based practice 90 mi. northwest of New York City. Excellent recreational activities and easy access to metropolis. All modalities available. Excellent salary and benefits leading to early partnership. Immediate availability, but can wait for right applicant. Call G. Bilick; (914) 794-3300, ext. 2216 or send CV to P.O. Box 144, Harris, NY 12742. 11–2ap

RADIOLOGIST—A 21-physician, multispecialty group practice is seeking a second radiologist. The practice, located in the mountains of beautiful southwest Virginia, covers 4 outpatient clinics with ultrasound, nuclear medicine, mammography, and diagnostic radiology. Competitive salary; excellent benefits. Send CV to Tommie Massey, Dickenson Wise Medical Group, P.O. Box 17, Wise, VA 24293; (703) 328-2631. 11ap

COASTAL NORTHERN CALIFORNIA / SAN FRANCISCO BAY AREA—Progressive, diversified group of 16 board-certified diagnostic radiologists and 4 radiation oncologists seeks board-eligible/certified radiologists with fellowship training in MRI/neuroradiology. The group serves 4 small to medium-sized hospitals and a large outpatient imaging center. The imaging center includes GE 1.5-T MRI, CT, and Acuson ultrasound as well as CGR mammography and 3 RF rooms. Competitive salary, 2 yr to full partnership, and excellent benefits. Fast-growing suburban/rural community 50 min north of downtown San Francisco with sunny Mediterranean climate and very mild winters in the heart of the wine country. Excellent outdoor recreational opportunities including sailboating, ocean/steelhead fishing, backpacking, water skiing, and snow skiing in the Sierras. Please send initial inquiry and CV to John McGovern, 121 Sotoyome St., Santa Rosa, CA 95405. 11ap

RADIOLOGIST—Veterans Affairs Medical Center, Wilkes-Barre, PA, has an immediate vacancy for a board-certified radiologist. This 473-bed, teaching medical center with a 120-bed (plus 60 additional beds currently under construction) nursing home-care unit is affiliated with Temple University School of Medicine, Hahnemann University School of Medicine, and Episcopal Hospital, Philadelphia, PA. Wilkes-Barre is located near the Pocono Mountains resort area within a 2½-hr drive of New York City and Philadelphia. For additional information, contact William K. Grossman, M.D., Chief of Staff; (717) 821-7207. An equal opportunity employer. 11–1a

BOSTON ULTRASOUND CONSULTANTS is seeking a fellowship-trained radiologist for a growing, dedicated, ultrasound practice in the Boston area. Hands-on OB/GYN experience, preferably in a high-risk setting, is required. An excellent opportunity for the right person. For information, call or send CV to Boston Ultrasound Consultants, P.C., 77 Pond Ave., Ste. 104 C, Brookline, MA 02146; (617) 232-4600. 11ap

NEW ORLEANS PARTNERSHIP OPPORTUNITY—Would you like to live in "America's most interesting city"? Would you like to become a partner in a well-established, highly successful radiology group practice that has the latest technology, including a free-standing MRI center with a 1.5-T GE Advantage system? We are a large, multispecialty group practicing in hospital, outpatient offices, and a new breast center. We will offer a BC radiologist, with interest in MR and/or vascular procedures, an exciting job opportunity. Contact Harold R. Neitzschman, M.D., 4400 General Meyer Ave., Ste. 211, New Orleans, LA 70131; (504) 368-5074. 11–1ap

RADIOLOGISTS—Seven-member group seeks board-certified radiologists to join a progressive, hospital/clinic practice in scenic western Arkansas town of approximately 100,000. All modalities represented in practice. Competitive salary leading to early, full partnership. Liberal fringe benefits and vacation. At least 3 mo documented MRI training necessary. Interested parties please send CV to W. T. Huskison, M.D., P.O. Box 3887, Fort Smith, AR 72913; (501) 452-9416 collect. 11–1ap

HOUSTON GROUP needs an additional board-certified diagnostic radiologist. Prefer training and/or experience in interventional (including angiography and percutaneous interventional procedures), guided biopsy, ultrasound, CT, nuclear medicine, and MRI. Please submit CV to Professional Practice Management, Inc., 1075 Kingwood Dr., Kingwood, TX 77339; (713) 358-8113. 11–12ap

DIRECTOR OF ULTRASONOGRAPHY—Position available for Director of Ultrasonography in 700-bed, university-affiliated, teaching hospital with fully approved residency program. Modern equipment including 5 ultrasound units (performing 7,000 procedures annually, including all obstetric studies), 2 CT scanners, and 1 MRI unit. Staff of 12 full-time radiologists. Send CV to David Bryk, M.D., Dept. of Radiology, Maimonides Medical Center, 4802 Tenth Ave., Brooklyn, NY 11219. 11ap

MAINE—Excellent opportunity for BC/BE, fellowship-trained neuroradiologist with progressive, well-established, small group. Live and work in college community in southern region close to coast, mountains, and lakes. Competitive compensation package leading to partnership. Affiliated with 200-bed, modern community hospital. Send CV to New England Health Search, 63 Forest Ave., Orono, ME 04473; (207) 866-5680 or (207) 866-5685. 11–2ap

STAFF RADIOLOGIST—The VA Medical Center, Bay Pines, FL, affiliated with the University of South Florida School of Medicine, is currently accepting applications for a staff radiologist, board-certified in general diagnostic radiology with MRI experience. This medical center is located on the beautiful West Coast of FL, only min from the Gulf of Mexico. Send CV and/or call Ann C. Esquerra, M.D., Chief, Radiology Service (114), VA Medical Center, Bay Pines, FL 33504; (813) 398-9363. EOE/MFHV. 11–12a

CHIEF OF RADIOLOGY—St. Paul-Ramsey Medical Center, a major affiliate hospital of the University of Minnesota, is seeking a well-qualified radiologist to head the Section of Radiology. This acute-care, 275-bed hospital is 1 of the primary teaching institutions of the University of Minnesota and is a designated regional center for trauma and burns. This 9-member section is fully equipped with state-of-the-art facilities for ultrasonography, CT, and MRI. The successful candidate for this position will have well-developed administrative and managerial skills and an unequivocal commitment to patient care, education, and collaborative interaction with other hospital depts. Development of a radiology residency program in conjunction with the University of Minnesota is seen as a highly desirable near-term goal. Research will be encouraged. Faculty rank and salary depend on past scholarly productivity and post-M.D. experience. Applicants must be able to obtain a license to practice medicine in the state of Minnesota before the appointment date, which is negotiable. Applications will be accepted through Nov. 30, 1990. Send letters to John J. Marini, M.D., Chair, Radiology Search Committee, St. Paul-Ramsey Medical Center (Division of Pulmonary Medicine), 640 Jackson St., St. Paul, MN 55101-2595. The University of Minnesota is an equal opportunity educator and employer, and specifically invites and encourages applications from women and minorities. 11a

PEDIATRIC RADIOLOGIST—The Nemours Children's Clinic and the University of Florida are seeking a board-certified/eligible radiologist to join the expanding program in Jacksonville, FL. The Nemours Children's Clinic is a multidisciplinary pediatric medical and surgical specialty clinic. The clinic is located in a beautiful, new, 11-story building with state-of-the-art technology on the cutting edge of pediatric health care. The radiology program is a rapidly expanding service providing community-wide service for a city of 800,000, with a large referral base in south Georgia and northeast Florida. The candidate will be offered University appointment at the assistant/associate professor level. Teaching and research are strongly encouraged and funds are available for establishment and maintenance of quality research programs. Salary will be commensurate with experience. Interested applicants should send their CV to Ian T. Nathanson, M.D., Chairman, Search Committee, Nemours Children's Clinic, P.O. Box 5720, Jacksonville, FL 32247. Academic status is offered by the University of Florida, an equal opportunity/affirmative action employer with whom Nemours is affiliated. Recruiting deadline is Dec. 1, 1990. Anticipated starting date is Jan. 1, 1991. 11a

MRI RADIOLOGIST—An 8-person radiology group in southern New Jersey, 15 min from Philadelphia, seeks a board-certified radiologist with specialty training in body MRI to help run a new GE 1.5-T Signa MRI. Busy, dynamic practice consists of 2 hospitals as well as a full-service private office which also houses the MRI unit. Competitive compensation package will lead to full partnership. Send CV or call Steven Singer, M.D., Kings Highway and Princeton Ave., Woodbury, NJ 08096; (609) 848-4998. 11–1ap

RADIOLOGIST—Hospital-based practitioner seeks board-certified associate. Services include all phases of diagnostic radiology, ultrasound, CT, and nuclear medicine. Practice in a 149-bed, Catholic hospital located in a city of 20,000 near Albany and Saratoga. Excellent schools and recreational facilities nearby. Reply with CV and references to Ruperto S. Young, M.D., P.C., 427 Guy Park Ave., Amsterdam, NY 12010. 11ap

IMMEDIATE OPENING, DIAGNOSTIC RADIOLOGIST—Excellent opportunity for a young, dynamic, preferably board-certified radiologist to join an active, 9-member group. Growing practice includes a 700-bed hospital system with state-of-the-art equipment and excellent working facilities. Skills in all phases of diagnostic radiology desired. Attractive and competitive benefits package leading to full partnership. Contact Sanford E. Rabushka, M.D., 11133 Dunn Rd., Ste. 1017, St. Louis, MO 63136; (314) 653-4300. 11–4ap

THE DEPT. OF RADIOLOGY, VIRGINIA COMMONWEALTH UNIVERSITY/MEDICAL COLLEGE OF VIRGINIA (VCU/MCV), AND THE MCGUIRE VA MEDICAL CENTER (VAMC) RICHMOND, VA, seek faculty for positions in diagnostic radiology (chest, GI, mammography, CT/ultrasound/MR, musculoskeletal, pediatrics, ER, angio/interventional, and neuroradiology), nuclear medicine, and radiologic physics. MCV is a 1,058-bed facility (205 for pediatric patients) and a level I trauma center. The McGuire VAMC is an 800-bed facility (pediatrics excluded). ABR certification or eligibility required. Applicant should have experience working in a culturally diverse environment. Academic rank and salary commensurate with experience. For position description or to submit CV, write or phone A. V. Proto, M.D., Dept. of Radiology, MCV Box 470, Richmond, VA 23298-0470; (804) 786-7212. VCU/MCV is an equal opportunity/affirmative action employer. Women and minorities are encouraged to apply. 11a

SKELETAL RADIOLOGIST—A staff position is available at the Cleveland Clinic Foundation in the 4-member Section of Musculoskeletal Radiology. The Cleveland Clinic is a 1,000-bed, academic, tertiary-care facility with a large outpatient population and international referral base. The section provides CT and MR as applied to the musculoskeletal system. In addition, the section performs bone biopsies, quantitative bone densitometry, arthrography, and reads a large volume of plain films. There is a large radiology residency at the Cleveland Clinic. A musculoskeletal fellowship will begin in 1991. Applicants should be fellowship-trained or possess equivalent experience. Send CV to Bradford J. Richmond, M.D., Head, Section of Musculoskeletal Radiology, Clinic Radiology, Desk A21, Cleveland Clinic Foundation, 9500 Euclid Ave., Cleveland, OH 44195. The Cleveland Clinic is an equal opportunity employer. M-F-H-V. 11–1a

RADIOLOGIST, CHICAGO AREA—A 7-member radiology group in far southwest suburb of Chicago metropolitan area is currently interviewing BC/BE radiologists for a position available July 1991. Fellowship training attractive but not essential. A highly recommended candidate directly from residency will be given equal consideration. Expertise in general radiology, imaging, and angiography required. Radiology services are provided for 524-bed community hospital and soon-to-be-completed joint venture MRI center, together generating 85,000 exams/yr. Number of exams, as well as group revenue, has steadily increased in the past several years and is likely to continue as we are in a rapidly growing, middle/upper class area. We are oriented toward providing top-quality radiology to referring physicians, as well as a pleasant work environment and significant leisure time for ourselves. Features include competitive starting salary, full benefit package, full partnership after 3 yr, equal division of call among group members, generous vacation time (8 wk to start), and teleradiography. Equipment includes the following state-of-the-art items: Siemens Hi-Q CT; 2 Acuson units with color-flow Doppler and endovaginal probe (third unit ordered); Phillips ARC-14 DVI-S specials room with full digital capability; fully equipped nuclear medicine dept. with dual head bone table and third SPECT camera ordered; 1.5-T Siemens SP MRI with MR angiography; and GE Senographe 600-T mammography unit. RSNA interview possible. Send CV to Box G73, *AJR* (see address this section), or contact Bruce Linder, M.D., (708) 910-3850. 11–1ap

TEMPLE UNIVERSITY SCHOOL OF MEDICINE is seeking a chair of the Dept. of Diagnostic Imaging. This expanding dept. consists of 3 divisions: diagnostic radiology and nuclear medicine at Temple University Hospital, and pediatric radiology at St. Christopher's Hospital for Children. Candidates should have demonstrated leadership in clinical practice, teaching, and research and must have strong administrative skills. Inquiries and nominations should be addressed to Jeffrey I. Greenstein, M.D., Chairman, Search Committee, Dept. of Neurology, Temple University School of Medicine, 3401 N. Broad St. (5PP), Philadelphia, PA 19140. Temple University is an equal opportunity/affirmative action employer. 11a

BODY MRI/ABDOMINAL IMAGING—Board-certified radiologist with fellowship training in MRI needed for a position beginning July 1, 1991. Must have fellowship training in MRI, and an interest in CT and GI studies for practice in 578-bed, advanced, metropolitan, tertiary-care teaching hospital. Radiology group is an academically oriented private practice. Send inquiries to Harvey L. Neiman, M.D., Chairman, Dept. of Radiology, The Western Pennsylvania Hospital, 4800 Friendship Ave., Pittsburgh, PA 15224. 11–1a

ANGIO/INTERVENTIONAL—Large, private-practice group in suburb of Detroit is looking for an additional interventional/angio radiologist with expertise in general radiology also. Send letters and resume to Vjeko Mikelic, M.D., St. John Hospital & Medical Center, 22101 Moross Rd., Detroit, MI 48236. 11–12ap

FACULTY NEURORADIOLOGIST, THOMAS JEFFERSON UNIVERSITY HOSPITAL—The Dept. of Radiology at Thomas Jefferson University Hospital in Philadelphia has an immediate opening for a faculty neuroradiologist. This can be either at a very senior or junior level. Our dept. currently operates 4 GE 1.5-T Signa MRI units, and also has a modern neurosciences imaging center. Aside from the MRI units, this facility has a Philips angio room with DSA, a myelography room, 2 CT scanners, reading rooms, and faculty offices. There are 6 faculty members in the neuro division, as well as 5 2-yr neuro fellows. Our practice is growing rapidly and close clinical and research relationships exist with neurosurgery, neurology, orthopedic surgery, and a large spinal-cord-injury center. The dept. also maintains experimental laboratories of its own. Candidates should ideally have broad clinical, research, and teaching interests. Excellent salary and fringe benefits. Interested persons should contact David C. Levin, M.D., Chairman, Dept. of Radiology, Thomas Jefferson University Hospital, Philadelphia, PA 19107; (215) 955-7264. Jefferson is an equal opportunity/affirmative action employer. 11–1a

RADIOLOGIST—Seven-person group seeks general radiologist with fellowship training and special interest in MRI for 92-bed hospital and several imaging centers. Practice in the rapidly growing north San Diego and Temecula Valley areas. Send CV to North Coast Imaging Radiology Medical Group, Inc., 1582 W. San Marcos Blvd., Ste. 104, San Marcos, CA 92069; (619) 744-6442. 11–2ap

MINNEAPOLIS, MINNESOTA—Practice opportunity for a board-certified radiologist with subspecialty interest in musculoskeletal imaging. MR experience is required. Procedural skills are desirable, as there is a growing volume of invasive orthopedic procedures. Practice is based at a rapidly growing, privately owned, freestanding outpatient imaging center equipped with 2 GE 9800 CT scanners, 2 GE Signa 1.5-T MR scanners, and related fluoroscopic-radiographic and ultrasound equipment. Practice also includes coverage of a 750-bed, tertiary-care medical center and adjacent satellite clinic. Five radiologists in practice currently. One distant MR facility operating and plans for more. Investment opportunities for radiologists involved in the practice as well as academic orientation and opportunity for subspecialization. Excellent benefits. Send CV and responses to Cooper R. Gundry, M.D., Center for Diagnostic Imaging, 5775 Wayzata Blvd., Ste. 190, Minneapolis, MN 55416. No telephone calls please. All inquiries confidential. 11–1ap

ANGIOGRAPHER/INTERVENTIONAL RADIOLOGIST—Nationally known, university medical center in the Washington, DC, vicinity seeks qualified radiologist for special procedures. Responsibilities include all visceral angiography and special procedures, resident training, and some general diagnostic radiology. University faculty appointment available to qualified persons. Applicants must be graduate of U.S. medical school, board-certified, fellowship-trained in angio/interventional, and SCVIR eligible or member. Excellent opportunity for new fellowship graduate. Position available July 1991. Generous compensation package. Respond with CV to S. Markovitz, S.M.D., 7826 Eastern Ave., N.W., Ste. 402, Washington, DC 20012. 11–12ap

A 42-PHYSICIAN, MULTISPECIALTY CLINIC serving central and western Kansas has an immediate position for an additional board-certified/eligible radiologist to join 2 others. Excellent facilities include diagnostic radiography, CT, diagnostic ultrasound, nuclear medicine, and MR services. No call, weekends, or holidays. An excellent opportunity in a dynamic practice setting 45 mi. from Wichita. Please send CV to Administrator, Hutchinson Clinic, 2101 N. Waldron, Hutchinson, KS 67502, or call collect (316) 669-2626. 11–12ap

BC/BE DIAGNOSTIC RADIOLOGIST with skills in all aspects of radiology, including CT, ultrasound, nuclear medicine, interventional, MR, and mammography sought to join a dynamic group of 6 BC radiologists covering a busy, progressive, community hospital, 2 private offices, and an outpatient women's center. Modern dept., state-of-the-art equipment, attractive vacation, CME, and benefits package. 30 min west of Philadelphia. Position available immediately but will wait for right person. Reply with CV to L. Griska, M.D., Dept. of Radiology, Montgomery Hospital, Powell and Fornance Sts., Norristown, PA 19401. 11–2ap

BOARD-CERTIFIED, DIAGNOSTIC RADIOLOGIST sought by 8-member, community-based, university-affiliated hospital in Hartford, CT. Practice includes outpatient office with the latest equipment, including MRI, CT, ultrasound, and angiography. Send CV to Harold Moskowitz, M.D., FACR, Director, Dept. of Radiology, Mount Sinai Hospital, 500 Blue Hills Ave., Hartford, CT 06112. 11ap

SIX-PERSON, WELL-ESTABLISHED GROUP of radiologists in western Pennsylvania seeks a well-qualified, board-certified/eligible radiologist. Large hospital practice. Group owns CT scanner, and new freestanding MRI installation. Partnership available; good opportunity for the right candidate. Contact Jose C. Guinto, M.D., Chairman, Dept. of Diagnostic Radiology, McKeesport Hospital, 1500 Fifth Ave., McKeesport, PA 15132. 11ap

RADIOLOGIST—The Dept. of Radiology at the Beth Israel Hospital in Boston, MA, is seeking a radiologist with broad experience in general radiology. Special expertise in body CT and ultrasound is desirable as position involves teaching and consultation responsibilities to junior staff and trainees. The hospital is a 504-bed, voluntary, teaching hospital affiliated with the Harvard Medical School. Candidates should meet the requirements for faculty appointment, preferably at the associate professor level. Please send inquiries with a CV to Sven Paulin, M.D., Radiologist-in-Chief, Beth Israel Hospital, 330 Brookline Ave., Boston, MA 02215. The hospital is an affirmative action/equal opportunity employer. Minority and female candidates are encouraged to apply. 11ap

ISRAEL, DIAGNOSTIC RADIOLOGY. Opportunities for 3–4 week or longer working vacations in a number of Israeli medical centers, on a volunteer basis. Positions varied, arrangements flexible. For information contact: Jonathan H. Fish, M.D., 1844 San Miguel Dr., #302, Walnut Creek, CA 94596; (415) 947-0560. 11–1xa

NUCLEAR MEDICINE—Excellent opportunity for a diagnostic radiologist with special interest in nuclear medicine (special competency preferred) to join a private-practice group of 13 radiologists. 600-bed, university-affiliated community hospital, with radiology residency, in a pleasant suburban setting 25 mi. from New York City. State-of-the-art equipment including Acuson with color Doppler, Siemens Somatom Plus CT, and 1.5-T Magnetom. Competitive salary leading to partnership. Please send CV to A. Salomon, M.D., 151 Summit Ave., Summit, NJ 07901. 9–12ap

THE DIVISION OF VASCULAR AND INTERVENTIONAL RADIOLOGY of Emory University, Dept. of Radiology, is seeking a fellowship-trained, interventional radiologist to join our staff. This is an exciting opportunity for an individual with clinical, teaching, and/or research interest. We are involved in all aspects of interventional radiology including angioplasty, atherectomy, laser angioplasty, thrombolysis, and biliary and GU intervention. Our equipment is state-of-the-art. Research opportunities are available in a fully equipped research laboratory. Atlanta is a cosmopolitan city with ample cultural and recreational resources and a mild climate. Interested candidates should contact Stephen L. Kaufman, M.D., Dept. of Radiology, Emory University Hospital, 1364 Clifton Rd., N.E., Atlanta, GA 30322. Emory University is an equal opportunity, affirmative action employer. 9–11a

THE DIVISION OF NUCLEAR MEDICINE, Oregon Health Sciences University, Portland, OR, invites applications for a faculty position available immediately either part-time in nuclear medicine or full-time divided between nuclear medicine and another division of diagnostic radiology. Board-certification in nuclear medicine is required. Send CV to Richard W. Katzberg, M.D., Chairman, or Jeffrey S. Stevens, M.D., Dept. of Diagnostic Radiology, UHN72, Oregon Health Sciences University, 3181 S.W. Sam Jackson Park Rd., Portland, OR 97201-3098. OHSU is an affirmative action, equal opportunity employer. 9–12a

OUTPATIENT CLINIC-RADIOLOGIST, UNIVERSITY OF PITTSBURGH—We are seeking an additional radiologist for the Falk Clinic—Outpatient Division. This is an attractive, modern facility with state-of-the-art equipment, including plain radiography, fluoroscopy, mammography, sonography, and CT. The appointment will be at the assistant or associate professor level, with rank appropriate with experience. Salary and fringe benefits are very competitive. This is an academic appointment with emphasis on clinical service and teaching. The University of Pittsburgh is an equal opportunity employer. Contact Michael P. Federle, M.D., Professor and Chairman, Dept. of Radiology, Presbyterian-University Hospital, DeSoto at O'Hara Sts., Pittsburgh, PA 15213. 9–11ap

ANGIOGRAPHY/INTERVENTIONAL RADIOLOGIST—Excellent opportunity for diagnostic radiologist with additional training in angiography and interventional radiology to join private practice group of 13 radiologists. Practice in 600-bed, university-affiliated, community hospital, with radiology residency, in a pleasant suburban setting 25 mi. from New York City. State-of-the-art equipment including Acuson with color Doppler, Siemens Somatom Plus CT, and 1.5-T Magnetom. Competitive salary leading to partnership. Please send CV to A. Salomon, M.D., 151 Summit Ave., Summit, NJ 07901. 9–12ap

ULTRASOUND/CT/MRI—Opportunity for a board-certified radiologist specializing in ultrasound, body CT, and body MRI to pursue an academic career at the New York Hospital-Cornell Medical Center. Dept. provides state-of-the-art equipment, including Acuson ultrasound, GE 9800 CT, and GE Signa 1.5-T MR. Wide variety of ultrasound exams include abdominal, OB-GYN, color Doppler, small parts, neonatal head, transvaginal, and transrectal. Prefer candidate with prior fellowship in sectional imaging or ultrasound. Responsibilities include clinical practice, teaching, and research. Position available 7/1/91 or earlier. Please send CV to Elias Kazam, M.D., Dept. of Radiology, The New York Hospital-Cornell Medical Center, 525 E. 68th St., New York, NY 10021. 9–12ap

ULTRASOUND SECTION CHIEF, UNIVERSITY OF MARYLAND—The University of Maryland Hospital seeks a chief for the ultrasound section of the Dept. of Radiology. Although already well-equipped, this position offers a great opportunity for expansion and development, both with the new all-digital Dept. of Radiology under construction at the adjoining VA Hospital and in a new planned all-digital Dept. of Radiology to be constructed at the University Hospital. Applicants should have specialist training and fellowship in ultrasound and a willingness to be involved in the teaching of residents and students. Academic rank and salary are commensurate with experience. The radiologists are organized as a professional corporation, offering excellent fringe benefits. Baltimore is a superb place to live and work. It has all the amenities of a large metropolitan center, yet is small enough to avoid most of the problems (traffic, inflated property values, etc.) of our largest cities. It is only 3 hr from the ocean and Washington, Philadelphia, and New York are readily accessible. Submit CV to Gerald S. Johnston, M.D., Dept. of Diagnostic Radiology, 22 S. Greene St., Baltimore, MD 21201; (800) 866-8667, ext. 3477. Affirmative action/equal opportunity employer encourages applications from members of minority groups. 9–2ap

UNIVERSITY OF ILLINOIS COLLEGE OF MEDICINE AT CHICAGO has an opening for a board-certified, diagnostic radiologist with interest in abdominal imaging including CT, MRI, ultrasound, GI, and GU radiology. The position offers a balance of clinical, teaching, and research activities. Salary and faculty rank are appropriate to experience. Please send inquiries along with CT to Steven Pinsky, M.D., Professor and Head of Radiology, University of Illinois at Chicago, 1740 West Taylor Street, Chicago, IL 60612; (312) 996-0234. UICOMC is an AA/EO employer offering competitive salary and benefit package. 9–12a

VASCULAR/INTERVENTIONAL AND DIAGNOSTIC IMAGING, 2 POSITIONS—The 11-member imaging section of Guthrie Clinic-Robert Packer Hospital desires associates with fellowship training and/or expertise in the above areas. The Guthrie Clinic provides tertiary care in the southern tier of New York and the northern tier of Pennsylvania in the beautiful, endless mountains. Outstanding practice opportunities in an environment free of urban hassle. Please send letter of inquiry with CV or call Thomas F. Bednarek, M.D., Chairman, Dept. of Radiology, Guthrie Healthcare System, Sayre, PA 18840; (717) 882-4025. 9–11a

ACADEMIC POSITION, UNIVERSITY OF CALIFORNIA, LOS ANGELES (UCLA)—The UCLA Dept. of Radiological Sciences is recruiting an individual with an established record in MRI and/or spectroscopy to develop a basic and clinical MR research program. The dept. has 5 MR scanners in operation and the medical imaging division has an extensively equipped image processing laboratory and directs a biomedical physics graduate program. The candidate is expected to coordinate the overall MR research programs, attract extramural research support, integrate MR research into the graduate program, and participate in the teaching and administration of graduate students and residents. For the initial application, candidates should submit CV, names and addresses of 5 references, a synopsis of their current research program (including past, present, and pending grant support), representative recent publications, and a statement of teaching and administrative experience to Zoran L. Barbaric, M.D., Chairman of Search Committee, Dept. of Radiological Sciences, UCLA School of Medicine, 10833 Le Conte Ave., Los Angeles, CA 90024-1721. UCLA is an equal opportunity/affirmative action employer. 9–11a

THE UNIVERSITY OF ARIZONA, DEPT. OF RADIOLOGY, seeks 2 full-time, general radiologists to participate in clinical, teaching, and research activities at its university and affiliated hospitals. Applicants should be experienced in plain film interpretation, cross-sectional imaging, and mammography. Rank, salary, and time allotted to research are related to the applicant's credentials and interests. The review of applications will begin Sept. 15, 1990, and will continue until the position is filled. The University of Arizona is an equal opportunity employer. Contact Bruce J. Hillman, M.D., Vice-Chairman, Dept. of Radiology, University Medical Center, Tucson, AZ 85724; (602) 694-7368. 9–12a

POSITION AVAILABLE IN PALM SPRINGS, CA for a radiologist to join a 10-person group in a community hospital/office practice. Contact Marvin J. Friedenberg, M.D., Dept. of Radiology, Desert Hospital, 1150 N. Indian, Palm Springs, CA 92262. 9–11ap

BOSTON, IMMEDIATE OPENING—Radiologist wanted to join busy, well-established, private-practice group with 4 outpatient facilities. Expertise in ultrasound and mammography. No evening or weekend call. Excellent life-style, partnership opportunity. Send letter and CV to Box E49, *AJR* (see address this section). 9–2ap

INDIANAPOLIS, IN—Practice opportunity for a radiologist to serve as medical director of a new, freestanding, privately owned, high-field MR imaging center. Facility will be managed by and affiliated with the Center for Diagnostic Imaging in Minneapolis, MN. MR experience mandatory. Subspecialty experience in MR desirable. Board certification and licensure in Indiana required. Please send inquiries with CV to Kenneth B. Heithoff, M.D., Center for Diagnostic Imaging, 5775 Wayzata Blvd., Ste. 190, Minneapolis, MN 55416. All inquiries entirely confidential. No telephone calls please. 9–11ap

THE UNIVERSITY OF ARIZONA seeks part-time general radiologists to participate in its clinical and research programs at its university and affiliated hospitals. Applicants should be experienced in plain film interpretation and cross-sectional imaging; expertise in mammography is desirable. Rank and salary are related to the applicant's credentials. The review of applications will begin Sept. 15, 1990, and will continue until the position is filled. The University of Arizona is an equal opportunity employer. Contact Bruce J. Hillman, M.D., Vice-Chairman, Dept. of Radiology, University Medical Center, Tucson, AZ 85724; (602) 694-7368. 9–12a

THE DEPT. OF RADIOLOGY AT TRIPLER ARMY MEDICAL CENTER, HONOLULU, HI, is recruiting academic radiologists for several divisions of the dept. including ultrasound, chest, skeletal, neuro, and general diagnostic radiology. Our dept. offers a fully accredited residency program with 20 residents and 16 attending full-time staff. Numerous consultants from across the country lecture on a continuing and regular basis. The hospital is a modern, tertiary-care center serving Hawaii and the entire Pacific Basin. A strong residency program, diverse and interesting patient population, excellent equipment, and a tropical lifestyle are positive aspects of the practice. Academic credentials and/or experience are necessary. Recently graduated fellows are encouraged to apply. Board certification is mandatory. Candidates should be particularly interested in patient care, teaching, and research. Salary and benefits are competitive and generous. Tripler is an EO/EEO employer. Please contact Mark F. Hansen, M.D., CoL., MC, Chief, Dept. of Radiology, TAMC, HI 96859-5000; (808) 433-6393. 8–7a

NORTHERN CALIFORNIA/SAN FRANCISCO BAY AREA—The Permanente Medical Group is seeking a BC radiologist with multimodality interests and fellowship training in MR or interventional radiology to join a 10-person group serving a 337-bed, acute-care hospital and 2 outpatient clinics. Teaching opportunities are available with residents of subspecialty services on rotation from Stanford University Hospital as well as our own medical residents. We are currently siting a GE 1.5-T MRI system and installing a new LU arm. Competitive salary and excellent benefits. Please send inquiries and CV to Bruce Baker, M.D., Chief, Dept. of Radiology, Kaiser Permanente Medical Center, 900 Kiely Blvd., AD-AJR, Santa Clara, CA 95051; (408) 236-4444. EOE. 11–12a

DIAGNOSTIC RADIOLOGIST—Eight board-certified radiologists in expanding, hospital-based private practice seek BC/E general radiologist to associate. Competence in all modalities expected with need for MRI training emphasized. Opportunity in midwestern city of 72,000 offers generous compensation/vacation. Full partnership after 2 yr. Reply to Box D33, *AJR* (see address this section). 8–11ap

TWO BC RADIOLOGISTS, KANSAS CITY, MO Six radiologists currently covering a 600-bed, tertiary medical center seek a radiologist experienced in angio/interventional and a 2nd, well-rounded radiologist with all capabilities. Positions open immediately. Salary and fringe benefits competitive. Both positions lead to full partnership. Send CV and letter of inquiry to J. M. Speckman, M.D., 6400 Prospect, Ste. 310, Kansas City, MO 64132. 8–11ap

UTMB, GALVESTON, TX—The Dept. of Radiology of The University of Texas Medical Branch in Galveston has openings for persons trained and experienced in ultrasound, mammography, and abdominal imaging. The opportunity for academic advancement is great and benefits are generous. Salaries are competitive and living conditions are desirable. Interested persons should contact Melvyn H. Schreiber, M.D., Chairman, Dept. of Radiology, UTMB, Galveston, TX 77550; (409) 761-1823. UTMB is an equal opportunity M/F/H/V affirmative action employer. UTMB hires only those authorized to work in the United States. 7–12a

FACULTY ULTRASOUND RADIOLOGIST, THOMAS JEFFERSON UNIVERSITY HOSPITAL Jefferson's Dept. of Radiology wishes to recruit a faculty radiologist to work in our division of diagnostic ultrasound. Candidates at all levels will be considered. This division is housed in 1 of the largest and best equipped facilities in the world and is extensively involved in the full range of ultrasound studies including obstetrical, vascular, echocardiography, invasive, endoluminal, and both biliary and kidney stone lithotripsy. A new outpatient ultrasound facility is under construction adjacent to the main campus. The position provides excellent salary and benefits, protected research time each wk, and an opportunity to become associated with 1 of the most academically productive ultrasound groups anywhere. Interested individuals should contact either Barry Goldberg, M.D. (Director of Ultrasound), or David C. Levin, M.D. (Dept. Chairman), at the Dept. of Radiology, Thomas Jefferson University Hospital, Philadelphia, PA 19107. Jefferson is an equal opportunity/affirmative action employer. 11xa

FULL-TIME BC RADIOLOGIST needed to staff outpatient women's diagnostic center in suburban Dallas. Experience in mammography and OB/GYN sonography preferred. No call responsibilities. Attractive compensation package. Send CV to Box Y56, *AJR* (see address this section). 11xa

DIAGNOSTIC RADIOLOGIST—Board-certified/eligible radiologist with expertise in CT, ultrasound, nuclear medicine, mammography, angiography, and MRI needed to join group of 4 board-certified radiologists. Hospital-based practice in acute-care, 300-bed hospital with high risk OB and neonatal ICU. Excellent relationship with hospital administration. Annual volume, 85,000 exams. State-of-the-art equipment including Siemens Hi-Q CT, 2 Acuson 128 ultrasound units, and SPECT. Siemens 1.5-T MRI being installed. Pleasant living area, within 4-hr drive from ski/mountain areas of New Mexico and Colorado, draws from regional patient population of 350,000. Generous salary and benefits leading to early partnership. Contact Gayle H. Bickers, M.D., P.O. Box 3460, Amarillo, TX 79116-3460; (806) 378-4708. 7–12ap

DIAGNOSTIC RADIOLOGIST with skills in CT, MR, interventional, ultrasound, and nuclear medicine to join group of 8 board-certified radiologists. Growing practice in eastern Washington. 200-bed hospital and 4 private offices. Long-term potential of practice is excellent. Top-notch school system, including 3 first-rate universities. Excellent hunting, fishing, boating, and skiing. Contact L. E. Crecelius, M.D., N. 5901 Lidgerwood, Ste. 18B, Spokane, WA 99207; (509) 482-2385. 7–12ap

DIAGNOSTIC RADIOLOGISTS — Progressive 3-member group in North Carolina Coastal Plain seeks 2 BC/BE radiologists. ACR-accredited practice includes 350-bed, regional referral hospital, outpatient office, and women's diagnostic center. State-of-the-art equipment. Excellent financial package. Send letter and CV to Box C13, *AJR* (see address this section). 7–12ap

IMMEDIATE OPENING FOR BOARD-CERTIFIED DIAGNOSTIC RADIOLOGIST to join a 3-member group in desirable north Dallas location. Must have expertise in all aspects of diagnostic radiology including angiography and MRI. Hospital and outpatient office practice. Salary commensurate with experience. Serious inquiries only. Send CV to Jeffrey Kam, M.D., 11617 N. Central Expressway, Ste. 132, Dallas, TX 75243. 7–12ap

IMMEDIATE OPENING - BOSTON SUBURBAN RADIOLOGY GROUP — 300-bed, university-affiliated, community hospital seeks partner with skills or experience in all modalities. Send CV to Box B2, *AJR* (see address this section). 9–11ap

IMMEDIATE OPENING, PART-TIME, SUBURBAN BOSTON — 300-bed, university-affiliated, community teaching hospital seeks BE/BC radiologist. Flexible hours. Send CV to Box B6, *AJR* (see address this section). 9–11ap

NEURORADIOLOGIST, BRIGHAM & WOMEN'S HOSPITAL—The Dept. of Radiology at Brigham and Women's Hospital/Harvard Medical School is seeking a neuroradiologist for a full-time academic position. Research and teaching opportunities are available. Candidate must be BC/BE, with fellowship training in neuroradiology. Please send CV to B. Leonard Holman, M.D., Chairman, Dept. of Radiology, Brigham and Women's Hospital, 75 Francis St., Boston, MA 02115. Brigham and Women's Hospital/Harvard Medical School is an affirmative action/equal opportunity educator and employer. 6–11a

IMMEDIATE OPENING—BC/BE neuroradiologist to join medium-sized group in Austin, TX. Practice covers major trauma center and outpatient radiology facility. In addition to general diagnostic services, outpatient facility also provides CT and MRI service on 2 GE 9800 scanners, GE 1.5-T, and 0.5-T MR units. Applicants are requested to contact Drs. Boyd, Gray, or Lava, 711 W. 38th St., Ste. B-8, Austin, TX 78705; (512) 454-8718. 6–11ap

TWO BOARD-CERTIFIED/ELIGIBLE GENERAL DIAGNOSTIC RADIOLOGISTS to join expanding, 11-person group covering 2 hospitals and 2 MR sites. Ideal private practice in a stable midwest community using all imaging modalities and interventional techniques. Can start immediately or wait until July 1990. Excellent opportunity with excellent salary and benefits. Send CV to Joseph F. Norfray, M.D., MR Center of Springfield, 319 E. Madison, Springfield, IL 62701. 8–11ap

THE DEPT. OF RADIOLOGY, MEDICAL CENTER HOSPITAL OF VERMONT, Burlington, VT, is seeking board-certified radiologists for academic positions in neuroradiology, angio/interventional radiology, body imaging with substantial training or experience in MRI, and general diagnostic radiology. Applicants should send letters of interest to John P. Tampas, M.D., Professor and Chairman, Dept. of Radiology, Medical Center Hospital of Vermont, 111 Colchester Ave., Burlington, VT 05401-1435. 10–1ap

ASSOCIATE POSITION, VASCULAR/INTERVENTIONAL, BOSTON—A full-time associate position is available for July 1, 1991, or sooner, at Tufts-New England Medical Center Hospitals. The section has 2 staff, 2 fellows, 5 RTs, and 1 secretary and performs 1500 exams/yr (40% interventional and pediatric angio). Responsibilities are only in the section. Academic appointment will be at Tufts University School of Medicine. Starting salary will be based on candidate's experience. Must be ABR-certified, have interventional fellowship, and full Massachusetts license. Contact Victor G. Millan, M.D., Tufts-New England Medical Center Hospitals, Box 253, 750 Washington St., Boston, MA 02111; (617) 956-5961 (Barbara). 10–12ap

BC/BE RADIOLOGIST, SUBURBAN PHILADELPHIA—Tired of hospital-based radiology? Opportunity to join private imaging facility with state-of-the-art equipment, including fourth-generation CT. Competency in CT, ultrasound, mammography, and general radiography is a must. Compensation includes salary for the first yr with an opportunity for partnership after first yr. Send CV to Box F61, *AJR* (see address this section). 10–1ap

IMMEDIATE OPENING, DIAGNOSTIC RADIOLOGY—Midwest city of 55,000 in metropolitan area of 600,000. Abundant recreational opportunities to complement hospital-based, 3-person group practice with very up-to-date equipment including MRI, CT, color ultrasound, SPECT nuclear, and angio with DSA. University appointment may be available if desired. Medical staff is highly specialist oriented. Competitive salary and benefit package including pension, health and disability insurance, and time off. Contact Charles Morris, M.D., P.O. Box 279, Council Bluffs, IA 51502; (712) 328-7646 (office) or (712) 328-2074 (home). 10–1ap

DIAGNOSTIC RADIOLOGIST sought to join a fee-for-service group practice at 2 mid-Bronx hospitals. Board-certification with expertise in imaging and in special procedures/interventional radiology preferred. Please send CV to Arthur Avenue Radiology, P.C., P.O. Box 4332, Great Neck, NY 11027. 10–3ap

DIAGNOSTIC RADIOLOGIST—A 4-member radiology group located in beautiful southwestern Montana is currently seeking an additional board-certified/eligible radiologist. Expertise in MRI preferred. Hospital-based and office practice. Excellent school system and outstanding, year-round recreational activities. Approximately 35,000 exams last yr. Hospital is acquiring MRI and updating CT services. One yr to full partnership. Contact Dennis L. Rich, M.D., 300 N. Willson, Bozeman, MT 59715; (406) 587-8631. 10–3ap

NEURORADIOLOGIST—The University of Louisville, Dept. of Diagnostic Radiology is seeking a BC/BE diagnostic radiologist to fill a full-time faculty position as chief of neuroradiology. The candidate must have had additional training in neuroradiology and be willing to participate in undergraduate and graduate teaching and in research activities. This is a fine opportunity in a growing and busy dept. with excellent equipment. Tenure-track and non-tenure-track appointments available; academic rank commensurate with training and experience; compensation negotiable and competitive. Send inquiries with CV and 3 references to Hollis A. Thomas, M.D., Professor and Chairman, Dept. of Diagnostic Radiology, Humana Hospital - University of Louisville, 530 S. Jackson St., Louisville, KY 40202. The University of Louisville is an equal opportunity/affirmative action employer and encourages women and minority candidates to apply. 10–11a

MAMMOGRAPHY, UNIVERSITY OF PENNSYLVANIA—Exceptional opportunity in academic mammography within a high-volume, rapidly expanding, breast imaging section. Ongoing screening and problem-solving mammography, breast ultrasound, and collaborative projects. Academic rank and salary commensurate with credentials. Resident and student teaching responsibilities along with negotiable participation in bone and chest outpatient radiology. Position available immediately. Applicant must be ABR-certified and able to obtain license in Pennsylvania. University of Pennsylvania is an affirmative action, equal opportunity employer and specifically encourages applications from women and minorities. Send letter and CV to Rosalind H. Troupin, M.D., Dept. of Radiology, H.U.P., 3400 Spruce St., Philadelphia, PA 19104. 10–1ap

NEURORADIOLOGIST AND INTERVENTIONAL RADIOLOGIST—The Dept. of Diagnostic Imaging/Radiology of Sinai Hospital of Detroit is seeking individuals who would practice primarily in the areas of neuroradiology and vascular/interventional radiology, respectively. Our hospital is a tertiary-care, university-affiliated institution with a thriving residency program. The dept. consists of 13 radiologists with private practice on a fee-for-service, separate billing arrangement. Individuals should have an interest in teaching and research. Apply to Philip N. Cascade, M.D., Chairman, Dept. of Diagnostic Imaging/Radiology, Sinai Hospital, 6767 West Outer Drive, Detroit, MI 48235-2899; (313) 493-5906. 10–11ap

DIAGNOSTIC RADIOLOGIST, IMMEDIATE OPENING: DENVER, CO, AT ROSE MEDICAL CENTER (RMC)—A 7-person radiology group is recruiting a radiologist with fellowship training in body imaging or invasive radiology. The practice involves all imaging modalities. RMC is affiliated with the University of Colorado. Salary, benefits, and location are highly attractive. Contact David W. Wilder, M.D., or Jeffrey A. Levy, M.D., at (303) 320-2256. 10–1ap

HIGHLAND GENERAL HOSPITAL—Diagnostic radiologist needed for Highland General Hospital. This is a level II trauma center, 20 min from downtown San Francisco. The hospital performs 66,000 exams/yr. Equipment includes Picker CT 1200 SX, Picker Digicon angiography suite, and 3 ultrasound machines including Acuson with Doppler. There are 6.2 FTE radiologists and over 50 technical and secretarial personnel. Limited private practice available. Applicant with some MRI training or experience desired, but not essential. Clinical faculty appointment available for suitable candidate. Board certification and California license necessary. Highland General Hospital is an EOE. Reply to Leslie Preger, M.D., Highland General Hospital, 1411 E. 31st St., Oakland, CA 94602; (415) 437-4204. 10–12a

PENN STATE UNIVERSITY, FACULTY POSITION IN CARDIOVASCULAR / INTERVENTIONAL RADIOLOGY—The Penn State University, Dept. of Radiology, is seeking a full-time faculty member in the Section of Cardiovascular/Interventional Radiology for July 1, 1991. The section provides a wide range of services in all aspects of diagnostic and interventional angiography (including neuro- and pulmonary angiography), percutaneous and combined percutaneous/peroral biliary interventions, genitourinary interventions, central and peripheral venography (with IVC filter placement), traumatic and oncological embolizations, foreign body retrievals, complex biopsy and drainage procedures (under multiple imaging modalities), and is currently an FDA test site for a new holmium:YAG intravascular laser. Clinical responsibility at the assistant professor level is required, necessitating a Pennsylvania medical license, University Hospital medical staff privileges, and ABR certification. Although seeking a junior faculty person at the assistant professor level, the academic rank will be commensurate with previous academic performance, recommendations, and Penn State University guidelines. Independent original research is expected and is amply funded, both in time and money. The animal research facility at Penn State University is one of the finest facilities of its kind in the country and is coupled with a dedicated MR research facility with angiographic and spectroscopic capability. Both research facilities are staffed by full-time research associates and research faculty, and are equipped with modern, state-of-the-art equipment. The position is open to persons who have completed an accredited residency program in radiology and an accredited fellowship in CV/I radiology, can obtain a Pennsylvania medical license, and have fulfilled ABR requirements for board certification. A generous and competitive salary and benefits package are offered. National meeting presentation is encouraged and fully supported. Exceptional academic, biophotographic, and secretarial support are also provided. Applicants should respond as soon as possible with a letter of interest and current CV. Please direct inquiries and requests for application forms to John F. Cardella, M.D., Associate Professor and Chief, Cardiovascular / Interventional Radiology Section, Penn State University/ Hershey Medical Center, Box 850, Hershey, PA 17033. Penn State University is an affirmative action, equal opportunity employer. Women and minorities are encouraged to apply. 10–1a.

BOARD-CERTIFIED RADIOLOGIST to join hospital-based group of 3 radiologists. Teaching hospital close to San Francisco and Sierras. Approved residencies in surgery, internal medicine, family practice, and OB / GYN. Salary 6 figures, negotiable dependent on training and experience with subsequent increases. California license required. Submit CV to Douglas McGirr, M.D., P.O. Box 1020, Stockton, CA 95201; (209) 468-6225. 10–11ap

NEURORADIOLOGIST—Excellent, young, 12-person radiology group has an opening for a well-trained neuroradiologist. Practice is hospital-based with 2 GE CT 9800 scanners, 1 high-field MRI, 1 mid-field MRI, new GE angio. Please contact Richard D. Herman, M.D., Dept. of Radiology, St. Luke's Hospital, Bethlehem, PA 18015; (215) 691-4200. 10–1ap

RADIOLOGIST, SAN FRANCISCO BAY AREA New, hospital-based, private practice with all modalities including MRI center. Comfortable practice, beautiful area, and excellent medical staff. Recently trained radiologist with angio/ interventional or neuroradiology skills desired. Available 1991. Send CV to James E. Remkus, M.D., 6001 Norris Canyon Road, San Ramon, CA 94583. 10–11ap

VASCULAR/INTERVENTIONAL RADIOLOGIST Progressive, private-practice group is seeking a second fellowship-trained vascular and interventional radiologist for its expanding interventional radiology service. We are currently performing more than 1000 procedures/yr. We are budgeted for 2 state-of-the-art vascular suites, the first to be installed early in 1991. We will break ground soon on a new imaging center to include 2 MRI and 2 CT (including a cine CT) scanners. We have a noninvasive lab and retain admitting privileges for our interventional service. We are located in Fresno, CA, at Saint Agnes Medical Center. Saint Agnes is a tertiary-referral center for the San Joaquin Valley, and Fresno is one of the fastest growing cities in CA. We are located 90 mi. from Yosemite National Park and less than 2 hr from excellent winter skiing and 2 hr from the coast. We offer 2 yr to full partnership with excellent salary and benefits. Please contact Art Fontaine, M.D., Dept. of Imaging, Saint Agnes Medical Center, 1303 E. Herndon, Fresno, CA 93710; (209) 449-3210. 10–3ap

RADIOLOGISTS — New York City, combined private radiology practice, and fee-for-service hospital practice has an immediate opening for a board-certified radiologist with experience in CT, ultrasound, and interventional radiology. In addition, MRI and mammography experience is preferred. This well-established practice has 3 private offices on the upper East Side of Manhattan as well as operations in 2 hospitals in Manhattan. Other studies performed in the practice are diagnostic radiology, nuclear imaging, and vascular duplex imaging. The practice continues to expand in all imaging modalities with its recent opening of a second state-of-the-art MRI unit. Excellent benefit package includes health, life, disability, and malpractice insurance; profit sharing plan; continuing medical education; and a travel and entertainment account for professional use. Send CV to Box F67, *AJR* (see address this section). 10–12ap

DIAGNOSTIC RADIOLOGIST, TEXAS—Progressive, well-diversified group (15 radiologists) has immediate opening for a BC/BE diagnostic radiologist with competence in a broad range of modalities. Additional consideration for fellowship. Excellent opportunity with excellent salary and benefits. Send CV with letter of inquiry to Will Gray, M.D., 1101 N. 19th St., Abilene, TX 79601. 10–1ap

HARTFORD, CT—Position available July 1991 for board-certified radiologist to join an established group of 8. Practice includes hospital and 4 private offices, all fully equipped including CT. Mammography experience is helpful. CT and MRI experience is essential. Competitive starting salary and benefits. Please enclose CV with initial correspondence to Jeffrey Blau, M.D., 40 Hart St., New Britain, CT 06052; (203) 229-2059. 11xa

BC GENERAL DIAGNOSTIC RADIOLOGIST—Immediate opening at the Dartmouth-Hitchcock Medical Center, Mary Hitchcock Memorial Hospital (420 beds, 58,000 inpatient, 48,000 outpatient exams/yr). Dept. consists of 13 staff and 9 resident radiologists with full range of modern radiologic practice. Seeking general diagnostic radiologist to be member of a 200-physician, academic, multispecialty group that forms the clinical faculty of Dartmouth Medical School. Strong clinical orientation and interest in teaching is essential. Board certification or eligibility is required. Write to Peter K. Spiegel, M.D., Dept. of Radiology, Dartmouth-Hitchcock Medical Center, 2 Maynard St., Hanover, NH 03756. The Dartmouth-Hitchcock Medical Center is an affirmative action/equal opportunity employer, and applications from women and minority groups are encouraged. 11a

SALT LAKE CITY, UT—Opportunity for board-certified diagnostic radiologist, with recent MRI fellowship training, to join group of 7 board-certified radiologists. Experience in all aspects of general radiology required. Practice includes 2 hospitals, 2 private offices, and a freestanding MRI center. Send letter and CV to Neel E. Bennett, M.D., Medical Director and Chairman, Dept. of Radiology, Holy Cross Hospital, 1050 E. S. Temple, Salt Lake City, UT 84102; (801) 350-4636. 11xa

DIAGNOSTIC RADIOLOGIST—Immediate opening. Seeking a board-certified radiologist with specialty in ER radiology. Academic rank of assistant or associate professor level. Dept. currently performs 87,000 exams/yr and has a residency training program. Strong teaching background required. Compensation commensurate with qualifications and experience. Must possess or be able to obtain Missouri licensure. Send letter of interest and CV to Fong Y. Tsai, M.D., Professor and Chairman, University of Missouri-Kansas City, Dept. of Radiology, 2301 Holmes, Kansas City, MO 64108. 9–11ap

THE NEW YORK HOSPITAL, CORNELL MEDICAL CENTER, DEPT. OF RADIOLOGY has a position available for a junior attending in an expanding uroradiology section beginning July 1991. Position involves responsibilities in clinical aspects of GU imaging, teaching, and research. Applicants should be board-certified/eligible with experience in cross-sectional imaging. Please send CV to Susan Krysiewicz, M.D., Dept. of Radiology, NYH-CUMC, 525 E. 68th St., Starr 8A15, New York, NY 10021; (212) 746-2557. 10–1a

PHYSICIAN/RADIOLOGIST—Large radiology group with multiple private offices seeks a board-certified radiologist interested in a full-time position. Responsibilities include general radiography. Special training in CT, ultrasound, and nuclear medicine is desirable but not required. Desirable southern New Jersey location. Competitive salary and benefit package. Send CV to RABC, P.O. Box 729, Mt. Holly, NJ 08060. 11–1ap

PHYSICIAN/RADIOLOGIST—Large radiology group with 2 hospitals and multiple private offices with state-of-the-art equipment seeks a radiologist who is board-certified in nuclear medicine. Competitive salary and benefit package. Send CV to Radiology Associates of Burlington County, P.A., 175 Madison Ave., Mt. Holly, NJ 08060. 11–1ap

TEN-PERSON RADIOLOGY GROUP located in Corpus Christi is seeking a new associate to start July 1990 or as late as July 1991. Must be board-certified or eligible. Will perform all diagnostic studies, including interventional, CT, MRI, nuclear medicine, and ultrasound. Please send CV to Search Committee, P.O. Box 5608, Corpus Christi, TX 78465-5608. 11–12ap

PEDIATRIC RADIOLOGIST, PORTLAND, OR—Immediate opening for a pediatric radiologist at Emanuel Hospital in Portland, OR. Either a pediatric fellowship or significant work experience is required. Opportunity to do general radiology as well. The hospital is a Level I trauma center, as well as a major pediatric referral center. The position leads to full partnership after second year. Please send CV to Blaine E. Kozak, M.D., Chairman, Dept. of Radiology, Emanuel Hospital, 2801 N. Gantenbein, Portland, OR 97227; (503) 280-4032. 11ap

Positions Desired

BC NUCLEAR MEDICINE & RADIOLOGY—Available July 1991. Six yr in busy military hospitals. CT, ultrasound, nuclear medicine with SPECT, and some angio/interventional. Able to expand and improve nuclear medicine service. Prefer medium-sized to large group practice with emphasis on high-quality care. Consider busy, half-time partnership. Commercial pilot, SEL/IFR, can circuit ride. Now in Wiesbaden, W. Germany. Write Charles Girard, M.D., Chairman, Radiology Dept., 7100 CSW MEDCEN, Box 411, APO, NY 09220. 11bp

SENIOR NEURORADIOLOGY FELLOW, ABR/BC seeks academic position in a large community/small university hospital with radiology residency program. Small- or medium-sized dept. with emphasis on teaching desirable. High-field MRI/1024 biplane digital angiography preferred. Hard worker who will relocate for quality position. References/CV available. Please respond to Box F63, *AJR* (see address this section). 10–11bp

BC NEURORADIOLOGY FELLOW desires partnership-track position in private practice in greater Philadelphia metropolitan area (Harrisburg/Allentown/Wilmington/Philadelphia) beginning summer 1991. Greater than 75% neuroradiology, mid- and high-field MRI. Digital angiography an asset. Highly motivated physician with entrepreneurial skills. Excellent references. CV on request. Please reply Box F65, *AJR* (see address this section). 10–11bp

Fellowships and Residencies

VASCULAR/INTERVENTIONAL RADIOLOGY FELLOWSHIP, ST. LOUIS VASCULAR INSTITUTE AT THE CHRISTIAN HOSPITAL, ST. LOUIS, MO—A 1- to 2-yr fellowship in vascular and interventional radiology is offered beginning July 1, 1991. Training includes all aspects of diagnostic angiography and vascular and nonvascular interventional techniques. Candidates must have completed a diagnostic radiology residency in an accredited training program, must be certified by or eligible for certification by the ABR, and must be able to obtain a Missouri license. Direct inquiries to Saadoon Kadir, M.D., Dept. of Radiology, Christian Hospital Northeast, 11133 Dunn Rd., Ste. 1017, St. Louis, MO 63136. 11–4cp

THORACIC RADIOLOGY FELLOWSHIP, Massachusetts General Hospital, 1 yr beginning July 1, 1991. Participation in standard film interpretation, CT of the thorax, MRI, and interventional procedures. Opportunity for clinical and academic research. Send inquiries and CV to Theresa C. McLoud, M.D., Dept. of Radiology, Massachusetts General Hospital, Boston, MA 02114. 11cp

FELLOWSHIP IN NEURORADIOLOGY—The Dept. of Radiology at Henry Ford Hospital in Detroit, MI, offers a 2-yr neuroradiology fellowship. The Division of Neuroradiology performs a high volume of interesting neuropathologic cases including 14,000 neuro CT, 5,000 neuro MRI, 1,000 neuro angiography, 1,000 myelograms, and 50 neurointerventional studies annually. State-of-the-art equipment includes 2 GE 1.5-T Signa systems, 3 GE 9800 Quick CT scanners with independent 3-D ISG work stations, biplane DSA angio room for interventional neuroradiologic procedures, biplane Siemens angio room for magnification angiography, and biplane fluoroscopy equipped for myelography. Applicants must have completed a diagnostic radiology residency and be board-certified or eligible. Please contact Suresh C. Patel, M.D., Division Director, Neuroradiology, Dept. of Diagnostic Radiology, Henry Ford Hospital, 2799 W. Grand Blvd., Detroit, MI 48202; (313) 876-1357. 11–12cp

FELLOWSHIPS IN PEDIATRIC RADIOLOGY, JULY 1991—The Dept. of Radiology, Children's Hospital Medical Center, Cincinnati, OH, offers 1- or 2-yr fellowships in pediatric radiology beginning July 1991. Children's Hospital Medical Center is a 355-bed institution where approximately 100,000 radiological exams are performed annually by 13 full-time faculty radiologists. Four fellowship positions are available annually. Training includes all aspects of pediatric imaging: neonatal radiology, neuroimaging, musculoskeletal radiology, cardiovascular and thoracic imaging, abdominal imaging, oncologic imaging, ultrasonography, nuclear medicine, CT, MRI, and vascular/interventional techniques. Facilities include digital fluoroscopy, Acuson and ATL ultrasound units with Doppler and color-flow Doppler capabilities, Gamma and SPECT tomographic nuclear cameras, GE 9800 Quick CT scanner, 1.5-T GE MRI, and cardiac catheterization/angiographic suite with digital vascular imaging. Numerous opportunities to participate in both clinical and basic research. Salary and fringe benefits are highly competitive. Candidates must be board-certified or board-qualified in diagnostic radiology and must be able to obtain an Ohio medical license. Children's Hospital Medical Center and the University of Cincinnati College of Medicine are affirmative action/equal opportunity employers. Address inquiry and CV to Donald R. Kirks, M.D., Director, Dept. of Radiology, Children's Hospital Medical Center, Elland and Bethesda Aves., Cincinnati, OH 45229-2899; (513) 559-8058. 1–12cp

CARDIOVASCULAR/INTERVENTIONAL RADIOLOGY FELLOWSHIP, PENN STATE UNIVERSITY The Penn State University, Dept. of Radiology, offers 1- or 2-yr fellowships in cardiovascular/interventional radiology, with a primary purpose of preparing graduates for academic careers in the subspecialty of CV/I radiology. Fellows will receive training in all aspects of diagnostic and interventional angiography (including neuro and pulmonary angiography), percutaneous and combined percutaneous/peroral biliary interventions, genitourinary interventions, central and peripheral venography (with IVC filter placement), traumatic and oncological embolizations, foreign body retrievals, and complex biopsy and drainage procedures (under multiple imaging modalities). Clinical responsibility at the instructor level is required, necessitating a Pennsylvania medical license, university hospital medical staff privileges, and ABR eligibility (at time of application) and certification (during first program yr). Independent original research is expected and is amply funded, both in time and money. The animal research facility at Penn State University is one of the finest facilities of its kind in the country and is coupled with a dedicated MR research facility with angiographic and spectroscopic capability. Both research facilities are staffed by full-time research associates and research faculty, and are equipped with modern state-of-the-art equipment. The fellowship is open to individuals who have completed an accredited residency program in radiology, can obtain a Pennsylvania medical license, and have fulfilled ABR requirements for board-certification or eligibility. A generous competitive salary and benefits package are offered. Academic, biophotographic, and secretarial support are also provided. Applicants should respond as soon as possible with a letter of interest and current CV. Please direct inquiries and requests for application forms to John F. Cardella, M.D., Associate Professor and Chief, Cardiovascular/Interventional Radiology Section, Penn State University/Hershey Medical Center, Box 850, Hershey, PA 17033. Penn State University is an affirmative action, equal opportunity employer. Women and minorities are encouraged to apply. 10–1c

FELLOWSHIP IN ULTRASOUND / CT / ANGIO-INTERVENTIONAL—A 1-yr fellowship program available beginning July 1991 at Lehigh Valley Hospital Center in Allentown, PA. LVHC is a 492-bed, acute-care, university-affiliated hospital. The fellowship program offers training in CT (head and body), ultrasound, angiography (neuro and visceral), and interventional radiography. MRI experience is also available. For further information, contact Robert Kricun, M.D., Dept. of Radiology, Lehigh Valley Hospital Center, P.O. Box 689, Allentown, PA 18105. 9–11cp

THE UNIVERSITY OF ARIZONA, DEPT. OF RADIOLOGY, offers a 1-yr fellowship in abdominal, chest, and musculoskeletal cross-sectional imaging that includes CT, MRI, ultrasound, and interventional techniques. University Medical Center is a tertiary-care hospital and trauma center with 3 CT scanners, 3 ultrasound devices including color Doppler, and 2 MRI scanners. There is an active research program including 4.7-T MRS. Fellows will oversee daily clinical activities, participate in teaching and conferences, and conduct research. The review of applications will begin Sept. 15, 1990, and will continue until the position is filled. The University of Arizona is an equal opportunity employer. Contact Bruce J. Hillman, M.D., Vice-Chairman, Dept. of Radiology, University Medical Center, Tucson, AZ 85724; (602) 694-7368. 9–12c

FELLOWSHIP IN ULTRASOUND AND BODY CT/MRI—July 1, 1992, to June 30, 1993, at the New York Hospital-Cornell Medical Center. Dept. provides state-of-the-art equipment including Acuson ultrasound, GE 9800 CT, and GE Signa 1.5-T MR. Wide variety of ultrasound exams include abdominal, OB-GYN, color Doppler, small parts, neonatal head, transvaginal, and transrectal. Applicant should be ABR eligible or certified. Send CV to Elias Kazam, M.D., Dept. of Radiology, The New York Hospital-Cornell Medical Center, 525 E. 68th St., New York, NY 10021. 9–12cp

ABDOMINAL IMAGING FELLOWSHIP—The Dept. of Radiology at the University of Florida is offering 1-yr fellowships in abdominal imaging beginning July 1, 1991, and July 1, 1992. Minimum requirements include successful completion of an accredited radiology residency. The fellowship includes training in all aspects of abdominal imaging (gastrointestinal and genitourinary radiology, CT, ultrasound, and MRI) by a 3-person subspecialty faculty. The program offers full clinical experience and research opportunities. Applicants must be eligible to obtain a license in the state of Florida. For additional information, contact Pablo R. Ros, M.D., Professor, Dept. of Radiology, Box J-374, Gainesville, FL 32610-0374; (904) 395-0288. The University of Florida is an equal opportunity/affirmative action employer and encourages applications from women and minorities. 10–6c

THE DEPT. OF RADIOLOGY, UNIVERSITY OF ARKANSAS FOR MEDICAL SCIENCES, LITTLE ROCK, AR, has openings for fellowships to begin July 1991. Positions are available in body imaging/intervention, neuroradiology, vascular and interventional radiology, and pediatric radiology. Interested candidates should contact these program directors: imaging/intervention — Teresita L. Angtuaco, M.D., or Steven K. Teplick, M.D.; neuroradiology — Edgardo A. Angtuaco, M.D.; vascular and interventional radiology — Timothy C. McCowan, M.D.; pediatric radiology — Joanna J. Seibert, M.D. All program directors listed above can be contacted at the Dept. of Radiology, University of Arkansas for Medical Sciences, Slot 556, 4301 W. Markham St., Little Rock, AR 72205; (501) 686-5740. 11c

THE UNIVERSITY OF MIAMI/JACKSON MEMORIAL MEDICAL CENTER, RADIOLOGY DEPT., has fellowship openings for July 1, 1991, in body imaging and vascular interventional radiology at a 1500-bed combination regional tertiary referral center and primary care facility. The body imaging fellowship includes CT, ultrasound, and MRI, and interventional procedures under these modalities. The vascular/interventional fellowship includes diagnostic angiography and vascular and nonvascular interventions. For more information, call or write Jorge J. Guerra, Jr., M.D., P.O. Box 016960 (R-109), Miami, FL 33101; (305) 549-6894. 10–11cp

NUCLEAR MEDICINE RESIDENCY, SEPT. 1, 1990 San Francisco General Hospital Medical Center, University of California, San Francisco, Program B, 2-yr ACGME-approved program satisfying American Board of Nuclear Medicine training requirements both in basic science and performance/interpretation of imaging and nonimaging *in vivo* procedures, radioimmunoassay, and radionuclide therapy. Emphasis on SPECT, nuclear cardiology, use of computers. Prerequisite: 2-yr ACGME-approved residency in internal medicine, pathology, pediatrics, or radiology. Send CV to Myron Pollycove, M.D., Chief, Nuclear Medicine Dept., San Francisco General Hospital Medical Center, San Francisco, CA 94110. Equal opportunity/affirmative action employer. 10–11c

IMMEDIATE UNEXPECTED OPENING FOR FELLOWSHIP IN CARDIOVASCULAR-INTERVENTIONAL RADIOLOGY—One-yr fellowship program at 750-bed teaching hospital. Extensive clinical experience involving all aspects of cardiovascular imaging and interventional vascular and nonvascular procedures. Availability for clinical or animal research. Send CV and inquiries to Oscar H. Gutierrez, M.D., Dept. of Radiology, Box 648, University of Rochester Medical Center, Rochester, NY 14642. AA/EO/M-F employer. 10–1cp

NATIONAL INSTITUTES OF HEALTH (NIH) FELLOWSHIP IN RADIOLOGIC RESEARCH—The newly established Radiology Research and Training Program at NIH is offering 2-yr fellowships to encourage young men and women to pursue a program of original basic research in laboratories on the NIH campus. Candidates who have recently completed clinical training in diagnostic radiology or nuclear medicine or, under special circumstances, are currently in residency, would be considered for these positions. The fellowship emphasizes basic research with no clinical responsibilities, except as they relate to the candidate's project. Fellows will have access to the imaging laboratories of the Radiology Research and Training Program, facilities in the In Vivo NMR Center, the PET program of the Dept. of Nuclear Medicine, the Biomedical Engineering and Instrumentation Branch, and other laboratories on the NIH campus. The position would involve a full-time appointment, either in the Civil Service or Public Health Service, with an annual salary starting at $37,000. Initial appointments will begin July 1991. Candidates should submit a CV, at least 2 letters of reference, and a preliminary statement concerning area of research interest to John Doppman, M.D., Bldg. 10, Room 1C-660, National Institutes of Health, Bethesda, MD 20892 or fax (301) 496-9933. 10–12c

BODY IMAGING FELLOWSHIP, CT/ULTRASOUND/MRI—Clinical and research activities in all areas tailored to the fellow's and dept.'s goals. Should have interest in teaching and research. GE 9800 CT, GE 1.5-T Signa MRI, and Acuson Diasonics ultrasound. Full resident complement. Four body-imaging faculty. Send CV to Fred W. Flickinger, M.D., Body Imaging Section, Dept. of Radiology, Medical College of Georgia, 1120 15th St., Augusta, GA 30912-3900. EEO/AA. Women/minorities encouraged to apply. 10–12c

WOMEN'S IMAGING FELLOWSHIP—A 1- or 2-yr comprehensive experience in women's imaging modalities is offered in Tucson, AZ. Procedures in which we expect the fellow to gain expertise include high-volume, low-cost screening mammography and its associated administrative, financial, and epidemiological aspects; problem-solving diagnostic mammography, including invasive mammographic procedures (e.g., stereotactic guided cytology and galactography); high-volume obstetric and gynecologic sonography. Annual stipend is $50,000. Contact Arizona State Radiology, 7250 E. Ventana Canyon Dr., Tucson, AZ 85715; (602) 620-4911. 10–1cp

FELLOWSHIP IN ULTRASOUND AND BODY CT/MRI, DENVER, CO—The University of Colorado Health Sciences Center has fellowship openings for July 1992 through June 1993. The dept. provides state-of-the-art equipment including Acuson, ATL UM-9, and Acoustic Imaging ultrasound and color Doppler capability; Toshiba 900S and Picker 1200SX CT scanners; and GE Signa 1.5-T and Toshiba 0.35-T MRI units. The wide variety of ultrasound exams includes OB/GYN, transplant studies, Doppler, small parts, and intracavitary studies. In addition to the breadth of diagnostic uses of body CT and MRI, therapeutic and diagnostic interventional procedures are performed. Applicants should be ABR-eligible or certified. Please send CV to Michael Manco-Johnson, M.D., Chairman, Dept. of Radiology, Box C-277, 4200 E. 9th Ave., Denver, CO 80262. EEO/AA employer. 10–11c

FELLOWSHIPS AT THOMAS JEFFERSON UNIVERSITY HOSPITAL—The Dept. of Radiology at Thomas Jefferson University Hospital in Philadelphia offers the following fellowship programs each yr. Ultrasound/CT/MRI — Jefferson's ultrasound division is 1 of the largest in the world and performs all currently available exams including obstetric, vascular, lithotripsy, invasive, and endoluminal. We also operate 4 GE 1.5-T MRI units and 3 CT scanners. Contact Barry Goldberg, M.D., regarding this program. Cardiovascular/interventional — this division is housed in a new suite containing Philips angio units with DSA and performs the full range of vascular and nonvascular interventional procedures. Contact Geoffrey Gardiner, Jr., M.D. Neuro/ENT radiology — very active clinical services supply a wealth of material to this division, which is housed in a neurosciences imaging center containing all imaging modalities. Contact Carlos Gonzalez, M.D. Breast imaging — Jefferson's new breast imaging center performs approximately 85 studies/day including ultrasound and needle localizations. Contact Stephen Feig, M.D. Chest — includes biopsies and CT. Contact Robert Steiner, M.D. MRI — a dedicated body MRI program including excellent research opportunities in addition to a large clinical case load. Contact Matthew Rifkin, M.D. Ultrasound — a dedicated ultrasound program. Contact Barry Goldberg, M.D. Musculoskeletal — includes MRI of the musculoskeletal system. Contact David Karasick, M.D. All program directors listed above can be contacted at the Dept. of Radiology, Thomas Jefferson University Hospital, Philadelphia, PA 19107. Jefferson is an equal opportunity/affirmative action employer. 11xc

NEURORADIOLOGY FELLOWSHIP — Two yr beginning July 1, 1991. Exposure to all aspects of clinical/academic neuroradiology. Participation in research/teaching. Send cover letter/CV to John R. Jinkins, M.D., Director, Neuroradiology Section, University of Texas Health Science Center, 7703 Floyd Curl Dr., San Antonio, TX 78284-7800. The University of Texas Health Science Center at San Antonio is an affirmative action/equal opportunity employer. 10–11c

IMMEDIATE OPENING, FELLOWSHIP IN PEDIATRIC RADIOLOGY—Position available for fellowship in pediatric radiology, 1 or 2 yr beginning July 1, 1991, or July 1, 1992. Full training with abundant hands-on experience with all imaging modalities. Supported by strong Dept. of Pediatrics with a good mixture of patient material. Excellent teaching on a 1-to-1 basis and ample opportunity for pursuing academic interests. Apply to Leonard E. Swischuk, M.D., Dept. of Radiology, The University of Texas Medical Branch, Child Health Center, C-65, Galveston, TX 77550; (409) 761-2096. UTMB is an equal opportunity M/F/H/V affirmative action employer. UTMB hires only individuals authorized to work in the United States. 10–12c

Tutorials/Courses

CARIBBEAN CRUISE, MRI AT SEA—Jan. 5–12, 1991. Medical Seminars International, 18981 Ventura Blvd., #303, Tarzana, CA 91356; (818) 700-9821. 10–12d

CARIBBEAN CRUISE, BREAST IMAGING AT SEA—Jan. 12–19, 1991. Medical Seminars International, 18981 Ventura Blvd., #303, Tarzana, CA 91356; (818) 700-9821. 10–12d

NINTH WINTER DIAGNOSTIC IMAGING CONGRESS, VAL D'ISERE, FRANCE—March 2–9, 1991. MRI, CT, ultrasound. Medical Seminars International, 18981 Ventura Blvd.,#303, Tarzana, CA 91356; (818) 700-9821. 10–2d

Other

VISITING PROFESSORSHIPS, THOMAS JEFFERSON UNIVERSITY HOSPITAL—The Dept. of Radiology at Thomas Jefferson University Hospital in Philadelphia is offering visiting professorships over the next several yr, while some of our faculty members are on sabbatical leave. These positions can have either a 6-mo or 1-yr term. In particular, we are seeking candidates with expertise in either ultrasound or general diagnostic radiology, but emphasis in other areas may be acceptable as well. Funding for these positions is appropriate for a senior faculty member from another institution on sabbatical with partial funding of his/her own, or for a junior faculty member. These positions are also open to highly qualified foreign radiologists with current academic appointments at prestigious foreign medical schools. Visiting faculty members will do some clinical work in our dept. and also have access, for research or educational purposes, to state-of-the-art imaging modalities of all types, as well as well-equipped physics and physiology research laboratories. Interested persons should contact David C. Levin, M.D., Chairman, Dept. of Radiology, Thomas Jefferson University Hospital, Philadelphia, PA 19107. Jefferson is an equal opportunity/affirmative action employer. 11xe

MRI/CT INTERPRETATIONS—Overreads or primary reads of MRI/CT exams via teleradiology or overnight mail. Teleradiology Associates, P.A., One University Pl., Ste. 350, Durham, NC 27707; (919) 419-1000. 11ep

AJR Classified Advertisements Information

Box Responses and Address for Ad Placement

Write Box ______, *AJR*, 2223 Avenida de la Playa, Suite 103, La Jolla, CA 92037-3218; Telephone: (619) 459-2229; FAX: (619) 459-8814.

How to Place an Ad

AJR accepts classified advertising for Positions Available, Positions Desired, Fellowships and Residencies, and Tutorials/Courses. Ads are accepted by mail or FAX.

Rates: $6.00/line with a $30 minimum charge. Box service is $10 additional for each month the ad appears. There are discounts for multiple insertions: 10% for 2–3 insertions; 20% for 4 or more. To estimate lines, count all words and divide by 7.

Billing: Ads *must* be prepaid, or advertisers will be billed after the ad appears *providing* a purchase order number is submitted with the advertising copy. Terms are net 30 days.

Deadlines: 6 weeks prior to issue date. For specific deadlines, telephone the *AJR* editorial office.

Estimating Ad Charges

Line charge: divide total words by 7 and multiply by $6.00 . . . . . $ ________
Multiple insertions? If so, multiply by number . . . . × ________
Subtotal . . . . $ ________
Discount applies to two or more insertions. Subtract 10% if ad appears 2–3 months; 20% if 4 months or more . . . . . . – ________
Subtotal . . . . $ ________
Box response requested? If so, multiply number of months by $10.00 . . . . + ________
Approximate advertising charge . . . . $ ________

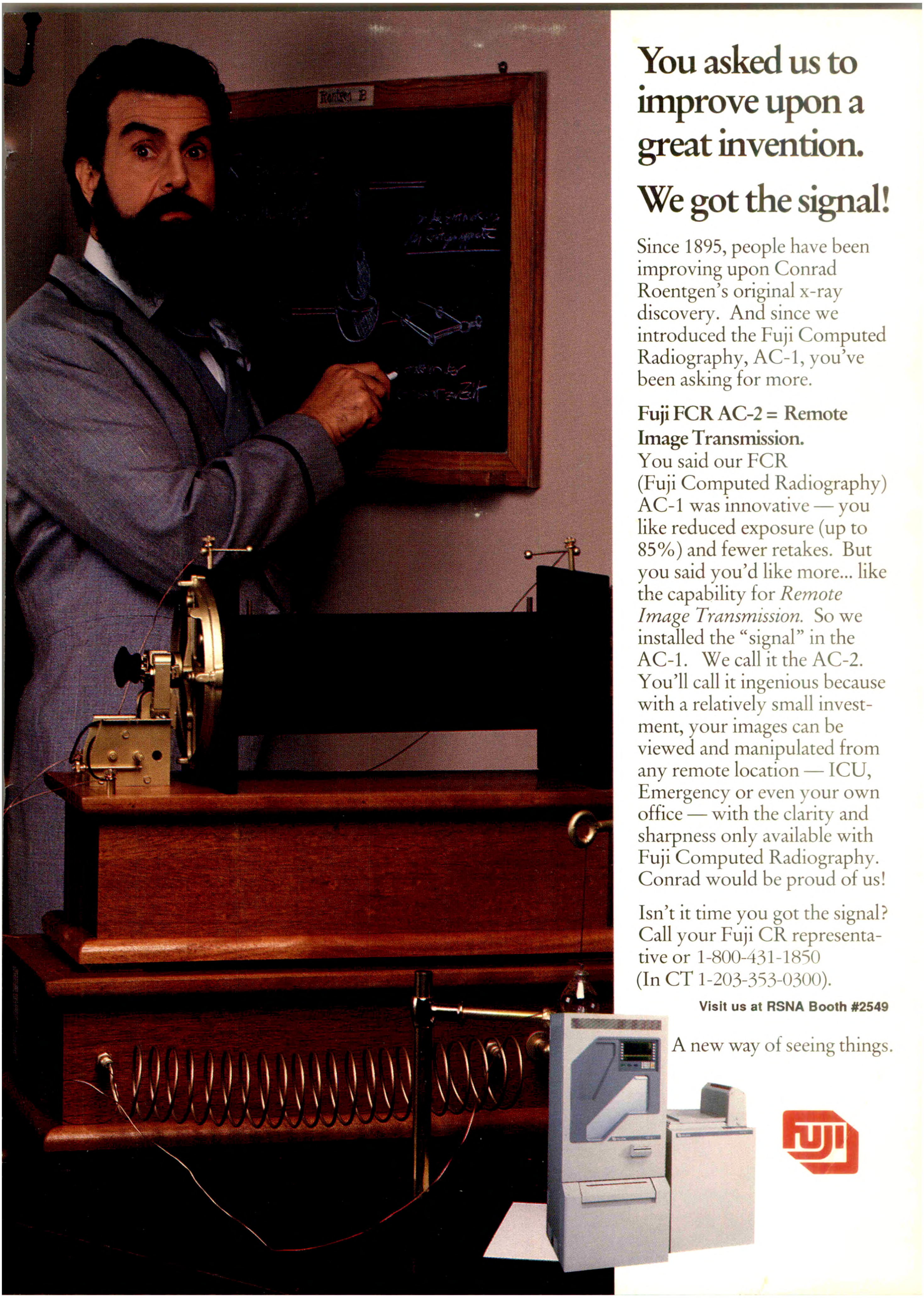

You asked us to improve upon a great invention.

We got the signal!

Since 1895, people have been improving upon Conrad Roentgen's original x-ray discovery. And since we introduced the Fuji Computed Radiography, AC-1, you've been asking for more.

Fuji FCR AC-2 = Remote Image Transmission.
You said our FCR (Fuji Computed Radiography) AC-1 was innovative — you like reduced exposure (up to 85%) and fewer retakes. But you said you'd like more... like the capability for *Remote Image Transmission.* So we installed the "signal" in the AC-1. We call it the AC-2. You'll call it ingenious because with a relatively small investment, your images can be viewed and manipulated from any remote location — ICU, Emergency or even your own office — with the clarity and sharpness only available with Fuji Computed Radiography. Conrad would be proud of us!

Isn't it time you got the signal? Call your Fuji CR representative or 1-800-431-1850 (In CT 1-203-353-0300).

Visit us at RSNA Booth #2549

A new way of seeing things.

Fuji

Volume 155 **American Journal of Roentgenology** November 1990

SPECIAL ARTICLE

925 **Merrill C. Sosman Lecture. Drugs, behavior, and brain chemistry.** *Wagner HN Jr*

REVIEW ARTICLES

933 **Update on esophageal radiology.** *Levine MS, Rubesin SE, Ott DJ*

943 **Iron oxide-enhanced MR imaging of the liver and spleen: review of the first 5 years.** *Ferrucci JT, Stark DD*

951 **Fast MR imaging: techniques and clinical applications.** *Haacke EM, Tkach JA*

PULMONARY RADIOLOGY

965 **Pictorial essay. Malignant pleural mesothelioma: CT manifestations in 50 cases.** *Kawashima A, Libshitz HI*

971 **Tuberculous bronchial stenosis: CT findings in 28 cases.** *Choe KO, Jeong HJ, Sohn HY*

BREAST RADIOLOGY

977 **Mammography-guided stereotactic fine-needle aspiration cytology of nonpalpable breast lesions: prospective comparison with surgical biopsy results.** *Fajardo LL, Davis JR, Wiens JL, Trego DC*

GASTROINTESTINAL RADIOLOGY

983 **Radiologic evaluation of esophageal motility: results in 170 patients with chest pain.** *Ott DJ, Abernethy WB, Chen MYM, Wu WC, Gelfand DW*

986 **Technical note. Use of C-arm fluoroscope to examine patients with swallowing disorders.** *Davis M, Palmer P, Kelsey C*

989 **Case report. Primary aortoesophageal fistula after chronic aortic dissection.** *Rose BS, Gordon DM, Geihsler JD*

991 **Obliteration of the fat surrounding the celiac axis and superior mesenteric artery is not a specific CT finding of carcinoma of the pancreas.** *Baker ME, Cohan RH, Nadel SN, Leder RA, Dunnick NR*

995 **Case report. Low-density insulinoma on dynamic CT.** *Smith TR, Koenigsberg M*

997 **Detection of pancreatic fluid and urine leakage after pancreas transplantation: value of CT and cystography.** *Longley DG, Dunn DL, Gruessner R, Halvorsen RA Jr, Sutherland DER, Letourneau JG*

1001 **Review. Radiologic findings of clonorchiasis.** *Lim JH*

1009 **Case report. MR imaging of hepatic adenoma.** *Gabata T, Matsui O, Kadoya M, et al.*

1013 **Case report. Percutaneous cholecystostomy drainage for the treatment of acute emphysematous cholecystitis.** *Vingan HL, Wohlgemuth SD, Bell JS III*

GENITOURINARY RADIOLOGY

1015 **Carcinoma of the prostate: value of transrectal sonography in detecting extension into the neurovascular bundle.** *Hamper UM, Sheth S, Walsh PC, Holtz PM, Epstein JI*

1021 **Cysts of the prostate and seminal vesicles: MR imaging findings in 11 cases.** *Gevenois PA, Van Sinoy ML, Sintzoff SA Jr, et al.*

MUSCULOSKELETAL RADIOLOGY

1025 **Soft-tissue tumors of the foot: value of MR imaging for specific diagnosis.** *Wetzel LH, Levine E*

1031 **Injury of the achilles tendon: diagnosis with sonography.** *Kainberger FM, Engel A, Barton P, Huebsch P, Neuhold A, Salomonowitz E*

1037 **Congenital absence of a cervical spine pedicle: clinical and radiologic findings.** *Wiener MD, Martinez S, Forsberg DA*

1043 **Detection of malignant bone tumors: MR imaging vs scintigraphy.** *Frank JA, Ling A, Patronas NJ, et al.*

1049 **Osteochondral impaction of the femoral head associated with hip dislocation: CT study in 35 patients.** *Tehranzadeh J, Vanarthos W, Pais MJ*

1053 **K-edge digital subtraction arthrography of the painful hip prosthesis: a feasibility study.** *Kelcz F, Peppler WW, Mistretta CA, DeSmet A, McBeath AA*

NEURORADIOLOGY

1059 **Diffusion-weighted MR imaging of the brain: value of differentiating between extraaxial cysts and epidermoid tumors.** *Tsuruda JS, Chew WM, Moseley ME, Norman D*

1066 **Commentary. Diffusion-weighted MR imaging: a useful adjunct to clinical diagnosis or a scientific curiosity?** *Henkelman RM*

1069 **MR imaging of CSF-like choroidal fissure and parenchymal cysts of the brain.** *Sherman JL, Camponovo E, Citrin CM*

1077 **Spinal cord pial metastases: MR imaging with gadopentetate dimeglumine.** *Lim V, Sobel DF, Zyroff J*

VASCULAR RADIOLOGY

1085 **Determination of the extent of lower-extremity peripheral arterial disease with color-assisted duplex sonography: comparison with angiography.** *Polak JF, Karmel MI, Mannick JA, O'Leary DH, Donaldson MC, Whittemore AD*

1091 **Duplex Doppler sonography of the carotid artery: false-positive results in an artery contralateral to an artery with marked stenosis.** *Beckett WW Jr, Davis PC, Hoffman JC Jr*

1097 **Percutaneous placement of Hickman catheters: comparison of sonographically guided and blind technique.** *Laméris JS, Post PJM, Zonderland HM, Gerritsen PG, Kappers-Klunne MC, Schütte HE*

1100 **Case report. The mechanism of peripheral recanalization by laser-assisted thermal angioplasty: confirmation by intravascular sonography.** *Tobis JM, Miranda CP, Deutsch L, et al.*

1103 **Case report. Splaying of titanium Greenfield inferior vena caval filter.** *Ramchandani P, Koolpe HA, Zeit RM*

MR IMAGING

1105 **Thermal effects of MR imaging: worst-case studies on sheep.** *Barber BJ, Schaefer DJ, Gordon CJ, Zawieja DC, Hecker J*

1111 **Fat-saturation MR imaging of the upper abdomen.** *Semelka RC, Chew W, Hricak H, Tomei E, Higgins CB*

1117 **Spatial misregistration of vascular flow during MR imaging of the CNS: cause and clinical significance.** *Larson TC III, Kelly WM, Ehman RL, Wehrli FW*

MEETING NEWS

1125 **Liver imaging—current trends in MRI, CT, and US: International Symposium and Course, June 1990.** *Whalen E*

OTHER CONTENT

Book reviews 932, 970, 982, 1020, 1042, 1076, 1090
1012 **Forthcoming articles**
1095 **ARRS 1991 resident award papers information**
1096 **Memorial, John T. Keller**
1133 **Letters**
1144 **Review of current literature**
1148 **News**
1152 **American Roentgen Ray Society information**
1153 **Classified advertisements**
A10 ***AJR* business and subscriber information**
A19 **Guidelines for authors**

1991 ARRS Meeting: May 5–10, Boston, MA

AJR

American
Journal of
Roentgenology

December 1990

PICTURE PERFECT

IF YOUR MAMMOGRAPHY EQUIPMENT ISN'T THE "PICTURE" OF EFFICIENCY,

YOUR PRODUCTIVITY AND PERFORMANCE WILL BE OUT OF FOCUS!

For over 40 years, specially-dedicated S & S x-ray equipment and accessories have been improving Radiologists' efficiency and productivity. Specially-dedicated mammography equipment includes:

MOBILE *MOTORIZED VIEWERS*

Hold *Mammography* radiographs for random access recall and viewing within 7 seconds! Individual on-off light switches control divided viewing areas.

MODELS:

MV810-170: 10 viewing areas for 170 8x10″ films

MV 1824-272: 16 viewing areas for 272 18x24cm films

MV2430-204: 12 viewing areas for 204 24x30cm films

S & S *MAMMOGRAPHY ILLUMINATORS:*

The standard for illumination excellence. Surface or recessed mounting is available for 1 to 6 banks—1 over 1 up to 6 over 6. Individual on-off light controls for ***each*** viewing section reduce glare and prevent spill-over. Single or two tier models for straight or angulated viewing include:

MODELS:

147000: Series for 8x10/ 18x24cm films

146000: Series for 24x30cm films

MAMMOGRAPH-SIZED VERTIFILE:

Doubles capacity over conventional drawer files. Adjustable partitions. Available with or without sliding door closures.

MODELS:

871: 1 shelf (2 doors) 14x30x13½″

873: 3 shelves (6 doors) 14x30x37¾″

876: 6 shelves (12 doors) 14x30x74½″

ADD-ON *MOVING GRID BUCKY SYSTEM:*

Converts existing non-Bucky mammography equipment. Improves contrast and micro-calcification visibility. Eliminates grid lines. Reduces scattered radiation.

MODELS:

MB-12: for 18x24cm film

MB-24: for 24x30cm film

See your local x-ray dealer or call S & S directly for *Picture Perfect* mammography equipment and our expanded line of radiological equipment and accessories.

S & S X-RAY PRODUCTS, INC.
1101 Linwood Street, Brooklyn, NY 11208
TOLL FREE: 800/347-XRAY ■ **NY STATE:** 718/649-8500 ■ **FAX:** 718/257-0219

12. 4. 91

Official Journal of the American Roentgen Ray Society

AJR

American Journal of Roentgenology
Diagnostic Imaging and Related Sciences

Editor-In-Chief	Robert N. Berk, *La Jolla, California* *University of California, San Diego* *School of Medicine and Medical Center*
Editor Emeritus	Melvin M. Figley, *Seattle, Washington*
Associate Editor	Saskia von Waldenburg Hilton, *San Diego, California*
Consulting Editor	Michael S. Huckman, *Chicago, Illinois*
Statistician	Charles C. Berry, *San Diego, California*

Editorial Board

John R. Amberg
Itamar Aviad
Mark E. Baker
Lawrence W. Bassett
Michael A. Bettmann
Felix S. Chew
N. Reed Dunnick
David K. Edwards
Ronald G. Evens
David S. Feigin
Sandra K. Fernbach
Richard H. Gold
William R. Hendee
John R. Hesselink
Charles B. Higgins
Melvyn T. Korobkin
Faye C. Laing
Thomas L. Lawson
Robert G. Levitt
Bruce L. McClennan
Richard P. Moser
Albert A. Moss
Jeffrey H. Newhouse
Donald L. Resnick
Stewart R. Reuter
Charles A. Rohrmann, Jr.
Peter M. Ronai
Sjef H. J. Ruijs
Stuart S. Sagel
David J. Sartoris
Stefan C. Schatzki
William P. Shuman
Edward A. Sickles
Barry A. Siegel
David D. Stark
Edward T. Stewart
Murali Sundaram
Eric vanSonnenberg
Robert K. Zeman

Editorial Staff: Margaret Levene, *managing editor*; Katie L. Spiller, Barbara Rose, Barbara L. Halliburton, and Janine Anderson, *manuscript editors*; Nancy Rydbeck, *office manager*; Sheri Smith, *administrative assistant*; Linda J. Waggoner, *administrative secretary*.

AJR, AMERICAN JOURNAL OF ROENTGENOLOGY (ISSN 0361 803X) is the official journal of the American Roentgen Ray Society and is published monthly by Williams & Wilkins, 428 E. Preston St., Baltimore, MD 21202. Annual dues include $50 for journal subscription. Second-class postage paid at Baltimore, MD, and at additional mailing offices. Postmaster, send address changes (Form 3579) to AJR, 428 E. Preston St., Baltimore, MD 21202. Subscription rates $125 ($180 foreign); institutions $135 ($190 foreign); in training $25 ($80 foreign); single copy $18 ($22 foreign). Airmail rates furnished on request. Indexed by *Current Contents* and *Index Medicus*. Copyright © 1990 by American Roentgen Ray Society. 0361–803X/90$3.00

FROM MAL

[98]
Technetium
$4d^55s^2$
$^6S_{2\frac{1}{2}}$
98
97
99
53
Iodine
$4d^{10}5s^25p^5$
-1
5
7
$P^o_{1\frac{1}{2}}$
126.9045
I
127
75
Rhenium
SHELLS

AJR Guidelines for Authors

Address new and revised manuscripts, correspondence, and classified ads to the Editor:

AJR Editorial Office
2223 Avenida de la Playa, Suite 103
La Jolla, CA 92037-3218
Telephone: (619) 459-2229; FAX: (619) 459-8814

Inquiries regarding subscriptions, display advertising, reprints, or permission to republish *AJR* material should be addressed to the publisher:

The Williams & Wilkins Co.
428 E. Preston St.
Baltimore, MD 21202 Telephone: 1-800-638-6423

The *AJR* publishes original contributions to the advancement of medical diagnosis and treatment. Submitted manuscripts should not contain previously published material and should not be under consideration for publication elsewhere. Papers dealing with neuroradiology should be addressed to: American Journal of Neuroradiology, Dept. of Diagnostic Radiology, 1653 W. Congress Pkwy., Chicago, Il 60612. At the discretion of the *AJR* Editor, *AJNR* articles that are of interest to the general reader may be republished in the *AJR*. Neuroradiologic papers sent to the *AJR* will be forwarded to the Editorial Office of the *AJNR*.

Manuscript decisions are based on peer review. Reviewers receive manuscripts without title pages to ensure an unbiased review. Statements made in the article, including changes made by the Editor or manuscript editor, are the responsibility of the author and not of the *AJR* or its publisher. Authors will be sent the edited manuscript, galley proof, and proofs of illustrations. If the corresponding author will be unavailable to review galleys, arrangements should be made for a coauthor or colleague to read and return the proof.

The following guidelines are based on instructions set forth in the **Uniform Requirements for Manuscripts Submitted to Biomedical Journals** (*Ann Intern Med* **1988;**108:258–265). Articles will be edited, however, to conform to the individual style of AJR.

General Guidelines for Major Papers

Abstract. Clearly state (in 200 words or less) the purpose, methods, results, and conclusions of the study. Include actual data.

Introduction. Briefly describe the purpose of the investigation and explain why it is important.

Methods. Describe the research plan, the materials (or subjects), and the methods used, in that order. Explain in detail how disease was confirmed and how subjectivity in observations was controlled.

Results. Present results in a clear, logical sequence. If tables are used, do not duplicate tabular data in text, but do describe important trends and points.

Discussion. Describe the limitations of the research plan, materials (or subjects), and methods, considering both the purpose and the outcome of the study. When results differ from those of previous investigators, explain the discrepancy.

AUTHOR'S CHECKLIST

For priority handling, complete the following checklist, sign the copyright form on the reverse side of this page, and include both with the manuscript.

________ Two copies of the manuscript (the original and a photocopy) and two complete sets of figures are submitted. One copy has been retained by the author.

________ If appropriate, *AJR* Guidelines for case reports, technical notes, pictorial essays, or letters to the Editor have been followed. (See page A10.)

________ The manuscript, including references, figure legends, and tables, is typed double-spaced on 8½ × 11 in. (21.6 × 27.9 cm) *nonerasable* paper. Right-hand margins are not justified.

________ All manuscript pages are numbered consecutively beginning with the abstract. Authors' names do not appear on the manuscript pages.

________ The manuscript is organized as follows: title page, blind title page (title only), abstract, introduction, methods, results, discussion, acknowledgments, references, tables, figure legends, and figures.

________ Informed consent has been obtained from patients who participated in clinical investigations. If experiments were performed on animals, authors complied with NIH guidelines for use of laboratory animals.

________ Use of unfamiliar acronyms and abbrevations is kept to a minimum. When abbreviations are used they are defined at first mention, followed by the abbreviation in parentheses.

________ Metric measurements are used throughout, or the metric equivalent is given in parentheses.

________ Names and locations (city and state only) of manufacturers are given for equipment and nongeneric drugs.

Title Page

________ The following information is given: title of article; names and complete addresses (including zip code) of all authors; current addresses of authors who have moved since study; acknowledgment of grant or other assistance. The corresponding author is clearly identified, and a current address, phone number, and FAX number are given.

________ A blind title page is included in each copy of the manuscript, giving only the title (without the authors' names) for use in the review process.

Abstract

________ An abstract of approximately 200 words concisely states the purpose, methods, and results of the study in one paragraph. Actual data are included. Conclusions are stated in a second, summary paragraph.

________ No abbreviations or reference citations are used.

Case Reports

A case report is a brief description of a special case that provides a message that transcends the individual patient.

Format. There is no abstract. The introduction should be a short paragraph giving the general background and the specific interest of the case. No more than one case should be described in detail (similar ones can be mentioned briefly in the discussion). Emphasis should be on the radiologic aspects; clinical information must be limited to that necessary to provide a background for the radiology. The discussion should be succinct and should focus on the specific message and relevance of radiologic methods. A review of the literature is not appropriate.

Length. Maximum of five double-spaced, typewritten pages, including the references but not the title page or figure legends.

References. Maximum of eight.

Figures. Maximum of four, unless the text is shortened accordingly. Legends must not repeat the text.

Tables and Acknowledgments. Not appropriate in case reports.

Pictorial Essays

A pictorial essay is an article that conveys its message through illustrations and their legends. Unlike other *AJR* articles, which are based on original research, pictorial essays serve primarily as teaching tools, like exhibits at a scientific meeting. They are not encyclopedic book chapters. The abstract should be a short, introductory paragraph.

Length. Maximum of four double-spaced, typewritten pages, including the references but not the title page or figure legends.

References. Maximum of four.

Figures. Maximum of 30 figure *parts*. Number should be as few as necessary to convey the message of the paper.

Tables and Acknowledgments. Not appropriate in pictorial essays.

Opinions, Commentaries, and Perspectives

Opinions, commentaries, and perspectives are special articles dealing with controversial topics or issues of special concern to radiologists.

Format. Include a title page but no abstract. Headings may be used to break up the text.

Length. Maximum of five double-spaced, typewritten pages.

References. Maximum of five.

Tables and Figures. Maximum of four.

Technical Notes

A technical note is a brief description of a specific technique or procedure, modification of a technique, or equipment of interest to radiologists.

Format. No abstract, headings, or subheadings are required. If headings are used, they should be a combination of "Case Report," "Materials and Methods," "Results," and "Discussion." A brief one-paragraph introduction should be included to give the general background. Discussion should be limited to the specific message, including the uses of the technique or equipment. Literature reviews and lengthy case reports are not appropriate.

Length. Maximum of five double-spaced, typewritten pages, including the references but not the title page or figure legends.

References. Maximum of eight.

Figures. Maximum of two, unless the text is shortened accordingly.

Tables and Acknowledgments. Not appropriate in technical notes.

Letters to the Editor and Replies

Letters to the Editor and Replies should offer objective and constructive criticism of published articles. Letters may also discuss matters of general interest to radiologists. Do not end a letter with a hand-written signature.

Format. All letters should be typed double-spaced on nonletterhead paper, with no greeting or salutation. Name and affiliation should appear at the end of the letter. Titles for letters should be short and pertinent. The title for a reply is simply "Reply."

Length. Maximum of two double-spaced, typewritten pages, including references.

References. Maximum of four.

Figures. Maximum of two.

Tables and Acknowledgments. Not appropriate in Letters to the Editor and Replies.

Computer Page Articles

Articles published on the computer page deal with practical computer applications to radiology.

Format. Include a title page and an abstract.

Length. Maximum of eight double-spaced, typewritten pages.

References. Maximum of five.

Figures and Tables. Maximum of five. Computer printouts are not acceptable. Figures must be submitted as 5 × 7 in. glossy prints.

All submissions to the *AJR* must be accompanied by a completed copy of the Author's Checklist and the signed Copyright Agreement.

References

________ References (not to exceed 35) are typed double-spaced starting on a separate page and are **numbered consecutively in the order in which they appear in the text.**

________ All references are cited in the text and are enclosed in brackets and typed on line with the text (not superscript).

________ Unpublished data are not cited in the reference list, but are cited parenthetically in the text, for example, (Smith DJ, personal communication), (Smith DJ, unpublished data). This includes papers submitted, but not yet accepted, for publication.

________ Papers presented at a meeting are not cited in the reference list, but are cited parenthetically in the text (e.g., Smith DJ et al., presented at the annual meeting of the American Roentgen Ray Society, May 1990). After first mention, use (Smith DJ et al., ARRS meeting, May 1990).

________ Inclusive page numbers (e.g., 333–335) are given for all references.

________ Journal names are abbreviated according to *Index Medicus*.

________ Style and punctuation of references follow the format illustrated in the following examples (all authors are listed when six or fewer; when seven or more authors, the first three are listed, followed by "et al."):

Journal article

1. Long RS, Roe EW, Wu EU, et al. Membrane oxygenation: radiographic appearance. *AJR* **1986**;146:1257–1260

Book

2. Smith LW, Cohen AR. *Pathology of tumors*, 6th ed. Baltimore: Williams & Wilkins, **1977**:100–109

Chapter in a book

3. Breon AJ. Serum monitors of bone metastasis. In: Clark SA, ed. *Bone metastases*. Baltimore: Williams & Wilkins, **1983**:165–180

Tables

________ Each table is typed double-spaced on a separate page without vertical or horizontal rules; each has a short, descriptive title. Tables do not exceed two pages in length and contain at least four lines of data.

________ Tables are numbered in the order in which they are cited in the text.

________ Abbreviations are defined in an explanatory note below each table.

________ Tables are self-explanatory and do not duplicate data given in the text or figures.

________ All arithmetic (percentages, totals, differences) has been double checked for accuracy, and tabular data agree with data given in the text.

Figures and Legends

________ Two complete sets of original figures are submitted unmounted in labeled envelopes.

________ Figures are clean, unscratched, 5 × 7 in. (13 × 18 cm) glossy prints with **white borders.** A separate print is submitted for each figure *part.*

________ All figure parts relating to one patient have the same figure number.

________ Each figure is labeled on the back with the figure number and an arrow indicating "top." For black-and-white figures, labeling is done on a gummed label, which is then affixed to the back of the print. **Never** use labels on **color** figures, but write figure number on the back lightly in pencil. *Never* use ink on front or back of any figures.

________ Author's names are *not* written on the backs of figures.

________ Only removable (rub-on) arrows and letters are used on the figures. Symbols are uniform in size and style and are not broken or cracked.

________ Images are uniform in size and magnification.

________ Line drawings are done in black ink on a white background. They are professional in quality, and all use the same size type. (Only glossy prints are acceptable.)

________ Written permission has been obtained for use of all previously published illustrations (and copies of permission letters are included), and an appropriate credit line is given in the legends.

________ Legends are typed double-spaced, and figure numbers correspond with the order in which the figures are cited in the text.

Transfer of Copyright Agreement, Conflict of Interest Acknowledgment, Certification of Coauthors, and Exclusive Publication Statement

Complete copyright to the article entitled: ________________________________

____

is hereby transferred to the American Roentgen Ray Society (for United States government employees to the extent transferable), effective if and when the article is accepted for publication in the *American Journal of Roentgenology*. In the case of the authors who are officers or employees of the United States government, the American Roentgen Ray Society recognizes that works prepared by officers or employees of the United States government as part of their official government duties are in the public domain.

Authors reserve all proprietary rights other than copyright, such as patent rights and the right to use all or part of this article in future works of their own. The authors retain the right of replication, subject only to crediting the original source of publication and receiving written permission from the publisher.

Authors guarantee that this manuscript contains no matter that is libelous or otherwise unlawful, invades individual privacy, or infringes any proprietary rights.

Authors understand that they will receive no royalty or other compensation from the American Roentgen Ray Society or the publisher.

Authors guarantee that the editor has been or will be informed of any proprietary or commercial interest or conflicts of interest the authors may have that relate directly or indirectly to the subject of this article.

All authors certify that they have made substantive and specific intellectual contributions to the article and assume public responsibility for its content.

Finally, the authors certify that none of the material in this manuscript has been published previously or is currently under consideration for publication elsewhere.

________________	________________	________________
First author/date	Second author	Third author
________________	________________	________________
Fourth author	Fifth author	Sixth author

This agreement must be signed by all authors in order for the manuscript to be published.

AJR Business and Subscriber Information

The American Roentgen Ray Society

AJR, American Journal of Roentgenology, is published monthly to disseminate research on current developments in the radiologic sciences and commentary on topics related to radiology. It is published by the American Roentgen Ray Society, 1891 Preston White Dr., Reston, VA 22091; (703) 648-8992. Inquiries regarding society business, the annual ARRS meeting, and membership should be addressed to the Society at the above address.

Correspondence Concerning the *AJR*

Correspondence regarding display (not classified) advertising, subscriptions, address changes, reprints, and permission requests should be addressed to Williams & Wilkins, 428 E. Preston St., Baltimore, MD 21202; (301) 528-4000.

Correspondence regarding editorial matters and classified advertising should be addressed to Editorial Office, AJR, 2223 Avenida de la Playa, Ste. 103, La Jolla, CA 92037-3218; telephone (619) 459-2229; FAX (619) 459-8814. For information on manuscript submission, see Guidelines for Authors, pages A3–A5.

Subscriber Information

Subscription requests and inquiries should be sent to Williams & Wilkins, 428 E. Preston St., Baltimore, MD 21202. ARRS annual dues include $50 for journal subscription. Subscription rates are as follows: nonmembers, $125/year ($180 foreign); institutions, $135 ($190 foreign); nonmember in-training, $25 ($80 foreign). Single copies of the Journal may be purchased for $18 ($22 foreign). Airmail rates will be furnished on request.

Call toll-free, 1-800-638-6423 (in Maryland call 1-800-638-4007), with subscription questions or problems. Please have the mailing label from your latest issue available when you call.

If a subscriber receives a damaged copy of the *AJR* or fails to receive an issue, the subscriber should notify Williams & Wilkins (428 E. Preston St., Baltimore, MD 21202) within 60 days of publication (90 days for foreign subscribers) and that issue will be replaced.

Change of address information should be sent to Williams & Wilkins, 428 E. Preston St., Baltimore, MD 21202. Allow 90 days for address changes.

Copyrights, Permissions, and Reprints

The American Roentgen Ray Society holds the copyright for all material published in the *AJR*. No part of this publication may be reproduced without permission from the ARRS. Requests for such permission should be addressed to Williams & Wilkins, 428 E. Preston St., Baltimore, MD 21202.

For reprints of a particular article, please contact the author designated in the footnotes for that article.

Indexes

The *AJR* provides volume and yearly indexes (subject and author) in the June and December issues each year. *AJR* articles are also indexed in *Current Contents*, *Index Medicus*, and the cumulative index published by *Radiology*.

1990 ARRS President's Award

MR Receptor Imaging:

Ultrasmall Iron Oxide Particles Targeted to Asialoglycoprotein Receptors

Ralph Weissleder[1]
Peter Reimer
Albert S. Lee
Jack Wittenberg
Thomas J. Brady

Previously we have reported that ultrasmall superparamagnetic iron oxide (USPIO) particles migrate across capillary endothelium, a prerequisite for the design of particulate pharmaceuticals for MR receptor imaging. In the current study, USPIO particles are directed specifically to asialoglycoprotein (ASG) receptors by coupling galactose terminals in the form of arabinogalactan (AG) to these particles. Biodistribution data showed that ASG-directed, AG-coated USPIO (AG-USPIO) particles selectively accumulate in the liver but not in other organs. Electron microscopy of liver showed electron-dense iron oxide particles bound to hepatocyte cell-surface membranes and in large numbers within intracellular lysosomes. The specificity of AG-USPIO for asialoglycoprotein receptors was confirmed by incubation experiments with and without ASG-blocking agents such as D(+)galactose and asialofetuin. In vivo MR imaging in rats showed a significant decrease in liver signal intensity at low doses (2 μmol Fe/kg); no significant changes were observed in the spleen. This decrease in signal intensity is larger than that observed with conventional iron oxides at equal doses.

These initial data suggest that, for the first time, superparamagnetic agents can be directed to specific sites for MR imaging by strategies such as receptor targeting.

AJR **155:1161–1167, December 1990**

Superparamagnetic iron oxides in the size range of 30–1000 nm have been used to reduce relaxation times of liver and spleen [1–9] and lymph nodes [10]. After IV administration, these agents are cleared from the blood within minutes, rapidly accumulating in cells of the mononuclear phagocytic system [9]. As superparamagnetic iron oxides possess high relaxivity, arguments have been made for their use in antibody-labeled and receptor-directed MR imaging. Although antibodies have been labeled with iron oxide particles in vitro [11–15], in vivo results are less encouraging because rapid clearance of these agents by cells of the mononuclear phagocytic system occurs before significant antibody antigen binding can take place.

We recently developed an ultrasmall superparamagnetic iron oxide (USPIO) that is not phagocytosed immediately by liver and spleen [16]. These particles have a mean size of 11.5 ± 6.3 nm, high R2 relaxivity (i.e., 1/T2 as a function of molar concentration, 44.1 $(\text{mmol/l})^{-1}\text{sec}^{-1}$), a relatively long blood half-life (81 min), and they migrate through capillary endothelium [16]. We have reported previously on the IV use of USPIO to enhance lymph nodes in rodents [17]. These favorable characteristics suggest that, with appropriate modification, tissue biodistribution of USPIO can be altered selectively.

In this report, we present data on asialoglycoprotein (ASG) receptor-directed, arabinogalactan (AG)-coated USPIO (AG-USPIO). The ASG receptor system was chosen as a target because it is biochemically well characterized [18], it is an abundant receptor protein with as many as 500,000 surface ligand-binding sites per cell [19], the receptor can be targeted easily by attaching terminal galactose sugars to the desired pharmaceutical [20, 21], and the method has been used

Received March 21, 1990; accepted after revision July 9, 1990.

Presented at the the annual meeting of the American Roentgen Ray Society, Washington, DC, May 1990.

This work was supported in part by a grant from the National Institutes of Health (P01-CA48729), by the Massachusetts General Hospital NMR development fund. P. Reimer supported by the Deutsche Forschungsgemeinschaft (RE 758/1-1).

[1] All authors: Department of Radiology, Massachusetts General Hospital and Harvard Medical School, Boston, MA 02114. Address reprint requests to R. Weissleder.

0361-803X/90/1556-1161

© American Roentgen Ray Society

successfully to separate membrane vesicles of hepatocytes with ferromagnetic iron oxide microspheres [22]. The physical properties, pharmacologic behavior, and initial MR receptor imaging studies with AG-USPIO are reported.

Materials and Methods

Iron Oxide Preparations

USPIO was obtained by size fractionation of a heterogeneous dextran-stabilized iron oxide preparation as previously described [16] and was used at a concentration of 8.6 mg/ml (Advanced Magnetics, Inc., Cambridge, MA). USPIO has a molecular weight of approximately 700,000 by gel filtration, similar to that of endogenous ferritin (11 nm; molecular weight, 440,000–600,000) [23].

AG-USPIO was prepared by stabilizing iron oxide particles [24] with arabinogalactan, a galactose-terminated polysaccharide [25]. AG-USPIO (Advanced Magnetics, Inc.) was supplied at a concentration of 17 mg/ml [26].

Relaxation Time Measurements

T1 and T2 relaxation times were measured by using a nuclear magnetic resonance (NMR) spectrometer operating at 0.47 T at 37°C (PC-20 Minispec, IBM, Danbury, CT) and are reported in milliseconds. Before each measurement, the spectrometer was tuned and calibrated. T1 was measured from eight data points generated by an inversion-recovery pulse sequence. T2 was measured from 10 data points by using a Carr-Purcell-Meiboom-Gill pulse sequence with a tau of 1 msec. Timing intervals for different tissues were always optimized so that the multiexponential decay was sampled adequately. Each value is the mean of three separate measurements.

To determine the relaxivity of USPIO and AG-USPIO, we prepared solutions of decreasing concentrations (0.4, 0.2, 0.1, 0.05, 0.0025, and 0.00125 mg/ml) and measured their relaxation times. T1 and T2 relaxation times were expressed as the inverse (1/T1, 1/T2) and plotted against the concentration. The slopes ($[\text{mmol/l}]^{-1}\text{sec}^{-1}$) of these two curves correspond to R1 and R2 relaxivity. In all experiments, the linear correlation coefficient (r) of the curve fit was larger than .95.

Blood half-life of AG-USPIO was calculated after IV injections of 10 µmol Fe/kg into Sprague-Dawley rats. Blood samples were drawn at multiple time points up to 4 hr from six different animals. Blood relaxation times were determined at 37°C. Blood half-life was calculated by fitting mean 1/T1 values of blood to a single exponential equation: $1/T1_t = 1/T1_{t0} + C \times e^{-kt}$ (Systat Inc., Evanston, IL), where $1/T_{t0}$ is the spin-lattice relaxation rate of blood before injection of the preparation, $1/T1_t$ is the relaxation rate at time t after injection, C is the concentration in the blood at the moment of injection, and k is the rate constant for the decay.

The effect of AG-USPIO on various tissues was determined by injection of AG-USPIO at a dose of 10 µmol Fe/kg. Thirty minutes (> three half-lives) after injection of the agent, animals ($n = 15$) were sacrificed by exsanguination, and tissues were removed and blotted dry. Then tissues were placed in 5-ml NMR tubes for measurements of relaxation times. Values were expressed as mean plus or minus standard deviation of the mean.

AG-USPIO (10 µmol Fe/kg) was injected into 15 animals to study liver relaxation times as a function of time. Previous experiments had shown that these time-response curves are an accurate method for determining biodegradability of iron oxide particles [9]. T1 and T2 relaxation times of liver were determined at 0.5 and 6 hr and at 1, 2, 4, and 14 days after injection of the agent.

Pathologic Studies

Liver specimens were examined histologically to study the cellular distribution of AG-USPIO in a rat 30 min after injection of 150 µmol Fe/kg. The high dose was chosen because cellular iron oxides are barely visible on histologic specimens when lower doses are used. After removal, the liver was fixed in buffered 10% formaldehyde for 24 hr. Subsequently, tissue samples were embedded in paraffin and stained for iron with Perls' Prussian-blue stain. In this stain, ferric iron (Fe^{3+}) is dissolved from organic iron-containing complexes by hydrochloric acid and then reacted with potassium ferrocyanide [$K_4Fe(CN)_6$] to form a visible blue precipitate: ferric ferrocyanide [$Fe_4(Fe(CN)_6)_3$].

Electron microscopy of hepatic parenchymal cells was performed to study the receptor membrane and intracellular distribution of AG-USPIO. A rat was injected with 150 µmol Fe/kg of AG-USPIO and sacrificed after 30 min. Liver tissue was fixed in situ by perfusion with cold fixative and then studied by electron microscopy without previous staining. The fixative (2.5% glutaraldehyde in 0.1 mol/l cacodylate buffer, pH 7.4, cooled to 3 C°) was perfused through the rat's vascular system and dripped into the abdominal cavity. Electron microscopy also was used to determine the particle size of USPIO and AG-USPIO as previously described [16]. After removal and successive dehydration in graded alcohols, specimens were embedded in Epon (Fluka Chemical Corp., Ronkonkoma, NY), and sections 60-nm thick without previous staining were obtained by using an ultratome. Electron microscopy was performed on a JEOL Jelectron microscopy 100S (JEOL Instruments, Palo Alto, CA). The voltage was 60 kV. Micrographs were taken at magnifications of 3000–100,000× and enlarged photographically 2.6 times.

Receptor Experiments

Uptake of asialoglycoproteins by the liver is mediated specifically by ASG receptors on hepatocytes and can be blocked with D(+) galactose and asialofetuin [27–29]. For in vitro experiments, rodent hepatocyte membranes with ASG surface receptors were isolated by using a modification of a previously described technique [30, 31]. Livers from Sprague Dawley rats ($n = 2$) were perfused in vivo for 5 min with Hanks solution (Sigma Chemicals, St. Louis, MO) buffered with 0.05 mol/l HEPES and 0.5 mmol/l EGTA (Sigma Chemicals). After this initial perfusion to remove erythrocytes, the livers were perfused with collagenase solution (100 U/ml) in Williams E medium (Sigma Chemicals) buffered with 0.05 mol/l HEPES. Livers then were washed in complete medium and sieved through a number 60 stainless steel mesh (Sigma Chemicals). The resulting tissue fragments and cells were incubated in complete medium containing 0.3 mg/ml collagenase. Subsequently, the cells were washed, centrifuged at 1500*g* for 10 min, sonicated (10 W for three 20-sec cycles on ice, Branson sonifier 450; Branson Ultrasonics Corp, Danbury, CT) and washed again.

Samples of the membrane suspensions enriched with ASG receptors were then incubated for 30 min at 37°C with D(+) galactose (0.1 mg/ml; Sigma Chemicals) and asialofetuin (2 mg/ml; Sigma Chemicals) to saturate ASG binding sites on the membrane or complete medium (control). After this incubation, USPIO or AG-USPIO was added to the test tubes (10 µmol Fe), and samples were washed and ultracentrifuged twice to remove excess iron oxide particles. Finally, T1 and T2 measurements were obtained as described earlier.

MR Imaging

All in vivo MR imaging experiments were performed on anesthetized rats (intraperitoneal phenobarbital, 35 mg/kg). Rats ($n = 4$) were imaged before and after administration of AG-USPIO (2 and 10 µmol

Fe/kg) or USPIO (10 μmol Fe/kg). One of the rats received asialofetuin (4 mg/100 g body weight) 30 min before administration of AG-USPIO to show the feasibility of receptor blockade in vivo.

MR imaging was performed on a 0.6-T (25.1 MHz) Technicare superconducting magnet. Coronal multislice images were obtained by using a slice thickness of 4 mm and a 128 × 256 matrix. When the head coil with a field of view (FOV) of 16 cm was used, pixel dimensions were 0.6 × 1.2 × 4.0 mm. Images were acquired by using a variety of spin-echo (SE) pulse sequences, including SE 250/20/6 (TR/TE/number of signal averages), SE 500/40/4, and SE 1500/40/2. Homogeneous regions of interest (21 pixels) within individual livers and spleens were used to calculate signal-to-noise ratios (SNR, mean signal intensity divided by the standard deviation of noise). MR images of ASG-receptor distribution were obtained by subtracting AG-USPIO images obtained before and after administration of contrast material.

Animals

A total of 43 male Sprague-Dawley rats (Charles River Laboratories, Wilmington, MA) were used in the study. One animal was used for histopathologic studies, six for determination of blood half-life, 15 for biodistribution studies, 15 for time course studies, two for receptor studies, and four for MR imaging experiments.

Statistical Analysis

Differences in measurements of relaxation time and half-lives were evaluated statistically by using the nonparametric Wilcoxon test [32].

Results

Physical Properties

Magnetic properties.—The T1 relaxivity (R1) of USPIO was 21.6 $(\text{mmol/l})^{-1}\text{sec}^{-1}$, and the T2 relaxivity was 44.1 $(\text{mmol/l})^{-1}\text{sec}^{-1}$ (37°C and 0.47 T). The R1 of AG-USPIO was 23.3 $(\text{mmol/l})^{-1}\text{sec}^{-1}$, and the R2 was 48.9$(\text{mmol/l})^{-1}\text{sec}^{-1}$. The r value of the linear curve fits was greater than .95 for both substances. The R2/R1 ratio of both preparations was approximately two, which is lower than ratios obtained with larger iron oxide particles.

The mean particle sizes of USPIO (11.5 ± 6.3 nm) and AG-USPIO (12.2 ± 6.5 nm) were similar. For both agents, 96% of the particles were smaller than 20 nm, 70% were smaller than 10 nm, and 26% were smaller than 5 nm. USPIO and AG-USPIO were present as polycrystalline (each particle contained several electron-dense crystals), multidisperse particles (i.e., particles of different sizes) showing a more heterogeneous size distribution than ferritin (measured particle size, 9.3 ± 3.6 nm). USPIO has an apparent molecular weight by gel filtration of approximately 700,000 [16].

Pharmacology

Blood half-life.—The blood half-life of the T1 effect of USPIO is 81 min [16]. Compared with conventional superparamagnetic iron oxide preparations (AMI-25: half-life of 6 min), this half-life is significantly longer ($p < .001$), indicating that USPIO are recognized, opsonized, and/or phagocytosed less readily by the mononuclear phagocytic system of liver and spleen [16]. The half-life of AG-USPIO of 8 min was significantly shorter than that of USPIO ($p < .001$) despite the similar size, suggesting that AG-USPIO are effectively removed from the circulation by a high-affinity receptor system.

Biodistribution.—Thirty minutes after IV administration of 10 μmol Fe/kg of AG-USPIO, the only significant ($p < .001$) decrease in tissue relaxation times was noted in liver (Table 1). T1 decreased from 260.0 ± 6.2 msec to 224.3 ± 5.9 msec, and T2 decreased from 35.3 ± 2.1 to 19.7 ± 1.9 msec. Specifically, the spleen did not show a significant change in tissue relaxation time (Table 1), indicating selectivity of this agent for hepatocytic parenchyma rather than phagocytic cells. Relaxation times of small intestine and contents were not changed after IV administration of AG-USPIO, suggesting that this agent is not excreted via the biliary system and is therefore not a hepatobiliary contrast agent.

Time course (biodegradation).—To determine the intrahe-

TABLE 1: Biodistribution Studies

Tissue	T1 Control	T1 After AG-USPIO[a]	T2 Control	T2 After AG-USPIO[a]
Liver	260.0 ± 6.2	224.3 ± 5.9[b]	35.3 ± 2.1	19.7 ± 1.9[b]
Spleen	614.7 ± 37.8	605.7 ± 9.5	61.6 ± 1.0	60.0 ± 0.6
Muscle (flank)	590.5 ± 12.0	579.0 ± 4.2	39.0 ± 2.1	38.6 ± 0.4
Fat (peritoneal)	183.5 ± 2.1	183.0 ± 1.4	97.7 ± 6.2	107.3 ± 0.9
Kidney	458.0 ± 8.5	466.5 ± 6.4	48.6 ± 2.2	53.1 ± 1.5
Heart	620.5 ± 6.4	626.5 ± 17.7	42.9 ± 0.9	42.5 ± 1.7
Lungs	749.0 ± 2.8	745.5 ± 19.1	60.8 ± 4.7	52.8 ± 4.0
Testes	1002.0 ± 33.9	969.5 ± 40.3	128.2 ± 3.5	128.7 ± 1.0
Urine	1532.5 ± 40.3	1569.5 ± 35.7	203.2 ± 4.5	246.0 ± 20.2
Small intestine	366.3 ± 7.6	373.3 ± 7.2	50.9 ± 1.3	50.3 ± 0.5
Large intestine	428.5 ± 31.8	442.0 ± 67.9	42.4 ± 1.3	42.4 ± 2.3

Note.—Tissue relaxation times (in msec) without ($n = 7$) and with ($n = 8$) IV injection of 10 μmol Fe/kg of AG-USPIO in rats.

[a] AG-USPIO = arabinogalactan ultrasmall superparamagnetic iron oxide.

[b] Significantly ($p < .001$) lower values after administration of AG-USPIO.

patic degradability (i.e., loss of magnetic properties) of AG-USPIO, we determined liver relaxation times at various intervals after injection of 10 μmol AG-USPIO (Fig. 1). Thirty minutes after injection, liver T2 had decreased 44%. Twenty-four and 48 hr after administration, T2 was 24% and 14% lower than precontrast values, respectively. After 14 days, liver T2 had returned to precontrast values. These data suggest a liver half-life of AG-USPIO of approximately 24 hr. This rapid return to normal values indicates efficient degradation of the ultrasmall particles by hepatocytes.

Receptor Experiments

Cellular and intracellular distribution.—Histologically, stainable iron was detected in the cytoplasm of hepatic parenchymal cells (Fig. 2A). The iron stain also was shown in Kupffer cells, but not to the degree expected with conventional iron oxides [9].

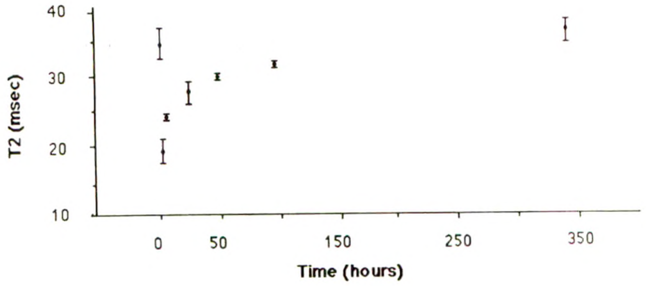

Fig. 1.—Degradation of ultrasmall iron oxide particles coated with arabinogalactan (AG-USPIO). T2 relaxation times of liver are mapped as a function of time before and after administration of 10 μmol Fe/kg of AG-USPIO. 30 min after administration, T2 decreases 44%. Within 24 hr T2 is 24%, and after 48 hr it is 14% lower than control values. Liver T2 has returned to baseline values after 14 days.

By electron microscopy, AG-USPIO was identified on the surface of hepatocyte membranes, presumably attached to ASG surface receptors (Fig. 2B). This distribution was such that most particles were seen close to coated pits. In addition, large amounts of electron-dense deposits were identified within cellular lysosomes. No particles were seen in the nucleus or the hepatic cytoplasm.

Membrane receptor studies.—T2 relaxation times of medium containing ASG membrane receptors were significantly ($p < .005$) shorter after incubation with AG-USPIO than after incubation with USPIO alone or with AG-USPIO after blockade (Fig. 3). This is best explained by the retention of AG-USPIO on membrane receptors despite repeated washing cycles. When ASG membrane receptors were blocked with D(+) galactose and asialofetuin before incubation with AG-USPIO, T2 values were significantly higher ($p < .001$). Membranes incubated with USPIO with and without blocker showed similar T2 values, confirming the hypothesis that there is no specific attachment of USPIO to ASG receptors. T2 values of membrane solutions incubated with USPIO and blocked with AG-USPIO are somewhat lower than those of the control experiment, presumably because not all particles had been removed during the two washing cycles.

MR Imaging Experiments

AG-USPIO vs USPIO imaging.—On unenhanced images, liver SNR was 42.9 ± 0.9 (SE 250/14) and spleen SNR was 24.5 ± 1.8 (Fig. 4A, spleen darker than liver). After administration of 10 μmol Fe/kg of AG-USPIO (Fig. 4B), liver SNR decreased from 42.9 ± 0.9 to 13.1 ± 0.2 ($p < .001$), whereas spleen SNR did not change significantly (24.5 ± 1.8 compared with 23.3 ± 0.2) (spleen brighter than liver). This biodistribution was different from that after administration of USPIO (Fig. 4D), which is known to be cleared by the mononuclear phag-

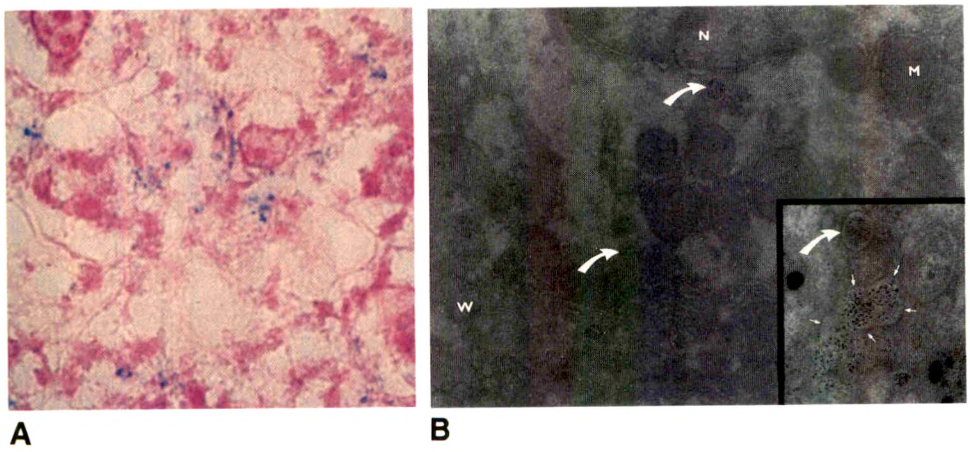

Fig. 2.—Cellular and intracellular distribution of ultrasmall iron oxide particles coated with arabinogalactan (AG-USPIO).

***A*, Photomicrograph of a liver specimen stained with Prussian blue shows iron preparation in blue and overall distribution of AG-USPIO particles. Blue $Fe_4(Fe(CN)_6)_3$ complex is seen within cytoplasm of polygonal hepatocytes. Cell nuclei do not contain stainable iron.**

***B*, Transmission electron micrograph (×20,000) of hepatocyte shows intracellular distribution of AG-USPIO. Electron-dense particles are seen in large numbers within lysosomes (*curved arrows*). Cell nucleus (N) is seen at top, mitochondria (M) to right and center, and cell wall (W) at lower left. At high power magnification (×100,000, inset) high-density AG-USPIO particles can be seen clearly along a hepatocyte cell membrane (*straight arrows*). Uptake by hepatocytes occurs by invagination of receptor-bound particles into membrane vesicles (*curved arrow*, inset).**

ocytic system. After administration of 10 μmol Fe/kg of USPIO, liver SNR decreased from 42.9 ± 0.9 to 20.4 ± 0.1 ($p < .001$) and spleen SNR decreased from 24.5 ± 1.8 to 18.6 ± 2.1 (Fig. 4C, spleen and liver are hypointense). The signal intensity of the liver after administration of contrast material was lower in animals injected with AG-USPIO than in animals that had received USPIO (13.1 ± 0.2 compared with 20.4 ± 0.1; $p < .05$).

In vivo blockade of ASG-receptors.—An experiment was performed to show in vivo that ASG receptors can be blocked competitively and that subsequently the biodistribution of the IV administered AG-USPIO (Fig. 4C) is altered. When ASG receptors were blocked with asialofetuin before administration of AG-USPIO, liver SNR was higher (31.5 ± 0.5 compared with 13.1 ± 0.2), and spleen SNR was lower (20.7 ± 0.7 compared with 23.3 ± 0.2) (compare Figs. 4B and 4C). These SNR changes in spleen and liver suggest that AG-USPIO had been redistributed into cells of the mononuclear phagocytic system. Indeed, this biodistribution was similar to that of USPIO (Fig. 4D).

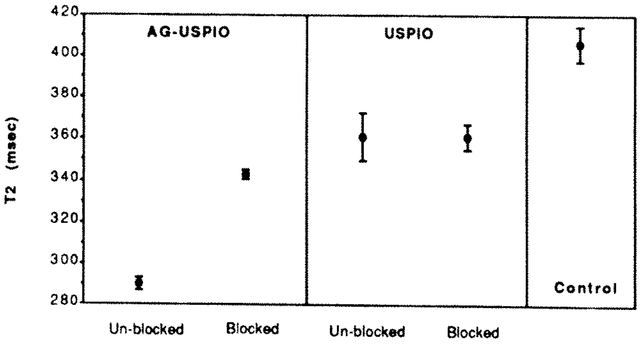

Fig. 3.—Graph shows T2 relaxation times (37°C, 0.47 T, Carr-Purcell-Meiboom-Gill sequence) of aqueous solutions containing asialoglycoprotein membrane receptors before (control) and after incubation in vitro with different iron oxide preparations. The solution of membrane receptors incubated with ultrasmall iron oxide particles coated with arabinogalactan (AG-USPIO) has a significantly lower T2 than that of the solution incubated with USPIO or AG-USPIO after the receptor was blocked with D(+)galactose and asialofetuin. T2 values of membrane solutions incubated with USPIO and blocked AG-USPIO are somewhat lower than those in control experiment, as not all particles had been removed during the two wash cycles.

MR receptor image.—In order to map the receptor distribution of the ASG receptor in vivo, coronal images were acquired as SE 500/40 and displayed as subtraction images ("receptor images") before and after administration of 2 μmol Fe/kg of AG-USPIO (Fig. 5). This dose is 10 times lower than that used in conventional iron oxide imaging [33]. On these receptor images, areas of high signal intensity represent regions with ASG receptors, whereas low-signal-intensity areas indicate the absence of receptors. The heart and some bowel loops appear bright because of motion-induced subtraction errors. No receptors were detectable in spleen, brain, lung, kidney, and muscle (Fig. 5). This biodistribution of receptors is consistent with previous reports of ASG receptor biodistribution [21].

Discussion

We have established that iron oxide particles can be targeted specifically to ASG receptors on hepatocytes. The findings are supported by biodistribution and MR imaging data and confirmed by in vitro and in vivo ASG blockade experiments. The characteristics of this novel receptor-specific iron oxide preparation that cause these results are the smallness of the particle and the receptor targeting.

We recently have shown that the biodistribution of superparamagnetic iron oxide particles can be altered by reducing the size of the particles [16]. USPIO particles have a mean size of 11.5 ± 6.3 nm compared with 30–100 nm for conventional iron oxide particles. The smaller size of USPIO and prolonged blood half-life (81 min vs 6 min for conventional iron oxide preparations) facilitate delivery into the interstitium by nonspecific vesicular transport and through transendothelial channels [16]. It has been shown that the transcytosis of USPIO into the interstitium results in significant delivery of the agent to regional and central lymph nodes [17]. The ability of an iron oxide particle to enter the interstitium is a prerequisite for successful MR receptor or antibody imaging.

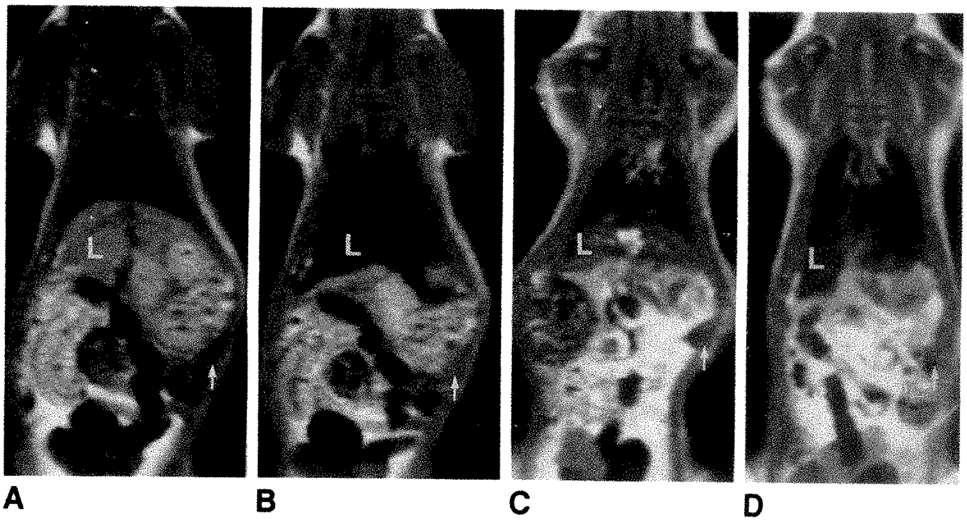

Fig. 4.—A–D, MR images of receptor blockade in rat. Images (SE 250/20) were obtained before (*A*), after 10 μmol Fe/kg of ultrasmall iron oxide particles coated with arabinogalactan (AG-USPIO, *B*), after blockade of asialoglycoprotein (ASG) receptors with D(+)galactose and asialofetuin and subsequent injection of 10 μmol Fe/kg of AG-USPIO (*C*), and after administration of 10 μmol Fe/kg of USPIO (*D*). Administration of AG-USPIO decreases liver (L) but not spleen (*arrow*) signal intensity (*B*), unlike USPIO, which decreases both (*D*). After in vivo blockade of ASG receptors (C), reduction of liver signal intensity is less pronounced (compare *B* and *C*) but still is present, as AG-USPIO now is diverted to Kupffer cells; similarly spleen (*arrow*) signal intensity is decreased, indicative of reticuloendothelial biodistribution.

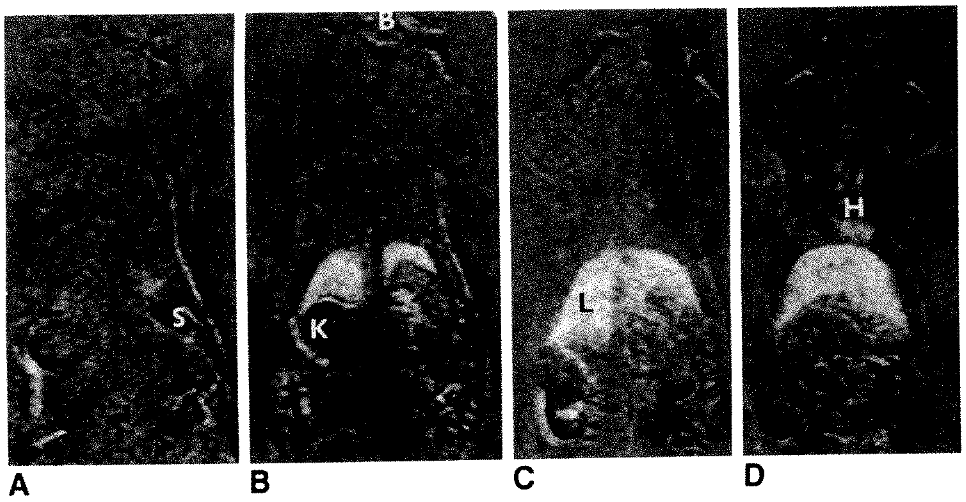

Fig. 5.—A–D, Receptor images of rat. MR images (SE 500/40) were obtained before and immediately after IV administration of 2 μmol Fe/kg of ultrasmall iron oxide particles coated with arabinogalactan (AG-USPIO). Images then were subtracted electronically and are displayed as four consecutive coronal slices from posterior to anterior (*A–D*). Only liver (L) appears white (indicating presence of receptor), whereas brain (B), lung, heart (H), kidney (K), muscle, and spleen (S) are dark (no receptor). Heart and some bowel loops appear bright because of motion-induced subtraction errors.

In the current study, USPIO was targeted to ASG receptors. Of the many different carbohydrate receptor systems on hepatocytes, the ASG receptor system was chosen because it is the most completely investigated and best understood carbohydrate-specific receptor system [18]. Asialoglycoprotein receptors are responsible for the plasma clearance of desialylated glycoproteins by the liver. The discovery of the ASG receptor system has led to the development of both diagnostic [21, 34] and therapeutic agents [35]. The ASG receptor has specificity for a large variety of desialated serum proteins in vivo, including follicle-stimulating hormone, human chorionic gonadotropin, transferrin, IgG, prothrombin, fetuin, and orosomucosoid [18]. The number of ASG binding sites per hepatocyte (as high as 500,000) [19] and the rapid internalization and reutilization of the receptor [36] indicate that a single dose of AG-USPIO will not interfere significantly with receptor binding of biological ligands.

Pharmaceuticals with terminal galactose groups are recognized by ASG receptors and thus can be directed to hepatocytes [18]. AG-USPIO particles differ from conventional USPIO in that they have been stabilized with arabinogalactan, a galactose-containing polysaccharide [25]. The terminal galactose groups are recognized by the ASG receptors, and the agent is taken up rapidly by hepatocytes before major uptake by the mononuclear phagocytic system occurs. The avidity of AG-USPIO uptake by ASG receptors is reflected by the reduction in blood half-life of these small particles from 81 to 6 min.

The initial interaction of the AG-USPIO with receptors in the course of endocytosis is at the hepatocyte plasma membrane. Our electron microscopy experiments confirm that this interaction occurs at least in part in coated pits, a membrane structure that has been implicated in adsorptive endocytosis [37]. It is well documented that internalization of the ASG-receptor-bound ligand is rapid. A first-order rate constant of ASG-receptor-bound ligands at 37°C has been calculated to be 3.7×10^{-3} sec^{-1} [36]. This corresponds to a half-life of approximately 3 min for the occupied receptor on the cell surface. The intracellular catabolic site of ASG-bound ligands is in lysosomes [38, 39]. Our electron microscopy results are in accordance with these observations, as electron-dense AG-USPIO could be shown within lysosomes (Fig. 2). Time-response curves support the observation that AG-USPIO are degraded completely in vivo and that liver relaxation times return to normal baseline values. The liver organ half-life of AG-USPIO as determined by T2 measurements is approximately 24 hr.

In vivo receptor imaging experiments and biodistribution studies confirm that AG-USPIO is taken up by liver tissue, with little or no uptake by the spleen, bone marrow, or lymph nodes, as would be expected for a mononuclear phagocytic system agent such as USPIO (Fig. 4). Proof that AG-USPIO is a receptor-specific agent was established with in vitro (Fig. 3) and in vivo (Fig. 4) receptor blockade experiments. MR imaging studies (Fig. 4) indicate that after the ASG receptor is blocked with D(+) galactose and asialofetuin, the agent redistributes to organs of the mononuclear phagocytic system (spleen, bone marrow), where it decreases signal intensity of these organs.

ASG receptor targeting of USPIO has several advantages over the use of conventional iron oxide preparations. First, because the majority of the dose reaches the liver, the injection dose can be decreased considerably (Fig. 3). Good liver enhancement was achieved with a dose of 2 μmol Fe/kg at 0.6 T, a dose 10 times lower than that proposed for MR imaging with conventional iron oxide preparations (Fig. 5). Second, AG-USPIO may provide a quantitative in vivo measure of ASG-receptor function that may be clinically useful for monitoring disease states and therapeutic response. Third, because most malignant tumors are devoid of ASG receptors, AG-USPIO is expected to provide excellent contrast between normal liver and metastases.

The current data on AG-USPIO provide new directions in development of tissue-specific contrast enhancement with MR imaging. Soon after the introduction of contrast agents for MR imaging, investigators proposed strategies for attaching antibodies to paramagnetic [40] and subsequently to iron oxide particles [13]. Early in vivo attempts were unsuccessful because of the combination of the low relaxivity of paramagnetic metal ions and the low concentration of antigenic sites.

Attempts at attachment of multimetal ions to organic backbones (e.g., polylysine) have been successful in vitro, but not in vivo (B. A. Khaw, personal communication). Conventional iron oxide particles also have been attached to antibodies [11, 12, 15]; however, in vivo these large particles are taken up quickly by cells of the mononuclear phagocytic system, and in vivo antibody binding to tumor cells is not reproducible in murine models with large tumors [14]. Ultrasmall iron oxide particles have the characteristics (small size, high relaxivity, extended blood half-life, and transcytosis) that are essential for receptor-directed MR imaging. Although AG-USPIO is specific for ASG receptor imaging, surface modification of these small particles should enable the development of a variety of receptor- and antibody-specific agents.

REFERENCES

1. Wolf G, Burnett K, Goldstein E, Joseph P. Contrast agents for magnetic resonance imaging. In: Kressel H, ed. *Magnetic resonance annual*. New York: Raven, **1985**:231-265
2. Mendonca-Dias M, Lauterbur P. Ferromagnetic particles as contrast agents for magnetic resonance imaging of the liver and spleen. *Magn Reson Med* **1986**;3:328-330
3. Renshaw P, Owens C, McLaughlin A, Frey T, Leigh J. Ferromagnetic contrast agents: a new approach. *Magn Reson Med* **1986**;3:217-255
4. Widder D, Greif W, Widder K, Edelman R, Brady T. Magnetite albumin microspheres: a new MR contrast material. *AJR* **1987**;148:399-404
5. Bacic G, Niesman M, Magin R, Wright S, Swartz H. The use of dextran-magnetite for liver enhancement. In *Proceedings of the Sixth Annual Meeting of the Society of Magnetic Resonance in Mecicine*, **1987**:328
6. Saini S, Stark D, Hahn P, Wittenberg J, Brady T, Ferrucci J. Ferrite particles: a superparamagnetic MR contrast agent for the reticuloendothelial system. *Radiology* **1987**;162:211-216
7. Hemmingson A, Carlsten J, Ericsson A, Klaveness J, Spreber G, Thomas K. Relaxation enhancement of the dog liver and spleen by biodegradable superparamagnetic particles in proton magnetic resonance imaging. *Acta Radiol* **1987**;28:703-705
8. Majumdar S, Zoghbi S, Pope C, Gore J. Quantitation of MR relaxation effects of iron oxide particles in liver and spleen. *Radiology* **1988**;169:653-655
9. Weissleder R, Stark D, Engelstad B, et al. Superparamagnetic iron oxide: pharmacokinetics and toxicity. *AJR* **1989**;152:167-173
10. Weissleder R, Elizondo G, Josephson L, et al. Experimental lymph node metastases: enhanced detection with MR lymphography. *Radiology* **1989**;171:835-839
11. Owen C, Sykes N. Magnetic labeling and cell sorting. *J Immunol Methods* **1984**;73:41-48
12. Molday R, Molday L. Separation of cells labeled with immunospecific iron dextran microspheres using high gradient magnetic chromatography. *FEBS Lett* **1984**;170:232-238
13. Renshaw P, Owen C, Evans A, Leigh J. Ferromagnetic antibody relaxation technique. *Proceedings of the Fifth Annual Meeting of the Society of Magnetic Resonance in Medicine*, **1986**:17
14. Cerdan S, Lötscher H, Künnecke B, Seelig J. Monoclonal antibody-coated magnetic particles as contrast agents in magnetic resonance imaging of tumors. *Magn Reson Med* **1989**;12:151-163
15. Molday R, Mackenzie D. Immunospecific ferromagnetic iron-dextran reagents for the labelling and magentic separation of cells. *J Immunol Methods* **1982**;52:353-367
16. Weissleder R, Elizondo G, Wittenberg J, Rabito C, Bengele H, Josephson L. Ultrasmall superparamagnetic iron oxide (USPIO): characterization of a new class of contrast agents for MR imaging. *Radiology* **1990**;175:489-493
17. Weissleder R, Elizondo G, Wittenberg J, Lee A, Josephson L, Brady T. Ultrasmall superparamagnetic iron oxide (USPIO): an intravenous contrast agent for asesssing lymph nodes with MR imaging. *Radiology* **1990**;175:494-498
18. Ashwell G, Harford J. Carbohydrate-specific receptors of the liver. *Ann Rev Biochem* **1982**;51:531-554
19. Schwartz A, Rup D, Lodisch H. Difficulties in the quantification of asialoglycoprotein receptors on the rat hepatocyte. *J Biol Chem* **1980**;255:9033-9036
20. Gregoriadis G. Targeting of drugs: implications in medicine. *Lancet* **1981**;2:241-246
21. Vera D, Stadalnik R, Krohn K. Technetium-99m galactosyl-neoglycoalbumin: preparation and preclinical studies. *J Nucl Med* **1985**;10:1157-1167
22. Sato S, Sako Y, Yamashina S, Ohnishi S. A novel method for isolating specific endocytic vesicles using very fine ferrite particles coated with biological ligands and the high gradient magnetic separation technique. *J Biochem* **1986**;100:1481-1492
23. Clough G, Michel C. The role of vesicles in the transport of ferritin through frog endothelium. *J Physiol* **1981**;315:127-142
24. Josephson L, Groman E, Menz L, Luis J, Bengele H. A functionalized superparamagnetic iron oxide colloid as a receptor-directed MR contrast agent. *Magn Reson Imaging* **1990** (in press)
25. Beuth J, Ko H, Oette K, Pulverer G, Roszkowski K, Uhlenbruck G. Inhibition of liver metastasis in mice by blocking hepatocyte lectins with arabinogalactan infusions and D-galactose. *J Cancer Res Clin Oncol* **1987**;113:51-55
26. Groman E, Josephson L, Lewis J. Biologically degradable superparamagnetic materials for use in clinical applications. United States Patent 4,827,945, **1989**
27. Hildenbrandt G, Aronson N. Uptake of asialo-glycophorin by the perfused rat liver and isolated hepatocytes. *Biochim Biophys Acta* **1979**;587:373-380
28. Clarke B, Oka J, Weigel P. Degradation of asialoglycoproteins mediated by the galactosyl receptor system in isolated hepatocytes: evidence for two parallel pathways. *J Biol Chem* **1987**;262:17384-17392
29. Regoeczi E, Debanne M, Hatton M, Koj A. Elimination of asialofetuin and asialoorosomucoid by the intact rat. *Biochim Biophys Acta* **1978**;541:372-384
30. Harford J, Ashwell G. Assessment of receptor recycling in mammalian hepatocytes: perspectives based on current techniques. In: Birnbaumer L, O'Malley B, eds. *Methods in enzymology*, vol. 109. New York: Academic Press, **1979**:232
31. Leffert H, Koch K, Moran T, Williams M. Liver cells. In: Jacoby W, Pastan I, eds. *Cell culture*. New York: Academic Press, **1979**:536-544
32. Armitage P, Berry G. *Statistical methods in medical research*. Oxford, England: Blackwell Scientific, **1987**
33. Fretz C. Elizondo G, Weissleder R, Hahn P, Stark D, Ferrucci J. Superparamagnetic iron oxide enhanced MR imaging: pulse sequence optimization for detection of liver cancer. *Radiology* **1989**;172:393-397
34. Sobue G, Kosaka A. Asialoglycoproteinemia in a case of primary hepatic cancer. *Hepatogastroenterology* **1980**;27:200-203
35. Gregoriadis G, Senior J, Poste G. *Targeting of drugs with synthetic systems*. New York: Plenum Press, **1986**
36. Tolleshaug H. Binding and internalization of asialo-glycoproteins by isolated rat hepatocytes. *Int J Biochem* **1981**;13:45-51
37. Goldstein J, Anderson R, Brown M. Coated pits, coated vesicles, and receptor-mediated endocytosis. *Nature* **1979**;279:679-685
38. Gregoriadis G, Morell A, Sternlieb I. Catabolism of desialated ceruloplasmin in the liver. *J Biol Chem* **1970**;245:5833-5837
39. Haimes H, Stockert R, Morell A, Novikoff A. Carbohydrate-specified endocytosis: localization of ligand in the lysosomal compartment. *Proc Natl Acad Sci USA* **1981**;78:6936-6939
40. Brady T, Rosen B. *Diagnostic specificity of nuclear magnetic resonance*. Washington, DC: National Academy Press, **1984**:65-76

1990

Happy Holidays

To All Our
Readers, Authors, and Reviewers
from the
American Journal of Roentgenology
Editorial Staff

Review Article

Fracture of the Pelvis: Current Concepts of Classification

Jeremy W. R. Young[1] and Charles S. Resnik

Historically, pelvic fractures have been classified according to whether there is pelvic stability or instability, although confusion has been caused by the inclusion of many eponyms that mainly reflect the observation of a single author on a particular fracture pattern. Pennal and Tile were the first authors to attempt to classify pelvic fractures according to the force vector causing them. This concept was refined by Young and Burgess, who provided a more detailed classification system, again relating to force vectors. This article focuses on this classification and its significance with regard to pelvic stability, type of pelvic disruption, and hence the type of corrective forces that should be applied in the surgical management. Use of a classification system of pelvic fractures based on force vectors allows the orthopedic surgeon to apply external fixation in the most appropriate manner to correct pelvic deformity and to maximize patients' survival.

General Considerations

Fractures of the pelvis have long been a dilemma, both diagnostically and therapeutically. Much of this has been because of the lack of a standardized classification system. In the past, the relative rarity of pelvic fractures resulted in a modest neglect of this part of the anatomy. With the coming of what might be termed the high-speed era, however, pelvic injury has become an increasingly important subject and has been cited as the primary cause of death in multiple-trauma victims [1–7]. Furthermore, with the advent of specialized trauma centers, large numbers of pelvic fractures are now seen in short periods. For example, Dunn and Morris [2] reported 149 patients with pelvic fractures treated during a 15-year period ending in 1967, whereas Young et al. [8] more recently reported over 300 cases seen in less than 3 years.

Radiologic examination of the pelvis is more complex than that of most areas of the skeleton, because standard lateral views are impractical in severely traumatized patients and are of limited value because of overlying bony structures. To combat this, additional views have been devised. Judet et al. [9] emphasized the importance of oblique views in the evaluation of the pelvis and acetabula, and angled "inlet" and "outlet" views have been shown to provide useful information about the integrity of the sacrum and sacroiliac joints. These views also provide the only means whereby the spatial relationship of the bones of the pelvic ring can be assessed on plain film radiographs [10–12]. This is of importance with regard to classifications based on force vectors, because the integrity of the pelvic ring, particularly the posterior elements, together with the position of fracture fragments, will provide the information needed to determine the disruptive force on the pelvis and hence the corrective forces needed for external stabilization.

The advent of CT has simplified radiologic evaluation of the pelvis and acetabulum [13]. CT is superior to plain films in providing detail of fractures, position of fracture fragments, and extent of diastasis of the sacroiliac joints and pubic symphysis. It is superior also in the evaluation of the sacrum and acetabulum, particularly with its ability to detect small intraarticular bone fragments [14]. In the acute setting, however, CT scanning is more time consuming than obtaining plain radiographs and is better performed at a later date when life-threatening complications are not a consideration and

---

Received February 22, 1990; accepted after revision June 22, 1990.

[1] Both authors: Department of Radiology, University of Maryland Medical System/Hospital, 22 S. Greene St., Baltimore, MD 21201. Address reprint requests to J. W. R. Young.

AJR 155:1169–1175, December 1990 0361-803X/90/1556-1169 © American Roentgen Ray Society

when time is available for definitive evaluation for surgical reconstruction [8]. In view of the superiority of CT, conventional tomography is rarely, if ever, indicated in the evaluation of pelvic fractures.

The importance of pelvic fractures lies in the high rates of associated complication and mortality. Reported frequencies of pelvic fractures in fatal accidents range from 18% to 24% [15-17], and according to Braunstein et al. [18], may be as high as 45% for pedestrians. In addition, pelvic fracture has been cited as the main factor contributing to death in multiple-trauma victims [1-7]. Mortality rates in patients with pelvic fractures have been quoted from 9% to 19% [3, 4, 15-19]. In Rothenberger's series, however, 60% of the deaths in patients with pelvic fractures were primarily due to the pelvic fracture, and of those, 65% were caused by hemorrhagic shock or coagulopathy [4]. Additional deaths were due to sepsis arising in the pelvic hematoma (9%) and renal failure resulting from blood loss or sepsis (9%). The control of hemorrhage is therefore of great importance.

Major blood loss usually occurs as a result of bleeding from the superior gluteal artery or anterior branches of the internal iliac artery [8, 12, 20]. This can be alleviated by a variety of embolization techniques [21-25]. Goris et al. [26] have suggested that early external fixation reduces blood loss associated with pelvic fractures and thus improves survival for patients with these injuries. This has been corroborated by extensive clinical experience.

Apart from causing severe hemorrhage, pelvic fractures also may cause injury of the urethra and bladder. Harris and Harris [27] state that "Malgaigne" fractures commonly cause such injury, with rupture of the bladder and urethra occurring in 20% of patients. Clark and Prudencio [28] and Flaherty et al. [29] suggest that urinary tract injuries are more commonly associated with separation of the symphysis pubis and frac-

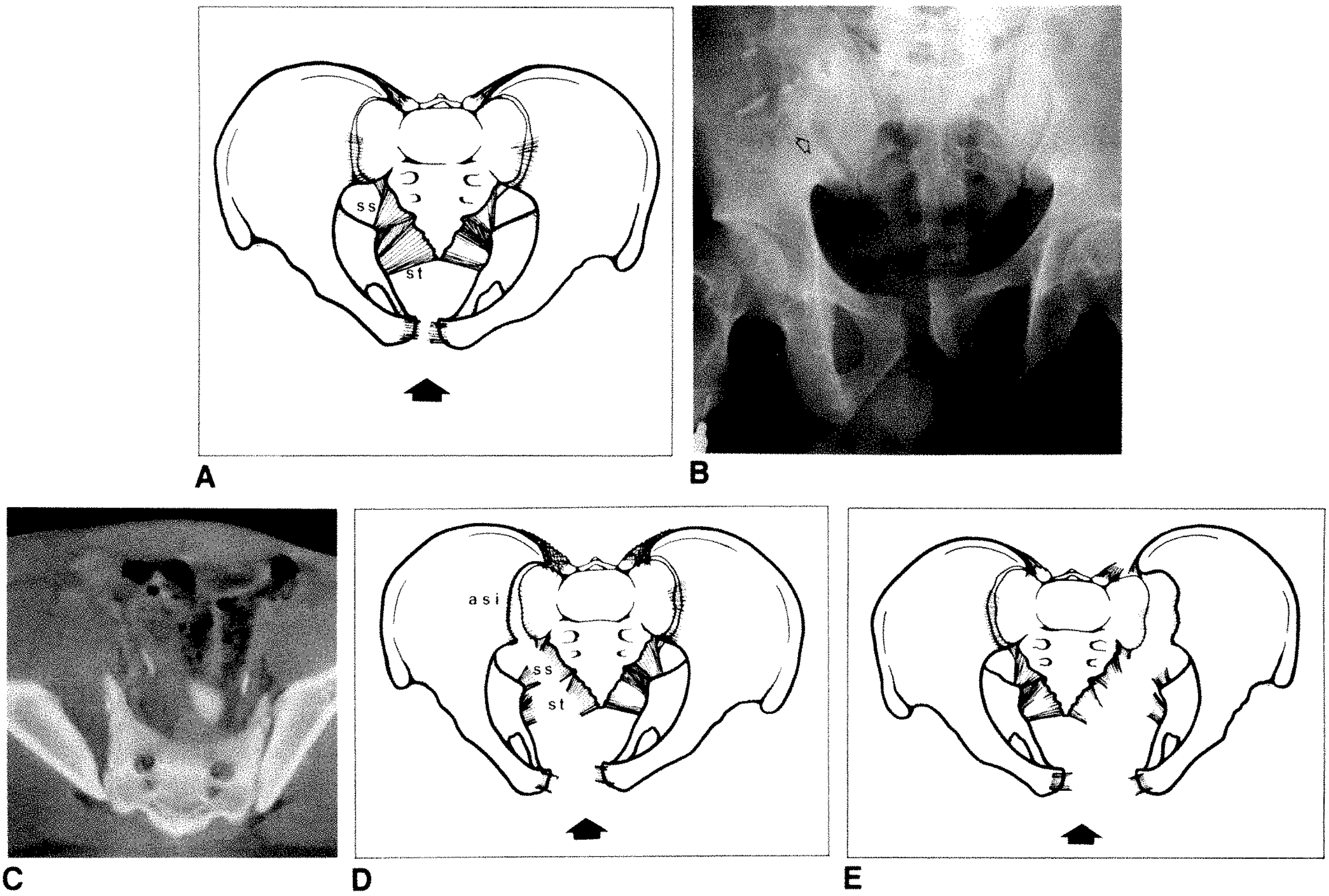

Fig. 1.—*A*, Anteroposterior compression injury (Young-Burgess Type I). Diagram shows mild diastasis of symphysis pubis with no evidence of sacroiliac joint disruption. Sacrospinous (ss) and sacrotuberous (st) ligaments are intact. Arrow = direction of force causing fracture. (Reprinted with permission from Young and Burgess [12].)

B, Anteroposterior compression injury (Young-Burgess Type II). Radiograph shows diastasis of symphysis pubis (*large arrow*) and anterior right sacroiliac joint (*small arrow*).

C, CT scan shows that sacroiliac joint disruption involves only anterior aspect.

D, Diagram of Young-Burgess Type II injury. Posteriorly directed force (*arrow*) has "opened" anterior pelvis more than 2.5 cm with disruption of symphysis pubis, anterior sacroiliac (asi), sacrospinous (ss), and sacrotuberous (st) ligaments on right. (Reprinted with permission from Young and Burgess [12].)

E, Anteroposterior compression injury (Young-Burgess Type III). Diagram shows complete disruption of symphysis pubis, left sacroiliac joint, sacroiliac and sacrotuberous ligaments. Left hemipelvic fragment has no ligamentous support. Arrow = direction of force causing fracture.

tures of the pubic rami, and the frequency is reported to increase with increasing diastasis of the symphysis pubis [30]. Berquist [31] also suggests a figure of 20% for urinary tract injury in patients with significant anterior pelvic injury. Other figures, however, suggest urethral injury in 4–17% and bladder injury in only 4% [30, 32, 33], and in a recent large series, Dalal et al. [34] found an overall frequency of urogenital injury of approximately 7%, suggesting that urinary tract injury is not as common as was previously reported.

Classification

A variety of classification systems have been used and reported in the literature. The most common systems of classification have regarded pelvic fractures predominantly as either stable or unstable, depending on radiologic appearances and physical findings [2, 3, 9, 33, 35–39]. Stable fractures have been reported to include "single" fractures of the pelvic ring, pure acetabular fractures, so-called straddle fractures of the pubic rami, and chip fractures or avulsion fractures. Unstable fractures, conversely, are those in which the pelvic ring is disrupted in more than one location, or more particularly, those in which the posterior pelvis, sacrum, or sacroiliac complex are disrupted. This includes Malgaigne or "bucket handle" fractures and "open-book" fractures [36, 37]. Malgaigne fractures consist of fractures of both pubic rami plus a posterior fracture of the sacroiliac complex. Open-book fractures consist of diastasis of the symphysis pubis and external rotation of one or both iliac bones, "hinging" at the sacroiliac joint (Fig. 1).

In severe cases, it is clear when pelvic instability is present, because the pelvic ring is obviously disrupted. However, where fracture fragments are not displaced or minimal diastasis of the symphysis pubis is seen, the radiologic determination of instability is difficult. Categorization of pure acetabular fractures and "single" fractures of the pelvic ring as stable also is confusing. The concept of single fractures was refuted by Gertzbein and Chenoweth [40], who, using radioisotope bone scanning, demonstrated the invariable presence of a second site of injury in fractures of the pelvic ring. This second injury may be a fracture, may occur at a site of ligament attachment, or may be to the ligaments themselves. Such injuries may give rise to significant pelvic instability, even when a second overt fracture is not present.

Confusion over the classification of pelvic fractures is highlighted by the variety of systems proposed. Older classification systems are predominantly a historical documentation of individual fracture patterns or use radiologic criteria to judge stability or lack of stability. Unfortunately, most of these systems have no logical basis and are therefore of limited practical value. In practice, instability is reliably detected only by clinical evaluation, as described by both Bucholz [41] and Tile [11]. Furthermore, diagnosis of instability also is of somewhat limited value in the treatment of the patient, indicating only the need for surgical stabilization rather than the type of stabilization required.

Another system of classification categorizes pelvic fractures according to whether the fractures occurred with or without a break in the pelvic ring, and if so, whether the fractures were single or double [4]. Kane [39] again uses a classification whereby one of the major groups is of single fractures of the pelvic ring. Once again, these authors acknowledge the concept of single injuries of the pelvic ring, which is not only scientifically unsound but is diagnostically hazardous, ignoring the presence of a second fracture and/or possible serious ligamentous injury. Monahan and Taylor [6] devised a system of classification whereby the pelvic fractures were divided into three groups, depending on whether the sacroiliac joints or symphysis pubis were diastatic and in what combination. The groups were further subdivided according to the associated fracture pattern. Again, this classification referred to traumatic points of instability in the pelvic ring and defined the clearly unstable fractures of the pelvis. As with other systems, difficulties of diagnosis often arose in less clear-cut cases. Conolly and Hedberg [5] used interruption of the major line of weight transmission as a basis of classification, and Looser and Crombie [42] grouped severe pelvic fractures into anterior and posterior fractures, which, as demonstrated by Tile [11], Pennal et al. [10], and Young and Burgess [12], is technically unsound.

One possible reason for the lack of a standardized classification is that the historical methods of treatment were confined to postural reduction, slings, or skeletal traction, which could apply only compressive forces to the pelvis [8, 38, 43]. The advent of external fixation devices has altered surgical management dramatically [11, 44–47]. The orthope-

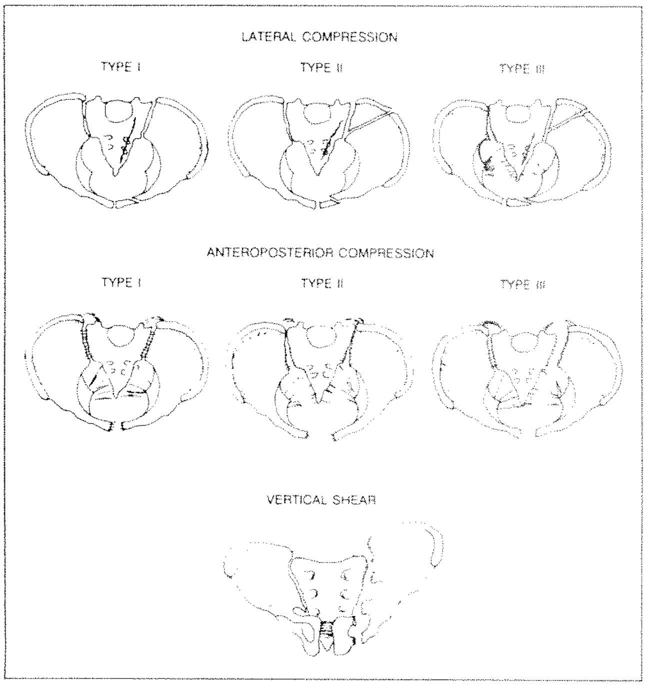

Fig. 2.—Classification of pelvic ring fractures.

dist is not able rapidly to apply a device that can provide either compressive or distractive forces on the pelvic ring. This has created a need to understand the force vectors causing the fracture so that the correct countering forces can be applied by the fixation. Huittinen and Slatis [7] were the first authors to realize the significance of force vectors in pelvic injury, but it was Pennal et al. [10] and Tile [11] who initiated a classification system based on the direction of injurious forces. This concept was refined by Young and Burgess, who classify all pelvic ring fractures as one of four major groups: lateral compression, anteroposterior compression, vertical shear, or combined mechanical injury [8, 12]. This provides a logical approach to pelvic ring trauma and provides the surgeon with the information needed to decide not only whether external fixation is required, but also what corrective forces should be applied. An overview of the major patterns of injury is shown in Figure 2.

With the Young-Burgess system, stability or lack of stability can be judged by knowledge of the ligamentous anatomy of the pelvis coupled with the fracture pattern and direction of the force of injury. In lateral compression fractures, the force of injury is from the side and is associated with horizontally oriented pubic fractures (Fig. 3). Impacted fractures of the sacrum also may occur. These fractures thus correspond to impacted fractures of the posterior sacroiliac complex, one of the unstable fractures in the older classification systems.

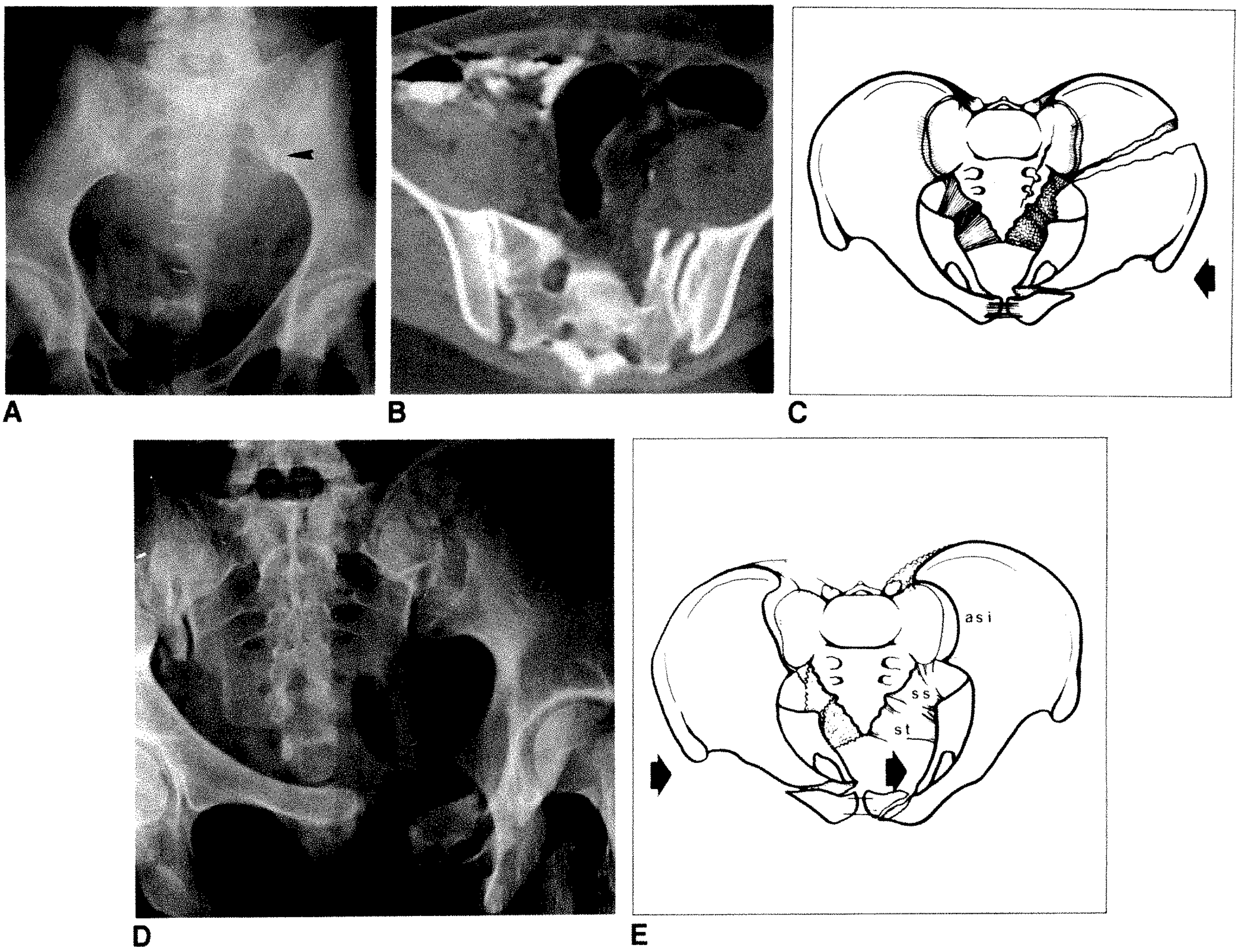

Fig. 3.—*A*, Lateral compression fracture (Young-Burgess Type I). Radiograph shows a crush fracture of sacrum with irregularity of sacral arcuate lines on left, in conjunction with overlap fractures of pubic rami on right. Apparent diastasis of left sacroiliac joint is seen (*arrowhead*).

B, CT scan of same patient indicates that diastasis of left sacroiliac joint is due to traumatic reorientation of sacroiliac joint into more sagittal plane. Fracture of sacrum is well seen.

C, Lateral compression fracture (Young-Burgess Type II). Diagram illustrates typical "horizontal" fractures of pubic rami and oblique fracture of iliac wing on left, giving rise to posterior pelvic instability and internal rotation of anterior hemipelvic fragment. Arrow = direction of force causing fracture. (Reprinted with permission from Young and Burgess [12].)

D, Radiograph of lateral compression fracture (Young-Burgess Type III). Lateral force from right has caused typical "overlap" fractures of left pubic rami, oblique fracture of right iliac wing, diastasis of left sacroiliac joint, and obvious shift of anterior pelvis to left. (Reprinted with permission from Young and Burgess [12].)

E, Diagram of Young-Burgess Type III lateral compression fracture shows similar pattern. On left, lateral force (*arrow*) has been transmitted, causing "external" displacement of right hemipelvis with rupture of anterior sacroiliac (asi), sacrotuberous (st), and sacrospinous (ss) ligaments. In this case, posterior instability on side of lateral force is achieved by rupture of posterior sacroiliac ligaments rather than fracture of iliac wing. (Reprinted with permission from Young and Burgess [12].)

However, the commonest and least destructive lateral compression injury (Type I) is not as a rule an unstable fracture clinically, because even if a sacral fracture is present, it is of the impacted variety (Figs. 3A and 3B). With increasing lateral force, usually imparted to the anterior pelvis, the major fracture fragment is rotated inward, with the anterior sacrum acting as a pivot. This gives rise to either a disruption of the posterior sacroiliac joint, allowing the posterior portion of the iliac wing to hinge outwards, or to an oblique fracture of the posterior ilium, usually extending laterally from the sacroiliac joint (Type II, Fig. 3C). Either of these patterns thus renders the pelvis unstable to additional compressive forces. The most severe form of lateral compression (Type III) is severely unstable, because the lateral compressive force on one side of the pelvis continues to the contralateral side where it becomes a distracting force, externally rotating the anterior pelvis (Figs. 3D and 3E).

In the Young-Burgess classification system, anteroposterior compression fractures are those in which the disruptive force is in the sagittal plane. In practice, this is usually seen in blows to the front of the pelvis, commonly occurring in automobile accidents (Fig. 1). This gives rise to forces that tend to disrupt the anterior pelvis, either by fracturing the pubic rami or by rupturing the ligaments of the symphysis pubis (Type I) (Fig. 1A). Additional anteroposterior forces tend to cause splaying of the anterior pelvis, with external rotation of the iliac wings "hinging" at the posterior aspect of the sacroiliac joints (Type II). This corresponds to the open-book fracture of older classifications. Stability, however, depends on the various ligaments involved. Bucholz [41] provided pathologic proof of the various degrees of instability by observing pelvic ligamentous damage in cadavers after pelvic ring disruption. Tile [11] demonstrated that division of the symphysis pubis allows approximately 2.5 cm of diastasis of the symphysis. Additional division of the anterior sacroiliac, sacrospinous, and sacrotuberous ligaments allows further diastasis (Type II) (Figs. 1B–1D), but complete instability is not achieved until all of the sacroiliac ligaments are disrupted (Type III) (Fig. 1E).

The third major variety of pelvic ring disruption is the vertical shear fracture, usually resulting from a fall from a height onto the lower limbs (Fig. 4). This injury is most nearly represented by the Malgaigne fracture, with a vertically oriented fracture through the anterior and posterior pelvis together with superior displacement of the lateral "acetabulum-containing" fragment of the pelvis. In the series of Young and Burgess, every vertical shear fracture was markedly unstable owing to the significant posterior pelvic disruption [8, 12].

The final group of fractures is the complex or mixed fracture pattern, due to a combination of fracture forces. In the patients studied by Young and Burgess, these accounted for 23% of pelvic fractures and were predominantly a combination of anteroposterior and lateral compression giving rise to fracture patterns with features of both of these types of injuries. Of particular interest in this group is the pattern of disruption of the sacroiliac joint, with posterior and medial displacement of the major hemipelvic fracture fragment, the forces of injury being directed along the plane of the affected sacroiliac joint (Fig. 5).

In review of the literature, this classification system provides a logical basis for the observations made by other authors in their own classification systems. For example, Conolly and Hedberg [5] classified injuries as minor or major; the major fractures including fractures of the hemipelvis (Malgaigne), bilateral pubic ramal fractures, symphysis pubis separations, and fractures of the acetabulum. These can be appreciated as representing vertical shear fractures, and the more significant anteroposterior or lateral compression fractures respectively, of the Young-Burgess classification. As such, the fact that 28 of the 109 patients with major fractures in Conolly and Hedberg's series died of their injury is not surprising, because these are the most serious injuries of the Young-Burgess classification.

Acetabular fractures are often regarded as separate injuries, although they are frequently associated with pelvic ring injury. In view of Gertzbein and Chenoweth's demonstration that double injury to the pelvic ring is the rule [40], fractures of the acetabulum should encourage a search for additional

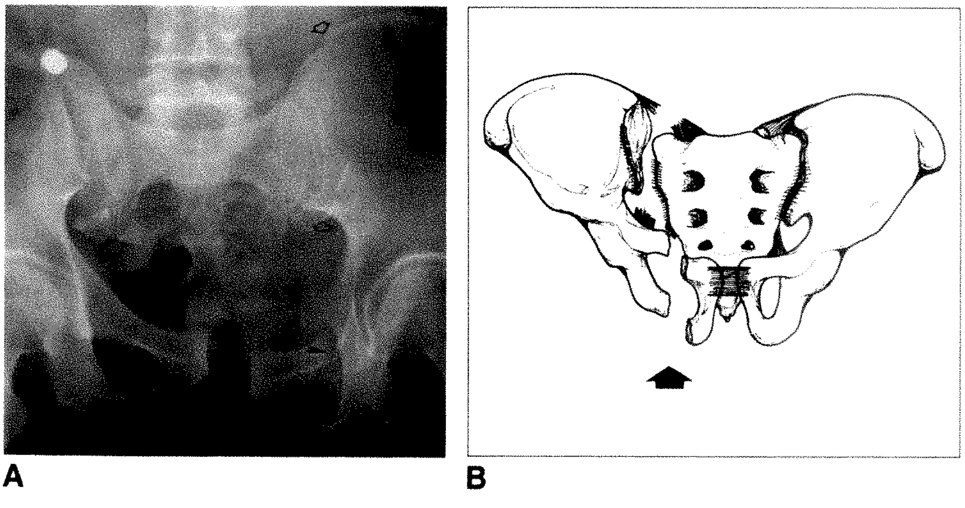

Fig. 4.—*A*, Radiograph of type of "double Malgaigne fracture," better classified as vertical shear fracture. Fracture dislocations are seen through both sacroiliac joints with significant superior displacement of major right hemipelvic fragment (*large open arrow*). Fracture on left extends through entire iliac bone (*small open arrows*). Left pubic ramal fractures are vertically oriented (*arrowheads*), and there is diastasis of symphysis pubis.

B, Diagram of unilateral vertical shear fracture. Force of injury (*arrow*) is from below, causing vertical fractures through pubic rami and sacroiliac joint with ligamentous disruption. Note superior displacement of left hemipelvic fragment. (Reprinted with permission from Young and Burgess [12].)

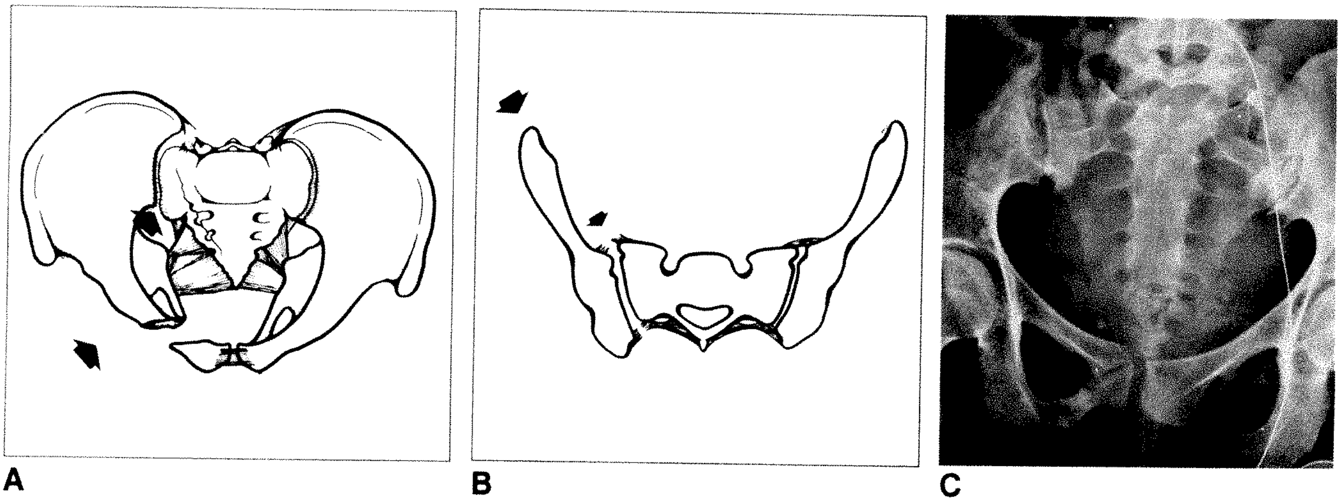

Fig. 5.—*A*, Diagram of complex fracture pattern: anterolateral compression fracture. Force of injury (*arrows*) is directed along plane of sacroiliac joint, with both anteroposterior and lateral compression. (Reprinted with permission from Young and Burgess [12].)

B, Fractured hemipelvis is driven along plane of injury, resulting in posterior and medial displacement. Arrow = direction of force of injury. (Reprinted with permission from Young and Burgess [12].)

C, Radiograph of complex fracture pattern. Horizontal fracture of symphysis argues for lateral compression. Diastasis of ipsilateral sacroiliac joint, however, indicates associated anteroposterior force vector.

pelvic injury. Lansinger [48] found acetabular fractures in approximately 20% of pelvic fractures.

The acetabulum can be conveniently divided into three major anatomic areas: the posterior column, the anterior column, and the quadrilateral plate. Fractures have been classified as occurring through each of these regions, either alone or in combination, and through the posterior rim of the acetabulum [9, 48–51]. Fractures of the posterior rim and posterior column are frequently seen in automobile accidents, most likely as a result of a posteriorly directed force on the flexed femur from dashboard impact. This is often associated with posterior dislocation of the femur. These are therefore frequently accompanied by anteroposterior compression fractures, and additional diastasis of the symphysis pubis or sacroiliac joints should be sought (Table 1). Fractures of the anterior column are seen as a result of direct blows onto the acetabulum, again often resulting from anterior compression forces [8, 10, 12] (Table 1).

Transverse fractures involving the quadrilateral plate frequently extend into the anterior or posterior column or both. Although they occur most commonly from a lateral compressive force and may be associated with central femoral head

TABLE 1: Features of Pelvic Fracture Patterns

Fracture Classification	Pubic Ramal Fractures	Acetabular Fractures	Sacral Fractures	Symphysis Pubis Diastasis	Sacroiliac Diastasis	Iliac Wing Fractures	Hemipelvic Displacement
Lateral Compression							
Type I	Horizontal	Medial wall ±central hip dislocation	Ipsilateral	No	No	Rare	No
Type II	Horizontal		Fractures of lateral sacrum	No	No	Oblique	Minimal: medial
Type III	Horizontal			No	Yes: anterior contralateral	Oblique or crush	Ipsilateral medial: contralateral lateral
Anteroposterior Compression							
Type I	Vertical	Anterior pillar ± posterior pillar	No	<2.5 cm	No	No	No
Type II	Vertical		No	>2.5 cm	Anterior	No	Lateral of anterior hemipelvis
Type III	Vertical		Rare: lateral sacral avulsion	Variable	Anterior and posterior	No	Lateral
Vertical shear	Vertical	±Roof	Vertical	Variable; vertical displacement	Variable; vertical displacement	Variable; vertical	Vertical

dislocation [49-52], they can be seen with any severe fracture extending between the anterior and posterior columns (Table 1). CT remains the method of choice for evaluating the acetabulum, with its superior detail of the fracture patterns and position of bone fragments.

That pelvic injury is regarded as the major cause of death indicates the importance of these fractures in multiple-trauma patients. The advent of external fixation has revolutionized the management of pelvic ring fractures and has allowed rapid pelvic stabilization with decrease in blood loss and significant improvement in morbidity and mortality [53]. A classification system based on the mechanism of injury and direction of injury force has allowed correct and timely application of external fixation, thus directly contributing to a more favorable outcome [53].

REFERENCES

1. Slatis P, Karaharju EO. External fixation of unstable pelvic fractures. *Clin Orthop* **1980**;171:73-80
2. Dunn AW, Morris MD. Fractures and dislocations of the pelvis. *J Bone Joint Surg [Am]* **1968**;50-A:1639-1648
3. Peltier LF. Complications associated with fractures of the pelvis. *J Bone Joint Surg [Am]* **1965**;47-A:1060-1069
4. Rothenberger DA, Fischer RP, Strare R, et al. The mortality associated with pelvic fractures. *Surgery* **1978**;84:356-361
5. Conolly WB, Hedberg EA. Observations on fractures of the pelvis. *J Trauma* **1969**;9:106-127
6. Monahan PRW, Taylor RG. Dislocation and fracture dislocation of the pelvis. *Injury* **1975**;6:325-333
7. Huittinen VM, Slatis P. Fractures of the pelvis: trauma mechanism, types of injury and principles of treatment. *Acta Chir Scand* **1972**;138:563-569
8. Young JWR, Burgess AR, Brumbach RJ, Poka A. Pelvic fractures: value of plain radiography in early assessment and management. *Radiology* **1986**;160:445-451
9. Judet R, Judet J, Letournel E. Fractures of the acetabulum: classification and surgical approaches for open reduction. *J Bone Joint Surg [Am]* **1964**;46-A:1615-1646
10. Pennal GF, Tile M, Waddell JP, Garside H. Pelvic disruption: assessment and classification. *Clin Orthop* **1980**;151:12-23
11. Tile M. *Fractures of the pelvis and acetabulum*. Baltimore: Williams & Wilkins, **1986**
12. Young JWR, Burgess AR. *Radiologic management of pelvic ring fractures*. Baltimore: Urban & Schwartzenberg, **1987**
13. Gilula LA, Murphy WA, Tailor CC, Patel RB. Computed tomography of the osseous pelvis. *Radiology* **1979**;132:107-114
14. Harley JD, Mack LA, Winquist RA. CT of acetabular fractures: comparison with conventional radiography. *AJR* **1982**;138:413-417
15. Patterson FP, Morton KS. The cause of death in fractures of the pelvis. *J Trauma* **1973**;13:849-856
16. Slatis P. Injuries in fatal traffic accidents. *Acta Chir Scand (Suppl)* **1962**; 297:1-15
17. Sevitt S. Fatal road accidents. Injuries, complications and causes of death in 250 subjects. *Br J Surg* **1968**;55:481-505
18. Braunstein PW, Skudder PA, McCarrol JR, Mussolina A, Wade PA. Concealed hemorrhage due to pelvic fracture. *J Trauma* **1964**;4:832-846
19. Reynolds BM, Balsano A, Reynolds FX. Pelvic fractures. *J Trauma* **1973**;13:1011-1020
20. Smith K, Ben-Menachem Y, Duke JH, Hill GL. The superior gluteal: an artery at risk in blunt pelvic trauma. *J Trauma* **1976**;16:273-279
21. Sheldon GF, Winestock DP. Hemorrhage from open pelvic fracture controlled intraoperatively with balloon catheter. *J Trauma* **1978**;18:68-70
22. Ayella RJ, DuPriest RW, Khaneja SC, et al. Transcatheter embolization: a technique for the control of arterial hemorrhage caused by pelvic trauma. *Surg Gynecol Obstet* **1978**;167:849-852
23. Paster SB, Van Houten FW, Adams DF. Percutaneous balloon catheterization: a technique for the control of arterial hemorrhage caused by pelvic trauma. *JAMA* **1976**;230:573-575
24. Matalon TSA, Athanasoulis CA, Margolies MW, et al. Hemorrhage with pelvic fractures: efficacy of transcatheter embolization. *AJR* **1979**;133: 859-864
25. Margolies MN, Ring EJ, Waltman AC, et al. Arteriography in the management of hemorrhage from pelvic fractures. *N Engl J Med* **1972**;287: 317-321
26. Goris RJA, Gimbere JSF, van Niekerk, et al. Improved survival of multiple injured patients by early external fixation and prophylactic mechanical ventilation. *Injury* **1982**;12:39-47
27. Harris JM, Harris WM. *The radiology of emergency medicine*. Baltimore: Williams & Wilkins, **1982**
28. Clark SS, Prudencio RF. Lower urinary tract injuries associated with pelvic fractures. *Surg Clin North Am* **1972**;52:183-189
29. Flaherty JS, Kelley R, Burnett B, et al. Relation of pelvic bone fracture patterns to injuries of the urethra and bladder. *J Urol* **1968**;99:297-305
30. Colapinto V. Trauma to the pelvis: urethral injury. *Clin Orthop* **1980**;151: 46-52
31. Berquist TM. *Diagnostic imaging of the acutely injured patient*. Baltimore: Urban & Schwartzenberg, **1985**
32. Pokorny M, Porkes JE, Pierce JM. Urological injuries associated with pelvic trauma. *J Urol* **1979**;121:455-461
33. Thaggard A, Mark TS, Carlson V. Fractures and dislocations of the bony pelvis and hip. *Semin Roentgenol* **1978**;13:117-126
34. Dalal SA, Siegel JH, Burgess AR, et al. Pelvic fractures in multiple trauma: classification by mechanism is key to pattern of organ injury, resuscitative requirements and outcome. *J Trauma* **1984**;29:981-1002
35. Trunkey DD, Chapman MW, Lim RC, et al. Management of pelvic fractures in blunt trauma injury. *J Trauma* **1974**;24:912-923
36. Rogers LF. *Radiology of skeletal trauma*. New York: Churchill Livingstone, **1982**
37. Edeiken-Monroe BS, Browner BD, Jackson H. The role of standard roentgenograms in the evaluation of instability of pelvic ring disruption. *Clin Orthop* **1989**;240:63-76
38. Holdsworth TW. Dislocation and fracture dislocation of the pelvis. *J Bone Joint Surg [Br]* **1972**;30-B:461-466
39. Kane WJ. Fractures of the pelvis. In: Rockwood CA, Green DD, eds. *Fractures in adults*, 2nd ed. Philadelphia: Lippincott, **1984**:1093-1209
40. Gertzbein SD, Chenoweth DR. Occult injuries of the pelvic ring. *Clin Orthop* **1977**;128:202-207
41. Bucholz RW. The pathological analog of Malgaigne fracture dislocations of the pelvis. *J Bone Joint Surg [Am]* **1981**;63-A:400-404
42. Looser KG, Crombie HD. Pelvic fractures: an anatomic guide to severity of injury. Review of 100 cases. *Am J Surg* **1976**;132:638-645
43. Sharp K. Plate fixation of disrupted symphysis pubis. *J Bone Joint Surg [Br]* **1973**;55-B:618-620
44. Mears DC, Freddie HF. Modern concepts of external fixation of the pelvis. *Clin Orthop* **1980**;151:65-73
45. Karaharju EO, Slatis P. External fixation of double vertical fractures with a trapezoid compression frame. *Injury* **1978**;10:142-143
46. Muller J, Bachman B, Berg M. Malgaigne fractures of the pelvis: treatment with percutaneous pin fixation. *J Bone Joint Surg [Am]* **1978**;60-A: 992-993
47. Wild JJ, Hanson GW, Tullos HS. Unstable fractures of the pelvis treated by external fixation. *J Bone Joint Surg [Am]* **1982**;64-A:1010-1020
48. Lansinger O. Fractures of the acetabulum: a clinical, radiological and experimental study. *Acta Orthop Scand* **1977**;165:1-11
49. Eichenholtz AN, Stark R. Central acetabular fractures. *J Bone Joint Surg [Am]* **1964**;46-A:695-714
50. Dunn AW, Russo CL. Central acetabular fractures. *J Trauma* **1973**;13: 695-705
51. Letournel E. Acetabulum fractures: classification and management. *Clin Orthop* **1980**;151:81-93
52. Young JWR, Burgess AR, Brumbach RJ, Poka A. Lateral compression fractures of the pelvis: the importance of plain radiographs in the diagnosis and surgical management. *Skeletal Radiol* **1986**;15:103-109
53. Burgess AR, Eastridge BJ, Young JWR, et al. Pelvic ring disruptions: effective classification system and treatment protocols. *J Trauma* **1990**; 30:1-9

Book Review

Imaging Principles of Cardiac Angiography. By Robert J. Moore. Rockville, MD: Aspen, 258 pp., 1990. $59

The author has addressed an imaging subject heretofore unavailable in the literature, namely, the imaging principles of cardiac angiography. Given the exacting requirements of this imaging task and the large number of physics investigations reported on cardiac imaging, it is surprising that a quality text has not been written before. *Imaging Principles of Cardiac Angiography* is pleasurable reading—for both information and content. The balance achieved in the text is extremely good. Chapter 1 devotes 25 pages to the basic concepts of image quality. Although nothing extra is included in the discussion, the uninitiated clinician will find the examples and presentation quite informative and logical. Users of cardiac imaging equipment will feel comfortable with concepts of image quality after reading this short discussion.

Chapters 2 and 3 address the formation of X-rays and their capture on film-screen and image-intensification tubes. The author is particularly good at the specification of instrumentation for measuring image quality. Extremely practical direction is given, and the author obviously is writing from a wealth of experience in performing numerous and varied radiologic measurements. The discussion on the cinefluorographic image chain is particularly helpful to the biomedical engineer or technical supervisor in a cardiac catheterization laboratory. The chapter on the fluoroscopic image chain includes a concise discussion of the rotatable spoke test-pattern examination for image quality. Particularly helpful is the specification of appropriate performance standards for image quality when these methods are used. These data are hard to find. Thus, the text is as much a handbook or instruction manual on testing and measurement of equipment for cardiac catheterization as it is a physics text.

Although the chapter on digital angiography is brief, its clinical application is evenhanded and practical. No serious discussion is made of digital imaging techniques, processing, and so forth. However, I think this chapter represents the clinical experience currently present in the world of cardiac catheterization, and therefore this brevity is not a limitation. The final chapter deals with radiation safety. It is brief, yet it contains quite useful information that is difficult to find on the specific radiation safety considerations of the cardiac catheterization laboratory. Recommendations are given for exposure of personnel who operate X-ray equipment, and this advice is well presented and practical.

In conclusion, I think this text is a long-overdue entry in the imaging physics library. Its readers will be residents in cardiac imaging, cardiac radiologists and cardiologists, biomedical engineers in the cardiac laboratory, and medical physicists who perform laboratory measurements. I highly recommend the purchase of this text by these individuals, and the author is to be congratulated for his contribution to diagnostic imaging.

William Pavlicek
Mayo Clinic
Rochester, MN 55905

Assessing the Patency of Mediastinal and Thoracic Inlet Veins: Value of MR Imaging

Margaret E. Hansen[1,2]
Charles E. Spritzer[1]
H. Dirk Sostman[1]

To assess the accuracy of MR imaging in the evaluation of patients with suspected thoracic venous obstruction, hospital records and MR studies of 31 such patients were reviewed. Gradient-recalled echo, spin-echo, or cine MR techniques were used. In 26 of the 31 patients, venous obstruction was confirmed by CT, venography, sonography, surgery, or autopsy. Causes included tumor invasion, compression of veins, coagulopathy, or indwelling catheters. MR detected an abnormality of the superior vena cava in all 16 cases in which it was seen on other tests. Abnormality of the internal or external jugular veins was detected in all six cases in which other studies were abnormal. Abnormality of veins in the shoulder region was detected by MR in 10 of 12 patients in whom such disease was seen on other tests. The two interpretive errors were caused by nonocclusive clot, short (<2-cm) occlusions, and metallic artifact. Overall, MR correctly identified abnormality in 32 of 34 vessels (sensitivity, 94%). In all cases, a negative MR study was found to be a true negative (no false positives in 42 normal vessels; specificity, 100%).

We conclude that MR is an accurate means of assessing patency of the thoracic inlet and mediastinal veins. Its noninvasive nature and multiplanar capability contribute to its usefulness in this clinical setting.

***AJR* 155:1177-1182, December 1990**

Compromise of mediastinal and thoracic inlet veins occurs frequently in a variety of benign and malignant conditions, such as inflammation, fibrosis, and neoplasm. Indwelling vascular devices also contribute to this problem by serving as foci for thrombosis. Although CT and venography have been the preferred techniques for evaluation of the mediastinal and thoracic inlet veins [1-4], several reports [5-7] have described the use of MR imaging in this setting. However, these studies were relatively early evaluations and used only spin-echo (SE) techniques.

We describe 31 patients with suspected obstruction of the superior vena cava or thoracic inlet veins who were studied with MR at 1.5 T, including gradient-recalled echo (GRE) techniques in 30 cases. Potential advantages and limitations of MR imaging in this setting are discussed, and optimal pulse sequences and imaging planes for different anatomic regions are considered.

Materials and Methods

Fifty-one patients with clinical and/or radiologic evidence of thoracic venous abnormality had MR imaging between December 1986 and October 1989. All patients were studied for clinical purposes rather than for research interest. In some cases, MR was requested because allergy to contrast material or lack of venous access precluded other studies. Patients were excluded from the study if hospital charts or radiologic studies were not available for review (two cases) or there was no confirmation of the MR results by other imaging studies or by operative or pathologic correlation (18 cases). A total of 31 patients met the necessary conditions for analysis.

Received April 12, 1990; accepted after revision July 10, 1990.

[1] Department of Radiology, Box 3808, Duke University Medical Center, Durham, NC 27710. Address reprint requests to C. E. Spritzer.

[2] Present address: Department of Radiology, Angiography Section, Massachusetts General Hospital, Boston, MA 02114.

0361-803X/90/1556-1177
© American Roentgen Ray Society

The patients were 4 months to 76 years old (mean, 45 years); there were 18 females and 13 males. Primary diagnoses included malignancy (22), hypercoagulable state (three), benign disease requiring indwelling central venous catheter (two), IV drug abuse (two), and trauma (one). In one case, no underlying condition was identified. Venous obstruction or thrombosis was due to complications of treatment (indwelling catheters or chemotherapy) or of underlying disease (hypercoagulability, invasion of veins by tumor, or drug abuse) in 15 patients. In 11, venous stasis and subsequent thrombosis were caused by compression by an extrinsic tumor.

All MR examinations were performed on a superconducting imager operating at 1.5 T (Signa, General Electric, Milwaukee, WI). All patients were imaged in the supine position with arms at their sides. Thirty-five studies were performed in the 31 patients.

Multislice SE imaging was used in 28 studies, with T1-weighted images, 500–600/20,25 (TR/TE), or T2-weighted sequences, 2000–2500/60–80. When cardiac gating was used (18 studies), TR was determined by heart rate. Two echoes were obtained in gated studies, typically at 20 and 60 msec. Only spatial presaturation was used routinely on SE studies; no motion compensation was employed. For axial scans, saturation pulses were applied in superior and inferior axes; for sagittal scans, saturation pulses were applied in the right-left axis as well as in the superior-inferior directions. Slice thickness ranged from 4 to 10 mm, with an interslice gap of 0–10 mm; a slice thickness of 7 mm with gap of 3 mm was used most commonly. Two excitations were performed in most cases, with a range of 1–4.

GRE techniques were used in 30 cases. GRASS (gradient-recalled acquisition in the steady state) is the acronym for the GRE technique most widely used on General Electric scanners; details of this technique have been reported [8]. GRASS imaging parameters were 22–41/12–17/30–80° (TR/TE/flip angle) with a slice thickness of 5–10 mm and interslice gap of 0–10 mm. In most cases, there were two excitations (range, 1–4). Images were obtained singly during suspended respiration. Cine GRASS images, 21–35/13/30–45°, were used in 14 cases to obtain 10-mm-thick contiguous sections. Three slices were obtained in each cine acquisition; from one to three acquisitions were done in each case.

GRE phase-reconstructed images were obtained in five cases. Two GRE images were acquired with complete and partial flow compensation and subtracted to provide the phase data. This technique (velocity imaging with gradient recalled echoes, VIGRE) has been described elsewhere [9].

For each MR examination, the exact parameters used were chosen by the attending radiologist involved in the case. Prior experience with lower extremity deep venous thrombosis [10], indicating increased sensitivity to slow flow with greater flip angles, thinner sections, and longer TR, influenced selection of these parameters in the more current cases. Image data were acquired by using a 256 × 128 matrix, interpolated to a 512 × 512 matrix for display.

Thirty-four MR scans were obtained in 30 patients for suspected abnormality of the superior vena cava. Axial images were obtained in 34 (SE in 30, GRE in 24); coronal scans were obtained in 14 (SE in nine, GRE in 10); and sagittal scans were obtained in 11 (SE in six, GRE in seven).

Fifteen MR scans in 14 patients were obtained for suspected neck vein abnormality. Axial scans were obtained in all 14 (SE in 14, GRE in 10), coronal scans were obtained in two (SE in one, GRE in one), and sagittal scans were obtained in four (SE in three, GRE in one).

Twenty-five MR scans were obtained in 22 patients with suspected venous abnormality in the shoulder region. Axial scans were obtained in 22 cases (SE in 21, GRE in 17), coronal in six (SE in four, GRE in five), and sagittal in 11 (SE in six, GRE in nine).

MR scans were reviewed by one interpreter and assigned values of positive, negative, or equivocal for the presence of venous obstruction or thrombosis. Scans were also interpreted as positive or negative for the presence of collateral venous channels. Efficacy of the different techniques and imaging planes in making these findings was assessed as well. Cases were reviewed without knowledge of prospective interpretations or the results of other tests. In all cases, axial images were evaluated first, followed by coronal and sagittal images. Within each plane, SE images were interpreted first, followed by GRE scans.

These results were correlated with those of other imaging studies and with surgical or autopsy findings obtained within 14 days of the MR scan and without pertinent intervening therapy. Confirmation was provided by CT alone (13 cases); CT and venography (five cases); CT and surgery (three cases); CT and sonography (two cases); CT, surgery, and venography (one case); venography alone (eight cases); surgery alone (two cases); and autopsy (one case). All CT scans were obtained on a General Electric 9800 scanner using a 512 × 512 matrix. Contiguous slices 10 mm thick were obtained in most cases, with a pixel size of 0.7 mm or less (depending on field size and target factor). CT contrast material was administered by bolus IV injection followed by drip infusion via the antecubital vein. In cases of suspected thoracic inlet venous abnormality, injection was into the ipsilateral side if venous access was available and the contralateral side if not.

The sensitivity and specificity of MR imaging relative to these reference methods were determined for each of three anatomic regions including (1) chest (superior vena cava), (2) neck (both internal and external jugular veins), and (3) shoulder area (axillary, subclavian, and brachiocephalic veins), as well as for the entire group.

Results

Thirty-four scans in 30 patients were obtained for suspected abnormality of the superior vena cava. Sixteen scans were interpreted as abnormal and 18 as normal. Confirmatory studies agreed with the MR interpretation in all cases, giving a sensitivity of 100%. As there were no false positives, specificity was also 100%.

The neck veins (internal and external jugular) were evaluated on 15 scans in 14 patients. Six scans were interpreted as abnormal and nine as normal. MR interpretations were corroborated by other studies in all cases. Sensitivity and specificity were 100%.

Twenty-five scans obtained in 22 patients assessed suspected venous disease in the shoulder area. Ten scans were interpreted as positive and 15 as negative. MR scans in two patients with proved venous thrombosis were interpreted as negative. In the first case, a short (<2-cm) occlusion of the left brachiocephalic vein was not identified owing to partial-volume effects. Venography demonstrated the focal occlusion and collateral vessels (Fig. 1). The second patient had nonocclusive clot in the left subclavian vein on venography; MR showed the vessel to be patent but with slow flow. Difficulty in this case was compounded by an artifact from a subcutaneous chemotherapy catheter in the area of interest (Fig. 2). Although specificity in this group was 100% (no false positives), sensitivity was only 83% (10/12 positives detected).

For all groups considered together, MR detected venous abnormality in 32 of the 34 vessels in which disease was shown on other tests, yielding a sensitivity of 94%. None of the 42 vessels shown to be normal on another study was termed abnormal on MR, yielding a specificity of 100%.

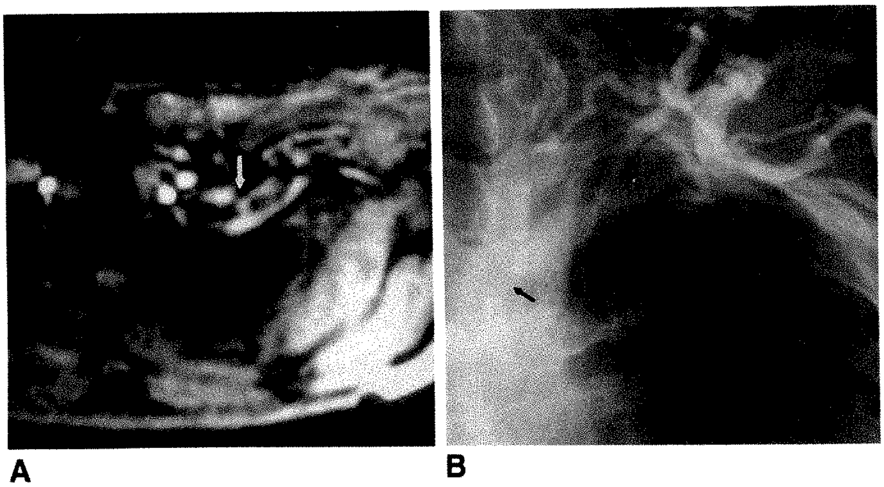

Fig. 1.—*A*, Axial GRASS MR image (33/16/45°) shows poor delineation of brachiocephalic vein medially (*arrow*). Subclavian vein was well seen laterally on higher sections.

B, Venogram shows focal occlusion of brachiocephalic vein (*arrow*) due to thrombus.

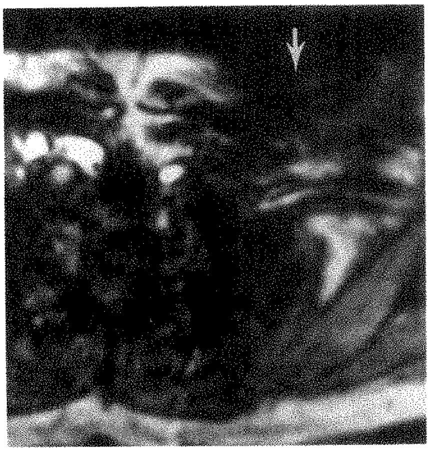

Fig. 2.—Axial GRASS MR image (33/16/60°) shows large artifact (*arrow*) from metallic hub of subcutaneous chemotherapy catheter; veins are not well seen. Venography showed nonocclusive clot in subclavian vein.

Axial images provided the correct diagnosis in all cases involving the superior vena cava or neck veins. Additional sagittal or coronal images did not increase the diagnostic accuracy or confidence in interpretation beyond that afforded by the axial images alone. However, diagnostic accuracy and confidence for the shoulder region veins was increased by the addition of sagittal images. Axial images were diagnostic in this region in only 15 of 22 cases. In five cases, the axial images were equivocal but the sagittal images provided the correct diagnosis. Two studies were interpreted incorrectly (false negative) on the basis of axial images. In one, no sagittal scans were obtained; in the second case, sagittal images were equivocal.

Early in our experience, it was decided that coronal images were of limited usefulness in the shoulder region owing to partial-volume averaging caused by the anterior and lateral curvature of these veins. While the coronal images contained diagnostic information in four of six cases, in no case were they the only diagnostic sequence. In the other two cases they were not diagnostic. In one case, the coronal scans showed no evidence of subclavian vein abnormality, but thrombus was clearly seen on sagittal images. In the last case, the coronal images were equivocal but axial scans proved diagnostic.

Collateral venous channels were identified by MR in 13 cases. In eight cases, they were seen only on GRE images; in five they were visible on both GRE and SE scans. In all 13, collaterals were shown by other means as well. In one case, collaterals were seen on venography but not detected on MR imaging. In the remaining 12 patients with venous abnormality, no collaterals were detected on any imaging study, including MR.

In five of 26 cases in which both SE and GRE scans were obtained, the SE images were equivocal but GRE images were diagnostic. In 20 cases, both sequences provided diagnostic information. Both were equivocal in the remaining case.

Phase images were obtained in five cases. In two cases they provided unique information regarding collaterals and direction of venous flow as well as the clearest depiction of venous disease; SE or GRE images were equivocal in these two cases. In the remaining three patients, no additional information or diagnostic confidence was provided.

Although this study is based on a retrospective review of MR cases, these interpretations were later compared with the prospective readings. For only one of the 35 scans was there a difference between the retrospective and prospective interpretations. In this case, thrombosis of the subclavian vein was considered on retrospective review, while no abnormality was diagnosed prospectively. Venography confirmed the presence of clot.

Discussion

As MR imaging becomes more widely available and techniques become more sophisticated, potential advantages over more invasive studies are apparent. Because no contrast agent is needed to image flowing blood, MR can be performed safely in patients with allergies to iodinated contrast media or in those for whom such media are contraindicated medically. In addition, MR imaging is particularly useful when no venous access can be obtained for enhanced studies.

Contrast-enhanced CT and contrast venography have traditionally been the mainstays in the diagnosis of thoracic and mediastinal venous obstruction [1–4]. However, both contrast-enhanced CT and venography are potentially subject to artifacts related to contrast administration [11]. MR imaging is not subject to such mixing artifacts because the inherent contrast between flowing blood and surrounding soft tissue is excellent on both SE and GRE images. Contrast between clotted and nonclotted blood is generally high as well [12, 13]. Inadequate venous access or allergic contrast reactions can also present problems in CT and venography. Three

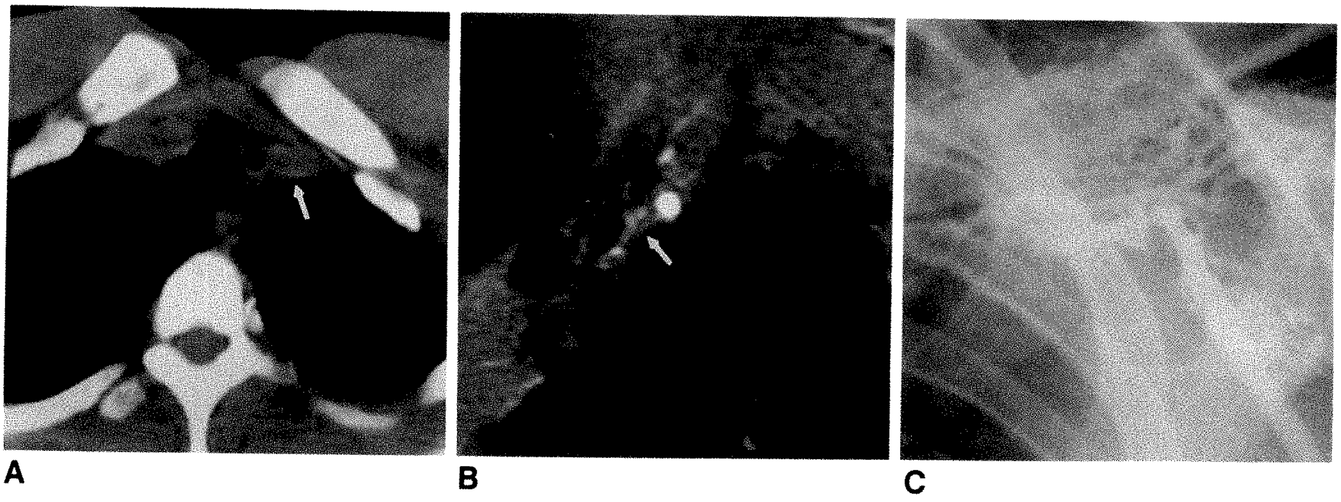

Fig. 3.—*A*, Unenhanced CT scan in patient with allergy to contrast medium shows enlargement of left brachiocephalic vein (*arrow*), but no definite clot.
B, Sagittal GRASS MR image (33/16/45°) through same region shows no flow in subclavian vein (*arrow*).
C, Venogram (after steroid treatment) confirms findings.

patients in our series had MR imaging because of these problems (Fig. 3). In all three, MR clearly depicted the vessels, and results were later confirmed (sonography in one, venography after steroid treatment in two).

The accuracy of MR imaging of the thoracic inlet and mediastinal veins was quite high in our retrospective review. It is of note that agreement between retrospective and prospective interpretations was excellent, with only one discrepancy in 35 scans. As the prospective interpretations were done by a larger number of individuals with various levels of experience in MR imaging, this suggests that interobserver consistency is easily achieved. In addition, the prospective accuracy of MR imaging in this clinical setting appears high.

One of the greatest advantages of MR imaging is its multiplanar capability. This is particularly useful in assessing thoracic inlet and mediastinal veins, which may be difficult to image entirely in a single plane. We found the axial plane to be excellent for evaluation of the superior vena cava and jugular veins, which are nearly perpendicular to the transverse plane throughout their course. However, the axillary, subclavian, and brachiocephalic veins normally curve slightly in both coronal and axial dimensions and are more difficult to image completely in these planes. In our series, accuracy of MR imaging in this region was significantly affected by imaging plane. In general, delineation of these veins was better on sagittal images than in the axial plane. However, the axial images were interpreted more easily in one case. As a result of this experience, we have found the combination of axial and sagittal planes most useful in evaluating these vessels. Other investigators have found coronal images helpful [6]. If imaging can be done in only one plane owing to time constraints or lack of patient cooperation, we now choose the sagittal plane for the shoulder area (Fig. 4).

GRE sequences offer advantages of speed, lack of respiratory motion, and high accuracy in the detection of venous thrombosis. In our series, GRE scans were the best sequence for suspected venous disease, although SE images often were necessary for confirmation. Experience with GRE imaging of lower extremity deep venous thrombosis has yielded similar results [10], though other authors prefer SE imaging in this setting [14]. A recent report [15] describing phase imaging of arterial and venous disease indicates that this method increases the level of confidence in detecting thrombi in both arteries and veins. Our own experience, although limited, would support such a position.

A potential advantage of MR imaging lies in the detection of collateral vessels. Although the extent of collaterals is probably not assessed better with MR than with CT if only SE techniques are used [6], collaterals are often quite striking on GRE images. In addition, direction of flow can be determined by using phase-reconstructed MR images (Fig. 5). Direction of flow in collaterals such as the azygos system may influence treatment and outcome [16] and cannot be determined reliably on CT. MR imaging may be able to identify patients at risk for development of serious sequelae, much as venography now does, though more work is needed to determine whether the same classification system would be useful [17].

MR imaging may provide additional information not available with other techniques. Most promising is its ability to differentiate tumor from fibrous tissue owing to their different T1 and T2 relaxation times [18, 19]. Other useful information more easily obtained with MR includes assessment of other vessels (e.g., thoracic aorta, central pulmonary vessels, and carotid arteries) and the heart, particularly on cine sequences [20, 21]. In four of our cases, compromise of pulmonary vessels or involvement of cardiac chambers was appreciated on GRASS or cine images. In another case, narrowing of the common carotid artery was seen on GRASS and SE images but not appreciated on CT or sonography.

General limitations of MR imaging are well known. Potential sources of misinterpretation in MR vascular imaging include nonocclusive clot, focal occlusions, slow flow, and metallic foreign bodies. The two interpretive errors in our series were

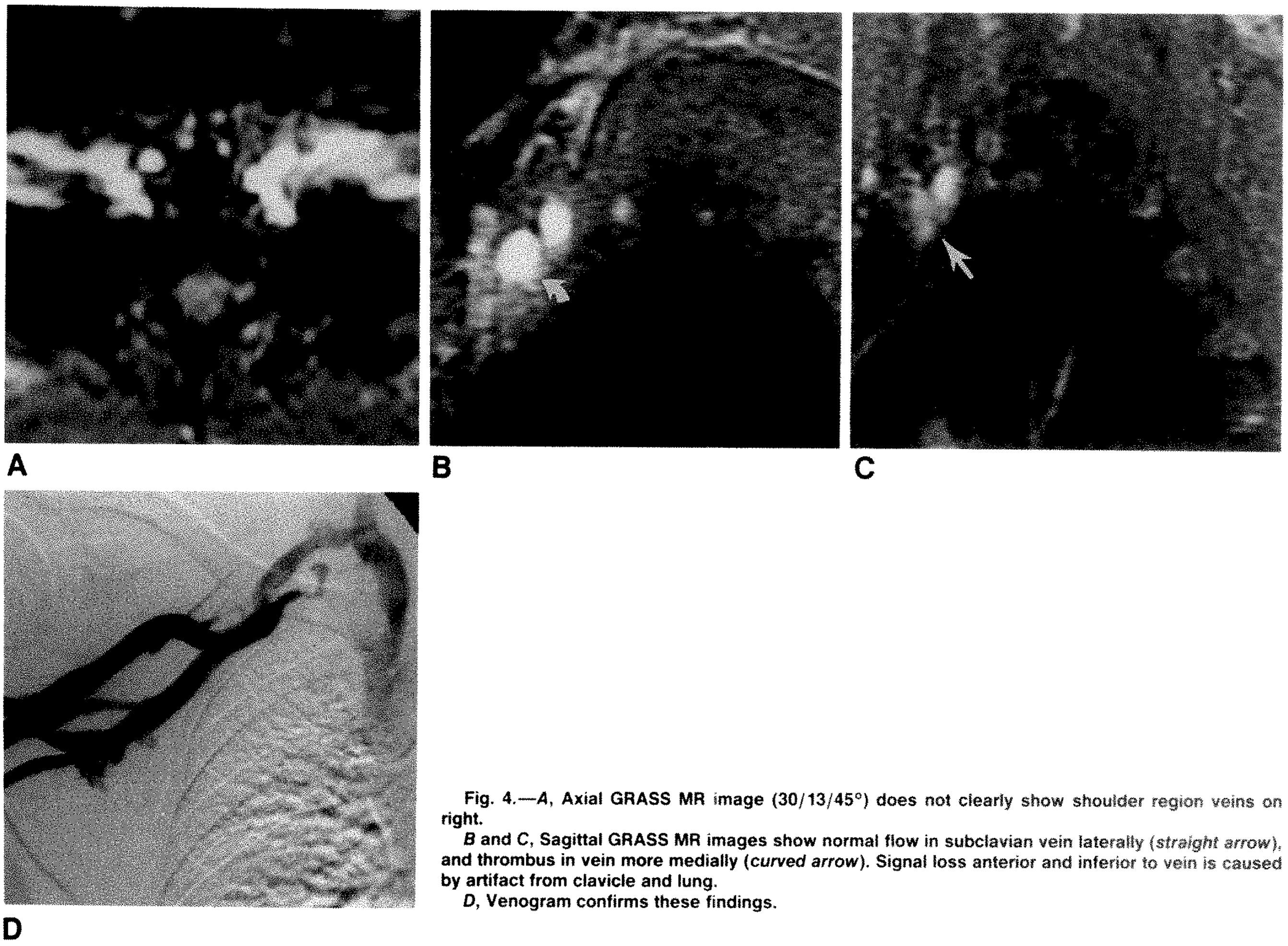

Fig. 4.—*A*, Axial GRASS MR image (30/13/45°) does not clearly show shoulder region veins on right.

B and *C*, Sagittal GRASS MR images show normal flow in subclavian vein laterally (*straight arrow*), and thrombus in vein more medially (*curved arrow*). Signal loss anterior and inferior to vein is caused by artifact from clavicle and lung.

D, Venogram confirms these findings.

due to nonocclusive clot and a metal artifact in one case and a focal (<2 cm in length) thrombus and slow flow in the second case.

Nonocclusive clot may be difficult to detect, as antegrade flow remains present in the affected vessel. Flow is generally slowed, but this may be the only detectable abnormality if the thrombus itself is small, as seen in one of our cases.

Very short occlusions are problematic for any sectional imaging technique owing to partial-volume artifacts. This problem can be reduced, but not eliminated, by decreasing slice thickness and interslice gap.

Another potential problem in GRE imaging is high-signal thrombus [6, 12], which may have less contrast with adjacent flowing blood. The signal, while higher than that of more solid clot, is often less than that of flowing blood, allowing correct identification. Questionable cases can be resolved readily with phase or SE images.

Flow artifacts on MR images have been well described [19, 22]. Slow flow mimicking clot is probably the most common potential pitfall, but other artifacts are also important. Use of spatial presaturation, gradient moment nulling (flow compensation), cardiac gating, and asymmetric first and second echoes can greatly reduce these problems [23–26]. The most common flow artifacts on SE images create specious intraluminal signal mimicking clot, while those on GRE images may obscure intraluminal clot that is truly present. Accordingly, SE and GRE sequences are complementary and the use of both should reduce diagnostic confusion due to flow artifacts. Phase images are perhaps the best way to confirm the presence or absence of flow in difficult cases [9, 15, 26].

Magnetic field inhomogeneity (susceptibility) caused by metal is a well-known problem in MR imaging. GRE methods, while highly sensitive to flow, are also more sensitive to susceptibility artifact. This is a problem in patients with surgical clips or metallic catheter components in the area of interest, as seen in one of our cases (Fig. 2). SE images are less sensitive to susceptibility effects, and may complement GRE images in such cases. In addition, changing the image plane may be useful in minimizing such artifacts.

Cardiac gating is necessary for cine studies, and improves image quality on SE studies as well. In patients with cardiac arrhythmias, however, image quality can be significantly degraded. In such cases, nongated SE and single breath-hold GRE images may be useful.

In this series, MR imaging accurately detected the presence or absence of thoracic venous disease in a representative clinical population. Larger experience in a prospective study is needed to further define the applicability of MR in this setting, as well as to refine and standardize optimal imaging strategies.

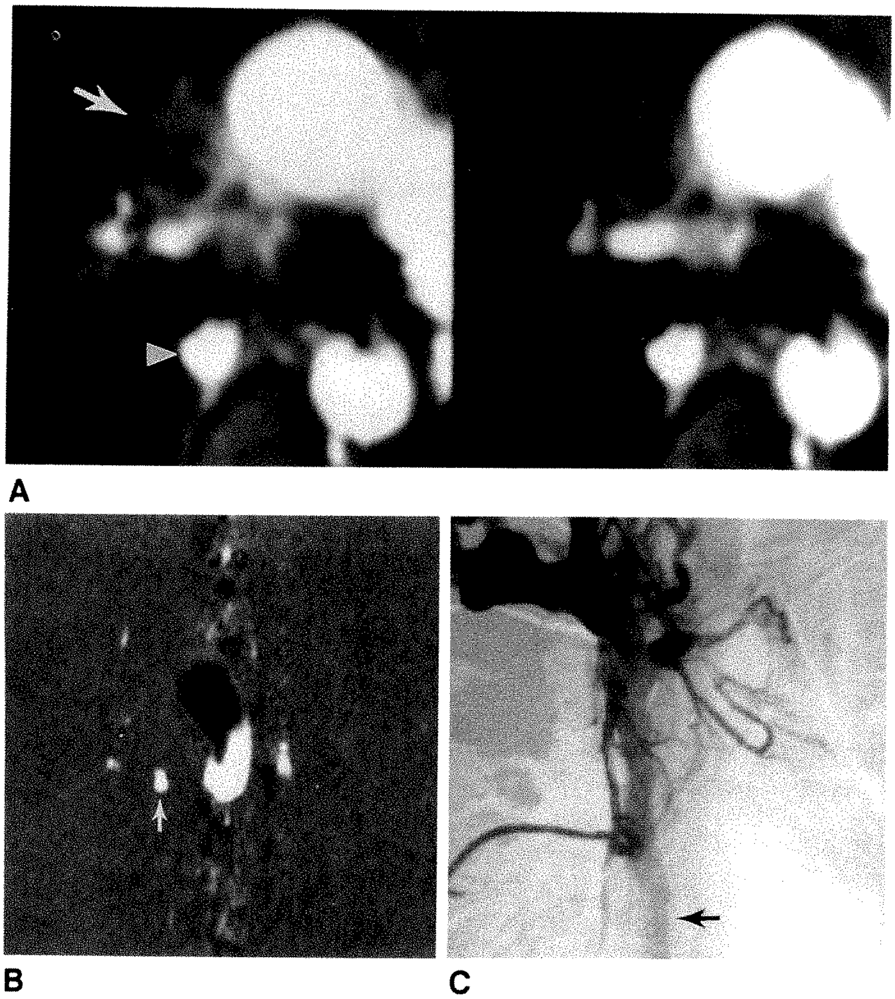

Fig. 5.—*A*, Axial cine GRASS MR image (33/13/60°) shows lack of flow in superior vena cava (*arrow*) and enlargement of azygos vein (*arrowhead*).

B, Axial phase MR image (100/13/45°) confirms caval occlusion and shows reversal of flow in azygos vein (*arrow*).

C, Venogram corroborates caval occlusion and reversed azygos flow (*arrow*).

REFERENCES

1. Moncada R, Cardella R, Demos TC, et al. Evaluation of superior vena cava syndrome by axial CT and CT phlebography. *AJR* **1984**;143:731-736
2. Benenati JF, Becker GJ, Mail JT, Holden RW. Digital subtraction venography in central venous obstruction. *AJR* **1986**;147:685-688
3. Yedlicka JW, Cormier MG, Gray R, Moncada R. Computed tomography of superior vena cava obstruction. *J Thorac Imaging* **1987**;2(1):72-78
4. Albertyn LE, Alcock MK. Diagnosis of internal jugular vein thrombosis. *Radiology* **1987**;162:505-508
5. Weinreb JC, Mootz A, Cohen JM. MRI evaluation of mediastinal and thoracic inlet venous obstruction. *AJR* **1986**;146:679-684
6. McMurdo KK, de Geer G, Webb WR, Gamsu G. Normal and occluded mediastinal veins: MR imaging. *Radiology* **1986**;159:33-38
7. Braun IF, Hoffman JC, Malko JA, Pettigrew RI, Dannels W, Davis PC. Jugular venous thrombosis: MR imaging. *Radiology* **1985**;157:357-360
8. Gullberg GT, Wehrli FW, Shimakawa A, Simons MA. MR vascular imaging with a fast gradient refocusing pulse sequence and reformatted images from transaxial sections. *Radiology* **1987**;165:241-246
9. Spritzer CE, Pelc NJ, Lee JN, Evans AJ, Sostman HD, Riederer SJ. Rapid MR imaging of blood flow with a phase-sensitive, limited-flip-angle, gradient recalled pulse sequence: preliminary experience. *Radiology* **1990**;176:255-262
10. Spritzer CE, Sussman SK, Blinder RA, Saeed M, Herfkens RJ. Deep venous thrombosis evaluation with limited-flip-angle, gradient-refucosed MR imaging: preliminary experience. *Radiology* **1988**;166:371-375
11. Godwin JD, Webb WR. Contrast-related flow phenomena mimicking pathology on thoracic computed tomography. *J Comput Assist Tomogr* **1982**;6:460-464
12. Rapoport S, Sostman HD, Pope C, Camputaro CM, Holcomb W, Gore JC. Venous clots: evaluation with MR imaging. *Radiology* **1987**;162:527-530
13. Erdman WA, Weinreb JC, Cohen JM, Buja LM, Chaney C, Peshock RM. Venous thrombosis: clinical and experimental MR imaging. *Radiology* **1986**;161:233-238
14. Erdman WA, Jayson HT, Redman HC, Miller GL, Parkey RW, Peshock RW. Deep venous thrombosis of extremities: role of MR imaging in the diagnosis. *Radiology* **1990**;174:425-431
15. Tavares NJ, Auffermann W, Brown JJ, Gilbert TJ, Sommerhoff C, Higgins CB. Detection of thrombus by using phase-image MR scans: ROC curve analysis. *AJR* **1989**;153:173-178
16. Stanford W, Doty DB. The role of venography and surgery in the management of patients with superior vena cava obstruction. *Ann Thorac Surg* **1986**;41:158-163
17. Stanford W, Jolles H, Ell S, Chiu LC. Superior vena cava obstruction: a venographic classification. *AJR* **1987**;148:259-262
18. Glazer HS, Lee JKT, Levitt RG, et al. Radiation fibrosis: differentiation from recurrent tumor by MR imaging. *Radiology* **1985**;156:721-726
19. Ebner F, Kressel HY, Mintz MC, et al. Tumor recurrence versus fibrosis in the female pelvis: differentiation with MR imaging at 1.5 T. *Radiology* **1988**;166:333-340
20. Spritzer C, Gamsu G, Sostman HD. Magnetic resonance imaging of the thorax: techniques, current applications, and future directions. *J Thorac Imaging* **1989**;4(2):1-18
21. Spritzer CE, Blinder RA. Vascular applications of magnetic resonance imaging. *Magn Reson Q* **1989**;5:205-227
22. Bradley WG, Waluch V. Blood flow: magnetic resonance imaging. *Radiology* **1985**;154:443-450
23. Felmlee JP, Ehman RL. Spatial presaturation: a method for suppressing flow artifacts and improving depiction of vascular anatomy in MR imaging. *Radiology* **1987**;164:559-564
24. Dumoulin CL, Hart HR. Magnetic resonance angiography. *Radiology* **1986**;161:717-720
25. Lenz GW, Haacke EM, Masaryk TJ, Laub G. In-plane vascular imaging: pulse sequence design and strategy. *Radiology* **1988**;166:875-882
26. White EM, Edelman RR, Wedeen VJ, Brady TJ. Intravascular signal in MR imaging: use of phase display for differentiation of blood-flow signal from intraluminal disease. *Radiology* **1986**;161:245-249

Case Report

Misdiagnosis or Missed Diagnosis? Thoracic Actinomycosis and Carcinoma on Sequential CT-Guided Lung Biopsies

Shane E. Macaulay,[1,2] Eric vanSonnenberg,[1,3] Giovanna Casola,[1] and James H. Harrell II[3]

Percutaneous thoracic biopsy under fluoroscopic or CT guidance is a well-established method of diagnosing the cause of a lung nodule [1–4]. Cytologic or histologic demonstration of malignant cells is definitive. However, establishing the diagnosis of a benign lesion is more difficult. Finding inflammatory cells is not specific enough for a firm diagnosis of benignity, nor is it sufficient for excluding malignancy. The consensus is that a specific organism must be demonstrated or grown to be certain of a benign diagnosis [5]. Importantly, making a specific benign diagnosis usually is considered sufficient to exclude malignancy.

This report describes a particularly bothersome pitfall of thoracic biopsy. A specific benign diagnosis was established, presumably excluding malignancy. However, follow-up studies showed growth of the lesion, leading to a second biopsy at which malignancy was proved.

Case Report

During hospitalization for a myocardial infarction, a 72-year-old woman was noted to have a new 1.2 × 1.0 cm solitary nodule in the right upper lobe on a chest radiograph. No other lesion or mediastinal adenopathy was noted. No further workup was initiated, as the patient elected to have the lesion monitored radiologically. Seven months later, a follow-up chest radiograph showed the nodule had increased to 1.5 × 1.5 cm (Fig. 1A). Transbronchoscopic biopsy was nondiagnostic. Three weeks later the patient was referred to our hospital for CT-guided fine-needle biopsy of the lesion. The patient had chronic cough, but no fever, chills, diaphoresis, hoarseness, hemoptysis, anorexia, or weight loss. She had a 50-pack-per-year history of smoking. There was no occupational exposure and no history of tuberculosis.

CT-guided lung biopsy (Fig. 1B) results were negative for malignancy. *Actinomyces naeslundii* was cultured 9 days after biopsy. Oral penicillin was administered, and the patient was followed up by her referring physician. The nodule appeared enlarged on 3-week and 5-month follow-up chest radiographs (Fig. 1C). She remained asymptomatic except for the chronic cough. The nodule increased in size, and a second CT-guided biopsy revealed poorly differentiated epidermoid carcinoma (Fig. 1D). The patient declined surgery and chose to undergo radiation therapy. She received a total of 6500 rad (65 Gy). Postirradiation fibrosis obscured the lesion and prevented subsequent radiologic observation. In the year after completion of radiotherapy, her condition did not worsen.

Discussion

Our case illustrates a rare pitfall of radiologically guided biopsy of lung lesions. Although a definite benign diagnosis is considered acceptable to exclude malignancy, it was misleading in our patient. The original diagnosis of actinomycosis was firm enough to begin appropriate antibiotic therapy, to guide follow-up, and to inform the patient that malignancy

---

Received March 16, 1990; accepted after revision May 7, 1990.

[1] Department of Radiology, University of California, San Diego, Medical Center, 225 Dickinson St., San Diego, CA 92103. Address reprint requests to E. vanSonnenberg.

[2] Present address: Department of Radiology, University of Washington, Seattle, Medical Center, Seattle, WA 98195.

[3] Department of Medicine, University of California, San Diego, Medical Center, San Diego, CA 92103.

AJR 155:1183–1184, December 1990 0361–803X/90/1556–1183 © American Roentgen Ray Society

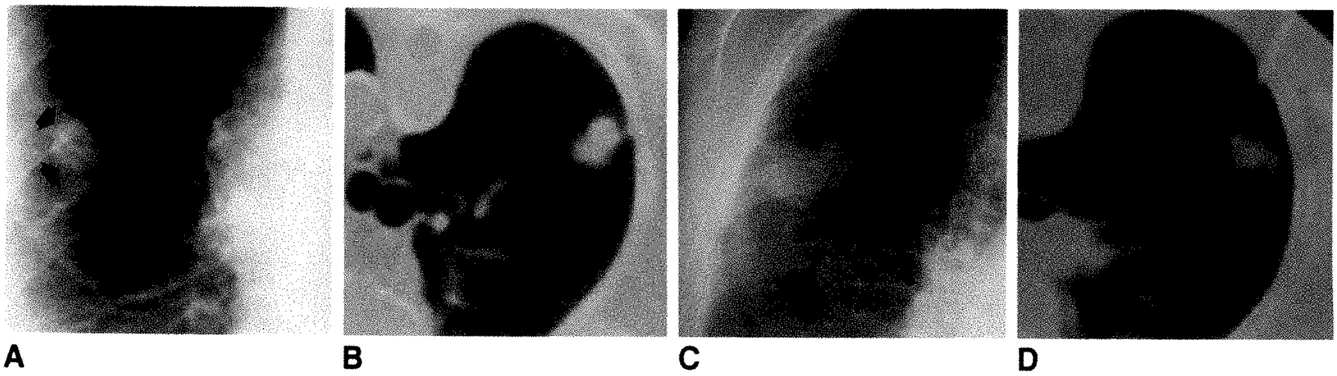

Fig. 1.—*A*, Chest film shows 1.5 × 1.5 cm nodule (*arrows*) in right upper lobe of lung.
B, Diagnosis on CT-guided biopsy of prone patient was *Actinomyces naeslundii*.
C, Follow-up chest radiograph obtained 5 months after *B* shows nodule has enlarged despite penicillin therapy.
D, Second CT-guided biopsy of prone patient yielded malignant cells; second biopsy site was more caudal than initial biopsy site.

was excluded. *Actinomyces* and malignancy probably coexisted; a sampling error probably resulted in the initial missed diagnosis of carcinoma. Although sequential development of actinomycosis and then carcinoma is possible, it is less likely. Another possibility is that *Actinomyces naeslundii* was a contaminant; however, this organism has not been recorded before as a contaminant of lung biopsy in our hospitals.

Reports of coexistent tumor and a benign lesion are rare [2, 6, 7]. One report of actinomycosis and lymphoma has been published [6]. Ballard and Boyd [1] describe a series of 102 patients who underwent thoracic biopsy; on a second biopsy, six patients were found to have malignancy after the first biopsy had established a benign diagnosis. However, the specific benign diagnoses are not mentioned.

Although tuberculosis or coccidioidomycosis may be concurrent with cancer, it is far more common to have pulmonary fungal or bacterial infections alone that mimic cancer, both clinically and radiologically [2]. Histoplasmosis, coccidioidomycosis, and tuberculosis are examples [2]. Radiologically, this mimicry is manifested as solitary pulmonary nodules, cavitating lesions, or large perihilar masses [2, 3].

Actinomyces infection is a well-known mimic of malignancy clinically, radiologically, and pathologically [7–9]. Actinomycotic pulmonary nodules or hilar lesions may resemble neoplasms. Actinomycosis associated with malignancy may be found in drainage from an infected tumor site [1].

Just as benign lesions may resemble malignant ones, neoplasms may at first appear to be benign lesions. Clinical or radiologic signs may suggest tuberculosis, manifested by apical lesions on chest films, along with cough, hemoptysis, fever, and weight loss. Rarely, even with tumor, biopsy may suggest only a nonspecific granulomatous inflammation [4].

When concurrent benign and malignant processes exist, it is possible to sample just the infectious organism and miss the malignant tumor altogether. In such cases, discovery of the causative organism in the biopsy sample (either by direct stain or by culture) may mask a potentially treatable malignant tumor. The diagnosis of actinomycosis in our patient delayed the recognition of a coexistent carcinoma that might have been cured surgically. Nevertheless, the patient refused surgery.

This case emphasizes the importance of correlative clinical and radiologic follow-up, even when a pulmonary nodule is diagnosed conclusively as benign or when the diagnosis might be due to a contaminant. Radiologic resolution of the pulmonary lesion during antibiotic therapy is important to support a benign diagnosis, but initial improvement can occur with concurrent processes, such as an infection associated with partial bronchial obstruction from a malignant tumor. Actinomycosis, tuberculosis, and other bacterial and fungal infections that are treated medically must be followed up until they have resolved completely [10] or until they are proved to be stable, that is, showing no change for at least 2 years.

ACKNOWLEDGMENTS

Our appreciation to Paul Friedman and Peggy Clark for their assistance.

REFERENCES

1. Ballard GL, Boyd WR. A specifically designed cutting aspiration needle for lung biopsy. *AJR* **1978**;130:899–903
2. Sinner WN. Needle biopsy and tumor staging (TNM-system). *ROFO* **1982**;136:270–276
3. Sinner WN. Needle biopsy and histoplasmosis. *ROFO* **1980**;133:590–593
4. Calhoun P, Feldman PS, Armstrong P, et al. The clinical outcome of needle aspirations of the lung when cancer is not diagnosed. *Ann Thorac Surg* **1986**;41:592–596
5. Balikian JP, Cheng TH, Costello P, Herman PG. Pulmonary actinomycosis: a report of 3 cases. *Radiology* **1978**;128:613–616
6. Winter RJ, Hoffbrand BI, Souhami RL. Simultaneous occurrence of actinomycosis and lymphocytic lymphoma. *J R Soc Med* **1983**;76:1071–1072
7. James R, Heneghan MA, Lipkansky V. Thoracic actinomycosis. *Chest* **1985**;87:536–537
8. Bennhoff DF. Actinomycosis: diagnosis and therapeutic considerations and a review of 32 cases. *Laryngoscope* **1984**;94:1198–1217
9. Rippon JW, Kathuria SK. *Actinomyces meyeri* presenting as an asymptomatic lung mass. *Mycopathologia* **1984**;84:187–192
10. Slade PR, Slesser BV, Southgate J. Thoracic actinomycosis. *Thorax* **1973**;28:73–85

Case Report

Peripheral Carcinoid Tumor of the Lung: CT Diagnosis

Sheila D. Davis,[1] Jonathan R. Zirn,[2] Antonio F. Govoni,[1] and David F. Yankelevitz[1]

The CT appearance of bronchial carcinoid tumors has been well described [1–6]. Because the majority of these tumors are central—in the trachea or the main, lobar, or proximal segmental bronchi—they are thought to be ideally situated for detection by CT [1, 2, 4]. In fact, to our knowledge, in all previous descriptions of carcinoid tumors examined by CT, endobronchial lesions have been located in the proximal bronchial tree. In this report, we present a case of peripheral carcinoid tumor for which an endobronchial component within a subsegmental bronchus was visualized on thin-section CT. This finding, together with significant contrast enhancement of the mass on a subsequent dynamic scan, provided a clue to the appropriate diagnosis.

Case Report

A 32-year-old woman was referred to our institution for evaluation of a nodule in the right lower lobe incidentally discovered on a chest radiograph (Fig. 1A). The patient was asymptomatic except for a history of some shortness of breath, which had improved after cessation of heavy smoking. Comparison with previous radiographs revealed that the mass had not changed in size for at least 1 year. On a contrast-enhanced CT scan at another hospital, the lesion was interpreted as representing a pulmonary arteriovenous malformation.

A second CT scan was obtained in our department. A preliminary scan without contrast material included contiguous 3-mm sections through the lesion. It showed a clearly defined, somewhat lobulated mass associated with a smooth endobronchial lesion in a subsegmental bronchus of the right lower lobe (Figs. 1B and 1C). No evidence was present for hilar or mediastinal lymphadenopathy. Because the diagnosis of an arteriovenous malformation had been raised at another institution, a dynamic CT scan was obtained; marked enhancement of the lesion occurred, from 50 H before administration of contrast material to about 160 H afterward. This enhancement occurred only after opacification of the left ventricle (Fig. 1D).

The patient subsequently had an exploratory right thoracotomy. Fiber-optic bronchoscopy during surgery revealed a moderate amount of mucus in the basilar segments of the right lower lobe. After removal of the mucus, an additional obstruction was faintly visualized more distally in a subsegmental bronchus. A solid parenchymal mass deep within the medial basal segment was then resected through a right lower lobectomy. The fresh, gross surgical specimen showed a yellow-white lobulated mass, 3 × 3 × 1 cm, related to a subsegmental bronchus (Fig. 1E). Microscopic examination was consistent with carcinoid tumor, revealing a characteristic cellular architectural pattern within a prominent vascular stroma. Seven regional lymph nodes did not show metastases.

Discussion

Certain characteristic CT features of bronchial carcinoid tumors have been described. Carcinoid tumors tend to arise centrally within the bronchial tree, so secondary signs of obstruction such as atelectasis, bronchiectasis, and recurrent pneumonia often are seen [1–5]. The intraluminal component of tumor or "tip of the iceberg," as well as the extraluminal mass, also may be visualized on CT [3, 4]. Hilar or mediastinal lymphadenopathy due to metastasis of the carcinoid tumor or hyperplasia from recurrent pneumonia may be present [2]. Calcification or ossification within the tumor mass has been described [5, 6]. Bronchial carcinoid tumors are quite vascular, and significant enhancement of these tumors has been noted on CT [3].

Received April 16, 1990; accepted after revision June 1, 1990.

[1] Department of Radiology, The New York Hospital-Cornell Medical Center, 525 E. 68th St., New York, NY 10021. Address reprint requests to S. D. Davis.

[2] Department of Pathology, The New York Hospital-Cornell Medical Center, 525 E. 68th St., New York, NY 10021.

AJR 155:1185–1187, December 1990 0361–803X/90/1556–1185 © American Roentgen Ray Society

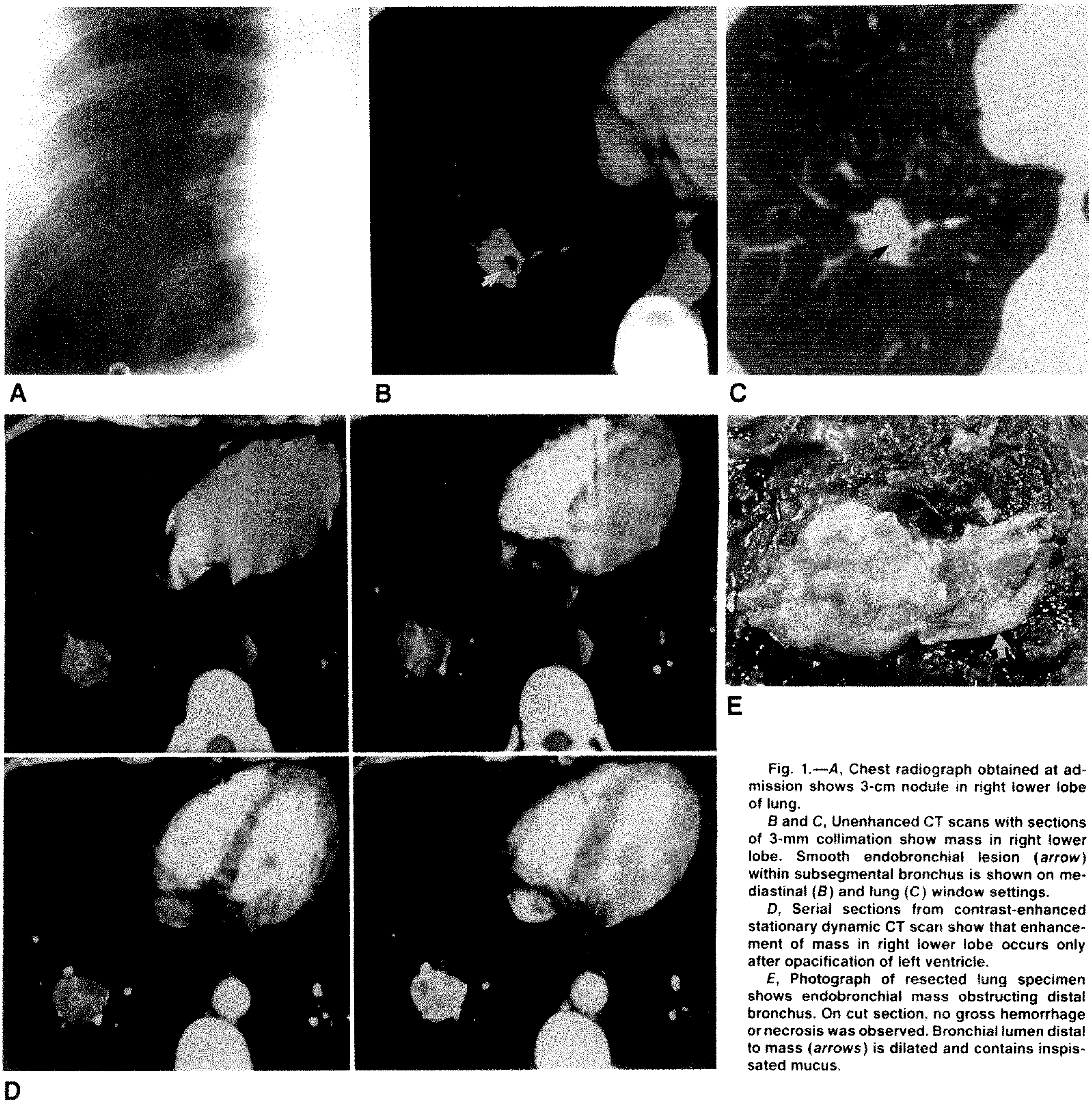

Fig. 1.—*A*, Chest radiograph obtained at admission shows 3-cm nodule in right lower lobe of lung.

B and *C*, Unenhanced CT scans with sections of 3-mm collimation show mass in right lower lobe. Smooth endobronchial lesion (*arrow*) within subsegmental bronchus is shown on mediastinal (*B*) and lung (*C*) window settings.

D, Serial sections from contrast-enhanced stationary dynamic CT scan show that enhancement of mass in right lower lobe occurs only after opacification of left ventricle.

E, Photograph of resected lung specimen shows endobronchial mass obstructing distal bronchus. On cut section, no gross hemorrhage or necrosis was observed. Bronchial lumen distal to mass (*arrows*) is dilated and contains inspissated mucus.

Carcinoid tumors that arise distal to segmental bronchi are termed peripheral carcinoid tumors. These tumors are not visualized bronchoscopically and rarely cause signs and symptoms of bronchial obstruction [7]. Radiologically, peripheral carcinoid tumors must be distinguished from solitary pulmonary nodules of other causes. In the descriptions or illustrations of previous reports, the endobronchial components of carcinoid tumors on CT have been located centrally within the trachea or the main, lobar, or segmental bronchi. It has been observed that the tumor mass of peripheral carcinoid tumors may closely abut a segmental or subsegmental bronchus [1, 4, 6]. In our case, an endobronchial component of a peripheral carcinoid tumor was visualized within a subsegmental bronchus of the right lower lobe on a preliminary scan with 3-mm collimation. It is expected that small endobronchial lesions would be visualized better on thin-section scans than on routine sections 10-mm thick. In one report [8], recognition of peribronchial thickening within a subsegmental bronchus on a 1.5-mm collimation scan allowed correct localization of an occult squamous cell carcinoma.

An enhancing pulmonary mass may be mistaken for a vascular lesion, as was initially the case for our patient. Simulation of an arteriovenous malformation on dynamic CT has previously been described for metastatic choriocarcinoma [9] and a peripheral adenosquamous carcinoma of the lung [10]. Stationary dynamic CT, that is, rapid serial scans at a single level after bolus injection of contrast material, has been advocated as a method for diagnosing vascular lung lesions and for differentiating a pulmonary arterial from a systemic arterial supply [11]. In the three cases reported by Aronchick et al. [3], incremental dynamic scans were obtained, and as the authors point out, the carcinoid tumors were not differentiated clearly from vascular lesions, although they did show significant enhancement. By using stationary dynamic CT scanning, we showed that the mass in our case had a systemic arterial supply. It was clearly not a pulmonary arteriovenous malformation or varix, although these diagnoses also were excluded by the finding of an endobronchial lesion.

In the evaluation of a pulmonary nodule, thin-section scanning without administration of contrast material often is performed. If an endobronchial component is detected, the differential diagnosis includes bronchogenic carcinoma, endobronchial metastases, and lymphoma in addition to bronchial adenoma. Nevertheless, the finding of a smooth-surfaced endobronchial lesion within a segmental or subsegmental bronchus should strongly suggest the presence of a peripherally situated carcinoid tumor. If a dynamic scan is performed, significant enhancement of the tumor mass also favors this diagnosis, although lack of enhancement still does not exclude the possibility of carcinoid tumor.

REFERENCES

1. Naidich DP, McCauley DI, Siegelman SS. Computed tomography of bronchial adenomas. *J Comput Assist Tomogr* **1982**;6:725–732
2. Webb WR, Gamsu G, Birnberg FA. CT appearance of bronchial carcinoid with recurrent pneumonia and hyperplastic hilar lymphadenopathy. *J Comput Assist Tomogr* **1983**;7:707–709
3. Aronchick JM, Wexler JA, Christen B, Miller W, Epstein D, Gefter WB. Computed tomography of bronchial carcinoid. *J Comput Assist Tomogr* **1986**;10:71–74
4. Naidich DP, Zerhouni EA, Siegelman SS. *Computed tomography of the thorax.* New York: Raven Press, **1984**:94–96
5. Shin MS, Berland LL, Myers JL, Clary G, Zorn GL. CT demonstration of an ossifying bronchial carcinoid simulating broncholithiasis. *AJR* **1989**;153:51–52
6. Magid D, Siegelman SS, Eggleston JC, Fishman EK, Zerhouni EA. Pulmonary carcinoid tumors: CT assessment. *J Comput Assist Tomogr* **1989**;13:244–247
7. Maier HC, Fischer WW. Adenomas arising from small bronchi not visible bronchoscopically. *J Thorac Surg* **1947**;16:392–398
8. Foster WL, Roberts L, McLendon RE, Hill RC. Localized peribronchial thickening: a CT sign of occult bronchogenic carcinoma. *AJR* **1985**;144:906–908
9. Cirimelli KM, Colletti PM, Beck S. Metastatic choriocarcinoma simulating an arteriovenous malformation on chest radiography and dynamic CT. *J Comput Assist Tomogr* **1988**;12:317–319
10. Halbsguth A, Schulze W, Ungeheur E, Hoer PW. Pitfall in the CT diagnosis of pulmonary arteriovenous malformation. *J Comput Assist Tomogr* **1983**;7:710–712
11. Godwin JD, Webb WR. Dynamic computed tomography in the evaluation of vascular lung lesions. *Radiology* **1981**;138:629–635

Book Review

MacDose. Version 2.1; User's Manual. By Russell K. Hobbie. Madison, WI: Medical Physics Publishing, 28 pp., 3.5-in. disk included. 1989. $30

MacDose is a simulation program that illustrates the basic interactions of radiation with matter. It is furnished as a single 3.5-in. diskette with a 28-page instruction manual for use with a Macintosh computer. MacDose is based on a program originally written by Tao-Qu Chen as part of the requirements for a master of science degree in physics. The present version and the associated instruction manual were written by Russell K. Hobbie.

MacDose provides a graphic presentation of the statistical variations of the photoelectric, Compton, and pair production interactions by using Monte Carlo techniques. Secondary electron and photon interactions can be displayed as an option. Compton scattering is approximated with a reasonable degree of accuracy. In the case of photoelectric interactions, all photoelectrons are assumed to be emitted in the forward direction, resulting in some inaccuracies. In pair production, the secondary electron trajectories are assumed to be straight lines. Options include choice of number and energy of incident photons, thickness of absorber, inclusion of all subsequent interactions, and choice of whether to have all photons interact. Our review configuration was a Macintosh IIcx with 4 megabytes of random access memory, an Apple high-resolution RGB color monitor, an 80-megabyte hard disk, and a Hewlett Packard Desk Writer ink-jet printer.

The screen display shows photons entering in a beam horizontally from left to right until they either interact or exit the absorber (water). Twenty-five photons are displayed in a single window, with each interaction observed at the time of occurrence. The speed of the display varies with the clock speed of the central processing unit in the Macintosh computer. The manual indicates that typical execution speeds for 100-keV photons are 180 photons/min on a Macintosh Plus or SE and 850 photons/min on a Macintosh II or SE/30. Our observations indicate that higher speeds would be desirable for long runs (1000 to 10,000 photons), particularly if secondary interactions are included. For our system, the measurement of 10,000 photons at 10 MeV in a 1-m sample, including secondary interactions, required 42 mins for completion. Photon interactions in water from 30 keV to 25 MeV were displayed successfully as part of our evaluation. The absorber size was varied from 10 cm to 1 m in length and was infinite in vertical extent.

Three types of display are provided simultaneously: (1) the graphic display of the photons together with scattering effects; (2) a tabular report showing the parameters of the interaction; and (3) a graphic report of the energy transferred, energy absorbed, and energy transferred by secondaries. In order to compare small photon runs at different energies or with different absorber thicknesses, the program can be restarted with the same seed number to obtain the same set of pseudorandom numbers for each group of photons.

Nine exercises are included for the student. They range from the different kinds of photon interactions, showing the basic scattering phenomena and the statistical nature of photon interactions, through the differences between energy transferred and energy absorbed, the effect of subsequent interactions, energy transferred vs depth, and photon energy. The author includes thought-provoking questions to stimulate further understanding of the simulations observed with each exercise.

This software is recommended for radiology residents and students of radiation physics. The program display is optimal if run on a Macintosh II or SE/30 with a color monitor, as primary and secondary photon and electron paths can be differentiated by color.

Carroll R. Markivee
Jeffrey L. Chenoweth
William J. Nalesnik
St. Louis University
St. Louis, MO 63106

Value of Increasing Film Processing Time to Reduce Radiation Dose During Mammography

Stanley E. Skubic[1]
Rauf Yagan
Dubravka Oravec
Zahid Shah

We systematically tested the effects on radiation dose and image quality of increasing the mammographic film processing time from the standard 90 sec to 3 min. Hurter and Driffield curves were obtained for a Kodak Min-R-OM1-SO177 screen-film combination processed with Kodak chemistry. Image contrast and radiation dose were measured for two tissue-equivalent breast phantoms. We also compared sequential pairs of mammograms, one processed at 90 sec and one at 3 min, from 44 patients on the basis of nine categories of image quality. Increased processing time reduced breast radiation dose by 30%, increased contrast by 11%, and produced slight overall gains in image quality. Simple modifications can convert a 90-sec processor to a 3-min unit. We recommend that implementation of extended processing be considered, especially by those centers that obtain a large number of screening mammograms.

Three-minute film processing can reduce breast radiation dose by 30% and increase contrast by 11% without compromising image quality.

***AJR* 155:1189–1193, December 1990**

Reducing radiation dose in mammography is increasingly important as more asymptomatic women undergo recommended screening mammography. A technique attracting special interest in recent years is increased film processing time, which has been shown to potentially reduce dose while increasing image contrast [1–4]. Previous reports have described extensive phantom studies but only anecdotal patient cases. Dependence on particular film and processing chemicals in those studies limits their usefulness [1, 2].

Our goal was to determine the feasibility of applying increased processing time to grid mammography in a high-volume department. To warrant adoption, the technique must reduce the radiation dose significantly without compromising image quality. The current study was performed to document the reduction in radiation dose to the breast and to systematically compare key image features between mammograms produced with grid and extended-time processing and those with grid and normal-time processing.

Equipment and Methods

Film Processors and Chemistry

Two Kodak M6AN processors (Eastman Kodak Co., Rochester, NY) in the same darkroom were modified to run at both 90-sec and 3-min processing times by replacing the standard processor drive motors with variable-speed motor systems. The standard developer crossover rollers were also replaced with softer silicon rollers. Changing between 90-sec and 3-min processing times required changing a switch setting and adjusting the replenishment rates. Developer immersion times were 23 and 47 sec, respectively; the developer used was the Kodak RP X-OMAT solution at 35°C (95°F) and the fixer solution as Autex RP (Allied Photo Products, Norcross, GA). Autex RP is considered equivalent to Kodak RP X-OMAT. Quality control procedures, including light sensitometry, developer temperature measure-

Received April 6, 1990; accepted after revision July 10, 1990.

Presented in part at the annual meeting of the American Roentgen Ray Society, New Orleans, May 1989.

[1] All authors: Department of Radiology, MetroHealth Medical Center/Case Western Reserve University, 3395 Scranton Rd., Cleveland, OH 44109. Address reprint requests to S. E. Skubic.

0361-803X/90/1556-1189

© American Roentgen Ray Society

ments, and replenishment rate measurement [5], were performed daily.

Radiographic Units and Image Receptors

Patient images used in the paired-image comparison were obtained with a Philips Diagnost UM dedicated mammography unit (Philips Medical Systems, Shelton, CT) by using automatic exposure. The unit has a 5:1 moving grid; molybdenum target and filtration; measured focal spot size of 0.65 mm; and measured half-value layers between 0.34 and 0.37 mm Al, depending on kilovoltage. A Picker Sureview dedicated mammography unit (Picker International, Inc., Highland Heights, OH) was chosen to obtain the Hurter and Driffield (H and D) curve data and the phantom images used for dose assessment because it has an mAs meter. This unit has molybdenum target and filtration; a 4:1 moving grid; and half-value layers that range from 0.29 to 0.37 mm Al, depending on kilovoltage.

Image receptors for both phantom and patient studies consisted of Kodak Min-R intensifying screens and Kodak OM1-SO177 film.

Intensity scale H and D curve data were obtained on a Picker GX1050 general-purpose radiographic unit operating at 50 kVp with the mirror removed from the beam. H and D curve measurements used the same pair of screens and film from the same box.

Film and Calibration Equipment

Exposure readings used a Keithley 96035 parallel-plate ion chamber connected to a Keithley 35614 electrometer (Keithley Instruments, Inc., Cleveland, OH). Both the chamber and electrometer have National Bureau of Standards traceable calibrations. Optical density values were obtained with a Macbeth TD932 densitometer (Kollmorgen Co., Newburgh, NY). Densitometer calibration was checked prior to each use with a Kodak photographic step tablet No. 2.

Physical Measurements

X-ray-generated H and D curves for the two processing techniques were obtained by using a two-part intensity-scale sensitometry technique. Standard irradiance-scale sensitometric values [6], obtained on the general radiographic unit, were normalized to absolute screen-film speed values obtained on the mammographic unit. The two-part technique provided absolute H and D curves that were accurate at mammographic kilovoltages and that were free from reciprocity law failure artifacts.

The differences in radiation dose to the breast between 3-min and 90-sec processing predicted by the difference in the two H and D curves were tested by imaging a CIRS model X breast phantom (Computerized Imaging Reference Systems, Inc., Norfolk, VA; 5 cm thick, 50% adipose-50% glandular tissue simulated composition) and a CIRS model XII breast phantom (4 cm thick, 30% glandular-70% adipose tissue simulated composition) in the standard craniocaudal projection on the Picker mammographic unit at 3 kVp. The images were obtained with a grid in the phototiming mode for each processing condition. Optical densities were measured at midbreast on all images at a point just posterior to the step wedge embedded in the phantom. Average glandular dose (D_g) was calculated in the standard manner as the product of X_{air} and $D_{g,N}$, with the $D_{g,N}$ values coming from Rosenstein et al. [7]. X_{air} was readily determined from measurements with the electrometer and ion chamber. Contrast was determined as the optical density difference between the steps of the embedded step wedge. Owing to differences in phototimer settings, there were variations in midphantom densities of 0.12–0.30 between the images processed at 3 min and 90 sec. To correct for the density differences between the image pairs, the X_{air} and contrast values were normalized to the lower of the two optical densities by using the gamma value from the appropriate measured H and D curve.

Image Acquisition

Pairs of sequential mammograms for each of 44 patients were used in image comparison. Four images of a standard two-projection mammogram were compared unless the patient had only one breast, in which case two images were compared. The first mammogram of the pair was obtained with 90-sec processing and the second with 3-min processing. This has been recommended as a means of allowing each patient to serve as her own control, and allows for variations in breast composition and architecture [2]. The compression and kilovoltage used for each of the sequential mammograms and the optical density of the images were similar but not necessarily identical. The interval between mammograms varied from 6 to 18 months depending on the reason for the second mammogram.

Image Comparison

Three experienced mammographers at our institution performed the image comparison. Before the comparison, individual mammograms of the pairs were randomly assigned one of two color codes, and the date of acquisition hidden, for blinded evaluation. Mammograms were compared projection by projection and breast by breast. Each evaluator could reject any image for technical inadequacy or artifacts, which dropped that image pair from that reviewer's subsequent analysis. An average of two images per evaluator were dropped.

Clinical comparison categories were chosen by the senior mammographer of the evaluator group in consultation with the other evaluators. These categories were:

1a. Does the image have sufficient uniformity of density (sufficient latitude) to permit proper evaluation of the entire breast without use of bright light? (yes or no)
1b. The degree or extent of uniformity of image density from chest wall to skin (on a scale of 1–10).
2a. Does the use of bright light permit adequate evaluation of the entire skin line? (yes or no)
2b. Fraction (%) of skin line that requires a bright light for proper evaluation.
2c. Extent of visibility of skin line (1–10 scale).
3. Extent of visualization of breast parenchyma, including ducts and Cooper ligaments (1–10 scale).
4. Extent of visualization of microcalcifications (1–10 scale).
5. Extent of visualization of asymmetric densities (1–10 scale).
6. Extent of visualization of masses (1–10 scale).

These categories were considered to be key features in the analysis of mammograms. In categories 1a, 2a, and 2b, each image of the pair was evaluated. In categories 1b, 2c, and 3–6, the images were evaluated as a pair and a comparison score determined; a score of 1 indicated that the 90-sec processed image was much superior and a score of 10 indicated that the 3-min processed image was much superior. On this scale, a score of 5.5 meant that the two images were considered equal.

Statistical Analysis

Image comparison used the statistical analysis programs of PC SAS [8]. The programs generated means, frequency distributions, and tests of statistical significance. Because data did not follow a normal distribution in any analysis category, the Wilcoxon signed rank test was used to determine statistical significance. Data were analyzed collectively as a composite of all patients and all evaluators.

Results

H and D curve measurement results are shown in Figure 1. The speeds [9] of the screen-film combination at 90-sec and 3-min processing times were 7.5 mR (1.9 μC/kg) and 5.3 mR (1.4 μC/kg), respectively. Curve gammas at a density of 1.0 above base fog were 2.7 and 3.0, respectively. Thus, 3-min processing showed a speed 30% less and gamma 11% greater than did 90-sec processing.

Dose savings predicted by this H and D behavior were confirmed in phantom imaging. Dose savings with 3-min processing ranged from 31% to 36% depending on phantom and kilovoltage, in good agreement with the 30% predicted by H and D speed measurements. Phantom images also demonstrated more contrast with 3-min processing. Contrast gains ranged from 7% to 18%, in good agreement with H and D gamma values.

Reviewer rejections and single-breast mammograms reduced the number of image comparisons to 150 image pairs for categories 1a–3. Categories 4–6, requiring the presence of abnormal conditions, yielded fewer pairs for comparison; the numbers of image pairs for these categories were 39, 30, and 38, respectively.

Figure 2 shows the average evaluation score for categories 1b, 2c, and 3–6. Differences in image quality were generally small, but were statistically significant for (2c) skin line visibility (p = .0001), (3) parenchyma evaluation (p = .0001), (4) evaluation of microcalcification (p = .0001), and (5) asymmetric density evaluation (p = .0037). Differences were suggested but not statistically significant (p = .105) for category 6, mass evaluation, and were very small (p = .326) for category 1b, uniformity of density.

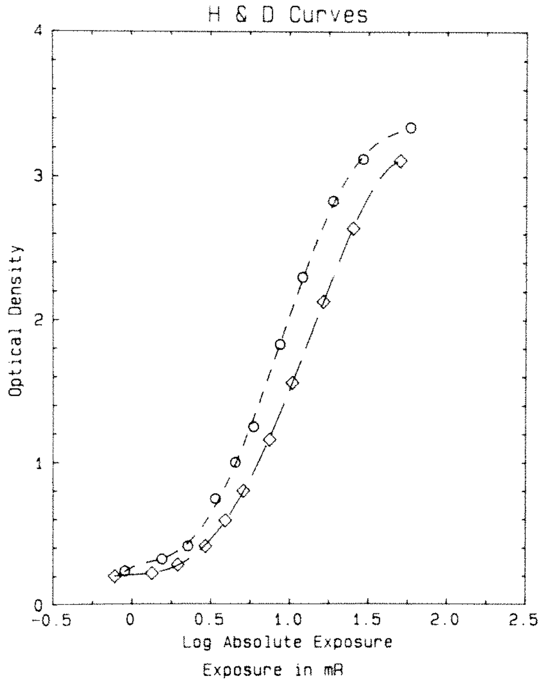

Fig. 1.—Absolute Hurter and Driffield (H & D) curves for the Kodak Min R-OM1-SO177 screen-film combination for two processing times. Curve connecting circles is for 3-min processing time; curve connecting diamonds is for 90-sec processing time. Curves are least-squares best fits to data. Error bars are not shown because they are smaller than the shapes marking the data points.

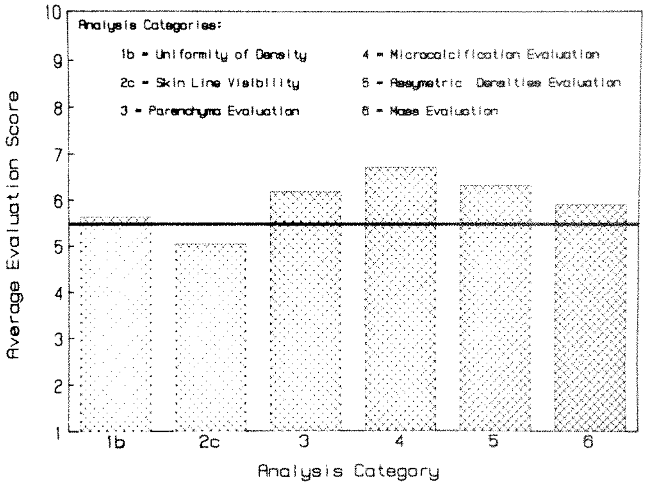

Fig. 2.—Composite average evaluation scores (all patients and all evaluators) for analysis categories of paired-image comparison. Dark horizontal line is at evaluation score value of 5.5, where the quality of 90-sec processed images equals that of 3-min processed images. Bars protruding above and below the line represent 3-min images that are superior and inferior, respectively, to 90-sec images.

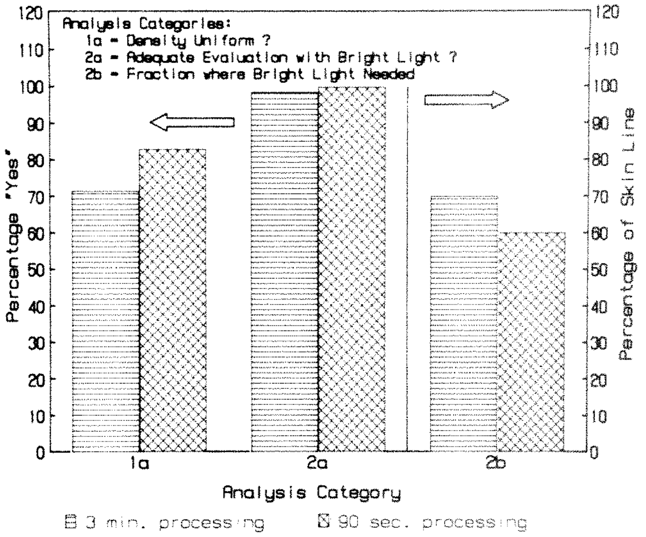

Fig. 3.—Composite average evaluation scores (all patients and all evaluators) for yes/no and percentage analysis categories of paired-image comparison. Striped bars are for images processed at 3 min; crosshatched bars are for images processed at 90 sec.

Note that images processed at 3 min were superior or equivalent to 90-sec processing for all image categories except skin line visibility.

Results for Yes/No and percentage evaluations, displayed in Figure 3, show that image latitude was sufficient to permit

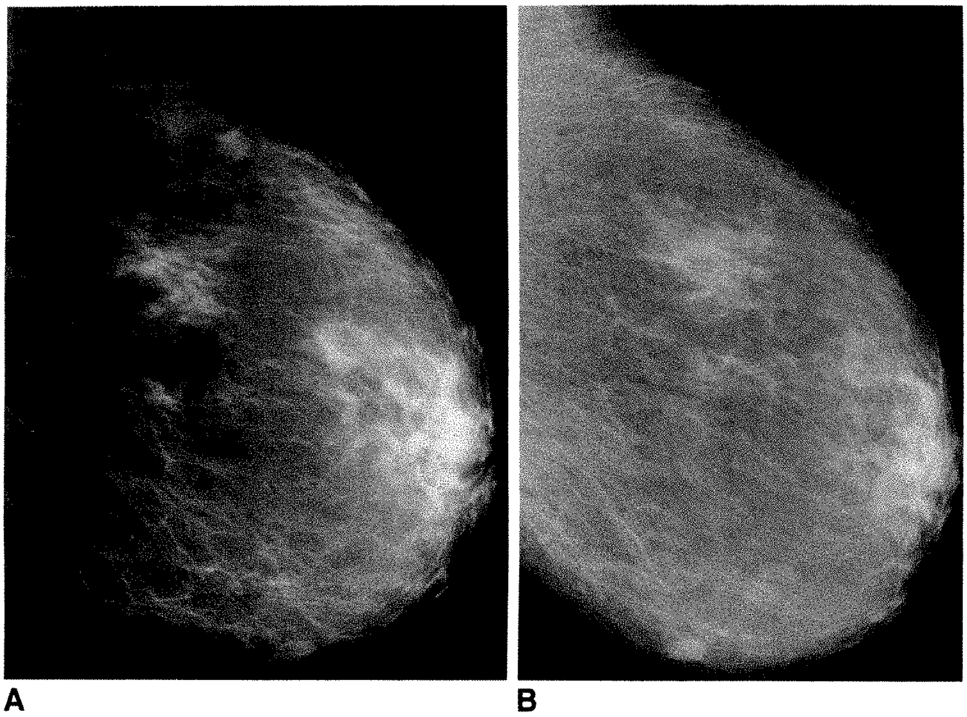

Fig. 4.—Mediolateral, time-sequential images of the same breast processed under normal and extended time processing.

A and *B*, Images processed at 3 min (*A*) and at 90 sec (*B*). Increased contrast seen in *A* allows better definition of breast parenchyma and aids in analysis of irregular, benign, increased density seen in central, upper portion of breast. Also, a small nodule noted in lower part of breast is much better defined in *A*. However, latitude of image is greater in *B*.

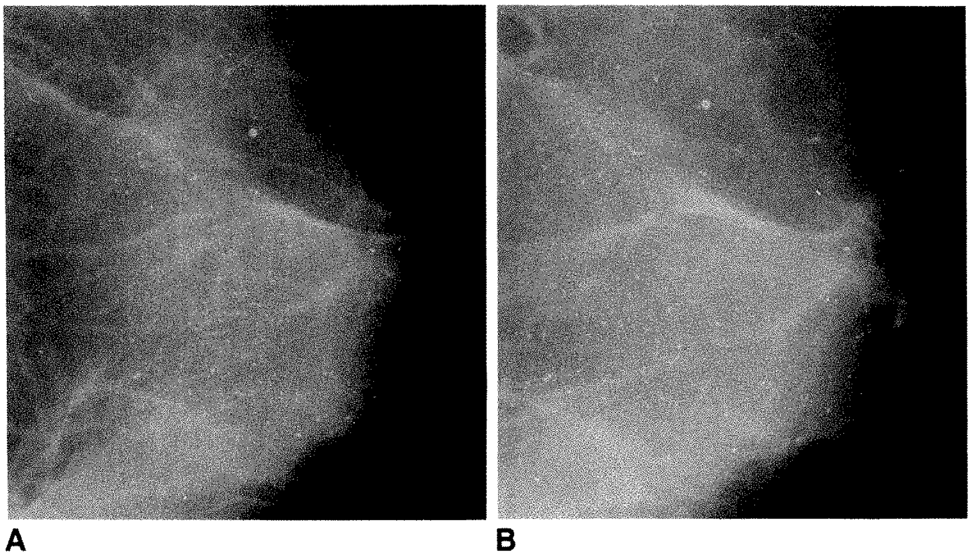

Fig. 5.—Close-up views of mediolateral, time-sequential breast images for paired image comparison.

A and *B*, Images processed at 3 min (*A*) and at 90 sec (*B*) show effect of different processing conditions on visualization and evaluation of microcalcifications. Microcalcifications in central, lower portion of the two images are more easily seen and evaluated in *A*.

proper evaluation of whole-breast parenchyma without bright light in 12% more images with 90-sec than with 3-min processing. An average of 10% more skin line evaluations required bright light with 3-min processing. These differences were small but statistically significant ($p = .0001$) in both cases.

Discussion

The general results of this work are demonstrated in the images shown in Figures 4 and 5. The 3-min images display greater contrast between breast structures and background, aiding in the evaluation of irregular increased density such as that in the central upper portion of the breast in Figure 4. This asymmetric density did not appear on the images of the contralateral breast. On the 90-sec image, the density could be mistaken for a masslike lesion. However, on the 3-min image, the margins and inner architecture of the density are better appreciated, so that it can be readily interpreted as a normal variation or benign alteration of breast parenchyma. It should be noted, however, that the appearance of the breast from the chest wall to the skin line is more uniformly dense on the 90-sec images.

Increased contrast on the 3-min images allows microcalcifications to be seen more easily (Fig. 5). The shape of the calcifications is also better appreciated on this image, aiding the determination of whether the calcifications have a benign or malignant indication.

To test whether the overall differences in patient image quality were due to consistent, small differences or to a small number of cases with large differences, we analyzed frequency of response for the categories assessed on a 1–10 scale. Differences in the evaluation of skin line, parenchyma, and microcalcifications generally are due to consistent small differences, although for microcalcifications there were a number of cases in which the differences were large (3 min greatly superior). For evaluation of asymmetric densities and masses, there were nearly equal numbers of cases favoring one time over the other, and the overall difference was due to a relatively small number of cases in which 3-min films were much superior.

The use of a 3-min processing time does effectively require a dedicated processor for mammography, but this is consistent with current recommendations [4]. The 3-min processing time is easily obtainable at small cost and little difficulty by simple modifications to a standard 90-sec processor. The extended processing time was readily accepted by our technical staff, has not proved inconvenient in practice, and has not reduced throughput. The ability to quickly switch back to 90-sec processing when time is of the essence, such as for needle localization, has proved quite useful.

Processing time extended from 90 sec to 3 min provides about a 30% reduction in breast radiation dose, which is important in the evaluation of symptomatic women, who may undergo increased mammographic surveillance. It is also significant for the increasing number of women undergoing screening mammography. Along with dose reduction, there is an overall gain in image quality. Differences in image quality are best appreciated by improved visibility and evaluation of microcalcifications and the analysis of asymmetric densities. Gains in contrast come at the expense of reduced latitude and the necessity to use bright light to properly evaluate the skin line. Such use should present no great inconvenience to the practicing mammographer. Extended-time processing ought to be seriously considered for routine implementation, especially by those centers obtaining a large number of screening mammograms.

ACKNOWLEDGMENTS

We thank Dawn Finn and Ruthellen Harris, the X-ray technologists who obtained the mammograms in this study.

REFERENCES

1. Tabar L, Haus AG. Processing of mammographic films: technical and clinical considerations. *Radiology* **1989**;173:65–69
2. Kimme-Smith C, Rothschild PA, Bassett LW, Gold RH, Moler C. Mammographic film-processor temperature, development time, and chemistry: effect on dose, contrast, and noise. *AJR* **1989**;152:35–40
3. Law J, Kirkpatrick AE. Film processing for mammography. *Br J Radiol* **1988**;61:939–942
4. Tabar L, Dean PB. Screen/film mammography: quality control. In: Feig SA, McLelland R, eds. *Breast carcinoma: current diagnosis and treatment*. New York: Masson, **1983**:161–168
5. National Council on Radiation Protection and Measurements. *Quality assurance for diagnostic imaging equipment: recommendations of the National Council on Radiation Protection and Measurements*, report No. 99. Washington, DC: National Council on Radiation Protection and Measurements, **1988**
6. Gray JE, Haus AG. Practical sensitometry in medical imaging. In: Waggener RG, Kereiakes JG, Shalek RJ, eds. *Handbook of medical physics*, Vol. 2. Boca Raton, FL: CRC, **1984**:229–258
7. Rosenstein M, Anderson L, Warner G. *Handbook of glandular doses in mammography*, HHS publication No. FDA85-8243. Washington, DC: Health and Human Services, **1985**
8. SAS Institute Inc. *SAS/STAT guide for personal computers*, version 6 ed. Cary, NC: SAS Institute, **1985**
9. Johns HE, Cunningham JR. *The physics of radiology*, 4th ed. Springfield, IL: Thomas, **1983**:581

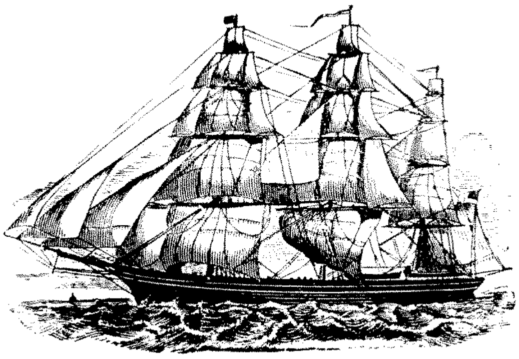

Come to the
American Roentgen Ray Society
91st
ANNUAL MEETING

Boston, MA

Sheraton Boston Hotel
May 5-10, 1991

Scientific Program (200 papers)
Instructional Courses (60 hours)
Categorical Course on Body MR Imaging
The Caldwell Lecture
Award Papers
Scientific Exhibits
Social, Golf, and Tennis Programs
Guest Programs

Perspective

Nonpalpable, Probably Benign Breast Lesions: Follow-up Strategies After Initial Detection on Mammography

Dorit D. Adler,[1] Mark A. Helvie, and Debra M. Ikeda

Numerous studies have established the efficacy of mammographic screening in the detection of early, clinically occult breast cancer [1]. As expected, the combination of improved image quality and increased use of mammography has led to detection of smaller and prognostically more favorable breast lesions. In addition, however, a large number of clinically occult benign breast lesions also are being identified. Some such lesions have pathognomonic benign radiologic features, obviating additional workup or intervention. These include masses such as calcified degenerating fibroadenomas; intramammary lymph nodes; and lipid-containing masses such as lipomas, some hamartomas, and oil cysts [2]. Similarly, some calcifications can be clearly identified as benign in origin, as in the case of dermal and vascular calcifications, secretory disease, and milk of calcium. It is, however, lesions that are not considered malignant, but do not demonstrate sufficient characteristic benign mammographic features to allow precise diagnosis, that result in management problems and are the subject of this discussion. Inasmuch as palpable findings frequently change the relative significance of a lesion, only nonpalpable, clinically occult lesions will be considered here.

Ultimately, the decision is whether or not to recommend surgical biopsy for definitive diagnosis of the mammographically detected finding. Alternatives to excision include examination by sonography, fine-needle aspiration biopsy, and mammographic follow-up. Few published reports address the option of periodic follow-up [3–5]. As will be discussed, a combination of these options may prove most useful in some circumstances.

Advantages and Disadvantages of Nonsurgical Follow-up

Although the surgical biopsy can be regarded as the "gold standard," in that excision allows complete pathologic inspection and diagnosis, it is not without shortcomings. At times, even when aided by mammographically guided localization techniques, surgical biopsy may not successfully excise a lesion. Surgical failure rates as high as 17% have been reported [6]. Despite documentation of excision by specimen radiology, some lesions may be missed on initial pathologic sectioning, requiring radiographs of tissue blocks to find the resected abnormality [7].

Mammographic follow-up spares a woman a surgical procedure with its albeit relatively minor morbidity and potential complications. Clinical and mammographic examinations are more easily performed and interpreted in the absence of postoperative scarring. Although the cost of the biopsy should not be considered a basis for determining whether or not a specific lesion requires excision, the monetary savings to the individual woman spared a surgical biopsy can be substantial.

The cost of surgical biopsy for a benign lesion has more widespread implications. Surgeons' fees and biopsy costs have been shown to account for over half of total costs (excluding treatment) in detecting small breast cancers in a population of screened women [8]. As many breast biopsies are generated on the basis of nonpalpable, mammographically detected lesions, and since cost has been shown to be a major obstacle to widespread acceptance of mammographic screening [9–11], the indirect costs generated from false-

---

Received May 11, 1990; accepted after revision July 3, 1990.

Presented in part at the annual meeting of the American Roentgen Ray Society, New Orleans, LA, May 1989.

[1] All authors: Department of Radiology, University of Michigan Hospitals, Taubman Center, 2910/0326, 1500 E. Medical Center Dr., Ann Arbor, MI 48109-0326. Address reprint requests to D. D. Adler.

AJR 155:1195–1201, December 1990 0361-803X/90/1556-1195 © American Roentgen Ray Society

positive mammographic interpretations resulting in benign biopsies should not be underestimated. Some have taken an extreme view that current data suggest that the net harm (cost plus morbidity) caused by breast cancer screening should result in ignoring the American Cancer Society recommendations, and that screening be reserved only for women at high risk for developing breast cancer [12].

Studies have suggested that providing mammographic follow-up [13], in some cases combined with fine-needle aspiration cytology [14], as an option to surgical biopsy can markedly decrease the number of biopsies performed on benign lesions, while not sacrificing the opportunity to detect early breast cancers. However, this requires a high level of interpretive expertise combined with a properly performed examination. The latter may frequently include additional tailored views [15] as well as sonography and/or aspiration.

The major argument against periodic mammographic follow-up lies in the inability to provide absolute assurance that the lesion in question is benign, and the potential of missing the opportunity of detecting a small, occult breast cancer when a successful clinical outcome is most likely. Some, like Moskowitz [16], believe that a benign-to-malignant biopsy ratio as high as 10:1 is acceptable so that mammographic screening can affect mortality statistics. Concern also exists about potential litigation resulting from a delay in the diagnosis of breast cancer. Although these considerations cannot be taken lightly, the radiologist interpreting mammograms cannot practically approach every visualized lesion with the attitude that "malignancy cannot be excluded." To do so would result in a clinically impractical and meaningless service. Rather, proper degrees of care and skill are expected of the radiologist [17]. The intent of this article is to provide such reasonable options without losing sight of the potential difficulties. One needs to consider that strong support of mammographic screening exists despite a true-positive rate for mammography of only 80–85% [18]. The prevalence of breast cancer found at autopsy in a population of young and middle-aged women has been surprisingly high, yet few would advocate routine prophylactic mastectomy to reduce this risk. Nielsen et al. [19] found malignancy in 20% of the deceased women examined, 45% having multicentric carcinoma and 41% having bilateral carcinoma. In their study, women younger than 20 years or over 54 years were excluded.

Finally, little formal consideration has been given to the potential anxiety that women may experience knowing that a lesion remains within the breast. Physicians of such patients may be similarly concerned whether such management is prudent. Little is known about these subjective factors and may be a subject for future investigation. A clear understanding by both the woman and her physician of the rationale for the approach chosen should, however, be provided.

Lesions That May Be Candidates for Mammographic Follow-up

The most common benign-appearing lesions considered for mammographic follow-up rather than surgical excision are (1) the well-circumscribed, noncalcified solitary mass; (2) punctate or oval clustered microcalcifications; and (3) asymmetric breast tissue. Optimal mammographic technique is a prerequisite for any examination. Once a lesion is identified, special tailored views frequently will be necessary to determine whether the abnormality fits into one of these categories. Such techniques as magnification [20], spot compression [21], and angled or rotated projections [22] can provide important information not available on a routine examination. Similarly, follow-up films must be obtained with a high-quality, tailored examination of the area of interest. Incomplete examination or improper technique could result in the mammographer recommending a workup very different from one that would have been suggested had these factors been employed. In addition, considerable diagnostic expertise generally is required in order to assess mammographic lesions without characteristic features. Such experience can be gained by meticulous mammographic/pathologic correlation and documentation of cases from one's own practice [17]. Double reading of difficult cases may be valuable as well [4].

The Solitary Well-Circumscribed Mass

Determination of the marginal characteristics of a mass can provide important diagnostic information. By using some of the techniques described above, separation of a mass with irregular margins from one with smooth margins can mean a high likelihood of malignancy vs a high likelihood of benignity (e.g., a cyst or fibroadenoma) (Figs. 1 and 2). Moskowitz [23] found a risk of malignancy of approximately 2% for mammographically benign masses, such as those with well-defined margins. The risk increased to 5% or 10% if there was partial loss of the margin. Others have reported similar results with a 5% risk of malignancy for lobulated nonpalpable masses [24] and a 2–7% risk depending on whether the mammographic suggestion of malignancy was minimal or slight, respectively [25].

Sonography has been useful in the characterization of masses inasmuch as definitive identification of a simple cyst ends the need for further concern. Its limitations, however, are the inconsistent identification of small (<5 mm) solid masses, especially in the fatty breast, and lack of specific gray-scale features to differentiate benign from malignant solid masses.

Cytologic results of breast aspirates obtained by fine-needle aspiration biopsy are known to be of value in the management of breast cancer, particularly when a preoperative diagnosis of malignancy can be obtained. Cyst puncture is also accepted as both therapeutically and diagnostically valuable. Fine-needle aspiration biopsy has been used less widely in further supporting the impression of a benign lesion, although its value has been documented [13, 26–28]. The specific cytologic diagnosis of a fibroadenoma can certainly be useful in electing mammographic follow-up rather than excision of a solitary nodule (Fig. 2). Such use of cytologic results requires an experienced breast cytopathologist and correlation with the mammographic impression. In addition, close radiologic follow-up, as we will describe, should be part of the protocol after such a lesion is aspirated.

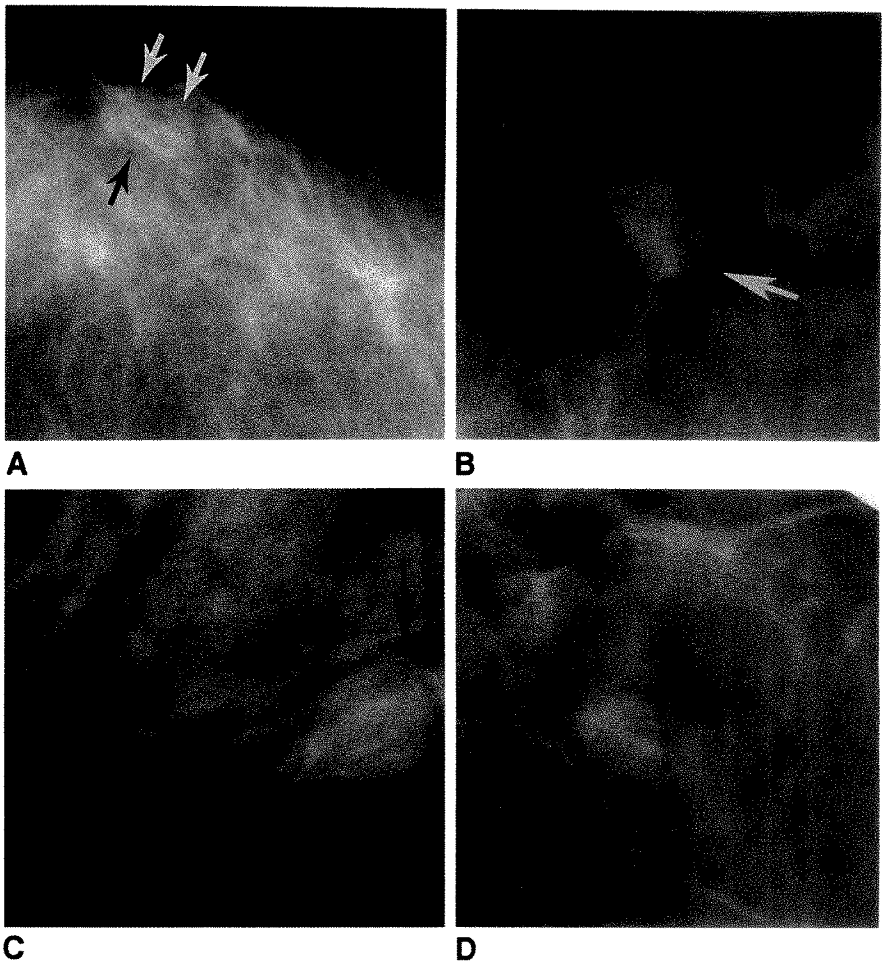

Fig. 1.—Solitary, well-circumscribed masses.

***A*, Magnification view (×1.5) of left breast in a 48-year-old woman shows well-circumscribed 1-cm nodule (*arrow*). No discrete lesion seen with sonography. Radiographically guided needle aspiration provided benign but nonspecific cytology. No change was seen on mammographic follow-up of nodule for 3 years.**

***B*, Magnification spot compression (×1.5) of 6-mm well-circumscribed nodule (*arrow*) identified on screening mammogram in a 47-year-old woman shows margins to be slightly lobular and smooth, suggesting a benign cause. The lesion remained stable on 4-, 12-, and 24-month follow-up examinations and was no longer seen on a 39-month follow-up examination. Lobular margins are known to occur with fibroadenomas, which may explain this nodule.**

***C*, Baseline mammogram in a 72-year-old woman reveals a well-circumscribed, benign-appearing nodule (*arrows*) deep within left breast. Mammographic follow-up for 4½ years showed no change in nodule size.**

***D*, Baseline mammogram in a 37-year-old woman reveals a 6-mm well-circumscribed nodule in central left breast. Spot compression view shows predominantly smooth margins (*arrows*), although overlying glandular tissue obscures part of periphery. The nodule was unchanged for more than 3 years.**

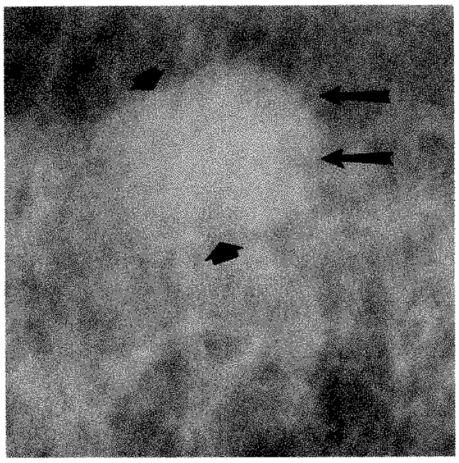

Fig. 2.—Solitary, well-circumscribed mass in a 53-year-old asymptomatic woman referred for a second opinion regarding a suspicious lesion seen on a mammogram obtained elsewhere. Left craniocaudal view shows a 1.3-cm nodule close to chest wall. Visualized margins appear smooth (*long arrows*), although part of margin is obscured by overlying glandular tissue (*short arrows*). Angled views (*not shown*) were not helpful in clarifying obscured margins. Fine-needle aspiration biopsy under radiologic guidance provided cytologic diagnosis of fibroadenoma. The nodule was unchanged on follow-up studies at 4, 12, 24, and 33 months.

Microcalcifications

Owing to the wide spectrum of appearances of microcalcifications, this group probably represents the most difficult differential diagnostic category. Magnification mammography is essential in order to allow careful analysis of calcific shape, number, and size. Calcifications that may be considered candidates for periodic follow-up rather than excision are most often round or oval and frequently tightly grouped (Fig. 3). However, there are frequent variations in the shape and size of the calcifications within these clusters.

Interpretive skill is perhaps most critical for this category. Lanyi [29] was able to show that after implementation of a detailed differential diagnostic system for microcalcifications, the true-positive yield for carcinoma improved from 27% to 52% over a period of approximately 5 years. In following up over 1000 round or oval clusters of microcalcification, Sickles [30] found carcinoma developed in only six patients, and none of these occurred in the area of calcification for which follow-up had been recommended.

Although Moskowitz [23] reported a relatively high (11.5%) positive predictive value for punctate calcifications, one should realize that the term "punctate" was used loosely inasmuch as some clusters with branching patterns and thin

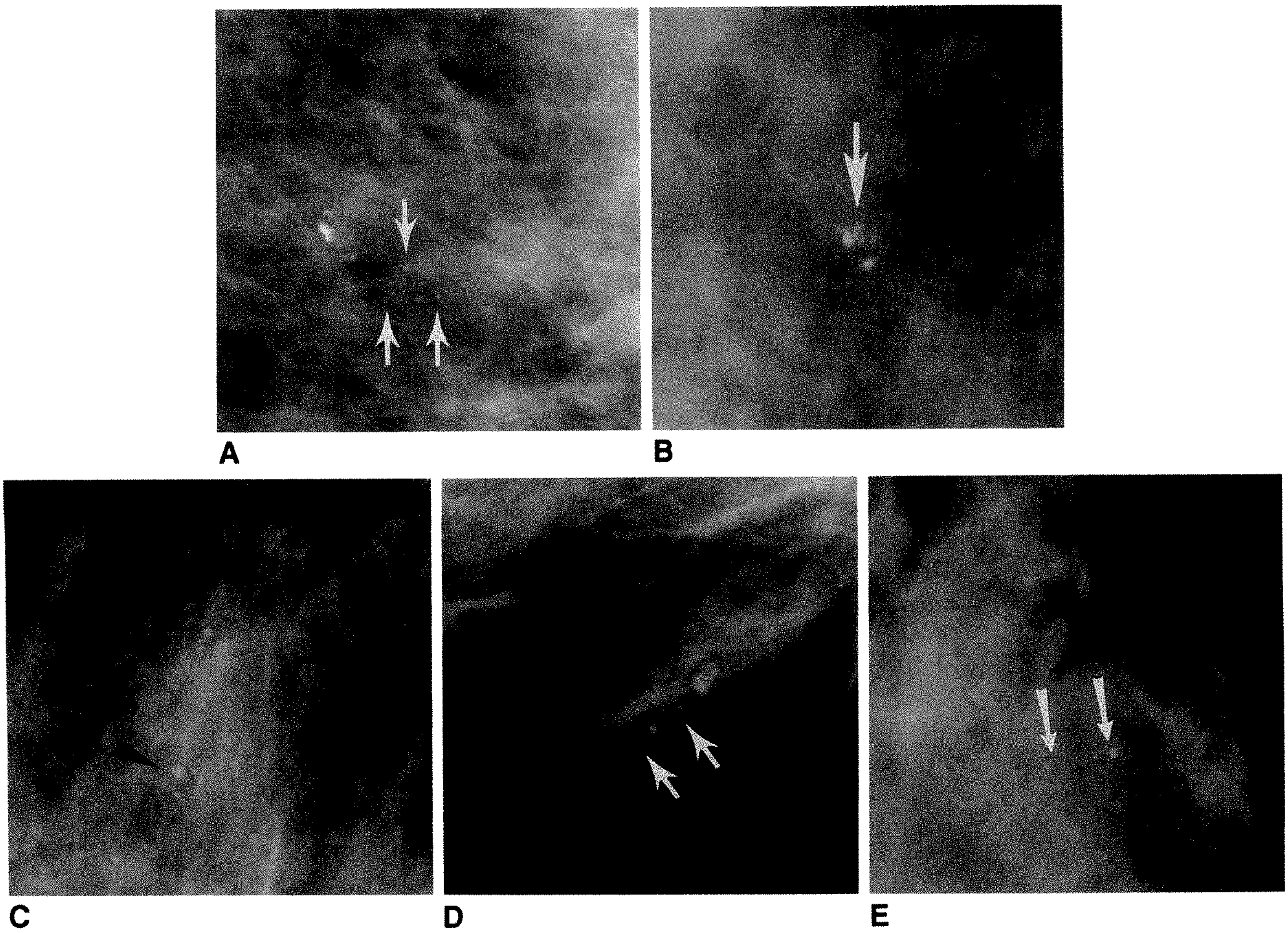

Fig. 3.—Microcalcifications.

A, Routine mammogram in asymptomatic 48-year-old woman showed left breast calcifications. Magnification film (×1.5) shows grouping of four punctate calcifications (*arrows*). Incidentally noted is a large, coarse calcification with contiguous faint calcifications, possibly representing degenerating fibroadenoma adjacent to group. Calcifications were unchanged at 4- and 12-month follow-up studies (*not shown*). Two years after initial study (*not shown*), calcifications were less apparent; 3 years after initial study, only a solitary dense calcification was seen in area of previous group.

B, Cluster of round calcifications (*arrow*) was found at baseline screening mammogram of a 39-year-old woman (magnification, ×1.5). Follow-up studies 4, 12, and 29 months later showed no change.

C, Group of punctate microcalcifications (*arrowheads*) in central right breast of a 66-year-old woman with a previous carcinoma in contralateral breast was unchanged over 4 years.

D, Despite some variation in size, relatively homogeneous and round or oval appearance of a cluster of microcalcifications (*arrows*) in the right breast of asymptomatic 50-year-old woman were radiologically followed up without interval change for 3½ years.

E, Several punctate calcifications (*arrows*) are seen in left breast of a 67-year-old woman in whom surgical biopsy had been recommended at another hospital. Mammographic follow-up was elected and calcifications remained stable for 3 years.

small rods were included. Hall et al. [25] found a 6% risk of malignancy for microcalcifications classified mammographically as minimally suggestive of malignancy, and follow-up rather than surgical excision was suggested for this group. Other investigators have advocated mammographic follow-up for calcifications with a round or cloudy appearance, because malignancy was found so infrequently in this setting that biopsy was not believed to be warranted [31].

Asymmetric Breast Tissue

A precise definition of this entity must be met for inclusion in this category. As described by Kopans et al. [32], the term is best used to identify an asymmetric volume of breast tissue, asymmetrically dense tissue without architectural distortion, and asymmetrically prominent ducts. Not to be considered in this group are developing densities, any suggestion of a mass, calcifications, or distortion. The prospective study of Kopans et al. of approximately 8400 mammograms found a 3% prevalence of asymmetric tissue. Less than 2% of the asymmetric cases followed up for at least 36 months proved to be malignant, and in no case was malignancy present when the physical examination was normal. On review of the mammographic features of 300 nonpalpable cancers, Sickles [33] found that only 3% were detected on the basis of an asymmetric density. Additional helpful mammographic criteria to separate benign asymmetric breast tissue from a significant true lesion include a relatively superficial location, lack of volumetric shape, and marked variation in appearance of the asymmetric tissue on different projections (Fig. 4) [34].

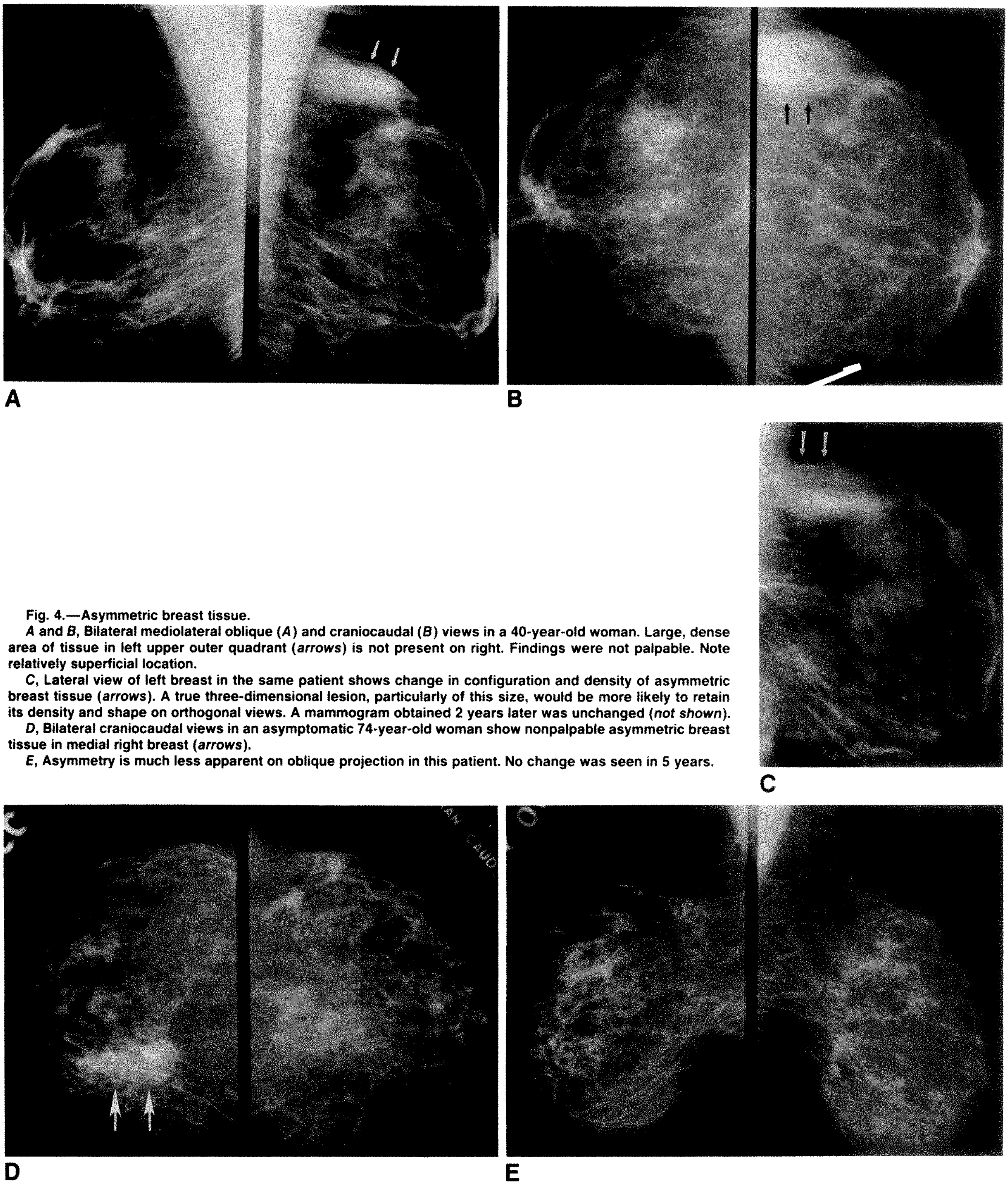

Fig. 4.—Asymmetric breast tissue.

A and *B*, Bilateral mediolateral oblique (*A*) and craniocaudal (*B*) views in a 40-year-old woman. Large, dense area of tissue in left upper outer quadrant (*arrows*) is not present on right. Findings were not palpable. Note relatively superficial location.

C, Lateral view of left breast in the same patient shows change in configuration and density of asymmetric breast tissue (*arrows*). A true three-dimensional lesion, particularly of this size, would be more likely to retain its density and shape on orthogonal views. A mammogram obtained 2 years later was unchanged (*not shown*).

D, Bilateral craniocaudal views in an asymptomatic 74-year-old woman show nonpalpable asymmetric breast tissue in medial right breast (*arrows*).

E, Asymmetry is much less apparent on oblique projection in this patient. No change was seen in 5 years.

Performing Mammographic Follow-up

Once it has been determined that a lesion has the features of one of the three categories described and radiologic follow-up is elected in lieu of surgical biopsy, a limited tailored examination can be performed at the designated time. Generally, this should require only unilateral examination of the involved breast, unless bilateral benign-appearing lesions are present. It is important that comparable examinations be performed to allow an accurate determination as to whether the finding remains stable over time (e.g., if magnification was used for better visualization, a magnification film in the same projection should be obtained at the follow-up examination). Similarly, if the lesion was seen only on a particular view such as the exaggerated craniocaudal view, no purpose is served initially in obtaining a standard craniocaudal view. The exception would be interval progression of the lesion, which would necessitate initiation of a complete diagnostic study of the breast in question.

Timing of the mammographic follow-up study has been based on estimates of mean tumor doubling time, recognizing that such estimates do not generally include very slowly or very rapidly growing tumors [35]. In one study, it was found that the majority of radiologists recommended initial follow-up at 3-6 months, irrespective of whether the abnormality was a mass, asymmetric density, or area of microcalcifications [36]. Over 50% of those polled followed up such lesions for a minimum of 2 years. Wolfe et al. [37] have advocated differentiating asymmetric densities and masses from calcifications, with the former reexamined at 3 months and the latter at 4-6 months. Moskowitz [16] has emphasized the importance of age, with a benign-appearing mass in a woman 40-49 years old followed up initially at 3 months, whereas the same mass in an older woman would first be reexamined at 6 months. There is general agreement that if the first follow-up study shows stability, the subsequent examination is performed 12 months after the original examination, at which time both breasts are imaged. Interval progression of the mammographic finding at any of these intervals usually prompts a surgical biopsy. Other factors that might sway the radiologist to recommend biopsy rather than follow-up include a previous personal history of breast cancer; strong family history; or a mass greater than 1 cm in diameter for which there is no specific cytology (e.g., fibroadenoma), particularly in a woman over 50 years of age. Ideally, mammographic follow-up of at least 2 years would be performed for lesions that are not excised, with the understanding that some cancers remain stable in size for several years [38].

Among 1356 lesions for which mammographic follow-up was recommended by Wolfe et al. [37], only 0.6% were cancers. We found similar results in a much smaller patient population [5], in which approximately 1% of lesions followed up with mammography in 144 women were found to be malignant.

Compliance with Periodic Follow-up Recommendations

In the 144 patients we studied for whom mammographic follow-up of a lesion was elected, diminishing compliance with the recommended follow-up was found with increasing time [5]. Eighty-eight percent of women returned for the 4-month study, 71% for the 12-month examination, 60% at 24 months, and 47% at 3 years. In order for mammographic follow-up to be a feasible alternative to surgical excision, compliance with the follow-up schedule must be addressed.

Problems encountered with compliance to mammographic screening guidelines on the part of both patients and their physicians are well known [9, 39, 40]. Lack of compliance is not unique to mammography. Noncompliance may be one of the most important issues facing medical practice [41]. Patient noncompliance is generally not detected unless specific efforts are made to determine adherence. Physicians may be unaware of the problem or its magnitude, and no easily identifiable patient characteristics distinguish those who will comply with recommendations from those who will not. Estimates of noncompliance with medication regimens have been reported to be as high as 92% for short-term medication and 50% for medication for chronic diseases [41]. Although numerous variables affect adherence to medical recommendations, among those shown to reduce compliance that would be applicable to mammographic follow-up are long duration (at least 2-3 years of follow-up needed), inconvenience (additional appointments required, particularly during first year), expense, and complexity of regimen (different from routine mammographic protocol, which may be familiar to the patient). Data have shown that physicians who have received additional training regarding issues of noncompliance spend more time on patient education, which ultimately results in better compliance [42]. Other mechanisms that have been used to improve compliance with mammography include reminder postcards [43] and increased involvement by women themselves, accomplished by sending the patient a copy of her report [44].

Conclusions

Once careful mammographic evaluation has identified a nonpalpable lesion meeting the criteria previously described and thereby carrying a high probability of benignity, radiologic follow-up can be considered a reasonable alternative to surgical biopsy. Any lesion not meeting these criteria and for which there is a suggestion of malignancy should undergo biopsy without delay. Noninvasive management is recommended with the expectation that the lesion is probably benign. Should a progressive change occur, however, intervention—frequently in the form of a surgical biopsy—should be recommended. Such an approach can be undertaken with the understanding on the part of both the patient and her physician that only excision with complete pathologic study can provide definitive information regarding the cause of the lesion. With few exceptions, absolute 100% assurance of benignity based on the mammographic appearance generally is not possible. Data from published series, and most importantly from one's own practice, however, can provide reasonable supportive information to make such an option feasible. Finally, patient compliance with the recommended follow-up is critical to the success of this alternative management approach.

REFERENCES

1. Feig SA. Decreased breast cancer mortality through mammographic screening: results of clinical trials. *Radiology* **1988**;167:659-665
2. Homer MJ. Imaging features and management of characteristically benign and probably benign lesions. *Radiol Clin North Am* **1987**;25:939-951
3. Brenner RJ, Sickles EA. Acceptability of periodic follow-up as an alternative to biopsy for mammographically detected lesions interpreted as probably benign. *Radiology* **1989**;171:645-646

4. Hall FM. Follow-up as an alternative to biopsy for mammographically detected lesions interpreted as probably benign. *Radiology* **1989**;173: 284-285
5. Helvie MA, Pennes DR, Rebner M, Adler DD. Mammographic follow-up of low-suspicion lesions: compliance rate and diagnostic yield. *Radiology* (in press)
6. Norton LW, Zeligman BE, Pearlman NW. Accuracy and cost of needle localization breast biopsy. *Arch Surg* **1988**;123:947-950
7. Rebner M, Helvie MA, Pennes DR, Oberman HA, Ikeda DA, Adler DD. Paraffin tissue block radiography: adjunct to breast specimen radiography. *Radiology* **1989**;173:695-696
8. Cyrlak D. Induced costs of low-cost screening mammography. *Radiology* **1988**;168:661-663
9. 1989 Survey of physicians' attitudes and practices in early cancer detection. *CA* **1990**;40:77-101
10. O'Leary TJ, deParedes ES, Tritschler J, Barr M. Utilization of screening mammography by primary care physicians. *Appl Radiol* **1989**;18:28-33
11. Bassett LW, Bunnell DH, Cerny JA, Gold RH. Screening mammography: referral practices of Los Angeles physicians. *AJR* **1986**;147:689-692
12. Wright CJ. Breast cancer screening: a different look at the evidence. *Surgery* **1986**;100:594-598
13. Meyer JE, Sonnenfeld MR, Greenes RA, Stomper PC. Preoperative localization of clinically occult breast lesions: experience at a referral hospital. *Radiology* **1988**;169:627-628
14. Ciatto S, Del Turco MR, Bravetti P. Nonpalpable breast lesions: stereotaxic fine-needle aspiration cytology. *Radiology* **1989**;173:57-59
15. Meyer JE, Sonnenfeld MR, Greenes RA, Stomper PC. Cancellation of preoperative breast localization procedures: analysis of 53 cases. *Radiology* **1988**;169:629-630
16. Moskowitz M. Impact of a priori medical decisions on screening for breast cancer. *Radiology* **1989**;171:605-608
17. Brenner RJ. Medicolegal aspects of screening mammography. *AJR* **1989**;153:53-56
18. Baker LH. Breast cancer detection demonstration project: five-year summary report. *CA* **1982**;42:4-35
19. Nielsen M, Thomsen JL, Primdahl S, Dyreborg U, Anderson JA. Breast cancer and atypia among young and middle-aged women: a study of 110 medicolegal autopsies. *Br J Cancer* **1987**;56:814-819
20. Sickles EA. Magnification mammography. In: Feig SA, McLelland R, eds. *Breast carcinoma: current diagnosis and treatment*. New York: Masson, **1983**:177-182
21. Berkowitz JE, Gatewood OMB, Gayler BW. Equivocal mammographic findings: evaluation with spot compression. *Radiology* **1989**;171:369-371
22. Logan WW, Janus J. Use of special mammographic views to maximize radiographic information. *Radiol Clin North Am* **1987**;5:953-959
23. Moskowitz M. The predictive value of certain mammographic signs in screening for breast cancer. *Cancer* **1983**;51:1007-1011
24. Kopans DB, Swann CA. Observations on mammographic screening and false-positive mammograms. *AJR* **1988**;150:785-786
25. Hall FM, Storella JM, Silverston DZ, Wyshak G. Nonpalpable breast lesions: recommendations for biopsy based on suspicion of carcinoma at mammography. *Radiology* **1988**;167:353-358
26. Hann L, Ducatman BS, Wang HH, Fein V, McIntire JM. Nonpalpable breast lesions: evaluation by means of fine-needle aspiration cytology. *Radiology* **1989**;171:373-376
27. Löfgren M, Andersson I, Bondeson L, Lindholm K. X-ray guided fine-needle aspiration for the cytologic diagnosis of nonpalpable breast lesions. *Cancer* **1988**;61:1032-1037
28. Helvie MA, Baker DE, Adler DD, Andersson I, Naylor B, Buckwalter KA. Radiographically guided fine-needle aspiration of nonpalpable breast lesions. *Radiology* **1990**;174:657-661
29. Lanyi M. Historical review, critical analysis of the literature, statement of problem and goals. In: Diagnosis and differential diagnosis of breast calcifications. New York: Springer-Verlag, **1986**:1-14
30. Sickles EA. Breast calcifications: mammographic evaluation. *Radiology* **1986**;160:289-293
31. Sigfusson BF, Andersson I, Aspegren K, Janson L, Linell F, Ljungberg O. Clustered breast calcifications. *Acta Radiol* **1983**;24:273-281
32. Kopans DB, Swann CA, White G, et al. Asymmetric breast tissue. *Radiology* **1989**;171:639-643
33. Sickles EA. Mammographic features of 300 consecutive nonpalpable breast cancers. *AJR* **1986**;146:661-663
34. Homer MJ, Doherty F. Evaluation and management of the solitary asymmetric breast density. *Breast Dis* **1989**;2:175-186
35. Fournier DV, Weber E, Hoeffken W, Bauer M, Kubli F, Barth V. Growth rate of 147 mammary carcinomas. *Cancer* **1980**;45:2198-2207
36. Homer MJ. Nonpalpable mammographic abnormalities: timing the follow-up studies. *AJR* **1981**;136:923-926
37. Wolfe JN, Buck KA, Salane M, Parekh NJ. Xeroradiography of the breast: overview of 21,057 consecutive cases. *Radiology* **1987**;165:305-311
38. Meyer JE, Kopans DB. Stability of a mammographic mass: a false sense of security. *AJR* **1981**;137:595-598
39. Rimer BK, Keintz MK, Kessler HB, Engstrom PF, Rosan JR. Why women resist screening mammography: patient-related barriers. *Radiology* **1989**;172:243-246
40. Fox SA, Klos DS, Tsou CV. Underuse of screening mammography by family physicians. *Radiology* **1988**;166:431-433
41. Eraker SA, Kirscht JP, Becker MH. Understanding and improving patient compliance. *Ann Intern Med* **1984**;100:258-268
42. Inui TS, Yourtee EL, Williamson JW. Improved outcomes in hypertension after physician tutorials: a controlled trial. *Ann Intern Med* **1976**;84:646-651
43. Bird RE, McLelland R. How to initiate and operate a low-cost screening mammography center. *Radiology* **1986**;161:43-47
44. Monsees B, Destouet JM, Evens RG. Communication problems after mammographic screening (letter). *Radiology* **1990**;175:877-878

Book Review

Primer of Medical Radiobiology, 2nd ed. By Elizabeth LaTorre Travis. Chicago: Year Book Medical, 302 pp., 1989. $29.25, softcover

This second edition of *Primer of Medical Radiobiology* is well written and deserves attention. Since the first edition in 1976, considerable advances in the radiation sciences have occurred, and, correctly, the author has either expanded previous material or added completely new information. She describes her book as a primer, and that is exactly what it is. It has 10 self-contained chapters, and each patiently introduces basic material to prepare the reader for the radiation science to follow. Chapter 1 deals with cells and cell populations and introduces the fundamental biological material that is needed to begin an odyssey in clinical radiobiology. This chapter is timely, although the list of references, which is short, appears somewhat dated. Chapter 2 concentrates on the basic radiobiological response of cells and introduces some limited material on physics and radiation chemistry. The sections on effects on DNA and chromosomes are clear and uncluttered, and the line drawings are helpful. Chapter 3 begins a discussion of the cellular response to irradiation, particularly the response of cultured mammalian cells. The graphs of the survival curves are adequate, and the reference list is satisfactory.

Chapter 4 discusses tissue radiation biology. The early work of Bergonie and Tribondeau through to the current trends of Withers functional clongenic assay systems in vivo are reviewed. Chapter 5 is the major part on radiation effects, cell and tissue responses, and the factors that modify cell and tissue responses. Physical and chemical factors, sensitizers and protectors, and biological factors are reviewed. The text is sufficient to bring the information together as a whole. Attractively, this chapter deals solely with experimental results and their interpretation; the reader is required to think. The graphs and illustrations are good. The references may be too numerous. Chapter 6 deals with radiation pathology. In this chapter, the author has had some difficulty bringing the wealth of material together. Although the underlying processes of acute radiation injury in the various organs and tissues of the body are described, the obvious practical applications (e.g., pathologic changes in normal tissue caused by radiation therapy) are not included.

Chapter 7 satisfactorily discusses whole-body irradiation and tissue response in adults, embryos, and fetuses. Perhaps too much emphasis is placed on the older high-dose animal experiments and not enough on the current observations in humans. Chapter 8 deals with the late effects of radiation, primarily cancer and genetic disorders induced by exposure to low-dose radiation. This chapter has too many references to the older literature and not enough to the current reports. Although all the bases are covered, the importance of this chapter with regard to matters that affect societal concerns, low-level radiation, nuclear energy, and medical radiation cannot be underestimated. I hope this chapter is expanded in the next edition. Chapter 9 deals with human radiobiology and diagnostic medical radiation. It introduces concepts of radiologic protection and dose limitation and will be helpful to new radiologists and radiologic technologists who must find their way through the maze of information relevant to their work. Chapter 10 deals with human radiobiology and therapeutic radiology. This is one of the best chapters. Its high level challenges the reader, and it is a good way to end the book. Finally, the glossary and index are done well and add to the value of the primer.

In all, Dr. Travis has written a good introductory text that is readable, clearly compiled, lucid, and digestible. The illustrations are satisfactory; however, the photomicrographs are not well reproduced. The book covers all the highlights of cell and tissue radiobiology and does it well. However, it needs more emphasis on current information on the late effects of irradiation and on the philosophy supporting radiation protection. The book deserves the attention of the new radiologist, physician, graduate student, or allied health scientist who is interested in understanding enough radiobiology to have a solid foundation in clinical radiology and radiologic protection.

Jacob I. Fabrikant
University of California, Berkeley
Berkeley, CA 94720

Case Report

Mammographic Appearance of the Retained Dacron Cuff of a Hickman Catheter

Gary A. Beyer,[1] M. Kristin Thorsen,[1] Katherine A. Shaffer,[1] and Alonzo P. Walker[2]

Central venous catheters, including Hickman catheters, are being inserted with increasing frequency. These catheters have multiple uses, including administration of chemotherapeutic agents or antibiotics, parenteral nutrition, and venous access for maintenance fluids. We describe the appearance of the retained Dacron cuff after removal of a Hickman catheter. This foreign body may cause a density on mammography and may be palpable on physical examination, prompting additional films or an unnecessary biopsy.

Case Report

Mammograms of the right breast were obtained in a 63-year-old woman who had had a left modified radical mastectomy 2 years before because of stage III breast carcinoma. Two weeks after her mastectomy, a Hickman catheter was inserted for infusion of chemotherapeutic agents. One year after mastectomy, the carcinoma recurred in the chest wall and was treated with radiation therapy. The Hickman catheter was removed 2 months before the current mammogram was obtained. On physical examination of the breast, a hard, fixed nodule was palpated in the upper inner quadrant of the right breast. Mammograms of the right breast showed a rectangular increased density in the upper inner quadrant with some surrounding soft-tissue density, which represented the retained Dacron cuff from the Hickman catheter that had been removed (Fig. 1).

Discussion

In a 2-year period, during routine mammographic screening, we saw 10 patients who had a retained Dacron cuff after removal of a Hickman catheter. Hickman catheters are constructed of silicone and have a proximal Dacron felt cuff that anchors the catheter to the subcutaneous tissue (Fig. 2). Hickman catheters are used for long-term venous access and are placed by using a cutdown technique [1, 2]. Hickman catheters commonly are inserted into either the cephalic vein at the deltopectoral groove (preferred site) or the axillary subclavian vein. A subcutaneous tunnel is made over the medial aspect of the chest. The catheter is threaded through the vertical tunnel to its venous entry point at the level of the cutdown site. Subcutaneous tunnels are 4–6 in. (10–15 cm) long, and the Dacron cuff rests approximately midway between the catheter exit point and the venous entry point. The Dacron felt cuff anchors the catheter to the subcutaneous tissue and provides a physical barrier to infection [3]. Intercostal positioning of the cuff is desired, because it makes the cuff less conspicuous [1]. Ideally, the distal tip of the catheter should be positioned in the right atrium. Hickman catheters are removed by applying a constant, steady pressure, stretching the line until it is freed and can be withdrawn easily [3].

Dacron cuffs elicit a fibrous reaction in the surrounding tissue, making simultaneous removal of cuff and catheter difficult [3]. Therefore, the cuff often is left behind. This has no clinical significance unless the cuff is infected. Dacron cuffs are approximately 7 × 5 mm and are cylindrical. The CT appearance of the Dacron cuff has been previously described [4]. On physical examination, these cuffs are palpable, firm, and often fixed. The patient's medical history and the presence of a cutaneous scar from the exit port for a Hickman catheter are clues to the origin of the palpable lesion.

Mammographically, the Dacron cuffs characteristically are located in the upper inner quadrant, usually on the right side, less commonly on the left side. The density of the cuff is between the densities of water and calcium. Soft-tissue struc-

---

Received April 9, 1990; accepted after revision May 21, 1990.

[1] Department of Radiology, Medical College of Wisconsin, Milwaukee County Medical Complex, 8700 W. Wisconsin Ave., Milwaukee, WI 53226. Address reprint requests to M. K. Thorsen.

[2] Department of Surgery, Medical College of Wisconsin, 8700 W. Wisconsin Ave., Milwaukee, WI 53226.

AJR 155:1203–1204, December 1990 0361–803X/90/1556–1203 © American Roentgen Ray Society

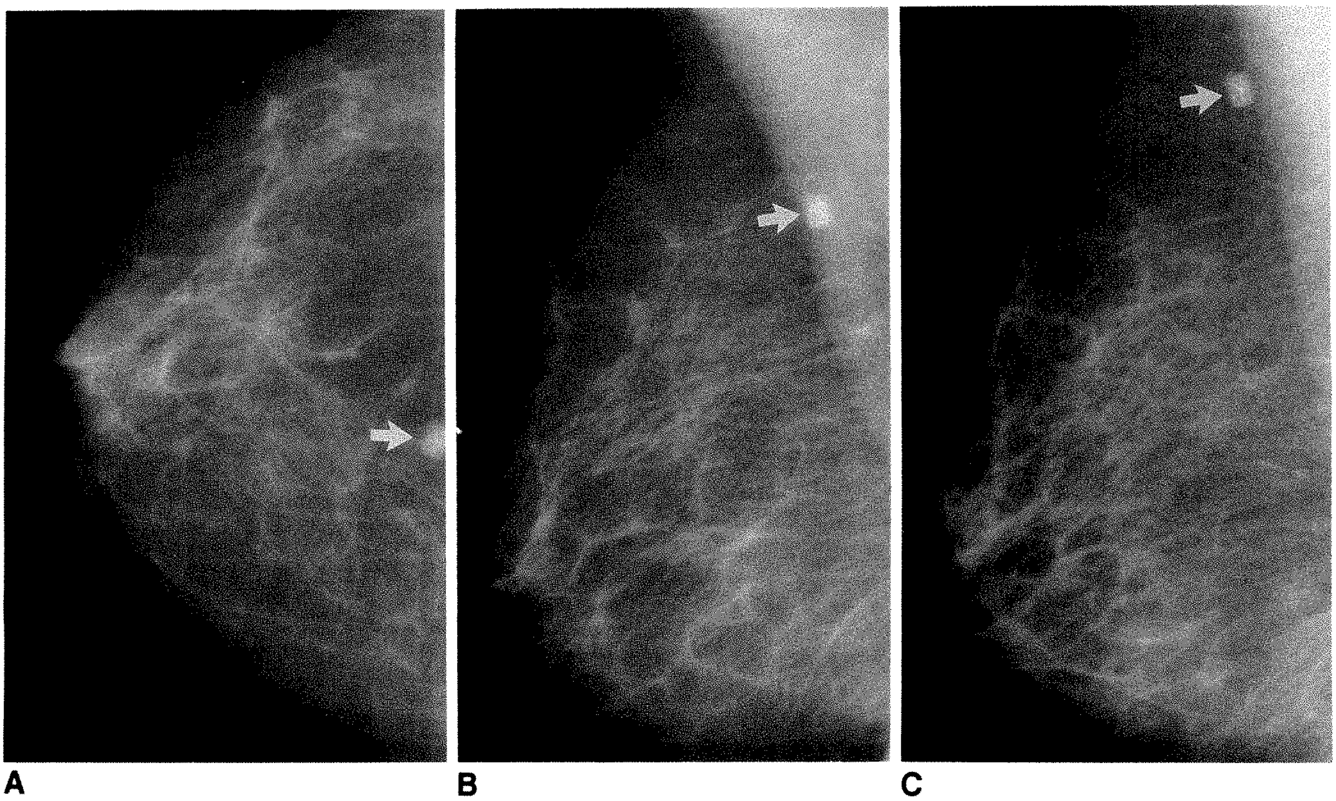

Fig. 1.—*A–C*, Craniocaudal (*A*), mediolateral oblique (*B*), and lateral (*C*) mammograms of right breast show retained Dacron cuff in upper inner quadrant (*arrows*) and an associated soft-tissue density adjacent to cuff, which most likely represents fibrosis.

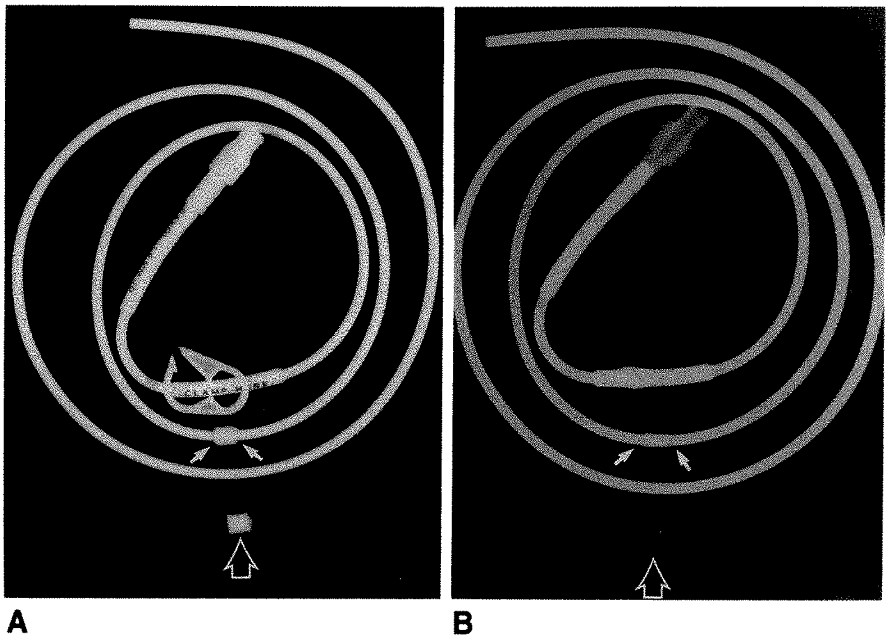

Fig. 2.—*A* and *B*, Photograph (*A*) and radiograph (*B*) show Hickman catheter with Dacron cuff in normal position (*arrows*) and cuff after removal from catheter (*open arrows*).

tures and glandular tissue can be seen through the cuff. An associated soft-tissue density that surrounds the cuff most likely represents fibrosis. The cuff may appear crenated and often has stellate soft-tissue strands extending from its periphery into surrounding tissue. This constellation of findings may be quite confusing to the uninformed interpreter. However, with a good history and physical examination, as well as knowledge of the radiologic appearance, a retained Dacron cuff should be distinguished easily from a neoplastic process.

REFERENCES

1. Heimbach DM, Ivey TD. Technique for placement of a permanent home hyperalimentation catheter. *Surg Gynecol Obstet* **1976**;143:634–636
2. Hickman RO, Buckner CD, Clift RA, Sanders JE, Stewart P, Thomas ED. A modified right atrial catheter for access to the venous system in marrow transplant recipients. *Surg Gynecol Obstet* **1979**;148:871–875
3. Bjeletich J, Hickman RO. The Hickman indwelling catheter. *Am J Nurs* **1980**;80:62–65
4. Fernandez GC, Coblentz CL, Cooper C, Sallee DS. Hickman nodule: a mimic of metastatic disease. *Radiology* **1989**;171:401–402

Pictorial Essay

Gastrointestinal Lipomas: A Radiologic and Pathologic Review

Andrew J. Taylor,[1] Edward T. Stewart, and Wylie J. Dodds

Lipomas of the gastrointestinal tract are an infrequent finding on radiologic examination; however, they occur often enough to warrant consideration in the differential diagnosis of mass lesions of the gut. In many instances, their morphologic characteristics allow the specific diagnosis of a lipoma. In this report, we review gastrointestinal lipomas with an emphasis on their radiologic and pathologic correlation.

General Considerations

Lipomas of the gastrointestinal tract are uncommon, slow growing, fatty tumors that can occur anywhere along the gut. Although generally single, they may be multiple. Peak occurrence is in the fifth to seventh decade of life, with a slight female preponderance. The tumor itself is composed of well-differentiated adipose tissue surrounded by a fibrous capsule. The cut surface is yellow and lobulated with a gross appearance of subcutaneous fat (Fig. 1D).

Approximately 90% to 95% of lipomas are located in the submucosa; the remaining 5% to 10% are subserosal [1]. Because of its usual position immediately superficial to the muscularis propria, underlying muscular contractions tend to draw the tumor into the bowel lumen, forming an intraluminal polyp on a pseudopedicle (Figs. 2A, 3B, 4A).

Lipomas usually are found incidentally during an examination done for another reason (Fig. 5). The size and location of the lipoma and the mobility afforded by the pseudopedicle, when present, account for the clinical signs and symptoms produced. Lesions larger than 2 cm may produce abdominal pain, intussusception, diarrhea, constipation, or gastrointestinal blood loss [1, 2]. The gastrointestinal blood loss is usually chronic and can cause anemia [1]. Acute hemorrhage, however, can occur and usually is caused by ulceration of the overlying mucosa (Figs. 6C, 3E) or possibly intussusception (Figs. 1B, 3A).

Diagnosis

Endoscopy

Endoscopy and radiology play a major role in the diagnosis of lipomas. Endoscopy relies on the gross appearance of the mass to suggest the correct diagnosis. A smooth-surfaced mass that may vary from red-orange to yellow suggests the diagnosis of lipoma (Fig. 7C). Various maneuvers are used to confirm the diagnosis: (1) The "tenting" sign consists in grasping the mucosa with forceps and pulling or "tenting" it away from the underlying mass. (2) The "cushion" sign reflects the spongy nature of the mass when indented with a closed forceps. (3) The "naked fat" sign is produced when fat protrudes from the mass after multiple biopsies remove the overlying mucosa. A lipoma occasionally can be lobulated or have an apical ulceration (Fig. 3D). At times, ulceration can be fairly extensive, (Fig. 1C), leading to the false impression of a more aggressive lesion.

Received May 21, 1990; accepted after revision July 2, 1990.

[1] All authors: Department of Radiology, The Medical College of Wisconsin, Milwaukee, WI 53226. Address reprint requests to A. J. Taylor, Department of Radiology, Froedtert Memorial Lutheran Hospital, 9200 W. Wisconsin Ave., Milwaukee, WI 53226.

AJR 155:1205-1210, December 1990 0361-803X/90/1556-1205 © American Roentgen Ray Society

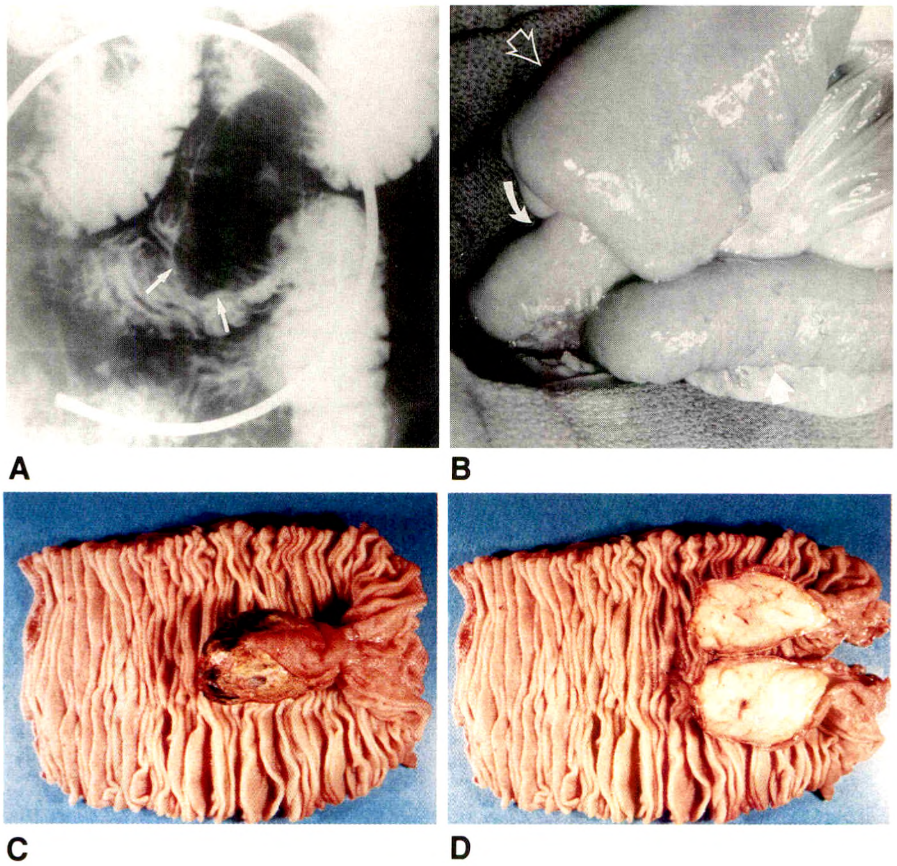

Fig. 1.—Small-bowel lipoma. A 39-year-old man had a 1-week history of increasing, intermittent, crampy epigastric pain. He had been followed up for 5 years because of a low hematocrit and guaiac-positive stools, thought to be a result of "runner's anemia."

A, On small-bowel series, a 3 × 4 cm polypoid mass was seen just distal to ligament of Treitz. At fluoroscopy, there was intermittent intussusception. Note subtle irregularity of mass, particularly at its apex (*arrows*).

B, At surgery, intussusception of jejunum was found. Point of intussusception (*curved arrow*) is seen between dilated jejunum proximally (*open arrow*) and normal caliber of jejunum just distally (*straight solid arrow*).

C, Resected specimen shows marked irregularity of mucosal surface due to healing of overlying ulcerated and necrotic mucosa.

D, Bivalved specimen shows fatty internal architecture of a lipoma.

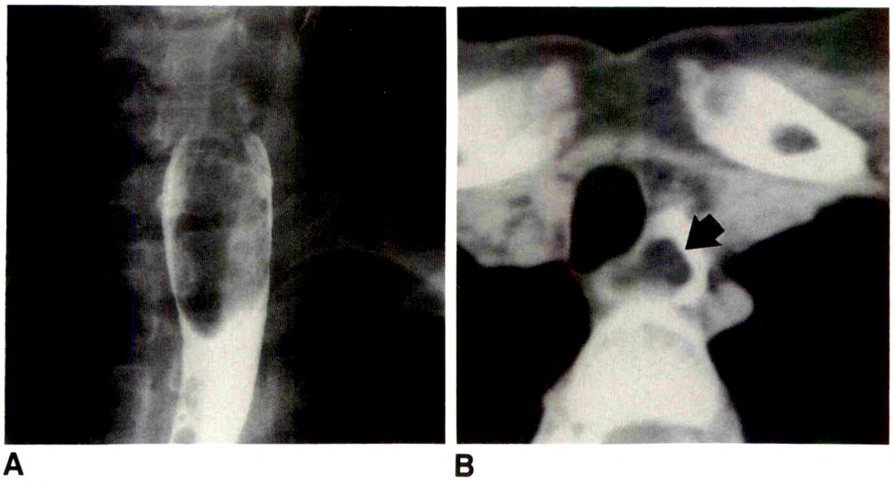

Fig. 2.—Esophageal lipoma. A 50-year-old woman had intermittent dysphagia. (Courtesy of J. Lammers, Brookfield, WI).

A, Anteroposterior view from an esophagogram shows a large, smooth, mobile, pedunculated polyp in upper esophagus.

B, Subsequent CT scan shows homogeneous internal architecture of mass (*arrow*) with an attenuation similar to that of subcutaneous fat. These findings are diagnostic of a lipoma, which subsequently was proved by surgery. Lipoma had its origin just distal to cricoid cartilage.

Radiology

Increased sophistication of radiologic studies now enables lipomas larger than 2 cm to be diagnosed with a high degree of accuracy [2]. The classic findings of a sharply marginated, smooth, ovoid or spherical mass with compressibility on fluoroscopic examination are supportive evidence of a lipoma (Figs. 7A and 7B). Other findings seen during studies follow directly from the gross appearance of lipoma wherein lobulation and ulceration can be seen (Fig. 6A). However, with the use of a positive-contrast examination, it is only rarely possible to discern the relative low density of a mass when outlined by barium (Fig. 5). The imaginative water enema, developed to circumvent this problem (Fig. 8), has fallen from favor with the advent of newer imaging techniques.

CT, in the properly prepared patient, is able to take advantage of the fat content, thereby identifying a mass as a lipoma. CT examination is now an appropriate first step for a definitive

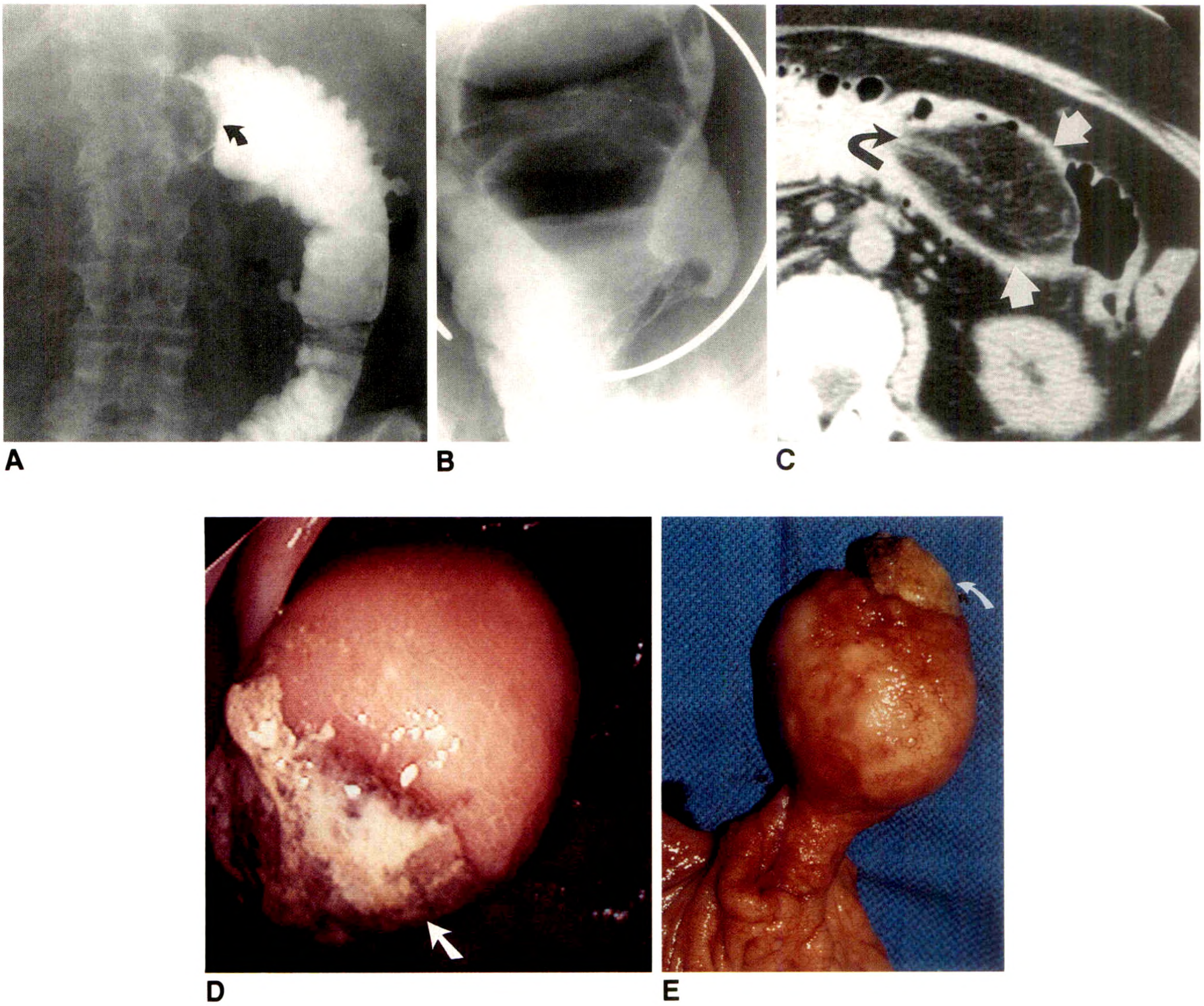

Fig. 3.—Colonic lipoma. A 67-year-old woman with 2-year history of vague pain in right lower quadrant had a recent change in bowel habits. She was having three to four loose stools each day and associated crampy pain and blood.

A, Single-contrast barium enema shows a colonic intussusception with tip of intussusceptum (*arrow*) at tip of distal transverse colon.

B, On reduction of intussusception during barium enema, a large mass with a wide stalk is seen originating from ileocecal valve.

C, CT scan shows mass (*straight arrows*) intussuscepted to distal transverse colon once again. Low attenuation value of mass is compatible with fat. Note central linear strand of higher attenuation material at base of mass (*curved arrow*).

D, At colonoscopy, a large pinkish-orange mass capped with an ulcer (*arrow*) is seen.

E, Surgical specimen shows a 6 × 5 × 4 cm mass with a broad-based pseudostalk and a large superficial ulcer at apex of mass (*arrow*). Note discolored fat protruding through ulcer.

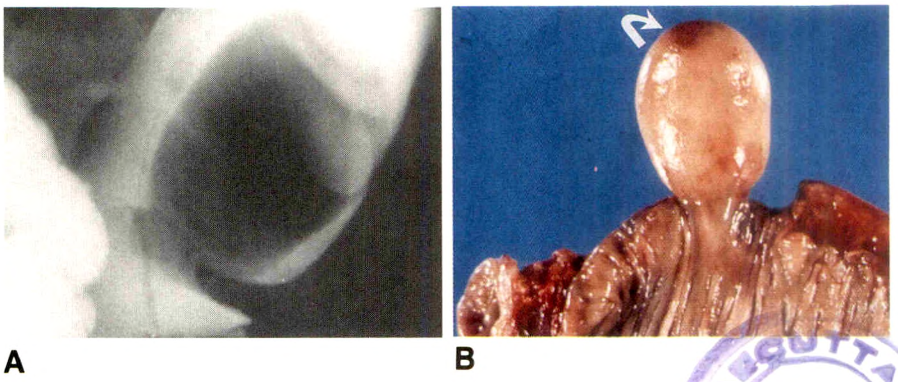

Fig. 4.—Lipoma of sigmoid colon. A 36-year-old woman had a 2-day history of crampy pain in left lower quadrant. She recently had passed bright red blood per rectum.

A, Anteroposterior view of sigmoid colon from a single-contrast barium enema shows an oval, well-circumscribed mass with a short, thick pedicle.

B, Surgical specimen shows a lipoma with superficial ulceration at apex (*arrow*).

CALCUTTA CENTRAL

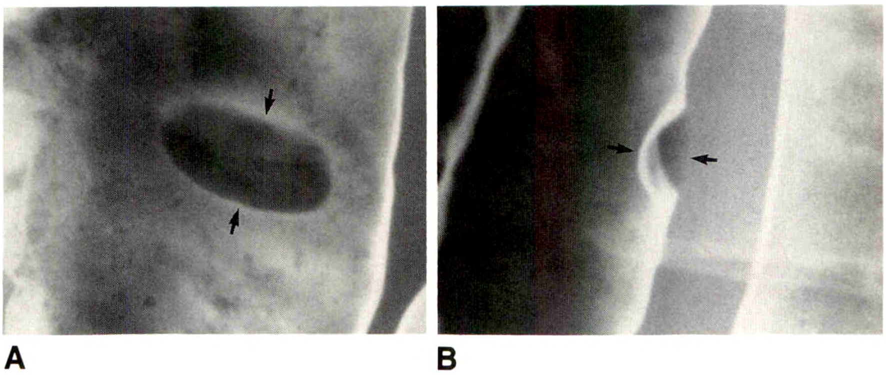

Fig. 5.—Small incidental colonic lipoma. A 27-year-old man had bright red blood per rectum.

A, Anteroposterior coned-down view from a double-contrast barium enema shows sessile mass (*arrows*) in distal transverse colon. Mass was 1.0 × 2.5 cm, smooth and oval, with a very low density.

B, A lateral view of same bowel segment shows mass in profile (*arrows*). Better visualized in this view is low density of mass, which is compatible with fat. Patient had endoscopy to locate source of bleeding: an anal fissure. Lipoma was not seen.

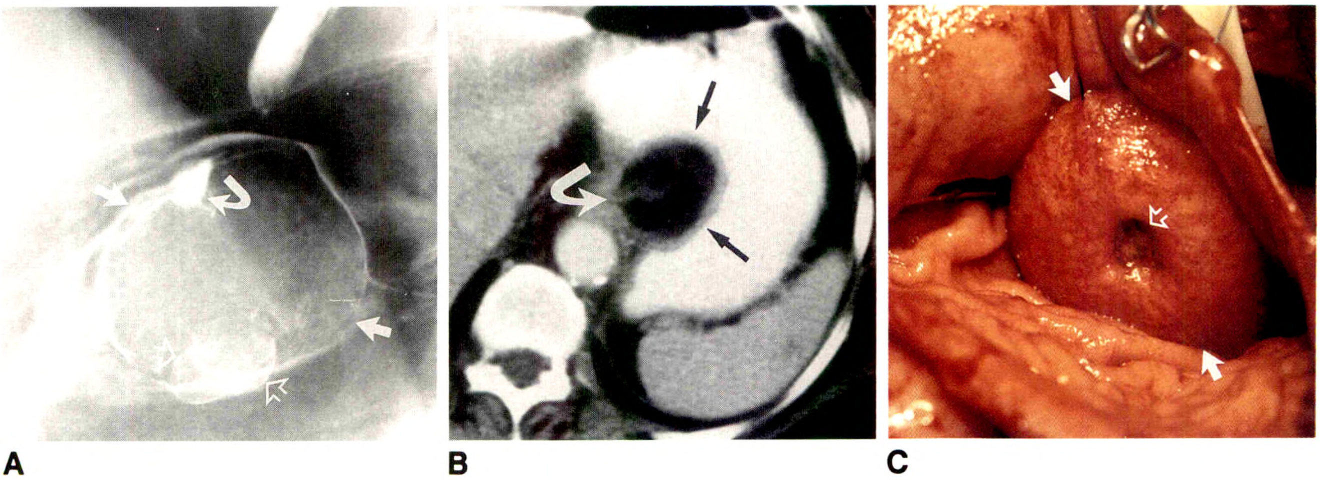

Fig. 6.—Gastric lipoma. An 83-year-old woman had a 2-week history of melena and decreasing hematocrit, necessitating transfusion of 5 units of blood.

A, Upper gastrointestinal examination shows a relatively smooth gastric mass (*straight solid arrows*) with an ulcer (*curved arrow*), and a lobulation off side of mass (*open arrows*).

B, CT scan shows a mass (*straight arrows*) of fatty internal architecture, −50 HU, with a curvilinear density (*curved arrow*) extending into fat from base of mass.

C, At surgery, mass (*solid arrows*) shows an ulcer (*open arrow*).

diagnosis of a lipoma. The finding of a homogeneous mass with Hounsfield units between −80 and −120 is nearly pathognomonic for a lipoma (Fig. 2B). Heiken et al. [2] reported that lipomas seen on CT did not have nonfatty elements. However, in two of our cases (Figs. 3, 6), linear strands of soft-tissue attenuation were shown at the base of the lipomas (Figs. 3C, 6B). Both of these tumors had an associated ulcer. On pathologic examination, these strands seen on CT correlated with prominent fibrovascular septa, which are normally microscopic. These septa presumably enlarged from drainage of the inflammation associated with an ulcer. We therefore suggest that the presence of basilar strands of nonfatty elements in an otherwise uniform fatty tumefaction would qualify the lesion as a benign lipoma, probably containing an ulcer. This pattern should not be mistaken for a liposarcoma, which is extremely rare in the alimentary tract [2].

Location Within Alimentary Tract

Pharynx and Esophagus

Lipomas may develop in the pharynx or in the esophagus, although these are the least common areas of involvement in the alimentary tract. Pharyngeal involvement is usually in the hypopharynx. The lipoma commonly takes its origin from structures lying between and including the aryepiglottic folds to the pyriform sinuses [3]. Of the pedunculated pharyngeal polyps, the simple lipoma is relatively uncommon compared with the more frequent fibrolipoma [4]. The potential mobility of a hypopharyngeal lipoma and its location at the bifurcation of the aerodigestive tract accounts for the signs and symptoms of dysphagia, fullness in the throat, change in voice, sudden episodic attacks of dyspnea, and sleep apnea (Fig. 7)

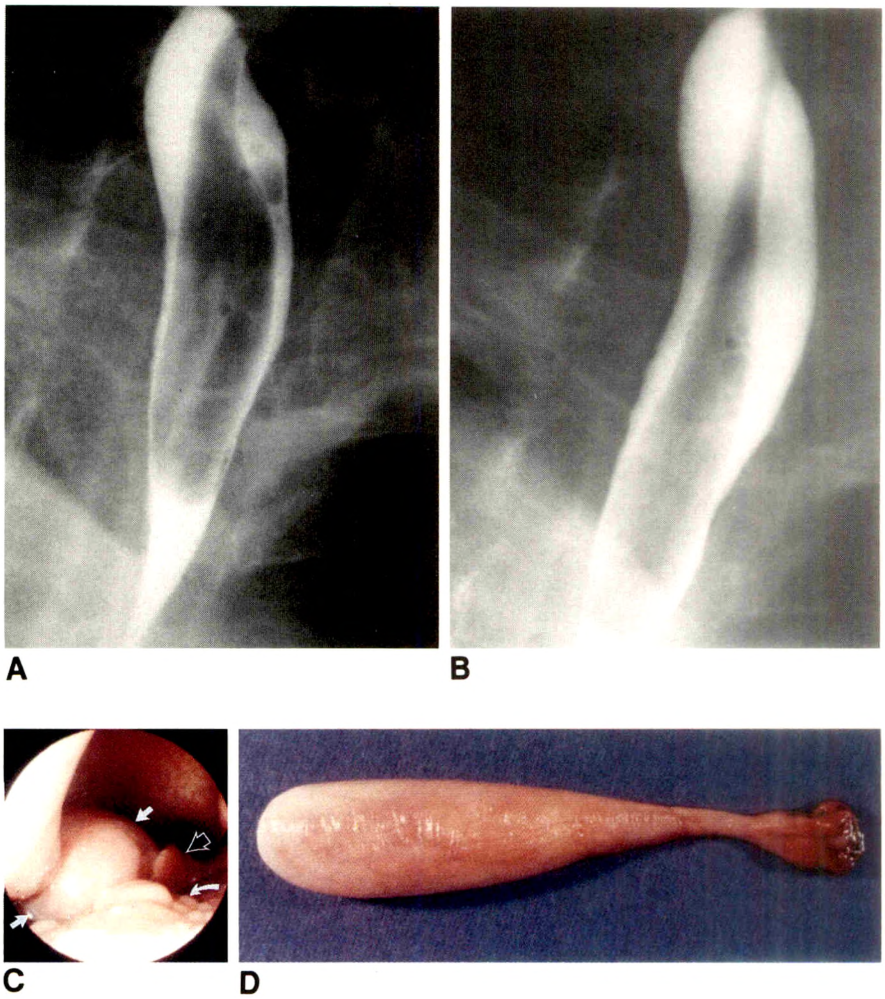

Fig. 7.—Lipoma of hypopharynx. A 66-year-old man had an 18-month history of dysphagia and episodic paroxysms of cough.

A, Oblique view from an esophagogram shows a smooth, pedunculated 7-cm mass that appears to emanate from hypopharynx. (Reprinted with permission from Olson et al. [4].)

B, Immediately after a swallow, mass elongates. In this case, intrinsic peristalsis of viscus shows compliance of mass. This phenomenon is referred to as "autopalpation." (Reprinted with permission from Olson et al. [4].)

C, Image from pharyngeal endoscopy shows a smooth pinkish-orange mass (*straight solid arrows*) in left pyriform sinus. (*Open arrow* = free edge of epiglottis, *curved arrow* = base of tongue).

D, Gross specimen shows mass has a pseudostalk.

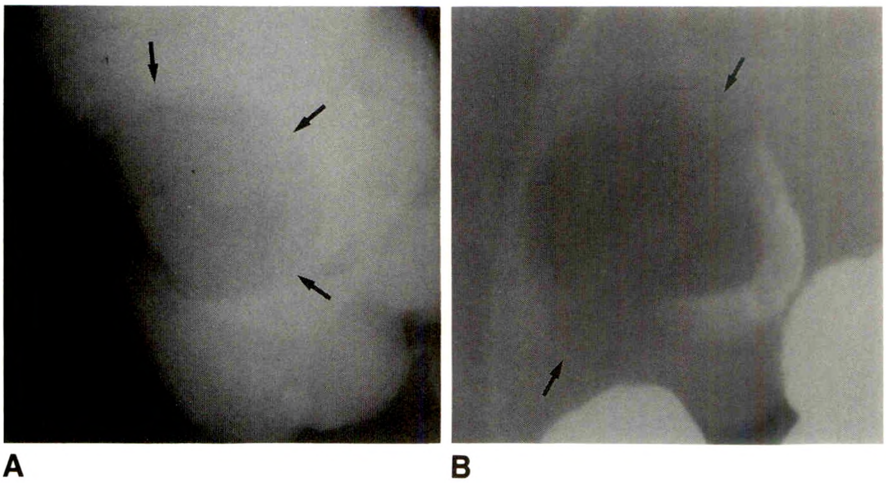

Fig. 8.—Lipoma shown by water enema.

A, Initial single-contrast barium enema shows a smooth mass (*arrows*) opposite ileocecal valve.

B, Subsequent enema with water shows mass (*arrows*) is lucent compared with surrounding water. This finding is compatible with a lipoma, which subsequently was proved at surgery. (Barium-filled appendix projects over part of lipoma).

[4]. In some cases, the polyp may prolapse into the esophagus (Figs. 7A, 7B) and be mistaken for a mass of esophageal origin.

Of benign esophageal tumors, the sessile leiomyoma is most frequent; the fibrovascular polyp is the most common pedunculated esophageal polyp [4]. The lipoma is next in frequency, generally arising from the upper one third of the esophagus near the level of the cricoid cartilage (Fig. 2) [4].

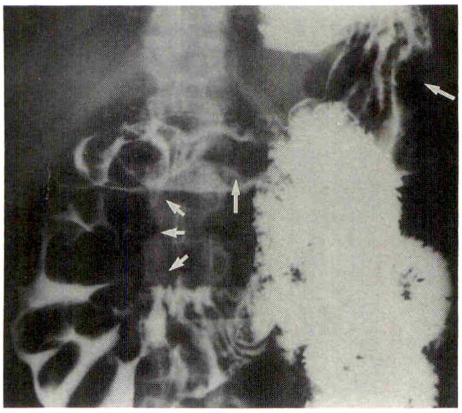

9

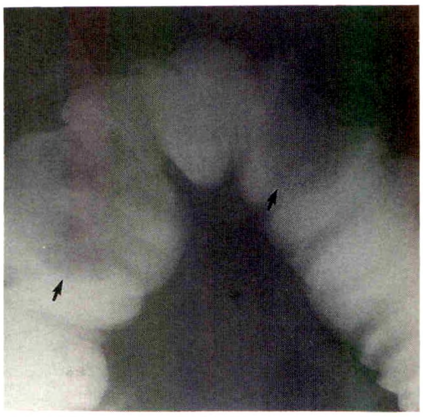

10

Fig. 9.—Multiple gastric and duodenal lipomas. A 50-year-old woman had a 4-month history of epigastric pain, with recent onset of intermittent vomiting. Single anteroposterior view from an upper gastrointestinal series shows multiple smooth masses along greater curvature of stomach (*long arrows*). Mass lesions (*short arrows*) continue into duodenum. At surgery, mass lesions were found to be lipomas. (Reprinted with permission from Deeths et al. [6].)

Fig. 10.—Multiple colonic lipomas. An oblique view from single-contrast barium enema shows two smooth, well-circumscribed masses (*arrows*) at splenic flexure. At surgery, these proved to be lipomas.

Stomach

Gastric lipomas are a rare lesion accounting for only 5% of alimentary tract lipomas and for only 3% of all benign gastric masses [5]. Most gastric lipomas are located in the antrum; the remainder are spread throughout the body and fundus (Fig. 6). The usual antral location accounts for a high frequency of prolapse into the pylorus. Because of the lipoma's supple nature, however, complete obstruction of the gastric outlet seldom occurs. As in other segments of the gut, lipomas are usually single but may be multiple (Fig. 9).

Small Bowel

The small bowel ranks as the second most common location for lipomas of the gut. About 20–25% of lipomas occur here [7], most frequently in the ileum. Lipomas are found less frequently in the jejunum (Fig. 1) and duodenum (Fig. 9) [7]. The lipoma is the second most common benign tumor of the small bowel; the first is leiomyoma [7].

Colon

The colon is the most frequently involved segment of the bowel, accounting for 65–75% of lipomas [7]. In fact, lipomas are the second (albeit a distant second) most common benign tumor of the colon, after the adenomatous polyp [1]. Lipomas are found most commonly in the cecum (Fig. 6) and the right side of the colon, and next most commonly in the sigmoid colon (Fig. 4). The true lipoma of the ileocecal valve should not be confused with the more frequent lipomatosis of the valve. In the former case, the fat is encapsulated, causing a well-defined mass emanating from the valve instead of the generalized enlargement seen with diffuse fatty infiltration.

Most colonic lipomas are solitary, but occasionally they may be multiple (Fig. 10). A rare condition of colonic lipomatosis exists in which innumerable small fatty deposits are present [8].

REFERENCES

1. Fernandez MJ, Davis RP, Nora PF. Gastrointestinal lipomas. *Arch Surg* **1983**;118:1081–1083
2. Heiken JP, Forde KA, Gold RP. Computed tomography as a definitive method for diagnosing gastrointestinal lipomas. *Radiology* **1982**;142:409–414
3. Som PM, Scherl MP, Rao VM, Biller HF. Rare presentations of ordinary lipomas of the head and neck: a review. *AJNR* **1986**;7:657–664
4. Olson DL, Dodds WJ, Stewart ET, Helm JF, Duncavage JA. Pedunculated pharyngeal lipoma presenting as an esophageal polyp. *Dysphagia* **1987**;2:113–116
5. Chu AG, Clifton JA. Gastric lipoma presenting as peptic ulcer: case report and review of the literature. *Am J Gastroenterol* **1983**;78:615–618
6. Deeths TM, Madden PN, Dodds WJ. Multiple lipomas of the stomach and duodenum. *Dig Dis Sci* **1975**;20:771–774
7. Agha FP, Dent TL, Fiddian-Green RG, Braunstein AH, Nostrant TT. Bleeding lipomas of the upper gastrointestinal tract: a diagnostic challenge. *Am Surg* **1985**;51:279–285
8. Yatto RP. Colonic lipomatosis. *Am J Gastroenterol* **1982**;77:436–437

Piezoelectric Biliary Lithotripsy:

An in Vitro Study of Factors Affecting Gallstone Fragmentation

Scott J. Schulte[1]
Richard L. Baron

Factors affecting the fragmentation of gallstones with piezoelectric lithotripsy were studied in vitro, with a goal of providing data that will help direct treatment with piezoelectric lithotriptors. Two hundred fifty-seven stones from 50 patients were treated with the EDAP LT.01 lithotriptor until all fragments measured 2 mm or less in diameter. The fragmentation process was observed, and two patterns were evident: central fragmentation and peripheral chipping. The majority of stones fragmented centrally. Fragmentation characteristics in different stones from the same patient were compared with those from different patients. Stone diameter, shock-wave frequency and power, and CT appearance were examined and correlated with fragmentation. Gallstones from the same patient showed uniform fragmentation patterns and consistent relationships between fragmentation time and gallstone size, shock-wave frequency, and power. In stones from the same patient, gallstone size had a marked effect on fragmentation time, which correlated with the cube of the stone diameter, and shock-wave frequency and power had a proportional inverse linear relationship with fragmentation time. When controlling for stone size and treatment parameters, stones from multiple patients showed marked differences in fragmentation time, and because of this, poor correlation between stone size and fragmentation time. Stones grouped according to CT pattern and attenuation showed wide variation and no correlation between CT characteristics and fragmentation pattern or fragmentation time.

Our results show that a great variability exists in fragmentation time of gallstones, making it impossible to accurately predict fragmentation time at a given stone size. Only rough estimates of longer fragmentation times with increasing stone size can be made. The linear relationships between shock-wave frequency or power and fragmentation time allow one to easily predict the effect of manipulating these variables and to tailor treatment to each patient's tolerance. Finally, CT appearance does not appear to be predictive of fragmentation outcome.

***AJR* 155:1211–1216, December 1990**

Biliary lithotripsy is currently performed worldwide to treat patients with symptomatic cholelithiasis. Early enthusiasm for biliary lithotripsy, based on reports from Europe using spark-gap technology [1], has begun to subside as trials in the United States have been less encouraging [2]. Other United States trials with piezoelectric technology have begun, and initial results are more promising and closer to the original European data [3]. The results of these clinical trials will be critical in determining the future of biliary lithotripsy in the United States. Unfortunately, few in vitro investigations that could provide a basis for in vivo biliary lithotripsy have been reported. We undertook this study to provide basic in vitro data on piezoelectric lithotripsy, with a goal of investigating factors that affect gallstone fragmentation, to help direct and optimize the treatment of patients.

The variables that were examined and compared with fragmentation were shock-wave frequency and shock-wave power (which are frequently manipulated during the course of therapy with piezoelectric lithotriptors), gallstone size, and CT appearance. Other experimental goals were to study the fragmentation process

---

Received May 3, 1990; accepted after revision July 9, 1990.

[1] Both authors: Department of Radiology (SB-05), University of Washington Medical Center, Seattle, WA 98195. Address reprint requests to S. J. Schulte.

0361-803X/90/1556-1211
© American Roentgen Ray Society

with piezoelectric lithotripsy and to determine the variability in fragmentation in gallstones from and between individual patients.

Materials and Methods

Two hundred fifty-seven human gallstones were collected during surgery from 50 patients. All stones were stored in bile or normal saline at room temperature for up to 2 months. The diameter of each stone was measured with calipers and the maximal diameter was recorded in millimeter increments (range, 4–17 mm). The gallstones were grouped into 51 stone families (each family comprising stones from the same patient), with a similar external appearance (color and texture), other than size and shape. One patient had two distinctive populations of gallstones. There were 33 one-stone families and 18 multiple stone families, with an average of 12.4 stones per family in those with multiple stones.

One gallstone from each family underwent in vitro CT, by using a custom-made plastic body phantom and a GE 9800 scanner (GE Medical Systems, Milwaukee, WI). All stones were scanned while immersed in normal saline by using 1.5-mm collimation, 140 kVp, and 170 mA. The CT appearance of the stone was analyzed, and region-of-interest attenuation coefficients were obtained by using a standard, previously described method [4].

All stones underwent in vitro lithotripsy with the EDAP LT.O1 lithotriptor (EDAP International Corp, Westford, MA). A single stone and 25 ml normal saline were placed in a plastic bag with a size and shape simulating a human gallbladder. These were then placed in a water-bath body phantom, coupled by sonographic gel to the treatment head of the EDAP LT.O1 lithotriptor (Fig. 1). The stone was optimally placed and maintained in the focal zone of the lithotriptor by using a combination of the on-line sonographic image, stone fragment motion, and shock-wave sound, which has a distinctive tone when accurately focused on the stone. Fragmentation was continuously observed and treatment intermittently interrupted to measure fragment size with calipers. Treatment was continued until all fragments measured 2 mm or less in diameter, and the treatment time required was recorded as fragmentation time.

Six separate experiments were devised by using data from the 257 stones. Individual stone data were used in one or more experiments and were included in all experiments where appropriate.

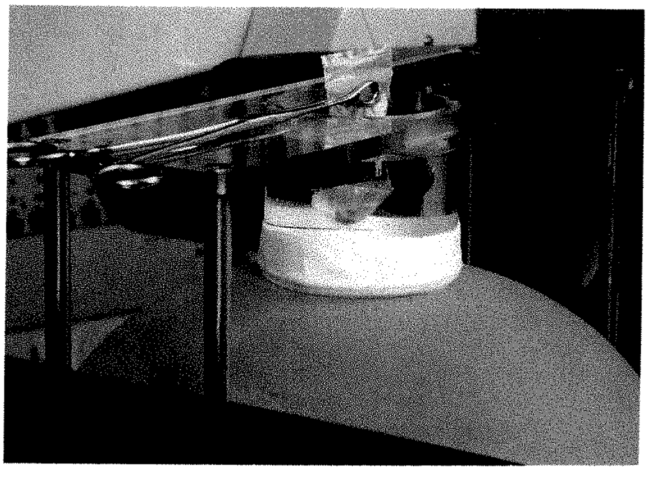

Fig. 1.—In vitro lithotripsy apparatus. Plastic bag containing single gallstone and saline is suspended within water-filled chamber of body phantom, coupled to treatment head of EDAP LT.O1 lithotriptor.

Experiment 1: Character of Fragmentation Process

For all stones (257), the character of the fragmentation process was assessed, and the fragmentation patterns were categorized. The variability in fragmentation patterns within stone families was investigated by analyzing the fragmentation patterns within the 14 stone families (209 stones) that contained four or more stones.

Experiment 2: Fragmentation Time Variability

The variability in fragmentation time was investigated by comparing fragmentation times in stones of a similar diameter, both without family grouping and within stone families. In order to determine the variability in fragmentation time without family grouping, the fragmentation times of all stones (138) shocked at 5.0 Hz shock-wave frequency and 100% shock-wave power (maximum FDA allowed in vivo shock-wave parameters) were grouped by stone diameter in 1-mm increments. For each different stone diameter, the variability in fragmentation time was assessed by determining the mean fragmentation time (for each stone diameter) and calculating the maximum variation in fragmentation time from this mean, in percent. These maximum variations from the mean fragmentation time were calculated for each of the 14 different stone diameters.

Fragmentation time variability within stone families was determined by comparing the fragmentation times in all possible family groups, each group containing stones of the same family and diameter, and treated with a uniform shock-wave frequency and power. Sixty groups (206 stones) meeting these qualifications could be compiled. The mean fragmentation time in each group was calculated, and the maximum variation in fragmentation time, in percent, was determined for each group.

Experiment 3: The Effect of Stone Diameter on Fragmentation Time

The fragmentation times of all stones (138) shocked at 5.0 Hz shock-wave frequency and 100% shock-wave power were compared with stone diameter. The correlation between fragmentation time and stone diameter, stone diameter squared, and stone diameter cubed was determined.

The effect of stone diameter on fragmentation time also was investigated within stone families. The fragmentation times of 54 stones, within the six stone families that contained stones with three or more different diameters, were compared with stone diameter. A constant shock-wave frequency of 5.0 Hz and shock-wave power of 100% were used. When possible, more than one stone of each different stone diameter was fragmented. The correlation between fragmentation time and stone diameter, stone diameter squared, and stone diameter cubed was determined for each of the six family groups.

Experiment 4: The Effect of Shock-Wave Frequency on Fragmentation Time

One hundred nineteen stones from 15 family groups (each containing stones of the same family and diameter), were treated at a controlled shock-wave power of 100% and a variable shock-wave frequency. Twelve stones from five family groups were shocked at 5.0 and 1.25 Hz only, and 107 stones from 10 family groups were shocked at 5.0, 2.5, and 1.25 Hz (shocks per second). When possible, multiple stones were fragmented at each shock-wave frequency, and the fragmentation times were averaged. Comparisons were made between shock-wave frequency and fragmentation times within each of the 15 family groups.

Experiment 5: The Effects of Shock-Wave Power on Fragmentation Time

Seventy-five stones from nine family groups (each containing stones of the same family and diameter) were treated at a controlled shock-wave frequency of 5.0 Hz and a variable shock-wave power. Twenty-five stones from four family groups were shocked at 100% and 54% of maximum power, and 50 stones from five family groups were shocked at 100%, 75%, and 54% of maximum power. When possible, multiple stones were shocked at each power setting, and the fragmentation times were averaged. Comparisons were made between shock-wave power and fragmentation times for each of the nine family groups.

Experiment 6: CT Correlation With Fragmentation Pattern and Fragmentation Time

Based on CT appearance and attenuation, the 51 stones that underwent CT were categorized into dense (homogeneous appearance and attenuation >90 H), faint/isodense (homogeneous appearance and attenuation ≤90 H), laminated (multiple concentric layers of varying attenuation), and rimmed (single peripheral rim of increased attenuation surrounding a homogeneously lower attenuation central region) groups.

Fragmentation patterns and fragmentation times were compared in the four CT groups. Because of variable stone size in each of the four CT groups and because of results obtained from experiment 3, fragmentation times were corrected to an equivalent stone diameter of 10 mm. As fragmentation time correlated best with the cube of the stone diameter, the fragmentation times of stones less than 10 mm in diameter were corrected up to the standard of 10 mm, and the fragmentation times of stones greater than 10 mm in diameter were corrected down to the standard of 10 mm by using the cubic power.

Statistics

Statview II software package (Abacus Concepts, Berkeley, CA) was used for all statistical analysis. Simple linear regression and one-way analysis of variance were used.

Results

Experiment 1: Character of Fragmentation Process

Two distinctive patterns of fragmentation were evident. One, termed central fragmentation, was a process with central fissures and fractures splitting the stone into large fragments, which then fractured into progressively smaller fragments. The second pattern, termed peripheral chipping, appeared as small chips or flakes off the surface, which gradually reduced the size of the stone. All stones showed some combination of these two patterns. For categorization, however, the stones were grouped according to the predominant pattern seen. Central fragmentation was predominant in 183, peripheral chipping predominant in 20, and both patterns of fragmentation roughly equal in 54.

Within the 14 stone families (209 stones) containing four or more stones, there was complete uniformity in fragmentation patterns in six of these families (118 stones). In the remaining eight families (91 stones), all showed a predominant fragmentation pattern, with 15 stones fragmenting by a method different from the predominant pattern. Therefore, only 15 (7%) of 209 stones fragmented in a manner different from the rest of the stone family. In all cases, the differing fragmentation patterns were either central fragmentation and mixed fragmentation, or peripheral chipping and mixed fragmentation. No families contained stones that fragmented by central fragmentation and peripheral chipping.

Experiment 2: Fragmentation-Time Variability

In all stones (138) shocked at 5-Hz frequency and 100% power, and from 4 to 17 mm in diameter, fragmentation times ranged from 22 sec to 115 min (mean, 23 min). Even when grouped by stone diameter (Fig. 2), the fragmentation times of these 138 stones showed wide variation, with the maximum variation from the mean fragmentation time, for each different stone diameter, ranging from 16% to 563%. The average maximum variation from the mean fragmentation time, for the 14 different stone diameters, was 165%.

In the 60 family groups (206 stones), each group containing stones of the same family and diameter and treated at a uniform shock-wave frequency and power, the maximum variation from the mean fragmentation time ranged from 0.5% to 98%. The average maximal variation from the mean fragmentation time, for the 60 groups, was 29%.

Experiment 3: The Effect of Stone Diameter on Fragmentation Time

In the 138 stones shocked at 5-Hz frequency and 100% power, the correlation between fragmentation time and stone diameter was .56. The correlation between fragmentation time and stone diameter squared was .55, and that between fragmentation time and stone diameter cubed was .52.

Within the six families (54 stones) containing three or more different stone diameters, the correlation between fragmentation time and stone diameter varied from .62 to .89, with a mean for all six groups of .74. The correlation between fragmentation time and stone diameter squared varied from .78 to .98 (mean, .86). The correlation between fragmentation time and stone diameter cubed ranged from .74 to .99 (mean, .89).

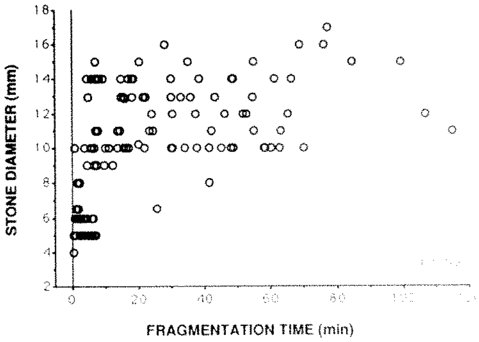

Fig. 2.—Graph shows correlation between stone diameter and fragmentation time in all stones treated at 5 Hz and 100% power. Fragmentation time varies widely at each stone diameter. Generally, fragmentation time increases with stone diameter (r = .56).

Experiment 4: The Effects of Shock-Wave Frequency on Fragmentation Time

Five family groups (12 stones) were shocked at 5.0 and 1.25 Hz. At 1.25 Hz, complete fragmentation took 2.0–4.8 (mean, 3.9 for the five groups) times longer than it did at 5.0 Hz. Ten family groups (107 stones) were shocked at 5.0, 2.5, and 1.25 Hz. At 2.5 Hz, complete fragmentation took 1.3–2.8 (mean, 2.0) times longer than it did at 5.0 Hz. At 1.25 Hz, complete fragmentation took 1.5–3.5 (mean, 2.1) times longer than it did at 2.5 Hz.

Experiment 5: The Effect of Shock-Wave Power on Fragmentation Time

Four family groups (25 stones) were shocked at 100% and 54% of maximum shock-wave power. At 54% power, complete fragmentation took 2.0–3.1 (mean, 2.2 for the four groups) times longer than it did at 100% power. Five family groups (50 stones) were shocked at 100%, 75%, and 54% power. At 75% power, complete fragmentation took 1.1–1.9 (mean, 1.5) times longer than it did at 100% power. At 54% power, complete fragmentation took 1.2–2.6 (mean, 1.8) times longer than it did at 75% power.

Experiment 6: CT Correlation With Fragmentation Pattern and Fragmentation Time

In the 51 stones examined with CT (one from each stone family), there were 13 dense, 20 faint/isodense, seven laminated, and 11 rimmed stones. In the dense group, seven predominantly fragmented centrally, four predominantly chipped peripherally, and two fragmented by a roughly equal mixture of both methods. In the faint/isodense group, 10 fragmented centrally, five chipped peripherally, and five fragmented by a mixture of both methods. In the laminated group, five fragmented centrally and two fragmented by a mixture of central fragmentation and peripheral chipping. In the rimmed group, six fragmented centrally, two chipped peripherally, and three fragmented by a mixture of both methods. No significant correlation was found between CT group and fragmentation pattern.

Fragmentation times from each CT group are shown in Table 1. No significant correlation was found between CT group and fragmentation time.

Fragmentation times corrected to an equivalent stone diameter of 10 mm also are shown in Table 1. Although mean corrected fragmentation times tended to be shorter in the heterogeneous stone groups (laminated and rimmed), statistical analysis showed no significant correlation between CT groups and corrected fragmentation time.

TABLE 1: CT Appearance vs Fragmentation Time

CT Group (No. of Stones)	Mean Fragmentation Time in Sec (Range)	Mean Corrected Fragmentation Time[a] in Sec (Range)
Dense (13)	2107 (242–4209)	1981 (182–5801)
Faint/Isodense (20)	2470 (432–6435)	1747 (108–4736)
Laminated (7)	1846 (346–6922)	1566 (324–5191)
Rimmed (11)	2449 (1222–3996)	1314 (354–2875)

[a] Fragmentation time corrected to an equivalent stone diameter of 10 mm, by using cubic power (see experiment 3).

Discussion

These experiments provide basic in vitro data on piezoelectric biliary lithotripsy, information on fragmentation properties of gallstones, and information of practical value when operating piezoelectric lithotriptors and optimizing treatment parameters.

These data reveal the great variability in fragmentation times of gallstones. In stones 4–17 mm in diameter, and treated at maximal in vivo shock-wave parameters (5 Hz frequency and 100% power) allowed by the Food and Drug Administration (FDA), fragmentation times ranged from 22 sec to 115 min (mean, 23 min). Even in stones of similar diameter (Fig. 2), fragmentation time was highly variable, ranging up to 563% from the mean fragmentation time for a specific stone diameter. The average maximal variation from the mean fragmentation time for the 14 different stone diameters fragmented was 165%. This great variability in fragmentation time most likely reflects differences in structure and composition of gallstones, because shock-wave frequency, power, and focusing were held constant. Some of this variability also may be due to differences in stone volume, as stones were grouped by maximum diameter, and differences in stone shape would mean different stone volumes, and therefore different stone burdens for lithotripsy. Despite this limitation, we elected to use maximum stone diameter as a measure of stone size because it is what is most often used clinically, in vivo, to estimate stone size by sonography, oral cholecystography, or plain film. Thus, we revealed what is most relevant clinically, that is, the great variability in fragmentation time that can occur at similar stone diameters.

Gallstone families (a population of stones from the same gallbladder that have a similar external appearance other than shape and size) have much greater uniformity in fragmentation time. In the 60 family groups examined, the average maximum variation from the mean fragmentation time was 29%, which is much less than the 165% without family grouping. Even within families, stones are often of different shapes, and again, some of this fragmentation time variability is probably the result of differences in stone volume. However, the much greater uniformity in fragmentation time most likely reflects more uniformity in gallstone structure and composition within stone families, and also emphasizes the relative importance of structural differences in producing the variability in fragmentation time of gallstones between family groups. Although gallstones from an individual gallbladder are assumed to have a similar chemical composition (R. D. Soloway, personal communication), this has not been scientifically documented. This experiment provides indirect evidence of this, by demonstrating the much greater uniformity in fragmentation time within stone families.

Because of the great variability in fragmentation time of gallstones, the experiments on the effects of stone diameter, shock-wave frequency, and shock-wave power were all performed within family groups, where fragmentation times are much more uniform, and this variable could be controlled. Data from several family groups were then averaged into an overall result. Although this method is cumbersome, and makes statistical analysis awkward, it is the optimal experimental design, because without family grouping, the variability in fragmentation time is so great that it often overrides the variable being examined. An example of the benefit of this experimental design is evident in determining the effects of stone diameter on fragmentation time. When fragmentation time and stone diameter for all stones treated at 5 Hz and 100% power are graphed (Fig. 2), fragmentation time generally increases with increasing stone diameter. Correlation is poor, however (r = .56), and this is probably related to the wide range of fragmentation times. Analyzed within family groups, the true effect of stone diameter on fragmentation time is revealed. Within the six family groups with stones of three or more different diameters, significantly better correlation between stone diameter and fragmentation time was found. Figure 3 shows data from a single stone family that contained stones of three different diameters. In Figure 3A, the fragmentation times of stones of the three diameters are graphed, with a linear correlation of .87. When comparing fragmentation times against the cube of the stone diameters (Fig. 3B), the correlation improves to .98. Overall, in the six family groups, correlation was better between the cube of the stone diameter and fragmentation time, where r ranged from .74 to .99 (mean, .89). Formulas for volumes of spheres, cubes, and other polyhedrons are all based on the cube of the diameter or side. As all stones involved in these experiments were closely related to these shapes, stone diameter cubed provides an estimate of stone volume and therefore stone burden, and this correlates highly with fragmentation time. Because of this cubic relationship, relatively small increases in stone diameter result in much greater increases in stone volume and fragmentation time (Fig. 3). Stone diameters of 10, 13, and 16 mm correspond to estimated stone volumes of 1000, 2197, and 4096 mm^3, and fragmentation times of 11, 29, and 73 min, respectively.

It should be emphasized that these correlations are only accurate within family groups, that is, in stones from the same patient. Between individuals, fragmentation time varies widely at specific stone diameters, and thus poor correlation is seen between stone diameter and fragmentation time. This corresponds to the clinical setting, that is, an unknown population of gallstones in which it is impossible to accurately predict fragmentation time at a given stone diameter. One can only conclude that it will tend to take longer to fragment larger stones.

The experiments on the effects of shock-wave frequency and power on fragmentation time indicate that there is an inverse linear relationship between these variables and fragmentation time. With decreasing shock-wave frequency and power, there is a proportional increase in fragmentation time (Figs. 4 and 5). Shock-wave frequencies of 5.0, 2.5, and 1.25 Hz were examined because these are the three frequency settings on the EDAP LT.O1 that are currently approved by the FDA for the treatment of patients. The power settings (100%, 75%, and 54% of maximum power) were chosen because they provide a proportional range of power settings, in the upper half of the power range, which is most often used clinically. The present FDA-approved EDAP protocol limits biliary lithotripsy treatment time to a maximum of 75 min, regardless of the shock-wave frequency or shock-wave power. Thus, our results indicate that to optimize fragmentation, the maximal FDA-allowed shock-wave frequency of 5.0 Hz, and maximal shock-wave power should be used, if tolerated by the patient. Additionally, the proportional inverse linear relationship between these variables and fragmentation time is valuable. Thus, decreasing shock-wave frequency from 5.0 to 2.5 Hz has the same effect as reducing power from 100% to 50%. This basic knowledge allows one to predict the effect of manipulating shock-wave parameters and to optimize treatment to patients' tolerance.

The CT correlation experiments suggest that CT is unable to depict the structure or composition properties of gallstones that determine fragmentation pattern or fragmentation time. The four CT groups were based on both CT pattern and attenuation; fragmentation time, corrected fragmentation time, and fragmentation pattern were not significantly different in these four groups. This corroborates what previous investigators have shown [5, 6], that is, CT is unable to predict fragmentation rates of gallstones. Unlike these previous experiments, we also correlated CT group with fragmentation time corrected for stone size. We feel this correction is critical to accurate comparison between groups, because of the proved dominant effect of stone size on fragmentation time.

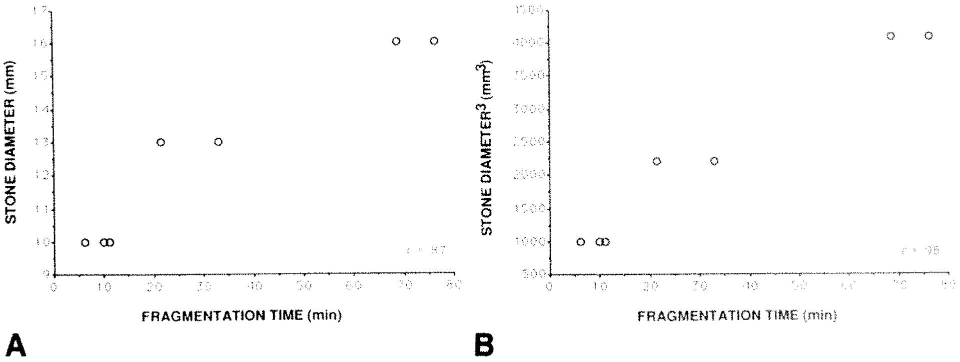

Fig. 3.—*A*, Graph shows correlation between stone diameter and fragmentation time for a single stone family with three stone diameters. Linear correlation coefficient = .87.

***B*, Graph shows correlation between cube of stone diameter and fragmentation time for same stone family. Note improved correlation (r = .98).**

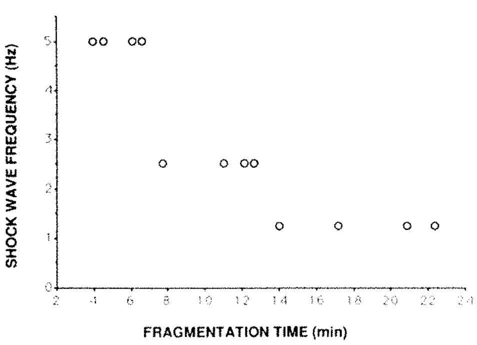

4

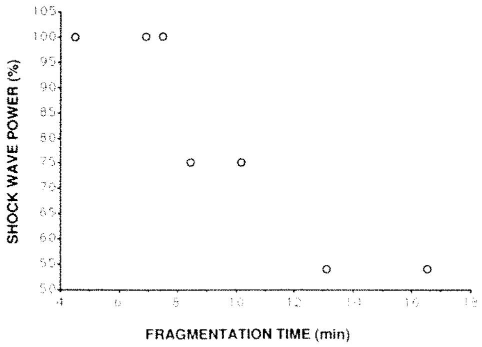

5

Fig. 4.—Graph shows correlation between shock-wave frequency and fragmentation time in a single stone family. All stones were 6 mm in diameter and were treated at a constant shock-wave power (100%).

Fig. 5.—Graph shows correlation between shock-wave power and fragmentation time in a single stone family. All stones were 9 mm in diameter and were treated at a constant shock-wave frequency (5 Hz).

Of interest is a tendency for the mean corrected fragmentation time to be shorter in the heterogeneous stones (laminated and rimmed CT groups) than in the homogeneous stones (faint and dense CT groups). Although our results were not statistically significant, Valette et al. [7] reported a statistically significant difference in fragmentation rates of heterogeneous and homogeneous stones on CT with spark-gap technology.

Observing fragmentation revealed that all stones fragmented by a combination of two distinctive patterns: central fragmentation and peripheral chipping or flaking. The majority of stones (71%) predominantly fragmented centrally; only 8% predominantly chipped peripherally. This is contrary to some previously held beliefs that stones primarily chip or flake peripherally with piezoelectric lithotripsy [8]. Within stone families, the fragmentation pattern was nearly completely uniform, and this is further evidence of the similarity in structure and composition of gallstones within stone families and the importance of gallstone structure in lithotripsy fragmentation.

In summary, our experiments document the wide variation in fragmentation time of gallstones, even those of similar diameter, and this most likely reflects structural differences between stones. Despite these structural differences that affect fragmentation, CT does not appear capable of depicting them. Stones from the same patient have much greater uniformity in fragmentation time, which implies structural similarity. Fragmentation time correlates with the cube of the stone diameter, which is an estimate of stone volume; however, this correlation is only accurate in stones from the same patient. Between patients, fragmentation time varies so widely that correlation between stone size and fragmentation time is poor, making it impossible to accurately predict fragmentation time at a given stone diameter. Shock-wave frequency and power have a proportional inverse linear relationship with fragmentation time. Finally, most gallstones fragment centrally with piezoelectric lithotripsy, which is contrary to previously held beliefs.

REFERENCES

1. Sackmann M, Delius M, Sauerbruch T, et al. Shock-wave lithotripsy of gallbladder stones: the first 175 patients. *New Engl J Med* **1988**;318:393–397
2. Torres WE, Steinberg HV, Davis RC Jr, Nelson RC, Casarella WJ. Shock wave lithotripsy of gallstones: preliminary results and 6-month follow-up in 146 patients. *Radiology* **1989**;173(P):203
3. Baron RL, Moss AA, Fromm H, et al. Piezoelectric biliary lithotripsy: multicenter clinical trial. *Radiology* **1989**;173(P):203
4. Baron RL, Rohrmann CA Jr, Lee SP, Shuman WP, Teefey SA. CT evaluation of gallstones in vitro: correlation with chemical analysis. *AJR* **1988**;151:1123–1128
5. Schachler R, Sauerbruch T, Wosiewitz U, et al. Fragmentation of gallstones using extracorporeal shock waves: an in vitro study. *Hepatology* **1988**;8:925–929
6. Schwab F, Albert M, Shehan C. Radiology of gallstones: in vitro correlation with efficacy of shock wave lithotripsy. *Radiology* **1989**;173(P):204
7. Valette PJ, Barkun AN, Ponchon T, Cathignol D. Radiologic variables that determine the success of in vitro solitary gallstone lithotripsy. *Radiology* **1989**;173(P):245
8. Ferrucci JT. Biliary lithotripsy: 1989. *AJR* **1989**;153:15–22

Nonaspiration Fine-Needle Cytology of the Liver: A New Technique for Obtaining Diagnostic Samples

Donald Fagelman[1]
Quintus Chess[2]

We studied a new method of obtaining diagnostic cytology samples from the liver that differs from fine-needle aspiration cytology in that no suction is used to obtain the sample. This method is simpler to perform than traditional aspiration biopsy and yields concentrated cell smears that are easier to interpret. The sample enters the needle because of capillary action, a physical property of fluid that causes it to flow into the lumen of a narrow channel. This nonaspiration technique was used in 40 consecutive patients undergoing fine-needle biopsy of mass lesions of the liver. A 22-gauge spinal needle was used in all procedures. The cytology smears obtained were prepared, stained, and interpreted by the same methods used for conventional fine-needle cytology specimens. Specific diagnoses were rendered in 36 patients (90%) and in 32 (94%) of those patients with malignant tumors. An average of 1.7 needle passes (range, 1–4) was needed per patient.

We conclude that the results from nonaspiration fine-needle cytology of the liver are as good as those from conventional aspiration technique, and the nonaspiration technique is easier to perform and results in smears that are easier to interpret.

AJR **155:1217–1219, December 1990**

Radiologically guided percutaneous fine-needle biopsy of the liver is an accepted diagnostic procedure in wide use for many clinical indications. A variety of needle designs have been used, but no matter which needle is selected, the cytologic specimen is virtually always obtained by aspiration [1]. According to this traditional method, a syringe is attached to the needle to maintain suction during the biopsy, and strong suction in the range of 5–10 ml negative pressure is advised.

Santos and Leiman [2] discuss a new technique for fine-needle cytology sampling that eliminates active aspiration. This technique is based on capillary action, a physical property in which fluid is drawn into narrow channels. These investigators compared this technique with traditional aspiration in a controlled series of 50 thyroid nodules. They concluded that aspiration is not only unnecessary, but actually reduces diagnostic yield. The result was attributed in part to the highly vascular structure of the thyroid gland, where suction frequently causes rapid filling of the syringe with fresh blood, which dilutes the sample and obscures cell detail. We reasoned that the same factors would apply in the liver, another vascular organ. This study was done to assess the effectiveness of nonaspiration fine-needle cytology for the diagnosis of hepatic tumors.

Subjects and Methods

Forty consecutive percutaneous fine-needle liver biopsies were performed during 1 year by using the nonaspiration technique. All procedures were performed by the same radiologist, who used CT guidance on an outpatient basis. Intraperitoneal bleeding requiring hospitalization developed in one patient; no other complications occurred. A standard 22-gauge spinal needle was used in every case. The same cytopathologist attended each procedure to ensure

Received April 16, 1990; accepted after revision June 26, 1990.

[1] Great Neck Imaging, P.C., 310 E. Shore Rd., Great Neck, NY 11023. Address reprint requests to D. Fagelman.

[2] Cytopath Biopsy Laboratory, Inc., 1495 Pine Knoll Lane, Mamaroneck, NY 10543 and Department of Pathology, Cornell University Medical College, 1275 York Ave., New York, NY 10021.

0361–803X/90/1556–1217
© American Roentgen Ray Society

the adequacy of the sample and to avoid excessive punctures.

The patients ranged from 26 to 77 years old, with an average age of 61 years. Twenty-two were women and 18 were men. Eight patients had solitary lesions, 32 had multiple hepatic lesions. Thirteen of the lesions were in the left lobe, and 27 were in the right lobe of the liver. The lesions ranged in size from 2 to 15 cm.

The lesion to be sampled by biopsy was localized by CT. A 22-gauge spinal needle was inserted into the lesion. The needle tip was confirmed to be within the lesion, and the stylet was removed. Without attaching a syringe, the needle was gently but rapidly moved with an in-and-out motion until fluid was seen in the hub, but for no longer than 10 sec. The needle was then withdrawn. At this point, a syringe was attached to the needle to express the sample onto glass slides. Smears were prepared in standard fashion, rapidly stained by Diff-quik (American Scientific Products, Philadelphia, PA) and assessed under the microscope for cellularity. If the volume of material within the needle was judged to be inadequate after two attempts, the traditional aspiration technique (suction) was used for subsequent needle passes. If, however, the volume was adequate (two complete smears), but the quality of the sample was judged inadequate, the nonaspiration technique was continued. If the initial microscopic assessment indicated the need for special studies such as immunoperoxidase tests, additional needle passes without suction were done. The number of needle passes required was recorded for each patient. All smears were then restained by the standard Papanicolaou method, and the final diagnosis was rendered by the same cytopathologist who attended the procedure. The diagnoses were tabulated and the overall sensitivity of the nonaspiration technique was compared with the sensitivity reported recently in a series of fine-needle aspiration biopsies of the liver.

Thirty-two (80%) of 40 samples were diagnostic of malignancy (30 metastases and two primary hepatocellular carcinomas). In all but three of the metastases, the primary site was established. Specific benign conditions were diagnosed in four (10%) cases, including two cases of focal hepatocellular steatosis, one case of atypical hemangioma, and one case of cirrhosis with dysplasia. Four (10%) of the procedures were not diagnostic. One of these was classified as "suspicious" but marked necrosis was present, which was attributed to recent chemotherapy. Follow-up has confirmed that the lesion was metastatic carcinoma. Another lesion yielded only necrotic material, even when aspiration was applied in the last two needle passes. Follow-up surgical biopsy results in this case showed the lesion to be necrotic carcinoma. The other two nondiagnostic lesions yielded scanty specimens; additional needle passes with vigorous aspiration did not produce better material. Both of these patients underwent surgical biopsy, and again no specific diagnosis could be made; clinical findings remain normal 1 year and 1½ years later.

Results

Specific diagnoses were obtained in 36 of 40 cases by using the nonaspiration technique. This indicates an overall diagnostic sensitivity of 90%. Thirty-two cases were diagnosed as malignant and four were diagnosed as a specific benign condition. An average of 1.7 needle passes per patient was needed. No patient underwent more than four needle passes. Clinical and radiologic follow-up to date confirms that these diagnostic samples are representative. In the four cases that could not be diagnosed by the nonaspiration technique, the use of suction did not produce a better diagnostic sample. Clinical follow-up including surgical biopsy indicates that two of these four nondiagnostic cases were benign and two were malignant. Thus, in this series of 40 patients, nonaspiration technique obtained specific pathologic diagnoses in 32 of 34 malignant tumors; the diagnostic sensitivity for the detection of malignancy is 94%.

Discussion

It has been established that radiologically guided fine-needle cytology is a safe, accurate, and sensitive method for the diagnosis of liver masses [1]. Prior and coworkers [3] compared surgical tissue biopsy with sonographically guided percutaneous fine-needle aspiration biopsy in 36 patients, each of whom had both procedures. They report a diagnostic sensitivity of 82% for tissue biopsy and 86% for aspiration biopsy. Leiman and coworkers [4], in a multicenter series of 160 fine-needle aspiration liver biopsies, correctly diagnosed 101 of 108 malignant tumors and report a sensitivity of 94% for malignancy. However, that figure excludes 47 cases that were classified as "nondiagnostic" and analyzed separately. The authors attribute the problem in these nondiagnostic cases, in part, to smears that were obscured by blood. Despite the presence of a cytopathologist at each procedure, up to seven needle passes were done on some patients in that study.

Many other series of liver fine-needle biopsy have differed in selection of patients, type of radiologic guidance, needle type, and numerous other ways; however, all report the use of aspiration in order to obtain the diagnostic sample. The diagnostic sensitivity of liver aspiration cytology ranges from 80% to 90%. In our series of 40 consecutive fine-needle liver biopsies performed by using the nonaspiration technique, the diagnostic sensitivity for malignancy is 94% and the diagnostic sensitivity for all cases is 90%. These results show that the nonaspiration method is as sensitive as is traditional aspiration fine-needle biopsy of the liver.

Nonaspiration works because of the physical property of capillary action. Capillary action is a phenomenon in which the surface of a liquid is elevated where it comes into contact with a solid. This adhesive force causes the sample to flow into a narrow channel such as a 22-gauge needle. A recent semiquantitative analysis of biopsies of 103 different lesions showed that needle biopsy without aspiration yields the same amount of *cellular* material as does aspiration biopsy [5]. Diagnostic specificity is also comparable, but depends more directly on the skill of the cytopathologist.

There are several practical and theoretical advantages to avoiding aspiration, both for the radiologist and for the cytopathologist. Rapid filling of the hub of the needle and syringe with bloody fluid does not occur; therefore, there is more time to manipulate the needle. With nonaspiration, the cytopathologist receives a precise volume of highly cellular sample, usually about enough to prepare two complete thin smears from each needle pass. The initial assessment of cellularity at the time of the biopsy is more rapid and also more accurate. Screening a single smear allows the cytopathologist to view half of the specimen. When suction is used, the cytopathologist may have to prepare seven or eight smears. These are often thick, bloody, or partly clotted. It may be difficult to select the right smear(s) for immediate assessment of cellularity. This may lead to unnecessary, time-consuming, and possibly harmful additional needle punctures. Most series do not report the number of needle passes needed per diagnosis, but our average of 1.7 is certainly acceptable. If a differential diagnosis is considered at the time of immediate assessment, the material from a second needle pass can be fixed appropriately for whichever special studies the pathologist anticipates (e.g., immunoperoxidase, Gram strain/culture, electron microscopy). In fact, one of the major advantages of having a cytopathologist present, the need for special handling, is enhanced by this approach. Conversely, there is no need to "rescue" material from the syringe by rinsing and no need to resort to any of the blood-lysing or cell-enrichment procedures that have been needed in the past [6, 7].

In addition to these practical advantages, there are theoretical advantages to nonaspiration. The application of suction to draw cells through a fine needle traumatizes fragile cells. In particular, aspiration of neoplasms of the clear-cell type, including renal and adrenal tumors, results in artifacts that may lead to diagnostic error. For example, Min et al. [8] report two cases of adrenal cortical nodules mimicking small round cell malignant tumor because of stripping of cytoplasm during aspiration. Avoidance of suction may minimize this and other misleading artifacts.

We selected the liver for our study because, like the thyroid, it is a highly vascular organ that tends to yield bloody aspirates. By the same logic, we have sampled other vascular targets such as bone lesions without aspiration. Furthermore, certain tumor types are inherently vascular, such as renal cell carcinoma or neuroendocrine carcinoma. Certain other tumors, such as most forms of lymphoma, also yield abundant diagnostic material without suction because the cells do not stick together. Although this study was restricted to liver biopsy, we have used nonaspiration successfully in other parts of the body for these tumors. Yue and Zheng [9] report favorable results in 10 out of 11 cases of transthoracic fine-needle sampling without suction. Mair et al. [10] report a series of 100 masses in various sites sampled by using fine needles with and without suction, and they found no statistical difference in the efficacy of the two methods.

It must be recognized that characteristically fibrotic neoplasms such as certain primary breast or pancreas carcinomas may require vigorous biopsy technique including suction or, rarely, a larger bore needle. However, fine needles should be used whenever possible because they are less traumatic. In fact, since the completion of this study, we have used the nonaspiration technique successfully with 25-gauge needles.

ACKNOWLEDGMENT

The authors express their deepest gratitude for the preparation of the manuscript to Jane Ryan.

REFERENCES

1. Pincus D, Weyman PJ, Anderson DJ. Interventional computed tomography. In: Lee JKT, Sagel SS, Stanley RJ, eds. *Computed body tomography*, 2nd ed. New York: Raven Press, **1989**:89–108
2. Santos JEC, Leiman G. Nonaspiration fine needle cytology: application of a new technique to nodular thyroid disease. *Acta Cytol* **1988**;32:353–356
3. Prior C, Kathrein H, Mikuz G, Judmaier G. Differential diagnosis of malignant intrahepatic tumors. *Acta Cytol* **1988**;32:892–895
4. Leiman G, Leibowitz CB, Dunbar F. Fine needle aspiration of the liver. *Diagn Cytopathol* **1989**;5:35–39
5. Akhtar M, Ali MA, Hug M, Faulkner C. Fine needle biopsy: comparison of cellular yield with and without aspiration. *Diagn Cytopathol* **1989**;5:162–165
6. Umlas J. Preparation of bloody specimens for cytologic examination using saponin. *Acta Cytol* **1972**;16:186–188
7. Axe S, Erozon Y, Ermatinger S. Fine needle aspiration of the liver: a comparison of smear and rinse preparation in the detection of cancer. *Am J Clin Pathol* **1986**;86:281–285
8. Min KW, Song J, Boesenberg M, Acebey J. Adrenal cortical nodule mimicking small round cell malignancy on fine needle aspiration. *Acta Cytol* **1988**;32:543–546
9. Yue X, Zheng S. Cytologic diagnosis by transthoracic fine needle sampling without aspiration. *Acta Cytol* **1989**;33:805–808
10. Mair S, Dunbar F, Becker PJ, PuPlessis W. Fine needle cytology: is aspiration suction necessary? *Acta Cytol* **1989**;33:809–813

Book Review

Endosonography. Edited by Bruno D. Fornage. Boston: Kluwer, 186 pp., 1989. $129

This volume, number 17 in the publisher's Series in Radiology, deals with various topics in the expanding realm of endosonography. After a brief review of transducer design, chapters discuss endoscopic sonography, transrectal prostate imaging, and laparoscopic and transurethral sonography. The book concludes with four chapters devoted to transvaginal sonography. Transesophageal cardiac imaging is mentioned only in passing, and intravascular applications are not described at all. Each chapter concludes with a list of references current through mid-1988.

As stated in the preface, this book's purpose is to "help newcomers get started in the field of endosonography" by describing techniques and clinical applications. The degree to which the various contributors accomplish this goal varies considerably, however. The chapter on upper abdominal endoscopic sonography is the most disappointing, suffering from an insufficient number of illustrations and poor-quality reproductions. Esophageal and rectal sonography, discussed in separate chapters, fares much better, incorporating sections describing sonographic staging of esophageal and rectal neoplasms. The chapter on transrectal prostatic sonography also is well done, although several of the images are not well reproduced. (The image of the prostate on the cover, rendered in pale yellow and white, is especially difficult to see.)

Written by several different authors, the final chapters on transvaginal sonography do not hold together as well as they ought to. For example, the technique is described twice, once under gynecology and once under obstetrics. The quality of some of the transvaginal images also is poor. The chapters on laparoscopic and transurethral sonography and transvaginal sonography of urinary disorders are fascinating but are unlikely to be of wide interest to radiologists.

This book is recommended for anyone who desires a rapid overview of endosonography. In general, the text is well written, and the entire volume can be read easily in 1 day. However, sonographers interested in actually performing the techniques described would be served better by texts that deal with the individual topics.

Franklin N. Tessler
University of California, Los Angeles
Los Angeles, CA 90024-1721

Percutaneous Ethanol Injection Therapy of Hepatocellular Carcinoma: Analysis of 77 Patients

Shuichiro Shiina[1]
Kazumi Tagawa[2]
Tadao Unuma[2]
Hitoshi Fujino[2]
Yoshiki Uta[2]
Yasuro Niwa[1]
Yasuo Hata[1]
Yutaka Komatsu[1]
Yasushi Shiratori[1]
Akira Terano[1]
Tsuneaki Sugimoto[1]

Although sonographically guided percutaneous ethanol injection therapy has been attracting a great deal of attention in the treatment of liver neoplasms, few reports regarding long-term results of this therapy have been published. We report here our 4-year experience, in which ethanol injection was performed 419 times on 108 lesions in 77 patients with hepatocellular carcinoma. Histopathologic examination performed in 14 cases after the therapy revealed that the lesion was completely necrotic in 10 cases, 90% necrotic in three cases, and 70% necrotic in the remaining case. Angiography performed after the therapy showed complete disappearance of tumor stain in 37 of 42 cases treated with ethanol injection. CT after the therapy showed no enhancement of the treated lesion in 55 of 56 cases. Elevated serum levels of α-fetoprotein decreased in 21 of 24 cases. Ethanol injection improved the long-term prognosis of the patients. Among the 50 patients in whom there were three or fewer lesions and all lesions were treated by ethanol injection, the 1-, 2-, 3-, and 4-year survival rates were 89%, 74%, 68%, and 60%, respectively. Factors that significantly affected the prognosis were the goal of the treatment, liver function, and size of the largest lesion. Serious complications rarely occurred even in patients with severe liver dysfunction.

Percutaneous ethanol injection therapy appears to be valuable for treatment of hepatocellular carcinoma.

***AJR* 155:1221–1226, December 1990**

Hepatocellular carcinoma is one of the most common malignant neoplasms in the world [1]. Various imaging techniques and measurement of serum levels of α-fetoprotein have been used widely in the screening of hepatocellular carcinoma among high-risk groups, such as hepatitis B surface-antigen carriers and patients with chronic liver disease. Thus, more and more cases have recently been detected at an early stage [2, 3].

Prognosis of patients with hepatocellular carcinoma in general has been dismal [4, 5]. Surgical resection has been the only curative therapy. Unfortunately, most patients with this cancer have underlying liver cirrhosis, and severe liver dysfunction often makes hepatectomy impossible, even when the cancer is found at an early stage [6]. In cases of hepatocellular carcinoma that is unresectable because of the advanced state of the cancer or because of poor surgical risks, transcatheter arterial embolization [7, 8] or chemotherapy [9] has been performed.

Recently, sonographically guided percutaneous ethanol injection therapy (PEIT) has been attracting a great deal of attention in the treatment of liver neoplasms [10–19]. However, few reports on its long-term results have been published. This report summarizes our clinical experience with PEIT in 77 patients during a 4-year period.

Subjects and Methods

From December 1985 to December 1989, PEIT was performed 419 times on 108 lesions in 63 men and 14 women who had hepatocellular carcinoma. The age range of the patients

Received May 10, 1990; accepted after revision June 29, 1990.

[1] Second Department of Internal Medicine, Faculty of Medicine, University of Tokyo, Hongo 7-3-1, Bunkyo-ku, Tokyo 113, Japan. Address reprint requests to S. Shiina.

[2] Department of Gastroenterology, Mitsui Memorial Hospital, Kandaizumi-cho 1, Chiyoda-ku, Tokyo 101, Japan.

0361-803X/90/1556-1221
© American Roentgen Ray Society

was 39–82 years (mean, 58 years). Histopathologic diagnosis of the lesion was made by fine-needle biopsy.

Seventy-three patients had liver cirrhosis. According to the Child's classification [20], 34 patients were in class A, 14 were in class B, and 25 were in class C. The four other patients had chronic hepatitis.

In 50 of the 77 cases, the goal of PEIT was to destroy the lesion or lesions completely (potentially curative group). In these cases, the patients had three or fewer lesions, and PEIT was used on all of the lesions. In these patients, 41 had a single lesion, eight had two lesions, and one had three lesions. The diameter of the largest lesion in each patient who had PEIT ranged from 1.0 to 6.0 cm.

In the remaining 27 cases, PEIT was performed to reduce the tumor burden (palliative group). These patients had four or more lesions, and PEIT was used only on the main lesions—some lesions were left untreated. In this group, the diameter of the largest lesion in each patient who had PEIT ranged from 1.2 to 10.0 cm.

Patients with ascites or a tendency for marked bleeding were excluded from this therapy. Absence of ascites was confirmed by sonography. In an early stage of this study, we had a case of intraperitoneal hemorrhage due to necrosis of the tumor. We thereafter performed PEIT only on patients whose prothrombin times were more than 35% and whose platelet counts were more than 40,000/μl. Informed consent was obtained from each patient.

PEIT was combined with transcatheter arterial embolization in 54 cases. In the remaining 23 cases, transcatheter arterial embolization was not performed because hepatocellular carcinoma was not diagnosed at the time of angiography (15 cases), because unfavorable anatomic variations made arterial embolization impossible (six cases), because an allergy to iodine prevented arterial embolization (one case), and because a poor general condition due to chronic obstructive lung disease and diabetes mellitus made arterial embolization risky (one case). In transcatheter arterial embolization, a vascular catheter was inserted superselectively into the hepatic artery that fed the tumor. Under fluoroscopic guidance, 10 mg of mitomycin C, 3 to 5 ml of lipiodol, and 1- to 2-mm pieces of Gelfoam (Upjohn Co., Kalamazoo, MI) were infused into the feeding artery through the catheter, with care being taken not to allow backflow of these agents into the proximal arteries.

For sonographic guidance, real-time linear-array scanners (SAL-55AS, Toshiba, Tokyo, or SSD-650, Aloka, Tokyo) were used with 3.5-MHz transducers (GCE-406M, Toshiba, Tokyo, or UST-5037P-3.5, Aloka, Tokyo) for the puncture. Commercially available 21-gauge, 15-cm or 20-cm needles (Hanaco, Tokyo), suitable for sonographic guidance, were used for the tumor puncture.

In most cases, 2–8 ml of 99.5% absolute ethanol was injected into the tumor at one or more locations in one treatment session, and the injection was performed two or three times each week until the total of the injected ethanol reached the intended volume. The total volume of injected ethanol ranged from 4 to 95 ml. The general guideline for the total volume of injected ethanol to destroy the lesion completely was calculated according to the following equation:

$$V = \frac{4}{3}\pi(r + 0.5)^3,$$

where V (in milliliters) is the volume of ethanol and r (in centimeters) is the radius of the lesion; 0.5 is added to provide a safety margin, which is based on the concept that a certain amount of the surrounding tissue at the periphery of the lesion as well as the lesion itself must be destroyed to ensure the cure of the lesion. However, the volume and the number of injections were modified depending on the patient's compliance, the number of lesions, the location of the lesions, the findings on CT with contrast enhancement after the therapy, and the goal of the treatment. Forty-seven of the 77 patients received an approximately equal volume as determined by the formula.

Responses to therapy were evaluated by histopathologic examination (14 cases), angiography (42 cases), CT (56 cases), serum levels of α-fetoprotein (all cases), and survival rates (all cases). For histopathologic examination, the resected liver was cut into slices of less than 1 cm in thickness after fixation in formalin. Every slice containing the lesion was sectioned for the observation. Hematoxylin and eosin, azan, orcein, and silver stains were used. CT with contrast enhancement was performed 1–6 months after the therapy in most cases. Angiography was performed 3–6 months after the therapy in most cases. The Kaplan-Meier method [21] was used to calculate survival rates, and the generalized Wilcoxon test [22] was used for statistical analysis. The date of the initial injection was the starting point for the calculations.

Results

Histopathologic Findings

Fourteen cases, 12 in the potentially curative group and two in the palliative group, were evaluated histopathologically. In 11 cases, the liver was resected 16–66 days after the final injection of ethanol; in the remaining three cases, the liver was removed at autopsy 28, 32, and 136 days after the final injection of ethanol, respectively. In these 14 cases, the tumor was completely necrotic in 10 cases, 90% necrotic in three cases, and 70% necrotic in one case. Incidentally, in the seven patients who underwent only PEIT, the tumor was completely necrotic in five cases and 90% necrotic in two cases. In the other seven patients who underwent both PEIT and transcatheter arterial embolization, the tumor was completely necrotic in five cases, 90% necrotic in one case, and 70% necrotic in one case.

In the four cases in which some portions of the lesion remained undestroyed, viable tumor tissue was found in small tumor nodules present around the main tumor, in portions isolated by septa, or along the edge of the lesion.

Imaging Findings

The efficacy of PEIT was evaluated angiographically [7] in 42 cases, 25 in the potentially curative group and 17 in the palliative group. The tumor stain had disappeared completely in 37 cases. The tumor stain was smaller but remained in some portions in one case in the palliative group. In the remaining four cases, all of which were in the palliative group, the tumor stain apparently had not changed.

Follow-up CT was performed to evaluate the effectiveness [7] in 56 cases, 33 in the potentially curative group and 23 in the palliative group. The treated lesion was enhanced in only one case in the palliative group, which suggested the remains of the viable cancer tissue. In this case, angiography also showed an apparent tumor stain. In the remaining 55 cases, CT showed the therapy's effectiveness.

Serum Levels of α-Fetoprotein

In the potentially curative group, 16 cases had elevated serum levels of α-fetoprotein (>100 ng/ml); the levels decreased in all of these cases after PEIT. In the palliative group, eight cases had elevated serum levels of α-fetoprotein (>100 ng/ml); the levels decreased in five cases and increased in the remaining three cases after PEIT.

Survival Rates

The 1-, 2-, 3-, and 4-year survival rates of all 77 patients were 82%, 67%, 53%, and 47%, respectively (Fig. 1). The survival rates were not different between the 23 patients who had PEIT alone and the 54 patients who underwent PEIT and transcatheter arterial embolization (Fig. 2).

When the survival rates were analyzed in the potentially curative group and the palliative group separately, they were significantly ($p < .05$) different between the two groups (Fig. 3). The 1-, 2-, and 3-, and 4-year survival rates of the potentially curative group were 89%, 74%, 68%, and 60%, respectively, whereas the 1-, 2-, and 3-year survival rates of the palliative group were 71%, 54%, and 24%, respectively.

The survival rates were then evaluated with regard to liver function (Fig. 4). The patients in Child's class A had significantly ($p < .05$) higher survival rates than the patients in Child's class C did. Furthermore, the effect of liver function on the survival rates was evaluated separately in the potentially curative group and in the palliative group. In the potentially curative group, the survival rates were significantly different not only between the patients in Child's class A and the patients in Child's class C ($p < .01$) but also between the patients in Child's class A and the patients in Child's class B ($p < .05$) (Fig. 5), whereas degree of liver dysfunction did not cause different prognoses in the palliative group.

With regard to the number of lesions, although the patients who had a single lesion tended to have higher survival rates than those who had multiple lesions, the difference was not statistically significant (Fig. 6).

As for the size of the largest lesion, there was a significant ($p < .05$) difference in the survival rates when the sizes were

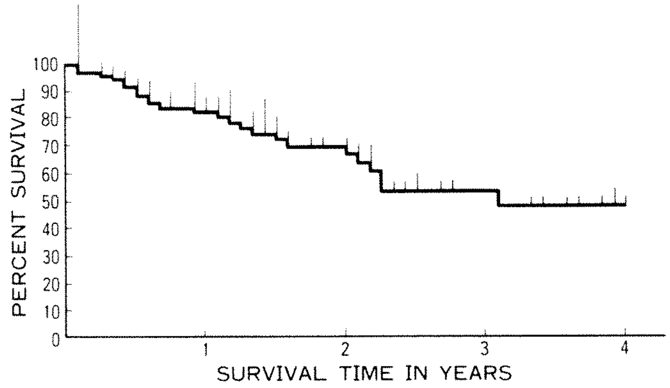

Fig. 1.—Survival of 77 patients who had percutaneous ethanol injection therapy for hepatocellular carcinoma.

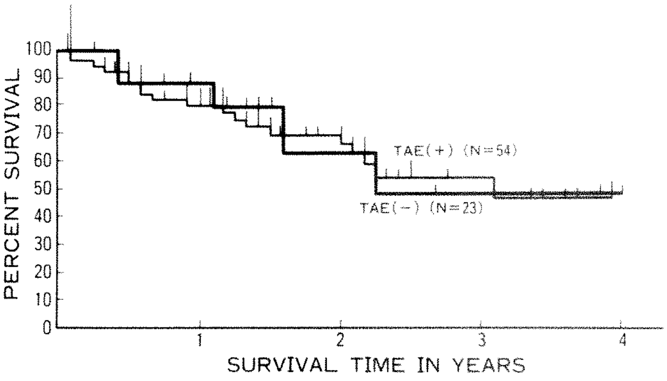

Fig. 2.—Survival of patients who had percutaneous ethanol injection therapy (PEIT) alone and those who had combination of PEIT and transcatheter arterial embolization. Prognosis was not different between two groups. TAE = transcatheter arterial embolization.

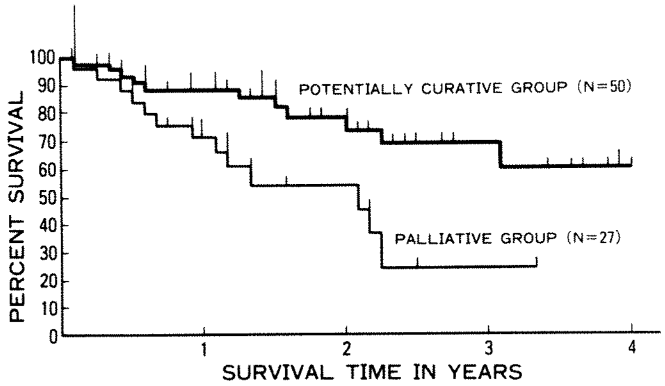

Fig. 3.—Survival of potentially curative group and palliative group who had ethanol injection for hepatocellular carcinoma. Potentially curative group had significantly ($p < .05$) higher survival rates than palliative group did.

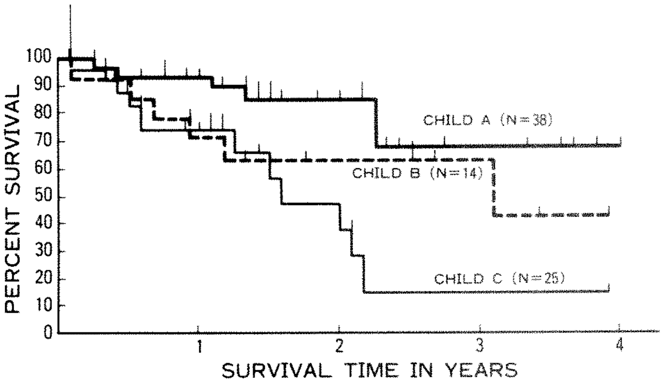

Fig. 4.—Survival of patients treated with ethanol injection in regard to liver function. Patients in Child's class A had significantly ($p < .05$) higher survival rates than did those in Child's class C.

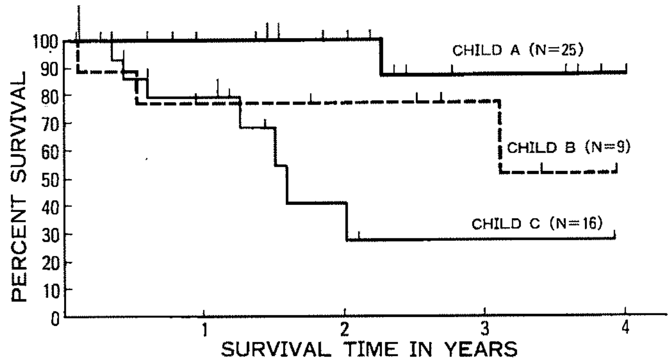

Fig. 5.—Survival of patients treated with ethanol injection in regard to liver function (potentially curative group). Patients in Child's class A had significantly higher survival rates than those in Child's class B ($p < .05$) and those in Child's class C ($p < .01$).

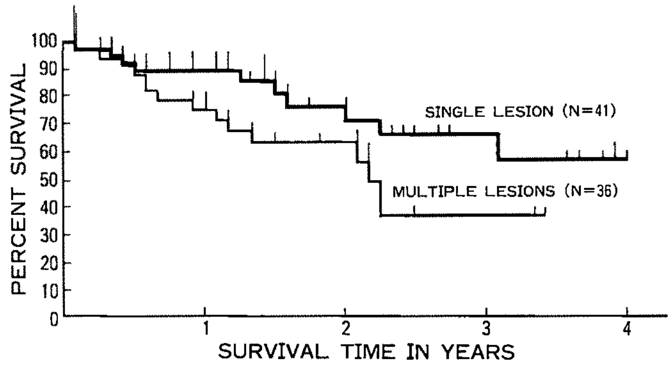

Fig. 6.—Survival of patients treated with ethanol injection in regard to number of lesions. Although patients with single lesion had higher survival rates than those with multiple lesions, difference was not statistically significant.

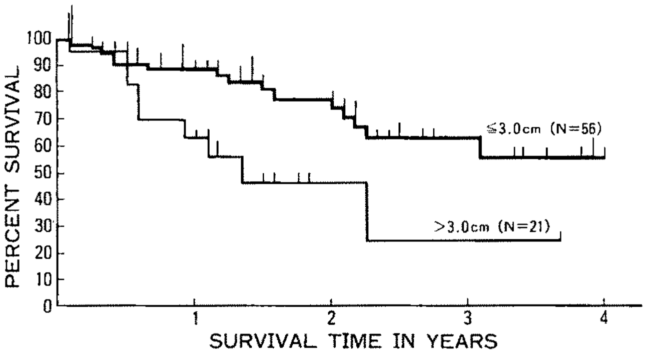

Fig. 7.—Survival of patients treated with ethanol injection in regard to size of largest lesion. Patients with largest lesion ≤3.0 cm in diameter had significantly ($p < .05$) higher survival rates than did those with largest lesion of >3.0 cm.

divided at 3.0 cm (Fig. 7). When the sizes were divided at 2.0, 2.5, or 5.0 cm, although patients with smaller lesions tended to have higher survival rates than patients with larger lesions, the difference was not statistically significant.

Causes of Death

Eleven patients in the potentially curative group and 13 patients in the palliative group died during the 4-year period. In the potentially curative group, only one patient died of hepatocellular carcinoma; other causes of death were variceal bleeding (five patients), hepatic failure (four patients), and pneumonia (one patient). In the palliative group, the causes of death were variceal bleeding (five patients), hepatocellular carcinoma (two patients), hepatic failure (two patients), pneumonia (two patients), gastric cancer (one patient), and pseudomembranous coli (one patient).

Complications

After the injection of ethanol, transient pain, fever, or mild alcohol intoxication were encountered in about one third of the patients. None of these required any special treatment.

The change in liver function after PEIT was mild and transient. Encephalopathy, jaundice, or ascites did not occur after PEIT in any case. Local dissemination of the cancer cells was not encountered in any case. The only serious complication encountered was intraperitoneal hemorrhage due to necrosis of the tumor in one patient, which occurred 2 days after the injection. The patient recovered with conservative treatment. No deaths were directly related to PEIT.

Discussion

Improvements in sonography have made it possible to guide needles percutaneously into abdominal organs more precisely and safely [23]. In PEIT, absolute ethanol is injected into the lesion through fine needles under sonographic observation. Absolute ethanol, which has been used in various therapeutic procedures [24–26], destroys the cancer tissue immediately and directly, mainly through its dehydrative and protein degenerative effects and partly through its thromboembolic effect [24, 25].

As a general rule, we combined PEIT with transcatheter arterial embolization, because the effect of PEIT is local only. Even small hepatocellular carcinomas frequently invade vessel systems, followed by intrahepatic metastasis. Thus, we believe that the main lesion or lesions should be treated by the combination of PEIT and transcatheter arterial embolization and that the lesions undetected by sonography should be controlled by arterial embolization.

The combination of PEIT and transcatheter arterial embolization in many patients made it difficult to evaluate the efficacy of PEIT alone. The best way to examine the short-term efficacy is to compare the histopathologic findings between the seven patients who had PEIT alone and the other seven patients who had both PEIT and transcatheter arterial embolization. This comparison showed that the proportion of lesions that were completely necrotic did not differ between the two groups. Furthermore, survival rates (the best measure of long-term efficacy) were not different between the 23 patients who had PEIT alone and the 54 patients who underwent both PEIT and transcatheter arterial embolization. Probably the local effect of PEIT is much stronger than that of transcatheter arterial embolization, and thus transcatheter arterial embolization adds little efficacy to that of PEIT.

With regard to the short-term efficacy of this therapy, histopathologic examination, which can definitively identify necrosis of the lesion, revealed that the treated lesion was completely destroyed in most cases. The findings in the imaging techniques and the changes in serum levels of α-fetoprotein also showed PEIT to have remarkable short-term efficacy.

The long-term survival rates of the patients who had PEIT may be even better than those of patients treated by surgery, although the size and number of lesions and the degree of liver dysfunction differ between patients treated with PEIT and those treated with surgery. The 1-, 2-, 3-, and 4-year survival rates of all 77 patients who had PEIT were 82%, 67%, 53%, and 47%, respectively. Furthermore, the 1-, 2-, 3-, and 4-year survival rates of the potentially curative group were 89%, 74%, 68%, and 60%, respectively. On the other hand, according to the latest report by the Liver Cancer Study Group of Japan [6], the 1-, 2-, 3-, 4-, and 5-year survival rates of 2478 patients treated by hepatic resection were 67%, 51%, 40%, 29%, and 29%, respectively. The patients treated by surgery frequently had larger lesions (44% had tumors larger than 5 cm in diameter). However, more than two thirds of them (71%) had only one lesion, and most of them probably had better liver function. Patients in Child's class C usually are not considered candidates for surgery.

When a patient had four or more lesions, we treated only the main lesions. This was because we assumed that small undetectable intrahepatic metastases were present in these cases, which would make curative treatment impossible even if PEIT was used on all of the detected lesions. In those cases, because the purpose of PEIT was to reduce the tumor mass, the total volume of injected ethanol tended to be less than that suggested by the general treatment guideline. Survival rates in the palliative group were worse than those in the potentially curative group.

Patients with better liver function had a better prognosis. This tendency was more remarkable in the potentially curative group than in the palliative group, probably because in the potentially curative group, the cancer was cured or at least controlled, and it was not the cancer itself but complications of liver cirrhosis that determined the prognosis. Actually only one patient in the potentially curative group died of hepatocellular carcinoma.

The difference in the number of the lesions did not cause a significantly different prognosis. However, this may be because the number of subjects was not large enough to be statistically significant.

As for the size of the largest lesion, although a statistical significance was obtained only when the sizes were divided at 3.0 cm, this may be simply because the number of subjects was not large enough. Patients with smaller lesions tended to have better prognoses than those with larger lesions did, even when the size of the lesions was divided at 2.0, 2.5, or 5.0 cm.

The death rate from hepatocellular carcinoma may be lower in patients who have PEIT than in those treated by surgery or chemotherapy. This is mainly because patients who undergo PEIT can undergo PEIT again when any recurrence of the cancer is found, and partly because many of the patients who undergo PEIT have such advanced liver cirrhosis that they frequently die of complications of cirrhosis.

The only serious complication experienced in the 419 procedures was intraperitoneal hemorrhage, probably due to necrosis of the treated tumor, in one case. Since this difficulty, we have performed PEIT only on patients whose prothrombin times are more than 35% and whose platelet counts are more than 40,000/μl. PEIT is a safe procedure; other investigators also have reported low complication rates with this therapy [11–17, 19].

Alterations in liver function after PEIT were much milder than changes that occur after surgical resection or transcatheter arterial embolization. Thus, PEIT can be considered for patients with severe liver dysfunction who cannot be treated by other procedures. No deaths were directly related to PEIT. In surgical resection, postoperative hepatic failure often occurs, and the operative mortality rate has been about 10% in Japan [27, 28].

REFERENCES

1. Prevention of liver cancer: report of WHO meeting. In: *World Health Organization Technical Report Series*. Geneva: World Health Organization, **1983**:7–8
2. Kubo Y, Okuda K, Musha H, et al. Detection of hepatocellular carcinoma during a clinical follow-up of chronic liver disease. *Gastroenterology* **1978**;74:578–580
3. Liaw YF, Tai DI, Chu CM, et al. Early detection of hepatocellular carcinoma in patients with chronic type B hepatitis. *Gastroenterology* **1986**;90:263–267
4. McDermott WV. Surgical disease in East Africa. *Arch Surg* **1987**;122:397–402
5. Lee Y-TN. Primary carcinoma of the liver: diagnosis, prognosis, and management. *J Surg Oncol* **1983**;22:17–25
6. Liver Cancer Study Group of Japan. *Survey and follow-up study of primary liver cancer in Japan*, report 8. Kyoto: Shinkoinsatsu, **1988**:63–85
7. Nakamura H, Tanaka T, Hori S, et al. Transcatheter embolization of hepatocellular carcinoma: assessment of efficacy in cases of resection following embolization. *Radiology* **1983**;147:401–405
8. Yamada R, Kitayama K, Sato M, et al. Transcatheter arterial embolization in the treatment of primary liver cancer. In: *Diseases of the liver and biliary system*, vol. 2. Tokyo: Nihon Rinsho, **1988**:161–166
9. Bhardwaj S, Bruckner HW, Holland JF. Therapy of malignant tumors of the liver. In: Berk JE, Haubrich WS, Kalser MH, Roth JLA, Schaffner F, eds. *Gastroenterology*, 4th ed. Philadelphia: Saunders, **1985**:3388–3397
10. Sugiura N, Takara K, Ohto M, et al. Percutaneous intratumoral injection of ethanol under ultrasound imaging for treatment of small hepatocellular carcinoma. *Acta Hepatol Jpn* **1983**;24:920
11. Livraghi T, Festi D, Monti F, Salmi A, Vettori C. US-guided percutaneous alcohol injection of small hepatic and abdominal tumors. *Radiology* **1986**;161:309–312
12. Shiina S, Yasuda H, Muto H, et al. Percutaneous ethanol injection in the treatment of liver neoplasms. *AJR* **1987**;149:949–952

13. Sheu JC, Sung JL, Huang GT, et al. Intratumor injection of absolute ethanol under ultrasound guidance for the treatment of small hepatocellular carcinoma. *Hepatogastroenterology* **1987**;34:255-261
14. Suyama Y, Horishi M, Ebisui S, et al. US guided intratumoral ethanol injection therapy of small liver cancer: clinical evaluation for twenty cases. *J Jpn Soc Cancer Ther* **1987**;22:818-826
15. Fujimoto T. The experimental and clinical studies of percutaneous ethanol injection therapy (PEIT) under ultrasonography for small hepatocellular carcinoma. *Acta Hepatol Jpn* **1988**;29:52-59
16. Ebara M, Nihei T, Ohto M. Intratumoral injection of absolute ethanol for treatment of small hepatocellular carcinoma. *Naika* **1988**;61:665-669
17. Livraghi T, Salmi A, Bolondi L, et al. Small hepatocellular carcinoma: percutaneous alcohol injection: results in 23 patients. *Radiology* **1988**;168:313-317
18. Kubota Y, Nakano T, Seki T, et al. Validity of MR imaging for monitoring effects of percutaneous ethanol injection for HCC. *Hepatogastroenterology* **1989**;36:262-265
19. Shiina S, Tagawa K, Unuma T, Terano A. Percutaneous ethanol injection therapy for the treatment of hepatocellular carcinoma. *AJR* **1990**;154:947-951
20. Child CG III. Hepatic circulation and portal hypertension. Philadelphia: Saunders, **1954**
21. Kaplan EL, Meier P. Nonparametric estimation from incomplete observations. *J Am Stat Assoc* **1958**;53:457-481
22. Gehan E. A generalized Wilcoxon test for comparing arbitrarily singly-censored samples. *Biometrika* **1965**;52:203-223
23. Ohto M, Karasawa E, Tsuchiya Y, et al. Ultrasonically guided percutaneous contrast medium injection and aspiration biopsy using a real-time puncture transducer. *Radiology* **1980**;136:171-176
24. Ellman BA, Parkhill BJ, Curry TS, et al. Ablation of renal tumors with absolute ethanol: a new technique. *Radiology* **1981**;141:619-626
25. Yune HY, Klatte EC, Richmond BD, Rabe FE. Absolute ethanol in thrombotherapy of bleeding esophageal varices. *AJR* **1982**;138:1137-1141
26. Solbiati L, Giangrande A, Pra LD, Bellotti E, Cantù P, Ravetto C. Percutaneous ethanol injection of parathyroid tumors under US guidance: treatment for secondary hyperparathyroidism. *Radiology* **1985**;155:607-610
27. Nagasue N, Yukaya H, Ogawa Y, Sasaki Y, Chang YC, Niimi K. Clinical experience with 118 hepatic resections for hepatocellular carcinoma. *Surgery* **1986**;99:694-701
28. Nagao T, Goto S, Kawano N, et al. Hepatic resection for hepatocellular carcinoma: clinical features and long-term prognosis. *Ann Surg* **1987**;205:33-40

American Roentgen Ray Society Residents' Award Papers, 1991

The ARRS announces competition for the 1991 President's Award and two Executive Council Awards for the best papers concerning the clinical application of the radiologic sciences.

Awards

The winner of the President's Award will receive a certificate and a $2000 prize. The winners of the two Executive Council Awards will each be given a certificate and a prize of $1000. The winners will be announced on March 15, 1991. Winning papers will be presented at the ARRS annual meeting at the Sheraton Boston Hotel, Boston, MA, May 5-10, 1991. Winning papers will be submitted for early publication in the *American Journal of Roentgenology*. All other papers will be returned to the authors.

Regulations

Eligibility is limited to residents or fellows in radiology who have not yet completed 4 years of approved training in a radiologic discipline. A letter from the resident's department chairman attesting to this status must accompany the manuscript. The resident must be the sole or senior author and be responsible for all or most of the project.

Submitted manuscripts must not exceed 5000 words and have no more than 10 illustrations. Four copies of the manuscript and illustrations are required. Submitted manuscripts should not contain previously presented or published material and should not be under consideration for publication elsewhere.

Deadline for submissions is February 15, 1991. Send papers to

Nancy O. Whitley, M.D.
Chairman, Committee on Education & Research
American Roentgen Ray Society
Department of Radiology
University of Maryland Medical Systems Hospital
22 S. Greene St.
Baltimore, MD 21201

Regenerating Nodules in Hepatic Cirrhosis: MR Findings with Pathologic Correlation

Takamichi Murakami[1]
Chikazumi Kuroda[1]
Taro Marukawa[1]
Koushi Harada[1]
Kenichi Wakasa[2]
Masami Sakurai[2]
Morito Monden[3]
Akinori Kasahara[4]
Sumio Kawata[5]
Takahiro Kozuka[1]

To establish clearly the pathologic basis for small low-intensity nodules seen on MR images of the cirrhotic liver, we obtained MR images in 26 patients with cirrhosis in whom partial hepatectomy for hepatoma (15 patients), laparoscopy for cirrhosis (10 patients), or autopsy (one patient) was subsequently performed. Small low-intensity nodules were seen on gradient-echo images with short TEs (10–13 msec) in 13 of the 26 patients. In 12 of these 13 patients, small low-intensity nodules appeared larger and clearer as the TE was prolonged (14–25 msec). On T2-weighted spin-echo images, small low-intensity nodules were seen in 12 of the 13 patients, but not seen as well as on gradient-echo images. Pathologic correlation in these 13 patients revealed that the nodules on the MR images corresponded to iron deposits in regenerating nodules. Small low-intensity nodules were observed only on T2-weighted spin-echo images in two of the remaining 13 patients, in whom microscopic examination of the liver revealed marked inflammatory cell infiltration in the fibrous septa and no iron deposition.

We conclude that small low-intensity nodules observed on MR images are caused by iron deposits in regenerating nodules, and that gradient-echo images with short and prolonged TEs are useful to confirm the presence of iron deposits in regenerating nodules.

***AJR* 155:1227–1231, December 1990**

A study published in 1987 reported that regenerating nodules were sometimes demonstrated as small low-intensity nodules on T2-weighted spin-echo or gradient-echo MR images [1]. It was suggested in other previously published papers that small low-intensity nodules seen on MR images of the liver in cirrhotic patients might represent signal loss due to the magnetic susceptibility effect caused by deposited iron in regenerating nodules [2–4]. However, direct correlations of MR and pathologic findings had not been performed. In this study, we correlated MR images of cirrhotic patients with gross and microscopic findings to establish more clearly the pathologic basis for small low-intensity nodules. Moreover, optimal sequences to demonstrate small low-intensity nodules also were determined with spin-echo and gradient-echo techniques.

Materials and Methods

Between October 1988 and September 1989, 78 consecutive patients with clinically diagnosed liver cirrhosis were studied by using MR imaging to screen for liver tumors. A histologic diagnosis of liver cirrhosis was made within 3 months after MR examination in 26 of these patients at the time of partial hepatectomy for hepatoma (15 patients), laparoscopy with liver biopsy (10 patients), or autopsy (one patient). We analyzed the MR and pathologic findings in these 26 patients. The cause of liver cirrhosis was alcoholism in four patients, hepatitis in 18, and unknown in four. Twenty-two of the 26 patients were men and four were women; they were 35–69 years old.

Received April 19, 1990; accepted after revision June 28, 1990.

[1] Department of Radiology, Osaka University Medical School, 1-1-50 Fukushima, Fukushima-ku, Osaka 553, Japan. Address reprint requests to T. Murakami.

[2] Department of Pathology, Osaka University Medical School, Osaka 553, Japan.

[3] The Second Department of Surgery, Osaka University Medical School, Osaka 553, Japan.

[4] The First Department of Internal Medicine, Osaka University Medical School, Osaka 553, Japan.

[5] The Second Department of Internal Medicine, Osaka University Medical School, Osaka 553, Japan.

0361-803X/90/1556-1227
© American Roentgen Ray Society

MR imaging was performed with a superconducting magnet operating at 1.5 T (Magnetom, Siemens). MR images were obtained by using spin-echo sequences with 600–850/15 (TR/TE) and 1800–2600/70 with ECG gating. Gradient-echo (fast low-angle shot imaging) sequences were performed with 150/10–13,14–25/30–90° (TR/TE/flip angle). The slice thickness was 8–10 mm. Two signal acquisitions were used for T1- and T2-weighted spin-echo images and one signal acquisition for gradient-echo images. Spin-echo images were acquired with a 256 × 256 matrix and gradient-echo images with a 256 × 256 rectangular matrix. A body coil was used with a field of view of 33.3 cm. The gradient moment nulling technique was used for the T2-weighted spin-echo images, and the presaturation technique eliminating flow artifacts was used for T1- and T2-weighted spin-echo images. For gradient-echo images, the gradient moment nulling technique was used in 16 patients and the presaturation technique was used in 10 patients. The gradient-echo images were obtained with breath-holding (about 20 msec).

Three radiologists evaluated the MR images of the 26 patients without knowledge of the pathologic findings, paying special attention to the detectability, variations in intensity, and size of small low-intensity nodules.

In all 26 cases, specimens of the liver were stained with hematoxylin and eosin and Prussian blue. The degree of inflammatory cell infiltration into the fibrous septa and the amount of iron deposited in liver cells and Kupffer cells in regenerating nodules and fibrous septa were estimated by two pathologists.

In 14 of the 26 patients, formalin-fixed liver specimens were studied with MR images by using the same pulse sequences that had been used for in vivo MR images. MR images of the remaining 12 liver specimens could not be obtained because of their small size.

Results

Small low-intensity nodules in the liver were seen on gradient-echo images using short TEs in 13 of the 26 patients. In these 13 patients, slight-to-marked iron deposits in both liver cells and Kupffer cells of regenerating nodules were recognized by histologic examination. Low-intensity nodules appeared larger and clearer on gradient-echo images as the TE was prolonged in 12 of the 13 patients in whom slight-to-moderate iron deposits in regenerating nodules were recognized histologically (Fig. 1). In the remaining patient with marked iron deposits in both liver cells and Kupffer cells of regenerating nodules, low-intensity nodules appeared larger and fused; as the TE was prolonged, there was an apparent decrease in the signal intensity of the liver and no low-intensity nodules were seen on gradient-echo images (Fig. 2). No low-intensity nodules were seen on gradient-echo images in the 13 patients in whom no, or very slight, iron deposits in regenerating nodules were shown by histologic examination.

Small low-intensity nodules were seen on T1-weighted spin-echo images in only three of the 13 patients with iron deposits and in none of the 13 patients without iron deposits. The number of low-intensity nodules seen in patients with iron deposits was small and their outlines were obscure.

On T2-weighted images, small low-intensity nodules were seen in 12 of the 13 patients with iron deposits, but the number of small low-intensity nodules was smaller and their contours were more obscure than when gradient-echo images were used (Figs. 1 and 2). In two of the 12 patients in whom marked iron deposits in liver cells and moderate or marked iron deposits in Kupffer cells of regenerating nodules were recognized histologically, low-intensity nodules were obscure, and the signal intensity of the liver surrounding low-intensity nodules apparently was low on T2-weighted spin-echo images (Fig. 2).

Iron deposits in the fibrous septa were seen in five patients in whom low-intensity nodules were seen only on gradient-echo images, but the deposition was slight. Small low-intensity nodules surrounded by high-intensity septa were seen only on T2-weighted spin-echo images in two of the 13 patients without iron deposits. Microscopic examination of the liver revealed marked inflammatory cell infiltration into the fibrous septa in these two patients (Fig. 3). In the other 11 patients without iron deposits, mild-to-moderate inflammatory cell infiltration into the fibrous septa was recognized microscopically.

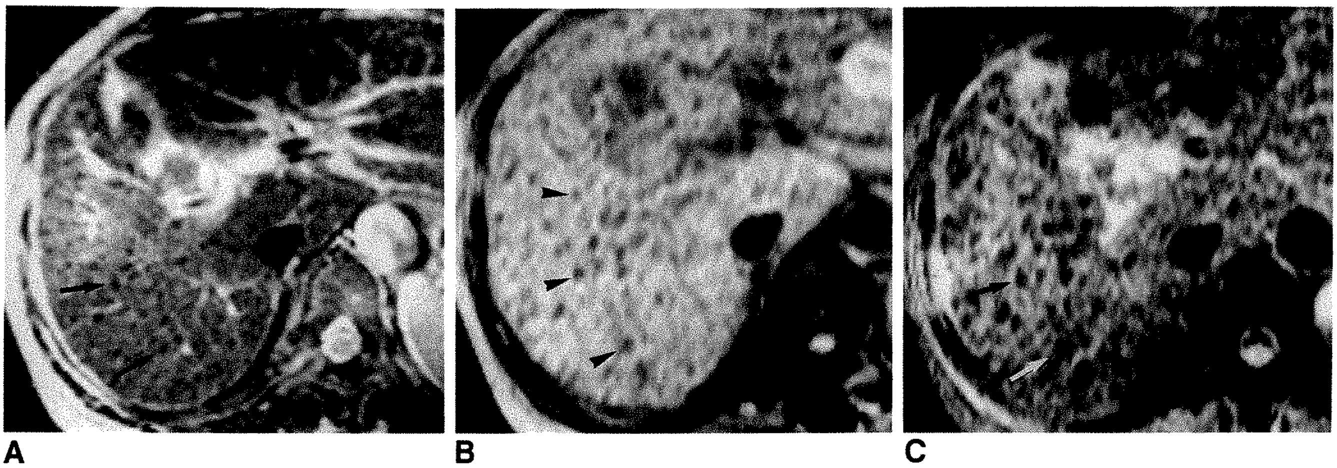

Fig. 1.—Cirrhosis with moderate iron deposition in regenerating nodules.
***A*, T2-weighted spin-echo MR image, 2400/70, shows small low-intensity nodules (*arrows*).**
***B*, Gradient-echo MR image with a short TE, 150/10/55°, shows small low-intensity nodules clearly (*arrowheads*).**
***C*, Small low-intensity nodules appear larger and clearer on gradient-echo MR image as TE is prolonged, 150/23/55° (*arrows*).**

Direct correlation of MR images of resected specimens with gross and microscopic findings revealed that small, low-intensity nodules seen on gradient-echo images were iron deposits in regenerating nodules (Fig. 4). Low-intensity nodules in the resected specimens with iron deposits in regenerating nodules appeared larger and clearer on gradient-echo images as the TE was prolonged (Fig. 4); these findings coincided with gradient-echo images obtained in vivo (Figs. 1 and 2). Small low-intensity nodules were not observed on MR images of resected specimens that did not have iron deposits in regenerating nodules. The two patients with marked inflammatory cell infiltration into the fibrous septa were not included in this direct correlation study.

Discussion

Siderosis of the liver is common in patients with liver cirrhosis [5–8]. However, since iron deposits in regenerating nodules are small [6, 7] and their distribution is patchy [9], imaging techniques other than MR fail to depict the deposition of iron in the liver. In patients with cirrhosis, regenerating nodules were reported to appear as small low-intensity nodules on MR images [1]. We [2] and Ohtomo et al. [3, 4] hypothesized that the small low-intensity nodules might represent signal loss due to the magnetic susceptibility effect caused by deposited iron in regenerating nodules in the cirrhotic liver. Our direct pathologic-MR correlation in this

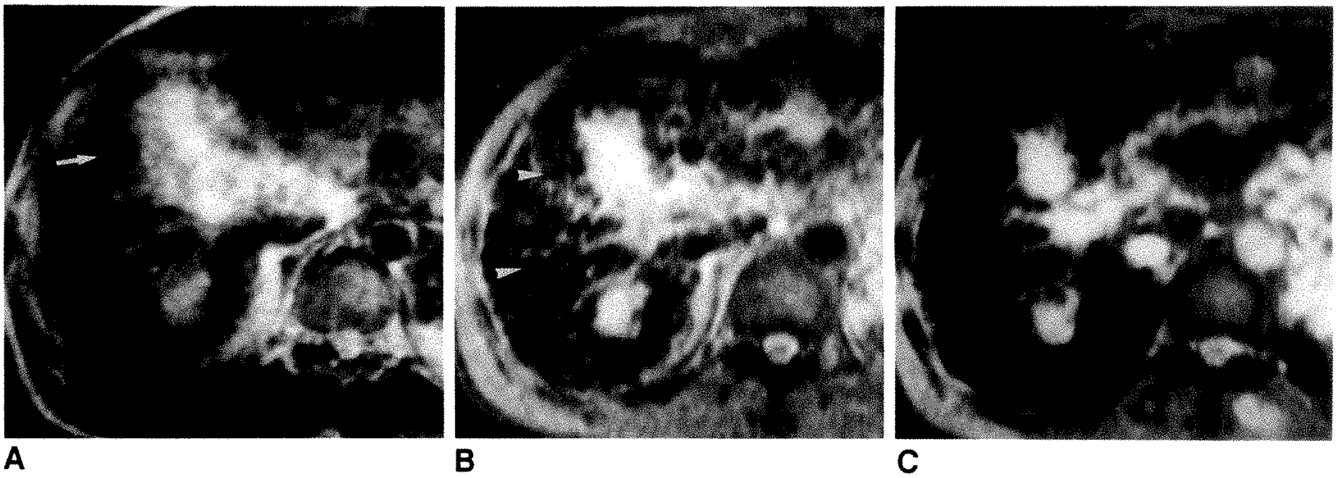

Fig. 2.—Cirrhosis with marked iron deposition in regenerating nodules.

A, T2-weighted spin-echo MR image, 2000/70, shows apparent low signal intensity of liver and small low-intensity nodules (*arrow*), but they are somewhat obscured by respiratory motion and magnetic susceptibility caused by deposited iron.

B, Gradient-echo MR image with a short TE, 150/12/30°, shows small low-intensity nodules more clearly (*arrowheads*).

C, Gradient-echo MR image with prolonged TE, 150/18/30°, shows apparent decrease in signal intensity of liver and no low-intensity nodules because of enhancement of magnetic susceptibility effect.

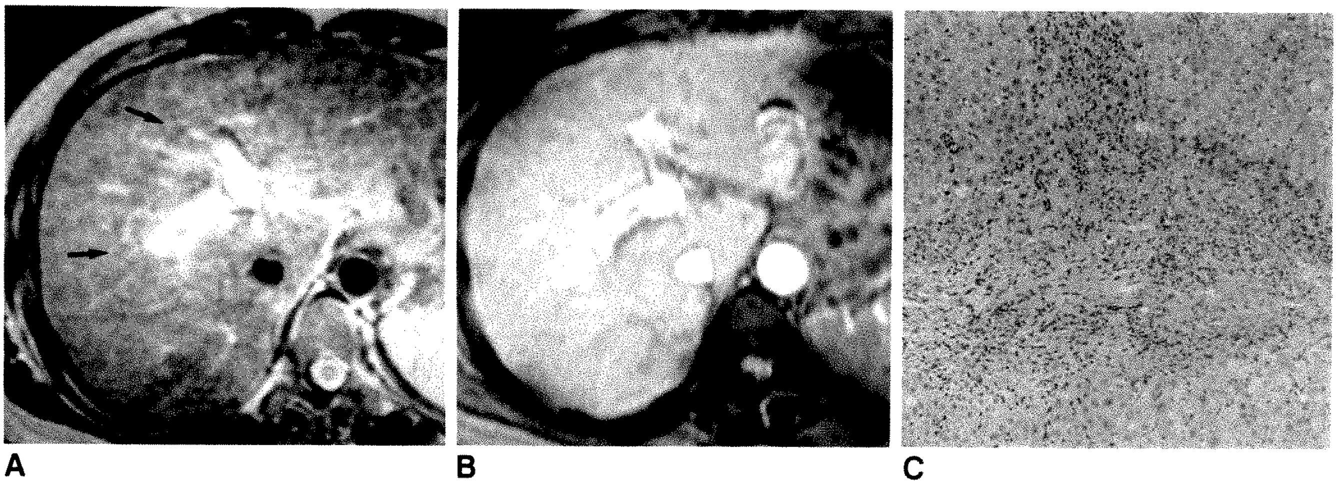

Fig. 3.—Cirrhosis without iron deposition in regenerating nodules.

A, T2-weighted spin-echo MR image, 2000/70, shows small low-intensity nodules surrounded by high-intensity septa (*arrows*).

B, Gradient-echo MR image, 150/12/60°, does not show nodules.

C, Marked inflammatory cell infiltration into fibrous septa is noted. (H and E stain)

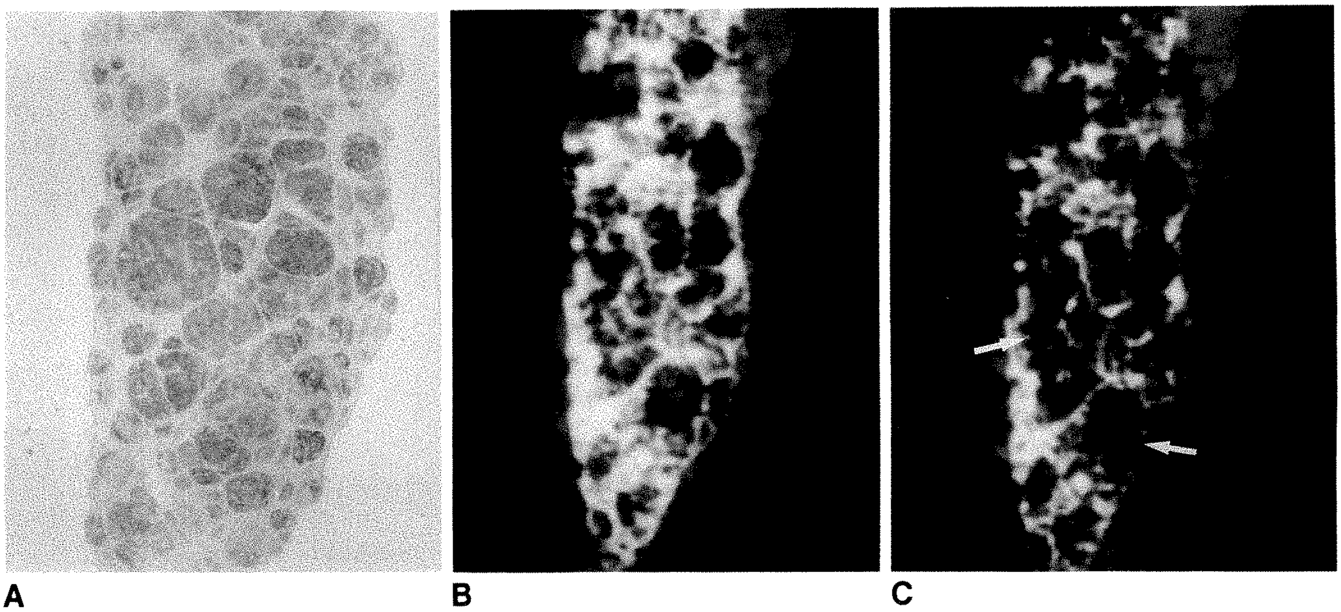

Fig. 4.— Formalin-fixed liver specimen with iron deposits in regenerating nodules.

A, Regenerating nodules contain iron deposits ranging from 2 to 9 mm. (Prussian blue stain)

B, Gradient-echo MR image with a short TE, 150/10/90°, shows low-intensity nodules (3–11 mm) corresponding to iron deposits in regenerating nodules.

C, Low-intensity nodules (4–35 mm) appear larger and fused (*arrows*) on gradient-echo MR image as TE is prolonged, 150/15/90°. These findings coincided with in vivo gradient-echo MR images.

series confirmed that the low-intensity nodules observed on gradient-echo images were iron deposits in regenerating nodules.

The gradient-echo technique without a refocusing 180° pulse is useful in depicting iron deposits in regenerating nodules because it is more sensitive than the spin-echo technique to the magnetic susceptibility effect caused by the presence of iron [10–14]. Small low-intensity nodules appear larger and sometimes clearer on gradient-echo images as the TE is prolonged, because the magnetic susceptibility effect is enhanced as TE is prolonged [10, 11, 14]. Therefore, in general, gradient-echo images with prolonged TEs are more useful than gradient-echo images with short TEs in depicting iron deposits in regenerating nodules. However, in patients with marked iron deposits in regenerating nodules, it is difficult to demonstrate small low-intensity nodules because low-intensity nodules are fused and become unclear on gradient-echo images with prolonged TEs. Therefore, gradient-echo images with short and prolonged TEs should be obtained in patients with liver cirrhosis to confirm iron deposits in regenerating nodules.

In this study, we obtained gradient-echo images with variable TEs, but we think that it is adequate and better to obtain only in-phase images with short and prolonged TEs in order to eliminate the chemical-shift effect.

The T2-weighted spin-echo technique is also influenced by the magnetic susceptibility effect [15, 16]. However, low signal-to-noise ratios and contrast-to-noise ratios due to respiratory motion and the magnetic susceptibility effect caused by deposited iron obscured low-intensity nodules on T2-weighted spin-echo images withouth breath-holding. Therefore, T2-weighted spin-echo images are not useful in confirming iron deposits in regenerating nodules.

The regenerating nodules might be shown as low-intensity nodules because the fibrous septa infiltrated by inflammatory cells had relatively high intensities on T2-weighted images (Maeda et al., presented at the annual meeting of the Radiological Society of North America, November 1989). However, in this study, small low-intensity nodules surrounded by high-intensity septa were seen only on T2-weighted spin-echo images in the two patients with marked inflammatory cell infiltration into the fibrous septa, but they were not seen in the remaining 11 patients with mild or moderate inflammatory cell infiltration into the fibrous septa. No iron deposits in regenerating nodules were seen in these 13 patients. Therefore, our results suggest that small low-intensity nodules observed only on T2-weighted spin-echo images in cirrhotic patients without iron deposition may depend on the degree of inflammatory cell infiltration into the fibrous septa. As to the cause of the small low-intensity nodules, Ohtomo et al. [4] suggested that regenerating nodules surrounded by vascular fibrous septa might be another possible reason for the presence of small low-intensity nodules [4]. In our series, there were no cases in which regenerating nodules were surrounded by vascular fibrous septa.

On the basis of our results, we conclude that small low-intensity nodules seen on MR images are iron deposits in regenerating nodules. Gradient-echo images with short and prolonged TEs are useful to confirm regenerating nodules with iron deposition noninvasively.

ACKNOWLEDGMENT

We thank Nobuhiro Satoh for suggestions.

REFERENCES

1. Itai Y, Ohnishi S, Ohtomo K, et al. Regenerating nodules of liver cirrhosis: MR imaging. *Radiology* **1987**;165:419–423
2. Murakami T, Marukawa T, Kuroda C, et al. Siderotic regenerating nodules in liver cirrhosis: evaluation by gradient echo (FLASH) imaging 1.5T. *Nippon Igaku Hoshasen Gakkai Zasshi* **1989**;49:1427–1429 (in Japanese)
3. Ohtomo K, Itai Y, Ohtomo Y, Shiga J, Minami M, Iio M. MRI demonstration of pseudolobules of liver cirrhosis: particular reference to iron deposits on autopsied specimens. *Nippon Igaku Hoshasen Gakkai Zashi* **1989**;49(5): 681–683 (in Japanese)
4. Ohtomo K, Itai Y, Ohtomo Y, Shiga J, Iio M. Regenerating nodule of liver cirrhosis: MR imaging with pathologic correlation. *AJR* **1990**;154:505–507
5. Runge VM, Clanton JA, Smith FW, et al. Nuclear magnetic resonance of iron and copper disease states. *AJR* **1983**;141:943–948
6. Williams R, Williams HS, Scheuer PJ, Pitcher CS, Loiseau E, Sherlock S. Iron absorption and siderosis in chronic liver disease. *Q J Med* **1967**;141:151–166
7. Kent G, Popper H. Liver biopsy in diagnosis of hemochromatosis. *Am J Med* **1968**;44:837–841
8. Pachet GS, French SW, Levy J, MacDonald RA. Histologic and chemical tissue iron: significance for hemochromatosis. *Arch Pathol Lab Med* **1965**;79:452–461
9. Searle JW, Kerr JFR, Halliday JW, Powell LW. Iron storage disease. In: MacSween RNM, Anthony PP, Scheuer PJ, eds. *Pathology of liver.* New York: Churchill Livingstone, **1987**:181–201
10. Frahm J, Melboldt KD, Hanicke W. Direct FLASH MR imaging of magnetic field inhomogeneities by gradient compensation. *Magn Reson Med* **1988**;6:474–480
11. Hendric RE, Kneeland JB, Stark DD. Maximizing signal-to-noise and contrast-to-noise ratios in FLASH imaging. *Magn Reson Imaging* **1987**;5: 117–127
12. Buxton RB, Edelman RR, Rosen BR, Wismer GL, Brady TJ. Contrast in rapid MR imaging: T1- and T2-weighted imaging. *J Comput Assist Tomogr* **1987**;11(1):7–16
13. Wendt RE III, Wilcott MR III, Nitz W, Murphy PH, Bryan RN. MR imaging of susceptibility-induced magnetic field inhomogeneities. *Radiology* **1988**;168:837–841
14. Haacke EM, Tkach JA, Parrish TB. Reduction of T2* dephasing in gradient field-echo imaging. *Radiology* **1989**;170:457–462
15. Edelman RR, Johnson KA, Buxton RB, et al. MR of hemorrhage: a new approach. *AJNR* **1986**;7:751–756
16. Winkler ML, Thoeni RF, Luh N, Kaufman L, Margulis AR. Hepatic neoplasia: breath-hold MR imaging. *Radiology* **1989**;170:801–806

Book Review

Nonionizing Radiation Protection, 2nd ed. (WHO Regional Publications, European Series, No. 25.) Edited by Michael J. Suess and Deirdre A. Benwell-Morison. Copenhagen: World Health Organization, Regional Office for Europe, 346 pp., 1989. $34.40

For most radiologists and radiotherapists, the term *radiation hazard* has been associated with ionizing radiation. Recently, however, interest has increased in the biological effects of nonionizing radiation, which includes ultraviolet, infrared, and the whole spectrum of RF electromagnetic radiation. It also includes mechanically produced radiation, such as ultrasound. In contrast to ionizing radiation, nonionizing radiation does not have sufficient energy to remove electrons from atoms and thus cause direct chemical and consequent biochemical changes. In general, however, it can produce heating effects at sufficiently high intensities. Other more subtle and controversial effects have been proposed as mechanisms for biological damage at exposure levels far below those required for thermal effects.

This book is the second edition of the original 1982 World Health Organization summary of current knowledge of the physical properties of nonionizing radiation and its effects on humans. Most chapters have been updated, and the chapters on RF and extra low frequency (ELF) electromagnetic radiation have been rewritten completely to reflect current areas of concern and interest.

The book has seven main sections. The first five are organized in order of decreasing electromagnetic energy and cover ultraviolet; optical radiation, with particular reference to lasers; infrared; and RF and ELF electromagnetic radiation. These are followed by a section on ultrasound. The final section of regulation and enforcement procedures probably will be of more interest to organizations than to individual physicians.

The format for each section is fairly standard. A physical description and methods of production for each type of radiation are followed by discussions of the mechanisms of interaction with biological tissue and the resultant effects in humans. Safety standards and control measures to achieve these standards are given. Each section ends with a short summary of conclusions and recommendations.

In contrast to some other publications that deal with this subject material, the text is lucid and uses a minimum of mathematics and technical jargon. Système International d'Unités (SI units) are used throughout. Although it has a few typographic errors (e.g., on page 182, the magnetic field during a thunderstorm is given as 0.5 μT instead of 0.5 mT), the book appears to be edited meticulously and is both informative and pleasant to read. The introduction apologizes for the fact that the bibliographies are necessarily incomplete, particularly in those areas such as ELF in which much current work is occurring. However, the wealth of references cited at the end of each section is an indication of the care that has gone into compiling this volume.

Of particular interest to a medical audience are the sections with direct medical application, such as the use of RF fields in diathermy, hyperthermia, and MR imaging. These chapters cover exposure of both patient and operator. The diagnostic and therapeutic uses of ultrasound are covered fully. With the rapid spread of laser applications in medicine, the section on lasers is recommended. The book is complete enough that it can be used as a text for college level courses on nonionizing radiation and its effects on human health.

Physicians often are called on to act as scientific advocates in areas that may be beyond their expertise. For example, in many communities, debates are occurring as to the effects of high-voltage power transmission lines and of magnetic fields from domestic appliances and so forth on human health. This book is a valuable resource to check out source material for extravagant claims of health hazards from sources such as these. In view of increasing public concern about environmental issues, particularly those involving radiation, physicians can benefit from the easily accessible and authoritative information in this volume. This book is an extremely worthwhile purchase.

Douglas R. Shearer
Rhode Island Hospital
Providence, RI 02902

Case Report

Familial Splenic Epidermoid Cyst

Mark W. Ragozzino,[1] Henry Singletary,[2] and Ronald Patrick[3]

The differential diagnosis of cystic lesions of the spleen includes cystic neoplasms (sarcoma, lymphangioma, hamartoma), parasitic cysts (echinococcosis), nonparasitic abscess, pseudocysts (without an epithelial lining), and epithelial cysts [1-3]. Epithelial cysts can be classified as mesothelial, epidermoid, and dermoid. Epidermoid cysts are now generally believed to be due to squamous metaplasia within preexisting mesothelial cysts [2, 4]. Dermoid cysts possess skin adnexa and squamous epithelium. Very few have been reported, and their existence is controversial [5]. We observed three siblings with splenic epidermoid cysts. Splenic rupture occurred in two of the three siblings. The familial occurrence of epidermoid cysts and their apparent tendency to rupture prompted this case report.

Case Reports

A 16-year-old boy collided with another player while playing baseball and later developed pain and fullness in the left upper quadrant. Abdominal CT showed a large splenic cyst and a large amount of intraperitoneal fluid or hemorrhage. Splenectomy was performed. There was 2000 ml of old intraperitoneal blood. There was an 11 × 12 × 9 cm unilocular cyst lined by firm, white, trabeculated tissue containing hemorrhagic material. Microscopic analysis of the cyst revealed an inner lining of stratified squamous epithelial cells with some areas of nonciliated, nonsecretory cuboidal (mesothelial) cells. The cyst wall was partially calcified.

The 23-year-old pregnant sister of the index patient was incidentally observed to have a large splenic cyst on screening obstetric sonography. She came to the emergency department 3 weeks postpartum complaining of pain in the back and left upper quadrant. Abdominal CT showed a complex splenic cyst and free intraperitoneal fluid or hemorrhage. Splenectomy was performed. There was 1300 ml of gray-green intraperitoneal fluid. The spleen weighed 1150 g and measured 20 × 10 × 10 cm. Cultures of the intraperitoneal fluid were negative. Gross section of the spleen contained three cysts measuring 14.5, 4.0, and 3.0 cm, respectively. The three cysts were lined almost entirely by stratified squamous epithelium and had a trabeculated appearance.

The 21-year-old sister of the index patient was brought to the emergency department. She complained of persistent, dull, upper abdominal pain with radiation to the back; nausea; and weight loss during the past year. Results of esophagogastroduodenoscopy 6 months earlier had been normal. Sonography showed a 3.5-cm simple cyst and a separate 4.5-cm cyst with low-level echoes compatible with either hemorrhage or infection (Fig. 1A). A follow-up CT scan obtained 3 days later (Fig. 1B) confirmed the sonographic findings. The patient's persistent symptoms, active life-style (which included frequent backpacking trips to remote areas), and familial history prompted prophylactic splenectomy. Gross and microscopic analysis revealed two splenic epidermoid cysts (Figs. 1C and 1D).

Review of the health of the siblings' grandparents, parents, aunts, uncles, cousins, nephews, and nieces revealed no other splenic abnormalities.

Discussion

Epithelial cysts of the spleen are uncommon, making up approximately 10% of benign, nonparasitic cysts [6], as determined on the basis of referral practices. Approximately 200 cases of splenic epidermoid cysts have been described in the English literature. The mean age of patients diagnosed with epidermoid cysts is approximately 20 years, with a range

---

Received February 22, 1990; accepted after revision May 20, 1990.

[1] Delaney Radiologists, 2212 Delaney Ave., Wilmington, NC 28401. Address reprints requests to M. W. Ragozzino.

[2] Wilmington Pathology Associates, 1626 Harbour Dr., Wilmington, NC 28402.

[3] Department of Surgery, New Hanover Memorial Hospital, Wilmington, NC 28402.

AJR 155:1233-1234, December 1990 0361-803X/90/1556-1233 © American Roentgen Ray Society

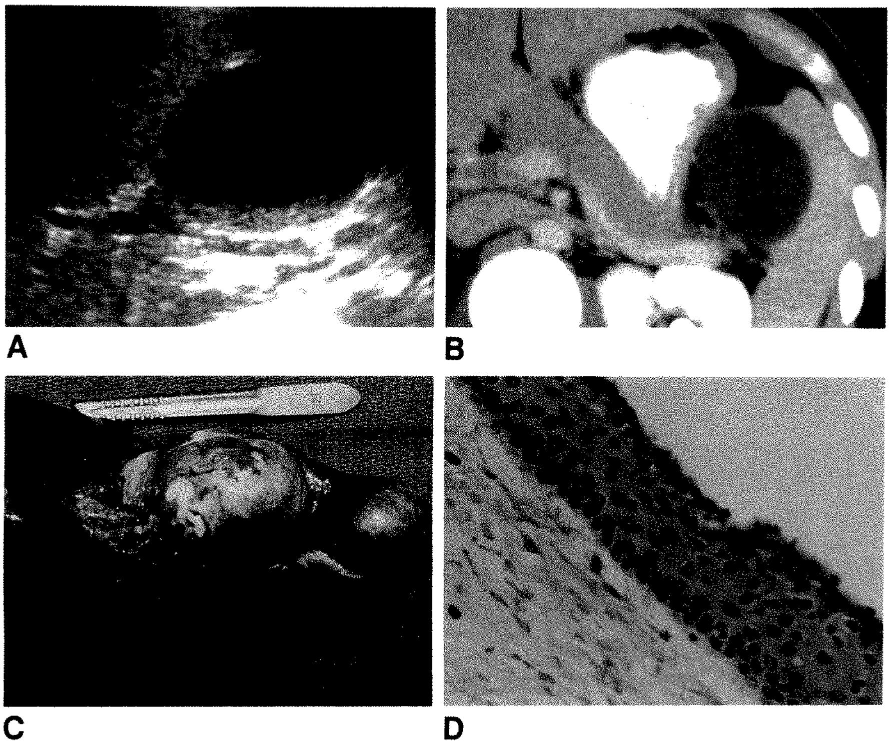

Fig. 1.—*A*, Sonogram shows simple cyst of spleen.

B, CT scan shows simple cyst of spleen.

C, Photograph of surgical specimen shows enlarged spleen with two cysts.

D, Photomicrograph of well-formed stratified squamous epithelial lining in dense connective tissue. (H and E ×250)

from 6 months to 62 years [7]. No strong sexual predominance is observed.

The natural history of splenic epidermoid cysts is unknown; no reports of long-term follow-up of a cohort of persons with splenic cysts have been published. Clinical presentations include painless or painful splenomegaly, spontaneous or posttraumatic splenic rupture, infection, intractable nausea, and dyspnea [3, 5-12]. Several authors describe exacerbation of the signs and symptoms during menstruation [9] and pregnancy [8, 10].

Epidermoid cysts of the spleen are now generally believed to represent metaplasia within mesothelial cysts. These are postulated to arise from invagination of the surface mesothelium during spleen formation [1, 3, 4] or trapping of peritoneal mesothelium after rupture of the splenic capsule [1, 2]. Splenic epidermoid cysts are not associated with cysts in any other organ. The overwhelming majority of cases are sporadic, as would be expected from the theories of epidermoid formation and the absence of associated abnormalities.

Two case reports of familial splenic epidermoid cysts have been published [11, 12]. Two of five siblings in one family were diagnosed with epidermoid splenic cysts [11]. Three of six siblings in another family had epidermoid cysts of the spleen [12]. Clinical presentations included asymptomatic splenomegaly, dyspnea, left shoulder pain, tenderness in the left upper quadrant, and persistent vomiting. Splenic rupture or infection was not observed in these five patients. No evidence or history of splenic disease was elicited in either of the families.

Our observation of splenic epidermoid cysts in siblings and two prior case reports [11, 12] suggest an autosomal recessive, organ-specific defect of mesothelial migration in a small proportion of persons with splenic epidermoid cysts. The rarity of this observation and the lack of associated disorders do not allow confident genetic mapping of this trait and elucidation of possible mechanisms.

An accurate assessment of the natural history of sporadic or familial splenic epidermoid cysts remains unknown. However, given the potential for splenic rupture, noninvasive sonographic screening of siblings of persons with epidermoid cysts may be warranted so that appropriate precautions and prophylaxis can be undertaken by those, albeit rare, persons found to have splenic cysts. Management depends on presentation and the life-style of the patient. Options include careful observation, partial or complete splenectomy [7, 8], marsupialization, and percutaneous aspiration.

REFERENCES

1. Dachman A, Ros P, Muran P, Olmsted W, Lichtenstein J. Non-parasitic splenic cysts: a report of 52 cases with radiologic-pathologic correlation. *AJR* **1986**;147:537–542
2. Burrig K. Epithelial (true) splenic cysts: pathogenesis of the mesothelial and so-called epidermoid cyst of the spleen. *Am J Surg Pathol* **1988**; 12:275–281
3. Fowler RH. Non-parasitic benign cystic tumors of the spleen. *Int Abstr Surg* **1953**;96:209–227
4. Ough Y, Nash H, Wood D. Mesothelial cysts of the spleen with squamous metaplasia. *Am J Clin Pathol* **1981**;76:666–669
5. Pujari B, Phatah A, Jayaranariah M, Deodhare S. Dermoid cyst of the spleen. *Int Surg* **1976**;61:603–604
6. Ross M, Ellwood R, Yang S, Lucas R. Epidermoid splenic cysts. *Arch Surg* **1977**;112:596–599
7. Park J, Song T. Splenic cyst: a case report and review of the literature. *Am Surg* **1971**;37:544–547
8. Doolas A, Nolte M, McDonald O, Economu S. Splenic cysts. *J Surg Oncol* **1978**;10:369–387
9. Tamaki H. Splenic cysts. *Arch Pathol* **1948**;46:550–557
10. Aiengar N. Solitary splenic cysts. *Indian Med Gazette* **1945**;80:131–138
11. Ahlgren L, Beardmore H. Solitary epidermoid splenic cysts: occurrence in sibs. *J Pediatr Surg* **1984**;19:56–58
12. Gilmartin D. Familial multiple epidermoid cysts of the spleen. *Conn Med* **1978**;42:297–300

Case Report

Hemangiomatosis of the Liver and Spleen: Successful Treatment with Embolization and Splenectomy

Pavel G. Tarazov,[1] Vladimir N. Polysalov, and Vladimir K. Ryzhkov

Hemangioma is the most common benign tumor affecting both the liver and spleen. Hepatic resection and splenectomy should be done in symptomatic cases. When multiple or diffuse hemangiomatosis of the liver is diagnosed, radical surgery is impossible. Hepatic artery ligation or embolization is the treatment of choice in such patients. We present a case of simultaneous involvement of the liver and spleen treated with arterial embolization and splenectomy.

Case Report

A 38-year-old woman complained of abdominal pain in the right upper quadrant, dyspepsia, and weight loss. The left lobe of the liver was enlarged. Endoscopy showed moderately sized gastroesophageal varices. Sonography and scintigraphy showed unresectable diffuse hepatic tumor. Needle biopsy showed capillary hemangiomatosis.

Angiography revealed enlargement of hepatic arteries with increased blood flow to the liver, hypervascularization, and arterioportal shunting. No malignant neovascularity was seen. These changes were noticed in all liver segments, especially in the left lobe. The left hepatic artery (arising from the celiac artery) was embolized with 1 cm^3 of 2 × 2 × 5 mm particles of Spongostan (Ferrosan Co., Copenhagen, Denmark) and three modified Gianturco coils (Cook Co., Bloomington, IN). The coils were homemade of stainless steel guidewire 0.95 mm in diameter. The coils were 5 to 15 cm long when stretched and had five to 10 spires of 0.3–0.8 cm in diameter [1]. Additional embolization of the proximal segment of the gastroduodenal artery with part of the last coil was performed.

For 5 days after embolization, the patient had pain in the right upper abdomen, fever, and moderate elevation of liver enzyme levels. By the 10th day, the liver was noted to have decreased in size. The patient was discharged on the 14 day.

Fourteen months later, the patient was hospitalized for a second time with recurrent abdominal pain and hepatomegaly. Superior mesenteric angiography showed two enlarged right hepatic arteries supplying the tumor (Fig. 1A). Embolization of both vessels was performed during 14 days with six coils. By the 12th day, the abdominal pain had diminished and the liver had decreased in size. Endoscopy showed no gastroesophageal varices.

Celiac angiography performed before the first hepatic artery embolization revealed partial revascularization of the left lobe from arterial collaterals. Multiple hypovascular nodules in the spleen were seen and interpreted as hemangiomatosis (Fig. 1B). Embolization of the splenic artery with three coils was performed (Figure 1C), followed 2 hr later by splenectomy. Splenic hemangiomatosis was confirmed pathologically. The postoperative course was uneventful.

The patient had no other signs or symptoms of hemangiomatosis until she died of Ewing sarcoma of the pelvic bone 2 years later. The hemangiomatosis and the malignant bone tumor were not related. The latter appeared clinically and radiologically 18 months after splenectomy. Autopsy and pathologic investigation of the removed spleen showed no metastases of Ewing sarcoma.

Discussion

Treatment of hepatic hemangiomatosis in our patient was considered necessary because of the presence of symptoms and esophageal varices.

Received March 9, 1990; accepted after revision May 29, 1990.

[1] All authors: Central Research Institute of Roentgenology and Radiology, Ministry of Public Health, ul. Leningradskaja 70/4, Pesochny-2, Leningrad 189646, U.S.S.R. Address reprint requests to P. G. Tarazov.

***AJR* 155:1235–1236, December 1990** 0361-803X/90/1556-1235 © American Roentgen Ray Society

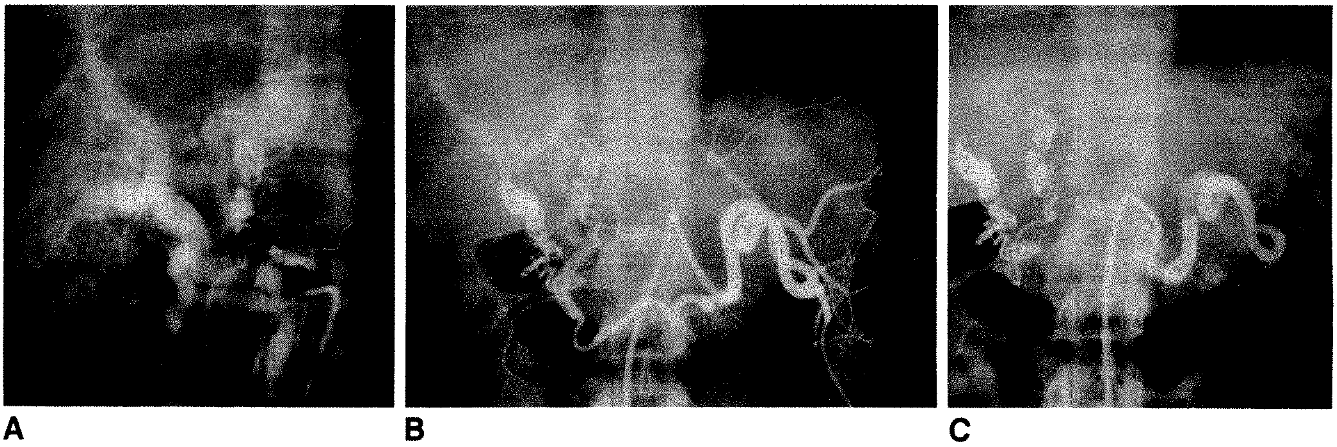

Fig. 1.—*A*, Superior mesenteric angiogram shows two enlarged right hepatic arteries supplying tumor. Note arterioportal shunting within hemangioma. *B*, Celiac angiogram shows partial revascularization of liver from dorsal pancreatic artery. Multiple zones of hypovascularization in spleen are seen. *C*, Angiogram obtained after splenic artery embolization shows significant reduction of blood flow to spleen. Collateral flow to liver disappeared.

Hepatic artery ligation in patients with extensive hepatic hemangiomas results in cure of congestive heart failure, decrease of tumor size, and normalization of liver function [2–4]. However, the procedure may be difficult, and laparotomy and anesthesia are needed.

Successful treatment with hepatic artery embolization has been reported [4–7]. However, one death due to embolization of gallbladder, kidneys, and lungs with Gelfoam (Upjohn, Kalamazoo, MI) particles has been described [8].

Our patient survived all of the devascularization procedures well. A postembolization syndrome was moderate or mild and lasted only a few days. A good palliative effect developed shortly after hepatic artery embolization and lasted for a considerable length of time. This effect included an improvement of overall condition, disappearance of abdominal pain, and decrease in size of both the tumor and the liver. After the completion of hepatic hemangiomatosis devascularization, the gastroesophageal varices disappeared.

We used only large Spongostan particles and steel coils for embolization in our patient because of the high risk of hepatic failure resulting from massive tumor necrosis. The use of small embolic materials was dangerous because they could pass into the portal circulation via arterioportal shunts. Preoperative embolization of the splenic artery minimized intraoperative hemorrhage and interrupted the hepatic arterial collateral flow.

REFERENCES

1. Ryzhkov VK, Borisova NA, Gapchenco EM, Dmitrijeva IA. Verschluß von Arterien durch vergrößerte Spiralembolisate. *Radiol Diagn* (Berl) **1988**;29:713–718
2. Shannon R, Buchanan GR, Votteber TP. Multiple hepatic hemangiomas: failure of corticosteroid therapy and successful hepatic artery ligation. *Am J Dis Child* **1982**;136:275–276
3. Nishida O, Sato N, Alam S, Uchino J. The effect of hepatic artery ligation for irresectable cavernous hemangioma of the liver. *Am Surg* **1988**;54:483–486
4. Reading NG, Forbes A, Nunnerley HB, Williams R. Hepatic haemangioma: a critical review of diagnosis and management. *Q J Med* **1988**;67:431–445
5. Stanley P, Grinell VS, Stanton RE, Williams KO, Shore NA. Therapeutic embolization of infantile hepatic hemangioma with polyvinyl alcohol. *AJR* **1983**;141:1047–1051
6. Burrows PE, Rosenberg HC, Chuang HC. Diffuse hepatic hemangiomas: percutaneous transcatheter embolization with detachable silicone balloons. *Radiology* **1985**;156:85–88
7. Jimenez FF, Albanil R, Lopez-Panero A, Gordillo I, Melero C, Lopez J. Hemangimatosis hepática: embolización terapéutica con polivinil alcohol (Ivalon). *An Esp Pediatr* **1988**;28:588–590
8. Tegtmeyer CJ, Smith TH, Shaw A, Barwick KW, Kattwinkel J. Renal infarction: a complication of Gelfoam embolization of a hemangioendothelioma of the liver. *AJR* **1977**;128:305–307

Bright Pleural Effusion and Ascites on Gradient-Echo MR Images: A Potential Source of Confusion in Vascular MR Studies

Bernd Wallner[1,2]
Robert R. Edelman[1]
John Paul Finn[3]
Heinrich P. Mattle[1,3]

Motion of fluids other than blood can cause flow-related signal enhancement on MR images, including MR angiograms. In order to study this problem, the appearance of ascites (20 patients) and pleural effusions (five patients) was assessed on MR images made during suspended respiration with flow-compensated gradient-echo sequences as well as T1- and T2-weighted sequences. Signal intensities of vessels, fluid collections, and muscle were measured and vessel/muscle and vessel/fluid contrast were calculated. Fluid motion was measured with a bolus tracking technique that tags a selected volume of fluid with an RF presaturation. Fluid collections had a bright signal in four of five patients with pleural effusion and in 15 of 20 patients with ascites. The average contrast ratio between bright components of the fluid collections and vessels was only 0.03 ± 0.09. Bright fluid collections were seen on MR angiograms and could obscure blood vessels. Bolus tracking measurements of ascites revealed multidirectional flow, suggesting that its bright signal is related to motion that continues during suspended respiration. Fluid collections appeared dark on T1-weighted images in all patients, indicating that a short T1 relaxation time was not a cause of the high signal intensity.

The results indicate that, despite breath-holding, ascites and pleural effusions can show bright signal intensity on gradient-echo images. Awareness of this phenomenon will avoid confusion between moving fluid collections and flowing blood and identify a source of image degradation on both gradient-echo and T2-weighted spin-echo MR acquisitions.

***AJR* 155:1237–1240, December 1990**

MR images obtained with gradient-echo sequences are used widely in vascular MR imaging [1–3]. When short repetition times and moderate flip angles are used, stationary protons become partially saturated and give only low signal relative to inflowing unsaturated protons within vessels. Although flowing blood appears bright on these images, moving protons of any kind can enhance signal.

Ascites and pleural effusion are fluid collections that are subject to various degrees of bulk motion. This motion can be induced by respiration, cardiac and arterial pulsation, bowel peristalsis, and muscular activity. The signal intensities of these fluid collections on images (such as gradient-echo acquistions) that are sensitized to flow may differ therefore from the appearance expected on the basis of T1 and T2 relaxation times. We assessed the appearance of pleural effusions and ascites on gradient-echo images and studied their effects on image quality.

Materials and Methods

Twenty-five patients with ascites (20 patients) and/or pleural effusion (five patients) were included in the study. Nineteen with ascites associated with portal hypertension and one with ascites caused by the Budd-Chiari syndrome had abdominal MR angiography for evaluation of the portal venous system. Two patients with pleural effusions had thoracic MR studies for dissecting aortic aneurysm, and three were evaluated for suspected occlusion of the superior

Received April 4, 1990; accepted after revision July 9, 1990.

[1] Department of Radiology, Beth Israel Hospital, 330 Brookline Ave., Boston, MA 02215. Address reprint requests to R. R. Edelman.

[2] Department of Radiology I, University of Ulm, D-7900 Ulm, Germany.

[3] Department of Radiology, New England Deaconess Hospital, Boston, MA 02215.

0361–803X/90/1556–1237
© American Roentgen Ray Society

vena cava. The studies were performed on two MR systems, a 1.5- and a 1.0-T imager (Magnetom, Siemens Medical Systems, Erlangen, FRG). Breath-hold images were acquired during end-expiration by using a spoiled fast low-angle shot (FLASH), 30-64/10/30° (TR/TE/flip angle), sequence with flow compensation. T1-weighted gradient-echo images, 110/5/80°, and T2-weighted spin-echo images, 2500/40,90/2 (TR/TE/excitations), also were obtained in 14 patients. The angiograms were postprocessed with a maximum-intensity-projection algorithm to generate projection angiograms. Generally, five projections were produced (at −30°, −15°, 0°, 15°, and 30° rotations from the coronal view).

The signal intensities of blood vessels, fluid collections, muscle, and background were measured by using standard region-of-interest measurements. The background signal was measured by using a large rectangular volume filling the space anterior to the abdomen on axial images; signal also was measured over muscles of the abdominal or thoracic wall. Vessel/muscle and vessel/fluid contrast were calculated according to the following formula [4]: Contrast = (S1 − S2)/(S1 + S2), where S1 and S2 are the signal intensities of the vessel and muscle or vessel and fluid, respectively. The muscle signal-to-noise ratio (S/N = signal intensity of muscle/standard deviation of background signal) also was determined and compared with that in a group of patients without fluid collections (*n* = 10). The signal intensities of fluid collections were related to location (abdominal or thoracic, proximity to a vessel, contact with the diaphragm).

For the fluid collections, flow-velocity measurements with bolus tracking were performed to document bulk flow and determine its direction. Bolus tracking uses an in-plane RF presaturation to tag moving protons. Thus, displacement over time is shown, and the direction and velocity of flow can be determined [5].

Results

In seven of the 20 patients with ascites, the fluid appeared uniformly bright; in eight patients, the signal intensity was mixed; and in five patients, the fluid appeared homogeneously dark (Fig. 1). The bright areas showed higher signal intensity than intraluminal flowing blood in five patients. The average contrast between bright components of the fluid collections and vessels was only 0.03 ± 0.09; the contrast with muscle was 0.44 ± 0.06 for arteries, 0.46 ± 0.06 for veins, and 0.43 ± 0.07 for ascites. When bright fluid was intimately associated with blood vessels, the latter were obscured on projection angiograms. The portal vein, however, was visualized in all of these patients because the fluid was not in contact with the vessel. Bolus tracking revealed multidirectional flow of fluid (Fig. 2). None of the fluid collections appeared bright on T1-weighted images, and all of them showed high signal intensity on T2-weighted images.

Pleural effusions also showed high signal intensities on MR angiograms. In three patients, there was a homogeneously bright appearance with signal intensities similar to those of flowing blood within the aorta. In one patient, the effusion presented a layered appearance, with low signal from fluid adjacent to the thoracic wall and high signal from fluid close to the visceral pleura. In these patients, the fluid was located on the left side and was contiguous with the descending aorta. The effusions also appeared brighter in the lower thoracic regions adjoining the diaphragm than in the upper regions. In one patient, the interpretation of gradient-echo images was confounded by a bright effusion contiguous with a dissecting aneurysm (Fig. 3), but T2-weighted images allowed a correct evaluation. In another patient, the pleural effusion obscured the aortic arch because of direct contact. In one patient, the pleural effusion showed homogeneously low signal intensity. In this case, the fluid collection was located on the right side.

There was no significant difference in muscle S/N between patients with and without fluid collections (12.3 ± 2.1 vs 10.7 ± 2.9). Because of its high signal intensity, similar to blood flow, ascites was seen on the projection angiograms in

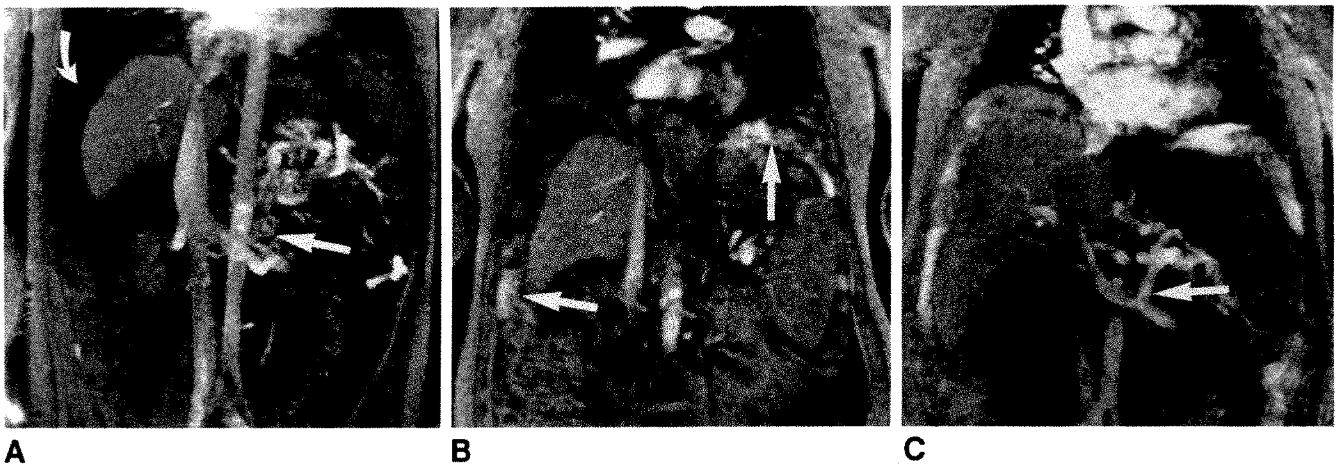

Fig. 1.—Variable appearance of ascites on MR images. MR angiograms were created by postprocessing a series of breath-hold spoiled FLASH images (30–64/10/30°) with flow compensation.

***A*, MR angiogram in patient with spontaneous splenorenal shunt shows fluid (*curved arrow*) around liver is uniformly dark. Shunt (*straight arrow*) and paragastric varices are well seen.**

***B*, Single MR image in patient with portal hypertension shows bright collections of ascites adjacent to spleen and bowel loops (*arrows*). Fluid around liver appears dark.**

***C*, MR angiogram in patient with surgical splenorenal shunt shows ascites, which is predominantly bright. Note that portions of ascites have higher signal intensity than flowing blood within splenic vein and shunt (*arrow*).**

15 patients (Fig. 4). Overlap among laterally located bright fluid collections and centrally located vessels was worst on rotated projections. Pleural effusion appeared partly bright on the projection angiograms in four of the five cases.

Discussion

The influence of flow on the appearance of pleural effusion and ascites on MR images has not been addressed before. Articles on the imaging of fluid collections focus on the characteristics of the collections on spin-echo images and highlight the dependence on protein and hemorrhagic components [6, 7].

Two types of gradient-echo sequences commonly are used in MR imaging of flowing blood. One type (e.g., FLASH) uses a spoiler gradient after each data collection in order to destroy residual transverse magnetization. When this kind of sequence is used, a short TR in combination with moderate flip angles permits only slight T1 relaxation of stationary protons, and good contrast between flowing and stationary protons is achieved. This sequence type was used in our study. The other group of sequences (e.g., gradient-recalled acquisition in the steady state and fast imaging steady precession) is designed to maintain a nonzero steady-state component of transverse magnetization. The contrast behavior of flowing blood on images obtained with these steady-state types of sequences is more complicated. For short TR times, stationary fluid looks bright because of its long T2 relaxation time. The combination of this effect and flow-related enhancement can produce complex signal patterns [8, 9].

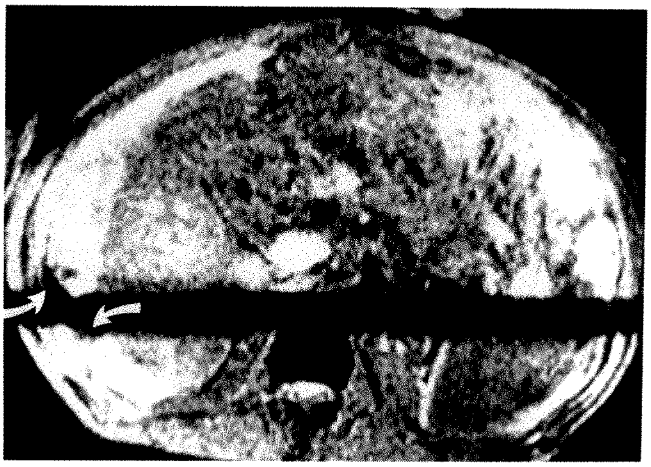

Fig. 2.—MR image shows bolus tracking of ascites in axial plane. Dark horizontal stripe represents a region to which an RF presaturation was applied; data were acquired 30 msec after each application of presaturation. Flow occurring during this interval results in displacement of dark, tagged bolus. Flow is simultaneous from anterior to posterior regions and in opposite direction, indicated by displacement of black stripe (*arrows*).

Pleural effusion and ascites exhibit certain flow dynamics. In ascites, two forces mainly determine the direction of flow. During quiet respiration the pressure in the subphrenic region falls with inspiration and rises with expiration. The outward movement of the ribs enlarges the volume in the upper abdomen more than it is decreased by the descent of the diaphragm. It has been shown that the resulting pressure differences are capable of transferring fluid from the lower to the upper abdomen, even when the person is in an upright position. Against this acts the pull of gravity, which tends to pool fluid in dependent peritoneal recesses [10, 11]. In our series, measurements of flow during suspended respiration showed multidirectional motion of fluid collections. This result suggests that the bright appearance of ascites on gradient-echo images is due to persistent fluid movement after suspension of respiration. In addition to flow-related enhancement, fluid motion also causes ghost artifacts that degrade image quality. Although not specifically evaluated in this study, fluid motion can be expected to cause degradation on T2-weighted spin-echo images as well.

The bright appearance of ascites was an inconsistent finding in our study, presumably because of differences in fluid flow dynamics among patients. The dark appearance on T1-weighted images excludes a short T1 relaxation time as the reason for the high signal intensities.

Fig. 3.—Breath-hold spoiled FLASH image (30/10/30°) with flow compensation in patient with dissecting aneurysm of thoracic aorta shows bright pleural effusion (*arrow*).

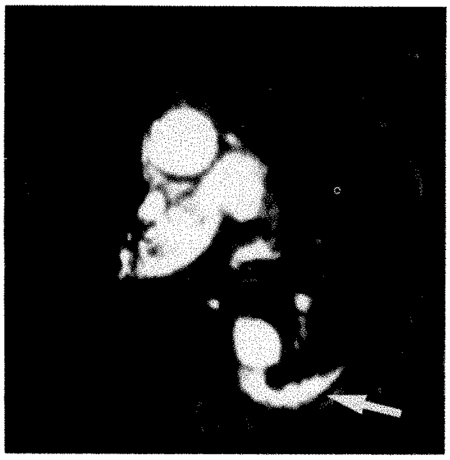

3

Fig. 4.—Rotated view (15°) of MR angiogram in patient with portal hypertension and ascites shows paragastric varices (*long solid arrow*) and compression of upper inferior vena cava (*short solid arrow*) by caudate lobe of liver. Ascites has inhomogeneously bright signal (*open arrows*). Because projection angiogram was created from only a limited number of gradient-echo sections (30 mm total thickness, 64/10/30°), only portions of some blood vessels are seen. Presaturation was applied to lower thoracic aorta to eliminate arterial signal within abdomen.

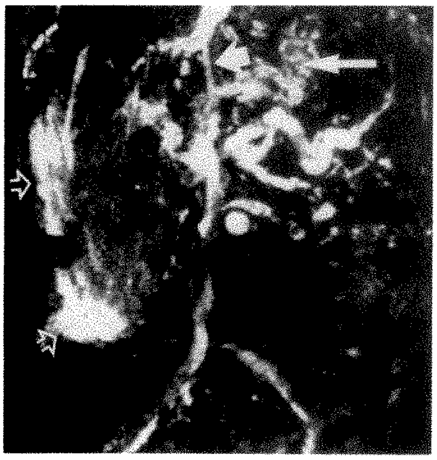

4

Pleural effusion also shows dynamic behavior. It has been shown that there is a rapid turnover of labeled tracers in the pleural space [12]. Unlike a right pleural effusion, all the pleural fluid collections in contact with the aorta appeared at least partly bright, suggesting that motion of a pleural effusion may be induced to some extent by vascular pulsations.

In conclusion, pleural effusion and ascites exhibit flow phenomena that can cause them to give signal as high as that of intravascular flowing blood on gradient-echo images. They therefore have the potential to obscure vessels of interest and to degrade image quality in gradient-echo and T2-weighted spin-echo acquisitions. Awareness of this phenomenon is helpful for proper image interpretation and to avoid confusion between flow in blood vessels and fluid collections in MR angiography.

REFERENCES

1. Frahm J, Haase A, Matthaei D. Rapid NMR imaging of dynamic processes using the FLASH technique. *Magn Reson Med* **1986**;3:321-327
2. Laub GA, Kaiser WA. MR angiography with gradient motion rephasing. *J Comput Assist Tomogr* **1988**;12:377-382
3. Edelman RR, Mattle H, Atkinson DJ. Magnetic resonance angiography. *AJR* **1990**;154:937-946
4. Hendrick RE. Image contrast and noise. In: Stark DD, Bradley WG, eds. *Magnetic resonance imaging*. St. Louis: Mosby, **1988**:66-83
5. Edelman RR, Mattle H, Kleefield J, Silver MS. Dynamic MRI and quantification of flow using presaturation bolus tracking. *Radiology* **1989**; 171:551-556
6. Mulvagh SL, Rokey R, Vick GW, Johnston DL. Usefulness of nuclear magnetic resonance imaging for evaluation of pericardial effusion and comparison with 2D echocardiography. *Am J Cardiol* **1989**;64:1002-1006
7. Tscholakoff D, Sechtem U, de Greer G, et al. Evaluation of pleural effusion by magnetic resonance imaging. *Eur J Radiol* **1987**;7:169-174
8. Martin JF, Edelman RR. Fast MR imaging. In: Edelman RR, Hesselink JR, eds. *Clinical magnetic resonance imaging*. Philadelphia: Saunders, **1990**:183-220
9. Winkler ML, Ortendahl DA, Mills TC, et al. Characteristics of partial flip angle and gradient reversal MRI. *Radiology* **1988**;166:17-26
10. Meyers MA. The spread and localization of acute intraperitoneal effusions. *Radiology* **1970**;95:547-554
11. Overholt RH. Intraperitoneal pressure. *Arch Surg* **1931**;22:691-703
12. Nakamura T, Iwasaki Y, Tanaka Y, Fukabori T. Dynamics of pleural effusion estimated through urea clearance. *Jpn J Med* **1987**;26:319-322

Sonography of Abnormal Lymph Nodes In Vitro: Correlation of Sonographic and Histologic Findings

Leopoldo Rubaltelli[1]
Enrico Proto[1]
Roberto Salmaso[2]
Paolo Bortoletto[1]
Francesco Candiani[1]
Pierpaolo Cagol[3]

The sonographic evaluation of lymph nodes is based primarily on evaluation of their shape and size. Recently, however, the availability of high-frequency transducers has made consideration of internal structure possible. An important objective is to determine whether node enlargement is due to inflammatory or neoplastic processes. To determine the accuracy of sonography for this purpose, we obtained in vitro sonograms of 53 enlarged lymph nodes excised from 41 patients during surgery for neoplastic or non-neoplastic disease. The sonograms were obtained with 7.5- and 10-MHz transducers. They were interpreted by a radiologist who was unaware of the clinical diagnosis. The nodes were subsequently processed for anatomohistologic study; findings were compared side by side. In 26 of the 53 nodes, sonograms showed an identifiable central echogenic line, which on histologic specimen corresponded to the internal part of the medulla where the lymphatic sinuses converge. All these nodes were benign. Two other nodes had an echogenic internal structure not resembling the normal hilum; in one case this was caused by metastatic disease and in the other by fibrosis. Sonograms of the remaining 25 nodes showed no detectable hilar structure; 21 were involved by a tumor and four had diffuse fatty replacement.

Our results suggest that the sonographic finding of a central echogenic line is a valid criterion of benignity. Absence of this finding may be due to factors other than neoplastic disease, such as fatty replacement.

***AJR* 155:1241–1244, December 1990**

Sonography is useful for studying enlarged lymph nodes in superficial regions, where it can detect impalpable lymph nodes [1–7]. An important objective is distinguishing between inflammation and tumor as a cause of the lymphadenopathy. Detection of an oval shape and an echogenic hilum have been proposed as sonographic evidence of benignity. Roundness and absence of an echogenic hilum are considered signs of malignancy [8–12]. To determine the accuracy of these findings, and to shed additional light on the subject, we performed in vitro sonography on excised abnormal lymph nodes and compared the sonographic and histologic findings.

Materials and Methods

Fifty-three lymph nodes obtained surgically from 41 patients were studied by sonography in a water bath. This prospective study included lymph nodes that were enlarged and affected by various diseases. Among the 41 patients, 32 had a clinical diagnosis of neoplastic disease: thyroid cancer (eight cases), breast cancer (five cases), gastric adenocarcinoma (five cases), colonic cancer (four cases), esophageal cancer (two cases), soft-tissue sarcoma (two cases), and non-Hodgkin lymphoma (six cases). The diagnoses in the remaining nine patients were gallstones (six cases), chronic pancreatitis (two cases), and AIDS (one case). Forty-six specimens consisted of single lymph nodes and seven were masses comprising several unseparable lymph nodes. In 29 cases, nodes were taken from a superficial site (neck, groin, axilla); in 24 they were obtained from the abdomen. The maximal diameters of the nodes ranged from 6 to 24 mm (mean ± SD, 14.8 ± 5.8 mm).

Received March 29, 1990; accepted after revision May 30, 1990.

[1] Istituto di Radiologia, Università di Padova, Via Giustiniani 2, Padova, Italy 35128. Address reprint requests to L. Rubaltelli.

[2] Istituto di Anatomia Patologica, Università di Padova, Padova, Italy 35128.

[3] Istituto di Patologia Chirurgica, Università di Padova, Padova, Italy 35128.

0361-803X/90/1556-1241
© American Roentgen Ray Society

Sonography was performed with a 7.5-MHz linear-array transducer (RT 2800, General Electric, Milwaukee, WI) and a 10-MHz mechanical sector transducer (AU 530, Esaote Biomedica, Genoa, Italy). Morphology, size, and echo structure were evaluated by a radiologist who was unaware of the clinical diagnosis. For each lymph node the following were considered: (1) degree of echogenicity, (2) presence or absence of an echogenic midline hilum, and (3) focal or diffuse changes in echogenicity. A sonographic diagnosis of benignity or malignancy was reached in every case.

Gross and histologic studies of the nodes were performed by a pathologist; sections were stained by the hematoxylin-eosin and Giemsa procedures. Anatomopathologic findings indicated that 31 nodes were reactive or inflammatory; four of these showed adipose replacement. Twenty-two specimens were neoplastic, comprising 15 instances of metastasis and seven of non-Hodgkin follicular lymphoma [13].

Lastly, the results of sonography and anatomohistologic studies were correlated by the radiologist and pathologist.

Results

In 26 (49%) of 53 lymph nodes, sonograms showed an echogenic line crossing the central portion of the node (Fig. 1A). Microscopic study of these lymph nodes excluded the presence of tumor, and showed that the line corresponded to the innermost part of the medulla, where the lymphatic sinuses converge toward the hilum and produce numerous interfaces (Fig. 1B).

In two cases, sonograms showed a central focus of echoes in the nodes (Figs. 2 and 3). In one of these nodes, histologic examination showed metastatic gastric adenocarcinoma with a small central necrotic zone; in the other, a lymph node from a patient with AIDS, a central area of fibrosis was found.

In 25 nodes, sonograms showed no central line. Histologic examination revealed that 21 (84%) of these were involved by tumor. In four lymph nodes from four different patients, histologic results showed adipose replacement in the medulla and cortex, which had increased the echogenicity of the internal structures (Fig. 4).

In six cases of lymphoma (five patients), the internal echo structure of the lymph node was characterized by small areas of irregular echogenicity both at the medulla and the cortex, conferring an overall "micronodular" aspect (Figs. 5A and 5B); this picture corresponded perfectly to that seen on the cut

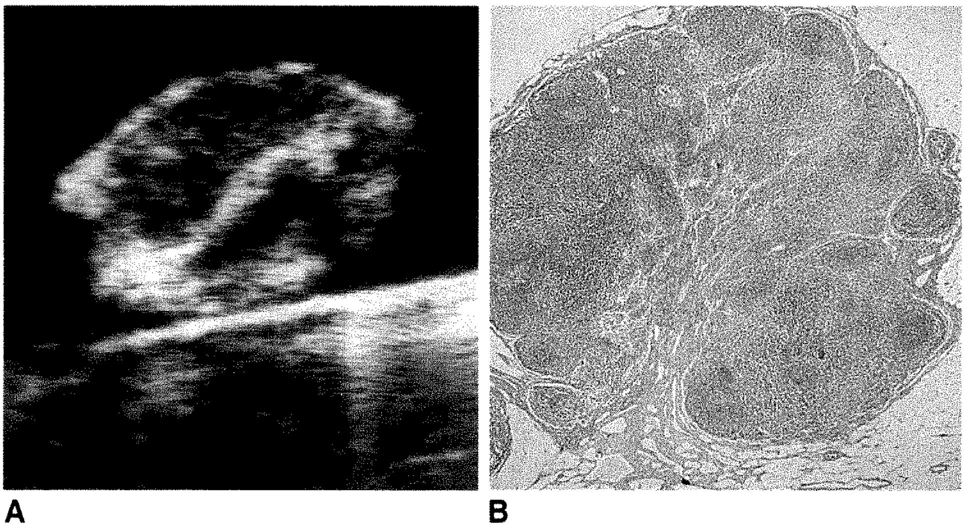

Fig. 1.—*A*, In vitro sonogram (10 MHz) shows echogenic line running through center of lymph node.

B, Histologic section shows echogenic central line is caused by interfaces in internal part of medulla. Hilum is evident also.

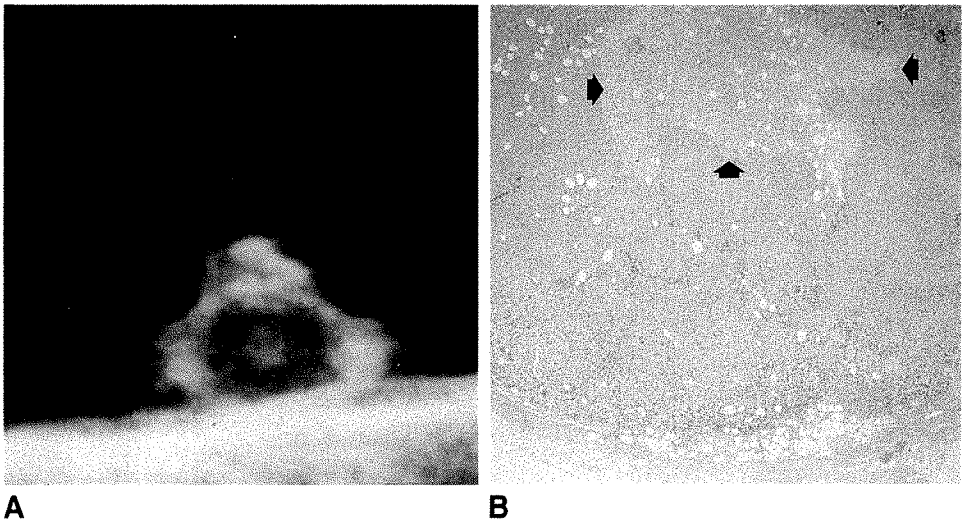

Fig. 2.—*A*, In vitro sonogram shows small central echogenic area.

B, Histologic section of metastasis from gastric adenocarcinoma. Area of necrosis (*arrows*) corresponds to echogenic zone.

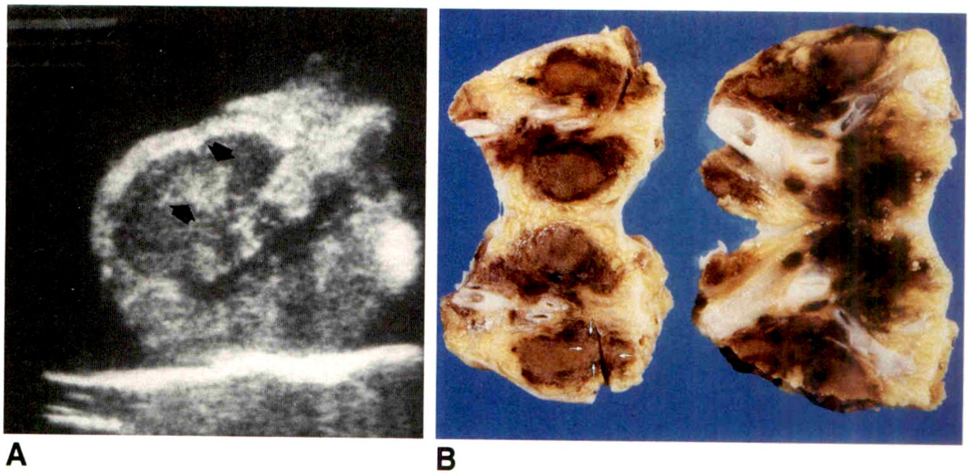

Fig. 3.—*A*, In vitro sonogram of large lymph-node mass in a patient with AIDS. One lymph node has a prominent central echogenic zone (*arrows*).
B, Gross specimen of sectioned lymph-node mass shows area of fibrosis corresponding to echogenic focus (*arrows*).

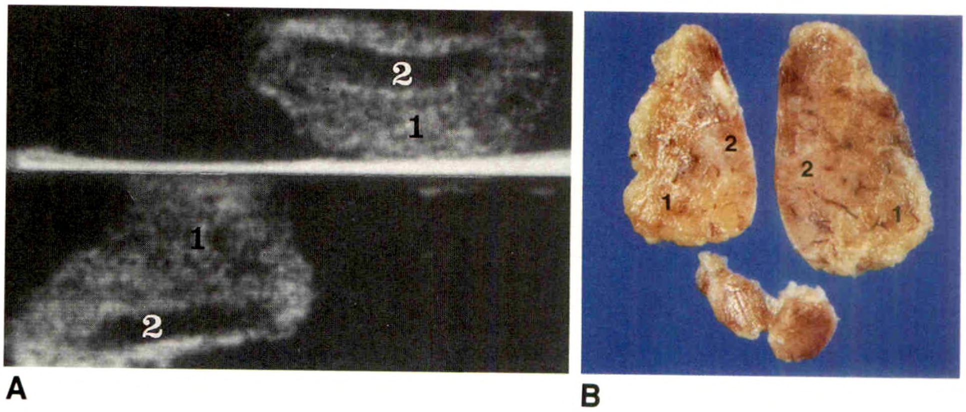

Fig. 4.—*A*, In vitro sonogram of lymph node in two opposing positions clearly shows hyperechoic (1) and smaller hypoechoic (2) zones.
B, Gross specimen shows that hyperechoic zone corresponds to adipose replacement (1) and hypoechoic zone to normal lymphatic tissue (2).

surface (Fig. 5C), and histologic results confirmed the presence of large, round, hypertrophic follicles (Fig. 5D).

Discussion

Only recently has the use of high-frequency transducers (7.5–10 MHz) permitted a detailed sonographic analysis of the internal architecture of lymph nodes. Detection of the hilum of the node (central echoes [8, 14] or an echogenic line [11, 12]) has been reported as an indication of normality. Small echogenic foci in the nodes caused by calcium or amyloid deposits were found in the lymph nodes involved by metastases from medullary thyroid carcinoma [12]; it was shown that liquefaction and coagulation necrosis may cause hypoechoic and hyperechoic areas, respectively [9].

Our findings showed that the central echogenic line detected in 25 lymph nodes (47%), and previously described as the hilum, is produced by numerous interfaces present in the internal part of the medulla, where the lymphatic sinuses converge at the hilum (Fig. 1). Although this finding has been attributed to the presence of fat [14], in our experience fat makes the central echogenic line thicker and more evident, but is not essential for its visualization.

Our in vitro findings demonstrated, however, that the central echogenic line was valid as a diagnostic marker in 48 (90%) of 53 cases; in fact, it was not present in any neoplastic lymph node and was seen in 26 of 31 benign nodes. In four reactive nodes, this sign was not recognized owing to the presence of diffuse adipose infiltration, which made the nodes hyperechoic. This situation occurs frequently in nodes of elderly or immunosuppressed patients, and may partly explain the in vivo diagnostic errors arising from recognition of a central echogenic line.

In both inflammatory and neoplastic lymph nodes, hypoechoic (liquefaction necrosis) or hyperechoic (fibrosis, coagulation necrosis) zones may be present; the latter generally appear as irregular spots that should not be confused with the central echogenic line.

In six of seven lymph nodes with non-Hodgkin follicular lymphoma, we found a characteristic micronodular configuration that corresponded perfectly to that seen on the cut surface. This finding obviously needs further confirmation in a larger series of cases, as well as by in vivo verification. In this regard, it is worth mentioning that the technical conditions during in vivo examinations are optimal only for nodes in superficial locations, especially when transducers of 10 MHz or more are used. Identification of such fine details on sonograms of nodes in the abdomen is unlikely.

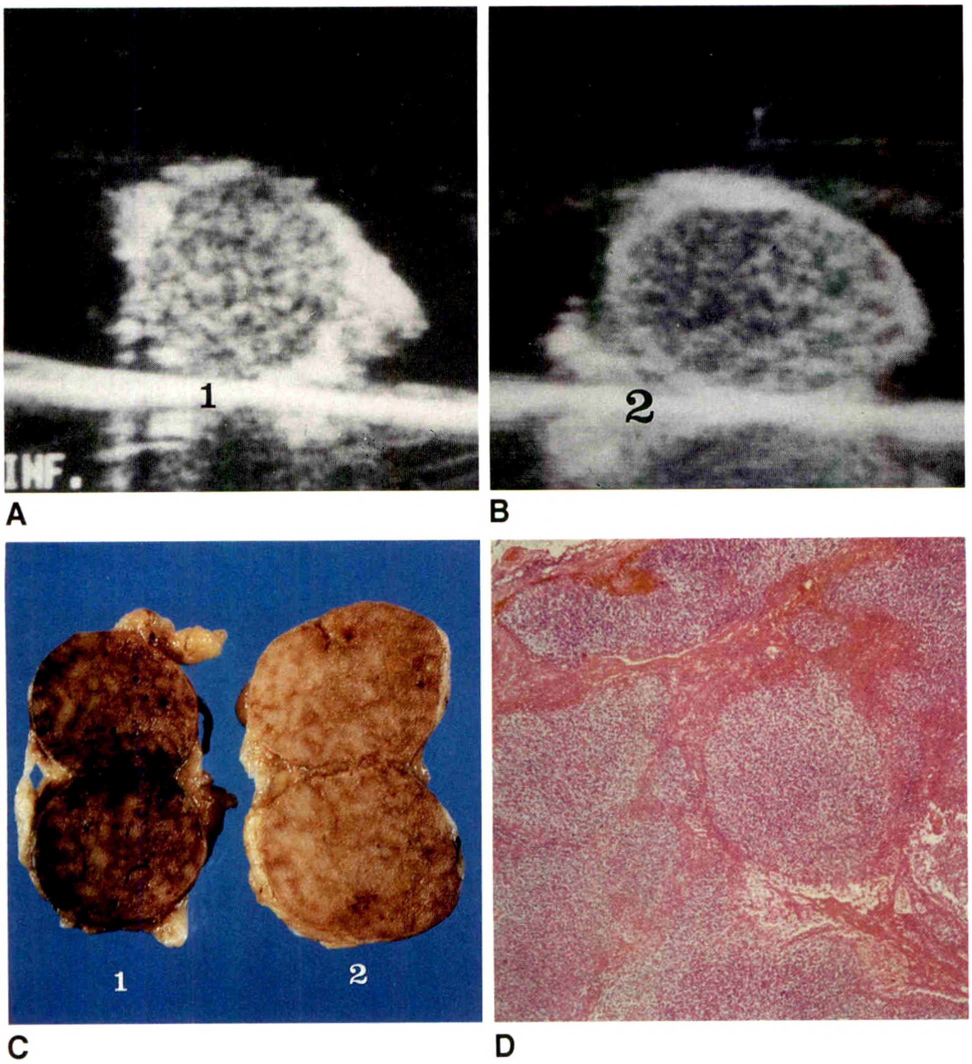

Fig. 5.—*A* and *B*, In vitro sonograms of lymph nodes (1 and 2) involved by non-Hodgkin follicular-type lymphoma show absence of central echogenic line and inhomogeneous echo structure with small micronodular aspects.

C, Gross specimen. Cut surface shows diffuse micronodular infiltration.

D, Histologic section shows large, round, hypertrophic follicles indicative of follicular lymphoma.

REFERENCES

1. Bruneton JN, Roux P, Caramella E, Demard F, Vallicioni J, Chauvel P. Ear, nose, and throat cancer: ultrasound diagnosis of metastasis to cervical lymph nodes. *Radiology* **1984**;152:771–773
2. Bruneton JN, Caramella E, Héry M, Aubanel D, Manzino JJ, Pichard JL. Axillary lymph node metastases in breast cancer: preoperative detection with US. *Radiology* **1986**;158:325–326
3. Hajek PC, Salomonowitz E, Turk R, Tscholakoff D, Kumpan W, Czembirek H. Lymph nodes of the neck: evaluation with US. *Radiology* **1986**;158:739–742
4. Bruneton JN, Roux P, Caramella E, Manzino JJ, Vallicioni J, Demard F. Tongue and tonsil cancer: staging with US. *Radiology* **1986**;158:743–746
5. Bruneton JN, Normand F, Balu-Maestro C, et al. Lymphomatous superficial lymph nodes: US detection. *Radiology* **1987**;165:233–235
6. Von Prayer L, Winkelbauer F, Gritzmann N, Weislein H, Helmer M, Pehamberger H. Untersuchung der primaren Lymphkenotenstationen beim malignem Melanom mittels hochauflosender real-time-sonographie-stellenwert und Indikation. *ROFO* **1989**;151:294–297
7. Pamilo M, Soiva M, Lavast EM. Real-time ultrasound, axillary mammography, and clinical examination in the detection of axillary lymph node metastases in breast cancer patients. *J Ultrasound Med* **1989**;8:115–120
8. Perin B, Gardellin G, Nisi E, Perini L, Lunghi F, Frasson P. Identificazione ecografica di area iperecogena centrale nei linfonodi. Segno di linfoadenopatia benigna. *Radiol Med* (Torino) **1987**;74:535–538
9. Sakai F, Kiyono K, Sone S, et al. Ultrasonic evaluation of cervical metastatic lymphadenopathy. *J Ultrasound Med* **1988**;7:305–310
10. Thnosu N, Onoda S, Isono K. Ultrasonographic evaluation of cervical lymph node metastases in esophageal cancer with special reference to the relationship between the short to long axis ratio (S/L) and the cancer content. *J Ultrasound Med* **1989**;17:101–107
11. Gordon PB, Gilks B. Sonographic appearance of normal intramammary lymph nodes. *J Ultrasound Med* **1988**;7:545–548
12. Sutton RT, Reading CC, Charboneau JW, James EM, Grant CS, Hay ID. US-guided biopsy of neck masses in postoperative management of patients with thyroid cancer. *Radiology* **1988**;168:769–772
13. Bragg DG, Colby TV, Ward JH. New concepts in the non-Hodgkin lymphomas: radiologic implications. *Radiology* **1986**;159:289–304
14. Marchal G, Oyen R, Verschakelen J, Gelin J, Baert AL, Stessens RC. Sonographic appearance of normal lymph nodes. *J Ultrasound Med* **1985**;4:417–419

Case Report

Well-Differentiated Papillary Mesothelioma of the Peritoneum

F. Alan Lovell[1] and Philip E. Cranston

Abdominal mesotheliomas are rare neoplasms and account for approximately 33% of all mesotheliomas [1]. Histopathologically, mesotheliomas are divided into epithelial, connective tissue, and mixed varieties. Well-differentiated papillary mesothelioma of the peritoneum is a type of epithelial mesothelioma that occurs mainly in females and usually has an indolent course [2, 3].

This case shows an unusual CT presentation of this abnormality in which tumor plaque calcification diffusely involves the visceral and parietal peritoneum. This CT pattern of calcification has been described before in association with ovarian carcinomatosis [4].

Case Report

An 11-year-old girl presented to another hospital with acute abdominal pain. Laparotomy was performed for possible appendicitis. Operative findings included what was thought to be carcinomatous seeding of the omentum, right fallopian tube, and appendix. The ovaries appeared normal. The local pathologist diagnosed the process as a papillary adenocarcinoma from a probable fallopian tube or ovarian primary tumor.

The patient was referred to our hospital for further evaluation and treatment. Plain film of the abdomen revealed faint, stippled calcifications perihepatically and within the pelvis (Fig. 1A). Abdominal CT scans showed psammoma body calcifications without significant associated soft-tissue mass effect around the right and caudate lobes of the liver, at the falciform ligament, gastrosplenic ligament, lesser sac, porta hepatis, Morison pouch, left paracolic gutter, greater omentum, pouch of Douglas, paravesical spaces, and near both ovaries (Figs. 1B–1D). A small amount of ascites was noted.

The initial pathologic specimens were reviewed by pathologists at our hospital and other expert pathologists. The differential diagnosis was well-differentiated papillary mesothelioma of the peritoneum or papillary serous adenocarcinoma of low potential for malignancy from an unknown primary tumor. During pathologic review, the patient was begun on a six-treatment course of cisplatin and cyclophosphamide.

After three chemotherapy treatments, the patient was readmitted for a second exploratory laparotomy and restaging. At laparotomy a right oophorectomy, biopsy of the hemidiaphragms and peritoneal surfaces, and removal of the remaining omentum were performed. Pathologic examination revealed papillary mesothelioma containing numerous psammoma bodies.

Ultrastructural analysis with electron microscopy revealed features characteristic of a mesothelioma.

Postoperatively, the patient did well and was discharged. As no standard treatment has been established for this disease, our gynecologic oncologist elected to treat this patient empirically with Lupron (TAP Pharmaceuticals, North Chicago, IL), a gonadotropin-releasing hormone agonist. Recent follow-up 9 months after the initial presentation revealed the patient to be free of symptoms. An abdominal CT study done at that time revealed no change in the diffuse calcifications throughout the peritoneal cavity, and no soft-tissue masses were identified.

Discussion

Peritoneal mesotheliomas occur predominantly in men and have an extremely dismal prognosis. Well-differentiated papillary mesotheliomas of the peritoneum usually occur in females and have a favorable prognosis. A series of 22 cases of this disease has recently been described [2]. Eighteen of the 22 patients were women. The peritoneal tumor was usually multifocal, and psammoma bodies were found in five of the 22 cases. Psammoma bodies are generally considered to be rare in this disease. The patients ranged from 25 to 69 years old. Our case is unusual in that this patient is only 11 years old.

The diagnosis of mesothelioma requires biopsy. Pathologists may disagree with respect to the exact diagnosis in as

---

Received March 19, 1990; accepted after revision May 21, 1990.

[1] Both authors: Department of Radiology, University of Mississippi Medical Center, 2500 N. State St., Jackson, MI 39216-4505. Address reprint requests to P. E. Cranston.

AJR 155:1245–1246, December 1990 0361–803X/90/1556–1245 © American Roentgen Ray Society

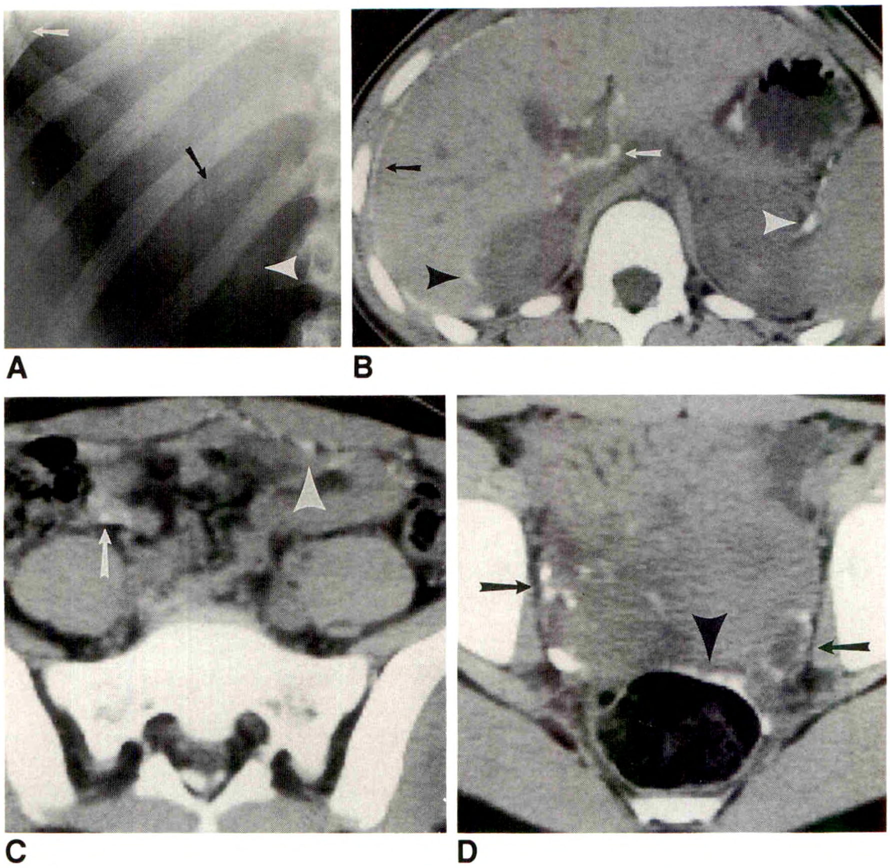

Fig. 1.—Diffuse psammoma body calcifications in patient with well-differentiated papillary mesothelioma of peritoneum.

***A*, Abdominal radiograph shows faint calcifications in right upper quadrant consistent with location around right lobe of liver (*white arrow*), at Morison pouch (*black arrow*), and at porta hepatis (*arrowhead*).**

***B*, Axial CT scan shows calcium at right perihepatic region (*black arrow*), Morison pouch (*black arrowhead*), porta hepatis (*white arrow*), and gastrosplenic ligament (*white arrowhead*).**

***C*, Axial pelvic CT scan shows psammoma body calcification at greater omentum (*arrowhead*) and at appendiceal area (*arrow*).**

***D*, Axial pelvic CT scan shows calcification near both ovaries (*arrows*) and at pouch of Douglas (*arrowhead*).**

many as one third of the cases. For suspected peritoneal mesotheliomas, electron microscopic features of the neoplasm are used as the definitive criteria for determining the diagnosis [5]. It is important to differentiate this disease from ovarian carcinomatosis, because in the latter, response to chemotherapy is very good; whereas, in the former, chemotherapy is not warranted because of the more indolent nature of the disease [2].

Peritoneal mesothelioma has been described relatively infrequently in the radiology literature. Peritoneal mesothelioma is generally considered to have nonspecific radiologic features and tends not to show any specific characteristics that help to differentiate it from other serosal neoplasms. CT is thought to be superior to sonography for the evaluation of peritoneal mesothelioma, especially for the detection of small tumor nodules and for mesenteric or peritoneal thickening; sonography may be superior for the evaluation of pelvic involvement [6]. In some cases with small tumor nodules, CT findings may be normal [4]. In a series of eight cases, frequent CT findings included nodularity and thickening of the peritoneum, ascites, mesenteric thickening, peritoneal masses, and retroperitoneal lymph node enlargement [7].

Radiologic evidence of intraabdominal calcification may be observed in certain primary intraabdominal tumors and in metastatic tumors [8]. Recently, a report of six patients with ovarian carcinomatosus described the "perihepatic calcification sign" in which calcified peritoneal plaques were shown surrounding the liver [4]. Additionally, calcified tumor nodules were noted in the right paracolic gutter and anterior abdominal wall in some of their cases. This pattern is very similar to the pattern seen in the case described in this report. It is interesting that in three of these six patients, the calcifications were the only abnormality identified by CT. The peritoneal calcification shown by plain film and CT in this case is caused by the abundant psammoma bodies shown histologically within the tumor plaques.

We suggest that well-differentiated papillary mesothelioma of the peritoneum should be included in the differential diagnosis with ovarian carcinomatosus when the previously described "perihepatic calcification sign" or other psammomatous calcifications are encountered on abdominal radiographs or CT.

REFERENCES

1. Moertel CG. Peritoneal mesothelioma. *Gastroenterology* **1972**;63:346–350
2. Daya D, McCaughey WTE. Well-differentiated papillary mesothelioma of the peritoneum: a clinicopathologic study of 22 cases. *Cancer* **1990**; 65:292–296
3. McCaughey WTE. Papillary peritoneal neoplasms in females. In: Sommers SC, Rosen PP, Fechner RE, eds. *Pathology annual*, Part 2. Norwalk, CT: Appleton-Century-Crofts, **1985**:387–404
4. Mitchell DG, Hill MC, Hills S, Zaloudek C. Serous carcinoma of the ovary: CT identification of metastatic calcified implants. *Radiology* **1986**;158: 649–652
5. Bollinger DJ, Wick MR, Dehner LP, Mills SE, Swanson PE, Clarke RE. Peritoneal malignant mesothelioma versus serous papillary adenocarcinoma: a histochemical and immunohistochemical comparison. *Am J Surg Pathol* **1989**;13:659–670
6. Reuter K, Raptopoulos V, Reale F, et al. Diagnosis of peritoneal mesothelioma: computed tomography, sonography, and fine-needle aspiration biopsy. *AJR* **1983**;140:1189–1194
7. Whitley NO, Brenner DE, Antman KH, Grant D, Aisner J. CT of peritoneal mesothelioma: analysis of eight cases. *AJR* **1982**;138:531–535
8. Fred HL, Eiband JM, Collins LC. Calcifications in intraabdominal and retroperitoneal metastases: review of the roentgenographic features. *AJR* **1964**;91:138–148

Extraadrenal Retroperitoneal Paraganglioma: Clinical, Pathologic, and CT Findings

Wendelin S. Hayes[1]
Alan J. Davidson[2,3]
Philip M. Grimley[4]
David S. Hartman[5]

Paragangliomas of the retroperitoneum arise from specialized neural crest cells distributed along the aorta in association with the sympathetic chain. In order to ascertain characteristic CT features of extraadrenal retroperitoneal paragangliomas to differentiate them from other retroperitoneal tumors, 31 discrete tumors and two cases of paragangliomatosis in 28 patients were reviewed retrospectively, and the CT features were correlated with clinical and pathologic findings. There were 16 men and 12 women. Average age was 37 years (range, 11–70 years). Twenty-four patients (86%) had hypertension. Of these, catecholamine levels were elevated in all 18 patients who had biochemical studies. Four patients (14%) had malignant paragangliomas. The discrete tumors were classified by location as suprarenal (26%), renal hilar (32%), or infrarenal (42%). Suprarenal paragangliomas could not be distinguished from the ipsilateral adrenal gland on CT. The average size of functional tumors was smaller (7.0 cm) than that of nonfunctional tumors (12.0 cm), but the sizes of the two groups overlapped. Smaller tumors were more likely to be homogeneous and have well-defined margins than were larger tumors.

Our findings indicate that extraadrenal retroperitoneal paragangliomas are functionally active more often than previously reported and that they are readily detected by CT as soft-tissue masses closely associated with the entire length of the abdominal aorta. However, no CT feature was found that was unique for paraganglioma.

***AJR* 155:1247–1250, December 1990**

Retroperitoneal paragangliomas arise from paraganglia, collections of specialized neural crest cells symmetrically distributed along the aorta in close association with the sympathetic chain. This tissue either aggregates in the adrenal medulla, where it gives rise to intraadrenal paraganglioma, also known as pheochromocytoma, or remains in its paraaortic sites, where it may develop into extraadrenal, retroperitoneal paragangliomas.

The clinical and pathologic features of extraadrenal retroperitoneal paragangliomas have been reviewed [1–3]. The CT characteristics of these tumors have been described either as isolated case reports or as inclusive series that did not discriminate between adrenal paragangliomas or paragangliomas arising outside the retroperitoneum [4–11].

This study describes the CT characteristics of 28 proved cases of extraadrenal retroperitoneal paragangliomas. Its purpose is to correlate clinical and pathologic features with CT findings.

Materials and Methods

This report is based on a retrospective review of 23 patients with a single extraadrenal retroperitoneal paraganglioma, three patients with multiple discrete tumors, and two patients with continuous paraaortic tumors. These cases were accessioned into the archives of the Department of Radiologic Pathology at the Armed Forces Institute of Pathology between

Received April 24, 1990; accepted after revision July 9, 1990.

The opinions expressed herein are those of the authors and are not to be construed as reflecting the views of the Department of Defense, the Department of the Army, the Department of Navy, or the Uniformed Services University of the Health Sciences.

Presented at the annual meeting of the Society of Uroradiology, Naples, FL, September 1989.

[1] Department of Radiology, Georgetown University Hospital, 3800 Reservoir Rd., N.W., Washington, DC 20007.

[2] Department of Radiology and Radiological Sciences, Johns Hopkins University, School of Medicine, Baltimore, MD 21205.

[3] Present address: Radiologic Pathology, Armed Forces Institute of Pathology, Washington, DC 20306-6000. Address reprint requests to W. S. Hayes, % A. J. Davidson.

[4] Department of Pathology, F. Edward Hebert School of Medicine, Uniformed Services University of the Health Sciences, Bethesda, MD 20814-4799.

[5] Department of Radiology/Nuclear Medicine, F. Edward Hebert School of Medicine, Uniformed Services University of the Health Sciences, Bethesda, MD 20814-4799.

0361-803X/90/1556-1247

1979 and 1989. Paragangliomas of the urinary bladder were excluded.

The study population was characterized as to age, sex, and clinical presentation. Asymptomatic hypertension or hypertension associated with headaches, sweating, or palpitations was tabulated. The level of catecholamine or its metabolites in urine or plasma was noted, as was the presence of associated tumors or syndromes.

The diagnosis of paraganglioma was confirmed by established criteria. These included a tumor that is well demarcated by a fibrous pseudocapsule and one or both of the two major histopathologic patterns: small compartmentalized cell nests (the classical "zellballen" pattern of carotid body and related head and neck paragangliomas) or larger cell islands or confluent sheets of epithelioid cells frequently associated with adrenal medullary paragangliomas [12]. In either pattern, numerous cells stained for chromogranin, a typical finding in cells of neuroendocrine phenotype [13]. All tumors were richly vascularized.

Tumor size was obtained from the description of the gross specimen if resection was complete. In those cases in which resection was incomplete, size was determined by CT. Encapsulation of the tumor was evaluated from photographs of specimens or from pathology reports. Histopathologic growth patterns and cytologic features were reviewed without knowledge of clinical or radiologic data.

On the basis of CT data, the tumors were classified by location: suprarenal (above the upper pole of the kidney), renal hilar, or infrarenal (below the lower pole of the kidney). Infrarenal tumors were considered to have arisen in the organ of Zuckerkandl, which was defined as the area from the origin of the inferior mesenteric artery to the bifurcation of the abdominal aorta into the iliac arteries [1, 3, 14]. Tumors located in the suprarenal region were evaluated as to whether the ipsilateral adrenal gland could be identified as separate from the paraganglioma. For renal hilar tumors, note was taken of compression of the renal artery. Homogeneity, tumor margin (smooth or irregular), calcification within the tumor, and ability to distinguish the primary tumor from the aorta and inferior vena cava also were determined.

Results

The patients ranged in age from 11 to 70 years, with an average of 37 years. There were 16 males and 12 females.

Twenty-four patients (86%) had hypertension; 14 (58%) of the 24 were asymptomatic. Of these, hypertension developed in four during surgery or during induction of anesthesia for a procedure unrelated to the paraganglioma, which was discovered subsequently. Ten (42%) of the 24 patients had signs and symptoms related to excess secretion of catecholamines. These included headache, sweating, palpitations, and hypertension.

Plasma or serum levels of catecholamines were elevated in nine of the 14 patients with asymptomatic hypertension and in nine of the 10 patients with symptomatic hypertension. Data for catecholamines were not available in the remaining six patients with hypertension.

Blood pressure measurements were not available in three patients and were normal in one who also had normal biochemical studies.

None of the patients in this series had evidence of any of the syndromes that have been associated with neural crest tumors, such as the multiple endocrine adenoma syndrome or Carney triad.

No correlation was noted between histologic characteristics, tumor location, functional status, or malignancy. Benign and malignant lesions could not be distinguished on the basis of histopathologic criteria alone. Distant metastases and invasion of adjacent organs were the only reliable indicators of malignancy. An unusual degree of nuclear pleomorphism and multinucleation in two cases with metastasis and one case with multiple paragangliomas was noted.

Seven CT studies without contrast enhancement and 21 with enhancement were performed. No studies combined both. Thus, tumor enhancement could not be evaluated. No complications due to the use of contrast material were reported.

All of the tumors were closely related to the abdominal aorta, following the distribution of the aorticosympathetic chain. Average diameter of all tumors was 8.6 cm (range, 1.6–30.0 cm). Twenty-three (70%) of the tumors had smooth, well-defined margins.

In the 23 patients with single tumors, six tumors were localized as suprarenal, seven were renal hilar, and 10 were infrarenal. In the three patients with multiple discrete tumors, one patient had one suprarenal, one infrarenal and two renal hilar tumors; the second patient had one renal hilar and one infrarenal tumor; and the third patient had one suprarenal and one infrarenal tumor. Thus, eight (26%) of the 31 discrete tumors were localized as suprarenal, 10 (32%) were hilar, and 13 (42%) were infrarenal (Figs. 1–3). In the two patients with contiguous tumors (paragangliomatosis), distribution of involvement followed the course of the aorticosympathetic chain (Fig. 4). Suprarenal tumors could not be separated from the ipsilateral adrenal gland on the basis of CT criteria. Separation of the tumor from the normal adrenal gland was noted at the time of surgery or during gross pathologic inspection. Two renal hilar tumors were associated with renal artery encasement, one of which had an associated small kidney. Three of four nonfunctional tumors were infrarenal; one was suprarenal.

Of all tumors studied, 18 (55%) had homogeneous soft-tissue density (Figs. 1 and 2). Thirteen (39%) tumors had central areas of low density (Fig. 5). Two tumors (6%) had areas that were slightly greater in density than soft tissue; trauma preceded surgery in one of these patients, and the higher density represented acute hemorrhage. Punctate calcification was present in five tumors (15%) (Fig. 3).

Seventeen (89%) of 19 tumors less than 7 cm in diameter were of homogeneous density and sharply marginated. Of the 12 that were greater than 7 cm in diameter, eight (67%) had heterogeneous density and irregular margins.

Four patients (14%) had malignant paragangliomas as established by metastases to the liver (one patient), liver plus adjacent bowel (one patient), or bone (one patient). In one patient, invasion of adjacent bowel that had been suspected on preoperative CT was discovered at surgery. The malignant paragangliomas had an average diameter of 13.8 cm (range, 10.7–17.0), irregular margins, and, in three of the four tumors, low-density areas of necrosis (Figs. 5 and 6). Two patients with malignant paragangliomas did not have hypertension, suggesting nonfunctional tumors. Catecholamine levels were not measured in these two patients.

Discussion

The demographic features of extraadrenal retroperitoneal paragangliomas noted in this series are consistent with those previously described [1, 2, 14]. Men are affected more frequently than women, and most patients are between the ages of 30 and 45 years [11, 14].

Paragangliomas can be detected early if clinical findings

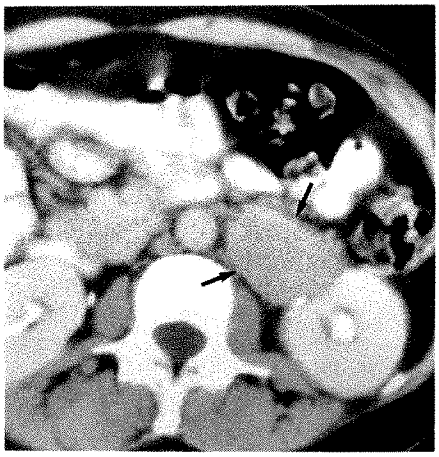

1

Fig. 1.—Renal hilar paraganglioma in a 25-year-old woman with hypertension, headaches, and diaphoresis. CT scan at level of left renal vein shows a smoothly marginated, homogeneous soft-tissue mass (*arrows*).

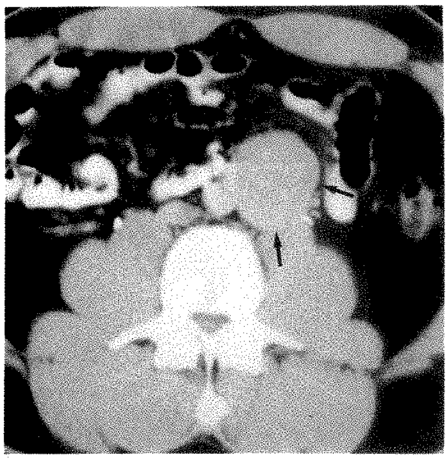

2

Fig. 2.—Infrarenal (Zuckerkandl) paraganglioma in a 29-year-old man with hypertension and clinically suspected paraganglioma. CT scan of lower abdomen shows a homogeneously solid, well-defined mass at Zuckerkandl region (*arrows*) adjacent to abdominal aorta.

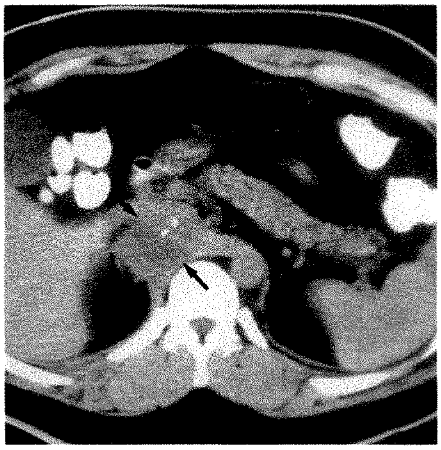

Fig. 3.—Suprarenal paraganglioma in a 24-year-old man with hypertension that developed during induction of anesthesia. CT scan through suprarenal area shows a soft-tissue mass (*arrows*) with small areas of calcification. Mass cannot be separated from right adrenal gland or inferior vena cava.

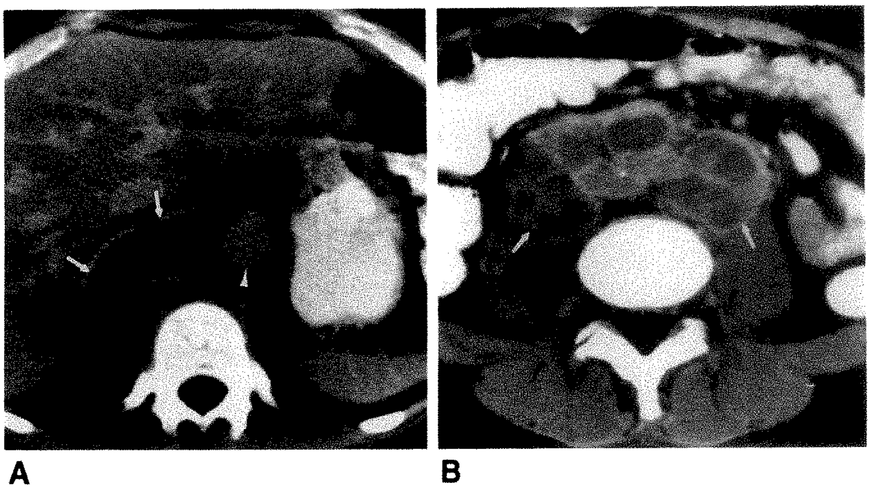

Fig. 4.—*A* and *B*, CT scans of upper (*A*) and lower (*B*) abdomen of a 43-year-old man with hypertension, palpitations, diaphoresis, and flushing show multiple, continuous, rounded soft-tissue masses (*arrows*) following the course of the aorticosympathetic chain, displacing inferior vena cava and aorta (*arrowhead*) anteriorly.

caused by excess secretion of catecholamines are present. The literature states that extraadrenal retroperitoneal paragangliomas are functional in only up to 60% of patients [2, 3, 14]. However, the data from this study indicate that symptomatic hypertension is, in fact, more common. For those patients with nonfunctional extraadrenal retroperitoneal paragangliomas, diagnosis usually depends on nonspecific factors related to the growth of a retroperitoneal mass [2, 6, 15].

In this study, the preponderant location of extraadrenal retroperitoneal paraganglioma was infrarenal, as has been described in previous reports [2, 14]. This area, known as the organ of Zuckerkandl, encompasses all chromaffin-cell-bearing tissue along the lower abdominal aorta, its bifurcation, and the iliac vessels [3].

Our data show that malignant tumors tend to be large, necrotic, and poorly marginated. However, these same features may be found in tumors that are not malignant, and therefore, they cannot be used as predictors of the benign or malignant nature of the tumor. Local invasion and distant metastases are reliable criteria for this determination [1].

The observations in this study illustrate that the CT features of extraadrenal paraganglioma overlap those of other types of tumors found in the retroperitoneum. Specifically, tumors of neural or mesodermal origin and those of metastatic disease must be considered.

Other tumors of neurogenic origin may resemble paragangliomas in both distribution and appearance. Neurofibromas appear as well-rounded, solid soft-tissue masses on CT [16], whereas neurilemomas are generally well-circumscribed homogeneous or inhomogeneous soft-tissue masses [17, 18].

Primary retroperitoneal tumors of mesodermal origin, specifically lipomatous tumors, may be differentiated from paragangliomas on CT only if fat can be identified within the tumor. Poorly differentiated liposarcomas with little or no fat, regardless of whether they are solid or necrotic [19–21] are difficult to distinguish from paragangliomas. This is also true of leiomyosarcomas. However, a necrotic or cystic liver metastasis would be more likely to occur in leiomyosarcomas than in paragangliomas [22]. Malignant fibrous histiocytomas arising near the kidney or adrenal gland would be indistinguishable from renal hilar paragangliomas [23].

The close relationship of paragangliomas to the aorta in all

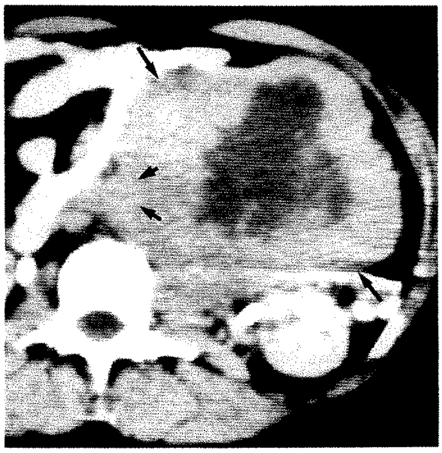

Fig. 5.—CT scan of mid abdomen in a 47-year-old man with a malignant paraganglioma shows a lobulated paraaortic mass (*long arrows*) with central necrosis adherent to aorta (*short arrows*). Resection and grafting of distal aorta were required at surgery.

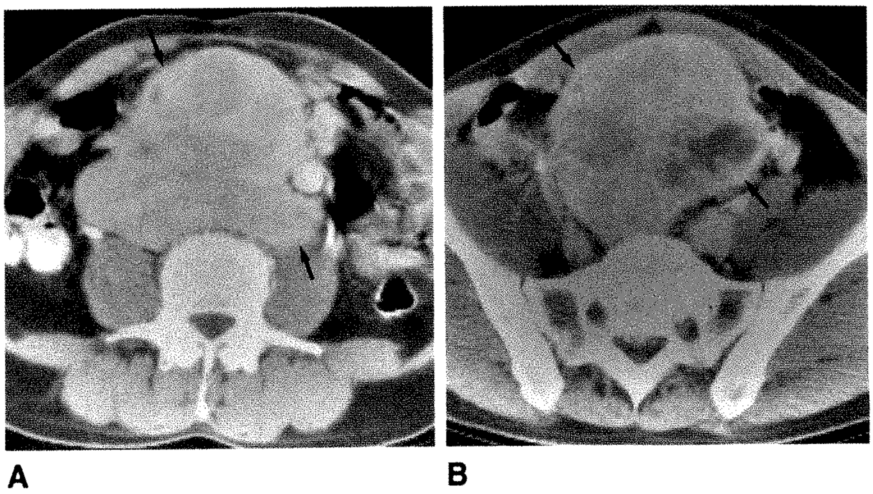

Fig. 6.—*A* and *B*, CT scans of pelvis of a 37-year-old man with a malignant infrarenal paraganglioma show an inhomogeneous soft-tissue mass with areas of low density and irregular margins in region of organ of Zuckerkandl (*arrows*).

instances may be of some value in differentiating these tumors from other primary retroperitoneal tumors. Tumor location away from the aorta should eliminate paragangliomas from the differential diagnosis. Paraaortic lymph node involvement from lymphoma or metastases to retroperitoneal nodes from a variety of primary neoplasms can resemble extraadrenal paragangliomas.

Correlation of symptoms and laboratory values of catecholamines is the most efficacious way of identifying a soft-tissue retroperitoneal mass detected by CT as an extraadrenal retroperitoneal paraganglioma. With nonfunctional paragangliomas, the CT features of extraadrenal paragangliomas overlap those of other retroperitoneal neoplasms, and the diagnosis is more difficult.

Certain limitations must be considered in interpreting the data. This study is a retrospective review of images obtained at multiple institutions without the advantage of uniform protocol and standardization of CT technique. Selection of patients may be biased for functional tumors and for tumors with surgical correlation. Because of these selection factors, this series may not be representative of retroperitoneal paragangliomas occurring in the general population. Despite these limitations, our results emphasize the need to consider paragangliomas in the differential diagnosis of a soft-tissue retroperitoneal mass that is suprarenal, renal hilar, or infrarenal, especially when hypertension is present. Further, the combination of large size, heterogeneous density, and irregular margins may increase the likelihood of malignancy and suggest the need for careful follow-up.

REFERENCES

1. Glenn F, Gray GF. Functional tumors of the organ of Zuckerkandl. *Ann Surg* **1976**;183:578–586
2. Lack EE, Cubilla AL, Woodruff JM, Lieberman PH. Extraadrenal paragangliomas of the retroperitoneum: a clinicopathologic study of 12 tumors. *Am J Surg Pathol* **1980**;4:109–120
3. Melicow MM. One hundred cases of pheochromocytoma (107 tumors) at the Columbia-Presbyterian Medical Center, 1926–1976: a clinicopathological analysis. *Cancer* **1977**;40:1987–2004
4. Francis IR, Glazer GM, Shapiro B, Sisson JC, Gross BH. Complementary roles of CT and ^{131}I-MIBG scintigraphy in diagnosing pheochromocytoma. *AJR* **1983**;141:719–725
5. Laursen K, Damgaard-Pederson K. CT for pheochromocytoma diagnosis. *AJR* **1980**;134:277–280
6. Law NW, Alfano L. Non-functioning retroperitoneal paraganglioma. *J R Soc Med* **1987**;80:246–247
7. Patel YD, Morehouse HT. Malignant paragangliomas of the retroperitoneum: value of computed tomography and angiography. *Clin Radiol* **1984**;35:185–188
8. Quint LE, Glazer GM, Francis IR, Shapiro B, Chenevert TL. Pheochromocytoma and paraganglioma: comparison of MR imaging with CT and I-131 MIBG scintigraphy. *Radiology* **1987**;165:89–93
9. Thomas JL, Bernardino ME, Samaan NA, Hickey RC. CT of pheochromocytoma. *AJR* **1980**;135:477–482
10. Welch TJ, Sheedy PF II, van Heerden JA, Sheps SG, Hattery RR, Stephens DH. Pheochromocytoma: value of computed tomography. *Radiology* **1983**;148:501–503
11. Mikhail RA, Moore JB, Reed DN Jr, Abbott RR. Malignant retroperitoneal paragangliomas. *J Surg Oncol* **1986**;32:32–36
12. Grimley PM, DeLellis RA. Multisystem neuroendocrine neoplasms. In: Albores-Saavedra J, Henson DE, eds. *Pathology of incipient neoplasia*. Philadelphia: Saunders, **1986**:425–454
13. Grimley PM. Multicentric paragangliomas and associated neuroendocrine tumors. In: Kaiser HE, ed. *Progression of human cancer*. Boston: Kluwer Academic, **1989**:49–61
14. Enzinger FM, Weiss SW. Paraganglioma. In: Enzinger FM, Weiss SW, eds. *Soft tissue tumors*. St. Louis: Mosby, **1988**:836–860
15. Kryger-Baggesen N, Kjaergaard J, Sehested M. Nonchromaffin paraganglioma of the retroperitoneum. *J Urol* **1985**;134:536–538
16. Biondetti PR, Vigo M, Fiore D, De Faveri D, Ravasini R, Benedetti L. CT appearance of generalized von Recklinghausen neurofibromatosis. *J Comput Assist Tomogr* **1983**;7:866–869
17. Ghiatas AA, Faleski EJ. Benign solitary schwannoma of the retroperitoneum: CT features. *South Med J* **1989**;82:801–802
18. Donnal JF, Baker ME, Mahony BS, Leight GS. Benign retroperitoneal schwannoma. *Urology* **1988**;31:332–334
19. Friedman AC, Hartman DS, Sherman J, Lautin EM, Goldman M. Computed tomography of abdominal fatty masses. *Radiology* **1981**;139:415–429
20. Waligore MP, Stephens DH, Soule EH, McLeod RA. Lipomatous tumors of the abdominal cavity: CT appearance and pathologic correlation. *AJR* **1981**;137:539–545
21. Lane RH, Stephens DH, Reiman HM. Primary retroperitoneal neoplasms: CT findings in 90 cases with clinical and pathologic correlation. *AJR* **1989**;152:83–89
22. McLeod AJ, Zornoza J, Shirkhoda A. Leiomyosarcoma: computed tomographic findings. *Radiology* **1984**;152:133–136
23. Goldman SM, Hartman DS, Weiss SW. The varied radiographic manifestations of retroperitoneal malignant fibrous histiocytoma revealed through 27 cases. *J Urol* **1986**;135:33–38

Value of MR Imaging in Differentiating Benign from Malignant Soft-Tissue Masses:

Study of 95 Lesions

Thomas H. Berquist[1]
Richard L. Ehman[1]
Bernard F. King[1]
Charles G. Hodgman[1]
Duane M. Ilstrup[2]

MR imaging has largely replaced CT as the technique of choice for preoperative staging of patients with soft-tissue masses. Whether MR imaging can be used to differentiate benign from malignant masses is controversial. Our experience suggests that MR imaging often can characterize soft-tissue masses accurately. To evaluate this question further, we studied 95 consecutive lesions (50 benign and 45 malignant). Consecutive cases were selected to simulate our clinical practice. Surgical proof was available for all masses except hematomas, for which clinical follow-up confirmed the diagnosis. MR images were interpreted twice by three radiologists. The first review was accomplished without any clinical history and the second review with clinical history. Reviewers were asked to classify the lesion as benign or malignant on the basis of their clinical knowledge and analysis of MR image features (size, lesion margin, signal homogeneity, and neurovascular or bone involvement). Although interpretation varied somewhat because of the experience of the reviewers, the specificity and accuracy of diagnosis averaged 90% for both benign and malignant lesions. Negative predictive value for malignancy averaged 94% among the three reviewers.

MR imaging is the technique of choice for identification and characterization of soft-tissue masses. The nature of the lesion (benign vs malignant) can be determined in the majority of cases.

***AJR* 155:1251–1255, December 1990**

MR imaging has become the premier method for identifying and staging soft-tissue masses of the musculoskeletal system. Although MR imaging is sensitive, many authors have reported that it is not useful in differentiating benign from malignant soft-tissue masses [1–5].

Our experience indicates that certain image features are useful in differentiating benign from malignant lesions. Therefore, we elected to perform a blind study of MR images of benign and malignant soft-tissue masses. Images were obtained and interpreted before biopsy or surgical data were obtained. Ninety-five (50 benign and 45 malignant) consecutive soft-tissue masses were studied to determine the usefulness of MR imaging features in differentiating benign from malignant lesions. Nonneoplastic lesions such as abscess and hematoma were included with benign tumors. The primary goal of this study was to determine the value of morphologic characteristics (e.g., lesion size, margins, signal intensity, and neurovascular involvement) in predicting the nature of soft-tissue masses. We also chose radiologists with different levels of experience with MR imaging to determine what effect experience has on the accuracy of interpretation.

Materials and Methods

MR examinations of 95 consecutive patients with soft-tissue masses who had not had biopsies were selected for review. This series included 45 malignant and 50 benign masses. The specific diagnoses are given in Table 1. Benign masses included hematomas, abscesses, and other lesions that mimic neoplasms. Surgical proof was available in all cases except for

Received April 5, 1990; accepted after revision June 26, 1990.

[1] Department of Diagnostic Radiology, Mayo Clinic and Mayo Foundation, Rochester, MN 55905. Address reprint requests to T. H. Berquist.

[2] Section of Biostatistics, Mayo Clinic and Mayo Foundation, Rochester, MN 55905.

0361–803X/90/1556–1251
© American Roentgen Ray Society

TABLE 1: Diagnoses of 95 Soft-Tissue Masses

Type of Mass	No. of Patients
Benign	
Cyst	12
Hematoma	9
Lipoma	8
Hemangioma	5
Desmoid	4
Neuroma	4
Abscess	2
Myxoma	2
Thrombosed aneurysm	1
Thrombosed vein	1
Epidermoid	1
Angiolipoma	1
Total	50
Malignant	
Malignant fibrous histiocytoma	17
Liposarcoma	7
Synovial sarcoma	6
Mesenchymal sarcoma	3
Rhabdomyosarcoma	3
Chondrosarcoma (soft tissue)	2
Leiomyosarcoma	2
Neurofibrosarcoma	2
Fibrosarcoma	1
Epithelioid sarcoma	1
Lymphoma	1
Total	45

TABLE 2: MR Features of Soft-Tissue Masses

Feature	No. (%)	
	Malignant (n = 45)	Benign (n = 50)
Size (cm)		
<1	0	1 (2)
1–3	0	10 (20)
3–5	6 (13)	14 (28)
>5	39 (87)	25 (50)
Margin		
Well defined	7 (15)	22 (44)
Partially irregular	13 (29)	20 (40)
Irregular	25 (56)	8 (16)
Signal intensity		
Homogeneous	2 (5)	21 (42)
Majority of mass homogeneous	11 (24)	17 (34)
Inhomogeneous	32 (71)	12 (24)

posttraumatic hematomas. In these patients, follow-up with resolution of symptoms and hematomas confirmed the clinical diagnosis. This information was not available to the reviewers.

The majority of all lesions were in the lower extremity: 29 (31%) in the thigh, 17 (18%) in the leg, and 11 (12%) around the knee. The remainder of the lesions were in the upper extremity and trunk. The majority of malignant lesions (32/45, 71%) also were in the lower extremity. Benign cysts were almost always immediately adjacent to joints in both upper and lower extremities.

MR images were obtained on either a 0.15-T resistive system (25 patients) or a 1.5-T Signa system (70 patients). Both T1-weighted, 500/20 (TR/TE), and T2-weighted, 2000/60, spin-echo (SE) sequences were available for each examination. Only pertinent images were selected for review. All patient data were removed from the images, and all cases were randomized (benign and malignant were not separated) before evaluation.

Images were interpreted blindly in separate sessions by three different radiologists. Two radiologists were fellows in cross-sectional imaging and in the process of taking a 3-month MR imaging fellowship when they began their participation in the study. The third radiologist was a consultant with 5 years of experience in musculoskeletal MR imaging. Images were randomized and reviewed by each radiologist in two different settings. In the first part of the study, the radiologists were given images to review without any clinical information or other imaging studies to compare with the MR study. After 3–6 months, the images were put in a different order and given to the interpreters for a second evaluation. At this time, the clinical history and results of other imaging studies were made available. CT scans were available in only about one-third of cases because MR imaging is the technique of choice for soft-tissue masses at our institution.

The reviewers were instructed to categorize cases according to several specific criteria. The size and location of each lesion were recorded by each radiologist. Other features included the margins of the lesions (which were to be defined as smooth, partially well defined, or irregular) and the signal intensity and/or homogeneity (recorded on both T1- and T2-weighted sequences). Also evaluated were neurovascular encasement or displacement, hemorrhage and/or edema in or around the lesion, and bone involvement. After each of these features was evaluated, the reviewers were asked to categorize the lesion as benign or malignant and, when possible, to provide a histologic diagnosis. Specific diagnoses for benign lesions such as hematoma or abscess were also requested when it was possible to provide one. Data were tabulated for both reviews for each of the three examiners. The final diagnoses (lesions benign vs malignant) were evaluated for accuracy, sensitivity, specificity, and positive and negative predictive values.

Results

For lesion size, as measured on MR images, the average of the three measurements was used. The sizes of lesions are summarized in Table 2. No malignant lesions were less than 3 cm in diameter. On the other hand, 22% of benign lesions were less than 3 cm in diameter. Thirteen percent of malignant lesions were 3–5 cm; 87% were larger than 5 cm. On the surface this may seem important; however, 50% of benign lesions also were larger than 5 cm.

Forty-four percent of benign lesions had well-defined or sharp margins (Table 2). Slight irregularity was described in 40% of benign masses. Only eight (16%) showed total or nearly complete irregularity of margins. Most of the tumor margin was irregular in 38 malignant lesions (85%). However, sharp margins were noted in seven cases (15%).

At least some inhomogeneous signal intensity was noted in 43 malignant lesions (95%) (Table 2). Homogeneous signal intensity was unusual in malignant lesions. Small areas of inhomogeneity were present in 12 benign lesions (24%).

Neurovascular involvement was not common in either benign or malignant lesions; however, some displacement of neurovascular structures occurred in 32 malignant lesions (71%). Three malignant lesions (7%) had neurovascular encasement. This was also observed with desmoid tumors (which are considered benign). Hemorrhage or edema or both were present in 27% of benign and 54% of malignant lesions. The prevalence of hemorrhage and edema in benign lesions was due to the number of hematomas (9/50) included in this group of patients. Bone involvement was noted with malignant lesions and desmoid tumors.

Accuracy of interpretation varied somewhat among the reviewers. There were also differences in diagnostic ability related to the type of lesions (benign vs malignant) and availability of clinical data. The latter was especially important for the less experienced radiologists. Accuracy in predicting whether lesions were benign or malignant ranged from a low of 88% in the less experienced group to 93% for the physician experienced in MR imaging (Table 3). Radiologists were able to predict the histology of the lesions in up to 26% of cases, mostly for benign lesions, when no history was available. When a history was available, the two less experienced reviewers changed their diagnoses 13% and 19% of the time overall. The more experienced physician changed the diagnosis only once on the basis of historical information.

The less experienced physicians predicted the nature of benign lesions 38–40% of the time without clinical data and 50–52% of the time when history was available. The physician more experienced in MR imaging accurately predicted the nature of a benign lesion in 74% of cases. The reviewers were not successful in predicting the histology of malignant lesions.

The sensitivity, specificity, positive predictive value, negative predictive value, and accuracy were calculated for benign and malignant lesions (Table 4). The data for malignant lesions are particularly important. The specificity for malignant lesions ranged from 82% to 96%, with a negative predictive value of 92–96% and a positive predictive value of 88–90%.

Discussion

An increasingly common indication for MR imaging is to determine the presence or absence of musculoskeletal masses. When a mass is found in such an examination, the immediate challenge is to characterize it. Several authors [3, 6–9] have noted that clinical data, especially patient age, lesion location, and duration of symptoms, are helpful in addition to image features for characterizing lesions. Some authors [5, 7, 10–12] have reported, however, that differentiation of benign and malignant lesions is inconsistent when MR features are used. Manipulation of T1 and T2 relaxation times has not improved specificity [1, 6].

TABLE 3: Accuracy in Predicting Benign and Malignant Lesions

Observer No.	No. (%) (n = 95)		% of Diagnoses Changed with History
	Accuracy	Exact Histology	
1	85 (90)	15 (16)	13[a]
2	84 (88)	25 (26)	19[a]
3[b]	88 (93)	24 (25)	1

[a] Diagnosis less accurate after history in 11% of patients when initial interpretation was changed.

[b] Physician experienced in MR imaging.

TABLE 4: Observer Performance for Detection of Soft-Tissue Masses

Type of Mass/ Statistical Measure	Observer No.			Average
	1	2	3[a]	
Benign				
Sensitivity (%)	90	82	90	88
Specificity (%)	90	83	96	90
Positive predictive value (%)	92	95	96	94
Negative predictive value (%)	88	83	90	87
Accuracy (%)	90	88	93	90
Malignant				
Sensitivity (%)	90	96	96	94
Specificity (%)	90	82	96	90
Positive predictive value (%)	88	93	90	87
Negative predictive value (%)	92	95	96	94
Accuracy (%)	90	88	93	90

[a] Physician experienced in MR imaging.

Our results provide support for using MR imaging to characterize soft-tissue masses. By using traditional radiologic criteria, such as homogeneity and boundary characteristics, experienced and inexperienced observers were able to identify malignant lesions with an average sensitivity of 94% in this series. The negative predictive value of an interpretation that a mass was not malignant also was high (94%).

Classic benign and malignant lesion characteristics are illustrated in Figures 1 and 2, respectively. Benign lesions (Fig. 1) tend to be well marginated, have homogeneous signal intensity, and do not encase neurovascular structures or invade bone. Malignant lesions (Fig. 2) generally have irregular margins and inhomogeneous signal and more often encase neurovascular structures and involve bone [3, 6].

The benign lesions that most often were classified incorrectly as malignant in this series were desmoid tumors and necrotic benign neoplasms (neurofibromas). A single hemangioma was considered malignant by one observer (Fig. 3); this was a solid inhomogeneous cavernous hemangioma [13, 14]. The difficulty of correctly classifying desmoid tumors is not surprising in view of the infiltrative, locally aggressive nature of the lesions [3, 6].

Many of the benign lesions (ganglionic cysts, lipomas, hemangiomas, neuromas [because of location], and most hematomas) were diagnosed correctly on the basis of imaging features alone [13, 15–17]. When the MR images were interpreted with knowledge of the clinical findings, the specific histologic diagnosis for benign lesions could be predicted in 38–40% of cases by the inexperienced reviewers and in 74% by the more experienced MR imaging consultant. These percentages are higher than the 24% reported by Kransdorf et al. [18].

The malignant lesion most commonly misclassified as benign was synovial sarcoma. Three of the six synovial sarcomas in this group of lesions had smooth margins and a cystic appearance or mimicked hematomas (Fig. 4). Errors in diagnosis were made in more than half of the observations.

The results show that historical data can be helpful in lesion classification. The accuracy improved for the less experienced reviewers when history was available. The more experienced

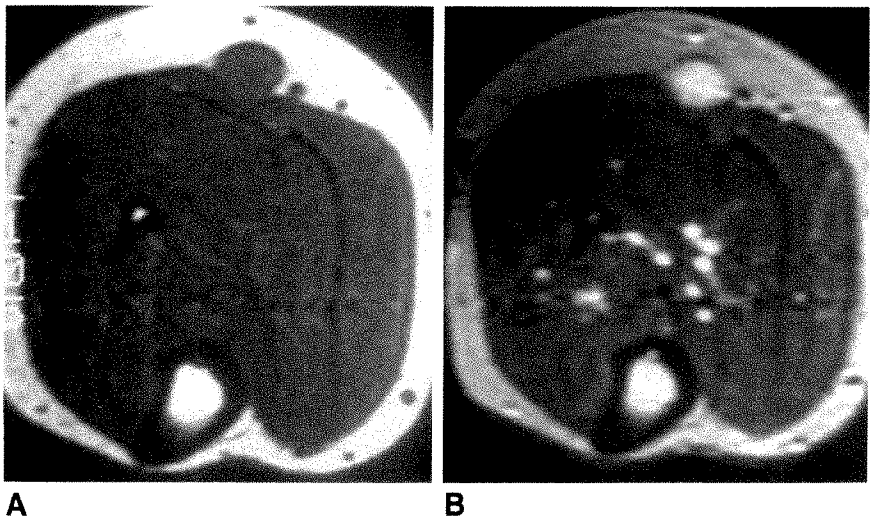

Fig. 1.—Benign neuroma.

A, Axial T1-weighted MR image (SE 500/20) shows a well-marginated homogeneous low-intensity mass.

B, Axial T2-weighted MR image (SE 2000/60) shows uniform high signal intensity. Margination and signal intensity are typical of a benign lesion. Change in signal intensity between the two images indicates lesion is not a lipoma.

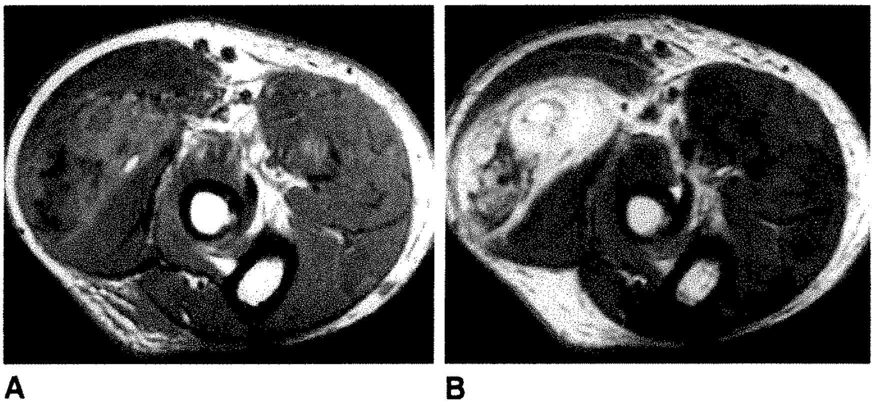

Fig. 2.—Fibrosarcoma of forearm.

A, Axial T1-weighted MR image (SE 500/20) shows mass with mixed or inhomogeneous signal intensity.

B, Axial T2-weighted MR image (SE 2000/60) shows mass has irregular margins and inhomogeneous signal intensity. These features are typical of a malignant mass and appreciated more easily on T2-weighted image.

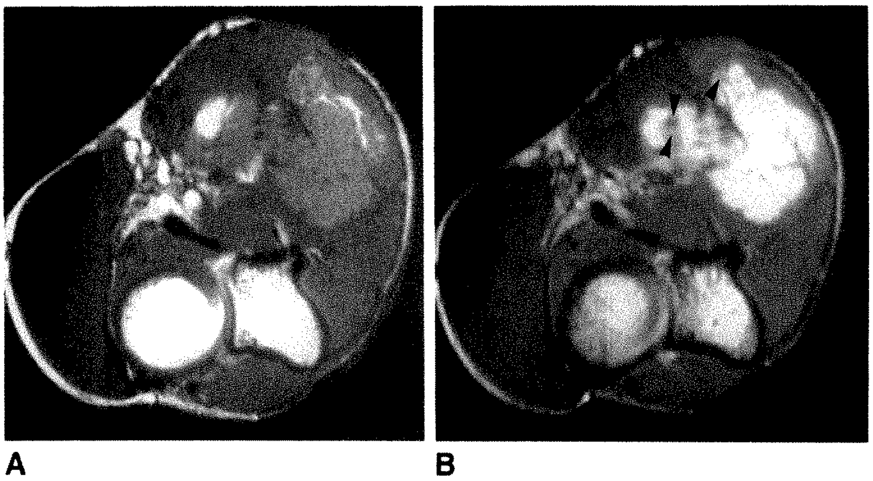

Fig. 3.—Cavernous hemangioma in proximal forearm.

A, Axial T1-weighted MR image (SE 500/20) shows scattered areas of increased signal intensity due to blood.

B, Axial T2-weighted MR image shows areas of high and low intensity (*arrowheads*) due to paramagnetic effects of blood. Inhomogeneous signal intensity and irregular margins may cause this lesion to be confused with a malignant mass.

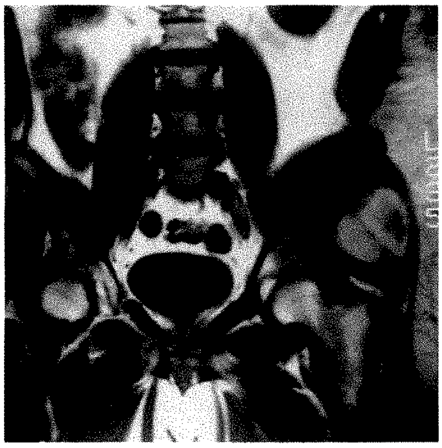

Fig. 4.—Synovial sarcoma in gluteal region. Coronal SE 500/20 MR image of pelvis shows well-marginated cystic lesion with appearance similar to that of hematoma. Three of six synovial sarcomas were considered benign because of this appearance.

MR imaging reviewer relied on history minimally, and the overall specificity of 96% for all lesions did not change between the first and second portions of the study.

REFERENCES

1. Beltran J, Simon DC, Katz W, Weis LD. Increased MR signal intensity in skeletal muscle adjacent to malignant tumors: pathologic correlation and clinical relevance. *Radiology* **1987**;162:251-255
2. Bland KI, McCoy DM, Kinard RE, Copeland EM III. Application of magnetic resonance imaging and computerized tomography as an adjunct to the surgical management of soft tissue sarcomas. *Ann Surg* **1987**;205:473-481
3. Berquist TH. Magnetic resonance imaging of musculoskeletal neoplasms. *Clin Orthop* **1989**;244:101-118
4. Sundaram M, McGuire MH, Herbold DR, Beshany SE, Fletcher JW. High signal intensity soft tissue masses on T1 weighted pulsing sequences. *Skeletal Radiol* **1987**;16:30-36
5. Sundaram M, McGuire MH, Herbold DR. Magnetic resonance imaging of soft tissue masses: an evaluation of fifty-three histologically proven tumors. *Magn Reson Imaging* **1988**;6:237-248
6. Berquist TH, Ehman RL, Richardson ML. *Magnetic resonance of the musculoskeletal system*. New York: Raven, **1987**:85-108
7. Dooms GC, Hricak H, Sollitto RA, Higgins CB. Lipomatous tumors and tumors with fatty component: MR imaging potential and comparison of MR and CT results. *Radiology* **1985**;157:479-483
8. Weekes RG, Berquist TH, McLeod RA, Zimmer WD. Magnetic resonance imaging of soft-tissue tumors: comparison with computed tomography. *Magn Reson Imaging* **1985**;3:345-352
9. Weekes RG, McLeod RA, Reiman HM, Pritchard DJ. CT of soft-tissue neoplasms. *AJR* **1985**;144:355-360
10. Petasnick JP, Turner DA, Charters JR, Gitelis S, Zacharias CE. Soft-tissue masses of the locomotor system: comparison of MR imaging and CT. *Radiology* **1986**;160:125-133
11. Sundaram M, McGuire MH, Schajowicz F. Soft-tissue masses: histologic basis for decreased signal (short T2) on T2-weighted MR images. *AJR* **1987**;148:1247-1250
12. Totty WG, Murphy WA, Lee JKT. Soft-tissue tumors: MR imaging. *Radiology* **1986**;160:135-141
13. Cohen EK, Kressel HY, Perosio T, et al. MR imaging of soft-tissue hemangiomas: correlation with pathologic findings. *AJR* **1988**;150:1079-1081
14. Cohen JM, Weinreb JC, Redman HC. Arteriovenous malformations of the extremities: MR imaging. *Radiology* **1986**;158:475-479
15. Cohen MD, McGuire W, Cory DA, Smith JA. MR appearance of blood and blood products: an in vitro study. *AJR* **1986**;146:1293-1297
16. Ehman RL, Berquist TH. Magnetic resonance imaging of musculoskeletal trauma. *Radiol Clin North Am* **1986**;24(2):291-319
17. Swensen SJ, Keller PL, Berquist TH, McLeod RA, Stephens DH. Magnetic resonance imaging of hemorrhage. *AJR* **1985**;145:921-927
18. Kransdorf MJ, Jelinek JS, Moser RP Jr, et al. Soft-tissue masses: diagnosis using MR imaging. *AJR* **1989**;153:541-547

Book Review

Radiology of Bone Diseases, 5th ed. By George B. Greenfield. Philadelphia: Lippincott, 1024 pp., 1990. $95

This fifth edition of a deservedly popular one-volume textbook contains 82 more pages than the previous edition published 4 years ago, 192 new illustrations (mostly MR images and CT scans), and a 25% increase in the number of references, which now extend through 1988. As in previous editions, the material is organized according to the main radiologic features of the lesions rather than according to etiology. Thus, an introductory chapter detailing an analytic approach to bone radiology is followed by chapters titled "Loss of Bone Density," "Alteration of Bone Texture," "Epiphyseal Region" (stretched to include the metaphysis), "Changes in Size and Shape of Bone" (including dysplasias and congenital malformation syndromes), "Cardinal Roentgen Features" (a grab bag), "The Solitary Lesion," "The Soft Tissues," and "The Joints." The obvious advantage of this arrangement is the transformation of the table of contents into a table of differential diagnosis. The inevitable disadvantage, repetition of textual and illustrative material, is minor and does not destroy the natural flow of information. The text abounds with gamut lists of radiologic features and differential diagnoses. An introduction to each disorder or group of disorders features clinical and pathologic information set forth clearly and concisely. The text is enhanced by pertinent CT, radionuclide, and MR images and by explanation of the indications and comparative usefulness of these techniques for each disorder. No attempt has been made to explain the physics of MR imaging. Sentences are short and pithy, and radiologic descriptions are crisp and to the point.

As in previous editions, the book strikes appropriate balances between text and pictures and between the common and esoteric. Discussions of the dysplasias, metabolic diseases, and anemias are especially well organized and reasonably up to date. However, sections on MR imaging of the knee and intervertebral disk herniation are too skimpy to be of much value, and the legends for the images sometime lack such basic information as TR and TE values or, at the very least, whether they are T1- or T2-weighted.

Occasionally, errors from earlier editions persist or, through editorial lapses, are preserved on one page only to be corrected on another. For example, the existence of transphyseal blood vessels in infancy is denied on page 5 and accepted on page 482. Malignant degeneration is stated to occur "in a significant number of cases" of Paget disease (page 115) vs "the incidence may be far less than 1%" (page 130). "Gross bending of bone" rather than recurrent fractures with remodeling is stated to be responsible for the shepherd's crook deformity of fibrous dysplasia. The physis mistakenly is stated to form an effective barrier against the epiphyseal spread of osteosarcoma, when actually it is breached by most metaphyseal osteosarcomas. The characteristic site of origin of periosteal osteosarcoma is said to be the tibia on page 585 and the femur on page 609. No mention is made of the probable traumatic origin of the distal femoral periosteal desmoid. Multicentric reticulohistiocytosis is called by the obsolete term reticulohistiocytoma. Vertebral osteomyelitis unaccountably is placed on a list of disorders associated with a "vacuum disk," and spondylolysis is stated to be of congenital origin, without mention of the more likely possibility of stress fracture. Excessive use is made of the bogus term "softening of bone."

Although the illustrations are plentiful (1685) and show a wide variety of diseases, they include too many gross abnormalities and too few subtleties. Many are mottled or blotchy. Although this problem occurred in previous editions, it has been exaggerated in this one by increased image contrast and lack of gray tones. The resultant loss of detail means that a few illustrations fail to show what they are supposed to show, and others show findings that are so indistinct as to be almost invisible. Some of the less obvious findings might have benefited from judicious use of arrows.

In summary, this book maintains its place as a practical introduction to skeletal radiology. The text, for the most part, is clear and concise. Primary drawbacks include occasional errors of fact and, more important, the variable quality and sometimes downright impenetrability of the illustrations. I hope that in the next edition, these disappointing illustrations will have been rephotographed or replaced.

Richard H. Gold
University of California, Los Angeles, Medical Center
Los Angeles, CA 90024

MR Imaging Findings in Patients with Bone-Chip Allografts

James S. Jelinek[1-3]
Mark J. Kransdorf[1,2,4]
Richard P. Moser[2,4]
H. Thomas Temple[5]
Martha K. Lenhart[5]
B. Hudson Berrey[2,5]

Increasing use of MR to evaluate primary bone neoplasms has stimulated numerous articles on the initial assessment of these lesions. However, scant MR literature has been written about the postoperative MR appearance. We studied the MR appearance of lesions treated by curettage followed by packing with cancellous bone-chip allograft. We retrospectively reviewed the MR scans of 18 consecutive patients treated in this way. Pathologic diagnoses of these lesions were confirmed according to commonly accepted criteria. The allograft sites showed a distinctive pattern of speckled bright signal on T1-weighted images in eight cases. Thirteen of 18 grafts showed a whorled or speckled pattern of increased signal on the T2-weighted images. Only four allograft regions had predominantly low signal on both T1- and T2-weighted images. Two of 18 patients had recurrent tumor proved by open biopsy. MR images in these cases showed areas of homogeneous signal that replaced areas of speckled hyperintensity on both T1- and T2-weighted images. In both these recurrences the tumor had signal intensity similar to that seen on the preoperative MR study.

We conclude that knowledge of the MR appearance of cancellous bone chip allografts is important to avoid misinterpreting areas of high signal on T1- or T2-weighted images as areas of recurrence of tumor and/or hemorrhage.

***AJR* 155:1257-1260, December 1990**

The increasing use of MR in assessing primary bone neoplasms has stimulated publication of articles on the MR appearance of these lesions [1-5]. However, very little has been written on the postoperative MR appearance, specifically in those lesions curetted and packed with cancellous bone-chip allograft [6-9]. Cancellous bone chip allograft is harvested from cadaver sites (femur, tibia, and humeral condyles) and then is ground into different-sized fragments. It serves as a milieu to foster new bone formation and promote healing of the curetted area of bone. In this study, we review the MR appearance of 18 postoperative cancellous bone allografts and discuss the possible causes for their distinctive appearance.

Materials and Methods

Since 1986, 18 patients with a variety of primary bone tumors or tumorlike processes underwent bone curettage and cancellous bone allografting. Pathologic diagnoses, confirmed according to commonly accepted criteria, included giant-cell tumor (eight cases), fibroxanthoma (two cases), fibrous dysplasia (two cases), bone cyst (two cases), and eosinophilic granuloma, intraosseous lipoma, liposclerosing myxofibromatous tumor, and a desmoplastic fibroma (one case each). MR scans were performed from 1 month to 3 years after surgical grafting. Three patients had more than one follow-up examination, and only the most recent findings were used in the tabulation of results.

MR technique included axial and either sagittal or coronal scans with both T1-weighted (200-700/20 [TR/TE]) and T2-weighted (1600-2800/60-100) sequences. Depending on

Received April 23, 1990; accepted after revision June 11, 1990.

[1] Department of Radiology, Walter Reed Army Medical Center, Washington, DC 20307-5001.

[2] Departments of Radiology and Orthopedic Surgery, Uniformed Services University of Health Sciences, Bethesda, MD 20814.

[3] Present address: Department of Radiology, Washington Hospital Center, 110 Irving St., N.W., Washington, DC 20010.

[4] Department of Radiologic Pathology, Armed Forces Institute of Pathology, Walter Reed Army Medical Center, Washington, DC 20306. Address reprint requests to R. P. Moser.

[5] Department of Orthopedic Surgery, Walter Reed Army Medical Center, Washington, DC 20307-5001.

0361-803X/90/1556-1257

lesion size and location, slice thickness varied from 3 to 10 mm with an approximate 20–33% gap. Field of view ranged from 12 to 40 cm, and two to four repetitions were used. Additionally, the bone allograft chips in their original shipped glass containers were imaged by MR using T1- and T2-weighted techniques with parameters as described previously. These samples were imaged with two test tubes containing water and vegetable oil. Images were obtained with a 1.5-T GE Signa MR unit (General Electric, Milwaukee, WI) or a 1.5-T Technicare MR unit (Technicare, Solon, OH). Images were interpreted by two radiologists experienced in musculoskeletal MR, with full knowledge of the clinical history and with corresponding radiographs. No attempt was made to review the images in a blinded fashion.

After harvest from a cadaver, the bone is cultured and postmortem blood samples are screened for infectious agents. The bone is then ground into different-sized fragments and processed by using either a saline, hydrogen peroxide, or sterile water/alcohol cleansing. Tissue is freeze-dried and later tested for residual moisture (recommend 5% by weight).

Two samples of cancellous allograft that had undergone morcellation were reconstituted in saline, and the supernatant was smeared on a glass slide and stained with hematoxylin and eosin (H & E). Further processing was performed on the allograft chips by whole-mount, plastic-embedded sections on H & E stained specimens. Microscopic evaluation was then performed. Histologic examination of dried smears and plastic-embedded bone allograft specimens showed fat and crenated RBCs interspersed within cellular bone marrow. A background of necrotic marrow elements and bony trabeculae also was noted (Fig. 1).

Results

MR imaging of the cancellous bone allografts in vitro in their original shipped containers was performed. On T1-weighted images, one jar of allograft had a markedly speckled hyperintense MR appearance equal to the signal intensity of fat. The second sample's appearance was uniformly hypointense. All samples were of mildly speckled hyperintensity on T2-weighted images and equal in signal intensity to fat.

The results of MR imaging of the patients' allografted sites are summarized in Table 1. MR imaging of the 18 bone sites after cancellous bone allografting showed only four lesions to be relatively hypointense on both T1- and T2-weighted images. Ten grafted lesions were uniformly hypointense on T1-weighted images (Fig. 2), and eight showed at least a minimally speckled pattern of signal intensity (Fig. 3). On T2-weighted images, 13 of 18 allograft sites showed a speckled or whorled pattern of alternating high and low signal (Figs. 2 and 3). Three bone allografts showed only minimal foci of hyperintense signal compared with skeletal muscle. One allograft was uniformly hyperintense, and one allograft was uniformly hypointense on the T2-weighted images. Three patients had more than one follow-up MR examination. The intervals between follow-up examinations ranged between 4 and 12 months, and no significant change in appearance was

TABLE 1: Results of MR Imaging of Allografted Sites

Primary Tumor	Months After Surgery	T1 Appearance		T2 Appearance	
		SI	SP	SI	SP
Bone cyst	1	=SM	No	>F	No
Fibroxanthoma	1	=SM	No	=F	Yes
Giant cell	1	>SM	Yes	>F	Yes
Giant cell	2	>SM	Yes	>F	Yes
Fibroxanthoma	3	>SM	Yes	>F	Yes
Giant cell	4	=SM	No	=F	Yes
Giant cell with recurrence	4	=SM	Yes	>F	Yes
Intraosseous lipoma	4	=SM	No	=F	Yes
Fibrous dysplasia	6	=SM	No	<F	Minimal
Eosinophilic granuloma	8	<SM	No	=SM	No
Bone cyst	11	=SM	No	=F	Yes
Giant cell	12	=SM	No	>F	Yes
Giant cell	13	=SM	No	>F	Yes
Desmoplastic fibroma with recurrence	16	>SM	Minimal	>F	Yes
Cystic giant cell	26	>SM	Yes	=F	Yes
Fibrous dysplasia	27	>SM	Minimal	<F	Minimal
Giant cell	30	=SM	Minimal	>F	Yes
Liposclerosing myxofibromatous tumor	36	=SM	No	<F	Minimal

Note.—SI = signal intensity, SP = speckled pattern present or not, SM = skeletal muscle intensity, F = fat signal intensity.

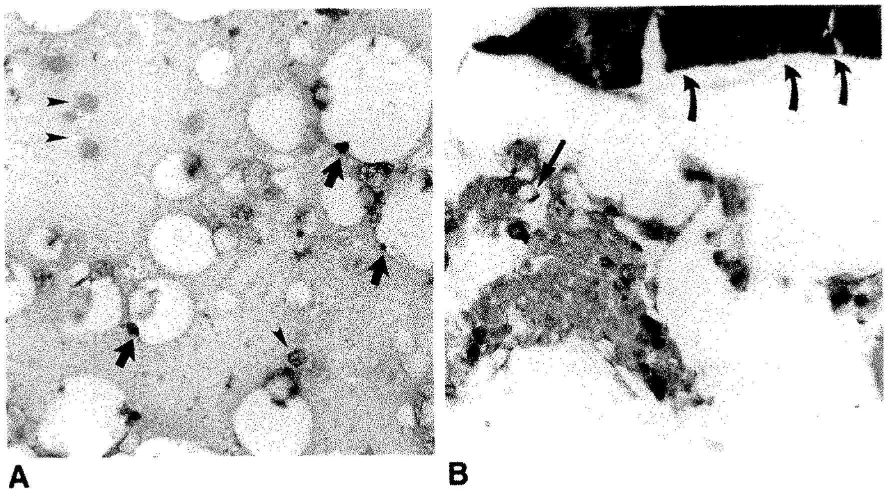

Fig. 1.—Histologic examination of sample of reconstituted cancellous bone allograft.

***A*, Supernatant smear stained with hematoxylin and eosin (H & E) shows intact fat cells (*arrows*) and crenated RBCs (*arrowheads*) in a background of proteinaceous debris. (Magnification ×480)**

***B*, Plastic-embedded allograft sample stained with H & E shows hemopoietic marrow elements, fat cells (*straight arrow*), and bony trabeculae (*curved arrows*). (Magnification ×200)**

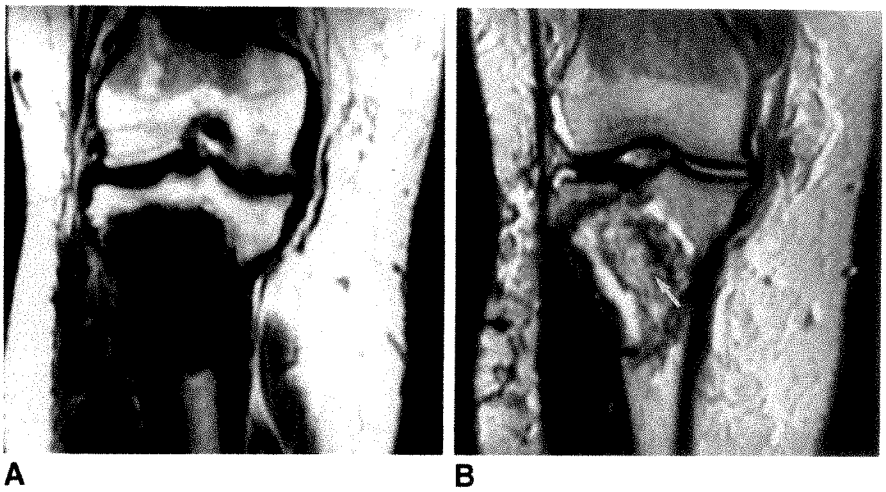

Fig. 2.—Site of curettage of giant-cell tumor and cancellous bone allograft packing 4 months previously.

A, Coronal T1-weighted MR image (600/20) shows relatively uniform hypointense signal throughout graft site.

B, Coronal T2-weighted MR image (1800/80) shows a whorled central pattern (*arrow*) with minimal fluid at margins of graft site.

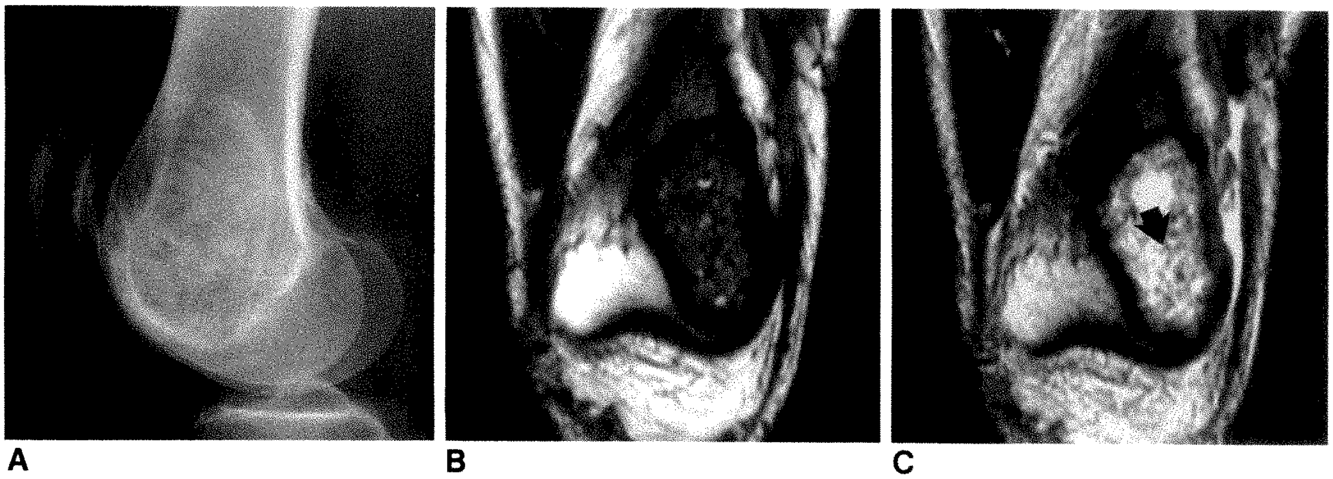

Fig. 3.—Cancellous bone allograft status after curettage of a giant-cell tumor 2 months previously. Patient has no evidence of recurrence.

A, Radiograph shows well-healed bony allograft in distal femur.

B, Coronal T1-weighted MR image (617/20) shows a speckled pattern of hyperintensity.

C, Coronal T2-weighted MR image (1800/80) shows speckled areas of hyperintensity (*arrow*).

noted. Two recurrences occurred at the allograft sites, which showed areas of homogeneous dark T1 and homogeneously intermediate T2 signal replacing the speckled pattern (Fig. 4). There was one recurrent giant-cell tumor and one recurrent desmoplastic fibroma with areas of sarcomatous elements within.

Discussion

Although MR has been used in the preoperative imaging evaluation of patients with primary bone lesions [1-5], little has been written about the postoperative MR appearance, particularly after cancellous bone allografting [6]. The general assumption would be that in the early postoperative period, MR images of the grafted bone would reveal areas of inhomogeneous hyperintense signal on T2-weighted images attributable to postoperative hemorrhage/fluid. However, on studies of healed sclerotic bone allograft (months or years later), one would not expect areas of hyperintensity on T1- or T2-weighted images. The presence of areas of speckled hyperintensity reflects the underlying morphology of the cancellous bone allograft.

In the samples examined histologically, a combination of intact fat cells and partially crenated RBCs were seen against a background of necrotic marrow elements and bony trabeculae. We believe it is these components that are responsible for the heterogeneous, speckled appearance observed on MR images. Sites of vascularized granulation tissue and necrotic bone marrow elements would be hyperintense on T2-weighted images. But one would not expect this tissue signal on T1-weighted images. The presence of fat cells on the histologic examination and the same signal intensity as that of fat on the in vitro MR images suggests the fat cells cause the bright signal on T1-weighted images. Bone tra-

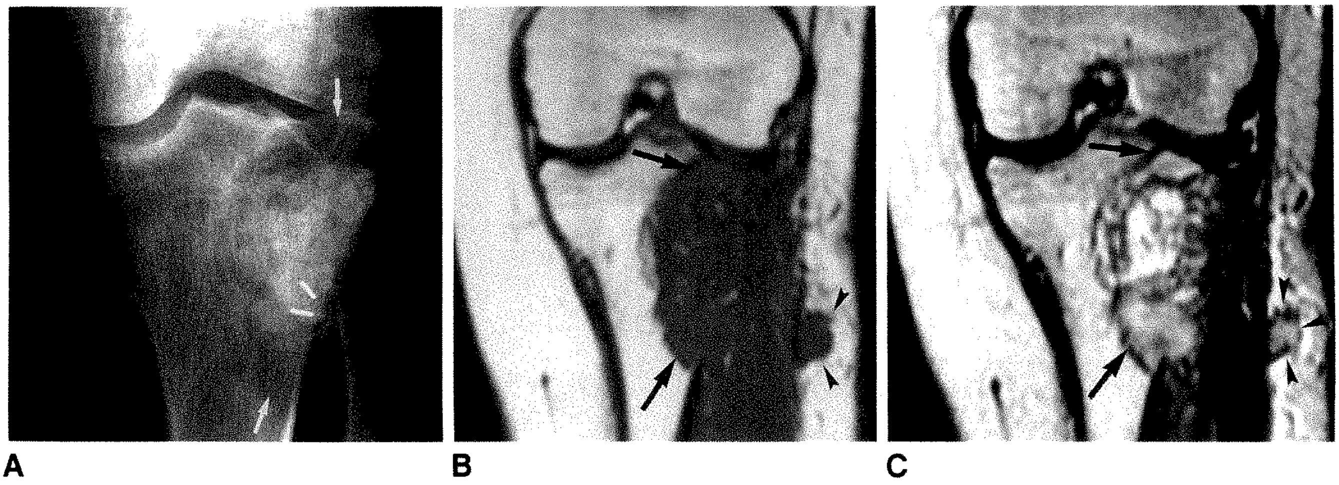

Fig. 4.—Recurrent desmoplastic fibroma of proximal lateral tibia.

***A*, Radiograph shows increased lucency (*arrows*) along superior and inferior margins of allograft. This appearance was seen in both cases of recurrence of tumor and in two cases without evidence of recurrent tumor.**

***B* and *C*, T1-weighted (600/20) and T2-weighted (1800/80) coronal images show biopsy-proved tumor recurrence at superior and inferior edge of allograft site (*arrows*) and a recurrence within soft tissues (*arrowheads*). Note recurrent tumor replaces areas of speckled hyperintensity.**

beculae most likely are the source of the dark signal on both T1- and T2-weighted images. It is interesting that no change in signal intensity occurred in the three patients who did have follow-up examinations up to 12 months later. Unfortunately, we do not have follow-up on patients for a longer postoperative period to see when this signal pattern disappears.

In the two cases of tumor recurrence that followed curettage and bone grafting, focal areas of homogeneously dark T1 and intermediate T2 signal replaced the usual speckled appearance. The signal intensity of the recurrent tumor was identical to the appearance of the tumor seen on the MR studies before the initial surgery.

In summary, the typical MR appearance of cancellous bone-chip allograft sites is frequently speckled and hyperintense, especially on T2-weighted images. This reflects the underlying morphology of the cancellous bone allograft and should not be misinterpreted as recurrent tumor.

ACKNOWLEDGMENTS

Special thanks to Mary Mood and Wendy Baker for preparation and revision of this manuscript.

REFERENCES

1. Tehranzadeh J, Mnaymneh W, Ghavam C, Morillo G, Murphy BJ. Comparison of CT and MR imaging in musculoskeletal neoplasms. *J Comput Assist Tomogr* **1989**;13:466–472
2. Sundaram M, McGuire MH. Computed tomography or magnetic resonance for evaluating the solitary tumor or tumor-like lesions of bone. *Skeletal Radiol* **1988**;17:393–401
3. Bloem JL, Bluemm RG, Taminiau AHM, van Oosterom AT, Stolk J, Doornbos J. Magnetic resonance imaging of primary malignant bone tumors. *RadioGraphics* **1987**;7:425–445
4. Petterson H, Slone RM, Spanier S, Gillespy T III, Fitzsimmons JR, Scott KN. Musculoskeletal tumors: T1 and T2 relaxation times. *Radiology* **1988**;167:783–785
5. Petterson H, Gillespy T III, Hamlin DJ, et al. Primary musculoskeletal tumors: examination with MR imaging compared with conventional modalities. *Radiology* **1987**;164:237–241
6. Vanel D, Lacombe MJ, Couanet D, Kalifa C, Spielmann M, Genin J. Musculoskeletal tumors: follow-up with MR imaging after treatment with surgery and radiation therapy. *Radiology* **1987**; 164:243–245
7. Kattapuram SV, Phillips WC, Mankin HJ. Giant cell tumor of bone: radiographic changes following local excision and allograft replacement. *Radiology* **1986**;161:493–498
8. Sartoris DJ, Gershuni DH, Akeson WH, Holmes RE, Resnick D. Coralline hydroxyapatite bone graft substitutes: preliminary report of radiographic evaluation. *Radiology* **1986**;159:133–137
9. Kusnick C, Haywood I, Sartoris DJ, et al. Radiographic evaluation of joints resurfaced with osteochondral shell allografts. *AJR* **1987**;149:743–748

MR Imaging of Fractures of the Growth Plate

Diego Jaramillo[1, 2]
Fredric A. Hoffer[1]
Frederic Shapiro[3]
Frank Rand[3]

In order to assess whether MR imaging could be used to evaluate posttraumatic abnormalities of the growth plate cartilage, 28 MR imaging examinations of 26 physeal fractures were performed from 4 days to 2 years after injury. Twelve patients were studied within 6 months of the fracture. MR imaging changed the Salter-Harris classification in six. Interruption of the growth plate detected on T2-weighted images was associated with subsequent growth anomaly in six of eight patients. Horizontal fracture of the physis without interruption was associated with growth disturbance in only one of four patients. Sixteen growth plates were studied beyond 6 months after injury. Twelve had physeal bars and abnormal growth. Of four patients without physeal abnormality on MR imaging, two had normal growth and two had mild deformity.

Our results show that MR imaging detects abnormalities in the cartilage that are associated with subsequent growth disturbances and provides accurate mapping of physeal bridging and associated growth abnormalities that have already occurred.

***AJR* 155:1261–1265, December 1990**

The Salter-Harris classification describes growth plate fractures according to the direction of the fracture line as seen on plain radiographs [1–3]. The prognosis following growth plate fractures is dependent not only on the type of fracture but also on the age of the patient, the epiphysis involved (greatest potential for growth abnormalities in the distal femur and the least in the distal radius), the intensity of the trauma, and the size of the fibrous or bony lesion and its location within the plate [4–6]. For example, some type II fractures of the distal femur heal uneventfully while others, which are radiologically indistinguishable, go on to premature growth plate arrest and severe deformity [5]. Increasing awareness of the limitation of radiologic methods for evaluating abnormalities of the growth plate [4–7] has led to the use of axial and coronal CT [8–10]. However, as with radiographs and tomograms, only ossified lesions can be detected, and, by definition, these bony bridges have already been formed. Quantitative scintigraphy [11] detects differential rates of activity in the injured physis, but lacks the spatial resolution of the other techniques.

Our studies in a rabbit model of growth plate injury suggest that MR imaging has the capability of showing the early cartilaginous and vascular abnormalities that eventually lead to growth disturbances [12]. If MR imaging could detect bony bar formation in its early stages of development, as well as assess later sequelae of trauma to the growth plate, it would be a useful tool in the early detection of posttraumatic growth abnormalities and potentially prevent their occurrence. We report our preliminary experience with MR imaging of high-risk fractures of the growth plate and their complications. This work in progress attempts to assess whether MR imaging provides information beyond that obtained with other radiologic techniques. Further work is needed to determine the definitive role of MR imaging in the evaluation of growth disturbances.

Received April 4, 1990; accepted after revision July 10, 1990.

Presented in part at the annual meeting of the Society for Pediatric Radiology, San Antonio, TX, April 1989.

[1] Department of Radiology, Children's Hospital and Harvard Medical School, 300 Longwood Ave., Boston, MA 02115. Address reprint requests to F. A. Hoffer.

[2] Present address: Department of Radiology, Massachusetts General Hospital, Fruit St., Boston, MA 02114.

[3] Department of Orthopaedic Surgery, Children's Hospital and Harvard Medical School, Boston, MA 02115.

0361-803X/90/1556-1261
© American Roentgen Ray Society

Materials and Methods

During an 18-month period, 28 MR imaging studies were done in 26 patients 1–15 years old. Two patients had two injuries each and two others were studied 5 and 8 months after the initial imaging. The majority of fractures studied were evaluated because they involved the distal tibia ($n = 11$), distal femur ($n = 7$), and proximal tibia ($n = 2$), where there is a high likelihood of posttraumatic growth arrest, irrespective of whether the Salter-Harris type was II, III, or IV [4–6]. Four MR imaging studies of the distal humerus were done in children less than 5 years of age to clarify the fracture pattern through the unossified epiphysis. A single distal radial study was performed to confirm the plain film findings of a rare growth arrest, and a study of the distal fibula was done in a patient who had had partial amputation of this bone.

In all patients, the initial diagnosis of a growth plate injury was made with plain radiographs. Tomograms were obtained in seven patients and a coronal CT scan in one; these studies were performed within 1 month of the MR studies. MR imaging was not used as a primary diagnostic technique.

All MR studies were performed on a 1.5-T unit (Signa, General Electric, Milwaukee, WI) by using an extremity coil or a 3-in. (7.6-cm) circular surface coil. An examination typically included the following sequences: coronal T1-weighted spin-echo (SE), 400–600/20 (TR/TE); coronal T2* or T2-weighted gradient-echo (GRE), 39/15/30° or 100/25/10° (TR/TE/flip angle) respectively; and sagittal T2-weighted SE 2000/20,80. Fat-suppression imaging was done in two patients. The frequency-encoding direction was perpendicular to the long axis of the bone to avoid chemical shift in the physis. Patients younger than 7 years of age were sedated with chloral hydrate, 50–75 mg/kg orally, or with Demerol compound (Demerol, Phenergan, Thorazine) intramuscularly. Some patients were scanned with a cast on but none had metallic internal fixation devices at the time of imaging.

Fractures imaged within 6 months of injury (when the physeal abnormalities are evolving and the fracture lines are consistently visualized) were classified with MR imaging by using the Salter-Harris classification [1]. Interruption of the growth plate on SE or GRE T2-weighted images was classified as small (<25% of the plate) or large, and as central or peripheral. In patients examined beyond 6 months after injury (when bony bridge formation has occurred), the signal intensity of the interrupted portion of the plate on T1-weighted images was judged as being low (similar to fibrous tissue) or high (similar to medullary fat).

Seven patients had surgery after MR imaging and 11 patients have been followed up with radiographs ($n = 9$) or MR imaging ($n = 2$) for more than 3 months after the initial MR study.

The MR images were first interpreted without knowledge of the radiologic findings. Subsequently, a combined analysis of the MR images, radiographs, and clinical outcome was performed. MR studies were compared with tomograms according to the adequacy of definition of fracture lines, bony bridge, growth plate distortion, growth deformity, and associated findings.

Results

MR Imaging Findings

Abnormalities of the growth plate cartilage.—Interruption of the growth plate was seen as a focal dark area within the bright physeal cartilage on T2- or T2*-weighted sequences (Fig. 1). Of the eight patients with growth plate interruptions imaged within 6 months of injury, six had abnormal growth: two developed angular deformity requiring surgery and the physes in four closed prematurely.

Horizontal fracture without interruption of the physeal cartilage was seen in four patients (Fig. 2). In the only one of these who had abnormal growth, MR showed that the fracture had occurred along the epiphyseal side of the growth plate. Of the other three, one had physeal separation along the metaphyseal side of the cartilage and two had physeal widening without a clear plane of cleavage. The area of fractured cartilage did not correlate with the outcome.

Fracture pattern.—By MR criteria, fractures examined within 6 months of injury included Salter-Harris II ($n = 7$), Salter-Harris III ($n = 1$), and Salter-Harris IV ($n = 4$). MR imaging changed the radiologic Salter-Harris classification in six, or half, of the cases. Extension of the fracture into the unossified distal humeral epiphysis was detected by MR imaging in two cases (Fig. 3). Bright fracture lines were seen on T2 or T2*-weighted images in eight of 10 fractures examined within 3 months after injury and in only three of 16 fractures studied later than 6 months after trauma. Two of these last three showed evidence of nonunion on radiographs (Fig. 3).

Formation of a bony bridge.—The signal of the interrupted growth plate on T1-weighted images obtained more than 6 months after injury was increased in six cases (suggesting fatty marrow within the bridge) and decreased in six (sug-

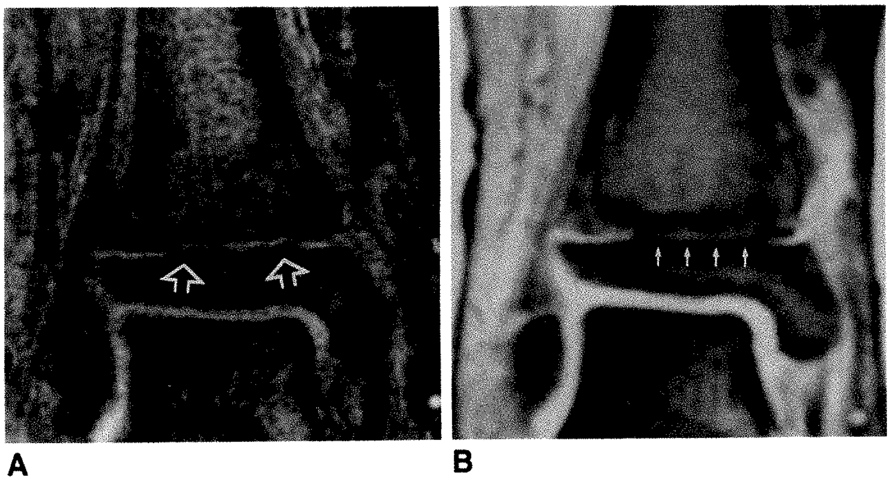

Fig. 1.—11-year-old boy with Salter II fracture of distal tibia.

A, Gradient-echo (GRE) 39/15/30° MR image obtained 2 months after injury shows several interruptions of signal from plate (*arrows*). Patient was in cast at the time of study, and radiographs had not shown any abnormality of the growth plate.

B, GRE 330/10/40° MR image obtained 7 months after injury shows large area of interruption of growth plate (*arrows*). This has resulted in arrest of growth with 4 mm of shortening. Further follow-up was to continue because patient had not reached skeletal maturity.

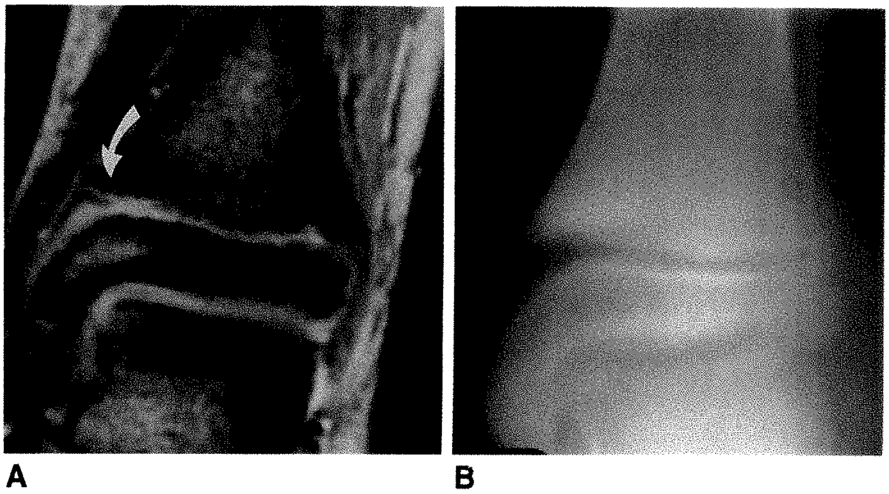

Fig. 2.—11-year-old boy with Salter IV fracture of distal tibia.

***A*, Gradient-echo 39/15/30° MR image obtained 3 weeks after injury. Plane of cleavage extends into metaphyseal bone immediately adjacent to physis (*arrow*), indicating that separation is on metaphyseal side of plate.**

***B*, Anteroposterior tomogram obtained 2 weeks earlier shows medial widening of plate but no indication of subchondral abnormality. Metaphyseal component of fracture is not apparent on MR image but was seen on T1-weighted images. A coronal CT scan showed a nondisplaced, incomplete fracture in epiphysis, which was not evident on other studies.**

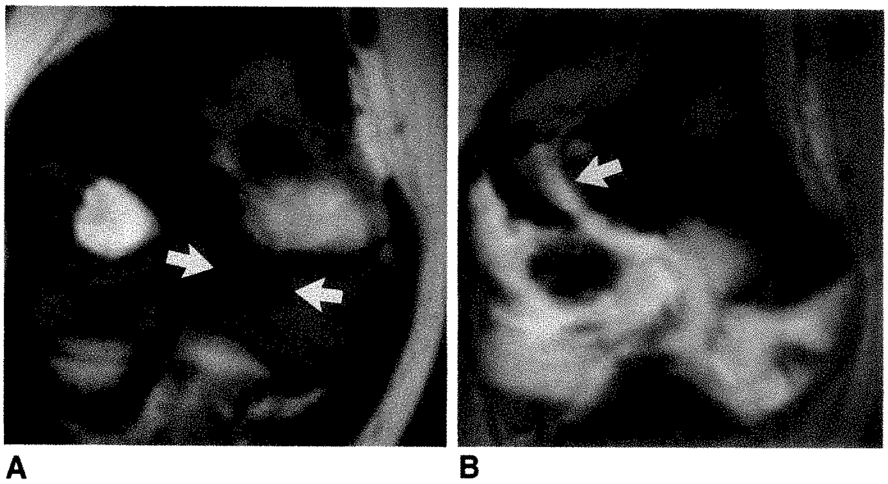

Fig. 3.—4-year-old boy with lateral condylar fracture.

***A*, Spin-echo 600/20 MR image of distal humerus obtained 14 months after injury. Fracture (*arrows*) extends into unossified epiphysis.**

***B*, Gradient-echo 67/20/13° MR image shows increased signal along fracture line (*arrow*). This patient had delayed union of fracture.**

gesting fibrosis or dense bone, Fig. 4). All patients in whom interruptions of the growth plate were present 6 or more months after the injury had abnormal growth. Of the four patients without growth plate interruptions more than 6 months after trauma, two had mild deformity that has been improving and two had normal growth.

Metaphyseal abnormalities.—Growth recovery lines were seen on T1-weighted MR images and on radiographs in patients studied 3 or more months after the fracture. Of 12 patients with abnormal growth recovery lines, five of the lines were tilted (Fig. 5), two were focally curved (Fig. 4), two were delayed (Fig. 6), and three were absent in the fractured bone but present in neighboring ones (complete growth arrest). All patients with angular deformity had peripheral lesions and all patients with arrested or delayed growth had central lesions.

Focal extension of the growth cartilage into the metaphysis was seen in five patients (Fig. 6). There was no evidence of deformity at the site of the metaphyseal abnormality.

Lack of ossification of a portion of the metaphysis was seen in a patient with varus deformity of the distal humerus. Although the deformity was evident on radiographs, MR imaging demonstrated an unsuspected focal absence of the dark zone of provisional calcification suggesting growth plate dysfunction.

Abnormalities of surrounding structures.—Two patients had avascular necrosis which was seen as decreased signal intensity on T1-weighted images in the marrow contiguous to the fracture. One patient had a tear of the collateral ligament of the knee, and one had narrowing of the popliteal artery adjacent to the injury. One patient developed an exostosis at the site of cartilaginous injury (Fig. 5).

Contributions and Limitations of Imaging Studies

Two patients with only minimal evidence of fracture on radiographs developed growth arrest (Fig. 5). In five of seven patients who had tomograms, MR imaging and tomography showed bony abnormalities equally well; in the other two, MR imaging was superior to tomography. In one case, a bridge and the associated growth deformity were not well demonstrated with tomograms but were well seen with MR imaging (Fig. 4). In another one, tomograms failed to show separation of the physis, which was demonstrated on MR imaging (Fig. 2). Associated soft-tissue findings not seen radiologically were detected in three patients.

Surgical and Imaging Follow-up

MR imaging findings were confirmed surgically in seven patients. Four of these patients underwent bridge resection; two bridges were bony and two were fibrous.

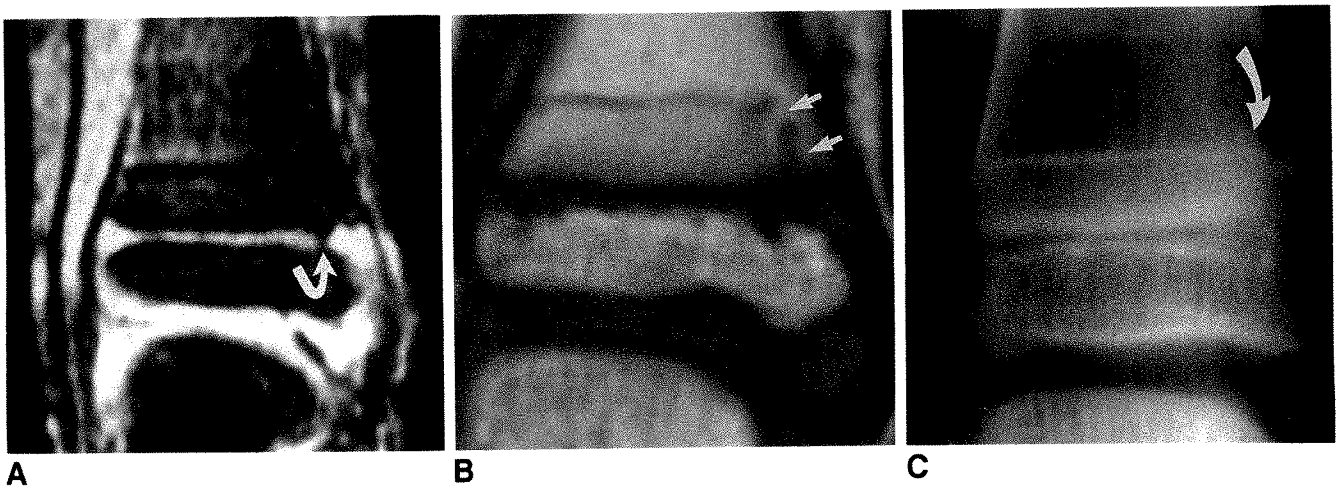

Fig. 4.—5-year-old girl with Salter IV fracture of distal tibia.

A, Gradient-echo 100/25/10° MR image obtained 15 months after injury. Focal interruption of medial growth plate is manifested by a lack of bright signal (*arrow*). At surgery, a fibrous bridge was found in region of interruption.

B, Spin-echo 500/20 T1-weighted MR image shows focal curving of growth recovery line medially (*arrows*). More lateral growth recovery line is not affected.

C, Anteroposterior tomogram close to time of MR examination. Although there is local curving of growth recovery line (*arrow*), it is less apparent than on MR imaging. Fibrous bridge is not detectable.

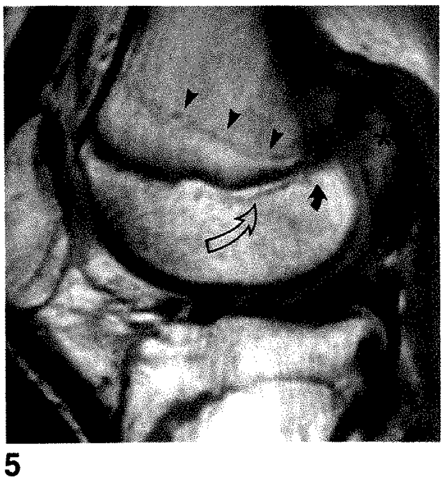
5

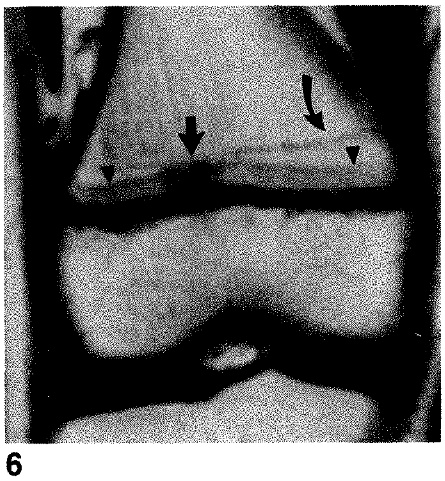
6

Fig. 5.—11-year-old boy with Salter IV fracture of proximal tibia and subtle avulsion of periphery of distal femoral physis. Sagittal spin-echo (SE) 2000/20 MR image of knee obtained 17 months after injury shows a tilted, dark growth recovery line in distal femur (*arrowheads*), indicating ongoing anterior but no posterior growth since injury. Bright signal from physis (*open arrow*) is interrupted in region of posterior bridge (*solid arrow*). Signal from proximal tibial physis is absent, indicating posttraumatic fusion. An exostosis has developed in region of avulsion (*asterisk*).

Fig. 6.—10-year-old girl with Salter II fracture of distal right femur. SE 600/20 MR image obtained 8 months after injury shows healed metaphyseal fracture (*curved arrow*) and more distal growth recovery line (*arrowheads*). Focal widening of growth plate (*straight arrow*) extends to growth recovery line. Femoral growth recovery line is not as advanced as proximal tibial growth recovery line, suggesting a delay in femoral growth.

Of 11 patients who had long-term follow-up, six had early physeal closure with slight shortening, two had mild angulation that has been improving, one had extensive bridging (Fig. 1), and two had no growth abnormality.

Discussion

Current treatment of posttraumatic growth abnormalities attempts to prevent deformity. Peripheral lesions causing angular deformity require early correction, usually by excision of the bony bridge. The management of central lesions producing shortening varies because up to 2 cm of limb length discrepancy can be tolerated. Therefore, patients close to maturity may not require therapy, whereas younger patients may be treated with bridge resection or closure of the contralateral growth plate [13]. Only a small group of patients with growth plate fractures develop physeal damage that is clinically significant. Patients with high-risk fractures are followed to skeletal maturity as growth plate damage can become radiologically and clinically apparent years after injury [6, 13].

MR imaging can show initial and evolving posttraumatic abnormalities of the growth cartilage [12]. In the small group of patients studied in the first months after injury, MR imaging defined the path of injury within the cartilage. Our experience suggests that vertical interruption of the growth plate is frequently associated with subsequent growth abnormality, whereas horizontal fracture of the physis is not. The exact plane of separation within the physis can, on occasion, be determined with MR imaging. Although our experience is limited, such definition is potentially significant, because fractures involving the resting and proliferative zones have more complications than those involving the hypertrophic zone [14, 15].

Improved detection of the adjacent epiphyseal and/or metaphyseal components of growth plate fractures changes the radiologic Salter-Harris classification. MR is particularly useful for distinguishing between Salter-Harris II and IV injuries of the unossified distal humerus (Fig. 3) and detecting metaphyseal extension of an apparent Salter-Harris III fracture, thus defining it as a more worrisome type IV injury in which communication between epiphyseal and metaphyseal circulations forms a bony bridge [5, 16]. Imaging of abnormalities in the ligaments, menisci, and vessels adjacent to the injured bone is an additional advantage of MR.

A bridge across the physis develops months after a growth plate fracture and causes deformity. If the bridge is fibrous, it may not be detectable radiologically or by CT but may be seen with MR imaging, as occurred in one of our cases (Fig. 4). Increased signal intensity on T1-weighted images indicates fatty bone marrow within the bridge. Differentiation between a small bony bridge and a fibrous bridge is not possible with MR imaging, because both are dark on all sequences. Clinically, both fibrous and osseous bridges may need to be resected. The multiplanar capability of MR imaging combined with the possibility of cross-referencing abnormalities on the display monitor facilitates the mapping of the bridge. The diagnosis of an uninvolved physis can be made with greater confidence by using MR imaging, as there is superior contrast resolution between the bright cartilage and the dark abnormalities.

Abnormal growth recovery lines, an early indication of deformity [17-20], are easily detected with MR imaging as dark lines on a bright background of fatty marrow. Extension of the growth cartilage into the metaphysis presumably is due to ischemic alteration of metaphyseal ossification and, as indicated by previous studies [2, 21] and by our own experience, does not cause growth abnormality. MR imaging can suggest abnormal fracture healing when there is persistent high signal intensity along the fracture margins (Fig. 3). This may represent cartilage and granulation tissue, which is seen in the callus in cases of delayed union [22]. Secondary findings such as osteonecrosis are well seen with MR imaging.

This report represents a preliminary study. All the fractures chosen for MR imaging presented specific clinical concerns regarding possible growth plate arrest and were expected to have a fairly high rate of problems. The patients studied varied widely in age, fracture type, and time from fracture to imaging. Also, we have not studied fractures expected to have an uncomplicated course. An accurate comparison between MR imaging and other techniques cannot be done on the basis of our data because tomograms were obtained only in a few patients. When both studies were performed, MR imaging was slightly superior to tomography for imaging disturbances of the cartilage and adjacent structures.

The growth cartilage has a great capability to recover after insult and can overcome some fibrous bridges and even some small bony bridges. It is currently uncertain whether some of the more subtle findings of MR imaging should mandate a change in therapy. Further studies (or possibly a multicenter study including a large number of patients) are necessary in order to assess the clinical significance of the MR findings.

In this study we have shown the value of MR imaging in defining evolving physeal bridge formation. Other techniques have defined bony bridges only after they have formed. We consider MR imaging not just another way of defining bony bridges but rather a way to image them earlier.

We are currently using MR imaging in the early days and weeks after injury to evaluate growth plate fractures that, by well-established clinical and radiologic criteria, have a significant risk of developing growth abnormalities. We are also using MR imaging several months after injury, when bars across the physis have already formed, to determine the size, location, and characteristics of the lesion. We believe that MR imaging provides a means to better assess growth plate injuries as it directly images the physeal cartilage and the changes produced by physeal injury. It is our hope that this improved imaging of injuries of the growth plate will eventually lead to earlier intervention and better long-term results.

ACKNOWLEDGMENTS

We thank James Kasser, John Emans, Anthony Weber, and Michael Millis for referring their patients for MR examinations and Robert Wilkinson and John A. Kirkpatrick, Jr., for helpful comments.

REFERENCES

1. Salter RB, Harris WR. Injuries involving the epiphyseal plate. *J Bone Joint Surg [Am]* **1963**;45-A:587-622
2. Ogden JA. Injury to the growth mechanisms of the immature skeleton. *Skeletal Radiol* **1981**;6:237-253
3. Rogers LF. The radiography of epiphyseal injuries. *AJR* **1970**;96:289-299
4. Shapiro, F. Epiphyseal disorders. *N Engl J Med* **1987**;317:1702-1710
5. Shapiro, F. Epiphyseal growth plate fracture-separations: a patho-physiologic approach. *Orthopedics* **1982**;5:720-736
6. Ogden JA. The evaluation and treatment of partial physeal arrest. *J Bone Joint Surg [Am]* **1987**;69-A:1297-1302
7. Carlson WO, Wenger DR. A mapping method to prepare for surgical excision of partial physeal arrest. *J Pediatr Orthop* **1984**;4:232-238
8. Murray K, Nixon GW. Ephiphyseal growth plate: evaluation with modified coronal CT. *Radiology* **1988**;166:263-265
9. Young JWR, Bright RW, Whitley NO. Computed tomography in the evaluation of partial growth plate arrest in children. *Skeletal Radiol* **1986**; 15:530-535
10. DeCampo JF, Boldt DW. Computed tomography of partial growth plate arrest: initial experience. *Skeletal Radiol* **1986**;15:526-529
11. Harcke HT, Zapf SE, Mandell GA, Sharkey CA, Cooley LA. Angular deformity of the lower extremity: evaluation with quantitative bone scintigraphy. *Radiology* **1987**;164:437-440
12. Jaramillo D, Shapiro F, Hoffer FA, et al. Post-traumatic growth-plate abnormalities: MR imaging of bony-bridge formation in rabbits. *Radiology* **1990**;175:767-773
13. Peterson HA. Partial growth arrest. In: Morrissy RT, ed. *Pediatric orthopedics*. Philadelphia: Lippincott, **1990**:1076-1077
14. Bright RW. Physeal injuries. In: Rockwood CA Jr, Wilkins KE, King RE, eds. *Fractures in children*. Philadelphia: Lippincott, **1984**:87-172
15. Johnston RM, James WW. Fractures through human growth plates. *Orthop Trans* **1980**;4:295
16. Riseborough EJ, Barrett IR, Shapiro F. Growth disturbances following distal femoral physeal fracture-separations. *J Bone Joint Surg [Am]* **1983**;65-A:885-89
17. Hynes D, O'Brien T. Growth disturbance lines after injury of the distal tibial physis. *J Bone Joint Surg [Br]* **1988**;70-B:231-233
18. O'Brien T, Millis MB, Griffin PP. The early identification and classification of growth disturbances of the proximal end of the femur. *J Bone Joint Surg [Am]* **1986**;68-A:970-980
19. Siffert RS, Katz JF. Growth recovery zones. *J Pediatr Orthop* **1983**;3: 196-201
20. Ogden JA. Growth slowdown and arrest lines. *J Pediatr Orthop* **1984**;4:409-415
21. Trueta J. *Studies of the development and decay of the human frame*. Philadelphia: Saunders, **1968**:90-118
22. Brand RA, Rubin CT. Fracture healing. In: Albright JA, Brand RA, eds. *The scientific basis of orthopedics*. Norwalk, CT: Appleton & Lange, **1987**: 327-329

Videotape Review

RSNA Today, Vol. 4. No. 1. Oak Brook, IL: The Radiological Society of North America, 1990. $55; by subscription, 6 issue annually at $185 for RSNA members and $225 for nonmembers (VHS videotape)

This videotape consists of five segments. It begins with a fascinating short segment by Robert S. Campbell, 1989 president of the Radiological Society of North America (RSNA), highlighting his presidential address, which traced the history and evolution of the RSNA, as well as the specialty of radiology, during the past 75 years. Dr. Campbell traces the RSNA from its beginning as the Western Roentgen Society in 1915, organized by four midwestern radiologists, to its current position as the largest radiologic society in the world, with more than 24,000 members.

The second segment, "Imaging Insights in Gastrointestinal Radiology," is designed to provide the radiologist with practical information on problems commonly encountered in everyday practice. This segment, by Alec J. Megibow, reviews the significance of the "target sign" in CT of the gastrointestinal tract. Dr. Megibow describes the target sign as a low-density ring within a thickened loop of bowel that may be accompanied by enhancement of the mucosal surface. He provides several excellent examples and thoroughly discusses the significance and pathogenesis of this sign (including its histologic correlation) and the appropriate differential diagnosis.

The third segment is a review, by John V. Crues III, of MR imaging of bone injuries of the knee. Dr. Crues reviews his experience with 434 MR examinations of the knee and describes three types of knee injuries that are undetectable on plain radiographs. These injuries are classified according to the pattern of signal loss in the epiphysis and metaphysis on T1-weighted or intermediate images and are designated as types 1 through 3. Correlation, where possible, with T2-weighted images, plain radiographs, and arthrograms suggests that type 1 and type 2 lesions are more acute in nature and represent injury to trabecular bone. Type 2 injury is associated with fracture of the cortical bone. Signal loss in a type 3 injury most likely is due to chronic, degenerative subchondral sclerosis. This information can be important in the clinical management of patients who have knee pain. The three different types of injuries are illustrated clearly with high-quality MR images.

Segment four, by David P. Naidich and Elias A. Zerhouni, is on high-resolution CT of the pulmonary parenchyma. This section begins with a discussion by Dr. Zerhouni of the appropriate technique for thin-section high-resolution CT, including a discussion of the basic signs of interstitial lung disease. Subsequently, Dr. Naidich discusses specific changes on high-resolution CT encountered in various interstitial diseases and develops criteria for the use of this technique. After their discussion, Drs. Zerhouni and Naidich are joined by Anthony V. Proto, a member of the RSNA editorial board, who asks several questions to put the topic of high-resolution in perspective.

The final segment is a special one by Elliot K. Fishman, Donna Magid, Derek R. Ney, and Janet E. Kuhlman on interactive two- and three-dimensional imaging of skeletal trauma. They use case presentations to illustrate the clinical application of these two types of imaging in complex skeletal trauma. Examples presented include an acetabular fracture, a proximal humeral fracture, and complex ankle fractures.

The tape is interesting and quite informative. In general, the image quality is good, the abnormalities are easily discernible, and arrows are used liberally to highlight the findings. The tape should be of great interest to the general radiologist.

Mark J. Kransdorf
Armed Forces Institute of Pathology
Washington, DC 20306-6000

Cloacal Exstrophy: Radiologic Findings in 13 Patients

Allen J. Meglin[1, 2]
Robert J. Balotin[1]
James S. Jelinek[1-3]
Elliot K. Fishman[4]
Robert D. Jeffs[5]
Victor Ghaed[1]

Cloacal exstrophy is a complex, multisystem malformation that has not received much attention in the radiologic literature. The clinical histories and imaging studies of 13 cases of cloacal exstrophy proved surgically or at autopsy were reviewed. Radiologic observations were based on skeletal plain films (13), contrast-enhanced examinations of the genitourinary system (12), abdominopelvic sonograms (nine), gastrointestinal studies (seven), CT scans of the pelvis and CNS (seven), MR images of the pelvis and CNS (six), renal nuclear medicine scans (three), myelography (three), and three-dimensional scans of the pelvis (two). Genitourinary and gastrointestinal abnormalities identified in our 13 patients included bladder malformations (13), hindgut anomalies (13), undescended testes (five), malrotation (five), duplicated müllerian structures (four), and renal ectopia (four). Skeletal abnormalities included symphysis pubis diastasis (13), posterior element dysraphism (12), vertebral segmentation anomalies (12), clubfeet (six), and hip dislocations (five). CNS anomalies included meningocele (nine) and Chiari malformation (one).

Immediate surgical closure of the defect with maximal bowel preservation and diverting colostomy offers optimal chances for survival. Appropriate preoperative gastrointestinal and genitourinary evaluation is essential.

AJR **155:1267–1272, December 1990**

Depending on the timing of the intrauterine insult, premature perforation of the cloacal membrane results in a spectrum of disease that ranges from epispadias of the glans penis to cloacal exstrophy. Cloacal exstrophy is the most severe and, fortunately, the rarest form of defect. Of the vesical exstrophy complex, it is estimated that 30% are epispadias, 60% are classic bladder exstrophy, and less than 10% are cloacal exstrophies [1, 2]. Extrapolated from this, approximately 15 new cases of cloacal exstrophy occur each year [1].

The embryonic insult causing cloacal exstrophy occurs during organogenesis and consequently affects multiple organ systems. Multidisciplinary surgical intervention can now offer marked improvement in the life quality and life expectancy in this previously fatal malformation [1, 3, 4]. The radiologist must have a working knowledge of the anatomic derangements and organ systems involved to prenatally diagnose and preoperatively evaluate cloacal exstrophy [5, 6]. The purpose of this report is to provide a detailed anatomic and pathologic description of cloacal exstrophy. We present an imaging approach that we believe is helpful in the assessment of cloacal exstrophy.

Materials and Methods

Thirteen cases of cloacal exstrophy proved surgically or at autopsy were reviewed retrospectively. Twelve patients were referred to tertiary care centers for surgical evaluation. In one patient, who died shortly after birth, the exstrophy was diagnosed antenatally. Complete medical records from the time of transfer, including surgical and autopsy reports, were

Received April 2, 1990; accepted after revision July 2, 1990.

The opinions or assertions contained herein are the private views of the authors and are not to be construed as official or as reflecting the views of the Department of the Army, the Department of Defense, or the Uniformed Services University of Health Sciences.

[1] Department of Radiology, Walter Reed Army Medical Center, Washington, DC 20307-5001. Address reprint requests to A. J. Meglin.

[2] Department of Radiology, Uniformed Services University of Health Sciences, Bethesda, MD 20814.

[3] Department of Radiology, Washington Hospital Center, 110 Irving St., N.W., Washington, DC 20101.

[4] Department of Radiology, Johns Hopkins University, Baltimore, MD 21205.

[5] Department of Urology, Johns Hopkins University, Baltimore, MD 21205.

0361-803X/90/1556-1267

available in all 13 cases. The age at the time of referral, sex, radiologic evaluation, case histories, and clinical findings were recorded. Plain film evaluation included the extremities (seven), spine (seven), skull (four), and hand for bone age (three). Barium studies of the gastrointestinal system included upper gastrointestinal series (seven), barium enema (four), and fistulogram (four) or defecogram (four). Excretory urograms (12), voiding cystourethrograms (10), sonograms of the abdomen and pelvis (eight), and antenatal sonograms (one) were available for review. Myelograms (three) and CT myelograms (three), unenhanced spinal CT scans (three), and spine (three) and brain (two) MR images were reviewed. MR of the pelvis and abdomen (five) and three-dimensional CT of the pelvis (two) were available. Surgical or pathologic correlation was available in all cases.

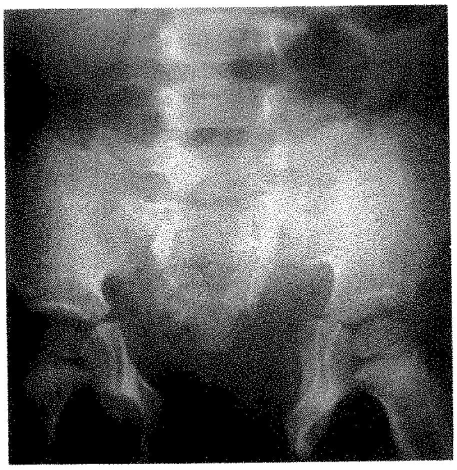

Fig. 1.—Frontal radiograph of pelvis shows wide pubic diastasis and widening of lumbosacral posterior elements. Ostomy is seen overlying left iliac wing.

Results

Skeletal System

The most common findings on radiographs were skeletal malformations. Symphysis pubis diastasis was present in all cases (13/13) and we considered it to be a prerequisite for the diagnosis of cloacal exstrophy (Fig. 1). The degree of underdevelopment of the pubic rami varied, but in most cases the diastasis was not accompanied by significant superior or inferior pubic rami dysplasia. The pubic rami were often so divergent that their anterior border was directed laterally rather than medially. Hip subluxations (5/9) or acetabular dysplasia (1/9) also were seen. Posterior element dysraphism (12/13) was present with hemivertebrae (six), vertebral fusions (five), or absence of vertebral bodies (five) (Fig. 2). Sacral dysplasia (12/13) occurred with combinations of posterior element dysraphism, widened neural foramina, axial torsion, and marked underdevelopment (Fig. 3. Scoliosis (6/9) occurred with one gibbous deformity. Rib series in five cases demonstrated three cases with 11 pairs of ribs and two with hypoplasia of the thoracic cage. Bone ages obtained at chronologic ages of 7, 11, and 16 months were below 2 SD in all three cases.

Limb anomalies (7/13) consisted of bilateral clubfeet (four), unilateral clubfoot (two), and a severely dysplastic lower extremity requiring amputation (one) (Fig. 4).

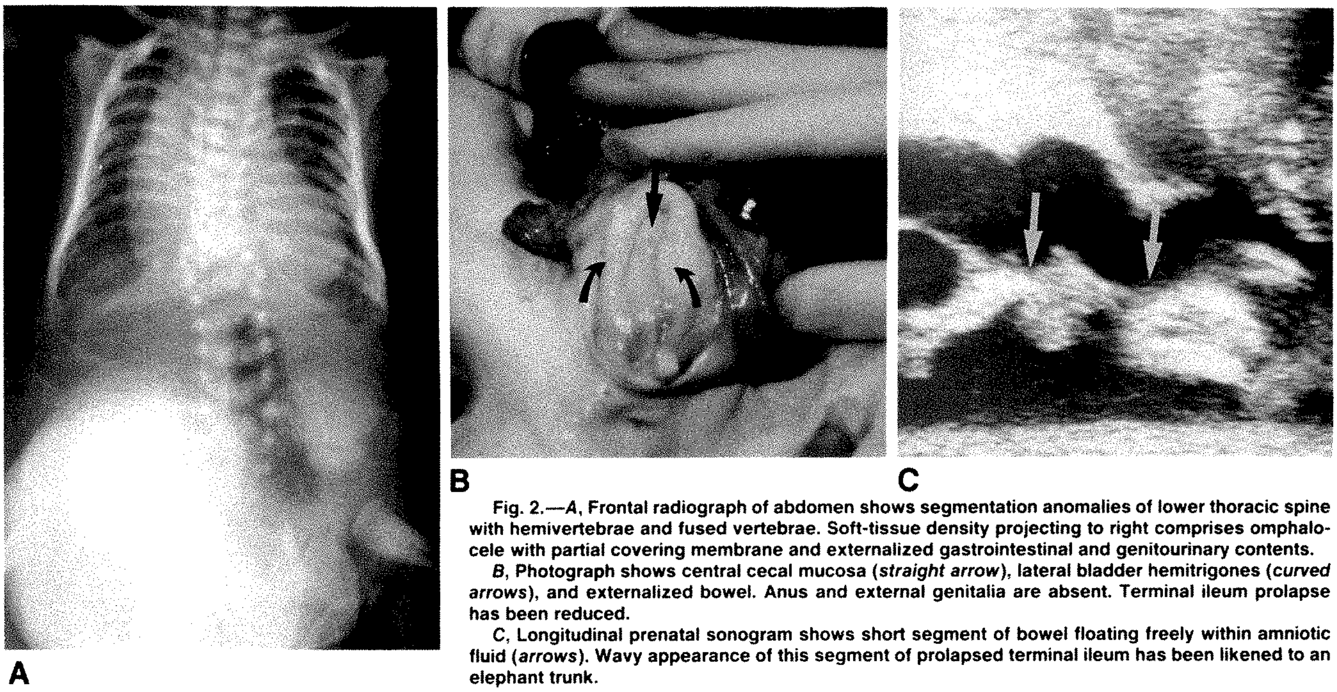

Fig. 2.—*A*, Frontal radiograph of abdomen shows segmentation anomalies of lower thoracic spine with hemivertebrae and fused vertebrae. Soft-tissue density projecting to right comprises omphalocele with partial covering membrane and externalized gastrointestinal and genitourinary contents.

***B*, Photograph shows central cecal mucosa (*straight arrow*), lateral bladder hemitrigones (*curved arrows*), and externalized bowel. Anus and external genitalia are absent. Terminal ileum prolapse has been reduced.**

***C*, Longitudinal prenatal sonogram shows short segment of bowel floating freely within amniotic fluid (*arrows*). Wavy appearance of this segment of prolapsed terminal ileum has been likened to an elephant trunk.**

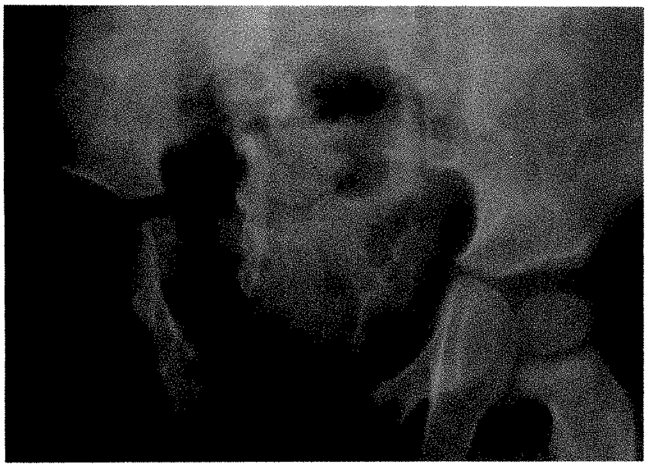

Fig. 3.—Frontal radiograph of pelvis shows incompletely formed sacral segments with distortion of neural foramina and pubic symphysis diastasis.

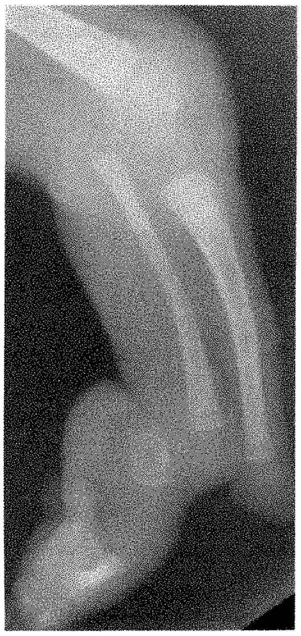

Fig. 4.—Frontal radiograph of severely dysplastic lower extremity. Orthopedic evaluation revealed this to be nonfunctional and amputation was performed. Gestational oligohydramnios was absent.

Genitourinary System

Classic cloacal exstrophy, in which the bladder is separated into two hemibladders by a portion of interposed bowel, occurred in 12 of 13 cases. One case had severe epispadias with partial bladder and bowel exstrophy. In all cases, the conglomerate mass of bowel and bladder was applied to the abdomen as a plaque with an otherwise absent or hypoplastic superior anterior abdominal wall (Figs. 2 and 5). The bowel represented at the plaque is the ileocecum with varying numbers of orifices. Abnormalities of the appendix included absence (one), enlargement (one), and duplication (one).

Renal anomalies were common and included bilateral renal ectopia (4/13), bilateral pelvic kidneys (1/13) (Fig. 6), unilateral renal ectopia (3/13), left-sided renal agenesis (3/13), right-sided renal atrophy (1/13), and complete bifid collecting systems (2/13). Eight of 13 had upper tract anomalies.

Genital anomalies occurred frequently in both the genotypic females (5/13) and genotypic males (8/13). All the males required conversion to female with orchiectomy (7/8) at the time of surgery for adequate social-sexual function. In males, cryptorchidism (5/7) and, in females, duplication of internal genitalia (4/5) with duplicated or bicornuate uterus (4/5), double cervix (1/5), duplicated vagina (2/5), and hypoplastic fallopian tube (1/5) were noted (Fig. 7).

CNS

Detailed radiologic examination of the brain and spinal cord was not available in all cases. Spinal dysraphism (12/13) was associated with lumbar lipomyelomeningocele (7/12), cord lipoma (1/12), simple meningocele (1/12), and myelomeningocele (1/12) (Fig. 8). Two cases, including the nonclassic cloacal exstrophy, had neither spinal cord nor meningeal abnormality. No cases of anterior sacral meningocele, cord tethering syndrome, dorsal dermal sinus, caudal regression, or presacral teratoma were identified.

Gastrointestinal System

There were 12 classic cloacal exstrophies and one combined gastrointestinal and genitourinary variant. The classic cloacal exstrophy cases had bladder bisection by the ileocecal portion of the bowel (Figs. 2B and 5A). The free-floating terminal ileum was either separate or had prolapsed through the ileocecal valve. When free, it hung down in front of the abdomen giving an elephant trunk appearance.

Other gut anomalies included blind-ending colon with imperforate anus (10/12), malrotation or nonrotation (5/10), large-bowel duplication (1/13), appendiceal duplication (1/7), and anatomically short small bowel (1/13). Both anus and rectum (1/13) were noted in the variant (nonclassic) cloacal exstrophy. The superior half of the anterior abdominal wall was markedly hypoplastic (13/13), with an omphalocele (10/10) (Fig. 3C). No cases had complete absence of the abdominal wall.

The pelvic floor was evaluated by MR (five) and three-dimensional CT (two) and demonstrated hypoplasia of the levator musculature (5/5). Total absence of the pelvic floor was not identified. Landmarks such as fat in the ischiorectal fossa (5/5) and muscular slips between the perineum and pelvic contents (5/5) could be identified easily (Fig. 6B).

Discussion

Advances in neonatology, surgical technique, and supportive care have improved the prognosis for patients with cloacal exstrophy. As recently as 1960, there were no reports of survival past early infancy [1]. Since then, particularly in the last decade, several centers have reported a 90% survival rate past infancy [4]. Care now includes early and aggressive multidisciplinary surgical intervention [3, 7]. Consequently,

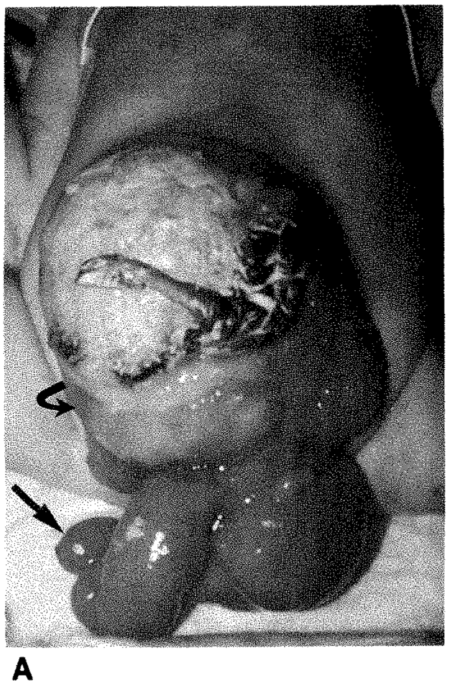

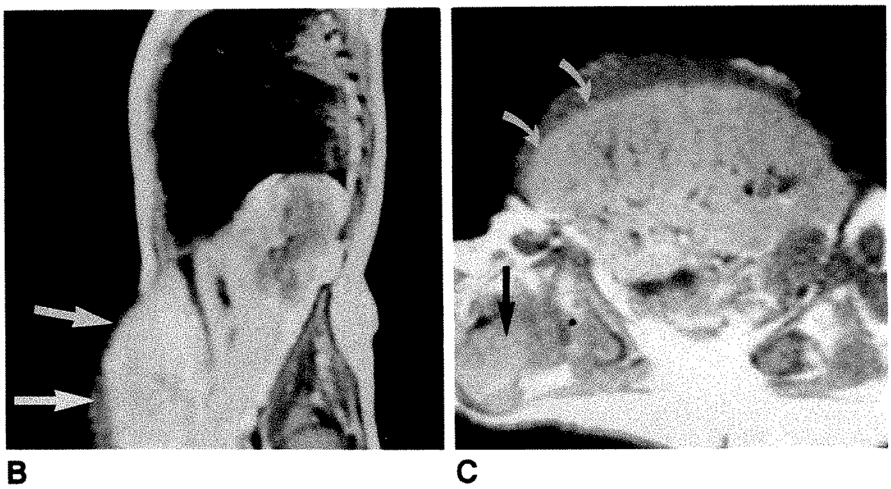

Fig. 5.—*A*, Photograph shows prolapsed terminal ileum (elephant trunk deformity) (*straight arrow*), omphalocele, and everted bladder mucosa (*curved arrow*). (Patient's chest is at top of picture, pelvis at bottom.)

B, Sagittal T1-weighted MR image shows markedly hypoplastic superior abdominal wall with liver protruding out of abdominal cavity (omphalocele) (*arrows*).

C, Axial T1-weighted MR image at level of dislocated right femoral head (*black arrow*) shows hypoplastic anterior abdominal wall. Liver (*white arrows*) is covered by thin membrane.

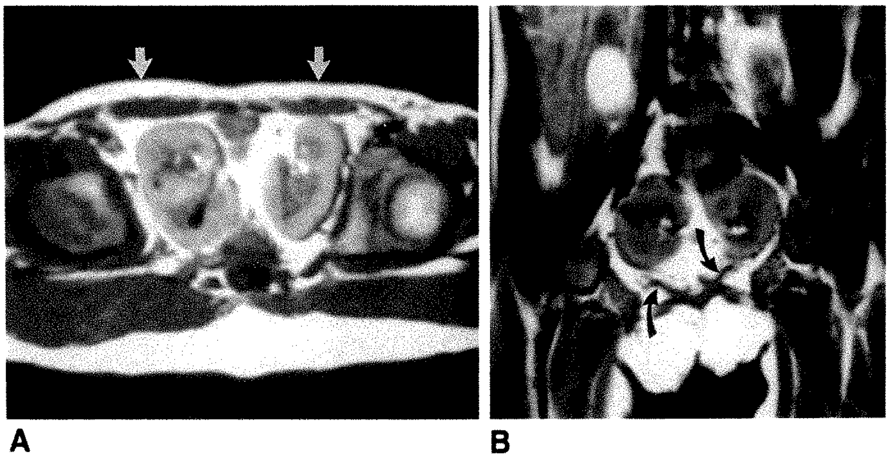

Fig. 6.—*A*, Axial T1-weighted MR image at level of acetabulum. Bilateral pelvic kidneys and hypoplastic but intact lower anterior abdominal wall (*arrows*).

B, Coronal T1-weighted MR image shows muscular slips between ischiorectal fossa fat and pelvic contents (*arrows*). Pelvic floor is abnormally elevated owing to bladder and rectosigmoid absence. Note bilateral pelvic kidneys.

the radiologist must be familiar with the multisystem effects of this disorder.

The anatomic derangements of cloacal exstrophy chiefly involve the gastrointestinal, genitourinary, nervous, and skeletal systems. A satisfactory embryologic explanation for the constellation of findings has not yet emerged [1–4, 8, 9]. Recent attempts to classify cloacal exstrophy have divided it into classic and nonclassic forms [4]. In both forms, there is incomplete formation of the inferior anterior abdominal wall with externalization of gastrointestinal and genitourinary contents. The bowel portion of the central mass is made up of externalized cecum, terminal ileum, and proximal colon. The colon usually ends blindly without communication to the anus. The proximal portion of the colon is usually present at the central gastrointestinal mucosal strip as an inferior orifice. The bladder is everted and represented by two separate hemibladders that are divided by the central gastrointestinal mass. In contrast, simple bladder exstrophy has a single everted bladder, which is not in communication with the gut. In all cases of cloacal exstrophy, the pubic rami are widely separated [1–4]. This serves as a differential feature, as epispadias and simple bladder exstrophy patients usually are not as severely diastatic as cloacal exstrophy patients.

In addition to the externalized gastrointestinal and genitourinary abnormalities that define cloacal exstrophy, we found a high prevalence of internal distortion of the gastrointestinal and genitourinary systems [1–4, 8, 9]. As reported in other series, malrotation (30%) and hindgut duplication (8%) were common in our series [1–4].

We also found that, owing to the hindgut malformation, the pelvic floor musculature was hypoplastic in all cases. Though this is well reported in the surgical literature, it has been

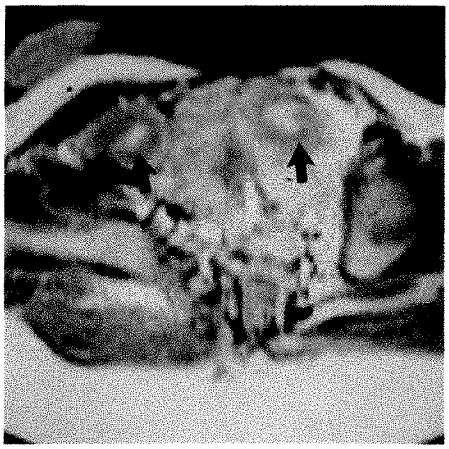
7

Fig. 7.—Axial proton-weighted MR image at level of acetabulum shows duplicated uterus (*arrows*). Maternal hormones have stimulated endometrium, which resulted in high signal intensity.

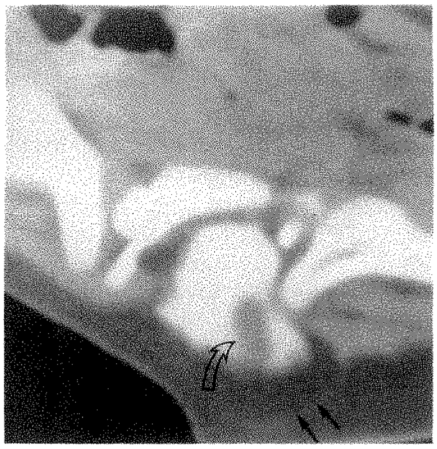
8

Fig. 8.—Axial CT scan after intrathecal injection of metrizamide shows dysraphism of posterior element of lumbosacral spine, posterior rotation of iliac wings, and lipomyelomeningocele. Spinal cord (*open arrow*); cord lipoma (*solid arrows*).

assessed only recently in the radiologic literature [10]. In our series, the hypoplastic pelvic musculature was well demonstrated by both MR and three-dimensional CT. This is particularly important in planning continence-maintaining procedures. In epispadias the pelvic floor develops normally as both the anus and rectum are normal.

In our series, as well as in others, the most common internal genitourinary abnormalities were renal ectopia (25%), agenesis (25%), and duplicated collecting systems (10%) [1, 2, 7, 11]. Similarly, five of seven males were found to have cryptorchidism [1–4]. Although this was not assessed radiologically in our series, testicular location can be ascertained by sonography, CT, and MR. This is particularly useful in cases of equivocal sex identification. Eighty percent (4/5) of genotypic females had duplication of müllerian structures [12]. This is not surprising, as cloacal exstrophy results from a midline embryologic malformation. Duplication of the uterus was seen particularly well on MR imaging and sonography.

It is important to assess orthopedic anomalies early in life. In the first 48 hr of life, the flexibility of pelvic bone is maximal owing to the effects of maternal hormones still circulating within the neonate. Exstrophy and omphalocele repair can be accomplished with accommodation of the neobladder and other structures within the pelvis [1–4]. Iliac osteotomy with closure of the pubic diastasis may have greater success if performed during the early neonatal period [1–4]. It has been our experience that the orthopedic surgeons benefit from animated video-loop three-dimensional CT display of the pelvis when planning the size, location, and angulation of the pelvic osteotomy (Fig. 9) [13–15].

We found a higher prevalence of CNS abnormalities in our series than has been previously reported [1–4, 7]. Only one case of intracranial disease, a Chiari I malformation, was identified. Patients with cloacal exstrophy generally have normal or nearly normal intelligence. Many of their deficits can be attributed to the psychosocial consequences of being incontinent, infertile, and nonambulatory. The oldest patient in our series is a successful college student at the time of this writing. Many of the lifestyle alterations result from the lower spinal anomalies including lipomyelomeningocele, spinal cord lipoma, meningocele, hydrosyringomyelia, and myelomeningocele [7].

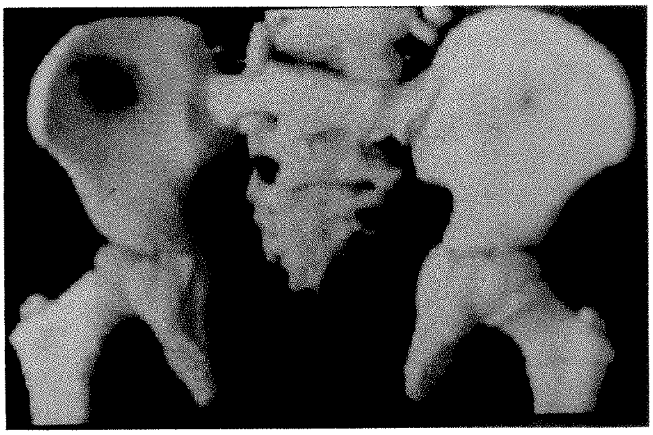
Fig. 9.—Three-dimensional CT scan of bony pelvis shows marked pubic diastasis, dysraphism of posterior element of sacrum, and bilateral normal hip location. This image can be rotated about a cephalocaudad, anteroposterior, or axial axis in an animated video loop for preoperative assessment.

The prenatal diagnosis of cloacal exstrophy has not been previously reported in the radiologic literature. The constellation of pubic diastasis, everted bladder and bowel, and lumbosacral anomalies should help differentiate cloacal exstrophy from classic bladder exstrophy, omphalocele, gastroschisis, body stalk anomalies, caudal regression syndrome, myelomeningocele, and possibly presacral teratoma [5, 6]. Visualization of the elephant trunk deformity or prolapsed terminal ileum on prenatal sonograms can help in the differentiation of bladder exstrophy from cloacal exstrophy (Fig. 2C). Everted hemibladders are visualized occasionally. It should be noted that there is generally no urinary obstruction, and, in the absence of renal agenesis, we cannot suggest a reason for oligohydramnios.

Cloacal exstrophy is a nonlethal, sporadic, nonhereditary malformation. The greatest risk to the infant occurs in the immediate neonatal period owing to dehydration and inability to maintain adequate nutrition. Immediate intervention with aggressive surgical management of the omphalocele, bladder, small bowel, and pubic diastasis enhances the chances for survival. Problems resulting from upper gastrointestinal, genital, and neurologic malformations can be addressed later in infancy. The life-threatening anomalies need immediate radiologic assessment, while those that affect quality of life can be delayed until after the immediate postoperative period.

In summary, we have discussed the multiple malformations that constitute cloacal exstrophy. Prenatal sonographic findings include pubic diastasis and an elephant trunk deformity. Postpartum plain films to image the spine and pelvis along with the clinical examination should be diagnostic of cloacal exstrophy. Immediate colostomy and closure of the defect can then be performed. Evaluation of renal anatomy and function and the three-dimensional relationships of the pelvis may help in planning this first-stage procedure. Subsequent radiologic assessment, in preparation for further reconstructive surgery, can be performed later in infancy or childhood. We think evaluation of the extremities for orthopedic anomalies; small bowel for malrotation; and pelvis for urologic, genital, neurologic, bony, and muscular wall anomalies is necessary.

ACKNOWLEDGMENT

We thank Mary S. Mood for clerical support.

REFERENCES

1. Ziegler MM, Duckett JW, Howell CG, et al. Cloacal exstrophy. In: Welch KJ, Randolph JG, Ravitch MM, O'Neill JA, Rowe MI, eds. *Pediatric surgery*, vol. 2, 4th ed. Chicago: Year Book Medical, **1986**:764–771
2. Fujiyoshi Y, Nakamura Y, Cho T, et al. Exstrophy of the cloacal membrane. *Arch Pathol Lab Med* **1987**;111:157–160
3. Jeffs RD. Exstrophy and cloacal exstrophy. *Urol Clin North Am* **1978**;5:127–140
4. Hurwitz RS, Manzoni GAM, Ransley PG, Stephens FD. Cloacal exstrophy: Report of 34 cases. *J Urol* **1987**;138:1060–1064
5. Patten RM, Van Allen M, Mack LA, et al. Limb-body wall complex: in utero sonographic diagnosis of a complicated fetal malformation. *AJR* **1986**;146:1019–1024
6. Sanders RC, Blakemore K. Lethal fetal anomalies: sonographic demonstration. *Radiology* **1989**;172:1–6
7. Karrer FM, Flannery AM, Nelson MD, et al. Anorectal malformations: evaluation of associated spinal dystrophic syndromes. *J Pediatr Surg* **1988**;23:45–48
8. Mildenberger H, Kluth D, Dziuba M. Embryology of bladder exstrophy. *J Pediatr Surg* **1988**;23:166–170
9. Van der Putte SCJ. Normal and abnormal development of the anorectum. *J Pediatr Surg* **1986**;21:434–440
10. Sato Y, Pringle KC, Bergman RA, et al. Congenital anorectal anomalies: MR imaging. *Radiology* **1988**;168:157–162
11. Herman TE, Cleveland RH, Kushner DC. Pelvic kidney in cloacal exstrophy. *Pediatr Radiol* **1986**;16:306–308
12. Gilsanz V, Cleveland RH, Reid BS. Duplication of the mullerian ducts and genitourinary malformations. *Radiology* **1982**;144:797–801
13. Robertson DD, Fishman EK, Walker PS, Magid D, Granholm JW, Weiss PJ. Advanced CT imaging methods: application to orthopedic surgery of the hip. *Electromedica* **1988**;56:24–29
14. Magid D, Fishman EK, Brooker AF, Mendelbaum BR, Siegelman SS. Multiplanar computed tomography of acetabular fractures. *J Comput Assist Tomogr* **1986**;10:778–783
15. Fishman EK, Magid D, Ney DR, Drebin RA, Kuhlman JE. Three-dimensional imaging and display of musculoskeletal anatomy. *J Comput Assist Tomogr* **1988**;12:465–467

Choledochal Cyst and Biliary Atresia in the Neonate: Imaging Findings in Five Cases

Jean M. Torrisi[1]
Jack O. Haller[1]
Francesca T. Velcek[2]

The radiologic findings in five neonates with choledochal cyst associated with extrahepatic biliary atresia are described. All five patients (age range, 13–72 days) presented with jaundice and acholic stools. In all four patients who underwent sonographic examination, a cystic structure separate from the gallbladder representing the choledochal cyst was shown. The diagnosis of atresia of the distal common bile duct was made preoperatively in all cases by hepatobiliary scintigraphy. Diagnosis was confirmed by surgical findings and was demonstrated by intraoperative cholangiography in four cases. All patients were successfully treated with surgical intervention within 1 month from the time of diagnosis. Early detection of this rare disorder, which may be distinct from choledochal cyst found in children and adults, is important to prevent fatal complications of biliary obstruction.

The combined use of sonography and hepatobiliary scintigraphy can correctly identify this subset of patients with persistent neonatal jaundice and provide valuable information for prompt surgical management.

***AJR* 155:1273–1276, December 1990**

Choledochal cyst is an infrequent cause of neonatal jaundice—it usually occurs in the older child or adult [1]. The choledochal cyst of the neonate may be a separate entity from the choledochal cyst that presents in childhood and adolescence, as they have different clinical and radiologic presentations and may have separate etiologies [2–4]. Choledochal cyst in the neonate may be associated with atresia of the distal common bile duct; when distal biliary atresia is present, the patient typically presents with obstructive jaundice and acholic stools. The older patient with a nonobstructive choledochal cyst presents later in life with any combination of intermittent jaundice, abdominal pain, and a palpable abdominal mass. The combined use of sonography, which can identify the choledochal cyst, and hepatobiliary scintigraphy, which can determine distal obstruction in the neonate and communication of the cystic structure with the biliary tree in the older child, can be successful in the diagnosis of choledochal cyst in both groups [5]. The pathogenesis of the choledochal cyst in these two groups differs in that the choledochal cyst in the neonate is congenital, whereas the choledochal cyst in the older child may be acquired in association with an anomalous pancreaticobiliary union [3, 4]. Distal atresia has been described only with choledochal cysts in the neonate and may represent a separate entity, as other authors have suggested [1–4].

We describe the sonographic and scintigraphic findings in five neonates with choledochal cyst and distal biliary atresia and discuss the anatomy, pathogenesis, clinical and radiologic findings, and surgical corrective procedures for this entity.

Materials and Methods

We retrospectively reviewed the imaging studies and medical records of five consecutive patients in whom choledochal cyst associated with atresia of the distal common bile duct

---

Received April 4, 1990; accepted after revision July 2, 1990.

Presented at the 34th annual meeting of the American Institution of Ultrasound in Medicine, New Orleans, LA, March 1990.

[1] Department of Radiology, SUNY Health Science Center at Brooklyn, 450 Clarkson Ave., Brooklyn, NY 11203. Address reprint requests to J. O. Haller.

[2] Department of Pediatric Surgery, SUNY Health Science Center at Brooklyn, 450 Clarkson Ave., Brooklyn, NY 11203.

0361-803X/90/1556-1273

© American Roentgen Ray Society

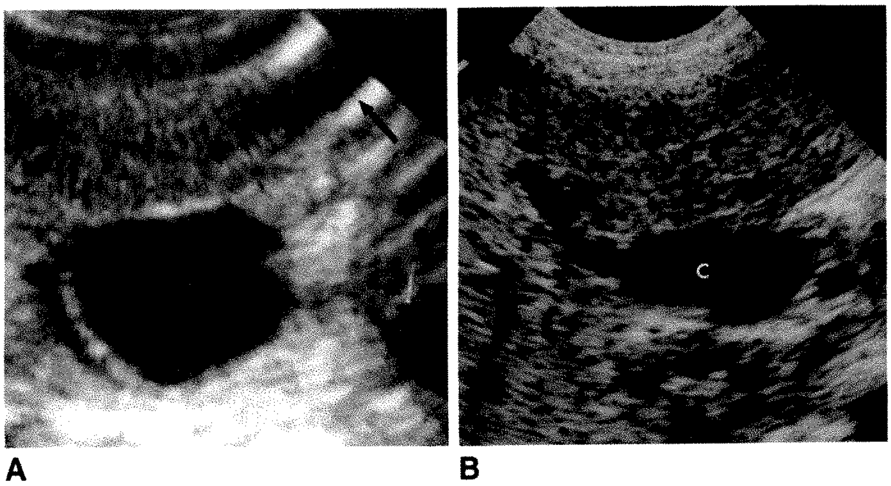

Fig. 1.—*A*, Longitudinal sonogram of right upper quadrant shows typical findings of surgically proven choledochal cyst, with large cystic structure in region of porta hepatis. Separate cystic structure (*arrow*) farther anterior represents gallbladder.

B, Longitudinal sonogram of right upper quadrant shows a choledochal cyst (c) with a dilated duct leading to it. At surgery, a choledochal cyst was found with a stricture just proximal to cyst and a dilated hepatic duct proximal to stricture.

was diagnosed at our Medical Center in the past 13 years. The age at presentation ranged from 13 to 72 days. Four of five patients underwent sonographic examination performed with conventional real-time sector scanners, and five of five had scintigraphy with early and delayed images performed with either rose bengal (two) or an iminodiacetic acid derivative (three). Intraoperative cholangiograms were obtained in four patients. The diagnosis of choledochal cyst with biliary atresia was confirmed by intraoperative observation and pathologic specimens in all cases.

Results

The age of the patients at the time of presentation ranged from 13 to 72 days. Most of the patients presented within the first 2 months of life; the delay in diagnosis of the oldest patient was due to an incorrect diagnosis of physiologic jaundice. The preponderance of females over males in our series (4:1) reflects the sex distribution reported elsewhere [2, 3].

The most common clinical findings in our patients were jaundice (five patients), acholic stools (five patients), and hepatosplenomegaly (four patients). Abdominal distension or hepatosplenomegaly was clinically suspected in all cases; however, there was no comment on liver size in either the sonographic reports or the intraoperative notes to confirm this clinical observation.

Liver echogenicity was normal in all four patients who underwent sonographic examination. All four sonograms showed a cystic structure in the region of the porta hepatis separate from the gallbladder (Fig. 1A). None of the sonographic examinations showed intrahepatic biliary dilatation. One case reported a dilated hepatic duct, a dilated cystic duct, and an elongated gallbladder (Fig. 1B). At surgery, a stricture of the hepatic duct proximal to the choledochal cyst with dilatation proximal to the stricture was found. An elongated yet hypoplastic gallbladder also was noted. The gallbladder was identified in all other sonographic examinations and was noted to be small in one case.

Scintigrams showed normal hepatic extraction of tracer from the blood pool in four patients and delayed uptake in one patient. Delayed uptake was observed in the oldest patient, who had gone longest without surgical management. None of the five patients' scintigrams showed excretion of hepatobiliary radionuclide into the gastrointestinal tract (Fig. 2). (Quantitative measurements were not taken at the duodenum.) The choledochal cyst was not visualized on scintigrams in any case.

Choledochal cyst with atresia of the distal common bile duct was confirmed by intraoperative observation and pathologic specimens in all cases. Intraoperative cholangiograms were obtained in four cases and showed drainage of contrast material from the gallbladder into a cystic common bile duct with no communication to the duodenum (Fig. 3). In all cases, an abnormality of the gallbladder was observed at surgery, which showed an atretic gallbladder (three patients), hypoplastic gallbladder (one patient), and an intrahepatic gallbladder (one patient), although these abnormalities were not always appreciated on sonography.

In all cases, the choledochal cyst was surgically repaired and the extrahepatic biliary tree was reconstructed to establish drainage. Three patients underwent cyst excision with Roux-en-Y hepatojejunostomy, portoenterostomy, or choledochojejunostomy. Two patients underwent choledochoduodenostomy. All five patients are doing well postoperatively up to 14 years later; none required revision of their primary surgical repair.

Discussion

In 1959 Alonso-Lej and coworkers [6] collected all known cases of choledochal cyst and devised a classification scheme of three major types: cystic, diverticular, and choledochocele. Type I choledochal cyst is a concentric dilatation of the common bile duct. This can be associated with proximal and/or distal atresia and obstruction. Type II choledochal cyst is

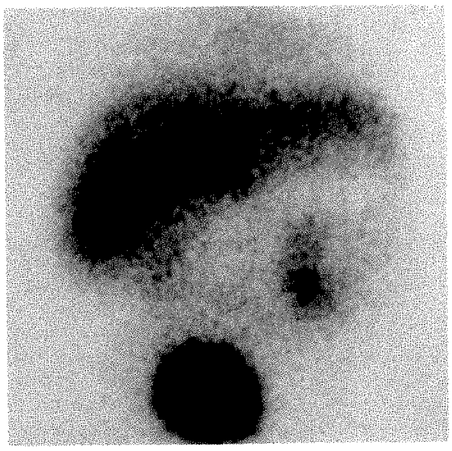

2

Fig. 2.—A 24-hr hepatobiliary scintigram shows no activity in gastrointestinal tract consistent with noncommunication of biliary tree. Choledochal cyst is not seen. Excretion in kidney and bladder is seen.

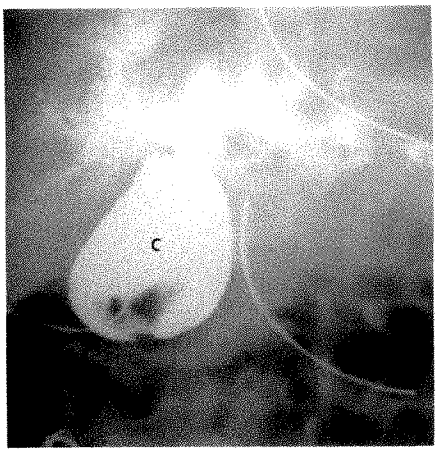

3

Fig. 3.—Operative cholangiogram shows contrast material injected into gallbladder has flowed into choledochal cyst (c) with reflux up hepatic duct and filling of intrahepatic bile ducts. There is no flow to duodenum.

a diverticular outpouching of the common bile duct. Type III, a choledochocele, is the rarest and is believed by some authors to have a different etiology [7]. Revisions of the original Alonso-Lej classification include two other morphologic types; a Type IV with multiple cysts of the intrahepatic and extrahepatic ducts and a Type V with isolated intrahepatic dilatation [2]. Type V is also known as Caroli disease.

The etiology of the choledochal cyst is not known. Theories concerning its pathogenesis proposed an inequality of epithelial proliferation in the developing choledochus, intrauterine rupture of the bile duct, vascular accidents, and weakness of the common duct wall [6–8]. As reviewed elsewhere, Alonso-Lej believed that a choledochal cyst was a congenital abnormality in which an inherent weakness in the common bile duct in its developmental stages allows dilatation in response to increased intraductal pressure due to obstruction of the distal common duct [8].

In 1974, Landing [9] hypothesized that neonatal hepatitis, biliary atresia, and choledochal cyst represented a spectrum of manifestations of what he called "infantile obstructive cholangiopathy." He thought that a perinatal infectious cholangitis (most likely of viral origin), which progressed to a fibrotic scarring of the biliary tract, caused the panductular sclerosis of biliary atresia and the extrahepatic distal obstruction responsible for the formation of the choledochal cyst. This was a possible explanation for common bile duct obstruction in the perinatal period.

Babbitt and coworkers [4] suggest a choledochal cyst is acquired as a result of an anomalous pancreaticobiliary union. In this anomalous union, the distal common bile duct inserts more proximally than usual into the pancreatic duct of Wirsung, resulting in loss of normal ampullary sphincter function. Chronic reflux of pancreatic fluid into the common bile duct may cause inflammation and weakening of the common bile duct wall with subsequent dilatation. Larger studies have since documented this anomalous union in patients with choledochal cysts [10, 11]. The subjects in these studies are primarily children and young adolescents, not neonates.

The presenting symptoms and diagnostic findings of our five patients are typical of those reported by other authors [2, 3] for choledochal cyst with distal biliary atresia in the neonate. Neonates with choledochal cyst present with jaundice and acholic stools characteristic of biliary obstruction. The clinical presentation is indistinguishable from neonatal hepatitis and biliary atresia, and differentiation from these more common entities requires radiologic evaluation. Older children with choledochal cyst, not associated with distal atresia, have any combination of the classic triad of jaundice, intermittent abdominal pain, and a palpable abdominal mass. Reports of the percentage of children who actually present with this triad range from 21% to 60–70%; this variability is in part due to the failure of some authors to exclude neonates from their populations [12]. This triad is not typical for neonates, and trying to identify these signs in a neonate may delay diagnosis.

The combination of hepatobiliary scintigraphy and sonography is diagnostic for choledochal cysts associated with atresia of the distal common bile duct [1, 5]. Sonography will show a cystic structure in the porta hepatis, separate from the gallbladder, representing the choledochal cyst. Nonvisualization of radionuclide activity in the bowel during hepatobiliary scintigraphy signifies noncommunication of the biliary system with the intestinal tract, consistent with distal biliary atresia. Nonvisualization of radioactivity in the bowel without the sonographic findings of a cystic structure is diagnostic of biliary atresia.

In the older patient, the combination of hepatobiliary scintigraphy and sonography is also diagnostic for choledochal cysts [1, 5]. Sonography shows a cystic structure in the porta hepatis, and scintigraphy classically shows a photopenic defect over the porta hepatis on early images, with delayed accumulation of tracer in the photopenic area indicating communication with the biliary system.

Association with intrahepatic atresia has been reported, and intraoperative cholangiography (Fig. 3) is routinely performed to exclude patients with intrahepatic biliary atresia, as these patients are more aptly treated with a Kasai procedure [2].

The treatment of choledochal cyst with distal atresia is surgical. Delayed surgery may result in cirrhosis with portal hypertension, cholangitis, and pancreatitis [1, 5, 12].

REFERENCES

1. Kirks DR, Coleman RE, Filston HC, Rosenberg ER, Merten DF. An imaging approach to persistent neonatal jaundice. *AJR* **1984**;142:461–465
2. O'Neill JA Jr, Templeton JM Jr, Schnaufer L, Bishop HC, Ziegler MM, Ross AJ III. Recent experience with choledochal cyst. *Ann Surg* **1987**;205:533–540
3. Barlow B, Tabor E, Blanc WA, Santulli TV, Harris RC. Choledochal cyst: a review of 19 cases. *J Pediatr* **1976**;89:934–940
4. Babbitt DP, Starshak RJ, Clemet AR. Choledochal cyst: a concept of etiology. *AJR* **1973**;119:57–63
5. Papanicolaou N, Abramson SJ, Teele RL, Treves S. Specific preoperative diagnosis of choledochal cysts by combined sonography and hepatobiliary scintigraphy. *Ann Radiol* **1985**;28:276–282
6. Alonzo-Lej F, Rever WB Jr, Pessagno DJ. Collective review: congenital choledochal cyst, with a report of 2, and an analysis of 94 cases. *Int Abst Surg* **1959**;108:1–30
7. Klotz D, Cohn BD, Kottmeier PK. Choledochal cysts: diagnostic and therapeutic problems. *J Pediatr Surg* **1973**;8:271–283
8. Howell CG, Templeton JM, Weiner S, Glassman M, Betts JM, Witzleben CL. Antenatal diagnosis and early surgery for choledochal cyst. *J Pediatr Surg* **1983**;18:387–393
9. Landing BH. Considerations of the pathogenesis of neonatal hepatitis, biliary atresia and choledochal cyst: the concept of infantile obstructive cholangiopathy. *Prog Pediatr Surg* **1974**;5:113–139
10. Kimura K, Ohto M, Ono T, et al. Congenital cystic dilatation of the common bile duct: relationship to anomalous pancreaticobiliary ductal union. *AJR* **1977**;128:571–577
11. Jona JZ, Babbitt DP, Starshak RJ, LaPorta AJ, Glicklich M, Cohen RD. Anatomic observations and etiologic and surgical considerations in choledochal cyst. *J Pediatr Surg* **1979**;14:315–320
12. Fonkalsrud EW, Boles ET Jr. Choledochal cysts in infancy and childhood. *Surg Gynecol Obstet* **1965**;121:733–742

Come to the
American Roentgen
Ray Society
91st
ANNUAL MEETING

Boston, MA

Sheraton Boston Hotel
May 5-10, 1991

Scientific Program (200 papers)
Instructional Courses (60 hours)
Categorical Course on
Body MR Imaging
The Caldwell Lecture
Award Papers
Scientific Exhibits
Social, Golf, and Tennis Programs
Guest Programs

Localization and Guided Removal of Soft-Tissue Foreign Bodies with Sonography

William E. Shiels II[1-3]
Diane S. Babcock[1]
James L. Wilson[2]
Reed A. Burch[2]

Sonography was used to detect, localize, and guide removal of foreign bodies in the soft tissues of the extremities and neck. Twenty localization procedures were performed in 19 patients (12 children and seven adults) with 21 foreign bodies including wood, glass, stone, metal, and lead pencil. Localization was accomplished by using anatomic landmarks, ink marks on the skin, and needle and hemostat markers. Localization was facilitated by the use of small standoff pads that were cut for use on small surfaces. The foreign bodies were visualized as hyperechoic foci with acoustic shadows that were partial or complete depending on the angle of insonation and foreign body composition. Hyperechoic comet-tail artifacts (reverberation artifacts) were seen with six metallic foreign bodies and one glass fragment. Nine foreign bodies were surrounded by hypoechoic halos caused by edema, abscess, or granulation tissue. A slow meticulous scanning technique and high-frequency transducer helped in detection of small foreign bodies. Sonographically guided removal of the foreign body was successful in all four patients in whom it was attempted. Scanning with the ultrasound beam parallel to the long axis of the hemostat and the foreign body was the fastest way to guide the hemostat to the tip of a foreign body. The procedure was accomplished most easily and quickly when one physician performed sonography and hemostat removal of the foreign body simultaneously.

Our experience with these cases indicates that sonography is a useful tool in the localization and removal of soft-tissue foreign bodies.

AJR **155:1277–1281, December 1990**

Soft-tissue foreign bodies are a common clinical problem in both children and adults. Traditionally, radiographs have been used to identify radiopaque foreign bodies and fluoroscopy has been used for guidance during surgical removal. Recent reports have demonstrated the usefulness of sonography in the detection, preoperative localization, and confirmation of surgical retrieval of foreign bodies in the distal extremities [1–4].

We report a series of patients in whom sonography was successfully used for detection, localization, and removal of soft-tissue foreign bodies in the extremities and the neck.

Materials and Methods

Twenty-six patients were referred for sonography because of possible retention of foreign bodies in soft-tissue between March 1986 and May 1990. The patients were referred by surgeons either before, during, or after exploration for possible soft-tissue foreign bodies. The 19 males and seven females were 1–37 years old (mean, 13 years). Nineteen of the patients were between 1 and 17 years old, and seven were between 22 and 37 years old.

In 24 patients, plain radiographs were obtained before sonography. In two patients, one with a known wooden splinter in the thigh and one with a lead pencil fragment in the hand, no radiographs were obtained. Surgical removal had been attempted unsuccessfully in five patients.

Received February 27, 1990; accepted after revision June 29, 1990.

The opinions or assertions contained herein are the private views of the authors and are not to be construed as official or as reflecting the views of the Department of the Army or the Department of Defense.

Presented at the annual meeting of the Society for Pediatric Radiology, San Antonio, TX, April 1989.

[1] Department of Radiology, Children's Hospital Medical Center, and the Departments of Radiology and Pediatrics, University of Cincinnati College of Medicine, Cincinnati, OH 45229-2899.

[2] Tripler Army Medical Center, Honolulu, HI 96859-5000.

[3] Present address: Department of Radiology, Walter Reed Army Medical Center, Washington, DC 20307-5001. Address reprint requests to W. E. Shiels II.

0361-803X/90/1556-1277

Sonograms were obtained with Acuson 128 (Mountain View, CA); ATL-Ultramark 8, ATL-Mark 4, or ATL-Mark 300 (Bothell, WA); and Picker Microview (Cleveland, OH) systems, using 5.0-, 7.5-, and 10.0-MHz transducers. Commercially available standoff pads (Kitecko, 3M, Roseville, MN, and Aquaflex, Parker Laboratories, Inc., Orange, NJ) were used to provide adequate visualization of the skin and superficial soft tissues. Preoperative localization was performed by marking the skin with permanent ink markers. Needle localization was performed with either 19- or 27-gauge needles. Sonographic confirmation of skin-marker positioning was performed with commercially available metal beads attached to disks of adhesive plastic (Beekley Spots, Beekley Corp., Bristol, CT). Hemostat localization was used during four intraoperative sonographically guided removal procedures. Comparison images of the opposite normal extremity were not obtained.

Imaging guidance was used for foreign body removal in six patients. Four of the six had sonographic guidance, two in the sonography suite and two in the operating room. One patient underwent fluoroscopically guided surgical exploration after sonographic localization of the foreign body. In another patient, a retained metal needle fragment was removed under fluoroscopic guidance after sonographic localization was unsuccessful. In this case there was extensive dissection and introduction of air into the operative bed. All operative sonographic studies were performed with sterile latex or polyethylene sonographic probe covers (Cone Instruments, Solon, OH).

Results

Of the 26 patients, radiographs or sonograms showed no evidence of a foreign body in six. In 19 patients, 21 foreign bodies were detected and localized by sonography. Sonography was unsuccessful in one case in which a retained metal needle fragment was not localized during intraoperative sonography after air was introduced into the wound after extensive dissection before sonography. Foreign bodies were detected in the feet, hands, finger, neck, thigh, knee, and calf; 19 of 21 foreign bodies were removed at surgery. Removal was not attempted in one patient because of the small size of the foreign body (2 × 1 mm). In another patient, a 3- by 1-mm splinter was not recovered at surgery (performed with only preoperative sonographic localization). One patient underwent two localization procedures, because sonography after initial surgical exploration revealed a retained wood fragment. The 21 foreign bodies that were removed consisted of ten wood fragments, six metal needles, two pencil fragments (one radiopaque, one without radiographs), one metal BB shot, one stone, and one glass fragment (radiopaque).

All of the sonographically detected foreign bodies were visualized as hyperechoic foci. Acoustic shadows were partial

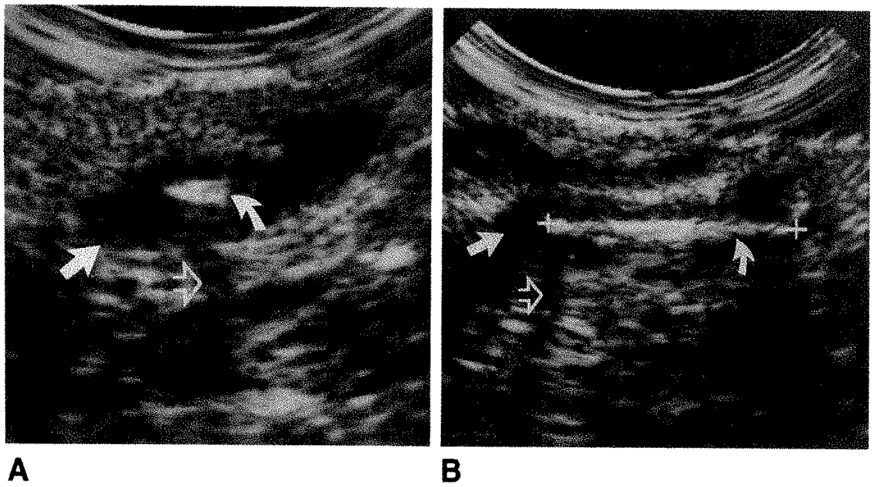

Fig. 1.—Retained wooden foreign body, 4 months after surgical removal failed.

A and *B*, Transverse (*A*) and longitudinal (*B*) sonograms show echogenic foreign body (*curved arrows*) surrounded by hypoechoic halo of inflammation (*solid straight arrows*) and partial acoustic shadowing (*open arrows*).

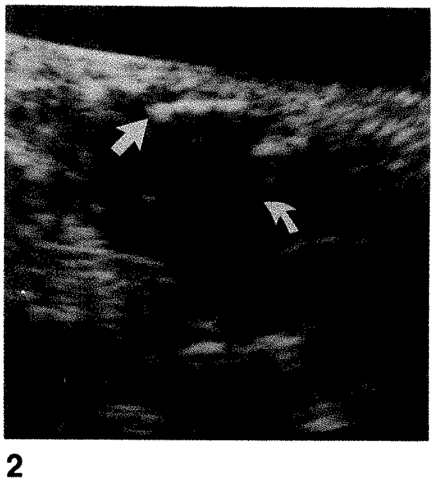

Fig. 2.—Wooden thorn. Longitudinal sonogram through palm of hand shows wooden thorn as markedly echogenic structure (*straight arrow*) with nearly complete shadowing (*curved arrow*). Thorn measured 5.6 mm in greatest length with exact correlation between preoperative sonographic measurement and measurement of specimen after recovery.

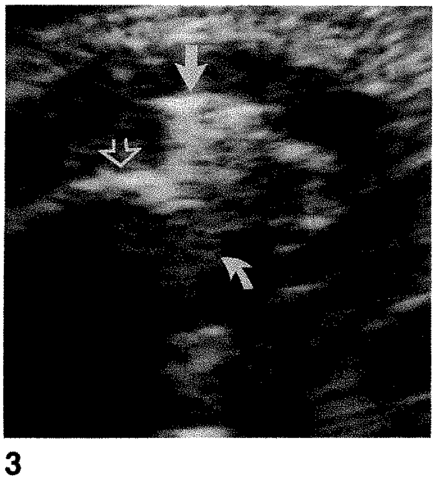

Fig. 3.—Glass. Transverse sonogram of hand shows echogenic glass foreign body (*solid straight arrow*) with comet-tail reverberation artifact (*curved arrow*) adjacent to a metacarpal (*open arrow*).

or complete depending on the angle of the beam and the composition of the foreign body (Figs. 1 and 2). Hyperechoic comet-tail artifacts (reverberation artifacts) were seen with six metallic foreign bodies and one glass fragment (Fig. 3). Nine foreign bodies were surrounded by hypoechoic halos (Fig. 1). The halos consisted of edema (four cases), abscess (two cases), and granulation tissue (four cases), either alone or in combination. The smallest foreign body detected (and recovered) was a nonradiopaque thorn measuring 5.6 mm in length. Two wooden splinters were the thinnest foreign bodies recovered, each measuring less than 1 mm in width.

Sonographically guided foreign body removal was successful in all four patients in whom it was used, including two needles from the feet, one needle from the knee, and one wooden pencil from the foot. No complications resulted from the sonographic localization and removal procedures. Two patients had retained wooden fragments after attempted surgical removal without sonographic guidance.

Discussion

Traditionally, plain films have primarily been used in the detection of soft-tissue foreign bodies. Fluoroscopy is often used for localization and guided removal. But these procedures are successful only if the foreign body is radiopaque, and radiation exposure is required.

Sonography provides an excellent alternative for identifying nonradiopaque foreign bodies. In cases of radiopaque foreign bodies, sonography complements the plain film evaluation by providing accurate three-dimensional localization for preoperative planning. Knowledge of the exact location of a foreign body relative to skin surfaces, adjacent muscles, tendons, neurovascular bundles, and other vascular structures allows more controlled surgical dissection. Doppler sonography is useful if the foreign body is near a vessel.

Slow, meticulous scanning technique is imperative in the detection of small foreign bodies. This is especially important

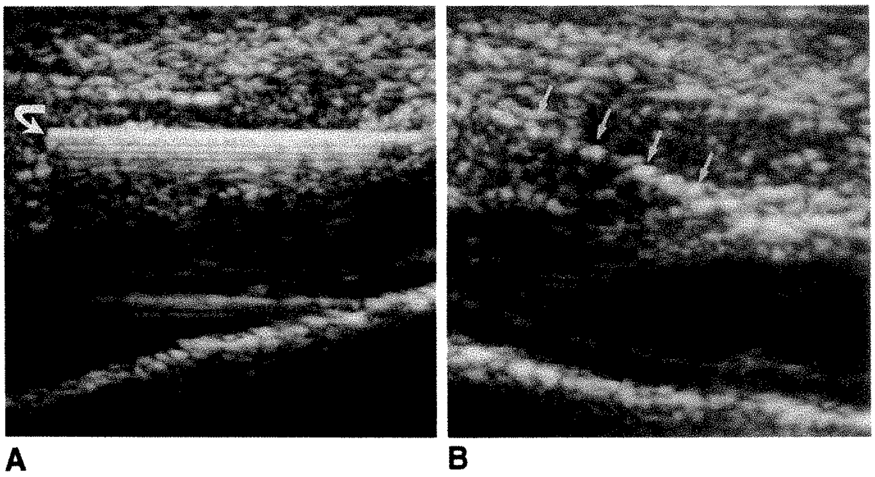

Fig. 4.—Sonograms of 19-gauge metallic needle in turkey breast.
A, Longitudinal scan with needle perpendicular to ultrasound beam shows clear definition of needle (*arrow*).
B, Sonogram with needle oblique to beam shows poorer definition of needle (*arrows*).

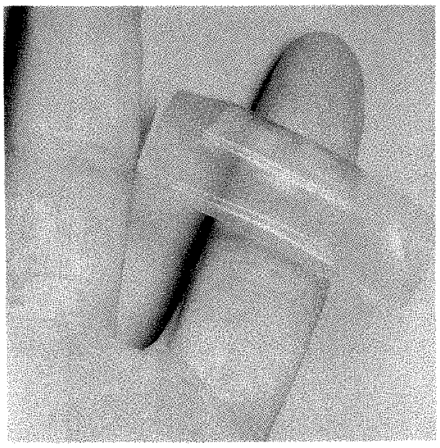

Fig. 5.—Standoff pad. Small rectangular acoustic standoff pad in place for scanning a finger.

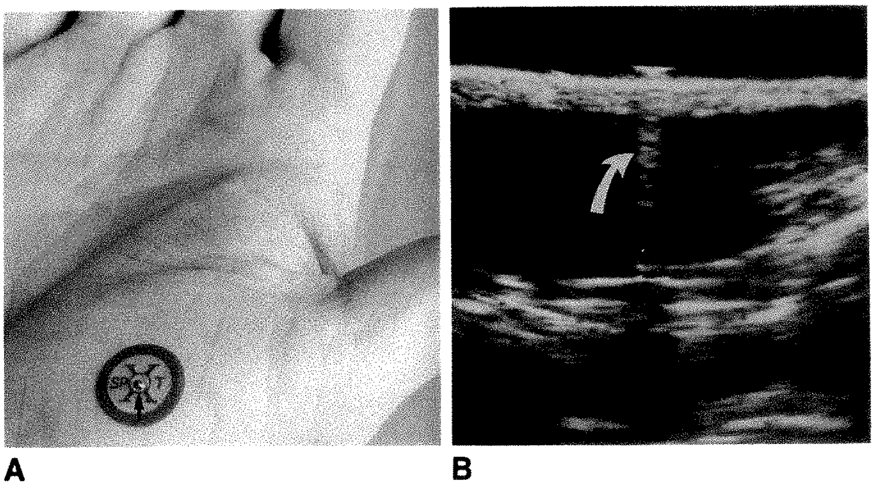

Fig. 6.—Skin-marking bead.
A, Photograph of a hand with adhesive disk and metallic bead (*arrow*) on hand for confirmation of skin marking.
B, Transverse sonogram through thenar eminence of hand shows reverberation artifact (*arrow*) produced with 7.5-MHz sector transducer.

in the hands and feet, where there are many echogenic structures and where small foreign bodies can be easily overlooked, and when foreign bodies do not lie parallel to the skin surface. When the transducer is perpendicular to the skin, foreign bodies lying perpendicular or oblique to the skin surface can be overlooked, only to be clearly delineated when the ultrasound beam is perpendicular to the long axis of the foreign body (Fig. 4). Although all foreign bodies in our series were echogenic, metallic foreign bodies were detected more readily than wood. The size of a foreign body contributes more to enhanced conspicuity than does foreign body composition. Small foreign bodies may be difficult to discern from surrounding tissues.

Both sector and linear-array transducers are useful. Linear-array transducers are helpful in the initial detection of the foreign bodies, when the larger scanning area of the linear probe accentuates the foreign body in an area of familiar anatomy. In this regard, high-frequency transducers have proved to be valuable not only for fine measurements of foreign bodies, but also in the initial detection of the foreign bodies. The higher-frequency transducers produce more vivid echoes from the foreign bodies. Sector transducers also can be used in the initial foreign body detection, and the smaller sector transducer heads are especially useful during intraoperative localization and removal procedures. The small sector transducer is less cumbersome than a linear-array transducer and allows greater flexibility while scanning next to an incision.

Standoff gel pads help in foreign body detection by placing the visualized anatomy in clearer perspective out of the transducer near field, enhancing foreign body conspicuity. The gel pads are cut with scissors or a scalpel blade to small

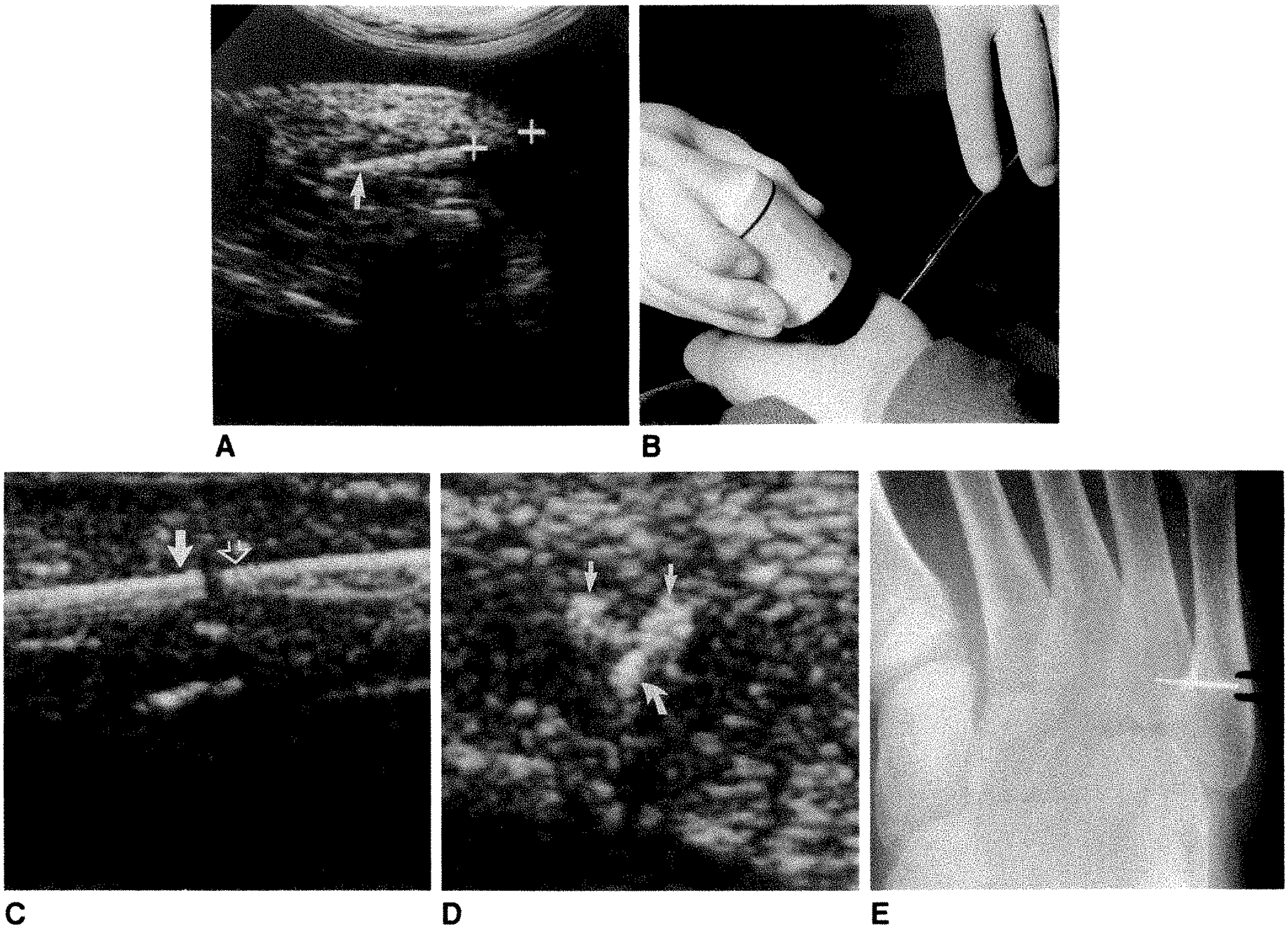

Fig. 7.—Metallic needle.

A, Preoperative sonogram of foot shows echogenic metallic needle (*arrow*).

B–E, Simulations of sonographically guided procedure for foreign body removal.

B, Photograph shows sector probe on plantar surface of foot, allowing surgeon to make a lateral incision and hemostat dissection in foot for retrieval of foreign body (as opposed to an incision on plantar weight-bearing surface of foot).

C, Sonogram with beam parallel to long axis of foreign body with tip of hemostat (*open arrow*) adjacent to tip of needle (*solid arrow*).

D, Sonogram with transducer beam transverse to long axis of foreign body. In this plane, we see open tips of hemostat (*straight arrows*) adjacent to tip of needle (*curved arrow*) for grasping and removal.

E, Plain radiograph of foot with superimposed hemostat shows lateral approach of hemostat with tips in position for sonographically guided removal.

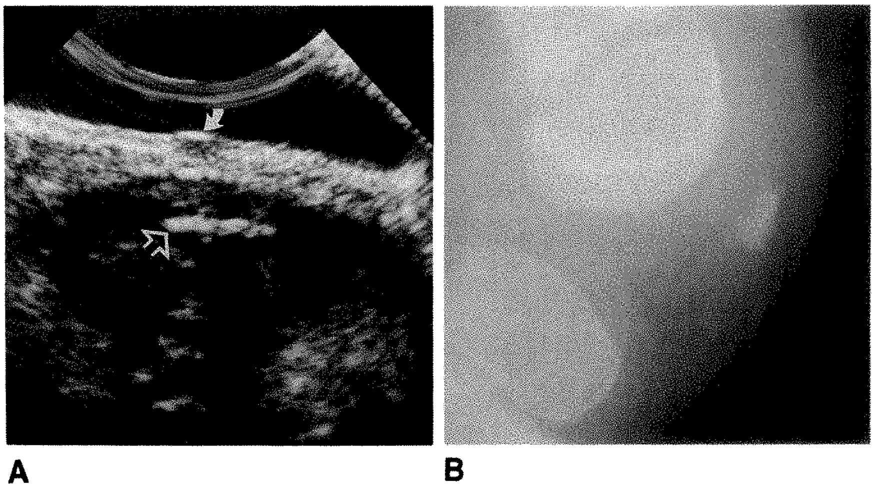

Fig. 8.—Pitfall caused by irregularly and partially ossified cartilage. A 4-year-old boy had fallen on knee on gravel and had persistent tenderness in area of healed wound. Initial scan revealed an irregular echogenic focus with sonographic shadowing beneath skin, looking like a retained foreign body. Further scanning revealed several such structures in the same area, all surrounded by a diskoid hypoechoic structure.

A, Sonogram in sagittal plane of knee shows echogenic cutaneous scar (*curved arrow*) as well as echogenic material in subcutaneous tissue (*straight arrow*) surrounded by elliptical hypoechoic zone. These specular echoes initially suspected to be a foreign body represent ossification center in diskoid cartilaginous patella.

B, Corresponding lateral knee radiograph confirms central speckled patellar ossification.

sizes for use on areas such as the hands, fingers, and neck (Fig. 5). The small standoff pads (3–6 cm long, either square or rectangular) are particularly useful in small children.

Metal beads are useful for verification of skin-marker position. Metal beads attached to adhesive disks used for lesion localization in CT-guided biopsies and drainage procedures (Fig. 6A) are ideal sonographic markers. The beads are sonographically visualized over the marked area, casting either an acoustic shadow or ring-down artifact beneath the bead (Fig. 6B). The adhesive disk transmits sound waves and does not obscure visualization of the underlying anatomy or foreign body. The adhesive disk is easily removed and replaced if repeated marking and verification are necessary. Standoff pads are used with bead verification.

Sonographic guidance of dissection and foreign body removal allows tailoring of the surgical approach, reducing the size of incision and depth of dissection (Fig. 7). Preoperative (or preincision) sonography is an essential element in successful sonographic detection, localization, and guided removal of foreign bodies. As demonstrated in our only case of unsuccessful detection, air introduced into tissues adjacent to a foreign body during dissection can obscure sonographic visualization of the foreign body. Care must be taken to avoid pitfalls in distinguishing foreign bodies from other body tissue such as ossified cartilage (Fig. 8), keratin plugs [3], and scar tissue.

A combination of longitudinal and transverse scanning planes facilitates removal. Scanning with the ultrasound beam aligned with the long axis of a hemostat and the foreign body is the fastest way to guide the hemostat to the tip of the foreign body (Fig. 7C). If the removal attempt with longitudinal scanning is unsuccessful, after the closed hemostat is visualized near the tip of the foreign body, transverse scanning best visualizes the tip of the foreign body as well as the two tips of the hemostat, in open and closed positions (Fig. 7D).

Skin incisions and dissections were performed by surgeons in the four sonographically guided removal cases. With experience and practice, including practice using beef tongue and turkey breast (Shiels et al., presented at the annual meeting of the Radiological Society of North American, November 1989), the time required for successful sonographically guided removal decreased. Our first attempt took nearly 1 hr from initial skin incision to successful removal. With better preoperative planning, improved communication with the surgeons, and practice, subsequent foreign bodies were removed in 11 min, 3 min, and 2 min, respectively. Sonographically guided foreign body removal is accomplished most easily and quickly when one physician performs sonography and hemostat removal of the foreign body simultaneously.

ACKNOWLEDGMENTS

We thank Juanita Hunter and Theresa Ricke for help in manuscript preparation and Corning Benton for editorial support.

REFERENCES

1. Fornage BD, Schernberg FJ. Sonographic diagnosis of foreign bodies of the distal extremities (case report). *AJR* **1986**;147:567–569
2. Fornage BD, Schernberg FJ. Sonographic pre-operative localization of a foreign body in the hand. *J Ultrasound Med* **1987**;6:217–219
3. Gooding GAW, Hardiman T, Sumers M, Stess R, Graf P, Grunfeld C. Sonography of the hand and foot in foreign body detection. *J Ultrasound Med* **1987**;6:441–447
4. Gordon D. Non-metallic foreign bodies (letter). *Br J Radiol* **1985**;58:574

Book Review

Stedman's Medical Dictionary, 25th ed. Baltimore: Williams & Wilkins, 1784 pp., 1990. $38.95

Stedman's Medical Dictionary, long one of the standard reference books for medical terminology, is now in its 25th edition. The most obvious improvement over the preceding edition is the increase in size to 8½ × 11 in., which makes the book much easier to read. The paper in the new edition seems a bit thinner than before, but the quality of the printing is high, so images do not bleed through the pages. A quick guide to use of the dictionary and its subentry locator has been added to the inside front cover. The subentry locator, an alphabetical list of subentries, each followed by the main entries under which they can be found, is quite handy. How many times have I looked under disease, syndrome, sickness, disorder, or other main entries to find a particular subentry? I must admit that the subentry locator was in the earlier edition, but I never noticed it buried in the appendixes in the back. In the new edition, the subentry locator is in the front and in much larger print.

Many features remain unchanged from the preceding edition. Each subentry is set out as a separate paragraph beneath the main entry, so you can scan the list of boldfaced subentries quickly to find the one you seek. This system has always been much easier to use than the run-on subentries clumped together in a block after the main entry, as for example, in *Dorland's Illustrated Medical Dictionary*. Each new letter of the alphabet starts on a fresh page, and the white space is plentiful. *Stedman's* is beautifully designed to make it as easy as possible to locate entries.

Two- and four-color plates of the skeleton, viscera, muscles, arteries, veins, and nerves remain conveniently grouped in the center of the volume, rather than scattered throughout the book wherever the main entry is located. The number of illustrations and the choice of which terms to illustrate seem appropriate. *Stedman's* illustrations of organs often are simple line drawings, whereas *Dorland's* tends to offer much more detailed and realistic reproductions (compare, for example, the drawings of the eye, endocrine glands, and kidney in the two dictionaries).

Dorland's also tends to be more encyclopedic in its definitions. Several of the *AJR's* editors say they have more luck finding terms in *Dorland's* than in *Stedman's*; I was shocked to find that *Stedman's* does not have an entry for extracorporeal shock-wave lithotripsy. However, *Dorland's* goes too far with its inclusion of "caudalward," when caudad or caudally would serve. (To *Dorland's* credit, it does not include cephalicward or cranialward.) On the whole, the definitions in *Dorland's* are longer, and I often find them clearer. The preface to *Stedman's* states that definitions were made "as readable as possible within the constraints of conciseness. . . . All major words in a definition . . . can be found as defined entries in the vocabulary." So at worst, you can decipher a definition in *Stedman's* if you are willing to look up any words you do not know. Neither *Stedman's* nor *Dorland's* shows the points at which each word can be divided at the end of a line, a feature we in the publishing business would find useful.

Stedman's 25th edition is an improvement over the last edition; the new design makes it even easier to use. You'll find the word you need quickly, and if you are familiar with medical terminology, the definition will be clear.

Katie L. Spiller
Senior Manuscript Editor
American Journal of Roentgenology
La Jolla, CA 92037

Case Report

Gastric Hematoma and Pneumatosis in Child Abuse

Ann S. Fulcher,[1] Lakshmana Das Narla, and William H. Brewer

Various visceral injuries have been described in association with the battered-child syndrome [1]. Intramural hematomas of the duodenum and proximal jejunum are the most commonly seen of such injuries. We report a case of an intramural hematoma and extensive pneumatosis of the stomach.

Case Report

A 21-month-old girl was brought to the emergency department, unresponsive and hypotensive. Physical examination revealed multiple bruises, lacerations, and human bite marks on the abdomen and back. Mild erythema around the vaginal introitus was present. Urinalysis showed a large quantity of myoglobin.

Radiologic workup included a normal chest radiograph, cranial CT, and skeletal survey. Abdominal CT performed shortly after admission showed low-density intraperitoneal fluid, gastric distension, and gastric antral thickening due to an intramural hematoma (Fig. 1A). An upper gastrointestinal examination showed passage of contrast material into the duodenum without evidence of duodenal hematoma (Fig. 1B).

After hydration, the patient became alert and active. However, on the second day after admission, she had increasing abdominal tenderness. The previously normal WBC count rose to 20×10^9/l with a shift to the left. Repeated abdominal radiographs and abdominal CT scans were remarkable for air within the gastric wall as well as for gastric distension and antral hematoma (Fig. 1C). The patient was treated with IV antibiotics and was monitored closely in the intensive care unit. An upper gastrointestinal examination performed 10 days after admission showed resolution of the hematoma but persistence of air within the gastric wall. A follow-up upper gastrointestinal examination done 17 days after admission showed resolution of the gastric pneumatosis.

Discussion

During the past two decades, physicians have become increasingly aware of the battered-child syndrome as a clinical entity. The skeletal and CNS manifestations of this syndrome have been documented extensively.

In recent years attention has been directed toward the visceral injuries associated with child abuse. Visceral injuries are estimated to occur in less than 2% of battered children [1]. Although intramural hematomas involving the duodenum and proximal jejunum are the most frequent visceral injuries detected radiologically, other injuries include pancreatitis; pancreatic pseudocysts; acute gastric distension and rupture; mesenteric injuries; and hepatic, splenic, and renal lacerations and hematomas [1-5].

Intramural hematoma of the intestine occurs as the result of extravasation of blood into the subserosal and interstitial tissues of the intestine [5]. Such injuries are usually the result of a direct blow to the anterior mid-abdomen [1]. Felson and Levin [6] noted the characteristic gastrointestinal series findings of a duodenal intramural hematoma: an intramural mass with a coiled-spring mucosal pattern.

The intramural hematoma of the gastric antrum and the gastric pneumatosis in this patient were clearly related to the battered-child syndrome. Although gastric hematomas have been described in association with hemophilia [7, 8], we are not aware of any reports of intramural gastric hematomas or pneumatosis resulting from child abuse. However, gastric hematomas may occur more frequently than previous reports suggest, particularly if such hematomas are not associated with obstruction.

Received December 26, 1989; accepted after revision May 21, 1990.

[1] All authors: Department of Diagnostic Radiology, Medical College of Virginia Hospitals, MCV Station, Box 615, Richmond, VA 23298-0615. Address reprint requests to L. D. Narla.

AJR 155:1283-1284, December 1990 0361-803X/90/1556-1283 © American Roentgen Ray Society

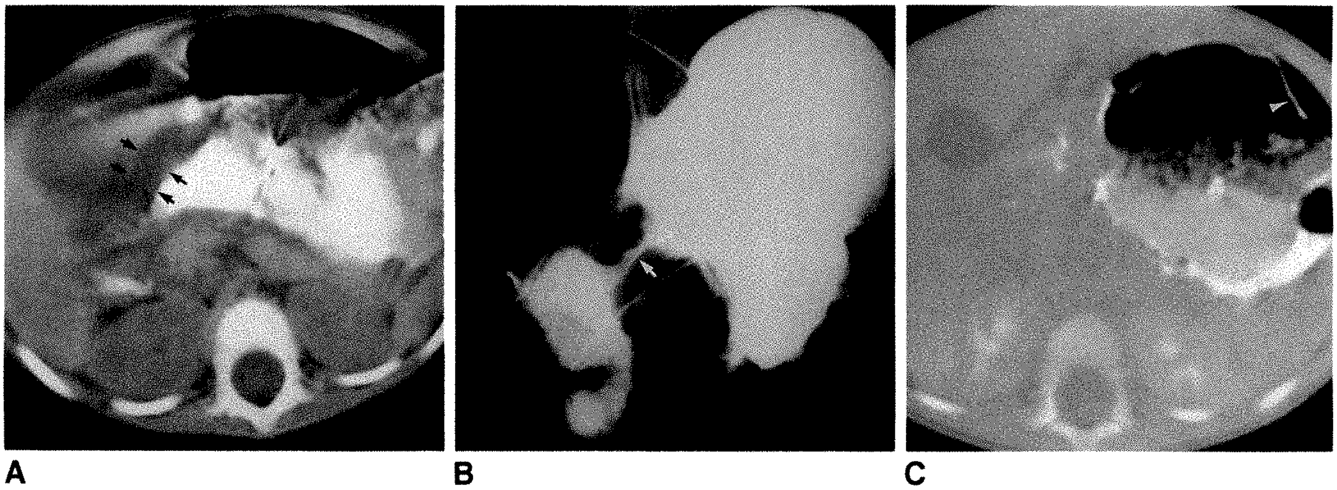

Fig. 1.—Gastric antral hematoma and pneumatosis of stomach in an abused child.
***A*, CT scan shows thickening of gastric antral wall (*arrows*) and obstruction of gastric outlet.**
***B*, Initial upper gastrointestinal examination shows circumferential, extrinsic compression of gastric antrum (*arrow*).**
***C*, Follow-up CT scan shows persistent antral hematoma and air within gastric wall (*arrowhead*) seen on abdomen and lung windows.**

In all likelihood, the traumatic event that results in intramural hematoma formation also results in a gastric mucosal tear. The subsequent dissection of air into the wall of the stomach is enhanced by partial or complete obstruction. Antral hematomas and pneumatosis thus are additional intraabdominal manifestations of child abuse.

REFERENCES

1. Kirks DR. Radiologic evaluation of visceral injuries in the battered child syndrome. *Pediatr Ann* **1983**;12:888-893
2. Kleinman PK, Raptopoulos VD, Brill PW. Occult nonskeletal trauma in the battered-child syndrome. *Radiology* **1981**;141:393-396
3. Franken ER, Fox M, Smith JA, Smith WL. Acute gastric dilatation in neglected children. *AJR* **1978**;130:297-299
4. Sivit CJ, Taylor GA, Eichelberger MR. Visceral injury in battered children: a changing perspective. *Radiology* **1989**;173:659-661
5. Kleinman PK, ed. *Diagnostic imaging of child abuse*. Baltimore: Williams and Wilkins, **1987**:116
6. Felson B, Levin EJ. Intramural hematoma of the duodenum: a diagnostic roentgen sign. *Radiology* **1954**;63:823-829
7. Bisset RAL, Gupta SC, Zammit-Maempel I. Radiographic and ultrasound appearances of intra-mural hematoma of the pylorus (case report). *Clin Radiol* **1988**;39:316-318
8. Grossman H, Berdon WE, Baker DH. Reversible gastrointestinal signs of hemorrhage and edema in the pediatric age group. *Radiology* **1965**;84:33-39

MR Imaging of the Normal and Abnormal Clivus

Fumiko Kimura[1]
Kwang S. Kim[1]
Harold Friedman[2]
Eric J. Russell[1]
Robert Breit[1]

We retrospectively reviewed 330 T1-weighted sagittal images, 80 T2-weighted sagittal images, and 83 gadopentetate-dimeglumine-enhanced scans of normal adults to determine the MR appearance of the normal adult clivus. MR images of 21 patients with an abnormal clivus (19 with tumor invasion and two with marrow reconversion) were also evaluated retrospectively and compared with those of the control group to assess MR features distinguishing the two groups. Our study revealed that a normal adult clivus consisted of low- and high-intensity portions mixed in various proportions on T1-weighted images. The low-intensity portion was isointense or hyperintense relative to the pons and always contained foci of bright signal intensity. The low-intensity tumor of a pathologic clivus tended to be hypointense relative to the pons (17/19), and was completely devoid of foci of bright signal intensity. The normal adult clivus was approximately isointense relative to the pons on T2-weighted images. Clival tumors were grossly hyperintense relative to the pons on T2-weighted images in 11 of 17 patients. In the remaining six patients, either a portion of or the entire lesion was isointense relative to the pons and, therefore, was not detectable on T2-weighted images. A normal adult clivus can enhance to some degree (19/83). Clival tumors were found to enhance intensely. A clivus of very low signal intensity (signal void) on T1- or T2-weighted images was always abnormal. The clivus with marrow reconversion was uniformly hypointense relative to the pons on T1-weighted images and isointense relative to normal marrow on T2-weighted images.

The intensity patterns of the normal clivus on T1- and T2-weighted MR images change predictably with advancing age. Intensity patterns of abnormal clivi differ from those of normal clivi. When contrast material is used, normal and abnormal clivi generally show different patterns of enhancement.

***AJNR* 11:1015–1021, September/October 1990; *AJR* 155:1285–1291,** December 1990

The superior sensitivity of MR in detecting bone-marrow diseases including tumor, inflammatory processes, and trauma has been well documented [1–10]. This results from the sensitivity of MR in detecting altered tissue constituents before any morphologic changes are detected. Alteration of the normal signal intensity of bone marrow is often the earliest and occasionally the only sign of diseased bone on MR.

The clivus, owing to its central location, is always well seen on T1-weighted sagittal scout MR images of the head. Thus, clinically suspected or unsuspected disease of the clivus may be detected on the routine cranial MR image. This prompted us to review the MR signal intensity of the clivus in both normal adults and those with disease. MR features that differentiate the two groups are discussed.

Materials and Methods

We retrospectively reviewed head MR images in a group of 330 adult patients (197 women and 133 men 20–88 years old) to establish the normal MR appearance of the clivus on T1-

Received December 12, 1989; revision requested January 30, 1990; revision received April 21, 1990; accepted April 25, 1990.

[1] Department of Radiology, Northwestern Memorial Hosital, Olson Pavilion, Suite 3416, 710 N. Fairbanks Ct., Chicago, IL 60611. Address reprint requests to K. S. Kim.

[2] Northeast Illinois MRI, 23196 N. Highway 45, Prairie View, IL 60069.

0361-803X/90/1556-1285
© American Roentgen Ray Society

TABLE 1: Graded Signal Intensity of Normal Adult Clivus: Correlation with Age

Grade	No. (%) of Patients in Each Age Group						
	20–29	30–39	40–49	50–59	60–69	70–79	80–89
1	16 (33)	13 (18)	5 (8)	0	1 (3)	0	0
2	16 (33)	31 (42)	28 (44)	19 (40)	9 (25)	9 (20)	0
3	17 (34)	29 (40)	31 (48)	28 (60)	26 (72)	36 (80)	16 (100)
Total	49	73	64	47	36	45	16

Note.—Grade 1 = predominantly low signal intensity, occupying more than 50% of clivus; grade 2 = low-signal-intensity portion occupying less than 50% but greater than 20% of clivus; grade 3 = predominantly high signal intensity, with low signal intensity occupying less than 20% of clivus.

weighted sagittal images. The age distribution of this group is shown in Table 1. Because of limited availability of cranial T2-weighted sagittal images, we retrospectively reviewed sagittal cervical spine MR images in a control group of 80 adult patients (46 men and 34 women 22–78 years old) in order to establish the normal MR appearance of the clivus on T2-weighted sagittal images. Patients with known or suspected abnormalities involving the skull base or bone marrow were excluded. Patients who had systemic disease or who had previous radiation or chemotherapy also were excluded.

We also retrospectively reviewed cranial MR images in 21 patients with an abnormal clivus. This group is summarized in Table 2. Although all of these patients had proved systemic or periclival tumor, in only three of 21 patients was histologic confirmation obtained directly from the clival lesion. The diagnosis in unproved cases (18/21) was based on other imaging techniques, such as radionuclide bone scanning, CT, or polytomography, as well as MR findings. The diagnosis was also supported by clinical information and follow-up MR scans, which showed regression following treatment or progressive change of the lesion.

The examinations were performed with a 1.5-T imager operating at 0.5 T or a 1.5-T imager operating at 1.5 T. Midline sagittal T1-weighted spin-echo (SE) images, SE 250–750/20–30/1–2 (TR/TE/excitations), with 5- to 10-mm slice thicknesses were used for evaluation of the signal intensity of the clivus. Midline sagittal T2-weighted images of the cervical spine, SE 1900–2000/80–100/2–4, with 4- to 7-mm slice thicknesses were compared with corresponding T1-weighted sagittal images. Only images that included the entire clivus were selected. In the pathologic group, cranial T2-weighted images, SE 2000–2200/70–100/2, were obtained with 5- to 10-mm slice thicknesses. Sagittal T2-weighted images were available in only seven of 21 patients. In the remaining 14 patients, the clival lesion was evaluated with axial or coronal T2-weighted images. All images were reviewed by at least three radiologists.

The signal intensity of the clivus on T1-weighted sagittal images consisted of relatively low- and high-signal-intensity portions. The low-signal-intensity portion was considered red marrow, while the high-signal-intensity portion was considered fatty marrow. The signal intensities of clival bone marrow were arbitrarily graded from 1 to 3: 1 = predominantly low signal intensity, occupying more than 50% of the clivus (Fig. 1); 2 = low-signal-intensity portion occupying less than 50% but greater than 20% of the clivus (Fig. 2); 3 = predominantly high signal intensity, with low signal intensity occupying less than 20% of the clivus (Fig. 3). The percentages used for grading may not precisely reflect the true composition of the low- and high-intensity portions of the clival marrow since they were evaluated on single midline sagittal images only. However, the observation of a general trend of age-related changes in the composition of the clival marrow may still be possible given our use of a large sample (330 subjects).

In 83 patients from the control group and 12 patients from the pathologic group, MR images were obtained before and after administration of gadopentetate dimeglumine. Images were obtained in the sagittal plane at 5-mm thicknesses in all 83 patients in the control group and at 5- to 10-mm thicknesses in 11 patients of the pathologic group. IV gadopentetate dimeglumine was administered in a dose of 0.1 mmol/kg; postinfusion T1-weighted images were obtained 3–4 min after injection. Pre- and postinfusion MR scans were compared side by side. The window levels and widths of the images were constant for the pre- and postinfusion scans.

TABLE 2: Diagnoses in Patients with an Abnormal Clivus

Diagnosis	No. of Patients
Metastases	
Breast carcinoma	5
Prostate carcinoma	2
Lung carcinoma	1
Subtotal	8
Lymphoma	2
Chordoma	3
Meningioma	3
Pituitary adenoma	2
Nasopharyngeal carcinoma	1
Reconversion from yellow to red marrow	2
Total	21

Results

Normal Adult Clivus on T1-Weighted Sagittal Images

The graded signal intensity of the clivus marrow in each age group is summarized in Table 1. A grade 1 clivus was observed in one third of patients in the third decade. The proportion of patients with grade 1 clivus gradually decreased, becoming zero by the sixth decade. A grade 2 clivus was observed in one third of patients in the third decade. The prevalence of grade 2 clivus peaked at 44% in the fifth decade and gradually decreased thereafter. A grade 3 clivus was observed in only one third of patients in the third decade. The proportion of grade 3 clivus gradually increased in older age groups and finally reached 100% in the ninth decade. The low-intensity portion of the normal adult clivus was isointense or slightly hyperintense relative to the pons on SE 250-750/20–30 images. The high-signal-intensity portion was isointense relative to subcutaneous fat.

Normal Adult Clivus on T2-Weighted Sagittal Images

The signal intensity of normal adult clivus was equal (45/80) (Fig. 4) or slightly hyperintense (25/80) or hypointense

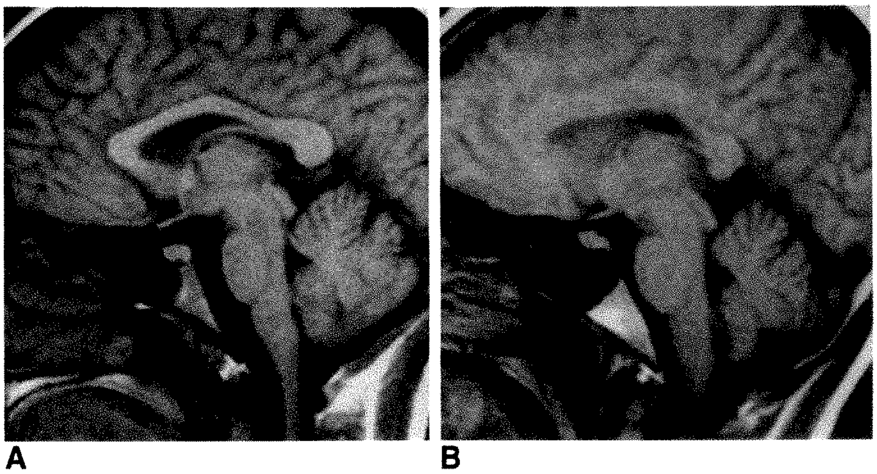

Fig. 1.—Grade 1 normal clivus on T1-weighted midline sagittal images, SE 350/30 (0.5 T), in a 25-year-old woman.

A, Clivus is of predominantly low signal intensity, approximately isointense relative to pons. A few foci of bright signal are seen in clival marrow.

B, 35-year-old woman. Clivus is of mixed signal intensity. Low-intensity portion, occupying greater than 50% of total marrow space, is hyperintense relative to pons.

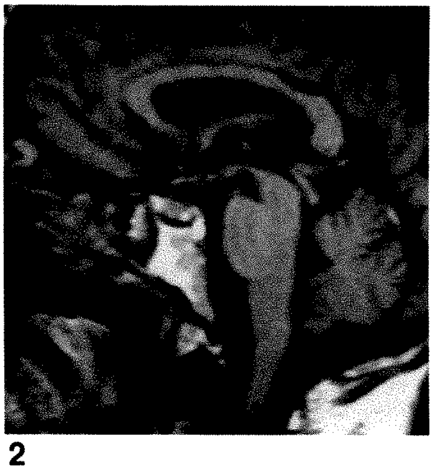

Fig. 2.—Grade 2 normal clivus with mixed signal intensity in a 77-year-old man. T1-weighted midline sagittal scan, SE 600/20 (1.5 T), shows a normal clivus with mixed low and high signal intensity. Area of low signal intensity is less than 50% but greater than 20% of entire marrow space. Low-signal-intensity area is hyperintense relative to pons. There are a few foci of bright signal intensity in low-signal-intensity portion.

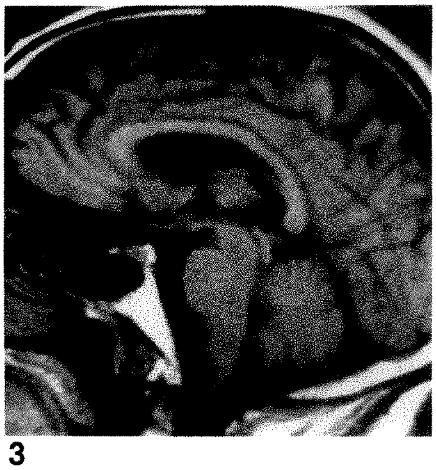

Fig. 3.—Grade 3 normal clivus in a 61-year-old woman. T1-weighted midline sagittal image, SE 350/30 (0.5 T), shows a normal clivus with uniformly bright signal intensity.

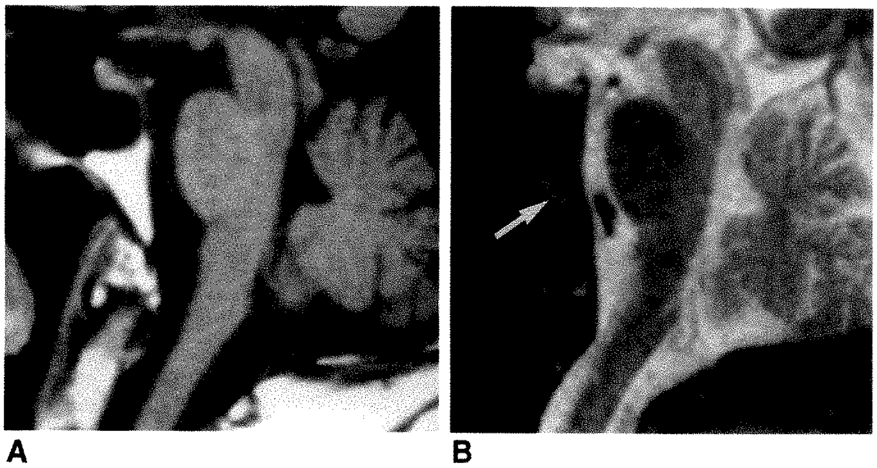

Fig. 4.—Normal clivus on T1- and T2-weighted midline sagittal images in a 63-year-old woman.

A, T1-weighted scan, SE 450/20 (1.5 T), shows a normal clivus with uniformly bright signal intensity (grade 3).

B, T2-weighted scan, SE 1900/80 (1.5 T), shows that signal intensity of clivus (*arrow*) becomes approximately isointense relative to the pons.

(10/80) relative to that of the pons on SE 1900–2000/80–100 images. Red and yellow discrimination diminished markedly. The fatty marrow was still slightly higher in signal intensity than red marrow on SE 1900-2000/80–100 images. The signal intensity from the clivus with a greater proportion of fatty marrow (high-grade clivus) tended to be isointense or slightly hyperintense relative to the pons. The clivus with a greater proportion of red marrow (lower-grade clivus) displayed the signal intensity equal to or slightly hypointense relative to the pons.

Gadopentetate Dimeglumine Enhancement of the Clivus in Normal Adult Patients

The prevalence of enhancement in the normal clivus in relation to the grade of preinfusion signal intensity is summarized in Table 3. Clival enhancement was observed in 19 (23%) of 83 normal patients, with greater prevalence when the preinfusion images revealed a lower grade of signal intensity. Enhancement was demonstrated in six (67%) of nine patients with grade 1 clivus intensity and in nine (26%) of 34 patients with grade 2. Enhancement was demonstrated in only four (10%) of 40 patients with grade 3 clival intensity. Contrast enhancement of the normal clivus was of mild intensity in 18 (95%) of 19 patients (Fig. 5). Enhancement was moderately intense in the remaining patient (5%) (Fig. 6).

TABLE 3: Gadopentetate Dimeglumine Enhancement of the Clivus in Normal Adults by Grade of Preinfusion Signal Intensity

Grade	Total	No. (%)	
		With Enhancement	Without Enhancement
1	9	6 (67)	3 (33)
2	34	9 (26)	25 (74)
3	40	4 (10)	36 (90)
Total	83	19 (23)	64 (77)

Note.—Grade 1 = predominantly low signal intensity, occupying more than 50% of the clivus; grade 2 = low-signal-intensity portion occupying less than 50% but greater than 20% of the clivus; grade 3 = predominantly high signal intensity, with low signal intensity occupying less than 20% of the clivus.

Abnormal Clivus

The signal intensity of the clivus was very low (signal void) in two patients with periclival meningioma on both T1-weighted (Fig. 7) and T2-weighted images. In the remaining 17 patients with tumor invasion of the clivus, the signal intensity on T1-weighted images was focally or diffusely low, hypointense relative to the pons in 15 patients (Figs. 8–10), and isointense relative to the pons in two patients. No foci of bright-signal-intensity fatty marrow were seen within the low-signal-intensity lesion in any of the patients with tumor invasion of the clivus. The signal intensity was uniformly low, hypointense relative to the pons, in two patients with yellow-to-red marrow reconversion (Fig. 11). The marrow reconversion resulted from prior repeated chemotherapy. The calvaria

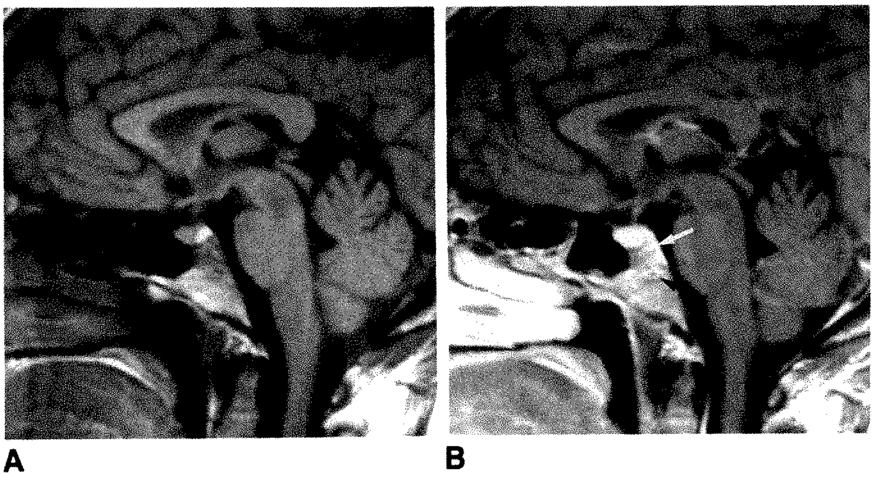

Fig. 5.—Enhancement of normal clivus in a 44-year-old woman.

***A*, Preinfusion scan, SE 600/20 (0.5 T), shows a normal clivus with mixed-signal-intensity portions (grade 2).**

***B*, Postinfusion scan shows mild enhancement of clivus near dorsum sellae. There is a curvilinear area of enhancement (*black arrow*), the morphology of which is suggestive of enhanced vascular structure. Enhancement is seen in basilar venous plexus (*white arrow*) behind upper clivus.**

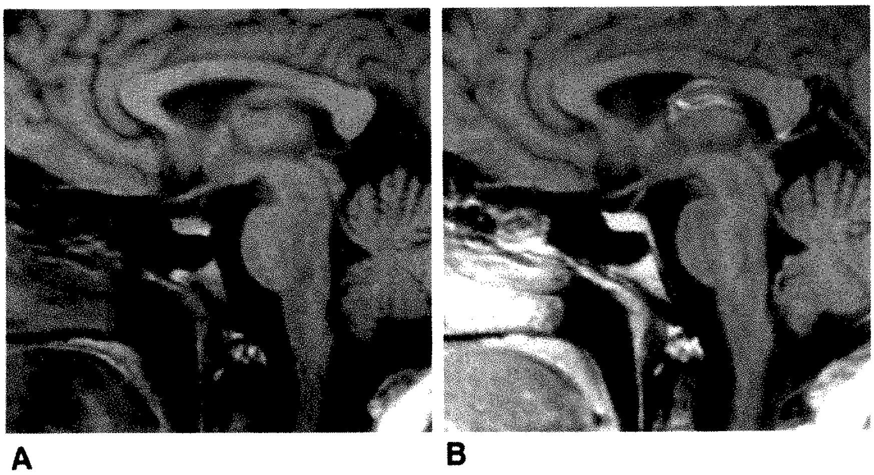

Fig. 6.—Enhancement of normal clivus marrow in a 26-year-old woman.

***A*, Preinfusion scan, SE 595/20 (1.5 T), shows a grade 1 clivus.**

***B*, Postinfusion scan shows moderately intense enhancement of clivus.**

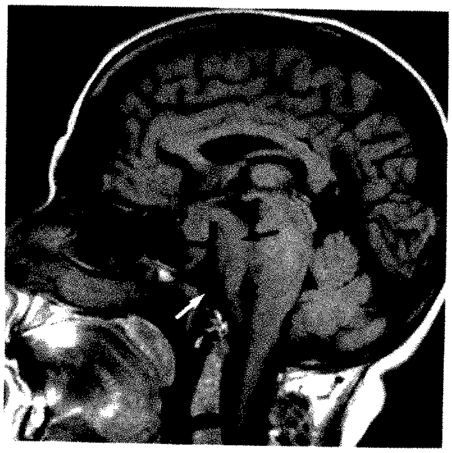

Fig. 7.—58-year-old woman with a periclival meningioma. T1-weighted midline sagittal scan, SE 750/30 (0.5 T). Very low signal intensity of clivus (*white arrow*) is caused by sclerotic change invoked by periclival meningioma (*black arrow*).

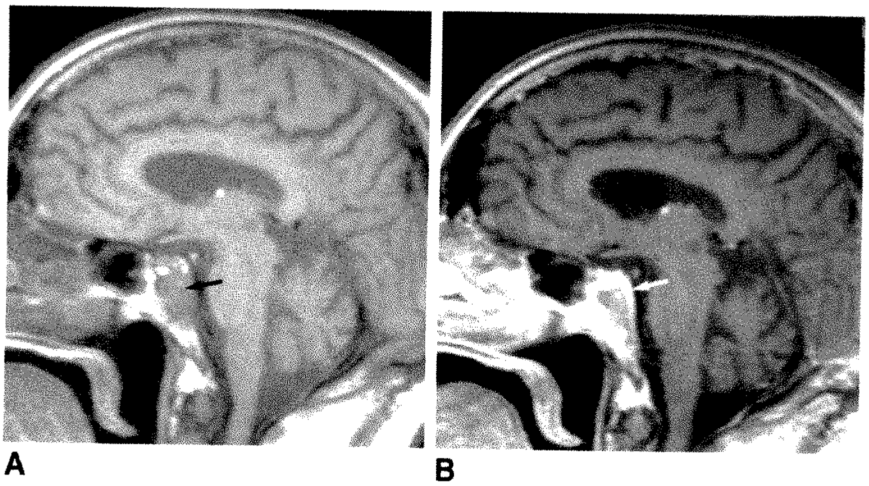

Fig. 8.—74-year-old man with metastasis from prostate carcinoma, presenting with isolated sixth-nerve palsy.

A, Preinfusion scan, SE 600/20 (1.5 T), shows focal area of low signal intensity (*arrow*) in clivus, representing metastatic tumor. Low-intensity lesion is hypointense relative to pons. No bright signal foci are seen within lesion.

B, Postinfusion scan shows intense enhancement in periphery of lesion. Central portion of lesion is poorly enhanced on scans obtained immediately after contrast infusion. Enhanced structure (*arrow*) behind clivus is basilar venous plexus.

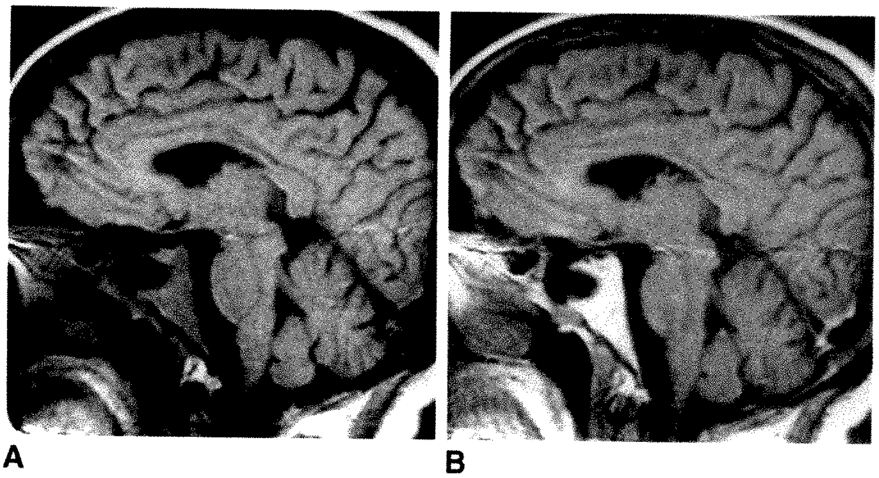

Fig. 9.—Lymphomatous infiltration of clivus in a 43-year-old woman with isolated right sixth-nerve palsy, which improved after radiation therapy.

A, Preinfusion scan, SE 600/30 (0.5 T), shows uniformly low signal intensity of clivus, which is slightly hypointense relative to pons. There are no bright signal foci within involved clivus. Contour of clivus is normal.

B, Postinfusion scan shows diffuse, intense enhancement of clivus, which is not discernible from a normal clivus with uniformly bright signal (grade 3).

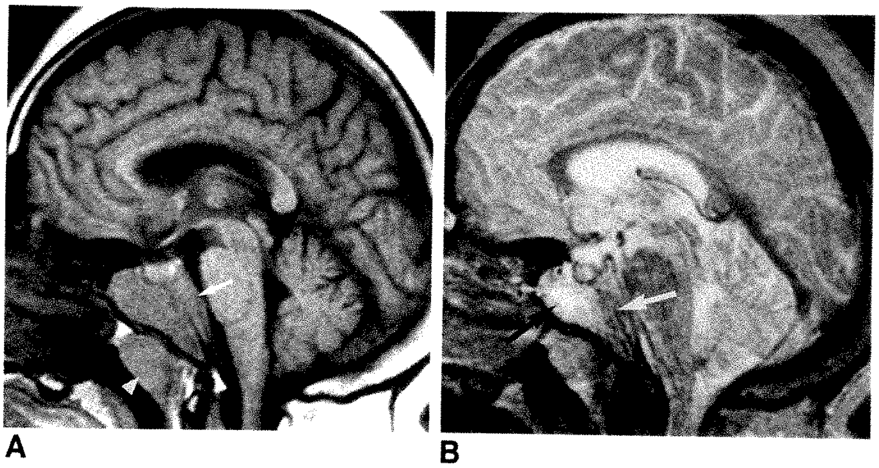

Fig. 10.—77-year-old woman with bilateral sixth-nerve palsy. Biopsy of clival lesion showed lymphoma.

A, T1-weighted midline sagittal scan, SE 750/30 (0.5 T), shows uniformly low signal intensity of clivus, which is hypointense relative to pons. There are no foci of bright marrow signal intensity within involved clivus. Lesion extends into sphenoid sinus anteriorly and into prepontine cistern posteriorly (*arrow*). There is also a soft-tissue mass (*arrowhead*) in retropharyngeal region.

B, T2-weighted sagittal scan, SE 2000/100 (0.5 T), shows that anterior two thirds (*black arrow*) of lesion becomes grossly hyperintense relative to pons. Remaining posterior one third (*white arrow*) is approximately isointense relative to pons and, therefore, is not detectable on T2-weighted images, resulting in underestimating true extent of lesion.

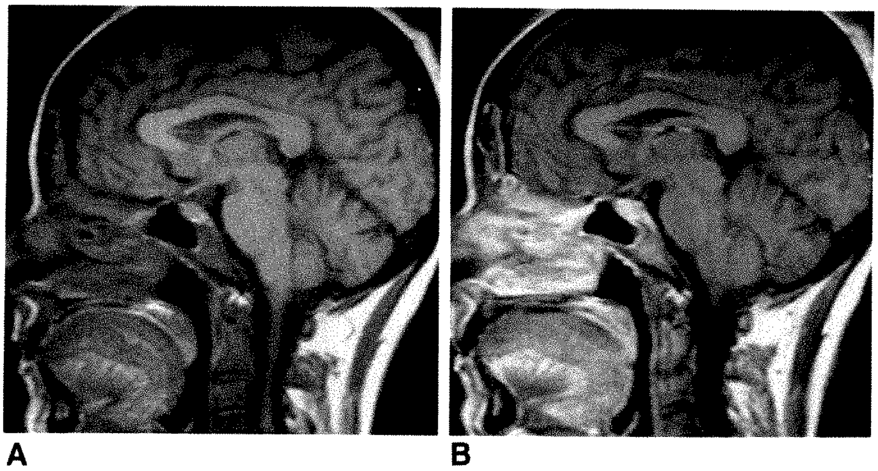

Fig. 11.—Yellow-to-red marrow reconversion in a 55-year-old woman who had prior chemotherapy for lymphoma.

A, Preinfusion midline sagittal scan, SE 425/25 (1.5 T), shows uniformly low signal intensity of clivus. Calvaria and upper cervical spine also show diffuse low-signal-intensity marrow.

B, Postinfusion scan shows moderate enhancement of clivus.

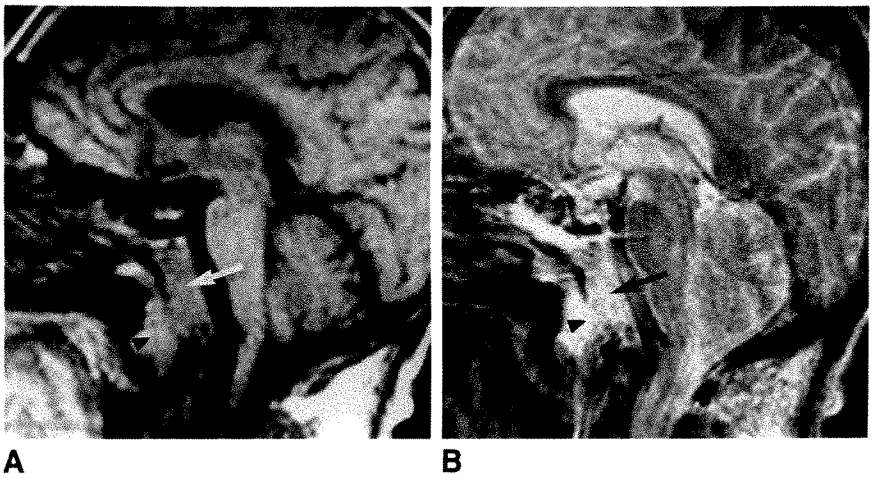

Fig. 12.—Nasopharyngeal carcinoma invading clivus in a 69-year-old man.

A, T1-weighted sagittal scan, SE 350/30 (0.5 T), shows a nasopharyngeal tumor (*arrowhead*) invading clivus (*arrow*). Involved clivus is slightly hypointense relative to pons.

B, T2-weighted sagittal scan, SE 2000/100 (0.5 T), shows that involved clivus (*arrow*) becomes grossly hyperintense relative to pons. Signal intensity of nasopharyngeal tumor (*arrowhead*) is bright also.

and the upper cervical spine, visualized on the cranial midline T1-weighted sagittal images, also showed diffuse loss of yellow marrow in these patients.

On T2-weighted images, lesions appeared as an area of homogeneously high intensity in three patients with chordoma, two with pituitary adenoma and one with nasopharyngeal carcinoma (Fig. 12). In five of eight patients with metastasis to the clivus, lesions were hyperintense relative to the normal clivus. The signal intensity was mixed with areas of iso- and hyperintensity in two patients with lymphomatous infiltration of the clivus (Fig. 10). The signal intensity was isointense relative to the normal clivus in three patients with metastasis, one with periclival meningioma and two with marrow reconversion. The diminished signal-to-noise ratio encountered on longer TR/TE images resulted in poorer anatomic definition of lesions.

Twelve of 21 patients with an abnormal clivus had gadopentetate-dimeglumine–enhanced scans. The low-intensity tumor, focal or diffuse, was intensely enhanced in all patients (Figs. 8 and 9). The reconverted clivus was mildly enhanced in one patient and moderately enhanced in the other (Fig. 11).

Discussion

Okada et al. [11], in their study of a group of normal children and young adults, demonstrated that signal from clival marrow was age-related and successively changed from uniformly low to uniformly high signal intensity on T1-weighted images. By the age of 24 years, 95% of their patients had a clivus of uniformly high signal intensity. The rate of conversion was somewhat slower in our patients. The clivus was uniformly bright in only one third of our normal patients in the third decade. The proportion of uniformly bright clivus gradually increases with advancing age. The rate increased to 80% by the eighth decade and reached 100% in the ninth decade. Our results show that interindividual variations are large in the composition of clival marrow in an adult population and that the conversion of red to yellow marrow occurs in a predictable and orderly pattern.

The hallmark of MR signal intensity caused by diseased marrow is T1 prolongation. The major factors determining the T1 changes are increased cellularity associated with tumor replacement of normal marrow and increased water content owing to bone marrow edema [10].

A clivus with uniformly low signal intensity that is hypointense relative to the pons should be considered abnormal in an adult patient. Conversely, a clivus of uniformly bright signal intensity is highly unlikely to be abnormal. The uniformly low signal intensity is attributable to diffuse tumor invasion of the clivus or marrow reconversion. In the normal adult, hematopoietic needs are met by the amount of red marrow existing in the axial skeleton and the proximal long bones. With increasing demand for red cells, a reconversion of yellow marrow to red marrow takes place. The causes of this process include chronic anemia, heart disease with chronic heart failure, and marrow replacement disorders [10, 12]. In our two patients, reconversion occurred after chemotherapy. In these patients, diffuse low signal intensity was demonstrated in other osseous structures such as the calvaria and the upper cervical spine, a feature differentiating this process from tumor invasion of the clivus (Fig. 11).

A clivus with a pattern of mixed signal intensity presented a greater challenge in differentiating normal from abnormal. The low-signal-intensity portion of the normal clivus was isointense or hyperintense relative to the pons on SE 250–750/20–30 images (Figs. 1 and 2), whereas the signal intensity of a clival lesion was hypointense relative to the pons (Fig. 8) in 15 of 17 patients with tumor invasion. In the remaining two patients, the low-signal-intensity lesion was isointense relative to the pons. The lesion could not be detected on the basis of signal intensity alone in these two patients. However, the low-signal-intensity lesion of a pathologic clivus is completely devoid of bright marrow signal foci (Fig. 8). Foci of bright marrow signal are always present within the area of relatively low signal intensity in a normal adult clivus (Figs. 1 and 2).

The normal adult clivus became approximately isointense relative to the pons on T2-weighted images on SE 1900–2000/80–100 images (Fig. 4). Red and yellow marrow discrimination was poorer, reflecting the diminished difference in T2 relaxation times between the two types of marrow. Our study in the evaluation of the clival lesion with T2-weighted images was less than optimal because of the limited availability of sagittal T2-weighted images. T2-weighted images were valuable in detecting tumor invasion of the clivus when the lesion was sufficiently hyperintense relative to normal marrow. This occurred in 11 of 17 patients with tumor invasion of the clivus. In two other patients, only a portion of the lesion became hyperintense, resulting in an underestimation of the true extent of tumor invasion (Fig. 10). The clival lesion was not detectable on T2-weighted images in the remaining four patients with tumor invasion. The anatomic definition of the lesions, if detected, was significantly poorer on T2-weighted images. It appears that T2-weighted images are useful in detecting tumor invasion of the clivus but are inferior to T1-weighted images because of their poor spatial resolution, higher false-negative rate, and longer examination time.

A clivus of very low signal intensity (signal void) was not observed on T1- or T2-weighted images of our normal adult population. The signal void in the clivus with periclival meningioma is related to a sclerotic change of the marrow produced by tumor invasion (Fig. 7). The signal intensity of the sclerotic bone is similar to that of compact bone, which has a very low spin density because of its low content of mobile protons.

Our results show that in 23% of adults, the normal clival marrow enhanced with gadopentetate-dimeglumine. The mechanism of enhancement of normal marrow is yet to be investigated. We have observed small punctuate or curvilinear areas of low signal intensity within the marrow that enhance with contrast administration (Fig. 5). The morphology of these enhanced structures suggests that they are enhanced vessels, probably slowly flowing venous channels. A more homogeneous pattern of contrast enhancement within the marrow presumably is related to contrast material pooling within the marrow sinusoids (Fig. 6). Enhancement is observed with greater frequency within the lower-grade clivus. The clivus with a lower grade of signal intensity contains a greater amount of red marrow, which is accompanied by greater vascularity [12]; hence, enhancement is observed more frequently in the lower-grade clivus. Furthermore, enhancement may be observed more readily in the red marrow, whereas the bright signal intensity of yellow marrow obscures contrast enhancement.

Enhancement of the normal clivus usually is mild. Contrast enhancement of low-intensity tumor tends to be intense (Figs. 8 and 9). A focally or diffusely enhanced lesion therefore, may not be detected on postinfusion scans alone (Fig. 9). Enhancement of reconverted clival marrow was mild in one patient and moderate in the other (Fig. 11). The number of cases in our study was too small to define the characteristic enhancement pattern of reconverted clivus.

REFERENCES

1. Cohen MD, Klatte EC, Baehner R, et al. Magnetic resonance imaging of bone marrow disease in children. *Radiology* **1984**;151:715–718
2. Zimmer WD, Berquist TH, McLead RA, et al. Bone tumor: magnetic resonance imaging versus computed tomography. *Radiology* **1985**;155:709–718
3. Daffner RH, Lupetin AR, Dash N, Deeb ZL, Sefczek RJ, Schapiro RL. MRI in the detection of malignant infiltration of bone marrow. *AJR* **1986**;146:353–358
4. Olson DO, Shields A, Scheurich CJ, Porter BA, Moss AA. Magnetic resonance imaging of the bone marrow in patients with leukemia, aplastic anemia and lymphoma. *Invest Radiol* **1986**;21:540–546
5. McKinstry CS, Steiner RE, Young AT, Jones L, Swirsky D, Aber V. Bone marrow in leukemia and aplastic anemia. MR imaging before, during, and after treatment. *Radiology* **1987**;162:701–707
6. Rehn RN, Hagberg GH, Hemmingsson A, Jung B, Simonsson B, Sundstrom C. Magnetic resonance imaging in diffuse malignant bone marrow diseases. *Acta Radiol [Diagn]* (Stockh) **1987**;28:199–205
7. Sze G, Krol G, Zimmerman RD, Deck MDF. Malignant extradural spinal tumors: MR imaging with Gd-DTPA. *Radiology* **1988**;167:217–223
8. Yao L, Lee JK. Occult intraosseous fracture: detection with MR imaging. *Radiology* **1988**;167:749–751
9. Unger E, Moldofsky P, Gatenby R, Hartz W, Broder G. Diagnosis of osteomyelitis by MR imaging. *AJR* **1988**;150:605–610
10. Vogler JB, Murphy WA. Bone marrow imaging. *Radiology* **1988**;168:679–693
11. Okada Y, Aoki S, Barkovich AJ, et al. Cranial bone marrow in children: assessment of normal development with MR imaging. *Radiology* **1989**;171:161–164
12. Kricun ME. Red-yellow marrow conversion: its effect on the location of some solitary bone lesions. *Skeletal Radiol* **1985**;14:10–19

Book Review

Clinical Magnetic Resonance Imaging. Edited by Robert R. Edelman and John R. Hesselink. Philadelphia: Saunders, 1192 pp., 1990. $165

The editors of this book have attempted to provide an up-to-date compendium of clinical MR. They do this by fusing what are really three separate books into one. The first, called part I, is the best clinically oriented review of MR physics and instrumentation that I have read to date. It manages to be lucid but not exclusive. The clinical practitioner will find complete yet practical explanations of the physics of MR and the engineering of daily practice. Artifacts, flow, fast MR, contrast agents, hemorrhage, spectroscopy, pulse-sequence design, site planning, and instrumentation are all covered. This part alone is worth the cost of the text.

The next "book," part II, "Central Nervous System," really covers more than just the CNS. It is a review of neuroradiologic diseases amenable to MR diagnosis. The usual sections on brain and spine are present. However, it also has separate sections on the orbit, head and neck, and brachial plexus. It is particularly refreshing to see the brachial plexus finally getting attention in a radiology textbook. The third "book," parts III through V, could be named "Body MR." The section on the chest concentrates on adult and congenital heart disease. Separate sections discuss the upper abdomen and adrenal glands and the kidneys and retroperitoneum. The part on the pelvis has separate sections on obstetric MR imaging, the scrotum and testes, developmental abnormalities of the female pelvis, and general pelvic imaging. The part on the musculoskeletal system is separated into six separate sections: one each on the knee, glenohumoral joint, temporomandibular joint, the wrist, the foot and ankle, and the hips. The last of these also reviews MR of the musculoskeletal system.

Two appendixes follow the text. The first provides MR imaging protocols. This is a carefully referenced compilation of published protocols for specific diseases. This is an efficient way to share the many different ways to use MR in disease evaluation and is really the only objective way to present all of these options. The second appendix provides staging systems of primary malignancies. This is followed by a glossary of MR terms.

As good as this book is, it does have problems. MR technology is changing so fast that no textbook can hope to be up to date. Such texts provide a review of the technology up to the time of composition, which can be 12–18 months before publication. General weaknesses include the variability in MR images. Some are poor-quality, low-field-strength images. The labeling of the images is not uniform. Many do not even provide the TR and TE. The next major weakness of the book is the poor presentation of the clinical impact of gadolinium. Too many statements are "promissory notes" suggesting that gadolinium might do this or that.

The weakest of the three "books" is the one on the CNS, which begins with a simplistic atlas of MR images of the normal brain. This is out of place in a state-of-the-art book. The chapter on brain neoplasia has too many sweeping statements and pathologic inaccuracies. Imaging-pathologic correlation is becoming quite precise, and neuropathology is changing dramatically. Work such as this really should be a joint effort by neuroradiologists and neuropathologists. The chapter on the orbit is composed enthusiastically but is strongly prejudiced against CT. A more balanced picture, comparing CT and MR, would be more appropriate. The few CT scans provided are not state of the art. The most significant advance in MR imaging in the orbit, routine fat-suppression studies with and without gadolinium, is not covered. These limitations are reasonable considering the usual lag time between writing a book and publishing it. Especially good chapters in the CNS section cover congenital malformations and the brachial plexus. The chapter on congenital malformations refreshingly is organized along major stages of brain development.

The appendix on staging systems of primary malignancies is injured by the exclusion of staging of head and neck cancer and the incorrect forced linear comparative classification of fibrillary astrocytic neoplasms. The Bailey and Cushing classification originated in 1926 and now is of historical interest only. The Ringertz, Dumas-Duport, and Brain Tumor Research Center of San Francisco grading systems are not even mentioned. The appendix has no discussion of immunohistochemistry, now important in classifying brain neoplasms. The World Health Organization classification is presented incorrectly.

The authors of this work have done a good job. The publishers provide their labors at an absolutely bargain price. I would buy a copy of this book myself.

Stephen S. Gebarski
University of Michigan Hospitals
Ann Arbor, MI 48109-0030

Sarcoidosis of the CNS: Comparison of Unenhanced and Enhanced MR Images

John L. Sherman[1, 2]
Barney J. Stern[3]

Sarcoidosis involving the CNS has a predilection for the leptomeninges, although parenchymal involvement occurs. We retrospectively evaluated the appearance of CNS sarcoidosis on unenhanced and enhanced MR images. MR studies were abnormal in 17 of 20 patients with CNS sarcoidosis. In all 17 patients, meningeal disease was detected on the gadopentetate-dimeglumine–enhanced T1-weighted images; the disease was detected on unenhanced images in three patients. Well-defined leptomeningeal patterns of enhancement were present in 15 patients. Other areas of involvement were the dura; brain parenchyma including hypothalamus, periventricular white matter, and ventricular ependyma; optic chiasm; and pituitary gland.

Gadopentetate dimeglumine optimally evaluates meningeal disease and highlights the importance of the leptomeninges and Virchow-Robin spaces in the pathogenesis of CNS sarcoidosis. Enhanced MR is the preferred imaging technique for the evaluation of CNS sarcoidosis.

AJNR 11:915–923, September/October 1990; *AJR* 155:1293–1301, December 1990

Neurologic manifestations of sarcoidosis occur in 5% of patients with this disease [1]. Postmortem studies demonstrate CNS and meningeal disease in as many as 14% of patients with known systemic sarcoidosis [2, 3]. Intracranial involvement is most often a diffuse or focal granulomatous leptomeningitis. Parenchymal inflammation is seen also. The MR appearance of neurosarcoidosis has been described [4–8]. Unenhanced MR is superior to CT in the evaluation of hypothalamic and periventricular involvement [3, 4]. However, unenhanced MR does not optimally evaluate inflammation of the meninges and does not evaluate the integrity of the blood-brain barrier. The use of gadopentetate dimeglumine has been recommended for brain MR imaging to evaluate the blood-brain barrier and whenever extraaxial disease is suspected [9–13]. In this study, we describe the gadopentetate-dimeglumine–enhanced MR appearance of CNS sarcoidosis and compare it with the unenhanced MR appearance.

Materials and Methods

Twenty patients with neurosarcoidosis underwent MR examinations of the brain before and after administration of gadopentetate dimeglumine. All but three patients had biopsy-proved systemic sarcoidosis. In those three patients, intracranial biopsies showed granulomatous inflammation consistent with sarcoidosis. The diagnosis of neurosarcoidosis was made clinically in the other 17 patients. There were 11 women and nine men 21–58 years old (average, 36 years). Table 1 is a clinical summary of the patients involved in this study.

MR examinations were performed on 1.5-T (n = 16 patients), 1.0-T (n = 1 patient), or 0.5-T (n = 3 patients) MR imagers. All unenhanced examinations used at least three techniques: T1-weighted spin echo (SE), 500–600/20–25/2 (TR/TE/excitations); intermediate SE, 2000–3200/30–40/1–2; and T2-weighted SE, 2200–3200/80–100/1–2. Section thickness was 5 or 7 mm, with an intersection gap of 1–2.5 mm. Gadopentetate dimeglumine (Magnevist, Berlex

Received December 6, 1989; revision requested February 15, 1990; revision received March 27, 1990; accepted March 29, 1990.

[1] Washington Imaging Center, 2801 University Blvd., Kensington, MD 20895. Address reprint requests to J. L. Sherman.

[2] Department of Radiology, Uniformed Services University of the Health Sciences, Bethesda, MD 20814, and George Washington University School of Medicine, Washington, DC 20037.

[3] Division of Neurology, Sinai Hospital of Baltimore, Baltimore, MD 21215, and Department of Neurology, The Johns Hopkins Medical Institutions, Baltimore, MD 21205.

0361-803X/90/1556-1293
© American Roentgen Ray Society

TABLE 1: Clinical Summary of Patients with CNS Sarcoidosis

Case No.	Age (yr)	Race	Sex	Neurologic Signs and Symptoms	Tissue Diagnosis	Systemic Disease	Steroid Therapy at Time of MR
1	34	B	F	Neuroendocrinologic dysfunction	Lung	Yes	Yes
2	49	B	M	Encephalopathy, ataxia	Brain	Yes	No
3	23	B	F	Papilledema, aseptic meningitis	Lung	Yes	No
4	34	B	F	Neuroendocrinologic dysfunction, aseptic meningitis	Nasal	Yes	No
5	21	B	M	Seizures, cranial nerve II	Node	Yes	Yes
6	27	B	M	Seizures, cranial nerves I, II, VIII	Node	Yes	No
7	58	W	F	Hypothalamic dysfunction, encephalopathy, cranial nerves I & II	Sinus	Yes	No
8	31	B	M	Hypothalamic dysfunction, cerebellar signs, ataxia	Testis	Yes	No
9	48	W	M	Seizures, encephalopathy, cranial nerves II & VIII	Brain	No	Yes
10	38	B	F	Neuroendocrinologic dysfunction	Lung	Yes	No
11	57	B	M	Cranial nerves II & VIII	Lung	Yes	No
12	39	W	M	Hemiparesis, cranial nerve II	Conjunctival	Yes	No
13	29	B	M	Papilledema, headache, cranial nerve I	Brain	No	Yes
14	31	B	F	Cranial nerves VII & VIII	Lung	Yes	No
15	40	B	F	Cranial nerves V & VIII	Node	Yes	No
16	30	B	F	Aseptic meningitis, cranial nerve VIII	Liver	Yes	No
17	32	B	F	Seizures, cranial nerves II & VIII; hypothalamic dysfunction	Brain	No	Yes
18	32	B	F	Seizures, cranial nerves I, II, & VIII; pituitary dysfunction	Brain	Yes	No
19	36	B	F	Encephalopathy, dysarthria pituitary dysfunction	Lymph node	Yes	No
20	29	B	M	Cerebellar signs, ataxia, encephalopathy	Lung	Yes	No

Laboratories, Wayne, NJ) was given in a concentration of 0.1–0.15 mmol/kg at a rate of 15–30 ml/min (Kashanian FK et al., presented at the annual meeting of the American Society of Neuroradiology March 1989). Patients were studied with short T1-weighted scans after the administration of contrast material. The matrix was 256 × 256 for all T1-weighted images and for most intermediate and T2-weighted images. A 128 × 256 matrix was used in a few instances.

In a nonblinded review, we retrospectively analyzed each set of images for abnormalities affecting the following areas: meninges, falx, hypothalamus/pituitary, periventricular white matter, parenchyma, and ependyma.

Results

The results of brain MR in our patients are summarized in Table 2. The enhanced MR studies revealed additional areas of involvement not suspected on the unenhanced examinations in 17 patients. We identified multiple lesions in most patients; for example, multiple meningeal foci, hypothalamic infiltration, and white or gray matter lesions. The scope and multiplicity of the variable MR findings on CNS sarcoid in our patients is reflected in Table 3. Of particular note is the observation of multiple areas of involvement that were visualized only on enhanced MR. Leptomeningeal involvement (Figs. 1–5) was most striking since none of the leptomeningeal disease was detected on unenhanced MR. Of interest is the observation of internal auditory canal enhancement in three patients with diffuse leptomeningeal disease. Other areas where enhanced MR was superior included the dura (Figs. 1 and 5), hypothalamus, and pituitary/infundibular disease (Figs. 1, 3, and 6). Periventricular enhancement (Figs. 6 and 7) was very prominent in several patients and could not be predicted on the basis of the appearance on the T2-weighted images.

Clinical Correlation and Follow-up Evaluation

The clinical summary of our patients is presented in Table 1. Three patients had a clinical diagnosis of CNS sarcoidosis with cranial neuropathies but had normal MR studies. Two of these patients were being treated with 40 mg/day of prednisone at the time of scanning.

Follow-up gadopentetate-dimeglumine–enhanced MR studies were available in four patients. Three of the patients were treated with 20–65 mg/day of prednisone. In one patient (case 13), a right cerebellopontine angle granuloma markedly decreased in size after 2 months of therapy but then stabilized over the next 12 months. A second patient (case 7, Fig. 6) had resolution of abnormal enhancement around the third ventricle but persistent chiasmatic enhancement after 6 months of corticosteroid therapy (40 mg of prednisone/day tapered to 10 mg/day). In a third patient (case 4), an unenhanced study initially revealed brain edema adjacent to an area of slight falcine thickening. Follow-up unenhanced and

TABLE 2: Summary of Brain MR Imaging in Patients with CNS Sarcoidosis

Case No.	Meningeal Disease		Hypothalamus and Pituitary	Periventricular White Matter Lesions	Ependymal Enhancement	Parenchymal Involvement	Hydrocephalus
	Leptomeningeal	Dural					
1	Diffuse (G)	None	G	U	No	None	No
2	Diffuse (G)	None	None	G/U	No	Edema, encephalopathy, meningovasculopathy (G/U)	No
3	Diffuse (G)	None	G/U	None	No	None	No
4	Diffuse (G)	None	G/U	None	No	Edema (U)	No
5	Diffuse (G)	G	G/U	G/U	No	Edema, encephalopathy (G/U)	No
6	Diffuse (G)	G/U	None	None	No	Two parenchymal nodules without surrounding edema (G)	No
7	Focal (G)	None	G	G/U	No	No	Yes
8	Focal (G)	None	None	None	Yes	Cerebellar peduncle infarct (U)	Yes
9	Focal (G)	None	None	U	No	None	Shunted
10	Focal (G)	None	G/U	G	No	None	No
11	Focal (G)	None	None	G/U	No	Enhancing cerebellar peduncle and posterior temporal lesions (G/U)	No
12	None	G	G	None	No	Internal capsule lacune (U)	No
13	None	G/U	None	None	No	None	Shunted
14	None	None	None	None	No	None	No
15	None	None	None	None	No	None	No
16	None	None	None	None	No	None	No
17	Diffuse (G)	None	G	G/U	No	Edema, confluent nodules causing mass in temporal lobe (G/U)	No
18	Diffuse (G)	G/U	G/U	None	No	Edema, encephalopathy (G/U)	No
19	Diffuse (G)	None	G	None	Yes	None	Yes
20	Diffuse (G)	G	None	None	No	Edema, subfrontal mass extending into frontal lobe (G/U)	No

Note.—G = enhancing abnormality identified on gadopentetate-dimeglumine–enhanced MR; U = abnormality identified on unenhanced MR.

TABLE 3: Summary of MR Characteristics of CNS Sarcoidosis

Involved Area	T2-Weighted Images	T1-Weighted Images	T1-Weighted Images with Gadopentetate Dimeglumine
Leptomeninges	No lesions detected	No lesions detected	Diffuse involvement ($n = 10$); focal involvement ($n = 5$)
Dura	Hypointense plaque ($n = 3$); isointense mass ($n = 1$) [4]	Isointense mass ($n = 1$)	Focal mass/plaque ($n = 3$); sheetlike involvement ($n = 3$) [13]
Pituitary and infundibulum	No lesions detected	Isointense enlargement ($n = 5$)	Increased enhancement of infundibulum ($n = 5$) and pituitary ($n = 1$)
Optic chiasm	No lesions detected	Enlarged chiasm ($n = 5$) [4]	Enhancement of chiasm ($n = 6$) and optic nerves/tracts ($n = 2$)
Hypothalamus	Hyperintensity in anterior perforated substance ($n = 4$) and anterior commissure ($n = 2$) [14]	No lesions detected	Enhancement of hypothalamic area ($n = 4$) and fornix ($n = 2$)
White matter	Vasogenic edema ($n = 6$); patchy periventricular/subcortical lesions ($n = 6$) [4, 6, 8]	No lesions detected	Enhancement near lateral ventricles ($n = 3$), near third ventricle ($n = 3$), and near fourth ventricle ($n = 3$)
Gray matter	Heterogeneous infiltrations with edema ($n = 5$) and without edema ($n = 1$) [4, 6, 7]	Hypointense area ($n = 2$)	Small discrete nodules ($n = 5$); linear/confluent nodular areas in continuity with pial disease ($n = 4$)
Ventricles	Hydrocephalus with periventricular edema ($n = 3$); "ballooning" of fourth ventricle ($n = 1$)	Hydrocephalus ($n = 3$) [4, 6]	Periaqueductal enhancement ($n = 2$); fourth ventricle enhancement ($n = 4$)

Note.—There was more than one area of involvement in most patients. Cited literature illustrates characteristics of CNS sarcoid.

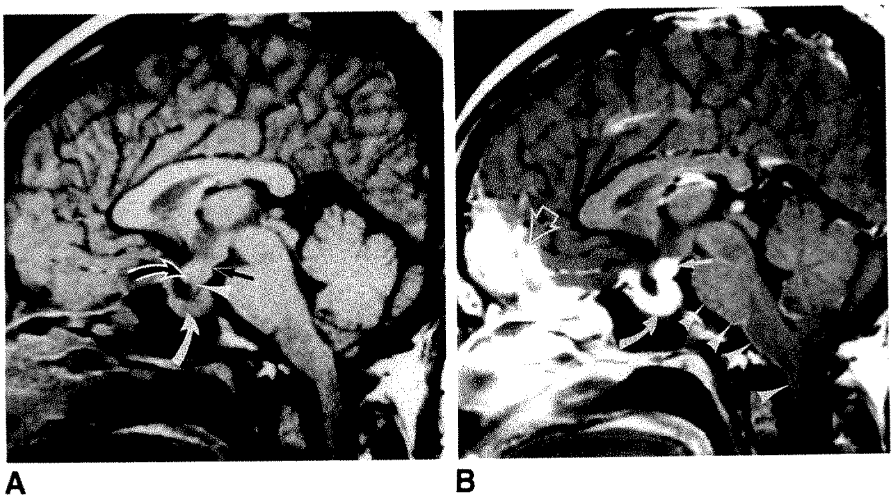

Fig. 1.—Case 4: 34-year-old woman with CNS sarcoidosis involving meninges, pituitary, and hypothalamus.

A, Unenhanced T1-weighted midsagittal image. Pituitary (*white arrow*), infundibulum (*arrowhead*), tuber cinereum (*straight arrow*), and chiasm (*curved black arrow*) are enlarged.

B, Contrast-enhanced T1-weighted midsagittal image shows extensive enhancement of falx and subfrontal meninges (*open arrow*). Note sharply demarcated enhancement of brainstem pia mater (*arrowheads*). Pituitary enhances intensely and is enlarged (*white arrow*). Enhancing pituitary infundibulum, tuber cinereum, and chiasm cannot be differentiated on enhanced image (*straight solid arrow*).

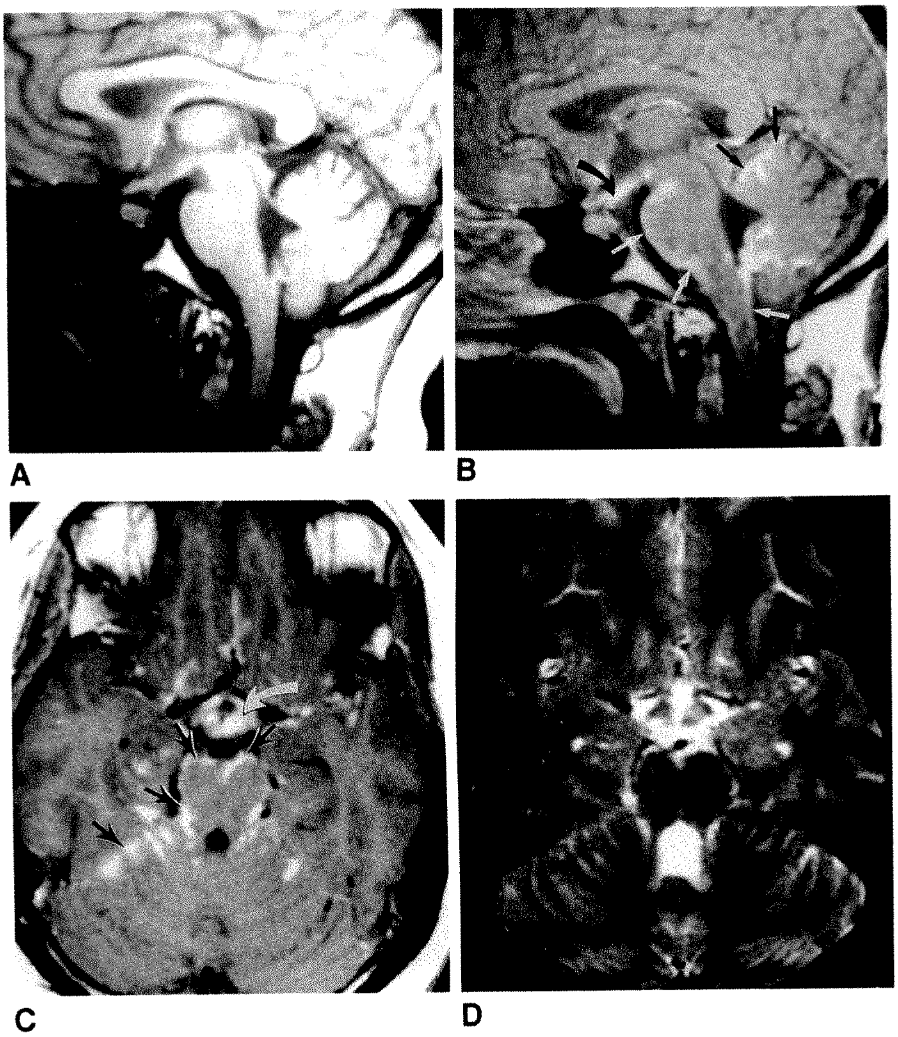

Fig. 2.—Case 1: 34-year-old woman with CNS leptomeningeal sarcoid.

A, Normal unenhanced T1-weighted midsagittal image.

B, Contrast-enhanced T1-weighted midsagittal image shows diffuse leptomeningeal enhancement. Note enhancement of chiasm (*curved arrow*), cerebellum, tectum, and margin of brainstem (*straight arrows*).

C, Enhanced T1-weighted axial image. Enhancement around midbrain and cerebellar hemisphere (*straight arrows*) indicates breakdown of blood-CSF barrier. Optic chiasm involvement (*curved arrow*).

D, T2-weighted image at same level shows no evidence of abnormal signal in brainstem. CSF-brain barrier is probably intact.

enhanced studies 10 months later revealed marked multifocal meningeal and hypothalamic enhancement (Fig. 1), but the brain edema had resolved without corticosteroid administration. The fourth patient (case 5), with extensive meningeal and hypothalamic involvement, was evaluated after 6 months and again after 10 months of suboptimal therapy (80 mg/day of prednisone was prescribed but the patient repeatedly missed doses). Brain edema initially improved but then remained unchanged. Extensive meningeal and parenchymal enhancement was present on the latest contrast-enhanced

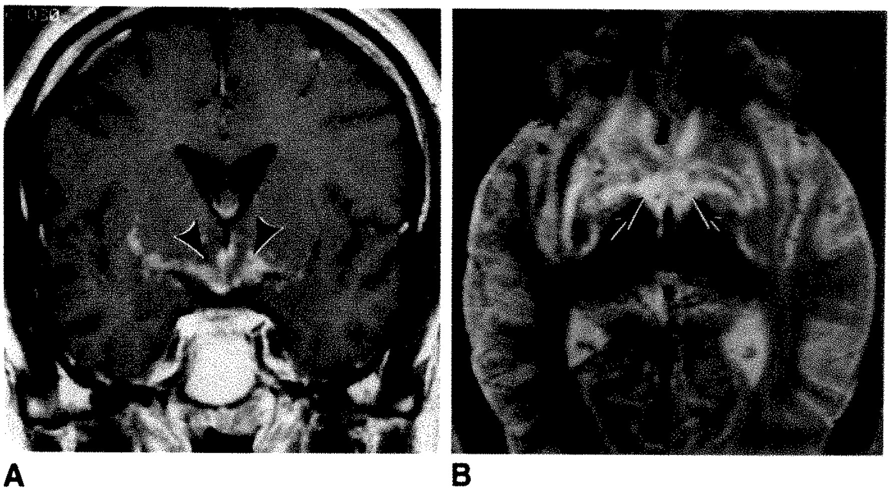

Fig. 3.—Case 5: 21-year-old man with leptomeningeal and hypothalamic involvement.

A, Coronal enhanced T1-weighted image. Note basilar leptomeningeal enhancement. Disease extends through anterior perforated substance into hypothalamus (*arrowheads*).

B, T2-weighted axial image reveals edema in base of brain (*arrows*).

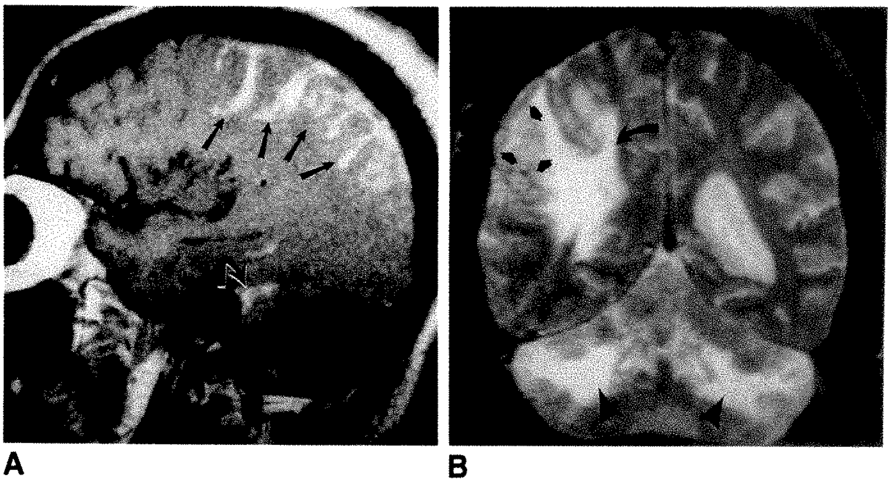

Fig. 4.—Case 2: 49-year-old man with meningoencephalovasculopathy.

A, Contrast-enhanced T1-weighted parasagittal image. Note extension of granulomatous disease deep into brain along Virchow-Robin spaces (*straight arrows*). Small area of enhancement (*curved arrow*) and large areas of hypointensity are noted in cerebellum.

B, T2-weighted coronal image. Cerebral cortical disease (*straight arrows*) and vasogenic edema (*curved arrow*). Cerebellar hyperintensity is not associated with mass effect and probably reflects chronic ischemic disease (*arrowheads*).

MR study (Fig. 3). Visual symptoms had increased. In case 17, CNS involvement increased despite chemotherapy with a regimen of prednisone (15 mg/day) and cyclosporine (trough blood level of 228 ng/ml).

Discussion

Our data concur with pathologic studies of CNS sarcoidosis that have shown that the most common sites of disease activity are the basal meninges; basal midline structures, especially hypothalamus; infundibulum; pituitary gland; and floor of the third ventricle [1, 14]. The pathologic manifestations of CNS sarcoidosis consist of granulomatous dural invasion with plaquelike or focal masses [4, 15], leptomeningitis, parenchymatous infiltration especially along the perivascular spaces of Virchow-Robin [16], and coalescence of granulomata in the brain parenchyma producing an intraaxial tumor [17]. Periventricular lesions in CNS sarcoidosis have been described also [1, 5, 8, 18].

Prior to the release of gadopentetate dimeglumine, our recommendation had been to perform both MR and contrast-enhanced CT [4]. Contrast-enhanced CT was most valuable in the detection of basal meningeal disease, while conventional unenhanced MR revealed involvement of the hypothalamus, optic chiasm, and brain parenchyma including periventricular white matter disease. However, this combined technique is still inadequate for evaluation of the meninges. Contrast-enhanced CT is suboptimal because of the Hounsfield artifact problem [13]. Unenhanced MR is suboptimal because of the poor contrast between bone, CSF, and meninges on both T1- and T2-weighted sequences.

The introduction of gadopentetate dimeglumine markedly increased the sensitivity of MR to the presence of meningeal disease [12]. We detected meningeal disease on the enhanced MR images in 17 patients, compared with unenhanced MR detection in three patients.

Sarcoidosis primarily involves the leptomeninges, which include both arachnoid and pia mater. The leptomeningeal pattern is recognized on enhanced MR images because the enhancement follows the contour of the brain, extending into the cortical sulci. Pial involvement can be differentiated from arachnoid involvement along the brainstem, where the arachnoid is separated from the pia by CSF in the cisternal subarachnoid space (Fig. 1). Here the pia mater is attached

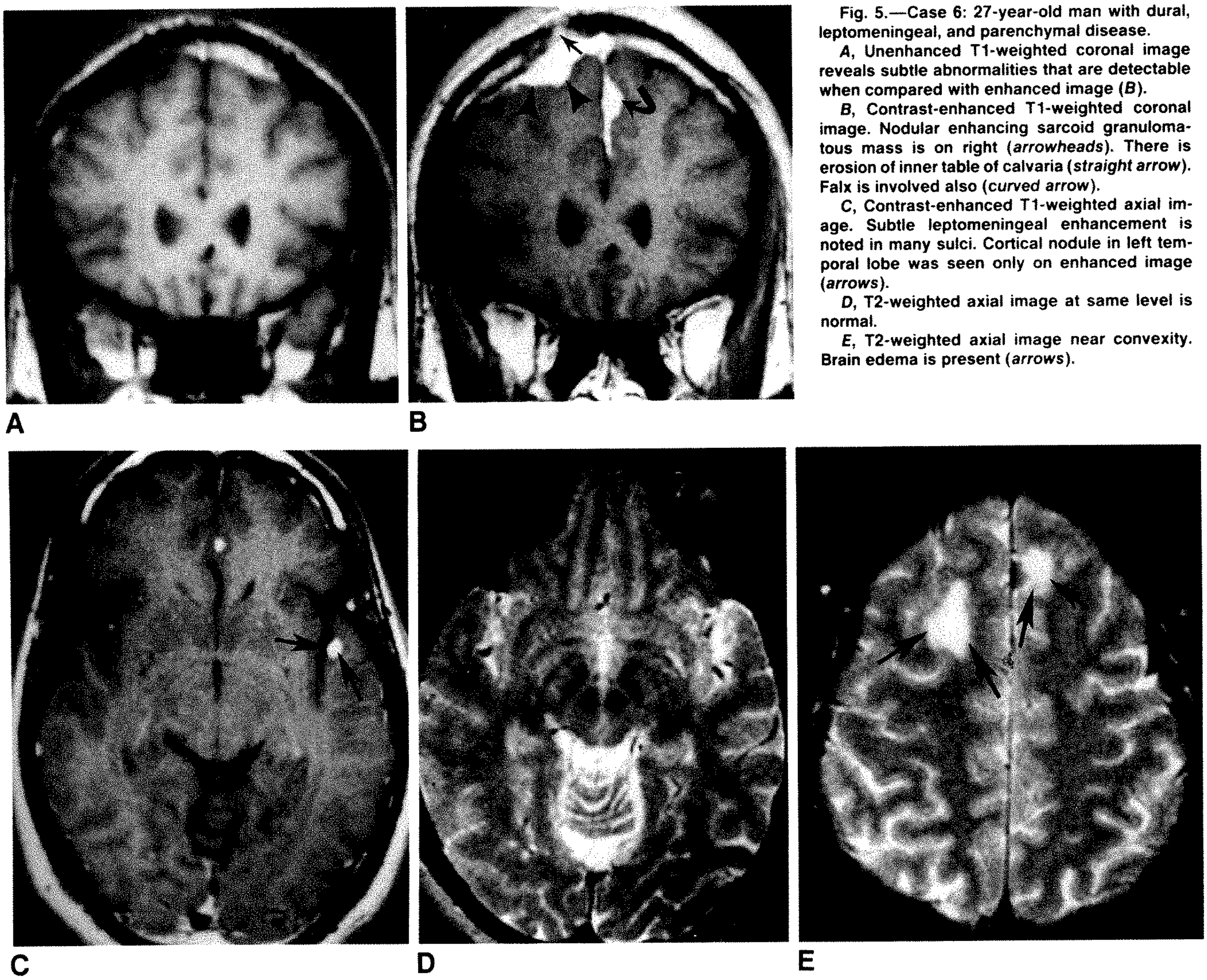

Fig. 5.—Case 6: 27-year-old man with dural, leptomeningeal, and parenchymal disease.

A, Unenhanced T1-weighted coronal image reveals subtle abnormalities that are detectable when compared with enhanced image (*B*).

B, Contrast-enhanced T1-weighted coronal image. Nodular enhancing sarcoid granulomatous mass is on right (*arrowheads*). There is erosion of inner table of calvaria (*straight arrow*). Falx is involved also (*curved arrow*).

C, Contrast-enhanced T1-weighted axial image. Subtle leptomeningeal enhancement is noted in many sulci. Cortical nodule in left temporal lobe was seen only on enhanced image (*arrows*).

D, T2-weighted axial image at same level is normal.

E, T2-weighted axial image near convexity. Brain edema is present (*arrows*).

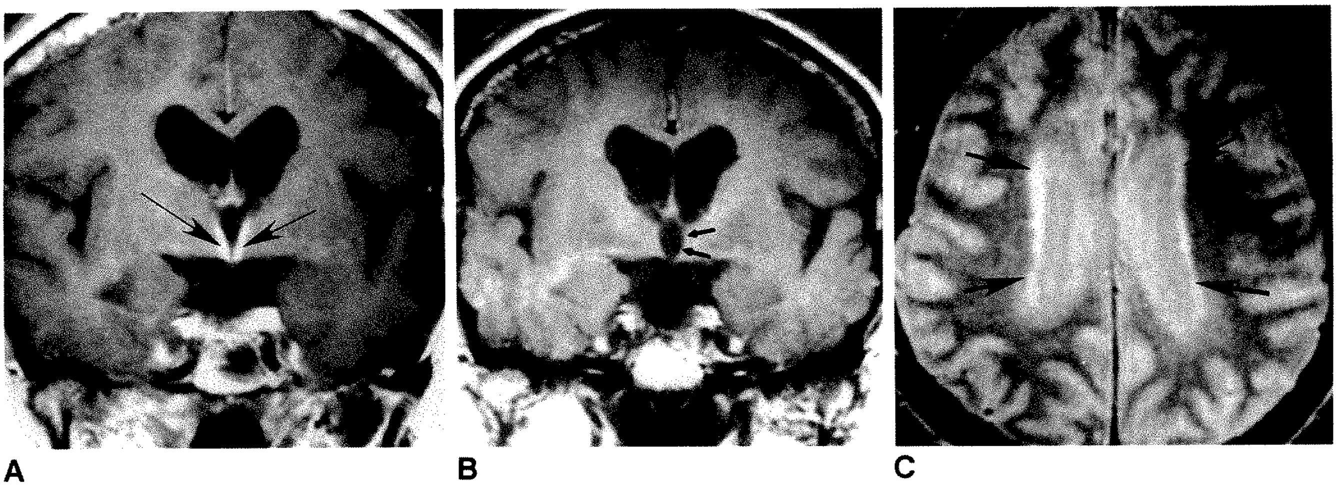

Fig. 6.—Case 7: 58-year-old woman with periventricular and hypothalamic disease.

A, Contrast-enhanced T1-weighted coronal image. Enhancing tissue along margin of third ventricle (*arrows*) causes slight compression of ventricle.

B, Contrast-enhanced T1-weighted image after 6 months of prednisone therapy. There has been resolution of enhancement and relief of mass effect (*arrows*). Note rounded appearance of third ventricle compared with *A*.

C, T2-weighted axial image (pretreatment). Note periventricular areas of increased intensity (*arrows*).

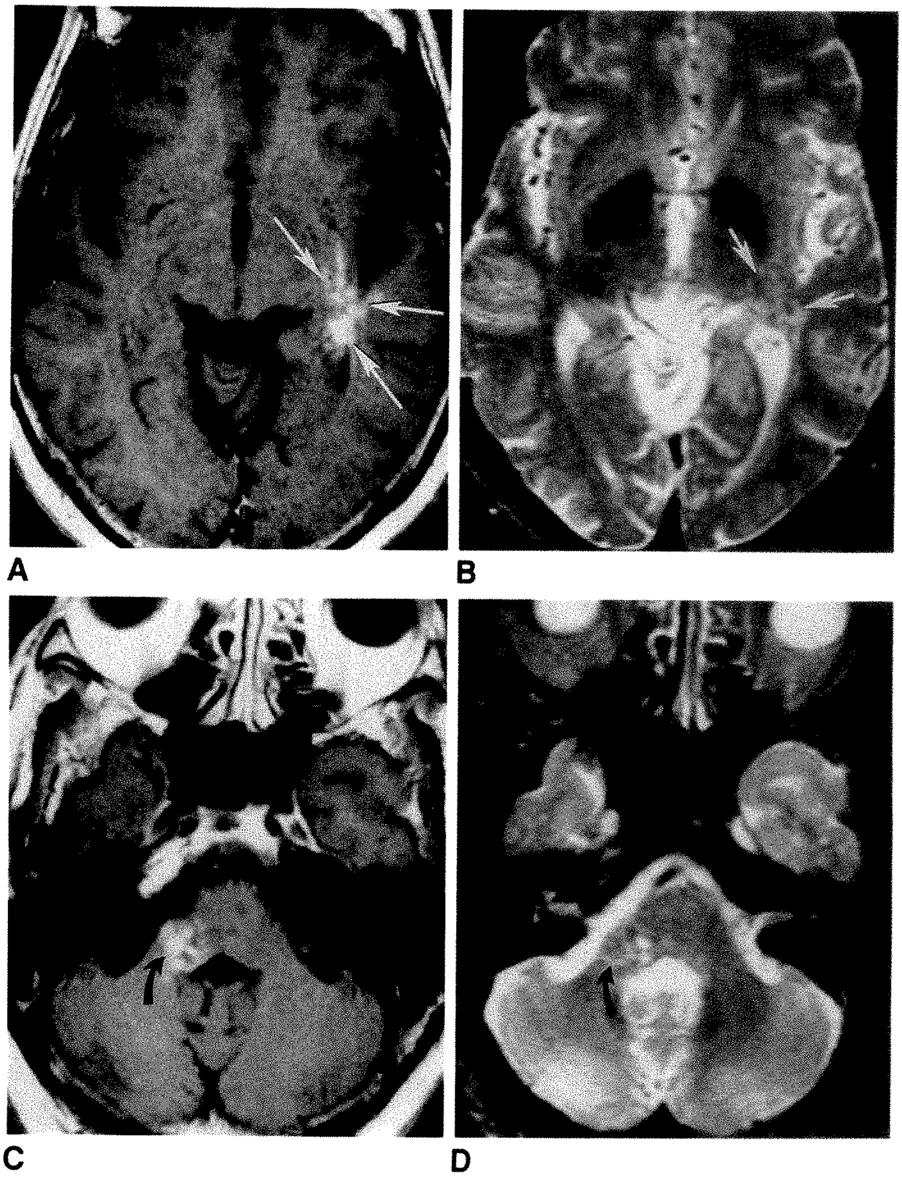

Fig. 7.—Case 11: 57-year-old man with parenchymal disease.

A, Contrast-enhanced T1-weighted axial image. Enhancing lesion involves subcortical and periventricular areas (*arrows*).

B, T2-weighted axial image. Small areas of increased intensity are present but there is no evidence of vasogenic edema (*arrows*).

C, Contrast-enhanced T1-weighted axial image in posterior fossa shows enhancing lesion in right middle cerebellar peduncle (*arrow*).

D, T2-weighted axial image. Small area of increased intensity indicates presence of granulomatous lesion (*arrow*). Note absence of vasogenic edema.

intimately to the neuroparenchyma and is detached from the arachnoid.

Capillary endothelial cells of the arachnoid have tight junctions, as do those in the brain, creating a CSF-blood barrier [19]. The basement membrane of the pia and adherent astrocytic foot processes creates a pial-brain barrier. In an animal model of meningeal carcinomatosis, Frank et al. [20] have shown that gadolinium not only enhances the infiltrated meninges but leaks into the contiguous CSF. Disruption of the capillary endothelial tight junctions of the arachnoid mater by disease most likely accounts for the passage of gadolinium into the adjacent pia mater and subarachnoid space [21].

Penetrating cerebral vessels are invested in a leptomeningeal sheath with a potential space continuous with subarachnoid space (the Virchow-Robin space) [16]. The first effect of leptomeningitis is meningeal vascular hyperemia. The ensuing inflammatory exudate spreads in the subarachnoid space and into the Virchow-Robin spaces to a variable degree. Infiltration may occur along the surface of the brain or extend deep into the brain along the Virchow-Robin spaces. The infiltrating process may appear intraparenchymal on gross examination or on MR images, but histologically the disease may remain restricted to the leptomeninges. A meningoencephalovasculopathy occurs when the pial-brain barriers are invaded by the inflammatory process [20].

Although we do not have direct pathologic correlation, progressive severity of the breakdown in the pial barriers can be inferred by noting the thickness of the pial enhancement, particularly along the brainstem. We speculate that if pial enhancement is seen as a sharply defined fine line there is disruption of the barriers, but probably no infiltration along perivascular spaces into the brain (Fig. 1). If the pial enhancement is thick and ragged (Fig. 4), then invasion along perivascular spaces has probably occurred, causing a meningoencephalovasculopathy, as has been shown on contrast-enhanced CT with pathologic correlation [16]. Enhancing linear and nodular areas extending from the pial surface into the white matter indicate infiltration along Virchow-Robin spaces (Figs. 3 and 4).

Inflammation originating in the Virchow-Robin space can spread and coalesce, in the case of sarcoidosis, into granulomatous masses (Figs. 5 and 7). When this occurs there is often adjacent edema due to disruption of the blood-brain barrier and increased vascular permeability that extends along white matter fascicles (vasogenic edema) [22–24]. However, areas of blood-brain barrier disruption may be present without associated edema (Fig. 7). Vasogenic edema should be differentiated from chronic ischemic gliosis secondary to vasculopathy and perforating vessel occlusion caused by infiltration of Virchow-Robin spaces [16].

Dural involvement, although less frequent, is more likely than leptomeningeal disease to be detected on unenhanced MR. As noted previously [4], the only manifestations of CNS sarcoidosis on unenhanced MR images may be subtle falcine thickening or focal plaque formation. We have seen meningeal sarcoid produce a mass over the convexity [4], in the middle cranial fossa, and in the cerebellopontine angle. The varied appearances of CNS sarcoidosis on unenhanced MR are reviewed in Table 3. Typically there is intense enhancement in the abnormal area if gadopentetate dimeglumine is administered (Fig. 5). Falcine disease may develop as a consequence of local leptomeningeal granulomatous inflammation.

Sze et al. [13] anecdotally reported one patient with CNS sarcoidosis in whom the most striking abnormality was diffuse dural enhancement with minimal leptomeningeal enhancement.

Any portion of the brain can be affected by sarcoidosis, but the basal portion is the most common location [2, 25]. This correlates with recent observations that CSF-filled Virchow-Robin spaces are routinely visualized in the basal areas of the brain [26, 27]. Anatomically this area includes the anterior perforated substance, which is characterized by numerous penetrating, small blood vessels [28]. In addition, the blood-brain barrier is absent in the tuber cinereum, hypophysis, and preoptic region [24].

Hypothalamic dysfunction is the most common manifestation of CNS parenchymatous disease in sarcoidosis [1]. Seven of our patients had disease of the hypothalamic-pituitary axis (Figs. 1, 3, and 6). Pituitary infiltration by sarcoidosis is often reported histologically in patients with systemic sarcoidosis, but we are unaware of any report in the imaging literature [2, 29]. Optic chiasm and infundibular "thickening" are other common manifestations of CNS sarcoidosis on MR. The optic chiasm is enveloped by pia mater and therefore is subject to granulomatous leptomeningitis. Thickening of the chiasmatic pia as well as infiltration of the optic pathway can cause enlargement of the chiasm.

Seven of our patients had diffuse or focal areas of increased intensity in the periventricular white matter on T2-weighted images (Figs. 6 and 7). In two patients, periventricular white matter disease was detected only on T2-weighted images. Periventricular white matter lesions in CNS sarcoidosis have been reported previously [4, 8, 30]. In two patients the periventricular white matter disease resembled the common pattern of multiple sclerosis [31, 32]; in three patients the pattern was more typical of ischemic disease [33, 34]. In two patients probable mild interstitial edema was associated with hydrocephalus. One patient had extensive bilateral cerebellar gliosis or white matter infarctions that were hyperintense on T2-weighted images. The typical pattern of vasogenic edema was not seen and there was only mild meningeal enhancement around the cerebellum after administration of gadopentetate dimeglumine.

Hydrocephalus is a common manifestation of CNS sarcoidosis [1–3]. Granulomatous leptomeningitis may cause extraventricular obstructive hydrocephalus (communicating hydrocephalus) [6] or fourth ventricular outlet obstruction [18, 35]. Granulomatous compression of the aqueduct [16] and fourth ventricle [18] also may occur. Infiltration of the ependyma and choroid plexus may alter CSF dynamics resulting in hydrocephalus [2, 18]. Ependymal enhancement and prominent enhancement of the choroid plexus at the foramina of Luschka was seen in one of our patients (case 8).

There are several possible explanations for normal gadopentetate-dimeglumine–enhanced MR studies in our three patients with cranial nerve involvement. There may be extracranial involvement of the cranial nerves. There may be focal leptomeningeal or endoneurial disease that is too small to visualize or does not disrupt the blood-brain and pial barriers [2]. For example, some patients with aseptic and bacterial meningitis have normal gadopentetate-dimeglumine MR studies even if extraventricular obstructive hydrocephalus is present [11, 36]. Studies of carcinomatous meningitis have suggested that a minimum amount of tumor is required before enhancement is observed in the meninges on the enhanced images [13, 20]. There may have been reestablishment of the CSF-pial-brain barrier, thus preventing contrast enhancement despite the presence of active meningeal disease [20, 36]. We observed one patient in whom abnormal periventricular enhancement resolved after 6 months of therapy (Fig. 6).

The differential diagnosis of CNS sarcoidosis is quite broad. None of the unenhanced MR or gadopentetate-dimeglumine–enhanced manifestations of sarcoidosis are specific. Tuberculosis [37], fungal diseases, and bacterial [11, 36, 38] infections can produce diffuse leptomeningitis that may enhance on gadopentetate-dimeglumine MR. Meningeal carcinomatosis, leukemia, and lymphoma are indistinguishable from CNS sarcoidosis on MR [13]. We have seen diffuse meningeal enhancement following subarachnoid and subdural hemorrhage. Diffuse dural fibrosis following ventricular shunting has been shown to enhance intensely, but leptomeningeal involvement has been absent [39]. Less common diseases that could be diagnostic considerations in some cases include meningiomatosis [40], lipogranulomatosis [41], and cranial pachymeningitis [42].

Summary

1. It is important to understand that CNS sarcoidosis is foremost a leptomeningeal disease and the Virchow-Robin spaces are extensions of the leptomeninges. Study of gadopentetate-dimeglumine–enhanced images of the brain has solidified this concept.

2. We recommend the use of gadopentetate dimeglumine in all patients being evaluated for CNS sarcoidosis. Unenhanced MR alone is unlikely to reveal the important leptomeningeal manifestations of this disease.

3. Normal unenhanced and gadopentetate-dimeglumine–enhanced MR does not exclude CNS sarcoidosis, especially in patients with only cranial neuropathy or in those patients being treated with corticosteroids.

4. Enhancement with gadopentetate dimeglumine can resolve with corticosteroid treatment.

ACKNOWLEDGMENTS

We thank Stephen Reich, John Griffin, Claudio Levin, Penelope Scott, Gary Cassel, Justin McArthur, Thomas Price, Thomas Kowalski, Barbara Joslow, Philip Pulaski, Ben Frishberg, Andy Barbash, Robert Baumgartner, Sharon Seltzer, Patricia Behlmer, and Don Wood for patient referrals and Andrea Zanin and Shirley Zabrek for organizational and administrative assistance.

REFERENCES

1. Stern BJ, Krumholz A, Johns C, Scott P, Nissim J. Sarcoidosis and its neurological manifestations. *Arch Neurol* **1985**;42:909–917
2. Delaney P. Neurologic manifestations of sarcoidosis. *Ann Intern Med* **1977**;87:336–345
3. Ricker W, Clark M. Sarcoidosis: a clinical pathologic review of 300 cases, including 22 autopsies. *Am J Clin Pathol* **1949**;19:725–749
4. Hayes WS, Sherman JL, Stern BJ, Citrin CM, Pulaski PD. MR and CT evaluations of intracranial sarcoidosis. *AJNR* **1987**;8:841–847, *AJR* **1987**;149:1043–1049
5. Ketonen L, Oksanen V, Kuuliala I. Preliminary experience of magnetic resonance imaging in neurosarcoidosis. *Neuroradiology* **1987**;29:127–129
6. Miller DH, Kendall BT, Barter S, et al. Magnetic resonance imaging in central nervous system sarcoidosis. *Neurology* **1988**;38:378–383
7. Martin N, Debroucker T, Mompoint D, et al. Sarcoidosis of the pineal region: CT and MR studies. *J Comput Assist Tomogr* **1989**;13:110–112
8. Smith AS, Meisler DM, Weinstein MA, et al. High-signal periventricular lesions in patients with sarcoidosis: neurosarcoidosis or multiple sclerosis? *AJNR* **1989**;10:485–490
9. Berry I, Brant-Zawadzki M, Osaki L, Brasch R, Murovic J, Norman D. Gd-DTPA in clinical MR of the brain. 2. Extraaxial lesions and normal structures. *AJR* **1986**;147:1231–1235
10. Hesselink JR, Healy ME, Press GA, Brahme FJ. Benefits of Gd-DTPA for MR imaging of intracranial abnormalities. *J Comput Assist Tomogr* **1988**;12:266–274
11. Mathews VP, Kuharik MA, Edwards MK, D'Amour PG, Azzarelli B, Dreesen RG. Gd-DTPA–enhanced MR imaging of experimental bacterial meningitis: evaluation and comparison with CT. *AJNR* **1988**;9:1045–1050
12. Runge VM, Schaible TF, Goldstein HA, et al. Gd-DTPA clinical efficacy. *RadioGraphics* **1988**;8:147–159
13. Sze G, Soletsky S, Bronen R, Krol G. MR imaging of the cranial meninges with emphasis on contrast enhancement and meningeal carcinomatosis. *AJNR* **1989**;10:965–975
14. Delaney P. Neurologic manifestations in sarcoidosis. Review of the literature, with a report of 23 cases. *Ann Intern Med* **1977**;87:336–345
15. Osenbach RK, Blumenkopf B, Ramirez H, Gutierrez J. Meningeal neurosarcoidosis mimicking convexity en-plaque meningioma. *Surg Neurol* **1986**;26:387–390
16. Mirfakhraee M, Crofford MJ, Guinto FC, Nauta HJ, Weedn VW. Virchow-Robin space: a path of spread in neurosarcoidosis. *Radiology* **1986**;158:715–720
17. Kumpe DA, Rao CVGK, Garcia JH, et al. Intracranial neurosarcoidosis. *J Comput Assist Tomogr* **1979**;3:324–330
18. Schlitt M, Duvall ER, Bonnin J, Morawetz RB. Neurosarcoidosis causing ventricular loculation, hydrocephalus and death. *Surg Neurol* **1986**;26:67–71
19. Dyer ML, Parker JC. The meninges and their reactions to injury. In: Davis RL, Robertson DM, eds. *Textbook of neuropathology*. Baltimore: Williams & Wilkins, **1985**:138–146
20. Frank JA, Girton M, Dwyer AJ, Wright DC, Cohen PJ, Doppman JL. Meningeal carcinomatosis in the VX2 rabbit tumor model: detection with Gd-DTPA–enhanced MR imaging. *Radiology* **1988**;167:825–829
21. Ushio Y, Shimizu K, Aragaki Y, Arita N, Hayakawa T, Mogami H. Alteration of blood-CSF barrier by tumor invasion into the meninges. *J Neurosurg* **1981**;55:445–449
22. Klatzo I. Neuropathological aspects of brain edema. *J Neuropathol Exp Neurol* **1967**;26:1–11
23. Klatzo I, Suzuki R, Orzi R, Schuier F, Nitsch C. Pathomechanisms of ischemic brain edema. In: *Proceedings of the fifth international symposium on brain edema. Gronningen, the Netherlands 1982*. New York: Plenum, **1984**:1–10
24. Sage MR. Blood-brain barrier: phenomenon of increasing importance to the imaging clinician. *AJR* **1982**;138:887–898
25. Clark WC, Acker JD, Dohan FC, Robertson JH. Presentation of central nervous system sarcoidosis as intracranial tumors. *J Neurosurg* **1985**;63:851–856
26. Heier LA, Bauer CJ, Schwartz L, Zimmerman RD, Morgello S, Deck MDF. Large Virchow-Robin spaces: MR-clinical correlation. *AJNR* **1989**;10:929–936
27. Jungreis CA, Kanal E, Hirsch WL, Martinez AJ, Moosey J. Normal perivascular spaces mimicking lacunar infarction: MR imaging. *Radiology* **1988**;169:101–104
28. Crosby EC, Humphrey T, Lauer EW. *Correlative anatomy of the nervous system*. New York: Macmillan, **1962**:412–433
29. Bleisch VR, Robbins SL. Sarcoid-like granulomata of the pituitary gland. *Arch Intern Med* **1952**;89:877–892
30. Miller DH, Kendall BE, Barter S, et al. Magnetic resonance imaging in central nervous system sarcoidosis. *Neurology* **1988**;38:378–383
31. Horowitz AL, Kaplan RD, Grewe G, White RT, Salbert LM. The ovoid lesion: a new MR observation in patients with multiple sclerosis. *AJNR* **1989**;10:303–305
32. Uhlenbrock D, Seidel D, Gehlen W, et al. MR imaging in multiple sclerosis: comparison with clinical, CSF, and visual evoked potential findings. *AJNR* **1988**;9:59–67
33. Awad IA, Spetzler RF, Hodak JA, et al. Incidental subcortical lesions identified on magnetic resonance imaging in the elderly. I. Correlation with age and cerebrovascular risk factors. *Stroke* **1986**;162:509–511
34. Awad IA, Johnson PD, Spetzler RF, et al. Incidental subcortical lesions identified on magnetic resonance imaging in the elderly. II. Postmortem pathological correlations. *Stroke* **1986**;17:1090–1097
35. Lukin RR, Chambers AA, Soleimanpour M. Outlet obstruction of the fourth ventricle in sarcoidosis. *Neuroradiology* **1975**;10:65–68
36. Matthews VP, Smith RR, Bognanno JR, Kuharik MA, Edwards MK, Harris TM. Gd-DTPA enhanced MRI of meningitis; initial clinical experience (abstr). *AJNR* **1989**;10:1020
37. Suss RA, Resta S, Diehl JT. Persistent cortical enhancement in tuberculous meningitis. *AJNR* **1987**;8:716–720
38. Brown E, DeLaPaz R. Enhancement of meningeal lesions with gadopentetate (Gd-DTPA) MRI (abstr). *AJNR* **1989**;10:877
39. Destian S, Heier LA, Zimmerman RD, Morgello S, Deck MDF. Differentiation between meningeal fibrosis and chronic subdural hematoma after ventricular shunting: value of enhanced CT and MR scans. *AJNR* **1989**;10:1021–1026
40. Aoki S, Barkovich AJ, Nishimura K, et al. Neurofibromatosis types 1 and 2: cranial MR findings. *Radiology* **1989**;172:527–534
41. Tien RD, Brasch RC, Jackson DE, Dillon WP. Cerebral Erdheim-Chester disease: persistent enhancement with Gd-DTPA on MR images. *Radiology* **1989**;172:791–792
42. Martin N, Masson C, Henin D, Mompoint D, Marsault C, Nahum H. Hypertrophic cranial pachymeningitis: assessment with CT and MR imaging. *AJNR* **1989**;10:477–484

Book Review

Magnetic Resonance Imaging and Computed Tomography of the Head and Spine. By C. Barrie Grossman. Baltimore: Williams & Wilkins, 465 pp., 1990. $125

It was a pleasure to read and review this book. In these days of edited books with multiple contributors, a book of this scope written by one author is a formidable achievement. The book is divided into four major sections: basic technical considerations; the brain; the skull base, skull, and face; and the spine. Each major section is divided into detailed subsections. The largest section is on the spine. A detailed table of contents is supplemented by a complete index. The topics are organized in a logical fashion, and needless repetition is avoided by having one author and good editing.

The illustrations are of uniformly high quality and have appropriate annotations and explanations. Because of its completeness, this book can be used as an atlas. The writing style is clear and terse, and the sections are distinct enough that the book can be used as a reference. Most entities have clinical and pathologic correlation, pertinent incidence statistics, and differential diagnostic considerations. The information is referenced heavily, and the bibliographies at the end of each subsection make an excellent up-to-date study guide.

The strength of this book is the smooth integration of the CT, MR, and clinicopathologic findings of each entity discussed. Where pertinent, illustrations and tables on differential diagnosis enrich and emphasize the salient points. The author frequently suggests the best and the most appropriate view to appreciate the pathologic lesions discussed. Although individual experiences may differ, these suggestions are consistently good places to start. In other instances, Grossman discusses MR technique, including the best choice of field of view or type of coil. I think this can be most helpful in cases of unusual disease processes or difficult diagnostic situations. The use of contrast material in each imaging technique is addressed for its effectiveness in showing pathologic changes. Although the book discusses pediatric neuroradiology, the cranial nerves, and AIDS as integral parts of different chapters, I would like to see separate sections on these topics in future editions. In addition, a separate index for illustrations would be helpful.

I have seen no other books in this field that have the same intense focus on CT and MR applications to neuroradiology. Because of this book's specific purpose and concise writing style, a level of previous experience and interest is assumed. Therefore, anyone who reads this book should be comfortable with the terminology of CT, MR, and neuroradiology.

In many ways, I think this is one book many have been looking for to tie together neuroradiology and the new technologies. It stands out among other books with similar titles and purposes as a standard for others to be compared with. I heartily recommend this book to all radiologists, neuroclinicians, and interested technologists. It is a worthwhile investment in time and money for the reader.

E. V. Grayson
Memorial Hospital
Hollywood, FL 33021

Spinal Cord Ischemia After Resection of Thoracoabdominal Aortic Aneurysms: MR Findings in 24 Patients

Michel E. Mawad[1]
Victor Rivera[2]
Stanley Crawford[3]
Ariel Ramirez[2]
Wini Breitbach[2]

MR images of the thoracic spinal cord were made in 24 patients who developed signs and symptoms of spinal cord ischemia or infarction following surgery for a thoracoabdominal aortic aneurysm. Findings consisted primarily of four different patterns of signal abnormalities in the distribution of the anterior spinal artery. These abnormalities were identified as types A–D, depending on the degree of involvement of the gray matter and surrounding white matter. We found good correlation between the distribution of the signal abnormalities in the cord, the severity of the neurologic deficits, and the clinical outcome.

MR is the imaging method of choice for diagnosing spinal cord ischemia or infarction. A thorough knowledge of the spinal cord arterial territories is crucial for characterizing ischemic MR signal abnormalities and for differentiating them from other causes of myelopathy.

***AJNR* 11:987–991, September/October 1990; *AJR* 155:1303–1307, December 1990**

Spinal cord ischemia or infarction is a rare clinical disorder that presents with signs and symptoms referable primarily to the lower thoracic cord and conus medullaris, and often results in the rapid onset of paraplegia and bowel and bladder dysfunction. It affects predominantly the older age group, particularly in the presence of risk factors such as atherosclerosis, diabetes, and hypertension. A major predisposing factor for spinal cord ischemia or infarction is the presence of a large thoracoabdominal aortic aneurysm involving the intercostal artery, which gives rise to the anterior spinal artery or artery of Adamkiewicz. All patients included in the present study had a thoracoabdominal aortic aneurysm and became symptomatic following surgical repair of the aneurysm. The diagnosis of spinal cord ischemia is based on the abrupt onset of the clinical symptoms and the predisposing factors. Nevertheless, other possible causes of lower thoracic myelopathy need to be excluded. MR has become the imaging method of choice for evaluating spinal cord ischemia, because it reliably excludes other causes of myelopathy such as extramedullary compressive lesions, intramedullary expansile neoplasms, or cavities. More important, it detects subtle signal abnormalities intrinsic to the spinal cord, which corroborate the clinical suspicion of spinal cord ischemia.

Materials and Methods

Forty patients developed symptoms of spinal cord ischemia following resection and graft replacement of thoracoabdominal aortic aneurysms. The patients consisted of 25 males and 15 females, 16 to 89 years old. In 24 patients, MR studies were obtained on a Siemens Magnetom 1.0-T scanner: these patients comprise the subjects of this report. Scanning parameters included sagittal T1-weighted images, 450/25/2 (TR/TE/excitations); axial T1-weighted images, 450/25/2; and axial T2-weighted double-echo images, 3000/90/1. Slice thickness was 4–5 mm, with an interslice gap of 1 mm.

Received September 23, 1989; revision requested December 20, 1989; revision received April 18, 1990; accepted April 26, 1990.

[1] Department of Radiology, The Methodist Hospital, Baylor College of Medicine, 6565 Fannin, M.S. 033, Houston, TX 77030. Address reprint requests to M. E. Mawad.

[2] Department of Neurology, The Methodist Hospital, Baylor College of Medicine, Houston, TX 77030.

[3] Department of Cardiovascular Surgery, The Methodist Hospital, Baylor College of Medicine, Houston, TX 77030.

0361–803X/90/1556–1303
© American Roentgen Ray Society

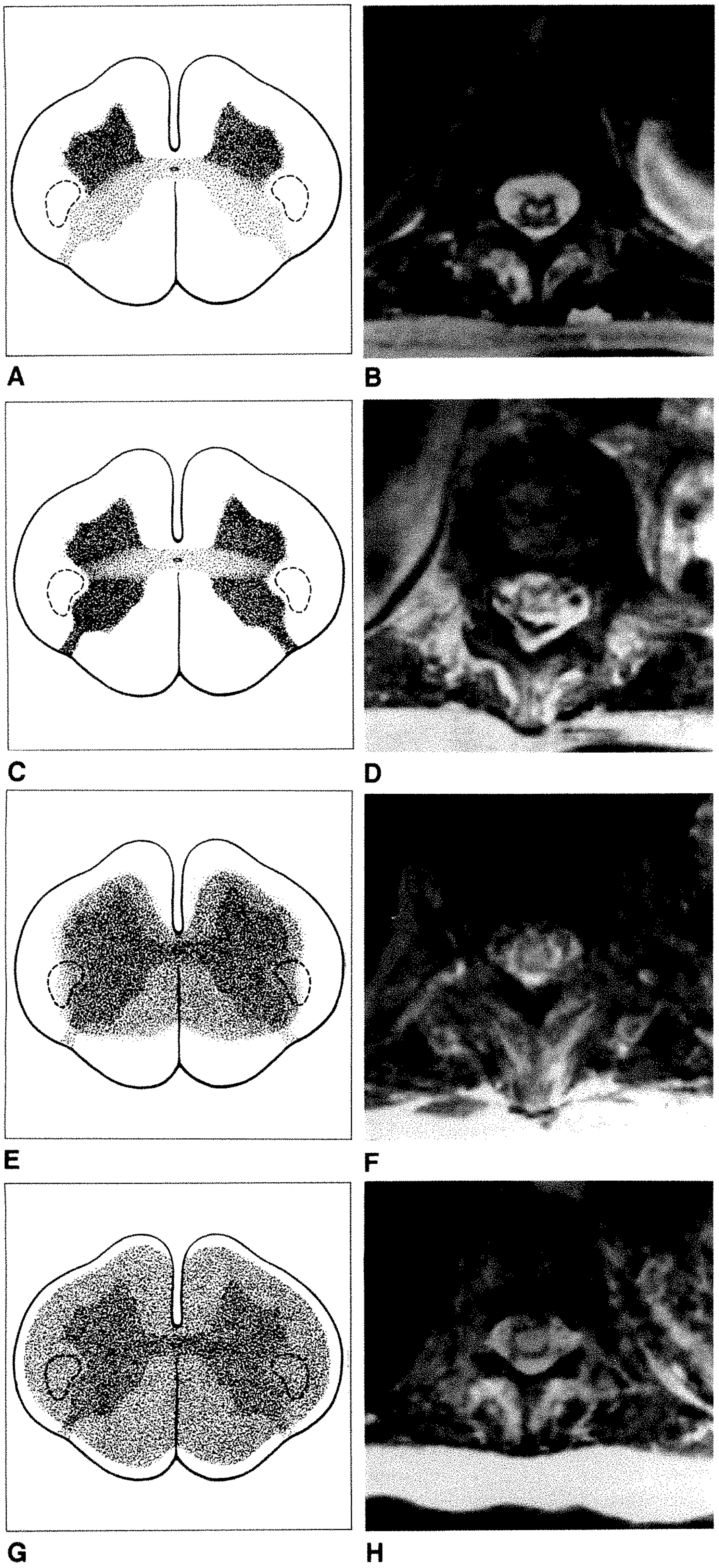

Fig. 1.—Patterns of MR signal abnormalities in spinal cord ischemia.

A and *B*, Type A: focal signal abnormality involving primarily the anterior horns of the gray matter: "owl's eyes" pattern. Schematic (*A*) and axial T2-weighted MR image, 3000/90/1, (*B*).

C and *D*, Type B: signal abnormality involving both the anterior and posterior horns of the gray matter. Schematic (*C*) and axial T2-weighted MR image, 3000/90/1, (*D*).

E and *F*, Type C: signal abnormality involving the entire gray matter and the adjacent central white matter. Schematic (*E*) and axial T2-weighted MR image, 3000/90/1, (*F*).

G and *H*, Type D: diffuse signal abnormality involving the entire cross section of the spinal cord. Schematic (*G*) and axial T2-weighted MR image, 3000/90/1 (*H*).

TABLE 1: Clinical/MR Correlation in Spinal Cord Ischemia (n = 17)

Initial Clinical Presentation	Location of Aneurysm	Location of MR Abnormality	Somatosensory Evoked Potential	MR Signal Abnormalities	Motor Function[a]
Spinal cord TIA (4)	Midthoracic	1 = Low thoracic 3 = Low thoracic and conus	Abnormal	Focal, limited to gray matter	Ambulatory (5/5)
Spinal cord RIND (1)	Midthoracic	Low thoracic	Abnormal	Focal, limited to gray matter	Ambulatory (5/5)
Completed spinal cord stroke (12)	Midthoracic and thoracoabdominal	1 = Low thoracic 1 = Low thoracic and conus 5 = Conus 5 = Mid-, low thoracic and conus	Abnormal	Diffuse, involving both gray and white matter	Nonambulatory (0/5)

Note.—RIND = reversible ischemic neurologic deficit.

[a] Motor function assessed on the muscle strength scale (range, 0–5).

Results

MR studies were abnormal in 17 patients, which correlated well with the results of the somatosensory evoked potential studies, which were abnormal in all 17 (see Table 1). All the signal abnormalities seen on the MR studies were found in the low thoracic cord and conus medullaris, regardless of the severity of the clinical findings. The MR signal abnormalities in the spinal cord were best seen on the axial proton-density-weighted (short TE/long TR) and T2-weighted (long TE/long TR) scans. The T1-weighted studies were equivocal at best; occasionally they showed ill-defined signal abnormalities intrinsic to the spinal cord manifested primarily by irregular and heterogeneous foci of prolongation of T1 without definite enlargement of the spinal cord. The abnormalities on the double-echo studies were more striking and were classified into four patterns depending on the distribution of the signal abnormalities inside the spinal cord (Fig. 1).

Table 1 correlates the findings between the initial clinical presentation, location of the operated aneurysms, MR signal abnormalities, results of the somatosensory evoked potential studies, and the clinical outcome.

All patients who developed spinal cord ischemia after aortic surgery and had abnormal MR scans also had predisposing risk factors such as hypertension, diabetes mellitus, atherosclerosis, chronic obstructive pulmonary disease, or a history of cerebral infarction. The majority of these patients had aneurysms of the descending aorta reaching to or extending below the diaphragm. Three major groups of neurologic signs and symptoms related to spinal cord ischemia can be identified: spinal cord TIAs manifested by transient motor deficit and sphincter dysfunction that resolve without residual neurologic deficit, spinal cord reversible ischemic neurologic deficit with minor residual neurologic deficit (motor = 4/5 on the muscle strength scale), and completed spinal cord stroke with devastating clinical outcome including flaccid paraplegia and complete sphincter dysfunction. All of the completed spinal cord strokes occurred in patients with thoracic and thoracoabdominal aortic aneurysms.

Discussion

Spinal cord ischemia or infarction is a rare clinical disease that affects primarily the older age group usually with a devastating outcome. Patients with atherosclerosis, hypertension, diabetes, or a history of cerebral stroke are at higher risk of developing spinal cord ischemia than are others in the same age group. Most cases of spontaneous spinal cord ischemia occur in patients with a thoracoabdominal aortic aneurysm; the presumed mechanism is the occlusion of the intercostal artery giving rise to the anterior spinal artery. Dissecting thoracoabdominal aortic aneurysms, especially those with a left-sided false lumen, are associated with a higher incidence of spinal cord ischemia, because in 85% of the population the anterior spinal artery arises from the left lower intercostal vessels.

Thirty-one pairs of radicular arteries [1, 2] penetrate the spinal canal through the intervertebral foramina; approximately seven or eight of these 62 radicular branches contribute to the vascularization of the spinal cord and define three major spinal arterial territories: cervicothoracic, midthoracic, and thoracolumbar (Fig. 2).

The cervicothoracic territory includes the cervical spinal cord, its brachial plexus enlargement, and the first two or three thoracic segments. This territory is richly supplied by the anterior spinal artery arising from the intracranial vertebral arteries, the midcervical radicular branches of the vertebral artery, and the branches of the costocervical trunk.

The midthoracic territory is usually supplied by a radicular branch arising at about the T7 level; it comprises the fourth to eighth segments of the thoracic cord.

The thoracolumbar territory includes, in addition to the lower thoracic segments, the lumbar enlargement, which relates to the lumbosacral plexus. This segment derives its blood supply from a single artery described in 1882 by Adamkiewicz. In about 75% of the cases, this artery originates from the ninth, 10th, 11th, or 12th intercostal arteries. In about 10% of cases, it arises from the first or second lumbar arteries. In about 15% of cases it arises from the higher intercostal vessels (i.e., from T5 through T8). When the artery of Adamkiewicz originates from a high intercostal vessel, there usually is a supplemental arterial supply to the conus medullaris from a smaller radicular branch originating more inferiorly.

When they reach the surface of the spinal cord, the radicular arteries form two distinct systems of intrinsic blood supply to the spinal cord (Fig. 3). The first system is a posterolateral

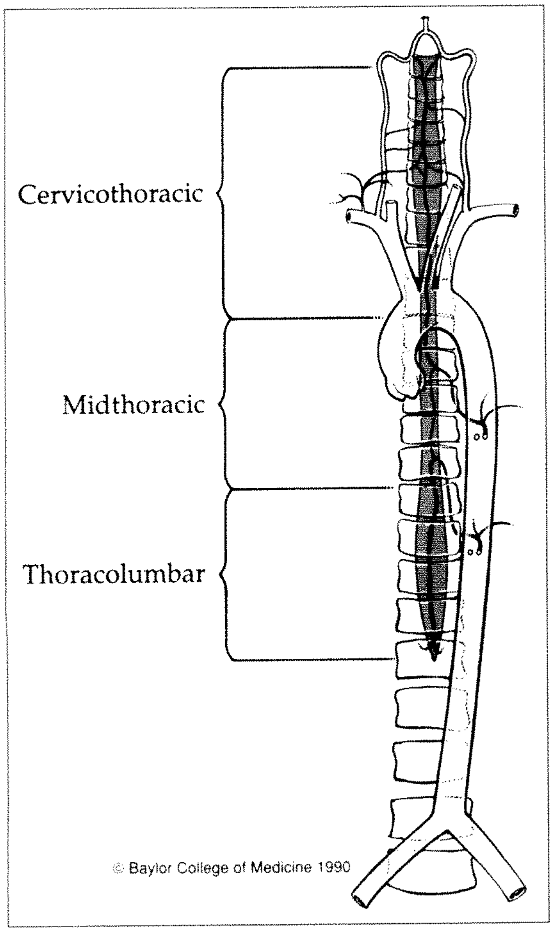

Fig. 2.—Schematic showing arterial territories of spinal cord.

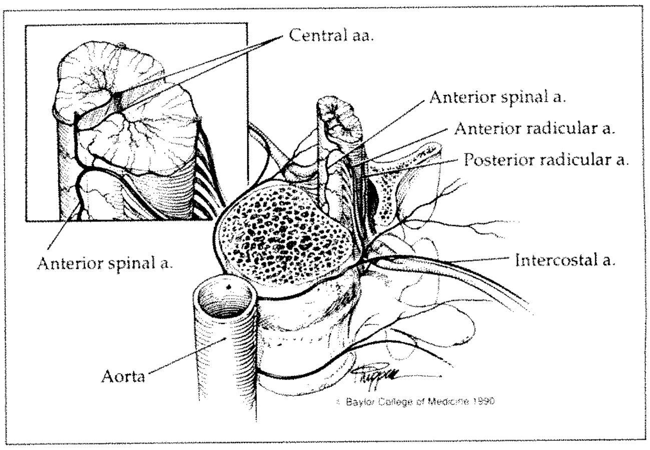

Fig. 3.—Schematic showing intrinsic blood supply of spinal cord.

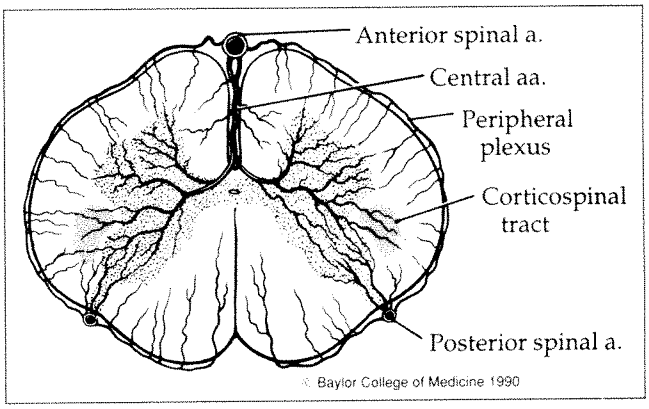

Fig. 4.—Schematic showing cross-sectional territory of anterior spinal artery.

and peripheral plexus formed primarily by the two posterior spinal arteries that run longitudinally along the posterolateral sulcus of the cord and are richly interconnected by anastomotic channels [3]. This is a centripetal vascular territory with penetrating branches that supply from one third to one half of the outer rim of the spinal cord. The second arterial system intrinsic to the spinal cord is a centrifugal system formed by numerous alternating central arteries that arise from the anterior spinal artery, run horizontally in the central sulcus, and turn alternately to the right and left [4]. This centrifugal system supplies the central gray matter and an adjacent mantle of central white matter, which includes the corticospinal tracts (Fig. 4).

The number of central arteries supplying each segment of the spinal cord varies with the region of the cord [5]. They are most numerous in the thoracolumbar segment and least numerous in the upper thoracic segment. The intrinsic arterial blood supply to the spinal cord is directly proportional to the cross-sectional area of the gray matter [6], which is most abundant in the thoracolumbar segment and has a much higher metabolic rate than the white matter. Therefore, in normal conditions, the blood flow to the spinal cord is highest in the thoracolumbar segment, which has the highest concentration of central arteries owing to the relative abundance of gray matter. Consequently, the same segment is the most vulnerable to hypoperfusion, particularly the gray matter that corresponds to the lumbar enlargement of the spinal cord. Ischemia or infarction in the distribution of the anterior spinal artery rapidly leads to cytotoxic and vasogenic edema in the gray matter with subsequent increase in mobile water. This is manifested by a focal increase in the proton density and a lengthening of the T2 relaxation time, which appears as distinct foci of increased signal intensity on the short TE/long TR and long TE/long TR pulse sequences. The signal abnormalities start in the anterior horns of the gray matter and, with increasing severity of ischemia, spread posteriorly to involve the posterior horns. Ultimately, the ischemic changes and corresponding MR signal abnormalities extend laterally to the posterolateral funiculi of the spinal cord, including the crossed corticospinal tracts. In severe cases, the whole cross section of the spinal cord is infarcted. The patterns of signal abnormality described above reflect a temporal sequence of ischemic changes that can often be recognized as distinct, separate stages. The MR appearance, however, is frequently a mixture of patterns, particularly in the patients with completed spinal cord stroke. The early stage of signal abnormalities, which is limited to the anterior horns of the gray matter and has an "owl's eyes" appearance, is the most characteristic of the four patterns and the most often recognized.

It becomes evident from the above discussion that axial double-echo MR studies are necessary for the diagnosis of spinal cord ischemia, since the geographic distribution of the signal abnormalities within the gray matter cannot be accurately displayed on sagittal scans. In addition, well-positioned scans with cardiac gating and motion-suppression gradients, as well as proper patient sedation, are necessary to avoid artifactual signal abnormalities in the center of the cord.

There seems to be a correlation between the distribution of the MR signal abnormalities and the severity of the clinical symptomatology seen in spinal cord ischemia. Cases in which the increased signal intensity was limited to the anterior horns of the gray matter had some preservation of motor function and a better clinical outcome than those in which the signal abnormalities were more diffuse and involved the adjacent central white matter. This region of the white matter may be supplied by either the centrifugal arterial system dependent on the anterior spinal artery or the centripetal peripheral system arising from the posterior spinal arteries. The collateral arterial circulation and the presence of small accessory anterior spinal arteries arising from the lower thoracic intercostal or upper lumbar vessels play a major role in the prevention of spinal cord ischemia when the anterior spinal artery is occluded. Infarction of the spinal cord related to aortic disease or corrective aortic surgery depends almost solely on the individual variation in spinal cord arterial blood supply and its potential collaterals. It would be beneficial to know the level of origin of the anterior spinal artery and the potential for collateral circulation to the lower thoracic cord in patients with thoracoabdominal aortic aneurysm undergoing surgical correction. This would, however, require spinal arteriography, which becomes technically difficult, if not dangerous, in patients with atherosclerotic aorta and a thoracoabdominal aneurysm.

Several theories have been advanced to explain the pathogenesis of spinal cord ischemia following corrective aortic surgery, and these involve major technical factors [7]. Hypoperfusion in the abdominal aorta due to clamping seems to play a major role in inducing spinal cord ischemia, particularly when the period of clamping exceeds a certain time limit. Several authors have recommended protective measures during surgery, such as hypothermia, left heart bypass, or jump grafts to avoid significant blood pressure drop in the aorta distal to the clamp. Others have abandoned these measures with no significant change in the occurrence of spinal cord ischemia following aortic surgery [8]. The declamping syndrome after declamping of the infrarenal aorta is another possible technical factor responsible for spinal cord ischemia. It may be circumvented by moderate volume loading prior to declamping in an effort to avoid hypoperfusion of the spinal cord.

Spinal cord tamponade by increased pressure of the CSF during clamping of the aorta may also lead to spinal cord ischemia during aortic surgery [9, 10]. Clamping of the aorta leads to an increase in intracranial pressure, which is followed by a shift of CSF into the spinal subarachnoid space and a subsequent rise in the spinal CSF pressure. This rise in CSF pressure can tamponade the spinal cord at a time when its blood supply is compromised, resulting in spinal cord ischemia.

Conclusions

Spinal cord ischemia or infarction involves primarily the lower thoracic cord and conus medullaris. It affects predominantly the central gray matter in a somewhat predictable fashion. In our series, all cases resulted from corrective surgery on the aorta to repair a thoracoabdominal aortic aneurysm. In these circumstances the onset of motor deficit in the lower extremities, particularly when associated with sphincter dysfunction, is strongly suggestive of spinal cord ischemia. MR of the lower thoracic cord and conus medullaris has become the imaging method of choice—not only to detect signal abnormalities intrinsic to the cord but also to exclude other causes of thoracic myelopathy. The abnormal signal intensities start in the territory of the anterior spinal artery and spread to the adjacent central white matter. The extent of signal abnormalities correlates well with the severity of the clinical findings and the potential for recovery. The frequency of spinal cord ischemia or infarction following corrective surgery of the aorta remains unpredictable given the individual variation of the spinal cord blood supply. Despite the refinement of surgical techniques and the various protective measures to diminish its risk, the rate of occurrence of this complication has perhaps reached an irreducible minimum.

REFERENCES

1. Lazorthes G, Gouaze A, Zadeh JO, et al. Arterial vascularization of the spinal cord. *J Neurosurg* **1971**;35:253–269
2. Lazorthes G, Poulhes J, Bastide G, et al. La vascularization arterielle de la moelle. *Neurochirurgie* **1958**;4:3–19
3. Gillilan L. The arterial blood supply of the human spinal cord. *J Comp Neurol* **1958**;110:75–103
4. Herren RY, Alexander L. Sulcal and intrinsic blood vessels of human spinal cord. *Archives of Neurology & Psychiatry* **1939**;41:678–687
5. Woollam DHM, Millen JW. The arterial supply of the spinal cord and its significance. *J Neurol Neurosurg Psychiat* **1955**;18:97–102
6. Suh TH, Alexander L. Vascular system of the human spinal cord. *Arch Neurol Psychiatry* **1939**;41:660–676
7. Ross RT. Spinal cord infraction in disease and surgery of the aorta. *Can J Neurol Sci* **1985**;12:289–295
8. DeBakey ME, McCullom CH, Crawford ES, et al. Dissection and dissecting aneurysm of the aorta: twenty year follow-up of five hundred twenty-seven patients treated surgically. *Surgery* **1982**;92:118–134
9. Brusoni B, Colombo A, Merlo L, et al. Hemodynamic and metabolic changes induced by temporary clamping of the thoracic aorta. *Eur Surg Res* **1978**;10:206–216
10. Blaisdell FW, Cooley DA. The mechanism of paraplegia after temporary thoracic occlusion and its relationship to spinal fluid pressure. *Surgery* **1962**;51:355–361

FORTHCOMING ARTICLES

SPECIAL ARTICLE

Barium enemas, latex balloons, and anaphylactic reactions. *Gelfand DW*

REVIEW ARTICLES

Color Doppler flow imaging. *Foley WD, Erickson SJ*

The evaluation of coronary bypass graft patency: a review of direct and indirect techniques other than coronary arteriography. *Stanford W, Galvin JR, Skorton DJ, Marcus ML*

CT of the gastrointestinal tract: principles and interpretation. *Balthazar EJ*

PROGRESS IN RADIOLOGY

Selective salpingography and fallopian tube recanalization. *Thurmond AS*

CARDIOPULMONARY RADIOLOGY

The detection of ACTH-producing bronchial carcinoid tumors: comparison of MR imaging with CT. *Doppman JL, Pass HI, Nieman LK, et al.*

Pictorial essay. High-density mediastinal masses on unenhanced CT. *Glazer HS, Molina PL, Siegel MJ, Sagel SS*

Diaphragmatic rupture due to blunt trauma: sensitivity of plain chest radiographs. *Gelman R, Mirvis SE, Gens D*

BREAST RADIOLOGY

Status of residency training in mammography in 1990. *Bassett LW, Cassady CI, Gold RH*

GASTROINTESTINAL RADIOLOGY

Pictorial essay. Endoscopic sonography of the upper gastrointestinal tract. *Botet JF, Lightdale C*

Thickening at the root of the superior mesenteric artery on sonography: evidence of vascular involvement in patients with cancer of the pancreas. *Kosuge T, Makuuchi M, Takayama T, Yamamoto J, Kinoshita T, Ozaki H*

Long-term soft-tissue effects of biliary extracorporeal shock waves: an animal study. *Rawat B, Wolber R, Burhenne HJ*

Technical note. Percutaneous transluminal biopsy of biliary strictures with a bioptome. *Terasaki K, Wittich GR, Lycke G, et al.*

Hepatic vein duplex Doppler sonographic findings in tricuspid regurgitation. *Abu-Yousef MM*

Portal venous system after portosystemic shunts or endoscopic sclerotherapy: evaluation with Doppler sonography. *Rice S, Lee KP, Johnson MB, Korula J, Ralls PW*

Case report. Peliosis hepatis in a patient with human immunodeficiency virus infection. *Radin DR, Kanel GC*

CT of acute pancreatitis: correlation between contrast enhancement and necrosis. *Johnson CD, Stephens DH, Sarr MG*

Case report. Pancreatitis with pseudoaneurysm formation: a pitfall for the interventional radiologist. *Lee MJ, Saini S, Geller SC, Warshaw AL, Mueller PR*

GENITOURINARY RADIOLOGY

Endoluminal sonography of the urinary tract: preliminary observations. *Goldberg BB, Bagley D, Liu J-B, Merton DA, Alexander A, Kurtz AB*

Renal transplant rejection: diagnosis using ^{31}P MR spectroscopy. *Grist TM, Charles HC, Sostman HD*

MUSCULOSKELETAL RADIOLOGY

Failure of MR imaging to detect reflex sympathetic dystrophy of the extremities. *Koch E, Hofer HO, Sialer G, Marincek B, von-Schulthess GK*

MR of the knee: a low-signal band parallel to the posterior cruciate ligament on sagittal images caused by a displaced bucket-handle tear. *Weiss KL, Morehouse HT, Levy IM*

MR imaging of displaced bucket-handle tear of the medial meniscus. *Singson RD, Feldman F, Staron R, Kiernan H*

Rheumatoid arthritis of the knee: value of gadopentetate dimeglumine–enhanced MR imaging. *Adam G, Dammer M, Bohndorf K, Christoph R, Fenke F, Günther RW*

Pictorial essay. MR imaging of the lateral collateral ligament of the ankle. *Erickson SJ, Smith JW, Ruiz ME, et al.*

PEDIATRIC RADIOLOGY

Urethral abnormalities in male neonates with VATER association. *Fernbach SK*

Sonography in neonatal congenital adrenal hyperplasia. *Sivit CJ, Hung W, Taylor GA, Catena LM, Brown-Jones C, Kushner DC*

Mediastinal pseudomass caused by compression of the thymus in neonates with anterior pneumothorax. *O'Keeffe FN, Swischuk LE, Stansberry SD*

Case report. Normal sonographic appearance of a thanatophoric-dwarf-variant fetus at 13 weeks gestation. *Macken MB, Grantmyre EB, Rimoin DL, Lachman RS*

Case report. CT of acute splenic torsion in children with wandering spleens. *Herman TE, Siegel MJ*

Case report. Pulmonary emboli as a primary manifestation of Wilms tumor. *Bulas DI, Thompson R, Reaman G*

NEURORADIOLOGY

Focal high signal on MR scans of the midbrain caused by enlarged perivascular spaces: MR-pathologic correlation. *Elster AD, Richardson DN*

Normal venous anatomy of the brain: demonstration with gadopentetate dimeglumine in enhanced 3-D MR angiography. *Chakeres DW, Schmalbrock P, Brogan M, Yuan C, Cohen L*

TECHNICAL NOTE

Atherectomy facilitated by long vascular sheaths. *Porter DH, Kim D, Siegel JB, Storella JM, Silverstone DZ*

PERSPECTIVE

Analysis of the cost effectiveness of PACS. *Hilsenrath PE, Smtih WL, Berbaum KS, Franken EA, Owen DA*

RADIOLOGY TEACHING

Effective audiovisual presentation. *Sagel SS, Ramsey RG*

MEETING NEWS

Tenth annual meeting and postgraduate course of the Society of Uroradiology, September 1990. *Whalen E*

Wernicke Encephalopathy: MR Findings in Five Patients

Massimo Gallucci[1]
Alessandro Bozzao
Alessandra Splendiani
Carlo Masciocchi
Roberto Passariello

Wernicke encephalopathy is a disease usually related to chronic alcoholism. The clinical diagnosis is often difficult to establish, and CT is unable to provide specific findings. MR follow-up studies in five patients affected by Wernicke encephalopathy were performed with the aim of establishing the sensitivity of MR in depicting the typical diencephalic/mesencephalic lesions. All subjects had MR imaging in the acute phase of the disease and were reexamined 6–12 months later, at which time they were in good health. Three of them also had CT scanning. On MR, hyperintense areas seen surrounding the third ventricle and aqueduct during the acute phase of the disease had disappeared or diminished on follow-up evaluations. The third ventricle and aqueduct were dilated. We suggest that these findings reflect the natural evolution of Wernicke encephalopathy.

The MR findings in Wernicke encephalopathy enable early diagnosis of the disease, which has a positive effect on both treatment and prognosis.

AJNR **11:887–892, September/October 1990;** ***AJR*** **155:1309–1314 December 1990**

Wernicke encephalopathy is the most severe neurologic complication of chronic alcoholism. It is caused by a nutritional deficiency of thiamine, which is why it is observed mainly, but not exclusively, in alcoholics.

Circumscribed mesencephalic/diencephalic lesions, which are typical of the disease [1–6], are responsible for a severe deterioration of consciousness as well as for focal neurologic symptoms. These symptoms, which may be single or multiple, usually occur suddenly. The clinical diagnosis is often difficult to establish, and CT findings are neither constant nor specific [7, 8]. MR is highly sensitive in detecting demyelinating, vascular, and degenerative diseases and therefore is a nearly ideal diagnostic tool for Wernicke encephalopathy. In this article, we report five cases of Wernicke encephalopathy in which typical mesencephalic and diencephalic lesions were documented by MR in the acute and chronic phases.

Subjects and Methods

Five patients, four men and one woman 22–47 years old (average age, 37), were admitted to the study. They had all been alcoholics at one time (with a daily consumption of ethanol of at least 80 g) and all presented suddenly with bilateral sixth cranial nerve palsy (one case), bilateral third cranial nerve palsy (one case), internuclear ophthalmoplegia (one case), right sixth cranial nerve palsy (one case), and vertical nystagmus (one case).

The neurologic symptoms started 4–72 hr before our examination, increased gradually, and were always associated with headache and vomiting. Neurologic examination revealed a global confusional state in three and ataxia of gait in four. Four patients also exhibited vestibular signs (vestibular paresis). Possible differential diagnoses included brainstem neoplasms (possibly metastatic in one patient who had undergone a laryngectomy 2 years before) and demyelinating or vascular diseases. Plain and enhanced CT examinations were obtained in three patients.

MR was performed with an Ansaldo Esatom/MR 5000 unit (Esaote-Biomedica, Genova, Italy) operating at a 0.5-T magnetic field. Spin-echo (SE) sequences, 1800/50–150/2 (TR/TE/

Received October 4, 1989; revision requested December 15, 1989; revision received February 2, 1990; accepted February 6, 1990.

[1] Cattedra di Radiologia, Università dell'Aquila, Ospedale "S.M. di Collemaggio," 67100 L'Aquila, Italy. Address reprint requests to M. Gallucci.

0361–803X/90/1556–1309
© American Roentgen Ray Society

excitations), were obtained with a 5- or 7-mm thickness (axial) for the whole brain and a 5-mm thickness (coronal) through the periaqueductal regions and third and fourth ventricles. Sagittal SE 350/30/2 scans with a 4-mm thickness were obtained also.

The patients were reexamined after 6–12 months. Neurologic evaluation showed normal ocular motility. Nystagmus on extreme gaze persisted in two patients. All were in good general health.

Results

Acute Phase

CT scans in three subjects showed a nonenhancing hypodense area around the aqueduct in one case (Figs. 1A and 1B). In all subjects T2-weighted sequences revealed a signal hyperintensity surrounding the third ventricle and aqueduct (Figs. 1C, 2A–2D, 3A, and 3B). In particular, the hyperintense area around the third ventricle showed a suggestive "double-wing" configuration (Figs. 2C, 2D, 3A, and 3B). Sagittal scans also showed no evidence of the mamillary bodies in four cases (Figs. 2I–2K).

The presence of these lesions and their correlation with pathologic periaqueductal changes described in postmortem studies, together with the history of chronic alcohol abuse and accompanying clinical symptoms, led to the diagnosis of Wernicke encephalopathy.

Laboratory findings showed moderate macrocytic anemia and platelet reduction, with sideropenia in four patients, while a marked elevation of blood pyruvate was evident in all cases. Blood transketolase assay performed in four subjects showed a marked reduction of the enzyme levels with a thiamine pyrophosphate effect up to 50%. For these reasons, medical therapy was prescribed, with 50 mg thiamine and 30 mg folate intramuscularly every day.

Follow-up

MR, performed with the same equipment and techniques as in the original study, showed lower intensities or fewer regions of hyperintensity than previously, and revealed third ventricle enlargement with aqueductal dilatation. The tissue degeneration, suggested by the hyperintensities detected on the first examinations, appeared to have developed into tissue atrophy (Figs. 1E, 1F, 2E–2H, 3C, and 3D). The CT scan was normal in the only case in which the brainstem lesion was evident. Laboratory findings were normal.

Discussion

Clinical and Physiopathologic Aspects

The true prevalence of Wernicke encephalopathy is clearly higher than is diagnosed clinically, since pathognomonic lesions have been found in up to 2.2% of consecutive series of autopsies in adults [6, 9]. It would seem that the prevalence of the disease is not influenced by the sex of the patients, though it is slightly higher in males [9]; the age of onset ranges from 30 to 70 years [5].

The symptomatology of Wernicke encephalopathy is characterized by nystagmus, abducens and conjugate gaze palsies, ataxia of the gait, and confusion [5, 9, 10]. Consequently, the triad of clinical features described by Wernicke (ophthalmoplegia, ataxia, and mental confusion) is still diagnostically useful [11]. These symptoms may follow a slowly evolving pattern or, conversely, be characterized by an abrupt onset. In either case, early thiamine therapy may successfully modify the evolution of the disease [5].

Capillary proliferation and myelin degeneration in Wernicke encephalopathy were described in 1928 [1]. Marked intracellular edema with swelling of astrocytes, oligodendrocytes, myelin sheaths, and neuronal dendrites is considered to be the earliest finding [12]. More advanced changes are represented by demyelination [10], petechial hemorrhage, and astrocytic, microglial proliferation with relative neuronal sparing. The lesions, always symmetric, are typically located around the third ventricle and involve the mamillary bodies, the pineal and periaqueductal regions, and the brainstem (Fig. 4) [1, 2, 10].

The exact mechanisms underlying the pathogenesis of the lesions observed in Wernicke encephalopathy are not understood completely. Thiamine's phosphoric esters are involved in the function of excitable membranes, glucose metabolism, and neurotransmitter production [2]. Thiamine-deficient membranes are unable to maintain osmotic gradients, resulting in swelling of intra- and extracellular spaces [13]. In the periventricular regions, the blood-brain barrier is defective [3, 14] and there is a high rate of thiamine-related glucose and oxidative metabolism [3]. For this reason thiamine deficiency may render this structure more susceptible to failure in transport mechanism [2]. Thiamine is administered to cause attenuation of the edema [15, 16] and promote reparative changes (glial and vascular proliferation) and remyelination [17, 18].

All these pathologic features, primarily resulting from vitamin B1 deprivation [4, 19], are generally, but not necessarily, related to chronic alcohol intoxication [20–22].

The diagnosis of Wernicke encephalopathy is generally based on the combination of history, clinical symptoms, and laboratory results; thus, many cases are misdiagnosed during the patient's lifetime, as has been reported by Harper [6].

Neuroradiologic Aspects

CT is usually of little help in the diagnosis of this disease [7], even if in some cases it is possible to show brainstem lesions. In fact, in only one of our cases was CT able to detect a hypodense area around the aqueduct. However, we should mention that this lesion was the largest observed in our series, and that it was shown by MR even on T1-weighted sequences (Fig. 1). MR offered the possibility of demonstrating similar lesions in all the cases studied, giving more satisfactory criteria for the identification of Wernicke encephalopathy.

To our knowledge the only study concerning the MR evaluation of Wernicke encephalopathy was the one published by Drayer [23] in 1988. Drayer reported a single case of Wernicke encephalopathy in which hyperintense areas were seen

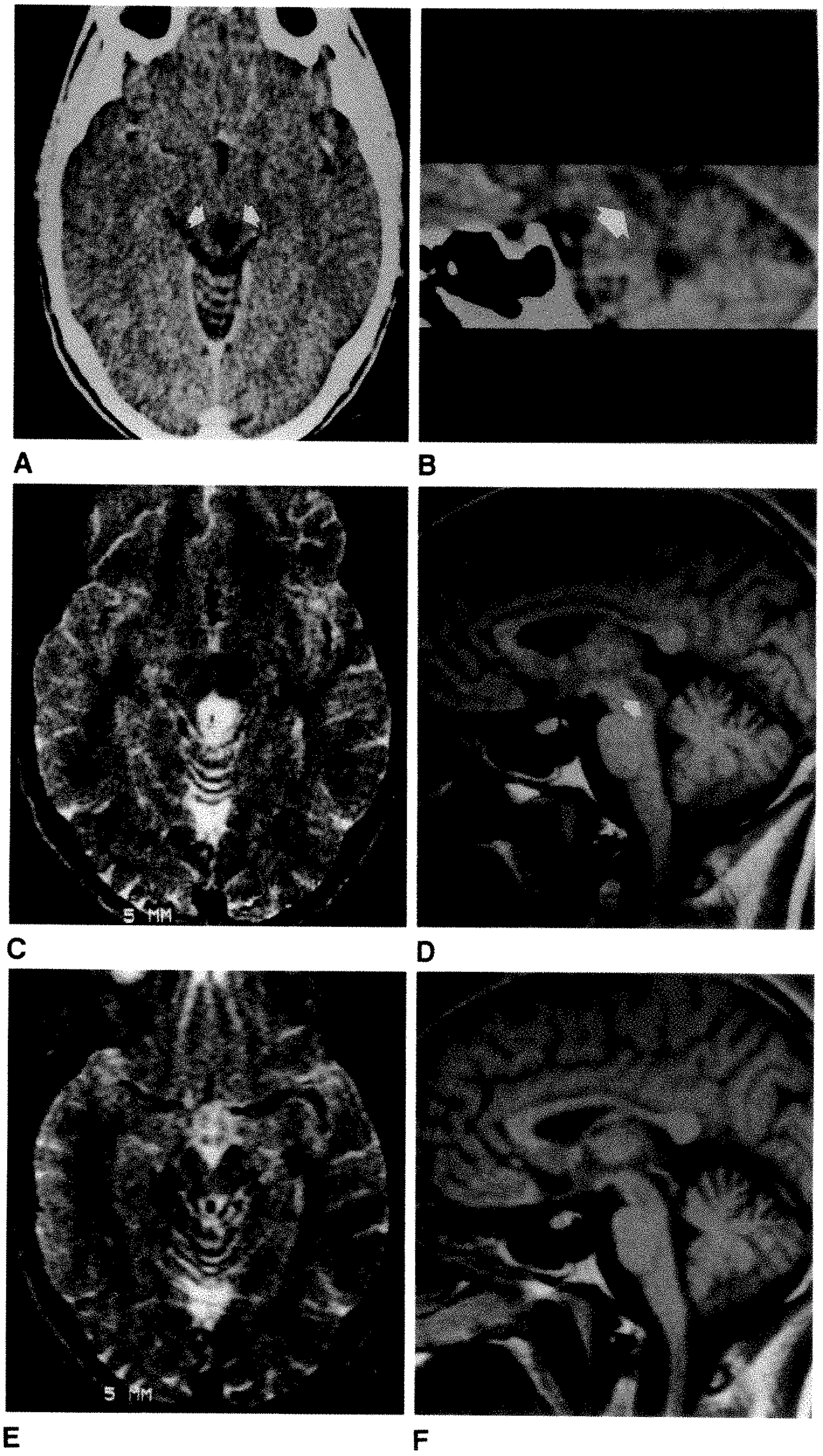

Fig. 1.—*A* and *B*, Axial (*A*) and sagittal (*B*) CT reconstructions in acute phase show hypodense area surrounding aqueduct (*arrows*).

C, T2-weighted MR image shows lesion to be hyperintense relative to normal parenchyma.

D, Lesion is also shown clearly on T1-weighted midsagittal scan (*arrow*).

E, Follow-up T2-weighted axial MR image 9 months later shows periaqueductal lesion to have almost disappeared. Aqueduct is now enlarged.

F, Midsagittal MR image confirms disappearance of periaqueductal lesion and aqueductal enlargement. Also note superior vermian atrophy.

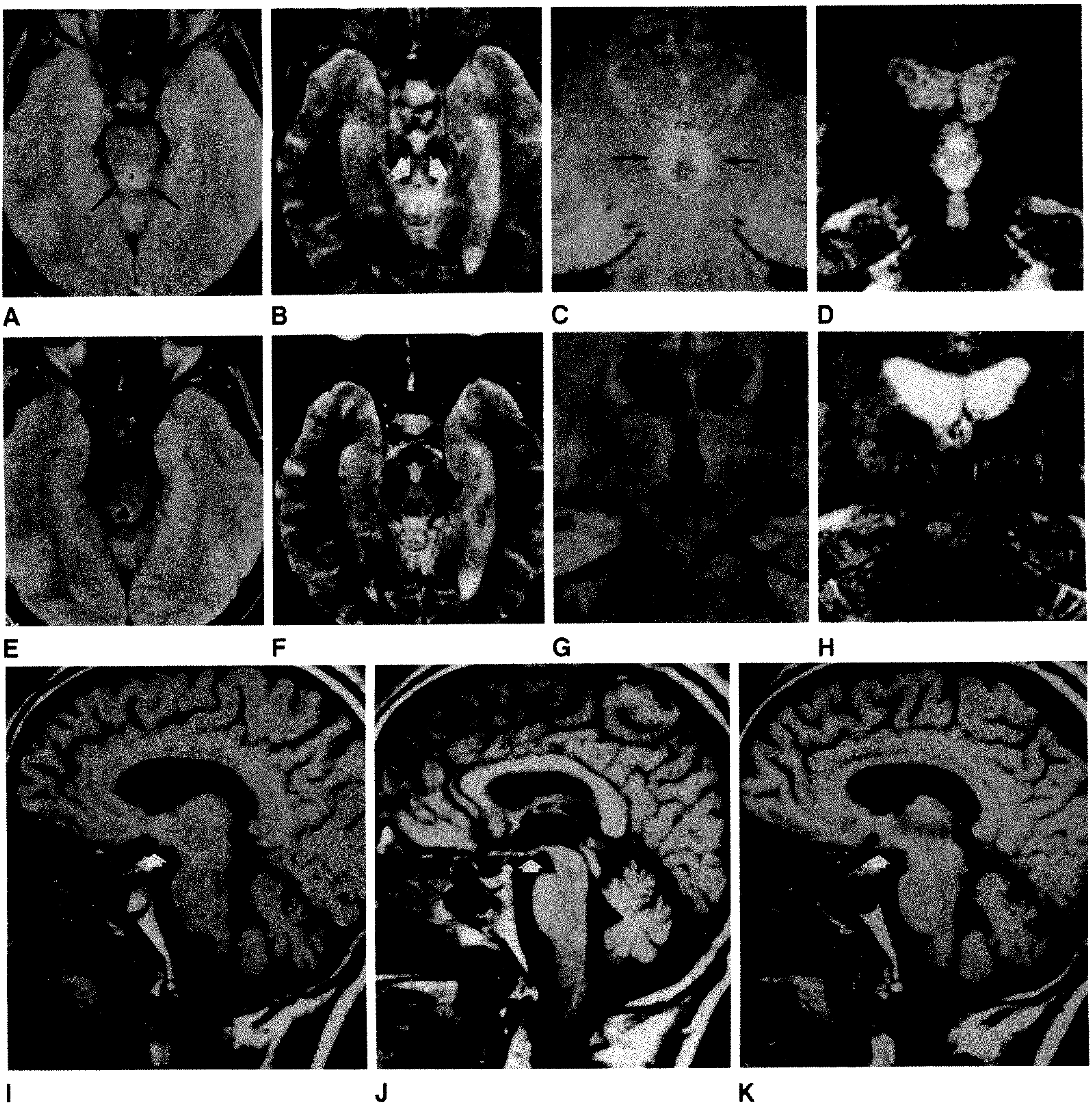

Fig. 2.—*A–D*, Proton-density- and T2-weighted axial and coronal MR images in acute phase show hyperintense areas (*arrows*) surrounding aqueduct (*A* and *B*) and third ventricle (*C* and *D*).

E–H, On follow-up, both periaqueductal (*E* and *F*) and periventricular (*G* and *H*) hyperintensities have almost disappeared. Note enlargement of aqueduct and third ventricle. Lack of signal and transverse artifact are attributed to flow effect (*H*).

I–K, Contiguous 4-mm sagittal T1-weighted MR images exhibit no evidence of mamillary bodies (*arrows*).

around the aqueduct and third ventricle; however, it was not specified whether the patient was observed in the acute or chronic phase or if the patient was an alcoholic.

In our study, MR was able to show many of the pathologic findings described in the medical literature, since typical changes were present both in the acute and chronic phases in the periventricular areas of all patients. Although the hyperintensities seen on the T2-weighted sequences were not specific to the pathology (edema, demyelination, gliosis), they can be considered typical of Wernicke encephalopathy, because their symmetric distribution permits differential diagnosis from other diseases (Fig. 5). Lack of MR evidence of hemorrhagic foci, as described in the pathology literature, is probably due to their presence in only a small percentage of

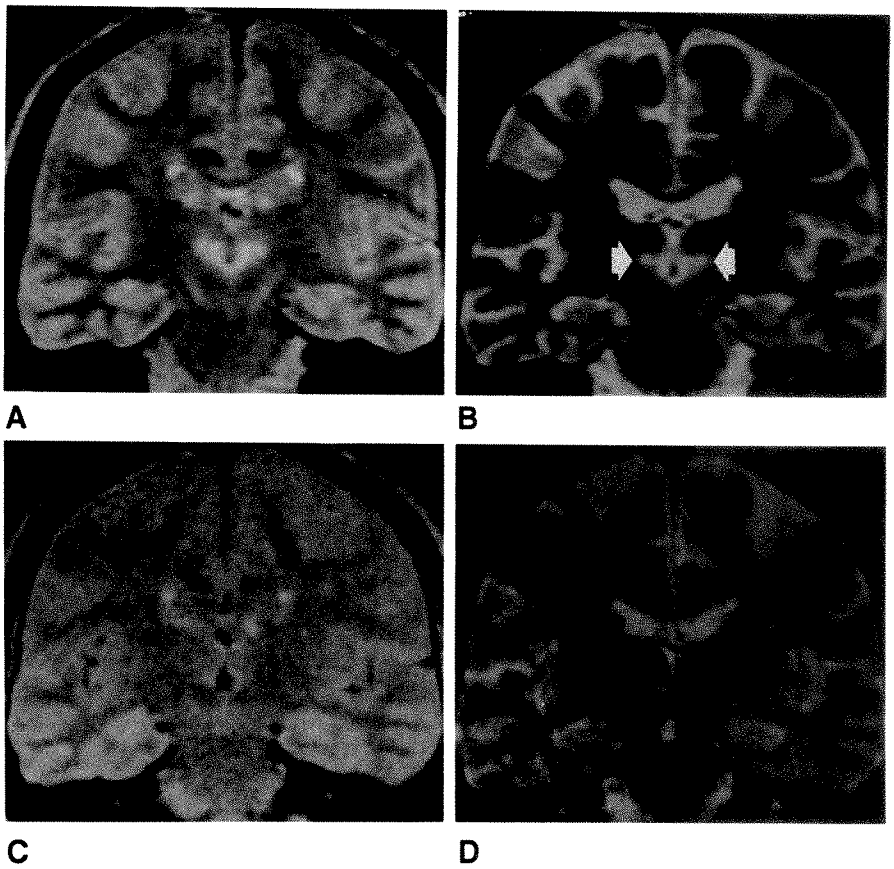

Fig. 3.—*A* and *B*, Coronal proton-density- and T2-weighted MR images in acute phase show hyperintense area surrounding third ventricle with suggestive double-wing configuration (*arrows*).

C and *D*, Follow-up study shows almost complete disappearance of hyperintensity and third ventricle enlargement.

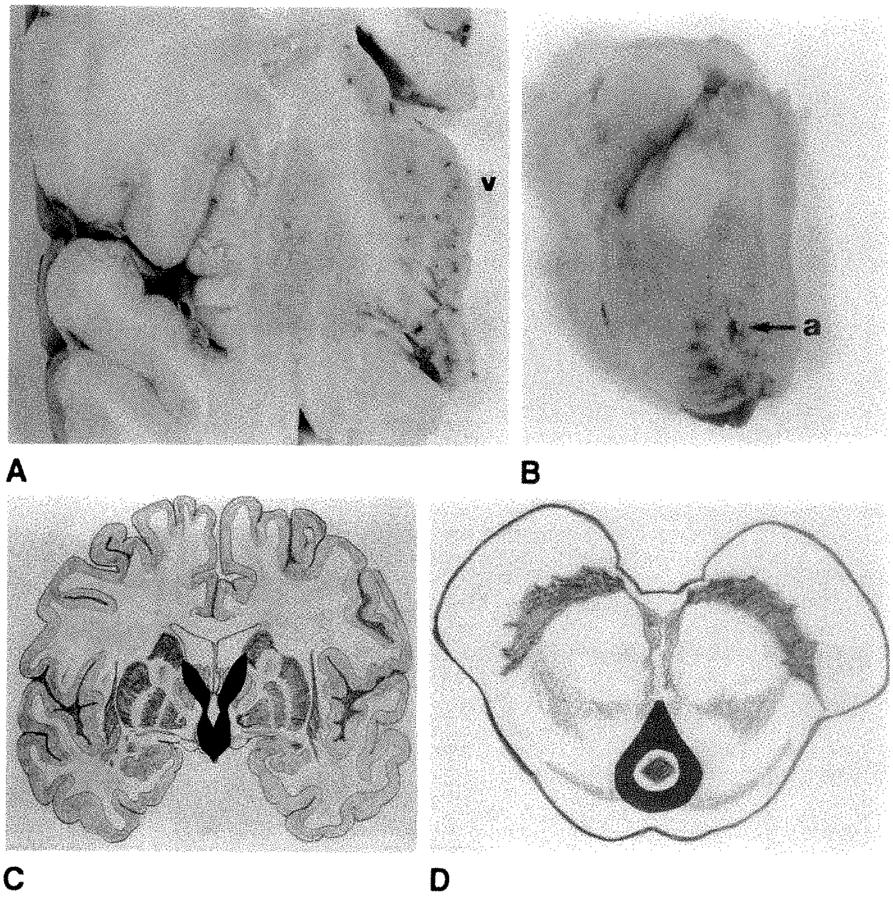

Fig. 4.—*A* and *B*, Pathologic specimens in Wernicke encephalopathy show petechial hemorrhage surrounding aqueduct (a) and third ventricle (v).

C and *D*, Schematic representation of sites and structures mostly involved in Wernicke encephalopathy.

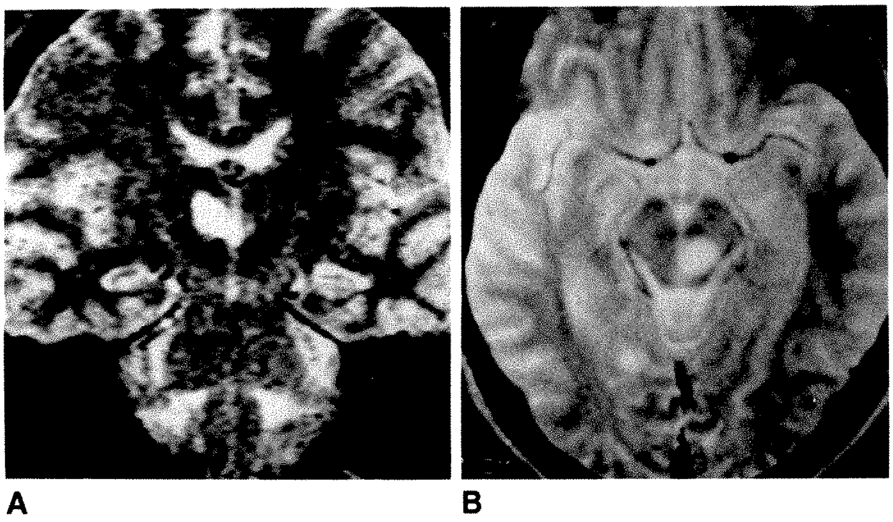

Fig. 5.—*A* and *B*, Thalamic infarction (*A*) and multiple sclerosis plaque (*B*). Both could simulate Wernicke encephalopathy at clinical onset; asymmetric involvement of periventricular and periaqueductal structures may help in the differentiation.

cases (20%), and when hemorrhage is present, many patients are agonal [5]. The reduction in hyperintense areas on the follow-up examination, also confirmed by ventricular and aqueductal dilatation, underscores the benign evolution of the pathology when appropriate therapy is applied and a correct diagnosis is made. Degeneration of the mamillary bodies and cerebellar atrophy were seen on CT in our patients and were in line with findings in other studies (Charness ME et al., presented at the annual meeting of the Radiological Society of North America, November 1986). However, these findings cannot be considered specific enough to enable more accurate diagnosis.

We did not find other focal lesions in the brain of patients affected by Wernicke encephalopathy, as was reported in one study of chronic alcohol abuse [24]. This may have been because of different pathophysiological mechanisms, different drinking habits, or to a younger age or longer duration of alcohol consumption.

In conclusion, the direct evidence of lesions provided by MR in Wernicke encephalopathy allows both early diagnosis and treatment, and therefore can successfully modify the prognosis of the disease. MR proved useful also when the history otherwise might have led to an incorrect diagnosis. Finally, we believe an early and definite identification of the disease may help establish the therapeutic approach as well.

REFERENCES

1. Gamper E. Zur Frage der Polio-encephalitis haemorragica des Chronischen Alkoholier: Anatomische Befunde beim alkoholischen Korsakow und ihre Benziehungen zum Klinischen Bild. *Dtsch Z Nervenheilk* **1928**;102:122-129
2. Witt ED. Neuroanatomical consequences of thiamine deficiency: a comparative analysis. *Alcohol Alcohol* **1985**;2:201-221
3. Gullotta F. Zur Localisation der Wernicke Encephalopatie im Kinder und Erwachsenelater. *Eur Arch Psychiatry Neurol Sci* **1968**;211:88-108
4. Thomson AD, Ryle PR, Shaw GK. Ethanol, thiamine and brain damage. *Alcohol Alcohol* **1983**;1:27-43
5. Adams RD, Victor M. *Principles of neurology*. New York: McGraw-Hill, **1985**
6. Harper C. Wernicke's encephalopathy: a more common disease than realised. A neuropathological study of 51 cases. *J Neurol Neurosurg Psychiatry* **1978**;42:226-231
7. McDowell JR, Le Blanc HJ. Computed tomography finding in Wernicke-Korsakoff syndrome. *Arch Neurol* **1984**;41:435-454
8. Cala LA, Mastaglia FL. Computerized axial tomography in the detection of brain damage. *Med J Aust* **1980**;2:193-198
9. Victor M, Adams RD, Collins GH. *The Wernicke-Korsakoff syndrome: a clinical and pathological study of 245 patients, 82 with post-mortem examinations*. Philadelphia: Davis, **1971**
10. Ghez C. Vestibular paresis: a clinical feature of Wernicke disease. *J Neurol Neurosurg Psychiatry* **1969**;178:134-139
11. Wernicke C. *Lehrbuch der Gehirnkrankheiten fur Aertre und Studiezenk*, vol. 2. Berlin: Theodor Fisher, **1881**:229-242
12. Collins GH, Converse WK. Cerebellar degeneration in thiamine deficient rats. *Am J Pathol* **1970**;29:57-69
13. Dreyfus PM. Thiamine and nervous system: an overview. *J Nutr Sci Vitaminol* (Tokyo) **1976**;22:13-16
14. Hofer H. Zur Morphologie der Circumventrikulare Organen des Zwishenhirns der Saugetiere. *Verh Dtsch Ges Zool* **1958**;202
15. Watanabe I, Iwasaki Y, Aikawa H, Satayashi E, Davis JW. Hemorrhage of thiamine-deficient encephalopathy in the mouse. *J Neuropathol Exp Neurol* **1981**;40:566-580
16. Watanabe I, Tomoto T, Hung KG, Iwasaki Y. Edematous necrosis in thiamine-deficient encephalopathy of the mouse. *J Neuropathol Exp Neurol* **1981**;40:454-471
17. Witt ED, Goldman-Rakic PS. Intermittent thiamine deficiency in the rhesus monkey. I. Progression of neurological signs and neuroanatomical lesions. *Ann Neurol* **1983**;13:376-395
18. Witt ED, Goldman-Rakic PS. Intermittent thiamine deficiency in the rhesus monkey. II. Progression of neurological signs and neuroanatomical lesions. *Ann Neurol* **1983**;13:396-401
19. Victor M, Adams RD. On the etiology of alcoholic neurologic disease, with special reference to the role of nutrition. *Am J Clin Nutr* **1961**;9:379-397
20. Lopez RI, Collins GH. Wernicke's encephalopathy. A complication of chronic hemodialysis. *Arch Neurol* **1968**;18:248-259
21. Frantzen E. Wernicke's encephalopathy: three cases occurring in connection with severe malnutrition. *Acta Neurol Scand* **1966**;42:426-441
22. Nixon PF. Is there a genetic component to the pathogenesis of the Wernicke-Korsakoff syndrome? *Alcohol Alcohol* **1984**;3:219-221
23. Drayer BP. Imaging of the aging brain. Part II. Pathologic conditions. *Radiology* **1988**;166:797-806
24. Gallucci M, Amicarelli I, Rossi A, et al. MR imaging of white matter lessions in uncomplicated chronic alcoholism. *J Comput Assist Tomogr* **1989**; 13(3):395-398

The reader's attention is directed to the commentary on this article, which appears on pages 1315-1316.

Commentary

MR in the Diagnosis of Wernicke-Korsakoff Syndrome

Maurice Victor[1,2]

Wernicke disease, or Wernicke encephalopathy, is a neurologic disorder of abrupt or saltatory onset, characterized by nystagmus, abducens and conjugate gaze palsies, unsteadiness of stance and gait, confusion, and apathy. These manifestations may occur singly or in various combinations. Korsakoff psychosis (better termed Korsakoff syndrome or Korsakoff amnesic state) refers to an abnormality of mentation in which learning and memory are affected out of proportion to other cognitive functions; the patient is otherwise alert and responsive. Most patients who present with the manifestations of Wernicke disease and survive the acute illness are left with an enduring amnesic state—in which case the term Wernicke-Korsakoff syndrome is appropriate. The syndrome is common; autopsy studies in disparate parts of the world (Oslo, Boston, Cleveland, and Western Australia) have shown a prevalence of between 2 and 3% of the adult population [1].

The Wernicke-Korsakoff syndrome is due to nutritional deficiency, more specifically to a deficiency of vitamin B_1, or thiamine. In the Western world, it occurs most often in alcoholics. Alcohol displaces food in the diet and also adds its own carbohydrate calories, thus increasing the need for thiamine. However, the syndrome is observed with some regularity in a wide variety of other medical settings: prolonged infectious-febrile conditions, carcinoma, hyperemesis gravidarum, small-bowel obstruction, anorexia nervosa, and prolonged voluntary starvation— to name the better documented ones.

Increasingly, in recent years, attention has been drawn to iatrogenic factors in the causation of the Wernicke-Korsakoff syndrome. From time to time, the syndrome is a complication of a prolonged course of dialysis or hyperalimentation. In a significant proportion of patients who have gastric partitioning or plication, for the treatment of morbid obesity, persistent vomiting and the Wernicke-Korsakoff syndrome develop. In confused alcoholics and otherwise nutritionally depleted patients, particularly those with other serious medical illnesses, the long-term administration of dextrose and water without supplemental vitamins may precipitate the syndrome or cause an early form of it to worsen. This is not an uncommon clinical event, even on the wards of teaching hospitals [2] and is all the more distressing because it can be prevented by the simple expedient of adding B vitamins to the parenteral fluids.

Patients who die in the acute stages of Wernicke disease show symmetrical lesions in the paraventricular regions of the thalamus and hypothalamus, in the mamillary bodies, periaqueductal region of the midbrain, floor of the fourth ventricle (particularly in the regions of the dorsal motor nuclei of the vagus and vestibular nuclei), and midline structures of the cerebellum. Histologically, the lesions are characterized by various degrees of necrosis, with prominence of blood vessels and a proliferation of astrocytic and microglial cells. Hemorrhages are found in only 20% of autopsied cases; they are usually petechial in size, and many of them appear to be agonal.

In this issue of the *AJNR*, two separate groups of neuroradiologists [3, 4] describe for the first time the MR appearance of the *acute* lesions of the Wernicke-Korsakoff syndrome. Bilaterally symmetrical diencephalic (medial thalamic) and mesencephalic (periaqueductal) lesions stand out with remarkable clarity, much more so than with CT scanning [5, 6]. This is a matter of more than theoretical interest. If early signs and symptoms of the syndrome are not recognized,

---

This article is a commentary on the preceding article by Gallucci et al.

[1] Dartmouth Medical School, Hanover, NH 03755.

[2] Veterans Administration Medical Center, White River Junction, VT 05001. Address reprint requests to M. Victor.

AJNR 11:895-896, September/October 1990; AJR 155:1315-1316, December 1990 0361-803X/90/1556-1315 © American Roentgen Ray Society

and specific treatment (parenteral administration of large doses of thiamine) is not undertaken immediately, the disease invariably will progress to a state of stupor, coma, and death. Conversely, early diagnosis and treatment halts the progression of the disease. The manifestations of Wernicke disease can be reversed partially or completely, depending on their duration before the institution of treatment, and the development of a Korsakoff amnesic state can be prevented, or an early form of the state can be kept from worsening. Thus, MR may be of critical importance, particularly in the cases that do not conform to the classic clinical picture.

The classic triad of signs described by Wernicke—ophthalmoplegia, ataxia, and an apathetic-confusional state—is still diagnostically useful, but it will be found on initial examination in only one third of patients. In the remainder, the signs occur singly or in some other combination. Moreover, the ocular and ataxic signs are so sensitive to thiamine that they can be attenuated greatly by a meal or two (e.g., before hospital admission) and then can be detected only if carefully sought. Thus, ophthalmoparesis can be reduced to a fine horizontal nystagmus on far lateral gaze, and ataxia may be so restricted as to be elicited only on tandem walking. The occurrence of coma as the initial event in Wernicke disease is rare; however, apathy, drowsiness, confusion, and profound fatigue are commonplace and will progress to coma if untreated, as they did in Wernicke's original cases [1]. Once coma has supervened, identification of the disease becomes more difficult; the presence of serious medical disease (e.g., sepsis, hepatic failure) compounds this difficulty.

In summary, an awareness of the commonality of the Wernicke-Korsakoff syndrome and the clinical settings (not only alcoholism) in which it occurs and some knowledge of the incomplete or attenuated forms of the syndrome and how to elicit them permit a diagnosis to be made in most cases. Even a suspicion of the disease calls for the immediate parenteral administration of large doses of thiamine, after which MR logically could be used to substantiate the diagnosis.

Finally, MR (and CT) may serve another purpose in the diagnosis of Wernicke-Korsakoff syndrome—namely, to identify the nature of a chronic Korsakoff amnesic state in patients who have never shown the ocular and ataxic signs of Wernicke disease or in whom these signs have been abolished. Occasionally, such an amnesic state may be the only manifestation of Wernicke-Korsakoff syndrome, or a clinically indistinguishable state may be due to other forms of diencephalic disease (infarction, tumor) or to discrete lesions in other parts of the brain (basal forebrain, hippocampal formations). Atrophy of the mamillary bodies, medial thalamic nuclei (widening of third ventricle), and periaqueductal gray matter (dilated aqueduct) mark the amnesic state as alcoholic-nutritional in origin. In cases of Korsakoff amnesic state due to basal forebrain or bilateral hippocampal lesions, MR and CT show characteristic abnormalities in these structures [7–10].

REFERENCES

1. Victor M, Adams RD, Collins GH. *The Wernicke-Korsakoff syndrome and related neurologic disorders due to alcoholism and malnutrition*, 2nd ed. Philadelphia; Davis, **1989**:1–117
2. Novak DJ, Victor M. The vagus and sympathetic nerves in alcoholic polyneuropathy. *Arch Neurol* **1974**;30:273–284
3. Donnal JF, Heinz ER, Burger PC. MR of reversible thalamic lesions in Wernicke syndrome. *AJNR* **1990**;11:893–894
4. Gallucci M, Bozzao A, Splendiani A, Masciocchi C, Passariello R. Wernicke encephalopathy: MR findings in five patients. *AJNR* **1990**;11:887–892; *AJR* **1990**;155:1309–1314
5. Mensing TWA, Hoogland PH, Sloof JL. Computed tomography in the diagnosis of Wernicke's encephalopathy: a radiological-neuropathological correlation. *Ann Neurol* **1984**;16:363–365
6. McDowell JR, LeBlanc HJ. Computed tomographic findings in Wernicke-Korsakoff syndrome. *Arch Neurol* **1984**;41:453–454
7. Charness ME, DeLaPaz RL. Mammillary body atrophy in Wernicke's encephalopathy: antemortem identification using magnetic resonance imaging. *Ann Neurol* **1987**;22:595–600
8. Shimamura AP, Jernigan TL, Squire LR. Korsakoff's syndrome: radiological (CT) findings and neuropsychological correlates. *J Neurosci* **1988**;8:4400–4410
9. Press GA, Amaral DG, Squire LR. Hippocampal abnormalities in amnesic patients revealed by high-resolution magnetic resonance imaging. *Nature* **1989**;341:54–57
10. Squire LR, Amaral DG, Press GA. Magnetic resonance measurements of hippocampal formation and mammillary nuclei distinguish medial temporal lobe and diencephalic amnesia. *Behav Neurosci* (in press)

Computer Page

Computer-Based Learning in Radiology: A Hypermedia Application in CT

Joseph G. Hennessey,[1] Elliot K. Fishman, Janet E. Kuhlman, Derek R. Ney, and Donna Magid

Multimedia is a form of computer data presentation that uses multiple formats (text, illustration, sound, and animation) to enhance attention to and retention of presented information. Hypermedia is a nonlinear, branched access version of this that allows the user to pursue information more freely and variably than a linear format does. We used the hypermedia format to create an interactive medical teaching program that we believe holds the user's interest and attention better than a straight-text style does.

The transfer of information in radiology, as in all of medicine, has traditionally been done in standard teaching formats with an instructor lecturing to a group of residents or students, one-to-one discussions, or direct hands-on experience. The "see one, do one, teach one" philosophy has always been strong in all facets of medicine.

The radiologist is now faced with an overwhelming amount of information that must be assimilated during training and in the postgraduate years. In the past decade, technology that was once unimaginable has developed into key techniques that affect the basic function of radiology. CT, MR imaging, and single-photon emission CT (SPECT) have rapidly emerged during this time. In teaching radiology residents and medical students, we are now faced with transmitting a larger amount of material in what seems to be an increasingly inadequate time span. Although traditional teaching methods undoubtedly will persist, new technology may facilitate new methods of teaching. Computer applications in primary radiologic teaching, for example, have not yet achieved widespread use or acceptance [1, 2]. We present our experience with the development of a computer-based teaching system that uses a hypermedia interface to the user. Hypermedia formats allow nonsequential, nonlinear, branched access to information stored in a number of media (multimedia) including text, static images, animated sequences, and sound.

Materials and Methods

The computer configuration used in the development of this project was a Macintosh II computer (Apple Computer, Cupertino, CA) with 8 megabytes of random access memory (RAM) and an 80-megabyte internal hard disk. The software used for creation of the program was the SuperCard hypermedia program (Silicon Beach Software, San Diego, CA). All radiologic images were entered via a Barneyscan slide scanner (Barneyscan Corp., Berkeley, CA) by using Barneyscan Mac 1.7 scanner software and the XP extended image-processing software.

In our teaching files, we have a library of 50,000 CT slides and over 1800 animated three-dimensional (3-D) studies on magnetic tape or slides. A Barneyscanner, a 24-bit color slide scanner that we use to scan the slides, is used to get selected images into the Macintosh. Most of our images are monochrome and are therefore scanned in as 256-gray-level images. The Barneyscanner also comes with software that allows us to convert our 3-D images into a format suitable for inclusion in our teaching program.

All commands were written in standard HyperCard (Apple Computer) or SuperCard (Silicon Beach Software) scripting language. HyperCard is easily programmable software for the nonexpert user, who can modify and add on to the basic program to tailor software for specific needs. SuperCard is slower than HyperCard but uses

---

Received January 3, 1990; accepted after revision June 26, 1990.

[1] All authors: The Russell H. Morgan Department of Radiology and Radiological Science, The Johns Hopkins Medical Institutions, Baltimore, MD 21205. Address reprint requests to E. K. Fishman, Department of Radiology, The Johns Hopkins Hospital, 600 N. Wolfe St., Baltimore, MD 21205.

AJR 155:1317–1320, December 1990 0361–803X/90/1556–1317 © American Roentgen Ray Society

larger (full screen) images and can incorporate color. SuperCard combines graphics, sound, and text; like HyperCard, it is user-friendly to those with limited expertise. The basic hardware required to use this approach includes a Macintosh II computer (Apple Computer), 2 megabytes of memory, a 40-megabyte hard disk, and a 13-in. (33 cm) monitor with 256 colors (an upgraded configuration would include 5 megabytes memory and an 80-megabyte hard disk). These parameters are well within the technical and economic limits of many individual users. The program currently contains 32 megabytes of questions, text, images, and audio.

Appropriate text, illustrations, and quiz sets were prepared for the initial test menus. "Computed Tomography: The Game" is a multiformatted or multimedia (sound, text, static, and animated illustrations) program first entered through a series of menus allowing the user to choose a section on the basis of keywords (e.g., by anatomic location, imaging technique, or disease) (Figs. 1 and 2). The user interface is a keyboard, mouse, color monitor, and monophonic speaker. This is a single-user system. Navigation buttons (Fig. 3) are programmed to facilitate rapid travel through the program and can be used for rapid return to the last position visited (vs a conventional next/last travel mode), to the main menu, or to additional stations appropriate to each section being visited. At any time, an alternative set of cards may be selected through the key-word indexes. Once a topic or anatomic focus of interest is selected, relevant text and illustrations are presented. A quiz is then provided that uses both text and voice (voice optional for feedback and further review; Figs. 3 and 4). A timer can be set for either 10 or 20 sec to encourage timely progression through the program.

Interlinking data of multiple media types in the essence of hypermedia [3-5]. It is vital that there may be many ways to access and reference that data. This program currently offers four ways to access information. First, there is a browser. This allows a user to rapidly go to a particular portion of the program by a visual representation of the structure. Second, the hierarchical tree structure of the program allows the user to access the different sections by going up or down the tree. Then, a dynamic linking allows the user to go to a relevant section dependent on the answer to various questions. Finally, a key word search defines a group of relevant cards on the basis of a word that is to be searched for and then allows the user to access any of them.

Discussion

Radiology now deals with an expanding base of images, many of which are digital. These images are an important source of learning and experience at all levels of training. However, these images of patients are not always readily accessible because of their display and filing format as film or hard copy. Teaching files are a classic method of supporting the patient-care learning process, with representative cases selected from the patients' files.

The film-based teaching files have several obvious disadvantages. They take up an enormous amount of space and require significant clerical attention. A misplaced or misfiled film is no longer available for further use. In addition, there is often little motivation to maintain and update the learning file, as its upkeep is often given to nonphysician employees who may have little interest in keeping it up to date or in order. A computer-based learning file uses far less space to store and retrieve images, and may be easier to update or expand in limited time and space. We also believe that the game-style presentation of text and images is conductive to extended use, engaging and holding the user's attention. This distinguishes "CT: The Game" from other medical teaching programs in a "video text" format.

HyperCard is widely used and readily available software. However, its limitations include small screen size and inability to present color images. SuperCard is a slower program, but offsets this with the use of color and full-screen images. SuperCard also may be easier to manipulate or program for the less experienced user. SuperCard and other hypermedia programs are dynamic environments incorporating text, figures, and sound. The hypermedia programs simplify inter-

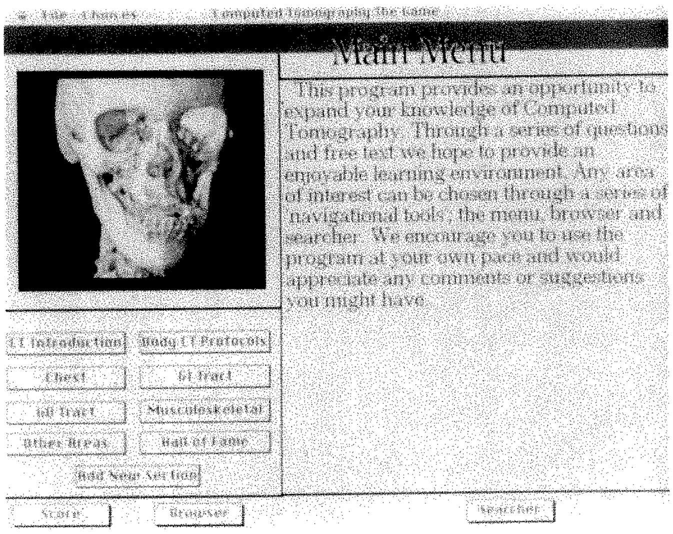

This program provides an opportunity to expand your knowledge of Computed Tomography. Through a series of questions and free text we hope to provide an enjoyable learning environment. Any area of interest can be chosen through a series of "navigational tools"; the menu, browser and searcher. We encourage you to use the program at your own pace and would appreciate any comments or suggestions you might have.

Fig. 1.—First card on entry into main portion of program. Choices of anatomic area (i.e., chest) are provided. If a more expanded menu of areas of interest is needed, "browser" or "searcher" buttons can be selected.

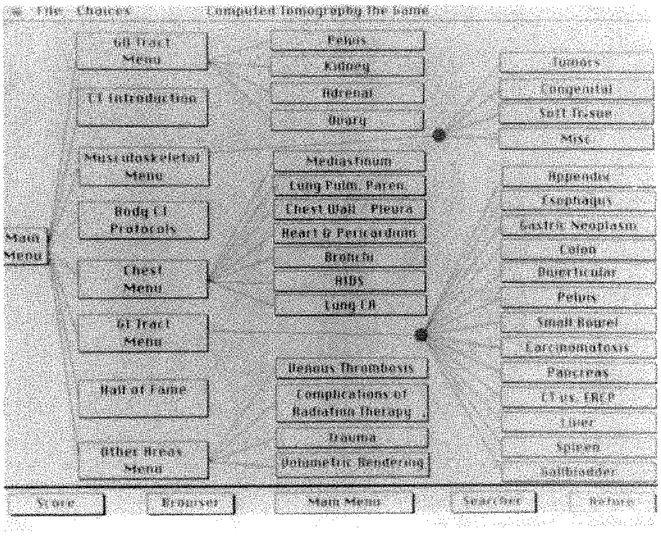

Fig. 2.—"Browser" card shows all areas available for study. This card can be as complicated or as simple as one would like.

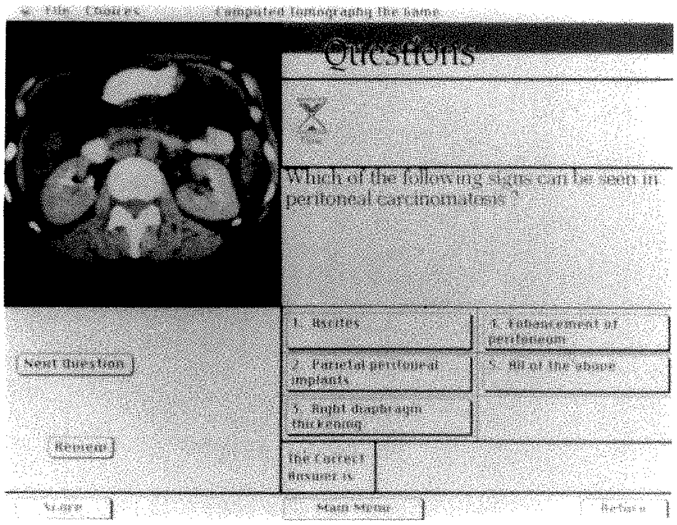

Which of the following signs can be seen in peritoneal carcinomatosis ?

1. Ascites
2. Parietal peritoneal implants
3. Right diaphragm thickening
4. Enhancement of peritoneum
5. All of the above

The Correct Answer is

Fig. 3.—Sample quiz card with standard format of image questions and answers. Timer and other navigation buttons are provided.

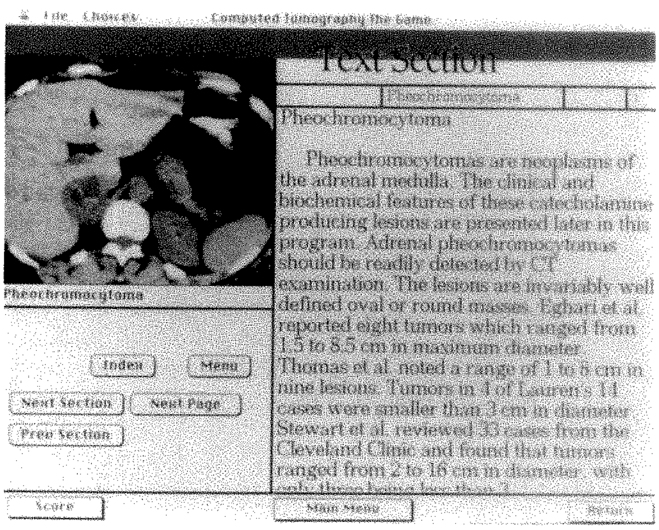

Pheochromocytoma

Pheochromocytomas are neoplasms of the adrenal medulla. The clinical and biochemical features of these catecholamine producing lesions are presented later in this program. Adrenal pheochromocytomas should be readily detected by CT examination. The lesions are invariably well defined oval or round masses. Eghari et al reported eight tumors which ranged from 1.5 to 8.5 cm in maximum diameter. Thomas et al. noted a range of 1 to 6 cm in nine lesions. Tumors in 4 of Lauren's 11 cases were smaller than 3 cm in diameter. Stewart et al. reviewed 33 cases from the Cleveland Clinic and found that tumors ranged from 2 to 16 cm in diameter, with

Fig. 4.—Sample text card combines images and text. Card is linked to questions, main menu, and entire adrenal section.

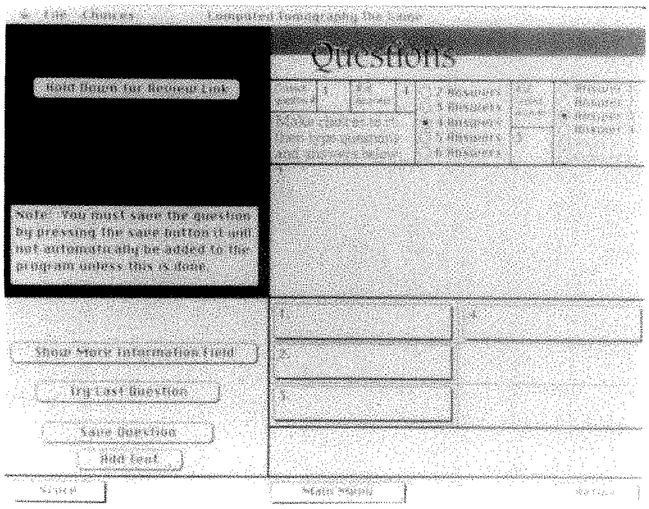

Note: You must save the question by pressing the save button it will not automatically be added to the program unless this is done.

Fig. 5.—Copy of entry card for additional text questions to be placed into program. No programming experience is necessary at user level.

faces with and access to referenced material, since the program's nonlinear branched format frees it from the next/last progression of standard linear programs. This makes such nonlinear formats markedly faster at retrieval than conventional linear formats. The user also can create additional links or add text, comments, questions, or images as desired. We take advantage of this user-friendly and flexible environment to encourage and coordinate multiple contributors to this project, allowing the rapid establishment, expansion, and as necessary, updating, of our data base. We have developed a series of form-enter cards (Fig. 5) that allow one to enter questions or text without any expertise at all. Twenty-five radiology residents and third and fourth year medical students have tested our teaching format as part of the development program. User suggestions have been incorporated as the program has grown. As of September 1990, "CT: The Game" will be part of the basic core curriculum for medical students rotating through our department.

One current limitation is storage size. We have been using an 80-megabyte hard disk for storage. SuperCard compresses images, but even so, we can store only about 1200 high-quality quarter-screen images on a disk. This capacity is adequate if one uses only conventional or two-dimensional (2-D) views, but limits the use of animated image sequences, which require multiple images per sequence and therefore consume disproportionate amounts of memory. Although we have made sample sections using compressed animated 3-D images at 1 megabyte each, it is not yet feasible to include extensive use of animated 3-D. We have found that motion and transparency cues enhance appreciation of 3-D images and detail, and we prefer to use these images as animated series. However, a full 360° of rotation requires a minimum loop of 64 individual images for smooth simulated rotation. This can require as much as 3.5 megabytes, limiting us to as few as 19 animated 3-D sequences per disk, far too limiting for current applications. However, still under investigation is the use of a videodisk or CD-ROM (compact disk read-only memory), either of which would expand storage significantly. Increased memory also would allow the addition of digitalized sound, such as more natural audio commentary or a teaching file of heart murmurs. Expanding memory, unfortunately, also increases costs.

At this time, we have 600 static slides (average size: 40 kilobytes) for a total of 24 megabytes and one compressed animation sequence (1 megabyte). We can store static images of up to 256 × 256 pixels at eight gray levels per pixel for a maximum storage requirement per images of 64 kilobytes (although our actual average has been 40 kilobytes). An 80-megabyte hard disk could be expected to store at least 1200 static images.

However, in the current format, "CT: The Game" runs on reasonably priced, widely available, and widely used hardware and software. The use of affordable and ubiquitous personal computers like the Macintosh also allows the user to share disks and information with colleagues in the same institution, state, or across the country. Ideally, in time, individuals could access large data bases of images and text developed at other institutions through cooperative relationships or central public resources like the National Library of Medicine. Access to information and images might be obtained with the ease of doing a search through Medline. We believe that the computer can become a true teaching resource that is affordable, available, and can be updated.

ACKNOWLEDGMENTS

We thank John Sculley, Kirsten Nelson, Nancy Eaton, John Lowe, and Susan Hammer of Apple Computer for their support and help in this project and Lyn Alonso for manuscript preparation.

REFERENCES

1. Greenes RA. "Desktop knowledge": a new focus for medical education and decision support. *Methods Inf Med* **1989**;28:332–339
2. Manning PR. The computer and the future of continuing medical education. *West J Med* **1986**;145:872–873
3. Yankelovich N, Meyrowitz N, van Dam A. Reading and writing of the electronic book. *Computer* **1985**;18:15–30
4. Conklin EJ. Hypertext: an introduction and survey. *Computer* **1987**;2: 14–17
5. Nielsen, J. The art of navigating through hypertext. *Association for Computing Machinery* **1990**;33:296–310

Radiology Outreach Foundation

The Radiology Outreach Foundation (ROF) is a nonprofit corporation whose goal is to help disadvantaged countries improve their health care by providing radiology equipment, books, consultation, education, and training to their practitioners. This assistance is on an application basis that is independent of political, ethnic, or religious orientation of the grantee. It depends on the need of the people and the ability of the ROF to meet that need. The ROF is approved by the U.S. Internal Revenue Service as a tax-exempt organization. It is endorsed by the following radiologic societies: American Association of Women Radiologists, American College of Radiology, American Roentgen Ray Society, Association of University Radiologists, Radiological Society of North America, Society of Chairmen of Academic Radiology Departments, Society for Pediatric Radiology, European Society of Pediatric Radiology.

All donations to the ROF are tax deductible. Persons who would like to contribute financially to the ROF, would be interested in being a visiting professor, would like to send books or journals to any of the institutions supported by the ROF, or would like further information about the ROF should write to Charles A. Gooding, M.D., President, Radiology Outreach Foundation, 3415 Sacramento St., San Francisco, CA 94118 USA.

Commentary

Europe 1992: Consequences for European Health Care and Radiology

Henri E. Schütte[1]

Health care and health care organizations in Europe have always been exclusively national affairs, but this may change in the near future. National politics are being influenced by the unifying changes taking place within the European Economic Community (EC), or what is generally referred to as "Europe 1992." To what extent unification will influence health care and radiology is still uncertain but is worthy of consideration.

The European Economic Community

The EC was created by the Treaty of Rome in 1957 primarily as a "custom-union." The founding member states, Belgium, West Germany, France, Italy, Luxembourg, and the Netherlands, were joined in 1974 by Denmark, Ireland, and the United Kingdom. In 1981 Greece followed, and in 1986 Spain and Portugal joined, bringing the total citizenry of the EC to 325 million. In 1983 and 1984, a number of leading businessmen from European multinational corporations (e.g., Dekker from Philips, Agnelli from Fiat) expressed concern for Europe's future competitive trade status, in particular with Japan and the United States. In 1985, the European Commission responded to the concerns of the captains of industry by publishing a "white paper" by one of their commissioners, Lord Cockfield. The white paper suggested measures for achieving a single European economic market, with an absolute free exchange of persons, services, goods, and capital and with no restrictive national regulations. A schedule was drafted with January 1, 1993, as the target starting date for the European Common Market.

The main goal of the EC is to facilitate trade within the member states, while maintaining national values and identifies under the structure of a European government. In the broadest terms, a united Europe will include: (1) economic integration based on stable relationships between the different currencies; (2) unification with respect to quality of life, environment, and education; and (3) maintenance of the national identities of the member states.

The Europe 1992 phenomenon is essentially economic. Leaders of the movement are guided by a determination to enhance Europe's ability to compete with Japan and the United States. But with economic integration, a certain political integration will be necessary, and that will affect social systems in the member states.

Some Legal Aspects

The Court of Justice of the European Communities, established in Luxembourg, is the highest authority within the Community for interpretation of Community laws and their relationship to the national laws of the member states [1]. The Court has ruled that within each of the member states two legal systems simultaneously apply: first, the traditional system governed by the national constitution and the laws of the country and second, a separate Community system with an independent set of Community laws. The Community law

---

Received January 25, 1990; accepted after revision June 14, 1990.

[1] Department of Diagnostic Radiology, Erasmus University and University Hospital Rotterdam-Dijkzigt, Dr. Molewaterpl. 40, 3015 GD Rotterdam, The Netherlands. Address reprint requests to H. E. Schütte.

AJR 155:1321-1325, December 1990 0361-803X/90/1556-1321 © American Roentgen Ray Society

CALCUTTA CENTRAL LIBRARY

can be found in the Treaty of Rome (1957) and in the legislation issued by the Community's law-making bodies. Community law binds both citizens and member states and is implemented in regulations and directives. A regulation binds both the member state and the individual; it should be applied by all administrative authorities and courts in the member states, and its purpose is to create uniform law throughout the Community. Directives are legally binding instructions addressed to every member state, to be incorporated within a certain time in its national legislation. Thus, the function of a directive is standardization of laws.

Effects on Health Care

Free Movement of Persons

One of the fundamental rights that the Treaty of Rome gives to all EC citizens is freedom to pursue their professional activity in any of the 12 member states of the Community. Specific directives concerning medical specialists and general practitioners, nurses responsible for general care, midwives, pharmaceutical chemists, and dentists have already been issued. These directives not only establish the right to practice in another member state, but also permit the rendering of services without actual establishment in another member state. In January 1989, a directive on the mutual recognition of diplomas of higher education came into force. Any EC citizen who presents a proper diploma must be admitted to the profession. The member state should treat the traveling professional and the immigrant professional the same way as they treat their own citizens, without any discrimination on grounds of nationality, neither in law, nor in administrative practice, nor in fact. As for the immigrant professional, all restrictions to their activities should be abolished if such restrictions are exclusively or principally to hinder the provision of services by nonnational EC citizens.

Free Trade for Pharmaceuticals

The pricing of medical products and their inclusion in the scope of national insurance systems came under regulation in 1989. On the basis of the provision for free trade of goods, the European Court ruled that a national measure, intended to control the price of pharmaceutical products, that differentiated between domestic and imported products conflicted with one of the EC articles. The Court acknowledged that member states have the responsibility to combat inflation, but that national price-restricting measures cannot be used to discriminate against imported medicine.

Health Care Eligibility

The social security objectives of the EC are limited to the coordination of existing national schemes, and as such do not affect the content of the individual national social security legislation. But the coordination of the almost incomparable social security schemes will be difficult, and applications in specific situations may be inequitable. One example is the provision that enables insured persons of one member state to receive treatment in another member state provided that such treatment has been authorized by a competent national health care authority. The costs of treatment are at the expense of that authority, yet expenditures for care vary greatly between the member states (Table 1). On the other hand, private health insurance is regarded as an object of trade between the member states, as a service to which the free movement/free establishment policy applies. Because almost 40% of the Dutch population is privately insured, the Netherlands is an attractive market to foreign health insurers, not only to insurance companies from the member states, but also via takeovers of established European insurance companies by companies from Japan, Switzerland, and the United States. In most member states (except for Belgium and West Germany), private health insurance is less competitively offered than it is in the Netherlands, being purchased by only 2–7% of the population.

Developments of Health Policy

The World Health Organization

In 1980, the European version of the "health-for-all" strategy was enunciated. Subsequently, in 1984, 38 regional targets were adopted by the 32 member states of the European Region of the World Health Organization (EURO), including the 12 EC member states. The core objective is that by the year 2000 "health for all" must be under way, and the first of the 38 outcome targets (namely, "equity in health") must be reached. The equity-in-health strategy of the World Health Organization [4] is to reduce differences in health status between countries and between groups within countries by 25%. This pan-European policy was adopted outside the political, institutional, and legal framework of the EC and therefore lacks a clear legal and constitutional basis. But it hardly lacks political support of the member states and the Community at large.

TABLE 1: Costs of Health Care per Capita in Member States of the European Community in 1986 vs Canada and the United States in 1985

Country	Cost (U.S. dollars)
United States	1710
Canada	1362
France	1039
Germany	1031
The Netherlands	984
Luxembourg	968
Belgium	826
Denmark	800
Italy	764
United Kingdom	711
Ireland	549
Spain	486
Portugal	310
Greece	245

Note.—Data on European Community from the Organization for Economic Cooperation and Development [2]. Data on Canada and United States from Evens et al. [3].

Professional Organizations

In 1956, the Union Européenne des Médicins Spécialistes (UEMS) was founded as a private union of European medical specialists to defend the title of medical specialist and the specialist's role in health care, to promote the quality of that care, to promote cooperation between national professional organizations and solidarity between specialists, to promote the free exchange of medical specialists, and to defend their moral and medical interests. With the establishment of the EC in 1957, the UEMS became an EC organization and a Standing Committee of Physicians, the Comité Permanente was established, in which all physicians of the EC member states are represented together with associate members from nonmember states as observers. The Comité Permanente is concerned with (1) promotion of the highest standard of medical training, practice, and health care within the EC; (2) promotion of free movement of medical specialists in the EC; and (3) representation of the medical profession to nonmedical authorities of the EC.

Recognition of Specialties

A medical specialty is recognized by the UEMS when it is represented in two thirds of the 12 member states. Each specialty that has been recognized is represented in a monospecialist section of the UEMS, which studies the problems raised by the Treaty of Rome concerning definition, training qualifications, and the practice of that particular specialty. To date, 27 specialties have been recognized. This achievement should not be underestimated. In Italy, for instance, 148 medical specialties are proclaimed, which requires the UEMS to group these numerous subspecialties into fewer more broadly accepted categories.

Despite recognition of specialties, the basic curriculum of each has not yet been established. This has led to a commission within the UEMS, the main function of which is the standardization of training programs and determination of what good training programs should encompass. The EC also has been interested in medical training. A directive has created the Advisory Committee of Medical Training, an official body with equal representation from the responsible authority, the medical faculties, and the professional organization of each member state. The goal of this committee is to promote an equal, high level of training and qualifications in the member states. Recently questionnaires were sent to organizations dealing with training programs in the member states to determine the status of these programs.

Consequences for Radiology

Professional organizations such as the European Federation of Organizations for Medical Physics (EFOMP) and the European Association of Radiology (AER) will undoubtedly attract the attention of the EC.

The EFOMP, formed in 1980, has surveyed the status of quality assurance among the 23 member countries in Europe and informed the EC Commission accordingly in October 1988.

The AER, founded in 1963, is an elected federation representing all 28 radiology societies in Europe, including those in the 12 EC member states. The AER is especially concerned with establishing and maintaining the highest educational standards. The unification of Europe undoubtedly has stimulated the AER to more activity. It organizes and sponsors European congresses and, with support from the Radiological Society of North America and the European radiologic industry, now plans congresses on a permanent site every 2 years, instead of every 4 years, as in the past. In 1991 and 1993, congresses will be held in Vienna, and to commemorate the 100th anniversary of Roentgen's discovery, Berlin has been chosen as the site for 1995.

EC Directive on Radiation Protection

The (84/466/Euratom) directive [5] compelling the EC member states to establish fundamental measures for the protection of persons exposed to radiation for diagnostic or therapeutic reasons will have a direct impact in the near future. The directive was issued in 1984 along with some guidelines on how to improve radiation protection. Since then, each member state is adjusting its own directives. The EC directive addressed the following issues: (1) medical justification—the exposure of any person to ionizing radiation should be medically justified and the radiation dose should subsequently decrease to "as-low-as-reasonably-achievable" levels; (2) standards of qualification for persons who use radiation in health care; (3) protocols for quality assurance for radiographic equipment; (4) reduction of the number of pieces of radiographic equipment; (5) availability of a competent medical physicist when equipment is used in radiotherapy and nuclear medicine.

European Journals

Journal publication has not been directly addressed by the EC, but some international cooperation may be desirable. In many European academic faculties, the journals in which publications appear and the number of citations these publications have received are used to measure the value of research. Journals are rated by their "impact factor" [6]. As a consequence of emphasis on publication in high-impact journals, it is time to start working on one core European radiologic journal. There is no dominant large-circulation European journal (Table 2).

Since 1987, the official journal of the Dutch Society has been the *Journal of Medical Imaging*. Stimulated by the Europe 1992 idea, I began, in my capacity as chief editor of that journal, calling on the editors of other European journals to explore the opportunities for possible mergers. Some lines from the letter I received from Terry Patton, who is associated with the *British Journal of Radiology*, reflect some nationalistic hesitancy. "In theory, I am sure that Europe could produce at least one journal comparable to *Radiology* or *AJR* and that we (Europeans) are losing out because we are all trying to 'go it alone.' There are also people in U.K. who think that it is anomalous that we (UK) produce two journals (BJR and Clin

TABLE 2: European Radiology Journals

Journal	Society/ Affiliation	No. of Members	No. of Full-Cost Subscriptions
Acta Radiologica (founded 1921)	Nordic countries	2500	1500
British Journal of Radiology (founded 1896)	British Institute of Radiology	1800	3000
Clinical Radiology (founded 1949)	Royal College of Radiologists	3300	1700
Journal Belge de Radiologie (founded 1917)	Belgian Society	900	<200
Journal of Medical Imaging (founded 1987)	Dutch Society	850	<100

Radiology). However, the reasons are historic. The BJR is the oldest radiological journal in the world, being the direct descendant of Archives of Roentgen Ray, founded in 1896, one year after Roentgen's discovery. The *British Journal of Radiology* is the official journal of the British Institute of Radiology, a multidisciplinary organization whose members are anyone interested in medical radiology, such as diagnostic and therapeutic radiologists, radiobiologists, technicians, physicists, and industrialists. *Clinical Radiology* is the official organ of the Royal College of Radiologists, a medical body with important academic and educational responsibilities. Its fellowship examination is the only radiologic qualification accepted for consultant appointments in the U.K." In 1989 *Clinical Radiology* became a monthly journal. It is obvious that the *British Journal of Radiology* and *Clinical Radiology* have a different pedigree, which interferes with merger ideas.

Acta Radiologica is produced by radiologists and oncologists from the Nordic countries. It is not yet ready to accept editors outside these countries. Furthermore, the editor wants the two journals *Acta Radiologica* and *Acta Oncologica* to be dominated by research from the Nordic countries. A new French journal, *Diagnostic and Interventional Radiology* was announced during the International Congress of Radiology in Paris last year. It is linked to the French Radiological Society, and the best papers from their national journal will be translated into English and published in *Diagnostic and Interventional Radiology* four times a year for international readers. The *Journal Belge de Radiologie* is considered to be instructive and educational and specifically focused on the home market. Articles are mainly in English. Extensive abstracts from other journals are furnished to the membership of the Belgian Society.

The *European Journal of Radiology* is more independent. It was founded 9 years ago, and claimed to be the "official journal of the European Association of Radiology" since 1986. Unfortunately, the AER, being a federation of national societies, had no individual members to guarantee adequate circulation. Convinced of the desirability of a larger European journal, and following discussions with the publishers concerned, the chief editor of the *European Journal of Radiology*, Jan Göthlin, and I are working together on the merger of the *European Journal of Radiology* and the *Journal of Medical Imaging*. Consequently, starting in January 1990, the two journals will appear under the title *European Journal of Radiology*, published by Elsevier Science Publishers.

In the meantime, the board of the AER has redesigned the European congresses, and a postgraduate journal (*European Radiology*) closely linked to the European congress, produced at regular intervals between the congresses, is under consideration. Consequently, the newly merged *European Journal of Radiology* will not be the official journal of the AER. Hence, it may be anticipated that a single large European journal in radiology will not meet the 1993 deadline of the Common Market.

Discussion

International cooperation between the EC and the World Health Organization has borne fruit in the past. Activities on environmental protection and health, such as a Smoke-Free Europe, Europe against Cancer, and pleas for the development of a common European policy to fight AIDS, are examples. In terms of health care and health care organizations, experience with these programs has revealed that the member states are at different stages of development. It will subsequently take a long time before a reasonable coordination between the national programs in the member states is achieved.

What influence the directives from Brussels may have on health care is uncertain. The regulation of physicians and health care personnel is most likely to remain the exclusive responsibility of the national authorities of the member states and, unlike the American states, these governments also will probably remain primarily responsible for financing or otherwise providing personal health care to their citizens. Thus, the EC seems unlikely to encounter the problems of divided responsibilities that have caused the U.S. federal government to assume a greater role in policing individual physicians [7]. Still there is the fear that brain drain will occur to states with attractive climates. Havinghurst [7] suggests "Although poorer Europeans are even more closely tied to their communities by culture and language than are Americans, the EC might be wise to adhere to an instrumental view of free movement guarantees and not to create a right to travel and relocate as extensive as the right created by the U.S. Supreme Court." Migration of medical professionals in Europe since

1957 has been on a very small scale, possibly because of national restrictions intended to minimize difficulties in local manpower planning. Some local restrictions are not in defiance of the EC Treaty. A local rule may declare that the practitioner must reside within the area of his practice in order to guarantee his availability to patients in that area. Requirement to possess a license granted by local authorities is not in defiance of the treaty either, provided that the chances of obtaining such a license are equal for physicians from other member states.

But other conditions are in defiance of the treaty, such as the provision in the French national health code that permanent employment as a health care professional in public hospitals is reserved for French nationals. A member state can refuse to hire nonnationals in public services but only for functions that are directly related to the public authority or the protection of the interests of the state.

There are also problems that may restrict the influence of professional organizations. The labors of individuals in the UEMS and its committees are offered voluntarily on a spare-time basis. Funds are lacking, and the road along which council and advice of the UEMS must go, via the Comité Permanente to the Advisory Committee of Medical Training and the European Commission, is a long and strenuous one, full of bureaucratic pitfalls.

Clearly, the evolving supranational processes and the ways in which EC policies will affect health care issues are less tangible than the consequences of the transfer of goods, services, and capital. That, at least, is what most health officials like to believe. Others, however, expect that the liberalization of the private insurance market in July 1990 may have an enormous impact on health care. Patients will no longer be restricted exclusively to local medical care and, assuming that their insurance company is obliged to reimburse the costs of treatment, will travel to prestigious hospitals abroad. This phenomenon can already be observed in border regions of some member states, where patients and medical groups are orienting themselves in neighboring states. Because the financial aspects of health care are dealt with in the Treaty of Rome and are regarded as an object of trade, the member states will not be able to use their own national budgetary provisions as an excuse. Subsequently, health care in Europe will inevitably become more expensive in the future. Competition between medical facilities in the member states will lead to a drive toward higher quality. If this change in attitude indeed does occur, national flavors will evaporate and will have to be replaced by community policies.

The realization of Europe 1992 will require many future discussions. But the year 1992 is not essential. What really counts is the vision of one and only one free Europe—the sooner, the better. The recent changes in Eastern Europe now compound the problems facing the original European Community. They are forces that will further compel realization of the economic goals of the Treaty of Rome and, with that, more unification of medicine and other social systems in Europe.

ACKNOWLEDGMENTS

I would like to express my gratitude to the editors in chief who provided me with information concerning their journals. Terry Patton, *Br J Radiol*; C. D. R. Flower, *Clin Radiol*; Erik Boijsen, *Acta Radiol*; Jacques Pringot, *J Belge Radiol*; and Jan Göthlin, *Eur J Radiol*. I thank A. J. Simons for his help in getting the material about the professional organizations of the EC straight. I am grateful to I. Isherwood, president of the AER, for his wise words concerning the AER.

REFERENCES

1. Ter Kuile BH, Du Pré FM, Sevinga K. The European dimensions. In: *Health care in Europe after 1992*, Symposion Rotterdam Oct. 16–19, 1989. Rotterdam: Erasmus Congress Bureau (in press)
2. Organization for Economic Cooperation and Development (OECD). *Financing and delivery health care, a comparative analysis of OECD countries*. Paris: OECD, **1987**
3. Evens RG, Lomas J, Barer ML, et al. Controlling health expenditures: the Canadian reality. *N Engl J Med* **1989**;320:571–577
4. World Health Organization Regional Office for Europe (WHOROE). *Evaluation of the strategy for health for all by the year 2000*, vol. 5. Copenhagen: WHOROE, **1986**
5. 84/466 Euratom, PB 1984 NR. L 265. European Commission, Brussels, **1984**
6. Garfield E. Citation analysis as a tool in journal evaluation. *Science* **1972**;178:471–479
7. Havinghurst CC. American federalism and American health care: lessons for the European community? In: *Health care in Europe after 1992*, Symposion Rotterdam 1989. Rotterdam: Erasmus Congress Bureau (in press)

Book Review

The Radiology Word Book. By Theresa Indovina and Wilburta Q. (Billie) Lindh. Philadelphia: Davis, 504 pp., 1990. $22.95, softcover

"*The Radiology Word Book* is designed to be used primarily by medical radiology transcriptionists. However, many other professionals, such as radiology personnel, radiology technicians, nurses, ward clerks, medical records administrators, etc., will find this book an excellent reference source." This is the beginning of the authors' preface. They suggest that the book, in the format of a standard dictionary, be used as such. The book has 465 pages of word lists, 12 pages of sample reports, an appendix with the physical constants of the elements, and a computer glossary. Four pages are devoted to fractures: the type, the definition of the type, the complications of the fracture, and some clinical information. This information is followed by Figures 1-14; most of these are drawings, but four are brain MR images.

It is clear that this book is a mixed bag. Segments are not for the medical transcriptionist, nor is all of the book applicable to any one group. The book contains a lot of information and at a modest price is a nice compendium of material grouped together that otherwise may be difficult for transcriptionists to find (i.e., the bones of the wrist all listed together on page 44). The illustrations are simple and clear, but it is difficult for me to understand who really would need to see the four MR images. Frequently, the medical transcriptionist needs to have the correct spelling but not the meaning of a word, and therefore this book can be helpful. Especially for a new medical secretary or transcriptionist, the ability to find a word rapidly is important.

The book does, however, have some shortcomings. First, it has some misspellings. For example, thallium is spelled thalium on the cover but is spelled correctly in the text. Similarly, yttrium is spelled correctly in the text but incorrectly on the cover. On page 309, potassium is spelled postassium, and therefore potassium chloride is listed incorrectly. I think that this sort of problem can be dealt with in editing the second printing. The need for sample reports, however, is something that escapes me. Each radiology department will have its own reports, and the format of these reports should be irrelevant to most people using the book.

Despite these comments, this is a detailed, informative, quick reference for a number of persons and, at a cost of $22.95, it is a bargain. I suggest that secretaries and transcriptionists in radiology departments, purchasing and billing personnel, and some medical libraries would benefit from this text.

Thomas L. Slovis
Children's Hospital of Michigan
Detroit, MI 48201

Perspective

Physician Referrals to Radiologists

Michael Lopiano,[1] Jonathan Stolz,[2] Jonathan Sunshine,[3] Trevor Fisk,[4] and Evan Leepson[3]

In 1989 the American College of Radiology (ACR), through its Commission on Marketing Communications, conducted a national survey of physicians about referral patterns for radiologic studies. It is believed to be the largest survey to date on this issue, with 2982 nonradiologist physicians responding. The findings confirm some of the assumptions that radiologists already make about the attitudes of referring physicians, but also suggest some other issues for consideration. The ACR has permitted the publishing of this study in order to share these findings as broadly as possible within the radiologic profession.

Methods

All of the approximately 3500 radiology practices (including solo practitioners and groups) in the United States that are known to the ACR were invited to participate in the survey. Each practice was sent a kit consisting of a recommended cover letter and questionnaires to be distributed to its 10 most important referral sources. Some 350 radiology practices throughout the United States agreed to mail surveys to their referral sources. Referring physicians were invited to respond directly and anonymously to the ACR. The ACR tabulated and analyzed 2982 responses.

Each of the 50 states was represented among the respondents. Their distribution by state was broadly proportional to population. The notable exceptions were that New Jersey, New York, and Massachusetts were somewhat underrepresented, and North Carolina and Virginia were somewhat overrepresented. These distortions in the sample were not large and do not invalidate the general findings.

By specialty, the respondents fairly closely reflected the overall distribution of United States physicians (excluding, of course, radiologists) reported by the American Medical Association [1] (Table 1).

Statistically, the overall sample is large enough to yield results accurate to within 1% at a 95% confidence level. However, this confidence interval does not recognize any error that may arise from limits in the representativeness of the sample. Larger confidence intervals apply to the responses of subgroups of the sample, for instance, physicians in a particular specialty.

The survey was intended to investigate the following issues: (1) To what extent do nonradiologists perform their own imaging? (2) Do physicians tend to concentrate their radiology referrals to one radiology practice or to divide them among several? (3) What are the most important factors in deciding where to refer patients for imaging, or in changing established referral patterns? (4) How do physicians feel about marketing communications that they may receive from radiologists? (5) How do referring physicians feel about radiologists disclosing the results of studies to their patients?

Results

Responding physicians each referred an average of 18 patients a week to radiologists. Two thirds of all respondents referred 10–30 patients to radiologists per week.

Amount of Imaging Done by Physicians Who Refer Patients to Radiologists

Thirty-one percent of responding physicians performed some radiology studies in their own practices; 67% did not (2% of respondents did not supply this information). Physi-

---

Received May 2, 1990; accepted after revision June 11, 1990.

[1] Department of Radiology and Nuclear Medicine, St. John's Hospital, 333 N. F St., Oxnard, CA 93030.
[2] Department of Radiology, Community General Hospital, 145 N. Sixth St., Reading, PA 19601.
[3] American College of Radiology, 1891 Preston White Dr., Reston, VA 22091. Address reprint requests to E. Leepson.
[4] Thomas Jefferson University Hospital, 1020 Walnut St., Philadelphia, PA 19107.

AJR 155:1327–1330, December 1990 0361–803X/90/1556–1327 © American Roentgen Ray Society

TABLE 1: Distribution of United States Physicians by Specialty

Specialty	Survey Respondents (%)	All U.S. Physicians (%)
Family/practice	24	17
Obstetrics/gynecology	8	8
Pediatrics	4	8
Internal medicine	25	21
Neurology	2	
Cardiology	3	3
Orthopedics	5	4
Other	29	39[a]

[a] Including neurology.

cians with their own imaging capabilities make, of course, fewer referrals to radiologists, but none of this third of the responding physicians was totally self-sufficient with regard to imaging. Because participants in the survey were recruited by the radiologists to whom they refer patients, physicians who never refer to radiologists (if any such physicians exist) were not included in the survey, and those who rarely refer to radiologists may be underrepresented in the survey.

As might be expected, the percentage of physicians with specific imaging capabilities in their own practices varies significantly by specialty and imaging techniques. In the following situations, more than 10% of physicians in a particular specialty reported having a given technique available in their own office: Radiographic equipment in 36% of family medicine practices, 21% of internal medicine, 12% of neurology, 15% of cardiology, 61% of orthopedics, and 12% of all other physicians. Thirty-nine percent of obstetrics/gynecology practices had sonographic equipment. Twelve percent of neurologists had CT equipment. Twelve percent of cardiologists had angiographic equipment. The confidence interval for family medicine, internal medicine, and other specialties was 2%. The confidence level for obstetrics/gynecology was 3% and for orthopedics 4%.

In no specialty did more than 10% of respondents indicate having MR, nonobstetric sonography, or other imaging resources not listed here.

In short, large numbers of physicians in certain specialties now perform specific types of diagnostic imaging in their own practices, but many primary care physicians and specialists do not. Moreover, physicians with their own imaging capabilities still refer to radiologists, some of them quite extensively.

Number of Radiology Practices Used by Referring Physicians

The number of radiology practices to which outpatient referrals were made was as follows: referrals to one radiology practice, 46%; referrals to two radiology practices, 32%; referrals to three radiology practices, 14%; referrals to four or more practices, 8%. Thus, nearly half of all physicians choose one practice for all their outpatient radiology needs. For the radiologists concerned, such 100% loyalty from referring physicians should, if possible, be identified, so that special attention can be paid to retaining their support.

Almost another half of all physicians split their referrals among two or three radiology practices. The reasons were not investigated, but may include specialization of the radiology practices in different imaging techniques, convenience for different populations, or scheduling problems for certain studies. Radiologists should be mindful of this large number of referring physicians who are unlikely to "put all their eggs in one basket." Clearly, marketing opportunities exist to meet part of the needs of many physicians, even if their total dependence on one practice is unobtainable.

Most Important Factors in Selecting Radiologists

Table 2 shows, in order of importance, how respondents ranked various factors involved in selecting a radiologist for an outpatient study.

The second column in Table 2 suggests that these factors fall into three categories of importance, with significant gaps between them: the most important are the ability to schedule quickly, quality, personal familiarity, and speed of reporting results. Convenient location and range of techniques available were found to be somewhat important, and hospital affiliation and patient's preference were found to be less important.

Clearly, speed of both scheduling and reporting results is a critical factor in referring physicians' satisfaction. Inability to meet these expectations all the time or some of the time causes many physicians to "hedge their bets" by not depending solely on one radiology practice.

The relatively high level of importance attached to "personal familiarity" with the radiologist suggests that the traditional approach to building peer respect—through direct professional contact with potential referral sources—remains an essential ingredient of a successful radiology practice. Other relationship-building tools, borrowed from marketing methods in other fields, have been used increasingly. These techniques include brochures, mailings to physicians, and systematically organized referral relations programs. However, this finding suggests that such activities should be viewed as supple-

TABLE 2: Most Important Factors in Selecting a Radiologist

Factor	Percentage of Respondents Choosing: As Most Important Factor	Percentage of Respondents Choosing: As One of Top Three Factors
Ability to schedule patients quickly	30	68
Personal familiarity with radiologist	29	55
Speed in receiving results	18	58
Convenient location	16	43
Range of techniques available	11	37
Hospital affiliation	8	20
Patient's preference	5	18
Other[a]	22	27

[a] Nearly all of the "other" responses concerned the quality/accuracy of the radiologist. As this factor was not offered in the multiple choice set, but was so frequently specified, it should be regarded as of at least equal importance to the top two or three factors in the list above.

mentary to rather than as a replacement for the development and maintenance of personal physician-to-physician relations.

Nevertheless, it is noticeable that with the possible exception of quality, no one factor was included among the top three by more than 68% (or approximately two thirds) of respondents. (It is not uncommon with similar surveys about consumer products, for example, to find one key "benefit" mentioned by close to 100% of respondents that is therefore considered indispensable to its marketing.) This situation allows competing radiology practices to differentiate themselves by emphasizing different factors within this list that matter to some significant segment of the local medical community. As an example, a practice that emphasizes convenient location may not have to emphasize speed of service, as there is a sizeable minority of physicians to whom convenience is more important than speed.

Hospital-based radiologists should heed the relatively low ranking given to hospital affiliation. It implies that most referring physicians will not necessarily direct outpatient studies to the radiology department of a hospital with which they are affiliated, unless that department also is perceived as desirable in terms of other factors to which the physician attaches more importance.

Respondents were asked to rank not only those factors important in selecting a radiologist for referral, but also those factors most likely to lead them to change established referral patterns for radiology (Table 3).

As would be expected, the responses to this question about negative features of radiology practices largely mirror the answers to the previous question about positive features. Three slight differences are worth noting.

The more frequent (72–78%) mention of speed issues as a reason for changing referral patterns, compared with its frequency of mention (58–60%) as a reason for choosing a radiologist, reflects a common result in customer surveys in fields other than radiology. The ill will generated by failure to meet an important service expectation exceeds the goodwill created by meeting that expectation. These results reinforce the important of speed of response (both in scheduling appointments and in reporting results) for most referral sources.

The higher rate of mention of patient's choice in this table compared with the previous one reflects the same phenomenon. Patients' agreement with a referral recommendation may do little to reinforce a physician's comfort with his or her choice of radiologist, but patients' resistance can do much to discomfort referring physicians, and in extreme cases, may lead to a change in referral patterns.

The rate of mention of HMOs/PPOs (30%) as a reason for changing radiology referral patterns is not far out of line with their degree of market penetration nationally and may be expected to grow if that penetration grows.

TABLE 3: Reasons for Changing Radiologists

Reason	Percentage of Respondents Choosing	
	As Most Important Reason	As One of Top Three Reasons
Patient scheduling delays	31	78
Reporting delays	29	72
Patient's choice	18	49
Radiologist's personality	17	48
HMO/PPO policies[a]	16	30
Other[b]	14	16

[a] HMO = health maintenance organization, PPO = preferred provider organization.

[b] Mainly issues of quality/accuracy. Please see note to Table 2.

Value of Literature Currently Received from Radiologists

Despite the importance of personal familiarity with a radiologist, other forms of communication may provide useful supplementary contact with referral sources. The survey investigated whether physicians currently receive mail materials about the capabilities of at least one local radiology practice and whether they find them useful.

Fifty-seven percent of those who receive mailings (51% of all respondents) find them useful; 43% do not find them useful. Fifty-seven percent of those who do not receive mailings (49% of respondents) would find them useful; 43% would not. Thus, approximately half of the respondents currently receive such literature from radiologists. A majority of those receiving such materials find it useful, but a significant minority do not. A majority of those not receiving such materials would find them useful but, again, a significant minority would not.

There is a clearly unmet interest currently, with 57% of physicians not receiving such materials but desiring them. The sizeable minority of current recipients not finding such materials useful also suggests that radiologists should consider how such literature might be improved.

However, the main issue may be not the quality of such literature, but differences among physicians in their interest levels. Clearly much of this literature is currently being sent to physicians unlikely to be responsive to it. That is true with all direct mailing. The individual radiology practice must decide for itself whether to continue with its current mailing list and accept that only approximately 60% of recipients will find the material valuable, or attempt to identify nonresponsive physicians and cull them from those mailing lists. These problems are not a case against such mailings, because they seem to fulfill a need of a large percentage of their recipients. They do illustrate, however, that any direct-mail program inevitably contains some waste circulation.

In addition to the respondents reporting that they receive literature from radiologists about their capabilities, other types of communication from radiologists were received by the following percentages of respondents: information about new imaging developments, 41%; telephone calls, 37%; referral, 34%; rolodex cards, 20%; patient information pamphlets, 19%; maps for patients, 18%; personal letters, 12%; personal visits, 11%; and business cards, 6%.

Respondents were not asked to rate their appreciation of these specific forms of communication, but one implication of these findings may be quite important. Given the high value attached by referring physicians to "personal familiarity" with a radiologist, it is noteworthy that less than half of the respondents report receiving telephone calls from radiology practices, and only one tenth report personal visits by radiologists. Both types of contact are, of course, time-consuming for the radiologist, but their cost-benefit may be worth testing.

Disclosing Results to Patients

In response to the question of whether radiologists should report results to patients, the responding physicians indicated that radiologists should report results only to the referring physician (34%); radiologists should report results to the referring physician and selectively to patients (55%); radiologists should routinely report results to both physician and patient (10%); no response (1%). Thus, a significant minority of referring physicians only want radiology results reported to them, but some two thirds now believe that radiologists also should report results to patients, at least on a selective basis.

The responses to this question did not vary widely by specialty (Table 4). Most of the differences in response shown in this table are well within the confidence interval given the number of respondents in each specialty and, consequently, are not of statistical significance.

The one specialty with a pattern of response that appears distinct is obstetrics/gynecology. The lesser support in that specialty for the radiologist withholding results from patients possibly reflects the growth of mammography. Although fewer physicians in this specialty believe that results should be reported to them only, the percentage of obstetricians/gynecologists who currently support results being shared with patients as a routine practice is still only slightly higher than in other specialties.

In light of these responses, it is not possible to recommend one clear policy on this issue for radiology practices. Opinions among referring physicians about the direct disclosure of results to patients may be changing. Only a minority now support the traditional approach of disclosing results only to the referring physician, but they remain a sizeable minority. Although a small minority of physicians favors routine disclosure to patients by radiologists, the majority clearly sees some need for selectivity in when and when not to do so.

TABLE 4: Reporting Results of Radiologic Examinations

Specialty	To Referring Physician Only (%)	To Physician and Selectively to Patient (%)	To Both as Routine (%)
Family medicine	38	53	9
Pediatrics	32	51	17
Internal medicine	38	56	6
Obstetrics/ gynecology	20	63	17
Neurology	37	52	11
Cardiology	34	54	12
Orthopedics	36	50	14
Other	32	56	12

Certainly, an individual radiology practice, in light of these findings, could develop a written set of guidelines on disclosure of results, including those selective circumstances in which results will be given to patients in addition to the referring physician, and circulate those draft guidelines for comment to referring physicians. As their opinions are likely to vary, and may be strongly held, it could be unwise to adopt the majority response as a standard policy. It may be preferable to develop a mechanism that allows individual referring physicians to elect their own policy regarding having results disclosed to patients. Such an administrative process may, however, be very cumbersome logistically. Moreover, this survey cannot show whether those who favor selective results disclosure are reasonably consistent or widely divergent in their definitions of the circumstances in which disclosure would be appropriate.

Conclusions

Radiologists' understanding of, and responsiveness to, the needs and preferences of their outpatient referral sources are of great importance to their practices, but there is a paucity of published research on referring physicians' attitudes. "Market research represents a deliberate commitment by a group to organize its efforts to create a favorable change" [2]. This survey by the ACR was conducted to assist its members and their radiology practices in determining how to "create a favorable change" in response to the changing attitudes and needs of referral sources. The findings confirm some common perceptions about referring physicians, but provide some greater assurance by quantifying them. They also shed new light on some aspects of referring physicians' relations with radiologists.

Radiology practices can only benefit from further research into these issues. Some of the findings in this survey show a need for more investigation. Because some of the attitudes studied may be in a state of flux, periodic repetitions of such surveys also may be valuable in providing a timely indication of any change.

The ACR gratefully acknowledges the contribution of the responding physicians to this study, which is designed to aid radiologists in being even more responsive to the diagnostic and therapeutic needs of the United States medical community and its patients.

Meanwhile, we believe, as did the ACR's Commission on Marketing Communications when reviewing these data, that the practicing radiologist can gain from reviewing such research and forming his or her own strategic conclusions from it.

REFERENCES

1. American Medical Association. *Physician marketplace statistics*. Chicago: AMA Center for Health Policy Research, **1989**
2. Marasco JA, Linton OW. Marketing radiology and radiologic services. *AJR* **1989;**152:191–194

Perspective

Antitrust Principles for Radiologists

Stewart R. Reuter[1]

As the practice of medicine becomes more competitive, the states' attorneys general, the Federal Trade Commission, the Justice Department, and individual competitors progressively will use the Sherman Antitrust Act to ensure a competitive market for the delivery of health care services. Therefore, radiologists must have an understanding of the purposes of the Sherman Act and an understanding of types of anticompetitive activities that will trigger civil and criminal penalties. Specifically, radiologists must avoid blatant violations, such as price fixing, division of markets, and group boycotts, any of which may elicit the interest of the Justice Department. Further, radiologists need to consult knowledgable legal counsel when carrying out peer review activities and when entering into exclusive contracts with hospitals, particularly hospitals that have significant market power.

Radiologists increasingly have become involved in antitrust litigation in recent years. Although they must therefore have some understanding of the Sherman Act to avoid becoming defendants, a detailed knowledge is not necessary. The use of the antitrust laws by the courts is complex, and an understanding of the nuances of antitrust principles is beyond the interest of the average radiologist. It is enough that they understand the purposes of the statutes and know the types of anticompetitive behavior that may result in antitrust litigation from the point of view of both a potential plaintiff and a defendant, either of whom might be a radiologist. Such an understanding is even more important today because of increased antitrust activity in the health care field by the Department of Justice.

The Antitrust Acts

In 1890, Congress passed the Sherman Act in an attempt to curb the abusive, monopolizing trade practices of American industry. The act has two primary sections. Section I prohibits competitors from joining together to restrain competition unreasonably. The section reads in part: "Every contract, combination in the form of trust or otherwise, or conspiracy, in restraint of trade or commerce among the several States, or with foreign nations, is declared to be illegal" [1]. Section II makes illegal the formation of a monopoly. It states: "Every person who shall monopolize, or attempt to monopolize, or combine or conspire with any other person or persons, to monopolize any part of the trade or commerce among the states, or with foreign nations, shall be deemed guilty of a felony . . . " [2].

In 1914, Congress passed the Clayton Act to clarify and augment provisions of the Sherman Act. From the radiologist's point of view, the provisions of the Clayton Act need not be separated from those of the Sherman Act. However, the Clayton Act also created the remedies of triple damages and the award of attorney's fees for antitrust violations [3], making loss of an antitrust case quite expensive and placing great pressure on defendants to settle.

During the first 85 years of the Sherman Act, most observers thought that it did not apply to the learned professions. During this period, only a handful of antitrust cases related to health care were litigated successfully. Most were suits by health maintenance organizations (HMOs) against medical

---

Received April 30, 1990; accepted after revision June 14, 1990.

[1] Department of Radiology, The University of Texas Health Science Center at San Antonio, 7703 Floyd Curl Dr., San Antonio, TX 78284-7800.

societies that recommended that the society's membership boycott the HMOs. In 1975, however, the United States Supreme Court decided the landmark case of *Goldfarb v. Virginia State Bar* [4] and in 1978, *National Society of Professional Engineers v. United States* [5]. These cases held that Virginia lawyers had fixed prices for real estate transactions in violation of the Sherman Act and that the engineers had restrained trade through a canon of ethics prohibiting competitive bidding by its members. In both cases the Court stated that the learned professions were trades and therefore subject to the antitrust statutes. In the years since 1975, antitrust litigation in the health care industry has increased rapidly. Suits by and against radiologists have been an important part of the explosion of litigation in the field. The American College of Radiology (ACR) has participated actively in some of the litigation.

In part, the increased litigation has resulted from the increased number of radiologists who are competing for the same patients. Another cause has been the rapid expansion of alternative health care delivery systems, such as HMOs and preferred provider organizations, and the threat that they pose to established patterns of medical practice. Also, nonphysician health care providers, such as chiropractors, have pushed aggressively for hospital privileges and a larger share of the health care dollar. Finally, radiologic services have moved to the outpatient setting, where competition is more intense than in the hospital. At a recent antitrust seminar, several hypothetical situations in which the antitrust laws were discussed involved a radiologist.

Enforcement

Several different groups enforce the federal and state antitrust laws. The Antitrust Division of the Department of Justice enforces the Sherman and Clayton acts when it determines that criminal violations of the acts have occurred. A violation of the Sherman Act can result in fines up to $1,000,000 for corporations, or $250,000 and up to 3 years in prison for individuals. Although any violation of the acts technically creates the possibility of exposure to criminal sanctions, the Department of Justice has not prosecuted physicians until recently. This reflects a change in policy by the Department of Justice. In a speech before the American Medical Association in 1988, Charles Rule, the Assistant Attorney General in the Antitrust Division of the Department of Justice, told physicians that they are no different from other competitors and that the department intended to prosecute physicians who use price fixing, allocation of territories, or boycotts of competing health care providers to interrupt the free operation of competitive processes without any possible economic benefits for consumers (Rule CF, presented at the interim meeting of the American Medical Association House of Delegates, Dallas, TX, December 1988). In fact, the Department of Justice is currently pursuing three grand jury investigations that allege criminal violations of the antitrust statutes by two groups of physicians and one group of dentists.

The Federal Trade Commission Act gives the Federal Trade Commission (FTC) broad powers to prosecute unfair methods of competition and unfair or deceptive trade practices. If the FTC determines that a trade practice is anticompetitive, it orders the defendant to terminate the practice. Such an order was issued to the ACR regarding its original relative-value scale, which the FTC found in 1977 to be a form of price fixing [6]. When such an order is entered, the defendant may either appeal to the federal courts or negotiate a consent decree with the FTC that spells out what the defendant will not do in the future. In regard to its original relative-value scale, the ACR signed a consent decree agreeing to abandon the relative-value scale and did not appeal to the courts. Because the FTC has limitless resources to prosecute a case, most defendants sign consent decrees; to fight the FTC in court entails enormous legal fees.

Private parties also may seek enforcement of the Sherman Act in federal court, either for an injunction against an anticompetitive practice or for damages suffered because of the violation. The great majority of antitrust litigation in the medical field has been instigated by individual plaintiffs. Many of these plaintiffs have been radiologists challenging exclusive contracts between hospitals and radiology groups.

Finally, most states have antitrust statutes similar to the Sherman Act. These are enforced by the states' attorneys general. For many years the states were more active than the federal government in enforcing their own antitrust laws in the health care field. One of the most important price fixing cases, *Arizona v. Maricopa County Medical Society* [7], arose out of state enforcement of antitrust laws.

Application of the Sherman Act by the Courts

When the Sherman Act was enacted a hundred years ago, Congress did not envision its application to the delivery of health services. Even if it had, no one could have predicted the types of competition that exist in today's health care system. Therefore, courts applying the Sherman Act today rely on the plain wording of the act and previous interpretations of the act in competitive settings both within and outside the health care field.

A discussion of the Sherman Act requires the preliminary introduction of three concepts: the "per se" violation, the "rule of reason," and exceptions to the act.

Long before *Goldfarb* [4], the Supreme Court determined that certain types of anticompetitive behavior had such an obviously negative effect on competition that they should be considered per se violations of the Sherman Act; that is, the behavior should be found to be anticompetitive regardless of the impact of the conduct on the consumer. Such behavior includes price fixing, division of markets, group boycotts, and tying arrangements. If the activity does not fall into one of these categories, it is analyzed according to the rule of reason and the anticompetitive aspects of the activity are balanced against the procompetitive consequences to see whether the activity has a positive or negative impact on the consumer.

Finally, a number of exceptions to the application of the Sherman Act have developed through the years. Congress enacted the McCarran-Ferguson Act, which exempts certain aspects of the insurance business from the provisions of the Sherman Act [8]. Congress has also exempted the collective bargaining activities of labor unions [9]. Other exceptions to the provisions of the Sherman Act have been created by the courts. For example, courts have determined that citizens have a right to petition the legislature for changes in the regulations and statutes governing their field of competition [10] and thus have allowed competitors to join together to petition governing bodies even though, ordinarily, such a combination of competitors would be a violation of the Sherman Act. Finally, if a state has developed an extensive scheme to regulate an industry, the courts recognize that the state, as part of its regulatory capacity, may allow competitors to enter into practices that otherwise would be violations of the Sherman Act [11]. The health care industry is perhaps the best example of an industry that is extensively regulated by states, and this exception, the so-called state action exception, is of importance to physicians.

During the course of antitrust litigation, the plaintiffs' attorneys try to present their clients' cases in a manner calculated to convince the court to see the facts as a per se violation of the Sherman Act. If they succeed, the courts will find the alleged anticompetitive activity to be a violation of the Sherman Act without considering the procompetitive aspects of the activity. The defendants, on the other hand, initially try to describe the alleged anticompetitive activity as falling into one of the exceptions of the Sherman Act. Failing this, the defendant tries to prove that his or her activities were not a per se violation and that the procompetitive aspects of the activity outweigh the anticompetitive aspects.

Competitors and Competition

The Sherman Act forbids contracts, combinations, or conspiracies in restraint of trade. Such acts require that two or more legal entities work together. A person is a legal entity, and a corporation is a legal entity. Thus, two persons or a person and a corporation may conspire to restrain trade. However, an individual person may commit many types of anticompetitive activity so long as he or she acts alone. Also, a group of potential competitors might incorporate to form a practice group, such as an HMO; so long as they share risks and practice as a unit, they are considered to be a single entity. If otherwise separate business entities act together to restrain competition, however, they will be in violation of the act.

Some groups have had problems establishing themselves as legal entities. Medical societies, for example, even though incorporated under state laws, are considered to be groups of individual competitors. When a medical society acts to restrain competition in any manner, it probably is in violation of the Sherman Act. Similarly, partnerships are not corporations, but are groups of individual radiologists. However, most radiologists in partnerships share capital and risks, compete as a unit, and are not competitors. Although a partnership may act in a manner to impede competition, the impact is not so great as when a group of competitors does the same act, and a partnership probably is an entity for the purposes of the Sherman Act.

It is important to remember that the Sherman Act protects competition, not necessarily competitors. All arguments made by the plaintiff and defendant in an antitrust suit must be framed in terms of the impact of the alleged act on the consumer, not the impact on the competitor. For example, radiologists being excluded from practice in a hospital because of an existing exclusive contract with other radiologists must show that because of their exclusion, services to the consumer are less available or more expensive than they would be if the excluded radiologists had been admitted to the staff.

Market Share

Perhaps the most important determination in any antitrust proceedings is an evaluation by the court of the market share (or market power) of the defendant. The greater the extent to which any given competitor dominates a market, the more opportunity he or she has to establish the price, quantity, quality, and availability of services. In *Jefferson Parish Hospital District No. 2 v. Hyde* [12], recently decided by the United States Supreme Court, the outcome turned in great part on the court's decision about the relevant market for anesthesiology service in the New Orleans area. In this case, an anesthesiologist who had been excluded from practice at East Jefferson Hospital by an exclusive contract between the hospital and a group of anesthesiologists alleged a violation of the Sherman Act. When the case was decided by the 5th Circuit Court of Appeals, the plaintiff won, in great part because the court found the relevant market for anesthesiology services to be the East Bank of Jefferson Parish. In that market, approximately 30% of patients used the East Jefferson Hospital. However, on appeal, the United States Supreme Court focused on the 70% of Jefferson Parish patients who went to hospitals other than East Jefferson Hospital. In effect, the Court found the relevant market for anesthesiology services to be the greater New Orleans area. In this market, East Jefferson Hospital did not have significant market power. Had the facts been otherwise, and had Dr. Hyde been excluded from the staff in an isolated community with a single hospital, the result might have been different.

No rule defines the percentage of a market that must be dominated in order for a competitor to have significant market share; each case varies with the facts. For example, if a plaintiff can introduce evidence of some significant detriment to the consumer, such as artificially elevated prices, this can be used as evidence of a significant market power.

Per Se Violations of the Antitrust Acts

Anticompetitive activities that are so obviously unreasonable restraints of trade that the courts traditionally have found them to be per se violations include horizontal price fixing, horizontal divisions of markets, group boycotts, and tying arrangements.

Price Fixing

Whenever two competitors agree on the price to be charged for a product, an obvious violation of the Sherman Act has occurred. Price fixing is a concept that we have no problem labeling anticompetitive. However, some subtleties exist. Although competitors obviously cannot set a minimum price that they will charge for a service, can they set the maximum price? In *Arizona v. Maricopa County Medical Society* [7], mentioned before, the medical association formed two nonprofit foundations to promote fee-for-service medicine. As part of their activities, the foundations established a schedule of maximum fees that members would charge for medical services. About 70% of Maricopa County physicians were members of these foundations. The attorney general of Arizona challenged the fee schedule as a price-fixing arrangement. The county medical society argued that it was not trying to fix prices, it was only setting maximum fees in an attempt to reduce medical costs. The United States Supreme Court said that price fixing is price fixing, whether it is minimum fees or maximum fees. All physicians would rapidly charge the maximum fee. Because it found the fee schedule to be a per se violation, the Court paid no attention to the procompetitive effect of potentially lower prices.

The United States Supreme Court has been relatively lenient with other types of per se violations in the health care areas, allowing the violator to escape the per se label if the defendant has a small market share or if the Court finds that the activity was motivated by adequate noneconomic considerations. This allows the defendant's actions to be evaluated by the rule-of-reason analysis. This is not so with price fixing. Agreements among competitors to fix prices invariably are considered to be per se violations. Therefore, radiologists must avoid any communications with competing radiologists about the price, quality, or quantity of services they provide. For example, if a radiologist starting a new procedure were to call across town to another radiologist to find out what an appropriate price for the new procedure should be, this is a potential violation of the Sherman Act.

Relative-value scales also may be considered to be a form of price fixing. As mentioned before, the FTC found the ACR's attempts at establishing a relative value scale to be a form of price fixing in 1977. Ironically, the ACR is again at the forefront of recommending to the Department of Health and Human Services that relative value scales be developed for medical services. However, the current effort is progressing under a mandate from Congress. Activities by competitors that ordinarily would be violations of the Sherman Act are all right if the government regulates and supervises the activities. This is an example of the state action exception to the Sherman Act.

Finally, physicians must consider the possibility of a Sherman Act violation when they enter into certain types of joint ventures. Joint ventures will be a problem if competitors set the fee schedules, if the number of participants in the venture constitute a majority of the physicians in the area, or if participants are not allowed by the terms of the agreement to participate in other alternative health care delivery systems. In evaluating the antitrust consequences of an alternative health care joint venture, the courts will look at the motivation of the participants. Is the joint venture a legitimate effort to introduce a new lower-cost product to the marketplace or is it simply a means of stifling competition?

Because the *legal theory* of conspiracy is available to prosecutors pursuing antitrust violations, they have some advantages not available in ordinary legal procedure. Evidentiary rules in conspiracy trials are less rigid than those for a normal trial, and concerted actions toward a common goal may be evidence of a conspiracy. Therefore, even though no agreement or conspiracy exists between two competing radiologists, if contacts or conversations between them were known, then the fact that the same price is charged as a result of the conversation could be evidence of price fixing. Often, the existence of equal prices for competing services or products alerts enforcement agencies to a price-fixing agreement.

Market Division

Antitrust cases involving the division of a market by competitors, either by territory or by customers, has long been held by the courts to be a per se violation of the Sherman Act. However, market division cases have not been a prominent part of antitrust litigation in the health care field. Such a case might occur, for example, if one hospital agreed with another that one of the two hospitals would take all of the pediatric patients and the other would take the obstetric patients and that neither would compete in the other's market. Radiologists rarely get involved in this type of tradeoff. In fact, most of the economic incentives in modern medical practice encourage radiologists to duplicate services.

Group Boycotts

A group boycott, also called a concerted refusal to deal, occurs when two or more competitors agree to refuse to supply services or products to another competitor, or when they conspire to restrict a competitor's access to the marketplace. From the beginning of antitrust litigation in the health care field, allegations of group boycotts have been a prominent part of the cases that have come before appellate courts. In part, this has stemmed from the natural defensive tactics used by established groups to preserve their market share against incoming competitors. Examples of such behavior include exclusion of physicians who treat HMO patients from membership in county medical societies, boycotts by physicians of hospital corporations that also have "doc-in-the-box" operations in competition with the physicians' office practices, and refusal of physicians to refer patients to hospitals that employ emergency-room physicians.

Radiologists are at the same risk as other physicians for entering into group boycotts. The ACR has just finished lengthy litigation in *Wilk v. American Medical Association* [13], a suit instituted by chiropractors who claimed that members of the ACR conspired to refuse their referrals. As a result of a trial court verdict in favor of the chiropractors, the ACR entered a settlement in which it agreed to let each individual radiologist determine what type of consultations best fit his or her practice situation but removed all objections to referrals from chiropractors. Pressures to join into group boycotts may come from many sources. For example, the orthopedic surgeons may threaten to send their patients to a different radiology group unless the radiologists refuse to accept referrals from podiatrists. Clearly, orthopedic surgeons who engage in this type of activity are violating the Sherman Act. However, the radiologist who agrees to the arrangement is also in violation. Individual radiologists always can follow their consciences and refuse to send patients to any entity so long as the radiologist acts alone. However, when two competing radiologists get together and refuse to send patients to a certain health care provider or refuse to see patients referred by a health care provider, they have joined in a group boycott and may be found to be in violation of the Sherman Act.

Although courts originally determined all group boycotts to be per se violations, they have eased the rules in recent years. Thus, if a boycott has no economic consequences and can be characterized as purely political, or if it seems genuinely motivated by a concern for the patient, it may avoid the label of a per se violation. In this regard, the *Wilk* decision states that such a "patient care" defense requires proof of a genuine, objectively reasonable concern for use of the scientific method in patient care, proof that the concern has been the dominant motivating factor in the establishment of ethical principles leading to the boycott and in the conduct intended to implement those principles, and proof that the concern for the use of the scientific method in patient care could not have been satisfied adequately in a manner that had a lesser impact on competition. In *Wilk* the defendants submitted evidence that chiropractic is an unscientific cult and claimed that they refused referrals from chiropractors in the interest of patient safety. However, the court evaluated the evidence and found that it did not meet these elements of proof. Rather, the court found significant evidence to indicate that the boycott was economic in nature.

Similarly, boycotts by entities that have no significant market share are treated more leniently and may escape the per se label. In this regard, exclusive contracts by radiologists with hospitals represent a form of boycott, that is, a concerted refusal to deal with a competitor. Yet, the courts consistently have evaluated exclusive contracts under the rule of reason analysis.

Tying Arrangement (or Tie-in)

A tie-in occurs when a seller of a product forces the buyer to purchase a second, unwanted product in order to obtain the desired product. For example, a patient would like to purchase a urinalysis from a pathology laboratory. However, the laboratory will sell the desired test only if the buyer also purchases an amylase test, the tied product, which is not wanted.

In *Hyde* [12], discussed in the section on market share, the anesthesiologist, who had been denied privileges to practice at East Jefferson Hospital because of an exclusive contract between the hospital and a group of anesthesiologists, argued that anesthesia services at East Jefferson Hospital were tied to surgical operations. That is, a patient could not get an operation at the hospital without also purchasing anesthesia services. Before *Hyde*, exclusive contracts uniformly had been analyzed under the rule-of-reason analysis, and the procompetitive effects of the contract always had outweighed the anticompetitive effects. If Dr. Hyde could get the court to label the arrangement a tie-in, he might have the exclusive contract designated a per se violation of the Sherman Act and avoid the rule-of-reason analysis. However, some justices on the present United States Supreme Court have felt that tying arrangements should not be per se violations of the Antitrust Act unless the defendant has adequate market power to force the purchase of the unwanted product. Since the Court in *Hyde* found the market for surgical and anesthesia services at East Jefferson Hospital to be the greater New Orleans area, the hospital and its anesthesiologists did not have significant market power. Also, a requirement for a tying arrangement is that the tying product and the tied product must be separate and distinct items. The Supreme Court in *Hyde* found that operations and anesthesia were not separate and distinct. No one would want an operation without also wanting the anesthesia.

Having found that no tying arrangement existed, the Court evaluated the exclusive contract under the rule of reason and found that the procompetitive effects to the consumer outweighed the anticompetitive effects. As a result of *Hyde*, plaintiffs will find the allegation of a tying arrangement to be a difficult legal theory to use in attacking exclusive contracts for medical services.

Rule-of-Reason Analysis

Every contract restrains trade to some degree. Over the years, therefore, the courts have determined that the Sherman Act does not prohibit all anticompetitive activity, only unreasonable anticompetitive activity. The per se violations, discussed previously, are obviously unreasonable. However, if a court does not find a per se violation, it analyzes the case according to the rule of reason, which is really only a balancing of the negative impact of the alleged anticompetitive activity on competition and the consumer against the procompetitive benefits gained from the activity. Simply stated, conduct is reasonable if it promotes competition and is unreasonable if it impedes competition. In other words, some mergers and agreements between competitors make better goods available at lower prices. Because the antitrust laws were designed to benefit consumers, the courts do not want to harm the consumer as long as the anticompetitive activity is not of the blatant, per se type.

The rule of reason is a comprehensive analysis of all the factors that go into the competitive setting. Market share is the most important. The larger the market area as defined by the court, the less likely it is that any individual defendant's activities will have a negative impact on the consumer. In addition to market share, courts look at the intent of the defendant in carrying out the alleged anticompetitive activity and to the positions of the plaintiff and defendant relative to their abilities to be competitive. The impact on the consumer is the most important factor.

Most hospitals have an exclusive contract with a group of radiologists for inpatient care. Although such a contract clearly restricts competition, it is not the type of activity that would be considered a per se violation. Therefore, courts consistently have used the rule of reason to determine whether an exclusive contract should be allowed to exist. In doing so, the courts have balanced the anticompetitive effects of excluding a radiologist from a specific hospital practice against the procompetitive effects of a specific contract. Procompetitive effects considered by the courts include ease of scheduling patients, 24-hr coverage, standardization of procedures and efficient use of equipment, uniformity of ordering equipment, uniform call schedules, and the ability of the hospital to monitor quality of services. As mentioned earlier, the anticompetitiveness of an exclusive contract depends in great extent on the courts' definition of the geographic area and market share of the hospital that has the exclusive contract. Although this has not been a major problem in exclusive contract cases to date, the wording of the Supreme Court in *Hyde* indicates that if the hospital's market power is so great that alternative radiologic services are not available to the consumer in that market, the court might go the other way and find that the anticompetitive effects outweigh the procompetitive effects.

Similarly, suits by physicians excluded from a medical staff have been considered by the courts to be a concerted refusal by the medical staff to deal with the excluded physician. Thus, peer review may be in conflict with the Sherman Act if it is carried out by competitors and results in a diminished ability of the accused physician to practice in the peer reviewers' marketplace and the peer review is not carried out in good faith. The leading case in this area is *Patrick v. Burget* [14], recently decided by the United States Supreme Court. Although the decision in that case went against the peer reviewers, who were found to be in violation of the Sherman Act, this was by no means a good faith peer review. The surgeons who removed Dr. Patrick from the medical staff were in direct competition with him, and Dr. Patrick was not afforded a fair and impartial due-process hearing. The United States Supreme Court's decision in *Patrick* should not deter fair-minded radiologists from participating in peer review. The case really stands for the proposition that peer review must be fair. Discussions by hospital peer review committees should relate only to the hospital's interest in physicians' personal qualifications, competence, ethics, and quality of care. Any discussion of economics must be avoided.

In response to the *Patrick* decision, Congress passed the Health Care Quality Improvement Act (HCQIA) of 1986 [15]. This act provides immunity from prosecution under the Sherman Act for good-faith peer review, that is, peer review that is conducted after a thorough and objective evaluation of the facts and that provides due process rights to the accused physician. All hospital staff bylaws and the bylaws of state radiologic societies should be amended to conform to the requirements of the HCQIA. In addition to the protection afforded by the HCQIA, most states also have statutes providing protection for good-faith peer review and for the confidentiality (nondiscoverability) of committee proceedings related to peer review activities.

The *Patrick* decision was also important because the United States Supreme Court placed some limitations on the state action exception, which gives protection to competitors for acts that are performed under a pervasive scheme of state regulation and supervision. The defendants in *Patrick* tried to bring themselves under the state action exception by arguing that the State of Oregon was involved extensively in the regulation of health care services and encouraged peer review. The Court agreed with the defendant in this contention but stated that Oregon did not have standards as to how peer review was to be carried out and did not become involved in the process of peer review. Thus, the court set out a two-step test that must be met before a state action exception can be claimed. The state must have a comprehensive regulatory scheme and also must become involved in following up this regulatory activity.

The Sherman Act and Third-Party Reimbursement

In recent years, the Blue Cross and Blue Shield plans have begun to use their dominant market power in the Northeast to reduce payments to physicians, including radiologists. The first case in which a physician challenged the Blue Shield practices was *Kartell v. Blue Shield of Massachusetts, Inc.* [16]. In this case, Dr. Kartell and three of his colleagues attempted to get an injunction against Massachusetts Blue Shield's prohibition on balanced billing by physicians caring for its subscribers. The United States district court denied the injunction but allowed the case to proceed as a potential violation of the Sherman Act. That Blue Shield had a dominant market share was not contested. It provided insurance coverage for about 74% of Massachusetts residents who were not covered by Medicare or Medicaid. Although the district court declined to find a per se violation by Blue Shield, it did find that Blue Shield's payment system to the physicians, when combined with Blue Shield's market power, unreasonably restrained the doctors' freedom to charge higher prices for more expensive services and discouraged them from developing and offering patients more expensive, and perhaps better, services. In other words, using the rule of reason, the court found that anticompetitive aspects of Blue Shield's ban on balanced billing outweighed the procompetitive effects.

Blue Shield appealed to the First Circuit Court of Appeals, which reversed the district court opinion and found that no unreasonable restraint of trade had occurred. In order to be unreasonable, said the court, Blue Shield would have to be a "third force" intervening in the marketplace to prevent the purchasing patients and the selling physicians from determining a fair market value for the physicians' services. Rather, said the court, Blue Shield was itself the purchaser of physician services. Even assuming that Blue Shield had significant market power and used that power to obtain lower than competitive prices, the fact that a buyer has a monopoly situation does not prevent it from obtaining the lowest possible prices. Therefore, if Blue Shield had simply purchased the services for itself, the prices paid, in and of themselves, would not have amounted to a violation of the antitrust laws. In addition, the court stated that no law forbids a legitimate insurance company from obtaining a complete set of goods and services for its customers. Therefore, the court found that a buyer, even a monopoly buyer, could insist that no additional charge be made to its customers. In reaching this decision, the court of appeals relied on three additional factors. First, the Sherman Act was enacted to aid consumers and Blue Shield was attempting to lower the cost of health care. Second, the subject of medical cost is an area of great complexity, and courts should move slowly in establishing antitrust law in this field. Third, the pricing system at issue was supervised by state regulators, invoking the state action exception to the application of the Sherman Act. Thus, *Kartell* gave Blue Shield a strong legal basis for new initiatives intended to control physician reimbursement.

One of those initiatives had a significant impact on radiologists. Empire Blue Cross/Blue Shield, operating in downstate New York, decided that it could save money if hospitals contracting with Blue Cross for radiologic services for its subscribers included the radiologists' incomes as part of the package of services covered by Blue Cross. Suddenly, radiologists who formerly had billed fee-for-service found themselves, in effect, to be hospital employees. Westchester Radiological Associates and some 60 other radiology groups sued Empire Blue Cross/Blue Shield for violations of the Sherman Act in federal district court [17]. Specifically, the radiologists alleged that Empire Blue Cross/Blue Shield had conspired with the hospitals in downstate New York to fix prices and to restrain the manner in which radiologists bill for their services. They also claimed that Empire Blue Cross attempted to monopolize the hospital insurance market, using its market power in that market to gain a competitive advantage for its less successful Blue Shield operation in the physician market.

Empire filed a motion with the district court to dismiss the complaint, relying primarily on the First Circuit Court of Appeals' decision in *Kartell*. Judge Kram, of the United District Court for the Southern District of New York, who heard the first motion to dismiss, affirmed that contracts between buyers of services, even monopolies, and sellers of services did not violate the Sherman Act. However, she found that the Empire contract that disallowed the fee-for-service billing by the radiologists was between Empire and the hospitals. In other words, Judge Kram felt that this was the triangular relationship in which Empire was acting as the third force that the *Kartell* court felt would bring the case under antitrust scrutiny. Judge Kram therefore dismissed Empire's motion and would have allowed the case to go to trial.

About a year later, Empire filed a motion with the United States District Court for the Southern District of New York for summary judgment, a motion similar to the previous motion to dismiss. Judge Kram was no longer the judge of record, and the motion was heard by Judge Wood, who dismissed the radiologists' suit. She found that, as a matter of law, Empire did not violate the Sherman Act. Judge Wood disagreed with the third force argument of the radiologists, deciding that Empire, as a buyer of health services for others, could buy those services through an intermediary, leaving the radiologists and hospitals free to bargain with one another. The fact that Empire had significant market power did not prevent it from obtaining the best prices possible for its subscribers so long as its practices were not predatory.

The Westchester Radiological Associates appealed to the United States Second Court of Appeals, which agreed with Judge Wood, calling her opinion well reasoned. The final appeal was to the United States Supreme Court, which declined to hear the case.

Westchester Radiological is a difficult case for radiologists and for physicians whose primary site of practice is hospitals, and it may be devastating if other insurors with monopoly power follow Empire's lead. Antitrust challenges by physicians to large insurance companies' efforts to contain costs of the physicians' services will be difficult. First, insurance companies enjoy protection under the McCarran-Ferguson Act for their activities so long as they are not conspiring with other insurance companies to fix prices. Most of the activities alleged by physicians to be in violation of the Sherman Act, including rate setting, determination of benefits for customers, and bargaining with providers for services, are examples of the business of insurance. Although the Court has not invoked the McCarren-Ferguson Act to dismiss suits against large insurors, the courts in *Kartell* and *Westchester Radiological* have been sensitive to the fact that an insurance company is being sued.

Second, health care reimbursement is an area of intense federal and state regulation and supervision, and the state action exemption to the application of the Sherman Act therefore comes into play. Blue Cross/Blue Shield plans are established by state legislation, are regulated by state insurance commissioners, and are intermediaries in Medicare and Medicaid reimbursement. Because of these factors, it is unlikely that activities of an insurance company acting to contain costs and to obtain the best bargain for its subscribers will be considered to be a per se violation of the Sherman Act in the absence of a clear conspiracy or predatory activity. This means that antitrust suits alleging violation of the Sherman Act by an insurance company will be decided by using the rule of reason. As the outcome of a rule-of-reason analysis is determined by what is best for the consumer, a court would be unlikely to uphold an antitrust challenge by a group seeking to maintain high prices (physicians) against a group seeking to lower prices (insurors).

ACKNOWLEDGMENT

I thank Tom Greeson, Internal Legal Counsel of the American College of Radiology, for guiding me around the pitfalls in this difficult area of the law.

REFERENCES

1. 15 U.S.C.A. §1 (**1890**)
2. U.S.C.A. §2 (**1890**)
3. 15 U.S.C.A. §15 (**1914**)
4. *Goldfarb v. Virginia State Bar*, 95 S.Ct. 2004, 421 U.S. 773 (**1975**)
5. *National Society of Professional Engineers v. United States*, 98 S.Ct. 1355, 435 U.S. 679 (**1978**)
6. *FTC v. American College of Radiology*, CC Trade Case #21, 236 (**1977**), *consent order modified* (**1985**)
7. *Arizona v. Maricopa Co. Med. Soc.*, 102 S.Ct. 2466, 451 U.S. 332 (**1982**)
8. 15 U.S.C.A. §1013 (**1945**)
9. 29 U.S.C.A. §105 (**1932**)
10. *Eastern RR Presidents Conference v. Noerr Motor Freight Inc.*, 81 S.Ct. 523, 355 U.S. 127 (**1961**); *United Mine Workers v. Pennington*, 85 S.Ct. 1585, 381 U.S. 657 (**1965**)
11. *Parker V. Brown*, 63 S.Ct. 307, 317 U.S. 341 (**1943**)
12. *Jefferson Parish Hospital District No. 2 v. Hyde*, 686 F.2d 286 (5th Cir. **1982**): 104 S.Ct. 1551, 446 U.S. 2 (**1984**)
13. *Wilk v. American Medical Association*, 671 F. Supp. 1465 (N.D. Ill. **1987**); 719 F.2d 207 (7th Cir. **1990**)
14. *Patrick v. Burget*, 108 S.Ct. 1658, 100 L.Ed.2d 83 (**1988**)
15. 42 U.S.C.A. §§11101–11137 (**1986**)
16. *Kartell v. Blue Shield of Massachusetts, Inc.*, U.S. Dist. Ct. for Mass. (Slip Opinion, Nov. 4, **1980**), 592 F.2d 1191 (1st Cir. **1979**); 542 F. Supp. 782 (D. Mass. **1982**); 687 F.2d 543 (1st Cir. **1982**); 749 F.2d 922 (1st Cir. **1984**)
17. *Westchester Radiological Associates, P.C. v. Empire Blue Cross and Blue Shield, Inc.*, 659 F. Supp. 132 (S.D. N.Y. **1987**); 707 F. Supp. 708 (S.D. N.Y. **1989**); 884 F.2d 709 (2nd Cir. **1989**); 1990 U.S. 869 (**1990**)

Recognition of Manuscript and Book Reviewers for 1990

The editors and the editorial staff wish to express their appreciation to the following colleagues, who as manuscript reviewers have spent many hours in 1990 helping to select only the most authentic, original, and useful articles for publication in the *AJR*, and to those responsible for book reviews.

Each manuscript received by the Journal is forwarded anonymously to two knowledgeable reviewers for their opinions concerning the worthiness of the paper for publication and/or their suggestions for improvement. The Journal receives 1400 manuscripts annually, of which only approximately 600 (43%) are published. The reviewers perform this service without compensation and with no recognition except for this acknowledgment.

The dedication of the reviewers is largely responsible for the exceedingly short mean time (3.3 weeks) between submission of manuscripts and notification of authors about the initial editorial decision. Initial editorial decisions are reached this quickly only because reviewers agree to judge manuscripts within 2 weeks, an enormous commitment considering the extent of their other responsibilities.

Book reviewers have been equally generous with their time, evaluating for the readers the burgeoning number of textbooks published each year.

These contributors have added immeasurably to the value, scientific merit, and relevance of the Journal. The quality of the Journal is in their hands. We are grateful for the erudite and conscientious manner in which they discharge these imposing responsibilities.

Robert N. Berk
Editor-in-Chief

Henry G. Adams
Alex M. Aisen
Abass Alavi
Philip O. Alderson
T. Noel K. Allan
John R. Amberg
Edward S. Amis Jr.
Gary M. Amundson
Dixie J. Anderson
James H. Anderson
Michael Andre
Jerry S. Apple
John D. Armstrong II
Judith M. Ash
William L. Ashburn
John H. M. Austin
Leon Axel
Diane S. Babcock
Jeanne W. Baer
David H. Baker
Mark E. Baker
Stephen R. Baker
Dennis M. Balfe
Emil J. Balthazar
Marc P. Banner
Richard L. Baron
Klemens H. Barth
Royal J. Bartrum Jr.
Lawrence W. Bassett
Solomon Batnitzky
Stanley Baum
Bruce R. Baumgartner
John W. Beabout
Gary J. Becker
Joshua A. Becker
Melvin H. Becker
Colin B. Begg
Beryl Benacerraf
Richard A. Benedikt
Carol B. Benson
Walter E. Berdon
Paul Berger
Leonard Berlin
Michael E. Bernardino
Charles C. Berry
Michael A. Bettmann
Gayle H. Bickers
Jeffrey Bisker
George S. Bisset III
Ann Bjorkengren
William C. Black
M. Donald Blaufox
Johan G. Blickman
J. Eric Blum
Stanley P. Bohrer
Nicole-Fr. Bolender
Joseph J. Bookstein
Gregory P. Borkowski
Lawrence M. Boxt
William G. Bradley Jr.
Thomas J. Brady
David G. Bragg
Folke J. Brahme
Robert T. Bramson
William E. Brant
Michael N. Brant-Zawadzki
Robert Brasch
Ethan M. Braunstein
Robert L. Bree
Alan S. Brody
Anne C. Brower
Jeffrey J. Brown
Reynold F. Brown
Patrick J. Bryan
James L. Buck
Edward Buonocore
H. Joachim Burhenne
Linda Warren Burhenne
Anthony J. Buschi
William H. Bush Jr.
Rodney James Butch
John B. Campbell
William L. Campbell
M. Paul Capp
Gary Caputo
David H. Carlson
Harley Carlson
Erik Carlsson
Barbara A. Carroll
William J. Casarella
Philip N. Cascade
Giovana Casola
Manuel Cerqueira
Arnold Chait
Paul Joseph Chang
Norman E. Chase
Charles H. Chesnut III
Felix S. Chew
Paul Chikos
Kyung J. Cho
Ross Christensen
Kyung Chung
Robert A. Clark
W. Peter Cockshott
Alan M. Cohen
Harris L. Cohen
Jesse M. Cohen
Mervyn D. Cohen
Beverly G. Coleman
Richard S. Colvin
Virgil R. Condon
James J. Conway
William F. Conway
Peter L. Cooperberg
Constantin Cope
Philip Costello
Craig M. Coulam
Michael Crade
Lawrence E. Crooks
Harte C. Crow
Andrew B. Crummy
Donald A. Cubberley
David J. Curtis
Horacio R. D'Agostino
Abraham H. Dachman
Richard H. Daffner
Michael D. Dake
Murray K. Dalinka
Michael David Darcy
Frederick L. Datz
Gary B. Davis
Patricia C. Davis
Peter L. Davis
Arthur A. De Smet
James B. Dealy Jr.
Terrence C. Demos
Joseph P. Dillard
Wilma C. Diner
Robert E. Dinsmore
Michael A. DiPietro
Karl T. Dockray
Gerald D. Dodd
James Donaldson
John L. Doppman
John P. Dorst
Peter J. Doubilet
Walter Drane
Gregory L. Dubuque
N. Reed Dunnick
Andrew Dwyer
Samuel J. Dwyer III
Marlene R. Eckstein
Steven Edell
Robert R. Edelman
David K. Edwards III
Juri Eenmaa
Eric L. Effmann
Georges Y. El-Khoury
Kent Ellis
Robert A. Ellwood
Barry L. Engelstad
Ronald G. Evens
Jacob I. Fabrikant
Joseph Fakhry
Gary E. Falkoff
Michael P. Federle
Stephen A. Feig
David S. Feigin
Sandra K. Fernbach
Joseph T. Ferrucci
Melvin M. Figley
Hossein Firooznia
Dale W. Fitting
Barry D. Fletcher
L. Christopher Foley
W. Dennis Foley
John Forrest
Lee A. Forstrom
Edmund A. Franken Jr.
Gerald S. Freedman

Patrick C. Freeny
Robert H. Freiberger
Irwin M. Freundlich
Donald G. Frey
Andrew M. Fried
Gerald W. Friedland
Arnold C. Friedman
Paul J. Friedman
J. James Frost
Dennis G. Fryback
Carl R. Fuhrman
Gary D. Fullerton
Raymond A. Gagliardi
Gordon Gamsu
Stephen S. Gebarski
David W. Gelfand
Harry Genant
Gary G. Ghahremani
Louis A. Gilula
John J. Gisvold
Seth N. Glick
Morton Glickman
J. David Godwin
Thomas C. Goergen
Richard H. Gold
Richard P. Gold
Robert E. Gold
Barry B. Goldberg
Leonard Goldberg
Marvin E. Goldberg
Amy Beth Goldman
Harold S. Goldman
Antoinette S. Gomes
Charles A. Gooding
Gretchen A.W. Gooding
Lawrence R. Goodman
David A. Goodwin
Roy L. Gordon
Richard M. Gore
Michael Goris
Antonio Govoni
Herbert F. Gramm
Edward G. Grant
Joel E. Gray
Edward V. Grayson
Curtis E. Green
Paul Greenberger
Reginald Greene
Robert A. Greenes
Adam Greenspan
Guerdon Greenway
N. Thorne Griscom
Julius Harry Grollman Jr.
Stuart A. Groskin
Marvin Guter
Diana F. Guthaner
Michael T. Gyepes
David B. Hackney
Ferris Hall
Jack O. Haller
Robert A. Halvorsen Jr.
William Hanafee
Roger K. Harned
Donald P. Harrington
A. Basil Harris
John H. Harris Jr.
Ronald D. Harris
David S. Hartman
Derek Harwood-Nash
Marvin E. Haskin
Robert R. Hattery
Irvin F. Hawkins Jr.
David R. Haynor
Mark Healy
Jay P. Heiken
Richard M. Heller
William R. Hendee
Mark Henkelman
Robert Herfkens
Hans Herlinger
John R. Hesselink
Charles B. Higgins
Saskia V. W. Hilton
Waldo S. Hinshaw
Charles P. Ho
Paul B. Hoffer
Alan D. Hoffman
Richard A. Holmes
Marc J. Homer
Steven Horii
Brian A. Howard
Hedvig Hricak
H.K. Huang
Karl F. Hubner
Terry M. Hudson
David W. Hunter
Douglas E. Hutchinson
Gerald A.L. Irwin
Kenneth L. Jackson
Valerie P. Jackson
Harold G. Jacobson
C. Carl Jaffe
Richard B. Jaffe
Edward Janon
Paul F. Jaques
R. Brooke Jeffrey
Maxine Jochelson
Mary Ann Johnson
Gordon C. Johnson
Irwin S. Johnsrude
Bronwyn Jones
R. Gilbert Jost
George W. Kabalka
Saadoon Kadir
Emanuel Kanal
Krishna Kandarpa
Robert A. Kane
Hooshang Kangarloo
Stephen A. Kanter
George W. Kaplan
Phoebe Ann Kaplan
David Karasick
Nolan Karstaedt
Richard W. Katzberg
Barry T. Katzen
Robert A. Kaufman
Stephen L. Kaufman
Chester Kay
Jeremy J. Kaye
Theodore E. Keats
Norman N. Keep
Frederick S. Keller
Frederick M. Kelvin
James G. Kereiakes
Pamela Kidd
Reiley Kidd
Stephen A. Kieffer
Thomas S. Kilcheski
Ray F. Kilcoyne
E. Edmund Kim
Carolyn Kimme-Smith
Michael S. Kipper
Peter T. Kirchner
John A. Kirkpatrick Jr.
Donald R. Kirks
Eugene C. Klatte
Richard M. Klein
Paul K. Kleinman
J. Bruce Kneeland
Nancy Knight
P. Ruben Koehler
Daniel B. Kopans
Kenyon K. Kopecky
Melvyn Korobkin
Kenneth L. Krabbenhoft
Elissa L. Kramer
Mark J. Kransdorf
Adrian G. Krudy
Robert A. Kubicka
Jerald P. Kuhn
Madan V. Kulkarni
Harold L. Kundel
Sevil Kursunoglu-Brahme
Alfred B. Kurtz
David C. Kushner
Ralph S. Lachman
Faye C. Laing
Michael J. Landay
Erich K. Lang
Elliott C. Lasser
Igor Laufer
Paul C. Lauterbur
Thomas L. Lawson
Edward A. Lebowitz
Robert L. Lebowitz
Joseph K.T. Lee
John C. Leonidas
George R. Leopold
Janis Gissel Letourneau
Anna S. Lev-Toaff
David C. Levin
Errol Levine
Marc S. Levine
Robert G. Levitt
Thomas K. Lewellen
David K. Li
King C. Li
Herman I. Libshitz
Joel E. Lichtenstein
Arthur Lieber
Karen K. Lindfors
Daniel P. Link
Joseph P. LiPuma
Martin J. Lipton
Hing-Har Lo
Gwilym S. Lodwick
K. William Logan
Juan F. Lois
H. Esterbrook Longmaid III
John W. Loop
Ronald J. Lorig
Leon Love
Mortimer Lubert
Robert B. Lufkin
Kenneth H. Luk
Caroline J. Lundell
Robert L. MacCarty
William J. MacIntyre
Laurence A. Mack
Heber MacMahon
Nabil F. Maklad
Michael L. Manco-Johnson
Frederick A. Mann
Carol Marcus
Stephen I. Marglin
Carroll Markivee
Richard I. Markowitz
William Martel
David S. Martin
Eric C. Martin
John E. Martin
Luis O. Martinez
Myron Marx
Alan H. Maurer
Gerald R. May
Richard B. Mazess
John G. McAfee
William H. McAlister
Ronald W. McCallum
Bruce L. McClennan
John P. McGahan
Richard A. McLeod
Theresa C. McLoud
Thomas F. Meaney
H. Erik Meema
Alec J. Megibow
G. Leland Melson
Christopher R.B. Merritt
Charles E. Metz
Morton A. Meyers
Peter Meyers
Reuben S. Mezrich
William A. Middleton
John R. Milbrath
Donald L. Miller
Edward I. Miller
Stephen W. Miller
Lee Milner
Howard J. Mindell
Jerrold H. Mink
Charles A. Mistretta
Donald G. Mitchell
Carol A. Mittlelstaedt
Harold A. Mitty
Roger E. Moe
Paul L. Molina
Sheila G. Moore
William E. Moore
Richard L. Morin
Thomas W. Morris
Richard P. Moser Jr.
Myron Moskowitz
Albert A. Moss
Peter R. Mueller
Lawrence R. Muroff
William A. Murphy Jr.
Howard J. Naidech
Harvey L. Neiman
Wil B. Nelp
David W. Nelson
James A. Nelson
Thomas Roy Nelson
Albert A. Nemcek Jr.
Arthur H. Newberg
Jeffrey H. Newhouse
Harris Newmark III
Alex Norman
Robert A. Novelline
Stanley Novy
Ray L. Nunnally
Michael J. O'Brien
Michael K. O'Connor
Robert E. O'Mara
Alan E. Oestreich
Linda K. Olson
Anne G. Osborn
David J. Ott
Theron W. Ovitt
Maer B. Ozonoff
Julio C. Palmaz
David M. Panicek
Bruce R. Parker
Robert W. Parkey
Suresh K. Patel
Mini Nutan Pathria
Heidi Patriquin
James A. Patton
Sven J. K. Paulin
David M. Paushter
William Pavlicek
Alan S. Pearlman
Wallace Peck
Rita Perrella
Jerry P. Petasnick
Warren C. Phillips
Daniel Picus
Howard M. Pollack
Andrew K. Poznanski
Satish C. Prasad
Leslie Preger
Gary A. Press
Dolores H. Pretorius
Leland A. Prewitt Jr.
Anthony V. Proto
Robert D. Pugatch
Jack G. Rabinowitz
Patricia Ann Randall
Vassilios Raptopoulos
Helen C. Redman
Barbara S. Reid
Donald L. Renfrew
Robert R. Renner
Donald L. Resnick
Charles S. Resnik
Stewart R. Reuter
Todd Richards
Michael L. Richardson
Paul A. Riemenschneider
Matthew D. Rifkin
Ernest J. Ring
Barry Robbins
Anne C. Roberts
Shauna R. Roberts
Arvin E. Robinson
Maurice A. Robkin
John O.F. Roehm Jr.
Charles A. Rohrmann Jr.
F. David Rollo
Pablo R. Ros
David M. Rosenbaum
Murray A. Rosenberg
Arthur Rosenfield
Harvey Rosenkrantz
Carl John Rosenquist
Daniel I. Rosenthal
Raymond P. Rossi
Allan Rowberg
Marshall Rowen
V. Allen Rowley
Deborah Rubens
Stephen E. Rubesin
Jonathan M. Rubin
Carol M. Rumack
Anthony H. Russell
Francis F. Ruzicka Jr.
Stuart S. Sagel
David J. Sahn
Sanjay Saini
Carl M. Sandler
Martin P. Sandler

E. Nicholas Sargent
David J. Sartoris
Mohammad Sarwar
Stefan C. Schatzki
William Scheible
Heinrich R. Schelbert
William L. Schey
Melvyn H. Schreiber
Scott J. Schulte
William B. Seaman
Jeno I. Sebes
Arthur J. Segal
Steven E. Seltzer
Jerome H. Shapiro
Marcelle J. Shapiro
Douglas R. Shearer
William H. Shehadi
William P. Shuman
Ferris J. Siber
Edward A. Sickles
Barry A. Siegel
Hano Armin Siegel
Marilyn J. Siegel
Michael E. Siegel
Edward B. Silberstein
Paul M. Silverman
Stuart G. Silverman
Allan L. Simon
M. Leon Skolnick
Jovitas Skucas
Thomas L. Slovis
James G. Smirniotopoulos
Claire Smith
Edward H. Smith
Julius Smith
F. Graham Sommer
Thomas A. Sos
Constantine Soter
Benigno Soto
Renate L. Soulen
Richard P. Spencer
Dimitrios Spigos
Hugo Spindola-Franco
Beverly A. Spirt
David B. Spring
Eugene L. St. Louis
Robert C. Stadalnik
Philip Stanley
Robert J. Stanley
Tom W. Staple
David D. Stark
Paul Stark
Richard Steckel
Harvey V. Steinberg
Robert M. Steiner
David H. Stephens
Richard K. Stevens
Giles Stevenson
Edward T. Stewart
William H. Straub
David A. Stringer
Charles M. Strother
John R. Sty
Murali Sundaram
Leonard E. Swischuk
Lee Talner
John P. Tampas
Juan M. Taveras
George A. Taylor
Kenneth J. W. Taylor
Charles D. Teates
Rita Teele
Charles J. Tegtmeyer
George Teitelbaum
Steven K. Teplick
Franklin N. Tessler
Elias G. Theros
Ruedi F. Thoeni
F. Deaver Thomas
William M. Thompson
John R. Thornbury
Robert D. Tien
Jaime Tisnado
Ina L. D. Tonkin
William G. Totty
Richard Towbin
Michael Trambert
Theodore A. Tristan
Rosalind H. Troupin
David A. Turner
James A. Usselman
Karim Valji
Ronald L. Van Heertum
Michael W. Vannier
Robert R. Varney
C. Whitley Vick III
Frederick Vines
Michael R. Violante
Robert L. Vogelzang
Kay H. Vydareny
Eric vanSonnenberg
Susan D. Wall
Sidney Wallace
William J. Walls
Joseph F. Walter
Arthur C. Waltman
Victor Waluch
Keith Y. Wang
Yen Wang
John F. Ward
W. Richard Webb
Felix W. Wehrli
Melvyn L. Weiner
Jeffrey C. Weinreb
Barbara N. Weissman
Heidi S. Weissman
Richard L. Wesenberg
Jack L. Westcott
John Wexler
Lewis Wexler
Joseph P. Whalen
Nancy O. Whitley
Mark H. Wholey
Stephen N. Wiener
William A. Wilcox
Susan M. Williams
Brian R.J. Williamson
John S. Wills
Stephanie Wilson
Gary G. Winzelberg
Jerome F. Wiot
Richard L. Witcofski
Jack Wittenberg
Gerhard Wittich
Gerald L. Wolf
John N. Wolfe
Michael K. Wolverson
Beverly P. Wood
Michael L. Wood
Peter Wootton
Joseph M. Yee
Isabel C. Yoder
Jeremy W. R. Young
Lionel W. Young
Heun Y. Yune
Albert B. Zajko
Robert A. Zamenhof
Robert K. Zeman
Michael B. Zlatkin
Carl J. Zylak

Letters

Referencing Trends in the Radiologic Literature, 1970–1990

This study was undertaken to evaluate general trends in referencing and, in particular, the prevalence of self-citation (authors' referencing their own papers) in the radiologic literature. With increased emphasis on publications in the academic environment, discussions of citation analysis have surfaced. Citation analysis refers to the use of the Science Citation Index [1] to determine the number of times an article was cited as a reference in subsequent publications. Some have proposed that such analysis be used as a criterion for academic advancement, suggesting that the number of citations is a measure of the quality and significance of a person's work [2]. Others have alluded to the fallacies of this reasoning [3]. Consciously or unconsciously, authors feel pressure not only to publish but also to be cited. Therefore, we hypothesized an increase in the prevalence of self-citations. To evaluate this, we reviewed the March issues of the *AJR* and *Radiology* from 1970, 1980, and 1990. The results are shown in Table 1.

From 1970 to 1990, the average length of an article decreased from 6 to 4.5 pages (25%), the mean number of authors increased from 2.6 to 4.3 (65%), and the mean number of references increased from 13 to 17 (31%). These findings correlate with other reports of an increase in the number of authors per article [4]. The average number of self-citations increased 64%, from 1.1 (8.5% of all references) in 1970 to 1.8 (10.5% of all references) in 1990 (Fig. 1). Consequently, the percentage of papers with at least one self-citation has increased, and the number with three or more has nearly doubled (Fig. 2).

TABLE 1: Referencing Trends in the Radiologic Literature

Variable	1970	1980	1990
Total number of articles (March issues of *AJR* and *Radiology*)	61	83	93
Mean number of authors per paper	2.6	3.3	4.3
Mean number of pages per paper	6	4.5	4.5
Mean number of references per paper	13	12	17
Self-citations			
Mean number per paper	1.1	1.1	1.8
Percentage of all references	8.5	9	10.5
Percentage of papers with at least one	48	41	64
Percentage of papers with three or more	15	19	27

Our results show an increase in self-citations both as an average number per paper and as a percentage of all references. A small increase would not be unexpected solely on the basis of the increased number of authors, which generates an increased likelihood that one of the authors of a paper is an author of a reference cited in that paper. The increase, however, seems disproportionate. The increase in the percentage of self-citations from 8.5% to 10.5% is an increase of 25%. Explanations include the increased complexity of research and subspecialization, resulting in fewer groups working on related projects, and the concept that research often builds on the investigator's previous experience. Other explanations include bias toward self-citation and publishing small portions of results separately, which

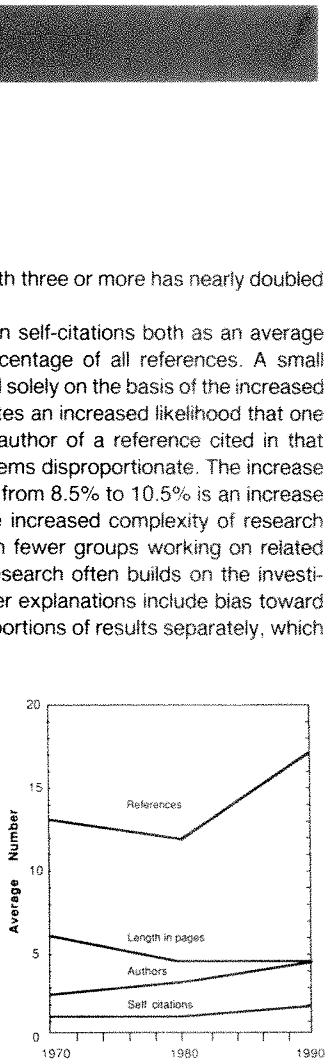

Fig. 1.—Graph shows trends in referencing in radiologic literature, 1970–1990.

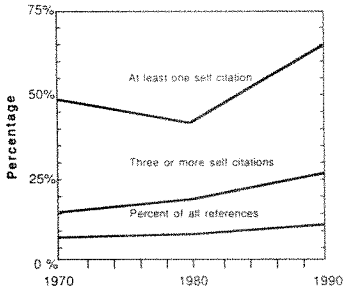

Fig. 2.—Graph shows changes in self-citation in radiologic literature, 1970–1990.

necessitates self-referral to fill in the gaps. Considering all these factors, we show evidence that the prevalence of self-citation has increased somewhat disproportionately to the increases in the number of authors and the total number of references, but we find insufficient evidence to attribute this to academic pressure to publish and be cited.

Richard M. Slone
Barbara S. Martineau
University of Florida, College of Medicine
Gainesville, FL 32610-0374

REFERENCES

1. *Science Citation Index*. Philadelphia: Institute for Scientific Information. Published monthly; compiled yearly and every 5 years.
2. MacRoberts MH, MacRoberts BR. Citation analysis and the science policy arena. *Trends Biochem Sci* **1989**;14(1):8, 10, 12
3. Cole S. Citations and the evaluation of individual scientists. *Trends Biochem Sci* **1989**;14(1):9, 11, 13
4. Chew FS. The scientific literature in diagnostic radiology for American readers: a survey and analysis of journals, papers, and authors. *AJR* **1986**; 147:1055–1061

Knowledge of Clinical History and the Accuracy of Interpretation of Chest Radiographs

We read with interest the article by Good et al. [1] on what effect knowing the clinical history has on the accuracy of interpretation of the chest radiograph. However, their conclusion that knowledge of the history does not affect the accuracy of interpretations is counterintuitive and at odds with our clinical experience. We think that their negative results can be explained by deficiencies in the design of their study.

According to the Methods section, each radiograph was read with the benefit of a scoring sheet that directed the radiologist to search for three diseases (interstitial disease, nodule, pneumothorax) whether or not the supplemental clinical history was available. Because the scoring sheet itself provided what is often the most relevant information that can be extracted from a patient's history—what to look for on the radiograph—a major effect of history was not assessed. From our personal experience, we know that our approach to the chest radiograph differs from routine when we are alerted to look for a particular abnormality. For example, when the abnormality in question is a pneumothorax, we scrutinize the apices and peripheral lung fields, use a bright light on these regions, and look specifically for a pleural border. We would be shocked to discover that these efforts did not improve our performance in detecting pneumothorax.

The definition by Good et al. of accuracy as the area under the receiver-operating-characteristic (ROC) curve precludes the assessment of another important effect of history. History on the likelihood and importance of the disease in question can influence where the radiologist chooses to operate along the ROC curve. However, the area under the ROC curve is not affected by history that influences this choice. On the other hand, accuracy defined in the more conventional manner as the proportion of correct interpretations [2] is affected by such history. Whether the effect of such history is to increase or decrease accuracy (conventionally defined) depends on the prevalence of disease in the tested population [2]. (The effect of such history on the clinical usefulness of testing depends on the prevalence and the relative costs of false-positive and false-negative errors [3].)

Although we disagree with their major conclusion, we believe that Good et al. are on the right trail when they question what constitutes "history" and suggest that different forms have different effects on how we interpret images. These are ideas worth pursuing.

William C. Black
Andrew J. Dwyer
Warren G. Magnuson Clinical Center
National Institutes of Health
Bethesda, MD 20892

REFERENCES

1. Good BC, Cooperstein LA, DeMarino GB, et al. Does knowledge of the clinical history affect the accuracy of chest radiograph interpretation? *AJR* **1990**;154:709–712
2. Phillips WC, Scott JA, Blasczcynski GI. How sensitive is "sensitivity"; how specific is "specificity"? *AJR* **1983**;140:1265–1270
3. McNeil BJ, Keeler E, Adelstein SJ. Primer on certain elements of medical decision making. *N Engl J Med* **1975**;293:211–215

Reply

Drs. Black and Dwyer think that because we investigated three particular abnormalities (pneumothorax, nodule, and interstitial disease) in our study [1], we de facto provided a history, of a kind, to the persons who interpreted the radiographs. It is important to remember, however, that in this study these three possibilities were presented on a checklist-type form for all the cases. The list gave no indication that other abnormalities were not present, and, in fact, a number of radiographs in the study did have abnormalities other than the three specifically investigated. Although having the interpreters deal with these three only may have narrowed the number of possible resultant diagnoses, this is not qualitatively the same thing as a radiologist's seeing, for example, "pneumothorax?" on a requisition form in the reading room when pneumothorax clearly is suspected in a particular case. As we make clear in our paper, the findings we reported have a number of qualifications. However, we do not think that the use of the three abnormalities we chose to examine invalidates these findings.

Black and Dwyer state that they would be "shocked to discover" that the special efforts they make when they have been alerted to look for a particular abnormality do not improve their performance. We ask them to consider the possibility that these special efforts may lead them to increase their false-positive rates at the same time they increase their true-positive rates. In our study, the benefit of having a more thorough history available (as opposed to simply a cue) appeared to be offset by the fact that this body of information, although accurate, sometimes contained data that were suggestive in the wrong direction and thus led to mistakes in diagnosis.

In our article, we provided only summary performance indexes (A_z); however, receiver-operating-characteristic methods do provide detailed information on relative performance of observers at different false-positive fractions (as is discussed in the third reference in Black and Dwyer's letter). If we had observed in our analyses significant differences between the two reading modes (i.e., with and without history) as a function of false-positive fraction, we would have discussed them; however, this was not the case.

We agree with Drs. Black and Dwyer that prior probabilities are affected by clinical history, but the precise impact a history has on an observer's performance has not been well documented, nor is it conclusive for posteroanterior chest radiographs that show multiple abnormalities.

Sometimes the results of a carefully planned study will conflict with the perceptions of those who have been performing in-the-field clinical work. For those who disagree with the findings of our study, it is important to remember that our findings were limited to a specific procedure, a certain type of history, and three particular abnormalities. Where our findings conflict with personal experience with the value of the clinical history, we ask readers to consider whether they might not tend to remember those cases for which clinical information is clearly of some help. It is no doubt difficult to remember or objectively account for cases in which the availability of such information led to an incorrect diagnosis.

David Gur
Barbara Good
Lawrence A. Cooperstein
University of Pittsburgh
Pittsburgh, PA 15261

REFERENCE

1. Good BC, Cooperstein LA, DeMarino GB, et al. Does knowledge of the clinical history affect the accuracy of chest radiograph interpretation? *AJR* **1990**;154:709-712

Imaging of Pulmonary Sequestration

The review article by Felker and Tonkin [1] is an integral presentation of the imaging of the pulmonary sequestration and the various abnormalities associated with such sequestration. In their conclusions, the authors suggest an imaging workup, stating that CT plays a lesser role in diagnosis. However, MR must be considered in terms of cost and availability. Therefore, when plain chest radiographs suggest the diagnosis, not uncommonly CT findings must be considered before arteriography is performed. Although Felker and Tonkin describe the CT findings as consisting of abnormal lung parenchyma, aberrant supplying vessels, and the uncommonly found calcification, I suggest that two more CT signs should be emphasized.

I recently saw a case of an angiographically proved pulmonary sequestration in which CT revealed localized emphysema. This finding, which is well documented even on plain chest radiographs [2], is shown better by CT [2, 3]. Reviewing the CT literature, I did not find any satisfying explanation for the presence of the localized emphysema. Oh et al. [2] state that emphysematous changes sometimes are seen in cystic pulmonary sequestration. In my opinion, the nonaerated abnormal lung parenchyma in intralobar pulmonary sequestration causes local atelectasis and therefore could be responsible for the localized emphysema. In addition, a rare supply by a renal artery [4] can be suspected when a vertically oriented aberrant vessel is seen on contrast-enhanced CT.

Apostolos H. Karantanas
Medical School, University of Ioannina
Ioannina 451 10, Greece

REFERENCES

1. Felker RE, Tonkin ILD. Imaging of pulmonary sequestration. *AJR* **1990**;154:241-249
2. Oh KS, Newman B, Bender TM, Bowenn AD. Pulmonary pseudofibrosis and pseudomass lesions. *Radiol Clin North Am* **1988**;26:365-375
3. Naidich DP, Rumancik WM, Ettenger NA, et al. Congenital anomalies of the lungs in adults: MR diagnosis. *AJR* **1988**151:13-19
4. Pedersen ML, LeQuire MH, Spies JB, Ladd WA. Computer tomography of intralobar bronchopulmonary sequestration supplied from the renal artery. *J Comput Assist Tomogr* **1988**;12:874-875

Reply

We agree with Dr. Karantanas that CT has a role in the workup of pulmonary sequestration, particularly if MR is not available. In our experience, CT is useful in showing the sequestration itself and the aberrant vessels. However, we do think that MR is more likely to be conclusive than CT for making the diagnosis and may circumvent the need for angiography. We have not observed localized emphysema in our cases of pulmonary sequestration, but we recognize that it may be difficult to distinguish localized emphysema from what we described as cystic changes in the nonaerated lung of pulmonary sequestration.

R. E. Felker
I. L. D. Tonkin
University of Tennessee, Memphis
Memphis, TN 38163

Left Main Bronchus on Lateral Chest Radiographs

The article by Lang and Friedman [1] provides concise and detailed information about the lobar and segmental bronchial trees in the hilar and perihilar areas. Special attention is paid to the anterior wall stripe of the left lower lobe bronchus. Knowledge of the anatomic variations in the relationship between blood vessels and the left lower lobe bronchus is useful in identifying pathologic changes in this area.

I learned much from this article, but I disagree on two points. First, in Figures 1A and 1B and 6A and 6B, Lang and Friedman show a structure that is labeled as the left upper lobe bronchus (LULB). I think that this structure is, in fact, the terminal part of the left main bronchus, which generally is positioned horizontally beneath the left pulmonary artery. Thus, it is visualized more frequently than the right upper lobe bronchus on lateral radiographs because it is parallel to the X-ray beam in this projection. It can be identified correctly on radiographs by applying the following criteria: (1) The caliber of the left main bronchus in cross section is larger than the caliber of the right upper lobe bronchus. This is well shown in Figures 1, 2, 3, and 6 in the paper by Lang and Friedman. (2) When the left main bronchus is seen end on, its anterior and posterior borders can be united with its anterior and posterior walls, which are observed easily and can be traced from the lower end of the trachea. (3) As Lang and Friedman emphasize, the left lower lobe bronchus comes from this ring shadow seen in cross section. Therefore, this end portion of the left main bronchus is the pivot of the left main bronchus and, at the same time, the starting point of the left lower lobe bronchus. (4) Anatomically, the LULB goes upward or slightly anteriorly at its origin from the left main bronchus. Sometimes, its lingual branch goes downward and is visible on lateral radiographs. Because it is parallel to the X-ray beam, the LULB cannot be seen in cross section on lateral radiographs. The LULB normally is visualized as a small tubelike air shadow just above the upper border of the cross section of the left main bronchus. Its size is usually about 50-60% of the caliber of the left main bronchus. (5) Both main bronchi commonly are visualized as the continuous portion of the trachea. They are shortened markedly, but they keep the normal anatomic relationships: the right main bronchus is slightly anterior and the left main bronchus is a bit behind.

Second, in Figures 1A and 1B, area 2 is labeled as the truncus anterior of the right pulmonary artery. However, according to Proto and Speckman [2], this area is occupied chiefly by the end portion of the main pulmonary artery, which is the part that will divide to form the right and left pulmonary arteries. In these figures, the truncus anterior of the right pulmonary artery is merely superimposed on the main pulmonary artery.

Lian Bi Hu
Staff Hospital, Petroleum Control Dept. of Sichuan Province
Zhong Xing Chang, Chengdu, 610212, China

REFERENCES

1. Lang EV, Friedman PJ. The anterior wall stripe of the left lower lobe bronchus on the lateral chest radiograph: CT correlative study. *AJR* **1990**;154:33-39
2. Proto AV, Speckman JM. The left lateral radiograph of the chest. Part II. *Med Radiogr Photogr* **1980**;56:38-64

Reply

The end-on bronchial shadow seen on the lateral chest film, labeled LULB in Figure 1B of our paper [1], is in fact the left upper lobe bronchus, rather than the left main bronchus. The way to distinguish these two was discussed in a previous review article [2]. The size comparison should not be made to the right upper lobe bronchus but to the diameter of the left main bronchus itself, which extends to the back of the vertical air shadow that is not delimited by the thin line of the back of the right bronchus intermedius. In Figure 1, the back of the left bronchus is clearly 2–3 mm more posterior than the back of the LULB. In Figure 3A, a radiograph of a different patient, the end-on bronchial shadow is tangential to the back wall of the vertical left bronchus as well as the front, so in this case, it *is* the left main bronchus that is projected on end. In Figure 2, both bronchial segments can be seen, partially superimposed.

Differences between patients and between radiographs do not allow a rigid set of criteria to be used to identify the relative position or size of various structures. The elevation of the left hilum and the angle of the X-ray beam in lateral projections determine which part of the bronchus is projected on end, as shown in Figure 13 of a previous paper [2].

With regard to Dr. Hu's second point, it is certainly correct that the truncus anterior of the right pulmonary artery, as projected on the lateral chest film, is superimposed on the main pulmonary artery; however, unless the patient has emphysema or pulmonary hypertension or both, the main pulmonary artery remains invisible (embedded in the mediastinal tissues), and the structure that casts the visible shadow seen on the radiograph is the truncus anterior.

Elvira V. Lang
Paul J. Friedman
Palo Alto VA Medical Center
Palo Alto, CA 94304

REFERENCES

1. Lang EV, Friedman PJ. The anterior wall stripe of the left lower lobe bronchus on the lateral chest radiograph: CT correlative study. *AJR* **1990**;154:33-39
2. Friedman PJ. Practical radiology of the hila and mediastinum. *Postgrad Radiol* **1981**;1:269-304

Broncholithiasis in Bronchogenic Carcinoma Shown by Digital Radiography

Broncholithiasis is a condition in which calcified material from peribronchial lymph nodes is present within a bronchus or a cavity [1]. Direct bronchoscopic visualization or broncholiths is diagnostic, but the broncholiths are seen in only 28% of cases [2]. Chest radiographs may not detect a small broncholith. Conventional tomography can detect a calcified focus, but its exact location in relation to the bronchus is often difficult to delineate. It is useful in the diagnosis of broncholithiasis [3]. Broncholithiasis is clinically important because it may cause a variety of nonspecific signs and symptoms of respiratory diseases before the onset of lithoptysis [4], and proper identification is important because the development of bleeding, recurrent pneumonias, or airway obstruction is an indication for bronchoscopic or surgical intervention [4].

We report a case of a 54-year-old man with hemoptysis in whom a conventional tomogram of the chest (Fig. 1A) showed a cavitating mass in the right upper lobe associated with two small calcifications that apparently were not related to the bronchial lumen. Digital processing ("edge-enhancement" technique) (Fig. 1B) of the conventional tomogram showed that the two calcifications were outlined with air. Squamous cell bronchogenic carcinoma was identified on the basis of bronchoscopy and biopsy. The calcified material could not be reached by the fiberbronchoscope. Lithoptysis occurred shortly thereafter, and the calcification was not present on subsequent radiographs. This case is of special interest because of the infrequent simultaneous occurrence of broncholithiasis and bronchogenic carcinoma (4% of surgical series) [2] and because the broncholiths were detected by digital radiography.

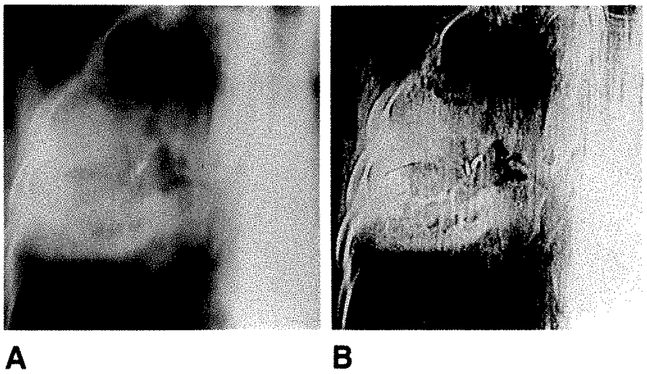

Fig. 1.—Broncholithiasis in bronchogenic carcinoma.
***A*, Conventional tomogram shows cavitation in right upper lobe of lung and two small calcifications.**
***B*, Digital radiograph shows calcifications are outlined with air.**

Juan J. Vidal
Miguel Souto
Pablo G. Tahoces
Carmen Gonzalez
José Correa
José Carreira
Hospital General de Galicia
University of Santiago de Compostela
Santiago de Compostela, Spain

REFERENCES

1. Schmidt HW, Clagget OT, McDonald JR. Broncholithiasis. *J Thorac Cardiovasc Surg* **1950**;19:226-245
2. Arrigoni MG, Bernatz PE, Donoghue FE. Broncholithiasis. *J Thorac Cardiovasc Surg* **1971**;62:231-237
3. Shin MS, Ho K-J. Broncholithiasis: its detection by computed tomography in patients with recurrent hemoptysis of unknown etiology. *J Comput Assist Tomogr* **1983**;7:189-193
4. Dixon GF, Donnemberg RL, Schonfeld SA, Whitcomb ME. Clinical commentary. Advances in the diagnosis and treatment of broncholithiasis. *Am Rev Respir Dis* **1984**;129:1028-1030

Radiologic Investigation of Dysphagia

We read with interest the report by Levine and Rubesin [1] on the radiologic investigation of dysphagia, and we commend them on the thoroughness of their approach to this common clinical problem. We have used a similar combination of techniques and agree that tailoring the examination to the presentation of the patient is important [2]. In addition to motion-recording and static-filming techniques, the supplemental use of a solid bolus is also important.

Although a variety of solid boluses have been recommended for evaluating dysphagia, the 12.5-mm barium tablet and the marshmallow are used most often [3]. We prefer using one third to one half of a standard marshmallow, which is swallowed with a diluted suspension of barium (36% w/v). The solid bolus may impact and produce dysphagia or occasionally may show an esophageal narrowing not seen on initial examination with liquid barium [4]. In a recent project, we detected nine (14%) of 63 mucosal rings on radiographs only when a marshmallow was used (Ott et al., scientific exhibit presented at the annual meeting of the American Gastroenterological Association, Dallas, May 1990). Thus, the use of a solid bolus should be considered in patients who have dysphagia, especially if the routine examination does not explain this symptom.

David J. Ott
David W. Gelfand
Michael Y. M. Chen
Bowman Gray School of Medicine
Winston-Salem, NC 27103

REFERENCES

1. Levine MS, Rubesin SE. Radiologic investigation of dysphagia. *AJR* **1990**;154:1157–1163
2. Gelfand DW, Ott DJ. Anatomy and technique in evaluating the esophagus. *Semin Roentgenol* **1981**;16:168–182
3. Somers S, Stevenson GW, Thompson G. Comparison of endoscopy and barium swallow with marshmallow in dysphagia. *J Can Assoc Radiol* **1986**;37:73–75
4. Ott DJ, Kelley TF, Chen MYM, Gelfand DW. Evaluation of the esophagus with a marshmallow bolus: emphasis on clarifying dysphagia. *Gatrointest Radiol* (in press)

Pancreatic Pseudonodule Due to Prepancreatic Fat

Intraabdominal fat is mostly hyperechoic [1]. Occasionally, however, fat may appear hypoechoic [1]. Prepancreatic fat with this sonolucent appearance may lead to the erroneous diagnosis of a diffuse pancreatic lesion [2]. To our knowledge, no reference has been made in the literature to prepancreatic fat simulating a nodular pancreatic lesion or peripancreatic adenopathy, as in the case presented here.

A 58-year-old man was admitted because of malaise and weight loss. Chest radiograph and CT revealed a mass in the right lung with invasion of the mediastinum and thoracic wall. The diagnosis at biopsy was undifferentiated carcinoma. Abdominal sonography showed two hypoechoic nodules in the pancreatic area consistent with pancreatic metastases (Fig. 1A). Abdominal CT was performed to confirm this diagnosis. Abundant prepancreatic fat was observed in the area separating the pancreas from the stomach (Fig. 1B). No pancreatic tumors or peripancreatic adenoapthy was observed.

Knowledge that prepancreatic fat may be hypoechoic may prevent a mistake in diagnosis. The distinction between sonolucent fat and pancreatic nodules is particularly important when a primary or metastatic tumor is suspected. In case of doubt, the presence of prepancreatic fat as the cause of the sonographic abnormality can be confirmed by CT.

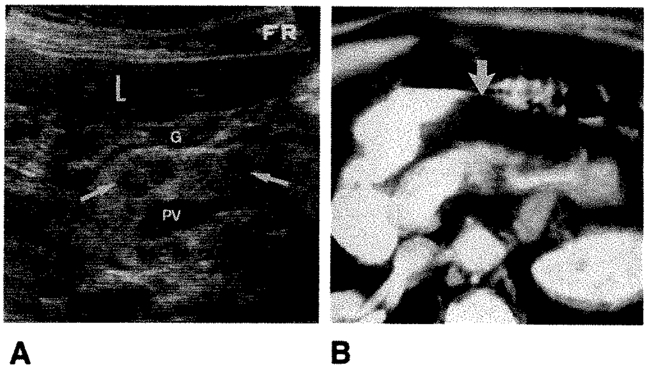

Fig. 1.—Pancreatic pseudonodule due to prepancreatic fat.
***A*, Transverse sonogram through pancreas shows two hypoechoic nodules (*arrows*) in area of pancreatic body and neck. L = left hepatic lobe, PV = main portal vein, G = gastric wall.**
***B*, CT scan at same level as *A* shows extensive prepancreatic fat (*arrow*) separating pancreas from posterior wall of stomach. No evidence of pancreatic lesions or peripancreatic adenopathy is seen.**

E. Sanchís Querol
L. Donoso Bach
A. Martínez-Noguera
Hospital de Sant Pau
08025-Barcelona, Spain

REFERENCES

1. Behan M, Kazam E. The echographic characteristics of fatty tissues and tumors. *Radiology* **1978**;129:143–151
2. Op den Orth JO. Prepancreatic fat deposition: a possible pitfall in pancreatic sonography. *AJR* **1986**;146:1017–1018

Mesothelial Cyst of the Round Ligament

Mesothelial cyst of the round ligament occurs infrequently; only 53 cases have been described [1]. The findings on physical examination are similar to those for an inguinal hernia, and preoperative diagnosis is not easy. To our knowledge, we present the first preoperative diagnostic images of a mesothelial cyst of the round ligament and establish criteria for diagnosis of this entity.

A 44-year-old woman had had pain associated with a mass in the left inguinal region for 3 months. Physical examination was inconclusive for inguinal hernia. Sonography, carried out with 7.5-MHz transducers, showed an anechoic ovoid area 4.0 × 2.5 cm (Fig. 1A) with the typical appearance of a cyst. "Dynamic" sonography, performed while the patient performed the Valsalva maneuver, showed no variation in the size of the mass and no signs of inguinal hernia (i.e., passage of intestinal contents to the interior of the mass). A clear yellow liquid was aspirated via puncture with a fine needle; results of cytologic examination of the liquid were inconclusive. No inguinal hernia was observed on cystography (Fig. 1B) or herniography (Fig. 1C). The preoperative diagnosis was mesothelial cyst of the round ligament. The cyst was extirpated, and histologic examination

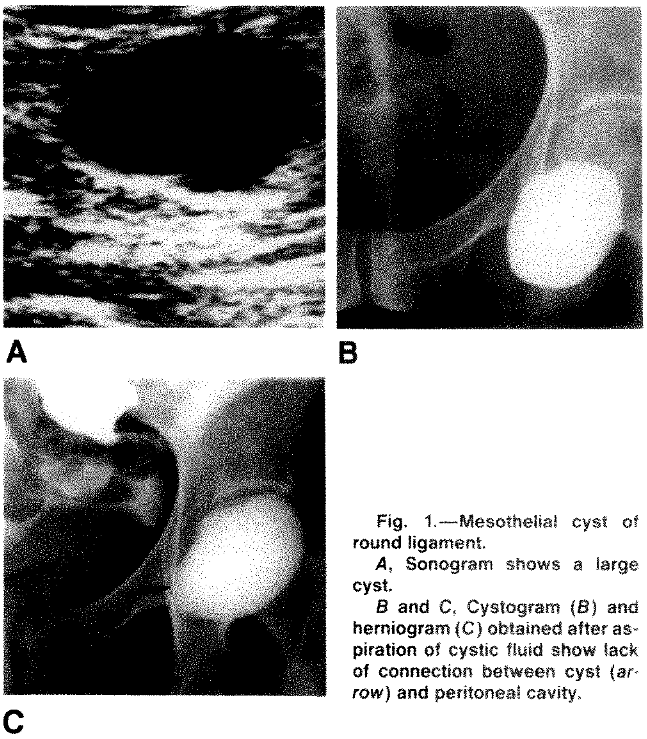

Fig. 1.—Mesothelial cyst of round ligament.
***A*, Sonogram shows a large cyst.**
***B* and *C*, Cystogram (*B*) and herniogram (*C*) obtained after aspiration of cystic fluid show lack of connection between cyst (*arrow*) and peritoneal cavity.**

showed a cyst with a fibrous wall lined with mesothelial cells and foci of chronic inflammatory reaction.

In women, the hernial sac follows the path of the round ligament as far as the labium. Usually the sac contains omentum and small intestine and, occasionally, ascites [2]. A number of different techniques can be used to study hernias of the abdominal wall: CT, MR, sonography, and herniography [2, 3].

The diagnostic sequence used in our case was (1) physical examination, (2) dynamic sonography, and (3) cystography and herniography. Dynamic sonography, performed while the patient performs the Valsalva maneuver, was performed because the results of physical examination were inconclusive for inguinal hernia. In the case of hernias, hyperechoic areas (gas, omentum, and intestine) are seen on dynamic sonography as they are displaced toward the hernial sac or inside it. In our case, no variation in the size or the content of the mass was observed as abdominal pressure was increased. Cystography and herniography were used to confirm the lack of a connection between the cyst and the peritoneal cavity and thus eliminate hernia as a diagnosis, as mesothelial cysts of the round ligament are associated with hernias in 50% of cases [1].

Mesothelial cyst of the round ligament, though rare, should be considered in the differential diagnosis of doubtful inguinal masses, especially in women 34–44 years old.

Juan D. Berná
Vicente García-Medina
José Guirao
Manuel Madrigal
Hospital General, Universidad de Murcia
30001 Murcia, Spain

REFERENCES

1. Harper GB, Awbrey BJ, Thomas CG, Askin FB. Mesothelial cysts of the round ligment simulating inguinal hernia. *Am J Surg* **1986**;151:515–517
2. Wechsler RJ, Kurtz AB, Needleman L, et al. Cross-sectional imaging of abdominal wall hernias. *AJR* **1989**;153:517–521
3. Ekberg O. Inguinal herniography in adults: technique, normal anatomy, and diagnostic criteria for hernias. *Radiology* **1981**;138:31–36

Differentiation of Child Abuse from Osteogenesis Imperfecta

Our attention has been drawn to a review article in the *AJR* by Ablin et al. [1] in which specific comments are made on our work and on the work of our colleagues. We would not wish anyone to underestimate the difficulties involved in differentiating nonaccidental injury from osteogenesis imperfecta (OI) and similar disorders. We are concerned that some of the misconceptions included in the paper by Ablin et al. could lead to serious diagnostic errors.

Our work is based on clinical records of more than 1000 patients with undoubted OI, 700 of whom we have seen personally. We have reviewed the radiographs of 150 patients to date, and our work is continuing. Since 1977, we have published in peer-reviewed journals 13 articles on different aspects of OI.

We recently published a much fuller account [2] of cases of OI in which a serious misdiagnosis of nonaccidental injury was made in the early days. These are patients in whom there is now no doubt about the diagnosis; the follow-up period has been not shorter than 4 years. In every case in which legal proceedings were held, the original radiographs have been reviewed, and attempts have been made to identify the reasons for the error in diagnosis. In many cases, the radiographs obtained at the time of the original fractures were normal, but it is important to recognize that substantial loss of bone mineral is needed before osteoporosis can be assessed with any confidence on ordinary radiographs. Although clear-cut osteoporosis is seen in the majority of patients who have type III OI, only a minority of patients who have type I and type IV OI show osteopenia at the time of the first few fractures. Indeed, the osteoporosis familiar to radiologists in major referral centers usually is that seen in patients with many previous fractures and periods of immobilization. We showed some time ago [3] that even in adult life, cortical thickness is usually normal in bones that have not had previous fractures. More recently, we have shown that single-photon absorptiometry with a precision of less than 1.5% gives normal values even in many adults with OI.

It is not surprising [2] that diagnostic difficulties occur most frequently with type IV OI. We suspect that this disorder is diagnosed less often than it should be. In detailed studies of families who have the type IV disease, the diagnosis was missed in many family members until detailed inquiries were made. The disorder can arise as a new mutation, as with most other dominant disorders [4]. It is not surprising that the milder cases of the type IV disease, particularly in patients without a clear-cut family history, can cause difficulties. None of the patients reported in our published work has lacked reliable evidence of OI. We challenge Dr. Ablin and her colleagues to visit and review our clinical records and our radiographs and to identify a single case included in a published report for which ample evidence is not available to support the diagnosis made.

We remain concerned about the view that wormian bones are an essential feature of OI. Our own experience, with both type I and type IV disease, is that an excess of wormian bones is seen in only a minority of cases. Detailed examination of the cited paper by Cremin et al. [5], in which all or most patients described had wormian bones, indicated that most of their patients had the type III disease, in which diagnosis should present no difficulty. We emphasize that radiographs of the cases we have published have been reviewed independently by a radiologic colleague without knowledge of the detailed clinical diagnosis.

We are concerned that the rather doubtful statsitics presented by Taitz should be given credibility when they are based on just nine patients with type IV OI. The diagnostic difficulties we have recorded do not occur often, but in the United Kingdom, with a population of about 56 million, the difficulties we have described occur too often for complacency [2]. In the worst case (identified only in retrospect), a child was in foster care from the age of 18 months to the age of 5.5 years and nearly was adopted before the correct diagnosis of OI became obvious. It is important to recognize that a misdiagnosis of nonaccidental injury causes immense harm.

Ablin et al. include in one table (Table 4) as one feature of child abuse a "lack of history of significant trauma in patient with fractures." This may be a feature of nonaccidental injury, but it is also a classical feature of OI of all types and does not help in making a diagnosis.

Ablin et al. comment on the types of fractures that may be associated with nonaccidental injury and with OI. Fractures in OI can be of all types and are not confined to the diaphysis. We have numerous OI patients with classical metaphyseal corner fractures and bucket-handle fractures both with and without other bony abnormalities. It is not true that such fractures are "virtually pathognomonic and highly specific for child abuse."

Ablin et al. report two cases in which judges rejected our evidence. What they did not mention was that over the last 16 years, no fewer than 65 children have been returned to their families as a result of our testimony in the courts and that not one of these children has had subsequent proved nonaccidental injury.

We support the authors' concluding sentence that the key to the distinction between OI and nonaccidental injury is correlation of clinical history, physical examination, family history, and the radiologic findings. Fewer of the tragedies that we have identified would have occurred if this correlation had been carried out adequately, and, in particular, if the radiologists concerned had recognized the limitations of their own skills. A child with fractures and apparently normal bones may have OI or some other bone disorder [6]. A competent radiologist should say that although nonaccidental injury can cause these findings, the same appearances also can be caused by OI. Such caution may prevent the gratuitous destruction of some normal families.

Colin R. Paterson
Susan J. McAllion
University of Dundee
Dundee DD1 9SY, Scotland

REFERENCES

1. Ablin DS, Greenspan A, Reinhart M, Grix A. Differentiation of child abuse from osteogenesis imperfecta. *AJR* **1990**;154:1035–1046
2. Paterson CR, McAllion SJ. Osteogenesis imperfecta in the differential diagnosis of child abuse. *Br Med J* **1989**;299:1451–1454
3. Paterson CR. Metacarpal morphometry in adults with osteogenesis imperfecta. *Br Med J* **1978**;1:213–214
4. Carothers AD, McAllion SJ, Paterson CR. Risk of dominant mutation in older fathers: evidence from osteogenesis imperfecta. *J Med Genet* **1986**;23:227–230
5. Cremin B, Goodman H, Spranger J, Beighton P. Wormian bones in osteogenesis imperfecta and other disorders. *Skeletal Radiol* **1982**;8: 35–38
6. Paterson CR. Osteogenesis imperfecta and other bone disorders in the differential diagnosis of unexplained fractures. *J R Soc Med* **1990**;83: 72–74

Reply

We would like to thank Drs. Paterson and McAllion for their specific comments on our review article, "Differentiation of Child Abuse from Osteogenesis Imperfecta" [1]. We agree with them that some forms of osteogenesis imperfecta (OI), particularly type IV, mistakenly can be diagnosed as child abuse, but we would like to emphasize that this occurrence is rare. This is supported by a commentary on our article by Paul Kleinman [2], an expert on child abuse. Unfortunately, when the misdiagnosis of child abuse is made, parents of children who actually have OI may be involved in protective care proceedings while the correct diagnosis is in doubt. It is true that misdiagnosing OI as child abuse causes immense harm. However, even more harm can be done by considering OI in an abused child. Currently, collagen analysis can be helpful in reaching the proper diagnosis.

We agree that some cases of OI type IV can show minimal or no osteoporosis at the time of first fracture and that a family history of OI may be lacking because in some cases the disease is caused by a new mutation. Two of the papers [3, 4] cited by Paterson and McAllion were published after the submission of our revised manuscript to *AJR*. One of these [3] described 15 (2%) of 802 children with OI who were subjects of formal case conferences and care proceedings. However, only two of these patients lacked blue sclera, wormian bones, or a family history that would have caused confusion in distinguishing type IV OI from child abuse. In 13 of these patients with OI, protective care proceedings could have been avoided if radiologic findings, clinical history, physical examination, and family history had been correlated.

Because, at least in the United States, child abuse is so much more common than OI (particularly, the rare type IV), it is essential that child abuse be considered in children who have unexplained fractures, particularly if metaphyseal corner fractures or bucket-handle lesions can be identified. Kleinman, a respected expert on child abuse, agrees with others that "the classic metaphyseal corner fracture and bucket-handle lesions are virtually pathognomonic for infant abuse" [5].

Radiologists, pediatricians, and geneticists must educate themselves to distinguish between OI and child abuse by considering not only radiologic findings but also clinical history, physical examination, and family history to avoid the tragedy of misdiagnosis. A team approach is essential.

Deborah S. Ablin
Adam Greenspan
Michael Reinhart
Arthur Grix
University of California, Davis Medical Center
Sacramento, CA 95817

REFERENCES

1. Ablin DS, Greenspan A, Reinhart M, Grix A. Differentiation of child abuse from osteogenesis imperfecta. *AJR* **1990**;154:1035–1046
2. Kleinman PK. Differentiation of child abuse and osteogenesis imperfecta: medical and legal implications. *AJR* **1990**;154:1047–1048
3. Paterson CR, McAllion SJ. Osteogenesis imperfecta in the differential diagnosis of child abuse. *Br Med J* **1989**;299:1451–1454
4. Paterson CR. Osteogenesis imperfecta and other bone disorders in the differential diagnosis of unexplained fractures. *J R Soc Med* **1990**;83: 72–74
5. Kleinman PK. *Diagnostic imaging of child abuse*. Baltimore: Williams & Wilkins, **1987**:10

A Pitfall in the Sonographic Diagnosis of Spina Bifida

Despite the growing use of sonography during pregnancy, spina bifida often remains undiagnosed before birth. Only 50% of such cases currently are diagnosed by using sonography [1]. We report a case that indicates that slightly angled longitudinal views may fail to show dysraphic defects.

A 24-year-old pregnant woman, para 2, gravida 2, had routine obstetric sonography at 24 weeks after her last menstrual period. Sonographic findings included intrauterine growth retardation; enlargement of lateral cerebral ventricles; and lumbar spina bifida, with V-shaped vertebrae on transverse views and a lumbar dysraphic defect on sagittal views (Figs. 1A and 1B). Longitudinal views, slightly angled from the sagittal midline view, did not show the defect (Figs. 1C and 1D). The patient had a therapeutic abortion, with vaginal

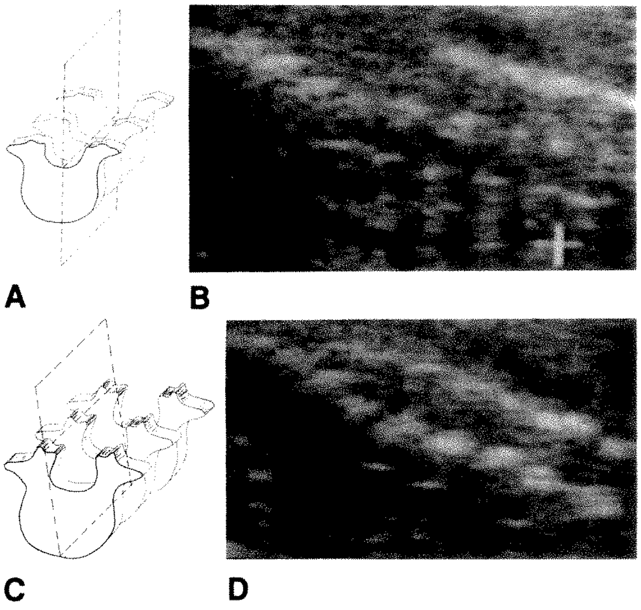

Fig. 1.—Fetal spinal bifida.
***A* and *B*, Sagittal midline view. Drawing (*A*) shows plane of view, and corresponding sonogram (*B*) shows posterior dysraphic defect of lumbar spine.**
***C* and *D*, Angled longitudinal view. Drawing (*C*) shows plane of view, and corresponding sonogram (*D*) does not show dysraphic defect.**

delivery of a female fetus that had lumbar spina bifida and myelomeningocele.

Ideally, sonographic examination of the fetal spine should include both transverse and sagittal views. However, these views are not always easy to obtain. The major obstacles are breech presentation, twin pregnancy, fetal lie with the spine posterior, and oligoamnios. In such situations, the fetal spine may be unaccessible to postero-anterior transverse views and to sagittal midline views. Figures 1C and 1D show that starting from a sagittal midline view, slight tilting of the transducer may give a false appearance of normal spine. This emphasizes the importance of sonographic signs associated with spina bifida, such as enlargement of cerebral ventricles [2].

L. R. M. Morin
Valognes Hospital
F50700 Valognes, France
J. C. Loisel
Meaux Hospital
F77104 Meaux, France

REFERENCES

1. Main DM, Mennuti MT. Neural tube defects: issues in prenatal diagnosis and couseling. *Obstet Gynecol* **1986**;67:1-15
2. Nicolaides KH, Gabbe SG, Campbell S, Guidetti R. Ultrasound screening for spina bifida: cranial and cerebellar signs. *Lancet* **1986**;2:72-74

Chronic Arterial Occlusion in a Canine Model: A Novel Technique

The introduction of new interventional means for vascular recanalization, such as lasers, stents, and atherectomy devices, has underlined the need for a suitable experimental animal model of arterial occlusion that can be used to evaluate new techniques and to gain the necessary hands-on experience with them. We describe a novel, yet familiar, technique for obtaining such a model occlusion.

Six mongrel dogs were anesthetized with ketamine, and their femoral arteries were exposed surgically. A short segment of vessel, 4-5 cm long and free of branches, was isolated between two clamps. Through a small arteriotomy, 0.2-0.3 ml of the polymer N-butyl cyanoacrylate was injected into this segment. When this liquid comes into contact with blood, it sets into a firm, solid mass and occludes the lumen of the vessel. Once the polymer had solidified, the clamps were released, and angiograms were obtained to confirm the occlusion. Short occlusive segments with well-developed collateral circulation were seen in all the dogs (Fig. 1A). In two dogs that were sacrificed immediately after angiography, the femoral arteries showed panarterial inflammation, disruption of the internal elastic lamina, and occlusion of the lumen by the refractile polymer. In two more dogs sacrificed 6 months after injection of the polymer, hyalinized thrombus was seen in the lumen, with small channels of recanalization in the periphery (Fig. 1B). Much of the refractile material was no longer present, and only a mild inflammatory reaction was seen.

Several techniques for producing model arterial occlusion have been described. However, an acceptable model continues to be elusive because it is difficult to simulate the slow and complex process of human arterial occlusion brought about by either atherogenesis or arteritis. Atheromata produced by high levels of cholesterol or other dietary changes are soft and friable and bear no resemblance to human lesions [1]. Occlusions caused by emboli of autogenous fat and clot have been tried [2], but these materials also have a soft consistency, and random embolization can result in occlusion of branch vessels, which hampers the development of collateral circulation. Ligation of a segment of the femoral artery with plain catgut has been described as a model that can be used to test laser angioplasty systems [3].

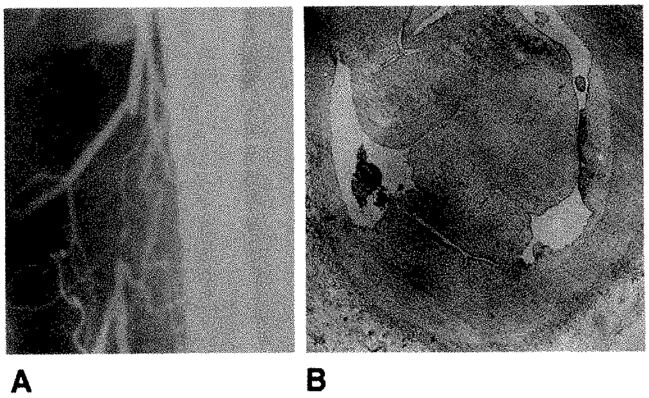

Fig. 1.—Chronic arterial occlusion in a canine model.

***A*, Femoral arteriogram obtained 6 months after occlusion of artery with N-butylcyanoacrylate shows persistent occlusion with good collateral circulation and distal runoff.**

***B*, Histologic section of femoral artery shows occlusion with organized thrombus and channels of recanalization in periphery. Internal elastic lamina is disrupted at some places. (H and E)**

We think our technique is superior to existing ones on several counts. Controlled occlusion of a segment of the vessel between two major side branches allows collateral circulation to develop, and the angiographic appearance of such an occlusion is similar to that of chronic arterial occlusion in the lower extremities in humans. Thus, practical problems in vascular intervention, such as entry into side branches and their inadvertent occlusion, are simulated effectively. The firm consistency of the occluding material resembles more closely the organized thrombus in chronic occlusion of human arteries. Finally, the mild panarterial inflammation that is produced resembles inflammatory arteriopathies like Takayasu and Buerger diseases.

K. Ravimandalam
V. R. K. Rao
Sunil Kumar
Santhosh Joseph
Arthur V. Lal
Mira Mohanty
Sree Chitra Tirunal Institute for Medical Sciences and Technology
Trivandrum-695 011, India

REFERENCES

1. Choy DSJ. Laser applications in cardiovascular disease. *Semin Intervent Radiol* **1986**;3:1-10
2. Doyle L, Litvack F, Grundfest W, et al. In vivo model for testing laser angioplasty systems. *Circulation* **1986**;74:II-361
3. Jain AC, Dhedhia HV, Savrin RA, Withers AS, Rochlani S. Laser and balloon angioplasty in chronic occlusion of femoral artery in a canine model. *Am Heart J* **1986**;111:794-795

Letters are published at the discretion of the Editor and are subject to editing.

Letters to the Editor must not be more than two *double-spaced*, typewritten pages. One or two figures may be included. Abbreviations should not be used. See Author Guidelines, page A5.

Material being submitted or published elsewhere should not be duplicated in letters, and authors of letters must disclose financial associations or other possible conflicts of interest.

Letters concerning a paper published in the *AJR* will be sent to the authors of the paper for a reply to be published in the same issue. Opinions expressed in the Letters to the Editor do not necessarily reflect the opinions of the Editor.

Review of Current Literature

Initials and addresses of corresponding authors are provided in parentheses for each article so that the reader can obtain reprints directly. Abstracts are printed verbatim from each journal.

The New England Journal of Medicine

Intermittent cyclical etidronate treatment of postmenopausal osteoporosis. Watts NB, Harris ST, Genant HK, et al. (NBW, The Emory Clinic, 1365 Clifton Rd., N.E., Atlanta, GA 30322). *N Engl J Med* 323(2):73–79, July 1990

Background. To determine the effects of etidronate (a bisphosphonate that inhibits osteoclast-mediated bone resorption) in the treatment of postmenopausal osteoporosis, we conducted a prospective, two-year, double-blind, placebo-controlled, multicenter study in 429 women who had one to four vertebral compression fractures plus radiographic evidence of osteopenia.

Methods. The patients were randomly assigned to treatment with phosphate (1.0 g) or placebo twice daily on days 1 through 3, etidronate (400 mg) or placebo daily on days 4 through 17, and supplemental calcium (500 mg) daily on days 18 through 91 (group 1, placebo and placebo; group 2, phosphate and placebo; group 3, placebo and etidronate; and group 4, phosphate and etidronate). The treatment cycles were repeated eight times. The bone density of the spine was measured by dual-photon absorptiometry, and the rates of new vertebral fractures were determined from sequential radiographs.

Results. After two years, the patients receiving etidronate (groups 3 and 4) had significant increases in their mean (±SE) spinal bone density (4.2 ± 0.8 percent and 5.2 ± 0.7 percent, respectively; $P < 0.017$). The rate of new vertebral fractures was reduced by half in the etidronate-treated patients (groups 3 and 4 combined) as compared with the patients who did not receive etidronate (groups 1 and 2 combined) (29.5 vs. 62.9 fractures per 1000 patient-years; $P = 0.043$); the effect of treatment was most striking in the subgroup of patients with the lowest spinal bone mineral density at base line, in whom fracture rates were reduced by two thirds (42.3 vs. 132.7 fractures per 1000 patient-years; $P = 0.004$). The addition of phosphate provided no apparent benefit. There were no significant adverse effects of treatment.

Conclusions. Intermittent cyclical therapy with etidronate for two years significantly increases spinal bone mass and reduces the incidence of new vertebral fractures in women with postmenopausal osteoporosis.

Transplacental passage of insulin in pregnant women with insulin-dependent diabetes mellitus: its role in fetal macrosomia. Menon RK, Cohen RM, Sperling MA, Cutfield WS, Mimouni F, Khoury JC (MAS, Dept. of Pediatrics, Children's Hospital of Pittsburgh, 1 Children's Pl., Fifth Ave., Pittsburgh, PA 15213). *N Engl J Med* 323(5):309–315, July 1990

Background and Methods. Fetal macrosomia occurs despite nearly normal maternal blood glucose levels in women with diabetes treated with insulin. We examined the hypothesis that it may be caused by insulin transferred as an insulin-antibody complex from the mother to her fetus. We adapted and validated a method based on high-performance liquid chromatography and used it to quantitate insulin in small volumes (0.5 to 1.0 ml) of cord serum from 51 infants born to mothers with insulin-dependent diabetes mellitus.

Results. In mothers receiving only human insulin ($n = 6$), only human insulin was detected in cord serum. Of the remaining 45 infants, whose mothers received animal insulin during pregnancy, 28 (group 1) had levels of animal (bovine or porcine) insulin (mean [±SE], 707 ± 163 pmol per liter) that constituted 27.4 ± 2.5 percent of the total insulin concentration (2393 ± 500 pmol per liter) measured in the cord serum. The cord-serum insulin concentration in the remaining 17 infants (group 2), in whom only human insulin was detected (381 ± 56 pmol per liter), was only 15 percent of that in group 1 ($P < 0.001$). There was a significant correlation between the maternal and the cord-serum concentrations of anti-insulin antibody and the concentration of animal insulin in the baby ($r = 0.77$, $P < 0.01$, and $r = 0.76$, $P < 0.001$, respectively), suggesting that the animal insulin was transferred as an insulin-antibody complex. In group 1 the mean concentration of animal insulin in cord serum was higher in the 12 infants with macrosomia than in the 16 infants without the condition (1113 ± 321 vs. 402 ± 110 pmol per liter; $P < 0.05$), and the concentration of animal insulin in cord serum correlated with birth weight ($r = 0.39$, $P < 0.05$). The maternal glycosylated hemoglobin values and the incidence of respiratory distress syndrome were similar in groups 1 and 2.

Conclusions. Considerable amounts of antibody-bound insulin are transferred from mother to fetus during pregnancy in some women with insulin-dependent diabetes mellitus; the extent of transfer correlates with the maternal concentration of anti-insulin antibody. The correlation between macrosomia and the concentrations of animal insulin in cord serum indicates that the transferred insulin has biologic activity and suggests that the formation of antibody to insulin in the mother is a determinant of fetal outcome independent of maternal blood glucose levels.

Enhanced detection of ischemic but viable myocardium by the reinjection of thallium after stress-redistribution imaging. Dilsizian V, Rocco TP, Freedman NMT, Leon MB, Bonow RO (VD, The National Institutes of Health, Bldg. 10, Rm. 7B-15, Bethesda, MD 20892). *N Engl J Med* 323(3):141-146, July 1990

Background. The identification of ischemic but viable myocardium by thallium exercise scintigraphy is often imprecise, since many of the perfusion defects that develop in ischemic myocardium during exercise do not "fill in" on subsequent redistribution images. We hypothesized that a second injection of thallium given after the redistribution images were taken might improve the detection of ischemic but viable myocardium.

Methods. We studied 100 patients with coronary artery disease, using thallium exercise tomographic imaging and radionuclide angiography. Patients received 2 mCi of thallium intravenously during exercise, redistribution imaging was performed three to four hours later, and a second dose of 1 mCi of thallium was injected at rest immediately thereafter. The three sets of images (stress, redistribution, and reinjection) were then analyzed.

Results. Ninety-two of the 100 patients had exercise-induced perfusion defects. Of the 260 abnormal myocardial regions identified by stress imaging, 85 (33 percent) appeared to be irreversible on redistribution imaging three to four hours later. However, 42 of these apparently irreversible defects (49 percent) demonstrated improved or normal thallium uptake after the second injection of thallium, with an increase in mean regional uptake from 56 ± 12 percent on redistribution studies to 64 ± 10 percent on reinjection imaging ($P < 0.001$). Twenty patients were restudied three to six months after coronary angioplasty. Of the 15 myocardial regions with defects on redistribution studies that were identified as viable by reinjection studies before angioplasty, 13 (87 percent) had normal thallium uptake and improved regional wall motion after angioplasty. In contrast, all eight regions with persistent defects on reinjection imaging before angioplasty had abnormal thallium uptake and abnormal regional wall motion after angioplasty.

Conclusions. These data indicate that the reinjection of thallium improves the detection of ischemic myocardium and that myocardial regions with improved thallium uptake on reinjection imaging represent viable but jeopardized myocardium.

Immunohistologic abnormalities of the microfibrillar-fiber system in the Marfan syndrome. Hollister DW, Godfrey M, Sakai LY, Pyeritz RE (DWH, Dept. of Pediatrics, University of Nebraska Medical Center, 600 S. 42nd St., Omaha, NE 68198-5430). *N Engl J Med* 323(3):152–159, July 1990

Background. Indirect-immunofluorescence studies of skin and cultured dermal fibroblasts from patients with the Marfan syndrome demonstrate apparent deficiency of one element of connective tissue—the microfibrillar-fiber system—in assays using specific antibodies against fibrillin, a major microfibrillar protein. This study was designed to test whether these immunostaining abnormalities are consistent and diagnostic features of the disease.

Methods. We studied patients with either the Marfan syndrome or various other inherited connective-tissue disorders and normal subjects according to a single-blind protocol in which coded samples of skin, fibroblast cultures, or both were analyzed without knowledge of the clinical diagnosis and classified as "Marfan" or "non-Marfan" before the sample codes were broken.

Results. Of the 27 patients with the Marfan syndrome, 24 were correctly identified by the decreased content of microfibrillar fibers in their skin, cultured fibroblasts, or both; in contrast, 19 of 25 patients with other heritable disorders of connective tissue and all 13 normal subjects were correctly classified as "non-Marfan" by these assays ($P < 0.001$).

Conclusions. These results document consistent, relatively specific abnormalities of microfibrillar fibers in the Marfan syndrome. The biomechanical incompetence of these structural elements, due to quantitative or qualitative abnormalities, may account for the pleiotropic clinical manifestations of the disease. Therefore, various defects in the expression, structure, assembly, or degradation of the constituent structural glycoprotein (or glycoproteins) of microfibrils may be implicated in the causation of the Marfan syndrome.

Stereotactic heavy-charged-particle Bragg-peak radiation for intracranial arteriovenous malformations. Steinberg GK, Fabrikant JI, Marks MP, et al. (GKS, Stanford University, Division of Neurosurgery, S006, 300 Pasteur Dr., Stanford, CA 94305). *N Engl J Med* 323(2):96–101, July 1990

Background. Heavy-charged-particle radiation has several advantages over protons and photons for the treatment of intracranial lesions; it has an improved physical distribution of the dose deep in tissue, a small angle of lateral scattering, and a sharp distal falloff of the dose.

Methods. We present detailed clinical and radiologic follow-up in 86 patients with symptomatic but surgically inaccessible cerebral arteriovenous malformations that were treated with stereotactic helium-ion Bragg-peak radiation. The doses ranged from 8.8 to 34.6 Gy delivered to volumes of tissue of 0.3 to 70 cm^3.

Results. Two years after radiation treatment, the rate of complete obliteration of the lesions, as detected angiographically, was 94 percent for lesions smaller than 4 cm^3, 75 percent for those of 4 to 25 cm^3, and 39 percent for those larger than 25 cm^3. After three years, the rates of obliteration were 100, 95, and 70 percent, respectively. Major neurologic complications occurred in 10 patients (12 percent), of whom 9 had permanent deficits. All these complications occurred in the initial stage of the protocol, before the maximal dose of radiation was reduced to 19.2 Gy. In addition, hemorrhage occurred in 10 patients from residual malformations between 4 and 34 months after treatment. Seizures and headaches were less severe in 63 percent of the 35 and 68 percent of the 40 patients, respectively, who had them initially.

Conclusions. Given the natural history of these inaccessible lesions and the high risks of surgery, we conclude that heavy-charged-particle radiation is an effective therapy for symptomatic, surgically inaccessible intracranial arteriovenous malformations. The current procedure has two disadvantages: a prolonged latency period before complete obliteration of the vascular lesion and a small risk of serious neurologic complications.

Chest

Computed tomography in the etiologic assessment of idiopathic spontaneous pneumothorax. Lesur O, Delorme N, Fromaget JM, Bernadac P, Polu JM (JMP, Maladies Respiratoires et Reanimation Respiratoire, CHU de Nancy-Brabois, F-54500 Vandoeuvre-les Nancy, France). *Chest* 98(2):341–347, Aug. 1990

In an attempt to elucidate the origin of the so-called idiopathic spontaneous pneumothorax (ISP), clinical examination, pulmonary function tests, and computed tomography (CT) with visual quantification and density analysis were performed in 20 young patients two months after an ISP episode. Twenty controls were recruited for CT. The chest roentgenograms were normal in the two groups. The results indicated the presence of various types of emphysematous lesions (EL) in the ISP group located predominantly in the apical fields with subpleural location in 16 patients. Interestingly, diffuse but moderate centrilobular emphysema was noted in 12 of 20 patients. The EL visual quantification was always less than 5 percent of the CT slices' total areas. The lung mean density shifted significantly toward the air density in the patient group (patients: −743±57.5 HU vs controls −713±59.5 HU, $p < 0.01$). These findings suggest that CT may be useful for early assessment of EL in patients with ISP.

Gastrointestinal Endoscopy

Push-enteroscopy for diagnosis of patients with gastrointestinal bleeding of obscure origin. Foutch PG, Sawyer R, Sanowski RA (PGF, Gastroenterology, Carl T. Hayden Veterans Administration Medical Center, Phoenix, AZ 85012). *Gastrointest Endosc* 36(4):337–341, 1990

Push-enteroscopy using a disinfected colonoscope was performed on 39 patients with gastrointestinal bleeding of obscure origin. Our results show that: (1) A high percentage of patients (38%) have pathological lesions responsible for bleeding located in the distal duodenum and proximal jejunum, which are readily detected by push-enteroscopy. (2) Duodeno-jejunal arteriovenous malformations (AVMs) are the most common cause for bleeding, and these lesions can be conveniently cauterized through the endoscope. (3) An efficient sequence of steps for diagnosis of patients with this problem includes push-enteroscopy when the initial EGD and colonoscopy are normal followed by small bowel radiography. Mesenteric angiography and intraoperative enteroscopy can be reserved for patients with severe bleeding when push-enteroscopy and small bowel radiography are negative. We conclude that push-enteroscopy has an important role to play in the early assessment of patients with gastrointestinal bleeding of obscure origin.

Endoscopic cholangiopancreatography in hepatic clonorchiasis—a follow-up study. Leung JWC, Sung JY, Banez VP, et al. (JWCL, Dept. of Medicine, Prince of Wales Hospital, Shatin, N.T. Hong Kong). *Gastrointest Endosc* 36:360-363, 1990

Cholangiographic changes by the biliary system in 16 patients with proven hepatic clonorchiasis, diagnosed by positive stool or bile ova isolates, were studied. All patients presented with epigastric pain. Other symptoms included jaundice in 31% (5 of 16) and fever in 12.5% (2 of 16). Praziquantel given at 25 mg/kg for three doses in 1 day were administered. Three consecutive stool tests were performed 3 months after treatment and were negative in 87.5% (14 of 16). ERCP studies were repeated at a mean interval of 31.6 months (range, 8 to 69 months). Measurements of the bile ducts on retrograde cholangiograms before and after treatment were compared using the paired Student's *t* test. Filling defects and blunting of the terminal bile ducts seen on the initial cholangiogram, interpreted as the presence of adult worms, disappeared after treatment. However, there was no significant change between pre- and post-treatment measurement of bile duct caliber. Bile duct dilation, irregularities, and ductal proliferation persisted despite eradication of the parasite.

Endoscopic ultrasonography for the evaluation of smooth muscle tumors in the upper gastrointestinal tract: an experience with 42 cases. Tio TL, Tytgat GNJ, den Hartog Jager FCA (TLT, Dept. of Gastro-Entero-Hepatology, Academic Medical Center, Meibergdreef 9, 1105 AZ Amsterdam, the Netherlands). *Gastrointest Endosc* 36:342-350, 1990

Before surgery, 12 patients with suspected leiomyoma and 12 patients with suspected leiomyosarcoma were studied by endoscopic ultrasonography (EUS), computed tomography (CT), endoscopy, and barium swallow. The results were correlated with surgery and histology. Ten leiomyomas, one benign gastric ulcer, one carcinoid metastasis, eight leiomyosarcomas, two leiomyoblastomas, one mucus secreting adenocarcinoma, and one bronchial carcinoma were diagnosed. Eighteen additional patients suspected to have benign submucosal lesions by endoscopy and barium meal were treated nonsurgically, and studied by EUS and CT. EUS was superior to other imaging techniques in the detection, staging, and follow-up of submucosal smooth muscle tumors because of clear imaging of the intramural abnormality and adjacent lymph nodes.

The Journal of Bone and Joint Surgery

B-mode ultrasound scanning in the detection of proximal venous thrombosis after total hip replacement. Woolson ST, McCrory DW, Walter JF, Maloney WJ, Watt JM, Cahill PD (STW, Ste. 202, 1220 University Dr., Menlo Park, CA 94025). *J Bone Joint Surg [Am]* 72-A(7):983-987, Aug. 1990

A prospective study of the accuracy of real-time B-mode ultrasonography in detecting deep venous thrombosis in the femoral and popliteal veins of the lower extremity was conducted on a consecutive series of patients who had had a total hip replacement. Ascending venography was used as a diagnostic standard. One hundred and forty-three patients had ultrasound studies of both lower extremities and a venographic study of the operatively treated lower extremity at an average of 7.6 days postoperatively. The two tests were done within twenty-four hours of each other.

Both ultrasonography and venography were done on 152 extremities. Two paired studies were excluded from the analysis of results because the ultrasound scans could not be interpreted. In 131 extremities, both diagnostic tests were negative for proximal thrombosis. Eight extremities had isolated thrombosis of a vein in the calf that was detected only by venography. In nineteen extremities, old or fresh thrombosis was diagnosed by venography. In four extremities, an old thrombosis of the superficial femoral vein was detected by both studies. In four of the extremities that had a new thrombus in the common femoral vein and in nine that had a new thrombus in the superficial femoral vein, abnormal findings on ultrasound scans correlated with those on venograms. There were two false-negative ultrasound scans and one false-negative venogram.

The sensitivity, specificity, and accuracy of ultrasonography were 89, 100, and 99 per cent for the diagnosis of thrombosis of the proximal veins of the lower limb and 63, 100, and 93 per cent for the diagnosis of thrombosis when the entire venous system of the limb was included. We believe that B-mode ultrasonography is accurate and compares favorably with venography for detection of deep venous thrombosis of the proximal veins after total hip replacement.

The Journal of Urology

Enlargement of regional lymph nodes in renal cell carcinoma is often not due to metastases. Studer UE, Scherz S, Scheidegger J, et al. (UES, Dept. of Urology, Inselspital, University of Berne, Berne, Switzerland). *J Urol* 144:243-245, Aug. 1990

Preoperative axial computerized tomography scans in 163 patients with renal cell carcinoma were reviewed to assess the predictive value for the diagnosis of regional lymph node metastases. Computerized tomography was falsely negative in 5 patients: 2 had metastatic lymph nodes in the renal hilus adjacent to the primary tumor measuring 2 and 2.5 cm., and 3 had micrometastases in nodes of less than 1 cm. In 43 patients enlarged lymph nodes with a diameter of 1 to 2.2 cm. (median 1.4 cm.) were diagnosed on the preoperative scan and this was confirmed at nephrectomy and pathologically. In 18 of these 43 patients (42%) histological study showed metastases of the renal cell carcinoma in the enlarged lymph nodes. In the other 25 patients (58%) the enlarged nodes showed only inflammatory changes and/or follicular hyperplasia. This finding was significantly more frequent in patients with tumor involvement of the renal vein and tumor necrosis ($p = 0.0044$).

We conclude that the sensitivity of preoperative computerized tomography is good for the detection of enlarged lymph nodes in patients with renal cell cancer (95%). However, significant lymph node enlargement frequently may be caused by inflammatory changes, especially in the presence of tumor necrosis. This radiological finding should not be misinterpreted as metastatic disease, unless it has been proved cytologically by fine needle aspiration.

Journal of Ultrasound in Medicine

Sonographically demonstrated intra-amniotic hemorrhage following transplacental genetic amniocentesis: frequency, sonographic appearance, and clinical significance. Chinn DH, Towers CV, Beeman RG (DHC, Dept. of Radiology, Hoag Memorial Hospital, 301 Newport Blvd., Newport Beach, CA 92663). *J Ultrasound Med* 9:495-502, Sept. 1990

Over a 9-month period 11 transplacental amniocenteses were performed. Following completion of amniocentesis, intra-amniotic hemorrhage occurred in all 11 cases. Amniotic masses and intra-amniotic strands occurred in three cases as a result of intra-amniotic hemorrhage. The 11 pregnancies in which transplacental amniocentesis were performed were uncomplicated, and they resulted in normal infants. Transplacental amniocentesis can yield unusual sonographic appearances, but does not appear to adversely affect pregnancy outcome.

Reprinted with permission by the American Institute of Ultrasound in Medicine.

Magnetic Resonance Imaging

Magnetic resonance imaging features in melanoma. Marx HF, Colletti PM, Raval JK, Boswell WD Jr, Zee CS (HFM, City of Hope National Medical Center, Dept. of Radiology, 1500 E. Duarte Rd., Duarte, CA 91010). *Magn Reson Imaging* 8:223–229, 1990

T_1 and T_2 relaxation time shortening secondary to paramagnetic compounds has been described in melanoma. The purpose of this paper is to evaluate the signal behavior of melanoma involved in various body areas using short TR, TE and long TR, TE sequences. Twenty-seven sites of melanoma were evaluated with MR using T_1-weighted and T_2-weighted techniques. Using fat and muscle signal intensities as references tissues, lesions were graded into high, low or intermediate intensity categories for each of the sequences. Four signal patterns emerged. The typical pattern characterized by high signal on T_1-weighted images and low signal on T_2-weighted images reflected T_1 and T_2 shortening. The other pattern categories comprised of lesions demonstrating low signal T_1-weighted images and high signal on T_2-weighted images, high signal on both T_1- and T_2-weighted images and lesions showing intermediate signal on either T_2- or T_2-weighted images. We observed a tendency away from the typical signal pattern in extraocular melanoma cases with only one of 14 demonstrating this pattern. Moreover, only seven of thirteen ocular melanomas exhibited such behavior. Possible explanations for this finding as well as the existence of a variety of MR appearances to melanoma are offered. We conclude that while signal patterns showing T_1 and T_2 shortening are typical of melanoma, the absence of these does not exclude the diagnosis.

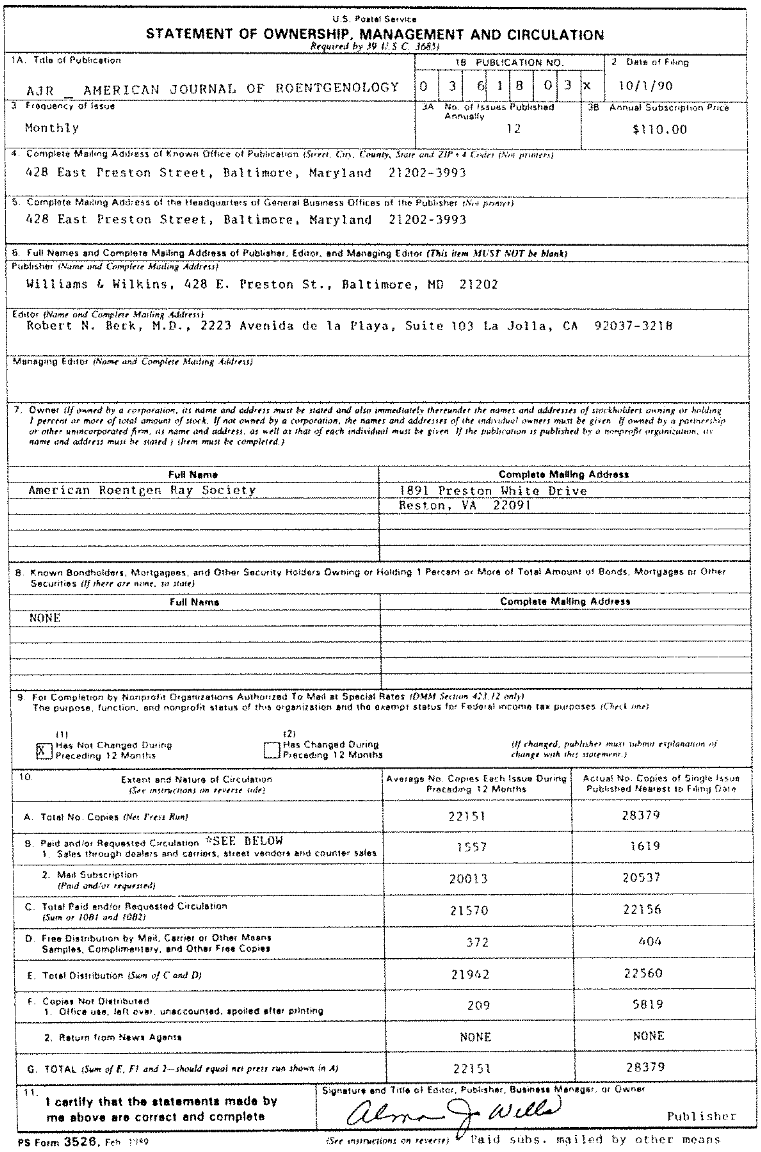

U.S. Postal Service

STATEMENT OF OWNERSHIP, MANAGEMENT AND CIRCULATION

Required by 39 U.S.C. 3685)

1A. Title of Publication AJR _ AMERICAN JOURNAL OF ROENTGENOLOGY	1B. PUBLICATION NO. 0 3 6 1 8 0 3 x	2. Date of Filing 10/1/90
3. Frequency of Issue Monthly	3A. No. of Issues Published Annually 12	3B. Annual Subscription Price $110.00

4. Complete Mailing Address of Known Office of Publication *(Street, City, County, State and ZIP+4 Code) (Not printers)*
428 East Preston Street, Baltimore, Maryland 21202-3993

5. Complete Mailing Address of the Headquarters of General Business Offices of the Publisher *(Not printer)*
428 East Preston Street, Baltimore, Maryland 21202-3993

6. Full Names and Complete Mailing Address of Publisher, Editor, and Managing Editor *(This item MUST NOT be blank)*

Publisher *(Name and Complete Mailing Address)*
Williams & Wilkins, 428 E. Preston St., Baltimore, MD 21202

Editor *(Name and Complete Mailing Address)*
Robert N. Berk, M.D., 2223 Avenida de la Playa, Suite 103 La Jolla, CA 92037-3218

Managing Editor *(Name and Complete Mailing Address)*

7. Owner *(If owned by a corporation, its name and address must be stated and also immediately thereunder the names and addresses of stockholders owning or holding 1 percent or more of total amount of stock. If not owned by a corporation, the names and addresses of the individual owners must be given. If owned by a partnership or other unincorporated firm, its name and address, as well as that of each individual must be given. If the publication is published by a nonprofit organization, its name and address must be stated.) (Item must be completed.)*

Full Name	Complete Mailing Address
American Roentgen Ray Society	1891 Preston White Drive
	Reston, VA 22091

8. Known Bondholders, Mortgagees, and Other Security Holders Owning or Holding 1 Percent or More of Total Amount of Bonds, Mortgages or Other Securities *(If there are none, so state)*

Full Name	Complete Mailing Address
NONE	

9. For Completion by Nonprofit Organizations Authorized To Mail at Special Rates *(DMM Section 423.12 only)*
The purpose, function, and nonprofit status of this organization and the exempt status for Federal income tax purposes *(Check one)*

(1) ☒ Has Not Changed During Preceding 12 Months
(2) ☐ Has Changed During Preceding 12 Months
(If changed, publisher must submit explanation of change with this statement.)

10. Extent and Nature of Circulation *(See instructions on reverse side)*	Average No. Copies Each Issue During Preceding 12 Months	Actual No. Copies of Single Issue Published Nearest to Filing Date
A. Total No. Copies *(Net Press Run)*	22151	28379
B. Paid and/or Requested Circulation *SEE BELOW 1. Sales through dealers and carriers, street vendors and counter sales	1557	1619
2. Mail Subscription *(Paid and/or requested)*	20013	20537
C. Total Paid and/or Requested Circulation *(Sum or 10B1 and 10B2)*	21570	22156
D. Free Distribution by Mail, Carrier or Other Means Samples, Complimentary, and Other Free Copies	372	404
E. Total Distribution *(Sum of C and D)*	21942	22560
F. Copies Not Distributed 1. Office use, left over, unaccounted, spoiled after printing	209	5819
2. Return from News Agents	NONE	NONE
G. TOTAL *(Sum of E, F1 and 2—should equal net press run shown in A)*	22151	28379

11. **I certify that the statements made by me above are correct and complete**

Signature and Title of Editor, Publisher, Business Manager, or Owner
Alma J. Wills Publisher

PS Form 3526, Feb 1989 *(See instructions on reverse)* * Paid subs. mailed by other means

News

Caribbean Cruise—MRI at Sea

Caribbean Cruise—MRI at Sea will be held Jan. 5–12, 1991. The course will include lectures, seminars, and case discussions. It will be presented by Chi-Shing Zee, director of the Diagnostic Imaging Center, Magnetic Resonance Imaging, University of Southern California/Los Angeles County Medical Center. Program director: Ronald J. Friedman. Category 1 credits will be awarded. Fee: $460. Information: Caribbean Cruise, c/o Medical Seminars International, Inc., 18981 Ventura Blvd., Ste. 303, Tarzana, CA 91356; (818) 700-9821.

Physics and Instrumentation

The Division of Diagnostic Ultrasound, Dept. of Radiology, Thomas Jefferson University Hospital, Philadelphia, will present Physics and Instrumentation, Jan. 14–18, 1991. The course is an introduction to physical principles and instrumentation for diagnostic sonography. No previous knowledge of physics is assumed. The focus will be on practical knowledge that will be immediately useful in performing and interpreting sonographic examinations. Hands-on experience with a wide variety of ultrasound instruments will be an integral part of the course. Program coordinator: Peter N. Burns. Category 1 credit: 26 hr. Fee: $675. Information: Judith Kaneff, Education Coordinator, Division of Diagnostic Ultrasound, Thomas Jefferson University Hospital, 7th Floor Main Bldg., Philadelphia, PA 19107; (215) 955-8533.

Cross-Sectional Anatomy

The Division of Diagnostic Ultrasound, Dept. of Radiology, Thomas Jefferson University Hospital, Philadelphia, will present Cross-Sectional Anatomy, Jan. 21–25, 1991. This introductory course is divided between a detailed review of sectional anatomy and correlation of anatomic findings with ultrasound images. Other correlative imaging techniques such as CT and MR will be included as appropriate. Program coordinator: Carol A. Williams. Category 1 credit: 27 hr. Fee: $675. Information: Judith Kaneff, Education Coordinator, Division of Diagnostic Ultrasound, Thomas Jefferson University Hospital, 7th Floor Main Bldg., Philadelphia, PA 19107; (215) 955-8533.

Annual AFIP Neuroradiology Review Course

The Armed Forces Institute of Pathology (AFIP), the American College of Radiology, and the American Registry of Pathology, are sponsoring the 6th annual AFIP Neuroradiology Review Course, Feb. 2–3, 1991, at the Hyatt Regency Bethesda, Bethesda, MD. The purpose of the course is to review basic concepts in neuroradiology, with an emphasis on pathologic correlation and pathophysiology. The course will precede the annual AFIP Neuropathology Course, which will begin Feb. 4 at the same hotel. Course directors: James G. Smirniotopoulos and Frances M. Murphy. Faculty: C. R. Fitz, F. M. Murphy, A. G. Osborn, J. L. Sherman, J. G. Smirniotopoulos, and R. A. Zimmerman. Category 1 credit: 13 hr. Information: Ms. Wendy S. Baker, Course Coordinator, (202) 576-2162 or 576-2973.

Practical Radiology 1991

The Dept. of Radiology, University of British Columbia, is sponsoring its 9th annual postgraduate course, Practical Radiology 1991, Feb. 3–8, 1991, at the Whistler ski resort, which is located approximately 120 km from Vancouver. The course is designed for the practicing radiologist. Faculty: Donald Resnick, Richard Webb, Patrick Freeny, Richard Gore, Jay Heiken, Edward Stewart, David Stephens, and William Thompson. Category 1 credit: 21 hr. Fee (American/Canadian dollars): physicians, $400/$465; residents and fellows, $300/$350. Information: H. Joachim Burhenne, M.D., Professor and Head, Dept. of Radiology, University of British Columbia, 10th Ave. and Heather St., Vancouver, B.C., Canada V5Z 1M9; telephone: (604) 875-4355; fax: (604) 875-4319.

Obstetrics and Gynecology

The Division of Diagnostic Ultrasound, Dept. of Radiology, Thomas Jefferson University Hospital, Philadelphia, is offering Obstetrics and Gynecology, Feb. 4–8, March 11–15, and April 22–26, 1991. The program will cover the full range of ultrasound applications in examination of the fetus and the female pelvis. Approximately two thirds of the course will be devoted to obstetrics and the other third to gynecology. The obstetrics part will include a review of current techniques of fetal measurement, an orderly approach to assessment of fetal growth and well-being, identification of abnormal echo patterns, and establishing a differential diagnosis. The gynecologic part will emphasize recognition of normal anatomy and characterization of gynecologic masses. Hands-on scanning of pregnant patients is not part of the course. Program coordinator: Alfred B. Kurtz. Category 1 credit: 30 hr. Fee $675. Information: Judith Kaneff, Education Coordinator, Division of Diagnostic Ultrasound, Thomas Jefferson University Hospital, 7th Floor Main Bldg., Philadelphia, PA 19107; (215) 955-8533.

Intraluminal Ultrasound Imaging

The Dept. of Radiology, University of California, San Diego, School of Medicine, will present Intraluminal Ultrasound Imaging: Focus on New Developments, Techniques, and Applications, Feb. 6, 1991, at the Le Meridien Hotel, Coronado (San Diego), CA. The course will include lectures on a wide variety of topics, including applications of ultrasound in pediatric cardiology and peripheral vascular disease and techniques and applications of sonographic imaging of the pelvis, abdomen, and renal area. Program directors: Barbara B. Gosink and Sandra L. Hagen-Ansert. Guest faculty: B. B. Goldberg, Phillip Gwinnup, and Natesa Pandian. Category 1 credit: 6.25 hr. Fee: physicians, $150; residents, fellows, nurses, and technologists, $100. Information: Dawne Ryals, Ryals & Associates, P. O. Box 1925, Roswell, GA 30077-1925; telephone: (404) 641-9773; fax: (404) 552-9859.

Duplex Imaging

The Department of Radiology, University of California, San Diego Medical Center, will present Duplex Imaging, Feb. 6–9, 1991, at the Le Meridien Hotel, Coronado (San Diego), CA. The course will be divided into two sections: Basic Introduction to Doppler Principles, Feb. 6, and Duplex Imaging Tutorial Conference and Exhibit, Feb. 7–9. The course is designed to provide practicing physicians, sonographers, and vascular technologists with instruction in the principles and clinical applications of duplex imaging. Imaging of the carotid and subclavian arteries, the upper and lower extremities, and the abdominal vessels will be covered. Program directors: Sandra L. Hagen-Ansert, John R. Forsythe, and Barbara B. Gosink. Guest faculty: Laurence Needleman, Brian Thiele, Washington C. Hill, Cindy Kallman, and Richard E. Rae II. Category 1 credit: Basic Introduction only, 7.25 hr; Conference and Exhibit only, 14 hr; combined course, 21.25 hr. Fee (physicians/residents, fellows, and technologists): Basic Introduction only, $150/$100; Conference and Exhibit only, $420/$295; combined course, $495/$300. Information: Dawne Ryals, Ryals & Associates, P.O. Box 1925, Roswell, GA 30077-1925; telephone: (404) 641-9773; fax: (404) 552-9859.

Obstetric and Gynecology Sonographic Update

The Dept. of Radiology and the Center for Fetal Diagnostic Studies, University of California, San Diego, School of Medicine, will present Obstetric and Gynecology Sonographic Update; Focus on CNS Abnormalities, Feb. 9–10, 1991, at the Le Meridien Hotel, Coronado (San Diego), CA. Didactic and workshop presentations will focus on CNS abnormalities in the fetus; however, other topics will be considered, including Doppler applications in obstetrics, evaluation and management of twin pregnancies, the pathologist's evaluation of the placenta, and infection with human immunodeficiency virus in pregnancy. The endovaginal technique for examination of women early in pregnancy and of postmenopausal patients will be presented. Course directors: Delores Pretorius and Sandra L. Hagen-Ansert. Guest faculty: Washington C. Hill. Category 1 credit: 10 hr. Fee: physicians, $150; residents, fellows, sonographers, and technologists, $100; U. S. Navy personnel, $100 (letter required). Information: Dawne Ryals, Ryals & Associates, P.O. Box 1925, Roswell, GA 30077-1925; telephone: (404) 641-9773; fax: (404) 559-9859.

Current Topics in Diagnostic Imaging

The NYU Medical Center, Post-Graduate Medical School, is offering Current Topics in Diagnostic Imaging, Feb. 11–15, 1991, at the Hyatt Regency Cerromar Beach, Puerto Rico. The program will touch on many of the latest developments in radiology and will review important issues and current approaches in this field. Topics to be covered include CT, sonography, MR imaging, neuroradiology, head and neck imaging, chest radiology, gastrointestinal radiology, uroradiology, bone and joint radiology, and pediatric radiology. Category 1 credit: 23 hr. Fee: $495. Information: NYU Medical Center, Post-Graduate Medical School, 550 First Ave., New York, NY 10016; (212) 340-5295.

Mammographically Detected Early Breast Cancer

The Dept. of Radiology, University of Alabama at Birmingham, will present Mammographically Detected Early Breast Cancer: Current Concepts and Controversies in Diagnostic Management, Feb. 14–17, 1991, at the Ritz-Carlton Resort Hotel, Naples, FL. The course will discuss the pathologic, radiologic, and clinical considerations involved in the diagnosis and management of mammographically detected early breast cancer. Current controversies regarding atypical and in situ lesions will be included. Workshops will be provided on mammographic technique, quality assurance, breast ultrasound, localization, aspiration of cysts, and biopsy procedures. Program directors: Eva Rubin and Wanda K. Bernreuter. Guest faculty: David Page, Ellen Mendelson, J. R. Harris, and Richard Margolese. Information: Dawne Ryals, Ryals & Associates, P.O. Box 1925, Roswell, GA 30077-1925; telephone: (404) 641-9773; fax: (404) 552-9859.

Positron Emission Tomography

The Division of Nuclear Medicine and Biophysics, University of California, Los Angeles, will present Positron Emission Tomography: Fundamentals and Clinical Applications, Feb. 24–27, 1991, at the Dana Point Resort, Dana Point, CA. Topics will include lowering health care costs with positron emission tomography (PET); fundamentals of instrumentation; radioisotope design and production; clinical applications of PET in cardiology, neurology, and oncology; competing techniques; and patterns of reimbursement. The application deadline is Dec. 1, 1990. Fee: physicians, $475; fellows, residents, and technologists, $375. Information: Wendy Hagar, Division of Nuclear Medicine and Biophysics, Dept. of Radiological Sciences, UCLA School of Medicine, 10833 Le Conte Ave., Los Angeles, CA 90024-1721; (213) 825-2724.

Winter Congress on Diagnostic Imaging

The American Institute of Ultrasound in Medicine is sponsoring the 9th Winter Congress, Diagnostic Imaging, March 2–9, 1991, in Val D'Isere, France. Program coordinator: Ronald J. Friedman. Faculty: Michael Bernardino, William Boswell, Neil Chafetz, Ronald Friedman, Dietbert Hahn, Anders Hemmingsson, Faye Laing, Angelo Lurus, Michael Manco-Johnson, Donald Resnick, Rudi Thoeni, Paul van Waes, and Francis Weill. Fee (up to/after Dec. 14, 1990): physicians, $460/$495; residents, interns, technologists, and nurses, $360/$395 (letter required). Information: Winter Congress, Medical Seminars International, Inc., 18981 Ventura Blvd., Ste. 303, Tarzana, CA 91311; (818) 700-9821.

Masters Diagnostic Radiology Conference

The 10th annual Masters Diagnostic Radiology Conference will be held March 3–8, 1991, at the Hyatt Regency Maui Hotel, Maui, HI. The course will emphasize lectures and discussions on chest, skeletal, gastrointestinal, and tropical radiology and on sonography, CT, and MR. Program director: Maurice M. Reeder. Guest faculty: H. Goldberg, Y. Hiramatsu, H. G. Jacobson, G. Leopold, P. E. S. Palmer, M. Reeder, S. Tada, and E. G. Theros. Category 1 credit: 23 hr. Fee: physicians, $545; residents, fellows, and U. S. military personnel, $425. Information: Maurice M. Reeder, M.D., Chairman, Dept. of Radiology, University of Hawaii School of Medicine, 1356 Lusitana St., Honolulu, HI 96813; (808) 531-6471.

Update on Body Imaging and Neuroradiology

The Dept. of Radiology and the Continuing Education Office, State University of New York, Health Science Center at Syracuse, are sponsoring the 10th annual Comprehensive Update: Body Imaging and Neuroradiology, March 4–8, 1991, at the Acapulco Princess Hotel, Acapulco, Mexico. This two-part course is designed to provide an update on state-of-the-art diagnostic imaging. The part on body imaging, March 4–6, will be an overview of current knowledge and concepts of imaging of the abdomen, pelvis, and extremities in children and adults. The advantages and limitations of MR imaging, CT, and sonography in each of these areas will be included. The part on neuroradiology, March 6–8, will be an overview of recent advances in imaging of the brain and spine, with emphasis on newer and improved imaging techniques that maximize the yield of information. The indications and contraindications for MR, CT, and other imaging techniques in evaluation of the CNS and the advantages and limitations of these techniques will be discussed. Category 1 credit: 21 hr. Program directors: E. Mark Levinsohn and Edwin D. Cacayorin. Fee: body imaging only, $300; neuroradiology only, $300; both courses, $575. Information: Office of Continuing Education, SUNY Health Science Center at Syracuse, 750 E. Adams St., Syracuse, NY 13210; (315) 464-4606 or (800) 283-4606.

Pediatric Radiology Course

The Dept. of Radiology, Children's Hospital Medical Center, Cincinnati, will present Magnetic Resonance Imaging, Color Flow Doppler Ultrasound, and Other Special Imaging Techniques in the Pediatric Patient, March 11–15, 1991, at the Resort Center Lodge and Inn, Park City, UT. Information: Cathy Laine, International Meeting Managers, Inc., 4550 Post Oak Pl., Ste. 248, Houston, TX 77027; telephone: (713) 965-0566; fax: (713) 960-0488.

Breast Imaging Conference

The Orlando Regional Medical Center and Medical Center Radiology Group are sponsoring the 1st Annual Breast Imaging Conference, March 21–24, 1991, at the Buena Vista Palace, Walt Disney World Village, Lake Buena Vista, FL. Program director: Anne K. Claiborne. Guest faculty: D. B. Kopans, S. A. Feig, N. L. Sadowsky, and V. Jackson. Category 1 credit: 16 hr. Fee: physicians, $325; residents, $225. Information: Patti L. Devlin, Orlando Regional Medical Center, Continuing Medical Education, 1414 Kuhl Ave., Orlando, FL 32806-2093; (800) 648-0450.

San Diego Residents' Radiology Review Course

The Dept. of Radiology, University of California, San Diego, School of Medicine, will present the 11th annual San Diego Residents' Radiology Review Course, April 21–26, 1991, at the Hyatt Regency Hotel, La Jolla, CA. The course is designed for senior radiology residents and practicing radiologists who desire a comprehensive review of the entire field of diagnostic radiology. It will cover all major techniques: plain films and routine radiographic procedures, angiography, neuroradiology, nuclear medicine, sonography, CT, MR imaging, and interventional radiology. Program directors: Folke J. Brahme and Saskia v.W. Hilton. Category 1 credit: 39 hr. Fee: $435. Information: Dawne Ryals, Ryals & Associates, P.O. Box 1925, Roswell, GA 30077-1925; telephone: (404) 641-9773; fax: (404) 552-9859.

Introduction to Interventional Radiology

The Dept. of Radiology, University of California, San Diego, School of Medicine, will present Introduction to Interventional Radiology, April 27, 1991, at the Hyatt Regency Hotel, La Jolla, CA. Program director: Eric vanSonnenberg. Category credit: 8.25 hr. Fee: $100. Information: Dawne Ryals, Ryals & Associates, P.O. Box 1925, Roswell, GA 30077-1925; telephone: (404) 641-9773; fax: (404) 552-9859.

Leeds Gastroenterology Course for Radiologists

The Leeds Gastroenterology Course for Radiologists will be held July 1–5, 1991, at St. James's University Hospital, Leeds, England. Fee: £260. Applications and information: Miss Pat Kentley, Level 7, Worsley Medical Bldg., University of Leeds, Leeds LS2 9JT, England.

Radiology Outreach Foundation News

The Radiology Outreach Foundation (ROF) is a nonprofit corporation whose goal is to help improve health care in disadvantaged countries by providing radiology equipment, books, consultation, education, and training to physicians in these countries. This assistance is on an application basis and is independent of political, ethnic, or religious orientation of the grantee. It depends solely on the need of the people and the ability of the ROF to meet that need.

Since its inception in 1988, the ROF has accomplished a number of philanthropic activities worldwide. A total of 2500 textbooks, with an estimated value of more than $125,000, were sent to 67 institutions in 40 countries. Complimentary subscriptions to scientific journals were sent to 15 countries. Radiographic film and processing chemicals were sent to an impoverished hospital in Africa and donated angiographic contrast media to a university medical center in an Eastern European country. One hundred seventy-five new radiographic cassettes with a retail value of $60,000 were donated and were sent to 10 different institutions. Two Eastern European academic radiologists were brought to the United States for postgraduate training, and the ROF subsidized the costs of their attendance at the annual meeting of the Radiological Society of North America. ROF sponsorship has been provided for an American radiologist to teach at Kenyatta Medical School in Nairobi, Kenya, a center that has trainees from several adjacent African countries. The ROF also is sponsoring American radiologists to teach at the medical school in Kathmandu, Nepal. A lending library was established in India with books donated by the ROF. The foundation also participated in funding the mission of 15 radiologists and technologists to 15 cities in India for the development of an on-site mammography training program. A training program is being initiated in American universities for radiology residents from Latin America. Trainees from a Pacific Rim country are now receiving part of their training at the Karolinska Hospital in Stockholm. Several other projects are in the negotiation and development phases.

The ROF has been chosen by the International Medical Scholars

Program, a subsidiary of the Educational Commission for Foreign Medical Graduates, to be an advisory board on the selection of trainees from foreign countries for receipt of federally funded assistance. This program is designed to provide training in the United States for foreign physicians who will return to their native country with improved skills. The ROF also has been selected by Project HOPE to be the advisory agency in the design, equipping, and staffing of the radiology department of a new 250-bed children's hospital to be established in Shanghai, China.

Subsidization of the ROF has been achieved by donations from individuals, foundations, universities, and industry. All donations are tax deductible. If you would like to contribute financially to the ROF, if you are interested in being a visiting professor, or if you would like to send books or journals to any of the institutions supported by the ROF, please write to Charles A. Gooding, M.D., President, Radiology Outreach Foundation, 3415 Sacramento St., San Francisco, CA 94118 U. S. A.

The American Board of Radiology Examinations

Written examinations for the American Board of Radiology (ABR) are scheduled for Oct. 3–4, 1991. Oral examinations will be held at the Executive West Hotel in Louisville, KY, June 3–7, 1991. The ABR will accept applications for admission to the examinations after July 1, but not later than Sept. 30, in the year *preceding* the year in which the examination is to be taken. For application forms and further information: Office of the Secretary, The American Board of Radiology, 300 Park, Ste. 440, Birmingham, MI 48009.

Meeting and Course Review

For the reader's convenience, a summary of upcoming meetings and courses is provided. Detailed listings are given in the *AJR* issue given in parentheses.

Cyanoacrylate Embolization Course, times arranged, Baltimore (July)
Visiting Fellowships in Ultrasound, times arranged, Baltimore (Aug)
Visiting Fellowships in Interventional Radiology, times arranged, Baltimore (Oct)
Courses in MR Imaging at Emory University: course for physicians, Dec. 3–7, Atlanta (June)
MRI for Radiologic Technologists, Dec. 7–8, Houston (July)
Advanced Seminars in Diagnostic Imaging, Dec. 7–9, Laguna Niguel, CA (Sept)
MRI Fellowships at Johns Hopkins, Dec. 10–14, 1990; Jan 7–11, 1991; April 8–12, 1991; and June 17–21, 1991, Baltimore (Oct)
MR Imaging Update, Dec. 13–15, New York City (Aug)
CT/MRI Head to Toe, Dec. 17–22, New York City (Nov)
Future and Present MRI, Jan. 9–13, 1991, Naples, FL (Aug)
Caribbean Cruise—Breast Imaging at Sea, Jan. 12–19, 1991 (Nov)
Advanced Seminars in Diagnostic Imaging, Jan. 19–21, 1991, Laguna Niguel, CA (Aug)
Seminars in MRI, Jan. 19–26, 1991, Vail, CO (Nov)
Park City 1991: MRI Update, Jan. 20–24, 1991, Park City, UT (Oct)
Diagnostic Imaging in Aruba, Jan. 20–26, 1991, Aruba (Aug)
International Symposium on MR Imaging, Jan. 23–27, 1991, Garmisch-Partenkirchen, Bavaria (Aug)
Society for Pediatric Radiology Research and Education Grants, application deadline, Feb. 1, 1991 (Sept)
Midwinter Radiological Conference, Feb. 1–3, 1991, Los Angeles (Nov)
Practical Aspects of Diagnostic Radiology/Medical Imaging IV, Feb. 2–8, 1991, Snowmass Village, CO (Nov)
Big Sky Radiology Conference, Feb. 3–7, 1991, Big Sky, MT (Nov)
Angio-Interventional Radiology, Feb. 4–5, 1991, Coronado (San Diego), CA (Oct)
Mid-Pacific Radiological Conference, Feb. 5–9, 1991, Maui, HI (Nov)
Computed Body Tomography 1991—The Cutting Edge, Feb. 7–10, 1991, Orlando, FL (Nov)
Annual Intermountain Imaging Conference, Feb. 9–16, 1991, Steamboat Springs, CO (Nov)
Contemporary Diagnostic Imaging, Feb. 11–15, 1991, Mauna Lani, HI (Oct)
Society of Gastrointestinal Radiologists Annual Meeting and Postgraduate Course, Feb. 17–21, 1991, Carlsbad, CA (Oct)
Imaging the Head, Spine, and Musculoskeletal System, Feb. 17–22, 1991, Kauai, HI (Oct)
MR Imaging Course at Disney World, Feb. 17–22, 1991, Orlando, FL (Oct)
Sun Valley Imaging Meeting, Feb. 23–March 2, 1991, Sun Valley, ID (Nov)
Principles and Practice of Clinical MRI, Feb. 28–March 3, 1991, Lake Buena Vista, FL (Nov)
Advanced Seminars in Diagnostic Imaging, March 1–3, 1991, Laguna Niguel, CA (Nov)
Practicum in Diagnostic Ultrasound, March 4–8, 1991, and April 22–26, 1991, Baltimore (Oct)
Course on MR Imaging, March 4–8, 1991, Coronado (San Diego), CA (Nov)
Musculoskeletal Imaging, March 4–8, 1991, Barbados (Nov)
Orthopedic Radiology 1991, March 25–27, 1991, Boston (Nov)
Ultrasound 1991, April 2–5, 1991, Boston (Nov)
National Council on Radiation Protection and Measurements Annual Meeting, April 3–4, 1991, Washington, DC (Nov)
Society for Magnetic Resonance Imaging Annual Meeting, April 13–17, 1991 (Nov)
Clinical Nuclear Medicine 1991, April 22–25, 1991, Boston (Nov)
International Pediatric Radiology '91, May 27–31, 1991, Stockholm (Aug)
International Congress of Radiation Research, July 7–12, 1991, Toronto. Deadline for abstracts, Jan. 15, 1991 (May)
World Congress in Ultrasound, Sept. 1–6, 1991, Copenhagen (Sept)
European Congress of Radiology 1991, Sept. 15–20, 1991, Vienna, Austria (Oct)

AJR carries announcements of courses, symposia, and meetings of interest to its readers if received a minimum of 5 months before the event. There is no charge; receipt of items by the *AJR* Editorial Office is not acknowledged. Submit items for publication typed double-spaced. Provide title, date, location, brief description, sponsor, course directors, fees, category I credit, and address and telephone number for additional information. Faculty from the host institution will not be listed. Guest faculty names will appear **only** if initials are provided. Mail news items to *AJR* Editorial Office, 2223 Avenida de la Playa, Suite 103, La Jolla, CA 92037-3218.

American Roentgen Ray Society:

Officers, Committees, and Membership Information

Officers

President: M. Paul Capp
President-elect: John A. Kirkpatrick, Jr.
1st Vice-president: A. Everette James, Jr.
2nd Vice-president: Andrew K. Poznanski
Secretary: Joseph T. Ferrucci, Jr.
Treasurer: Beverly P. Wood

Executive Council: R. J. Alfidi, R. N. Berk, M. P. Capp, W. J. Casarella, N. R. Dunnick, R. G. Evens, J. T. Ferrucci, Jr., A. E. James, Jr., J. A. Kirkpatrick, Jr., A. M. Landry, Jr., J. E. Madewell, A. A. Moss, A. K. Poznanski, L. F. Rogers, R. J. Stanley, J. H. Thrall, K. H. Vydareny, N. O. Whitley, B. P. Wood, G. R. Leopold, chairman

Committees

Editorial Policy: R. N. Berk, E. Buonocore, Melvin M. Figley, S. v. W. Hilton, M. S. Huckman, C. A. Rohrmann, Jr., R. J. Stanley, R. I. White, W. J. Casarella, chairman

Education and Research: C. B. Higgins, B. J. Hillman, R. A. McLeod, R. J. Stanley, W. M. Thompson, N. O. Whitley, chairman

Finance and Budget: R. J. Alfidi, R. K. Gedgaudas-McClees, J. R. Thornbury, K. H. Vydareny, J. H. Thrall, chairman

Nominating: G. A. W. Gooding, L. F. Rogers, K. H. Vydareny, chairman

Publications: E. Buonocore, C. A. Rohrmann, Jr., R. J. Stanley, R. I. White, W. J. Casarella, chairman

Membership: J. E. Madewell, A. A. Moss, K. H. Vydareny, R. J. Alfidi, chairman

Representatives to Other Organizations

American Board of Radiology: J. A. Kirkpatrick, Jr., E. C. Klatte, L. F. Rogers

American College of Radiology: J. M. Dennis, R. A. Gagliardi, J. E. Madewell, B. L. McClennan, R. J. Stanley

American Medical Association: S. F. Ochsner, delegate; K. L. Krabbenhoft, alternate; K. L. Kidd, CPT Advisory Committee

American National Standards Institute: M. E. Haskin

National Council on Radiation Protection and Measurements: F. Miraldi, E. L. Saenger

Armed Forces Institute of Pathology: J. E. Madewell

Meeting Arrangements

Annual Meetings: May 5–10, 1991, Sheraton Boston, Boston; May 10–15, 1992, Marriott's World Center, Orlando, FL

Annual Meeting Committee: H. C. Carlson, J. K. Crowe, N. R. Dunnick, R. R. Lukin, R. J. Stanley, R. D. Steele, Jr., A. M. Landry, Jr., chairman

Instructional Courses: R. J. Stanley, chairman

Scientific Program: P. Arger, E. Buonocore, D. O. Davis, K. B. Hunter, D. Kushner, T. C. McLoud, W. A. Murphy, Jr., L. B. Talner, J. H. Thrall, J. A. Kirkpatrick, Jr., chairman

Scientific Exhibits: J. R. Haaga, R. G. Ramsey, N. R. Dunnick, chairman

ARRS Membership

An application form is printed in the September issue of the Journal. For consideration at the 1991 ARRS meeting, send completed forms before February 1, 1991, to American Roentgen Ray Society, 1891 Preston White Dr., Reston, VA 22091. Active members are graduates of an approved medical or osteopathic school or hold an advanced degree in an allied science. They must practice radiology or work in an associated science in the United States or Canada and be certified by the American Board of Radiology, American Osteopathic Board of Radiology, or Royal College of Physicians of Canada or otherwise adequately document training and credentials. Corresponding members are foreign radiologists or scientists who are active in radiology or an allied science. Members-in-training are residents or fellows in radiology or postgraduate students in an allied science. Additional application forms can be obtained from the ARRS offices in Reston, VA.

Business Office

Paul Fullagar, Executive Director, American Roentgen Ray Society, 1891 Preston White Dr., Reston, VA 22091; (703) 648-8992.

Classified Advertisements

Positions Available

THE UNIVERSITY OF TEXAS HEALTH SCIENCE CENTER AT SAN ANTONIO announces formation of a Research Imaging Center. This center is designed to use modern imaging methods in evaluating pharmaceutical therapies in both animal and human models. Thirteen new positions are available in 1990/1991 and an equal number are anticipated the following yr. Applications are invited for the following faculty or administrative positions: Director of PET Facility—An M.D.- or Ph.D.-level scientist to provide overall direction of the PET facility operation, supervise personnel, and conduct an independent research program. Appointment at the assistant or associate professor level will depend on experience. Radiochemist—A Ph.D.-level scientist to direct operation of the cyclotron and radiochemistry hot lab in support of the PET operations and conduct an independent research program. Appointment at the assistant or associate professor level will depend on experience. Associate Radiochemist/Physicist—A Ph.D.-level scientist to be responsible for the operation of the cyclotron and related radiochemistry developments. Appointment as assistant professor or lecturer will depend on experience. Radiopharmacist—A Master's (or Ph.D.) level radiopharmacist who is licensed and certified to prepare, test, and certify radiopharmaceuticals for human use. The appointment will be at the assistant professor level. NMR Physicist or Chemist—A Master's (or Ph.D.) level scientist with a minimum of 2 yr experience operating and assisting others in the use of a 2-T (45-cm bore) MRI/MRS unit. The appointment will be at the level of lecturer. NMR Chemist or Biologist—A Master's (or Ph.D.) level scientist to operate high resolution NMR spectrometers and assist others in using these instruments. The appointment will be at the level of lecturer. All of the above faculty will have the opportunity to participate in both medical and graduate school (radiological sciences) educational programs with appointments depending on the interests and experience of the successful candidates. The University of Texas Health Science Center at San Antonio is an equal opportunity employer. Send cover letter/CV to Gary D. Fullerton, Ph.D., Dept. of Radiology, UTHSCSA, 7703 Floyd Curl Dr., San Antonio, TX 78284-7800. 12–2ap

RADIOLOGY/NUCLEAR MEDICINE—Group seeks third, full-time, BC/BE radiologist for all new multidiscipline imaging center with state-of-the-art equipment. Experience in nuclear medicine/SPECT desirable, but not necessary. All modalities except MRI. Located in large medical complex of physicians serving suburban area. Prefer individual with 5 yr demonstrated experience. Contact Marc B. d'Avignon, M.D., Westwood Imaging Center, 40 Dale Rd., Avon, CT 06001; (203) 677-1500. 12ap

STAFF PHYSICIAN/RADIOLOGY—Vacancies exist for 2 diagnostic radiologists, board-certified or in examining process, with experience in CT, ultrasound, and invasive diagnostic procedures. Hospital located in northeastern Tennessee near ski slopes and Appalachian Trail in Smoky Mountains. Great area for outdoor activities including hiking, golf, tennis, and all water sports. Affiliated with Quillen College of Medicine in Johnson City, TN. Direct inquiries to Harold Ross, M.D., Chief, Radiology Service, VA Medical Center, Mountain Home, TN 37684; (615) 926-1171 ext. 7401. An equal opportunity employer. 12–1a

RADIOLOGIST—A second radiologist is needed for a 54-physician, multi-specialty group located in western Montana. Experience or formal training in mammography a must; general radiologic procedures excluding CT and MRI. Offered salary and benefits generous. Send CV to Administrator, Western Montana Clinic, P.O. Box 7609, Missoula, MT 59807. 12–1ap

GENERAL DIAGNOSTIC RADIOLOGIST—Position available to join 11-member, private-practice group in 500-bed, university-affiliated, tertiary-care hospital in Allentown, PA. The position offers a competitive salary benefit package commensurate with training leading to full partnership. The Radiology Dept. offers a fellowship in CT, ultrasound, and angiography/interventional. The hospital has active residency programs in medicine and surgery. Allentown is located in the Lehigh Valley (population 250,000) and is 2 hr from New York City, 1 hr from Philadelphia, and 1 hr from the Pocono Mountains. For information, please contact Robert Kricun, M.D., or Alan Wolson, M.D., Lehigh Valley Hospital Center, 1200 S. Cedar Crest Blvd., P.O. Box 689, Allentown, PA 18105; (215) 776-8088. 12–2ap

ULTRASOUND RADIOLOGIST—The Dept. of Radiology at the University of Arkansas for Medical Sciences is inviting applications for a faculty radiologist at the instructor or assistant professor level to do primarily ultrasound. The position would require someone with a reasonable amount of ultrasound experience. Also included would be participation in CT and nonvascular interventional procedures. The UAMS is the only medical school and teaching hospital in the state of Arkansas. There are approximately 1150 beds in our institution, which includes the University Hospital, an adjacent VA Hospital, and a large Children's Hospital. For further information or to apply, please contact Steven K. Teplick, M.D., Vice-Chairman, Dept. of Radiology; (501) 686-6902. The University of Arkansas is an equal opportunity employer. 12–1ap

PEDIATRIC RADIOLOGIST—The Nemours Children's Clinic and the University of Florida are seeking a board-certified/eligible individual to join the expanding program in Jacksonville, FL, as chairman of the Dept. of Radiology. The Nemours Children's Clinic is a multidisciplinary, pediatric medical and surgical specialty clinic. The clinic is located in a beautiful new 11-story building with state-of-the-art technology on the cutting edge of pediatric health care. The radiology program is a rapidly expanding service providing community-wide service for a city of 800,000 with a large referral base in south Georgia and northeast Florida. The candidate will be offered university appointment as an associate professor and chief, or professor and chief. Teaching and research are strongly encouraged and funds are available for establishment and maintenance of quality research programs. Salary will be commensurate with experience. Interested applicants should send their CV to Ian T. Nathanson, M.D., Chairman, Search Committee, Nemours Children's Clinic, 807 Nira St., Jacksonville, FL 32207; (904) 390-3600. Academic status is offered by the University of Florida, an equal opportunity/affirmative action employer with whom Nemours is affiliated. Recruiting deadline is Jan. 15, 1991. 12a

NUCLEAR MEDICINE OR INTERVENTIONAL RADIOLOGIST—Progressive, 7-person group seeks to add an interventional radiology or nuclear medicine (special competency preferred) fellowship-trained radiologist for spring 1991. This busy, expanding practice is hospital- and recently full-service imaging center-based. Both institutions use leading edge technology. The proximity of Lake Tahoe, the gaming industry, the state capitol, and a major university provides many cultural, entertainment, and sporting opportunities. Send CV to Colby Laughlin, M.D., Reno Diagnostic Center, 590 Eureka Ave., Reno, NV 89512. 12–3a

DIAGNOSTIC RADIOLOGIST—Excellent opportunity for BC/BE radiologist to join established group of 4 in July 1991 providing all services for 380-bed hospital. Rewarding practice in university city of 200,000. Send CV and letter to N. Thomas Rice, M.D., Central Baptist Hospital, 1740 S. Limestone St., Lexington, KY 40503. 12–2ap

PHILADELPHIA, PA—Temple University Hospital and School of Medicine seeks the following board-certified radiologists: Vascular/Interventional Radiologists (2)—Section Head and staff positions available. Positions involve responsibilities in patient care and teaching. Candidates with fellowship training and research skills preferred. Abdominal imaging radiologist—Strong clinical skills in ultrasound, CT, MRI, urography, and gastrointestinal radiology. Fellowship training is preferred. An interest in medical student and radiology resident teaching is required. Interest in abdominal imaging research desirable. Pulmonary radiologist—Candidate should be a senior-level radiologist at the professor or associate professor level with a primary interest in pulmonary radiology. Ideal candidate will have fellowship training in pulmonary radiology and proficiency in all areas of radiologic practice. Candidates should have demonstrated skills as a teacher and an interest in research. Applicants should send current CV (indicate position of interest), bibliography, and 3 letters of recommendation to Temple University School of Medicine, Attn: Francis J. Shea, M.D., Deputy Chairman, Dept. of Diagnostic Imaging, Broad and Ontario Sts., Philadelphia, PA 19140. An equal opportunity/affirmative action employer. 12xa

DIAGNOSTIC RADIOLOGIST—Excellent opportunity in well-established, South Carolina hospital-based practice for BC/BE radiologist. Competitive salary. Full partnership in 1 yr. Send CV to Box H87, *AJR* (see address this section). 12–3ap

NEURORADIOLOGY—Position open at the University of Utah, Dept. of Radiology, for a neuroradiologist at the assistant or associate professor level. Job responsibilities would include acting as Clinical Director of the MR Center and would prefer expertise in MRA. Interested applicants please forward CV to H. Ric Harnsberger, M.D., Associate Professor of Radiology, Chief of ENT/Neuroradiology, University of Utah School of Medicine, 50 N. Medical Dr., Salt Lake City, UT 84132. The University of Utah is an equal opportunity employer. Applications must be received by the closing date of Jan. 31, 1991, or until a qualified candidate is identified. 12a

CHICAGO AREA—Opening for full- or part-time radiologist to join progressive, 8-member group in a large, community hospital in Harvey, IL (southern suburb of Chicago), beginning July 1991. State-of-the-art equipment in CT, ultrasound, nuclear medicine, angiography, MRI, and diagnostic radiology is available. Approximately 120,000 exams/yr. We are looking for a well-trained, flexible radiologist interested in both general radiology and all facets of imaging. Nuclear cardiology and mammography experience is preferred. Interested parties should contact Jay Bronner, M.D., or Peter Kucharski, M.D., Ingalls Hospital, Harvey, IL 60426; (708) 333-2300, ext. 5600. 12–1ap

CHIEF, RADIOLOGY DEPT.—The VA Medical Center in Louisville, a major affiliate of the University of Louisville, School of Medicine, is seeking applications for the Chief of Diagnostic Radiology. The radiology dept. is equipped with state-of-the-art equipment, which is the result of a recent $13 million clinical and educational addition. The dept. includes facilities for digital vascular imaging, CT, ultrasound, and all noncardiac nuclear medicine imaging. The radiology dept. is now staffed by a group of 6 physicians and performs approximately 50,000 exams/yr. Qualifications include board certification in diagnostic radiology and eligibility for an academic appointment at the University of Louisville School of Medicine. Please send inquiries to Hollis A. Thomas, M.D., Professor and Chairman, Dept. of Diagnostic Radiology, Humana Hospital-University of Louisville, 530 S. Jackson St., Louisville, KY 40202. An equal opportunity/affirmative action employer. 12–1ap

NEURORADIOLOGIST—The Dept. of Radiology at the University of Arkansas for Medical Sciences is inviting applications for a faculty radiologist at the assistant or associate professor level to perform neuroradiology. Excellent opportunity for academic growth. The UAMS is the only medical school in the state of Arkansas. There are approximately 1150 beds in our institution, which includes the University Hospital, an adjacent VA Hospital, and a large Children's Hospital. For further information or to apply, please contact Edgardo Angtuaco, M.D., Dept. of Radiology, (501) 686-6033. The University of Arkansas is an equal opportunity employer. 12a

MUSCULOSKELETAL RADIOLOGIST—The Dept. of Radiology at the University of Arkansas for Medical Sciences is inviting applications for a faculty radiologist at the assistant professor level. Excellent opportunity for academic growth. The UAMS is the only medical school in the state of Arkansas. There are approximately 1150 beds in our institution, which includes the University Hospital, an adjacent VA Hospital, and a large Children's Hospital. For further information or to apply, please contact Steve K. Teplick, M.D., Vice-Chairman, Dept. of Radiology; (501) 686-6902. The University of Arkansas is an equal opportunity employer. 12a

IMMEDIATE OPENING FOR BOARD-CERTIFIED/ELIGIBLE DIAGNOSTIC RADIOLOGIST with experience in CT, ultrasound, nuclear medicine, mammography, MRI, and basic angiography. Hospital-based practice joining a 4-person group located in the city of Houston. Salary competitive. Please write with CV to Gerald A. Jaffe, M.D., 5718 Grape, Houston, TX 77096; (713) 772-4714 (home) or (713) 675-3241 (work). 12ap

SECTION CHIEF, ABDOMINAL IMAGING—The University of Nebraska Medical Center, Dept. of Radiology, is recruiting a radiologist to head a section of 2 other GI radiologists. Responsibilities include traditional GI barium studies, abdominal CT, abdominal MRI, and biliary lithotripsy. The medical center specializes in tertiary care with emphasis on biliary disease and organ transplantation. The University of Nebraska Medical Center, Dept. of Radiology, currently has 22 faculty members and a very well-equipped dept. This is an academic position requiring strong interest in clinical teaching and research as well as patient care. Academic rank is commensurate with qualifications. Please send inquiries with a CV by Dec. 31, 1990, to Thomas J. Imray, M.D., Professor and Chairman, Dept. of Radiology, University of Nebraska Medical Center, 600 S. 42nd St., Omaha, NE 68198-1045. The University of Nebraska Medical Center is an equal opportunity/affirmative action employer M/F/H/V. 12a

PEDIATRIC RADIOLOGIST AND PEDIATRIC NEURORADIOLOGIST—Childrens Hospital Los Angeles, Dept. of Radiologic Imaging, has openings for faculty positions at the assistant professor level for persons who have completed appropriate fellowship training and ABR examination and desire an exciting opportunity in a strong academic setting. Varied clinical work, basic and clinical research, and teaching are an integral part of the program. The 331-bed pediatric hospital provides primary, secondary, and tertiary care and unique clinical programs to a large population with state-of-the-art equipment for ultrasound, CT, digital angiography, MR, and nuclear radiology. Opportunities for collaborative and individual projects are excellent. Childrens Hospital Los Angeles is the pediatric program of the University of Southern California. Childrens Hospital Los Angeles is an equal opportunity/affirmative action employer. Address inquiry and CV to Beverly P. Wood, M.D., Chief of Radiology, Dept. of Radiology, Childrens Hospital Los Angeles, 4650 Sunset Blvd., Los Angeles, CA 90027. 12ap

RADIOLOGIST WITH MRI, ULTRASOUND EXPERTISE for 3-person group near San Francisco. Office practice includes general radiology, ultrasound, mammography, and MRI. Stanford Hospital practice includes general radiology and resident teaching. Excellent salary leading to partnership. Wonderful area to live. Contact Dr. Reveno, Ste. C-3, 1101 Welch Rd., Palo Alto, CA 94304; (415) 323-1343. 12ap

NUCLEAR MEDICINE/NEURORADIOLOGIST—Expanding, 7-member diagnostic radiology group in Denver, CO, seeks 2 board-certified radiologists. Individuals must have fellowship training. We are soliciting an individual in nuclear medicine as well as neuroradiology. Group covers 3 hospitals offering all radiologic services including MRI, 2 private offices, and a successful free-standing MRI facility. Position leads to equal partnership. Send CV to Mitchell Achee, M.D., 1633 Fillmore, Ste. 2, Denver, CO 80206; (303) 388-4124. 12ap

NEURORADIOLOGIST with fellowship training in MR to join 7-member group in community practice. Candidate should be board-certified. Facilities include 2 community hospitals and several outpatient facilities, 2 MRI, 3 CT; installing new angio suite. Rapidly growing coastal community in southwest Florida with attractive cultural and recreational amenities. Generous salaried position leading to partnership. Reply to Box H83, *AJR* (see address this section). 12–1ap

INTERVENTIONAL RADIOLOGIST to join 7-member group in community practice. Candidate should be board-certified. Recent fellowship training preferred. Facilities include 2 community hospitals and several outpatient facilities. Installing new special procedure suite. Rapidly growing coastal community in southwest Florida with attractive cultural and recreational amenities. Generous salaried position leading to partnership. Reply Box H85, *AJR* (see address this section). 12–1ap

CHIEF RADIOLOGIST AND RADIOLOGISTS—In anticipation of the opening of our clinical addition, we are actively seeking BC radiologists for chief and staff positions. Facilities include fluoroscopy, tomography, diagnostic ultrasound, general radiology, CT, and angiography. Joint faculty appointment with our major affiliate, the Marshall University School of Medicine, dependent on candidate's clinical and academic experience. Our medical center is currently expanding to 250 beds and doubling facility size with a clinical addition. Radiology service will be located in new state-of-the-art facilities in the addition. Work with a rotating staff of radiologists, a chief technician, a permanent technical staff, and transitional residents in radiology. For more information on these challenging opportunities, please call or send your CV to Ms. R. Bookwalter, Office of the Chief of Staff, VA Medical Center, 1540 Spring Valley Dr., Huntington, WV 25704; (304) 429-6755, ext. 2517. 12–2a

IMMEDIATE OPENING—Radiologist needed to join 1 other in a 60-bed, hospital-based practice with GE 1.5-T MRI, 9800 CT, Doppler ultrasound, SPECT, nuclear, and biplane angio. Excellent salary leading to early partnership. Unique opportunity to join a sophisticated practice while living among the redwoods in a northern California coastal city with a referral population of over 100,000. Send CV to Dr. Jackson, 3560 N. St., Eureka, CA 95501; (707) 445-5993. 12–2ap

DIAGNOSTIC RADIOLOGIST—Eight board-certified radiologists in expanding, hospital-based private practice seek BC/BE general radiologist to associate. Competence in all modalities expected with need for MRI training emphasized for 2 MRI facilities in practice. Opportunity in midwestern city of 72,000 people offers generous compensation/vacation. Full partnership after 2 yr. Reply to Box H89, *AJR* (see address this section). 12–3ap

WEST RIVER REGIONAL MEDICAL CENTER of Hettinger, ND, is seeking a board-certified or eligible radiologist to join a progressive and innovative health-care team using state-of-the-art technology in a rural/frontier setting. General radiology including in-house mammography, ultrasound, nuclear medicine, echocardiography with color Doppler, and CT. MRI available. Unique medical staff (awarded 1982 Outstanding Rural Health Project Award) and 2 staff physicians (awarded North Dakota Physician of the Year). World-class upland game hunting, including pheasant, grouse, partridge, deer, and antelope. Superb fishing for walleye, trout, and salmon. Send CV and letter of inquiry to Bryon J. Dockter, President and CEO, West River Regional Medical Center, Rte. 2, Box 124, Hettinger, ND 58639; (701) 567-4561. 12–1ap

DIAGNOSTIC RADIOLOGIST needed in Conway Hospital, a community hospital located 10 mi. west of the resort/seaside community of Myrtle Beach, SC. The dept. performs 44,000 exams/yr including CT, MRI, nuclear medicine, ultrasound, mammography, and special procedures. All exams are done on state-of-the-art equipment. Our 3-person group offers a very strong financial package with all benefits including 17-wk vacation. Lovely, rapidly growing resort area includes 60 mi. of sandy beaches, 70 golf courses, and beautiful seaside homes. Contact Gary Rike, M.D., P.O. Box 917, Conway, SC 29526; (803) 347-7277. 12–5ap

PART-TIME MAMMOGRAPHY/ULTRASOUND RADIOLOGIST—Immediate opening for a half-time diagnostic radiologist with a 12-member group in a Pacific Northwest city of 60,000+. BC/BE with expertise/interest in mammography and ultrasound. Equipment is state-of-the-art. Competitive salary and benefits. Located amidst the recreational activities of the Puget Sound and Cascade Mountains. Send letter, personal sketch, and CV to J. W. Little, M.D., 3822 Colby Ave., Everett, WA 98201; (206) 259-3256. 12–2ap

THE DEPT. OF RADIOLOGY AT THE ALBERT EINSTEIN COLLEGE OF MEDICINE AND WEILER HOSPITAL are seeking a BC/BE, fellowship-trained radiologist in MR imaging with a special interest in body and musculoskeletal MRI. The position requires strong leadership skills in clinical and academic radiology. Competitive salary; excellent benefits. For additional information, contact Robert Bernstein, M.D., Director of Radiology, Weiler Hospital of the Albert Einstein College of Medicine, 1825 Eastchester Rd., Bronx, NY 10461; (212) 904-2965. 12ap

PEDIATRIC RADIOLOGIST—The Massachusetts General Hospital, Dept. of Radiology, is recruiting a staff radiologist to join the Division of Pediatric Radiology. Qualifications include board-eligibility/certification in radiology and completion of at least 1 yr pediatric radiology fellowship. Responsibilities include clinical teaching and research activities. The applicant must be versed in the imaging of children including CT, MRI, ultrasound, fluoroscopy, and plain film interpretation. Send a current CV and letter of inquiry to Robert H. Cleveland, M.D., Director, Division of Pediatric Radiology, Massachusetts General Hospital, Boston, MA 02114. The Massachusetts General Hospital is an equal opportunity employer. 12ap

DIAGNOSTIC RADIOLOGIST, SAN FRANCISCO BAY AREA—The Permanente Medical Group is seeking a progressive BC/BE diagnostic radiologist with special competency in MRI and cross-sectional imaging to join 5 other BC radiologists serving a 200-bed, acute-care hospital and outpatient clinic. This quality practice, located in a desirable suburban setting, offers all imaging modalities. Competitive salary and generous benefits. Send CV to Martin Portnoff, M.D., Kaiser Permanente Center, 200 Muir Rd., Martinez, CA 94553; (415) 372-1110. EOE. 12–2a

STAFF INTERVENTIONAL RADIOLOGIST SOUGHT at the New York Hospital-Cornell University Medical Center for July 1991. The position includes clinical and teaching responsibilities as well as the opportunity for research. Equipment includes 3 state-of-the-art Philips digital labs and a 4-bed recovery room. Applicants should be trained in all aspects of peripheral vascular and nonvascular interventions. For further information, please contact Thomas A. Sos, M.D.; (212) 746-2600. 12–1a

RADIOLOGIST, board-certified in radiology and nuclear medicine, will be responsible for the Nuclear Medicine Section of radiology. Will also have some responsibilities in diagnostic radiology. The VAMC Radiology Service is an active participant in the Medical University of South Carolina (MUSC) Radiology/Nuclear Medicine Residency Training Program. The position will also carry a faculty appointment with MUSC. Salary commensurate with qualifications and experience. For additional information, contact Philip N. Freedland, M.D., Chief, Radiology Service; (803) 577-5011, ext. 7332 or FTS 236-7332. 12a

VASCULAR/INTERVENTIONAL RADIOLOGIST The University of Texas Southwestern Medical School, Dept. of Radiology, is seeking BC/BE vascular/interventional radiologists at the rank of assistant/associate professor who have had a CVI fellowship or extensive experience in the subspecialty. Responsibilities will include clinical work in all aspects of the subspecialty at Parkland Memorial Hospital, Zale-Lipshy Hospital, and the VA Hospital as well as teaching of medical students, residents, and fellows. Clinical and basic research opportunities abound at this rapidly growing medical school complex. Salary negotiable and competitive and is dependent on the level of experience. Interested individuals should contact Helen C. Redman, M.D., Dept. of Radiology, The University of Texas Southwestern Medical School, 5323 Harry Hines Blvd., Dallas, TX 75235. UT Southwestern is an equal opportunity/affirmative action employer. 12–2a

IMMEDIATE OPENING—BC/BE radiologist to join medium-size group in Austin, TX. Practice covers major trauma center and outpatient radiology facility. In addition to general diagnostic services, outpatient facility also provides CT and MRI services on 2 GE 9800 scanners and on GE 1.5-T and 0.5-T MR units. Applicants are requested to contact Drs. Boyd, Gray, or Lava at 711 W. 38th St., Ste. B-8, Austin, TX 78705; (512) 454-8718. 12–5ap

RADIOLOGY/NEURORADIOLOGY, GEORGIA Group of 5 radiologists seeks individual with neuroradiology fellowship training and interest in continuing to practice other aspects of radiology. Well-established, private practice in 300-bed, acute-care hospital with neuro intensive care unit and private office. All imaging modalities are represented including MRI. Excellent benefits with full partnership in 2 yr. This is an opportunity to join an expanding practice in a beautiful coastal city with excellent recreational and cultural advantages. Send CV to Don Starr, M.D., Savannah Radiologists, P.A., 503 Eisenhower Dr., Savannah, GA 31499. 12–2ap

VACANCY EXISTS FOR A STAFF RADIOLOGIST The applicant should be board-certified, and should exhibit particular expertise and training in CT and ultrasound. The mission includes patient care, teaching, and research, and successful candidate will be expected to perform all 3 roles. EOE. Please write and submit CV to Gerald W. Friedland, M.D., Chief, Radiology Service, VA Medical Center, 3801 Miranda Ave., Palo Alto, CA 94304. 12a

DIAGNOSTIC RADIOLOGIST sought for July 1991 or sooner by 5-person group in eastern North Carolina. The group covers a 300-bed county hospital, outpatient facility, and 50-bed private hospital. State-of-the-art equipment including on-site MRI. Applicant must be skilled in all modalities including MRI and interventional. Please reply by letter and CV to Box H91, *AJR* (see address this section). 12ap

RURAL RADIOLOGY PRACTICE—Interested in being an extremely busy general radiologist in a rural midwest setting? We are seeking a fourth board-certified general radiologist to replace our recently retired senior partner. Hays is a town of 25,000 (5000 students at Fort Hays State University) in central Kansas, and functions as a regional medical center with 40–50 physicians. We are the sole radiology practice in northwest Kansas, reading about 70,000 exams/yr in Hays and surrounding towns. Equipment is state-of-the-art including 2 CT, a GE Signa MRI, 2 Acuson 128 color Doppler, angiography with DSA, nuclear medicine, and fluoro and plain films. The practice is egalitarian, with identical work schedules, call, and vacation times. Contact Robert F. Bowerman, M.D., Ph.D., for more details at Radiology Associates of Hays, P.A., P.O. Box 833, Hays, KS 67601; (913) 625-6521. 12–2ap

HOUSTON GROUP needs an additional board-certified diagnostic radiologist. Prefer training and/or experience in interventional (including angiography and percutaneous interventional procedures), guided biopsy, ultrasound, CT, nuclear medicine, and MRI. Please submit CV to Professional Practice Management, Inc., 1075 Kingwood Dr., Kingwood, TX 77339; (713) 358-8113. 11–12ap

MAINE—Excellent opportunity for BC/BE, fellowship-trained neuroradiologist with progressive, well-established, small group. Live and work in college community in southern region close to coast, mountains, and lakes. Competitive compensation package leading to partnership. Affiliated with 200-bed, modern community hospital. Send CV to New England Health Search, 63 Forest Ave., Orono, ME 04473; (207) 866-5680 or (207) 866-5685. 11–2ap

STAFF RADIOLOGIST—The VA Medical Center, Bay Pines, FL, affiliated with the University of South Florida School of Medicine, is currently accepting applications for a staff radiologist, board-certified in general diagnostic radiology with MRI experience. This medical center is located on the beautiful West Coast of FL, only min from the Gulf of Mexico. Send CV and/or call Ann C. Esquerra, M.D., Chief, Radiology Service (114), VA Medical Center, Bay Pines, FL 33504; (813) 398-9363. EOE/MFHV. 11–12a

MRI RADIOLOGIST—An 8-person radiology group in southern New Jersey, 15 min from Philadelphia, seeks a board-certified radiologist with specialty training in body MRI to help run a new GE 1.5-T Signa MRI. Busy, dynamic practice consists of 2 hospitals as well as a full-service private office which also houses the MRI unit. Competitive compensation package will lead to full partnership. Send CV or call Steven Singer, M.D., Kings Highway and Princeton Ave., Woodbury, NJ 08096; (609) 848-4998. 11–1ap

IMMEDIATE OPENING, DIAGNOSTIC RADIOLOGIST—Excellent opportunity for a young, dynamic, preferably board-certified radiologist to join an active, 9-member group. Growing practice includes a 700-bed hospital system with state-of-the-art equipment and excellent working facilities. Skills in all phases of diagnostic radiology desired. Attractive and competitive benefits package leading to full partnership. Contact Sanford E. Rabushka, M.D., 11133 Dunn Rd., Ste. 1017, St. Louis, MO 63136; (314) 653-4300. 11–4ap

BROAD SPECTRUM RADIOLOGIST/UPSTATE NEW YORK—Radiologist wanted for hospital-based practice 90 mi. northwest of New York City. Excellent recreational activities and easy access to metropolis. All modalities available. Excellent salary and benefits leading to early partnership. Immediate availability, but can wait for right applicant. Call G. Bilick; (914) 794-3300, ext. 2216 or send CV to P.O. Box 144, Harris, NY 12742. 11–2ap

RADIOLOGIST—Veterans Affairs Medical Center, Wilkes-Barre, PA, has an immediate vacancy for a board-certified radiologist. This 473-bed, teaching medical center with a 120-bed (plus 60 additional beds currently under construction) nursing home-care unit is affiliated with Temple University School of Medicine, Hahnemann University School of Medicine, and Episcopal Hospital, Philadelphia, PA. Wilkes-Barre is located near the Pocono Mountains resort area within a 2½-hr drive of New York City and Philadelphia. For additional information, contact William K. Grossman, M.D., Chief of Staff; (717) 821-7207. An equal opportunity employer. 11–1a

NEW ORLEANS PARTNERSHIP OPPORTUNITY—Would you like to live in "America's most interesting city"? Would you like to become a partner in a well-established, highly successful radiology group practice that has the latest technology, including a free-standing MRI center with a 1.5-T GE Advantage system? We are a large, multispecialty group practicing in hospital, outpatient offices, and a new breast center. We will offer a BC radiologist, with interest in MR and/or vascular procedures, an exciting job opportunity. Contact Harold R. Neitzschman, M.D., 4400 General Meyer Ave., Ste. 211, New Orleans, LA 70131; (504) 368-5074. 11–1ap

RADIOLOGISTS—Seven-member group seeks board-certified radiologists to join a progressive, hospital/clinic practice in scenic western Arkansas town of approximately 100,000. All modalities represented in practice. Competitive salary leading to early, full partnership. Liberal fringe benefits and vacation. At least 3 mo documented MRI training necessary. Interested parties please send CV to W. T. Huskison, M.D., P.O. Box 3887, Fort Smith, AR 72913; (501) 452-9416 collect. 11–1ap

RADIOLOGIST, CHICAGO AREA—A 7-member radiology group in far southwest suburb of Chicago metropolitan area is currently interviewing BC/BE radiologists for a position available July 1991. Fellowship training attractive but not essential. A highly recommended candidate directly from residency will be given equal consideration. Expertise in general radiology, imaging, and angiography required. Radiology services are provided for 524-bed community hospital and soon-to-be-completed joint venture MRI center, together generating 85,000 exams/yr. Number of exams, as well as group revenue, has steadily increased in the past several years and is likely to continue as we are in a rapidly growing, middle/upper class area. We are oriented toward providing top-quality radiology to referring physicians, as well as a pleasant work environment and significant leisure time for ourselves. Features include competitive starting salary, full benefit package, full partnership after 3 yr, equal division of call among group members, generous vacation time (8 wk to start), and teleradiography. Equipment includes the following state-of-the-art items: Siemens Hi-Q CT; 2 Acuson units with color-flow Doppler and endovaginal probe (third unit ordered); Phillips ARC-14 DVI-S specials room with full digital capability; fully equipped nuclear medicine dept. with dual head bone table and third SPECT camera ordered; 1.5-T Siemens SP MRI with MR angiography; and GE Senographe 600-T mammography unit. Send CV to Box G73, *AJR* (see address this section). 11–1ap

SKELETAL RADIOLOGIST—A staff position is available at the Cleveland Clinic Foundation in the 4-member Section of Musculoskeletal Radiology. The Cleveland Clinic is a 1,000-bed, academic, tertiary-care facility with a large outpatient population and international referral base. The section provides CT and MR as applied to the musculoskeletal system. In addition, the section performs bone biopsies, quantitative bone densitometry, arthrography, and reads a large volume of plain films. There is a large radiology residency at the Cleveland Clinic. A musculoskeletal fellowship will begin in 1991. Applicants should be fellowship-trained or possess equivalent experience. Send CV to Bradford J. Richmond, M.D., Head, Section of Musculoskeletal Radiology, Clinic Radiology, Desk A21, Cleveland Clinic Foundation, 9500 Euclid Ave., Cleveland, OH 44195. The Cleveland Clinic is an equal opportunity employer. M-F-H-V. 11–1a

RADIOLOGIST—Seven-person group seeks general radiologist with fellowship training and special interest in MRI for 92-bed hospital and several imaging centers. Practice in the rapidly growing north San Diego and Temecula Valley areas. Send CV to North Coast Imaging Radiology Medical Group, Inc., 1582 W. San Marcos Blvd., Ste. 104, San Marcos, CA 92069; (619) 744-6442. 11–2ap

MINNEAPOLIS, MINNESOTA—Practice opportunity for a board-certified radiologist with subspecialty interest in musculoskeletal imaging. MR experience is required. Procedural skills are desirable, as there is a growing volume of invasive orthopedic procedures. Practice is based at a rapidly growing, privately owned, freestanding outpatient imaging center equipped with 2 GE 9800 CT scanners, 2 GE Signa 1.5-T MR scanners, and related fluoroscopic-radiographic and ultrasound equipment. Practice also includes coverage of a 750-bed, tertiary-care medical center and adjacent satellite clinic. Five radiologists in practice currently. One distant MR facility operating and plans for more. Investment opportunities for radiologists involved in the practice as well as academic orientation and opportunity for subspecialization. Excellent benefits. Send CV and responses to Cooper R. Gundry, M.D., Center for Diagnostic Imaging, 5775 Wayzata Blvd., Ste. 190, Minneapolis, MN 55416. No telephone calls please. All inquiries confidential. 11–1ap

ANGIOGRAPHER/INTERVENTIONAL RADIOLOGIST—Nationally known, university medical center in the Washington, DC, vicinity seeks qualified radiologist for special procedures. Responsibilities include all visceral angiography and special procedures, resident training, and some general diagnostic radiology. University faculty appointment available to qualified persons. Applicants must be graduate of U.S. medical school, board-certified, fellowship-trained in angio/interventional, and SCVIR eligible or member. Excellent opportunity for new fellowship graduate. Position available July 1991. Generous compensation package. Respond with CV to S. Markovitz, S.M.D., 7826 Eastern Ave., N.W., Ste. 402, Washington, DC 20012. 11–12ap

A 42-PHYSICIAN, MULTISPECIALTY CLINIC serving central and western Kansas has an immediate position for an additional board-certified/eligible radiologist to join 2 others. Excellent facilities include diagnostic radiography, CT, diagnostic ultrasound, nuclear medicine, and MR services. No call, weekends, or holidays. An excellent opportunity in a dynamic practice setting 45 mi. from Wichita. Please send CV to Administrator, Hutchinson Clinic, 2101 N. Waldron, Hutchinson, KS 67502, or call collect (316) 669-2626. 11–12ap

BODY MRI/ABDOMINAL IMAGING—Board-certified radiologist with fellowship training in MRI needed for a position beginning July 1, 1991. Must have fellowship training in MRI, and an interest in CT and GI studies for practice in 578-bed, advanced, metropolitan, tertiary-care teaching hospital. Radiology group is an academically oriented private practice. Send inquiries to Harvey L. Neiman, M.D., Chairman, Dept. of Radiology, The Western Pennsylvania Hospital, 4800 Friendship Ave., Pittsburgh, PA 15224. 11–1a

ANGIO/INTERVENTIONAL—Large, private-practice group in suburb of Detroit is looking for an additional interventional/angio radiologist with expertise in general radiology also. Send letters and resume to Vjeko Mikelic, M.D., St. John Hospital & Medical Center, 22101 Moross Rd., Detroit, MI 48236. 11–12ap

FACULTY NEURORADIOLOGIST, THOMAS JEFFERSON UNIVERSITY HOSPITAL—The Dept. of Radiology at Thomas Jefferson University Hospital in Philadelphia has an immediate opening for a faculty neuroradiologist. This can be either at a very senior or junior level. Our dept. currently operates 4 GE 1.5-T Signa MRI units, and also has a modern neurosciences imaging center. Aside from the MRI units, this facility has a Philips angio room with DSA, a myelography room, 2 CT scanners, reading rooms, and faculty offices. There are 6 faculty members in the neuro division, as well as 5 2-yr neuro fellows. Our practice is growing rapidly and close clinical and research relationships exist with neurosurgery, neurology, orthopedic surgery, and a large spinal-cord-injury center. The dept. also maintains experimental laboratories of its own. Candidates should ideally have broad clinical, research, and teaching interests. Excellent salary and fringe benefits. Interested persons should contact David C. Levin, M.D., Chairman, Dept. of Radiology, Thomas Jefferson University Hospital, Philadelphia, PA 19107; (215) 955-7264. Jefferson is an equal opportunity/affirmative action employer. 11–1a

THE DIVISION OF NUCLEAR MEDICINE, Oregon Health Sciences University, Portland, OR, invites applications for a faculty position available immediately either part-time in nuclear medicine or full-time divided between nuclear medicine and another division of diagnostic radiology. Board-certification in nuclear medicine is required. Send CV to Richard W. Katzberg, M.D., Chairman, or Jeffrey S. Stevens, M.D., Dept. of Diagnostic Radiology, UHN72, Oregon Health Sciences University, 3181 S.W. Sam Jackson Park Rd., Portland, OR 97201-3098. OHSU is an affirmative action, equal opportunity employer. 9–12a

BOSTON, IMMEDIATE OPENING—Radiologist wanted to join busy, well-established, private-practice group with 4 outpatient facilities. Expertise in ultrasound and mammography. No evening or weekend call. Excellent life-style, partnership opportunity. Send letter and CV to Box E49, *AJR* (see address this section). 9–2ap

THE UNIVERSITY OF ARIZONA seeks part-time general radiologists to participate in its clinical and research programs at its university and affiliated hospitals. Applicants should be experienced in plain film interpretation and cross-sectional imaging; expertise in mammography is desirable. Rank and salary are related to the applicant's credentials. The review of applications will begin Sept. 15, 1990, and will continue until the position is filled. The University of Arizona is an equal opportunity employer. Contact Bruce J. Hillman, M.D., Vice-Chairman, Dept. of Radiology, University Medical Center, Tucson, AZ 85724; (602) 694-7368. 9–12a

BC/BE DIAGNOSTIC RADIOLOGIST with skills in all aspects of radiology, including CT, ultrasound, nuclear medicine, interventional, MR, and mammography sought to join a dynamic group of 6 BC radiologists covering a busy, progressive, community hospital, 2 private offices, and an outpatient women's center. Modern dept., state-of-the-art equipment, attractive vacation, CME, and benefits package. 30 min west of Philadelphia. Position available immediately but will wait for right person. Reply with CV to L. Griska, M.D., Dept. of Radiology, Montgomery Hospital, Powell and Fornance Sts., Norristown, PA 19401. 11–2ap

ISRAEL, DIAGNOSTIC RADIOLOGY. Opportunities for 3–4 week or longer working vacations in a number of Israeli medical centers, on a volunteer basis. Positions varied, arrangements flexible. For information contact: Jonathan H. Fish, M.D., 1844 San Miguel Dr., #302, Walnut Creek, CA 94596; (415) 947-0560. 11–1xa

NUCLEAR MEDICINE—Excellent opportunity for a diagnostic radiologist with special interest in nuclear medicine (special competency preferred) to join a private-practice group of 13 radiologists. 600-bed, university-affiliated community hospital, with radiology residency, in a pleasant suburban setting 25 mi. from New York City. State-of-the-art equipment including Acuson with color Doppler, Siemens Somatom Plus CT, and 1.5-T Magnetom. Competitive salary leading to partnership. Please send CV to A. Salomon, M.D., 151 Summit Ave., Summit, NJ 07901. 9–12ap

THE UNIVERSITY OF ARIZONA, DEPT. OF RADIOLOGY, seeks 2 full-time, general radiologists to participate in clinical, teaching, and research activities at its university and affiliated hospitals. Applicants should be experienced in plain film interpretation, cross-sectional imaging, and mammography. Rank, salary, and time allotted to research are related to the applicant's credentials and interests. The review of applications will begin Sept. 15, 1990, and will continue until the position is filled. The University of Arizona is an equal opportunity employer. Contact Bruce J. Hillman, M.D., Vice-Chairman, Dept. of Radiology, University Medical Center, Tucson, AZ 85724; (602) 694-7368. 9–12a

ANGIOGRAPHY/INTERVENTIONAL RADIOLOGIST—Excellent opportunity for diagnostic radiologist with additional training in angiography and interventional radiology to join private practice group of 13 radiologists. Practice in 600-bed, university-affiliated, community hospital, with radiology residency, in a pleasant suburban setting 25 mi. from New York City. State-of-the-art equipment including Acuson with color Doppler, Siemens Somatom Plus CT, and 1.5-T Magnetom. Competitive salary leading to partnership. Please send CV to A. Salomon, M.D., 151 Summit Ave., Summit, NJ 07901. 9–12ap

ULTRASOUND/CT/MRI—Opportunity for a board-certified radiologist specializing in ultrasound, body CT, and body MRI to pursue an academic career at the New York Hospital-Cornell Medical Center. Dept. provides state-of-the-art equipment, including Acuson ultrasound, GE 9800 CT, and GE Signa 1.5-T MR. Wide variety of ultrasound exams include abdominal, OB-GYN, color Doppler, small parts, neonatal head, transvaginal, and transrectal. Prefer candidate with prior fellowship in sectional imaging or ultrasound. Responsibilities include clinical practice, teaching, and research. Position available 7/1/91 or earlier. Please send CV to Elias Kazam, M.D., Dept. of Radiology, The New York Hospital-Cornell Medical Center, 525 E. 68th St., New York, NY 10021. 9–12ap

ULTRASOUND SECTION CHIEF, UNIVERSITY OF MARYLAND—The University of Maryland Hospital seeks a chief for the ultrasound section of the Dept. of Radiology. Although already well-equipped, this position offers a great opportunity for expansion and development, both with the new all-digital Dept. of Radiology under construction at the adjoining VA Hospital and in a new planned all-digital Dept. of Radiology to be constructed at the University Hospital. Applicants should have specialist training and fellowship in ultrasound and a willingness to be involved in the teaching of residents and students. Academic rank and salary are commensurate with experience. The radiologists are organized as a professional corporation, offering excellent fringe benefits. Baltimore is a superb place to live and work. It has all the amenities of a large metropolitan center, yet is small enough to avoid most of the problems (traffic, inflated property values, etc.) of our largest cities. It is only 3 hr from the ocean and Washington, Philadelphia, and New York are readily accessible. Submit CV to Gerald S. Johnston, M.D., Dept. of Diagnostic Radiology, 22 S. Greene St., Baltimore, MD 21201; (800) 866-8667, ext. 3477. Affirmative action/equal opportunity employer encourages applications from members of minority groups. 9–2ap

UNIVERSITY OF ILLINOIS COLLEGE OF MEDICINE AT CHICAGO has an opening for a board-certified, diagnostic radiologist with interest in abdominal imaging including CT, MRI, ultrasound, GI, and GU radiology. The position offers a balance of clinical, teaching, and research activities. Salary and faculty rank are appropriate to experience. Please send inquiries along with CT to Steven Pinsky, M.D., Professor and Head of Radiology, University of Illinois at Chicago, 1740 West Taylor Street, Chicago, IL 60612; (312) 996-0234. UICOMC is an AA/EO employer offering competitive salary and benefit package. 9–12a

THE DEPT. OF RADIOLOGY AT TRIPLER ARMY MEDICAL CENTER, HONOLULU, HI, is recruiting academic radiologists for several divisions of the dept. including ultrasound, chest, skeletal, neuro, and general diagnostic radiology. Our dept. offers a fully accredited residency program with 20 residents and 16 attending full-time staff. Numerous consultants from across the country lecture on a continuing and regular basis. The hospital is a modern, tertiary-care center serving Hawaii and the entire Pacific Basin. A strong residency program, diverse and interesting patient population, excellent equipment, and a tropical lifestyle are positive aspects of the practice. Academic credentials and/or experience are necessary. Recently graduated fellows are encouraged to apply. Board certification is mandatory. Candidates should be particularly interested in patient care, teaching, and research. Salary and benefits are competitive and generous. Tripler is an EO/EEO employer. Please contact Mark F. Hansen, M.D., CoL., MC, Chief, Dept. of Radiology, TAMC, HI 96859-5000; (808) 433-6393. 8–7a

NORTHERN CALIFORNIA/SAN FRANCISCO BAY AREA—The Permanente Medical Group is seeking a BC radiologist with multimodality interests and fellowship training in MR or interventional radiology to join a 10-person group serving a 337-bed, acute-care hospital and 2 outpatient clinics. Teaching opportunities are available with residents of subspecialty services on rotation from Stanford University Hospital as well as our own medical residents. We are currently siting a GE 1.5-T MRI system and installing a new LU arm. Competitive salary and excellent benefits. Please send inquiries and CV to Bruce Baker, M.D., Chief, Dept. of Radiology, Kaiser Permanente Medical Center, 900 Kiely Blvd., AD-AJR, Santa Clara, CA 95051; (408) 236-4444. EOE. 11–12a

UTMB, GALVESTON, TX—The Dept. of Radiology of The University of Texas Medical Branch in Galveston has openings for persons trained and experienced in ultrasound, mammography, and abdominal imaging. The opportunity for academic advancement is great and benefits are generous. Salaries are competitive and living conditions are desirable. Interested persons should contact Melvyn H. Schreiber, M.D., Chairman, Dept. of Radiology, UTMB, Galveston, TX 77550; (409) 761-1823. UTMB is an equal opportunity M/F/H/V affirmative action employer. UTMB hires only those authorized to work in the United States. 7–12a

FACULTY ULTRASOUND RADIOLOGIST, THOMAS JEFFERSON UNIVERSITY HOSPITAL Jefferson's Dept. of Radiology wishes to recruit a faculty radiologist to work in our division of diagnostic ultrasound. Candidates at all levels will be considered. This division is housed in 1 of the largest and best equipped facilities in the world and is extensively involved in the full range of ultrasound studies including obstetrical, vascular, echocardiography, invasive, endoluminal, and both biliary and kidney stone lithotripsy. A new outpatient ultrasound facility is under construction adjacent to the main campus. The position provides excellent salary and benefits, protected research time each wk, and an opportunity to become associated with 1 of the most academically productive ultrasound groups anywhere. Interested individuals should contact either Barry Goldberg, M.D. (Director of Ultrasound), or David C. Levin, M.D. (Dept. Chairman), at the Dept. of Radiology, Thomas Jefferson University Hospital, Philadelphia, PA 19107. Jefferson is an equal opportunity/affirmative action employer. 12xa

FULL-TIME BC RADIOLOGIST needed to staff outpatient women's diagnostic center in suburban Dallas. Experience in mammography and OB/GYN sonography preferred. No call responsibilities. Attractive compensation package. Send CV to Box Y56, *AJR* (see address this section). 12xa

DIAGNOSTIC RADIOLOGIST—Board-certified/eligible radiologist with expertise in CT, ultrasound, nuclear medicine, mammography, angiography, and MRI needed to join group of 4 board-certified radiologists. Hospital-based practice in acute-care, 300-bed hospital with high risk OB and neonatal ICU. Excellent relationship with hospital administration. Annual volume, 85,000 exams. State-of-the-art equipment including Siemens Hi-Q CT, 2 Acuson 128 ultrasound units, and SPECT. Siemens 1.5-T MRI being installed. Pleasant living area, within 4-hr drive from ski/mountain areas of New Mexico and Colorado, draws from regional patient population of 350,000. Generous salary and benefits leading to early partnership. Contact Gayle H. Bickers, M.D., P.O. Box 3460, Amarillo, TX 79116-3460; (806) 378-4708. 7–12ap

DIAGNOSTIC RADIOLOGIST with skills in CT, MR, interventional, ultrasound, and nuclear medicine to join group of 8 board-certified radiologists. Growing practice in eastern Washington. 200-bed hospital and 4 private offices. Long-term potential of practice is excellent. Top-notch school system, including 3 first-rate universities. Excellent hunting, fishing, boating, and skiing. Contact L. E. Crecelius, M.D., N. 5901 Lidgerwood, Ste. 18B, Spokane, WA 99207; (509) 482-2385. 7–12ap

DIAGNOSTIC RADIOLOGISTS—Progressive 3-member group in North Carolina Coastal Plain seeks 2 BC/BE radiologists. ACR-accredited practice includes 350-bed, regional referral hospital, outpatient office, and women's diagnostic center. State-of-the-art equipment. Excellent financial package. Send letter and CV to Box C13, *AJR* (see address this section). 7–12ap

IMMEDIATE OPENING FOR BOARD-CERTIFIED DIAGNOSTIC RADIOLOGIST to join a 3-member group in desirable north Dallas location. Must have expertise in all aspects of diagnostic radiology including angiography and MRI. Hospital and outpatient office practice. Salary commensurate with experience. Serious inquiries only. Send CV to Jeffrey Kam, M.D., 11617 N. Central Expressway, Ste. 132, Dallas, TX 75243. 7–12ap

THE DEPT. OF RADIOLOGY, MEDICAL CENTER HOSPITAL OF VERMONT, Burlington, VT, is seeking board-certified radiologists for academic positions in neuroradiology, angio/interventional radiology, body imaging with substantial training or experience in MRI, and general diagnostic radiology. Applicants should send letters of interest to John P. Tampas, M.D., Professor and Chairman, Dept. of Radiology, Medical Center Hospital of Vermont, 111 Colchester Ave., Burlington, VT 05401-1435. 10–1ap

ASSOCIATE POSITION, VASCULAR/INTERVENTIONAL, BOSTON—A full-time associate position is available for July 1, 1991, or sooner, at Tufts-New England Medical Center Hospitals. The section has 2 staff, 2 fellows, 5 RTs, and 1 secretary and performs 1500 exams/yr (40% interventional and pediatric angio). Responsibilities are only in the section. Academic appointment will be at Tufts University School of Medicine. Starting salary will be based on candidate's experience. Must be ABR-certified, have interventional fellowship, and full Massachusetts license. Contact Victor G. Millan, M.D., Tufts-New England Medical Center Hospitals, Box 253, 750 Washington St., Boston, MA 02111; (617) 956-5961 (Barbara). 10–12ap

BC/BE RADIOLOGIST, SUBURBAN PHILADELPHIA—Tired of hospital-based radiology? Opportunity to join private imaging facility with state-of-the-art equipment, including fourth-generation CT. Competency in CT, ultrasound, mammography, and general radiography is a must. Compensation includes salary for the first yr with an opportunity for partnership after first yr. Send CV to Box F61, *AJR* (see address this section). 10–1ap

IMMEDIATE OPENING, DIAGNOSTIC RADIOLOGY—Midwest city of 55,000 in metropolitan area of 600,000. Abundant recreational opportunities to complement hospital-based, 3-person group practice with very up-to-date equipment including MRI, CT, color ultrasound, SPECT nuclear, and angio with DSA. University appointment may be available if desired. Medical staff is highly specialist oriented. Competitive salary and benefit package including pension, health and disability insurance, and time off. Contact Charles Morris, M.D., P.O. Box 279, Council Bluffs, IA 51502; (712) 328-7646 (office) or (712) 328-2074 (home). 10–1ap

DIAGNOSTIC RADIOLOGIST sought to join a fee-for-service group practice at 2 mid-Bronx hospitals. Board-certification with expertise in imaging and in special procedures/interventional radiology preferred. Please send CV to Arthur Avenue Radiology, P.C., P.O. Box 4332, Great Neck, NY 11027. 10–3ap

DIAGNOSTIC RADIOLOGIST—A 4-member radiology group located in beautiful southwestern Montana is currently seeking an additional board-certified/eligible radiologist. Expertise in MRI preferred. Hospital-based and office practice. Excellent school system and outstanding, year-round recreational activities. Approximately 35,000 exams last yr. Hospital is acquiring MRI and updating CT services. One yr to full partnership. Contact Dennis L. Rich, M.D., 300 N. Willson, Bozeman, MT 59715; (406) 587-8631. 10–3ap

DIAGNOSTIC RADIOLOGIST, IMMEDIATE OPENING: DENVER, CO, AT ROSE MEDICAL CENTER (RMC)—A 7-person radiology group is recruiting a radiologist with fellowship training in body imaging or invasive radiology. The practice involves all imaging modalities. RMC is affiliated with the University of Colorado. Salary, benefits, and location are highly attractive. Contact David W. Wilder, M.D., or Jeffrey A. Levy, M.D., at (303) 320-2256. 10–1ap

HIGHLAND GENERAL HOSPITAL—Diagnostic radiologist needed for Highland General Hospital. This is a level II trauma center, 20 min from downtown San Francisco. The hospital performs 66,000 exams/yr. Equipment includes Picker CT 1200 SX, Picker Digicon angiography suite, and 3 ultrasound machines including Acuson with Doppler. There are 6.2 FTE radiologists and over 50 technical and secretarial personnel. Limited private practice available. Applicant with some MRI training or experience desired, but not essential. Clinical faculty appointment available for suitable candidate. Board certification and California license necessary. Highland General Hospital is an EOE. Reply to Leslie Preger, M.D., Highland General Hospital, 1411 E. 31st St., Oakland, CA 94602; (415) 437-4204. 10–12a

PENN STATE UNIVERSITY, FACULTY POSITION IN CARDIOVASCULAR/INTERVENTIONAL RADIOLOGY—The Penn State University, Dept. of Radiology, is seeking a full-time faculty member in the Section of Cardiovascular/Interventional Radiology for July 1, 1991. The section provides a wide range of services in all aspects of diagnostic and interventional angiography (including neuro- and pulmonary angiography), percutaneous and combined percutaneous/peroral biliary interventions, genitourinary interventions, central and peripheral venography (with IVC filter placement), traumatic and oncological embolizations, foreign body retrievals, complex biopsy and drainage procedures (under multiple imaging modalities), and is currently an FDA test site for a new holmium:YAG intravascular laser. Clinical responsibility at the assistant professor level is required, necessitating a Pennsylvania medical license, University Hospital medical staff privileges, and ABR certification. Although seeking a junior faculty person at the assistant professor level, the academic rank will be commensurate with previous academic performance, recommendations, and Penn State University guidelines. Independent original research is expected and is amply funded, both in time and money. The animal research facility at Penn State University is one of the finest facilities of its kind in the country and is coupled with a dedicated MR research facility with angiographic and spectroscopic capability. Both research facilities are staffed by full-time research associates and research faculty, and are equipped with modern, state-of-the-art equipment. The position is open to persons who have completed an accredited residency program in radiology and an accredited fellowship in CV/I radiology, can obtain a Pennsylvania medical license, and have fulfilled ABR requirements for board certification. A generous and competitive salary and benefits package are offered. National meeting presentation is encouraged and fully supported. Exceptional academic, biophotographic, and secretarial support are also provided. Applicants should respond as soon as possible with a letter of interest and current CV. Please direct inquiries and requests for application forms to John F. Cardella, M.D., Associate Professor and Chief, Cardiovascular/Interventional Radiology Section, Penn State University/Hershey Medical Center, Box 850, Hershey, PA 17033. Penn State University is an affirmative action, equal opportunity employer. Women and minorities are encouraged to apply. 10–1a.

MAMMOGRAPHY, UNIVERSITY OF PENNSYLVANIA—Exceptional opportunity in academic mammography within a high-volume, rapidly expanding, breast imaging section. Ongoing screening and problem-solving mammography, breast ultrasound, and collaborative projects. Academic rank and salary commensurate with credentials. Resident and student teaching responsibilities along with negotiable participation in bone and chest outpatient radiology. Position available immediately. Applicant must be ABR-certified and able to obtain license in Pennsylvania. University of Pennsylvania is an affirmative action, equal opportunity employer and specifically encourages applications from women and minorities. Send letter and CV to Rosalind H. Troupin, M.D., Dept. of Radiology, H.U.P., 3400 Spruce St., Philadelphia, PA 19104. 10–1ap

VASCULAR/INTERVENTIONAL RADIOLOGIST Progressive, private-practice group is seeking a second fellowship-trained vascular and interventional radiologist for its expanding interventional radiology service. We are currently performing more than 1000 procedures/yr. We are budgeted for 2 state-of-the-art vascular suites, the first to be installed early in 1991. We will break ground soon on a new imaging center to include 2 MRI and 2 CT (including a cine CT) scanners. We have a noninvasive lab and retain admitting privileges for our interventional service. We are located in Fresno, CA, at Saint Agnes Medical Center. Saint Agnes is a tertiary-referral center for the San Joaquin Valley, and Fresno is one of the fastest growing cities in CA. We are located 90 mi. from Yosemite National Park and less than 2 hr from excellent winter skiing and 2 hr from the coast. We offer 2 yr to full partnership with excellent salary and benefits. Please contact Art Fontaine, M.D., Dept. of Imaging, Saint Agnes Medical Center, 1303 E. Herndon, Fresno, CA 93710; (209) 449-3210. 10–3ap

RADIOLOGISTS — New York City, combined private radiology practice, and fee-for-service hospital practice has an immediate opening for a board-certified radiologist with experience in CT, ultrasound, and interventional radiology. In addition, MRI and mammography experience is preferred. This well-established practice has 3 private offices on the upper East Side of Manhattan as well as operations in 2 hospitals in Manhattan. Other studies performed in the practice are diagnostic radiology, nuclear imaging, and vascular duplex imaging. The practice continues to expand in all imaging modalities with its recent opening of a second state-of-the-art MRI unit. Excellent benefit package includes health, life, disability, and malpractice insurance; profit sharing plan; continuing medical education; and a travel and entertainment account for professional use. Send CV to Box F67, *AJR* (see address this section). 10–12ap

DIAGNOSTIC RADIOLOGIST, TEXAS—Progressive, well-diversified group (15 radiologists) has immediate opening for a BC/BE diagnostic radiologist with competence in a broad range of modalities. Additional consideration for fellowship. Excellent opportunity with excellent salary and benefits. Send CV with letter of inquiry to Will Gray, M.D., 1101 N. 19th St., Abilene, TX 79601. 10–1ap

HARTFORD, CT—Position available July 1991 for board-certified radiologist to join an established group of 8. Practice includes hospital and 4 private offices, all fully equipped including CT. Mammography experience is helpful. CT and MRI experience is essential. Competitive starting salary and benefits. Please enclose CV with initial correspondence to Jeffrey Blau, M.D., 40 Hart St., New Britain, CT 06052; (203) 229-2059. 12xa

NEURORADIOLOGIST—Excellent, young, 12-person radiology group has an opening for a well-trained neuroradiologist. Practice is hospital-based with 2 GE CT 9800 scanners, 1 high-field MRI, 1 mid-field MRI, new GE angio. Please contact Richard D. Herman, M.D., Dept. of Radiology, St. Luke's Hospital, Bethlehem, PA 18015; (215) 691-4200. 10–1ap

SALT LAKE CITY, UT—Opportunity for board-certified diagnostic radiologist, with recent MRI fellowship training, to join group of 7 board-certified radiologists. Experience in all aspects of general radiology required. Practice includes 2 hospitals, 2 private offices, and a freestanding MRI center. Send letter and CV to Neel E. Bennett, M.D., Medical Director and Chairman, Dept. of Radiology, Holy Cross Hospital, 1050 E. S. Temple, Salt Lake City, UT 84102; (801) 350-4636. 12xa

THE NEW YORK HOSPITAL, CORNELL MEDICAL CENTER, DEPT. OF RADIOLOGY has a position available for a junior attending in an expanding uroradiology section beginning July 1991. Position involves responsibilities in clinical aspects of GU imaging, teaching, and research. Applicants should be board-certified/eligible with experience in cross-sectional imaging. Please send CV to Susan Krysiewicz, M.D., Dept. of Radiology, NYH-CUMC, 525 E. 68th St., Starr 8A15, New York, NY 10021; (212) 746-2557. 10–1a

PHYSICIAN/RADIOLOGIST—Large radiology group with multiple private offices seeks a board-certified radiologist interested in a full-time position. Responsibilities include general radiography. Special training in CT, ultrasound, and nuclear medicine is desirable but not required. Desirable southern New Jersey location. Competitive salary and benefit package. Send CV to RABC, P.O. Box 729, Mt. Holly, NJ 08060. 11–1ap

PHYSICIAN/RADIOLOGIST—Large radiology group with 2 hospitals and multiple private offices with state-of-the-art equipment seeks a radiologist who is board-certified in nuclear medicine. Competitive salary and benefit package. Send CV to Radiology Associates of Burlington County, P.A., 175 Madison Ave., Mt. Holly, NJ 08060. 11–1ap

TEN-PERSON RADIOLOGY GROUP located in Corpus Christi is seeking a new associate to start July 1990 or as late as July 1991. Must be board-certified or eligible. Will perform all diagnostic studies, including interventional, CT, MRI, nuclear medicine, and ultrasound. Please send CV to Search Committee, P.O. Box 5608, Corpus Christi, TX 78465-5608. 11–12ap

DENVER, CO—Group of 8 diagnostic radiologists engaged in a predominantly hospital-based practice is seeking a new member on or about 10-1-90. The group provides diagnostic imaging services for a 565-bed, tertiary-care teaching hospital. The new member should be trained in diagnostic radiology and have fellowship training, and/or additional experience beyond residency level, in nuclear medicine. The new member will be primarily responsible for nuclear medicine but must be willing to participate in other modalities of diagnostic imaging. Salary, benefits, vacation time, and time to partnership are all competitive for the Rocky Mountain region. Interested parties should send their CV to Steve A. Holt, M.D., Western Radiologists, P.C., 3665 Cherry Creek Dr., N., Ste. 350, Denver, CO 80209. 12ap

DIAGNOSTIC RADIOLOGISTS—Owing to expansion and retirement, several positions are available with a large, dynamic radiology group in the Central New Jersey/Bucks County, PA, region. Openings for radiologists with expertise in 1 or more of the following: nuclear medicine, general, and angio/interventional. Immediate availability. Send letter and CV to E. Tarasov, M.D., 838 W. State St., Trenton, NJ 08618. 12–1a

INDIANAPOLIS, IN—Practice opportunity for a radiologist to serve as medical director of a new, freestanding, privately owned, high-field MR imaging center. Facility will be managed by and affiliated with the Center for Diagnostic Imaging in Minneapolis, MN. MR experience mandatory. Subspecialty experience in MR desirable. Board certification and licensure in Indiana required. Please send inquiries with CV to Cooper R. Gundry, M.D., Center for Diagnostic Imaging, 5775 Wayzata Blvd., Ste. 190, Minneapolis, MN 55416. All inquiries entirely confidential. No telephone calls please. 12–2a

CHALLENGING LOCUM TENENS POSITIONS AVAILABLE NOW—Work at your convenience, full- or part-time. Competitive compensation. No hassles, politics, or paperwork. Paid malpractice insurance, housing, and transportation. Put an experienced leader to work for you! Contact LOCUM Medical Group, 30100 Chagrin Blvd., Cleveland, OH 44124; (800) 752-5515. 12xa

Positions Desired

PGY-2 RADIOLOGY RESIDENCY POSITION SOUGHT—Radiology resident in second yr of training seeks position in University-based program. Interested in research and academic career. Strong credentials. Reply Box H93, *AJR* (see address this section). 12–1bp

Fellowships and Residencies

FELLOWSHIPS IN PEDIATRIC RADIOLOGY AND PEDIATRIC NEURORADIOLOGY—Childrens Hospital Los Angeles has 4 fellowship openings annually for 1 yr of training in all aspects of pediatric radiology and imaging. Applicants for the position should have completed a 4-yr training program in diagnostic radiology. There is a full-time faculty of 8 pediatric radiologists and equipment is state-of-the-art for ultrasound, CT, MR, digital angiography, and nuclear radiology. Opportunity for research and teaching experience. Excellent and varied career opportunities are available in the specialty of pediatric radiology. Address inquiry and CV to Beverly P. Wood, M.D., Chief of Radiology, Dept. of Radiology, Childrens Hospital Los Angeles, 4650 Sunset Blvd., Los Angeles, CA 90027. 12cp

DUKE UNIVERSITY, DEPT. OF RADIOLOGY offers 1- or 2-yr fellowship positions in chest radiology, neuroradiology, vascular/interventional radiology, musculoskeletal radiology, CT, ultrasound, MRI, abdominal imaging, mammography, pediatric radiology, and nuclear medicine beginning July 1991. The dept. runs an active clinical service with top quality equipment including 5 GE 9800 Quick CT scanners, 3 GE 1.5-T MRI units, and 4 fully equipped vascular/interventional laboratories. In addition to their clinical responsibilities, fellows are provided academic time to pursue investigational interests. Applications are due March 1, 1991, and interviews will be scheduled in the spring. For further information and application material, please contact Ms. Debbie Sykes at the Dept. of Radiology, Box 3808, Duke University Medical Center, Durham, NC 27710; (919) 660-2711, ext. 5228. Duke University is an equal opportunity/affirmative action employer. 12–2c

FELLOWSHIP IN VASCULAR/INTERVENTIONAL RADIOLOGY 1991—The University of New Mexico is offering a 1-yr fellowship in vascular/interventional radiology, beginning July 1, 1991. We perform all noncardiac diagnostic angiography, including neuroangiography, as well as a wide variety of vascular and nonvascular interventional procedures, with state-of-the-art equipment at the University Hospital (a level 1 trauma center) and the VA/Air Force Hospital. Applicants must have passed the ABR written exam, be eligible for ABR certification, and be eligible for medical licensure in the state of New Mexico. Contact Jerry King, M.D., University of New Mexico Hospital, Dept. of Radiology, Albuquerque, NM 87131; (505) 843-2269. 12–1c

FELLOWSHIP IN VASCULAR AND INTERVENTIONAL RADIOLOGY—A 1-yr fellowship position is available at the New York Hospital-Cornell University Medical Center for July 1991. Training includes experience in all aspects of peripheral vascular and nonvascular interventions. Equipment includes 3 state-of-the-art Philips digital labs and a 4-bed recovery room. For further information, please contact Thomas A. Sos, M.D.; (212) 746-2600. 12–1c

NUCLEAR MEDICINE RESIDENCY—University Health Center of Pittsburgh; 1- or 2-yr positions; July 1991. The division, within a progressive dept. of radiology, serves the 1300 beds of Presbyterian-University, Children's Montefiore University, and the VA Hospitals in the cultural-center area of Oakland. Resources include 7 physicians plus auxiliary and basic science faculty, and 17 scintillation cameras with single- and multi-detector SPECT. More than 11,000 imaging, 30,000 nonimaging, and 100 therapeutic procedures are performed annually. The fully accredited program incorporates nuclear cardiology, brain tomography, monoclonal antibodies, radioassay, thyroidology, computer applications, many research opportunities, and a PET rotation pending completion of our approved PET center. Contact Herbert A. Klein, M.D., Ph.D., Nuclear Medicine, Presbyterian-University Hospital, DeSoto at O'Hara Sts., Pittsburgh, PA 15213. 12cp

THE UNIVERSITY OF ARIZONA, DEPT. OF RADIOLOGY, offers a 1-yr fellowship in abdominal, chest, and musculoskeletal cross-sectional imaging that includes CT, MRI, ultrasound, and interventional techniques. University Medical Center is a tertiary-care hospital and trauma center with 3 CT scanners, 3 ultrasound devices including color Doppler, and 2 MRI scanners. There is an active research program including 4.7-T MRS. Fellows will oversee daily clinical activities, participate in teaching and conferences, and conduct research. The review of applications will begin Sept. 15, 1990, and will continue until the position is filled. The University of Arizona is an equal opportunity employer. Contact Bruce J. Hillman, M.D., Vice-Chairman, Dept. of Radiology, University Medical Center, Tucson, AZ 85724; (602) 694-7368. 9–12c

FELLOWSHIP IN ULTRASOUND AND BODY CT/MRI—July 1, 1992, to June 30, 1993, at the New York Hospital-Cornell Medical Center. Dept. provides state-of-the-art equipment including Acuson ultrasound, GE 9800 CT, and GE Signa 1.5-T MR. Wide variety of ultrasound exams include abdominal, OB-GYN, color Doppler, small parts, neonatal head, transvaginal, and transrectal. Applicant should be ABR eligible or certified. Send CV to Elias Kazam, M.D., Dept. of Radiology, The New York Hospital-Cornell Medical Center, 525 E. 68th St., New York, NY 10021. 9–12cp

FELLOWSHIPS IN PEDIATRIC RADIOLOGY, JULY 1991—The Dept. of Radiology, Children's Hospital Medical Center, Cincinnati, OH, offers 1- or 2-yr fellowships in pediatric radiology beginning July 1991. Children's Hospital Medical Center is a 355-bed institution where approximately 100,000 radiological exams are performed annually by 13 full-time faculty radiologists. Four fellowship positions are available annually. Training includes all aspects of pediatric imaging: neonatal radiology, neuroimaging, musculoskeletal radiology, cardiovascular and thoracic imaging, abdominal imaging, oncologic imaging, ultrasonography, nuclear medicine, CT, MRI, and vascular/interventional techniques. Facilities include digital fluoroscopy, Acuson and ATL ultrasound units with Doppler and color-flow Doppler capabilities, Gamma and SPECT tomographic nuclear cameras, GE 9800 Quick CT scanner, 1.5-T GE MRI, and cardiac catheterization/angiographic suite with digital vascular imaging. Numerous opportunities to participate in both clinical and basic research. Salary and fringe benefits are highly competitive. Candidates must be board-certified or board-qualified in diagnostic radiology and must be able to obtain an Ohio medical license. Children's Hospital Medical Center and the University of Cincinnati College of Medicine are affirmative action/equal opportunity employers. Address inquiry and CV to Donald R. Kirks, M.D., Director, Dept. of Radiology, Children's Hospital Medical Center, Elland and Bethesda Aves., Cincinnati, OH 45229-2899; (513) 559-8058. 1–12cp

CARDIOVASCULAR/INTERVENTIONAL RADIOLOGY FELLOWSHIP, PENN STATE UNIVERSITY The Penn State University, Dept. of Radiology, offers 1- or 2-yr fellowships in cardiovascular/interventional radiology, with a primary purpose of preparing graduates for academic careers in the subspecialty of CV/I radiology. Fellows will receive training in all aspects of diagnostic and interventional angiography (including neuro and pulmonary angiography), percutaneous and combined percutaneous/peroral biliary interventions, genitourinary interventions, central and peripheral venography (with IVC filter placement), traumatic and oncological embolizations, foreign body retrievals, and complex biopsy and drainage procedures (under multiple imaging modalities). Clinical responsibility at the instructor level is required, necessitating a Pennsylvania medical license, university hospital medical staff privileges, and ABR eligibility (at time of application) and certification (during first program yr). Independent original research is expected and is amply funded, both in time and money. The animal research facility at Penn State University is one of the finest facilities of its kind in the country and is coupled with a dedicated MR research facility with angiographic and spectroscopic capability. Both research facilities are staffed by full-time research associates and research faculty, and are equipped with modern state-of-the-art equipment. The fellowship is open to individuals who have completed an accredited residency program in radiology, can obtain a Pennsylvania medical license, and have fulfilled ABR requirements for board-certification or eligibility. A generous competitive salary and benefits package are offered. Academic, biophotographic, and secretarial support are also provided. Applicants should respond as soon as possible with a letter of interest and current CV. Please direct inquiries and requests for application forms to John F. Cardella, M.D., Associate Professor and Chief, Cardiovascular/Interventional Radiology Section, Penn State University/Hershey Medical Center, Box 850, Hershey, PA 17033. Penn State University is an affirmative action, equal opportunity employer. Women and minorities are encouraged to apply. 10–1c

VASCULAR/ INTERVENTIONAL RADIOLOGY FELLOWSHIP, ST. LOUIS VASCULAR INSTITUTE AT THE CHRISTIAN HOSPITAL, ST. LOUIS, MO—A 1- to 2-yr fellowship in vascular and interventional radiology is offered beginning July 1, 1991. Training includes all aspects of diagnostic angiography and vascular and nonvascular interventional techniques. Candidates must have completed a diagnostic radiology residency in an accredited training program, must be certified by or eligible for certification by the ABR, and must be able to obtain a Missouri license. Direct inquiries to Saadoon Kadir, M.D., Dept. of Radiology, Christian Hospital Northeast, 11133 Dunn Rd., Ste. 1017, St. Louis, MO 63136. 11–4cp

FELLOWSHIP IN NEURORADIOLOGY—The Dept. of Radiology at Henry Ford Hospital in Detroit, MI, offers a 2-yr neuroradiology fellowship. The Division of Neuroradiology performs a high volume of interesting neuropathologic cases including 14,000 neuro CT, 5,000 neuro MRI, 1,000 neuro angiography, 1,000 myelograms, and 50 neurointerventional studies annually. State-of-the-art equipment includes 2 GE 1.5-T Signa systems, 3 GE 9800 Quick CT scanners with independent 3-D ISG work stations, biplane DSA angio room for interventional neuroradiologic procedures, biplane Siemens angio room for magnification angiography, and biplane fluoroscopy equipped for myelography. Applicants must have completed a diagnostic radiology residency and be board-certified or eligible. Please contact Suresh C. Patel, M.D., Division Director, Neuroradiology, Dept. of Diagnostic Radiology, Henry Ford Hospital, 2799 W. Grand Blvd., Detroit, MI 48202; (313) 876-1357. 11–12cp

WOMEN'S IMAGING FELLOWSHIP—A 1- or 2-yr comprehensive experience in women's imaging modalities is offered in Tucson, AZ. Procedures in which we expect the fellow to gain expertise include high-volume, low-cost screening mammography and its associated administrative, financial, and epidemiological aspects; problem-solving diagnostic mammography, including invasive mammographic procedures (e.g., stereotactic guided cytology and galactography); high-volume obstetric and gynecologic sonography. Annual stipend is $50,000. Contact Arizona State Radiology, 7250 E. Ventana Canyon Dr., Tucson, AZ 85715; (602) 620-4911. 10–3cp

NATIONAL INSTITUTES OF HEALTH (NIH) FELLOWSHIP IN RADIOLOGIC RESEARCH—The newly established Radiology Research and Training Program at NIH is offering 2-yr fellowships to encourage young men and women to pursue a program of original basic research in laboratories on the NIH campus. Candidates who have recently completed clinical training in diagnostic radiology or nuclear medicine or, under special circumstances, are currently in residency, would be considered for these positions. The fellowship emphasizes basic research with no clinical responsibilities, except as they relate to the candidate's project. Fellows will have access to the imaging laboratories of the Radiology Research and Training Program, facilities in the In Vivo NMR Center, the PET program of the Dept. of Nuclear Medicine, the Biomedical Engineering and Instrumentation Branch, and other laboratories on the NIH campus. The position would involve a full-time appointment, either in the Civil Service or Public Health Service, with an annual salary starting at $37,000. Initial appointments will begin July 1991. Candidates should submit a CV, at least 2 letters of reference, and a preliminary statement concerning area of research interest to John Doppman, M.D., Bldg. 10, Room 1C-660, National Institutes of Health, Bethesda, MD 20892 or fax (301) 496-9933. 10–12c

BODY IMAGING FELLOWSHIP, CT/ULTRASOUND/MRI—Clinical and research activities in all areas tailored to the fellow's and dept.'s goals. Should have interest in teaching and research. GE 9800 CT, GE 1.5-T Signa MRI, and Acuson Diasonics ultrasound. Full resident complement. Four body-imaging faculty. Send CV to Fred W. Flickinger, M.D., Body Imaging Section, Dept. of Radiology, Medical College of Georgia, 1120 15th St., Augusta, GA 30912-3900. EEO/AA. Women/minorities encouraged to apply. 10–12c

IMMEDIATE UNEXPECTED OPENING FOR FELLOWSHIP IN CARDIOVASCULAR-INTERVENTIONAL RADIOLOGY—One-yr fellowship program at 750-bed teaching hospital. Extensive clinical experience involving all aspects of cardiovascular imaging and interventional vascular and nonvascular procedures. Availability for clinical or animal research. Send CV and inquiries to Oscar H. Gutierrez, M.D., Dept. of Radiology, Box 648, University of Rochester Medical Center, Rochester, NY 14642. AA/EO/M-F employer. 10–1cp

FELLOWSHIPS AT THOMAS JEFFERSON UNIVERSITY HOSPITAL—The Dept. of Radiology at Thomas Jefferson University Hospital in Philadelphia offers the following fellowship programs each yr. Ultrasound/CT/MRI — Jefferson's ultrasound division is 1 of the largest in the world and performs all currently available exams including obstetric, vascular, lithotripsy, invasive, and endoluminal. We also operate 4 GE 1.5-T MRI units and 3 CT scanners. Contact Barry Goldberg, M.D., regarding this program. Cardiovascular/interventional — this division is housed in a new suite containing Philips angio units with DSA and performs the full range of vascular and nonvascular interventional procedures. Contact Geoffrey Gardiner, Jr., M.D. Neuro/ENT radiology — very active clinical services supply a wealth of material to this division, which is housed in a neurosciences imaging center containing all imaging modalities. Contact Carlos Gonzalez, M.D. Breast imaging — Jefferson's new breast imaging center performs approximately 85 studies/day including ultrasound and needle localizations. Contact Stephen Feig, M.D. Chest — includes biopsies and CT. Contact Robert Steiner, M.D. MRI — a dedicated body MRI program including excellent research opportunities in addition to a large clinical case load. Contact Matthew Rifkin, M.D. Ultrasound — a dedicated ultrasound program. Contact Barry Goldberg, M.D. Musculoskeletal — includes MRI of the musculoskeletal system. Contact David Karasick, M.D. All program directors listed above can be contacted at the Dept. of Radiology, Thomas Jefferson University Hospital, Philadelphia, PA 19107. Jefferson is an equal opportunity/affirmative action employer. 12xc

ABDOMINAL IMAGING FELLOWSHIP—The Dept. of Radiology at the University of Florida is offering 1-yr fellowships in abdominal imaging beginning July 1, 1991, and July 1, 1992. Minimum requirements include successful completion of an accredited radiology residency. The fellowship includes training in all aspects of abdominal imaging (gastrointestinal and genitourinary radiology, CT, ultrasound, and MRI) by a 3-person subspecialty faculty. The program offers full clinical experience and research opportunities. Applicants must be eligible to obtain a license in the state of Florida. For additional information, contact Pablo R. Ros, M.D., Professor, Dept. of Radiology, Box J-374, Gainesville, FL 32610-0374; (904) 395-0288. The University of Florida is an equal opportunity/affirmative action employer and encourages applications from women and minorities. 10–6c

IMMEDIATE OPENING, FELLOWSHIP IN PEDIATRIC RADIOLOGY—Position available for fellowship in pediatric radiology, 1 or 2 yr beginning July 1, 1991, or July 1, 1992. Full training with abundant hands-on experience with all imaging modalities. Supported by strong Dept. of Pediatrics with a good mixture of patient material. Excellent teaching on a 1-to-1 basis and ample opportunity for pursuing academic interests. Apply to Leonard E. Swischuk, M.D., Dept. of Radiology, The University of Texas Medical Branch, Child Health Center, C-65, Galveston, TX 77550; (409) 761-2096. UTMB is an equal opportunity M/F/H/V affirmative action employer. UTMB hires only individuals authorized to work in the United States. 10–12c

Tutorials/Courses

CARIBBEAN CRUISE, MRI AT SEA — Jan. 5–12, 1991. Medical Seminars International, 18981 Ventura Blvd., #303, Tarzana, CA 91356; (818) 700-9821. 10–12d

CARIBBEAN CRUISE, BREAST IMAGING AT SEA—Jan. 12–19, 1991. Medical Seminars International, 18981 Ventura Blvd., #303, Tarzana, CA 91356; (818) 700-9821. 10–12d

NINTH WINTER DIAGNOSTIC IMAGING CONGRESS, VAL D'ISERE, FRANCE—March 2–9, 1991. MRI, CT, ultrasound. Medical Seminars International, 18981 Ventura Blvd., #303, Tarzana, CA 91356; (818) 700-9821. 10–2d

Other

VISITING PROFESSORSHIPS, THOMAS JEFFERSON UNIVERSITY HOSPITAL—The Dept. of Radiology at Thomas Jefferson University Hospital in Philadelphia is offering visiting professorships over the next several yr, while some of our faculty members are on sabbatical leave. These positions can have either a 6-mo or 1-yr term. In particular, we are seeking candidates with expertise in either ultrasound or general diagnostic radiology, but emphasis in other areas may be acceptable as well. Funding for these positions is appropriate for a senior faculty member from another institution on sabbatical with partial funding of his/her own, or for a junior faculty member. These positions are also open to highly qualified foreign radiologists with current academic appointments at prestigious foreign medical schools. Visiting faculty members will do some clinical work in our dept. and also have access, for research or educational purposes, to state-of-the-art imaging modalities of all types, as well as well-equipped physics and physiology research laboratories. Interested persons should contact David C. Levin, M.D., Chairman, Dept. of Radiology, Thomas Jefferson University Hospital, Philadelphia, PA 19107. Jefferson is an equal opportunity/affirmative action employer. 12xe

AJR Classified Advertisements Information

Box Responses and Address for Ad Placement

Write Box ______, AJR, 2223 Avenida de la Playa, Suite 103, La Jolla, CA 92037-3218; Phone: (619) 459-2229; FAX: (619) 459-8814.

Author Index Volumes 154–155

Authors of *AJR* articles are also included in the 5-year cumulative index published in *Radiology*.

A

Aabed MY, **154**:989
Abbitt PL, **154**:849
Abernethy WB, **155**:983
Ablin DS, **154**:1035, **155**:1347
Abu-Yousef MM, **154**:721, **155**:785
Adachi N, **154**:423
Adam A, **155**:391
Adler DD, **155**:39, **155**:1195
Aerts P, **155**:407
Agee MW, **154**:135, **155**:198
Aggarwal S, **155**:339
Agildere M, **155**:900
Ahuja GK, **155**:339
Aideyan OA, **154**:989
Aiman EJ, **155**:307
Aisen AM, **154**:1228
Aizpuru RN, **155**:420
Akhan O, **155**:197
Akins EW, **154**:1091
Akita Y, **154**:1257
Alberhasky MT, **154**:261
Albu E, **155**:1137
Alexander PW, **154**:493
Alford BA, **154**:785
Algra PR, **155**:899
Allen LC, **155**:67
Allgood M, **154**:181
Alper H, **155**:1142
Alrowaih A, **154**:331
Ambrosino MM, **154**:797
Amis ES Jr, **154**:1028, **155**:510
Anderson CM, **154**623
Anderson DJ, **155**:31
Anderson JC, **155**:237
Andersson I, **154**:1191
André MP, **154**:32
Ansari A, **154**:114
Ardill RH, **155**:91
Arena L, **155**:803
Arisawa J, **154**:1181
Ariyurek M, **155**:1142
Armato DP, **155**:659
Arrington LE, **154**:1237
Arthur RH, **154**:603
Aruny JE, **154**:1105
Atkinson DJ, **154**:937
Atlas SW, **154**:167, **154**:1069
Atri M, **155**:894
Avolio RE, **1127**, **154**:1128

B

Babcock DS, **154**:202, **155**:1277
Bach LD, **155**:1345
Bae WK, **154**:1346
Baert AL, **155**:407
Baines CJ, **155**:743, **155**:1133
Bair JH, **154**:405
Bakal CW, **154**:171
Baker EL, **154**:27
Baker KS, **154**:129
Baker LL, **154**:1251
Baker ME, **154**:67, **155**:55, **155**:291, **155**:991
Baker ML, **155**:177
Baker SR, **155**:803
Balistreri WF, **155**:351
Ball WS Jr, **154**:361
Balotin RJ, **155**:1267
Balthazar EJ, **154**:27, **154**:72, **154**:281, **154**:499
Banner H, **154**:797
Bansal SK, **155**:897
Barber BJ, **155**:1105
Barker WW, **154**:1285
Barkhof F, **155**:899
Barkoff ND, **154**:295
Barkovich AJ, **155**:143, **155**:855
Barloon TJ, **154**:271, **154**:301
Barnett TP, **155**:200
Baron NW, **154**:327
Baron RL, **154**:79, **155**:1211
Barr RG, **155**:656
Barth-Jones D, **155**:43
Barton P, **155**:1031
Barton R, **155**:153
Bartus SA, **155**:529
Basibüyük LN, **155**:135
Bassett LW, **154**:713, **154**:1196
Batnitzky S, **155**:1076
Baumann MH, **154**:481
Baumgartner BR, **154**:105, **154**:291, **155**:655
Baum JK, **155**:43
Baum PA, **154**:633
Bean WJ, **154**:659
Beatrous TE, **155**:85
Becker RD, **155**:739
Beckett WW Jr, **155**:1091
Beier-Hanratty S, **155**:91
Belhobek GH, **155**:555, **155**:1141
Bell JS III, **155**:1013
Bell SA, **154**:121
Beltran JL, **155**:337
Benedikt RA, **154**:16
Benjamin IS, **155**:391
Ben-Menachem Y, **155**:685, **155**:691
Bennett HT, **154**:1237
Benson LN, **154**:789
Berbaum KS, **154**:301
Bergfeld JA, **155**:1140
Bergin CJ, **154**:251, **154**:495, **155**:23, **155**:1137
Bergman A, **155**:1100
Berkowitz JE, **155**:89
Berland LL, **155**:651
Berman E, **154**:770
Berná JD, **155**:1345
Bernardino ME, **154**:45, **155**:73
Bernecker P, **155**:825
Berns M, **155**:1100
Bero LA, **155**:889
Berquist TH, **154**:323, **155**:424, **155**:1251
Berrey BH, **154**:563, **155**:1257
Berry CC, **154**:477, **155**:652
Berry GJ, **155**:23
Bescos JM, **154**:525
Besim A, **155**:197, **155**:900
Beyer GA, **155**:1203
Bhalla M, **154**:51
Bilaniuk LT, B154:585
Bindman DJ, **154**:533
Binkovitz LA, **154**:323, **155**:424, **155**:501
Birnbaum BA, **154**:761
Bisset GS III, **154**:202, **155**:351, **155**:831
Bjarke E, **155**:893
Bjorkengren AG, **154**:331, **154**:1025, **155**:329
Black WC, **154**:17, **155**:625, **155**:1342
Blandino A, **154**:654
Blank N, **155**:23
Blask AN, **154**:657
Blendis LM, **155**:76
Blinder R, **155**:55
Bloem JL, **154**:763
Boechat MI, **154**:573
Bogan ML, **155**:781
Bognanno JR, **154**:1299
Bogumill GP, **155**:659
Bohlman H, **154**:151, **155**:867
Boiskin I, **154**:529
Bortoletto P, **155**:1241
Borushok KF, **154**:275
Bory JL, **155**:545
Bosanko, **155**:43
Bosley TM, **154**:167
Bosmans H, **155**:407
Bowen BC, **154**:1285
Bowie JD, **154**:903, **155**:595
Boxt LM, **154**:788, **155**:34
Boyer RS, **155**:385
Bozzao A, **155**:1309
Bradley MJ, **154**:900
Brady TJ, **154**:1053, **155**:1161
Brahme F, **154**:158
Bramson RT, **155**:754
Brant-Zawadzki M, **154**:1284, **155**:359
Braunstein EM, **154**:134, **155**:526
Bree RL, **154**:656
Breed W, **155**:1139
Breen T, **155**:883
Breiman RS, **154**:1284
Breit R, **155**:1285
Breitbach W, **155**:1303
Brendler CB, **154**:741
Brenner B, **154**:175
Brenner JS, **154**:199
Brenner RJ, **154**:420
Brewer WH, **155**:1283
Briggs SE, **154**:1003
Brismar J, **155**:621
Brogdon BG, **154**:867, **154**:1111
Brooks BS, **154**:577
Broome DR, **154**:1299
Brower AC, **154**:309, **154**:1236
Brown AT, **154**:1003
Brown BP, **154**:721
Brown JJ, **155**:1
Brown MD, **154**:821
Brown RC, **154**:301
Brun A, **155**:135
Brunelle F, **155**:421
Bruner JM, **154**:351
Bryant RG, **154**:175
Budzik RF Jr, **154**:459, **155**:317
Buetow PC, **155**:587, **155**:896, **254**:563
Bunchman TE, **154**:785
Bungo M, **155**:1135
Burch RA, **155**:1277
Burger PC, **155**:581, **155**:595
Burhenne HJ, **154**:1015, **155**:771, **155**:775
Burk DL Jr, **154**:549
Burke DR, **154**:183
Burnstein MI, **154**:555
Burrows PE, **154**:789
Burton D, **154**:521
Busuttil RW, **154**:393, **154**:573

C

Cagol P, **155**:1241
Callen PW, **154**:459
Cammarata CA, **154**:893, **154**:1337
Campbell JA, **154**:1177
Candiani F, **155**:1241
Caponovo E, **155**:1069
Capp MP, **155**:451, **155**:639
Caputo GR, **155**:723
Carella I, **154**:654
Carlsen SE, **154**:495, **155**:1137
Caroline DF, **154**:1124
Carrasquillo JA, **155**:1043
Carreira J, **155**:1344
Carrera GF, **155**:323
Carroll BA, **154**:398, **155**:1090

Carson SC, **155:**595
Carter J, **154:**151
Carver CD, **155:**187
Carver DK, **155:**177
Casarella WJ, **154:**1007
Cascade PN, **154:**1117, **155:**886
Casola G, **155:**1183
Cassel D, **155:**658
Castellino RA, **154:**251, **154:**1251, **155:**23
Castillo M, **154:**607, **154:**1051, **155:**559, **155:**900
Cavouras D, **155:**541
Cekirge S, **155:**197
Cha SH, **155:**527
Chalif M, **154:**45
Chaloupka JC, **154:**1051
Chamberlain DW, **154:**999
Chan KK, **154:**415, **154:**635, **155:**183
Chandnani V, **154:**1025
Chang C-h, **154:**900
Chang KH, **154:**809
Chang P, **154:**521
Channin DS, **155:**658
Chapnick E, **155:**1134
Charboneau JW, **154:**1
Charles HC, **154:**67
Chaudhuri TK, **154:**1347
Chen C, **154:**1025
Chen MYM, **155:**983, **155:**1344
Chenoweth JL, **155:**1188
Chess Q, **155:**1217
Chew FS, **155:**199
Chew WM, **155:**1059, **155:**1111
Chi JG, **155:**799
Chi TL, **154:**1269
Chiles C, **155:**419
Cho PS, **154:**415, **154:**635, **155:**183
Choe KO, **155:**971
Choi BI, **155:**799
Choplin RH, **154:**23
Choyke PL, **155:**85
Chrysikopoulos H, **155:**196
Citrin CM, **155:**1069
Clark DC, **154:**989
Clark K, **155:**43
Clark LR, **154:**884, **154:**1318
Clark RA, **154:**54, **154:**744, **155:**401, **155:**762
Clore FC, **154:**655
Cohan RH, **155:**291, **155:**991
Cohen EP, **154:**1126
Cohen J, **154:**903
Colby JM, **154:**532
Coldwell DM, **154:**1101, **155:**685, **155:**691
Cole BA, **155:**267
Cole RA, **154:**1275
Conard FU III, **155:**529
Conrad MR, **155:**198
Cook KL, **155:**39
Coombs RJ, **154:**1011
Cooper CJ, **154:**119, **154:**888, **154:**1325
Cooper SG, **155:**887
Cooperstein LA, **154:**709, **155:**654, **155:**1342
Cope C, **154:**183, **154:**203, **154:**1256, **155:**515
Corcoran HL, **154:**255
Cormier JM, **154:**425, **155:**425
Corradino G, **154:**1293
Correa J, **155:**1344
Cossi AF, **154:**1343
Cotty Ph, **155:**895
Coulaud JM, **154:**1349
Coumas JM, **155:**883
Courchesne E, **154:**593
Cox JF, **154:**1124
Cox L, **155:**35
Crade M, **155:**316
Crain BJ, **155:**581
Cramer B, **155:**1142
Cranston PE, **155:**1245
Crawford ED, **155:**303
Crawford S, **155:**1303
Cronan JJ, **154:**851, **155:**81
Cumming WA, **155:**422
Curry NS, **154:**307
Curtin A, **155:**200
Cynamon J, **154:**171
Czarnecki DJ, **154:**902, **155:**95, **155:**659
Czervionke LF, **155:**849

D

Daffner RH, **154:**554
Daniel TB, **154:**1091
Daniels DL, **155:**849
Dännert W, **154:**691
Danovitch GM, **155:**295
Das KM, **154:**421
Das Narla L, **155:**1283
David G, **154:**863
Davidson AJ, **154:**888, **154:**1325, **155:**1247
Davis JR, **155:**977
Davis LP, **154:**327
Davis M, **155:**986
Davis PC, **154:**607, **154:**831, **155:**142, **155:**900, **155:**1091
Davis SD, **155:**1185
Day DL, **154:**729, **154:**785
Daza RC, **155:**547
De Courten-Meyers G, **154:**361
Defalque D, **154:**515
Degryse HRM, **154:**343
Del Pizzo W, **155:**829
DeMarino GB, **154:**709
Demeure R, **154:**515
Demirci A, **154:**1126
Demopoulos R, **154:**295
Denath FM, **155:**200
Denny DF Jr, **155:**887
den Toom R, **155:**655
De Pena CA, **154:**351
DeRemer DR, **154:**1275
Dershaw DD, **155:**35
Desai A, **155:**611
De Schepper AMA, **154:**343
De Smet AA, **154:**555, **155:**549, **155:**1053
Deutsch L, **155:**1100
Deveikis JP, **154:**893, **154:**1337
DeVivo DC, **154:**1269
Deyoe LA, **155:**81
Diamond JJ, **154:**867
Diaz MJ, **154:**315
Dickson BA, **154:**255
Diehl J, **155:**153
Diehl LF, **155:**267
Dillon WP, **154:**375, **155:**573
Diner WC, **154:**1217
DiPietro MA, **154:**1223
Distell BM, **154:**903
Djang WT, **155:**581
Dobkin GR, **154:**857
Dodd GD III, **154:**459, **155:**317
Dodds WJ, **154:**87, **154:**953, **154:**965, **155:**247, **155:**289, **155:**805, **155:**1205
Dodero P, **154:**1049
Doi K, **154:**1107
Donaldson MC, **154:**857, **155:**1085
Donaldson SS, **154:**1251
Done S, **155:**587
Doppman JL, **154:**1075
Dorfman GS, **154:**851, **155:**81
Dowling CA, **154:**1305
Downey DB, **155:**29
Doy M, **155:**283
Drake DG, **154:**785
Drayer BP, **154:**163
Dresel S, **154:**585
Drylie D, **155:**196
D'Souza VJ, **154:**621
Duara R, **154:**1285
DuBose TJ, **154:**1348, **155:**199
Duchesneau PM, **154:**1275
Duerinckx AJ, **154:**393
Dufretay X, **154:**1349
Dumoulin CL, **155:**167
Dunaway HE Jr, **154:**735
Dunbar JS, **154:**149
Dunn DL, **155:**997
Dunnick NR, **154:**927, **155:**291, **155:**713, **155:**991
Duvoisin B, **155:**105, **155:**1139
Dwyer AJ, **155:**1043, **155:**1342
Dyer RB, **154:**621

E

Eber O, **154:**423
Edeiken J, **155:**113
Edell SL, **154:**572
Edelman RR, **154:**901, **154:**937, **155:**1237
Edwards MK, **154:**1299
Edwards MSB, **155:**143
Ehara S, **154:**777
Ehman RL, **155:**1117, **155:**1251
Ehrlich SM, **154:**779
Einhorn LH, **154:**1299
Eisenberg RL, **154:**1125
Eismont F, **154:**821
Eklund GW, **154:**1345
Elfenbein DS, **155:**422
El Gammal T, **154:**577
Elizondo G, **154:**287, **155:**763
Elkadi TAF, **154:**1060
Elliott JA, **155:**79
Ellis JH, **154:**1223, **155:**197
Endo K, **155:**845
Endoh W, **154:**1124
Endress C, **154:**1346, **155:**333
Engel A, **155:**1031
Engelstad BL, **154:**73, **155:**158
English JT, **154:**199
Epstein JI, **154:**741, **155:**1015
Ercole C, **155:**91
Erdman WA, **155:**897
Erickson SJ, **154:**87, **154:**399, **154:**1126, **155:**307, **155:**323, **155:**805
Eryilmaz M, **155:**900, **155:**1142
Esparza J, **154:**525
Eulderink F, **154:**763

F

Fabrikant JI, **155:**1202
Fache JS, **155:**771, **155:**775
Fackler ML, **155:**685, **155:**691
Fagelman D, **155:**1217
Fagerholm M, **154:**545
Fajardo LL, **155:**977
Fakhry J, **154:**124, **155:**246
Fanney D, **154:**888, **154:**1325
Farmaka H, **155:**657
Farner RM, **154:**721, **155:**785
Faro SH, **154:**757
Fata J, **155:**333
Feczko PJ, , 154:199, **155:**654
Fedder SL, **155:**200
Fekete F, **155:**277
Felker RE, **154:**241, **155:**1343
Fell SC, **154:**73
Fellows KE, **155:**896
Felmlee JP, **154:**185
Fermand M, **154:**425, **155:**425
Fernback SK, **154:**142
Ferris EJ, **155:**177
Ferrucci JT Jr, **154:**287, **154:**1003, **155:**61, **155:**473, **155:**763, **155:**943
Fiala M, **155:**311
Fiessinger JN, **154:**425
Filly RA, **154:**459
Finck EJ, **154:**181
Finestone H, **154:**201, **154:**657
Fink S, **154:**1347
Finn JP, **155:**1237
Fish G, **154:**307
Fisher DR, **154:**555, **155:**549
Fishman EK, **154:**741, **154:**1017, **155:**99, **155:**1267, **155:**1317
Fisk T, **155:**1327
Fitting DW, **155:**404
Flack MR, **154:**1075
Flaherty LE, **154:**327
Flanigin HF, **154:**577
Flannigan B, **155:**829
Fleischer AC, **154:**529
Fletcher BD, **155:**343
Fletcher G, **154:**817
Foley WD, **154:**399, **154:**1126
Forcade C, **154:**51
Forer L, **154:**888, **154:**1325
Forman BH, **154:**1003
Formanek AG, **154:**898
Forsberg DA, **154:**751, **155:**1037
Fortin PR, **155:**1141
Foster MA, **154:**79
Foster TH, **154:**175
Fouquet B, **155:**895
Fournier D, **155:**1139
Francis CW, **154:**175
Frank JA, **155:**85, **155:**1043
Frank R, **155:**1134
Frank SJ, **154:**1075
Franken EA Jr, **154:**271, **154:**345, **154:**1123
Franquet T, **154:**525
Freed HA, **155:**555, **155:**1141
Freedom RM, **154:**789
Freeny PC, **154:**79
Fretz CJ, **155:**763
Frey GD, **154:**870
Fried AM, **154:**544
Friedland GW, 154:1100, **155:**1020
Friedman AC, **154:**1124, **154:**1222, **155:**739
Friedman AH, **155:**581
Friedman D, **154:**797
Friedman H, **155:**1285
Friedman PJ, **154:**33, **155:**738, **155:**1344
Friefeld GD, **154:**405
Froehlich JA, **154:**851
Fromowitz FB, **155:**739
Fueredi, GA, **155:**95
Fujino H, **155:**507, **155:**1221
Fujita J, **155:**653, **155:**1135
Fujita M, **154:**509
Fulcher AS, **154:**259, **155:**1283
Fullagar PR, **155:**643

G

Gaa J, **154:**1003
Gabata T, **155:**1009
Gado M, **154:**369
Gaeta M, **154:**654
Gage TS, **155:**529
Gagliardi RA, **154:**94, **154:**899, **154:**952, **155:**235, **155:**641
Gallego F, **154:**997
Gallucci M, **155:**1309
Gamstaetter G, **154:**654
García-Medina V, **155:**1345

Gareen IF, **154**:265
Garneau RA, **154**:271
Garrell RH, **155**:423
Garrett MK, **154**:1250
Garvin AJ, **154**:307
Gatewood OMB, **155**:89
Gaux JC, **154**:1349
Gay JN, **154**:577
Gay SB, **154**:55, **154**:871, **155**:195
Gayet B, **155**:277
Gebarski SS, **154**:360, **154**:1074, **155**:166, **155**:1292
Gebauer A, **154**:656
Geborek P, **155**:329
Gehman KE, **155**:79
Geihsler JD, **155**:989
Geisler FH, **155**:603
Gelfand DW, **154**:279, **155**:48, **155**:195, **155**:983, **155**:1344
Gelfand MJ, **154**:202
Genez BM, **154**:315
Genieser NB, **154**:797
Gennari RC, **154**:709
Gentili A, **155**:867
Gerard P, **155**:1134
Gerlach R, **154**:1305
Gerritsen PG, **155**:1097
Gerst PH, **155**:1137
Gessert J, **155**:1100
Geubel A, **154**:515
Gevenois PA, **155**:1021
Ghaed V, **155**:1267
Gibney RG, **154**:203, **154**:1015
Giger ML, **154**:1107
Gigot J-F, **154**:515
Gilula LA, **154**:129, **154**:559
Ginalski JM, **155**:299
Gingrich R, **154**:721
Giovanniello J, **154**:424
Glassberg RM, **154**:47, **155**:397
Glasser SA, **154**:1069
Glass-Royal M, **154**:890, **154**:1331, **155**:659
Glazer HS, **154**:200, **155**:31, **155**:495
Glenthøj A, **154**:1087
Glickstein MF, **155**:397
Godwin JD, **154**:41
Goell WS, **154**:902
Goerg C, **155**:795
Goerg K, **155**:795
Goga D, **155**:895
Gold RE, **154**:69
Gold RH, **154**:568, **154**:713, **155**:1256
Goldberg ME, **154**:286
Goldfarb CR, **154**:201, **154**:657
Goldman ML, **154**:1101
Goldstein RB, **154**:459
Goldwag S, **154**:849
Gomes AS, **154**:393, **154**:975
Gonzalez C, **155**:1344
Good BC, **154**:709, **155**:654, **155**:1342
Goodacre BW, **155**:771
Goodman P, **154**:1207
Goose PW, **154**:884, **154**:1318
Gopinath N, **155**:76
Gorden P, **154**:1075
Gordon CJ, **155**:1105
Gordon DM, **155**:989
Gordon RB, **154**:281, **154**:499, **154**:761
Gornbein JA, **154**:713
Gort HBW, **155**:422
Gotoh M, **154**:1124
Goulatia RK, **155**:339
Goulet RJ Jr, **155**:781
Goupille Ph, **155**:895
Gourtsoyiannis N, **155**:541
Govoni AF, **154**:265, **155**:1185
Graf BK, **154**:555, **155**:549
Grafe M, **154**:593
Grafton WD, **154**:1125
Gramm HF, **154**:476, **154**:1198
Grant EG, **154**:393, **154**:573, **154**:1349, **155**:295, **155**:538
Grantham JR, **154**:655
Grasl MCh, **154**:411
Gray JE, **154**:185
Grayson EV, **154**:576, **154**:1268, **155**:1302
Green BA, **154**:821
Green CE, **154**:884, **154**:1318, **155**:191
Greenspan A, **154**:1035, **155**:1347
Greenwood C, **155**:199
Grevers G, **154**:585
Griffith J, **155**:1100
Grimley PM, **155**:1247
Grissom LE, **155**:837
Gritzmann N, **154**:411
Grix A, **154**:1025, **155**:1347
Gross GM, **154**:1097
Gross GW, **154**:779
Grossman RI, **154**:167, **154**:1069
Gruessner R, **155**:997
Gudi K, **154**:424
Guenin M, **154**:897
Guenther RW, **154**:617
Guirao J, **155**:1345
Gundry CR, **154**:337, **154**:1233
Gur D, **154**:709, **155**:613, **155**:654, **155**:1342
Guyot DR, **155**:333

H

Haacke EM, **155**:159, **155**:951
Hackney DB, **154**:1069, **155**:108
Haddad MC, **154**:989
Haggerty MF, **155**:1136
Hahn PF, **154**:287, **154**:1003, **155**:61
Hall FM, **154**:897, **154**:903, **155**:195
Hall TR, **154**:573
Haller JO, **155**:1273
Hallin R, **155**:1141
Halvorsen RA Jr, **155**:997
Hamilton P, **154**:1187
Hamper UM, **155**:1015, **155**:1138
Han BK, **154**:202, **154**:361
Han JK, **155**:527, **155**:799
Han MC, **154**:809, **155**:527
Han MH, **154**:809
Hanafee W, **154**:374, **154**:584
Hansen ME, **155**:1177
Harada K, **155**:1227
Harcke HT, **155**:837
Hardy C, **155**:259
Harnsberger HR, **155**:385
Harrell JH II, **155**:1183
Harris K, **154**:424
Harris RD, **154**:1122
Harshfield DL, **154**:1217
Hartman DS, **154**:888, **154**:1325, **155**:1247
Hartman GW, **154**:645
Hasegawa H, **154**:1203, **155**:49
Hasson JH, **155**:735
Hata Y, **155**:421, **155**:507, **155**:653, **155**:1135, **155**:1221
Hatabu H, **155**:194, **155**:845
Hathorn JW, **154**:67
Haughton VM, **154**:817, **155**:849
Hawes DR, **154**:1345
Hawes RH, **155**:781
Hawkins IF Jr, **154**:1091
Hawkins RA, **154**:975
Hayes WS, **154**:888, **154**:1325, **155**:1247
Healy MV, **155**:357
Hecker J, **155**:1105
Hegedüs L, **154**:1087
Heinz ER, **155**:581
Heitbrink MA, **154**:202
Helmer E, **154**:603
Helmer M, **154**:411
Helms CA, **154**:319, **155**:896
Helvie MA, **155**:39, **155**:1195
Hendee WR, **154**:647
Henderson JM, **154**:1007
Hendrix LE, **155**:849
Henkelman RM, **155**:1066
Hennerici M, **154**:1061
Hennessey JG, **155**:1317
Henry W, **155**:1100
Herfkens RJ, **155**:55
Herman SJ, **154**:999
Herman TE, **154**:806
Hermans J, **154**:763
Hernandez RJ, **154**:1241
Hernanz-Schulman M, **154**:797
Herndon JH, **154**:851
Hertzberg BS, **154**:903, **155**:595
Hesselink JR, **154**:593, **154**:837
Heveron ED, **154**:867
Heydermann J, **155**:547
Hickey AM, **155**:1043
Hicks ME, **154**:725
Hidaka A, **155**:194, **155**:845
Higashihara H, **154**:1257, **155**:405
Higgins CB, **155**:259, **155**:723, **155**:1111
Higgins SS, **155**:259
Higgs JB, **154**:315
Higuchi K, **155**:194
Hilal SK, **154**:1269
Hill LW, **155**:199
Hindman BW, **154**:1127, **154**:1128
Hirohashi S, **155**:49
Hoashi T, **155**:405
Ho BKT, **154**:415, **154**:635
Ho C, **154**:1233
Ho CS, **155**:67
Hodgman CG, **155**:1251
Hoffer FA, **155**:1261
Hoffman JC Jr, **154**:607, **154**:831, **155**:1091
Ho K-C, **154**:817
Hollerman JJ, **155**:685, **155**:691
Holm HH, **154**:1087
Holmes CL, **154**:393
Holscher HC, **154**:763
Holtås S, **155**:135, **155**:329
Holtz PM, **155**:1015
Honda H, **154**:271
Hong KS, **155**:511
Hoogewoud HM, **154**:901, **154**:937
Hopper KD, **154**:115, **155**:267
Hopsu EVM, **154**:1259
Horvath K, **155**:1043
Houlle D, **154**:425, **155**:425
Howard JM, **154**:1011
Hricak H, **155**:1111
Hu LB, **155**:1343
Hua CL, **154**:1348
Huang HK, **154**:415, **154**:635, **155**:183
Hubner KF, **154**:1024
Hudgins PA, **154**:1051, **155**:559
Huebsch P, **155**:1031
Hughes JMB, **155**:455
Hull D, **155**:529
Hulnick D, **154**:499
Hunter DW, **154**:729
Hurst GC, **154**:1275
Huskison WT, **154**:118
Hyde JS, **155**:323

I

Iida Y, **155**:194, **155**:845
Iio M, **154**:505
Ikeda DM, **155**:39, **155**:1195
Ikeya S, **154**:1203
Ikezoe J, **154**:1079, **154**:1181
Ilstrup DM, **155**:1251
Imam N, **155**:61
Imazato M, **154**:201
Inculet RI, **155**:79
Ingram TL, **154**:893, **154**:1337
Irino S, **155**:653, **155**:1135
Ishibashi H, **155**:895
Isik V, **154**:1126
Isobe Y, **154**:201
Itai Y, **154**:505
Itoh K, **155**:61
Iyer GN, **155**:1137

J

Jackler RK, **155**:573
Jackson FI, **154**:899, **154**:1121, **155**:894
Jackson JE, **155**:391
Jackson VP, **154**:1196
Jacobsson B, **155**:621
Jacoby WT, **155**:291
Jaeger Ph, **155**:299
Jain CU, **154**:424
Jamart J, **154**:515
James SS, **155**:422
Janick PA, **154**:1069
Jaques PF, **155**:198
Jaramillo D, **155**:1261
Jeffrey RB Jr, **154**:27, **154**:275
Jeffs RD, **155**:1267
Jelinek JS, **154**:563, **155**:365, **155**:424, **155**:896, **155**:1257, **155**:1267
Jenkins JJ, **155**:343
Jeong HJ, **155**:971
Jesmanowicz A, **155**:323
Joffe N, **154**:897
Joffre F, **154**:613
Johnson CD, **154**:99, **155**:501
Johnson CE, **155**:873
Johnson JE, **155**:323
Johnson JO, **154**:539
Johnson KK, **154**:405
Johnson S, **155**:420
Jolles H, **154**:259
Joseph S, **155**:1348
Josephs SH, **154**:803, **155**:133
Joslyn JN, **154**:1293
Jóźwiak S, **155**:419
Julsrud PR, **155**:271

K

Kadoya M, **155**:1009
Kahn CE Jr, **154**:635
Kainberger FM, **155**:1031
Kairemo KJA, **154**:1259
Kanai T, **154**:1124
Kanal E, **154**:384, **155**:152
Kandarpa K, **154**:1105
Kang HS, **154**:337, **154**:1025
Kang K, **154**:585
Kangarloo H, **154**:635
Kanzer M, **155**:365
Kao SCS, **154**:345
Kaplan ID, **154**:745
Kaplan PA, **154**:319, **154**:1025, **155**:237, **155**:896
Kappers-Klunne MC, **155**:1097
Karantanas AH, **155**:893, **155**:1343
Karasick D, **154**:549, **155**:119
Karmel MI, **155**:1085
Karstrup S, **154**:1087
Karzel R, **155**:829

Kasagi K, **155**:194, **155**:845
Kasahara A, **155**:1227
Kasi LP, **154**:796
Kaszar-Seibert DJ, **154**:533
Kaude JV, **154**:199, **155**:196
Kaufman RA, **154**:569
Kaufman SL, **154**:1007
Kaveggia LP, **155**:295
Kawashima A, **155**:965
Kawata S, **155**:1227
Kay C, **155**:540
Kaya A, **155**:1142
Kedar R, **155**:423, **155**:655
Kelcz F, **155**:531, **155**:1053
Keller FS, **164**:1097
Kelly WM, **155**:1117
Kelsey C, **155**:986
Kenney PJ, **155**:485
Kerns SR, **154**:55, **155**:195
Kersting-Sommerhoff BA, **155**:259
Ketkar M, **155**:655
Kikuchi Y, **155**:283
Kilcoyne RF, **154**:1029, **155**:554
Kim C-W, **154**:809
Kim D, **154**:421, **154**:1213, **154**:1307, **155**:898
Kim EE, **154**:796
Kim IO, **154**:809
Kim KS, **155**:1285
Kim S, **155**:1137
Kim YH, **154**:1346
Kimizu K, **154**:385
Kimme-Smith C, **154**:713, **155**:124
Kimmey M, **154**:1101
Kimura F, **155**:1285
Kimura K, **154**:345
Kimura T, **155**:405
King BF, **154**:1219, **155**:1251
King DW, **154**:577
King GA, **154**:1346
Kirks DR, **154**:202, **155**:831
Kitagawa M, **154**:419
Kitamura T, **154**:509
Klatt EC, **154**:27
Klaus E, **155**:105
Klein MV, **154**:1245
Kleinman PK, **154**:1047, **155**:703
Kling GA, **154**:327
Klinkhamer PJJM, **155**:1139
Kloet AG, **155**:422
Kloetzsch C, **154**:1061
Kneeland JB, **155**:323, **155**:849
Knudson GJ, **154**:399
Ko YT, **154**:107, **155**:511
Kobayashi T, **154**:1079
Kochhar R, **154**:421
Koenigsberg M, **155**:995
Koga T, **155**:895
Koganemaru F, **155**:405
Koike K, **154**:789
Kok FP, **154**:202
Költringer P, **154**:423
Komatsu Y, **155**:1009, **155**:1221
Kondo C, **155**:259, **155**:723
Konishi J, **155**:194, **155**:845
Koolpe HA, **155**:1103
Kopans DB, **155**:743, **155**:748
Kopecky KK, **155**:781
Korn WT, **154**:533
Korobkin M, **154**:1096
Kostrubiak IS, **154**:125
Kowall NW, **154**:1053
Koyama H, **154**:1079
Kozuka T, **154**:1079, **154**:1181, **155**:1227
Kransdorf MJ, **154**:309, **154**:563, **155**:424, **155**:896, **155**:1257, **155**:1266
Krexner E, **155**:825
Kriegshauser JS, **154**:1219, **155**:271
Kronthal AJ, **154**:741
Krysiewicz S, **154**:1347
Kuboya Y, **154**:777
Kuhlman JE, **154**:741, **155**:1317
Kulik WJ, **154**:1127, **154**:1128
Kumar A, **155**:339
Kumar R, **155**:113
Kumar S, **155**:1348
Kuni CC, **155**:13
Kuroda C, **154**:1124, **155**:1227
Kursunoglu-Brahme S, **154**:337, **154**:1233, **155**:829
Kurtz AB, **154**:691
Kushner DC, **155**:133

L

LaBrecque D, **154**:721
Lack EE, **155**:659
La Fontaine RL, **154**:975
Lai A, **154**:1053
Laing FC, **154**:275
Lakshmiratnam K, **155**:655
Lal AV, **155**:1348
Lally JF, **154**:757
Lambiase RE, **155**:81
Laméris JS, **155**:1097
Lang EK, **154**:735
Lang EV, **154**:33, **154**:725, **155**:1344
Lange RH, **154**:555, **155**:549
Langsteger W, **154**:423
Lanzieri CF, **154**:1263
Larson TC III, **155**:1117
Lask D, **154**:111
Lasser EC, **154**:1343, **155**:652
Lathi SG, **155**:1096
Lauerman WC, **154**:315
Lautin EM, **155**:739
Lavis VR, **155**:611
Lawson TL, **154**:399, **155**:307, **155**:805, B154:87
Lebel F, **155**:1141
Lebowitz RL, **155**:125, **155**:561
Lecumberri FJ, **154**:525
Leder RA, **155**:291, **155**:713, **155**:991
Lee AS, **155**:1161
Lee DH, **154**:107, **155**:511
Lee EL, **154**:65
Lee G, **154**:1127, **154**:1128
Lee KS, **154**:1346
Lee MJ, **154**:1003
Lee RE, **154**:623
Lee SH, **154**:1015, **155**:775
Lee WJ, **155**:799
Lee Y-Y, **154**:351
Leeming BWA, **154**:1307
Leepson E, **155**:1327
Leetzow ML, **154**:185
Leitman BS, **154**:51
Lemmi MA, **155**:343
Lenhart MK, **155**:1257
Leonidas JC, **154**:1123, **155**:350
Lerner HH, **155**:420
Lerud KS, **155**:741
Letourneau JG, **154**:729, **154**:785, **155**:13, **155**:91, **155**:997
Leung AN, **154**:487
Levine AJ, **155**:43
Levine E, **154**:771, **155**:1025
Levine MS, **154**:1157, **155**:933
Lev-Toaff AS, **154**:982, **154**:1124
Levy A, **154**:903
Lewis CA, **155**:559
Libshitz HI, **155**:965
Lichter AS, **155**:39
Licigrai G, **154**:1049
Ligiéres G, **155**:425
Lile T, **155**:303
Lim JH, **154**:107, **155**:511, **155**:1001
Lim V, **155**:1077
Lindfors KK, **154**:261
Lindholm K, **154**:1191
Lind P, **154**:423
Lindstrand A, **154**:331
Ling A, **155**:625, **155**:1043
Lipchik EO, **154**:399
Lissac J, **154**:1349
Lissner J, **154**:585
Lituania M, **154**:1049
Liu SS, **154**:163
Lo H-H, **154**:1078
Loewenstein DA, **154**:1285
Löfgren M, **154**:1191
Logemann JA, **154**:953, **154**:965
Loisel JC, **155**:1347
Lombardo DM, **155**:55
Longley DG, **155**:997
Longmaid HE III, **154**:1034
Lopiano M, **155**:1327
Lorig RJ, **155**:656
Lossef SV, **155**:617
Lott SA, **154**:261
Lou SL, **155**:183
Lovell FA, **155**:1245
Low RA, **155**:13
Lowrey CE, **154**:315
Lowry PA, **155**:611
Lu CT, **154**:1107
Lu DSK, **155**:67
Lubat E, **154**:761
Luetkehans TJ, **155**:741
Luna-Fineman AS, **155**:357
Lund JT, **155**:271
Lusk RP, **155**:425
Lynch JC, **155**:267

M

Macaulay SE, **155**:1183
Mack LA, **154**:143
MacMahon H, **154**:1107
Madewell JE, **155**:113
Madrigal M, **155**:1345
Maeder PP, **155**:135
Magid D, **154**:1017, **155**:99, **155**:1317
Mahoney MC, **154**:255
Makuuchi M, **155**:49
Maldonado V, **154**:899
Mali WPTM, **154**:902, **155**:422
Malone DE, **155**:771
Manivel JC, **155**:91
Mann FA, **155**:336, **155**:816
Mann RW, 58, **154**:6, **154**:420, **154**:658, **154**:1347
Mannick JA, **154**:857, **155**:1085
Mansoory A, **154**:757
Mantineo G, **154**:654
Mantoni M, **154**:535
Manzione JV, **154**:1344
Maravilla KR, **154**:1305
Marchal G, **155**:407
Marcus RE, **154**:151
Marder VJ, **154**:175
Marina NM, **155**:343
Mark LP, **155**:849
Markivee CR, **154**:659, **155**:1188
Marks WH, **155**:536
Marom Z, **155**:275
Martin LG, **154**:1007
Martineau BS, **155**:1341
Martinez S, **154**:751, **155**:1037
Martínez-Noguera A, **155**:1345
Marukawa T, **154**:1124, **155**:1227
Marx MV, **154**:725
Masaryk TJ, **154**:151, **154**:159, **155**:159, **155**:867
Masciocchi C, **155**:1309
Matalon TAS, **154**:847
Matamoros A Jr, **155**:237
Mathews VP, **154**:1299
Matsen FA III, **154**:1029
Matsui O, **155**:1009
Mattle HP, **154**:901, **154**:937, **155**:1237
Mattrey RF, **154**:539
Mattsson TA, **154**:989
Mauer SM, **154**:785
Mauro MA, **155**:198
Mawad ME, **155**:1303
McAlister WH, **155**:425
McAllion SJ, **155**:1346
McAsey ME, **155**:307
McBeath AA, **155**:1053
McCabe DJ, **154**:656
McCauley DI, **154**:51
McCauslin MA, **155**:267
McClennan BL, **155**:225, B154:645
McCormick B, **155**:35
McCowan TC, **155**:177
McDiarmid SV, **154**:573
McGahan JP, **154**:143
McGrath FP, **154**:1015
McKee A, **154**:1053
McKinney M, **155**:729
McKinstry RC, **154**:1053
McKusick MA, **154**:422
McLaurin RL, **154**:361
McLeod RA, **154**:323, **155**:424, **155**:817
McNeal JE, **155**:811
McNeill GC, **155**:311
Meador K, **154**:577
Medina L, **154**:1269
Megibow AJ, **154**:27, **154**:281, **154**:295, **154**:761
Meglin AJ, **155**:1267
Meilstrup JW, **155**:267
Meizner I, **154**:903
Mellinger BC, **154**:1347
Mendelsohn D, **155**:153
Mendelson DS, **155**:275
Menu Y, **155**:277
Meranze SG, **154**:183
Mercanti AM, **155**:1134
Merchant SA, **154**:426, **155**:423, **155**:655, **155**:660
Merriam GR, **154**:1075
Merrick HW, **154**:1011
Mestayer RJ, **154**:893, **154**:1337
Metreweli C, **154**:900
Metz CE, **154**:419, **154**:1121, **155**:763
Metzger TS, **154**:847
Mewissen MW, **154**:399
Meyer A, **155**:193
Meyer WH, **155**:343
Meyers PC, **154**:86, **154**:1125
Meyers W, **155**:55
Meza MP, **154**:899
Mezwa DG, **155**:654
Micheli L, **154**:657
Michelson JD, **154**:1017
Miketic LM, **154**:709
Milam SG, **155**:785
Miller AB, **155**:743, **155**:1133
Miller DL, **154**:1075
Miller DP, **155**:307
Miller GJ, **155**:303
Miller MA, **155**:1141
Miller RR, **154**:487, **154**:983
Miller WT, **155**:653
Millikan WJ Jr, **154**:1007
Mills DG, **154**:375
Milner LB, **154**:486, **155**:22
Miranda CP, **155**:1100
Mirowitz SA, **154**:369, **155**:1
Mirvis SE, **154**:1293, **155**:603
Misaki T, **155**:845
Mistretta CA, **155**:580, **155**:1053

Mitchell DG, **154**:549
Mitchell MJ, **155**:339
Miyamoto Y, **155**:895
Miyata S, **154**:419
Modic MT, **154**:151, **154**:159, **155**:159, **155**:867
Moes CAF, **154**:789
Mohanty M, **155**:1348
Mojtahedi S, **154**:1107
Molina PL, **155**:31, **155**:495
Mompoint D, **155**:277
Monden M, **1541**124, **155**:1227
Montalvo BM, **154**:821
Montemayor KA, **154**:105, **155**:73
Montes M, **154**:525
Monticciolo DL, **155**:751
Moore J, **154**:1053
Moore SG, **154**:745
Morgan DE, **155**:735
Mori T, **154**:1124
Morimoto S, **154**:1079, **154**:1181
Morin LRM, **155**:1347
Moriyama N, **154**:1350, **155**:49
Morparia HK, **154**:426, **155**:660
Morris CS, **155**:337
Morris DM, **154**:1125
Morris M, **154**:1029
Morris S, **155**:198
Morris TW, **154**:300
Morrison MC, **154**:1003
Morse SS, **154**:1103, **155**:401
Moseley ME, **155**:1059
Moser RP Jr, **154**:309, **154**:563, **154**:1176, **154**:1240, **155**:113, **155**:1257
Moskowitz M, **155**:743
Moss GD, **154**:1086
Mostbeck G, **154**:656
Mostowfi K, **155**:547
Movson JS, **154**:903
Mowschenson PM, **154**:1213
Mueller PR, **154**:233, **154**:1003
Mukai K, **154**:1203
Müller NL, **154**:487, **154**:983
Mullhollan TJ, **154**:65
Mullin DM, **154**:659
Mulne A, **155**:153
Munk PL, **154**:391
Muñoz A, **B154**:997
Muntz HR, **155**:425
Murakami JW, **154**:593
Murakami T, **155**:1227
Muramatsu Y, **154**:1203, **154**:1350, **155**:49
Murphy FB, **154**45
Murphy TM, **155**:1136
Muz J, **154**:327

N

Nadel SN, **155**:291, **155**:991
Nahum H, **155**:277
Naidich DP, **154**:51
Nakahara K, **154**:1181
Nakamura H, **155**:653, **155**:1135
Nakanishi K, **154**:509
Nakasato T, **154**:777
Nalesnik WJ, **155**:1188
Nath H, **154**:493, **155**:735
Nawano S, **154**:1350
Neglia W, **155**:739
Nelson DW, **155**:970
Nelson MC, **155**:659
Nelson RC, **154**:291, **155**:655
Neuhold A, **155**:1031
Newbold R, **154**:119
Newmark H III, **154**:1164
Newton TH, **154**:375
Ney DR, **154**:1017, **155**:1317
Ng J, **154**:1237
Nijs HGT, **155**:655
Nino-Murcia M, **154**:521
Nishiyama K, **154**:1079
Niwa Y, **155**:421, **155**:507, **155**:1221
Nomura F, **155**:1135
Nooy MA, **154**:763
Norman D, **154**:375, **155**:1059
Numaguchi Y, **154**:1293
Nyberg DA, **154**:143
Nylander WA, **154**:529

O

Oates E, **155**:423
Oberly TD, **155**:531
O'Brien MJ, **154**:50
Oestreich AE, **154**:1250
Ohta Y, **155**:895
Ohtomo K, **154**:505
Ohtomo Y, **154**:505
Okamura J, **154**:1124
Okazaki M, **154**:1257, **155**:405
Okazaki N, **155**:49
Okimura T, **154**:385
Okuda S, **154**:509
Oldfield EH, **154**:1075
O'Leary DH, **154**:857, **155**:1085
Ollier P, **155**:277
Olmedilla G, **154**:997
Olson DL, **154**:1126
Omlie MR, **155**:373
O'Neil J, **154**:199
Ongseng F, **154**:201, **154**:657
Ono H, **155**:405
Oravec D, **155**:1189
Osborn AG, **154**:630, **155**:385
Osborne MP, **155**:35
Ott DJ, **154**:279, **155**:195, **155**:933, **155**:983, **155**:1344
Owsley DW, **154**:1347
Ozaksoy D, **155**:657
Ozcan U, **154**:1126

P

Pagny JY, **154**:1349
Pais MJ, **155**:1049
Palazzo L, **155**:277
Paley D, **154**:125
Palmer P, **155**:986
Pantelidis N, **155**:541
Parham DM, **155**:343
Parikh V, **155**:1137
Park JH, **154**:898, **155**:527
Parker BR, **154**:1251, **155**:357
Parkey RW, **155**:897
Parsi JE, **155**:365
Parvey HR, **154**:1125
Passariello R, **155**:1309
Patel V, **155**:655
Patel YD, **154**:179
Paterson CR, **155**:1346
Patrick R, **155**:1233
Patronas NJ, **154**:893, **154**:1075, **154**:1337, **155**:1043
Patt RH, **154**:633
Patten RM, **155**:109
Patterson K, **154**:803
Patterson RJ, **155**:831
Paulin S, **154**:898
Pavlicek W, **155**:1176
Payne WD, **154**:729
Pedersen JF, **154**:535
Pedersen MI, **154**:203
Peitschmann P, **155**:825
Peñarrocha L, **154**:997
Pendergrass TW, **155**:347
Pentecost MJ, **154**:181
Peppler WW, **155**:1053
Pera A, **155**:167
Perkash I, **154**:521
Perman WH, **155**:1
Pernicone JR, **155**:167
Perrella RR, **154**:393, **155**:295, **155**:538
Perret RS, **155**:307
Peterly CG, **155**:894
Petrik JH, **155**:659
Pettersson H, **154**:331, **155**:329
Pfister RC, **154**:233
Phillips WC Jr, **154**:1149
Phillipson J, **154**:539
Picus D, **154**:725
Pierce ME, **154**:1127
Pierro JA, **155**:545
Piper MA, **155**:373
Piraino DW, **155**:555, **155**:1140
Pirsch JD, **155**:531
Platt JF, **154**:1223, **155**:197
Poch-Broto J, **154**:997
Polak JF, **154**:857, **155**:1085
Pollak JS, **155**:887
Polysalov VN, **155**:1235
Poon PY, **155**:29
Popovich MJ, **154**:603
Porter D, **155**:93
Porter DH, **154**:421, **154**:1213, **155**:898
Porter LM, **155**:199
Porter RM, **154**:659
Portmann L, **155**:299
Post MJD, **154**:821
Post PJM, **155**:1097
Potchen EJ, **155**:167
Pozniak MA, **154**:545, **155**:531
Prasad K, **155**:339
Prassopoulos P, **155**:541
Preger L, **155**:282
Press GA, **154**:593, **154**:837
Price JC, **154**:185
Price SC, **154**:863
Pringot J, **154**:515
Proto AV, **154**:259
Proto E, **155**:1241
Pryce AP, **155**:881
Puffenbarger, **155**:401
Pyeritz RE, **155**:99

Q

Quencer RM, **154**:821
Querol ES, **155**:1345
Quinn SF, **154**:1103, **155**:323, **155**:1141
Quiroz F, **155**:307

R

Rabin AM, **154**:305
Rabinson S, **154**:111
Racette CD, **154**:757
Radecki PD, **154**:1124
Radin DR, **154**:27
Radtke RA, **155**:581
Ragozzino MW, **155**:1233
Rai AM, **155**:420
Raillat C, **154**:613
Ralls PW, **154**:27, **155**:517
Ramakantan R, **154**:61, **154**:200
Ramchandani P, **155**:1103
Ramirez A, **155**:1303
Rand F, **155**:1261
Randall PA, **155**:982
Rao VRK, **155**:1348
Rapaport SI, **154**:239
Raptopoulos V, **154**:532, **155**:506
Raval B, **154**:1207
Ravimandalam K, **155**:1348
Rawat B, **155**:771
Read RC, **154**:1217
Reading CC, **154**:1, **154**:1219
Reagan K, **154**:884, **154**:1318
Recht MP, **154**:183
Reed JC, **154**:23
Reid WM, **154**:893, **154**:1337
Reifsnyder AC, **154**:65
Reimer P, **155**:1161
Reinhart M, **154**:1025, **155**:1347
Relland J, **154**:1349
Remmele W, **154**:654
Renner JB, **154**:135
Rennie D, **155**:889
Resch H, **155**:825
Resnick D, 37, **154**:3, **154**:337, **154**:1025, **154**:1233, **154**:1245, **155**:829
Resnik CS, **154**:125, **155**:1169
Reuter SR, **155**:1331
Reyes N, **155**:153
Rice S, **154**:149
Richardson P, **155**:93
Richmond BJ, **155**:555, **155**:1141
Rifkin MD, **154**:549, **154**:691
Rivera V, **155**:1303
Robbins BS, **155**:780
Rockette HE, **154**:709
Rockwood CA, **154**:1029
Roddie ME, **155**:391
Roe D, **154**:975
Rogers LF, **155**:624
Roh JK, **154**:809
Rohrmann CA Jr, **154**:79, **154**:1002
Rollins N, **155**:153
Roniger WE, **154**:735
Rorke LB, **155**:865
Rose BS, **154**:425, **155**:989
Rosen BR, **154**:1053
Rosenbaum DM, **155**:347
Rosenberg MA, **154**:342, **154**:988, **155**:602
Rosenblatt M, **155**:739
Rosenquist CJ, **154**:644, **154**:652
Rosenthal JT, **155**:295
Rosenthal RE, **154**:658
Ross JS, **154**:151, **154**:159, **155**:159, **155**:867
Rothman B, **154**:1229
Rousseau H, **154**:613
Routh WD, **154**:1097
Roux D, **154**:613
Rowland GA, **154**:291, **155**:655
Rubaltelli L, **155**:1241
Rubesin SE, **154**:1157
Rubeson SE, **155**:933
Rubin JM, **154**:1223, **155**:197
Ruggieri PM, **155**:159
Rumancik W, **154**:797
Rummeney E, **154**:287
Russ PD, **154**:405
Russell EJ, **155**:1285
Rydholm U, **155**:329
Ryzhkov VK, **155**:1235

S

Sacks B, **155**:899
Sacks BA, **154**:422
Sacks EM, **154**:1344
Safirstein BH, **154**:897
Safrit H, **154**:119
Sagel SS, **154**:200, **155**:31
Sahn DJ, **154**:1060
Sahn SA, **154**:481
Saini S, **154**:287, **154**:1003, **155**:60, **155**:61
Saka H, **155**:1135
Sakai S, **155**:1135
Sakon M, **154**:1124
Sakurai M, **154**:1124, **155**:1227
Salciccioli G, **155**:333
Salerno MD, **154**:425
Salford LG, **155**:135
Salmaso R, **155**:1241

Salmon I, **155:**1021
Salomonowitz E, **155:**1031
Saloner D, **154:**623
Samuel E, **155:**425
Samuels T, **154:**1187
Sanders C, **154:**493, **155:**735
Sanders DE, **155:**743
Sanders RC, **154:**741
Sandler MP, **154:**529
Sandstrom JC, **155:**1
Sargent EN, **154:**64
Sarti D, **154:**1229
Sartor K, **154:**369
Sartoris DJ, **154:**337, **154:**882, **154:**1245
Sarwar M, **155:**384, **155:**848
Sasaki K, **154:**385
Sasaki M, **154:**777, **155:**1009
Sato K, **155:**653
Sato T, **154:**777
Sato Y, **154:**345
Savader BL, **155:**1138
Savino PJ, **154:**167
Saxey R, **154:**657
Scanlan KA, **154:**545
Schabel SI, **154:**307
Schaefer DJ, **155:**1105
Schaighofer B, **154:**1233
Scheinbaum K, **154:**171
Schellhas KP, **155:**373
Schellinger D, **154:**893, **154:**1337
Scheltens Ph, **155:**899
Schenck J, **154:**205
Schils JP, **154:**1025, **155:**555, **155:**1141
Schinella RA, **154:**281
Schlesinger AE, **154:**1241
Schlueter FJ, **154:**202
Schmidt RA, **154:**419, **154:**1107, **154:**1121
Schmiedl U, **154:**1305
Schnyder P, **155:**105
Schoeneman MJ, **154:**201
Schrader M, **155:**867
Schrock TB, **154:**73
Schulte SJ, **154:**79, **154:**1002, **155:**1211
Schütte HE, **155:**1097, **155:**1321
Schwaighofer BW, **154:**337, **154:**1245
Schwartz LH, **155:**617
Schwerk WB, **155:**795
Scott JA, **154:**1149
Scott LD, **155:**611
Scott MD, **154:**621
Scudamore CH, **154:**203
Sedman AB, **154:**1223
Seelos KC, **155:**259
Segal AJ, **155:**660
Seibert CE, **155:**652
Sekiya M, **154:**1107
Selby HG, **154:**871
Selby JB Jr, **154:**871
Selman WR, **155:**159
Semelka RC, **155:**1111
Semenkovich JW, **155:**611
Senaati S, **155:**197, **155:**900
Sener RN, **154:**1126, **155:**657, **155:**1142
Serchuk L, **154:**904, **155:**651
Sergott RC, **154:**167
Shaffer KA, **155:**1203
Shah P, **154:**61, **154:**200
Shah S, **155:**1137, **155:**1142
Shah Z, **155:**1189
Shanley DJ, **155:**741
Shapeero LG, **154:**623
Shapiro F, **155:**1261
Shapiro M, **155:**1136
Shapiro S, **154:**545
Share JC, **155:**561
Sharif HS, **154:**989
Shaw DWW, **154:**1101
Shaw P, **154:**1187
Shearer DR, **155:**1232
Sheflin JR, **154:**1177
Shelbourne KD, **154:**1237
Sheldon J, **154:**1285
Shellock FG, **154:**631, **154:**1229
Shen J-H, **155:**763
Shereff MJ, **155:**323
Sherman JL, **155:**1069, **155:**1293
Sherman M, **155:**76
Sherrier RH, **155:**419
Sheth S, **155:**1015, **155:**1138
Shiels WE II, **155:**1277
Shiga J, **154:**505
Shiina S, **154:**947, **155:**421, **155:**507, **155:**1221
Shimokata K, **155:**1135
Shiotani T, **155:**653, **155:**1135
Shipley RT, **154:**255
Shirahama M, **155:**895
Shirai Z, **154:**1257
Shiratori Y, **155:**507, **155:**1221
Shortsleeve MJ, **154:**533
Shuman WP, **154:**79, **154:**1029, **155:**109
Sibley RK, **154:**785, **155:**23
Sickles EA, **155:**743, **155:**751, **155:**755, **155:**1133
Siebert JE, **155:**167
Siegel HA, **154:**504, **154:**964, **155:**932
Siegel JB, **154:**1213, **155:**898
Siegel ME, **154:**114
Siegel MJ, **154:**139, **154:**200, **154:**806, **155:**495
Silver B, **154:**847
Silverman FN, **154:**784
Silverman PM, **154:**633, **154:**888, **154:**1325
Silverman SG, **154:**233, **154:**1003
Simeone J, **155:**763
Simon M, **155:**898
Singletary H, **155:**1233
Sintzoff SA Jr, **155:**1021
Sisler CL, **154:**139
Sisler WJ, **154:**1127
Sivit CJ, **154:**803, **155:**133
Sklar E, **154:**821
Sklar F, **155:**153
Skolnick L, **154:**1125
Skubic SE, **155:**1189
Slade W, **155:**343
Slimp G, **154:**631
Slone RM, **155:**1341
Slovis TL, **155:**12, **155:**187, **155:**1326
Small WC, **154:**45
Smerud MJ, **154:**99
Smirniotopoulos JG, **155:**365, **155:**587
Smit FW, **154:**202
Smith AS, **154:**1275
Smith DK, **154:**559
Smith GM, **154:**23
Smith HJ, **154:**65
Smith JL, **154:**271
Smith JR, **154:**577
Smith JW, **155:**323
Smith RR, **154:**1299
Smith TR, **155:**995
Smith WL, **154:**345
Smoker WRK, **155:**385
Snyder S, **155:**829
Sobel DF, **155:**1077
Sohn HY, **155:**971
Soleimanpour M, **155:**545
Solomon M, **154:**837
Solomon SL, **155:**31
Sonntag VKH, **154:**163
Sood A, **155:**339
Soper RT, **154:**345
Sorensen AG, **154:**1053
Sostman HD, **154:**67, **155:**1177
Soto B, **155:**131, **155:**130 Becker CJ
Souto M, **155:**1344
Souza SP, **155:**167
Speck U, **155:**407
Spencer RP, **154:**40
Spetzler RF, **154:**163
Spiller KL, **155:**1282
Splendiani A, **155:**1309
Spoto GP, **154:**837
Spouge AR, **154:**999, **155:**76
Sprayregen S, **154:**171
Sprecher S, **154:**904, **155:**651
Spritzer CE, **155:**55, **155:**1177
Stalker HP, **154:**569
Stallenberg B, **155:**1021
Stamey TA, **155:**811
Stancato-Pasik A, **155:**275
Stanton M, **154:**1217
Staples CA, **154:**983
Stark DD, **154:**287, **155:**763, **155:**943
Stark P, **155:**194, **155:**729, **155:**893
Starnes VA, **155:**23
Stedje K, **154:**569
Steele RD, **154:**899
Steer ML, **154:**1213
Steinberg FL, **154:**901
Steinberg GG, **155:**883
Steinberg R, **154:**904, **155:**651
Steiner E, **154:**411
Steiner RM, **155:**728
Steinke W, **154:**1061
Stephens DH, **154:**99, **154:**422, **155:**501
Stern BJ, **155:**1293
Stern E, **154:**51
Stevens SK, **154:**745
Stewart BK, **155:**183
Stewart ET, **154:**87, **154:**953, **154:**965, **155:**289, **155:**421, **155:**805, **155:**1205
Stolz J, **155:**1327
Stone J, **154:**521
Strange C, **154:**481
Straub WH, **155:**613
Strazzella WD, **154:**897
Strife JL, **154:**202, **155:**351
Strother CM, **155:**580
Struyven J, **155:**1021
Stubblebine J, **155:**198
Stulberg B, **155:**555
Stull MA, **154, 1337**, **154:**884, **154:**888, **154:**890, **154:**893, **154:**1317, **154:**1318, **154:**1325, **154:**1331, **154:**1337, **155:**659
Sugimoto T, **155:**507, **155:**1221
Sugisawa M, **154:**777
Suhocki PV, **154:**884, **154:**1318
Sundaram M, **154:**776, **155:**817, **155:**1042
Sunshine J, **155:**1327
Suri S, **154:**421
Surratt RS, **154:**725
Sussman SK, **154:**47, **155:**397, **155:**529
Sutherland DER, **155:**997
Suzuki J-i, **155:**723
Sweriduck S, **155:**60
Szabo J, **155:**311
Sze G, **155:**873
Szumowski J, **155:**849

T

Tagawa K, **154:**947, **155:**507, **155:**1221
Tahoces PG, **155:**1344
Taira RK, **154:**415, **154:**635
Takai S, **154:**1079
Takarada A, **154:**385
Takashima S, **154:**1079, **154:**1181
Takashima T, **154:**419, **155:**1009
Takasugi JE, **154:**41
Takayasu K, **154:**1203, **154:**1350, **155:**49
Takei Y, **154:**607, **154:**831
Talner LB, **155:**196
Tamakawa Y, **154:**777
Tamamura H, **154:**385
Taminiau AHM, **154:**763
Tanaka S, **154:**509
Tanaka TT, **154:**1245
Tapper UAS, **155:**135
Tarazov PG, **155:**1235
Tatsumi H, **155:**194
Taylor AJ, **154:**87, **154:**1126, **155:**289, **155:**805, **155:**1205
Taylor GA, **154:**803, **155:**133
Taylor KJW, **155:**536
Teefey SA, **154:**79, **155:**109
Teele RL, **154:**797
Tehranzadeh J, **155:**1049
Tein AB, **154:**305
Teitelbaum GP, **154:**633
Teixidor HS, **154:**265
Temple HT, **155:**1257
Teplick SK, **154:**1217
Terano A, **154:**947, **155:**507, **155:**1221
Terasaki KK, **154:**181
Terpstra OT, **155:**655
Terriff BA, **154:**203
Terris MK, **155:**811
Tessler FN, **154:**393, **155:**295, **155:**1220
Thaler H, **154:**423
Tham RTOTA, **155:**1139
Thickman D, **155:**303
Thoeni RF, **154:**73
Thomas P, **155:**29
Thomford NR, **154:**1011
Thompson BC, **155:**654
Thompson GP, **154:**1177
Thompson R, **154:**803
Thordarson S, **155:**729
Thorngren K-G, **154:**331
Thorsen MK, **155:**307, **155:**1203
Thulborn KR, **154:**1053
Tien RD, **154:**351, **155:**143, **155:**573
Tjon A Tham RTO, **154:**95
Tkach JA, **155:**951
To T, **155:**743
Tobis JM, **155:**1100
Tocino IM, **154:**1122
Toi A, **154:**1199, **155:**789
Tomà P, **154:**1049
Tomei E, **155:**1111
Tonami H, **154:**385
Tonkin ILD, **154:**241, **155:**1343
Toriya H, **154:**1257
Torres GM, **155:**196
Torres WE, **154:**291, **155:**655
Torrisi JM, **155:**1273
Totterman S, **154:**175, **155:**897
Totty WG, **154:**559
Towbin RB, **154:**149, **154:**361, **155:**131
Towers MJ, **155:**29
Townsend RR, **154:**275
Tracy CM, **154:**884, **154:**1318
Trambert JJ, **154:**305
Trego DC, **155:**977
Treves ST, **154:**657

Tristan TA, **155:**396
Truwit CL, **155:**855
Tsuruda JS, **154:**375, **154:**623, **155:**1059
Tung GA, **154:**1003
Tunuguntla K, **154:**1217
Tupler RH, **155:**897
Twedt G, **154:**203
Twigg HL, **154:**884, **154:**1318
Tyrrel RT, **154:**105, **155:**73

U

Uchida S, **155:**895
Ueda Y, **155:**1009
Ueno E, **154:**201
Umeshita K, **154:**1124
Unger EC, **154:**1344
Unger JM, **154:**1123
Unuma T, **154:**947, **155:**507, **155:**1221
Urbanek PJ, **154:**851
Urbanski S, **154:**849
Usselman JA, **154:**404
Uta Y, **155:**507, **155:**1221

V

Vahey TN, **154:**1237
Valat J-P, **155:**895
Valdivieso M, **154:**327
Valentino DJ, **155:**183
Valk J, **155:**899
Vanarthos WJ, **155:**420, **155:**1049
Van Beers B, **154:**515
VanBlarcom ST, **155:**95
Vandemark RM, **155:**465
Van Hecke P, **155:**407
van Heesewijk HPM, **154:**202
Vanhoenacker P, **155:**407
Vanness A, **155:**831
Van Regemorter G, **155:**1021
Van Sinoy ML, **155:**1021
vanSonnenberg E, **155:**1183
Van Tassel P, **154:**351
van Waes PFGM, **155:**422
Veith FJ, **154:**171
Velcek FT, **155:**1273
Vick CW, **154:**121
Victor M, **155:**1315
Vidal JJ, **155:**1344
Vilgrain V, **155:**277
Vingan HL, **155:**1013
Vitoux JF, **155:**425
Vlasveld LT, **154:**95
Vogl T, **154:**585
Vogler JB III, **154:**751
Volta S, **154:**654
Vontivillu JA, **155:**660
Vorwerk D, **154:**617

W

Wada M, **155:**283
Wagner HN, **155:**925
Wakao F, **154:**1350
Wakasa K, **154:**1124, **155:**1227
Wakhloo AK, **154:**654
Walker AP, **155:**1203
Wall C, **155:**743
Wallner B, **155:**1237
Walsh E, **155:**1142
Walsh PC, **155:**1015
Walter RM, **154:**656
Waltman AC, **154:**901
Wang Y, **154:**779
Wapner KL, **155:**119
Watanabe A, **155:**1136
Webb WR, **154:**701
Webber, MM, **154:**975
Wehrli FW, **154:**1069, **155:**1117
Weidenfeld M, **154:**654
Weinberger E, **155:**347
Weinreb JC, **154:**295
Weinstein MA, **154:**1275
Weintraub BD, **154:**1075
Weisbrod GL, **154:**999
Weiss KL, **154:**305
Weiss MA, **154:**656
Weissleder R, **154:**287, **155:**763, **155:**1161
Welch TJ, **154:**1, **154:**1219
Wenzel MS, **155:**95
Wesseling FJH, **155:**1139
West MS, **154:**888, **154:**1325
Westesson PL, **154:**1344
Wetzel LH, **154:**771, **155:**1025
Whalen E, **154:**11, **154:**875, **154:**1311, **155:**413, **155:**565, **155:**1125
Whittemore AD, **155:**1085
Whittemore AR, **154:**204
Wichman RD, **154:**45, **154:**831
Wiedmeyer DA, **154:**399
Wiener MD, **154:**751, **155:**1037
Wiener SN, **155:**881
Wiens JL, **155:**977
Wilbur AC, **155:**547
Wilkinson A, **155:**295
Wilkinson WE, **155:**581
Willemze R, **154:**95
Williams AL, **155:**849
Williams KD, **154:**163
Williams WG, **154:**789
Williams WH, **155:**311
Willis JJ, **154:**315
Wills JS, **154:**757
Willvonseder R, **155:**825
Wilson G, **154:**789
Wilson JL, **155:**1277
Wilson SR, **154:**1199, **155:**76, **155:**789
Winer-Muram HT, **154:**69
Wingstrand H, **154:**331
Winters WD, **155:**125
Witko J, **154:**897
Witte CL, **155:**311
Witte MH, **155:**311
Wittenberg J, **154:**287, **155:**763, **155:**1161
Wohlgemuth SD, **155:**1013
Wojtasek DA, **154:**265
Wolf AL, **154:**1293
Wong AWK, **155:**183
Woodring JH, **154:**1165
Woodruff W, **154:**315
Wootton P, **154:**862, **155:**610
Wu WC, **155:**983

X

Xu X-W, **154:**1107

Y

Yachia D, **154:**111
Yagan R, **155:**1189
Yaghmai F, **154:**577
Yakes WF, **154:**115
Yamada A, **154:**201
Yamaji Y, **155:**653, **155:**1135
Yamamoto I, **154:**385
Yamamoto K, **155:**194, **155:**845
Yamasaki S, **154:**1257
Yamashita T, **154:**423
Yankelevitz DF, **155:**1185
Yeung EYC, **155:**391
Yoon Y, **154:**107
Yoshikawa J, **154:**419
Young JWR, **154:**125, **155:**93, **155:**1169
Young LW, **154:**1156
Yousem DM, **154:**167, **154:**1069
Yu S, **154:**817
Yucel EK, **154:**901

Z

Zagoria R J, **154:**521
Zawieja DC, **155:**1105
Zeck OF, **155:**611
Zeiss J, **154:**1011
Zeit RM, **155:**1103
Zheutlin J, **154:**713
Zirn JR, **155:**1185
Zissin R, **155:**1136
Zonderland HM, **155:**1097
Zyroff J, **155:**1077

Subject Index
Volumes 154–155

AJR articles are also included in the 5-year cumulative index published in *Radiology*.

Index Key: a = abstract, b = book review, e = editorial, l = letter, m = memorial, p = pictorial essay, v = videotape review

Subjects in this index are cataloged by body part where possible. Disease entities unique to a body part are listed by that part; other more general diseases have separate listings by name. Technical procedures are also listed by part, as appropriate. Because of general interest, subjects dealing with CT, MR imaging, sonography, radionuclide imaging, and pediatric radiology are listed under those headings as well as under appropriate body part and/or disease.

A

- **Abdominal aorta**
  - aneurysm
    - prognosis (a), **154:**661
    - spinal cord ischemia after, **155:**1303
  - ruptured stump, transcatheter embolization, **154:**181
- **Abdominal wall,** abnormalities, CT (p), **154:**1207
- **Abortion,** threatened, subchorionic hemorrhage in, sonography, **154:**535
- **Acetabulum**
  - allografts, after bipolar revision arthroplasty, hip (a), **154:**1131
  - following porous-coated hip arthroplasty (a), **155:**204
- **N-Acetyl-β-glucosaminidase,** urinary tract infection, children (a), **155:**1145
- **Achalasia,** diffuse esophageal leiomyomatosis and (a), **155:**428
- **Achilles tendon,** injury, sonography, **155:**1031
- **Acquired immune deficiency syndrome**
  - bowel obstruction in, infant, **154:**803
  - extrapulmonary *Pneumocystis carinii* in, **155:**76
  - ileocecal tuberculosis, CT, **154:**499
  - ileocolic intussusception in, **154:**1325
  - infection related to, visceral and nodal calcification, **154:**27
  - Kaposi sarcoma, lymphangioscintigraphy in, **155:**311
  - pneumatosis intestinalis, children, **155:**133
  - pulmonary tuberculosis in (a), **155:**665
- **Acromegaly,** diagnosis, inferior petrosal sinus sampling, **154:**1075
- **Acromion,** stress fracture (l), **155:**1140
- **Actinomycosis,** mediastinal, CT, **155:**735
- **Adrenal gland**
  - bilateral hemorrhage, adrenocorticotropic hormone-induced (l), **154:**424
  - imaging, **154:**927
  - mass, renal tissue (l), **155:**656
- **Adrenocorticotropic hormone,** bilateral adrenal hemorrhage induced by (l), 154:**424**
- **Airway,** collapse, infant, ultrafast CT, **154:**345
- **Aldosteronism,** hypokalemia, renal cysts and (a), **154:**1354
- **Allografts,** fracture (a), **155:**1145
- **American College of Radiology,** summit meeting, August 1989, **154:**645
- **American Roentgen Ray Society**
  - information and application for membership, **154:**220, **154:**448, **154:**1138, **155:**216, **155:**442, **155:**648
  - 1989 meeting, summary, **154:**219
  - 1990 meeting, Washington, DC, **154:**216, **154:**435, **154:**673
    - administrative report, **155:**643
    - award-winning scientific exhibits, **155:**644
    - 1990 gold medals, **155:**639
    - instructional courses and symposium, **154:**438, **154:**676, **154:**914
    - local activities and tennis and golf tournaments, **154:**441
    - meeting news, **155:**631
    - secretary's report, **155:**641
    - summary, **154:**437, **154:**675, **154:**913
  - 1991 meeting, Boston, MA, **154:**1364, **155:**210, **155:**436, **155:**672, **155:**910
  - Melvin M. Figley Fellowship in Radiology Journalism, **154:**470
  - new members, **155:**646
  - officers, committees, and membership information, **154:**223, **154:**444, **154:**682, **154:**917, **154:**1141, **155:**215, **155:**441, **155:**671, **155:**909, **155:**1152, **155:**1357
  - presidential address, **155:**451
- **Amiloride,** aerosolized, lung disease in cystic fibrosis (a), **155:**661
- **Amniocentesis,** transplacental, intra-amniotic hemorrhage after, sonography (a), **155:**1351
- **Amyloid goiter,** radiologic findings (l), **155:**193
- **Amyloidosis,** pleural disease and (a), **155:**1144
- **Anastomosis,** biliary-enteric, surgically created, biliary obstruction in, sonography, **155:**789
- **Anatomy**
  - Pernkopf anatomy (b), **154:**374
  - sectional (b), **154:**504
    - basic atlas (b), **154:**882, **154:**1034
    - color atlas (b), **155:**932
- **Aneurysm,** mesenteric, with ergotism (l), **155:**897
- **Angina,** stable, silent ischemia during (a), **154:**1355
- **Angiography**
  - cardiac, principles of (b), **155:**1176
  - coronary
    - CLIP system, on-line reporting, **154:**1307
    - pulmonary atresia, hypoplastic right ventricle, and ventriculocoronary communications, **154:**789
  - digital, cardiac applications (b), **154:**788
  - miniature catheters, high-flow jets from, **154:**1091
  - MR, **154:**937
    - gadopentetate dimeglumine-polylysine, **155:**407
    - intracranial aneurysms, **155:**159
    - maximum-intensity-projection display (p), **154:**623
    - portal vein (l), **154:**901
    - three-dimensional phase-contrast, head and neck, **155:**167
- **Angioplasty**
  - balloon on a guidewire in, **155:**887
  - coarctation of the aorta, intima and media dissection after (a), **154:**1355
  - femoral, ruptured polyester balloon (l), **155:**1141
  - laser-assisted thermal, peripheral recanalization by, **155:**1100
  - laser (b), **155:**780
  - long-term, treatment of Budd-Chiari syndrome, **154:**1007
  - percutaneous transluminal
    - Budd-Chiari syndrome, MR (l), **154:**1350
    - infrapopliteal arteries, **154:**171
- **Ano-rectal strictures,** balloon dilatation, infant (a), **154:**211
- **Anti-carcinoembryonic antigen,** immunoscintigraphy, parotid gland tumors, 154:**1259**
- **Aorta**
  - coarctation
    - after surgical correction (a), **154:**208
    - angioplasty of, intima and media dissection after (a), **154:**1355
- **Aortoesophageal fistula,** after chronic aortic dissection, CT, **155:**989
- **Appendicitis,** perforation with, sonographic diagnosis, **154:**275
- **Arachnoiditis,** lumbar, benign, **155:**873
- **Arterial occlusion,** chronic, model (l), **155:**1348
- **Arteriovenous malformations**
  - intracranial, stereotactic heavy-particle Bragg-peak radiation (a), **155:**1350
  - pulmonary, noncommunicating (l), **155:**893
- **Arthrectomy,** balloon dilatation and, intimal hyperplasia in vascular endoprostheses, **154:**617
- **Arthritis**
  - degenerative, atlantoodontoid joint, CT (p), **154:**315

- rheumatoid
  - knee, MRI, **155:**329
  - nodular pulmonary opacities in (a), **154:**663
- suppurative, percutaneous catheter drainage, **154:**135

Arthrography
- K-edge digital subtraction, hip prosthesis, **155:**1053
- MR, shoulder, **155:**829
- temporomandibular joint
  - coronal radiographs and videofluoroscopy with, **155:**105
  - reaction to nonionic contrast medium (l), 154:1344
- wrist ligaments, MR comparison, **154:**337

Arthroplasty
- bipolar revision, acetabular allografts after (a), **154:**1131
- total knee, bone scans after (a), **155:**203

Arthrotomography, conventional and computed, shoulder evaluation (a), 154:**666**

Artifacts, intracranial chemical-shift, brain, MR, **154:**1275

Asbestos, diseases associated with, cigarette filter workers (a), **154:**661

Ascites, extraperitoneal mass effect (a), **154:**908

Aspergilloma, giant, percutaneous intracavitary treatment of (l), 154:**1346**

Atlantoodontoid joint, degenerative arthritis, CT (p), **154:**315

Autoradiology, patient-performed procedures, **154:**871

Azygos system, retroaortic anastomoses, CT, **154:**41

B

Bacteriuria, untreated, renal scarring and, pediatric girls (a), **154:**907

Bacille-Calmette-Guérin, vaccine, granulomatous prostatitis induced by (l), **155:**195

Balloon dilatation, atherectomy and, intimal hyperplasia in vascular endoprostheses, **154:**617

Barium studies
- air-contrast, epigastric hernia during (l), **155:**420
- diffuse eosinophillic gastroenteritis (a), **155:**665
- double-contrast, sigmoidoscopy and (a), **154:**906
- hypersensitivity reaction during (l), **154:**199

Barth, Earl E. (m), 155:624

Bell's palsy, contrast-enhanced MR, **155:**573

Biello criteria, diagnosis of pulmonary emboli, lung scans, **154:**975

Bile duct
- benign strictures, endoscopic therapy for (a), **154:**428
- biopsy, Simpson atherectomy catheter, **154:**1213
- extrahepatic, CT, **154:**79
- hilar cholangiocarcinoma, enhanced CT, **154:**1203
- intraperitoneal leakage, cholecystectomy and (l), **155:**1137
- necrosis, after partial hepatectomy (l), **154:**1124
- papillary adenomatosis, obstructing villous adenoma and, **154:**1217
- stones
  - ESWL treatment of, **155:**775
  - sonography for localization, ESWL and (a), **154:**1356

Biliary atresia, choledochal cyst and, neonate, **155:**1273

Biliary endoprostheses, clogging, aspirin and doxycycline in (a), **154:**906

Biliary tract
- endoprosthesis dysfunction, malignant hilar tumors and, **155:**391
- fistulas, endoscopic treatment (a), **154:**906
- Hawkins-Hunter rocket wire in, **154:**1101
- motility, clinical disorders and, **155:**247
- obstruction, sonography, **155:**789

Biopsy
- bone, new method (l), **155:**658
- CT and sonographically guided, **154:**1
- CT-guided, thoracic actinomycosis and carcinoma, **155:**1183
- fine-needle aspiration
  - hepatic hemangioma, fatality from (l), **154:**203
  - hepatocellular carcinoma (a), **154:**664
  - mammography-guided, nonpalpable breast lesion, **155:**977
  - metastatic lung tumor (a), **154:**905
- fine-needle nonaspiration, liver, **155:**1217
- needle
  - pneumothorax as complication of, **155:**31
  - sonographically guided, hepatic cavernous hemangioma (a), **154:**908
  - sonographically guided, prostatic hypoechoic area (a), **154:**1357
  - sonographically guided, simple phantom for, **154:**847
- occult breast lesions, new device for evaluation, **154:**261
- percutaneous
  - adjunct to CT and sonographically guided procedures (l), **155:**198
  - thoracic lesions, **154:**1181
- Simpson atherectomy catheter, bile duct, **154:**1213
- stereotactic fine-needle, nonpalpable breast lesions, **154:**1191, **154:**1196 (commentary)

Bladder
- augmentation, malignancy (a), **155:**664
- inverted layering of contrast material and urine, CT (l), **155:**1139
- transitional cell carcinoma, cavitary pulmonary metastases in, **154:**493

Blastomycosis, pulmonary, chest radiographs, **154:**1177

Blood flow, cerebral, newborn, mechanical ventilation effects (a), **154:**211

Blood pressure, high, adult, childhood risk factors for (a), **154:**209

Blount's disease, late onset (a), **155:**903

Blue rubber bleb nevus syndrome, CT, **154:**105

Bone
- diseases (b), **155:**1256
- dome of talus, osteochondral fractures (a), **154:**208
- Ilizarov limb-lengthening procedures, sonography, **154:**125
- imaging (b), **154:**1236
  - pediatric (b), **154:**1250
- metabolic diseases (b), **155:**1042
- metastasis, hepatocellular carcinoma presenting as (a), **154:**662
- pathologic formation (a), **154:**208
- primary neoplasms, bone-chip allografts, MR, **155:**1257
- sarcoma, chemotherapy effects, MR monitoring of, **154:**763
- scan, ballet dancers (l), **154:**657
- tibia vara (a), **154:**208
- tumors (b), **154:**1240
  - malignant, MR vs scintigraphy, **155:**1043
  - tumorlike lesions and, MR, **155:**817

Bone marrow
- changes after irradiation, MR, **154:**745
- systemic disorders, photon chemical shift imaging (a), **155:**1147

Book reviews
- advances in cerebral SPECT imaging, **155:**158
- advances in hepatobiliary radiology, **155:**506
- assurance of quality in the diagnostic x-ray department, **154:**32
- atlas of radiologic imaging, **155:**60
- avulsion and stress injuries of the musculoskeletal system, **154:**134
- basic atlas of sectional anatomy with correlated imaging, **154:**882, **154:**1034
- basic medical techniques and patient care for radiologic technologists, **154:**476
- basic principles of radiographic exposure, **154:**862
- bone and joint imaging, **154:**1236
- bone tumors, **154:**1240
- breast imaging, **154:**572
- cardiac applications of digital angiography, **154:**788
- cerebral and spinal CT, **154:**1074
- cerebral CT, **154:**360, **155:**108
- chest radiographic analysis, **154:**486
- clinical implications of abnormal digestive tract radiographs, **155:**48
- clinical MR imaging, **155:**1292
- clinical pelvic imaging, **154:**988
- clinical radiology of the small intestine, **154:**72
- clinical renal imaging, **154:**1096
- clinical urography, **154:**1222
- computers in diagnostic radiology, **155:**754
- CT and MRI of the thorax, **155:**970
- CT and sonography of the acute abdomen, **154:**982
- dento maxillo facial radiology, **154:**584
- diagnosis of diseases of the chest, **155:**738
- Doppler ultrasound, **154:**398
- Duplex Doppler ultrasound, **155:**1090
- dynamic functional studies in nuclear medicine in developing countries (b), **154:**40
- dysphagia, **154:**532
- echocardiography and Doppler in cardiac surgery, **155:**130
- emergency interventional radiology, **154:**1028
- endosonography, **155:**1220
- ERCP atlas, **154:**1002
- essentials of body CT, **155:**540
- evaluation of renal function and disease with radionuclides, **154:**114
- exercises in diagnostic imaging, **155:**526
- exposure of the U.S. population from diagnostic medical radiation, **154:**50
- gastrointestinal radiology, **154:**1198
- gastrointestinal radiology reviews, **155:**282
- genitourinary radiology, **155:**1020
- guidance on radiation received in space activities, **154:**870
- guidelines for the routine performance checking of medical ultrasound equipment, **155:**124
- handbook of breast imaging, **154:**568
- house officer, becoming a medical specialist, **154:**16
- how to measure angles from foot radiographs, **155:**816
- imaging 1990, **155:**602
- imaging of sports injuries, **154:**342
- imaging of the pediatric urinary tract, **154:**142
- imaging principles of cardiac angiography, **155:**1176
- interventional ultrasound, **155:**510
- intraoperative ultrasonography in hepato-biliary and pancreatic surgery, **155:**246
- laser angioplasty, **155:**780
- MacDose, **155:**1188
- magnetic resonance imaging and computed tomography of the head and spine, **155:**1302
- magnetic resonance imaging of central nervous system diseases, **155:**848
- magnetic resonance imaging of the spine, **155:**1076
- magnetic resonance imaging of bone and soft tissue tumors and their mimics, 154:554
- magnetic resonance imaging, **154:**770
- magnetic resonance imaging workbook, **154:**1228
- magnetic resonance of the spine, **155:**384
- manual of diagnostic imaging, **155:**12
- manual of diagnostic radiology, **154:**286
- MRI atlas of the brain, **155:**580
- MRI/CT and pathology in head and neck tumors, **155:**166
- MRI in multiple sclerosis, **155:**152
- MRI of the body, **155:**762

  new techniques in metabolic bone disease, **155:**1042
  nonionizing radiation protection, **155:**1232
  nuclear medicine annual 1989, **154:**404
  pediatric bone imaging, **154:**1250
  pediatric neuroimaging, **155:**142
  Pernkopf anatomy, **154:**374
  pocket atlas of head and neck MR anatomy, **154:**630
  pocket atlas of spinal MR, **154:**1268
  positron emission tomography in clinical research and clinical diagnosis, 154:1024
  practical color atlas of sectional anatomy, **155:**932
  primer of medical radiobiology, **155:**1202
  principles of radiography for technologists, **155:**610
  procedures in diagnostic radiology, **154:**1164
  progress in cardiology, **155:**982
  pros and cons in PTA and auxiliary methods, **154:**1256
  radiographic anatomy, **155:**397
  radiographic measurements, **154:**744
  radiologic clinics of North America
    cardiopulmonary imaging, **155:**22
    CT of the gastrointestinal tract, 154:86
    fetal ultrasound, **155:**316
    MR of the head and neck, **154:**158
    musculoskeletal trauma, **155:**337
    orthopedics, **155:**554
  radiology administration (b), **154:**644
  radiology of bone diseases, **155:**1256
  radiology of occupational chest diseases, **154:**64
  scintigraphy of inflammation with nanometer-sized colloid tracers, **154:**796
  sectional human anatomy, **154:**504
  Stedman's medical dictionary, **155:**1282
  technical and physical parameters for quality assurance in medical diagnostic radiology, **155:**404
  textbook of color Doppler echocardiography, **154:**1060
  textbook of interventional cardiology, **155:**886
  the cath lab, **155:**34
  the nucleus of cardiac diagnosis, **155:**728
  the radiology word book, **155:**1326
  tomographic methods in nuclear medicine, **154:**1078
  Turner syndrome, **155:**350
  ultrasonography of muscles and tendons, **154:**124
  ultrasound and infertility, **154:**544
  urologic pathology with clinical and radiologic correlations, **154:**1100
  videofluoroscopic studies of speech in patients with cleft palate, 154:1156
Borgerson, Robert James (m), 154:1086
Bowel
  infarction, CT, **154:**99
  inflammatory disease, geographic origins of Jewish patients (a), **154:**208
  small, perforation, cocaine-induced (l), **154:**1346
Brain
  chemistry, drugs, behavior and, **155:**925
  choroidal fissure and parenchymal cysts, CSF-like, MR, **155:**1069
  extraaxial tumors, epidermoid tumors and, differentiation, MR, **155:**1059, **155:**1066 (commentary)
  intracranial chemical-shift artifacts, MR, **154:** 1275
  intraventricular membranes, congenital symmetrical (l), **155:**1142
  MR signal abnormalities, memory disorder and dementia, **154:**1285
  posttraumatic infarction, CT, **154:**1293
  tumor, neonatal, **155:**587
Breast
  Canadian screening study (l), **155:**1133
  cancer
    after irradiation of thymus in infancy (a), **154:**905
    irradiation for tuberculosis (a), **154:**905
    prognosis, cathepsin D and (a), **154:**1353
    silicone gel-filled implants (a), **155:**1144
  carcinoma
    optical spectroscopy and, **155:**43
    previous treatment for Hodgkin disease and, **155:**39
    recurrence after lumpectomy, **155:**35
    secondary acute myelocytic leukemia after (a), **154:**662
  imaging (b), **154:**568, **154:**572
  implant, collapse after mammography (l), **154:**1345
  lesions
    nonpalpable, mammography-guided stereotactic fine-needle aspiration of, **155:**977
    nonpalpable benign, mammography detection, **155:**1195
    nonpalpable, stereotactic fine-needle biopsy, **154:**1191, **154:**1196 (commentary)
    occult, biopsy specimens, **154:**261
  screening
    Canadian National Breast Screening Study, **155:**743, **155:**748 (commentary)
    mammography, computerized follow-up of abnormalities, **155:**751
    mammography, computers in, **155:**755
  simulation of mass on mammogram (l), **154:**900
Breast milk, gadopentetate dimeglumine excretion, **154:**1305
Broad ultrasound attenuation, osteoporosis, **155:**825
Bronchial stenosis, tuberculous, CT, **155:**971
Bronchoalveolar lavage, chest radiographs with, interstitial lung disease (a), **154:**905
Bronchogenic carcinoma, extrathoracic staging (a), **155:**662
Broncholithiasis, bronchogenic carcinoma, digital radiography (l), **155:**1344
Bronchopulmonary dysplasia, long-term diuretic therapy for (a), **154:**210
Bronchoscopy, flexible, pulmonary filtrates in pediatric cancer patients (a), 154:**209**
Bronchus
  left lower lobe, anterior wall stripe, CT, **154:**33
  left main, lateral chest radiograph (l), **155:**1343
Budd-Chiari syndrome
  angioplasty for long-term treatment, **154:**1007
  percutaneous transluminal angioplasty treatment, MR (l), **154:**1350
Bursography, current role of, **154:**129

C

Calculi, *see* specific type
***Campylobacter pylori*,** gastrointestinal disease related to, children (a), 154:**427**
Cancer
  see also specific type or site
  lung, radiologic diagnosis, pitfalls, **154:**1165
  metastatic, samarium-153 EDTMP (a), **154:**665
Carcinoma, *see* specific organ, region
Cardiology
  interventional (b), **155:**886
  progress (b), **155:**982
Carotid artery
  disease, color Doppler flow imaging, **154:**1061
  internal siphon, MR, **155:**359
  stenosis, duplex Doppler sonography in, **155:**1091
Case of the day
  abdominal, **154:**888, **154:**1325
  chest, **154:**884, **154:**1318
  musculoskeletal, **154:**890, **154:**1331
  neuroradiology, **154:**893, **154:**1337
Castleman disease
  greater omentum (l), **154:**654
  mother and daughter (l), **154:**899
  neck, CT, **154:**1051
Cathepsin D, breast cancer prognosis and (a), **154:**1353
Catheter
  coaxial, splanchnic arteries, **155:**405
  conversion of retrograde to antegrade, femoral artery, **154:**179
  double-J, transgastric cystogastrostomy (l), **154:**421
  Hickman
    Dacron cuff of, mammographic appearance, **155:**1203
    percutaneous placement, subclavian vein, **155:**1097
  magnetic, removal of foreign bodies, **154:**149
  miniature angiographic, high-flow jets from, **154:**1091
  modified cope loop, percutaneous gastrojejunostomy with, **155:**79
  percutaneous drainage, suppurative arthritis, **154:**135
  Simpson atherectomy, biopsy, **154:**1213
  small drainage, malignant pleural effusions (a), **154:**662
  transvaginal, selective osteal salpingography and, fallopian tube obstruction, **154:**735
  venous, malpositioned, redirection of, **154:**183
Catheterization
  cath lab (b), **155:**34
  gastrojejunal, directable cannula for (l), **154:**203
Cauda equina, ependymoma of, subarachnoid hemorrhage and, **154:**1342
Caudate lobe, liver (p), **154:**87
Cecum, diverticulitis, sonography, **155:**283
Celiac axis, fat obliteration around, pancreatic carcinoma and, CT, **155:**991
Central nervous system, vascular flow, spatial misregistration, MR, **155:**1117
Cerebellum, anatomic MR correlation, **154:**593
Cerebral hemorrhage, CT appearance, ferritin and hemosiderin role in, **154:**1053
Cerebral palsy, preterm infants, periventricular echodensities associated with (a), **155:**431
Cerebral ventricles
  colloid cysts, MR and CT, **155:**135
  lateral neoplasms, CT and MR, **155:**359
Cervical pedicle, congenital absence, **155:**1037
Chemotherapy
  bone sarcoma, MR monitoring of, **154:**763
  cytosine-arabinoside, GI complications of, **154:**95
  Ewing sarcoma, MR, **155:**343
  Hodgkin disease, pulmonary histiocytosis X after, **155:**741
  intraarterial infusion, metastatic liver tumors, lipid contrast medium and (a), **154:**662
Child abuse
  differentiation from osteogenesis imperfecta, **154:**1035, **154:**1047 (commentary)
  gastric hematoma and pneumatosis, **155:**1283
  infant, diagnostic imaging, **155:**703
  osteogenesis imperfecta, differentiation (l), **155:**1346
Cholangiography
  clonorchiasis, **155:**1001
  papillary adenomatosis, obstructing villous adenoma and, bile ducts, **154:**1217
Cholangiohepatitis, oriental, sonography, **155:**511
Cholangiopancreatography
  endoscopic
    hepatic clonorchiasis (a), **155:**1351
    retrograde, biliary complications in hydatid disease of liver (a), **154:**210
Cholecystectomy
  bile duct diameter after (a), **154:**664
  duodenoscopic sphincterotomy after (a), **155:**203
  intraperitoneal bile leakage and (l), **155:**1137
Cholecystitis, acute emphysematous, treatment with percutaneous cholecystostomy drainage, **155:**1013
Cholecystography, oral, nonvisualization of gallbladder, lithotripsy and (a), **154:**1358

Cholecystolithotomy
  percutaneous
    endoscopic lithotripsy with, pulsed-dye laser and, **155:**781
    nitinol basket instrument for, **155:**515
Cholecystostomy, percutaneous, acute emphysematous cholecystitis, **155:**1013
Choledochal cyst
  biliary atresia and, neonate, **155:**1273
  common channel ectasia (l), **155:**421
Choledochocele, intestinal intussusception (a), **155:**666
Cholelithiasis
  see also Extracorporeal shock-wave lithotripsy
  coincidental, sonographic detection (a), **155:**429
  dissolution
    methyl *tert*-butyl ether, **155:**67
    methyl *tert*-butyl ether (a), **155:**428
    oral dihydroxy bile acids (a), **155:**901
  early recurrence rate, after shock-wave therapy (a), **154:**1131
  ESWL and, **154:**291, **155:**655
  fragmentation, piezoelectric biliary lithotripsy, **155:**1211
  partially calcified, ESPL and methyl *tert*-butyl ether (a), **154:**427
  stone fragments, after biliary ESWL (a), **155:**663
Chondroblastoma, periostitis in, frequency and diagnostic significance, **154:**309
Chondroma, periosteal (a), **155:**1145
Chondrosarcoma, laryngeal, CT, **154:**997
Cigarette smoking
  cigarette filter workers, asbestos-associated diseases (a), **154:**661
  neutrophil kinetics and, lung (a), **154:**661
Cirrhosis
  alcoholic, peritoneovenous shunting compared with medical treatment (a), **154:**1129
  gastroesophageal endoscopic features in (a), **154:**906
  hepatic, regenerating nodules, **155:**1227
  portal flow, echo-Doppler measurement of (a), **155:**663
  portal hypertension, ultrasonographic signs (a), **155:**666
  regenerating nodules of, MR, **154:**505
Cisplatin, suspended in lymphographic agent, chemotherapy for hepatocellular carcinoma (a), **154:**662
Clivus, normal and abnormal, MR, **155:**1285
Cloacal exstrophy, radiology, **155:**1267
Clonorchiasis
  hepatic, endoscopic cholangiopancreatography in (a), **155:**1351
  radiologic findings, **155:**1001
Cocaine
  coronary artery vasoconstriction and (a), **154:**1130
  ingested packets, CT (l), **155:**419
  small bowel perforation and (l), **154:**1346
Colitis, *Escherichia coli* 0157:H7-associated (a), **155:**901
Colloid cyst, third ventricle, MR and CT, **155:**135
Coloboma, real-time sonography, **154:**391
Colon
  acute diverticulitis, sonography, **154:**1199
  cancer, diagnosis, cost containment and, **154:**875
  carcinoma, colonic anisakiasis simulating (l), **155:**895
  diverticulitis, sonography, **155:**283
  filling, double-contrast enema, **154:**279
  postprandial transit and motor activity, after chronic constipation (a), **154:**1355
Colonoscopy
  pediatric patient (a), **154:**429
  vs flexible sigmoidoscopy plus air contrast barium enema (a), **155:**202
Computer page
  computer-based learning, hypermedia application in CT, **155:**1317
  computerized literature reference system, **155:**617
  computers in mammography screening practice, **155:**755
  coronary angiogram, CLIP system, **154:**1307
  JCAHO dose calculations, microcomputer spreadsheet program, **154:**863
  radiologic image communication methods, **155:**183
  residents' on-call and vacation schedules, management of, **154:**641
Computers, diagnostic radiology (b), **155:**754
Connective tissue disorder, gastrointestinal manifestations of (a), **155:**428
Constipation, chronic, postprandial colonic transit and motor activity in (a), **154:**1355
Contrast media
  Bell's palsy, MR, **155:**573
  effects, pediatric (a), **155:**205
  Gd-DTPA
    extradural degenerative disease, spine, **154:**151
    tears of anulus fibrosus, **154:**159
  ionic, universal premedication before (l), **154:**1343
  ionic and nonionic, **155:**235
    a proposal (l), **155:**651
    corticosteroid pretreatment in private practice (l), **155:**652
  lipid, anti-cancer agents suspended in, chemotherapy (a), **154:**662
  nonionic, reaction during arthrography (l), **154:**1344
  reactions, corticosteroid pretreatment for, children, **155:**357
  retention, focal nodular hyperplasia of liver (l), **154:**422
Coronary artery
  left ventricle fistula (l), **154:**898
  vasoconstriction, cocaine-induced (a), **154:**1130
Corpus callosum, agenesis and lipoma of, MR (l), **154:**1348
Corticosteroids
  pretreatment, contrast media reactions, children, **155:**357
  withdrawal, sarcoidosis during, chest radiography, **154:**481
Cranial nerves, MR (p), **154:**1263
Craniosynostosis, enlarged parietal foramina and, American Indian child (l), **154:**658
Cranium, parosteal osteogenic sarcoma, **155:**113
Crohn's disease
  cyclosporine therapy (a), **154:**207
  evolution on prednisolone (a), **155:**202
Cronkhite-Canada syndrome, radiologic features (a), **154:**211
Cryomicrotomy, cervical facet joints, age-related changes, **154:**817
***Cryptococcus neoformans*,** intracranial infection, CT, **154:**603
CT
  biopsy guided by, **154:**1
  hypermedia application, **155:**1317
CT, abdomen
  abnormalities of abdominal wall (p), **154:**1207
  acute (b), **154:**982
  acute diverticulitis, **154:**281
  after Whipple procedure for malignancy, **154:**1011
  aortoesophageal fistula, after chronic aortic dissection, **155:**989
  blue rubber bleb nevus syndrome, **154:**105
  blunt trauma, hematuria in, children, **154:**569
  bowel infarction, **154:**99
  combined systemic and portal venous gas, **154:**1219
  congenital aneurysm, superior mesenteric artery (l), **155:**199
  endoscopic, esophageal carcinoma, **155:**277
  enterovaginal and veiscovaginal fistulas (a), **155:**666
  extraadrenal retroperitoneal paraganglioma, **155:**1247
  gallium scan comparison, synthetic vascular graft infection, **154:**405
  hilar cholangiocarcinoma, **154:**1203
  ileocecal tuberculosis, **154:**499
  ingested cocaine packets (l), **155:**419
  ovarian vein, oncology patients, **155:**291
  peritoneal leiomyosarcomatosis, **155:**799
  splenic abnormalities (p), **155:**805
  staging of Hodgkin disease, children, **154:**1251
  traumatic mesenteric venous thrombosis (l), **154:**425
CT, adrenal
  current status, **154:**927
  metastatic lesions, lung cancer patients (a), **155:**1144
CT, ankle, plain film comparison, adult fractures, **154:**1017
CT, biliary system, extrahepatic bile ducts, **154:**79
CT, bladder, inverted layering, contrast material and urine (l), **155:**1139
CT, body, essentials (b), **155:**540
CT, bone
  degenerative arthritis, atlantoodontoid joint (p), **154:**315
  malignant melanoma metastases to axial skeleton, **155:**109
  occult fractures, carpals and metacarpals (l), **154:**1127
  subtalar arthrorisis, **154:**559
CT, breast, internal mammary vessels, **155:**397
CT, cranium
  anoxic/ischemic cerebral injury, reversal sign, children, **154:**361
  cerebral (b), **154:**360, **155:**108
  colloid cysts of third ventricle, **155:**135
  head and neck tumors (b), **155:**166
  intracranial cryptococcosis, **154:**603
  intracranial ganglioglioma, **154:**607
  intracranial leptomeningeal metastases, **154:**351
  lateral ventricular neoplasms, brain, **155:**365
  meningitis, comparison with Gd-DTPA-enhanced MR, **154:**809
  multiple sclerosis, adolescents, **155:**385
  osteoid osteoma, **155:**883
  Paget disease, syringomyelia associated with, **155:**881
  posttraumatic cerebral infarction, **154:**1293
  primary cerebral neuroblastoma, **154:**831
  sinus disease (l), **155:**425
CT, fetus, estimated radiation dose, multislice studies, **154:**185
CT, gallbladder, high-density bile (a), **154:**908
CT, hip
  dislocation, osteochondral impaction of femoral head with, **155:**1049
  posterior dislocation, cortical fracture of femoral head and, **155:**93
  risk of fracture (a), **155:**902
CT, humerus, displaced proximal fractures, Neer classification of (p), **154:**1029
CT, kidney
  long-term dialysis patients (l), **154:**1125
  lymphoma and, children, **155:**347
  oncocytoma, intratumoral fat on, **154:**307
  parenchyma, thickness, **155:**541
  percutaneous procedures, risk of puncturing lung, spleen, and liver, **154:**115
CT, larynx, chondrosarcoma, **154:**997
CT, leg, intracapsular osteoid osteoma, proximal femur (p), **154:**1241
CT, liver
  after transplantation, biliary complications (p), **154:**729
  cirrhotic, mesenteric, retroperitoneal, and subcutaneous fat in, **155:**73
  focal lesions, MR comparison (a), **154:**1358

  - focal nodular hyperplasia, contrast material retention in (l), **154:422**
  - hemangiomatosis (l), **154:423**
  - metastases detection, **155:763**
  - pedunculated hemangioma (l), **155:1137**
  - tumor imaging, **155:473**
- **CT, lung**
  - adenoid cystic carcinoma, calcification in (l), **154:419**
  - bronchiolitis obliterans, organizing pneumonia, **154:983**
  - pulmonary infarction (a), **154:665**
- **CT, lymph nodes,** Hodgkin disease patients, **155:267**
- **CT, neck**
  - Castleman disease, **154:1051**
  - ultrafast, laryngeal and tracheobronchial obstruction in infants, **154:345**
- **CT, pancreas**
  - carcinoma, fat obliteration in, **155:991**
  - fluid and urine leakage, after transplantation, **155:997**
  - low-density insulinoma, **155:995**
- **CT, pelvis**
  - cancer patients, pelvic pain, **155:85**
  - clinical imaging (b), **154:988**
  - ovarian cyst, herniation through inguinal canal (l), **154:202**
  - posterior perineal hernia, **154:761**
  - postsurgical complications, ileoanal pouches, **154:73**
  - surgical lateral ovarian transposition, **154:119**
- **CT, spine**
  - cerebral and spinal (b), **154:1074**
  - cervical facet joints, age-related changes, **154:817**
  - cervical spondylolysis, **154:751**
  - traumatic lumbar hernia, **154:757**
- **CT, thorax**
  - before lung transplantation (l), **155:1136**
  - blunt chest trauma (p), **154:55**, (l), **155:194**
  - critically ill patients (a), **155:901**
  - diffuse pleural disease, **154:487**
  - foot-in-mouth disease, **155:651**
  - Kaposi's sarcoma (a), **154:427**
  - left lower lobe bronchus, anterior wall stripe of, **154:33**
  - lung
    - biopsy guided by, actinomycosis and carcinoma, **155:1183**
    - carcinoma, calcification in, **154:255**
  - malignant pleural mesothelioma (p), **155:965**
  - mediastinal actinomycosis, **155:735**
  - mediastinal lymph node enlargement, usual interstitial pneumonitis, **154:251**
  - mediastinal masses, low-attenuation (l), **154:199**
  - mediastinal masses (l), **155:893**
  - non-Hodgkin lymphoma, calcification in, **155:739**
  - peripheral carcinoid tumor, lung, **155:1185**
  - pneumothorax, idiopathic spontaneous (a), **155:1350**
  - pulmonary interventional procedures guided by, detection of pneumothorax after, **154:45**
  - retroaortic anastomoses, azygos system, **154:41**
  - review (b), **155:970**
  - solitary pulmonary nodules, **154:701**
  - superior pericardial recess, simulating mediastinal mass, **154:69**
  - tuberculous bronchial stenosis, **155:971**
  - Whipple disease, mediastinum, **154:1187**
  - wooden foreign body in lung parenchyma, **154:999**
- **CT, thyroid,** anaplastic carcinoma, **154:1079**
- **CT, uterus,** perforating, simulating urachal carcinoma, **154:741**
- **CT, wrist,** what is abnormal (l), **154:1127**
- **Cyclosporine**
  - organ transplant recipients, malignant neoplasms in, **154:271**
  - therapy, Crohn's disease (a), **154:207**
- **Cyst,** *see* specific organ or site
- **Cystic fibrosis**
  - lung disease in, aerosolized amiloride (a), **155:661**
  - neonatal screening program, pancreatic function in (a), **154:1353**
  - research (a), **155:204**
- **Cystic teratoma,** mediastinum, **154:259**
- **Cystogastrostomy, transgastric, double-J catheter for (l), 154:421**
- **Cystoscopy,** double collecting system, children, **155:561**
- **Cytomegalovirus,** congenital infection, spinal cord calcification in (l), **155:1142**
- **Cytosine arabinoside,** high-dose therapy, acute leukemia, fatal pulmonary failure and (a), **154:1355**

D

- **Dementia,** MR signal abnormalities in, **154:1285**
- **Diabetes,** insulin-dependent, transplacental passage of insulin in pregnancy (a), **155:1349**
- **Diagnosis,** statistics and (l), **155:193**
- **Diagnostic tests**
  - cost of (a), **155:662**
  - definition of terms, **155:621**
- **Diaphragm,** congenital defects, children (a), **155:431**
- **Diastematomyelia,** cervical and basicranial, neonate, **154:806**
- **Diffuse pleural disease,** CT, **154:487**
- **Digestive tract,** abnormal radiographs (b), **155:48**
- **Diverticulitis**
  - acute, colon, sonography, **154:1199**
  - cecum and ascending colon, sonography, **155:283**
  - CT diagnosis, **154:281**
- **Drugs,** brain chemistry, behavior and, **155:925**
- **Ductus arteriosus,** transcatheter closure, pediatric (a), **154:209**
- **Dysbaric osteonecrosis,** further hyperbaric exposure and, **155:95**
- **Dysphagia**
  - diagnosis and treatment (b), **154:532**
  - radiologic investigation, **154:1157**

E

- **Echocardiography,** color Doppler (b), **154:1060**
  - radiologic investigation of (l), **155:1344**
- **Echocardiography**
  - Doppler and, cardiac surgery, **155:130**
  - ventricular mass (a), **155:662**
- **Embolization**
  - arterial, life-threatening hemorrhage from Meckel's diverticulum, **154:1257**
  - transcatheter, ruptured abdominal aortic stump, **154:181**
- **Encephalopathy**
  - AIDS-related, MR (a), **155:205**
  - Wernicke, MR, **155:1309**, **155:1315** (commentary)
- **Endoprosthesis,** Wallstent, iliac artery stenoses, **154:613**
- **Endoscopic therapy**
  - benign bile duct strictures (a), **154:428**
  - biliary tract fistulas (a), **154:906**
  - CT, esophageal carcinoma, **155:277**
  - upper gastrointestinal tract, pediatric patient (a), **154:429**
- **Endosonography (b), 155:1220**
  - anal (a), **154:210**
  - esophagogastric carcinoma (a), **155:429**
- **Endotracheal tube,** malpositioning, radiologic detection, **154:23**
- **Enema**
  - contrast
    - acute diverticulitis, **154:281**
    - postsurgical complications, ileoanal pouches, **154:73**
  - double-contrast
    - filling the colon, **154:**279
    - pumps in (l), **155:**195
- **Ependymoma,** subependymoma and, intracranial, MR, **154:**831
- **Epidermoid cyst,** splenic, familial, **155:**1233
- **Epididymitis,** Müllerian duct cyst and calculus, sonography, **155:**91
- **Epigastric artery,** pseudoaneurysm, **155:**529
- **Epilepsy,** intractable complex partial seizures, MR, **154:**577
- **Epiphysis,** proximal humeral, sonography (a), **155:**203
- **ERCP,** *see* Cholangiopancreatography, endoscopic retrograde
- **Ergotism,** mesenteric aneurysm (l), **155:**897
- **Esophagitis,** reflux, patients with Zollinger-Ellison syndrome (a), **154:**1131
- **Esophagogastric carcinoma**, endosonography in (a), **155:**429
- **Esophagus**
  - acute food impaction, glucagon, effervescent agent, and water combination, **154:**533
  - acute leukemic infiltration, dysphagia caused by (l), **155:**654
  - carcinoma, staging, endoscopic CT, **155:**277
  - disease, plain chest radiography (p), **155:**729
  - function, bolus consistency and temperature (a), **154:**1356
  - jet phenomenon, **155:**289
  - Maloney dilation (a), **155:**902
  - malpositioning of endotracheal tubes, radiologic detection, **154:**23
  - motility
    - disorders, manometry and radiology in (a), **154:**1356
    - radiologic evaluation of, **155:**983
  - tuberculosis, peptic strictures and (l), **154:**200
  - update on radiology, **155:**933
- **ESWL,** *see* Extracorporeal shock-wave lithotripsy
- **Ethanol**
  - percutaneous injection therapy
    - hepatocellular carcinoma, **154:**947, **155:**1221
    - sonographically guided, hyperparathyroidism, **154:**1087
    - surface neoplasms of liver, **155:**507
- **Etidronate,** intermittent cyclical treatment, postmenopausal osteoporosis (a), **155:**1349
- **Ewing sarcoma,** chemotherapy for, MR, **155:**343
- **Extracorporeal membrane oxygenation**
  - neonatal, neurophysiologic outcome (a), **155:**431
  - respiratory syncytial virus bronchiolitis, children (a), **154:**1358
- **Extracorporeal shock-wave lithotripsy**
  - abdominal radiography, renal ultrasound and excretory urography comparison (a), **154:**1132
  - bile duct stones, **155:**775
    - sonography for localization of stones (a), **154:**1356
  - biliary, gallbladder stone fragments after (a), **155:**663
  - gallstones, **154:**291, **155:**655(l)
    - recurrence after (a), **154:**1131
  - methyl *tert*-butyl ether and, partially calcified gallstones (a), **154:**427
  - soft-tissue damage induced by, liver, **155:**771

F

- **Fallopian tube,** obstruction, selective osteal salpingography and transvaginal catheter in, **154:**735
- **Fatsat technique,** MR of abdomen, **155:**1111
- **Femoral artery**
  - angioplasty, ruptured polyester balloon (l), **155:**1141
  - catheterization
    - conversion of retrograde to antegrade, **154:**179
    - Doppler flow monitoring, **155:**131
- **Femoral head**

  - osteochondral impaction of, hip dislocation and, CT, **155:**1049
  - posterior dislocation, CT, **155:**93
- **Femur**
  - acute intracapsular fracture, MR (a), **154:**1357
  - fractures, scintimetry after, prognostic accuracy (a), **154:**1131
  - proximal
    - intracapsular osteoid osteoma, CT (p), **154:**1241
    - metastatic carcinoma, MR (l), **154:**902
- **Ferritin,** cerebral hemorrhage appearance on CT and, **154:**1053
- **Fetal lobation,** anatomo-ultrasonographic correlation (a), **155:**205
- **Fetus,** nuchal cystic hygroma, spontaneous resolution in second trimester of pregnancy (l), **154:**903
- **Fine-needle aspiration cytology,** mammography-guided, breast lesion, nonpalpable, **155:**977
- **Fine needle nonaspiration cytology,** liver, **155:**1217
- **Fleischner lecture,** radionuclides and the lung, **155:**455
- **Fluoroscope**
  - C-arm, swallowing disorders, **155:**986
  - Gadopentetate dimeglumine, excretion, breast milk, **154:**1305
- **Foot,** soft-tissue tumors, MR, **155:**1025

G

- **Gadopentetate dimeglumine**
  - benign lumbar arachnoiditis, **155:**873
  - fat suppression technique and, MRI of optic nerve lesions, **155:**849
  - postoperative imaging, lumbar spine, **155:**867
- **Gadopentetate dimeglumine-polylysine,** MR angiography, **155:**407
- **Gallbladder**
  - contractility, spinal cord injuries, sonography, **154:**521
  - nonvisualized, oral cholecystography, lithotripsy and (a), **154:**1358
  - percutaneous interventional procedures (a), **154:**1358
  - polyps in (a), **155:**203
- **Gallstones,** *see* Cholelithiasis
- **Ganglioglioma**
  - intracranial
    - MR, **155:**899
    - MR, CT and clinical findings, **154:**607
- **Gastric polyps,** gastric mucosal background study in (a), **154:**1357
- **Gastric ulcer,** malignancy (a), **155:**901
- **Gastrinomas,** duodenum (a), **155:**428
- **Gastroenterostomy,** percutaneous, fluoroscopically guided, **154:**725
- **Gastroesophageal reflux,** stridor and, infants (a), **155:**903
- **Gastrointestinal bleeding,** push-enteroscopy for diagnosis (a), **155:**1350
- **Gastrointestinal disease,** functional, idiopathic autonomic denervation in (a), **155:**664
- **Gastrointestinal tract**
  - complications, cytosine-arabinoside chemotherapy, **154:**95
  - CT (b), **154:**86
  - lipomas (p), **155:**1205
  - radiology (b), **155:**282
  - smooth muscle tumors, endoscopic sonography (a), **155:**1351
- **Gastrojejunostomy,** percutaneous, modified cope loop catheter and, **155:**79
- **Gastropexy,** with percutaneous gastrostomy, **154:**1003
- **Gastrostomy**
  - endoscopic vs operative (a), **154:**1357
  - percutaneous
    - fluoroscopically guided, **154:**725
    - gastropexy with, **154:**1003
    - percutaneous endoscopic, tube dysfunction following (a), **155:**902
- **Geniculate artery,** pseudoaneurysm (l), **155:**659
- **Germ cell tumors,** neuroimaging, **154:**1299
- **Gibbs phenomenon (l), 154:**204
- **Glazer, Norman (m), 154:**784
- **Glomus tumor,** thigh (l), **155:**423
- **Glossopalatal sphincter,** manometric characteristics (a), **154:**1356
- **Gorham syndrome,** right clavicle and scapula, **154:**1335
- **Graves disease,** ^{131}I nasogastric administration, uncooperative patient, **155:**611
- **Growth plate,** fracture, MR, **155:**1261
- **Guidewires,** floppy platinum-tip, complications from, **154:**1103
- **Gunshot wounds,** bullet, ballistics, and mechanisms of injury, **155:**685, **155:**691

H

- **Hallux valgus,** deformity (p), **155:**119
- **Halo vest,** cervical spine fixation during MR, **154:**631
- **Hartman, Glen W. (m), 154:**952
- **Hawkins-Hunter rocket wire,** biliary system, **154:**1101
- **Health care,** European, consequences, **155:**1321 (commentary)
- **Heart**
  - cyanotic congenital disease, MR of surgical procedures, **155:**259
  - diagnosis (b), **155:**728
  - fat in and around, MR (p), **155:**271
  - MR spectroscopy, **155:**1
  - valvular regurgitation, cine MR, **155:**723
- **Heart disease,** congenital, angiography in, **154:**789
- **Heart-lung transplant**
  - lung rejection after, **155:**23
  - postoperative pleural effusion (l), **154:**1344
- ***Helicobacter pylori***
  - histologic gastritis (a), **154:**1129
  - intrafamilial clustering of infection (a), **154:**1354
- **Hemangioma**
  - hepatic, fatality from fine-needle aspiration biopsy (l), **154:**203
  - intramuscular
    - radiologic appearance (l), **155:**896
    - MR (p), **154:**563
- **Hemangiomatosis,** liver and spleen, embolization and splenectomy treatment of, **155:**1235
- **Hematuria**
  - asymptomatic microscopic (a), **155:**1145
  - blunt abdominal trauma, children, CT, **154:**569
- **Hemosiderin,** cerebral hemorrhage appearance on CT and, **154:**1053
- **Hemostasis,** before abdominal interventions, **154:**233, **154:**239 (commentary)
- **Hepatectomy,** partial, bile duct necrosis after (l), **154:**1124
- **Hepatic artery**
  - color Doppler sonography, **155:**517
  - transcatheter embolization, bile duct necrosis after (l), 154:1124
- **Hepatocellular carcinoma**
  - comparison with other lesions, Doppler studies (a), **154:**664
  - encapsulated (a), **155:**666
  - ethanol injection therapy, percutaneous, **155:**1221
  - fine-needle aspiration biopsy (a), **154:**664
  - hepatic arterial injection chemotherapy, cisplatin suspended in lymphographic agent for (a), **154:**662
  - percutaneous ethanol injection therapy, **154:**947
  - presenting as bone metastasis (a), **154:**662
  - small, diagnosis, **155:**49
- **Hepaturia,** dipsticks, urinary tract cancer detected with (a), **154:**663
- **Heroin,** cervical osteomyelitis and, **155:**333
- **Hickey lecture**
  - historical perspective, **155:**235
  - ionic and nonionic iodinated contrast media, **155:**225
- **Hilar cholangiocarcinoma,** enhanced CT, **154:**1203
- **Hilar tumors,** malignant, biliary endoprosthesis dysfunction and, **155:**391
- **Hip**
  - dislocation, osteochondral impaction and, CT, **155:**1049
  - prosthesis, K-edge digital subtraction arthrography, **155:**1053
- **Histiocytoma,** malignant fibrous, lung, asbestos exposure and, **154:**65
- **Histiocytosis X,** pulmonary, after chemotherapy for Hodgkin disease, **155:**741
- **Histoplasmosis,** rounded atelectasis caused by, **155:**275
- **History,** clinical, value of (l), **155:**653
- **Hodgkin disease**
  - breast carcinoma after, **155:**39
  - chemotherapy for, pulmonary histiocytosis X after, **155:**741
  - children, CT and lymphography comparison with laparotomy, **154:**1251
  - leukemia after (a), **154:**1130
  - lymphocyte-predominant (l), **155:**658
  - newly diagnosed patients, CT of necrotic mediastinal lymph nodes, **155:**267
  - primary pulmonary (a), **154:**1354
- **Holoprosencephaly,** alobar and semilobar, sonography of fetal facial features, **154:**143
- **Human immunodeficiency virus**
  - transmission, children (a), **154:**1357
  - type 1, *Pneumocystis carinii* pneumonia risk in (a), **154:**1354
- **Humerus,** displaced proximal fractures, Neer classification of (p), **154:**1029
- **Hyaline membrane disease,** mechanical breathing, surfactant therapy effects, infant (a), **154:**1132
- **Hydatid cysts,** multiple (l), **154:**1126
- **Hydatid disease,** spleen, imaging findings, **154:**525
- **Hydronephrosis**
  - carcinoma of the vermiform appendix and (l), **154:**654
  - prenatal detection of, **155:**125
- **Hyperparathyroidism,** ethanol injection, sonographically guided percutaneous, **154:**1087
- **Hypertension**
  - portal, ultrasonic measurements (a), **154:**908
  - radiation and (l), **154:**659
- **Hypokalemia,** aldosteronism, renal cysts and (a), **154:**1354
- **Hypothalamic histiolleitis,** CT, **154:**1338

I

- **Ileitis,** pouch (a), **154:**428
- **Ileoanal pouches,** CT, scintigraphy, and contrast enema comparison, **154:**73
- **Iliac artery,** stenoses, Wallstent endoprosthesis treatment, **154:**613
- **Ilizarov limb-lengthening procedures,** distraction site, sonography, **154:**125
- **Imaging**
  - diagnostic (b), **155:**12, **155:**526
  - pancreas transplant, **155:**13
- **Immunoscintigraphy,** anti-CEA, parotid gland tumors, **154:**1259
- **Impotence**
  - diagnostic evaluation, role of imaging in (l), **154:**1347
  - vasculogenic erectile, penile duplex sonography (a), **154:**907
- **Infant**
  - abuse, diagnostic imaging, **155:**703
  - febrile, chest radiography in evaluation, **155:**833
  - hip, dynamic sonography, **155:**837
- **Infertility,** sonography (b), **154:**544
- **Inflammatory bowel disease,** DRG-based pro-

spective payment categories (a), **155:**664

Infrapopliteal arteries, percutaneous transluminal angioplasty, **154:**171

Insulin, transplacental passage, diabetic pregnant women (a), **155:**1349

Insulinoma, low-density, CT, **155:**995

Interleukin-2, shoulder pain caused by, scintigraphy, **154:**327

Intestine, small, clinical radiology (b), **154:**72

Intracranial aneurysms, MR angiography, **155:**159

Intracranial hemorrhage, sonography in, **155:**595

Intrahepatic shunt, portosystemic venous, **155:**527

Intraocular lesions, patients with systemic disease, MR, **154:**385

Intraurethral stent, self-retaining, alternative for prostatism, **154:**111

Intraventricular hemorrhage
  indomethacin and (a), **154:**210
  preterm infants (a), **154:**665

Intussusception, hydrostatic reduction of (l), **154:**1123

Iodine-131, nasogastric tube administration, Graves disease patients, **155:**611

Iron oxide
  MR enhanced by, hepatic metastases, **155:**763
  ultrasmall particles, MR receptor imaging, **155:**1161

Irradiation, bone marrow changes after, MR, **154:**745

Ischemia, recurrent (a), **154:**663

Islet cell tumors, von Hippel-Lindau disease, **155:**501

Islets of Langerhans, tumors, CT, **155:**995

J

Jejunostomy
  percutaneous endoscopic
    poor results with (a), **155:**902
    tube dysfunction following (a), **155:**902

Jugular vein, vena caval filter placement via (l), **155:**898

K

Kaposi sarcoma
  AIDS-associated, lymphangioscintigraphy in, **155:**311
  CT (a), **154:**427

Keller, John T. (m), **155:**1096

Kidney
  abnormalities, bacterial attachment and, boys with urinary tract infection (a), **154:**907
  abscesses, percutaneous drainage, **155:**81
  allografts, duplex Doppler sonography in, **155:**295
  blood flow, transcatheter thrombosis of leaking saccular aneurysm, **154:**1097
  calculi, multimodality treatment (a), **155:**665
  carcinoma, venacavography and MR comparison (a), **154:**428
  chronic infections, imaging, **155:**485
  clinical imaging (b), **154:**1096
  crossed renal ectopia without fusion, sonography (l), **154:**657
  function, evaluation with radionuclides (b), **154:**114
  imaging, long-term dialysis patients, CT and sonography comparison (l), **154:**1125
  intrarenal arteriovenous fistula, pseudoaneurysm and, duplex Doppler sonography (l), **154:**424
  lymphoma and, children, CT and sonography, **155:**347
  medullary sponge, nephrolithiasis and, **155:**299
  nonobstructive renal disease, intrarenal arterial Doppler sonography, **154:**1223
  parenchyma, thickness, CT, **155:**541
  pelvis, transitional cell carcinoma, **155:**713
  percutaneous procedures, posterior intercostal approach, **154:**115
  polycystic disease, pediatric (a), **154:**907
  tissue, simulating adrenal mass (l), **155:**656
  transplantation
    children, Doppler evaluation of, **154:**785
    rejection, pyramidal appearance and resistive index, **155:**531, **155:**536 (commentary), **155:**538 (commentary)

Kimray-Greenfield filter
  intracaval breakage (l), **154:**1349
  percutaneous insertion, **154:**621

Knee
  acute changes in joint, jogging and, MR, **154:**1233
  lateral meniscus, pseudotear, MR, **154:**1237
  spontaneous osteonecrosis, MR, **154:**331
  total replacement, porous-coated metal-backed patellar component, **155:**555

Kyphosis, radiographs (a), **155:**430

L

Laparatomy, comparison with CT and lymphography, staging of Hodgkin disease in children, **154:**1251

Larynx, chondrosarcoma, CT, **154:**997

Lead time bias, misleading effects, **155:**625

Leigh syndrome, MR, correlation with biochemical defect, **154:**1269

Leiomyoma, distinguished from pelvic masses, MR, **154:**295

Leiomyosarcomatosis, peritoneal, CT, **155:**799

Length time bias, misleading effects, **155:**625

Leptomeningeal metastases, intracranial, CT and MR, **154:**351

Leukemia
  acute, high-dose Ara-C therapy, fatal pulmonary failure and (a), **154:**1355
  after chemotherapy for ovarian cancer (a), **154:**1129
  after Hodgkin's disease (a), **154:**1130
  esophageal anomalies and (l), **155:**654
  myelocytic, secondary, after breast carcinoma therapy (a), **154:**662

Lidocaine, alkalinized (l), **155:**198

Ligaments, wrist, arthrography and MR comparison, **154:**337

Linguinal cortical defect, unknown cause (l), **154:**420

Lipoma
  gastrointestinal (p), **155:**1205
  intracranial, pathogenesis of, MR, **155:**855, **155:**865 (commentary)

Lipomatous tumors, pelvis, women (p), **155:**317

Literature, radiologic, referencing trends (l), **155:**1341

Lithotripsy
  see also Extracorporeal shock-wave lithotripsy
  biliary, hepatic subcapsular hematoma and, **154:**1015
  endoscopic, percutaneous cholecystolithotomy with, **155:**781
  piezoelectric biliary, gallstone fragmentation and, **155:**1211

Liver
  abscess (l), **155:**654
  adenoma, MR, **155:**1009
  ascariasis (l), **155:**421
  caudate lobe (p), **154:**87
  cavernous hemangioma
    differentiation from metastases by MR (a), **155:**432
    fine-needle aspiration biopsy (a), **154:**908
    MR (a), **155:**432
  cirrhosis
    focal ultrasound lesions (a), **155:**429
    mesenteric, retroperitoneal, and subcutaneous fat in, CT, **155:**73
    regenerating nodules, **155:**1227
  Clonorchis sinensis, **155:**1001
  extramedullary hematopoiesis, sonography (l), **154:**900
  fine-needle nonaspiration cytology, **155:**1217
  focal lesions
    CT and MR comparison (a), **154:**1358
    t-null inversion recovery sequence MR (a), **154:**1359
  focal nodular hyperplasia, contrast material retention in (l), **154:**422
  hemangioma, pedunculated, CT (l), **155:**1137
  hemangiomas vs metastases, MR, **155:**55, **155:**61
  hemangiomatosis, embolization and splenectomy treatment of, **155:**1235
  hydatid cysts (a), **155:**428
  hydatid disease, biliary complications, ERCP value in (a), **154:**210
  imaging
    current trends, International Symposium and Course, June 1990, **155:**1125
    ghost artifact on gradient-echo, **154:**633
  inflammatory pseudotumor (l), **154:**201
  intrahepatic abscess, ventriculoperitoneal shunt and (l), **155:**894
  iron overload, noninvasive imaging (a), **154:**908
  metastases, CT, MR, and enhanced MR, **155:**763
  MR, iron oxide-enhanced, **155:**943
  neoplasms, percutaneous ethanol injection therapy for (l), **155:**420
  ringed lesions, MR (p), **154:**287
  soft-tissue damage, after biliary lithotripsy, **155:**771
  subcapsular hematoma, complication of biliary lithotripsy, **154:**1015
  surface neoplasms, percutaneous ethanol injection therapy for, **155:**507
  transplantation
    biliary complications after (p), **154:**729
    children, MR and sonography, **155:**351
  tumors
    color Doppler imaging, **154:**509
    Gd-DTPA-enhanced spin-echo imaging, **154:**515
    imaging, **155:**473
  venocclusive disease, Doppler sonography, **154:**721

Lobectomy, MRI correlation, temporal lobe seizures, **155:**581

Lumpectomy, tumor recurrence after, **155:**35

Lung
  adenoid cystic carcinoma, calcification in, CT (l), **154:**419
  blastomycosis, chest radiographs, **154:**1177
  bronchoalveolar carcinoma, CT, **154:**1318
  calcification in carcinoma, CT, **154:**255
  cancer
    adrenal metastatic lesions, CT (a), **155:**1144
    radiologic diagnosis, pitfalls, **154:**1165
  CT-guided biopsy, thoracic actinomycosis and carcinoma, **155:**1183
  diffuse centrilobular lesions, *Staphylococcus aureus* (l), **155:**652
  endobronchial sarcoidosis, upper lobe collapse (l), **154:**897
  hernia, radiologic features, **154:**51
  infarction, CT (a), **154:**665
  interstitial disease, chest radiographs with bronchoalveolar lavage (a), **154:**905
  left lower lobe bronchus, anterior wall stripe, CT, **154:**33
  malignant fibrous histiocytoma, asbestos exposure and, **154:**65
  malignant pleural effusions, small bore catheter drainage and sclerotherapy (a), **154:**662
  metastatic osteosarcoma to, **154:**1321
  metastatic tumors, fine needle aspiration biopsy (a), **154:**905
  neutrophil kinetics, smoking effects (a), **154:**661
  parenchyma, wooden foreign body in, **154:**999
  peripheral carcinoid tumor, CT, **155:**1185
  radiation fibrosis, Gd-DTPA enhancement (a),

154:666

- radionuclides and, **155:455**
- rejection, after heart-lung transplant, **155:23**
- rounded atelectasis, caused by histoplasmosis, **155:275**
- scans, criteria for diagnosis of pulmonary emboli, **154:975**
- sequestration, imaging of, **154:241**, **155:1343**(l)
- solitary nodule, radiologic evaluation, **154:701**
- transplantation
  - bilateral pulmonary fibrosis (a), **155:427**
  - chest CT before (l), **155:1136**
  - reactivation of tuberculosis after, **154:495**

Lymphangioleiomyomatosis, pulmonary (l), **155:419**

Lymphangioma, peripancreatic retroperitoneal, similarities to other lesions (l), **154:1125**

Lymphangioscintigraphy, AIDS-associated Kaposi sarcoma, **155:311**

Lymphedema, periportal, trauma patients (l), **154:1124**

Lymph nodes

- abnormal, sonography of, **155:1241**
- metastases, carotid artery and jugular vein, sonography, **154:411**
- necrotic mediastinal, Hodgkin disease, CT, **155:267**

Lymphography, staging of Hodgkin disease, children, **154:1251**

Lymphoma

- gastrointestinal, sonography, **155:795**
- intraabdominal and retroperitoneal, fine needle aspiration diagnosis (a), **154:1130**
- non-Hodgkin, calcification, plain film and CT, **155:739**
- renal involvement, children, CT and sonography, **155:347**

M

Mammary artery, importance, percutaneous transthoracic intervention, **154:47**

Mammary vessels, internal, CT, **155:397**

Mammography

- abnormalities, computerized follow-up of, **155:751**
- appearance, retained Dacron cuff of Hickman catheter, **155:1203**
- breast mass simulation (l), **154:900**
- Canadian National Breast Screening Study, **155:743**, **155:748** (commentary)
- Canadian National Breast Screening Study (l), **155:1133**
- collapse of breast implant after (l), **154:1345**
- computers in, **155:755**
- dual-screen and dual-emulsion film combination, quality of, **154:265**
- follow-up studies, nonpalpable benign breast lesion, **155:1195**
- radiation dose during, film processing time effects, **155:1189**
- screen/film combinations, radiation dose, **154:713**
- sensitivity of (l), **154:419**
- stereotactic fine-needle aspiration guided by, breast lesion, nonpalpable, **155:977**

Mandible, incipient lingual cortical defect, American Indian child (l), **154:658**

Manometry

- anorectal (a), **155:429**
- glossopalatal sphincter (a), **154:1356**
- radiology and, esophageal motility disorders (a), **154:1356**
- sphincter of Oddi in (a), **154:1131**

Marfan syndrome

- microfibrillar-fiber system, immunohistologic abnormalities (a), **155:1350**
- musculoskeletal manifestations of (p), **155:99**

Mastication, muscles of (l), **154:658**

McNeil criteria, diagnosis of pulmonary emboli, lung scans, **154:975**

Meckel's diverticulum, life-threatening hemorrhage from, arterial embolization, **154:1257**

Mediastinum

- cystic teratoma, **154:259**
- fibrosis, dysphagia due to, pulmonary tuberculosis and, **154:61**
- masses
  - CT (l), **155:893**
  - low-attenuation CT (l), **154:199**
  - superior pericardial recess simulating, **154:69**
- Whipple disease, **154:1187**

Medulloblastoma, recurrent, Gd-DTPA MRI, **155:153**

Megalourethra, congenital (a), **155:903**

Melanoma

- malignant, metastases to axial skeleton, CT, **155:109**
- metastases, sonographic diagnosis, liver, gallbladder, and spleen (a), **154:211**
- MRI in (a), **155:1352**

Memorials

- Andrew Eccles Yeates, 1951–1989, **154:1284**
- Earl E. Barth, 1901–1990, **155:624**
- Glen W. Hartman, 1936–1990, **154:952**
- John T. Keller, 1922–1990, **155:1096**
- Norman Glazer, 1920–1989, **154:784**
- Paul L. Rogers, 1931–1989, **154:118**
- Robert James Borgerson, 1919–1989, **154:1086**

Memory disorder, MR signal abnormalities in, **154:1285**

Meningitis, Gd-DTPA-enhanced MRI, CT comparison, **154:809**

Mesenteric artery

- superior
  - congenital aneurysm, CT (l), **155:199**
  - fat obliteration around, pancreatic carcinoma and, CT, **155:991**

Mesothelial cyst, round ligament (l), **155:1345**

Mesothelioma

- malignant pleural, CT (p), **155:965**
- papillary, peritoneum, **155:1245**

Metal detector, ingested metal foreign bodies, **155:803**

Metastatic disease, long bones (a), **154:906**

Methylprednisolone, acute spinal-cord injury (a), **155:662**

Methyl *tert*-butyl ether

- gallstone dissolution, **155:67**
- gallstone dissolution (a), **155:428**

Microalbuminuria, angiotensin converting enzyme inhibitor therapy, diabetic children (a), **155:1146**

Microcoils, platinum, therapeutic embolization, **155:401**

Mitral commissurotomy, percutaneous transvenous, indications, complications, and outcome (a), **154:207**

Monochorionic twinning, sonography, **154:459**

Motility disorders, gastrointestinal, stress and (a), **154:664**

MR imaging

- angiography, **154:937**
- body (b), **155:762**
- cancer patients, pelvic pain, **155:85**
- clinical (b), **155:1292**
- fast, techniques and applications, **155:951**
- infant, feeding formula given prior to (a), **155:205**
- melanoma (a), **155:1352**
- physical principles and instrumentation (b), **154:770**
- thermal effects, worst case, sheep, **155:1105**
- ultrasmall iron oxide particles, asialoglycoprotein receptors, **155:1161**
- workbook (b), **154:1228**

MR imaging, abdomen

- Budd-Chiari syndrome, percutaneous transluminal angioplasty treatment (l), **154:1350**
- fat-saturation technique, **155:1111**
- femoropopliteal venous thrombosis, **154:175**
- prenatal detection of abdominal mass, pancuronium bromide and, **154:1049**
- thorax and, comparison with other procedures, **154:989**
- transposition of great vessels, congenitally corrected (l), **154:898**

MR imaging, adrenal gland, current status, **154:927**

MR imaging, ankle, osteochondritis dissecans, **154:555**

MR imaging, bone

- chemotherapy for Ewing sarcoma and, **155:343**
- malignant tumors, vs scintigraphy, **155:1043**
- primary neoplasms, bone-chip allografts, **155:1257**
- sarcoma, chemotherapy effects, **154:763**
- soft tissue tumors and their mimics (b), **154:554**
- tumor and tumorlike lesions, **155:817**

MR imaging, bone marrow, changes after irradiation, **154:745**

MR imaging, central nervous system

- sarcoidosis, **155:1293**
- spatial misregistration, vascular flow, **155:1117**

MR imaging, cranium

- AIDS-related encephalopathy (a), **155:205**
- basal ganglion lesions, neurofibromatosis, **154:369**
- brain (b), **155:580**
- cerebellum, **154:593**
- cerebral hemorrhage, ferritin and hemosiderin role in, **154:1053**
- choroidal fissure and parenchymal cyst, CSF-like, **155:1069**
- clivus, normal and abnormal, **155:1285**
- colloid cysts of third ventricle, **155:135**
- contrast-enhanced, Bell's palsy, **155:573**
- corpus callosum, agenesis and lipoma (l), **154:1348**
- cranial nerves (p), **154:1263**
- extraaxial brain tumors, epidermoid tumor differentiation, **155:1059**, **155:1066** (commentary)
- Gd-DTPA
  - meningitis, CT comparison, **154:809**
  - recurrent medulloblastoma, **155:153**
- head and neck
  - anatomy (b), **154:630**
  - tumors (b), **155:166**
- internal carotid artery siphon, **155:359**
- intracranial chemical-shift artifacts on, **154:1275**
- intracranial ependymoma, subependymoma and, **154:837**
- intracranial ganglioglioma, **154:607**, **155:899**
- intracranial leptomeningeal metastases, **154:351**
- intracranial lipoma, **155:855**, **155:865** (commentary)
- intractable complex partial epileptic seizures, **154:577**
- lateral ventricular neoplasms, brain, **155:365**
- Leigh syndrome, children, **154:1269**
- multiple sclerosis, adolescents, **155:385**
- optic nerve, lesions, **155:849**
- pineal tumors, **155:143**
- primary cerebral neuroblastoma, **154:831**
- sella and para-sella region (b), **154:384**
- signal abnormalities, memory disorder and dementia, **154:1285**
- temporal lobe seizures, **155:581**
- temporomandibular joint, **154:1245**
- Tolosa-Hunt syndrome, **154:167**
- trichilemmal cyst, scalp (l), **154:423**

MR imaging, extremities, deep venous thrombosis (l), **155:897**

MR imaging, eyes, intraocular lesions, patients with systemic disease, **154:385**

MR imaging, foot

- ankle and (v), **154:776**
- tumors, soft-tissue, **155:1025**

MR imaging, hand and wrist, detection of masses, **154:323**

MR imaging, heart

- cine, valvular regurgitation, **155:723**

cyanotic congenital heart disease, surgical procedures, **155:**259
fat (p), **155:**271
mitral regurgitation (a), **154:**1133
MR imaging, hip, metastatic carcinoma (l), **154:**902
MR imaging, kidney, renal carcinoma, extending to renal vein and inferior vena cava (a), **154:**428
MR imaging, knee
acute changes in joint, jogging and, **154:**1233
acute rheumatoid arthritis, **155:**329
leukemic children (a), **155:**205
medial meniscal flounce (l), **155:**199
meniscal pathology (a), **155:**430
osteochondritis dissecans, **155:**549
osteonecrosis, **154:**331
popliteal artery, entrapment, **154:**425
popliteal vein entrapment (l), **155:**424
pseudotear of lateral meniscus, **154:**1237
MR imaging, leg
femoral head, acute intracapsular fracture (a), **154:**1357
tarsal tunnel syndrome, **155:**323
MR imaging, liver
adenoma, **155:**1009
alveolar echinococcosis (a), **155:**1147
cirrhosis, regenerating nodules of, **154:**505
focal lesions
CT comparison (a), **154:**1358
t-null inversion recovery sequence (a), **154:**1359
Gd-DTPA-enhanced, spin-echo, differentiation of tumors, **154:**515
gradient-echo, ghost artifact on, **154:**633
hemangioma
differentiation from metastases (a), **155:**432
vs metastases, **155:**55, **155:**61
iron oxide-enhanced, liver and spleen, **155:**943
metastases detection, **155:**763
ringed lesions (p), **154:**287
t-null inversion recovery sequence, characterization of lesions (a), **154:**1133
transplantation, children, **155:**351
MR imaging, muscle, intramuscular hemangiomas (p), **154:**563
MR imaging, neck, Gd-DTPA-enhanced, tumors of nasopharynx and adjacent areas, **154:**585
MR imaging, pelvis
clinical imaging (b), **154:**988
leiomyoma, distinguished from pelvic masses, **154:**295
MR imaging, prostate, cysts, **155:**1021
MR imaging, sacrum, lesions (p), **154:**771
MR imaging, scrotum, high-field-strength, heating, **154:**1229
MR imaging, shoulder
arthrography, comparison with conventional MR, **155:**829
correlation with plain film radiographs (p), **154:**549
0.2T permanent-magnet unit, **154:**777
MR imaging, skeletal, growth plate fractures, **155:**1261
MR imaging, soft-tissue, masses (l), **155:**423
benign and malignant differentiation, **155:**1251
MR imaging, spine
central nervous system diseases (b), **155:**848
cervical, halo vest for fixation, **154:**631
cervical facet joints, age-related changes, **154:**817
cervical portion, pseudoatrophy, **154:**1069
comprehensive study (b), **155:**384
diagnostic applications (b), **155:**1076
Gd-DTPA-enhanced
central nervous system, von Hippel-Lindau disease (a), **154:**211
extradural degenerative disease, **154:**151
tears of anulus fibrosus, **154:**159
lumbar
benign lumbar arachnoiditis, **155:**873
postoperative, **155:**867
lumbosacral, synovial cysts, **154:**163
pial metastases, **155:**1077
pocket atlas (b), **154:**1268
three-dimensional gradient-recalled, cervical radiculopathy, **154:**375
MR imaging, spleen
iron oxide-enhanced, liver and spleen, **155:**943
visceroatrial situs (p), **154:**797
MR imaging, testes, seminomatous and nonseminomatous tumors, **154:**539
MR imaging, thorax
abdominal wall and, comparison with other procedures, **154:**989
ascending aortic prosthetic conduits by (a), **154:**1131
bright pleural effusion, ascites and, **155:**1237
mediastinal and inlet vein, patency, **155:**1177
pseudarthrosis, giant synovial cyst associated with, **155:**337
review (b), **155:**970
MR imaging, thymus, tumors (p), **155:**495
MR imaging, wrist, ligament evaluation, arthrography comparison, **154:**337
Müllerian duct, cyst and calculus, epididymitis associated with, sonography, **155:**91
Multiple sclerosis
adolescents, CT and MR, **155:**385
bowel dysfunction in (a), **155:**663
MR in (b), **155:**152
Musculoskeletal system
avulsion and stress injuries (b), **154:**134
sonography of, **155:**237
trauma (b), **155:**337
Mycobacterium tuberculosis, susceptibility to infection by, racial differences (a), **154:**1354
Myocardium
infarction, noninfarcted myocardium, functional significance of hypertrophy (a), **154:**207
ischemic, thallium detection of (a), **155:**1349
Myopathy, pentozacine-inuced, imaging in, **154:** 343

N

Naloxone, acute spinal-cord injury (a), **155:**662
Nasopharynx, tumors, MR, **154:**585
Necrotizing enterocolitis, neonates, portable abdominal radiography in, **154:**779
Nephrolithiasis, medullary sponge kidney and, **155:**299
Neuroblastoma, primary cerebral, CT and MR, **154:**831
Neurofibromatosis, basal ganglion lesions in, MR, **154:**369
Neurofibromatosis 2, etiology, **154:**1337
Neuroimaging, germ cell neoplasms, **154:**1299
Nitinol basket instrument, percutaneous cholecystolithotomy, **155:**515
Nuclear medicine
1989 annual (b), **154:**404
developing countries (b), **154:**40
pulmonary, thromboembolic disease (a), **154:**907
spine fracture probability, multi-site BMC measurements for (a), **154:**210
tomographic methods (b), **154:**1078
Nutcracker phenomenon, pericaliceal varices due to, **154:**305

O

Omentum, Castleman disease (l), **154:**654
Oncocytoma, renal, mimicking angiomyolipoma, CT, **154:**307
Optic nerve, lesions, MR, **155:**849
Organ transplantation, cyclosporine treatment, malignant neoplasms in, **154:**271
Osteoarthritis, knee, symptomatic idiopathic (a), **155:**430
Osteochondritis dissecans
knee, MR, **155:**549
staging, MR, **154:**555
Osteochondroma, parasellar, **155:**900
Osteodystrophy, renal, primary oxalosis with, **154:**1334
Osteogenesis imperfecta, child abuse, differentiation from, **154:**1035, **154:**1047 (commentary), **155:**1346(l)
Osteogenic sarcoma, bleomycin-related pulmonary injury in (a), **154:**661
Osteoid osteoma
intracapsular, proximal femur, CT (p), **154:**1241
preoperative CT, **155:**883
Osteomyelitis, cervical, IV heroin use and, **155:**333
Osteonecrosis, spontaneous, knee, MR, **154:**331
Osteopenia, insufficiency fracture of sternum and, **154:**1025
Osteoporosis
broad ultrasound attenuation, **155:**825
postmenopausal
fluoride treatment effects (a), **155:**427
intermittent cyclical etidronate therapy (a), **155:**661
intermittent cyclical etidronate treatment (a), **155:**1349
women with eating disorders (a), **155:**204
Osteosarcoma
extraskeletal (a), **155:**1144
parosteal, humerus, CT, **154:**1331
retroperitoneal extraskeletal (l), **155:**1139
Ovary
benign cystic teratoma (p), **155:**317
cancer, chemotherapy for, leukemia after (a), **154:**1129
herniation of cyst through inguinal canal, CT (l), **154:**202
surgical lateral transposition, CT, **154:**119
teratomas, sonographic appearance, **154:**139

P

Pancreas
function, neonatal screening for cystic fibrosis (a), **154:**1353
sonographic changes, renal failure (a), **154:**210
transplantation, acute venous thrombosis after, sonography and scintigraphy, **154:**529
vein, thrombosis, CT in oncology patients, **155:**291
Paget disease, skull, syringomyelia associated with, **155:**881
Pancreas
Clonorchis sinensis, **155:**1001
fat obliteration on CT, carcinoma and, **155:**991
insulinoma, low-density CT, **155:**995
pseudonodule, prepancreatic fat and (l), **155:**1345
transplant, imaging, **155:**13
transplantation, fluid and urine leakage after, CT and cystography, **155:**997
Pancreatitis, chronic, endoscopic biliary drainage (a), **155:**429
Pancuronium bromide, immobilization of fetus during MR, detection of abdominal mass, **154:**1049
Panniculitis, mesenteric, CT, **154:**1328
Paraganglioma
extraadrenal retroperitoneal, CT, **155:**1247
malignant extraadrenal retroperitoneal, CT, **154:**1329
Parasellar epidermoid, CT, **154:**1340
Parosteal osteogenic sarcoma, cranial bones, **155:**113
Parotid gland, tumors, anti-CEA immunoscintigraphy, **154:**1259
Patella, bilateral dorsal defect (l), **154:**1347
Pediatric radiology
AIDS, pneumatosis intestinalis in, **155:**133
ano-rectal strictures, balloon dilatation of, infant (a), **154:**211
anoxic/ischemic cerebral injury, CT, reversal sign on, **154:**361

- biliary atresia and choledochal cyst, sonographic localization and guided removal, **155:**1277
- biomedical research, informed consent (a), **154:**1132
- blunt abdominal trauma, hematuria in, **154:**569
- bone imaging (b), **154:**1250
- bowel obstruction, infant with AIDS, **154:**803
- *Campylobacter pylori*, gastrointestinal disease related to (a), **154:**427
- cerebral palsy, preterm infants (a), **155:**431
- childhood risk factors, adult high blood pressure (a), **154:**209
- choledochal cyst, biliary atresia and, neonate, **155:**1273
- colonoscopy (a), **154:**429
- congenital diaphragmatic defects (a), **155:**431
- congenital rubella syndrome, calcific epiphyseal stippling and peroxisomal dysfunction (a), **154:**1132
- contrast media reactions
  - corticosteroid pretreatment for, **155:**357
  - effects (a), **155:**205
- coronary angiography, pulmonary atresia, hypoplastic right ventricle, and ventriculocoronary communications, **154:**789
- craniosynostosis, enlarged parietal foramina and, American Indian child (l), **154:**658
- cystic fibrosis research (a), **155:**204
- cystoscopy, double collecting system, **155:**561
- diastematomyelia, cervical and basicranial, **154:**806
- endoscopy, upper gastrointestinal tract (a), **154:**429
- Ewing sarcoma, chemotherapy for, MR, **155:**343
- extracorporeal membrane oxygenation, neonatal (a), **155:**431
- extremity injuries, radiographic assessment (a), **155:**1145
- febrile infant, chest radiographs, **155:**833
- femoral artery, puncture, Doppler flow monitoring of dorsal artery of foot, **155:**131
- gastric hematoma, pneumatosis and, child abuse, **155:**1283
- hepatic artery thrombosis, after liver transplantation, duplex Doppler studies, **154:**573
- hip, infant, sonography, **155:**837
- HIV transmission (a), **154:**1357
- Hodgkin disease, CT and lymphography comparison with laparotomy, **154:**1251
- holoprosencephaly, sonography of fetal facial features, **154:**143
- hyaline membrane disease, mechanical breathing, surfactant therapy effects, infant (a), **154:**1132
- hydronephrosis, prenatal detection, **155:**125
- incipient lingual cortical mandibular defect, American Indian child (l), **154:**658
- infant feeding formula, MR (a), **155:**205
- intraventricular hemorrhage
  - indomethacin and (a), **154:**210
  - preterm infants (a), **154:**665
- laryngeal and tracheobronchial obstruction, ultrafast CT of, **154:**345
- Leigh syndrome, MR correlation with biochemical defect, **154:**1269
- leukemia, MR of knee region in (a), **155:**205
- liver transplantation, MR and sonography, **155:**351
- long-term diuretic therapy, bronchopulmonary dysplasia (a), **154:**210
- lymphoma, renal involvement, CT and sonography, **155:**347
- lymphoreticular cancer, contrast reactions, corticosteroid pretreatment for, **155:**357
- magnetic catheter, removal of foreign bodies, **154:**149
- mechanical ventilation effects, cerebral blood flow, newborn (a), **154:**211
- microalbuminuria, angiotensin converting enzyme inhibitor therapy (a), **155:**1146
- moderate head trauma, intracranial injury after (a), **154:**428
- necrotizing enterocolitis, neonates, portable abdominal radiographs in, **154:**779
- neonatal brain tumors, **155:**587
- neural tube defects, newborn (a), **155:**666
- neuroimaging (b), **155:**142
- ovarian teratomas, prepubertal and postpubertal, **154:**139
- pneumatosis intestinalis, AIDS and, **155:**133
- polycystic kidney disease (a), **154:**907
- pulmonary infiltrates, cancer patients, flexible bronchoscopy in (a), **154:**209
- recurrent febrile seizures (a), **155:**431
- renal abnormalities, boys with urinary tract infection (a), **154:**907
- renal transplants, Doppler evaluation of, **154:**785
- respiratory syncytial virus, extracorporeal membrane oxygenation for (a), **154:**1358
- sinus radiographs (a), **155:**430
- technologists necessary to image patients, **155:**187
- thalamic hemorrhage, with intraventricular hemorrhage, full-term newborn (a), **155:**665
- thyroiditis, acute suppurative, pyriform sinus fistula and, **155:**845
- toxic shock syndrome (a), **155:**431
- transcatheter closure, patient ductus arteriosus (a), **154:**209
- untreated bacteriuria, renal scarring and, girls (a), **154:**907
- urinary tract imaging (b), **154:**142
- urinary tract infection, N-acetyl-β-glucosaminidase in (a), **155:**1145
- vasoparalysis, brain damage and, asphyxiated term neonates (a), **155:**1146
- ventilation, liquid, preterm neonates (a), **155:**1146

Pelvis
- fracture, classification, **155:**1169
- mass, solid, distinguished from leiomyoma, MR, **154:**295
- pain, cancer patients, scintigraphy, CT, and MR, **155:**85

Pentazocine, myopathy induced by, imaging in, **154:**343

Percutaneous transthoracic intervention, hemorrhage due to, **154:**47

Pericaliceal varices, due to nutcracker phenomenon, **154:**305

Perineal hernia, posterior, CT, **154:**761

Periostitis, chondroblastoma, **154:**309

Peripheral arterial disease, lower extremity, color-assisted duplex sonography, **155:**1085

Peritoneum, papillary mesothelioma, **155:**1245

Periventricular leukomalacia, sonography in, **155:**595

Phlegmasia cerulea dolens, after placement of bird's nest vena cava filter, **154:**1105

Picture archiving and communications systems
- implementation, delayed access to diagnostic imaging and, **155:**613
- Japan, **154:**415

Pineal gland, tumors, MR, **155:**143

PIOPED criteria, diagnosis of pulmonary emboli, lung scans, **154:**975

Pituitary adenoma, anterior communicating artery aneurysm and (l), **155:**200

Pneumatocele, traumatic, **154:**1323

Pneumatosis, gastric hematoma and, child abuse, **155:**1283

Pneumatosis intestinalis, AIDS and, children, **155:**133

Pneumocystis carinii
- AIDS-related infection, visceral and nodal calcification, **154:**27
- extrapulmonary, AIDS patient, **155:**76
- risk, HIV type 1 men (a), **154:**1354

Pneumonia
- bacterial, thoracic radiation therapy (l), **155:**1135
- bronchiolitis obliterans organizing, **154:**983

Pneumonitis, usual interstitial, lymph node enlargement on CT scans, **154:**251

Pneumoperitoneum
- acute abdomen, sonography, **154:**107
- catamenial pneumothorax with, **155:**29

Pneumothorax
- after CT-guided pulmonary interventional procedures, CT and chest radiographs, **154:**45
- catamenial, pneumoperitoneum with, **155:**29
- complication of needle biopsy, treatment for, **155:**31
- idiopathic spontaneous, CT (a), **155:**1350
- interlobar (l), **155:**1135

POEMS syndrome, plasma cell dyscrasia, **155:**339

Polyarthritis, chronic, **154:**1332

Popliteal artery, entrapment, MR, **154:**425

Portal vein, pulsatile flow, duplex Doppler sonography, **155:**785

Portal venous system, color Doppler sonography, **155:**517

Portosystemic shunts, color Doppler sonography, **154:**393

Positron emission tomography, clinical research and diagnosis (b), **154:**1024

Posttraumatic cerebral infarction, CT, **154:**1293

Pregnancy
- ectopic, endovaginal vs transabdominal sonography, **155:**307
- second trimester, nuchal fetal cystic hygroma, spontaneous resolution of (l), **154:**903
- transvaginal sonography in (l), **154:**656

Proctography, evacuation (a), **155:**429

Prostate
- cancer, invasion of seminal vesicles, transrectal sonography, **155:**811
- carcinoma, transrectal sonography, **155:**1015
- comedocarcinoma, sonography, **155:**303
- cysts, MR, **155:**1021
- endorectal sonography, **154:**691
- hypoechoic area, sonographically guided biopsy (a), **154:**1357
- midline cyst (l), **155:**656
- positional hypoechoic pseudolesions, transrectal sonography (l), **155:**1138

Prostatism, self-retaining intraurethral stent, **154:**111

Prune belly syndrome, comprehensive approach (a), **154:**209

Pulmonary artery, hypertension, right ventricular performance with, imaging techniques (a), **155:**1146

Pulmonary embolism
- natural course of (a), **155:**202
- single perfusion defect (a), **155:**204

Pulmonary sequestration, imaging of, **154:**241

Pyelocaliectasis, Doppler evaluation (l), **155:**196

R

Radiation
- diagnostic medical, exposure (b), **154:**50
- dose
  - estimated, multislice CT studies, fetus, **154:**185
  - film processing and, during mammography, **155:**1189
  - new mammography screen/film combinations, **154:**713
- hypertension and (l), **154:**659
- space activities (b), **154:**870
- nonionizing, protection (b), **155:**1232

Radiation therapy, thoracic, bacterial pneumonia after (l), **155:**1135

Radiculopathy, cervical, MR, **154:**375

Radiobiology, primer (b), **155:**1202

Radiography
- coloring digital, bone (l), **155:**657
- developed by new ultrarapid film processing system, **154:**1107
- exposure (b), **154:**862
- measurements (b), **154:**744

- plain chest, esophageal disease (p), **155:**729
- principles for technologists (b), **155:**610
- retained firearm projectiles, **154:**471

Radiography, technique
- chest
  - analysis (b), **154:**486
  - febrile infant, **155:**833
  - interpretation, clinical history effects, **154:**709
  - newer methods (a), **154:**1133
  - pulmonary blastomycosis, **154:**1177
  - sarcoidosis during corticosteroid withdrawal, **154:**481
- digital, broncholithiasis in bronchogenic carcinoma (l), **155:**1344
- foot, measurement (b), **155:**816
- GI complications, cytosine-arabinoside chemotherapy, **154:**95
- malpositioning of endotracheal tubes, esophagus, **154:**23
- portable abdominal, necrotizing enterocolitis in infants, **154:**779

Radiologic technologists, medical techniques and patient care (b), **154:**476

Radiologists
- antitrust principles, **155:**1331
- attitude toward practice, **154:**867
- implications of technology assessment (commentary), **154:**652
- medical decision making, **154:**1149
- physician referrals to, **155:**1327

Radiology
- administration (b), **154:**644
- diagnostic
  - manual for (b), **154:**286
  - proportions in, **154:**477
  - quality assurance (b), **155:**404
  - quality improvement (perspective), **154:**1117
- diagnostic (b), **154:**1164
- gastrointestinal (b), **154:**1198
- interventional, emergency (b), **154:**1028
- journalism, Melvin M. Figley Fellowship, **154:**470
- literature, evaluation of, **154:**17
- occupational chest diseases (b), **154:**64
- oral and pharyngeal phases of swallowing, **154:**953, **154:**965
- perception of images (l), **154:**1121
- statistical terminology, specifics of (l), **154:**1121
- subspecialization in, **155:**451

Radiology, technique
- cervical pedicle, congenital absence of, **155:**1037
- cervical spine, trauma patients, **155:**465
- dento maxillo facial (b), **154:**584
- diagnostic X-ray department, quality assurance (b), **154:**32
- dysphagia investigation, **154:**1157
- esophageal motility, **155:**983
- gunshot wounds, **155:**691
- hepatobiliary (b), **155:**506
- lung cancer diagnosis, pitfalls, **154:**1165

Radiology department, planning of (perspective), **154:**635

Radiology training
- fellowship training for all, **155:**191
- manpower equation (perspective), **154:**1111

Radionuclides
- evaluation of renal function (b), **154:**114
- lung and, **155:**455

Recanalization, laser-assisted thermal angioplasty, confirmation by intravascular sonography, **155:**1100

Referrals, from physicians to radiologists, **155:**1327

Renal artery, endovascular stented (l), **154:**902

Renal cell carcinoma
- inferior vena caval invasion by (a), **155:**204
- regional lymph node enlargement and (a), **155:**1351

Respiratory distress syndrome, adult, depressed bronchoalveolar urokinase activity (a), **155:**427

Reversal sign, CT and MR, anoxic/ischemic cerebral injury, children, **154:**361

Rhinovirus, transmission, radiologist and dictating machine in (l), **155:**1134

Roentgen diagnosis, index for (l), **154:**659

Rogers, Paul L. (m), 154:118

Rotator cuff
- incomplete tear (a), **155:**664
- tears, sonography, **154:**121

S

Sacrum, lesions, MR (p), **154:**771

Salpingography, selective osteal, fallopian tube obstruction, **154:**735

Samarium-153 EDTMP, pharmacokinetics of, metastatic cancer (a), **154:**665

Saphenous vein, arterial bypass graft stenosis, color Doppler sonography, **154:**857

Sarcoidosis
- central nervous system, MR, **155:**1293
- during corticosteroid withdrawal, chest radiographic findings in, **154:**481
- endobronchial, upper lobe collapse (l), **154:**897
- osseous, **154:**1332

Scintigraphy
- acute venous thrombosis, after pancreas transplantation, **154:**529
- cancer patients, pelvic pain, **155:**85
- gallium, CT comparison, synthetic vascular graft infection, **154:**405
- inflammation (b), **154:**796
- postsurgical complications, ileoanal pouches, **154:**73
- shoulder pain, caused by interleukin-2, **154:**327

Sclerotherapy, small drainage catheter and, malignant pleural effusions (a), **154:**662

Scoliosis, radiographs (a), **155:**430

Scrotum
- blunt trauma, ultrasound and (a), **154:**665
- skin temperature after MR, **154:**1229

Seizures
- febrile, predictors of (a), **155:**431
- temporal lobe, MRI, **155:**581

Seminal vesicles
- cysts, MRI, **155:**1021
- invasion by prostatic cancer, transrectal sonography, **155:**811

Septum pellucidum, hydrocephalic infant, sonography (a), **155:**904

Sequential images, method of identification (l), **154:**426

Sigmoidoscopy
- double-contrast barium enema and (a), **154:**906
- flexible, vs colonoscopy (a), **155:**202

Single photon emission CT, ^{99m}Tc-RBC, hemangiomatosis (l), **154:**423
- cerebral (b), **155:**158

Sinus, inferior petrosal, sampling, diagnosis of acromegaly, **154:**1075

Sinus disease
- abnormal radiographs, children (a), **155:**430
- CT and plain radiographs (l), **155:**425

Skull, tuberculosis (l), **155:**1141

Society for Pediatric Radiology, 1990 annual meeting, **154:**671, **155:**565

Society of Computed Body Tomography, 13th annual course, April 1990, **155:**413

Society of Gastrointestinal Radiologists, 19th annual meeting, **154:**1311

Society of Uroradiology
- abstracts from 1989 meeting, **154:**191
- 1989 scientific session, **154:**11
- survey of members, current status of adult uroradiology, **154:**301

Soft tissue
- foreign bodies, sonographic localization and guided removal, **155:**1277
- masses
  - benign and malignant differentiation, MR, **155:**1251
  - hand and wrist, MR, **154:**323
- tumor and tumorlike lesions, MR, **155:**817
- tumors, foot, MR, **155:**1025

Sonography
- biopsy guided by, **154:**1
  - needle placement for, **154:**847
- color Doppler
  - carotid artery disease, **154:**1061
  - hepatic artery and portal venous system, **155:**517
  - liver tumor, **154:**509
  - peripheral arterial disease, lower extremity, **155:**1085
  - physics, instrumentation, and clinical application (b), **154:**398
  - portosystemic shunts, **154:**393
  - saphenous vein arterial bypass graft stenosis, **154:**857
  - standards for (l), **154:**1348
  - upper-extremity deep venous thrombosis, **154:**399
- Doppler
  - black-and-white color (l), **155:**198
  - hepatic venocclusive disease, **154:**721
  - hepatocellular carcinoma and other lesions (a), **154:**664
  - renal transplantation in children, **154:**785
- duplex color Doppler
  - dysfunction in renal allografts, **155:**536 (commentary), **155:**538 (commentary)
  - pseudoaneurysm of epigastric artery, **155:**529
- duplex Doppler
  - applications (b), **155:**1090
  - carotid artery, **155:**1091
  - hepatic artery thrombosis after liver transplantation, children, **154:**573
  - intrarenal arteriovenous fistula and pseudoaneurysm (l), **154:**424
  - normal native kidneys with urinary tract obstruction (a), **154:**429
  - renal allografts, **155:**295
- equipment (b), **155:**124
- interventional (b), **155:**510
- muscles and tendons (b), **154:**124
- neonate, adrenal (a), **155:**432

Sonography, abdomen
- abdominal ectopic pregnancy (l), **155:**197
- acute appendicitis, perforation in, **154:**275
- acute (b), **154:**982
- biliary obstruction, surgically created biliary-enteric anastomosis, **155:**789
- cecum and ascending colon, diverticulitis, **155:**283
- combined systemic and portal venous gas, **154:**1219
- duplex Doppler, pulsatile portal vein flow, **155:**785
- endoscopic
  - colon and rectal disease (a), **155:**430
  - pancreatic tumors (a), **155:**430
  - smooth muscle tumors (a), **155:**1351
- endovaginal vs transabdominal, ectopic pregnancy diagnosis, **155:**307
- gallbladder contractility, spinal cord injuries, **154:**521
- gastrointestinal lymphoma, **155:**795
- hepato-biliary and pancreatic surgery (b), **155:**246
- melanoma metastases, liver, gallbladder, and spleen (a), **154:**211
- oriental cholangiohepatitis, **155:**511
- pneumoperitoneum, **154:**107

Sonography, adrenal gland, current status, **154:**927

Sonography, ankle, Achilles tendon injury, **155:**1031

Sonography, bone
- broad ultrasound attenuation, osteoporosis, **155:**825
- limb lengthening, Ilizarov procedures, **154:**125

Sonography, colon, acute diverticulitis, **154:**1199
Sonography, cranium
- acute suppurative thyroiditis, piriform sinus fistula and, **155:**845
- intracranial hemorrhage, periventricular leukomalacia and, **155:**595
- septum pellucidum (a), **155:**904

Sonography, eye, coloboma, **154:**391
Sonography, fetus
- alobar and semilobar holoprosencephaly, **154:**143
- femur length (a), **154:**665
- growth standards, racial differences (a), **154:**1358
- monochorionic twinning, **154:**459
- review (b), **155:**316
- spina bifida (l), **155:**1347
- transplacental genetic amniocentesis, intra-amniotic hemorrhage after (a), **155:**1351

Sonography, hip
- dynamic, infant, **155:**837
- lower-extremity venous thrombosis, acute fractures, **154:**851

Sonography, intrauterine, fetal growth, discordant twin gestations (a), **155:**1146
Sonography, kidney
- crossed renal ectopia without fusion (l), **154:**657
- intrarenal arterial Doppler, nonobstructive renal disease, **154:**1223
- long-term dialysis patients (l), **154:**1125
- lymphoma and, children, **155:**347
- transplant rejection, **155:**531, **155:**536 (commentary), **155:**538 (commentary)

Sonography, liver
- cirrhosis, ultrasonographic signs (a), **155:**666
- extramedullary hematopoiesis (l), **154:**900
- focal lesions, cirrhosis (a), **155:**429
- hemangiomatosis (l), **154:**423
- inflammatory pseudotumor (l), **154:**201
- portal vasculature, diagnosis of portal hypertension (a), **154:**908
- transplantation, children, **155:**351
- tumor imaging, **155:**473

Sonography, lymph node
  - abnormal, **155:**1241
  - metastases, carotid artery and jugular vein, **154:**411

Sonography, musculoskeletal, applications, **155:**237
Sonography, pancreas
- after transplantation, acute venous thrombosis, **154:**529
- changes in chronic renal failure (a), **154:**210

Sonography, pelvis
- clinical imaging (b), **154:**988
- endovaginal, draining pelvic fluid collections, **154:**849
- infertility (b), **154:**544
- ovarian teratomas, prepubertal and postpubertal, **154:**139
- threatened abortion, subchorionic hemorrhage in, **154:**535

Sonography, penis, vasculogenic erectile impotence (a), **154:**907
Sonography, prostate
- endorectal, **154:**691
- hypoechoic area, sonographically guided biopsy (a), **154:**1357

Sonography, scrotum, Müllerian duct cyst and calculus, epididymitis associated with, **155:**91
Sonography, shoulder, rotator cuff tears, **154:**121
Sonography, soft tissue, foreign bodies, localization and guided removal, **155:**1277
Sonography, spine
- intraoperative
  - cervical cord injury, **155:**603
  - lumbar disk herniation and canal stenosis, **154:**821
- neural tube defects (a), **155:**666

Sonography, thorax
- intravascular, peripheral recanalization by laser-assisted thermal angioplasty, **155:**1100
- percutaneous needle biopsy, lesions, **154:**1181
- subclavian vein, percutaneous placement of Hickman catheter, **155:**1097

Sonography, thyroid, hyperparathyroidism, sonographically guided percutaneous injection of ethanol, **154:**1087
Sonography, transabdominal, gynecologic disease (a), **154:**1133
Sonography, transperineal, assessment of vaginal atresia, **154:**545
Sonography, transrectal
- comedocarcinoma, prostate, **155:**303
- prostate, positional hypoechoic pseudolesions (l), **155:**1138
- prostate carcinoma, **155:**1015
  - invasion of seminal vesicles, **155:**811

Sonography, transvaginal
- early pregnancy (l), **154:**656
- gynecologic disease (a), **154:**1133

Spectroscopy
- MR
  - heart, **155:**1
  - radiation fibrosis and recurrent neoplasia, **154:**67
- nuclear MR, malignant tumors (a), **155:**661
- optical, detection of breast cancer and, **155:**43

Sphincter of Oddi, manometry in (a), **154:**1131
Spina bifida, sonography (l), **155:**1347
Spinal cord
- calcification, congenital cytomegalovirus infection (l), **155:**1142
- ischemia, after resection of thoracoabdominal aortic aneurysms, **155:**1303

Spine
- cervical
  - halo vest for fixation, **154:**631
  - intraoperative sonography, **155:**603
  - prevertebral fat stripe, **155:**559
  - pseudoatrophy, MR, **154:**1069
  - radiology in trauma patients, **155:**465
- cervical radiculopathy, MR, **154:**375
- cervical spondylolysis, CT, **154:**751
- cord compression, epidural, vertebral metastasis and (a), **154:**1130
- extradural degenerative disease, Gd-DTPA-enhanced MR, **154:**151
- injuries, gallbladder contractility and, sonography, **154:**521
- lumbar
  - benign lumbar arachnoiditis, **155:**873
  - postoperative, MR, **155:**867
  - traumatic hernia, CT, **154:**757
- lumbar disk herniation, canal stenosis and, intraoperative sonography, **154:**821
- lumbosacral, synovial cysts, MR, **154:**163
- MR diagnostic applications (b), **155:**1076
- pial metastases, MR, **155:**1077
- tears of anulus fibrosus, Gd-DTPA-enhanced MR, **154:**159

Spin-echo techniques, combined gradient and, variable flip angle imaging and fat suppression in (a), **155:**666
Splanchnic arteries, embolization, coaxial catheter and steerable guidewire, **155:**405
Spleen
- anomalies, imaging (p), **155:**805
- epidermoid cyst, familial, **155:**1233
- hemangiomatosis, embolization and splenectomy treatment of, **155:**1235
- hydatid disease, **154:**525
- MRI, iron oxide-enhanced, **155:**943

Splenosis, subcutaneous (l), **154:**655
Sports injuries, imaging (b), **154:**342
***Staphylococcus aureus*,** diffuse centrilobular lesions caused by (l), **155:**652
Sterility, MR heating of scrotum and, **154:**1229
Sternoclavicular joint, spontaneous atraumatic anterior subluxation of (a), **154:**428
Sternum, insufficiency fracture, osteopenia and, **154:**1025
Stopper fragments, technique for reduction (l), **155:**659
Subacute necrotizing encephalomyelopathy, *see* Leigh syndrome
Subtalar arthrorisis, CT, **154:**559
Swallowing
- disorders, C-arm fluoroscope use in, **155:**986
- oral and pharyngeal phases, physiology and radiology, **154:**953, **154:**965
- oropharyngeal, deglutitive glottic closure with (a), **155:**663
- upper esophageal sphincter opening and modulation during (a), **154:**663

Syringomyelia, Paget disease of the skull and, **155:**881

T

Talus, dome of, osteochondral fractures (a), **154:**208
Tarsal tunnel, MR, **155:**323
Technology assessment
- implications for the radiologist, **154:**652 (commentary)
- professional organizations and, **154:**647

Temporomandibular joint
- arthrography, **155:**105
- degeneration, facial skeleton remodeling, **155:**373
- diagnostic imaging, **154:**319, **155:**895(l)
- MR, **154:**1245

Tenography, current role of, **154:**129
Testes
- infarcted undescended, appearing as calcified abdominal mass, **155:**547
- seminomatous and nonseminomatous tumors, MR, **154:**539

Tetralogy of Fallot, pulmonary atresia with, **154:**1319
Thiazide, diuretic agent, hip fracture and (a), **154:**1353
Thorax
- blunt chest trauma, CT (p), **154:**55
- radiography
  - clinical history and accuracy of interpretation (l), **155:**1342
  - left main bronchus on (l), **155:**1343

Thromboembolic disease, pulmonary nuclear medicine (a), **154:**907
Thrombosis
- aortic, neonatal, tissue plasminogen activator and (a), **155:**904
- deep venous
  - extremities, MR (l), **155:**897
  - fracture of pelvis and (a), **155:**664
  - upper-extremity, color Doppler sonography, **154:**399
- hepatic artery, after liver transplantation, duplex Doppler studies in children, **154:**573
- mesenteric venous, CT (l), **154:**425
- proximal venous, hip replacement, ultrasound scanning (a), **155:**1351
- transcatheter, leaking saccular aneurysm, **154:**1097
- venous
  - after pancreas transplantation, sonography and scintigraphy, **154:**529
  - femoropopliteal, MRI, **154:**175
  - lower-extremity, compression sonography, **154:**851

Thymus
- irradiation, infancy, breast cancer after (a), **154:**905
- masses, MR (p), **155:**495

Thyroid gland
- anaplastic carcinoma, CT, **154:**1079
- metastatic anaplastic carcinoma, right heart ventricle (l), **155:**1136
- nodules, imaging comparison (a), **155:**665

Thyroiditis, acute suppurative, piriform sinus fistula and, **155:**845
Tibia vara, critical review (a), **154:**208
Tolosa-Hunt syndrome, MR, **154:**167
Trachea, rupture (l), **154:**1122
Transitional cell carcinoma
  bladder, cavitary pulmonary metastases in, **154:**493
  pelvicalices and ureter, **155:**713
Trauma, cervical spine, radiology in, **155:**465
Trichilemmal cyst, scalp, MR (l), **154:**423
Trisegmentectomy, right, percutaneous biliary drainage after (l), **154:**656
Tuberculosis
  ileocecal, CT and radiologic evaluation, **154:**499
  pulmonary, mediastinal fibrosis in, dysphagia and, **154:**61
  reactivation, after lung transplantation, **154:**495
  skull (l), **155:**1141
  treatment for, breast cancer after (a), **154:**905
  upper lobe, adult (a), **154:**1355
Turner syndrome, review (b), **155:**350

U

Ultrarapid film processing system, radiographs developed by, **154:**1107
Ulcerative colitis, dysplasia and cancer complicating (a), **155:**203
Ureter
  calculi, opaque presacral oblique plain radiographs, **155:**89
  left retrocaval, left inferior vena cava and, **155:**545
  transitional cell carcinoma, **155:**713
Ureteroileal stricture, metallic self-expandable stenting of (l), **155:**422
Urethra
  obstruction, self-retaining intraurethral stent, **154:**111
  stricture, sonourethrography and balloon dilatation (l), **155:**423
Urinary tract
  cancer, home screening with hematuria dipsticks (a), **154:**663
  imaging, pediatric (b), **154:**142
  infection
    boys, renal abnormalities and (a), **154:**907
    imaging (l), **154:**201
    vesicoureteral reflux relations (a), **155:**903
  obstruction, normal native kidneys with, duplex sonography evaluation (a), **154:**429
  upper, fungal bezoars of (a), **155:**203
Urography, clinical (b), **154:**1222
Urologic pathology, clinical and radiologic correlations (b), **154:**1100
Uroradiology
  adult, current status, **154:**301
  genitourinary radiology (b), **155:**1020
Uterus
  lipomatous tumors, sonography, CT, and MR (a), **155:**1147
  perforation, simulating urachal carcinoma, CT, **154:**741

V

Vaginal atresia, assessment, transperineal sonography, **154:**545
Vasoparalysis, brain damage and, asphyxiated term neonates (a), **155:**1146
Vena cava
  Amplatz filter, **155:**177
  bird's nest filter, phlegmasia cerulea dolens after, **154:**1105
  Greenfield filter, titanium, **155:**1103
  left inferior, left retrocaval ureter associated with, **155:**545
Venacavography, renal carcinoma, extending to renal vein and inferior vena cava (a), **154:**428
Ventriculoperitoneal shunt, intrahepatic abscess as a complication of (l), **155:**894
Videofluoroscopy
  coronal radiographs and, temporomandibular joint arthrography, **155:**105
  speech, cleft palate (b), **154:**1156
Videotape reviews
  MR of the foot and ankle, **154:**776
  MR of the sella and para-sella region, **154:**384
  RSNA today, vol. 3, no. 2, **154:**54
  RSNA today, vol. 3, no. 3, **154:**94
  RSNA today, vol. 3, no. 4, **154:**964
  RSNA today, vol. 3 special edition, **154:**300
  RSNA today, vol. 4, no. 1, **155:**1266
Villonodular synovitis, pigmented, knee, radiologic findings (a), **154:**664
Visceroatrial situs, abnormal (p), **154:**797
von Hippel-Lindau disease
  CT, **154:**1326
  islet cell tumors in, **155:**501
  radiologic screening (a), **154:**211

W

Wegener's granulomatosis, pulmonary (a), **155:**428
Wernicke-Korsakoff, encephalopathy, MR, **155:**1309, **155:**1315 (commentary)
Whipple disease, mediastinum, **154:**1187
Whipple procedure, recurrence of tumor, CT after, **154:**1011
White matter necrosis, very low birth weight infants (a), **155:**903
Wounds, gunshot, bullet, ballistics, and mechanisms of injury, **155:**685, **155:**691

Y

Yeates, Andrew Eccles (m), **154:**1284

Z

Zollinger-Ellison syndrome, reflux esophagitis in (a), **154:**1131

TIME TO RENEW?

To ensure uninterrupted service, please renew your journal subscription two months prior to the expiration date of your current subscription. To avoid renewal notices and price increases, consider a multiyear subscription. Current rates are available for up to three years.

For assistance with your renewal,
call TOLL-FREE:
1-800-638-6423
(from anywhere in the U.S.)
Or write:
Subscription Fulfillment Department
428 East Preston Street
Baltimore, MD 21202
Williams & Wilkins
at your service.

The First Century
1890-1990

ONCOLOGIC RADIOLOGY AND BREAST IMAGING

Roswell Park Cancer Institute is seeking Board certified radiologists with special interests in oncologic radiology, CT/MRI, breast imaging and angiography/interventional.

The modernization of the entire Radiology and Nuclear Medicine Departments includes a new multidisciplinary breast imaging center and a new magnetic resonance imaging center.

At this renowned comprehensive cancer center, currently entering a period of renewed growth, opportunity for research and academic activity is outstanding.

A faculty appointment will be at the School of Medicine and Biomedical Sciences, SUNY at Buffalo, according to the level of professional qualifications.

Please send curriculum vitae to:

Andrew A. Gage, M.D.
Deputy Institute Director
Roswell Park Cancer Institute
Elm and Carlton Streets
Buffalo, NY 14263.

Affirmative Action/Equal Opportunity Employer.

Get The Total Picture...

With The Only Text That Directly Describes And Correlates MR and CT Of The Head And Spine

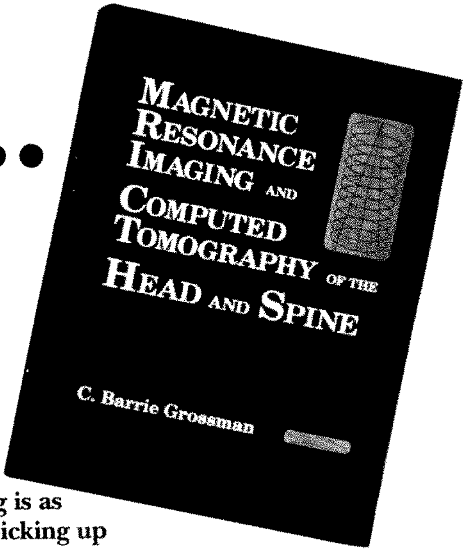
MAGNETIC RESONANCE IMAGING AND COMPUTED TOMOGRAPHY OF THE HEAD AND SPINE
C. Barrie Grossman

Featuring Full Coverage of Head and Spine Imaging in Both Adults and Children

This well-written and extensively illustrated text gives you a full understanding of these "hi-tech" methodologies, the indications for their use, and the important new techniques that lead to the best possible results. You get thorough coverage of both head and spine imaging along with full discussions of the most advanced techniques using state-of-the-art equipment.

Order today and see how this excellent text can enhance your practice.
1989/488 pages/882 illustrations/3768-4

Ordering is as easy as picking up your phone:
In the U.S. just dial toll free 1-800-638-0672.
Or fax your order to 1-800-447-8438. When calling please refer toorder #98562-0.
1 Year approval for this book! (US only)

Williams & Wilkins
428 East Preston Street,
Baltimore, Maryland 21202

Printed in the US
GROSSMAD
98562-0 09/90

New look.
New shape.

GoLYTELY®

PEG-3350 and Electrolytes for Oral Solution

NDC #52268-0100-01
GoLYTELY®
PEG – 3350 and Electrolytes
for Oral Solution
When reconstituted with water to a volume of 4 liters, this solution contains 125 mmol/L sodium, 10 mmol/L potassium, 40 mmol/L sulfate, 20 mmol/L bicarbonate, 35 mmol/L chloride, and 17.6 mmol/L polyethylene glycol 3350
Each disposable jug contains, in powdered form: polyethylene glycol 236 g, sodium sulfate (anhydrous) 22.74 g, sodium bicarbonate 6.74 g, sodium chloride 5.86 g, potassium chloride 2.97 g
CAUTION Federal law prohibits dispensing without prescription
LOT NO / EXPIRES } SEE BOTTOM
LABORATORIES INC
Braintree
Braintree, MA 02184
© 1985

The name that started a revolution now comes in a narrow, stackable container.

Now GoLYTELY takes up less storage space and less space in your patient's refrigerator.

More convenient for
- Patients
- Pharmacists
- Physicians
- Nurses

New look.
New shape.
GoLYTELY.

Made by Lyne Laboratories, Stoughton, MA 02072, for BRAINTREE LABORATORIES, INC., P.O. Box 361, Braintree, MA 02184.

LABORATORIES · INC
Braintree

© 1989 BRAINTREE LABORATORIES, INC.
TRE-1039

Volume 155 American Journal of Roentgenology December 1990

1990 ARRS PRESIDENT'S AWARD

1161 **MR receptor imaging: ultrasmall iron oxide particles targeted to asialoglycoprotein receptors.** *Weissleder R, Reimer P, Lee AS, Wittenberg J, Brady TJ*

REVIEW ARTICLE

1169 **Fracture of the pelvis: current concepts of classification.** *Young JWR, Resnik CS*

CHEST RADIOLOGY

1177 **Assessing the patency of mediastinal and thoracic inlet veins: value of MR imaging.** *Hansen ME, Spritzer CE, Sostman HD*

1183 **Case report. Misdiagnosis or missed diagnosis? Thoracic actinomycosis and carcinoma on sequential CT-guided lung biopsies.** *Macaulay SE, vanSonnenberg E, Casola G, Harrell JH II*

1185 **Case report. Peripheral carcinoid tumor of the lung: CT diagnosis.** *Davis SD, Zirn JR, Govoni AF, Yankelevitz DF*

BREAST RADIOLOGY

1189 **Value of increasing film processing time to reduce radiation dose during mammography.** *Skubic SE, Yagan R, Oravec D, Shah Z*

1195 **Perspective. Nonpalpable, probably benign breast lesions: follow-up strategies after initial detection on mammography.** *Adler DD, Helvie MA, Ikeda DM*

1203 **Case report. Mammographic appearance of the retained Dacron cuff of a Hickman catheter.** *Beyer GA, Thorsen MK, Shaffer KA, Walker AP*

GASTROINTESTINAL RADIOLOGY

1205 **Pictorial essay. Gastrointestinal lipomas: a radiologic and pathologic review.** *Taylor AJ, Stewart ET, Dodds WJ*

1211 **Piezoelectric biliary lithotripsy: an in vitro study of factors affecting gallstone fragmentation.** *Schulte SJ, Baron RL*

1217 **Nonaspiration fine-needle cytology of the liver: a new technique for obtaining diagnostic samples.** *Fagelman D, Chess Q*

1221 **Percutaneous ethanol injection therapy of hepatocellular carcinoma: analysis of 77 patients.** *Shiina S, Tagawa K, Unuma T, et al.*

1227 **Regenerating nodules in hepatic cirrhosis: MR findings with pathologic correlation.** *Murakami T, Kuroda C, Marukawa T, et al.*

1233 **Case report. Familial splenic epidermoid cyst.** *Ragozzino MW, Singletary H, Patrick R*

1235 **Case report. Hemangiomatosis of the liver and spleen: successful treatment with embolization and splenectomy.** *Tarazov PG, Polysalov VN, Ryzhkov VK*

1237 **Bright pleural effusion and ascites on gradient-echo MR images: a potential source of confusion in vascular MR studies.** *Wallner B, Edelman RR, Finn JP, Mattle HP*

1241 **Sonography of abnormal lymph nodes in vitro: correlation of sonographic and histologic findings.** *Rubaltelli L, Proto E, Salmaso R, Bortoletto P, Candiani F, Cagol P*

1245 **Case report. Well-differentiated papillary mesothelioma of the peritoneum.** *Lovell FA, Cranston PE*

GENITOURINARY RADIOLOGY

1247 **Extraadrenal retroperitoneal paraganglioma: clinical, pathologic, and CT findings.** *Hayes WS, Davidson AJ, Grimley PM, Hartman DS*

MUSCULOSKELETAL RADIOLOGY

1251 **Value of MR imaging in differentiating benign from malignant soft-tissue masses: study of 95 lesions.** *Berquist TH, Ehman RL, King BF, Hodgman CG, Ilstrup DM*

1257 **MR imaging findings in patients with bone-chip allografts.** *Jelinek JS, Kransdorf MJ, Moser RP, Temple HT, Lenhart MK, Berrey BH*

PEDIATRIC RADIOLOGY

1261 **MR imaging of fractures of the growth plate.** *Jaramillo D, Hoffer FA, Shapiro F, Rand F*

1267 **Cloacal exstrophy: radiologic findings in 13 patients.** *Meglin AJ, Balotin RJ, Jelinek JS, Fishman EK, Jeffs RD, Ghaed V*

1273 **Choledochal cyst and biliary atresia in the neonate: imaging findings in five cases.** *Torrisi JM, Haller JO, Velcek FT*

1277 **Localization and guided removal of soft-tissue foreign bodies with sonography.** *Shiels WE II, Babcock DS, Wilson JL, Burch RA*

1283 **Case report. Gastric hematoma and pneumatosis in child abuse.** *Fulcher AS, Narla LD, Brewer WH*

NEURORADIOLOGY

1285 **MR imaging of the normal and abnormal clivus.** *Kimura F, Kim KS, Friedman H, Russell EJ, Breit R*

1293 **Sarcoidosis of the CNS: comparison of unenhanced and enhanced MR images.** *Sherman JL, Stern BJ*

1303 **Spinal cord ischemia after resection of thoracoabdominal aortic aneurysms: MR findings in 24 patients.** *Mawad ME, Rivera V, Crawford S, Ramirez A, Breitbach W*

1309 **Wernicke encephalopathy: MR findings in five patients.** *Gallucci M, Bozzao A, Splendiani A, Masciocchi C, Passariello R*

1315 **Commentary. MR in the diagnosis of Wernicke-Korsakoff syndrome.** *Victor M*

COMPUTER PAGE

1317 **Computer-based learning in radiology: a hypermedia application in CT.** *Hennessey JG, Fishman EK, Kuhlman JE, Ney DR, Magid D*

COMMENTARY

1321 **Europe 1992: Consequences for European health care and radiology.** *Schütte HE*

PERSPECTIVES

1327 **Physician referrals to radiologists.** *Lopiano M, Stolz J, Sunshine J, Fisk T, Leepson E*

1331 **Antitrust principles for radiologists.** *Reuter SR*

OTHER CONTENT

Book and videotape reviews 1176, 1188, 1202, 1220, 1232, 1256, 1266, 1282, 1292, 1302, 1326

1226 **ARRS 1991 resident award papers information**

1308 **Forthcoming articles**

1338 **Recognition of manuscript and book reviewers 1990**

1341 **Letters**

1349 **Review of current literature**

1353 **News**

1357 **American Roentgen Ray Society information**

1358 **Classified advertisements**

1366 **Index, Volumes 154–155**

A9 **Guidelines for authors**

A12 ***AJR* business and subscriber information**

1991 ARRS Meeting: May 5–10, Boston, MA